



**4<sup>th</sup> International Students Science Congress  
Proceedings Book**

**4. Uluslararası Öğrenciler Fen Bilimleri Kongresi  
Bildiriler Kitabı**

**Editor-in-Chief / Sorumlu Editör**

Mehmet Çevik

**Co-editors / Yardımcı Editörler**

Alif Diambu Ngimbi

Furkan Emrem



İzmir Kâtip Çelebi Üniversitesi Yayın No: 17

Bu eserin, İzmir Kâtip Çelebi Üniversitesi Yönetim Kurulu'nun 12.01.2021 tarih ve 2021-02 sayılı toplantısında alınan 4 numaralı kararı uyarınca, elektronik kitap olarak yayımlanmasına karar verilmiştir.

Her hakkı saklıdır.

© İzmir Kâtip Çelebi Üniversitesi Yayınları  
Ocak 2021

Sertifika No: 46629

**Editör : Mehmet ÇEVİK**  
**Yardımcı Editörler : Alif Diambu NGIMBI**  
**Furkan EMREM**

**E-ISBN: 978-605-81050-6-5**

International Students Science Congress ( 4th : İzmir : 2020)

4th International Students Science Congress: Proceedings, 18-19 September 2020 =  
4. Uluslararası Öğrenciler Fen Bilimleri Kongresi: Bildiriler Kitabı, 18-19 Eylül 2020 /  
Sorumlu editör: Mehmet Çevik; Yardımcı editörler: Alif Diambu Ngimbi, Furkan Emrem —  
İzmir : İzmir Kâtip Çelebi Üniversitesi, 2020.

Çevrimiçi ( XIII, 495 Sayfa ; 26 cm.). -- (İzmir Kâtip Çelebi Üniversitesi ; Yayın No: 17)  
ISBN: 978-605-81050-6-5

1. Fen Bilimleri – Kongreler 2. Öğrenciler – Kongreler  
I. Çevik, Mehmet – II. Ngimbi, Alif Diambu – III. Emrem, Furkan

**Adres** : İzmir Kâtip Çelebi Üniversitesi Rektörlüğü, Balatçık Yerleşkesi, 35620 Çiğli  
İzmir, Türkiye

**Telefon** : +90 232 329 3535 / 1255

**E-posta** : ykb@ikc.edu.tr

**Belge-geçer** : +90 232 386 0888

**Web** : ykb.ikc.edu.tr

Eserin hukuki ve etik sorumluluğu yazarlara aittir. Tüm hakları saklıdır. Bu kitabın yayın hakkı İzmir Kâtip Çelebi Üniversitesi'ne aittir. İzinsiz kopyalanamaz ve çoğaltılamaz.

All rights reserved © İzmir Kâtip Çelebi University Press, 2021. No part of this book may be reproduced in any form or by any electronic or mechanical means including information storage systems without permission in writing from the publisher, except by a reviewer who may quote brief passages in a review.

## Preface

Dear Participants, Colleagues, and International Students,

It is a great honor and privilege for us to present the Abstract Book of the 4<sup>th</sup> International Students Science Congress to the authors and participants of the event. We hope that you will find it useful, exciting and inspiring.

In the last three years we organized our congresses in İzmir Kâtip Çelebi University campus in order to bring together young international researchers working in various science areas and this has really motivated all of us. In the same way, we planned the fourth congress on April 17-18 this year. However, due to the global Covid-19 pandemic, we had to postpone the event first; later it became clear that it was not possible to carry out an in-person congress. Therefore, we announced the online congress to be held on September 18-19. This was our first online congress experience, as many others all over the world. The congress was performed over Zoom and live-streamed on YouTube; you may access videos of the sessions on our Youtube channel.

Though it was an online event, we accomplished the fourth congress again with great enthusiasm. About one hundred young researchers from about twenty-five countries gathered for this congress and ninety-two papers were presented in 24 sessions. In addition to the contributed papers, two intriguing invited presentations were given: by Prof. Dr. Çetin Kaya Koç, Dean of Faculty of Engineering of İstinye University, who spoke about Machine Learning with Encrypted Data, and by Prof. Dr. Aydın Akan, the Head of Department of Electrical and Electronics Engineering at İzmir University of Economics, who spoke about Shaping the World as an Engineer and Current Biomedical Applications.

The congress particularly encouraged the interaction of international research students and developing academics with the more established academic community in an informal setting to present and to discuss new and current work. Their contributions helped to make the Congress as outstanding as it has been. The Congress provided a setting for discussing recent developments in a wide variety of topics including Agricultural Engineering, Architecture, Biology and Bioengineering, Chemistry and Chemical Engineering, Civil Engineering, Computer Science and Engineering, Electrical, Electronics and Communication Engineering, Geomatics Engineering, Food Engineering, Geology Engineering, Mechanical Engineering, Mathematics, Materials Science, Metallurgical and Materials Engineering, Nanotechnology, Renewable Energy, Urban and Regional Planning.

We would like to thank all participants for their contributions to the Congress program and for their contributions to these Abstract Proceedings. It is our pleasant duty to acknowledge the support from İzmir Kâtip Çelebi University, Federation of International Student Associations (UDEF) and İzmir International Guest Student Association.

I would like to express my sincere gratitude and appreciation to our organizing committee and all the students who worked voluntarily during the event.

The continuing success of this congress series means that planning can now proceed with confidence for the 5<sup>th</sup> International Students Science Congress to be held in 2021; probably both online and in-person.

We thank all authors, participants, and volunteers for their contributions.

Prof. Dr. Mehmet Çevik  
Congress Chair

## Önsöz

Değerli Katılımcılar, Meslektaşlarım ve Uluslararası Öğrenciler,

4. Uluslararası Öğrenciler Fen Bilimleri Kongresi Bildiri Özetleri Kitabını etkinliğin yazar ve katılımcılarına sunmak bizler için büyük bir onur ve ayrıcalıktır. Bunu yararlı, heyecan ve ilhm verici bulacağınızı umuyoruz.

Son üç yıldır İzmir Kâtip Çelebi Üniversitesi kampüsünde çeşitli bilim dallarında çalışan genç uluslararası araştırmacıları bir araya getirmek amacıyla kongrelerimizi düzenledik ve bu hepimizi gerçekten motive etti. Aynı şekilde bu yıl da 17-18 Nisan'da dördüncü kongreyi planladık. Ancak küresel Covid-19 salgını nedeniyle etkinliğimiz önce ertelemek zorunda kaldık; daha sonra ise yüzyüze kongre yapmanın mümkün olamayacağı anlaşıldı. Bu nedenle kongremizin 18-19 Eylül tarihlerinde çevrimiçi olarak yapılacağını kongreyi duyurduk. Bu, dünyanın her yerindeki diğerleri gibi ilk çevrimiçi kongre deneyimizdi. Kongre Zoom üzerinden yapıldı ve YouTube'da canlı yayınlandı; Youtube kanalımızdan oturumların videolarına ulaşabilirsiniz.

Çevrimiçi bir etkinlik olmasına rağmen dördüncü kongremizi de yine büyük bir istek ve heyecanla gerçekleştirdik. Bu kongre için yirmi beş ülkeden yaklaşık yüz genç araştırmacı bir araya geldi ve 24 oturumda doksan iki bildiri sunuldu. Bildirilere ek olarak, iki davetli konuşmacımız tarafından gerçekten ilgi çekici sunumlar yapıldı: İstinye Üniversitesi Mühendislik Fakültesi Dekanı Prof. Dr. Çetin Kaya Koç Şifrelenmiş Verilerle Makine Öğrenimi hakkında konuştu; İzmir Ekonomi Üniversitesi Elektrik-Elektronik Mühendisliği Bölüm Başkanı Prof. Dr. Aydın Akan ise mühendis dünyayı şekillendirmesi ve güncel biyomedikal uygulamalardan bahsetti.

Kongre, özellikle fen bilimleri alanında eğitimlerine devam eden uluslararası öğrencilerin ve genç akademisyenlerin önlerindeki akademik camia ile etkileşimlerini gayet samimi bir ortam sunarak teşvik ederken, yeni ve güncel çalışmalarını sunmaları ve tartışmaları için de güzel bir fırsat sağlamış oldu. Onların katkıları sayesinde Kongre olabildiğince seçkin ve nitelikli bir düzeye ulaşmış oldu. Kongre, Ziraat Mühendisliği, Mimarlık, Biyoloji ve Biyomühendislik, Kimya ve Kimya Mühendisliği, İnşaat Mühendisliği, Bilgisayar Bilimi ve Mühendisliği, Elektrik, Elektronik ve Haberleşme Mühendisliği, Harita Mühendisliği, Gıda Mühendisliği, Jeoloji Mühendisliği, Makine Mühendisliği, Matematik, Malzeme Bilimi, Metalurji ve Malzeme Mühendisliği, Nanoteknoloji, Yenilenebilir Enerji, Kentsel ve Bölgesel Planlama, vb. çok çeşitli konulardaki son gelişmeleri tartışmak için keyifli bir ortam sağladı.

Tüm katılımcılara kongre programımıza ve dolayısıyla bildiri özetleri kitabımıza yaptıkları katkılardan dolayı teşekkür ederiz. Ayrıca verdikleri destek ile bu kongrenin gerçekleşmesine katkı sağlayan İzmir Kâtip Çelebi Üniversitesi'ne, Uluslararası Öğrenci Dernekleri Federasyonu'na (UDEP) ve ana organizatörümüz İzmir Uluslararası Misafir Öğrenci Derneği'ne teşekkürlerimizi arz ederiz.

Organizasyon komitemize ve etkinlik süresince gönüllü olarak çalışan tüm öğrencilere içten şükran ve takdirlerimi sunuyorum.

Bu kongre dizisinin devam eden başarısı, 2021'de düzenlenmeyi hedeflediğimiz 5. Uluslararası Öğrenciler Fen Bilimleri Kongresi için planlamanın artık güvenle ilerleyebileceği anlamına geliyor; bu kongre muhtemelen hem çevrimiçi hem de yüz yüze olacak.

Katkılarından dolayı tüm yazarlara, katılımcılara ve gönüllülere teşekkür ederiz.

Prof. Dr. Mehmet Çevik  
Kongre Başkanı

## **Organizing Committee / Düzenleme Kurulu**

**Mehmet Çevik**

**Alif Diambu Ngimbi**

**Ahmet Aykaç**

**Faruk Özger**

**Kamil Şirin**

**Furkan Emrem**

**Ahenk Karcı Demirkol**

**Malath Thaer Nejres**

**Ala Jihad**

**Hande Gündel**

## Scientific Committee / Bilim Kurulu

- Prof. Dr. Abdelraouf A. Elmanama (Islamic University of Gaza, Palestine)  
Prof. Dr. Adnan Kaya (İzmir Kâtip Çelebi University, Turkey)  
Prof. Dr. Ahmed Hussein Kamel Ahmed Elshafie (University of Malaya, Malaysia)  
Prof. Dr. Ahmet Koyu (İzmir Kâtip Çelebi University, Turkey)  
Prof. Dr. Ahmet Türk (Manisa Celal Bayar University, Turkey)  
Prof. Dr. Akeel H. Ali Al-Assie (Tikrit University, Iraq)  
Prof. Dr. Ali Çelik (Manisa Celal Bayar University, Turkey)  
Prof. Dr. Ali Mutlu (Manisa Celal Bayar University, Turkey)  
Prof. Dr. Amin Solaiman Badawy (University of Tikrit, Iraq)  
Prof. Dr. Antonio Vargas-Berenguel (Universidad de Almería, Spain)  
Prof. Dr. Aydın Akan (İzmir Kâtip Çelebi University, Turkey)  
Prof. Dr. Aydoğan Savran (Ege University, Turkey)  
Prof. Dr. Ayşegül Alaybeyoğlu (İzmir Kâtip Çelebi University, Turkey)  
Prof. Dr. Bayram Şahin (Ege University, Turkey)  
Prof. Dr. Buket Okutan Baba (İzmir Kâtip Çelebi University, Turkey)  
Prof. Dr. Ekrem Alimi (“Kadri Zeka” University – Gjilan, Kosovo)  
Prof. Dr. Enver Atik (Manisa Celal Bayar University, Turkey)  
Prof. Dr. Erdal Çelik (Dokuz Eylül University, Turkey)  
Prof. Dr. Fatih Erdoğan Sevilgen (Gebze Technical University, Turkey)  
Prof. Dr. Figen Kırkpınar (Ege University, Turkey)  
Prof. Dr. İsmet Karaca (Ege University, Turkey)  
Prof. Dr. Md. Ashraful Hoque (Islamic University of Technology, Bangladesh)  
Prof. Dr. Mehmet Ali Yurdusev (Manisa Celal Bayar University, Turkey)  
Prof. Dr. Mehmet Çevik (İzmir Kâtip Çelebi University, Turkey)  
Prof. Dr. Mehmet Sezer (Manisa Celal Bayar University, Turkey)  
Prof. Dr. Muhammed Bahattin Tanyolaç (Ege University, Turkey)  
Prof. Dr. Musa Alcı (Ege University, Turkey)  
Prof. Dr. Nazar Mohammad Halim (Kabul University, Afghanistan)  
Prof. Dr. Nihat Sami Çetin (İzmir Kâtip Çelebi University, Turkey)  
Prof. Dr. Nilgül Çetin (İzmir Kâtip Çelebi University, Turkey)  
Prof. Dr. Nurcan Baykuş Savaşaneril (Dokuz Eylül University, Turkey)  
Prof. Dr. Özşen Çorumluoğlu (İzmir Kâtip Çelebi University, Turkey)  
Prof. Dr. Ramazan Karakuzu (Dokuz Eylül University, Turkey)  
Prof. Dr. Sahib Jumaa Abdurrahman (Tikrit University, Iraq)  
Prof. Dr. S. Bahadır Yüksel (Konya Technical University, Turkey)  
Prof. Dr. Şerafettin Demiç (İzmir Kâtip Çelebi University, Turkey)  
Prof. Dr. Roberta Katlen Fusco Marra (Universidade Salgado de Oliveira, Brazil)  
Prof. Dr. Tefvik Tansel Tanrikul (İzmir Kâtip Çelebi University, Turkey)  
Assoc. Prof. Dr. Ali Konuralp (Manisa Celal Bayar University, Turkey)  
Assoc. Prof. Dr. Aytuğ Onan (İzmir Kâtip Çelebi University, Turkey)  
Assoc. Prof. Dr. Berra Gültekin Sınır (Manisa Celal Bayar University, Turkey)  
Assoc. Prof. Dr. Cem Tozlu (İzmir Kâtip Çelebi University, Turkey)  
Assoc. Prof. Dr. Duygu Dönmez Demir (Manisa Celal Bayar University, Turkey)

- Assoc. Prof. Dr. Erkan Doğan (Manisa Celal Bayar University, Turkey)  
Assoc. Prof. Dr. Ersin Aslan (Manisa Celal Bayar University, Turkey)  
Assoc. Prof. Dr. Fabienne Anne Chantal Dumoulin (Gebze Technical University, Turkey)  
Assoc. Prof. Dr. Fethullah Güneş (İzmir Kâtip Çelebi University, Turkey)  
Assoc. Prof. Dr. Femin Yalçın (İzmir Kâtip Çelebi University, Turkey)  
Assoc. Prof. Dr. Gökçen Bombar (İzmir Kâtip Çelebi University, Turkey)  
Assoc. Prof. Dr. Hubert Chapuis (Université de Lorraine, France)  
Assoc. Prof. Dr. Kamil Şirin (Manisa Celal Bayar University, Turkey)  
Assoc. Prof. Dr. Levent Aydın (İzmir Kâtip Çelebi University, Turkey)  
Assoc. Prof. Dr. Levent Çetin (İzmir Kâtip Çelebi University, Turkey)  
Assoc. Prof. Dr. Merih Palandöken (İzmir Kâtip Çelebi University, Turkey)  
Assoc. Prof. Dr. Mücahit Sütçü (İzmir Kâtip Çelebi University, Turkey)  
Assoc. Prof. Dr. Muhammad Mukhlisin (Politeknik Negeri Semarang, Indonesia)  
Assoc. Prof. Dr. Mustafa Akyol (Manisa Celal Bayar University, Turkey)  
Assoc. Prof. Dr. Mustafa Can (İzmir Kâtip Çelebi University, Turkey)  
Assoc. Prof. Dr. Mustafa Erkan Turan (Manisa Celal Bayar University, Turkey)  
Assoc. Prof. Dr. Mustafa Erol (Dokuz Eylül University, İzmir, Turkey)  
Assoc. Prof. Dr. Neritan Shkodrani (Polytechnic University of Tirana, Albania)  
Assoc. Prof. Dr. Nesrin Horzum Polat (İzmir Kâtip Çelebi University, Turkey)  
Assoc. Prof. Dr. Ozan Karaman (İzmir Kâtip Çelebi University, Turkey)  
Assoc. Prof. Dr. Ömer Öztürkoğlu (Yaşar University, Turkey)  
Assoc. Prof. Dr. Özlem Çağındı (Manisa Celal Bayar University, Turkey)  
Assoc. Prof. Dr. Süleyman Murat Bağdatlı (Manisa Celal Bayar University, Turkey)  
Assoc. Prof. Dr. Utku Kürşat Ercan (İzmir Kâtip Çelebi University, Turkey)  
Assoc. Prof. Dr. Ümit İşci (Gebze Technical University, Turkey)  
Assoc. Prof. Dr. Yasin Ünlütürk (Kırklareli University, Turkey)  
Assist. Prof. Dr. Abdelkhalik Aboulouard (Université Sultan Moulay Slimane, Morocco)  
Assist. Prof. Dr. Abdulfetah Shobole (Istanbul Sabahattin Zaim University, Turkey)  
Assist. Prof. Dr. Adil Ali Haydir Hassan (University of Kirkuk, Iraq)  
Assist. Prof. Dr. Ahmet Aykaç (İzmir Kâtip Çelebi University, Turkey)  
Assist. Prof. Dr. Ali Yurddaş (Manisa Celal Bayar University, Turkey)  
Assist. Prof. Dr. Ali Ettehadı (İzmir Kâtip Çelebi University, Turkey)  
Assist. Prof. Dr. Ayşe Kalaycı Önaç (İzmir Kâtip Çelebi University, Turkey)  
Assist. Prof. Dr. Aytunga Bağdatlı (Manisa Celal Bayar University, Turkey)  
Assist. Prof. Dr. Ceyhun Araz (Manisa Celal Bayar University, Turkey)  
Assist. Prof. Dr. Daniel Hatungimana (Université du Burundi, Burundi)  
Assist. Prof. Dr. Derya Doğan Durgun (Manisa Celal Bayar University, Turkey)  
Assist. Prof. Dr. Ebubekir Atan (İzmir Kâtip Çelebi University, Turkey)  
Assist. Prof. Dr. Emine Kemiklioğlu (Manisa Celal Bayar University, Turkey)  
Assist. Prof. Dr. Faruk Özger (İzmir Kâtip Çelebi University, Turkey)  
Assist. Prof. Dr. Fatih Cemal Can (İzmir Kâtip Çelebi University, Turkey)  
Assist. Prof. Dr. İlker Polatoğlu (Manisa Celal Bayar University, Turkey)  
Assist. Prof. Dr. Mabvuto Mwanza (University of Zambia, Zambia)  
Assist. Prof. Dr. Mehmet Alper Çankaya (İzmir Kâtip Çelebi University)  
Assist. Prof. Dr. Mohammed Wadi (Istanbul Sabahattin Zaim University, Turkey)  
Assist. Prof. Dr. Moustapha Maman Mounirou (Abdou Moumouni University, Niger)



- Assist. Prof. Dr. Muhammad Imran Shakir (King Saud University, Saudi Arabia)  
Assist. Prof. Dr. Muhammad Shahid (The Islamia University of Bahawalpur, Pakistan)  
Assist. Prof. Dr. Mutlu Seçer (İzmir Kâtip Çelebi University, Turkey)  
Assist. Prof. Dr. Nihad A. Jafar (Tikrit University, Iraq)  
Assist. Prof. Dr. Onur Ertuğrul (İzmir Kâtip Çelebi University, Turkey)  
Assist. Prof. Dr. Oruç Altıntaş (İzmir Kâtip Çelebi University, Turkey)  
Assist. Prof. Dr. Özgün Yücel (Gebze Technical University, Turkey)  
Assist. Prof. Dr. Saim Kural (Manisa Celal Bayar University, Turkey)  
Assist. Prof. Dr. Samuel Bunani (Karlsruhe Institute of Technology, Germany)  
Assist. Prof. Dr. Sedat Yalçınkaya (İzmir Kâtip Çelebi University, Turkey)  
Assist. Prof. Dr. Sema Demirci Uzun (İzmir Kâtip Çelebi University, Turkey)  
Assist. Prof. Dr. Selçuk Saatici (İzmir Institute of Technology, Turkey)  
Assist. Prof. Dr. Sercan Acarer (İzmir Kâtip Çelebi University, Turkey)  
Assist. Prof. Dr. Simge Öztunç (Manisa Celal Bayar University, Turkey)  
Assist. Prof. Dr. Şeyma Aykaç (Ege University, Turkey)  
Assist. Prof. Dr. Tarkan Akderya (Bakırçay University, Turkey)  
Assist. Prof. Dr. Umut Ceyhan (İzmir Kâtip Çelebi University, Turkey)  
Assist. Prof. Dr. Violeta Rodriguez-Ruiz (The University of Cergy-Pontoise, France)  
Assist. Prof. Dr. Waleed Fadel (Girne American University, TRNC)  
Assist. Prof. Dr. Walid Sharmoukh Ahmed Moustafa (National Research Centre, Egypt)  
Assist. Prof. Dr. Yiğit Aksoy (Manisa Celal Bayar University, Turkey)  
Assist. Prof. Dr. Z. Haktan Karadeniz (İzmir Kâtip Çelebi University, Turkey)  
Dr. Alex Modi Lomoro Wani (Management System International, South Sudan)  
Dr. Amir Shirzadi (University of Cambridge, United Kingdom)  
Dr. Ansoumana Noumou Djite (Senegal)  
Dr. Ayşe Kurt Bahşı (Turkey)  
Dr. Hiba Yahyaoui (University of Tunis, Tunisia)  
Dr. Fakhra Liaqat (Pakistan)  
Dr. Ibrahim Karidio Diori (Niger)  
Dr. Ismael Abdou Souley (Niger)  
Dr. Juan Manuel Casas-Solvas (University of Almeria, Spain)  
Dr. M. Malick Diallo Nethehi (Guinea)  
Dr. M. Mustafa Bahşı (Manisa Celal Bayar University, Turkey)  
Dr. Muhammad İlyas Khazi (State Key Laboratory, China)  
Dr. Norhuda Bansil (Bangsa Moro)  
Dr. Ornela Lalaj Şen (Turkey)  
Dr. Sivarama Krishna Lakkaboyana (Universiti Teknologi Malaysia, Malaysia)  
Dr. Sümeyye Sınır (Turkey)  
Dr. Zoltán Fülöp (Budapest, Hungary)

## Invited Speakers / Davetli Konuşmacılar



### **Machine Learning with Encrypted Data**

**Prof. Dr. Çetin Kaya KOÇ**, Dean of Faculty of Engineering at İstinye University



### **Being an Engineer – Shaping the World**

**Prof. Dr. Aydın AKAN**, Head of the Department of Electrical and Electronics Engineering at İzmir University of Economics

## Table of Contents

Preface.....	iv
Önsöz.....	v
Organizing Committee / Düzenleme Kurulu.....	vi
Scientific Committee / Bilim Kurulu .....	vii
Invited Speakers / Davetli Konuşmacılar .....	x
Agricultural Engineering / Ziraat Mühendisliği.....	1
Comparative Study of Composted <i>Grevillea robusta</i> -Paspalum and <i>Alnus Acuminata</i> -Paspalum Biomasses.....	2
Uses of Bioslurry (Biogas Residue) as Inexpensive Product for Animal Feed.....	11
An Assessment on the Use and Application of Estrous Hormones in Dairy Cattle at Kiambaa Subcounty, Kiambu, Kenya .....	20
Hindilerde ( <i>Meleagris gallopavo</i> ) Yetiştirme Sisteminin Performans Üzerine Etkileri .....	29
Identification, the Best Wheat Cultivar Studied (5 Digits), by Comparing Physical and Chemical Properties, and Homology Results, in Order to Produce the Best, Hybrid Triticale.....	36
Identification of 3 Defense-Related Enzymes Activities by Using 2 Cell Damage Indices in 2 Chickpea Plants Genotypes under Cold Stress.....	44
Animal Nutrition / Hayvan Besleme .....	52
Cassava Root Silage as a Feed for Ruminants .....	53
Biochemistry / Biokimya .....	64
Uptake of Curcumin by Supported Metal Oxides (CaO and MgO) Mesoporous Silica Materials ...	65
Chemistry / Kimya .....	73
Characterization of Plasmid from Antibiotic-Resistant <i>Pseudomonas</i> spp. Isolated from Soil Sample .....	74
Civil Engineering / İnşaat Mühendisliği .....	79
Collapse Fragility of Wide Beam Frames using the Simplified Method of FEMA P-58 .....	80
An Alternative Approach to Produce Warm Mix Asphalt at Lower Temperatures.....	86
ACI318-14 ve TS500 Yönetmelikleri ile T En-Kesitli Betonarme Kirişlerin Davranışlarının Karşılaştırılması .....	93
TBDY-2018 ve ASCE 41-17'de Betonarme Kirişlerin Lineer Olmayan Analizleri için Modelleme Parametrelerinin Karşılaştırılması.....	104
Betonarme Kolonlar için Kesme Dayanımı ve Deformasyon Kapasite Modellerinin Araştırılması .....	118
Betonarme Taşıyıcı Sistem Elemanlarının Etkin Kesit Rijitliklerinin Araştırılması .....	129
Earthquake Resilience of Infilled Reinforced Concrete Frames with Innovative Wall Solutions ..	143
Derivation of Equation of Motions of Rotating Beams Using Biot Stress.....	154
Parametrical Resonance Analysis of a Rotating Beam .....	162
Punching Behavior of Fiber Reinforced Concrete Thin Panels .....	171
Unconfined Compression Strength of Polypropylene Fiber Reinforced Alluvial Deposits.....	178

Statistical Analysis of Monthly and Annual Precipitation and Monthly Mean Air Temperature in Black Sea (Turkey) .....	188
Computer Science and Engineering / Bilgisayar Bilimi ve Mühendisliği .....	193
Survey on Implementation of Lattice-based Identification Schemes .....	194
Support Vector Machines: From Classical Version to Quantum .....	207
Control and Automation Engineering / Kontrol ve Otomasyon Mühendisliği .....	217
An Application of Offset-Free Linear Quadratic Optimal Control .....	218
Electrical and Electronics Engineering / Elektrik ve Elektronik Mühendisliği .....	229
Photovoltaic Potential Assessment in the Democratic Republic of Congo .....	230
Environmental Engineering / Çevre Mühendisliği .....	238
Remediation of Nickel Ions from Contaminated Solutions Using Mandarin Peels as Non-Valuable Biosorbent Media .....	239
Fisheries / Balıkçılık .....	250
Utilization of Blood Meal as an Alternative Protein Source on Growth and Feed Efficiency in Fingerlings Nile Tilapia (Oreochromis Niloticus) .....	251
Food Engineering / Gıda Mühendisliği .....	258
Gıda Mühendisliğinde Dijitalleşme ve Önemi .....	259
Badem Sütü Üretimi ve Gıdalarda Kullanım Olanakları .....	269
Information Technologies / Bilgi Teknolojileri .....	272
Implementation and Evaluation of Distributed Algorithms in Peer-to-Peer and Multi-hop Smartphone Networks .....	273
Materials Science and Engineering / Malzeme Bilimi ve Mühendisliği .....	280
Stochastic Optimization of Graphene Sheets Subjected to Drilling Operation Using Neuro-Regression Approach for Maximum Mechanical Strength .....	281
Stochastic Optimization of Friction Stir Welded AA7039 Aluminum Alloy Joints Using Neuro-Regression Approach for Maximum Tensile Strength .....	290
Investigation in Graphene/Silicon-based Schottky Junction Solar Cell .....	297
Investigating the effect of Vacancy Defect on Graphene/Hexagonal Boron Nitride In-plane Heterostructure .....	302
Mathematics / Matematik .....	306
Numerical Solution of IVPs using Adaptive Nelder-Mead Optimization .....	307
A Numerical Algorithm to Solve a Class of Neutral Type Functional Integro-Differential Equations by Using Shifted Gegenbauer Polynomials .....	314
An Approximate Solution of 3D Partial Differential Equation by the Pell Matrix Collocation Method .....	321
Shifted Legendre Matrix Method for Solving Second Order Linear Neutral Integro Differential Equations Involving Delays .....	330
Approximation Properties of Some Bernstein Type Operators .....	340
A Numerical Approach Based on Bell Polynomials to Solve Volterra Integro Differential Equations with Variable Coefficients .....	343

Mechanical Engineering / Makina Mühendisliği.....	352
Compression-after Impact Behavior of Laminated Composites Plates.....	353
Cooling Analysis of a Horizontally Oriented Piezofan in Longitudinal Channel.....	361
Effects of Crosshead Speed and Penetrator Shape on the Punch Shear Behaviors of Sandwich Composites.....	369
Optimization Study of Ballistic Impact Tests on Carbon-Carbon Composites.....	375
Impact and Compression-after Impact Behaviors of Laminated Composite Plates.....	379
Linear Vibration Analysis of Axially Forced Euler-Bernoulli Beam Graded Trigonometric Material with Variable Cross-Section.....	385
Design of ABS Plastic Scrap Recycling Process for 3D Printer Filaments .....	392
Neuro-Regression Approach in Optimization of Predicted Enthalpy of a Refrigeration System with Two-Stage Compression and Intercooling .....	401
Cross Akışkanın Sınır Tabakası Denklemleri ve Benzerlik Çözümleri .....	409
Bir Gıda Üretim Tesisinde Konfor Soğutmada Amonyak ve Freon R-134a Akışkanlı Sistemlerin Verimliliklerinin Karşılaştırılması .....	419
Accurately Capturing Heat Transfer in a Turbulent U-Bend Flow .....	424
Hasara Uğramış Bir Manuel Vites Mekanizmasının Ömür ve Güvenirlik Analizi.....	431
Mining Engineering / Maden Mühendisliği.....	439
Characterization of Triple Superphosphate for Removal of Heavy Metals .....	440
Nanotechnology / Nanoteknoloji.....	446
Preparation and Characterization of Chitosan-Based Hydrogels Reinforced by Mesoporous Silica Nanoparticles.....	447
Petroleum and Natural Gas Engineering / Petrol ve Doğalgaz Mühendisliği.....	453
Miscible Displacement Simulator Using Novel Adjustable Flux Limiter .....	454
Physics / Fizik.....	461
Determination of Inelastic Longitudinal Electron Scattering Form Factors in <sup>58</sup> Ni.....	462
Urban Design / Kentsel Tasarım.....	466
Re-Examine Conventional Concepts in Urban Design: the Conflict Between Urban Space Utilization and The Elements of Power and Control - Case of Hawkers within Amman, Jordan ..	467
Congress Photograph Gallery / Kongre Fotoğraf Galerisi .....	477

# **Agricultural Engineering / Ziraat Mühendisliği**

## Comparative Study of Composted *Grevillea robusta*-Paspalum and *Alnus Acuminata*-Paspalum Biomasses

Jean Claude Tuyisenge\*, University of Rwanda, College of Agriculture, Animal Science and Veterinary Medicine, Department of Soil Science and Environmental Management, Huye, Rwanda

\*Corresponding author: jeanclaudetuyisenge3@gmail.com

**Keywords:** Compost; *Grevillea robusta*; *Alnus acuminata*; paspalum, fertilizer

**Discipline:** Agriculture

### Abstract

Intensive cultivation with reduced inputs, deforestation and tillage degrade soil organic matter and impoverish soil quality in tropics, especially in Rwanda. Inorganic fertilizers have been damaging environment (e.g., eutrophication and drinking water containing nitrogen). This study compares composted *Grevillea robusta* (GR)-Paspalum (P) and *Alnus acuminata* (AA)-Paspalum biomasses potential for improving and maintaining soil fertility, and assesses their best combination. Heap composting at Ruhande Arboretum, Rwanda for 6 weeks, with 3 treatments (GR-P, AA-P and GR-AA-P) and 2 replications with randomized complete block design was performed. After laboratory analysis of composts, Excel and GenStat Discovery Edition 4 were used for data management and analysis. No significant difference found between treatments means, as  $F_{pr} > 0.05$  at 5% (significance level) for considered compost characteristics. But a slight difference was found considering tables of means and histograms. The AA-P compost had high organic matter, organic carbon, extractable phosphorus, mineral nitrogen, and C/N ratio, with moderate pH, and having low total nitrogen, total phosphorus, cation exchange capacity (CEC), ash and moisture content. The GR-P compost possessed low organic matter, organic carbon, extractable phosphorus, pH, with moderate total nitrogen, mineral nitrogen, C/N ratio, and CEC, but possessing high total phosphorus, ash and moisture content. The GR-AA-P compost had high total nitrogen, CEC, and pH, with moderate total phosphorus, extractable phosphorus, organic matter, organic carbon, ash and moisture content, but with low mineral nitrogen, and C/N ratio. Due to similar abilities, all composts can serve as a cheap and organic fertilizer undoubtedly reducing environmental pollution.

### Introduction

#### Background of the Study

Intensive cultivation combined with insufficient inputs contributes to poor soil quality. Besides, given that most Rwandans rely on agriculture and considering the continuous population growth. Soil fertility solutions become of great need [1]. In Rwanda, agriculture is a sector for survival and development. Agriculture also induces land degradation, which is an environmental issue in the country [2]. In Tropics where Rwanda is found, mineral fertilizers contributes to health hazards through eutrophication and leaching of nitrates in drinking water [3]. It was mentioned that the nitrates leaching is an environmental threat in agriculture at the same time being a considerable global issue [4].

#### Problem Statement

Inorganic fertilizers damages environment [3]. Investigations of alternatives for increasing organic fertilizer quantities are carried out [1]. So, there is an urgent need for making organic fertilizers like composts available for use. Once a compost is tested, its application can be performed more accurately [5]. Organic fertilizers characterization can be more informative. This can contribute to crop production increase and a reduced environmental pollution and health hazards.

This study provides science-based information about the potential of composted *Grevillea robusta*-paspalum and *Alnus acuminata*-paspalum biomasses or their combination for supplying nutrients including nitrogen (N) and phosphorus (P), and for serving as the organic matter (OM) source. It also provides information about other important compost characteristics.

### Research Questions

- Does the composted *Grevillea robusta* (GR)-Paspalum (P) biomass have greater N, P, organic matter (OM), organic carbon (OC), ash, moisture, CEC, C/N ratio, and pH than for the composted *Alnus acuminata* (AA)-Paspalum biomass?
- Does the composted GR-AA-P biomass possess higher N, P, OM, OC, ash, moisture, CEC, C/N ratio, and pH than for the composted AA-P biomass?
- Are the C/N ratio, pH, CEC, N, P, OM, OC, ash, and moisture of the composted GR-AA-p biomass greater than those of the composted GR-P biomass?

### Literature Review

#### *Grevillea Robusta*

According to [6], *Grevillea robusta* is a medium to large tree commonly grown for ornamental use in warm-temperate and semitropical climates. It is widely planted on small farms, particularly in tropical highlands of Africa, where it is used in row and boundary plantings and grown within crop areas. Its leaves are used as materials for bedding in stables and as mulch.

#### *Alnus Acuminata*

According to [7], *Alnus acuminata* has leaves which are rich in nitrogen. It contributes in reclamation, nitrogen fixation, and soil improvement. It has been recommended in high altitude regions of Rwanda like Ruhengeri, parts of Kibuye and Gisenyi, Byumba, and Gikongoro along with other trees [8]. *A. acuminata* and *G. robusta* (generally in agroforestry), are in exotic species which mostly occur either in mixed or pure plantations and agroforestry [9]. Besides, It was reported that *alnus acuminata* leaves incorporation into the soil leads to a considerable rise in the yield of a crop as for potato [10].

#### Paspalum

The paspalum species whose biomass was used during composting is the *Paspalum Notatum Flugge*. According to [11], the *Paspalum Notatum Flugge* is known as Pensacola bahai, Bahiagrass, and Common bahai. *Paspalum Notatum* is a perennial herb which spread by seeds and by rhizomes. As reported by [12], in Rwanda, it is exotic and it is grown almost everywhere in Butare city gardens.

*Paspalum Notatum Flugge* is a C<sub>4</sub> grass, strongly resists stress, grows faster and yields high biomass. It has been greatly grown in tropical and subtropical regions for establishment of a lawn, for forage, for slope stabilization and for erosion control [13].

### Compost and Composting

Composting is known as a process for forming humus like organic materials outside the soil through piling, mixing, or storing organic materials under conditions leading to aerobic decomposition and conservation of nutrients [14 - 15]. The processes of decomposition and organisms involved are very identical to those involved in humus formation in soils. The principal difference is that with composting, decay process takes place outside the soil [14].

There are 3 stages for decomposition of organic materials including (i) initial mesophilic stage, (ii) thermophilic stage, and, (iii) second mesophilic or curing stage [14].

Important compost characteristics comprise pH (mostly from 5 to 8.5), soluble salts (conductivity), nutrient content, organic matter, moisture content, particle size, maturity (bioassay), stability (respirometry), inerts (physical contaminants), trace metals (chemical contaminants), and weed seeds and pathogens (biological contaminants) [16 - 17].

As composting methods include heap method, pit method, and NADEP Method. The heap method being the one in which organic materials like biomass, weeds, crop residues, and animal excreta are stacked together in alternating layers, and the surface is covered by a small layer of soil or dry leaves [18].



## Materials and Methods

### Materials

Composted materials included leaves and twigs of *Grevillea robusta* and *Alnus acuminata*, paspalum biomass, soil, rough materials (tree branches). During sampling, auger, plastic bags, and sack were utilized. During laboratory analysis, materials varied by tested parameter.

### Methods

Experimental Design: Heap composting by stacking materials in alternative layers [18].

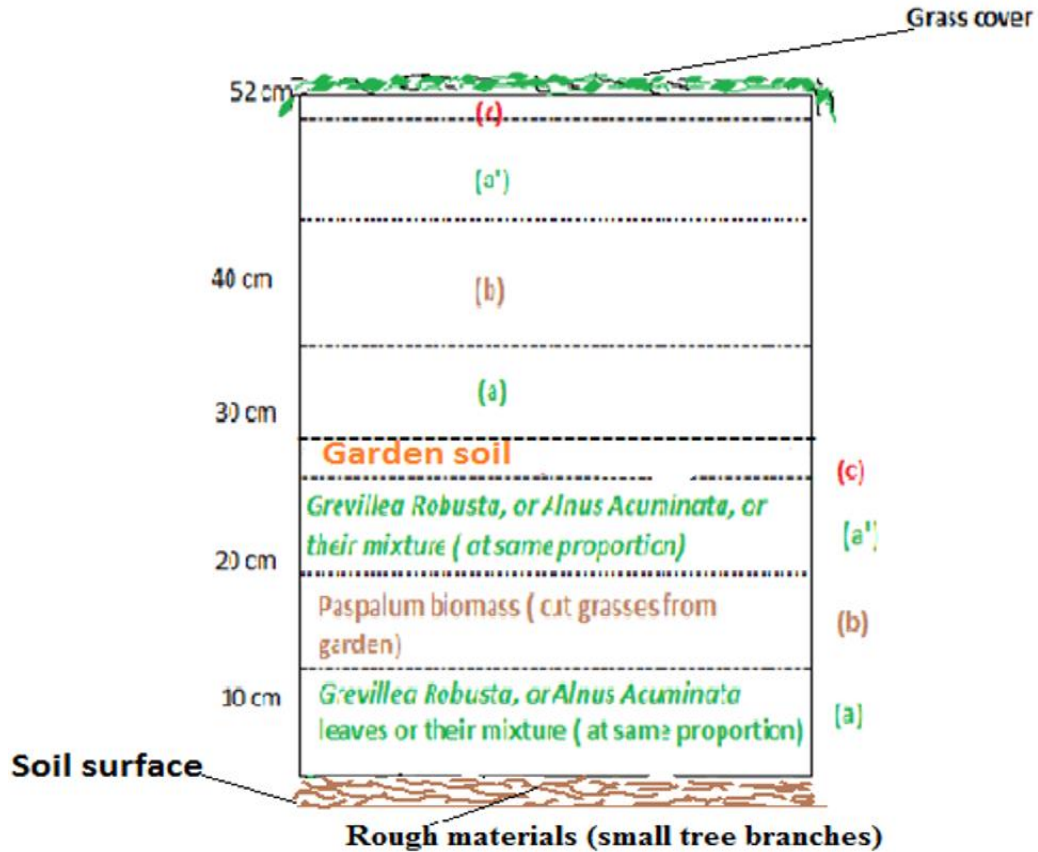


Figure 1. Compost heap design

1<sup>st</sup> day (Establishment of trials) → 10<sup>th</sup> day (Mixing) → 20<sup>th</sup> day (Mixing) → 30<sup>th</sup> day (Mixing) → 40<sup>th</sup> day (Mixing) → 42<sup>nd</sup> day (Sampling)

Laboratory Analysis: For total N and mineral N: Kjeldahl method [19 - 20], organic matter and ash content: Loss-on-Ignition [20 - 21], total P and extractable P : UV spectrophotometer [19 - 20], pH: potentiometric method [20], cation exchange capacity [20], moisture [19], organic carbon:  $OM \times 0.54$  [22], and C/N ratio [23].

Data Analysis: Microsoft Excel and GenStat Discovery Edition 4. Means were compared based on the LSD at 5% significant level.

## Results and Discussion

Since the soil organic matter always contains carbon (C), and various inorganic elements including nitrogen (N), and phosphorus (P). It has the capacity for holding enough moisture and for attracting up to 10 times more plant nutrients than can the clay minerals. In subtropical and tropical soils, the soil organic matter breakdown rate is high, and it is generally difficult to maintain high organic matter levels. But, as the organic matter has an effect on almost all soil processes, greater efforts have to be made for building up high levels [24]. Hence, it is usually better to put wastes (i.e. garden wastes like cut

paspalum, plant residues such as pruned tree biomass) through a composting process first, even if only for a short period of time without waiting for a complete breakdown and the compost maturity to be attained, especially where raising the production of food is vital [24].

For contributing to such effort, levels of some characteristics of compost were estimated from laboratory analysis of composted *Grevillea robusta*-Paspalum (GR-P) and *Alnus acuminata*-Paspalum (AA-P) biomasses, because by having compost tested, it can be applied more accurately [5]. Therefore, results of investigated compost characteristics are generally presented in Table 1, and specifically in different figures (histograms). From such results, composts produced were compared to other organic manures and chemical fertilizers used around the world. Additionally, as the plant needs a number of essential elements for a healthy growth [25]. Then, considering research findings, the potential of produced composts can be exploited for meeting plant needs through the use of compost as slow-release fertilizer, as an ingredient for potting mixes, as an organic soil conditioner, and as a mulching material [14].

Table 1. Mean Values of parameters after laboratory analysis

Compost	TN (%)	Min N (%)	NTP (mg/kg)	Ext P (mg/kg)	PCEC (meq/100g)	OM (%)	OC (%)	C/N	M (%)	A (%)	pH H <sub>2</sub> O	pH KCl
GR-P	0.95	0.024	313.770	11.125	52.8	42.100	24.477	27.565	61.99	57.900	6.42	5.92
AA-P	0.8	0.038	132.865	18.340	46	47.025	27.340	34.170	61.363	52.975	6.45	5.98
GR-AA-P1.6	0.021	156.635	14.365	60.4	45.585	26.503	23.835	61.541	54.415	6.50	6.19	

Where, TN: Total Nitrogen, Min N: Mineral Nitrogen, TP: Total Phosphorus, Ext P: Extractable Phosphorus, CEC: Cation Exchange Capacity, OM: Organic Matter, OC: Organic Carbon, C/N: Carbon to Nitrogen ratio, M: Moisture content, A: Ash content, pH: Hydrogen Potential, GR-P: *Grevillea robusta*-Paspalum, AA: *Alnus acuminata*-Paspalum, GR-AA-P: *Grevillea robusta*-*Alnus acuminata*-Paspalum, Rep: Replication, and Av.: Average.

### Total Nitrogen and Mineral Nitrogen Content

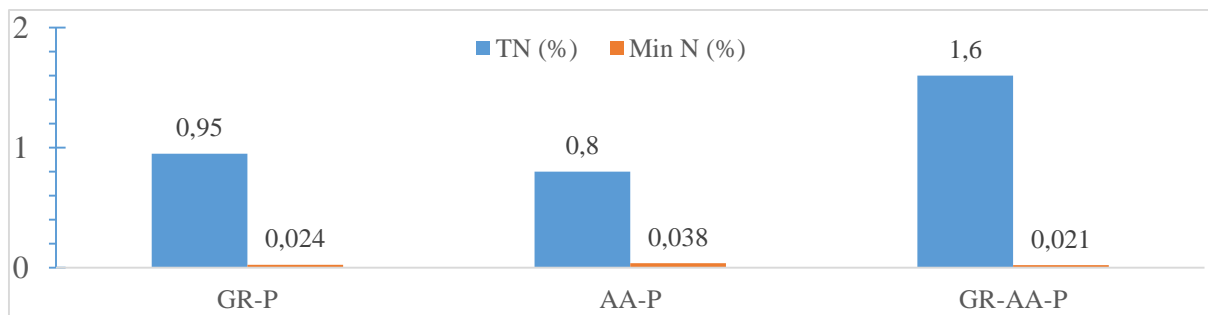


Figure 2. Total nitrogen and mineral nitrogen content in composts

### Total Nitrogen

The total N in finished compost falls in the range 0.4%-3.5% [26]. Total N often ranges from 0.5% to 2.5 % (dry weight basis) in finished composts [5, 27] which is met by studied composts. However, laboratory report data shows that the GR-AA-p compost can be considered as the best compost for supplying the total N in high amount.

### Mineral Nitrogen

Studied composts contain low amount of available N compared to the N level in most common manures and chemical fertilizers like urea. Low available N is also an important aspect for reducing nitrates leaching to drinking water and for eutrophication prevention [3 - 4].

Table 2. Standard range for commonly used organic materials

Parameter	Standard range	Type of organic material	Source
Nitrogen (N)	2.60%	Cow manure & straw bedding	[28]
	20-45 mg/g	Cattle dung	
	1.21%	Cattle urine	
	20-45 mg/g	pig, sheep and goat dung	[29]
	1.47%	sheep and goat urine	
	0.38%	pig urine	
	28-62 mg/g	Poultry dung	
Available N/ Mineral N	0.25-1.50%	Decomposed matter	[18]
Phosphorus (P)	2.60%	Cow manure & straw bedding	[28]
	4-10 mg/g	Cattle dung	
	0.01%	Cattle urine	
	4-11 mg/g	Sheep and goat dung	
	0.05%	Sheep and goat urine	[29]
	6-12 mg/g	pig dung	
	0.10%	Pig urine	
	9-26mg/g	Poultry dung	
Organic matter (OM)	2.60%	Cow manure & straw bedding	[28]
Organic Carbon (OC)	2.60%	Cow manure & straw bedding	[28]
	20-30%,	Decomposed matter	[18]
C/N ratio	10:1	Cow manure & Straw bedding	[28]
	14:1 to 20:1	Organic materials in pile	[14]
CEC	50 to 70 Cmolc / Kg	Organic matter of compost	[14]
Moisture Percent	30%	Cow manure & Straw bedding	[28]

### Total Phosphorus and Extractable Phosphorus

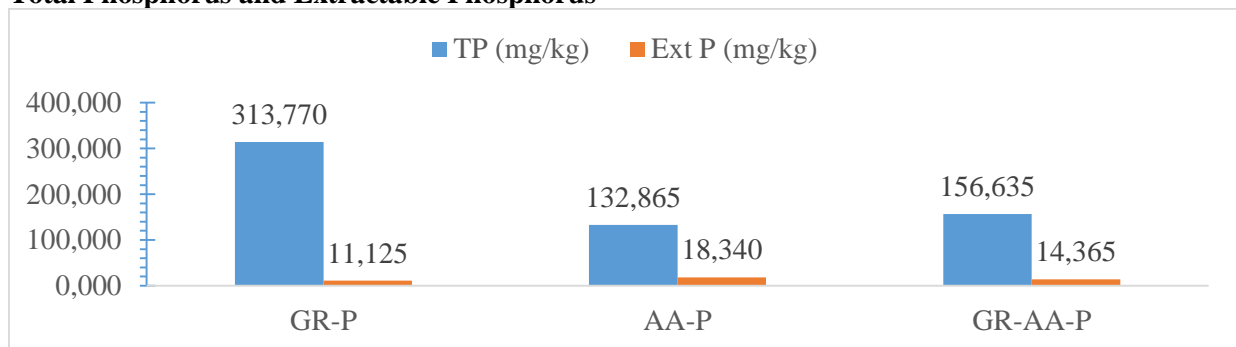


Figure 3. Total phosphorus and extractable phosphorus in composts

### Total Phosphorus

Total P level of quality compost varies between 0.6 % and 0.9% [30]. Total P in finished compost: 0.3 %  $P_2O_5$  (0.131% P) - 3.5%  $P_2O_5$  (1.528% P) [26]. Investigated composts possess low total P compared to some quality composts. For producing P rich composts, adding P rich materials where applicable is suggested.

### Extractable Phosphorus

Studied composts have low quantity of extractable P compared to the level mentioned by [19, 29] in dung and urine of goat, cattle and sheep. Their extrable P is also less than what was reported in straw bedding, cow manure, poultry manure, and farm yard manure (Table 2). Long composting period (> 6 weeks) is needed for composts to generate high P amount in plant available forms unless no phosphorus enrichment during composting.

### Cation Exchange Capacity

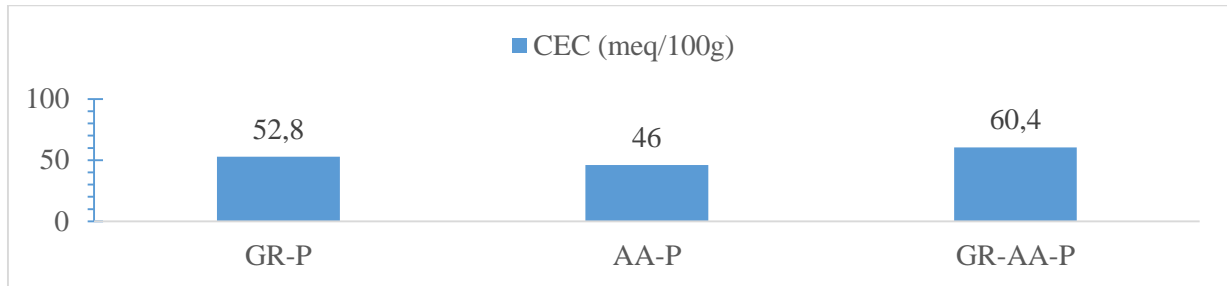


Figure 4. Cation exchange capacity of composts

[31] indicated that most composts possess the CEC > 60 meq/100g for fulfilling the quality standard of a finished compost. Research results show that only the GR-AA-P compost has the CEC falling above such critical CEC level for quality composts. But considering that [14] mentioned that the CEC of organic matter for compost is 50-70 Cmolc / Kg. Therefore, GR-AA-P and GR-P composts fall in such range, with only the AA-P compost having a slightly low CEC compared to a desired CEC.

### Organic Matter, Organic Carbon, Moisture and Ash Content

#### Organic Matter

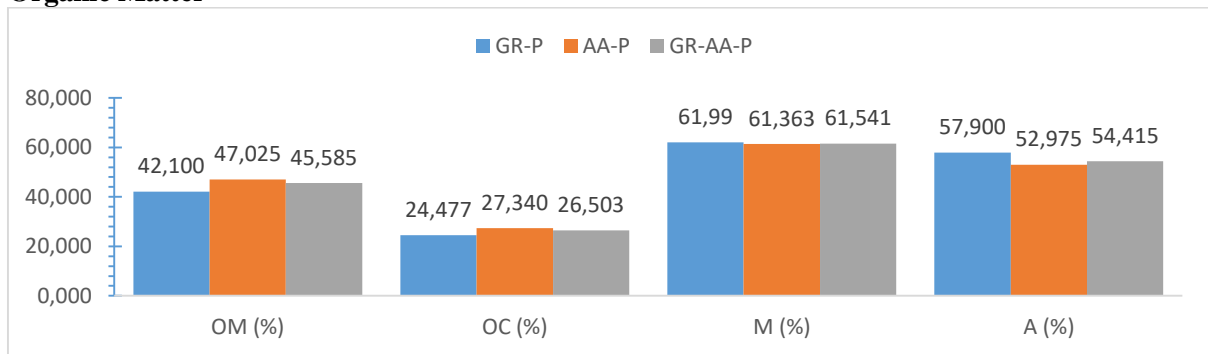


Figure 3. Organic matter, organic carbon, moisture and ash content

Compared to straw bedding and cow manure (Table 2), each compost has higher OM content. OM for finished compost: 25%-50% [26]. High quality compost possesses a minimum of 50% OM quantity based on dry weight [15] (Table 2), supporting investigated composts with OM amount that is not very low. It was reported that no ideal OM content in a finished compost. OM level decreases during composting. The OM content (dry weight basis) in finished compost varies from 30% to 70 %, with the range of 50-60 % considered as preferable for most compost uses [27]. Hence, studied composts can be used as a good source of OM for soil fertility improvement and maintenance.

#### Organic Carbon

Compared to decomposed matter, cow manure and straw bedding (Table 2). All composts possess higher OC content than the amount in straw bedding and cow manure. Each compost has the OC in the standard range mentioned by [18] for the decomposed matter. Also as the OC in finished compost is 8% - 50% (dry weight) [26] (Table 2). Therefore, each compost contains the OC in recommended range for a finished compost.

#### Moisture Content

Compared to straw bedding and cow manure (Table 2). Each compost can hold a lot of water than cow manure and straw bedding. As excessively wet compost with moisture amount at 60% and above can be clumpy and heavy presenting difficulties for uniform application and requiring high delivery cost. But very dry compost with less than 35% moisture quantity can be dusty as well as irritating during its use [17]. For investigated composts, the moisture level is very closer to the recommended range. This proves that studied composts can present no handling and application difficulty. Besides, they show a great potential for sufficiently holding water.

### Ash Content

Considering that the amount of ash varies with changes in OM content [32]. Investigated composts were burnt at 500-600°C leaving only mineral constituent known as ash greatly composed by Ca, P, K, Mg and other inorganic elements which are not oxidized. Moreover, as ash content in most composts ranges from 40% to 55 % [33]. Ash in AA-p compost falls in the range for most composts. Both GR-AA-P and GR-P composts possess slightly great ash quantity. Based on the ash content in such composts, it is expected that the overall total amount of other mineral elements like Ca, Mg, K and heavy metals follows this order: GR-P > GR-AA-P > AA-P.

### C/N Ratio

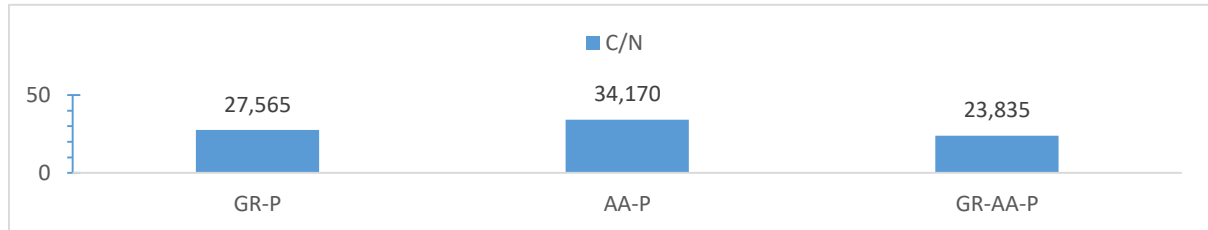


Figure 6. Carbon to nitrogen ratio (C/N)

Considering that the C/N ratio required by microorganisms is 25-35:1. Also as the C/N ratio < 20:1 shows excess of N and deficiency of C leading to ammoniacal N volatilization. This finally leading to fertilizer efficiency decrease due to the N loss [34]. Besides, as it was stressed that materials containing high C/N value are generally utilized as mulch owing to their slow decomposition rate after being spread on to the surface of the soil. Though, when materials high in C/N ratio are put into the soil, nitrogen available for plant may only decline in a short period. On the other hand, materials low in C/N ratio tend to decompose faster after being applied to the soil [35]. Therefore, it is clear that the AA-P compost can be considered as the compost which may release the plant available nitrogen after a long period compared to other investigated composts due to its high C/N ratio (34.2), whereas other composts are expected to release the nitrogen into a form available for the plant rapidly. It is also important to note that as the nitrogen availability can depend on the management of the organic input during its application; hence all studied composts may serve as a good source of plant available nitrogen if adequate compost application and good management practices are adopted.

### pH

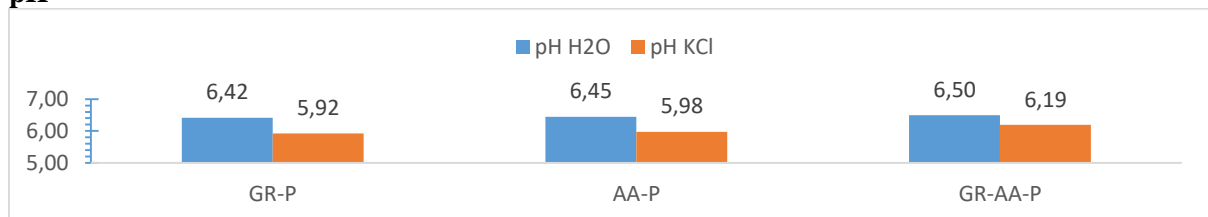


Figure 4. pH of composts

For aerobic decomposition, the acceptable pH is 5.5-9.0, while the ideal pH is 6.5-8.0. Data shows data for all studied composts the pH value at least falls in the acceptable range [34].

It was mentioned that most composts possess pH ranging from 6 to 8, with a range of 5.5-8.0 being common for yard waste (Table 2). Composts having very low pH level (<4.0) need to be utilized with attention, because the low level of compost pH can be a sign of poor composting which end up in the production of organic acids which are potentially toxic [15]. This justifies to a certain degree that composting method utilized in this study is undoubtedly a good composting practice based on pH levels. It was noted that the pH stands for active acidity in the compost or feedstock. The pH varies from 5.0 to 8.5 for most composts which are finished. The compost use defines the ideal compost. Even if for most compost uses a neutral pH is desired, for some ornamental plants, composts with lower pH levels are preferred [27]. Hence, GR-P, AA-P and GR-AA-P composts have both pH H<sub>2</sub>O and pH KCl values meeting the desired range for composts to be used for different purposes. This removes any hesitation for use of such composts as each of them presents the pH greater than 4.0 [15]. However, considering plant sensitivity to the pH should be given attention before use of these composts.

### Conclusion

Based on analysed parameters only, composts decomposition order is AA-P > GR-P > GRAA-P. On the other hand, the order for compost quality is GR-AA-P > AA-P > GR-P. But studying other parameters is essential.

It was found that the AA-P compost can serve as the best source of mineral N and available P. The GR-P compost was found as a good and cheap source of total N, and total P. All composts can serve as an important source of organic matter and organic carbon. During composting process, the C/N ratio and pH adjustment can enhance decomposition for achieving a good quality compost.

In terms of nutrient content, it was found that the content for all composts is low compared to nutrient content in chemical fertilizers. However, all studied composts showed high nutrient content compared to organic manures like cattle, goat and sheep urine.

Study findings suggest that paspalum biomass from gardens wastes can be used for producing a cheap and good quality soil amendment at the same time protecting the environment.

For appropriate use of composts that can be produced during composting as for the case of composted *Grevillea robusta*, paspalum and *Alnus acuminata* biomasses. It is recommended that heavy metals, K, Ca, Mg, and S content, biological and physical characteristics be analyzed for adequate use of produced composts and for ensuring the environment protection. Overall, all studied composts can serve as a cheap and good source of soil amendment for improving and maintaining soil fertility with reduced environmental pollution.

### Aknowledgement

The author would like to thank KASANZIKI Charles for helpful advice during the study. Many thanks to Prof. NARAMABUYE Francois Xavier for financial support during laboratory work.

### References

- [1] D. Eva, Soil Fertility Management and Socio-economic Factors in Small-scale Farming Systems in Southwest Rwanda: Interaction Between Research and Extension in Promoting Improved Compost Technology, Ghent University, Faculty of Agricultural and Applied Biological Sciences, 2004.
- [2] UNEP, «Agriculture and Land Degradation, » REMA, Kigali, 2008.
- [3] A. E. Hartemink, Soil Fertility Decline in the Tropics with Case Studies on Plantations, Wallingford: CABI Publishing, 2003, p. 33.
- [4] E. S. P. Rao ve K. Puttanna, «Nitrates, agriculture and environment, » Current Science, cilt 79, no. 9, pp. 1163-1168, 10 November 2000.
- [5] E. S. Sánchez ve T. L. Richard, Using Organic Nutrient Sources, Pennsylvania: The Pennsylvania State University, 2009.
- [6] C. E. Hardwood, *Grevillea robusta*: an annotated bibliography, Nairobi: International Council for Research in Agroforestry, ICRAT House, 1989, pp. 10-13.
- [7] C. Orwa, A. Mutua, R. Kindt, R. Jannadass ve A. Simons, Agroforestry Data base: a tree Reference and selection guide version 4.0, World Agroforestry Centre, 2009.
- [8] ICRAF, Kigali: World Agroforestry Center, n.d.
- [9] J. Nduwamungu, cilt 1, no. 14, pp. 17-20, 2011.
- [10] R. A. Cyamweshi, W. C. Muthuri, A. Mukuralinda ve S. Kuyah, *Alnus acuminata*: an effective fertilizer tree for smallholder farmers in sub-humid regions of Rwanda, World Agroforestry Centre, n.d.
- [11] P. J. Sekerman ve F. Riveros, Tropical Grasses, Rome: FAO [Food and Agriculture Organization of the United Nations], 1990, p. 832.
- [12] J. Ndayisenga, «Butare City Ornamental Plant Taxonomy and Phytogeography, » National University of Rwanda, Faculty of science, Department of Biology, Botany and Conservation, Huye, 2011.
- [13] J. Huang, H. Xia, Z. Li, Y. Xiong ve G. Kong, «Soil aluminium uptake and accumulation by *Paspalum notatum*, » Waste Management & Research, p. 668–675, 7 May 2009.
- [14] N. C. Brady ve R. R. Weil, The Nature and Properties of Soils, 13 dü., New Jersey: Prentice Hall, 2002, pp. 515-518.

- [15] W. Darlington, Compost – A Guide for Evaluating and Using Compost Materials as Soil Amendments, cilt 714, Soil & Plant Laboratory, Inc., n.d., pp. 282-877 .
- [16] AAFRD, Manure Composting Manual, Edmonton, Alberta, AAFRD [Alberta Agriculture, Food, and Rural Development], Livestock Engineering Unit & Environmental Practices Unit, Technical Services Division, Alberta Agriculture, Food and Rural Development, 2005.
- [17] USCC, Compost specification for soil incorporation, USCC [United States Composting Council], n.d.
- [18] P. P. Reddy, Organic farming for sustainable horticulture: Principles and practices, Scientific Publishers, 2008, pp. 11-12, 22-30.
- [19] P. K. Gupta, Soil, Plant, Water and Fertilizer Analysis, 2 dü., Jodhpur: Dr. Updesh Purohit for Agrobios, 2007, pp. 298-301, 307-313, 318-319.
- [20] J. R. Okalebo, K. W. Gathua ve P. L. Woomer, Laboratory Methods of Soil and Plant Analysis: A Working Manual, 2 dü., Nairobi: SACRED Africa [The Sustainable Agriculture Centre for Research Extension and Development in Africa], 2002, pp. 28, 77, 98, 100.
- [21] CCQC, Compost Maturity Index, 19375 Lake City Road, Nevada City, CA: CCQC [California Compost Quality Council], 2001.
- [22] Woods End Research Laboratory, «Interpretation of Waste and Compost Tests, » Journal of the Woods End Research Laboratory, cilt 1, no. 4, pp. 1998-2000, 2000.
- [23] T. Richard ve N. Trautmann, «[http://compost.css.cornell.edu/calc/cn\\_ratio.html](http://compost.css.cornell.edu/calc/cn_ratio.html), » Cornell University, Cornell Waste Management Institute, Cornell Composting Science and Engineering, 1996. [Çevrimiçi]. Available: [http://compost.css.cornell.edu/calc/cn\\_ratio.html](http://compost.css.cornell.edu/calc/cn_ratio.html). [Erişildi: 8 June 2020].
- [24] FAO, FAO Soils Bulletin 56, Oxford University Press & FAO [Food and Agriculture Organization of the United Nations], 1985, pp. 19-20, 22, 28.
- [25] K. Simpson, Fertilizers and Manures, London & New York: Longman, 1986, pp. 11-13, 83-84.
- [26] A. E. Baffour, «Co-Composting of Dewatered Sewage Sludge (Biosolids) and Sawdust for Agricultural use as an Organic Fertilizer: A Case Study of the KNUST Sewage Treatment Plant, » KNUST Space, Institutional Repository for KNUST, 2009.
- [27] AASLAB, Compost Analysis Report, Pennsylvania: Agricultural Analytical Services Laboratory, Pennstate Extension, Pennsylvania State University, 2019, p. 2.
- [28] Government of Alberta, «Compost Nutrients, » Alberta, 2014.
- [29] TNAU, Organic farming, TNAU Agritech Portal, TNAU [Tamil Nadu Agricultural University], Coimbatore, 2008.
- [30] Plant Natural Research Center, «Benefits of Using Compost in Your Garden, » Plant Natural Research Center, n.d. [Çevrimiçi]. Available: <https://www.planetnatural.com/composting-101/soil-science/compost-soil/>. [Erişildi: 12 June 2020].
- [31] NDEP, «Compost Specifications, » NDEP [Nevada Division of Environmental Protection], n.d.
- [32] Celnigns Analytical, Ash Content of Compost, n.d.
- [33] T. Richard, «Estimating Carbon Content, » Cornell Waste Management Institute, Cornell University, Ithaca, 1996.
- [34] Compost Tuner, « <https://compost-turner.net/>, » Compost Tuner, n. [Çevrimiçi]. Available: <https://compost-turner.net/composting-technologies/factors-affect-composting-process-and-compost-quality.html>. [Erişildi: 12 August 2020].
- [35] Hill Lab, Guidelines for interpreting your compost analysis report, Hill-laboratories, n.d., pp. 1-3.
- [36] C. F. Reed, Information summaries on 1000 economic plants. Typescripts submit to USDA, 1976.
- [37] C. Shouliang ve S. M. Phillips, «169. PASPALUM Linnaeus, Syst. Nat., ed. 10, 2: 855. 1759, » Flora of China, cilt 22, p. 526–530, 2006.

## Uses of Bioslurry (Biogas Residue) as Inexpensive Product for Animal Feed

*Abdol Hossain Ataei\**, Department of Animal Science, Graduate School of Natural and Applied Science, Ege University, İzmir, Turkey

*Figen Kırkpınar*, Department of Animal Science, Faculty of Agriculture, Ege University, İzmir, Turkey

*Helin Atan*, Department of Animal Science, Graduate School of Natural and Applied Science, Ege University, İzmir, Turkey

\*Corresponding author: [ab.ataei@gmail.com](mailto:ab.ataei@gmail.com)

**Keywords:** Animal feed, biogas, bioslurry, sustainable, waste

**Discipline:** Agricultural Engineering

### Abstract

Due to the increasing prices of fossil fuels and global warming, the extension and utilization of renewable energy resources has becoming an important component of a sustainable global energy strategy. Biogas is a clean, efficient, and renewable source of energy, which used as a substitute for other fuels in order to save energy. A biogas system is a combustible mixture of gases (mainly composed of 50 to 70 percent methane, 30 to 40 percent carbon dioxide) produced by micro organisms when livestock manure and other biological wastes are allowed to ferment in the absence of air in closed containers that it results in two end-products: energy-rich biogas and nutrient-rich digestion residue. Biogas can be used directly for cooking and for generation of electricity and heat. While biogas is used to produce energy, the large potential of bioslurry has often been overlooked. One of the outputs of a biodigester, next to the biogas, is bioslurry. The digested mixture of liquids and solids ‘bioslurry’ and ‘biosludge’ are mainly used as organic fertiliser for crops and many other purposes. Bioslurry is not only a good fertilizer; it also provides an excellent animal feed, both directly and indirectly.

Dried bioslurry can safely be used as a feed supplement to cattle, fish, and poultry. Most of ammonia nitrogen in bioslurry can be utilized by a growing bacterial biomass, to be converted into amino acids. Also, the fermentation process also produces B<sub>12</sub> vitamin in considerable amounts. Feeding animals with animal waste is a common practice, but since in the biodigester, pathogens from the livestock manure are mostly eliminated and minerals become more readily available for take-up, so uses of animal waste to run a biogas system and then feed the biogas slurry to animal feed, it is better than raw waste as feed. Also feeding of bioslurry results in reducing feed cost and a lower price of animal products; it contributes to self-sufficiency in protein, phosphorus and other expensive nutrients in feed rations.

It is concluded that bioslurry of biogas can be used as a locally sourced, reliable and inexpensive source of feed in countries where there is a shortage of animal feed, as well as a high rate of degradation of pastures and forests, leading to sustainable agricultural production.

The purpose of this review is to reveal the potential availability of biogas slurry that can be inexpensive product in animal nutrition and producing is to promote.

### Introduction

Due to the increasing prices of fossil fuels and global warming, the extension and utilization of renewable energy resources has becoming an important component of a sustainable global energy strategy. Climate change and greenhouse gases make matters more complex when developing an efficient and sustainable strategy for the animal production sector [1]. Also, slurries of animal farming and animal manure is an important part of the agricultural sector in most countries, accounting for 18% of worldwide greenhouse gas emissions [2]. At the global level, 80% of people without access to clean cooking in rural areas, and they have 60% of the world’s rural population. Also, less than 15% of the urban population globally lacks access to clean cooking, thanks to wider access to cleaner options [3]. Finding alternative, clean and economical sources of energy has nowadays become a major concern for households’ and nations’ economies. Besides, the increasing costs and pressure concerned with waste disposal stress the need for a reappraisal of the utilization of wastes. Therefore, modern science must emphasize for research on the management of wastes, its processing technology, and subsequent feeding value for livestock [4]. In fact, biological treatments are the clearest alternative for treating such waste, and these technologies can maximize the recycling and recycling of waste components. The recycling and utilization of organic wastes and by-products through development of a cost-effective, socially accepted and environmentally friendly technology is essential because the widespread accumulation of



this waste increases pollution and also causes disposal problems [5]. Among biological treatments, biogas technology can make a major contribution to climate protection and resource conservation, that it is one of the most potential technologies of biomass and bioenergy by using agricultural waste materials as feedstocks [6,7, 8, 9]. By-products of agriculture, mainly animal wastes and crop residues, are the primary inputs for biogas plants.

Biogas is a clean, efficient, and renewable source of energy, which used as a substitute for other fuels in order to save energy. A biogas system is a combustible mixture of gases (mainly composed of 50 to 70 percent methane (CH<sub>4</sub>), 30 to 40 percent carbon dioxide (CO<sub>2</sub>) produced by micro organisms when livestock manure and other biological wastes are allowed to ferment in the absence of air in closed containers that it results in two end-products: energy-rich biogas and nutrient-rich digestion residue [10].

Almost 95% of people in Africa use solid biomass, in the form of fuelwood, charcoal or dung in open fires [3]. Biogas can be used directly for cooking and for generation of electricity and heat. While biogas is used to produce energy, the large potential of bioslurry of biogas has often been overlooked. One of the outputs of a biodigester, next to the biogas, is bioslurry [11]. The digested mixture of liquids and solids 'bio-slurry' and 'bio-sludge' are mainly used as organic fertiliser for crops and many other purposes. Bioslurry is not only a good fertilizer; it also provides an excellent animal feed, both directly and indirectly. Bioslurry treatment increases the feed value of fodder with low protein content [12]. Bioslurry can safely be used as a feed supplement to cattle, fish, and poultry. Most of ammonia nitrogen in bioslurry can be utilized by a growing bacterial biomass, to be converted into amino acids. Also, the fermentation process also produces B<sub>12</sub> vitamin in considerable amounts.

Feeding animals with animal waste is a common practice, but since in the biodigester, pathogens from the livestock manure are mostly eliminated and minerals become more readily available for take-up, so uses of animal waste to run a biogas system and then feed the biogas slurry to animal feed, it is better than raw waste as feed. Also feeding of bioslurry of biogas results in reducing feed cost and a lower price of animal products; it contributes to self-sufficiency in protein, phosphorus and other expensive nutrients in feed rations [13, 14, 15, 16]. Bioslurry of biogas can be used as a locally sourced, reliable and inexpensive source of feed in countries where there is a shortage of animal feed, as well as a high rate of degradation of pastures and forests, leading to sustainable agricultural production.

The purpose of this review is to reveal the potential availability of bioslurry beside of biogas that can be inexpensive product in animal nutrition and producing is to promote.

### **Population, pollution and greenhouse gases**

World population is growing that estimated in 2050, the global population will reach around 9 billion, 50% increase since 2007. These people need to be fed. Therefore, agriculture production and efficiency must be increased. While, climate change and agriculture are interrelated [17]. Also, animal production systems are a major source of pollution affecting the quality of water, soil and air [17, 18]. Moreover, each year approximately 38 billion metric tons of organic wastes are produced all over the world in this regard was reported that, every year consumers in rich countries waste almost as much food (222 million tonnes) as the entire net production of food in Sub-Saharan Africa (230 million tonnes) [19]. As waste materials cannot always be used or are considered disposable so burning and precipitation have always been the result [20]. The changes in the global climate system and the demand for more food together with more meat production for the growing population will require innovations in policies as well as institutions. A solution can be found in a combination of energy optimization technology and agricultural productivity improving such as biodegrades [21].

The most important greenhouse gases from such activities include CO<sub>2</sub>, CH<sub>4</sub>, and N<sub>2</sub>O (US Environmental Protection Agency (EPA), 2007) while CH<sub>4</sub> is an important greenhouse gas with the ability of global warming 25 times greater than that of CO<sub>2</sub> [22].

When technical, economic, environmental, and social effects of alternative energy sources such as biogas, wind, hydroelectric, solar, and geothermal energy are evaluated, it is concluded that biogas technology is one of the alternative means regarding renewable energy [23]. Biogas produced from animals' dung and human excrement, together with the by-product bioslurry, can be a solution to poverty, climate change and soil fertility problems [17].

### **Biogas in the world**

It is very important that this increased energy requirement is from sustainable and environmentally friendly resources [24]. In 2019, bioenergy power generation increased an estimated 5%, and in the Sustainable Development Scenario (SDS), electricity generation from bioenergy increases 6% annually through 2030. Full utilisation of the sustainable potential could cover some 20% of today's worldwide gas demand [3].

Today there is around 18 GW (gigawatt) of installed power generation capacity running on biogas around the world, most of which is in Germany, the United States and the United Kingdom. Because of changes in policy support, although growth has started to pick up in other markets such as China and Turkey [3]. According to the World Energy Council, there is still significant potential to expand biogas for energy use by tapping the large volumes of unused residues and wastes [10].

The potential of biogas is significant in developed as well as developing countries. Some countries are using biogas energy at a significant level. Finland obtains 15% of its total energy this way, Sweden 9%, and the USA 4% [25]. In developing countries, however, biogas is mainly used for cooking and lighting purpose. In China for example, approximately 8 million small farm scale biogas digesters are generating gas for cooking and lighting [26].

### **Biogas in Turkey**

The impact of the oil crisis in the world in the early 1980s, Rural Services Ankara Soil Water a biogas unit was established at the Research Institute and dissemination activities throughout the country and studies of biogas accelerated [27, 28]. Animal wastes not used in biogas production in Turkey are mostly either directly burned or given to agricultural land as fertilizer. In this way, the desired quality of heat cannot be produced, and it is not possible to use the wastes as fertilizers after heat generation [29]. Furthermore, approximately 6.5 million houses use wood as the main fuel for heating purposes in Turkey [24]. However, Turkey has rich biogas potential, but there is not enough study regarding the evaluation of this potential and the contribution to the economy has not been calculated.

According to data for TÜİK (Turkish Statistical Institute) 2018, Turkey's energy import is 43 billion dollars that by conversion biomass waste will be meet 20% of energy import. Most of the people living in Turkey provide livelihood from livestock. Therefore, Turkey is rich in animal waste and manure.

Turkey has a total of 75.178 culture cattle, 73.716 breed cattle, 28.784 domestic cattle, and 1588 buffalos 2.525.385 meat-hen, 11.769 goose, 1.184.814 egg-hen, and 5624 ducks in 2007–2019 (\*thousand). The total amount of wet manure is calculated to be 1.472.223 kt (Kilotons) of bovine animal, 284.892 kt of sheep and goats, and 61.904 kt of poultry for Turkey between 2007 and 2019 [30, 31]. The finding of study by Caliskan and Ozdil [31] demonstrate that  $76.448 \times 10^6 \text{ m}^3$  potential of  $\text{CH}_4$  content can be obtained from biogas, and  $2.339.296 \times 10^6 \text{ MJ}$  potential of heating value can be obtained from this  $\text{CH}_4$  value. While the potential of electricity energy, which can be provided from animal manure wastes, has been  $231.009 \times 10^6 \text{ kW}$  between 2007 and 2019 in Turkey.

### **Biogas and biogas slurry**

Biogas is a mixture of  $\text{CH}_4$ ,  $\text{CO}_2$  and small quantities of other gases produced in biogas plants by the bacterial degradation of biomass under anaerobic conditions [3]. Depending on the feeding substance in the biogas plant, the  $\text{CH}_4$  content of the biogas slurry between 50% and 75%. The second main component of biogas is carbon dioxide ( $\text{CO}_2$ ) with a share between 25% and 50%. Other components of biogas are water ( $\text{H}_2\text{O}$ ), oxygen ( $\text{O}_2$ ) and traces of sulfur ( $\text{S}_2$ ) and hydrogen sulfide ( $\text{H}_2\text{S}$ ) [10]. The precise composition of biogas depends on the type of feeding substance and the production pathway [3]. The formation of biogas can occur either in natural environment or controlled conditions in constructed biogas plants (anaerobic degradation) [32]. However, biogas is a clean, environmental friendly and renewable form of energy.

Biogas slurry is a by-product of anaerobic digestion that produced from biogas plant and also produces biogas [16]. A biogas digester can be filled with locally-available raw materials, crop residues, and animal and human waste such as urine and dung. 'During digestion, about 25-30% of the total dry matter of animal/human wastes will be converted into a combustible gas and a residue of 70-75% of the total solids content of the fresh dung comes out as sludge which is known as digested slurry or biogas slurry [33]. The organic fraction of slurry may contain up to 30-40 percent of lignin, undigested cellulose

and lipid material, on a dry weight basis. The remainder consists of substances (mineral, salts, etc.) originally present in the raw materials but not subject to bacterial decomposition [34].

### **Benefits of biogas-slurry**

Biogas slurry has many positive effects to improving fertiliser qualities, reducing odours, it is pathogen-free and provide inexpensive feed for animals.

1. Soil conditioner as it contains 10-fold of humic acid.
2. Comprehensive nutrition and high quality.
3. Pro-biotic microbial-derived bioactivator
4. May serve as pesticide and organic fungicide and it is pathogen-free.
5. Good mixing materials for vermicompost fertilizer, mushroom culture media, pond fertilizer.
6. As animal feeds [35].

### **Forms of bioslurry**

There are many ways of using bioslurry, ranging from direct application as a liquid to solid application through drying or compositing.

**Liquid form:** The liquid form can be applied through foliar spraying, a bucket, or irrigation canal. In this way the bioslurry can be applied directly to the crops or feed to fish ponds [17]. But this method is mostly used to produce agricultural products.

**Dried form:** Farmers prefer the dry form of bioslurry because it is easier to transport and utilization than the liquid form. However, the dried bioslurry loses part of its nitrogen and therefore the nutrient value of the bioslurry is decreased [36].

**Composted form:** The composted form of bioslurry is the best way to overcome the transportation issue related to liquid bioslurry and the nutrient loss of the dried form. Indeed, this form is more used for production of agricultural products [11].

### **Feeding substance (feedstock)**

A range of different feedstocks can be used to produce biogas production. The different individual types of residue or waste were grouped into four broad feedstock categories: crop residues; animal manure, industrial organic waste and wastewater sludge [3, 32].

**Crop residues:** Residues from the harvest of wheat, maize, rice, other coarse grains, sugar beet, sugar cane, soybean and other oilseeds.

**Animal manure:** From livestock including cow, poultry, sheep or pig manure. The manure is an excellent feedstock substrate for biogas plants; with a carbon to nitrogen (C:N) ratio of around 25:1 and rich in various nutrients necessary for the growth of anaerobic microorganisms [10].

**Industrial organic waste:** Food and food-processing industry waste, green waste, paper and cardboard and wood that is not otherwise utilised.

**Wastewater sludge:** Solid organic waste and semi-solid organic matter that recovered in the form waste from private households and municipalities [3].

### **Nutrient values and composition of bioslurry**

Bioslurry is made up of 93% water and 7% dry matter, of which 4.5% is organic matter and 2.5% inorganic matter. Bio-slurry differs biochemically from the original raw material as it contains bioactive substances. The digested biogas slurry contains essential elements such as potassium, zinc, iron, manganese and copper among others [16]. So bioslurry of biogas contains a considerable amount of both macro and micro nutrients and easily-available plant nutrients than composted manure and farm yard manure [37]. In fact, Animals retain only 5-50% of the nutrient elements depending on animal species, in the feed. The major fraction (roughly 50-95%) is excreted via dung and urine, and animal manure therefore is a valuable source of nutrients [38]. The percentage of N, P and K content of the slurry on wet basis is 0.25, 0.13 and 0.12 while on dry basis it is 3.6, 1.8 and 3.6 respectively [35]. However, the form of nutrients is much more affected by anaerobic digestion. More than 50% of  $\text{NH}_4$  can be lost from uncovered bioslurry in one month. In addition, up to 50% of the organic N is converted to ammonium ( $\text{NH}_4$ ), while Because of the higher pH in bioslurry compared to farmyard manure; the fraction of available phosphorus (P) seems to be reduced during digestion [15]. Moreover, Nutrient availability in bioslurry is reported to be much higher than other undigested sources [39]. The digestion

process improves nutrient content of bioslurry [40]. Values between Nutritional value in biogas slurry 10% [41] and more than 70% [42] have been reported. Although, The nutrient composition of bioslurry of biogas varies between studies, that it depends upon several factors: the kind of dung and other feedstock, water, animals, and type of digester and the anaerobic process [11].

### **Biogas slurry as feed for animal**

The benefits of biogas systems not only collecting biogas for energy purpose but also taking bioslurry as fertilizer for fish raising [43]. Digested slurry has been experimentally used to supplement cattle, poultry and fish feed, ranging from direct application as a liquid to solid application through drying or compositing. Xi-Yan et al. [44] reported that biogas fermentative residue, which has abundant amino acid, vitamin, mineral and beneficial biology active matter, has been widely used in breeding industry. However, studies found on this subject recommended to use slurry as animal feed only in times of feed scarcity, or to use it as an additive to the normal diet. Experience also shows that the full potential of biogas use is often not fully utilized. Many farmers who use anaerobic digestion are not fully aware of the different benefits and risks of biogas use, and those who do are often not trained in how to apply biogas in each particular case [11]. The following subsections describe the various experiments performed in this field.

### **Bioslurry in aquaculture and fish feed**

For the aquaculture sector, the use of biogas slurry for fish pond fertilization has become increasingly important in recent years by small scale fish farmers basically to increase biological productivity of fish ponds. Duong et al. [45] concluded that supplementation of homemade feed to bioslurry and pig waste has positive effect on the growth and yield of fish species of Tilapia, Snakeskin gourami, Kissing gourami and Common carp. Ngan, et al. [43] found that feeding by 50% commercial feed and 50% bioslurry from biogas plant produces similar fish productivity to that of feeding by 100% commercial feed. Also, they reported that it is possible to raise fish with bioslurry feeding with or without giving any nutrients supplementary or chemical fertilizers [43]. However, in contrast to Ali et al. [46] concluded that growth and production performance of carp fish were higher in supplementary feed treatment compared with other treatments with biogas slurry or slurry + cow dung. But, Kaur et al. [47] reported growth rates of the fish were 3.54 times higher in biogas slurry-treated tanks than in the controls. Also, a study showed 10-fold increase of bioslurry over the control and 3.6-fold increase of bioslurry over the conventional feed in fish yield [48]. Seghal et al. [49] showed that both phyto- and zooplankton populations increased with addition of biogas slurry, compared to the control into the ponds.

In another study, results showed that the biogas slurry of using mango-processing wastes have been utilized for the production of fresh-water fishes, such as carp, rohu among others [50]. Indeed, the nutrients in biogas slurry and manure promote growth of algae and plankton that can serve as fish feed. So, biogas slurry can lead to similar fish production as with commercial fish feeds [15]. Sophin and Preston [51] concluded that all of the five fish species (Tilapia, Silver carp, Bighead carp, Silver barb and Mrigal) grew faster in ponds fertilized with biogas slurry than with manure. Biogas slurry is considered to be a suitable input to the fish ponds because of its high organic and N and P contents [52]. In addition, the application of bioslurry into a fish pond could keep the pH range at an optimal for fish growth and avoid growth of algae [43]. Therefore, it is necessary to address the organic aquaculture by applying biogas slurry and cow dung in polyculture system to enhance the fish production with low cost input and pollution free environment [46].

On the other hand, biogas slurry can be stimulated worm growing can be stimulated and the worms can be used as feed for fish. The worms can be utilized one to two weeks after the biodigester pit is filled [53]. In Vietnam, the use of biogas slurry as a feeder for fish nurseries saved 67% of fish feed costs, in addition, biogas slurry increases the yield by 12% [54]. Use of raw animal manure in fish ponds creates a greater demand for oxygen than bio digester slurry of animal manure. This can lead to more death of fish [53]. Islam et al. [55] concluded that the microbial load after treatment of animal manure via biogas system was grossly reduced and the reduction of bacterial pathogen depends on the duration and temperature of digestion.

### **Bioslurry as feed for monogastrics and poultry feed**

The experiment has revealed that the digested slurry from biogas plant provides 50% of the total feed requirement of ducks [56]. Also, in the poultry nutrition indirectly biogas slurry can be used as a fertilizer in water to allow algae to grow and then dried algal biomass has been used as a poultry feed component. In economic terms the system appears promising [57]. While, Wang et al. [58] showed that the average daily gain of experimental group fed with basal diet added 40%, 60% and 80% biogas slurry higher than that of control group fed with basal diet. However, the data revealed that the biogas slurry may be limited to 10 percent in growing pig diets. Zhang et al. [59] showed that nutrients needed for swine growth were contained in biogas slurry. They showed that apparent digestibility in various nutrients compared to control group non-significant difference. Also, the results of slaughtering trails these authors indicated that content of water, crude ash, protein and trace elements were increased in trace the diet containing biogas slurry; moreover, pork sensory and physical properties were within the pork health standards that indicated that pork with feeding biogas slurry was safe and edible [59]. In addition, negative effects on the flavor or hygienic quality of the meat were not noticed [60]. Also determined that the use slurry of biodigester for pig feed saves around €9 to €11 in feed costs. The biogas slurry can be used in rotation to feed pigs. Feed intake increase by 8 to 30% and the health of the pigs improves significantly. While, small piglets may have diarrhea by using it [53].

### **Bioslurry as feed for ruminants**

The experiment has revealed that the digested slurry from biogas plant provides 10 to 15% of the total feed requirement of some cattle [56]. Saxena et al [61] recommended that in times of fodder scarcity, bioslurry of biogas could be used as emergency feed. They found weight maintenance of crossbred bulls were stable who were partially fed with biogas slurry for 21 days. It was shown that the use of digested cattle slurry from a biogas plant in sheep nutrition in the form of oven-dried and sun-dried is edible when mixed with wheat bran, and can be fed to sheep according to a maintenance ration of up to 30% wheat bran replacement with bioslurry of biogas, and no significant effect was observed on the dry matter consumption and digestibility of nutrients or on the nutrient balances [62]. Additionally, the nutrients uptake and balance of N, K and P in sheep remained the same compared to the control group. However, they suggested that fed dried slurry of biogas with wheat bran (control group) together form a good and nutritious feed for sheep [62]. Saxena et al. [61] reported that protein content of dung enhances 8% to about 15% in the digested slurry, because of fermentative processes in the biogas plant.

### **Result and Conclusion**

Feeding of biogas slurry results in reducing feed cost and a lower price of animal products; it improves the quality of the manure that is fed into the bio digester, resulting in higher-quality nutrients for fish ponds and animals' feed. In theory, using biogas slurry for animal feed follows the same logic, yet studies on this particular topic are scarce [11].

Just, biogas slurry is low in energy content. In conclusion, big gas slurry can be a source to feed animals compared to the raw manure from which it is produced, since digestion upgrades even poor quality raw manure.

Different results were obtained from studies. However, the differences between the results of the studies can be due to several reasons, like the characteristics of different types of biogas source, storage and handling, crop types, soil and climate conditions, or differences in methodologies to assess the value of biogas slurry as a fertilizer.

However, to make the best use of biodigester as fish ponds and animals feed, it is necessary to improve our knowledge of the changes that occur in the biological and chemical properties of the substrate during the biological digestion process.

### **References**

- [1] Von Braun J. The role of livestock production for a growing world population. In Lohmann Information 2010 Aug (Vol. 45, No. 2, pp. 3-9).
- [2] Reist S, Hintermann F, Sommer R. La revolución ganadera: Una oportunidad para los productores pobres. InfoResources Focus. 2007;1 (07): 1-6.

- [3] IEA, Outlook for biogas and biomethane: Prospects for organic growth, IEA (2020), Paris <https://www.iea.org/reports/outlook-for-biogas-and-biomethane-prospects-for-organic-growth>
- [4] Ajila CM, Brar SK, Verma M, Tyagi RD, Godbout S, Valéro JR. Bio-processing of agro-byproducts to animal feed. *Critical reviews in biotechnology*. 2012 Dec 1; 32 (4): 382-400.
- [5] Raj D, Antil RS. Evaluation of maturity and stability parameters of composts prepared from agro-industrial wastes. *Bioresource Technology*. 2011 Feb 1; 102 (3): 2868-73.
- [6] Chung JN. Grand challenges in bioenergy and biofuel research: engineering and technology development, environmental impact, and sustainability. *Frontiers in Energy Research*. 2013 Sep 30;1:4.
- [7] Chung JN. A theoretical study of two novel concept systems for maximum thermal-chemical conversion of biomass to hydrogen. *Frontiers in Energy Research*. 2014 Jan 2; 1: 12.
- [8] Tonini D, Martinez-Sanchez V, Astrup TF. Material resources, energy, and nutrient recovery from waste: are waste refineries the solution for the future? *Environmental Science & Technology*. 2013 Aug. 6; 47 (15): 8962-9.
- [9] Wang J. Decentralized biogas technology of anaerobic digestion and farm ecosystem: opportunities and challenges. *Frontiers in Energy Research*. 2014 Mar 26; 2: 10.
- [10] Wellinger A, Murphy JD, Baxter D, editors. *The biogas handbook: science, production and applications*. Elsevier; 2013 Feb 19.
- [11] Groot LD, Bogdanski A. *Bioslurry= brown gold? A review of scientific literature on the co-product of biogas production*. Food and Agriculture Organization of the United Nations (FAO); 2013.
- [12] Consolidated Management Services. *Biogas Technology: A Training Manual for Extension*, Food and Agriculture Organization of the United Nations. Kathmandu, Nepal. (1996) Support for Development of National Biogas Programme (FAO/TCP/Nep/4451-T).
- [13] Muller ZO. *Feed from animal wastes: state of knowledge*. FAO; 1980.
- [14] Philipp W, Hoelzle LE. Germs in digestates from biogas plants? *Gefahrstoffe Reinhaltung der Luft*. 2012 May 1; 72 (5): 216-20.
- [15] Bonten LT, Zwart KB, Rietra RP, Postma R, De Haas MJ, Nysingh SL. *Bio-slurry as fertilizer: is bio-slurry from household digesters a better fertilizer than manure? A literature review*. Alterra, Wageningen-UR; 2014.
- [16] Kumar S, Malav LC, Malav MK, Khan SA. *Biogas slurry: source of nutrients for eco-friendly agriculture*. *International Journal of Extensive research*. 2015; 2: 42-6.
- [17] Warnars L, Oppenoorth H. *Bioslurry: A supreme fertilizer. A study on bioslurry results and uses*. Hivos, The Hague, Netherlands. 2014.
- [18] Liedl BE, Bombardiere J, Chatfield JM. *Fertilizer potential of liquid and solid effluent from thermophilic anaerobic digestion of poultry waste*. *Water Science and Technology*. 2006 Apr; 53 (8): 69-79.
- [19] Gustavsson J, Cederberg C, Sonesson U, van Otterdijk R, Meybeck A. *Global food losses and food waste-FAO Report*. Food and Agriculture Organization (FAO) of the United Nations. 2011: 1-37.
- [20] Kiyasudeen K, Ibrahim MH, Quaik S, Ismail SA. *Prospects of organic waste management and the significance of earthworms*. Springer; 2015 Dec 14.
- [21] Lybbert T, Sumner D. *Agricultural technologies for climate change mitigation and adaptation in developing countries: policy options for innovation and technology diffusion*. The International Food & Agricultural Trade Policy Council. May 2010 Issue Brief No. 6.
- [22] Change IP. *Climate change 2007: The physical science basis*. *Agenda*. 2007 May 31;6 (07): 333.
- [23] Baris K, Kucukali S. *Availability of renewable energy sources in Turkey: Current situation, potential, government policies and the EU perspective*. *Energy Policy*. 2012; 42: 377-391
- [24] Sarıkoç S. *Bioenergy Potential of Turkey's Forest Sources, Biomass Energy Conversion Methods, Products, and Applications*. *InRenewable Energy 2020 Jul 8*. IntechOpen.
- [25] Demirer GN, Duran M, Guven E, Ugurlu O, Erguder TH, Tezel U. *Biyokütle Enerjisine Bir Örnek: Anaerobik Yöntemlerle Organik Atıklardan Biyogaz Eldesi*. III. Ulusal Temiz Enerji Sempozyumu. 2000; 2: 15-7.
- [26] Anonymus. *Basic data on biogas*. SGC (Swedish Gas Company). Sweden. Available online at: <http://www.sgc.se/dokument/BiogasfolderengA5.pdf>. 2007.

- [27] Naçar Koçer N, Öner C, Sugözü İ. Türkiye’de hayvancılık potansiyeli ve biyogaz üretimi. Doğu Anadolu Bölgesi araştırmaları. Fırat Üniversitesi Mühendislik Fakültesi Çevre Mühendisliği Bölümü, Elazığ, Türkiye. 2006: 17-20.
- [28] Bilgin N. Biyogaz nedir? Tarım ve Köyişleri Bakanlığı Köy Hizmetleri Genel Müdürlüğü Ankara Araştırma Enstitüsü. 2003.
- [29] Tufaner F, Avşar Y, Dere T, Gönüllü MT. Türkiye’de biyogaz tesisi projelerinde başarı ve başarısızlık nedenlerinin analizi ve merkezi biyogaz tesislerinin önemi. Ulusal Kompost ve Biyogaz Çalıştayı. 2013: 11-4.
- [30] TÜİK, Turkish Statistical Institute. Turkey statistic for 2020. [http://www.turkstat.gov.tr/PreTablo.do?alt\\_id=1002](http://www.turkstat.gov.tr/PreTablo.do?alt_id=1002). 2020.
- [31] Caliskan M, Ozdil NF. Potential of Biogas and Electricity production from animal waste in Turkey. *BioEnergy Research*. 2020 Sep. 14: 1-0.
- [32] Yohannes MT. Biogas potential from cow manure–influence of diet. Master degree thesis. Swedish University of Agricultural Sciences. 2010.
- [33] Gurung B. Training programme on proper use of slurry for the technical staff of SNV/BSP. A training manual. 1998.
- [34] Lam J, ter Heegde F. Domestic biogas compact course. *Technology and Mass-Dissemination Experiences from Asia*. 2010.
- [35] Kalinda T. An assessment of the challenges affecting smallholder farmers in adopting biogas technology in Zambia. *Energy and Environment Research*; Vol. 9, No. 1; 2019.
- [36] Debnath G, Jain MC, Kumar S, Sarkar K, Sinha SK. Methane emissions from rice fields amended with biogas slurry and farm yard manure. *Climatic Change*. 1996 May 1; 33 (1): 97-109.
- [37] Ishikawa S, Hoshiba S, Hinata T, Hishinuma T, Morita S. Evaluation of a biogas plant from life cycle assessment (LCA). In *International Congress Series 2006 Jul 1*, Vol. 1293, pp. 230-233. Elsevier.
- [38] Oenema O, Oudendag D, Velthof G. Nutrient losses from manure management. *DIAS report*. 2006: 25.
- [39] Makádi M, Tomócsik A, Orosz V. Digestate: a new nutrient source–review. *Biogas*. 2012 Mar 14; 295: 312.
- [40] Chiyoka W. Characterization of nutrient release and greenhouse gas emission from Chernozemic soils amended with anaerobically digested cattle manure. Thesis of Master of Science. Faculty of Graduate Studies at the University of Manitoba, 2011.
- [41] Möller K, Müller T. Effects of anaerobic digestion on digestate nutrient availability and crop growth: a review. *Engineering in Life Sciences*. 2012 Jun; 12 (3): 242-57.
- [42] Massé DI, Croteau F, Masse L. The fate of crop nutrients during digestion of swine manure in psychrophilic anaerobic sequencing batch reactors. *Bioresource technology*. 2007 Nov 1; 98 (15): 2819-23.
- [43] Ngan NV, Van Be N, Du NX. Study on fish growing in hapa conditions using bio-slurry from co-digestion process. *International Journal of Advanced Scientific Research and Management*, Vol. 2 Issue 6, June 2017.
- [44] Xi-yan ZH. Comprehensive utilization of biogas fermentative residue in the breeding industry. *Journal of Anhui Agricultural Sciences*. 2009; 26.
- [45] Duong NL, Lam ML, Phan CO, Bui CT, Yamada R, Caldwell JS. Effects on fish yield and environmental quality of biogas digestion and supplemental fish feed in integrated pig–fish production in Tan Phu Thanh, Can Tho. In *Viet Nam: JIRCAS workshop, Cantho University 2010*.
- [46] Ali MH, Salam MA, Rashid MH, Barman AC, Bashar MA. Fish culture in ponds by using bio-gas slurry and raw cow dung in carp polyculture system. *Journal of Agro forestry Environment*. 2008; 2 (2): 151-4.
- [47] Kaur K, Sehgal GK, Sehgal HS. Efficacy of biogas slurry in carp, *Cyprinus carpio* var. *communis* (Linn.), culture-effects on survival and growth. *Biological Wastes*. 1987 Jan 1; 22 (2): 139-46.
- [48] Balasubramanian PR, Bai RK. Biogas-plant effluent as an organic fertiliser in fish polyculture. *Bioresource Technology*. 1994 Jan 1; 50 (3): 189-92.
- [49] Sehgal HS, Kaur K, Sehgal GK. Phytoplankton response to biogas slurry in carp ponds. *Bioresource Technology*. 1991 Jan 1; 37 (3): 229-34.

- [50] Mahadevaswamy M, Venkataraman LV. Integrated utilization of fruit-processing wastes for biogas and fish production. *Biological Wastes*. 1990 Jan 1; 32 (4): 243-51.
- [51] Sophea K, Preston TR. Comparison of biodigester effluent and urea as fertilizer for water spinach vegetable. *Livestock Research for Rural Development*. 2001 Dec; 13 (6).
- [52] Edwards P, Polprasert C, Rajput VS, Pacharaprakiti C. Integrated biogas technology in the tropics. 2. Use of slurry for fish culture. *Waste Management & Research*. 1988 Jan 1; 6 (1): 51-61.
- [53] Netherlands Development Institute (SNV). On: <http://www.snvworld.org/en/publications/bio-slurry-management-and-its-effect-on-soil-fertility-and-crop-production> Ssendangire, W. Application and utilization of bioslurry. 2013 Power point presentation.
- [54] Netherlands Development Institute (SNV). Technology and mass- dissemination experiences from Asia. Biogas compact course PPRE- Oldenburg University April 26 - 28, 2011.
- [55] Islam MA, Biswas P, Sabuj AA, Haque ZF, Saha CK, Alam MM, Rahman MT, Saha S. Microbial load in bio-slurry from different biogas plants in Bangladesh. *Journal of Advanced Veterinary and Animal Research*. 2019 Sep; 6 (3): 376.
- [56] [56] Gunnerson C, Stuckey D. Integrated resource recovery. *Anaerobic digestion: principles and practices for biogas systems*. The World Bank 1986 Apr 30.
- [57] Lansing S, Martin JF, Botero RB, Da Silva TN, Da Silva ED. Wastewater transformations and fertilizer value when co-digesting differing ratios of swine manure and used cooking grease in low-cost digesters. *Biomass and Bioenergy*. 2010 Dec 1; 34 (12): 1711-20.
- [58] Wang LK, Yuan BF, Guo WY, Chen K. Effect of biogas slurry on weight gain of fattening pigs. *Journal of Anhui Science and Technology University*. 2008; 22 (6): 5-8.
- [59] Zhang HB, Li JR, Shao KW. Safety and effect of biogas slurry in swine feed. *Acta Ecologiae Animalis Domastici*. 2009; 3: 68-72.
- [60] Tong: W. Research on feeding pigs with anaerobic digested effluent as supplementation of mixed concentrate rations. *Biogas Forum*. 1995. Vol. IV. No. 63. pp 8-15.
- [61] Saxena KK, Nath K, Srivastava SK. The effect of using dung from cattle fed high-, low-or no-concentrate rations, on the quality and nutritive value of slurry from a biogas plant. *Biological wastes*. 1989 Jan 1; 28 (1): 73-9.
- [62] Saxena KK, Ranjhan SK. Nutritive value of digested cattle slurry from a biogas plant in sheep. *Agricultural Wastes*. 1983 Jan 1; 8 (2): 119-24.



## **An Assessment on the Use and Application of Estrous Hormones in Dairy Cattle at Kiambaa Subcounty, Kiambu, Kenya**

*Ng'ang'a Zacharia Waithaka\* Ege University, Faculty of Agriculture, Dept. of Animal Breeding, 35100 Bornova, İzmir, Turkey*

*Dr. Lucas Asaava, Kenyatta University, School of Pure and Applied Sciences, Dept. of Zoological Sciences, Ruiru, Kenya*

*\*Corresponding author: zachariawaithaka96@gmail.com*

**Keywords:** Dairy cattle, estrous hormones, heat detection, synchronization

**Discipline:** Agriculture

### **Abstract**

The main aim of the research was to assess the use or utilization as well as the farmers view on the effectiveness of estrous hormonal control and synchronization in Kiambaa sub-county. Most people in Kiambaa sub-county which is located in Kiambu County, Kenya engage in agriculture especially dairy production. For improved production and reproduction efficiency of their dairy cows, proper methods of heat detection and synchronization have to be utilized to reduce breeding costs while achieving short calving intervals. The broad objective was to assess the popularity and the utilization of estrous hormones in dairy cattle production to achieve synchrony or heat detection. The commonly used hormones in estrous induction include Prostaglandins, Progesterone, Estrogens and Gonadotrophin-releasing hormones. This incorporated assessing the effectiveness, popularity and economic impact to the general production in the dairy enterprises. 83 farms were used in respect to the expected response rate. The methods of data collection used included direct observation, use of questionnaires, face to face interviews and use of secondary data from the veterinary department and agro-vet records in the area. The expectations of the research was to create awareness on the use of estrous hormones for improved reproduction rates and shortening of calving intervals as well as encouraging vets to motivate farmers and get better knowledge on estrous cycle and utilization of estrous hormones in the study area. The results proved only 20.5% awareness on estrous hormones while 79.5% had never heard about estrous hormonal control. Of the 83 farmers 91.6% of them had never applied estrous hormones in their farms with only 8.4% of them having utilized it at one point in time. The main limitation of using estrous hormones by farmers was noted to be lack of information followed by cost of the practice and ineffectiveness. Most of the farmers who had utilized the hormones before categorized the effectiveness of hormonal estrous control as fair i.e. not high nor low. The economic impact to the enterprise was fairly positive according to those who utilized the estrous hormones. The study drew several conclusions including that most farmers are unaware of estrous hormonal control. It also embraced the potential of the farmers to utilize the hormones in consultation with their veterinarians who are qualified and registered to administer them. The application of the estrous hormones also has an overall positive economic impact to the dairy enterprises. The research recommended that awareness on the use of estrous hormones should be raised among all stakeholders.

### **Introduction**

Dairy farming in Kenya is characterized by inefficient breeding practices and low usage of technology. There are new trends and innovations every day in the dairy sector due to technological advancement [1]. Some technologies such as estrus synchronization and embryo transfer among others are not common nor widely used [2]. Although Artificial Insemination (AI) for cattle breeding has been highly embraced by most dairy farmers especially in Kiambu County, long calving intervals, poor estrus detection skills and inappropriate timing of insemination are among the challenges that result to reproductive inefficiency. This results in the reduction of the overall productivity and profitability of dairy enterprises [3]. Other reasons for the poor reproductive efficiency in Kenya have been put across by past studies including inadequate and poor quality feeding, poor breeding techniques and lack of proper breeding records [4,5]. According to Patterson et al. [6], the problem of heat detection in dairy cattle AI service program can be minimized by effective estrus synchronization.

Hormonal oestrus synchronization [7] can be adopted by smallholder farmers to produce large number of dairy animals in a relatively short period of time, to match calving with feed availability and

market demand for dairy products and to improve the effectiveness and efficiency of AI. Macmillan [8] argues that estrus detection and animal identification have become increasingly difficult in many dairy enterprises where some crucial breeding decisions are being made even by herdsmen thus limiting expression of normal estrus behavioral signs. Estrus synchronization offers a solution for efficient and perfect estrus detection and observation which is crucial for proper management of dairy cows [9]. The synchronization enhances timed artificial insemination (TAI) utilizing different protocols which have been developed and applied in the high production dairy cows [10]. Most estrous synchronization systems utilize methods to control follicular wave development, promote ovulation in anestrous cows, regress the corpus luteum in cyclic cows, and synchronize estrus and (or) ovulation at the end of treatment. Most recent programs include protocols for re-synchronization following first or subsequent AI's. Almost all programs involve strategically timed treatment of prostaglandin F2 $\alpha$  (PGF) and gonadotropin releasing hormone (GnRH), though in some programs, an estradiol ester treatment and progesterone supplementation may be included [9].

The estrous cycle is under control of the reproductive hormones comprising of GnRH, Lutenising Hormone (LH), Follicle Stimulating Hormone (FSH) and gonadal hormones estrogen and progesterone [2]. The four main hormonal products used include Prostaglandins, Progesterones, Oestrogens and Gonadotrophin- releasing hormones. Prostaglandins are hormones that cause the active corpus luteum to lyse and allows the cows to come on heat. They only work to bring cows to heat when a corpus luteum is present. They also produce abortions in cows less than 5 months pregnant, induce calving in the last few weeks of pregnancy and treat some ovarian cysts. Progesterone releasing devices act to mimic the action of the active corpus luteum in producing progesterone. The hormone is important in priming the cow to display heat, control the number of growing follicles, and maintaining a pregnancy. They can be used to synchronize estrous and can get non-cycling cows to cycle. According to Chebel *et al.* [11] the most successful treatments of anestrus have usually involved as a period of progesterone supplementation almost invariably using an intravaginal insert. Oestrogen are always produced when cows are on heat. Estradiol esters have been successfully applied. As Sales *et al.*, [12] puts it the oestrogens administered after progesterone device removal or after monitoring the cycle were effective in inducing a LH surge that resulted in synchronized ovulations. Several GnRH products are available in the market. They turn over follicles, induce ovulation and induce corpus luteum formation [13]. The use of GnRH provides the platform to standardize the pattern of follicular growth in animals. This helps to evade development of persistent follicles and for estrous control systems in which the injection is used to synchronize ovulation time for timed artificial insemination. These hormones used in oestrus cycle provide the means for farmers to control the reproduction of their dairy herd. They aid in shortening the calving intervals and increasing conception rates. Improved and greater awareness and popularity of these hormonal products and how they are used can be of great value to farmers.

There are various signs of heat. The main is always standing heat when a cow stands to be mounted. The others include mucus discharge, bellowing, restlessness, trailing others, swelling and reddening of the vulva, rubbed tailhead hair, decreased feed intake, sniffing others genitalia and decline in milk yield [14]. The occurrence and detection of estrus, time to post-partum resumption of cyclic activity and fertility at service highly influences the interval between calving and conception which is the most critical variable since the gestation period is fixed. Accurate estrus determination is therefore very important when it comes to optimization of reproductive efficiency, especially where AI is used. Heat detection aids such as pedometers, teasers, chin-ball markers amongst others, can be used alongside visual observation to enhance the accuracy of heat detection on dairy farms [15,16]. However, most of these aids may not be practical in small holder dairy systems especially due to being unaffordable. Proper timing of AI is equally a critical factor in determination of fertility at service and is normally determined by when the animal was confirmed to be seen on heat. The need for a rapid, easy and affordable method for timely assessment of reproductive status of cows promotes the use of estrous hormones for optimum reproductive efficiency [2].

Kiambaa area has a high dairy cows' population which are the major source of livelihood to the residents of the area though the larger proportion experiences long calving intervals. Most farmers especially in Kiambaa sub-county are unable to make accurate observations especially heat signs where the cows may become unpredictable with irregular heat patterns. Incorrect detection of estrus is related to loss of income due to extended calving intervals, milk loss, increased veterinary cost, slowed genetic progress and increased heifer rearing cost. Farmers need the knowhow to apply these practice for

continued benefit to the enterprise. The project was to create awareness thus boosting the farmers through more income associated with improved production and as well as the county economy whereby this translates to the country's improved production. The veterinarians and animal health practitioners will have an easy time to accurately serve a cow that's on heat and avoiding risk or loss of customers trust. The project is also supposed to assist the national research and development partners in coming up with effective programs and policies for better and efficient delivery of breeding and AI services involving the high production areas like Kiambaa. The main objective of this study was therefore to assess and evaluate the use of estrus hormones in dairy cattle production of Kiambaa sub-county. Specific objectives were to determine the level of utilization of estrus hormone during breeding in Kiambaa sub-county and to determine the economic impact of estrus hormone utilization in breeding in Kiambaa sub-county.

### Methodology

**Study Area:** Kiambaa sub-county is located in Kiambu County in the Central region of Kenya. Its geographical coordinates: 1° 10' 0" South, 36° 45' 0" East. It's divided into five locations: Kiambaa, Waguthu, Ruaka, Cianda and Kihara. Cianda covers the largest area i.e. 38.3 km<sup>2</sup> with the highly urbanized Ruaka location being the smallest covering 7.1km<sup>2</sup>. Kiambaa has an arable land coverage of 80km<sup>2</sup> with average land size of 0.3 hectares. The average rainfall annually ranges from 1100-1400mm. The rains are normally concentrated in two short seasons; end of March to May, and end of October to December. The highest rainfall is received in April. The mean temperature ranges from 18.4°C- 19.5°C. The altitude ranges from 1520-1760 meters above sea level. Agriculture is the dominant economic activity especially dairy production and coffee production. According to the data in the agricultural office of Kiambaa there are about 7365 productive households and a population of around 126000.

**Study Design:** The study design used was a Cross sectional study. It involved conducting a survey of a sample of population elements at one point in time. It was used thereby to assess the use of estrus hormones in dairy farms of Kiambaa sub-county in Kiambu County.

**Study Population:** The target sample population was 67 household farm each with more than two dairy high producing cows. The expected response rate was 80% thereby dividing the target sample size of 67 with the expected response rate gave an appropriate sample size of 83 households.

**Sampling Procedure:** Simple random sampling was used to identify the 83 farms which were used to administer questionnaires and general interactions. The list of households was obtained from the agricultural office in the area and the Kiambaa Division Co-operative Veterinary Services Limited.

**Data Collection:** The methods used in collecting data included primary data collection through observation, use of questionnaires, interactions and interviews. Secondary data from the Veterinary office in the area was also used. Records from the local Agro vets on hormonal products was also used.

**Data Analysis:** Data was documented using Microsoft Excel. Statistical Package for Social Sciences software (SPSS Inc., Chicago, IL, USA) was used to conduct the statistical analyses. Frequency distribution tables and charts were also used in analysis and in data presentation.

### Results and Discussion

Use of hormones to induce estrus and mechanical aids to supplement visual detection of estrus have been shown to improve heat detection efficiency and accuracy [17]. There is a steady decline in the fertility of dairy cows with time hence increasing the assistance of hormones [18]. Shortened calving rates due to efficient heat detection and serving lead to increased milk production in dairy farms. The estrus hormones highly aid in heat detection and synchronization thus improving the general production of the herd. Use of estrus hormones, new innovations and modern mechanisms to enhance reproductive efficiency and production in dairy farms is increasing in Kenya. Adoption of this measures and technologies will highly enable farmers to produce more efficiently and effectively. The study assessed and evaluated the use of estrus hormones including the level of utilization and the economic impact of estrus hormone utilization in dairy cattle production in Kiambaa sub-county.

The farms involved in the study had a positive response rate. The number of male respondents was 55 compared to 28 females. Most of the farmers were aged between 51 and 60 years old i.e. 27/83. The smallest age grouping of farmers owning dairy cows was 20-30 years where only 5 farmers fell in that range. Different studies have shown the positive effect of education on the acceptance of different agricultural innovations and technologies by farmers [19–21]. It was clear that the area had literate

farmers with most of them (56/83) having reached the secondary level of education i.e. (67.5%). Those with tertiary education were 18 out of the 83 total respondents (21.7%). The primary school level farmers were only 9(10.8%). The levels of education have a high impact on use of technology and modern measures like hormonal control of estrus. The study showed that most of those using estrus hormones have tertiary education and are keen to use technology and innovations to improve the production of their farm units. This supports the findings by Njarui et al [22] research in Machakos that literacy levels in the region were high with most farmers having attained secondary education and above. This in his explanation implied that the utilization and acceptance of any newly introduced dairy technology is likely to be high since education levels correlates with the adoption [22].

The area has many small-scale dairy farmers where most of them keep about 2 cows. This is similar to the findings by Nabulindo [2], where he stated that about 52% of dairy farmers in Kiambu kept less than 5 cows. This is somehow related to the high populations in the area and the current real estate adoption trend in the region that negatively impacts on agricultural potential land resource. The long serving vets in the area could note that the numbers of dairy cows have decreased in Kiambaa Sub County over the decades. Almost all of them are small holder dairy livestock farmers rearing their cows in an intensive zero grazing system. The Friesian breed dominates the region. In this study most farmers kept Friesian breed followed by Ayrshire breed. This is because it's the best producer of large quantities of milk in the area. Those with an extra cow whether an Ayrshire, Guernsey or Jersey keep them to improve the quality of their milk through the butterfat content i.e. solidification. This agrees with a study conducted in eastern and central Africa specifically Machakos and Wote in Kenya where they stated and proved the significance that Holstein-Friesian breed is the dominant dairy breed in Kenya [22].

All the farmers were using the AI Technology to serve their animals. Use of bulls directly to serve cows in the area was very rare. All farmers involved in the study were aware and practices Artificial Insemination method of service in their farms. The adoption rate of artificial insemination for breeding in Kiambu County is very high and most farmers apply it [2]. This can be attributed to the fact that many veterinary professionals and para-professionals highly administer A.I services in these areas and farmers have been highly encouraged to apply this method to reduce breeding diseases, cost of raising a bull and for easy management of the dairy herd while avoiding inbreeding.

Out of the total 83 respondents, 75 of them had never received any extension service either from the government or organizations. 8 of them had received some extension services at any one point in time. 79.5% of the farmers in that area do not know or have never heard about estrus hormonal control. As shown in Table 1 only 17 of the total respondents said they have heard or have little knowledge on hormonal control to aid artificial insemination. More people are unaware of hormonal synchronization and hormonal heat detection. This is attributed to the low extension services and lack of information to farmers. The farmers are also expected to pay for training organized by groups or cooperatives which prove unaffordable to most of them. In fact Nabulindo [2] in his results of a study in Kiambu County stated that none of the dairy farmers were aware of p4 kits for heat detection. It requires expertise to administer estrus hormones and monitor the cycle effectively. Gatew et al [23] conducted a study on factors influencing the success of on-farm estrus synchronization of dairy cattle in in North Shewa Zone, Amhara Region, Ethiopia. About 53% of respondents did not have awareness in dairy cattle estrus synchronization technology at the time of implementation. The veterinarians have to take responsibility of these measures of which most do not recommend or explain to farmers the importance of utilizing hormones.

Table 3. The awareness levels of estrus hormones by the respondents

<b>Do you know about oestrus hormones?</b>					
		Frequency	Percent	Valid Percent	Cumulative Percent
Valid	NO	66	79.5	79.5	79.5
	YES	17	20.5	20.5	100.0
Total		83	100.0	100.0	

Use of hormones (prostaglandins, progesterone, oestrogens and GnRH) to synchronize estrus or ovulation reduce the need for direct heat signs observation and tend to increase the number of animals

being inseminated [18,24]. As it can be seen from Figure 1, out of the 83 respondents only 7 farmers (8.4%) had utilized estrus hormones either for accurate heat detection or for synchronization in their farms by the help of their veterinarians. Only a very small percentage of farmers in the study area apply estrus hormones in their dairy herds. This explains the poor reproductive efficiency of dairy cows in the area. This is contrary with a study in Europe where a research conducted in 714 non-organic farms resulted that only 4 farms never used hormones to assist the insemination of lactating dairy cows [18]. This brings about the low adoption rate and awareness in developing countries like Kenya. Most of those who apply estrus hormones in Kiambaa were found to keep fairly high numbers of dairy cows.

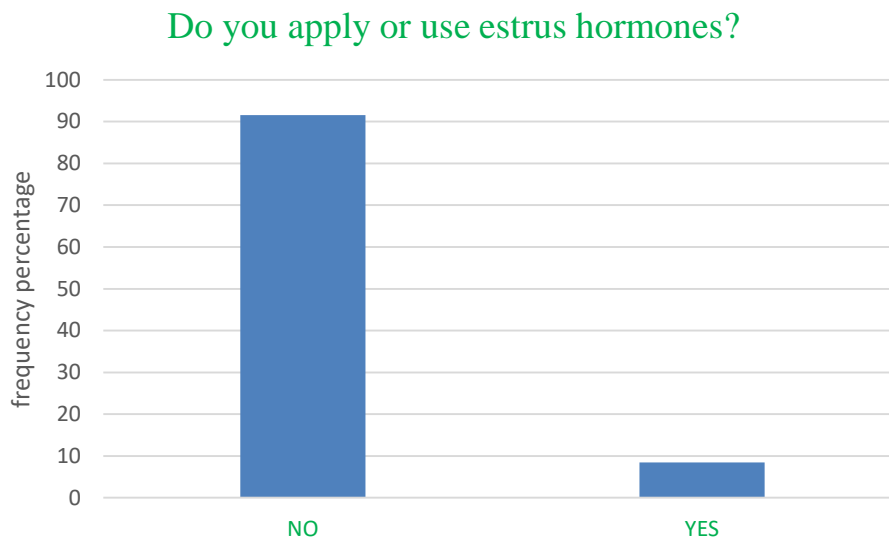


Figure 1. The percentage of estrus hormones usage by the respondent farms

The farmers highlighted the three main limitations of using estrus hormones in their farms. 67 out of the 83 were disadvantaged by lack of any information on the use of estrus hormones. For those aware of the hormones 11 of them were limited due to the high cost incurred in using them. 5 of the respondents said their main limitation is the ineffectiveness of the hormones as per the past experiences.

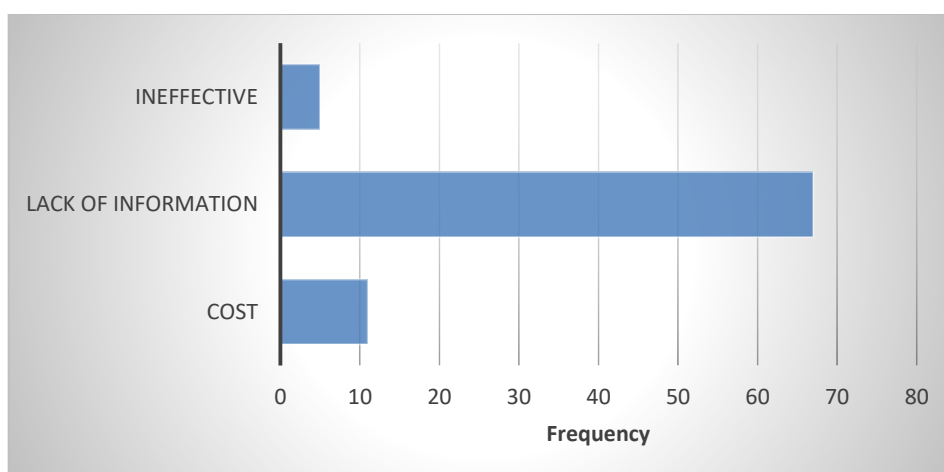


Figure 5. The main limitations to using estrus hormones by the respondents

A long postpartum anestrous period is a very common issue with cows reared in a tropical environment [25]. Heat detection is normally cited as the most important factor affecting the success of artificial insemination programs. There are various biological and managerial factors that can affect the interval between calving and conception including: silent heat, poor heat detection skills, poor heat detection efficiency and accuracy, delay in resumption of postpartum ovarian activity, postpartum diseases such as endometritis, increased cases of failed insemination, suboptimal voluntary waiting

period, and inadequate feeding [26–28]. A calving conception interval of 85-110 days should be the aim in order to attain the recommended calving interval of 365-390 days [27]. Kenyan dairy farms have reported long calving conception interval according to previous studies [4,5,29]. As this interval increases losses are incurred because fewer calves are produced, breeding costs increase due to higher number of inseminations per conception, veterinary costs increase due to more repeat breeders, days in milk increases and lifetime milk yield decreases [30].

92% of the respondents could not describe the effectiveness as they had never applied the estrus hormones before. For those who utilized hormones 6% of the total respondents said that the efficiency of the hormones was fair i.e. not high nor low. No respondent complained of very low effectiveness of the hormones. The remaining 2% were very confident in the use of hormones. The economic impact to the general production is fairly positive. The confident farmers attributed their productivity constancy to the use of hormones. Those with very few cows are more affected by using hormones due to the high cost involved.

According to a study conducted by Abera et al [31] in Ilu and Waliso districts of South West Shoa Zone of Oromio, Ethiopia, most of the respondents (67.15%) indicated that their satisfaction level towards synchronization and mass artificial insemination was low. The low satisfaction levels towards estrus synchronization in Ethiopia were associated with shortage of feed, silent heat, poor performance of the inseminator and low awareness of farmers on the technology [31]. The current study agrees that these reasons are similar to Kenyan situation. From the study in Ethiopia it was also noted that the overall percentage (26.22%) of calving rate to oestrus synchronization and mass artificial insemination was low mainly due to heat detection problem (36%); A.I technician efficiency (29.25%), absence of A.I technician (23.9%) and distance of A.I center (10.25%). In another study by H. Gatew [23] in Ethiopia, about 59.72% of farmers who were aware about estrus synchronization gave negative feedback towards the technology. In the same study the proportion of respondents who gave negative feedback towards the technology attributed to 88.3, 6.98 and 4.65% for poor pregnancy rate, poor heat response and unavailability of the service, respectively. In agreement with the current study, they also confirmed that due to lack of awareness and feed resources, the majority of farmers (68.48%) do not supplement breeding cows/heifers. Although in their study inaccessibility of AI and improved bull service was a major factor contrary to the current study in Kiambaa, Kenya, heat detection problems, lack of awareness of farmers and poor cattle management systems were also major factors which were responsible for the low pregnancy rate (20.18%) of the studied synchronization program in Ethiopia similar to our findings in the current study.

Efficiency of estrus hormones was found to be either fair or high. The utilization of hormones to induce estrus in place of visual detection has been proved to improve heat detection efficiency and accuracy [17]. This is also confirmed by an experiment that set to determine the economic outcome of estrus synchronization and timed artificial insemination in commercial cow/calf production. They concluded that estrous synchronization and TAI had positive economic impacts on subsequent weaning weights of exposed cows and reported increased returns per cow [32]. Higgins et al explained their findings in Europe that veterinary practitioners agreed (>80%) that estrus hormones improve fertility and the overall farm business profitability [18]. In his research, utilizing hormones to aid breeding in high producing dairy cows is cost effective for farmers and is an economic necessity for the UK dairy industry. This study confirms that the use and utilization of estrus hormones have a positive economic impact to the dairy enterprise. Fetrow [33] developed an economic model concerning the value of using prostaglandin (PG) in dairy cows with non-detected estrus. While considering assumptions, it was more profitable to treat cows with PG and to breed the cows at a detected estrus than it was not to treat the cows and to wait to breed the cows at a detected estrus. It was concluded that when using timed artificial insemination, it was also more profitable to breed PG-treated cows than it was not to use PG [33].

Estrus synchronization in dairy cattle is definitely beneficial in that it reduces the time devoted to estrus detection and reduces variability in days from parturition to first service thus reduced calving intervals [34]. Conception rates and calving rates were noted to be very low in the area. Parallel to the findings by Tegegn and Zelalem [35], the low conception rates observed in this study were associated with heat detection problems of farmers, poor timing of artificial insemination and poor husbandry practice of heifers and cows.

The agrovet personnel confirmed that very few veterinarians buy estrus hormones thus their stock is also very low. This proves the fact that hormones are not widely utilized and very few people have

the knowledge in the use of hormones for estrus control. Upon interviewing some veterinarians and animal health practitioners in Kiambaa, they pointed out that only a limited number of people had the knowledge on the utilization of hormones. Comparing out of 100, most of them affirmed that 95% of the farmers were unaware. On a scale of 10, they averagely rated the effectiveness of estrous hormones in small scale farming to about 6.5/10.

Stating the concept plainly; the main importance of estrus synchronization in dairy cows include saving time put in place for estrus or heat detection and reduction of days variability from the time of giving birth to the first service thus shorter calving intervals [34]. Teixeira [36] also highlights that the timed artificial insemination protocols increases the proportion of cows becoming pregnant sooner after the voluntary waiting period and decreases the interval from parturition to first service. The estrus protocols also minimizes time and labor while yielding good pregnancy results enhancing reproductive efficiency [1]. Synchronization of the estrous cycle has the potential to shorten the calving season, increase calf uniformity, and enhance the possibilities for utilizing AI [37]. It is therefore necessary for farmers especially in developing nations like Kenya through clear engagement with their animal health service providers to adopt the use of estrous hormones in heat detection and estrus synchronization in their dairy farms.

### Conclusion

The study shows that most farmers are unaware of estrus hormonal control including estrus synchronization and heat detection aids. It also establishes that farmers have embraced Artificial insemination thus if well taught on its importance and utilization they can embrace hormonal control too. It also helps to realize that hormones are effective in heat detection and to achieve synchrony. The application of estrus hormones has an overall positive economic impact to the dairy enterprise especially to those with high numbers of dairy cows.

### Recommendations

Awareness should be created on the use of estrus hormones. Veterinarians should take responsibility of educating their clients on new measures available especially on estrus hormones in case of silent heat and/or increased calving intervals. Further studies should be conducted on the effectiveness of estrus hormone synchrony especially in developing countries like Kenya and its impact in arid and semi-arid areas.

### References

- [1] Baruselli PS, Sales JNS, Sala R V, Vieira LM, Filho MFS. History , evolution and perspectives of timed artificial insemination programs in Brazil. *Anim Reprod* 2012;9:139–52.
- [2] Nabulindo WN. Blood Progesterone Determination by Lateral Flow Immunoassay for Assessment of Reproductive Status of Dairy Cattle in Kenya. University of Nairobi, 2016.
- [3] Muia JMK, Kariuki JN, Mbugua PN, Gachui CK, Lukibisi LB, Ayako WO, et al. Smallholder dairy production in high altitude Nyandarua milk-shed in Kenya: Status, challenges and opportunities. *Livest Res Rural Dev* 2011;23:108–20.
- [4] Bebe BO, Udo HMJ, Rowlands GJ, Thorpe W. Smallholder dairy systems in the Kenya highlands: Cattle population dynamics under increasing intensification. *Livest Prod Sci* 2003;82:211–21. [https://doi.org/10.1016/S0301-6226\(03\)00013-7](https://doi.org/10.1016/S0301-6226(03)00013-7).
- [5] OWEN E, KITALYI A, JAYASURIYA N, SMITH T. *Livestock and wealth creation: improving the husbandry of animals kept by resource-poor people in developing countries*. 1st ed. Nottingham University Press, UK.; 2005.
- [6] Patterson DJ, Thomas JM, Abel JM, Bishop BE, Locke JWC, Decker JE, et al. Control of estrus and ovulation in beef cows. *Appl. Reprod. Strateg. Beef Cattle*, Des Moines, Iowa: 2016.
- [7] Tegegne A, Hoekstra D, Gebremedhin B, Gizaw S. History and experiences of hormonal oestrus synchronization and mass insemination of cattle for improved genetics in Ethiopia: From science to developmental impact. 2016.
- [8] Macmillan KL. Recent advances in the synchronization of estrus and ovulation in dairy cows. *J Reprod Dev* 2010;56 Suppl:S42-7. <https://doi.org/10.1262/jrd.1056s42>.
- [9] Paul AK, Yoisungnorn T, Bunaparte N. Hormonal treatment and estrus synchronization in cows: A mini-review. *J Adv Vet Anim Res* 2015;2:10–7. <https://doi.org/10.5455/javar.2015.b45>.

- [10] Wiltbank MC, Sartori R, Herlihy MM, Vasconcelos JLM, Nascimento AB, Souza AH, et al. Managing the dominant follicle in lactating dairy cows. *Theriogenology* 2011;76:1568–82. <https://doi.org/10.1016/j.theriogenology.2011.08.012>.
- [11] Chebel RC, Santos JEP, Cerri RLA, Rutigliano HM, Bruno RGS. Reproduction in dairy cows following progesterone insert presynchronization and resynchronization protocols. *J Dairy Sci* 2006;89:4205–19. [https://doi.org/10.3168/jds.S0022-0302\(06\)72466-3](https://doi.org/10.3168/jds.S0022-0302(06)72466-3).
- [12] Sales JNS, Carvalho JBP, Crepaldi GA, Cipriano RS, Jacomini JO, Maio JRG, et al. Effects of two estradiol esters (benzoate and cypionate) on the induction of synchronized ovulations in *Bos indicus* cows submitted to a timed artificial insemination protocol. *Theriogenology* 2012;78:510–6. <https://doi.org/10.1016/j.theriogenology.2012.02.031>.
- [13] Lauderdale JW. WHERE WE'VE BEEN AND WHERE WE ARE TODAY: HISTORY OF DEVELOPMENT OF PROTOCOLS FOR HISTORY OF DEVELOPMENT OF PROTOCOLS FOR BREEDING MANAGEMENT OF CATTLE THROUGH BREEDING MANAGEMENT OF CATTLE THROUGH SYNCHRONIZATION OF ESTRUS AND OVULATION. *Appl. Reprod. Strateg. Beef Cattle, NCBA Conv., San Antonio, TX: 2010*.
- [14] Rao TKS, Kumar N, Kumar P, Chaurasia S, Patel NB. Heat detection techniques in cattle and buffalo. *Vet World* 2013;6:363–9. <https://doi.org/10.5455/vetworld.2013.363-369>.
- [15] Dalton JC. Strategies for Success in Heat Detection and Artificial Insemination. *Adv Dairy Technol J* 2011:215–29.
- [16] O'Connor ML. Estrus Detection. *Curr. Ther. Large Anim. Theriogenology Second Ed., Elsevier Inc.; 2006, p. 270–8. https://doi.org/10.1016/B978-072169323-1.50039-8*.
- [17] Holman A, Thompson J, Routly JE, Cameron J, Jones DN, Grove-White D, et al. Comparison of oestrus detection methods in dairy cattle. *Vet Rec* 2011;169:47. <https://doi.org/10.1136/vr.d2344>.
- [18] Higgins HM, Ferguson E, Smith RF, Green MJ. Using Hormones to Manage Dairy Cow Fertility: The Clinical and Ethical Beliefs of Veterinary Practitioners. *PLoS One* 2013;8:e62993. <https://doi.org/10.1371/journal.pone.0062993>.
- [19] Prokopy LS, Floress K, Klotthor-Weinkauff D, Baumgart-Getz A. Determinants of agricultural best management practice adoption: Evidence from the literature. *J Soil Water Conserv* 2008;63:300–11. <https://doi.org/10.2489/jswc.63.5.300>.
- [20] Howley P, O. Donoghue C, Heanue K. Factors Affecting Farmers' Adoption of Agricultural Innovations: A Panel Data Analysis of the Use of Artificial Insemination among Dairy Farmers in Ireland. *J Agric Sci* 2012;4. <https://doi.org/10.5539/jas.v4n6p171>.
- [21] Mwangi M, Kariuki S. Factors Determining Adoption of New Agricultural Technology by Smallholder Farmers in Developing Countries. *J Econ Sustain Dev WwvlisteOrg ISSN* 2015; 6:208–16.
- [22] Njarui DMG, Kabirizi JM, Itabari JK, Gatheru M, Nakiganda A, Mugerwa S. Production characteristics and gender roles in dairy farming in peri-urban areas of Eastern and Central Africa. *Livest Res Rural Dev* 2012;24.
- [23] Gatew H, Zewde T, Kassa G, Chanyalew Y, Gazu L. Factors influencing the success of on-farm estrus synchronization of dairy cattle in North Shewa Zone, Amahara Region, Ethiopia. *Int J Livest Prod* 2018;9:9–16. <https://doi.org/10.5897/IJLP2017.0408>.
- [24] Nebel RL, Jobst SM. Evaluation of Systematic Breeding programs for Lactating Dairy Cows: A Review. *J Dairy Sci* 1998;81:1169–74. [https://doi.org/10.3168/jds.S0022-0302\(98\)75679-6](https://doi.org/10.3168/jds.S0022-0302(98)75679-6).
- [25] Tadesse M, Thiengtham J, Pinyopummin A, Prasanpanich S, Tegegne A. Estrus Performance of Boran and Boran × Holstein Friesian Crossbred Cattle Synchronized with a Protocol based on Estradiol Benzoate or Gonadotrophin-Releasing Hormone. *Agric Nat Resour (Formerly Kasetsart J - Nat Sci* 2011;45:221–32.
- [26] Heersche G, Nebel RL. Measuring Efficiency and Accuracy of Detection of Estrus. *J Dairy Sci* 1994;77:2754–61. [https://doi.org/10.3168/jds.S0022-0302\(94\)77218-0](https://doi.org/10.3168/jds.S0022-0302(94)77218-0).
- [27] Hare E, Norman HD, Wright JR. Trends in calving ages and calving intervals for dairy cattle breeds in the United States. *J Dairy Sci* 2006;89:365–70. [https://doi.org/10.3168/jds.S0022-0302\(06\)72102-6](https://doi.org/10.3168/jds.S0022-0302(06)72102-6).
- [28] Kim IH, Kang HG. Risk factors for delayed conception in Korean dairy herds. *J Vet Sci* 2006;7:381–5. <https://doi.org/10.4142/jvs.2006.7.4.381>.
- [29] Ojango J, Pollott G. The productivity of holstein-friesian dairy cattle in different farming systems



- of Kenya. *Int J Agric Rural Dev* 2006;5:145–55. <https://doi.org/10.4314/ijard.v5i1.2576>.
- [30] Heuwieser W, Oltenacu PA, Lednor AJ, Foote RH. Evaluation of Different Protocols for Prostaglandin Synchronization to Improve Reproductive Performance in Dairy Herds with Low Estrus Detection Efficiency. *J Dairy Sci* 1997;80:2766–74. [https://doi.org/10.3168/jds.S0022-0302\(97\)76239-8](https://doi.org/10.3168/jds.S0022-0302(97)76239-8).
- [31] Abera F, Ulfina G, Lemma F, Chala M, Amanuel B. Dairy cattle producers' perception on Oestrus Synchronization and mass artificial insemination services in Waliso and Ilu Districts of South West Shoa Zone of Oromia, Ethiopia. *Insights Vet Sci* 2020; 4:010–3. <https://doi.org/10.29328/journal.ivs.1001020>.
- [32] Lamb C. What are the Long-Term Impacts of Estrus Synchronization and Artificial Insemination? | Panhandle Agriculture. Univ Florida 2015. <http://nwdistrict.ifas.ufl.edu/phag/2015/10/09/what-are-the-long-term-impacts-of-estrus-synchronization-and-artificial-insemination/> (accessed October 6, 2020).
- [33] Fetrow J, Blanchard T. Economic impact of the use of prostaglandin to induce estrus in dairy cows. *J Am Vet Med Assoc* 1987;190:163–9.
- [34] Waldmann A, Kurykin J, Jaakma Ü, Kaart T, Aidnik M, Jalakas M, et al. The effects of ovarian function on estrus synchronization with PGF in dairy cows. *Theriogenology* 2006;66:1364–74. <https://doi.org/10.1016/J.THERIOGENOLOGY.2006.04.030>.
- [35] Tegegn F, Zelalem A. Evaluation of oestrus synchronization and mass artificial insemination service of dairy cattle in Mizan Aman area, Bench Maji zone, South West Ethiopia. *Int J Livest Prod* 2017;8:1–4. <https://doi.org/10.5897/ijlp2016.0338>.
- [36] Teixeira AA. Impacto da inseminação artificial em tempo fixo na eficiência reprodutiva de vacas de leite de alta produção. Biblioteca Digital de Teses e Dissertações da Universidade de São Paulo, 2010. <https://doi.org/10.11606/D.10.2010.tde-16022011-150133>.
- [37] Lamb GC. Impacts of Estrus Synchronization on Cowherd Performance. *Range Beef Cow Symp. XXIV*, 2015, p. 81–8.

## Hindilerde (*Meleagris gallopavo*) Yetiştirme Sisteminin Performans Üzerine Etkileri

*Foudehou Issaka Ibrahima\**, Ege Üniversitesi, Fen Bilimleri Enstitüsü, Zootekni Anabilim Dalı, İzmir  
*Figen Kırkpınar*, Ege Üniversitesi, Ziraat Fakültesi, Zootekni Bölümü, İzmir  
*\*İletişimden sorumlu yazar: ifoudehou@hotmail*

**Anahtar Kelimeler:** *Meleagris gallopavo*, hindi yetiştiriciliği, yetiştirme sistemi, entansif, ekstansif  
**Disiplin:** Ziraat / Zootekni

### Özet

Bu çalışmada hindilerin yetiştirilmesinde uygulanan sistemin performans üzerine etkileri derlenmiştir. Özellikle hindilerde yetiştirme sisteminin sağlık, refah, üreme, besi performansı ve et kalitesi üzerine etkilerine değinilmiştir. Bu amaç doğrultusunda daha önce yapılmış çalışmaların yanı sıra ulusal ve uluslararası istatistik kurumlarının verileri kullanılmıştır.

Son zamanlarda kanatlı hayvan yetiştiriciliğindeki genetik ve teknolojik ilerlemeler sayesinde kanatlı hayvan eti üretimi ve tüketimi dünya çapında gittikçe artmaktadır. Hindinin hem entansif hem ekstansif koşullarda yetiştirilebilir olması yaygınlaşmasında olumlu bir etki sağlayabilmektedir. Hindilerde gözlenen performansın sadece %10-30'u genetik bileşenlerden kaynaklanmaktadır. Başka bir deyişle hindilerin performansının en az %70'i yetiştirme sistemine (barınma, beslenme, bakım ve sağlık faktörleri) bağlıdır. Bu nedenle sürdürülebilir bir hindi üretimi için en uygun yetiştirme sisteminin seçilmesi son derecede önemli bir husustur.

Hindilerde yetiştirme sisteminin canlı ağırlık üzerine etkisi 7.-8. haftadan itibaren görülmekte ve en iyi sonuç entansif yetiştirme sistemiyle elde edilmektedir. Ancak bu sistemde kullanılan ağır hatlar daha fazla yem tüketip yüksek canlı ağırlık kazanmakla birlikte kas içi yağ içeriği de yükselmektedir. Bu durum hindi eti tüketicilerinin tüketim tercihini olumsuz etkilemektedir. Karkas verimi bakımında ise ırk ve cinsiyetin etkisi, yetiştirme sistemine göre daha önemli olmaktadır. Hindiler, diğer kanatlılara göre kaba yemi daha iyi değerlendirebilir ve merada beslenme ile yaklaşık %30-40 oranında bir yem tasarrufu sağlayabilmektedir. Bu nedenle yemden yararlanma oranı ekstansif sistemlerde daha iyi olmaktadır. Hayvan sağlığı ve refahı açısından ekstansif ve yarı entansif sistemlerde hindiler yavaş büyüdükleri ve dış alana (güneş ve hareket) erişebildikleri için entansif sistemlerde karşılaşılan bacak kusurları, kalp yetmezliği ve kanibalizm gibi aksaklıklar görülmemektedir.

Tüm bu parametreler dikkate alındığında, hem sağlıklı bir ürün elde edilmesi hem de hayvan refahı açısından, hindi yetiştiriciliği için yarı entansif ve ekstansif sistemlerin tercih edilmesinin daha iyi olduğu söylenebilir.

### Giriş

Son zamanlarda kanatlı hayvan yetiştiriciliğindeki genetik ve teknolojik ilerlemeler sayesinde kanatlı hayvan eti üretimi ve tüketimi dünya çapında gittikçe artmaktadır (Chodova vd., 2014). Bu sektör, Dünya Gıda ve Tarım Örgütü'nün (FAO) 2019 verilerine göre 130,48 milyon ton karkas üretimiyle dünya et sektöründe hâkim konuma gelmiştir (FAO, 2019). Bunun yaklaşık %76'sını (99,572 milyon ton) sektörün önderi olarak etlik piliç üretimi oluşturmaktadır (United States Department of Agriculture Service, 2019). Hindi eti üretimi ise 2000 yılından itibaren karkas üretiminde 5-6 milyon ton arasında sabit kalmıştır (BESD-BİR, 2019). Bu rakam 2016 yılında 6,2 milyon tona yükselmiş ve 2025'te 6,7 milyon tona ulaşacağı tahmin edilmektedir (Johnson, 2018).

Türkiye'de hindi yetiştiriciliği entansif anlamda ilk kez 1960'lı yıllarda başlamıştır (Koyubenbe ve Konca, 2010). Hindi eti üretiminde 2000 yılından bu yana rakamsal olarak etlik piliç kadar olmasa da orantılı olarak önemli ilerlemeler elde edilmiştir. Hindi eti üretimi 2000 yılında 2,29 milyon adet hindi iken düzensiz bir değişiklik göstererek 2018 yılında 6,8 milyon adet üretime ulaşmıştır (2000 yılı üretiminin 2,95 katı). Ancak Dünya (2017 yılında 459,369 milyon adet), ABD (2017 yılında 242,5 milyon adet) ve Avrupa Birliği (2017 yılında 90,129 milyon adet) ülkelerine kıyasla bu üretim oldukça düşük kalmıştır.

Bu sektördeki üretim başarısı entansif yetiştirme sistemlerinde gerçekleşmekte ve söz edilen sistemin olumsuz tarafları gittikçe belirginleşmektedir. Bu nedenle dünya genelinde hayvan haklarını savunan kuruluşların öncülüğüyle hayvan refahı ile ilgili yasaların düzenlenmesi ve imkânları olan

tüketicilerin talepleri sonucunda, hayvancılık işletmeleri daha insani ve çevreyle dost üretime yönlendirilmektedir (Ferrante vd., 2019; İpek ve Sözcü, 2015). Bu piyasadaki büyüyen talep ve yetiştiriciler üzerindeki baskı nedenleriyle kanatlı hayvanlar başta olmak üzere tüm evcil hayvanların üretiminde yoğun yetiştirme sistemleri yerine artık alternatif olarak yarı-entansif, ekstansif, organik ve serbest dolaşım (free-range) yetiştirme sistemlerine tekrar geri dönülmektedir.

Hindi, kanatlı sektöründe verimlilik açısından piliçten sonra ikinci sırada bulunmaktadır (Sipahi, 2010). Ancak üretim maliyetinin yüksek olması, üretiminin uzun sürmesi ve daha az tüketilir olmasından dolayı bugüne kadar yetiştirilmesi pilice kıyasla çok az yaygınlaşmıştır (Özer ve Özbey, 2013a; Singh ve Sharma, 2005). Kanatlı hayvan etleri arasında piliç en fazla tüketilen et olsa da, hindi etinin daha kaliteli olduğu bilinmektedir (Özer ve Özbey, 2013b). Hindi eti yüksek besinsel ve duyuşal özelliklere sahip olduğu için (protein, vitamin B<sub>1</sub> ve B<sub>2</sub> bakımında zengin; yağ miktarı düşük ve çok az kolesterol içerir) sağlıklı beslenmede ideal ürün olarak sayılmaktadır (Jahan vd., 2018; Kırkpınar ve Mert, 2004). Ancak tüketilmesinin yaygınlaşmasını engelleyen önemli faktörlerden biri piliçten daha pahalı olmasıdır.

Hindinin hem entansif hem ekstansif koşullarda yetiştirilebilir olması (Jahan vd., 2018; Karaca vd., 1991; Kırkpınar ve Mert, 2004; Swalander, 2012) ve piliçlere göre daha dayanıklı ve yüksek karkas randımanına sahip olması (Koyubenbe ve Konca, 2010) yetiştiriciliğinin yaygınlaşmasında olumlu bir avantaj sayılmaktadır (Anna Anandh vd., 2012; Karaca vd., 1991). Ayrıca otlaklarda sürüler halinde yetiştirilebilir ve büyük hayvanların değerlendiremediği cılız otlar, hasat sonrası anızlarda kalan daneler, çekirge, solucanlar ve böcekler hindiler tarafından değerlendirilerek ete dönüştürülebilmektedir (Kırkpınar ve Mert, 2004). Böylece günde 8 saatlik merada beslenme ile yaklaşık %30-40 oranında bir yem tasarrufu sağlanmaktadır (Özer ve Özbey, 2013a).

Swalander (2012)'e göre hindilerde gözlenen performansın sadece %10-30'u genetik bileşenlerden, diğer kısmı (%70-90) ise barınma, beslenme, bakım ve sağlık faktörlerinden kaynaklanmaktadır. Başka bir deyişle hindilerin performansı en az %70 oranında yetiştirme sistemine bağlıdır. Bu nedenle sürdürülebilir bir hindi üretimi için en uygun yetiştirme sisteminin seçilmesi son derecede önemli bir husustur.

Bu çalışmada hindilerin yetiştirilmesinde uygulanan sistemin performans üzerine etkileri derlenmiştir. Özellikle hindilerde yetiştirme sisteminin sağlık, refah, üreme, besi performansı ve et kalitesi üzerine etkilerine değinilmiştir. Bu amaç doğrultusunda daha önce yapılmış çalışmaların yanı sıra ulusal ve uluslararası istatistik kurumlarının verileri ve raporları kullanılmıştır.

### Yetiştirme Sistemlerinin Sağlık Üzerine Etkisi

Kuluçkahanede ve çiftlikte karşılaşılan bakteri popülasyonları hayvanlar için potansiyel bir çevresel tehlikedir. Bu bakterilerin hindilerle temas ettiklerinde sindirim sisteminin bozulması, dolayısıyla besi performansında düşüş hatta ölümle sonuçlanabilen önemli bir ekonomik kayıp yaratabilmektedir (Fairchild vd., 2000). Bu bakteriler yemden kaynaklanabileceği gibi çevreden de (coğrafi konum, altlık, hava, diğer hayvanlar vs.) bulaşabilmektedir (Smith ve Rehberger, 2018). Bu bakımdan sağlıklı bir sürü oluşturabilmek için bölgeye adapte olan ırkların tercih edilmesi, kümesteki ortam ve çiftlik yönetimi (biyogüvenlik) çok önemlidir.

Entansif sistemlerde hindilerin kapalı barınaklarda (hepsi içeri - hepsi dışarı sistemi) yetiştirildiği düşünülürse, bu sistemin sağlık açısından daha riskli olduğu söylenebilir. Nitekim hastalık vektörleri dışkılarda daha çabuk çoğalabilir. Yarı entansif ve ekstansif yetiştirme sistemlerinde ise hindiler gündüzleri merada dışkıladıkları için entansif sisteme göre barınaklarda daha az dışkı bulunur. Ayrıca belli aralıklarla mera alanının değiştirildiği işletmelerde hastalık riskleri daha aza düşürülmektedir.

Hindilerin sağlığını etkileyen diğer faktör ise hızlı büyüme ve aşırı kilo alma kabiliyetleridir. Hızlı gelişme açısından ıslah edilmiş hindi hatlarının genellikle bağışıklık sistemleri daha hassas olup hastalıklara karşı daha duyarlı olmaktadır (Bayyari vd., 1997; Kırkpınar ve Mert, 2004). Ekstansif sistemlerde hızlı gelişen hindi hatları kullanılmakta ve büyümeyi azaltmak için kısıtlı yemleme programları uygulanmaktadır. Zira bu hızlı büyüme nedeniyle hindilerin sağlığını bozabilen hareketsizlik, ayak-bacak kusurları, göğüs ödemi (enfeksiyon riski), kanibalizm ve ani ölümler (kalp yetmezliği) sık sık görülebilir. Ayrıca verim ve ayak kusuru arasında negatif korelasyon olduğundan (Kapell vd., 2017) ekstansif sistemde yetiştirilse de küçük hat hindilere kıyasla hızlı büyüyen hatlarda ayak yaraları daha sık ortaya çıkmaktadır (McCrea vd., 2012).

### Yetiştirme Sistemlerinin Refah Üzerine Etkisi

Hayvanların refahı iki şekilde değerlendirilebilir (Ferrante vd., 2019):

i) Barınma ve ortam uygunluğuna bakarak değerlendirme

Bu açıdan, hindi refahını etkileyebilen faktörler barınma yoğunluğu, grup büyüklüğü, aydınlatma, beslenme ve taşıma sayılabilir (Watanabe vd., 2013).

ii) Hayvanların bireysel davranışı ve genel sağlık durumuna bakarak değerlendirme

Bu açıdan, hindi refahını etkileyebilen faktörler yukarıda sayılanlardan ziyade ırk, cinsiyet ve hayvanlar üzerinde yapılan uygulamalar (gaga kesme, yapay tohumlama vs.) değerlendirilir.

Yabani hindi türlerinin doğal davranışı ve yaşam alanı, et için ticari olarak yetiştirilen hindilerinkinden çok farklıdır. Otomatik barınaklarda aşırı kalabalık olan hindiler doğal davranışlarını sergileyemezler (The Humane Society of the United States (HSUS), 2008). Bu nedenle barınma yoğunluğu arttıkça, ayak yaraları, yürüyüş bozukluğu, diğer hindilere saldırı ve gagalama sıklığı artmakta ve bireysel düzeyde refah da düşmektedir (Martrenchar vd., 1999).

Gaga kesimi kanatlı hayvan işletmelerinde hayvanların refahını bozan önemli uygulamalardan biridir. Grigor vd., (1995) gaga kesiminin verim açısından daha yararlı olduğunu ortaya koymuşlardır. Nitekim yaptıkları çalışmada kanibalizm sonucunda ortaya çıkan yaralanmalarda (%68,1'den %9,8'e), ölümden (%8,7'den %1,6'ya) ve tüy hasarı puanlarında (%1,5'dan %0,29'a) gaga kesimi ile önemli düzeyde azalma saptamışlardır. Bu uygulama her ne kadar kümes içinde refahı artmışsa uygulamalarda bireysel hindi refahındaki azalma göz önünde bulundurulmalıdır. Çünkü Gillian vd., (1989) kanatlılar üzerinde yaptıkları çalışmada gaga kesimi sonucunda yem tüketme, su içme ve temizlenme için harcanan zaman azalmış, aktif olmayıp ayakta kalma ve çökme süreleri artmıştır. Diğer taraftan bu uygulama gibi stresli muamelelerin anestezi yapılmaması (AnimalsAsia, 2013) hayvan refahını olumsuz bir şekilde etkilemektedir. Ekstansif yetiştiricilikte gaga kesmeye gerek olmadığı için hayvanlar refah açısından daha avantajlıdır.

Hindi endüstrisindeki diğer önemli refah sorunlarından biri de hayvanların hızlı büyüyen kısa sürede daha ağır kesim ağırlığına ulaşmalarıdır (HSUS, 2008). Büyüme ve verime yönelik ıslah edilmiş hindi hatlarında bacak kusurları daha çok görülmektedir. Yaklaşık 50 yıl önce, ticari hindinin 16 haftalık ortalama canlı ağırlığı 5 ila 7 kg iken günümüzde ticari hindi aynı dönemde 17 kg'a ulaşabilmektedir (AnimalsAsia, 2013; Clark vd., 2019). Bu hızlı büyüme, hindilerin sağlık ve refahını daha da kötüleştirmekte ve sıklıkla görülen ayak-bacak kusurlarının yanı sıra iskelet bozukluğu, hareketsizlik-yatma, göğüs ödemi ve kalp yetmezliği gibi sorunlar da yaşanmaktadır. Hayvanın kaldıramayacağı kadar kilo alımı sonucunda aşım yapmak için yapay tohumlamaya başvurulur. Ticari işletmelerde yüzlerce hindi tohumlamak için hızlı çalışmak gerekir ve uygulamalar hayvan refahı dikkate alınmadan yapılabilir (AnimalsAsia, 2013; Glatz ve Rodda, 2013). Tüm bu olayların hayvan refahını bozduğu ve işletme kârlılığını etkilediği açıkça söylenebilir.

Kapell vd., (2017)'a göre verim ve ayak kusuru arasında negatif korelasyon söz konusudur. Yoğun yetiştirme sistemlerinde hızlı gelişen hatlar kullanılmakta ve erkek hindiler daha ağır oldukları için dişilere göre daha uzun yatma süresi göstermektedirler. Dolayısıyla dişilerle oranla ayakta durma için fazla, yürüme için ise daha az zaman harcamaktadırlar. Bunun sonucunda erkekler daha fazla kirlenmekte ve daha fazla göğüs yarası gelişmektedir ki refah açısından istenmeyen bir durumdur (Ferrante vd., 2019; Glatz ve Rodda, 2013). Bu sorunları engellemek için göğüs eti için ıslah edilmiş damızlık hindilerin canlı ağırlığını istenilen seviyede tutmak gerekir; dolayısıyla sürekli kısıtlı yemleme yapılmaktadır (HSUS, 2008).

Diğer taraftan gündüzleri dış alanlara sürekli erişebildikleri için yarı entansif ve ekstansif sistemlerde hindilere daha iyi refah koşulları sunulmaktadır. Hayvanların temiz havaya ve gün ışığına erişimi, daha güçlü ve sağlıklı bacak yapısı ve doğal davranışlarını yapabilmeleri avantaj sağlamaktadır. Ayrıca bu sistemlerde büyümenin yavaşlaması genellikle kalp yetmezliği veya hızlı büyüme ile ilişkili yukarıda sayılan sorunları engellemektedir (AnimalsAsia, 2013; Glatz ve Rodda, 2013).

### Yetiştirme Sistemlerinin Üreme Performansına Etkisi

Yetiştirme sistemi hindilerin üreme performansını önemli düzeyde etkilemektedir. Anna Anandh vd. (2012), yaptıkları çalışmada yumurta ağırlığı, kuluçkadan çıkış ve çıkışta yaşayan palaz oranları, dölsüz yumurta ve kuluçkada embriyonik ölüm oranları, döl verimi ve yaşama gücü değerleri açısından yetiştirme sistemlerini en iyiden başlayarak şu şekilde sıralamışlardır: entansif > yarı entansif > ekstansif (serbest dolaşım). Entansif ve yarı entansif sistemlerde istatistiksel olarak aynı palaz çıkış ağırlıkları

elde etmişlerdir.

Ancak palazlarda düşük kuluçkadan çıkış ağırlığı bir dezavantaj olarak algılanmamalıdır. Nitekim aynı ırktaki hafif palazlar ağır palazlardan daha az yem tüketip daha düşük kesim ağırlığına ulaşsa da tükettikleri yemi daha iyi değerlendirebilirler (Şengül ve Çetin, 2002). Başka bir deyişle kârlılık açısından önemli olan yemden yararlanma açısından daha üstün olmaktadır. Ayrıca kuluçkadan çıkış ağırlığı, karkas ağırlığı ve karkas randımanı önemli düzeyde etkilenmemektedir (Şengül ve Çetin, 2002).

Bu bulgular beraber değerlendirildiğinde aynı ırktaki hafif çıkan palazlar ağır olanlara kıyasla 1 kg et üretmek için daha az maliyet gerektirdikleri için tercih edilebilirler (yarı-entansif ve ekstansif sistemlere çok uygun).

### Yetiştirme Sisteminin Besi Performansı Üzerine Etkisi

Hayvanların besi performansı, canlı ağırlık kazancı ve yemden yararlanma değerleri ile ölçülür. Yetiştirme sistemleri hindilerin canlı ağırlıklarını önemli düzeyde etkilemektedir (İncil vd., 2016). Yapılan araştırmalara göre hindilerde yetiştirme sistemlerinin canlı ağırlık üzerine etkisi 7.-8. haftadan itibaren görülmektedir (İncil vd., 2016; Sarica vd., 2009; Sogut vd., 2016). Bunun nedeni hindilerin 7.-8. haftadan sonra sindirim sistemlerinin tamamen gelişmiş ve kaliteli yemden daha iyi yararlanabilmelerinden dolayı olabilir. Bu nedenle pratikte ekstansif koşullarda büyütülecek palazlar, genellikle 8. hafta itibarıyla meraya çıkarılmak üzere, öncesinde kapalı barınaklarda beslenmektedir.

Hindileri besi performansı, canlı ağırlık ve karkas verimi açısından değerlendiren çalışmalar incelendiğinde entansif sistem en avantajlı sistemdir. İncil vd., (2016)'a göre canlı ağırlık kazancı açısından 10-18. haftalarda entansif sistem daha kârlıdır. Ardından yarı-entansif ve ekstansif sistemler gelmektedir. Bu sistemler arasındaki performans farklılığının önemi, kullanılan yemin şekli ve içeriğine göre değişebilir. Genelde ekstansif yetiştiricilikte işlenmemiş daneler kullanılırken entansif yetiştiricilikte işlenmiş daneler kullanılır (öğütme, ısı muamele, enzim ilavesi vs.). Bu işlemler hayvanlarda yemden yararlanmayı iyileştirmektedir. Hindilerde öğütülmemiş daneler kullanıldığında ayrıca besi ve büyüme performansları düşmektedir (Ahmed vd., 2018). Aynı şekilde barınma yoğunluğunun artması ile hindilerin canlı ağırlığı önemli ölçüde azalmaktadır (Martrenchar vd., 1999).

Anna Anandh (2017)'in yaptığı çalışmada ortalama canlı ağırlık, karkas ağırlığı (g), karkas randımanı, kan (%), tüy (%), ayak (%), karın boşluğu yağı (%), baş (%), sırt (%), ve bacak (%) verim değerleri entansif sistem altında yetiştirilen hindilerde daha yüksek bulunmuştur. Entansif sistemi yarı-entansif ve ekstansif sistemler izlemiştir. Bununla birlikte, iç organlar (%), bağırsak (%), boyun (%), kanatlar (%) ve göğüs (%) veriminde ters eğilimler gözlenmiştir (ekstansif > yarı-entansif > entansif).

Başka bir çalışmada karkas verimi bakımından ırk, kesim yaşı ve cinsiyet etkiliyken yetiştirme sisteminin etkisi önemsiz bulunmuştur (McCrea vd., 2012; Sarica vd., 2009; Shamseldin vd., 2014).

Hindilerin besi performansı, yemden yararlanma açısından değerlendirildiğinde hindilerin günde 8 saat merada otlatılmasıyla entansif gruba göre daha az yem tüketip daha iyi yemden yararlanma oranı elde edilmiştir (Karaca vd., 1991; Özer ve Özbey, 2013a). Bu durumu daha iyi değerlendirilebilmek için meralarda iyi kaliteli kaba yemlerin bulunması şarttır. Ancak yemden yararlanma açısından farklı ırkların yetiştirme sistemlerine verdiği tepkiler farklıdır. Özer ve Özbey (2013a, 2013b) Beyaz ve Bronz hindilerle yaptıkları karşılaştırmalı çalışmada entansif gruplar yarı entansif gruplardan daha fazla yem tüketip daha yüksek kesim ağırlığına ulaşmıştır. Her iki ırk için dişi hindilerin karkas randımanı yarı entansif sistemde daha yüksek bulunmuştur. Fakat besi performansı açısından bronz hindilerin yarı entansif, beyaz hindilerin ise entansif tarzda yetiştirilmesinin daha uygun olduğu sonucuna varmışlardır. Bu bulgular ırk ve cinsiyete göre uygulanan sistemlerin farklı sonuç verebilirliğini vurgulamaktadır.

### Yetiştirme Sisteminin Et Kalitesi ve Kârlılık Üzerine Etkisi

Yetiştirme sistemi et kalitesini etkilemektedir. Sarica vd., (2011) 3 farklı hindi ırkı ile yaptıkları karşılaştırmalı çalışmada, aynı besleme programına tabi tutulduğunda açık alana (mera) erişen hayvan gruplarının göğüs etinin a\* değeri (kırmızı) ve bacak etinin b\* değeri (sarı) daha yüksek bulunmuştur. Ayrıca göğüs eti protein içeriği artmış (%21.98'den %22.42'ye), yağ ve kül içerikleri azalmıştır (sırasıyla %4.27'den %3.91'e ve % 1.06'den %1.04'e). Entansif yetiştiricilikte et verimine yönelik ıslah edilmiş hatlar kullanılmaktadır. Bu ıslahların sonucunda hindiler daha fazla canlı ağırlık kazanmakla birlikte kas içi yağ içeriği de yükselmektedir (Anna Anandh, 2017; Dewez vd., 2018). Bu durum, düşük yağ ve yüksek protein kaynağı olması nedeniyle hindi eti tüketicilerinin tüketim tercihini olumsuz etkilemektedir (Clark vd., 2019).

Ancak entansif ve yarı-entansif tarzda üretilen hindi etinin organoleptik özellikleri açısından istatistiki olarak önemli bir farklılık görülmemiştir. Fakat rakamsal olarak mera beslemesi yapılan yarı entansif grubun entansif gruba oranla daha fazla puan aldığı belirtilmiştir.

Bir yandan entansif yetiştiricilikte yem giderinin fazla olmasına karşın daha yüksek canlı ağırlıklar elde edilmektedir. Öbür yandan merada yetiştirme sisteminde yem gideri az olsa da düşük canlı ağırlık elde edilmektedir. Bu nedenle ekonomik olarak hangi sistemin daha üstün olduğunu belirlenmek için net kârın hesaplanması gerekmektedir (İncil vd., 2016). Lance (1983) çalışmasında performans ve maliyet analizlerini dikkate alarak, kapalı sisteme göre açık alanda hindi yetiştiriciliğinin daha kârlı olduğu sonucuna varmıştır. Ancak şimdiki hatların ıslah edilmiş olması, üretim maliyeti ve et fiyatının değişmiş olması nedeniyle güncel veriler değerlendirilerek yeni bir tahlil yapmak gerekmektedir.

### Sonuç ve Değerlendirme

Ekonomik bir aktivite olarak yapılan hayvancılıkta sisteme göre uygun bir hattın seçilmesi çok önemlidir. Nitekim her ırkın besi performansı ve çevreye duyarlılığı farklıdır. Islah çalışmalarıyla elde edilen hızlı gelişen hindiler refah ve sağlık sorunlarına daha duyarlıdır. Ayrıca kapalı entansif sistemde barınma koşulları hindilerin doğal davranışlarını bozmakta ve söz edilen duyarlılıkları artmaktadır.

Yetiştirme yöntemlerinin canlı ağırlık üzerinde etkisi hindilerde 7.-8. haftalardan itibaren görülmektedir. Hindilerin merada beslenmesi ile yem tasarrufu sağlandığı için yemden yararlanma oranı yarı entansif ve ekstansif sistemlerde daha iyi olmaktadır. Aynı zamanda bu tip sistemlerde hindilerin yavaş büyüdükleri ve dış alana (güneş ve hareket) erişebildikleri için entansif sistemlerde karşılaşılan bacak kusurları, kalp yetmezliği ve kanibalizm gibi aksaklıklar görülmemektedir. Ancak iyi bir besi performansı elde edebilmek için meradaki bitkilerin kaliteli olması gerekmektedir.

Tüm bu parametreler dikkate alındığında, hem sağlıklı bir ürün elde edilmesi hem hayvan refahı açısından, hindi yetiştiriciliğinin yarı entansif ve ekstansif sistemlerde yapılması tavsiye edilebilir. Kârlılık açısından ise her sistem için üretime giren tüm güncel masraflar dikkate alınarak net kârın hesaplanması gerekmektedir.

### Kaynakça

- [1] Ahmed, R., Juniper, D., Tonks, A., Rymer, C., 2018. The effect of incremental inclusion of whole grain wheat in the diet of growing turkeys on growth performance, feed conversion ratio, cecal health, and digesta characteristics. *Livest. Sci.* 214, 36-41. <https://doi.org/10.1016/j.livsci.2018.05.009>
- [2] *Animals Asia*, 2013. Intensive animal farming: Turkey. [https://www.animalsasia.org/us/assets/pdf/Turkey\\_Factsheet.pdf](https://www.animalsasia.org/us/assets/pdf/Turkey_Factsheet.pdf)
- [3] Anna Anandh, M., 2017. Effect of rearing systems on slaughter and carcass characteristics of turkey (*Meleagris gallopavo*). *Res. J. Anim. Husb. Dairy Sci.* 8, 46-50. <https://doi.org/10.15740/has/rjahds/8.1/46-50>
- [4] Anna Anandh, M., Richard Jagatheesan, P.N., Senthil Kumar, P., Paramasivam, A., Rajarajan, G., 2012. Effect of rearing systems on reproductive performance of turkey. *Vet. World* 5, 226–229. <https://doi.org/10.5455/vetworld.2012.226-229>
- [5] Bayyari, G.R., Huff, W.E., Rath, N.C., Balog, J.M., Newberry, L.A., Villines, J.D., Skeeles, J.K., Anthony, N.B., Nestor, K.E., 1997. Effect of the genetic selection of turkeys for increased body weight and egg production on immune and physiological responses. *Poult. Sci.* 76, 289-296.
- [6] BESD-BİR, 2019. İstatistikler - (Beyaz Et Sanayicileri ve Damızlıkçıları Birliği Derneği) [www Document]. BESD-BİR Derneği. URL <http://www.besd-bir.org/istatistikler> (erişim 12.12.19).
- [7] Chodova, D., Tümová, E., Svobodová, J., Uhlířová, L., 2014. Differences in carcass composition of males and females of two turkeys hybrids. *Acta Fytotech. Zootech.* 17, 72–74. <https://doi.org/10.15414/afz.2014.17.03.72-74>
- [8] Clark, D.L., Nestor, K.E., Velleman, S.G., 2019. Continual selection for increased 16 wk body weight on turkey growth and meat quality: 50 generation update. *J. Appl. Poult. Res.* 28, 658–668. <https://doi.org/10.3382/japr/pfz017>
- [9] Dewez, M.F., Etourneau, P., Lecompte, F., Briere, S., Froment, P., 2018. Use of computed tomography to determine body composition of heavy strain Turkey hens (*Meleagris gallopavo*) from rearing to early laying. *Poult. Sci.* 97, 4093-4106. <https://doi.org/10.3382/ps/pey267>

- [10] Fairchild, A.S., Grimes, J.L., Wineland, M.J., Jones, F.T., 2000. A comparison of the microbiological profile of poulters from young versus old turkey breeder hens. *J. Appl. Poult. Res.* 9, 476-486. <https://doi.org/10.1093/japr/9.4.476>
- [11] FAO, 2019. Food Outlook - Biannual report on global food markets. November 2019. Rome.
- [12] Ferrante, V., Lolli, S., Ferrari, L., Terumi, T., Watanabe, N., Tremolada, C., Marchewka, J., Estevez, I., 2019. Differences in prevalence of welfare indicators in male and female turkey flocks (*Meleagris gallopavo*). *Poult. Sci.* 98, 1568-1574. <https://doi.org/10.3382/ps/pey534>
- [13] Gillian, S.S., Seawright, E., Breward, J., 1989. Behavioural consequences of partial beak amputation (beak trimming) in poultry. *Br. Poult. Sci.* 30, 479-488. <https://doi.org/10.1080/00071668908417172>
- [14] Glatz, P., Rodda, B., 2013. Turkey farming: Welfare and husbandry issues. *African J. Agric. Res.* 8, 6149-6163. <https://doi.org/10.5897/AJAR12.034>
- [15] Grigor, P.N., Hughes, B.O., Gentle, M.J., 1995. An experimental investigation of the costs and benefits of beak trimming in turkeys. *Vet. Rec.* 136, 257-265. <https://doi.org/10.1136/vr.136.11.257>
- [16] İncil, H., Söğüt, B., Ayaşan, T., Çelik, Ş., Şengül, T., 2016. Farklı besleme yöntemlerinin hindilerde canlı ağırlık ve canlı ağırlık artışına olan etkilerinin belirlenmesi. *İğdır Üni. Fen Bilim. Enst. Der.* 6, 151-156. <https://doi.org/10.21597/jist.2016218858>
- [17] İpek, A., Sözcü, A., 2015. Alternatif kanatlı yetiştirme sistemlerinde yetiştirme pratikleri ve refah standartları. *J. Agric. Fac. Uludag Univ.* 29, 133-146.
- [18] Jahan, B., Ashraf, A., Rahman, M., Molla, M., Chowdhury, S., Megwalu, F., Asare, O., Shaikh, M., 2018. Rearing of high yielding turkey poulters : problems and future prospects in bangladesh : a review. *SF J. Biotechnol. Biomed. Eng.* 1, 1-8.
- [19] Johnson, R., 2018. Global turkey meat market: Key findings and insights. The Poultry Site [WWW Document]. *Poult. Site*. URL <https://thepoultrysite.com/news/2018/05/global-turkey-meat-market-key-findings-and-insights> (erişim 12.12.19).
- [20] Kapell, D.N.R.G., Hocking, P.M., Glover, P.K., Kremer, V.D., Avendaño, S., 2017. Genetic basis of leg health and its relationship with body weight in purebred turkey lines. *Poult. Sci.* 96, 1553-1562. <https://doi.org/10.3382/ps/pew479>
- [21] Karaca, O., Vanlı, Y., Demirel, M., Eratak, S., Çetin, M., Aydın, A., 1991. Bronz ırkı hindilerin kapalı ve açık yetiştirme koşullarında gelişme ve karkas özellikleri üzerinde araştırmalar. *Yüzüncü yıl Üniversitesi Ziraat Fakültesi Derg.* 1, 82-96.
- [22] Kırkpınar, F., Mert, S., 2004. Etlik Hindi Üretiminin Temel İlkeleri. *Hasad Hayvancılık Dergisi* 2, 24-27/16-21.
- [23] Koyubenbe, N., Konca, Y., 2010. Türkiye ve Avrupa Birliği'nde hindi eti üretimi, tüketimi ve politikaları, *Ege Üniv. Ziraat Fak. Derg.* 201-209.
- [24] Lance, G.C., 1983. Economic evaluation of total confinement and open range turkey production systems in Georgia. *Poult. Sci.* 62, 1142-1154. <https://doi.org/10.3382/ps.0621142>
- [25] Martrenchar, A., Huonnic, D., Cotte, J.P., Boillet, E., Morisse, J.P., 1999. Influence of stocking density on behavioural, health and productivity traits of turkeys in large flocks. *Br. Poult. Sci.* 40, 323-331. <https://doi.org/10.1080/00071669987403>
- [26] McCrea, B.A., Leslie, M.A., Stevenson, L.M., Macklin, K.S., Bauermeister, L.J., Hess, J.B., 2012. Live performance characteristics, pathogen load and foot pad lesions in range-reared heritage vs. conventional turkeys (*Meleagris gallopavo*). *Int. J. Poult. Sci.* 11, 438-444. <https://doi.org/10.3923/ijps.2012.438.444>
- [27] Özer, H., Özbey, O., 2013a. Beyaz ve Bronz hindilerin (*Meleagris gallopavo*) entansif ve yarı entansif şartlarda bazı verim özelliklerinin karşılaştırılması: 1. Büyüme performansı. *F.Ü. Sağ. Bil. Vet. Derg.* 27, 87-92.
- [28] Özer, H., Özbey, O., 2013b. Beyaz ve Bronz hindilerin (*Meleagris gallopavo*) entansif ve yarı entansif şartlarda bazı verim özellikleri: 2. Kesim ve karkas özellikleri. *F.Ü. Sağ. Bil. Vet. Derg.* 27, 135-140.
- [29] Sarica, M., Ocak, N., Karacay, N., Yamak, U., Kop, C., Altop, A., 2009. Growth, slaughter and gastrointestinal tract traits of three turkey genotypes under barn and free-range housing systems. *Br. Poult. Sci.* 50, 487-494. <https://doi.org/10.1080/00071660903110919>
- [30] Sarica, M., Ocak, N., Turhan, S., Kop, C., Yamak, U.S., 2011. Evaluation of meat quality from 3

- turkey genotypes reared with or without outdoor access. *Poult. Sci.* 90, 1313-1323. <https://doi.org/10.3382/ps.2009-00600>
- [31] Şengül, T., Çetin, M., 2002. Hindilerde kuluçkadan çıkış ağırlığı ve cinsiyetin besi performansı ve karkas verimine etkisi. *Tavukçuluk Araştırma Derg.* 4, 23-28.
- [32] Shamseldin, R.M., Gibril, S., Atta, M., Yassin, O.E., Hassan, A.A., 2014. Effect of rearing system, slaughter age and sex on turkey (*Meleagris gallopavo*) carcass components percentages. *Res. Opin. Anim. Vet. Sci.* 4, 198-202.
- [33] Singh, R., Sharma, D., 2005. Turkey and Guinea fowl : Role in Indian poultry production [www Document]. *Cent. Avian Res. Inst.* URL [http://www.poultvet.com/poultry/articles/turkey\\_guinea.php](http://www.poultvet.com/poultry/articles/turkey_guinea.php) (erişim 12.12.19).
- [34] Sipahi, C., 2010. Entansif hindi yetiştiriciliği işletmelerinde kârlılık ve verimlilik analizleri. Ankara Üniversitesi Sağlık Bilimleri Enstitüsü Doktora Tezi.
- [35] Smith, A.H., Rehberger, T.G., 2018. Bacteria and fungi in day-old turkeys vary among companies, collection periods, and breeder flocks. *Poult. Sci.* 97, 1400-1411. <https://doi.org/10.3382/ps/pex429>
- [36] Sogut, B., Celik, S., Ayasan, T., Inci, H., 2016. Analyzing growth curves of turkeys reared in different breeding systems (intensive and free-range) with some nonlinear models. *Brazilian J. Poult. Sci.* 18, 619–628. <https://doi.org/10.1590/1806-9061-2016-0263>
- [37] Swalander, M., 2012. Balanced breeding of turkeys for health & welfare traits. *Lohman Information* 47, 43-48.
- [38] The Humane Society of the United States, H., 2008. The welfare of animals in the turkey industry. [https://www.wellbeingintlstudiesrepository.org/cgi/viewcontent.cgi?article=](https://www.wellbeingintlstudiesrepository.org/cgi/viewcontent.cgi?article=1007&context=hsus_reps_impacts_on_animals)
- [39] 1007&context=hsus\_reps\_impacts\_on\_animals
- [40] United States Department of Agriculture Service, (USDA), 2019. Livestock and Poultry: World Markets and Trade. <https://www.fas.usda.gov/data/livestock-and-poultry-world-markets-and-trade>
- [41] Watanabe, T.T.N., Lolli, S., Ferrari, L., Ferrante, V., 2013. Review of the physiological and pathological welfare indicators applied in turkeys (*Meleagris gallopavo*). *Biotechnol. Anim. Husb.* 29, 727-740. <https://doi.org/10.2298/BAH1304727W>



## Identification, the Best Wheat Cultivar Studied (5 Digits), by Comparing Physical and Chemical Properties, and Homology Results, in Order to Produce the Best, Hybrid Triticale

*Yasaman Naziri\**, Ege Univ., Dept. of Seed Science and Technology, İzmir, Turkey  
*Houtan Vafaiefard*, Ege Univ., Dept. Of Seed Science and Technology, İzmir, Turkey  
*Raziyeh Sarabadani Tafreshi*, Department of Biotechnology, Payame Noor University, Tehran, Iran  
*Mohammad Ali Ebrahimi*, Department of Biotechnology, Payame Noor University, Tehran, Iran  
\*Corresponding author: nnyasan@yahoo.com

**Keywords:** Biotechnology, plant breeding, molecular biology, hybrid triticale, wheat, rye, bioinformatics  
**Discipline:** Agriculture, Plant Biotechnology

### Abstract

Triticale (Triticosecale) is a man-made hybrid through crossing between wheat and rye and is one of the plants that can play an important role in supplying most of human and livestock needs with its high production capacity. This plant was created to combine desirable traits of the two parental species, including high production capacity, wide adaptability, desirable wheat grain traits, and rye tolerance to abiotic stresses. In this study, five wheat varieties, namely Aflak, Ofogh, Gonbad, Navid, and Dena, were tested as the maternal base crossed with a fixed parental base variety, namely Nikita rye. In a first experiment, the sequences of organic bases from five base varieties were identified through the CLC main software. After elimination of the beginning and end of the band pattern, these sequences were evaluated by 19 primers as they were not identified by the software. After modeling the base sequence, five triticale  $F_1 \rightarrow F_5$  hybrids were also identified by the CLC main software. Then, its base sequence was examined to compare the characteristics of CG pair, annealing temperature, cross-examination of base patterns in the  $3' \rightarrow 5'$  direction, line alignment, and the line temperature similarity ( $P_1 \rightarrow P_5$ ) for the production of  $F_1 \rightarrow F_5$  hybrids. Finally, it was determined that  $P_1 \rightarrow P_5$  line could have the most effective bases and hybrid similarities in producing suitable lines for base alignment based on behavioral similarities in terms of physicochemical properties and band similarity, and the line among the maternal  $P_{11} \rightarrow P_{51}$  lines that could produce the best and most suitable hybrid. In order to identify a suitable hybrid band pattern among  $F_1 \rightarrow F_5$  hybrids, effective and important physicochemical properties were examined in  $P_{11} \rightarrow P_{51}$  lines. Results showed that P41 (Navid) wheat could be the best maternal line in the production of triticale ( $F_{41}$ ) hybrid. In terms of important physicochemical properties, Navid variety, for example, with a high probability was the suitable maternal line as indicated by the number of beta and alpha helix sheets and could have better yield in terms of other characteristics than the other four maternal line varieties.

### Introduction

Population growth and the need for more food along with the impossibility of increasing the cultivation area, excessive human pressure on existing resources, and its adverse effects on the environment are among the challenges causing a quantitative increase and quality improvement of crops per unit area. Thus, the cultivation of new and compatible plants is considered as one of the most appropriate solutions. Today, soil fertility issues, plant nutritional needs, and global food security are the frontispiece of the World Food Declaration [1]. Over the last few decades, the cultivation of triticale in different parts of the world shows its adaptation in a wide range of different climatic conditions. Evaluation of quantitative yield of triticale over successive years indicates that this plant has a better yield in cropping conditions equal to those of wheat. Triticale is highly tolerable to salinity and some varieties can compete with wheat and barley in tolerance to salinity in the early stages of growth [2]. Triticale has great potential for adaptation to a wide range of climatic conditions. It also performs better and is more adaptable than wheat in tolerance to acidic soils [3]. Most of triticale varieties that tolerate acidic and aluminum soils in areas with prevalent abiotic stresses, such as drought, salinity, toxicity, or nutrient deficiencies, are similar to their rye paternal parent. In vitro analysis of grains has shown that the percentage protein in triticale is higher than those of wheat, rice, rye, corn, and oats, and is in good condition in terms of essential amino acids. Also, the contents of leaf potash, phosphorus, and nitrogen are higher than wheat and rye during different stages of growth [1].

According to the above, there is a need to create a triticale hybrid that inherits desirable traits from its parents. In this study, endemic wheat line varieties were tried to be selected from desirable and highly cultivated varieties of the region. As such, the resulting hybrids are expected to have the positive traits of triticale mentioned earlier, in addition to the desirable traits of maternal lines so that they can replace part of the area under wheat cultivation. This study aims to investigate the similarity of triticale hybrids to their parents in order to create suitable, resistant, and high-yield hybrid varieties, and tries to elucidate the importance of using alternative triticale varieties in place of their parental lines that have maximum similarity to wheat and rye. The examination and production of the obtained triticale hybrid allow to obtain suitable cold- and drought-resistant varieties that can produce the traits of maternal lines as a hybrid crop. Thereby, triticale can be used both directly and indirectly as a suitable food hybrid source in terms of desired proteins and adaptability with the cultivation area.

### Materials and Methods

Five wheat varieties (Aflak = P<sub>11</sub>, Ofogh = P<sub>21</sub>, Gonbad = P<sub>31</sub>, Navid = P<sub>41</sub>, and Dena = P<sub>51</sub>) were used to perform genetic tests, examine alignments, and to compare maternal lines with the produced hybrids. The paternal line was the Nikita rye variety. Seeds of five wheat varieties, one Nikita rye variety, and five triticale hybrid varieties were planted in suitable plastic pots. After two weeks of germination, the leaves of the varieties were harvested as lines ready for the study, transferred to the laboratory, and the nuclear DNA was extracted using the Delaporta method. In the experimental stages, it was necessary to change the quantitative and qualitative indicators after each DNA extraction operation. To do this, the obtained DNA was electrophoresed in 1% agarose gel for 2 h. The resulting DNA formed only one band and had the least amount of fragmentation.

Then, the quality of DNA was determined using the adsorption ratio by the volume of 260 to 280 nm (the highest adsorption levels of DNA and protein are at 260 and 280 nm, respectively). To determine the sequence of products obtained from polymerase chain reaction (PCR), they were sent to the Fanavaran Gene Co. (the products were prepared according to the protocol provided by this company). Then, results obtained from computable analyses were evaluated by alignment multivariate analyses using sequences obtained from databases of other analyses by the CIC main software.

### Results

#### Correlation and percentage similarity of CG pairs of the maternal line to the resulting hybrid triticale

According to the results (Table 1), the maternal main line of Aflak wheat could transfer up to 55% of the CG base pair, line similarity, and base alignments in the amino acid sequence pattern. There is even moderate similarity in terms of forward and reverse sequences. On the other hand, it could not be the desired variety in terms of gradient slope temperature and self-annealing. Therefore, Aflak variety cannot function optimally to produce the hybrid triticale. According to the comparison of Ofogh maternal line and the resultant hybrid (Table 2), its similarity is higher than Aflak wheat in terms of CG pair percentage and forward and reverse sequences, hence Ofogh wheat can produce better hybrids. This means that it was relatively able to show 65% better alignment in terms of band pattern, due to forward and reverse sequences, and even the percentage of CG pairs.

As shown in Table 3, Gonbad variety failed to transfer organic bases to its hybrid and also showed less alignment than the other two varieties studied here. Additionally, it showed an alignment lower than 35% in terms of direct and reverse sequences, making Gonbad wheat an unsuitable variety. Consequently, it could not produce a desirable hybrid as a maternal base and was not successful as an effective genetic indicator in the selection and production of a suitable hybrid.

Based on the data in Table 4, Gonbad wheat could not successfully transfer organic bases to its hybrid, and also showed less alignment than the two other studied varieties. In addition, it presented an alignment lower than 35% in terms of direct and reverse sequences, making Gonbad wheat an unsuitable variety. Accordingly, it could not produce a desirable hybrid as a maternal base and was not successful as an effective genetic indicator in the selection and production of a suitable hybrid.

The results in Table 5 indicate that the P<sub>5.1</sub> maternal line could have up to 85% similarity of base pairs with its hybrid triticale. A comparison of amino acids in forward and reverse modes also showed a high level of similarity. After Navid variety, therefore, Dena maternal line had the best performance between the other two varieties and became of interest here.

### **Physicochemical properties and band patterns of endemic wheat maternal line varieties and the resulting triticale hybrids**

As shown in Table 6, the pattern obtained from Aflak wheat could have little overlap with triticale hybrid. It also had a low ancestral ratio for the transfer of organic bases to the produced hybrid. Also, there is a high difference between line P<sub>1.1</sub> and the produced hybrid with regard to the number of amino acids. Regarding the Gravy factor, which is related to a protein or peptide, it could be more compatible with the wheat and the produced triticale hybrid, but the different wheat varieties showed different compatibility spectra than the produced triticale. In this respect, Aflak wheat and its hybrids could not be effective in proper overlapping and alignment in the transfer of genes and organic bases making up the essential amino acids of the formed bond. Aflak wheat, therefore, cannot be a suitable variety for the transfer of effective genes to its triticale hybrid. Also, the abundance of hydrophobic amino acids, including alanine, phenylalanine, isoleucine, leucine, methionine, proline, valine, and tryptophan in wheat, are 42 and 44% in Aflak and Triticale varieties, respectively, which could not be a suitable maternal line for the production of hybrid triticale.

Based on the data in Table 4-7, the length of band patterns and organic bases for the amino acids, as well as the overlap and alignment of organic bases, Ofogh wheat and its resultant triticale hybrid had an acceptable percentage of transfer from Ofogh wheat maternal line to the produced hybrid triticale compared to Aflak variety. However, this transfer could create little similarity and alignment in the transfer of ancestral concerned genes. In terms of the length and weight of base patterns, Ofogh wheat was not adequately similar to the resultant hybrid. In addition, it showed a relative difference in terms of hydrophilic and hydrophobic frequencies, that is, it was different concerning the frequency of positive and negative charges and the number of beta and alpha helix sheets. As a result, the maternal line of Ofogh wheat is not suitable for the production of triticale hybrids. It was ranked the third with 85% gene balance in terms of the relation and relative transfer of effective organic bases, based on the information in Table 7.

According to Table 8, it can be inferred that Gonbad maternal line has a very low compatibility with its triticale hybrid in terms of the studied traits, which can be detected by the high difference between the numbers of alpha and beta helix sheets. This means that these sheets have little ability regarding the balance of positive and negative charges to transfer base similarities and the type of transfer. Hence, it is not adequately capable in terms of genetic transfer and ancestral kinship, and has little compatibility with the produced hybrid with regard to crossing with the maternal base, thus it acted differently regarding the number of beta sheets. It also showed significant differences concerning the physicochemical nature, alignment properties, and organic base pairs. Therefore, it can be said that Gonbad variety could not be a suitable maternal line. The data in Table 9 demonstrated that Navid wheat with a high percentage and an effective probability coefficient both concerning the alignment of organic base sequences and the sequence length obtained from the band pattern, even regarding the band pattern weight, was very consistent with the lowest error for effective transfer to triticale F4 hybrid, acting most properly in transferring the sequence detected by the CLC main software. This variety was also very successful in the amount and intensity of light absorption; hence it was identified as the best genetic inheritance pattern to its hybrid offspring and can be considered a suitable cultivar to be selected as the maternal line. Moreover, it was successful in the frequency of organic bases and transferable amino acids in the length and weight quality of the band pattern with a high confidence level. As a result, this variety was able to succeed in genetic relations and their proper transfer to the desired hybrid with the highest quality prioritization index. As Navid wheat was introduced as a semi-tolerant variety to cold and suitable for cultivation in cold regions by the Iranian Seed Breeding Institute (1990), a triticale hybrid from Navid wheat line with similar traits can be expected from the results of this study. Based on the results in Table 10, the study of physicochemical characteristics of Dena wheat as the maternal base and its resulting hybrid shows that the frequency of positive and negative charges is more different in Navid variety than Dena variety and the resultant hybrid. Subsequently, the alpha- and beta helix sheets behave differently, and was ranked after Navid variety with a slight difference. High similarity was also achieved in the alignment of bases, meaning that there are very small differences between the frequency of positive charges for Dena variety and the hybrid as well as the negative charges of this variety with hybrids. As a result, it is ranked the second after Navid wheat due to the high similarity of

organic bases, even in terms of the frequency and type of amino acids with the least difference compared to the produced hybrid.

### Discussion and Conclusion

The aim of this study was to obtain the best triticale hybrid from five studied wheat varieties as the maternal base or P<sub>1</sub> line and to compare the homology tables of wheat varieties and triticale. The physicochemical properties as well as the similarities and differences between wheat varieties and triticale were also investigated in terms of optical wavelength characteristics and their CG pairs.

Triticale was created to replace wheat and rye in suboptimal conditions for each of its parents. The difference between triticale and wheat is that the R genome has been replaced by the D genome in the former, which is more efficient than wheat R genome in such traits as yield, disease resistance, tolerance to the deficiency of trace elements, ion toxicity, and phosphorus uptake efficiency [4]. A number of scientists compared the band patterns of wheat, rye, and triticale, and concluded that the hybrid triticale plant was much more similar to its wheat maternal base than rye [5]. Therefore, the strengths of the hybrid triticale compared to its parents and a high genetic similarity of triticale to wheat were confirmed here by comparing the band patterns and examining the physicochemical properties. It is, therefore, concluded that triticale hybrid obtained from Navid wheat has the highest similarity to its maternal base (Navid variety) among the five selected wheat cultivars, in addition to having R-genome-dependent positive traits transferred from rye.

In a study on the genotypes of different triticale varieties, it is concluded that the utilization of genetic diversity and genetic structure is used as a preliminary recommendation for breeding programs [6]. In this regard, in addition to physicochemical comparisons between the hybrid triticale and its parent in the present study, the obtained results can be used to study triticale hybrids directly to select a suitable hybrid for cultivation.

Table 1. Correlation and percentage of similarity of CG pairs in Aflak maternal line with the resulting hybrid

Sequence / Variety	Forward	Reverse	Annealing temperature	Self-Annealing	CG pair (%)
Aflak P1	GTCATCGGGTAC GCGTATG	TATCCTTATC GGTTCTTTT	57	14	53
Hybrid F1	GTGGTCGCCTAC GGGTATC	TCTCCAAAT CGGTTCTTTT	54	12	56

Table 2. Correlation and percentage of similarity of CG pairs in Ofogh maternal line with the resulting hybrid

Sequence / Variety	Forward	Reverse	Annealing temperature	Self-Annealing	CG pair (%)
Ofogh P2	GTCCTCGGG TCCGTCTGCC	GGCAGACGGA CCCGAGGAC	56	13	54
Hybrid F2	GCGCACGCC TGGACCAG	GGATGACGGT CCCCACGAC	54	11	56

Table 3. Correlation and percentage of similarity of CG pairs in Gonbad maternal line with the resulting hybrid

Sequence / Variety	Forward	Reverse	Annealing temperature	Self-Annealing	CG pair (%)
Gonbad P3	GTCACCGGCT ACGGGAACG	CGTTCCCGTA GCCGGTGAC	58	14	51
Hybrid F3	GAGTGGGGCT TCCCCTACG	CCAAGCCGAA GCGCCAGTG	52	11	56

Table 4. Correlation and percentage of similarity of CG pairs in Navid maternal line with the resulting hybrid

Sequence Variety	Forward	Reverse	Annealing temperature	Self-Annealing	CG pair (%)
Navid P4	TACCTGGGTAC GGCATCTG	CAGATGCCGT ACCCAGGTA	56	13	54
Hybrid F4	TACCTGGGTAC GGCATCTG	CAGATGCCGT ACCCAGGTA	56	13	54

Table 5. Correlation and percentage of similarity of CG pairs in Dena maternal line with the resulting hybrid

Sequence Variety	Forward	Reverse	Annealing temperature	Self-Annealing	CG pair (%)
Dena P5	TACCTGGGTAC GGCATCTG	CAGATGCCGTAC CCAGGTA	56	13	54
Hybrid F5	TACCTGGGTAC GGCATCTG	CAGATGCCGTAC CCAGGTA	55	12	53

Table 6. Physicochemical properties and band pattern of Aflak wheat and its triticale hybrid

Varieties	Aflak wheat maternal base	Hybrid triticale
Traits		
Studied pattern length	142	144
Studied pattern weight	14.7	14.3
IP	7.27	7.10
Aliphatic index	53.67	54.19
Absorbance coefficient (260 nm)	33	32.14
Absorbance coefficient (280 nm)	2.17	2.27
HcNoS atomic frequency	0-10-8-30-46	0-10-9-30-46
Hydrophobic frequency	43	45
Hydrophilic frequency	35	37
Negative charge frequency	12	11
Positive charge frequency	10	8
Max. frequency of amino acids	<b>Serine 9</b>	<b>ValineSerine-9</b>
Number of alpha-helix	8	6
Number of beta sheets	2	1
Gravy	0.46	-0.47

Table 7. Physicochemical properties and band pattern of Ofogh wheat and its triticale hybrid

Varieties	Ofogh wheat maternal base	Hybrid triticale
Traits		
Studied pattern length	142	144
Studied pattern weight	14.7	14.3
IP	7.27	7.10
Aliphatic index	53.67	54.19
Absorbance coefficient (260 nm)	33	32.14
Absorbance coefficient (280 nm)	2.17	2.27
HcNoS atomic frequency	0-10-8-30-46	0-10-9-30-46
Hydrophobic frequency	43	45
Hydrophilic frequency	35	37
Negative charge frequency	12	11
Positive charge frequency	10	8
Max. frequency of amino acids	<b>Serine 9</b>	<b>Serine-Alanine -9</b>
Number of alpha-helix	8	6
Number of beta sheets	2	1
Gravy	0.46	-0.47

Table 8. Physicochemical properties and band pattern of Gonbad wheat and its triticale hybrid

Varieties	Gonbad wheat maternal base	Hybrid triticale
Traits		
Studied pattern length	141	145
Studied pattern weight	14.96	15.94
IP	7.91	5.84
Aliphatic index	58.21	54.16
Absorbance coefficient (260 nm)	31	34.11
Absorbance coefficient (280 nm)	2.11	3.16
HcNoS atomic frequency	0-10-8-30-48	0-11-7-30-49
Hydrophobic frequency	44	41
Hydrophilic frequency	31	38
Negative charge frequency	10	14
Positive charge frequency	11	6
Max. frequency of amino acids	<b>Serine 9</b>	<b>Valine -9</b>
Number of alpha-helix	9	6
Number of beta sheets	3	1
Gravy	-0.49	-0.47

Table 9. Physicochemical properties and band pattern of Navid wheat and its triticale hybrid

Varieties	Navid wheat maternal base	Hybrid triticale
Traits		
Studied pattern length	144	144
Studied pattern weight	15.68	15.67
IP	8.23	8.1
Aliphatic index	56.25	55.75
Absorbance coefficient (260 nm)	33	33.2
Absorbance coefficient (280 nm)	2.11	2.10
HcNoS atomic frequency	0-9-8-31-48	0-9-8-31-47
Hydrophobic frequency	42	43
Hydrophilic frequency	34	35
Negative charge frequency	12	12
Positive charge frequency	10	11
Max. frequency of amino acids	<b>Serine 9</b>	<b>Serine -9</b>
Number of alpha-helix	9	8
Number of beta sheets	3	3
Gravy	-0.48	-0.48

Table 10. Physicochemical properties and band pattern of Dena wheat and its triticale hybrid

Varieties	Dena wheat maternal base	Hybrid triticale
Traits		
Studied pattern length	142	142
Studied pattern weight	15.51	15.40
IP	8.41	7.90
Aliphatic index	2.21	2.27
Absorbance coefficient (260 nm)	34	34.51
Absorbance coefficient (280 nm)	2.21	2.27
HcNoS atomic frequency	0-9-8-30-49	0-10-8-30-49
Hydrophobic frequency	42	43.17
Hydrophilic frequency	34	35.17
Negative charge frequency	12	12.8
Positive charge frequency	10	11
Max. frequency of amino acids	<b>Serine 9</b>	<b>Serine 10</b>
Number of alpha-helix	9	7
Number of beta sheets	3	2
Gravy	-0.42	-0.494

### References

- [1] Hosseinzadeh, H., Hashemi, H., Quraishi, R. (2012). The impact of waste from four important crops on improving food security in the country. Second National Seminar on Food Security, Savadkuh, Islamic Azad University, Savadkuh Branch.
- [2] Francois, L.E., T.J. Donovan, E.V. Maas and G.L. Ruberenthaler. 1988. Effect of salinity on grain yield and quality, vegetative growth and germination of triticale. *Agron. J.*, 80: 642-647
- [3] Royo, C., Rodriguez, A. and Romagosa, I. (1993), Differential Adaptation of Complete and Substituted Triticale. *Plant Breeding*, 111: 113-119. doi:10.1111/j.1439-0523.1993.tb00616.x
- [4] Li, G., He, Z., Lillemo, M., Sun, Q., Xia, X., 2008, Molecular characterization of allelic variations at Pina and Pinb loci in Shandong wheat landraces, historical and current cultivars. *Journal of Cereal Science*, 47, 51.517-0
- [5] Kharrazi, Mohammad Ali Shirazi and Mohammad Reza Naroui Rad. Evaluation of sorghum genotypes under drought stress conditions using some stress tolerance indices. *African Journal of Biotechnology* 10 (2011): 13086-13089.
- [6] Niedziela, A., Orłowska, R., Machczyńska, J., & Bednarek, P. T. (2016). The genetic diversity of triticale genotypes involved in Polish breeding programs. *SpringerPlus*, 5, 355. <https://doi.org/10.1186/s40064-016-1997-8>



## Identification of 3 Defense-Related Enzymes Activities by Using 2 Cell Damage Indices in 2 Chickpea Plants Genotypes under Cold Stress

*Houtan Vafaeifard\**, Ege Univ., Dept. of Seed Science and Technology, İzmir, Turkey

*Yasaman Naziri*, Ege Univ., Dept. of Seed Science and Technology, İzmir, Turkey

*Samane Karami*, Shahid Beheshti Univ., Dept. of Agriculture, Tehran, Iran

*Reza Maali Amiri*, Tehran Univ., Dept. of Agronomy and Plant Breeding, College of Agriculture and Natural Resources, Karaj, Iran

\*Corresponding author: [h.vafaeifard@gmail.com](mailto:h.vafaeifard@gmail.com)

**Keywords:** Alternative oxidase, superoxide dismutase, catalase, reactive oxygen species, cold stress, electrolyte leakage, chickpea

**Disciplines:** Biotechnology, Agricultural Engineering, Plant Breeding, Molecular Biology, Genetics

### Abstract

Plants need diverse defensive mechanisms to survive and be tolerant under different environmental conditions. In the present study, the activity of 3 defense enzymes, namely, alternative oxidase (AOX), superoxide dismutase (SOD), catalase (CAT) in parallel with the amount of electrolyte leakage index (ELI) and hydrogen peroxide (H<sub>2</sub>O<sub>2</sub>) as cellular damage indices in two genotypes of chickpea, susceptible (ILC533) and tolerant (Sel96Th11439) was evaluated under 4°C cold stress. The analytical analysis of the results indicated that there is a remarkable difference between the genotypes under cold stress. Under cold stress, a decline in damage indices was accompanied by a significant elevation in the amount of AOX activity. The maximum activity of AOX was seen in the tolerant genotype on the sixth day of cold stress; However, AOX activity in the susceptible genotype significantly was lower compared to the tolerant genotype under such conditions. The rise in AOX activity that was accompanied by a drop in the evaluated cellular damage indicators, particularly on the sixth day of cold stress, demonstrated the vital role of AOX enzyme in the defense mechanism of chickpea plants at low temperatures. The simultaneous and notable increase in SOD and CAT activities, along with the results concluded from AOX activity analysis, may be beneficial and applicable in the assessment of chickpea genotypes under cold stress or considering them in breeding schemes.

### Introduction

Plants due to the lack of mobility are perpetually exposed to biotic and abiotic stresses. As a consequence, they must be able to sense and respond to their surroundings and therefore they must be agile in maintaining the homeostasis within the cell under the unsettled conditions [1]. Cold stress is a restrictive factor affecting the abundance and quality of crop plants. Cold stress tolerance elevation is directed by the cellular response in physiological, biochemical, and molecular levels. These responses are caused by gene induction and genome reprogramming in the cells. The plasma membrane is the first part of the cell response to cold stress. Therefore, evaluation of electrolyte leakage as a cell damage index can be an appropriate indicator in the early stages of the stress [2]. On the other hand, reactive oxygen species including superoxide (O<sub>2</sub><sup>-</sup>), hydroxyl radical (•OH), and non-radical molecules such as hydrogen peroxide are considered as cell damage causes [3]. ROS are produced by an unavoidable leakage of electrons into oxygen within the electron transport chain in the chloroplast, mitochondria, or plasma membrane. Besides, they can be generated as a natural by-product of the normal metabolic pathways [4]. Environmental stresses like cold stress as a result of the disruption in the cell homeostasis processes lead to a rise in the amount of ROS production. Excessive growth in ROS amount or inefficient removal of them puts the cell in the danger of oxidative stress which can be a serious threat for cells due to the lipid's peroxidation, proteins oxidation, oxidative nucleic acid damages, enzymes inhibition, and can lead to activation of cell death processes such as apoptosis [5]. Despite their destructive effects, they are known as secondary messengers in cellular processes such as cellular stress responses [6]. Whether the ROS act as a cellular messenger or oxidative stress depends on the scavenging systems and ROS generation balance. Cellular defense mechanisms such as enzymatic antioxidants including superoxide dismutase (SOD), catalase (CAT), Guaiacol peroxidase, Ascorbate peroxidase (APX), Glutathione reductase (GR) in cellular tissues and cellular organelles are needed for effective removal of produced ROS under cold stress [7]. Mitochondrial electron transport chain consists of diverse enzymatic complexes that play a significant role in forming a proton gradient required for ATP production. The

main pathway of this chain which provides needed energy is named cytochrome c oxidase (COX). COX catalyzes the transfer of electrons from ferrocytochrome c to molecular oxygen, converting the latter to water [8]. The plants have another Respiratory terminal oxidase in parallel with the COX pathway called alternative oxidase (AOX) which is a mitochondrial inner-membrane oxidase that accepts electrons directly from ubiquinol and reduces oxygen to water without being concerned with cytochrome-linked electron transport chain [9]. AOX is controlled by a gene family. This gene family is made up of two subfamilies named *aox1* and *aox2*. *Aox1* gene expression is affected in response to biotic, abiotic stresses (like *aox1a* in *Arabidopsis* and tobacco), and due to the improper mitochondrial electron transfer chain function [10]. AOX pathway probably plays a remarkable role in the mitigation of ROS that is formed through the electron transfer chain as AOX enzyme activity increases under environmental stresses and therefore the ROS amount and cell damage are reduced consequently [11]. Due to the restrictions of spring cultivation of chickpea plants (*Cicer arietinum* L.) like drought and lack of moisture that lead to yield reduction by 300 to 400 kilograms per hectare, fall cultivation regarding suitable rainfall and humidity appears to be more reasonable and practicable. However, the cold is a limiting factor in plant growth and development [1]. The study of alternative pathway respiration under cold stress in chickpea plants considering its possible role in ROS production regulation can be beneficial in the characterizing of defense mechanisms in plant breeding schemes. In the present study, the activity of the AOX enzyme along with several defensive responses under cold stress is evaluated under cold stress.

### Materials and Methods

The seeds of tolerant and susceptible genotypes were provided by National Rainfed Agricultural Research Institute. The seeds were disinfected by Sodium Hypochlorite solution 10% for ten minutes and after rinsing by distilled water the seeds germinated in the petri dish on filter paper soaked in water. The seedlings were transferred to pots. The ratio of sand, clay, and fertilizer was 1:3:1. The pots were placed in the growth chamber of the agronomy and plant breeding department of Tehran University. These plants were stored for 21 days at a temperature of 23 degrees Celsius, a light intensity of 220  $\mu\text{mol m}^{-2} \text{s}^{-1}$ , and a humidity of 75%. A part of the plants was kept as control samples in the mentioned condition and the other part was transferred and preserved at a temperature of 4 degrees Celsius for six days. Leaf sampling was performed at a temperature of 4 degrees Celsius on the first, third, and sixth days. Completely healthy leaves in the middle of the stem were used to measure the electrolytic conductivity. 80 mg of leaves were cut horizontally and transferred to the test tube containing 10 mg distilled water. For better water absorption, the air inside the test tube was removed using a vacuum pump and the test tubes were placed on a shaker for 30 minutes. The amount of electrolytic conductivity (EC1) of the samples were measured by an EC meter. (a Germany-made conductivity meter named Inolab). In the second stage, the amount of electrolytic conductivity of the test tube content was measured after placing the test tube in the boiling water bath at a temperature of 95 degrees Celsius for 10 minutes and then placing on the shaker board for 30 minutes. Eventually, the Electrolyte Leakage Index (ELI) amount was measured based on the formula  $I = \text{Ec1} / \text{Ec2} * 100$  [12]. To extract mitochondria, 5 mg leaf samples were homogenized in 20 ml of extraction buffer containing 0.4 mM mannitol, 50 mM Morpholino propane sulfonic acid (pH 7.2), 2 mM EGTA, 4mM L-cysteine, 20 mM  $\beta$ -mercaptoethanol, 0.6% polyvinylpyrrolidone, and 0.5% bovine serum albumin at a temperature of 4 degrees celsius. The resulting solution was centrifuged at 4000 X G for 5 minutes and the floating solution was centrifuged in two steps at 2000 X G for 10 minutes and 10000 X G for 30 minutes. The existing precipitate in the tube was washed by washing buffer containing 0.3 mM mannitol, 20 mM Morpholino propane sulfonic acid, 0.1% volume defatted BSA and 1 mM EGTA. Afterward, it was centrifuged at 2000 X G for 10 minutes. After centrifuging the supernatant at 15000 X G for 15 minutes, the existing precipitant at the bottom of the tube was homogenized by the washing buffer [13]. The activity of AOX was measured by the construction changes of oxidation (DQ) and reduction (DQH2) forms of duroquinol. The activity of AOX was evaluated using a spectrophotometer at 288 nm in S medium consisting of 5 mM  $\text{MgCl}_2$ , 10 mM  $\text{K}_2\text{HPO}_4$ , 10 mM sodium pyruvate, 5 mM dithiothreitol, 0.025% ethylenediaminetetraacetic acid, 1.8 mM myxothiazol, and 10 mM TES (pH was 6.8 and adjusted by KOH). The activity of AOX was obtained after adding 200  $\mu\text{l}$  DQH2 as a precursor to 2500  $\mu\text{l}$  of S medium and adding 20  $\mu\text{l}$  of extract containing mitochondria [14]. The activity of superoxide dismutase (SOD) was measured according to Beyer and Fridovich method [15]. The activity of this

enzyme was investigated photometrically. The major reaction buffer consisted of 100 mM phosphate buffer solution (pH=7.8), 12 mM methionine, 75 mM nitroblue tetrazolium, 100 mM EDTA, and 0.025% Triton X-100. 290  $\mu$ L major buffer, plus 5 $\mu$ L of riboflavin buffer (2 $\mu$ M) was added to a cuvette and the spectrophotometer was calibrated to a wavelength of 560 nm. For the measurement of each sample, 10  $\mu$ L of the protein extract was used. The method is based on *the reduction of nitroblue tetrazolium and the ability of the SOD in reduction inhibition. The amount of enzyme activity was measured based on the enzyme unit per minute per mg of protein.* The activity of the catalase enzyme at 25 degrees celsius was measured by the Scebba method [16]. The materials used consisted of 3000  $\mu$ L of 50mM potassium phosphate (pH:7), 5  $\mu$ L of 3.41 M hydrogen peroxide, and 100  $\mu$ L of enzyme extract. The activity of the enzyme was measured based on micromoles of hydrogen peroxide decomposed per minute in milligrams of protein. The required hydrogen peroxide was provided by 0.35 gram of leaf tissue. First, the leaves were ground in the liquid nitrogen mixed with 5 ml of 0.1% trichloroacetic acid completely in the ice bath. The homogenized mixture was centrifuged at 12000 X G at 4 degrees Celsius for 15 minutes. Afterward, 0.5 ml of supernatant was added to 0.5 ml of 10 mM potassium phosphate. Besides, 1 ml of 1M potassium iodide was added. Afterward, 0.5 ml of supernatant was added to 0.5 ml of 10 mM potassium phosphate. Besides, 1ml of 1M potassium iodide was added and the absorbance was measured at a wavelength of 390 nm [17]. Experimental data were analyzed based on a factorial experiment in a completely randomized design with three replications using SPSS 20 software and the means were compared based on Duncan's multiple range test.

### Conclusions

The results of the analysis of variance indicated that the interaction of genotype and temperature treatments had a meaningful difference ( $P \leq 0.01$ ) in terms of the studied traits, which demonstrates the existence of genetic diversity between genotypes and different responses of genotypes under temperature treatments. In the present study, ELI was considered as a physiological index for the determination of membrane damage in different genotypes of chickpea. The mean comparison test of ELI illustrated a meaningful difference among temperature treatments, which indicated the potential diversity of the responses in two genotypes under this condition (Figure 1). Under physiological temperature (23 degrees Celsius), the amount of ELI in the tolerant genotype was less than the susceptible genotype significantly that presents the distinctive genetic capacity of the tolerant genotype. Transfer the seedlings to the temperature of 4 degrees Celsius on the first day caused no remarkable change in the amount of ELI. However, the amount of ELI in the susceptible genotype on the third and sixth days of stress induction had a noticeable change, while a meaningful alteration was not observed in the tolerant genotype. The lowest and highest amount of ELI belonged to the tolerant and susceptible genotypes respectively on the sixth day. Therefore, probably the results of ELI under long-term tensions (6 days after the stress induction) shows the different tolerance levels of two genotypes in comparison with short-term tensions (after 1-day stress induction). Generally, the low level of electrolyte leakage in leaf cells deliberates the tolerance of the plant to cold stress [18]. As a result, it seems that the tolerant genotype under with less ELI under cold stress benefits from a more active defense mechanism, which leads to a kind of cellular compatibility. An increase of more than 50% indicates severe cell damage and eventually cell death [2]. Such a situation was observed in susceptible genotype.

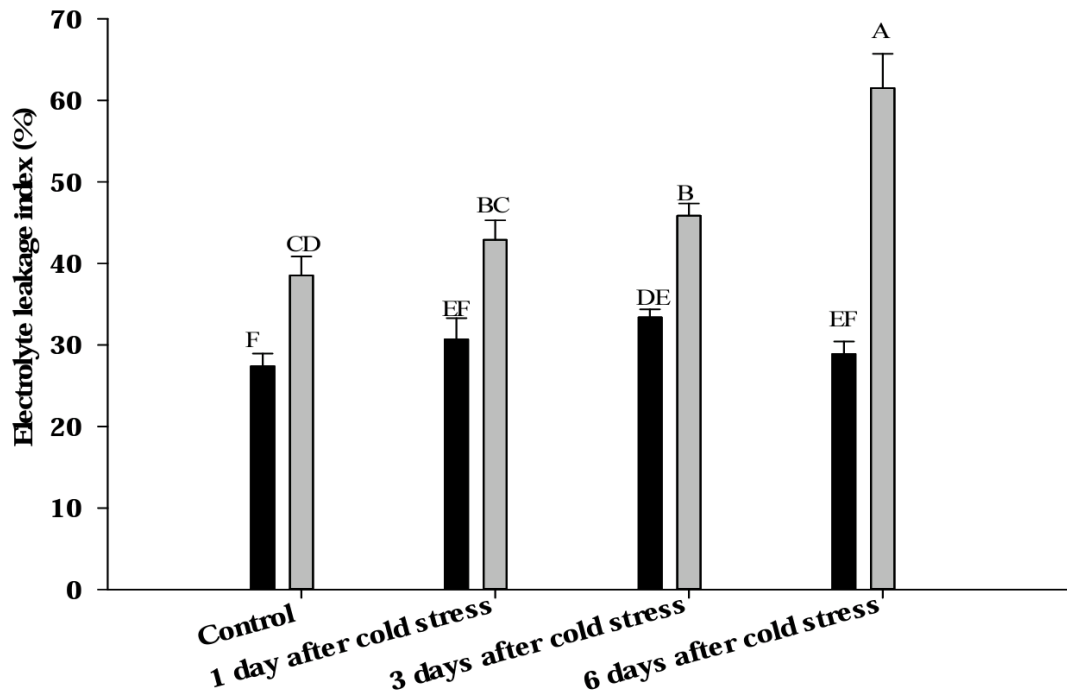


Figure 1. Change in electrolyte leakage index ELI in the leaves of tolerant (Sel96Th11439) and susceptible (ILC533) chickpea genotypes (black and light gray bars, respectively) grown under control (23°C) and day 1, day 3, and day 6 of cold stress (4°C).

The higher amount of ELI under cold stress was caused by ROS production that leads to oxidative stress consequently [19]. Accordingly, the changing pattern of H<sub>2</sub>O<sub>2</sub> production during different days of stress induction was measured. This molecule in contrast with other ROS has a longer half-life and can be diffused through biological membranes and as a messenger molecule triggers oxidative stress at plant cells in a place far from the place of production [20]. The results delineated that in the tolerant genotype the amount of H<sub>2</sub>O<sub>2</sub> after a meaningful rise during the first and third days of stress induction fell on the sixth day so that under such a condition the amount of H<sub>2</sub>O<sub>2</sub> reached the lowest level among the experimental treatments. In this condition, the amount of H<sub>2</sub>O<sub>2</sub> in the susceptible genotype soared considerably compared with the control sample by about 33%. (Figure 2). The result corroborated the results obtained from the examination of ELI. Furthermore, it represents the extension of oxidative stress under the influence of cold stress in comparison with the control condition in susceptible compared to the tolerant genotype. As a result, the level and intensity of stress response vary in different genotypes of chickpea, and also the study of the damage patterns under stress and normal conditions indicated this fact [21]. SOD and CAT are considered active molecules in the defense mechanisms of cells and play a vital role in the production and degradation of H<sub>2</sub>O<sub>2</sub> respectively [18]. The results manifested that the two genotypes respond differently in the face of cold stress. The level of SOD activity in the susceptible genotype after an imperceptible change in the first day, reduced gradually during the third and sixth days of stress induction so that it fell to the lowest level of activity, while a gradual upward trend was observed in the tolerant genotype. The highest amount of SOD, which was nearly 50% was on the sixth day of the stress induction. On the first day of stress, the amount of CAT activity in the tolerant genotype declined, whereas on the third and sixth days it was observed a substantial growth. In conclusion, its activity reached the level of the control sample. The activity of this enzyme in the susceptible genotype had about 52% reduction on the third day of stress induction compared to the control sample.

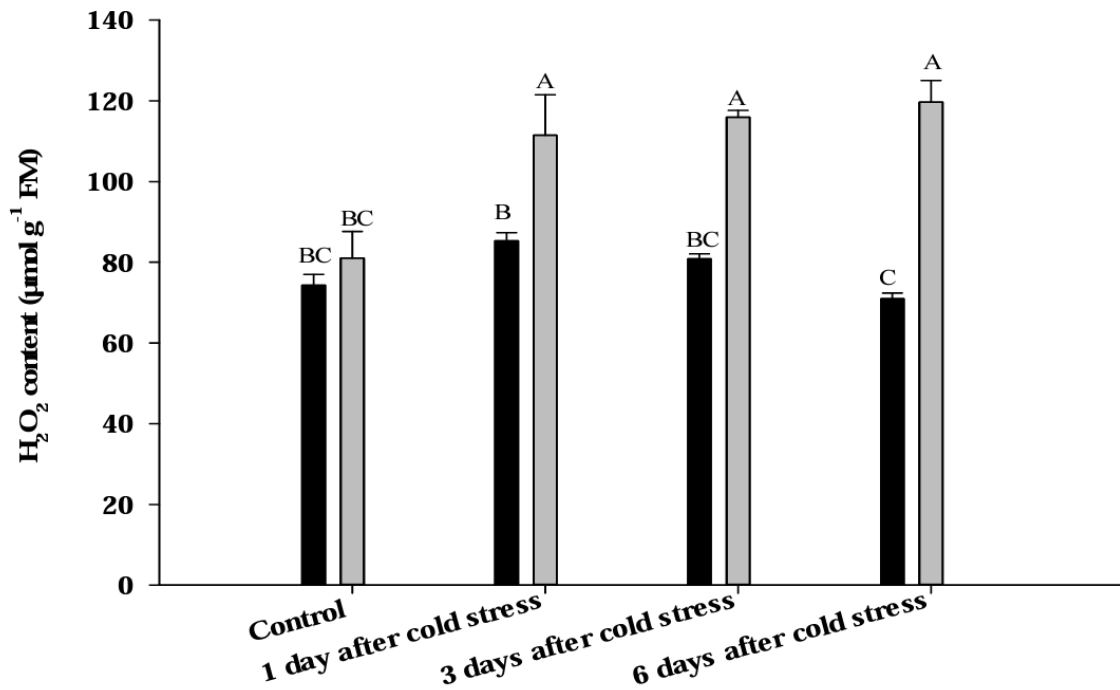


Figure 2. Change in hydrogen peroxide (H<sub>2</sub>O<sub>2</sub>) content in the leaves of tolerant (Sel96Th11439) and susceptible (ILC533) chickpea genotypes (black and light gray bars, respectively) grown under control (23°C) and day 1, day 3, and day 6 of cold stress (4°C).

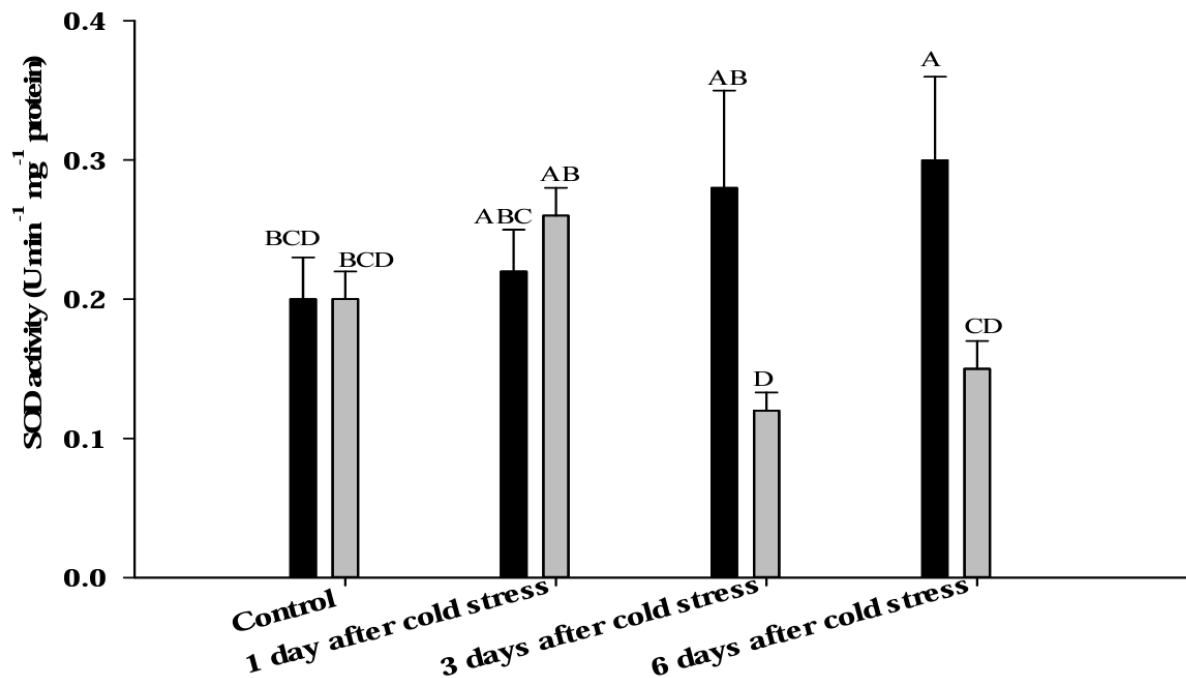


Figure 3. Change of activity in superoxide dismutase (SOD) in the leaves of tolerant (Sel96Th11439) and susceptible (ILC533) chickpea genotypes (black and light gray bars, respectively) grown under control (23°C) and day 1, day 3, and day 6 of cold stress (4°C).

Although the activity of CAT in susceptible genotype on the sixth day was higher than the third day, in comparison with the control sample a meaningful reduction in the enzyme activity was observed (Figures 3 and 4). Therefore, the studied antioxidant enzymes in the present study co-operate with each other, and an increase in their simultaneous activity leads to a decrease in the amount of cell damage (ELI) and also the amount of H<sub>2</sub>O<sub>2</sub> as one of the ROS produced in the cell. The process of electron

chain reaction, ROS formation, and finally the amount of ATP in the mitochondria are complicated, because under the stress an alternative electron pathway towards the AOX enzyme is activated which provides flexibility among carbon metabolism, electron transfer, and ATP production [9]. As a result, the activity of AOX as one of the most important enzymatic complexes in the mitochondrial electron chain reaction was measured. The activity of AOX increased with the prolongation of the stress period from the first to the sixth day in both genotypes after a significant decrease had an upward trend again, which indicates the effective role of this enzyme in the plant biochemical responses to cold stress.

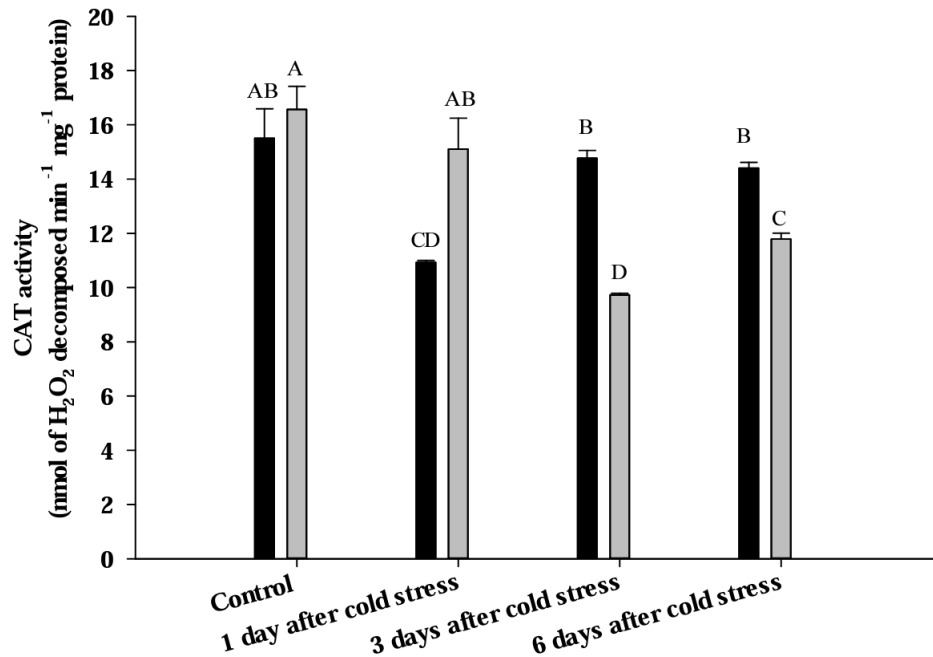


Figure 4. Change of activity in catalase (CAT) in the leaves of tolerant (Sel96Th11439) and susceptible (ILC533) chickpea genotypes (black and light gray bars, respectively) grown under control (23°C) and day 1, day 3, and day 6 of cold stress (4°C).

However, the level of AOX activity in the tolerant genotype was much higher than the susceptible genotype, so that this upward trend, unlike the susceptible genotype, started on the third day after stress and reached its maximum on the sixth day after stress (Figure 5). Research has shown that AOX activity modulates  $\text{O}_2^-$  production, which in turn reduces its conversion to other ROS species such as  $\text{H}_2\text{O}_2$  and  $\text{OH}^-$  [22]. It seems that under stress, oxidative stress messengers and plasma membrane properties (ELI and  $\text{H}_2\text{O}_2$  results) acted as key factors in regulating the activity of AOX genes, which ultimately inhibited ROS production ( $\text{H}_2\text{O}_2$  in this experiment) (Figures 1 and 2).

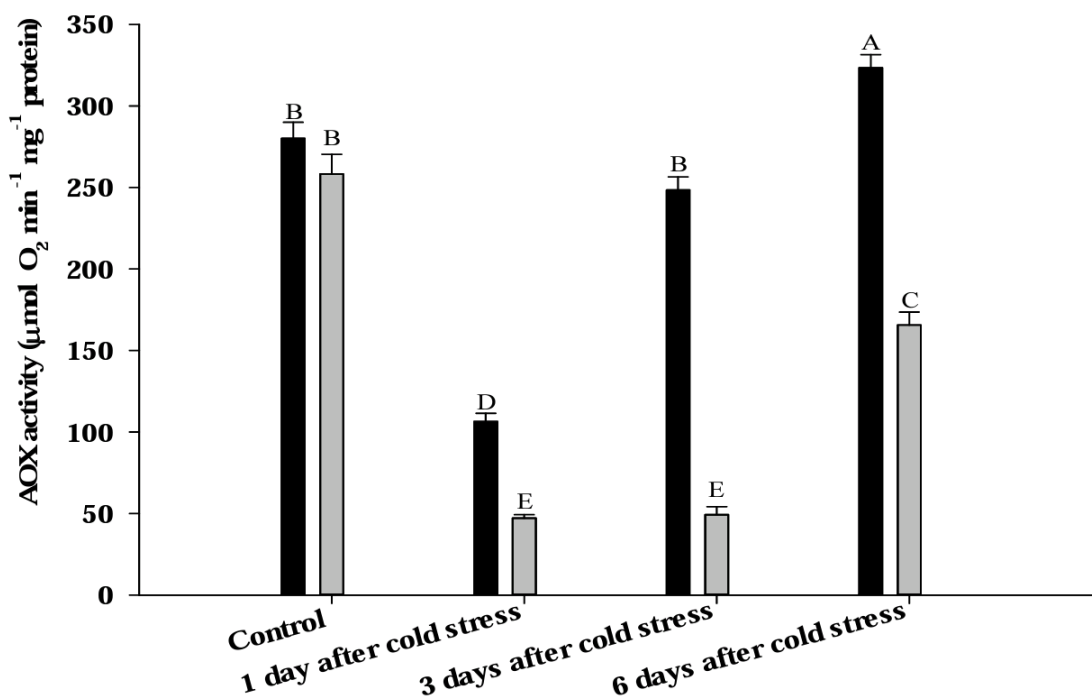


Figure 5. Change of activity in alternative oxidase (AOX) in the leaves of tolerant (Sel96Th11439) and susceptible (ILC533) chickpea genotypes (black and light gray bars, respectively) grown under control (23°C) and day 1, day 3, and day 6 of cold stress (4°C).

Tobacco-related researches suggested that plant transfer to cold conditions induces AOX enzyme activity so that the amount of Malondialdehyde as one of the cell damage indices decreases [23].

Thus, the alteration in ROS production is due to the changes in ROS inhibition capacity. It states that the control mechanisms of mitochondrial ROS production such as AOX can be critical to identify how the host cell manages the amount of ROS and how it determines the fixed level of cellular ROS [24]. The relationship between cell damage (ELI) and AOX enzyme activity in this experiment was inverse so that higher activity of this enzyme in the tolerant genotype was associated with a reduction in the cell damage. Besides, the activity of antioxidant enzymes increased in parallel with the rise of AOX activity, particularly in the tolerant genotype of chickpea. It seems that the AOX pathway and the pathway of antioxidant responses in the cell are associated and as a result of that the highest amount of inhibition in H<sub>2</sub>O<sub>2</sub> production and ELI was correlated with the highest amount of AOX and antioxidants activity. The increase of AOX enzyme activity indicated that the induction of cellular adaptation processes to reduce the amount of ROS may take place in the level of transcription or translation as the seedlings transfer to the lower temperatures caused a disruption of mitochondrial electron chain reaction. Thus, the plant responds to cold stress by increasing the AOX protein synthesis and as a result, the amount of ROS reduces (H<sub>2</sub>O<sub>2</sub> and ELI results). The susceptible genotype of chickpea sustains more damages compared with the tolerant genotype due to the less activity of AOX and reduced capacity of other antioxidant enzymes. Wider studies about these enzymes, their families, and the strategies to increase their gene expression in chickpea can be a principal approach to ease the fall cultivation of chickpea.

### References

- [1] Kazemi Shahandashti SS, MaaliAmiri R, Ramezanpour SS, Zeinali H (2013). Change in membrane fatty acid compositions & cold-induced responses in chickpea. *Molecular Biology Repts.* 40: 893-903.
- [2] Heidarvand L, Maali Amiri R, Naghavi MR, Farayedi Y, Sadeghzadeh B, AlizadehKh (2011). Physiological and morphological characteristics of chickpea accessions under low temperature stress. *Russian Journal of Plant Physiology* 58: 157-163.
- [3] Gill SS, Tuteja N (2010). Reactive oxygen species and antioxidant machinery in abiotic stress tolerance in crop plants. *Plant Physiology and Biochemistry* 48: 909-930.

- [4] Heyno E, Krieger-Liszky A, Mary V, Schopfer P (2011). Oxygen activation at the plasma membrane: relation between superoxide and hydroxyl radical production by isolated membranes. *Planta* 234: 35-45.
- [5] Mishra S, Jha AB, Dubey RS (2011). Arsenite treatment induces oxidative stress, upregulates antioxidant system & causes phytochelatin synthesis in rice seedlings. *Protoplasma* 248: 565-577.
- [6] Heidarvand L, MaaliAmiri R (2010). What happens in plant molecular responses to cold stress? *Acta Physiologiae Plantarum* 32:419-432.
- [7] Foyer CH, Noctor G (1998). Ascorbate and glutathione: keeping active oxygen under control. *Annual Review of Plant Biology* 49: 249-279.
- [8] Wang J, Rajakulendran N, Amirsadeghi S, Vanlerberghe GC (2011). Impact of mitochondrial alternative oxidase expression on the response of *Nicotiana tabacum* to cold temperature. *Physiologia Plantarum* 142: 339-351.
- [9] Vanlerberghe GC (2013). Alternative oxidase: a mitochondrial respiratory pathway to maintain metabolic and signaling homeostasis during abiotic and biotic stress in plants. *International Journal of Molecular Science* 14: 6805-6847.
- [10] Gandin A, Duffes C, Day DA, Cousins AB (2012). The absence of alternative oxidase AOX1A results in altered response of photosynthetic carbon assimilation to increasing CO<sub>2</sub> in *Arabidopsis thaliana*. *Plant and Cell Physiology* 53: 1627-1637.
- [11] Vanlerberghe GC, Cvetkovska M, Wang J (2009). Is the maintenance of homeostatic mitochondrial signaling during stress a physiological role for alternative oxidase? *Physiologia Plantarum* 137: 392-406.
- [12] Popov VN, Orlova IV, Kipaikina NV, Serebriiskaya TS, Merkulova NV, Nosov AM, Trunova TI, Tsydendambaev VD, Los A D (2005). The effect of tobacco plant transformation with a gene for acyl lipid  $\Delta 9$ -desaturase from *Synechococcus vulcanus* on plant chilling tolerance. *Russian Journal of Plant Physiology* 52: 664-667.
- [13] Erdal S, Genisel M, Turk H, Dumlupinar R, Demir Y (2015). Modulation of alternative oxidase to enhance tolerance against cold stress of chickpea by chemical treatments. *Journal of Plant Physiology* 175: 95-101.
- [14] Affourtit C, Moore AL (2003). Purification of the plant alternative oxidase from *Arum maculatum*: measurement, stability and metal requirement. *Biochimicae Biophysica Acta* 1608: 181-189.
- [15] Beyer WF, Fridovich I (1987). Assaying for superoxide dismutase activity: some large consequences of minor changes in condition. *Analytical Biochemistry* 161: 559-566.
- [16] Scebba F, Sebastiani L, Vitaglianpo C (1998). Changes in activity of antioxidative enzymes in wheat (*Triticumaestivum*) seedlings under cold acclimation. *Physiologia Plantarum* 104:747-752.
- [17] Loreto F, Velikova V (2001). Isoprene production by leave protects the photosynthetic apparatus against ozone damage, quenches ozone products, and reduces lipid peroxidation of cellular membranes. *Plant Physiology* 127: 1781-1787.
- [18] Kazemi Shahandashti SS, Khazaei M, Maali-Amiri R, Ramezanpour SS, Talei AR, Zeinali H (2014). Effect of short-term cold stress on oxidative damage and transcript accumulation of defense-related genes in chickpea seedlings. *Journal of Plant Physiology* 171: 1106-1116.
- [19] Heidarvand L, Maali-Amiri R (2013). Physio-biochemical and proteome analysis of chickpea in early phases of cold stress. *Journal of Plant Physiology* 170: 459-469.
- [20] Bienert GP, Kristiansen KA, Møller ALB (2007). Specific aquaporins facilitate the diffusion of hydrogen peroxide across membranes. *Journal of Biological Chemistry* 282: 1183-1192.
- [21] Nazari M, MaaliAmiri R, Mehraban FH (2012). Change in antioxidant responses against damage in black chickpea following cold acclimation. *Russian Journal of Plant Physiology* 59: 183-189.
- [22] Rogov AG, Sukhanova EI, Uralskaya LA, Aliverdieva DA, Zvyagilskaya RA (2014). Alternative oxidase: distribution, induction, properties, structure, regulation, and functions. *Biochemistry (Moscow)* 79: 1615-1634.
- [23] Huang GT, Ma SL, Bai LP, Zhang L, Ma H, Jia P, Liu J, Zhong M, Guo ZF (2012). Signal transduction during cold, salt, and drought stresses in plants. *Molecular Biology Reps* 1: 969-987.
- [24] Amirsadeghi, S, McDonald AE, Robson, C.A, Vanlerberghe GC (2006). Changes in plant mitochondrial electron transport alter cellular levels of reactive oxygen species and susceptibility to cell death signaling molecules. *Plant Cell Physiology* 47: 1509-1519.



## **Animal Nutrition / Hayvan Besleme**

## Cassava Root Silage as a Feed for Ruminants

*Jacob Matovu, Ege University, Faculty of Agriculture, Department of Animal Science, İzmir, Turkey*  
*Ahmet Alçiçek, Ege University, Faculty of Agriculture, Department of Animal Science, İzmir, Turkey*  
*\*Corresponding author: matoisrael@gmail.com*

**Keywords:** Cassava root silage, hydrocyanic acid, feed, ruminant  
**Discipline:** Animal Nutrition

### Abstract

Roots and tubers have high moisture content which makes them difficult to handle. During harvesting, transporting, and storage, roots can get damaged which makes them get spoiled quickly. The poor storage life of cassava roots necessitates rapid processing into a stable product. Normally the commonly used method of processing cassava is sun drying. Sun-dried cassava chips are susceptible to attack by several insect pests, even when stored for a short period, making an economical and eco-friendly storage impossible. Furthermore, in seasons of heavy rains, sun drying is hard to be done and is accompanied by the need for much labor force and there are high risks of aflatoxin contamination. To ensure the supply of safe animal feed all year round the technique of ensiling cassava has been constantly investigated. Cassava root is rich in energy and has a high amylopectin content (83%) that makes it a good energy feed for ruminants. Cassava silage has been used in areas where feeds become inadequate, especially during the dry seasons. Several studies have stated the use of cassava silage in livestock feeding, especially for monogastric. However, little or no information has critically analyzed cassava root silage as a potential feed for ruminants. This review paper discusses cassava production and world distribution, utilization of cassava root silage as feed-in ruminants, effects of ensiling on hydrocyanic acid, and its effects on ruminants.

### Introduction

Cassava cultivation dates back between 6,500 –5,500 BC, in the Amazon lowlands and has since been extensively cultivated in the tropics and subtropics of the world [1]. The first European travelers quickly recognized this crop's virtues in South America and the major area of concern is Brazil, since they had already colonies held in Africa and Asia they quickly spread it in these areas [2]; [3]. It is cultivated mainly by resource-limited small farmers for its starchy roots, which are used as human food either fresh or in many processed forms and products also used as animal feed [4]. Because of its inherent tolerance to stressful environments, where other food crops would fail, it is often considered a food security source against famine, requiring minimal care, it can easily grow in sandy-loam soil, in areas receiving low rainfall and high temperature [5].

About 70% of world cassava root production is used for human consumption then the remaining 30% is used for animal feed and other industrial products like starch or alcohol [5]. Currently, we are seeing an increase in the use of cassava in animal nutrition mainly because of its high energy value [6], in a way that it can partially or completely replace maize as an energy source in animal diets. Cassava starch has a large amylopectin content (83%) making it a suitable energy source for ruminants when combined with non-protein nitrogen in feeds [7].

Constraints to increased utilization of cassava in ruminants are mainly because of getting sufficient amounts, their low protein content, and the hydrogen cyanides [8]. The scenario of sufficient amount comes as a result of rapid perishability of cassava, meaning if much is harvested and brought to the farm, will get spoiled in few days thus causing a deficiency. Cassava root silage has been used when feeds are inadequate especially during the dry season in many areas where grazing is the main form of feeding for ruminant livestock. This season is associated with lower quantity and quality of grasses, especially in its energy and nitrogen. As a consequence, feed intake declines, and animal productivity is curtailed [9].

Furthermore, a commonly used crop for making silage is maize. Unfortunately, the ever-increasing stiff competition between humans and other local industries for maize is making higher demands on the crop. This is in addition to the massive requirements for the monogastric animals (poultry) [7]; [10]. The necessity to reserve any available maize for the above priorities calls for investigations into alternative dry season feeds. According to [11], the two most widely used processing methods are sun-

drying and ensiling. In the tropics, especially in the wet season, sun drying is difficult and may result in the production of a low-quality product with intense *Aspergillus* and aflatoxin contamination. Artificial drying is relatively expensive which makes the use of the root meal non-competitive with cereal by-products such as broken rice and bran. Ensiling of the cassava root appears to be a more feasible alternative.

### Cassava Production and World Distribution

Cassava (*Manihot esculenta Crantz*) is one of the major food crops, 6<sup>th</sup> after rice, maize, wheat potato, and barley, and acts as a staple food for more nearly one billion people in 105 countries, in the tropics, contributing above 60% of daily calorific needs [12];[13]. Developed countries grow most of the maize, wheat, potatoes, whereas developing countries grow most of the sweet potatoes and the cassava [14]. In previous years world, cassava production (based on the years 1988-1990) was approximately 144 million tons of fresh roots (equivalent to 48 million tons dry matter), of which 44% came from Africa, 37% from Asia, and 19% from Latin America [15]. For the period from the year 1995 to the year of 1997, world annual cassava production was 165.3 million tons, with an approximate value of US\$8800 million [16]. General, there has been a gradual increase in world cassava production. Recently Africa is still considered as the highest producer in the world accounting for 61.1% (more than 88 million tons), followed by Asia with 29%, Americas 9.8%, and lastly 0.1% Oceania according to Table 1 [17].

Table 1. showing cassava production and distribution [17]

Region	Area (ha)	Production (t)	Yield (hg/ha)
Africa	18681232	169673737	90826
Asia	3754922	80637819	214752
Americas	214752	27245826	127658
Oceania	20389	251376	123290
World	24590818	277808759	112973

### Nutrient composition of cassava tuber

The cassava plant is a woody shrub of 2 to 4 metres in height depending on the variety. Cassava tubers constitute 50% and the leaves makeup 6% of the mature plant and are the nutritionally valuable parts of the plant [18]. The root consists of the bark (outermost layer, 0.5- 2% of the tuber), then peel (1-2 mm thick; 8-15% of the tuber, and contains most of the toxic hydrogen cyanogenic glucosides) and then the fleshy starchy parenchyma (comprising of 83-92% of the tuber) which is the eaten part [12]; [19]. In most cases, each plant consists of 5 to 20 starchy elongated tubers. The tuber may be from 20 to 80 cm long and having a diameter of 5 – 10 cm. Average tuber weight ranges between 4 and 7 kg however specimens up to 40 kg have been reported [20].

The proximate and mineral contents of cassava products are shown in Table 2. The variability in the values shown in the tables is due to strain and varietal differences, location, fertilizer applications, soil type, environmental conditions, and the method of chemical analysis [13];[21].

Table 2. The proximate and mineral composition of cassava tuber and its products

Product	DM%	CP%	EE%	CF%	Ash %	CHO %	Ca g/kg	Pg/kg
Root	91.39	2.44	1.64	4.13	2.46	80.68	2.00	2.29
Root meal	89.51	2.65	0.56	2.19	3.63	60.00	1.60	3.70
Flour	85.43	1.90	1.53	1.74	1.76	64.47	0.90	4.01
Leave	86.90	21.64	4.99	13.05	5.90	46.83	20.90	5.01
Pulp	89.20	1.97	0.31	16.7	2.49		0.54	0.36
Peel	83.18	5.07	2.49	16.28	6.52	47.44	3.41	1.40

Sources; Root = [22];[23];[6];[7] Root meal = [24];[25];[26];[27] Flour = [28];[6];[29];[30]; Leaves = [31];[32];[33];[34] Pulp = [35]; [36]; [37];[38] Peel = [39];[40];[41];[37]; [42]

The starchy flesh consists of 80% to 90% total weight of the root with water forming the main components. The root contains a lot of water contributing to its poor storage, the water content of cassava ranges from 60.3% to 87.1% [18];[23]. Moisture is an important parameter in the storage of cassava root and its products, very high levels greater than 12% allow for microbial growth and thus low levels are favorable and give relatively longer shelf life [30]

In cassava root, carbohydrate content is 320.0–350.0 g/kg on a fresh weight (FW) basis and 80%-90% on a (dry weight) DW basis, which is higher than that of potatoes, but lower than that of wheat, rice, and sorghum. Carbohydrate and energy densities are high, suggesting that these could be used as a reliable food and energy source [43]. Cassava is an energy-dense food and therefore ranked high for its calorific value of  $250 \times 10^3$  cal/ ha/day as compared to  $176 \times 10^3$  for rice,  $110 \times 10^3$  for wheat,  $200 \times 10^3$  for maize, and  $114 \times 10^3$  for sorghum. It has an energy value of more than 3000 MJ metabolizable [44]. The cassava starch is highly digestible. Comparing cassava starch to maize starch, cassava starch contains 17% amylose and 83% amylopectin, with maize starch which has 28% amylose and 72% amylopectin. This shows how the digestible starch of cassava is compared with traditional common starch sources used in animal feeds [7].

The protein content is low ranging between 1% to 3% (Table 2) on a dry matter basis and between 0.4 and 1.5 g/100g of fresh weight [45]. However different researchers have reported higher or lower protein values, but generally, cassava tubers are said to have lower protein content[46]; [43].

Cassava is very low in lipids, in cassava roots ranges from 0.1% to 0.3% on a fresh weight (FW) basis, it ranges 0.1% to 0.4% and 0.65% on a dry weight (DW) basis[7];[23]. This content is relatively low compared to maize(6%) and sorghum, but higher than potato and comparable to rice [47]. The low level of lipids in cassava implies that there is also a poor source of fat-soluble vitamins.

The fiber content of the tuber does not exceed 1.5% in fresh roots and 4% in root flour. Cassava consists of 2% dry weight (DW) soluble fibers along with 7.1% insoluble fibers [48]. However, according to [49], showed that cassava can act as a replacement for maize as fiber sources when they showed cassava containing 8.23% crude fiber.

Different reports have given varying ash compositions depending on the varieties and other factors ranging from 1- 2.34 % in the root [43]. Ash content is an indicator of mineral contents, the higher the ash content the higher the mineral content [35]; [23]. Cassava is a good source of these minerals; K, Ca, Fe, Mn and Cu Ca, Cu, Fe, K, Mg, Mn, Na, P, and Zn. The Potassium (0.327 to 1.087%) and calcium (1083 to 1858 ppm) have been shown by [32] to be the most abundant minerals present in cassava tuber. Iron, magnesium, copper, zinc, and manganese are present in cassava at lower concentrations than those found in sorghum and maize [43];[48]. The low level of lipids in cassava implies that it is also a poor source of fat-soluble vitamins (ADEK), also it has low levels of vitamin B1, B2, and niacin but high levels of vitamin C [7];[47].

#### **Antinutritional substances (HCN) in cassava.**

Cassava contains anti-nutrients and toxic compounds which reduce its nutrient bioavailability, nutrient uptake, and digestibility during feeding including: (1) cyanogenic glucosides, the most toxic compounds depending on the cultivars and environmental conditions (2) oxalate, an anti-nutrient to negatively affect the bioavailability of magnesium and calcium; (3) anti-nutritional factors, such as high fiber content, tannins, polyphenols, and phytic acid; (4) non-protein amino acids (such as alanine, aspartic and glutamic acids), considered as the etiology of clinical disorders. Therefore cassava consumption without adequate processing could cause serious illness or death [34]; [50].

Besides all this, the most important antinutritional component are the glycosides [51], when studying molecular differentiation, diversity, and folk classification of “sweet” and “bitter” cassava (*Manihot esculenta*), reported that the cassava plant contains 2 glycosides, linamarin (80% of total glycoside) it's synthesized from valine and lotaustralin (20%) synthesized from isoleucine. These two glycosides are acted upon by a cell-wall enzyme to liberate hydrogen cyanide (HCN), which is lethal to animals. The amount of HCN in a given plant will depend on the cultivar, environmental conditions, plant age, number of harvests (for the foliage), and on the organ considered [52], [53].

The bitter varieties have been reported to have higher HCN than sweet varieties. Bitter varieties have roots containing 0.02-0.03% HCN (DM basis) while sweet varieties have roots containing less than 0.01% [54].

### Cassava root silage

Cassava roots need rapid processing into a stable product that can't get spoilt easily. Normally cassava tubers will get spoilt within 3 days. In humid places where sun-drying is not easy, or during excess production cassava roots can be ensiled alone or with cassava leaves or other feeding materials [55],[11]. A commonly used method of preservation is sun drying but dried cassava during storage can be easily attacked by insect pests, to ensure animal feed supply all year-round cassava ensiling has been investigated.

Cassava ensiling is very similar to that of forages, however, the high-water content of the root and its loss during the ensiling process should be put into consideration during the construction of the silos. Following this, solid, non-absorbent floor, and drainage should be provided to avoid excessive water accumulation and alcoholic fermentation or putrefaction from occurring[55].

According to Phnom [56], after cassava harvest the fresh roots are cleaned, wilted for 3-5 hours, chopped in 2-3 cm or grated finely mixed with additives like salt, molasses, the mixture is then packed into the silo, pressed tightly to expel all the air. It is then left to ferment naturally, the mixture can be used after 2-3 weeks of ensiling and kept for at least 3-4 months. Asaolu, [57] in his experiment cassava peels' moisture contents was reduced from 70-75 % to about 40% by wilting (air drying) for 2 days before ensiling. The silage after 21 days was firm in texture, light brown in colour, and had a pleasant odor. The pH was 4.4 acceptable for good silage, and no fungal growth was observed.

### Effects of ensiling on the nutritional value of Cassava

According to [58], the ensiling of cassava causes the following effects to the nutritional value of cassava that's; **i.** Detoxification of feed anti-nutrients during the process of fermentation (HCN reduction); **ii.** Biological enhancement of food substrates with proteins, essential amino acids, essential fatty acids, and vitamins; **iii.** Enrichment of the fermented products through the impartation of a range of aroma, flavours, and textures; and **iv.** Preservation of the fermented products through the production of lactic acid, acetic acid, alcohol, and alkali in the substrate as a result of fermentation. The ensiling process has shown to be more effective in reducing the HCN than sun drying, it causes disintegration of intact glucoside through cell disruption, a drop in pH of the ensiled medium, and an intense heat generation that reduces moulding [59]. The microorganisms produced during ensilage by the process of fermentation are capable of producing linamarase which then hydrolyzes the glycosides hence reducing the cyanide content [60]. Gomez and Valdivieso [61], showed that ensiling cassava chips reduced the hydrogen cyanide content to 36% of the initial value after an ensiling period of 26 weeks. Also in another experiment was found that about 98% of the free cyanide was lost by ensiling cassava roots with poultry litter for 8 weeks [62]. During the ensiling process, the increase in growth and proliferation of fungi or bacterial complex also helps to improve the crude protein content, lipid content, minerals, and vitamins content of cassava silage [63]. Fermentation of cassava peels has been shown to increase crude protein in the peels from less than 2% to 13-26% [64]. Oboh and Akindahunsi [63], in an attempt to enhance the nutritional quality of cassava products (flour and gari). The study showed that there were significant increases in the protein flour (10.9%), gari (6.3%), and fat flour (4.5%), gari (3.0%) contents. However, there were significant decreases in the cyanide content flour (9.5 mg/kg), gari (9.1 mg/kg). Okhonlaye and Foluke [42] fermented for 96 hours, then proximate and mineral composition of the was carried out. The proximate composition showed an increase in the nutritive value and mineral composition of the fermented sample when compared with raw samples as shown in Table 3.

Table 3. Proximate and mineral composition of fermented cassava [42].

Parameter	DM%	Ash %	Fat%	CF %	CP %	CHO %	Na(ppm)	Ca(ppm)	K(ppm)	Zn(ppm)	Fe (ppm)
Fermented	92.96	16.5	3.2	7.5	15.66	50.01	12.9	36.5	21.63	0.85	20
Raw	92.28	10.01	4.08	22.91	12.51	45.76	12.2	29.46	12.92	0.65	19.5

An experiment by Zanine and co-authors [62], whereby cassava scrapings were mixed with elephant grass and ensiled for 40 days, it was found out that cassava scrapings reduced losses and increased dry matter recovery, and Contents of N-NH<sub>3</sub> and butyric acid decreased quadratically, making the silage good for feeding.

### Effects of hydrogen cyanide (HCN) to ruminants

Intensive use of cassava products in animal feeding is possible after reduction of the cyanogenic glucosides. Cassava varieties containing HCN levels above 100 mg/kg are considered very toxic, then between 50–100 mg/kg moderately toxic, with those containing less than 50 mg/kg are preferred due to lower toxicity risk. In ruminants, cyanide can be toxic at 2 to 4 mg/ kg body weight [65] while in monogastric diets should contain less than 100 mg/kg HCN [59] [66]. According to [67] explained that ruminants can tolerate high levels of cyanide. Since rumen bacteria have the capacity to hydrolyze  $\beta$ -D-glucosides and to utilize the glucose as an energy source. The toxic Hydrogen cyanide can be quickly absorbed, belched, or further metabolized in the rumen [68];[69]. Earlier reports indicated that feeding large amounts of untreated cassava products could result in the death of animals, particularly non-ruminants [65].

### Utilization of cassava root silage as feed-in ruminants

#### Nutritive value of cassava silage for Cattle

In an earlier research, supplementing with ensiled cassava peels increased the Average daily gain of grazing cross-bred cattle from 0.07 kg/d to 0.33 kg/d compared to 0.29 kg/d for the dried peel [70]. Bureenok and co-authors [71] studied cassava root ensiled with Cassava leaves or Legumes on feed Intake and milk production of dairy cows and concluded that the dry matter intake was the highest ( $P < 0.05$ ) in cow fed with a combination of cassava root and cassava leave silages. Milk production in cow fed silages-based diets was much higher than cow fed with control diets. Also, milk compositions were not affected by feeding diets. Furthermore, 4% FCM was highest in cow fed with cassava root + cassava top-silages.

Table 4. Feed intakes and digestibility in cows fed with different silage-based diets[71]

Item	T1	T2	T3	T4
Total intake				
Kg DM/d	12.98	13.85	11.3	11.48
%BW	2.67	2.9	2.35	2.43
g/kg BW <sup>0.75</sup>	125.48	135.3	110.75	113.43
Milk production				
kg/d	11.68	13.75	13.4	12.25
4% FCM, kg/d	9.77	11.82	11.3	10.48
Milk fat %	2.92	3.05	2.92	3.02
Milk protein, %	3.37	3.18	3.48	3.42

Values in the same row followed by different letters are significantly different ( $p < 0.05$ ) T1 = control, T2 = cassava root +cassava top-silages, T3 = cassava root +hamata - silages and T4 = cassava root + Thapra stylo-silages.

In evaluating [72] feeding of an ensiled total mixed ration containing fresh cassava root on rumen characteristics, microbial protein synthesis, and blood metabolites in Thai native beef cattle according to Table 5, there was a positive effect on all these parameters after 7 days of ensiling. The dry matter voluntary intake for zero ensiling days was 107.3 g/kg BW<sup>0.75</sup> after 7 days ensiling, the dry matter voluntary intake was 109.1 g/kg BW<sup>0.75</sup>.

Table 5. Effects of ensiled total mixed ration containing fresh cassava root on rumen ecology, microorganisms, blood urea-nitrogen, and blood thiocyanate in Thai native beef cattle [72]

Parameter	0 days ensiling	7 days ensiling
Rumen Ecology		
Ruminal pH	7.1	6.9
Ruminal temperature, °C	39.1	38.7
NH <sub>3</sub> -N concentration, mg/dL	21	18.7
Ruminal microbes, cell/mL		
Protozoa, ×10 <sup>6</sup>	10.3	10.4
Bacteria, ×10 <sup>9</sup>	35.1	36.3
Blood parameters		
Blood urea-N concentration, mg/dL	9.9	9
Blood thiocyanate concentration, mg/dL	10.8	16.6

To the diet of ensiled cassava root-urea with rice straw, when 5% of brewers' grains were added, increased the dry matter intake, the apparent dry matter digestibility and N retention in local Yellow cattle was observed [73]. In another experiment supplementation of a basal diet of ensiled cassava root – urea and fresh cassava foliage with rice wine by-product improved the growth rate of local “Yellow” cattle by 37% and feed conversion by 21% [74].

In an experiment by [75], showed that feeding of ensiled cassava peels with elephant improved intake and milk production in Sokoto Gudali cows. Dry matter intake of cows increased from 2.56 to 3.84% of body weight (BW) and milk yield from 2.90 to 6.70 kg/d as the proportion of cassava peel in the grass silage increased. The feed conversion ratio (FCR) of cows ranged between 2.08 to 3.23 and improved with the inclusion of cassava peel in the silage. Cassava chip or other forms of cassava roots can be successfully ensiled with nutritional yeast (*Saccharomyces cereviceae*) to obtain a final product, with high crude protein and a relatively balanced profile of amino acids [76]. Supplementation of this product in replacement of soybean meal in lactating dairy cows resulted in very good milk yields (15.7 kg/d) [77].

#### Nutritive value of cassava silage for Small ruminants

Asaolu [57] fed West African Dwarf sheep on diets made of 80 percent dried or ensiled cassava peel, supplemented in each case with 20 percent *Gliricidia* leaves. The sheep were compared to a control group fed solely on *Gliricidia*. The performance of the sheep is summarized in Table 6 which shows that sheep fed mainly on ensiled cassava peel with a small supplement of protein-rich *Gliricidia* efficiently put on weight during this period. The sheep consumed more of the ensiled cassava which had low HCN and showed greater performance. The differences observed in the performance of the sheep were attributed in part, to the different levels of HCN in the diets.

Table 6. Performance of sheep fed ensiled or dried cassava peel [57]

Parameter	Control	Test 1	Test 2
	100% <i>Gliricidia</i>	20% <i>gliricidia</i> + 80% ECP	20% <i>gliricidia</i> + 80% DCP
DM intake (kg/day)	1	0.7	0.6
Daily gain(g)	106	81	59
Feed efficiency	9.9	9.8	10.8
DM digestibility %	81.6	76	72

ECP = ensiled cassava peel, DCP = dried cassava peel

In another report [78], 20 local sheep were fed with ensiled cassava peels, inclusion rates in the diet were 0%, 20%, 40%, and 60% of ensiled cassava peels. The conclusion was that a high percentage of ensiled cassava peels increased slaughter weight, empty body weight, carcass weight, and the percentage of carcass weight. Adebowale [79], also fed fermented cassava peels to sheep at 0, 20, 40, and 60% levels of inclusion to replace equivalent amounts of maize in the control diet and observed average daily gain of 60, 38, 31, and 67 g/d and feed/gain ratios of 7.8, 10.9, 11.8 and 7.4 kg feed/kg gain respectively.

Sheep fed a diet containing 80% ensiled cassava peels had a higher daily gain of 81 g/d as compared to those fed sun-dried peels which gained 59 g/d [80].

In an experiment were grass-legume foliage, cassava peel, and poultry excreta were evaluated by Okeke and Oji [81]. The three feed materials were ensiled in the ratio of 60:20:20 on a wet basis, and fed to West African Dwarf goats. Control goats were fed a maize silage diet. Based on favorable consumption and digestibility of the cassava peel diet, as well as normal rumen and blood metabolites, the cassava peel mixture gave good quality silage which was consumed in equal amounts as the maize silage. Also recommended that in anticipation of dry-season feeding, cassava peel could be used as an energy supplement in an ensiled mixture of grass-legume foliage and poultry excreta. Other authors [82] in their experiment were 100% ensiled re-growths of vetiver grass without cassava peels exhibit poor silage characteristics and were rejected by the experimental WAD goats. Un ensiled regrowth of vetiver grass was poorly accepted while ensiling with cassava peels enhanced the acceptability by WAD goats.

### Conclusion

These are the points to consider when feeding ruminants with ensiled cassava tubers; (i). Due to the low protein content of cassava, there is a need to supplement it with a better protein source. (ii). The high-water content of the tubers may prevent the animals from consuming sufficient amounts to satisfy the given ruminant daily requirement, therefore ad libitum systems are mostly encouraged when feeding with ensiled cassava.

Due to the increasing cassava cultivation especially in Africa and the tropical countries, this means more cassava is going to be produced, the increased supply will require more advanced techniques like silage making to preserve it for longer periods especially in feeding cattle. This review suggests the need for much more research. Some areas in which research is required are; How best can the ensiled cassava be kept for quite long for example more than a year and remain in a suitable form. Silage keeping qualities of the sweet and bitter cassava varieties. Development of appropriate feeding systems (feeding trials) and technologies suited in most economic ways for cassava silage utilization by the ruminants.

### References

- [1] Watling J, Shock MP, Mongeló GZ, Almeida FO, Kater T, De Oliveira PE, Neves, EG. (2018). Direct archaeological evidence for Southwestern Amazonia as an early plant domestication and food production centre. *PLoS One*. 13(7):1–28.
- [2] Howeler R. (2020). Cassava in Asia : Trends in Cassava Production, Processing and Marketing. In Workshop on “Partnership in modern science to develop a strong cassava commercial sector in Africa and appropriate varieties by (pp. 2-6).
- [3] Liu Q, Liu J, Zhang P, He S. (2014). Root and Tuber Crops. *Encycl Agric Food Syst*. 5:46–61.
- [4] Pushpalatha R, Gangadharan B. (2020). Is Cassava (*Manihot esculenta* Crantz) a Climate “Smart” Crop? A Review in the Context of Bridging Future Food Demand Gap. *Trop Plant Biol*. 1-11.
- [5] El-sharkawy MA. (2004). Cassava biology and physiology (2003). *Plant Molecular Biology* vol. 56: 481-501.
- [6] Chisenga SM, Workneh TS, Bultosa G, Laing M. (2019). Proximate composition, cyanide contents, and particle size distribution of cassava flour from cassava varieties in Zambia. *AIMS Agric Food*. 4(4):869–91.
- [7] Morgan NK, Choct M. (2016). Cassava: Nutrient composition and nutritive value in poultry diets. *Anim Nutr* [Internet]. 2(4):253–61. Available from: <http://dx.doi.org/10.1016/j.aninu.2016.08.010>
- [8] Oresegun A, Fagbenro OA, Ilona P, Bernard E. (2016). Nutritional and anti-nutritional composition of cassava leaf protein concentrate from six cassava varieties for use in aqua feed Cogent Food Agric [Internet]. 62(1). Available from: <http://dx.doi.org/10.1080/23311932.2016.1147323>
- [9] Ayano RT. (2013). Nutritive value of ensiled cassava (*manihot esculentus*, crantz) tops and guinea grass (*Panicum maximum*) for the West African dwarf sheep. (Doctoral Diss. :1–28.
- [10] Sugiharto S. (2019). A review on fungal fermented cassava pulp as a cheap alternative feedstuff in poultry ration. *J World’s Poult Res*. 9(1):1–6.
- [11] Loc NT, Preston TR, Ogle B. (1997). Cassava root silage for crossbred pigs under village conditions in Central Vietnam. *Livest Res Rural Dev*. 9(2):12-19.
- [12] Lebot V. (2009). Tropical root and tuber crops: cassava, sweet potato, yams and aroids. Wallingford, UK: Crop production science in horticulture (17), CAB books, CABI; 2009.



- [13] Iulianelli GCV, Tavares MIB. (2016). Application of solid-state NMR spectroscopy to evaluate cassava genotypes. *J Food Compos Anal* [Internet]. 48:88–94. Available from: <http://dx.doi.org/10.1016/j.jfca.2016.02.009>
- [14] Rehm S, Espig G. (1991). The cultivated plants of the tropics and sub-tropics (translated by G. McNamara & C. Ernsting). *Eng Geol.* 31(3–4):369–70.
- [15] El-Sharkawy MA. Drought-tolerant cassava for Africa, Asia, and Latin America: breeding projects work to stabilize productivity without increasing pressures on limited natural resources. *Bioscience.* 43(7):441–51.
- [16] Scott GJ, Rosegrant MW, Ringler C. (2000). Roots and tubers for the 21st century. *2020 Vis Briefs* [Internet]. (May):1–28. Available from: <http://ideas.repec.org/p/fpr/2020br/66.html>
- [17] FAOSTAT. (2018). (Food and Agriculture Organization of the United Nations). Accessed Sept 12, 2020 <http://www.fao.org/faostat/en/#data>.
- [18] Padonou SW, Nielsen DS, Akissoe NH, Hounhouigan JD, Nago MC, Jakobsen M. (2010). Development of starter culture for improved processing of Lafun, an African fermented cassava food product. *J Appl Microbiol.* 109(4):1402–10.
- [19] Tewe OO. (1992). Detoxification of cassava products and effects of residual toxins on consuming animals. [Internet]. Roots, tubers, plantains and bananas in animal feeding.(D. Machin and S. Nyvold, editors) *FAO Animal Production and Health.* 1992. 81–98 p. Available from: <http://www.fao.org/docrep/003/T0554E/T0554E17.htm>
- [20] El-Sharkawy MA. (2004). Cassava biology and physiology Cassava: a crop for sustainable agriculture and food security in developing countries. *Plant Mol Biol.* 56:481–501.
- [21] Bechoff A, Tomlins K, Fliedel G, Becerra Lopez-lavalle LA, Westby A, Hershey C, et al. (2018). Cassava traits and end-user preference: Relating traits to consumer liking, sensory perception, and genetics. *Crit Rev Food Sci Nutr* [Internet]. 58(4):547–67. Available from: <https://doi.org/10.1080/10408398.2016.1202888>
- [22] Shimber T, Agza B, Abebe W, Habte G, Shiferaw L, Yilma S. (2018). *Food Science and Nutrition Completed Research and Completed Research.* 2018. 177–187 p.
- [23] Manano J, Ogowok P, Byarugaba-Bazirake GW. (2017). Chemical Composition of Major Cassava Varieties in Uganda, Targeted for Industrialisation. *J Food Res.* 7(1):1.
- [24] Ande KO, Oso AO, Oluwatosin OO, Sanni LO, Bello KO, Adebayo K, et al. (2018). Performance and economic benefits of meat-type chicken fed diets containing white and yellow cassava supplemented with different additives. *Food Chain.* 7(2):71–86.
- [25] Boitai SS, Babu LK, Panda AK. (2019). Effect of dietary replacement of maize with cassava root meal on production performance , egg quality and serum biochemical parameters of Vanaraja laying hens. 8(7):365–8.
- [26] Diarra S. (2015). Utilisation of cassava products-copra meal based diets supplemented with or without Allzyme SSF by growing pullets. *Malaysian J Anim Sci.* 18(1):67–76.
- [27] Adeyemi, O.A., D. Eruvbetine, T. Oguntona, M.A. Dipeolua JAA. (2007). Enhancing the nutritional value of whole cassava root meal by rumen filtrate fermentation. *Arch Zootec.* 56:261–4.
- [28] Akmal S, Hidayat B, Muslihudin M. (2018). ISBB Development of Processing Technology of High-Protein Cassava Flour Made from High-Cyanide Cassava. :5–10.
- [29] Lu H, Guo L, Zhang L, Xie C, Li W, Gu B, et al. (2020). Study on quality characteristics of cassava flour and cassava flour short biscuits. *Food Sci Nutr* [Internet]. [cited 2020 Mar 27];8(1):521–33. Available from: <https://onlinelibrary.wiley.com/doi/abs/10.1002/fsn3.1334>
- [30] Hasmadi M, Harlina L, Jau-Shya L, Mansoor A., Jahurul MH., Zainol M. (2020). Physicochemical and functional properties of cassava flour grown in different. 4(August):991–9.
- [31] Pereira IG, Vagula JM, Marchi DF, Gleice R, Almeida S, Maruyama SA. (2016). Easy Method for Removal of Cyanogens from Cassava Leaves with Retention of Vitamins and Omega-3 Fatty Acids. 27(7):1290–6.
- [32] Mohan G, Raju J, Shiny R, Abhilash P V, Soumya S. (2019). Biochemical , mineral and proximate composition of Indian cassava varieties Biochemical , mineral and proximate composition of Indian cassava varieties. 7(January):1059–65.
- [33] Li M, Zi X, Tang, JuXu T, Gu L, Zhou H. (2020). Effects of cassava foliage on feed digestion, meat quality, and antioxidative status of geese. *Poult Sci* [Internet]. 99(1):423–9. Available from:

- <http://dx.doi.org/10.3382/ps/pez522>
- [34] Oresegun A, Fagbenro OA, Ilona P, Bernard E. (2016). Nutritional and anti-nutritional composition of cassava leaf protein concentrate from six cassava varieties for use in aqua feed. *Cogent Food Agric* [Internet]. 2(1). Available from: <http://dx.doi.org/10.1080/23311932.2016.1147323>
- [35] Ogunbode A, Akinosun A, Olajide T. (2019). Nutrients and Anti – Nutrient Content of Sundried Cassava Starch Extract Pulp. *J. Appl. Sci. Environ. Manage.* 23 (6) 1133-1135
- [36] Abouelezz K, Yuan J, Wang G, Bian G. (2018). The nutritive value of cassava starch extraction residue for growing ducks. *Trop Anim Health Prod.* 50(6):1231–8.
- [37] Napasirth V, Napasirth P, Sulinthone T, Phommachanh K, Cai Y. (2015). Microbial population, chemical composition and silage fermentation of cassava residues. *Anim Sci J.* 86(9):842–8.
- [38] Keaokliang O, Kawashima T, Anghong W, Suzuki T, Narmseelee R. (2018). Chemical composition and nutritive values of cassava pulp for cattle. *Anim Sci J.* 89(8):1120–8.
- [39] Okechukwu SO, Jiwuba PC, State E. (2019). Effects of cassava and yam peel meals on carcass traits and economics of production of finishing broilers. *Sustain Agri, Food Environ Res.* 7(3):221–9.
- [40] Idugboe OD, Nwokoro SO, Masuen JA. (2015). Chemical Composition of Cassava Peels Collected from Four Locations (. *Int J Sci Res* [Internet]. 6(4):2319–7064. Available from: [www.ijsr.net](http://www.ijsr.net)
- [41] Gabriel OS, Fajemisin AN, Onyekachi DE. (2018). Nutrients Digestibility, Nitrogen Balance and Blood Profile of West African Dwarf (Wad) Goats Fed Cassava Peels with Urea-molasses Multi-nutrient Block (UMMB) Supplements. *Asian Res J Agric.* 9(4):1–11.
- [42] Okhonlaye O, Foluke O. (2016). Fermentation of Cassava (*Manihot esculenta*) and Ripe Plantain Peels (*Musa paradisiaca*) in the Production of Animal Feed. *J Adv Microbiol.* 1(2):1–15.
- [43] Chiwona-Karlton L, Nyirenda D, Mwansa CN, Kongor JE, Brimer L, Haggblade S, et al. (2015). Farmer Preference, Utilization, and Biochemical Composition of Improved Cassava (*Manihot esculenta* Crantz) Varieties in Southeastern Africa. *Econ Bot.* 69(1):42–56.
- [44] Sriroth K, Piyachomkwan K, Wanlapatit S, Oates CG. (2000). Cassava Starch Technology: The Thai Experience. *Starch/Staerke.* 52(12):439–49.
- [45] Somendrika M.A.D, Wickramasinghe I, Wansapala MAJ, Peiris S. (2016). Analyzing Proximate Composition Of Macro Nutrients of Sri Lankan Cassava Variety Kirikawadi.pdf. 2016. p. 283–7.
- [46] Rafiu TA. (2015). Effects of f Replacement of Maize With ith Graded Levels of Cassava Grit on n Growth Performance , Nutrient Utilization and nd Carcass Characteristics of Broiler Chickens. 3(5):1426–30.
- [47] Bayata A. (2019). Review on Nutritional Value of Cassava for Use as a Staple Food. 7(4):83–91.
- [48] Panghal A, Munezero C, Sharma P, Chhikara N. (2019). Cassava toxicity , detoxification and its food applications : a review. *Toxin Rev* [Internet]. 0(0):1–16. Available from: <https://doi.org/10.1080/15569543.2018.1560334>
- [49] Dastu AJ, Doma UD, Yakubu RN, Damter SA, Sudik SD, Dikwahal SH. (2019). Comparative proximate analysis of some conventional and unconventional energy feed ingredients in jos town, nigeria. *Int J Sci Appl Res.* 3(2):48–54.
- [50] Tambo Tene S, Klang JM, Ndomou Houketchang SC, Teboukeu Boungo G, Womeni HM. (2019). Characterization of corn, cassava, and commercial flours: Use of amylase-rich flours of germinated corn and sweet potato in the reduction of the consistency of the gruels made from these flours— Influence on the nutritional and energy value. *Food Sci Nutr.* 7(4):1190–206.
- [51] Peroni N, Kageyama PY, Begossi A. (2007). Molecular differentiation, diversity, and folk classification of ‘sweet’ and ‘bitter’ cassava (*Manihot esculenta*) in Caiçara and Caboclo management systems (Brazil). *Genet Resour Crop Evol.* 54(6):1333–49.
- [52] Srisaikhon S, Jaijapo W, Lounglawan P, Suksombat W. (2018). Effect of feeding fermented fresh cassava pulp on lactoperoxidase activity and performance of holstein friesland crossbred lactating. *PIM 1st International Conference* :1–38.
- [53] Melesse A, Masebo M, Abebe A. (2018). The Substitution Effect of Noug Seed ( *Guizotia Abyssinica* ) Cake with Cassava Leaf ( *Manihot Escutulata C .* ) Meal on Feed Intake , Growth Performance , and Carcass Traits in Broiler Chickens. *Journal of Animal Husbandry and Dairy Science*, 2(2):1–9.
- [54] Ho O, Se K. (2016). Comparative Study on the Nutritional and Anti-Nutritional Compositions of Sweet and Bitter Cassava Varieties for Garri Production. *J Nutr Heal Sci.* 3(3).

- [55] Premkumar T, Padmaja G, Moorthy SN, Nanda SK, George M. (2001). New Cassava Products of Future Potential in India. Central Tuber Crops Research Institute (CTCRI) India:564–77.
- [56] Phnom P. (2015). Cassava handbook. Support by China-Cambodia-UNDP Trilateral Coop Cassava Proj Phase II Cambodia.
- [57] Asaolu VO. (1988). Utilization of cassava peels and *Gliricidia septum* in the diet of the West African Dwarf sheep. Obafemi Awolowo University, Nigeria. MPhil. thesis; 1988.
- [58] Aro SO. (2008). Improvement in the nutritive quality of cassava and its by-products through microbial fermentation. *African J Biotechnol.* 7(25):4789–97.
- [59] Lukuyu B, Okike I, Duncan A, Beveridge M, Blümmel M. (2014). Use of Cassava in Livestock and Aquaculture Feeding Programs. *ILRI (aka ILCA and ILRAD);* 25. :1–83.
- [60] Okafor N, Ejiofor MAN. (1986). The microbial breakdown of linamarin in fermenting pulp of cassava (*Manihot esculenta* Crantz). *MIRCEN J Appl Microbiol Biotechnol.* 2(2):327–38.
- [61] Gomez G, Valdivieso M. (1988). The effects of ensiling cassava whole-root chips on cyanide elimination. *Nutr Reports Int [Internet].* 37(6):1161–6. Available from: <http://dx.doi.org/10.1016/B978-0-444-52512-3.00160-1>
- [62] Zanine A de M, Santos EM, Dórea JRR, Dantas PA de S, da Silva TC, Pereira OG. (2010). Evaluation of elephant grass silage with the addition of cassava scrapings. *Rev Bras Zootec.* 39(12):2611–6.
- [63] Oboh G, Akindahunsi AA, Oshodi AA. (2002). Nutrient and Anti-nutrient Contents of *Aspergillus niger* -Fermented Cassava Products (Flour and Gari). *J Food Compos Anal.* 15(5):617–22.
- [64] Adamafio NA, Sakyiamah M, Tettey J. (2010). Fermentation in cassava (*Manihot esculenta* Crantz ) pulp juice improves nutritive value of cassava peel. *J Biochem.* 4(March):51–6.
- [65] Kumar R. (1992). Anti-nutritional factors, the potential risks of toxicity and methods to alleviate them. *FAO Animal Production and Health Paper, 102,* 145-160.
- [66] Buitrago J, Ospina B, Gil JL, Aparicio H. (2007). Cassava Root and Leaf Meals As the Main Ingredients in Poultry Feeding: Some Experiences in Colombia. :523–41.
- [67] Hill DC. (1973). Chronic cyanide toxicity in domestic animals. In *Chronic cassava toxicity.* IDRC, Ottawa, ON, CA.
- [68] Majak W, McDiarmid RE, Hall JW, Cheng KJ. (1990). Factors that determine rates of cyanogenesis in bovine ruminal fluid in vitro. *J Anim Sci.* 68(6):1648–55.
- [69] Anaeto M, Sawyerr A, Alli TR, Tayo GO, Adeyeye JA, Olarinmoye AO. (2013). Cassava leaf silage and cassava peel as dry season feed for West African dwarf sheep. *Glob J Sci Front Res.* 13(2):1–4.
- [70] Larsen RE, Amaning-Kwarteng K. (1976). Cassava peels with urea and molasses as dry season supplementary feed for cattle. *Ghana J Agric Sci [Internet].* 9:43–7. Available from: <http://mutagens.co.in>
- [71] Bureenok S, Yuangklang C, Vasupen K. (2013). Effect of Cassava Root Ensiled with Cassava Top or Legumes on Feed Intake and Digestibility of Dairy Cows. *47160(1):*4–6.
- [72] Supapong C, , Anusorn Cherdthong MW, And PC, Uriyapongson S. (2019). E ff ects of Sulfur Levels in Fermented Total Mixed Ration Containing Fresh Cassava Root on Feed. :1–11.
- [73] Inthapanya S, Preston TR, Leng RA. (2016). Ensiled brewers’ grains increased feed intake, digestibility and N retention in cattle fed ensiled cassava root, urea and rice straw with fresh cassava foliage or water spinach as main source of protein. *Livest Res Rural Dev.* :28.
- [74] Vongkhamchanh B, Preston T, Leng RA, L. A Van, Hai D. (2018). Effect of biochar on growth performance of local “Yellow” cattle fed ensiled cassava roots, fresh brewers’ grains and rice straw. *Growth.* 221(3.20):0–223.
- [75] Olorunnisomo OA, Ibhaze GA. (2014). Original Research Article Milk Yield and Feed Conversion of Sokoto Gudali Cows Fed Elephant Grass Ensiled with Cassava Peel. *Agric Trop Subtrop.* 46(4):123–8.
- [76] Polyorach S, Wanapat M, Cherdthong A. (2014). Influence of yeast fermented cassava chip protein (YEFECAP) and roughage to concentrate ratio on ruminal fermentation and microorganisms using in vitro gas production technique. *Asian-Australasian J Anim Sci.* 27(1):36–45.
- [77] Wanapat M, Polyorach S, Chanthakhoun V, Sornsongnern N. (2011). Yeast-fermented cassava chip protein ( YEFECAP ) concentrate for lactating dairy cows fed on urea – lime treated rice straw. *Livest Sci [Internet].* 139(3):258–63. Available from:

<http://dx.doi.org/10.1016/j.livsci.2011.01.016>

- [78] Nasution A, Ginting N, Hasnudi, Umar S, Yunilas. (2018). The use of fermented cassava peel (Manihot Utilisima) in the Ration on Carcass Quality of Male Local Sheep. 2018. p. 220–5.
- [79] Adebowale EA. (1981). The maize replacement value of fermented cassava peels (. (1979):54–9.
- [80] Heuzé V, Tran G, Bastianelli D, Archimède H, Lebas F. (2012). Cassava peels, cassava pomace and other cassava tubers by-products. Feed Tables Régions Chaudes A Proj by INRA, CIRAD AFZ with Support FAO [Internet]. :Accessed september 12, 2020. Available from: <http://www.feedipedia.org/node/526>
- [81] Okeke GC, Oji U. (1989). The nutritive value of grass ensiled with cassava peel and poultry excreta for goats. In Smith O. B, Bosman HG Proceedings of Workshop on Goat Production in the Humid Tropics. Obafemi Awolowo University, Ile-Ife, Nigeria.; 1989. 101–106 p.
- [82] Falola OO, Alasa MC, Babayemi OJ. (2013). Assessment of silage quality and forage acceptability of vetiver grass (*Chrysopogon zizanioides* L. Roberty) ensiled with cassava peels by wad goat. Pakistan J Nutr. 12(6):529–33.

## **Biochemistry / Biokimya**

## Uptake of Curcumin by Supported Metal Oxides (CaO and MgO) Mesoporous Silica Materials

Nihal S. Tabasi\*, Ege Univ., Dept. of Chemistry, İzmir, Turkey  
Issa M. El-Nahhal, Al azhar Univ., Dept. of Chemistry, Gaza, Palestine  
\*Corresponding author: nihaltabasi@gmail.com

**Keywords:** Curcumin; mesoporous silica; uptake of curcumin; curcumin metal complexes; metaloxide /mesoporous silica

**Discipline:** Biochemistry

### Abstract

Curcumin has received high attention as potential drug because of various pharmaceutical applications. Different metal oxide encapsulated mesoporous silica were used to investigate uptake capacity of curcumin by batch method. The structural properties of these materials were investigated using several characterization techniques such as FTIR, XRD, TGA and UV-vis. UV-vis analysis shows that curcumin have higher uptake capacity for CaO/mesoporous silica. It also found that the hexagonal-SiO<sub>2</sub>-SBA-15 have the highest capacity for curcumin than other lamellar-SiO<sub>2</sub> structures.

### Introduction

Curcumin is the major curcuminoid and the main bioactive component of *Curcuma longa*. Due to its various pharmaceutical applications [1-7], it has the interest of research as potential drug. The very low solubility of curcumin in water reduced its efficiency and bioavailability as potential drug [8]. Different materials were used to increase the bioavailability of curcumin. Anitha et al. have loaded curcumin into O- Carboxymethyl chitosan and investigated its oral bioavailability as anti-cancer drug [9]. Bahawana et al. have developed a method for the preparation of nanoparticles of curcumin with a view to improve its aqueous-phase solubility and examine the effect on its antimicrobial properties [10]. Modasiya & Patel have studied increasing solubility of curcumin as drug using solid dispersion technique. The solid binary systems were prepared using different drug: polymer ratio (1:1, 1:4 and 1:8) with polyethylene glycol 4000 and 6000 by different techniques like physical mixing, melting method and solvent evaporation method. PVP K 30 was also used as a polymer [11]. Here in, different mesoporous silica-based formulations have been developed to enhance bioavailability of curcumin as drug [12, 13]. Mesoporous silica with high surface area, large pore volume and narrow pore size distribution [14] are highly promise for drug delivery systems [15]. Incorporation of metal oxide in mesoporous silica has been a promising field of research such as catalysis [16], optics [17] and drug delivery [18]. In our present research, we aimed to synthesize an inert mesoporous silica with avoiding hazard materials. Four different mesoporous silica materials were firstly synthesized using triblock copolymer surfactants (Pluronic P123 gives hexagonal structures whereas L81, L61 and L31 give lamellar structures) [19]. Supported metal oxides (ZnO, CuO, CaO and MgO) mesoporous silica were synthesized using impregnation method [19, 20]. Curcumin uptake percentage, by four different metal oxides supported onto four different mesoporous silica (hexagonal and lamellar structures) are investigated using batch method. The synthesized encapsulated metal oxides-mesoporous silica materials and their curcumin complexes were characterized using several methods and techniques to examine their structural properties. These methods include X-ray diffraction (XRD), thermal gravimetric analysis (TGA) and Ultraviolet-Visible spectroscopy (UV-vis).

### Experimental

#### Materials

All the chemicals used were analytical grade and directly used as received without further purification. Triblock copolymer Pluronic P123 (EO<sub>20</sub> PO<sub>70</sub> EO<sub>20</sub>, 99%), Pluronic L81 (EO<sub>3</sub> PO<sub>43</sub> EO<sub>3</sub>, 99%), Pluronic L61 (EO<sub>2</sub> PO<sub>31</sub> EO<sub>2</sub>, 99%), Pluronic L31 (EO<sub>2</sub> PO<sub>16</sub> EO<sub>2</sub>, 99%), Tetra ethoxy ortho silane (TEOS) (Si(OC<sub>2</sub>H<sub>5</sub>)<sub>4</sub>), absolute ethanol (C<sub>2</sub>H<sub>6</sub>O) were purchased from Aldrich company. Magnesium acetate tetrahydrate (Mg(CH<sub>3</sub>COO)<sub>2</sub>.4H<sub>2</sub>O), curcumin (C<sub>21</sub>H<sub>20</sub>O<sub>6</sub>) were purchased from Sigma-Aldrich Company. Calcium carbonate (CaCO<sub>3</sub>) was purchased from Sigma Company. Hydrochloric

acid (HCl, 37%) and acetic acid (CH<sub>3</sub>COOH, 99.8%) were purchased from Merck Company. All the glassware used in this experimental work washed with distilled water and dried at 100 °C.

### Methodology

Thermogravimetric analysis (TGA) was carried out using Mettler Toledo TGA/SDTA 851e analyzer in the range of 25–600 °C of heat rate of 10 °C/min. The system was purged with nitrogen using a flow rate of 50 mL/min. Powder X-ray diffraction (XRD) patterns were recorded on Analytical Expert Pro diffractometer utilizing Cu K $\alpha$  radiation ( $k = 1.54$  Å). Ultraviolet–visible absorption spectra were recorded on a UV-vis spectrophotometer Shimadzu, UV-2400 in the wavelength range from 200 to 800 nm.

### Determination of curcumin uptake

Mesoporous silica (hexagonal and lamellar structures) were synthesized as previously reported in our work [19], The supported metal oxides (ZnO, CuO, CaO and MgO)/mesoporous silica materials were prepared using impregnation method as previously reported in our work [19, 20]. Curcumin uptake for ZnO, CuO, CaO [20] and MgO [20]/mesoporous silica was determined using batch method. 0.2 g of supported metal oxide/mesoporous silica was shaking with 25 mL of (6\*10<sup>-5</sup> M) ethanolic curcumin solution for 72 hours. Then, curcumin-metal (II) complexes/mesoporous silica were separated by centrifuge (3500 rpm for 15 minute), were washed with 5 mL ethanol and were dried at 80 °C. The curcumin uptake capacity was quantified measured by spectrophotometric method, a complete release of curcumin was also observed upon mild acidic treatment the loaded samples, where the orange color of the Ca(II) curcumin complex is converted into yellow color of free curcumin [20].

## Result and discussion

### X-ray Diffraction analysis (XRD)

CaO/SiO<sub>2</sub>-81, curcumin-Ca/SiO<sub>2</sub>-81, MgO/SiO<sub>2</sub>-81 and curcumin-Mg/SiO<sub>2</sub>-81 are shown previously in our last work [20]. The XRD patterns of SiO<sub>2</sub>-81, CuO/SiO<sub>2</sub>-81, and curcumin-Cu(II)/SiO<sub>2</sub>-81 are shown in Figure 1. XRD pattern (Figure 1 (red)) exhibits reflection peaks corresponded to monoclinic phase of CuO [19, 21]. Similar diffraction pattern was detected for curcumin-Cu(II)/SiO<sub>2</sub>-L81 (Figure 1 (black)) with less intense reflection peaks in comparison with CuO/SiO<sub>2</sub>-L81. The presence of these reflections suggest that CuO is not completely react with curcumin.

The XRD pattern of SiO<sub>2</sub>-81, ZnO/SiO<sub>2</sub>-L81 and curcumin-Zn(II)/SiO<sub>2</sub>-L81 are shown in Figure 2. ZnO/SiO<sub>2</sub>-L81 (Figure 2 (red)) exhibits reflection peaks correspond to wurtzite ZnO structure [19, 22]. Curcumin-Zn(II)/SiO<sub>2</sub>-L81 XRD pattern (Figure 2 (black)) has similar diffraction pattern of ZnO/SiO<sub>2</sub>-L81 (Figure 2 (red)) with a small decreasing in reflection intensities. The decreasing of intensity of reflection peaks of ZnO components indicates the curcumin complexation with Zn(II). The presence of ZnO reflections for curcumin-Zn(II)/SiO<sub>2</sub>-L81 prove the presence of unreacted ZnO nanoparticles.

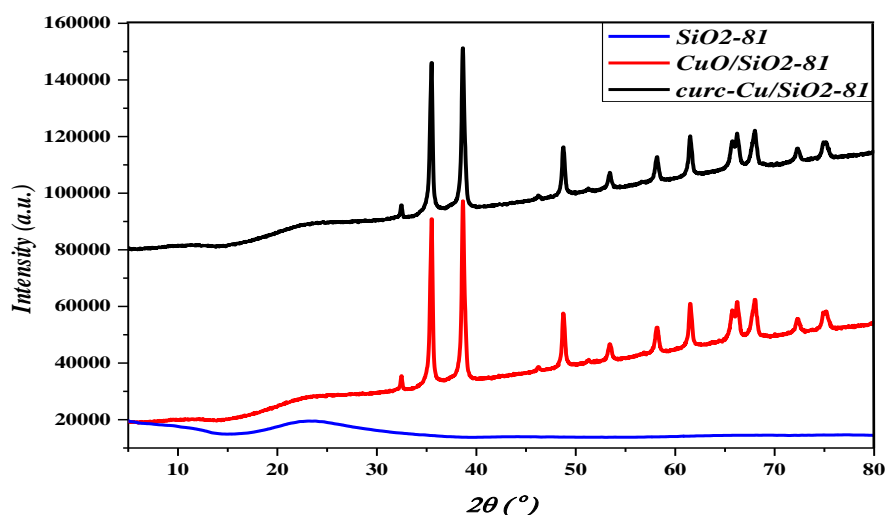


Figure 1. XRD patterns of SiO<sub>2</sub>-81 (blue), CuO/SiO<sub>2</sub>-81 (red) and Curcumin-Cu/SiO<sub>2</sub>-81 (black)

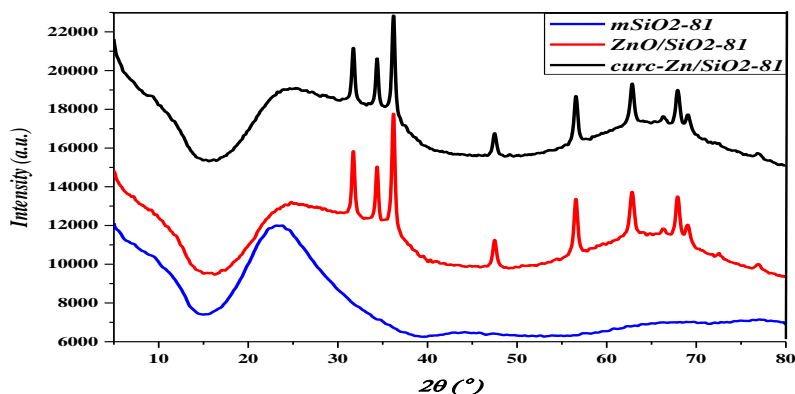


Figure 2. XRD patterns of SiO<sub>2</sub>-81 (blue), ZnO/SiO<sub>2</sub>-81 (red) and Curcumin-Zn/SiO<sub>2</sub>-81 (black)

### Thermal gravimetric analysis (TGA)

TGA and differential thermo-gravimetric analysis (DTA) for encapsulated CaO, MgO, CuO and ZnO/mesoporous silica and their curcumin complexes are examined under nitrogen at 25–600 °C at rate 10 °C/min (Figs. 3 and 4). TGA-DTA pattern of CaO/SBA-15, curcumin-Ca/SBA-15, MgO/SBA-15, curcumin-Mg/SBA-15, CaO/SiO<sub>2</sub>-81, curcumin-Ca/SiO<sub>2</sub>-81, MgO/SiO<sub>2</sub>-81 and curcumin-Mg/SiO<sub>2</sub>-81 are shown previously in our last work [20]. Figures 3 and 4 show TGA-DTA pattern of curcumin-Cu(II)/SiO<sub>2</sub>-L81, curcumin-Cu(II)/SBA-15, curcumin-Zn(II)/SiO<sub>2</sub>-L81 and curcumin-Zn(II)/SBA-15.

TGA – DTA pattern of curcumin-Cu(II)/SiO<sub>2</sub>-L81 (Figures 3 and 4 (blue)) show three loss weight steps. The first step occurs at 65 °C corresponds to loss of adsorbed water. The second step at 287 °C that is probably due to condensation of silanols of silica precursors. The third step above 410 °C is due to curcumin decomposition [23, 24]. The detailed specifications are summarized in Table 1.

TGA – DTA patterns of curcumin-Cu(II)/ SBA-15 (Figures 3 and 4 (black)) show three loss weight steps. The first at about 65 °C corresponds to loss of adsorbed water. The second step at 287 °C is probably due condensation of silanols of silica precursors. The third step above 410 °C is due to curcumin decomposition [23, 24]. The detailed specifications are summarized in Table 1.

TGA-DTA patterns of curcumin-Zn(II)/SiO<sub>2</sub>-L81 (Figures 3 and 4 (pink)) show three steps of weight loss. The first at 72 °C corresponds to loss of adsorbed water. The second step at 250 °C probably due to condensation of silanols of silica precursors. The third step at 400 °C is due to curcumin decomposition [24]. The detailed specifications are summarized in Table 1.

TGA-DTA patterns of curcumin-Zn(II)/SBA-15 (Figure 3 and 4 (red)) show three steps of weight loss. The first at about 72 °C corresponds to loss of adsorbed water. The second step at 250 °C probably due to condensation of silanols of silica precursors. The third step above 400 °C is due to curcumin decomposition [24]. The detailed specifications are summarized in Table 1.

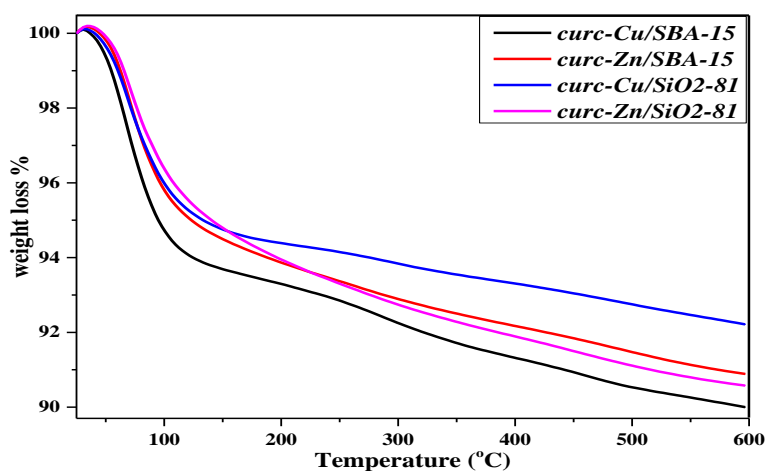


Figure 3. TGA patterns of curcumin-Cu/SiO<sub>2</sub>-81 (blue), curcumin-Cu/SBA-15 (black), curcumin-Zn/SiO<sub>2</sub>-81 (pink) and curcumin-Zn/SBA-15 (red)



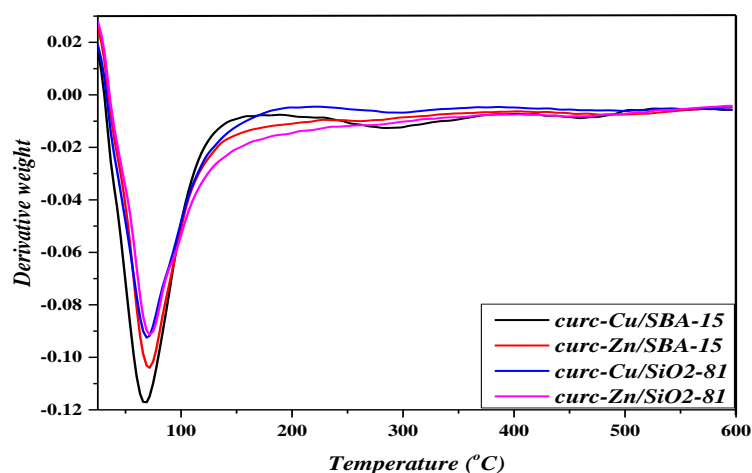


Figure 4. DTA patterns of curcumin-Cu/SiO<sub>2</sub>-81 (blue), curcumin-Cu/SBA-15 (black), curcumin-Zn/SiO<sub>2</sub>-81 (pink) and curcumin-Zn/SBA-15 (red)

Table 1. Weight loss step and temperature of CuO and ZnO supported mesoporous silica and their curcumin complexes

Compound	Adsorbed water		Curcumin decomposition		Silica condensation		Ref.
	T (°C)	Weight loss %	T (°C)	Weight loss %	T (°C)	Weight loss %	
CuO/SBA-15	80	3	–	–	> 200	2.2	[19]
CuO/SiO <sub>2</sub> -81	80	5	–	–	> 200	2.1	[19]
Curcumin-Cu/SBA-15	65	6	> 200	2.3	> 200	1.5	This work
Curcumin-Cu/SiO <sub>2</sub> -81	65	5	> 200	1.6	>200	1.1	This work
ZnO/SBA-15	80	2.5	–	–	> 200	3.5	[19]
ZnO/SiO <sub>2</sub> -81	75	5.5	–	–	> 200	3	[19]
Curcumin-Zn/SBA-15	72	5.4	> 200	1.6	> 200	2	This work
Curcumin-Zn/SiO <sub>2</sub> -81	72	5	> 200	1.9	> 200	2.6	This work

#### Ultraviolet-Visible spectroscopy (UV-vis)

Figure 5 shows UV-vis spectra of curcumin with different concentrations. A UV-vis spectrum of the curcumin in ethanol shows absorption maximum at 429 nm assigned to the band  $\pi \rightarrow \pi^*$ . As concentration decrease, the absorbance also decreases. The spectrum is maintained the absorption peak at 429 nm [20].

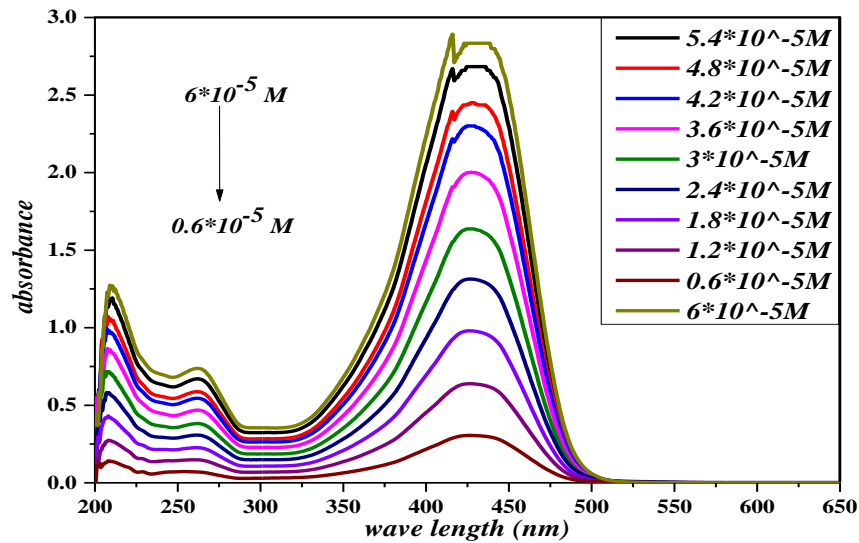


Figure 5. UV-vis spectra of different curcumin concentration for standard curve [20].

Figure 6 shows the standard curve of curcumin. The relation between absorbance and concentration is linear [20].

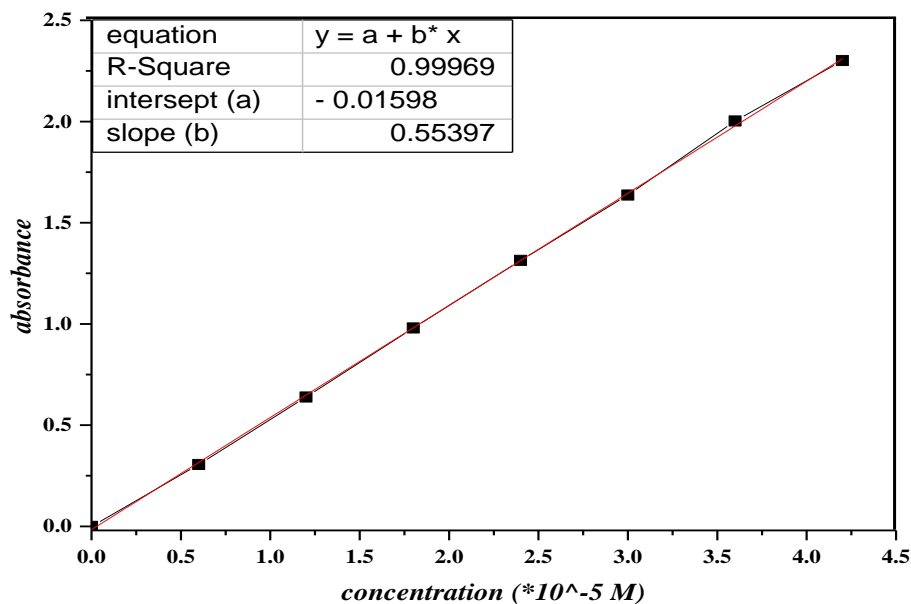


Figure 6. Curcumin standard curve [20].

Figure 7 (a-c) shows UV-vis spectra of curcumin, curcumin-Cu/SiO<sub>2</sub>-L81 and curcumin-Zn/SiO<sub>2</sub>-L81, respectively. UV-vis spectrum of curcumin in ethanol shows absorption maximum at 429 nm assigned to the band  $\pi \rightarrow \pi^*$  [3, 20]. For the curcumin-M(II) complex (Figure 7 (b, c)), the maximum absorption peak of curcumin decreases due to the formation of curcumin—metal (II) complexes [3, 24, 25].

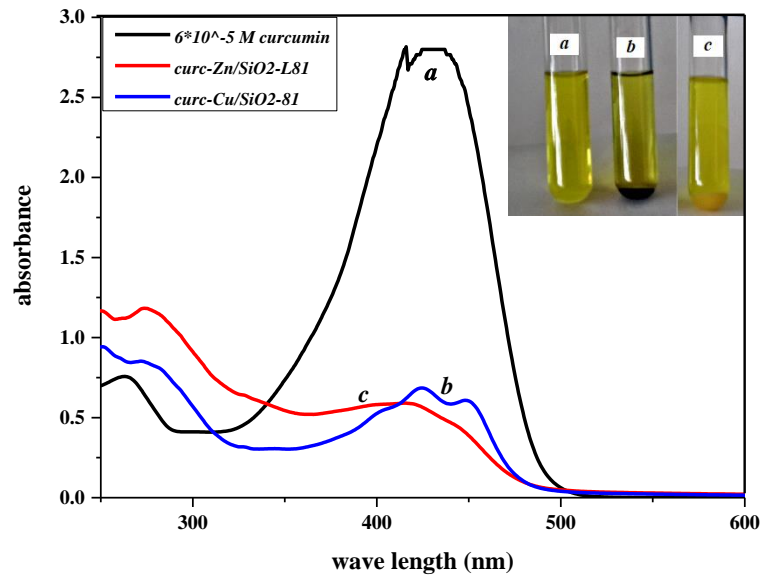


Figure 7. UV-vis spectra of (a) curcumin solution, (b) curcumin-Cu/SiO<sub>2</sub>-L81 solution and (c) curcumin-Zn/SiO<sub>2</sub>-L81 solution

Table 2 and Figure 8 show curcumin uptake capacity for metal oxide encapsulated mesoporous silica with different metal oxides (CaO, MgO, CuO and ZnO) and different mesoporous silica (SBA-15, SiO<sub>2</sub>-81, SiO<sub>2</sub>-61 and SiO<sub>2</sub>-31). It describes the curcumin uptake capacity as curcumin (mg)/1g sample for all metal oxide/mesoporous silica systems. There is a decreasing of curcumin uptake in the following order:  
SBA-15 > SiO<sub>2</sub>-L81 > SiO<sub>2</sub>-L61 > SiO<sub>2</sub>-L31.  
CaO > MgO > CuO > ZnO.

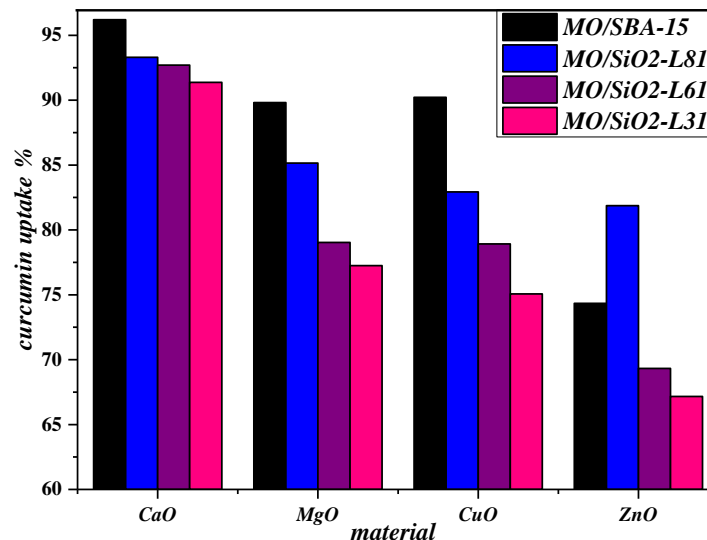


Figure 8. Curcumin uptake (%) by metal oxide encapsulated mesoporous silica after 72 h(s)

Table 2. Metal oxide/silica capacities for curcumin uptake (mg/1 g) and %

Materials	Curcumin uptake/Material (mg /1g)	Curcumin uptake %	Ref.
CaO/SBA-15	2.657	96.2	[20]
CaO/SiO <sub>2</sub> -L81	2.578	93.3	[20]
CaO/SiO <sub>2</sub> -L61	2.56	92.7	[20]
CaO/SiO <sub>2</sub> -L31	2.524	91.37	[20]
MgO/SBA-15	2.484	89.91	[20]
MgO/SiO <sub>2</sub> -L81	2.352	85.15	[20]
MgO/SiO <sub>2</sub> -L61	2.183	79.03	[20]
MgO/SiO <sub>2</sub> -L31	2.134	77.25	[20]
ZnO/SBA-15	2.054	74.34	In this work
ZnO/SiO <sub>2</sub> -L81	2.261	81.87	In this work
ZnO/SiO <sub>2</sub> -L61	1.915	69.33	In this work
ZnO/SiO <sub>2</sub> -L31	1.855	67.17	In this work
CuO/ SBA-15	2.492	90.22	In this work
CuO/SiO <sub>2</sub> -L81	2.291	82.93	In this work
CuO/SiO <sub>2</sub> -L61	2.18	78.917	In this work
CuO/SiO <sub>2</sub> -L31	2.074	75.072	In this work

### Conclusion

Curcumin–metal(II) complexes encapsulated mesoporous silica were synthesized by treatment of curcumin with metal oxide encapsulated mesoporous silica. The synthesized materials were characterized using X-ray diffraction (XRD), thermal gravimetric analysis (TGA) and ultraviolet-visible spectroscopy (UV-vis). XRD analysis shows that not all the metal oxide reacts with curcumin. This is confirmed by a slight decrease of all diffraction peaks intensity of metal oxide. TGA and UV-vis analysis shown that the uptake of curcumin is decreased in the following order for the complexes of Ca(II) > Mg(II) > Cu(II) > Zn(II), respectively. Curcumin uptake % studies show that CaO/SBA-15 is the best for curcumin uptake, curcumin uptake % was 96.2 %.

### Reference

- [1] Ruby A, Kuttan G, Babu K, Rajasekharan K, Kuttan K (1995). *Cancer Lett* 94:79.
- [2] Lantza R, Chena G, Solyomb A, Jolad S, Timmermann B (2005). *Phytomedicine* 12:445.
- [3] Patra D, Barakat C (2011). *Spectrochim Acta Part A Mol Biomol Spectrosc* 79:1034.
- [4] Yang F, Lim G, Begum A, Ubada O, Simmons M, Ambegaoka S, Chen P, Kayed R, Glabe C, Frautschy S, Cole G (2005). *J Biol Chem* 280:5892.
- [5] Egan M, Pearson M, Weiner S, Rajendran V, Rubin V, Glöckner- Pagel J, Caplan M (2004). *Science* 304:600.
- [6] Maheshwari R, Sing A, Gaddipati J, Srimal R (2006). *Life Sci* 78:2081.
- [7] Krishnaswamy K, Raghuramulu N (1998). *Indian J Med Res* 108:167.
- [8] Pang S, Tay S, Chin S (2014). *J Nanomater* 2014:22.
- [9] Anithaa A, Mayaa S, Deepaa N, Chennazhia K P, Naira S V, Tamurab H, Jayakumar R (2011). *Carbohydrate Polymers* 2011:83.
- [10] Bahawana, Basniwal R K, Buttar H S, Jain V K, Jain N (2011). *Journal of agricultural and food chemistry*, 59:5.
- [11] Modasiya, M. K., & Patel, V. M. (2012). *International Journal of Pharmacy & Life Sciences*, 3:3.

- [12] Wang A, Muhammad F, Qi W, Wang N, Chen L, Zhu G (2014). ACS Appl Mater Interfaces 6:14377.
- [13] Muhammad F, Wang A, Guo M, Zhao J, Qi W, Yingjie G, Gu J, Zhu G (2013). ACS Appl Mater Interfaces 5:11828.
- [14] Kresge C, Leonowicz M, Roth W, Vartuli J, Beck J (1992). Nature 359:710.
- [15] Slowing I, Vivero-Escoto J, Wu C, Lin V (2008). Adv Drug Deliv Rev 60:1278.
- [16] Barreca D, Blau W, Croke G, Deeney F, Dillon F, Holmes J, Tondello J (2007). Microporous Mesoporous Mater 103:142.
- [17] Hornebecq V, Antonietti M, Cardinal T, Treguer-Delapierre M (2003). Chem Mater 15:1993.
- [18] Li Z, Barnes J, Bosoy A, Stoddart J, Zink J (2012). Chem Soc Rev 41:2590.
- [19] El-Nahhal I M, Salem J K, Tabasi N S, Hempelmann R, Kodeh F S (2018). Chemical Physics Letters, 691, 211-218.
- [20] El-Nahhal I M, Salem J K, Tabasi N S (2018). Journal of Sol-Gel Science and Technology, 87:3, 647-656.
- [21] Dong C, Xiao X, Chen G, Guan H, Wang Y (2015). Applied Surface Science, 349, 844-848.
- [22] İpeksaç T, Kaya F, Kaya C (2013). Materials Letters, 100, 11-14.
- [23] Mohanan P V (2014). Curcumin and its derivatives as Antioxidants and DNA Intercalators.
- [24] Zebib B, Mouloungui Z, Noirot V (2010). Bioinorganic chemistry and applications, 2010.
- [25] Banerjee, R. (2014). Bioinorganic chemistry and applications, 2014.

## **Chemistry / Kimya**

## Characterization of Plasmid from Antibiotic-Resistant *Pseudomonas* spp. Isolated from Soil Sample

Sulaiman Anas Lawan, Kano University of Science and Technology Wudil, Dept. of Biochemistry, Kano, Nigeria  
Yunusa Umar Muazu\*, Dokuz Eylul University, Graduate School of Natural and Applied Sciences, Department of Biochemistry, İzmir, Turkey

Mukhtar Yau, Bayero University Kano, Department of Plant Biology, Kano, Nigeria

Aliyu Abubakar Aliyu, COMSATS University Islamabad, Department of Bioscience, Pakistan

Joseph Dasoem Naanswan, Federal University Wukari, Department of Microbiology, Taraba, Nigeria

\*Corresponding author's email: umarmuazu.yunusa@ogr.deu.edu.tr

**Keywords:** *Pseudomonas* spp., plasmid, antibiotics

**Discipline:** Chemistry

### Abstract

Antibiotic resistance plasmids pose threats to global health and food security. This study aims to determine the resistant of *Pseudomonas* spp against some antibiotics and to isolate and characterize plasmid DNA from the bacterial species. The soil sample was collected from the Department of Biochemistry, Bayero University Kano, Kano State, Nigeria. The bacterial strain was isolated from the soil sample and identified with the aid of cetrimide agar. It was then inoculated with tetracycline, ampicillin, chloramphenicol, and a combination of ampicillin and chloramphenicol into four different plates. Two creamy colonies from a plate containing a combination of ampicillin and chloramphenicol were harvested and stored in nutrient broth for 48 hours before subjected to DNA extraction. The plasmid DNA was extracted using a modified alkaline lysis method utilizing Zyppy™ Plasmid Miniprep Kit. The size of the eluted plasmid was determined through gel electrophoresis. A DNA plasmid of approximate size 7kb (fig. 1) was obtained from one of the colonies. The approximate size was estimated by corresponding it to the DNA ladder. No plasmid was extracted from the other colony. The isolated *Pseudomonas* spp from a soil sample was resistant to ampicillin and chloramphenicol antibiotics. The extracted plasmid of molecular weight 7kb may be responsible for the resistant of the strain to the two antibiotics.

### Introduction

*Pseudomonas* spp. are aerobic nonfermenting Gram-negative, rod-shaped bacteria of the pseudomonadaceae family with fast growing capabilities and adaptability to oxidative, nutritional, and other stresses conditions. It has an important feature in the production of a wide variety extracellular polymeric substances such as enzymes, proteins, polysaccharides, extracellular DNA which are mainly involved in biofilm formation, virulence and attachment processes [1]. Besides these, *Pseudomonas* spp. has the ability to grow under anoxic conditions and limited susceptibility to many antimicrobials and disinfectants [2]. Due to the remarkable plasticity of their genome, the members of *Pseudomonas* spp. are suspected to be able to acquire almost all known antimicrobial-resistance mechanisms [3].

Antibiotic resistance, which occurs naturally or artificially through the misuse of antibiotics in humans and animals, is one of the biggest threats to global health and food security. A growing number of deadly infections – such as tuberculosis, salmonellosis, gonorrhoea, and pneumonia – are becoming harder to treat as the antibiotics used to treat them become less effective. These can lead to longer hospital stays, higher medical costs, increased mortality, and can also compromise the success of major surgery and cancer chemotherapy [4]. There are two distinct types of antibiotic resistance: intrinsic and acquired. In intrinsic a particular antibiotic as a result of inherent structural or functional characteristics may be unable to penetrate the outer membrane of certain microorganisms or the antibiotic entering the membrane is removed by efflux pumps. While acquired resistance can be obtained via chromosomal mutations or, more commonly, by acquiring an antibiotic resistance gene from another bacterium via mobile plasmids or transposons by a process known as horizontal gene transfer [6]. There are currently five main targets (membrane structure, cell wall synthesis, folate mechanism, and protein synthesis, DNA gyrase and RNA polymerase) for antibiotics, and antibiotic resistance can essentially be acquired through mutation, conjugation, transduction, and transformation; and expressed by four different mechanisms (inactivating proteins, prevention of cell penetration, modification of the target, and expulsion via efflux pumps) [6,7].

Plasmids (often referred to as extra-chromosomal DNA) is a small DNA molecule within the cytoplasm of a bacterium or protozoan cell that can replicate independently. They have self-replicating genetic modules capable of dissemination through conjugation and transformation [8]. Conjugated resistance plasmids produce a pilus that attaches to target cells and facilitates the transfer of the conjugative element to the recipient [9]. This has been found to be an effective approach to limit the spread of antibiotic resistance by chemically blocking conjugation factors in either donors or recipients [10]. Conjugative elements vary in host range, suggesting that plasmid donation or reception often also depends on chromosomally encoded factors in donors and recipients. The current study aimed to identify the plasmid causing antibiotics resistance in *Pseudomonas* specie.

## Materials and Methods

### Sample Collection

The soil sample was collected in a sterilized bottle (to avoid further contamination) from the Department of Biochemistry, Bayero University Kano, Kano State, Nigeria.

### Chemicals and Equipment

Ethanol, izal (disinfectant), chloramphenicol, ampicillin, tetracycline, ethidium bromide (dye), loading dye, agarose gel, media (cetrimide, nutrient agar and broth), Zyppy TM Plasmid miniprep kit, plates, wire loop, autoclave, spirit lamp, micropipette, incubator, refrigerator, weighing balance, conical flask, measuring cylinder, shaker, centrifuge, test tubes, microwave and bioimaging system (imager) were some of the reagents and equipment used during the study.

### Preparation of Cetrimide Agar

Cetrimide agar was prepared by suspending 45.3 grams of the purchased solid medium in one litre of distilled water, shook to dissolved, followed by addition of 10ml of glycerol and boil for one minute to dissolve completely. The resulting mixture was sterilized by autoclaving at 121°C for 15 minutes and cooled to approximately 50°C before poured into sterile Petri dishes. This agar was prepared for the purpose of selective isolation and presumptive identification of *Pseudomonas* spp.

### Preparation of Nutrient Broth

Exactly eight 8 grams of the medium was suspended in one litre of distilled water, shook to dissolved and boiled for one minute until complete dissolution. Sterilization in an autoclave was followed at 121°C for 15 minutes.

### Preparation of Nutrient Agar

Exactly twenty-eight (28) grams of the medium was suspended in one litre of distilled water, shook to dissolved, boiled for one minute until complete dissolution, and followed by autoclaving at 121°C for 15 minutes.

### Isolation and Identification of *Pseudomonas* spp.

The soil sample was inoculated on the already prepared cetrimide agar plate using streak plate technique. Streaked plates were incubated at 37°C for 24 hours followed by colonies grown examination. Typical *Pseudomonas* colonies appearing green were isolated purified, and then stored in nutrient broth (Merck, Germany) supplemented with 15 % glycerol (Merck, Germany) at -80 °C for further analysis.

### Antimicrobial Susceptibility Testing

The isolates from the nutrient broth were picked and tested for susceptibility to some antibiotics on Mueller-Hinton agar plates by the disc diffusion method [11]. The isolates were inoculated with tetracycline, ampicillin, chloramphenicol, and combination of ampicillin and chloramphenicol into the four different plates before pouring the nutrient agar into the plates. The plates were then incubated at 37°C for 24 hours before growth examination.

Few colonies growth which were cream in colour and circular in shape were observed in each of ampicillin plate and chloramphenicol plate. Moreover, two creamy colonies were also observed in a plate containing combination of the two antibiotics. These two colonies were picked again and stored in nutrient broth and incubated for 24 hours. The nutrient broth was shaken in a water bath for two days before taken to National Research Institute (NARICT), Zaria for plasmid extraction.



### Plasmid Extraction

The plasmid was extracted using Zyppy™ plasmid miniprep kit (developed by Zymo Research Corporation: Catalog Nos. D4036, D4019, D4020 & D4037). About 600 µl of bacterial cultures grown in nutrient broth containing appropriate antibiotics was transferred to 1.5 ml microfuge tubes and spun at 11,000xg for 60 seconds to pellet down the cells. The supernatant was carefully removed with a fine-tip pipette and discarded. To the reaction mixture, 100µL of 7X lysis buffer (alkaline SDS solution: 1% NaOH and 2% sodium dodecyl sulfate) was added and the tube was gently inverted 5 times to get a clear suspension, indicating complete lysis. Within 2 minutes, 350 µl of cold neutralization buffer (3M guanidine HCl) was added to the suspension and the contents of the tube were gently mixed by inverting 3 times to ensure complete neutralization. The mixture turned to yellow colour when the neutralization was completed. The tube was then centrifuged for 4 minutes and the clear supernatant (around 900 µl) was transferred into the provided Zymo-Spin™ IIN column and placed into a collection tube and re-centrifuged at the same speed for 15 seconds.

After discarding the flow-through, 200 µl of endo-wash buffer was added to the Zymo-Spin™ IIN column and centrifuge for 30 seconds. This followed with addition of 400 µl of Zyppy™ wash buffer and centrifuged for 1 minute before the content of the column transferred into a clean 1.5 ml microcentrifuge. To the resulting mixture, 30 µl of Zyppy™ elution buffer (10 mM Tris-HCl, pH 8.5 and 0.1 mM EDTA) directly added to the column matrix and let stranded for one minute at room temperature before it was centrifuged for 30 seconds to eluted the plasmid DNA. Relative centrifugal force of 11,000xg and room temperature was maintained throughout the processed. The procedure was repeated for the second isolate. The eluted plasmid was then taken for gel electrophoresis for size determination.

### Gel Electrophoresis

In gel electrophoresis, 2.0% agarose gel was prepared by dissolving 1g of agarose powder (electrophoresis grade) to 50 ml TBE electrophoresis buffer (45 mM Tris-borate, 1 mM EDTA) of 0.5x working concentration (i.e. 1:10 dilution of the concentrated stock) in a 200 ml beaker. The beaker was heated uncovered for 3 minutes in a microwave oven at high setting until all agarose is dissolved. A 3µl ethidium bromide staining solution was added to the solution. The gel was then poured into the gel electrophoresis tray and allowed to set at room temperature cooled before using an appropriate comb into the gel mold to create the wells. The comb was carefully removed from the solidified gel.

Enough running buffer was poured inside the electrophoresis tray to cover up to the surface of the gel. The loading dye (0.25 g bromophenol blue: m.w. 669.96; 0.25 g xylene cyanol: m.w. 538.60; 50.00 g sucrose: m.w. 342.30/50 ml of glycerol; 1.00 ml 1M Tris (pH 8.0)) was added to our eluted DNA samples. Loading dye helps to track how far the DNA sample has traveled, and also allows the sample to sink into the gel. A 10 µl DNA sample was slowly and carefully measured and loaded into the gel wells. An appropriate DNA size marker was also loaded along with experimental sample. The electrophoretic machine was turn on allowed to run at 120 volts for 45 minutes. When electrophoresis has completed, the gel was removed and placed on paper towels to absorb any extra running buffer before it was visualized on a 302 nm UV transilluminator (Model TM-36, UV products, Inc.).

## Results

### Identification of the Isolates

After the isolate was inoculated on the cetrimide agar (a *Pseudomonas* selective agar) plate using streak plate technique and incubated for 24 hours at 37°C few colonies which were circular in shape and green in colour was observed. This agar was used for the selective isolation and presumptive identification of *Pseudomonas* spp.

### Antimicrobial Susceptibility

According to the obtained results as presented in Table 1, the resistance to ampicillin, chloramphenicol, and a combination of ampicillin & chloramphenicol antimicrobial agents was observed among *Pseudomonas* spp. of the soil sample. Morphological characteristics shows scanty growth which were circular in shape are cream in color. No growth was observed when isolate was inoculated in nutrient agar with tetracycline plate. This has showed that the *Pseudomonas* spp. of the soil sample under study was not resistance to tetracycline antibiotic.

Table 1. Antimicrobial susceptibility

Isolates in Agar (s)	Morphological characteristics	Colour
Isolates in nutrient agar with ampicillin	scanty growth, circular shape	cream
Isolates in nutrient agar with chloramphenicol	scanty growth, circular shape	cream
Isolates in nutrient agar with tetracycline	no growth	-
Isolates in nutrient agar with ampicillin and chloramphenicol	two colonies growth, circular shape	cream

### Plasmid Profile of Resistant Isolates

The electrogram of the DNA isolate was presented in the Figure 1. After complete separation by electrophoretic machine the DNA fragments are visible according to their sizes. From the figure letter A shows the one DNA fragments of the first isolate. By corresponding it with the DNA ladder (letter D), the plasmid was estimated to be approximately 7kb in size. Letter B which is isolate of the second sample shows no plasmid. Letter C was positive control.

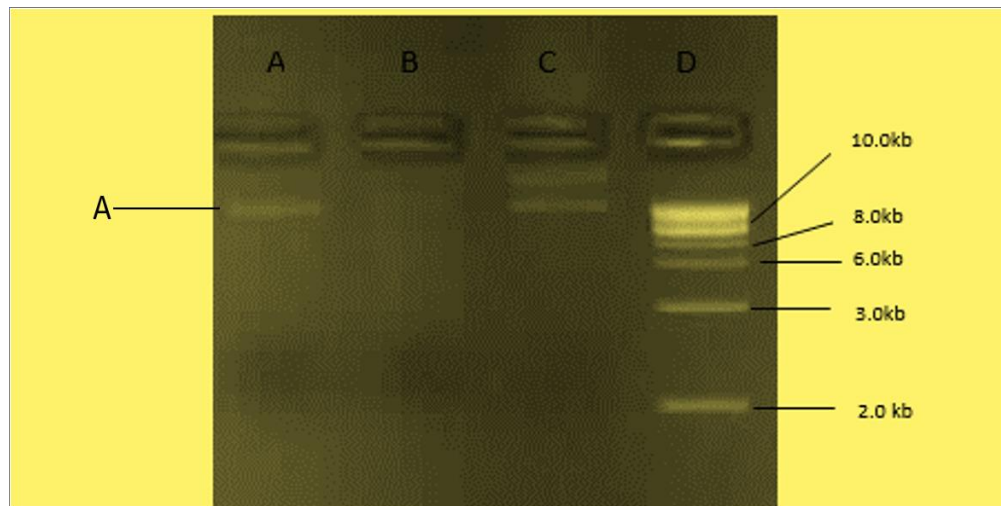


Figure 1. An image of a gel post electrophoresis of the isolates.

Keys: A= shows the plasmid (one) of the first isolate; B= shows no plasmid of the second isolate; C= positive control; D= DNA ladder

### Discussion

*Pseudomonas* spp. can be isolated from different environments depending on cultural, morphological and biochemical tests. These bacteria are pathogenic causing aggressive infections in the lungs, skin, eye and sometime ear. In the current study, the *Pseudomonas* spp. was isolated from the soil sample using cetramide agar. This agar is used for presumptive identification of *Pseudomonas* spp. It is known to inhibits most bacteria by acting as a detergent (cetyltrimethylammonium bromide, a quaternary ammonium, cationic detergent). This microorganism was found to be resistance to ampicillin, chloramphenicol, and combination of ampicillin & chloramphenicol antibiotics. The resistance of ampicillin to microorganisms involves irreversible inhibition of an enzyme transpeptidase, which is needed by bacteria to make the cell wall. By doing so it inhibits the final stage of bacterial cell wall synthesis in binary fission and cause cell lysis. For this reason, ampicillin is regarded as bacteriolytic [12]. However, resistance to chloramphenicol is mainly due to the production of a specific inactivating chloramphenicol acetyltransferase (CAT). Chloramphenicol is known to enters the bacteria through energy-dependent process and hinders protein chain elongation. It is antibiotic activity is due to competitive inhibition for the binding of aminoacyl tRNA to the peptidyltransferase domain of the 50S subunit. This induces conformational change in the ribosome, which slows or even inhibits the incorporation of the aminoacyl tRNA and in turn the transpeptidation reaction [13].

Following complete separation using electrophoretic machine the first isolate showed a plasmid with molecular weight of the plasmid of 7kb while the second isolate showed no plasmid. Plasmid have known to contribute significantly to bacterial genetic diversity and plasticity by encoding functions that might not be specified by the chromosome. As a tool, it can also be modified to express the protein of interest and served as invaluable model systems for the study of processes such as DNA replication, segregation, conjugation, and evolution [14]. Akrayi and Khider [15] opined that conjugation and transduction process, and poor quality of antibiotics available to the public to enhanced antibiotic resistance genes among naturally occurring bacteria.

### Conclusion

The extracted plasmid of molecular weight 7kb may be responsible for the resistant of the strain to the two antibiotics.

### References

- [1] van Delden C. Virulence factors in *Pseudomonas aeruginosa*. In *Virulence and Gene Regulation* 2004 (pp. 3-45). Springer, Boston, MA.
- [2] Luczkiewicz A, Kotlarska E, Artichowicz W, Tarasewicz K, Fudala-Ksiazek S. Antimicrobial resistance of *Pseudomonas* spp. isolated from wastewater and wastewater-impacted marine coastal zone. *Environmental Science and Pollution Research*. 2015 Dec 1;22(24):19823-34.
- [3] Livermore DM. Multiple mechanisms of antimicrobial resistance in *Pseudomonas aeruginosa*: our worst nightmare. *Clinical infectious diseases*. 2002 Mar 1;34(5):634-40.
- [4] WHO, 2018. Antimicrobial resistance. <https://www.who.int/news-room/fact-sheets/detail/antibiotic-resistance>
- [5] Blair JM, Webber MA, Baylay AJ, Ogbolu DO, Piddock LJ. Molecular mechanisms of antibiotic resistance. *Nature reviews microbiology*. 2015 Jan;13(1):42-51.
- [6] Chellat MF, Raguž L, Riedl R. Targeting antibiotic resistance. *Angewandte Chemie International Edition*. 2016 Jun 1;55(23):6600-26.
- [7] Li B, Webster TJ. Bacteria antibiotic resistance: New challenges and opportunities for implant-associated orthopedic infections. *Journal of Orthopaedic Research®*. 2018 Jan;36(1):22-32.
- [8] Lacroix B, Citovsky V. Transfer of DNA from bacteria to eukaryotes. *MBio*. 2016 Sep 7;7(4).
- [9] Alalam H, Graf FE, Palm M, Abadikhah M, Zackrisson M, Mattsson M, Hadjineophytou C, Persson L, Stenberg S, Ghiaci P, Sunnerhagen P. Conjugation factors controlling F-plasmid antibiotic resistance transmission. *bioRxiv*. 2018 Jan 1:271254.
- [10] Getino M, Fernandez-Lopez R, Palencia-Gándara C, Campos-Gómez J, Sánchez-López JM, Martínez M, Fernández A, de la Cruz F. Tanzawaic acids, a chemically novel set of bacterial conjugation inhibitors. *PloS one*. 2016 Jan 26;11(1):e0148098.
- [11] Bauer AW. Antibiotic susceptibility testing by a standardized single disc method. *Am J clin pathol*. 1966 ;45 :149-58.
- [12] Fauci AS, Hauser SL, Jameson JL, Kasper DL, Longo DL, Loscalzo J, editors. *Harrison's Principles of Internal Medicine*. McGraw-Hill Education LLC.; 2012.
- [13] Van Bambeke F, Mingeot-Leclercq MP, Glupczynski Y, Tulkens PM. Mechanisms of action. *Infect Dis*. 2017 Jan 1; 2:1162-80.
- [14] Khan S, Ullah MW, Siddique R, Nabi G, Manan S, Yousaf M, Hou H. Role of recombinant DNA technology to improve life. *International journal of genomics*. 2016 Jan 1;2016.
- [15] Akrayi HF, Khider AK. Genetic Site Determination of Antibiotic Resistance Genes in *Escherichia Coli* Isolated from Different Sources of Human Infection. *Medical Journal of Islamic World Academy of Sciences*. 2013 Apr;109(892):1-8.

## **Civil Engineering / İnşaat Mühendisliği**

## Collapse Fragility of Wide Beam Frames using the Simplified Method of FEMA P-58

Ornela Lalaj Şen\*, İzmir Kâtip Çelebi Univ., Dept. of Civil Engineering, İzmir, Turkey  
Mehmet Çevik, İzmir Kâtip Çelebi Univ., Dept. of Mechanical Engineering, İzmir, Turkey  
\*Corresponding author: lalaj.ornela@gmail.com

**Keywords:** Collapse fragility, idealized pushover curve  
**Discipline:** Civil Engineering

### Abstract

Wide beam framed (WBF) structures are very common in Turkey, however their performance is debatable. TBEC2018 designates WBF without shear walls as Limited Ductility Class, not able of resisting high levels of seismic loads. In this study, WBF are compared to frames with normal beams using their collapse fragility functions. The results indicate that the wide beam frames performed satisfactorily. It should be noted that the frames were designed according to the most recent seismic code of Turkey.

### Introduction

In some types of reinforced concrete construction, hidden beams are used instead of the normal beams, whose depth is typically greater than the width and hang below the slabs. These hidden beams instead have depth equal to the depth of the slab they support, and their widths are greater, to compensate for the limited depth, and provide the required moment and ductility capacities. In Turkey, this type of beams is often found in ribbed slab structures, in which the depth of the slab and the beams is 30-40 cm. The seismic performance of wide beam frames is debatable, which is why TBEC2018 provides limiting clauses for the design of wide beam frames.

Fragility curves summarize important building structural performance information, such as performance parameter versus earthquake hazard intensity. Generation of fragility curves is done through a tedious and time-consuming procedure. A large batch of time history analyses, at different earthquake intensity levels should be performed. FEMA P-58 [1] introduces a simplified procedure to generate the fragility curves, which requires only pushover analysis results from a comprehensive model. The method is discussed in detail in other studies [2]. In this study, the procedure above mentioned is applied to three reinforced concrete frames, designed according to TBEC2018 [3]. The frames are two-dimensional, represent residential structures and are designed for soil class D and earthquake design level 3.

### Methodology

FEMA P-58 introduces three methods to compute the collapse fragility of structures. *Nonlinear Response History Analyses* makes use of time history analyses to obtain demand parameters calculated for different levels of hazard intensity. *Incremental Dynamic Analysis (IDA)* uses thousands of ground motion records to calculate the seismic demand. *Limited-Suite Nonlinear Analyses* can be performed instead, using ground motion records organized in sets, and incrementally scaled to higher intensities to obtain the demand parameters. *Simplified Procedure (SPO2IDA)* makes use of the results of pushover analysis and an assigned dispersion of 0.6 to obtain the collapse fragility curves. *Judgment-Based Collapse* fragility curves can be derived based on engineering judgment of the expected collapse capacity of code-conforming structures.

Nonlinear Response History Analysis method yields the most accurate results, but it is considerably computationally consuming. The Simplified Method is suitable for simple, low-rise structures, and can be applied more readily since less analyses are required. FEMA P-58 presents a computational tool, SPO2IDA\_Tool.xls which was used in this study. This tool, which stands for Simplified Push Over To Incremental Dynamic Analysis, converts the pushover load versus displacement curve into IDA data. The pushover curve should be smoothed into a trilinear or quadrilinear curve in order to be used with the SPO2IDA tool. Figure 1 summarizes the steps of the Simplified method.

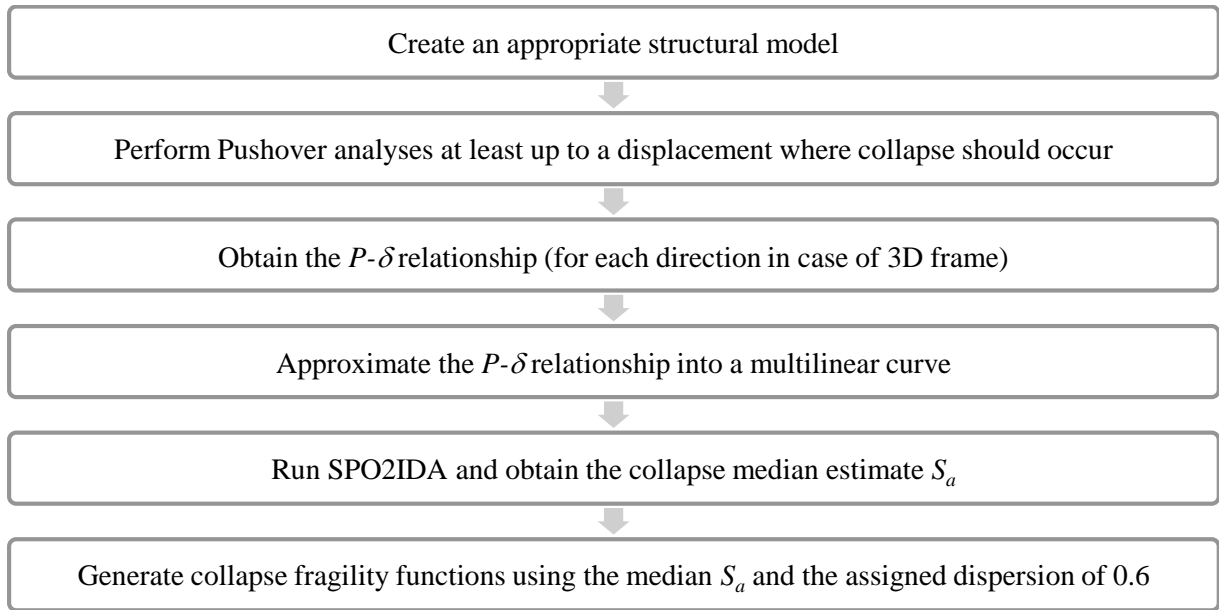
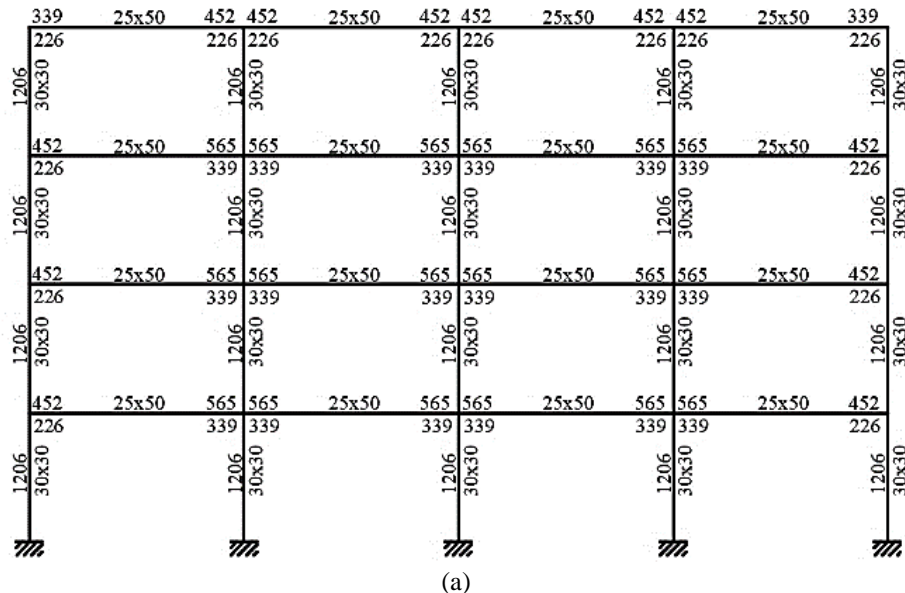


Figure 1. Steps of the simplified procedure for calculating collapse fragility functions

The 2D frames that were used in this study were modeled in SAP2000 using line elements for beams and columns, and plastic hinges to describe nonlinear behavior. The nonlinear behavior of columns was modeled with axial load – moment interaction hinges, and the nonlinear behavior of beams was modeled with moment hinges. The shear capacity of both beams and columns was calculated per TS500 (*çit.*) and modeled as brittle hinges. The load versus displacements were obtained in terms of base shear and roof top drift ratios. The idealization of the pushover curves and the generation of the collapse fragility functions is explained in detail in the next sections.



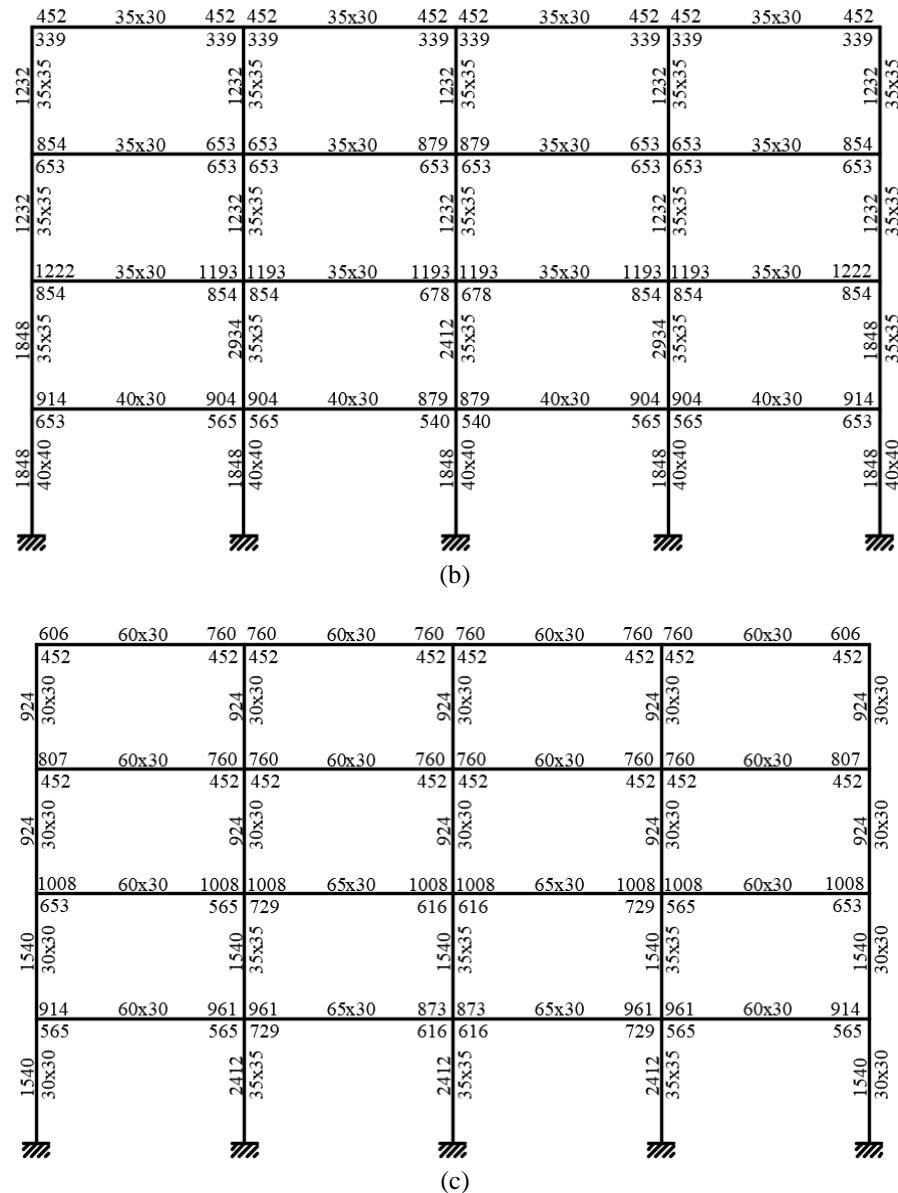


Figure 2. Cross-section sizes (in cm) and reinforcement areas (in mm<sup>2</sup>) for frames (a) CB; (b) WB1; (c) WB2

3 frame models, designed for soil class D and earthquake design level 3, according to TBEC2018 were considered in this paper. The cross-section sizes and reinforcement areas of the frames models are given in Figure 2. The frames had story heights of 2.9 m, and 5 m bay lengths. The materials used for the design and subsequent analyzes are C30 and B420C. The models are designated as CB – conventional beam frame; WB1 – wide beam frame of type 1, the width of the wide beams is the same as the width of the columns; WB2 – wide beam frame of type 2, the width of the wide beam is equal to the summation of column depth and beam depth.

### Idealized Pushover Analyzes

The idealization of the pushover curves is described in several sources, such as ASCE/SEI 41-06 [4] and FEMA356 [6]. FEMA P-58 suggests the procedure described in ASCE/SEI 41-06 for the idealization of pushover curves. The pushover curves are idealized as quadrilinear curves, an example of which is shown in Figure 3. Point 1 defines the yield, point 2 is the point of maximum base shear, point 3 and point 4 are in the collapse region. Point 2 is easily determined from the pushover curves of the frame models. The yield point of the structures is determined by setting the energy dissipated up to the maximum base shear (point 2) equal for both the actual and idealized curves. Additionally, segment

01 should be secant to the actual pushover curves at a point which has a base shear of  $0.6S_y$ . Point 3 defines the post-peak stiffness degradation. The strength degradation corresponding to point 3 can be anywhere between 20-40%. The ASCE/SEI 41-06 procedure, in which the rest of the idealization was based determines the point 3 as the secant at  $0.6S_y$ . However, wide beam frames do not display such strength degradation. Therefore point 3 was taken as a secant at  $0.8S_{max}$ . The coordinates of point 4 were taken the same as the coordinates of point 3. A Matlab code was written to perform the idealization.

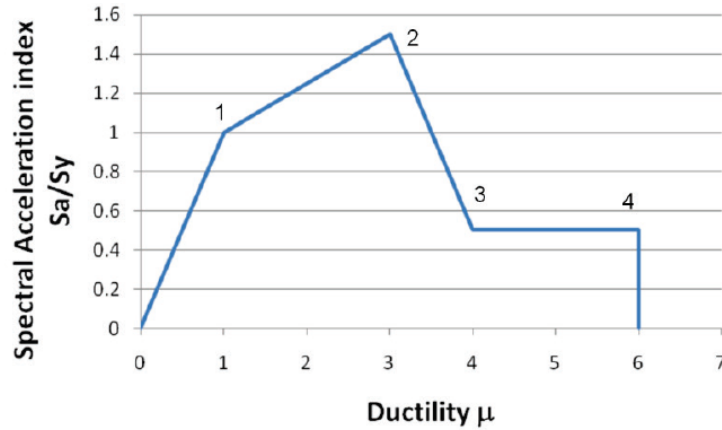
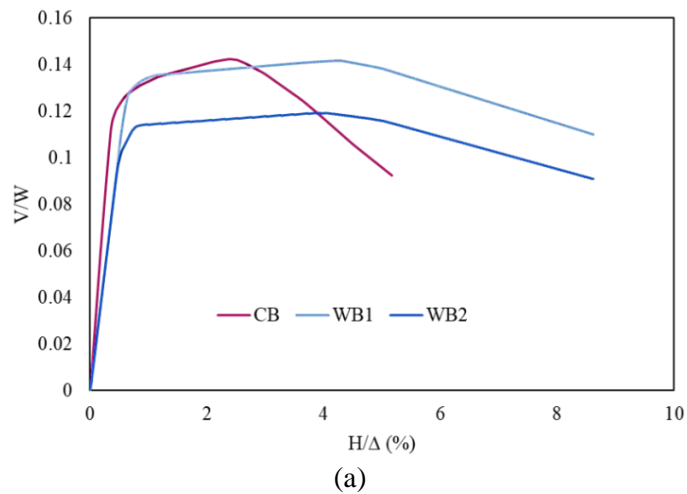
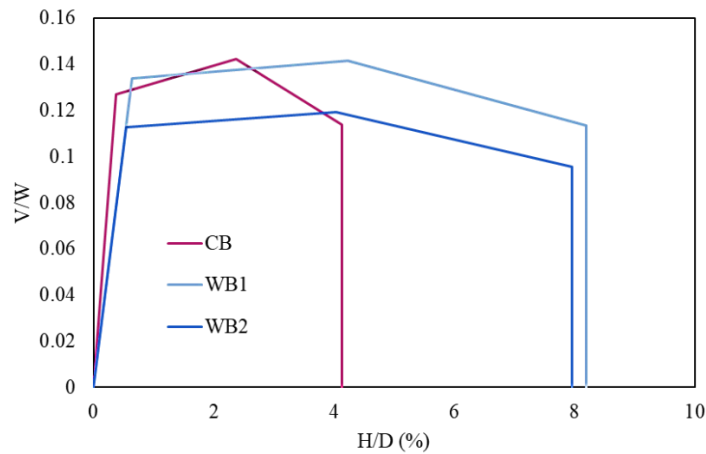


Figure 3. Example of an idealized pushover curve, required as an input for SPO2IDA tool



(a)



(b)

Figure 3. (a) The pushover curves of the frames express in terms of base shear coefficient ( $V/W$ ) versus rooftop drift ratio; (b) Idealized pushover curves of the frame models



The pushover curves of the 3 frame models are shown in Figure 3 (a), while Figure 3 (b) the idealized pushover curves.

### SPO2IDA and Collapse Fragility Functions

The SPO2IDA tool was used together with the idealized pushover curves displayed in Figure 3 (b). The pushover curves are converted into IDA curves, for selected percentiles. In this case, 16<sup>th</sup>, 50<sup>th</sup> and 84<sup>th</sup> percentile IDAs are generated. The outcome of the tool is expressed in terms of normalized spectral acceleration  $S_a/S_y$  and ductility  $\Delta/\Delta_y$ . Figure 4 shows the percentile IDA curves for frames CB, WB1 and WB2. The green dots represent the median demand  $S_a$ .

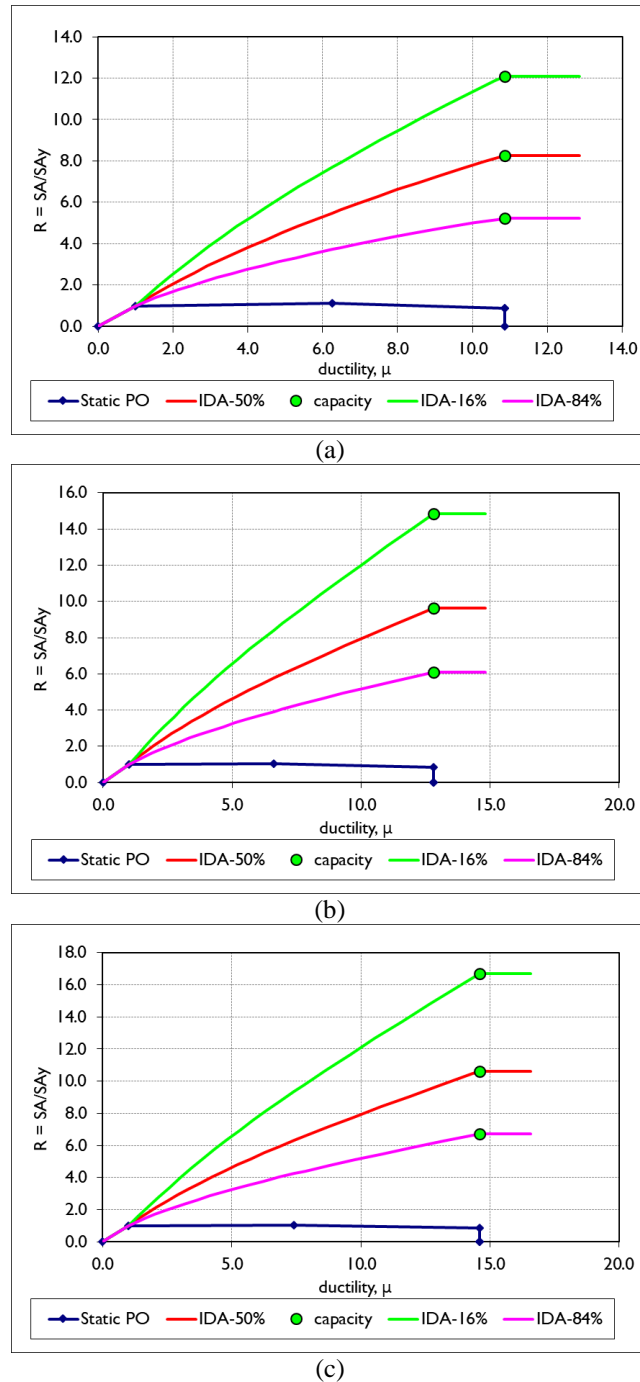


Figure 4. IDA curves for frames (a) CB; (b) WB1; (c) WB2

The dispersion of the fragility functions is suggested to be 0.6 when the simplified method of FEMA P-58 is used. The median collapse fragility functions for the frames considered in this study are

displayed in Figure 5. These curves relate any value of spectral acceleration  $S_a$  to a collapse fragility to each of the frames. For instance, the median collapse probabilities for a spectral acceleration of 0.5g is 68.1%, 46.5% and 54.8% for frames CB, WB1 and WB2 respectively. On the other hand, the collapse probabilities for the elastic design spectral acceleration (around 0.2g) are 25.9%, 6.8% and 9.1% for frames CB, WB1 and WB2 respectively. From these results it is observed that wide beam frames have lower collapse fragilities than the conventional beam frame, for the same values of spectral acceleration.

The collapse fragility functions were generated for 3 frames, two of which were wide beam frames. The frames were designed for similar conditions, according to TBEC2018. The collapse fragility functions were calculated based on the simplified procedure presented in FEMA P-58. The median spectral accelerations were obtained by using FEMA P-58 accompanying tool SPO2IDA, and the collapse fragility curves were generated.

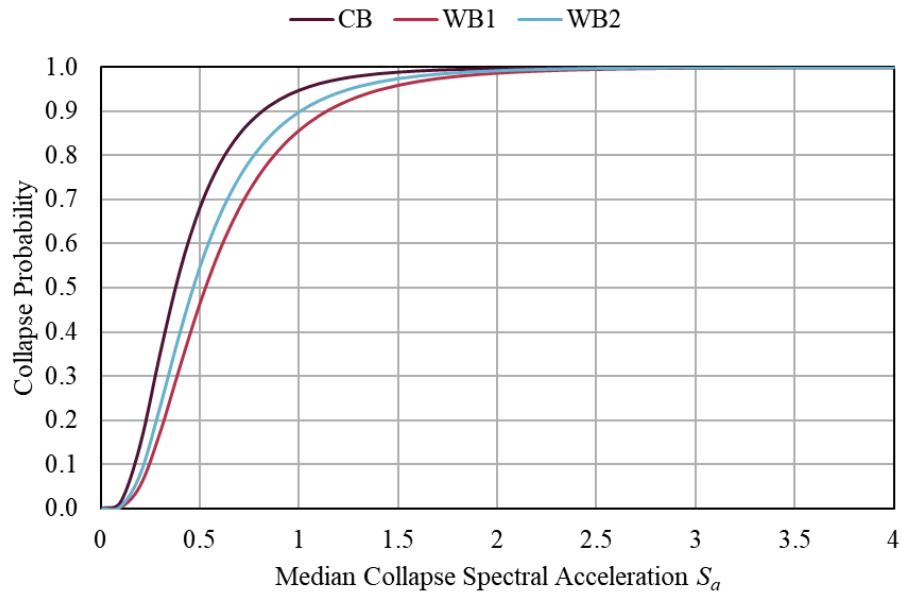


Figure 5. Collapse fragility curves for the 3 frames

### Conclusions

Wide beam frames have lower collapse probabilities than the conventional beam frame for any given spectral acceleration. The collapse probabilities for the elastic spectral acceleration corresponding to the fundamental period of each frame were also calculated. These probabilities are of course low, ranging 7-9% for the wide beam frames, and 25% for the conventional beam frame. From the point of view of collapse probability, well designed and detailed wide beam frames perform satisfactorily.

### References

- [1] ATC. Seismic Performance Assessment of Buildings, Volume 1 – Methodology, FEMA P-58-1. Washington D.C.; 2012.
- [2] Fragiadakis M, Vamvatsikos D. Fast performance uncertainty estimation via pushover and approximate IDA. Earthq Eng Struct Dyn. 2010; 39(6):683-703.
- [3] Disaster and Emergency Management Authority. Turkish Building Earthquake Code. Ankara; 2018
- [4] ASCE. Seismic Rehabilitation of Existing Buildings, ASCE/SEI 41-06. Washington, D.C.; 2007.
- [5] Zarfam P, Massood M. On the incremental dynamic analysis of reinforced concrete structures using a trilinear idealization model. Eng Struct. 2011; 33(4):1117-1122.
- [6] ASCE. Prestandard and Commentary for the Seismic Rehabilitation of Buildings. FEMA 356. Washington, D.C. 2000.

## An Alternative Approach to Produce Warm Mix Asphalt at Lower Temperatures

*Ali Almusawi\**, Graduate School of Natural and Applied Sciences, Dokuz Eylul University, Turkey

*Burak Şengöz*, Department of Civil Engineering, Dokuz Eylul University, Turkey

*Ali Topal*, Department of Civil Engineering, Dokuz Eylul University, Turkey

\*Corresponding author: [ali89.engin@yahoo.com](mailto:ali89.engin@yahoo.com)

**Keywords:** Hot bitumen, warm mix asphalt, steady shear flow

**Discipline:** Civil Engineering

### Abstract

The utilization of hot asphalt mixture may lead to environmental problems such as carbon dioxide emissions. In order to overcome these issues, in the last few years, a new bitumen technology has been developed named warm mix asphalt (WMA) which requires lesser temperatures than the conventional bitumen. The WMA technology is produced by mixing the hot bitumen with different types of Chemical and Organic additives which work on reducing the bitumen resistance to flow. In other words, the viscosity of the WMA becomes lesser and the workability increases during construction. However, the application of the standard method (ASTM D2493) to determine the required construction temperatures may not be suitable since the obtained temperatures do not exhibit much difference compare to the hot bitumen. In this study, an alternative approach called Steady Shear Flow (SSF) has been applied aiming to obtain lesser temperatures than the traditional method. The WMA samples have been prepared by using two different Chemical and Organic additives within 50/70 and 160/220 penetration grade base bitumen. The results showed that the application of the new proposed approach has led to lower temperatures than the standard method.

### Introduction

The idea of producing bituminous mixtures at lower temperatures has been an issue that has been studied for many years. The first study was made in 1956 from Iowa State University made by Csanyi [1]. In this study, Csanyi designed a metal conditioning cabinet on the field. This cabin has two entrances and one exit section. Hot bitumen injection is made from the upper entrance, and cold water is added to the cabinet from the other entrance. Cold water sprayed into the cabin foamed hot bitumen, causing a decrease in its viscosity. The foamed bitumen obtained from the outlet in the cabin was mixed with aggregate and paved [2].

Other studies were carried out by Chevron in the early 1970s by developing asphalt emulsions and some mixture and thickness design methods. Chevron has determined some important rules to be followed in the design and production works of bituminous mixtures prepared with asphalt emulsions [3]. In the ongoing studies, it was stated that the mixes prepared by using asphalt emulsions are prepared at a lower temperature and that they are easy to transport and can be used easily on rural roads, and the investment costs are very low in the plants where asphalt emulsions are produced [4].

The first modern WMA studies have started from the second half of the 90s and the findings have been published in the German Bitumen Forum (GBF) held in 1997. In the organization, it was aimed to introduce bitumen producers and academicians with WMA technology and direct the works in line with the requirements of the contractor companies. In the process that followed, Shell Bitumen Company implemented trial ways and laboratory experiments with WMA in Norway, England, and the Netherlands [5]. Shell Bitumen Company has developed a WMA additive named WAM - Foam in the light of the data obtained from Harrisons' experimental studies using intensive gradation. In the subsequent works, Sasol Wax International AG in Europe introduced Sasobit®, a fully organic wax-based WMA additive, to the market in 1997. As of this date, this process has started to be called WMA technology [6].

The aforementioned studies have started to be applied primarily in places such as Europe, South Africa, and Australia where fossil fuels are costlier [6]. Today, although warm mix asphalt additives are available in the market, it is not a technology used as intensely as HMA. However, its potential effects are being investigated. Recently, in many states of the USA, both laboratory experiments and field studies are applied intensely on a bituminous mixture prepared with WMA additives [7]. Studies have

shown that it is possible to use WMA additives for applications with different aggregate gradations such as open gradation, gap gradation, and stone mastic asphalt (SMA), although it is generally utilized with dens gradation mixtures [5].

However, the determination of the required construction temperature is observed to be high when the standard method (ASTM D2493) is applied [8-11]. Thus, in this paper, an alternative method proposed in the literature has been implemented aiming to determine lower temperature than the standard method.

### Materials and Experimental

In this study 50/70 and 160/220 base bitumen grades supplied by DERE ASFALT were used. Some of the conventional tests have been conducted for the base bitumen such as penetration test, softening point test, and Rolling thin film oven test to measure the bitumen characteristics. Table 1 shows the test results according to the ASTM specification.

Table 1. Properties of the base bitumen

Test	Specification	Results		Specification limits	
		50/70	160/220	50/70	160/220
Penetration (25 °C; 0.1 mm)	ASTM D5	65	190	50-70	160-220
Softening point (°C)	ASTM D36	51	41	46-54	35-43
Penetration index (PI)	-	0.35	0.123	-	-
Rolling thin film oven test (RTFOT)	ASTM D2872-12				
Change of mass (%)	-	0.160	0.94	0.5 (max.)	0.5 (max.)
Penetration (25 °C; 0.1 mm)	ASTM D5	53	97	50 (min.)	50 (min.)
Retained penetration (%)	ASTM D5	82	51	50 (min.)	50 (min.)
Softening point after RTFOT (°C)	ASTM D36	58	50	48 (min.)	48 (min.)

In order to prepare warm mix asphalt samples, two types of additives organic (Sasobit®) and chemical (Rediset®) have been used. The organic WMA additive, which has been supplied from a South African Company, is a long-chain aliphatic polymethylene hydrocarbon produced from the Fischer-Tropsch chemical process with a melting temperature of 120 °C. The longer chains help keep the wax in solution, which reduces bitumen viscosity at typical asphalt production and compaction temperatures. Chemical WMA additive is a combination of cationic surfactants and organic additive-based rheology modifier. The additive chemically modifies the bitumen and obtains active adhesion force that improves coating of aggregates with bitumen [12].

### Preparation of Warm Mix Asphalt Samples

The content of both organic and chemical is determined based on the recommendations by the suppliers as well as literature [12]. The content of both organic additive (Sasobit®) and the chemical additive (Rediset®) is selected as 3% to produce WMA samples. The virgin bitumen is heated until it becomes fluid and has been poured into a 500 ml glass beaker. The Sasobit® is then mixed gradually and the rotation speed was fixed at 1000 rpm for 10 minutes. Whereas for the chemical additive the rotation speed was 1000 rpm for 15 minutes [10].

### Mixing and Compaction Temperatures Determination Methods

Production temperatures are determined through the standard method (ASTM D2493). In this paper, another method named as steady shear flow (SSF) is applied for WMA samples.

### ASTM D 2493 Method

Brookfield viscometer is performed to determine the required mixing and compaction temperatures. As stated by the ASTM D 2493 standard, this method is utilized to measure the viscosity of the bitumen at two temperatures 135 °C and 165 °C at a constant shear rate of 6.8 1/s. The measured viscosity values are plotted against the temperature as shown in Fig. 1. The mixing and compaction temperature limits are  $0.17 \pm 0.02$  and  $0.28 \pm 0.03$ , respectively [13].

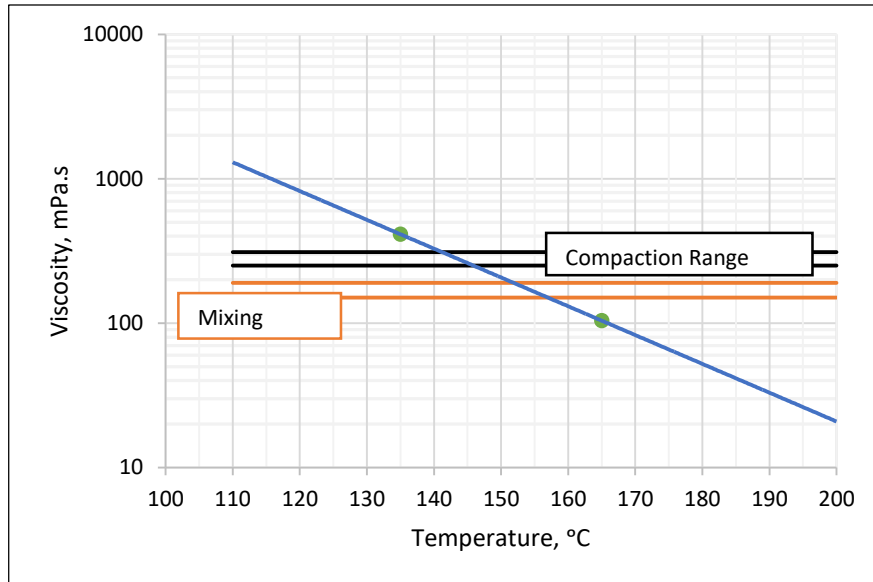


Figure 1. ASTM D 2493 Method [9]

### Steady Shear Flow Method (SSF)

This method which is recommended by Reink is based on the shear dependency of the bitumen. The steady shear flow test is conducted using Dynamic Shear Rheometer (DSR). The target shear stress of 500 Pascal is chosen as a value where the viscosity measurements appeared more stable and the bitumen sample reaches the steady-state condition. In this method, Viscosities are measured at three temperatures (76°C, 82°C, and 88°C) over a series of stress levels from 0.33 Pa to 500 Pa as shown in Fig. 2. The measured viscosity values at steady state-condition (500 Pa) are then plotted using a log viscosity versus log temperature chart and extrapolated to determine the mixing and compaction temperatures based upon specified viscosity ranges of  $0.17 \pm 0.02$  Pa. s and  $0.35 \pm 0.03$  Pa. s, respectively [14].

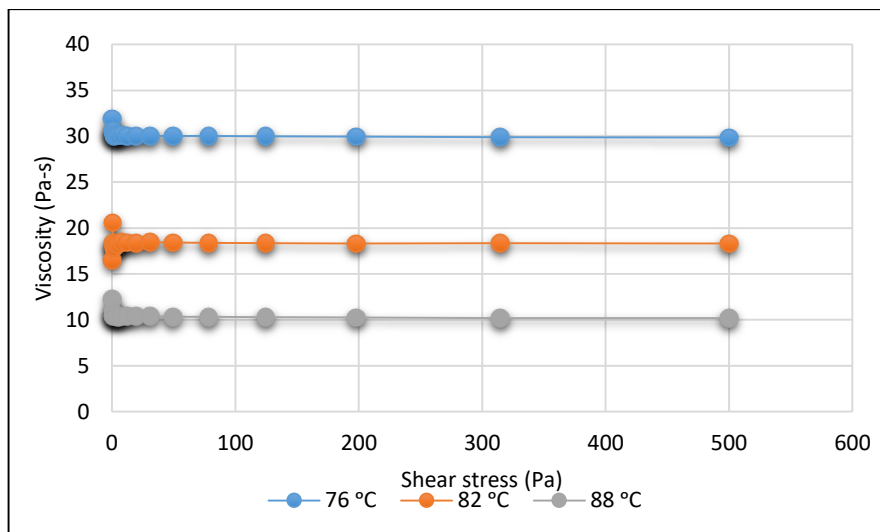


Figure 2. Example of SSF method

### Results and Discussion

The mixing and compaction temperatures are determined based on ASTM D2493. The mixing and compaction temperatures calculation for 50/70 and 160/220 penetration grade bitumen involving WMA additives is presented in Fig. 3.

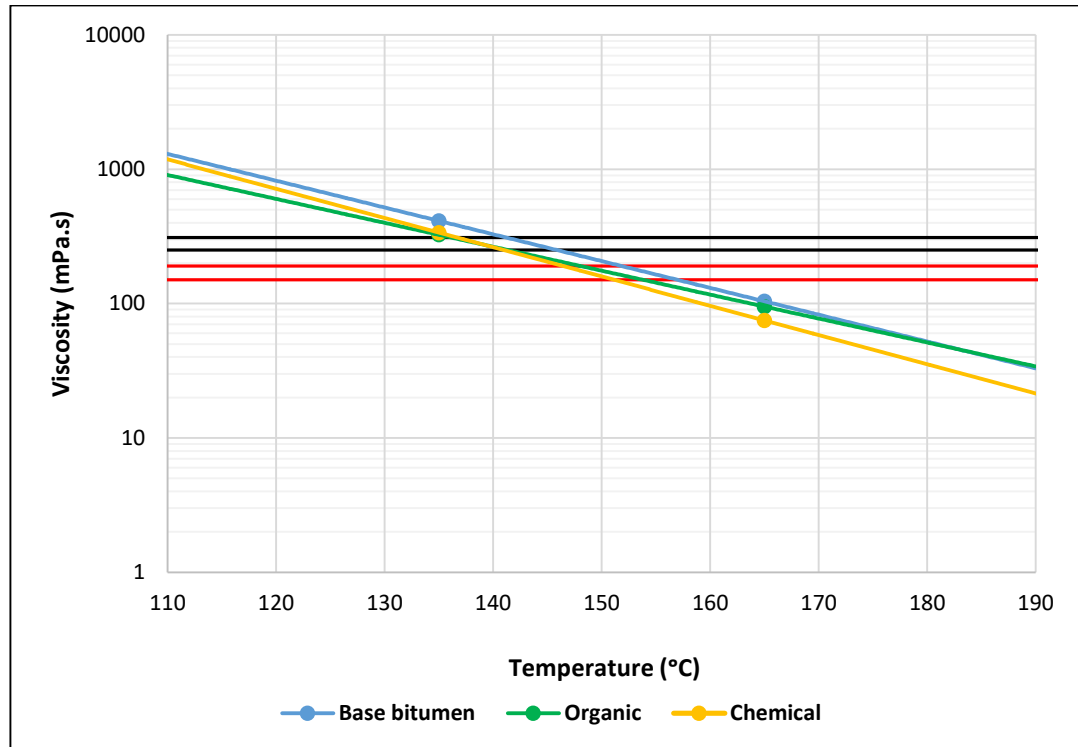


Figure 3. Example Data of (50/70 Bitumen) mixing and compaction temperatures determination

The mixing and compaction temperatures corresponding to  $0.17 \pm 0.02$  Pa. s and  $0.28 \pm 0.03$  Pa. s are presented in Table 2. Both warm mix asphalt additive work on reducing the viscosity of the bitumen samples so the required mixing and compaction temperatures become lesser than the base bitumen.

Table 2. Mixing and compaction temperatures results

Material	50/70		160/220	
	Mixing Temp. (°C)	Compaction Temp. (°C)	Mixing Temp. (°C)	Compaction Temp. (°C)
Base bitumen	152-158	141-146	140-147	125-131
WMA (Organic)	146-153	135-140	134-140	123-128
WMA (Chemical)	146-151	136-141	135-140	124-128

Fig. 4 presents an example for the test results for bitumen sample involving organic additives at a different set of temperatures (76 °C, 82 °C, and 88 °C). All the bitumen samples have reached a steady-state condition (no variation in the viscosity readings) when the stress level is about 500 Pa.

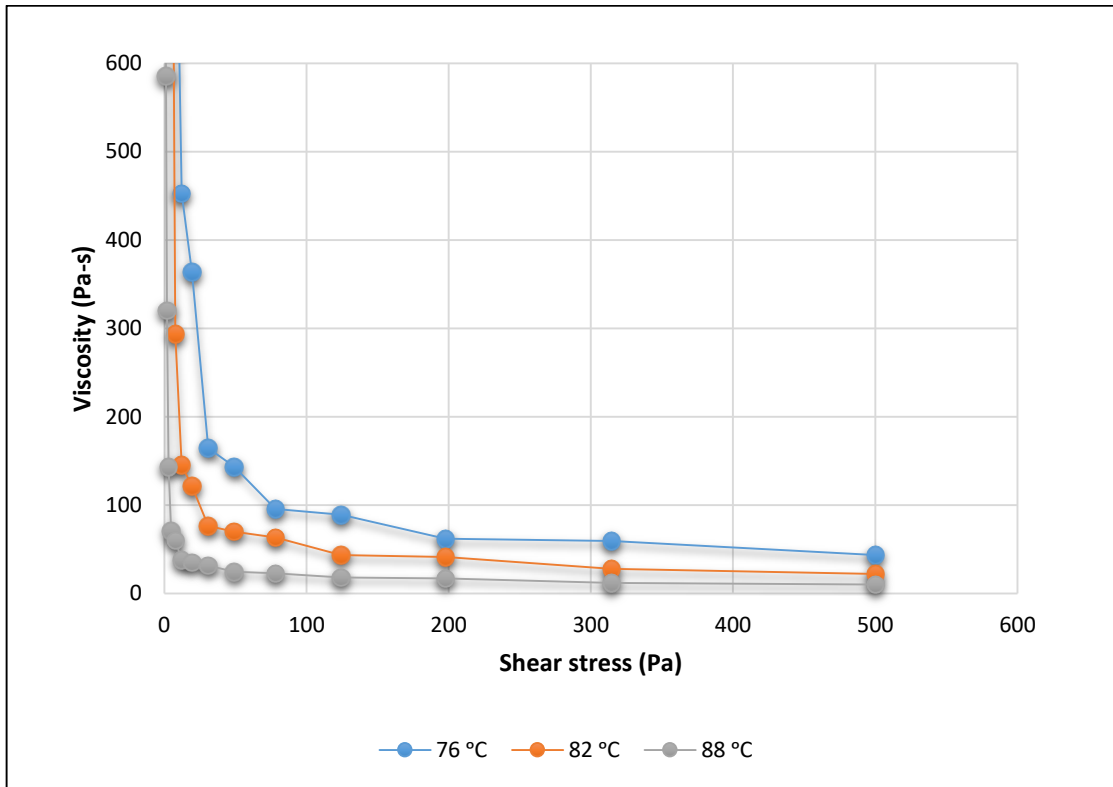


Figure 4. Example data of steady shear flow measurements for 50/70 (Organic)

In order to obtain the mixing and compaction temperatures, the viscosity values at steady-state conditions are plotted and extrapolated against the temperature as illustrated in Fig. 4.

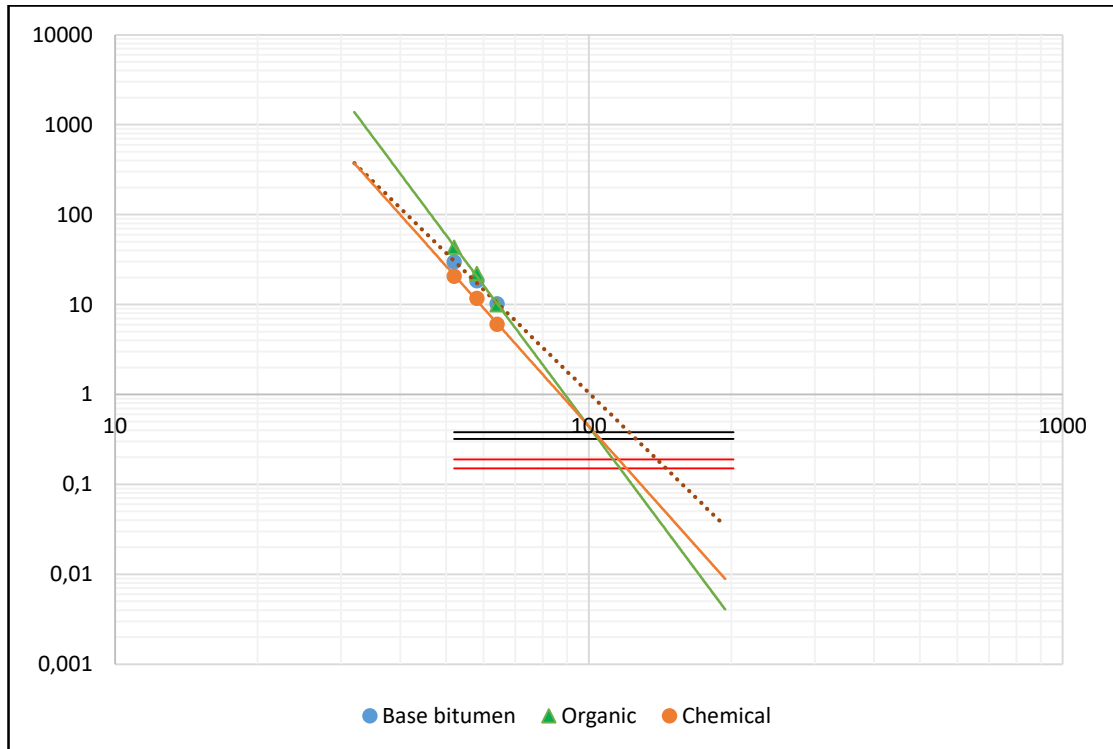


Figure 5. Example data for SSF of 50/70 bitumen mixing and compaction temperatures determination

Table 3. SSF method results

Material	50/70		160/220	
	Mixing Temp. (°C)	Comp. Temp. (°C)	Mixing Temp. (°C)	Comp. Temp. (°C)
Base bitumen	152	140	140	125
WMA (Organic)	133	124	120	115
WMA (Chemical)	136	124	129	118

The steady shear flow method can be applied for different penetration bitumen grades with both WMA and polymer additives. As expected, as the penetration value of the bitumen increases, that is, the bitumen becomes more fluid, the required bitumen and aggregate mixing and compaction temperatures decrease (Table 3).

For the base bitumen sample, the steady shear flow method yielded almost similar temperatures compared to the ASTM method. While for WMA samples, the determined temperatures are considerably decreased. It has been noticed that the detected behavior was non-Newtonian and the viscosity value decreased with the increase of the shear stress. This can be attributed to the sensitivity of the Dynamic Shear Rheometer (DSR) machine which used to perform this test and also to the low range of temperatures (76°C, 82°C, and 88°C) utilized in this method. The mixing and compaction temperature values of 50/70 and 160/220 penetration bitumen samples containing organic and chemical WMA additives produced close results.

### Conclusion

Based on the obtained results, it can be concluded that the implementation of the standard method for bitumen samples involving WMA additives has not led to a significant reduction in the obtained mixing and compaction temperatures. On the other hand, the application of the SSF method has exhibited a considerable reduction in the obtained temperatures in comparison to the standard methods. It is much more practical to use the SSF method to determine the mixing and compaction temperatures for WMA instead of the standard method.

### Acknowledgment

This research was sponsored by the Department of Scientific Research projects, Dokuz Eylül University under the project number 2019.KB.FEN.021 for which the authors are greatly indebted. The authors are also thankful to the Graduate School of Natural and Applied Sciences of Dokuz Eylül University for its support.

### References

- [1] Chowdhury A, Button JW. A review of warm mix asphalt. Texas Transportation Institute; 2008 Dec 1.
- [2] P Csanyi LH. Foamed asphalt in bituminous paving mixtures. Highway Research Board Bulletin. 1957(160).
- [3] Manual BM. Chevron USA. Asphalt Division, San Francisco, Calif. 1977 Jan.
- [4] Kuennen T. Warm mixes are a hot topic. Better roads. 2004 Jun;74(6).
- [5] Harrison T, Christodoulaki L. Innovative processes in asphalt production and application: "Strengthening asphalt's position in helping to build a better world". In World of Asphalt Pavements, International Conference, 1st, 2000, Sydney, New South Wales, Australia 2000.
- [6] Button JW, Estakhri CK, Wimsatt AJ. A synthesis of warm-mix asphalt. Texas Transportation Institute; 2007 Jul 1.
- [7] Zettler R. Warm mix stands up to its trials. Better roads. 2006 Feb;76(2).
- [8] Almusawı A , Şengöz B , Kaya Özdemir D , Topal A . Predicting Mixing and Compaction Temperatures of Polymer Modified Bitumen. Celal Bayar University Journal of Science. 2020; 16(3): 263-268.
- [9] Almusawı A , Sengoz B , Topal A, Oner J . Comparison Between Zero Shear Viscosity and Steady Shear Flow Methods To Determine Mixing and Compaction Temperatures of PMB.



- Eurasian Journal of Civil Engineering and Architecture. 2019 Dec 1;3(2):1-8.
- [10] Almusawi, A., Sengoz, B., Topal, A. Investigation of Mixing and Compaction Temperatures of Modified Hot Asphalt and Warm Mix Asphalt. *Periodica Polytechnica Civil Engineering*. 2020.
- [11] Almusawı A, Şengöz B, Özdemir DK, Topal A. Determination of Mixing and Compaction Temperatures of Polymer Modified Bitumen through High Shear Rate Method. in 3<sup>rd</sup> International Students Science Congress. 2019; pp. 110–115.
- [12] Sengoz B, Topal A, Gorkem C. Evaluation of natural zeolite as warm mix asphalt additive and its comparison with other warm mix additives. *Construction and Building Materials*. 2013 Jun 1;43:242-52.
- [13] ASTM International. D2493-01 Standard Viscosity-Temperature Chart for Asphalts. West Conshohocken, PA; ASTM International, 2001.
- [14] West RC, Watson DE, Turner PA, Casola JR. Mixing and compaction temperatures of asphalt binders in hot-mix asphalt. 2010.

## ACI318-14 ve TS500 Yönetmelikleri ile T En-Kesitli Betonarme Kirişlerin Davranışlarının Karşılaştırılması

Rohullah Jamal\*, Konya Teknik Üniversitesi, Mühendislik ve Doğa Bilimleri Fakültesi, İnşaat Mühendisliği Bölümü, Konya, Türkiye

Süleyman Bahadır Yüksel, Konya Teknik Üniversitesi, Mühendislik ve Doğa Bilimleri Fakültesi, İnşaat Mühendisliği Bölümü, Konya, Türkiye

\*İletişimden sorumlu yazar: jamal.rohullah@gmail.com

**Anahtar Kelimeler:** Akma moment taşıma kapasitesi, beton basınç dayanımı, basınç donatısı, T en-kesitli betonarme kirişle, donatı çeliği

**Disiplin:** İnşaat Mühendisliği

### Özet

Bu çalışmada T en-kesitli betonarme kirişlerde farklı parametre olarak beton sınıfı, boyuna donatı olarak çekme ve basınç donatısı oranlarının eğilme momentine etkisi ACI 318-14 ve TS500-2000 yönetmeliklerin elde edilen sonuçlar araştırılarak karşılaştırılmıştır. Parametrelerin değerleri değiştirilerek sayısal bir çalışma yapılmıştır. Bu amaçla, 55 adet farklı parametrelere sahip T en-kesitli betonarme kiriş tasarlanmıştır. Betonarme kiriş elemanların moment taşıma kapasitesi malzemelerin yönetmeliklere uygun şekilde ele alınarak hesaplanmıştır. Analizlerde kiriş kesitlerinde beton basınç dayanımı TS500-2000'e göre  $f_{cd}$  ve ACI 318-14'e göre  $f_{ck}$  donatı çeliğin akma dayanımı TS500-2000'e göre  $f_{yd}$  ve ACI 318-14'e göre  $f_{yk}$  olarak alınmıştır. Analiz sonuçları kullanılarak güç tükenmesi durumunda eğilme moment kapasitesinin değerleri elde edilmiştir. Analiz sonuçlarından farklı parametrelerden elde edilen verilerin sonuçları çizelgeler halinde sunulmuş ve sonuçlar değerlendirilmiştir. T en-kesitli kirişlerde iki farklı yönetmeliğe göre hesaplanan moment kapasiteleri kıyaslanarak yorumlanmıştır. Betonarme kiriş elemanlarında basınç donatısı oranının artması ile moment kapasitesi değerleri artmaktadır. Çalışmadan elde edilen sonuçlardan ACI 318-14 ve TS500-2000 yönetmeliklerinden elde edilen moment kapasiteleri arasında farklılıklar olduğu gözlemlenmiştir.

### Giriş

Betonarme yapılardaki kiriş ve döşeme gibi yatay taşıyıcı elemanlar, uygulanan düşey ve yatay yükler nedeni ile eğilmeye çalışmaktadır. Taşıyıcı sistem içinde kirişlerin iki temel görevinden söz edilebilir. Bunlardan birincisi, düşey doğrultuda etkilenen ve döşemeden aktarılan kalıcı ve hareketli yükler ile varsa üzerindeki duvar yüklerini mesnetlenmiş kolon ve ya perdelerle aktarmaktadır. İkinci etki ise deprem ve rüzgâr nedeniyle oluşan yatay yükleri döşemelerle birlikte düşey taşıyıcı elemanlara aktarmaktadır [1]. Bu elemanların kesitlerinde eğilmeye ek olarak kesme kuvveti, yüklemeye ve sistemi oluşturan elemanların düzenlenmesine bağlı olarak burulma ve eksenel yük de oluşabilmektedir. Betonun çekme dayanımının çok düşük olması nedeniyle, donatısız eğilme elemanı yapmak pratik ve ekonomik olmamaktadır. Kiriş ve döşeme gibi eğilmeye çalışan elemanlarda, çekme bölgesinde yerleştirilen donatılar, basınç bölgesindeki betonun tam kapasite ile çalışmasını sağlamaktadır. Betonarme T en-kesitli kiriş kesit hesabı ve tasarımı yapılırken dikkat edilmesi gereken en önemli husus, elde edilen kesitteki donatı oranının, dengeli donatı orandan küçük olmasını sağlamaktır. Betonarme T en-kesitli kirişlerde sünek davranışın sağlanabilmesi için, çekme donatısı oranının dengeli donatı oranından küçük olması gerekmektedir. Betonarme T en-kesitli kirişlerin çekme donatısı oranı maksimum donatı oranına eşit tutulmuş ve Denklem (1) ile hesaplanmıştır.

$$\bar{\rho}_b = 0.85 \frac{f_{cd}}{f_{yd}} \left[ k_1 \frac{600}{600 + f_{yd}} + \left( \frac{h_f}{d} \right) \left( \frac{b}{b_w} - 1 \right) \right], \quad \rho_{max} = 0.85 \bar{\rho}_b, (\rho - \rho') \leq \rho_{max} \quad (1)$$

Sabit geometride, farklı beton sınıfı, boyuna donatı olarak sabit çekme ve farklı basınç donatı oranlarına sahip 5 tip toplam 55 adet betonarme T en kesitli kiriş modeli tasarlanmıştır. Betonarme T en kesitli kiriş modellerinin tasarımında Türkiye Bina Deprem Yönetmeliği (TBDY, 2018), Betonarme Yapıların Tasarım ve Yapım Kuralları (TS500, 2000) ve ACI 318-14'te verilen hükümler dikkate alınmıştır. Farklı parametrelerde tasarlanan betonarme T en-kesitli kiriş modellerinde çekme donatısı oranı olarak;  $\rho = \rho_{max}$  ve basınç donatı oranı olarak;  $\rho'_s = 0.0, 0.1\rho, 0.2\rho, 0.3\rho, 0.4\rho, 0.5\rho, 0.6\rho,$

0.7 $\rho$ , 0.8 $\rho$ , 0.9 $\rho$  ve  $\rho$  değerleri değiştirilerek dikkate alınmıştır. Betonarme T en-kesitli kiriş modellerinde C30, C35, C40, C45 ve C50 olarak beş farklı beton sınıfı dikkate alınmıştır. Betonarme T en-kesitli kiriş modellerinde her beton sınıfı için çekme donatısı oranı  $\rho = \rho_{max}$  ve beton basınç dayanımı olacak şekilde sabit tutulmuş basınç donatısı oranları değiştirilerek kesitlerin taşıma gücü momentleri araştırılarak hesaplanmıştır. Araştırılmış betonarme T en-kesitli kirişlerin taşıma gücü momentleri TS500 ve ACI 318-14'e göre hesaplanarak karşılaştırılmıştır. Betonarme T en-kesitli kiriş kesitlerin moment taşıma kapasitesi EXCEL2016 programı ile hesaplanmıştır. EXCEL2016 programında tanımlanan beton ve donatı çeliği için hesaplarda kullanılan dayanım ve katsayılar ACI 318-14 ve TS500-2000'e göre hesaplanarak Tablo 1 ve 2'de özetlenmiştir. Betonarme T en-kesitli kirişlerin çekme ve basınç donatı alanları Tablo 3'te özet olarak verilmiştir. Kirişlerde eksenel yükün maksimum değeri  $N = 0.10 \times A_c \times f_c$  olacak şekilde sınırlandırılmış ve eksenel yük sıfır olarak alınmıştır [2].

Tablo 1. AC318-14'te farklı beton basınç dayanımı için kullanılan katsayılar [3]

$\alpha$	$\beta$	$\beta_1$	$\gamma$	$f_{ck} = f_{cd}$ (MPa)	$f_{yk} = f_{yd}$ (MPa)
0.720	0.425	0.85	0.85	25	420
0.706	0.420	0.84	0.85	30	420
0.677	0.400	0.80	0.85	35	420
0.648	0.380	0.76	0.85	40	420
0.620	0.365	0.73	0.85	45	420
0.590	0.345	0.69	0.86	50	420

Tablo 2. TS500-2000'de farklı beton basınç dayanımı için kullanılan katsayılar [4]

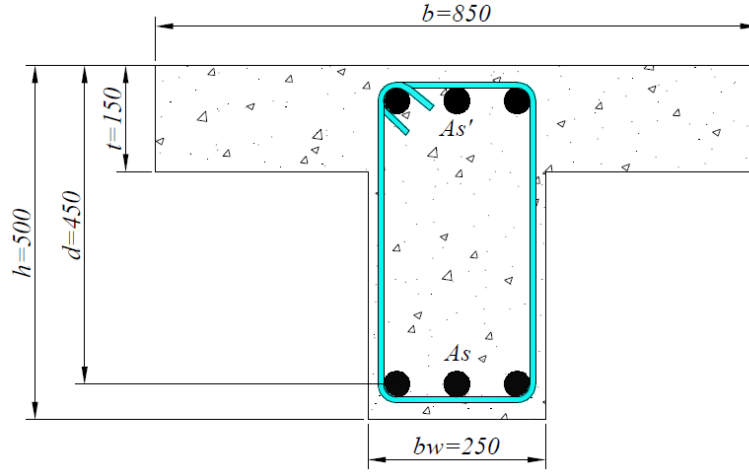
$k_1$	$\gamma_{mc}$	$\gamma_{ms}$	$f_{ck}$ (MPa)	$f_{cd}$ (MPa)	$f_{yk}$ (MPa)	$f_{yd}$ (MPa)
0.85			25	16.7	420	365
0.82			30	20.0	420	365
0.79	1.5	1.15	35	23.3	420	365
0.76			40	26.7	420	365
0.73			45	30.0	420	365
0.70			50	33.3	420	365

Tablo 3. T en-kesitli betonarme kirişlerin çekme ve basınç donatısı oranı ve alanı

Tip-1		Tip-2		Tip-3		Tip-4		Tip-5	
$\rho$	$A_s$ (mm <sup>2</sup> )	$\rho$	$A_s$ (mm <sup>2</sup> )	$\rho$	$A_s$ (mm <sup>2</sup> )	$\rho$	$A_s$ (mm <sup>2</sup> )	$\rho$	$A_s$ (mm <sup>2</sup> )
0.0518	5829.8	0.0596	6704.5	0.0671	7551.7	0.0744	8371.1	0.0814	9162.9
$\rho'$	$A'_s$ (mm <sup>2</sup> )	$\rho'$	$A'_s$ (mm <sup>2</sup> )	$\rho'$	$A'_s$ (mm <sup>2</sup> )	$\rho'$	$A'_s$ (mm <sup>2</sup> )	$\rho'$	$A'_s$ (mm <sup>2</sup> )
0.0000	0.0	0.0000	0.0	0.0000	0.0	0.0000	0.0	0.0000	0.0
0.0052	583.0	0.0060	670.5	0.0067	755.2	0.0074	837.1	0.0081	916.3
0.0104	1166.0	0.0119	1340.9	0.0134	1510.3	0.0149	1674.2	0.0163	1832.6
0.0155	1748.9	0.0179	2011.4	0.0201	2265.5	0.0223	2511.3	0.0244	2748.9
0.0207	2331.9	0.0238	2681.8	0.0269	3020.7	0.0298	3348.4	0.0326	3665.2
0.0259	2914.9	0.0298	3352.3	0.0336	3775.8	0.0372	4185.6	0.0407	4581.4
0.0311	3497.9	0.0358	4022.7	0.0403	4531.0	0.0446	5022.7	0.0489	5497.7
0.0363	4080.8	0.0417	4693.2	0.0470	5286.2	0.0521	5859.8	0.0570	6414.0
0.0415	4663.8	0.0477	5363.6	0.0537	6041.3	0.0595	6696.9	0.0652	7330.3
0.0466	5246.8	0.0536	6034.1	0.0604	6796.5	0.0670	7534.0	0.0733	8246.6
0.0518	5829.8	0.0596	6704.5	0.0671	7551.7	0.0744	8371.1	0.0814	9162.9

### Materyal ve Metot

Uygulamada kirişler genellikle döşemeler ile birlikte dökülmektedir. Bu durumda kiriş açıklığı tablalı kesit olarak davranmaktadır. Basınç bölgesindeki donatılarının dikkate alınması durumunda, kesit çift donatılı tablalı kesit olarak tasarlanmaktadır. Betonarme T en-kesitli kirişler tek donatılı ve çift donatılı kiriş olarak tasarlanmaktadır. Bu çalışmada tek donatılı ve çift donatılı T en-kesitli kirişler tasarlanmıştır. Betonarme T en-kesitli kirişlerin kesit boyutları ve donatı yerleşim planı Şekil 1’de verilmiştir.



Şekil 1. T en-kesitli kirişlerin boyutları ve donatı yerleşimi

Şekil 1’de  $b$ ; tabla genişliğini,  $b_w$ ; kiriş gövde genişliğini,  $h$ ; kiriş yüksekliğini,  $d$ ; faydalı yüksekliği,  $t$ ; döşeme kalınlığını  $A_s$  ve  $A_s'$  sırasıyla çekme ve basınç donatısı alanlarını göstermektedir. Betonarme kesitlerin moment taşıma kapasitesini etkileyen parametreler, beton basınç dayanımı, çekme donatısı oranı ve basınç donatısı oranı gibi faktörlerdir. Bu çalışmada betonarme T en-kesitli kirişlerin çekme donatısı oranını sabit tutulmuş, basınç donatı alanı ve beton basınç dayanımını değiştirerek moment taşıma kapasiteleri ACI 318-14 ve TS500-2000’e göre hesaplanmıştır. İki farklı yönetmeliğine göre elde edilen moment taşıma kapasiteleri karşılaştırarak değişen parametrelerin moment taşıma kapasitesine etkisi araştırılmıştır. Çalışmanın amacı etkilenen parametrelerin moment taşıma kapasitesine etkisi ve iki farklı yönetmeliğine göre hesaplanan betonarme T en-kesitli kirişlerin moment taşıma kapasitelerinin karşılaştırılmasıdır. Bu nedenle, ACI 318-14 ve TS500-2000 yönetmeliklerine göre moment taşıma kapasitesi elde edilmesinin prosedürü iki farklı başlık altında verilmiştir.

### $\alpha$ - Moment Taşıma Kapasitesinin ACI318-14’e göre Hesaplanması

Betonarme inşaatın bir döküm özelliği nedeniyle döşeme ve kirişler tek döküm olarak inşa edilmekte ve birlikte çalışmaktadır. Bu nedenle kesit hesabı yapılırken, döşeme kiriş kesite dahil edilmekte ve birlikte çalışmaktadır. Elde edilmiş kesitler T kesit (tablalı kesit) olarak adlandırılır. Şekil 1’de T en-kesitli betonarme kiriş verilmiştir. T en-kesitli kirişlerde tarafsız eksen tablanın içinde kalırsa kiriş dikdörtgen kiriş gibi tasarlanmaktadır. Eğer tarafsız eksen tablanın altında kalırsa, kiriş T en-kesitli kiriş olarak tasarlanmalıdır. Bu çalışmada tek donatılı ve çift donatılı T en-kesitli kirişler tasarlanmıştır. Betonarme T en-kesitli kirişlerde çekme donatısı oranı ( $\rho = \rho_{max}$ ) sabit alınmış ve basınç donatı oranı ise  $\rho_s' = 0.0, 0.1\rho, 0.2\rho, \dots$  ve  $\rho$  olacak şekilde değiştirilmiştir. Beton basınç dayanımının kiriş davranışı üzerinde etkisini araştırmak için 5 farklı beton sınıfı (C30, C35, C40, C45 ve C50) dikkate alınarak tasarım yapılmıştır. Betonarme T en-kesitli kirişlerde statik denge kuvvetleri ayrı ayrı Denklem (2) ile hesaplanmıştır.

$$F_c = 0.85\beta_1 c f_c' b, \quad F_s = A_{s1} f_y, \quad F_s' = A_{s2} f_{s2} = A_{s2} 600 \left( \frac{c - d'}{c} \right) \quad (2)$$

Denklem (2)’de;  $\beta_1$ ; eşdeğer dikdörtgen beton gerilme dağılımı katsayısını,  $c$ ; tarafsız eksen derinliğini,  $f_c'$ ; betonun karakteristik basınç dayanımını,  $b$ ; etkili tabla genişliğini,  $A_{s1}$ ; kirişin çekme

donatısı alanını,  $A_{s2}$ ; basınç donatısı alanını,  $f_y$  donatının karakteristik akma dayanımını,  $f_{s2}$ ; basınç donatısındaki gerilmeyi ve  $d'$ ; beton basınç yüzünden basınç donatısı ağırlık merkezine olan mesafeseyi göstermektedir. Kuvvet bileşkelerinden denge denklemi Denklem (3)'te verilmiştir. Eşdeğer dikdörtgen beton gerilme dağılımı katsayısı Denklem (4) ile hesaplanmıştır.

$$\Sigma F = 0, \quad F_c + F'_s - F_s = 0 \quad (3)$$

$$\begin{cases} 17MPa \leq f'_c \leq 28MPa & \beta_1 = 0.85 \\ 28MPa < f'_c < 55MPa & \beta_1 = 0.85 - \frac{0.05(f'_c - 28)}{7} \\ f'_c \geq 55MPa & \beta_1 = 0.65 \end{cases} \quad (4)$$

Denklem (3)'te sırasıyla  $F_c$ ,  $F'_s$  ve  $F_s$  basınç bölgesindeki betona uygulanan bileşke kuvveti, basınç ve çekme donatılara uygulanan bileşke kuvvetleri temsil etmektedir. Denklem (2)'de verilen  $F_c$ ,  $F'_s$  ve  $F_s$ 'nin değerlerini Denklem (3)'e yerleştirerek Denklem (5) elde edilmiştir.

$$\begin{cases} (0.85\beta_1 f'_c b) \cdot c + (600A_{s2} - A_{s1} f_y) \cdot c + (-600A_{s2} d') = 0 \\ A \cdot c^2 + Bc + D = 0 \end{cases} \quad (5)$$

Denklem (5)'te verilen A, B ve D ikinci derece denklemin sabit katsayılarıdır. Denklem (5)'ten basınç bloğunun derinliği (c) elde edilmiştir. Basınç bloğun derinliği (c), ve eşdeğer basınç bloğun değerleri (a) Denklem (6) ile hesaplanmıştır.

$$c_{1,2} = \frac{-B \pm \sqrt{B^2 - 4AD}}{2A}, \quad a = \beta_1 c \quad (6)$$

Eğer eşdeğer basınç bloğunun derinliği (a) tabla kalınlığından küçük ise, dikdörtgen en-kesitli kirişlerin taşıma gücü mometi Denklem (7) ile hesaplanmaktadır.

$$M_n = A_{s2} f_{s2} (d - d') + 0.85 f'_c b a \left( d - \frac{a}{2} \right), \quad M_r = \phi M_n \quad (7)$$

Eğer eşdeğer basınç bloğun derinliği (a) tabla kalınlığından büyük ise T en-kesitli betonarme kirişlerin taşıma gücü momenti denklem (10) ile hesaplanmaktadır. Akma birim uzaması ve basınç donatısının birim kısalması Denklem (8) ile hesaplanmıştır.

$$\varepsilon_{sy} = \frac{f_y}{E_s}, \quad \varepsilon'_s = 0.003 \left( \frac{c - d'}{c} \right) \quad (8)$$

Eğer  $\varepsilon'_s \geq \varepsilon_{sy}$ ; T en-en kesitli betonarme kirişlerde basınç donatısı akma konumuna ulaşmıştır. Betonarme T en-kesitli kirişlerin ağırlık merkezinin en dış beton basınç lifine olan mesafesi ( $\bar{x}$ ) Denklem (9) ile hesaplanmıştır.

$$\bar{x} = \frac{0.5b_w a^2 + 0.5(b - b_w) t^2}{b_w a + (b - b_w) t} \quad (9)$$

T en-kesitli betonarme kirişlerin moment taşıma kapasitesi Denklem (10) ile hesaplanmıştır.

$$M_n = (A_{s1} f_y - A_{s2} f_{s2}) (d - \bar{x}) + A_{s2} f_{s2} (d - d'), \quad M_r = \phi M_n \quad (10)$$

Denklem (10)'da  $M_n$  nominal taşıma kapasite momenti ve  $\phi$  dayanım azaltma katsayısıdır. Azaltma katsayısı  $\phi$  Denklem (11) ile hesaplanmıştır.

$$\left\{ \begin{array}{ll} \varepsilon_s \leq \varepsilon_{sy} & \phi = 0.65 \\ \varepsilon_{sy} < \varepsilon_s < 0.005 & \phi = 0.65 + 0.25 \frac{0.05(\varepsilon_s - \varepsilon_{sy})}{(0.005 - \varepsilon_{sy})} \\ \varepsilon_s \geq 0.005 & \phi = 0.9 \end{array} \right. \quad (11)$$

### b- Moment Taşıma Kapasitesinin TS500'göre Hesaplanması

Kirişler betonarme taşıyıcı sistemlerde düşey yüklerin karşılanmasında döşemelere mesnetlik yaparak, gelen yükleri kolonlara aktarmaktadır. Kirişler ve döşemeler genellikle tek döküm özelliğine sahiptir. Bu durumda kirişler T kesit (tablalı kesit) olarak adlandırılır. T en-kesitli kirişler tek ve çift donatılı kirişler olarak tasarlanmaktadır. Şekil 1'de T en-kesitli betonarme kiriş kesit boyutları ve donatı yerleşim planı gösterilmiştir. T en-kesitli kirişler tarafsız eksenine bağlı olarak iki farklı yöntem ile hesaplanmaktadır. Eğer tarafsız eksen tablanın içinde kalırsa kiriş dikdörtgen kiriş gibi tasarlanmaktadır. Eğer tarafsız eksen tablanın altında kalırsa kiriş T en-kesitli kiriş olarak tasarlanmalıdır. Bu çalışmada T en-kesitli kirişler çift donatılı olarak tasarlanmıştır. Kirişlerde çekme donatı olarak maksimum donatı oranı ( $\rho = \rho_{max} = 0.85\bar{\rho}_b$ ) ve basınç donatısı oranı  $\rho'_s = 0.0, 0.1\rho, 0.2\rho, 0.3\rho, 0.4\rho, 0.5\rho, 0.6\rho, 0.7\rho, 0.8\rho, 0.9\rho$  ve  $\rho$  olacak şekilde ele alınmıştır. Beton basınç dayanımının kiriş davranışı üzerinde etkisini araştırmak için farklı beton basınç dayanımları (C30, C35, C40, C45, C50) dikkate alınmıştır. T en-kesitli kirişlerin statik denge kuvvetleri Denklem (12) ile hesaplanmıştır.

$$F_c = 0.85k_1Cf_{cd}b, \quad F_s = A_s f_{yd}, \quad F'_s = A'_s f'_s = A'_s 600 \left( \frac{c - d'}{c} \right) \quad (12)$$

Denklem (12)'de;  $k_1, c, f_{cd}, b, A_s, A'_s, f_{yd}, f'_s$  ve  $d'$  sırasıyla eşdeğer dikdörtgen basınç bloğu derinlik katsayısını, tarafsız eksen derinliğini, betonun tasarım basınç dayanımını, etkili tabla genişliğini, çekme donatısı alanını, basınç donatısı alanını, donatının tasarım akma dayanımını, basınç donatısındaki gerilmeyi ve beton basınç yüzünden basınç donatısı ağırlık merkezine olan mesafeyi göstermektedir. Statik denge kuvvetleri Denklem (13)'te verilmiştir.

$$\sum F = 0, \quad F_c + F'_s - F_s = 0 \quad (13)$$

Denklem (13)'te  $F_c, F'_s$  ve  $F_s$  sırasıyla, basınç bölgesindeki betona uygulanan bileşke kuvveti, basınç ve çekme donatılara uygulanan bileşke kuvvetlerdir. Denklem (12)'de verilen bileşke kuvvetlerin değerleri Denklem (13)'e yerleştirilerek ikinci derece bir denklem elde edilmiştir. Elde edilen ikinci derece denklem Denklem (14)'te verilmiştir.

$$\left\{ \begin{array}{l} (0.85k_1f_{cd}b).C + (600A'_s - A_s f_{yd}).C + (-600A'_s d') = 0 \\ A.C^2 + BC + D = 0 \end{array} \right. \quad (14)$$

Denklem (14)'te A, B ve D ikinci derece denklemin katsayılarıdır. Denklem (14) ile basınç bloğunun derinliğini hesaplanmıştır. Basınç bloğun derinliği (c), ve eşdeğer basınç bloğun derinliği (a) Denklem (15) ile hesaplanmaktadır.

$$c_{1,2} = \frac{-B \pm \sqrt{B^2 - 4AD}}{2A}, \quad a = k_1 c \quad (15)$$

Eğer eşdeğer basınç bloğun derinliği (a) tabla kalınlığından küçük ise, taşıma gücü momenti ( $M_r$ ) dikdörtgen kesitlerdeki gibi Denklem (16) ile hesaplanmaktadır.

$$M_r = A'_s f'_s (d - d') + 0.85f_{cd}ba \left( d - \frac{a}{2} \right) \quad (16)$$

Eğer eşdeğer basınç bloğunun derinliği ( $a$ ) tabla kalınlığından büyük ise, taşıma gücü momenti ( $M_r$ ) T en-kesitli kirişler gibi denklem (19) ile hesaplanmaktadır. Akma birim uzama ve basınç donatısının birim kısalması Denklem (17) ile hesaplanmıştır.

$$\varepsilon_{sy} = \frac{f_{yd}}{E_s} , \quad \varepsilon'_s = 0.003 \left( \frac{c - d'}{c} \right) \quad (17)$$

Eğer  $\varepsilon'_s \geq \varepsilon_{sy}$  olursa, T en-kesitli betonarme kirişlerde basınç donatısı akmıştır. Eşdeğer basınç bloğunun ağırlık merkezinin en dış basınç lifine olan mesafesi Denklem (18) ile hesaplanmıştır.

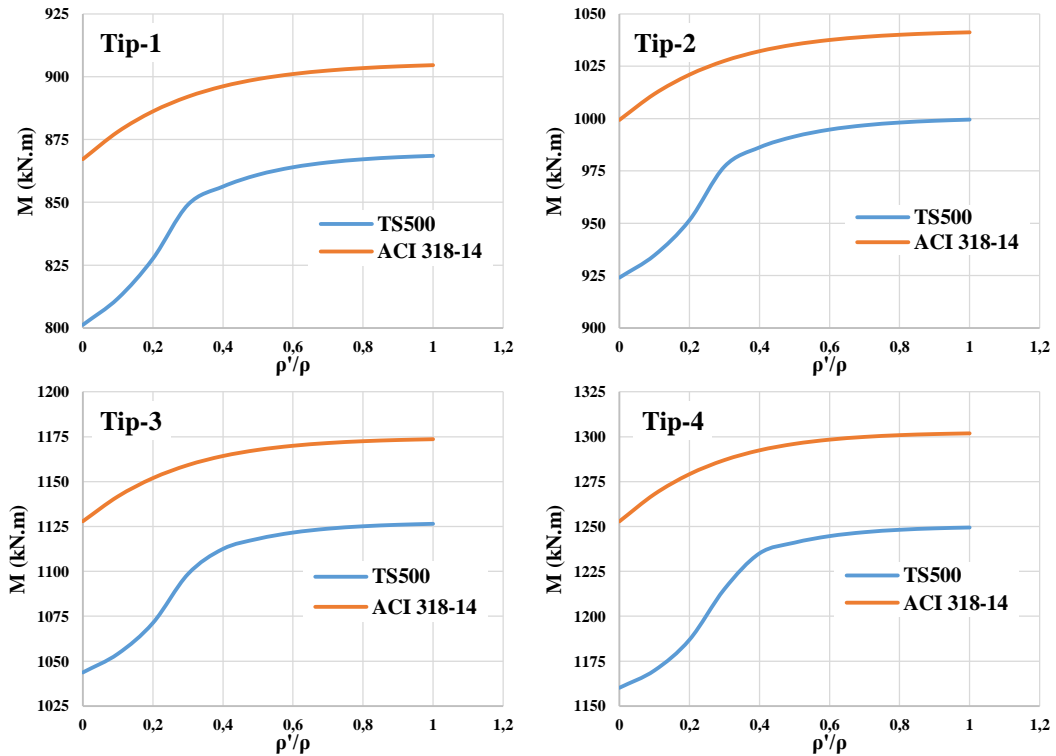
$$\bar{x} = \frac{0.5b_w a^2 + 0.5(b - b_w)t^2}{b_w a + (b - b_w)t} \quad (18)$$

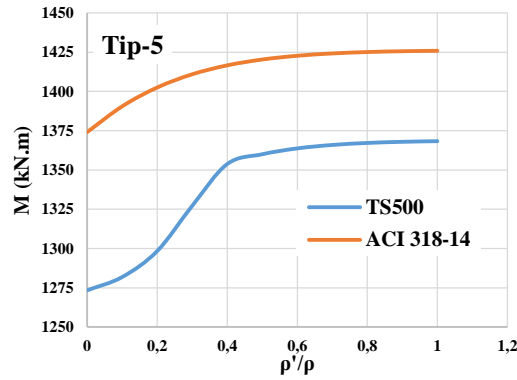
T en-kesitli kirişlerin moment taşıma kapasitesi Denklem (19) ile hesaplanmıştır.

$$M_r = (A_s f_{yd} - A'_s f'_s)(d - \bar{x}) + A'_s f'_s(d - d') \quad (19)$$

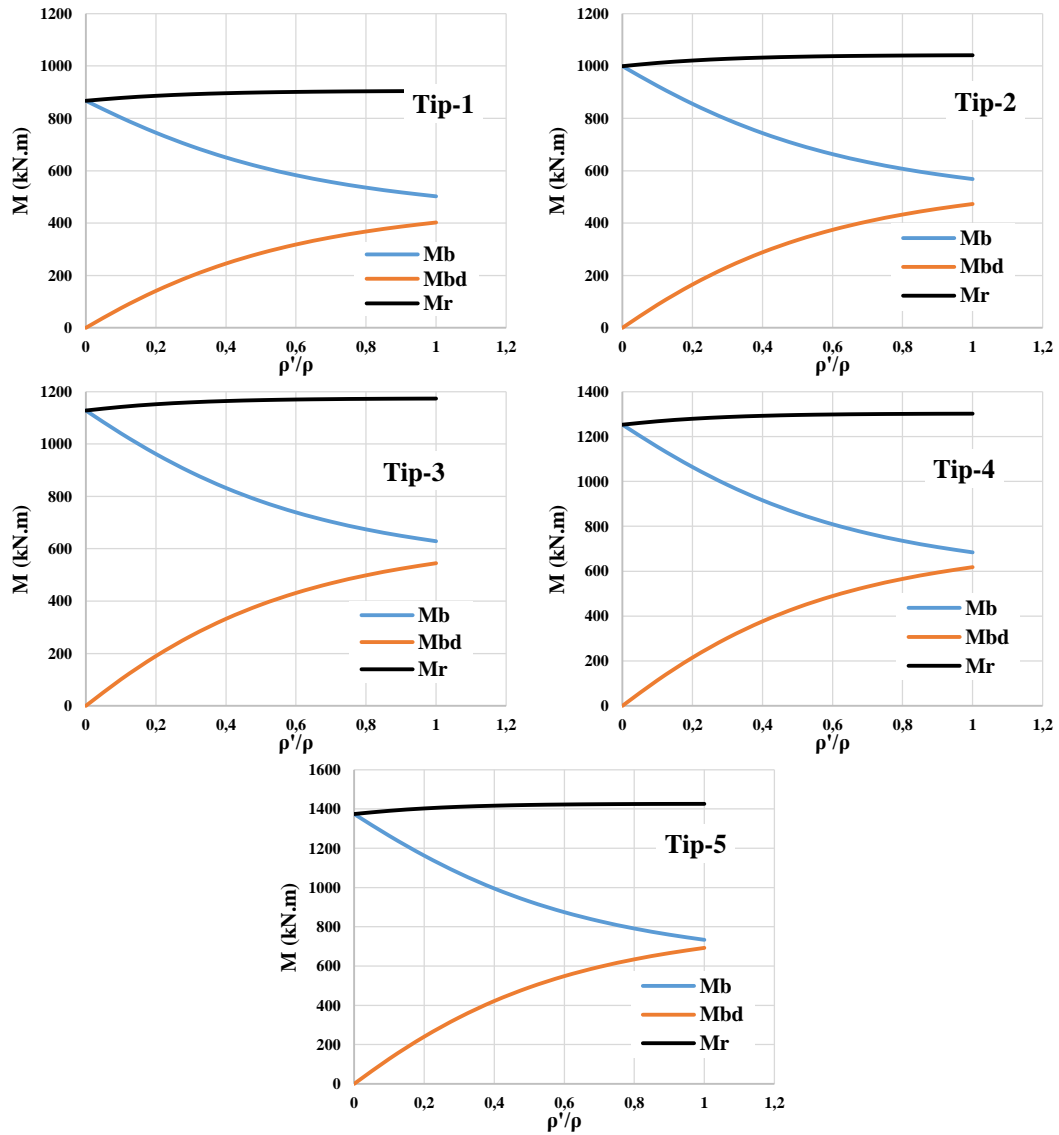
### Analitik Çalışma

Betonarme T en-kesitli kiriş elemanlarının moment taşıma kapasiteleri ACI318-14 ve TS500-2000 yönetmeliklere göre hesaplanmıştır. Tasarlanmış T en-kesitli betonarme kirişlerde, beton basınç dayanımı ve basınç donatısı oranının değişiminin moment taşıma kapasitesine etkisi araştırılarak iki farklı yönetmeliğe göre elde edilen moment taşıma kapasiteleri karşılaştırılmıştır. Analitik çalışmanın kapsamında toplam 55 adet farklı parametrelere sahip T en-kesitli betonarme kirişlerin analizi yapılmıştır. Elde edilen sonuçlar karşılaştırmalı olarak çizelgeler halinde özetlenmiştir. İki farklı yönetmeliğe göre elde edilen moment taşıma kapasitelerinin grafikleri Şekil 2’de verilmiştir. ACI 318-14 ve TS500 2000’e göre hesaplanan taşıma gücü momentleri ve  $\rho'/\rho$  oranının karşılaştırmalı grafikleri Şekil 2’de verilmiştir. ACI 318-14’e göre hesaplanan T en-kesitli kirişlerin taşıma gücü momenti, beton ve basınç donatısı tarafından karşılanan momentlerin grafikleri Şekil 3’te karşılaştırmalı olarak verilmiştir. TS500-2000’e göre hesaplanan T en-kesitli kirişlerin taşıma gücü momenti, beton ve basınç donatısı tarafından karşılanan momentleri Şekil 4’te karşılaştırmalı olarak verilmiştir.



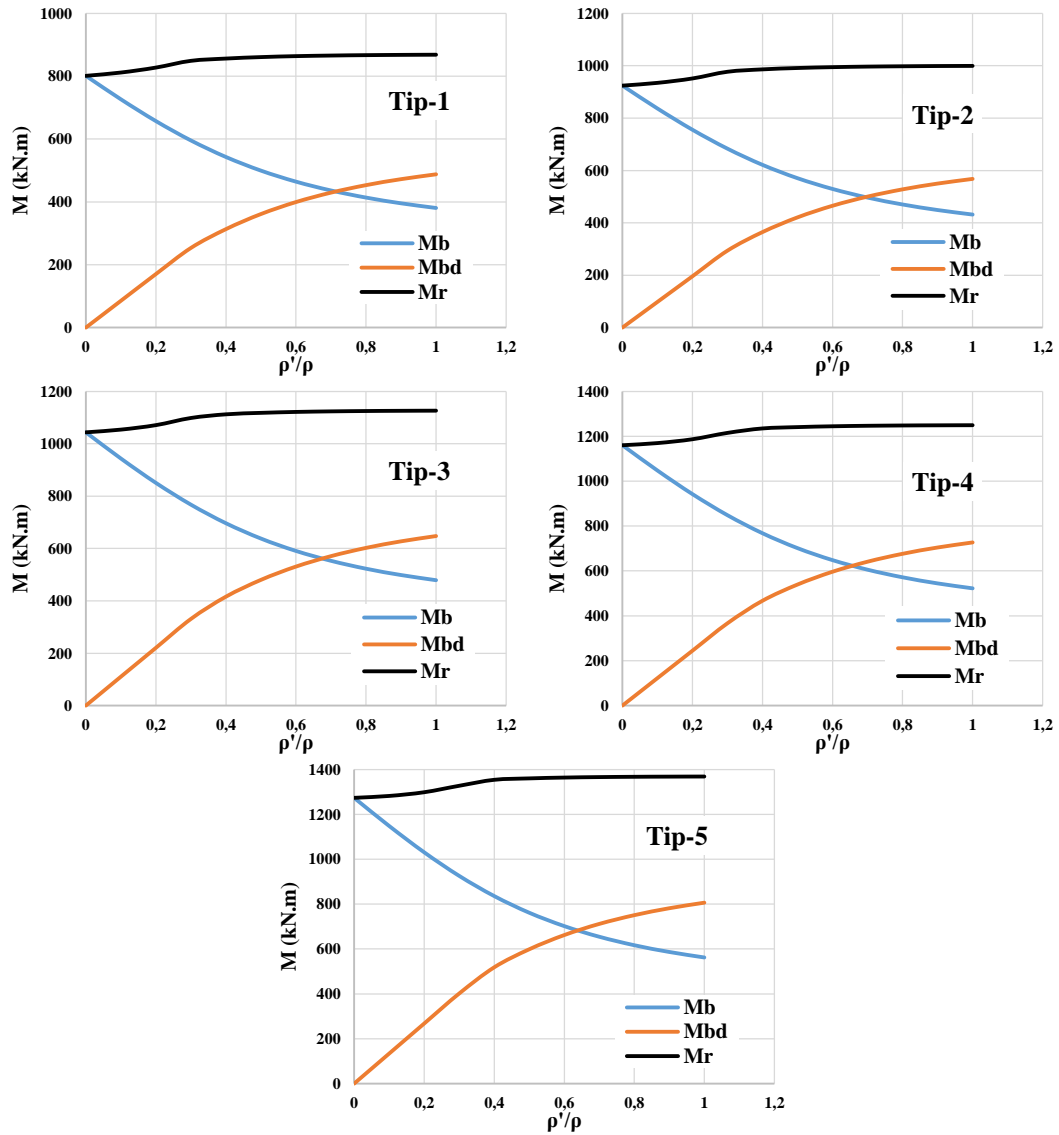


Şekil 2. ACI 318-14 ve TS500 yönetmeliğe göre hesaplanan Moment taşıma kapasitesi-basınç donatı oranı/çekme donatı oranının grafikleri



Şekil 3. ACI 318-14'e göre hesaplanan beton ve basınç donatısı tarafından karşılanan taşıma gücü momenti-basınç/çekme donatısı oranının grafikleri





Şekil 4. TS500'e göre hesaplanan beton ve basınç donatısı tarafından karşılayan taşıma gücü momenti-basınç/çekme donatısı oranının grafikleri

### Araştırma Bulgular ve Tartışma

Tasarlanan T en-kesitli betonarme kiriş kesitlerinin farklı parametrelere göre analiz ve hesap sonuçlarından elde edilen değerler karşılaştırmalı olarak Tablo 3, 4 ve 5'te verilmiştir. Betonarme kirişler için ACI 318-14 ve TS500-2000'e verilen beton basınç dayanımı, donatı akma dayanımı ve betonarmede kullanılan katsayılar Tablo 4'te verilmiştir. Farklı parametrelere göre elde edilen kapasite momenti değerleri karşılaştırılmalı olarak verilmiştir (Tablo 5 ve 6). ACI318-14 ve TS500-2000 ile hesaplanan taşıma gücü momentlerinin değerleri Tablo 5 ve 6'da verilmiştir. Her iki yönetmeliğine göre hesaplanan taşıma gücü momenti karşılaştırma grafiği Şekil 5'te verilmiştir.

Tablo 4. Beton basınç dayanımı, donatı akma dayanımı ve kullanılan katsayılar (AC318-14 ve TS500)

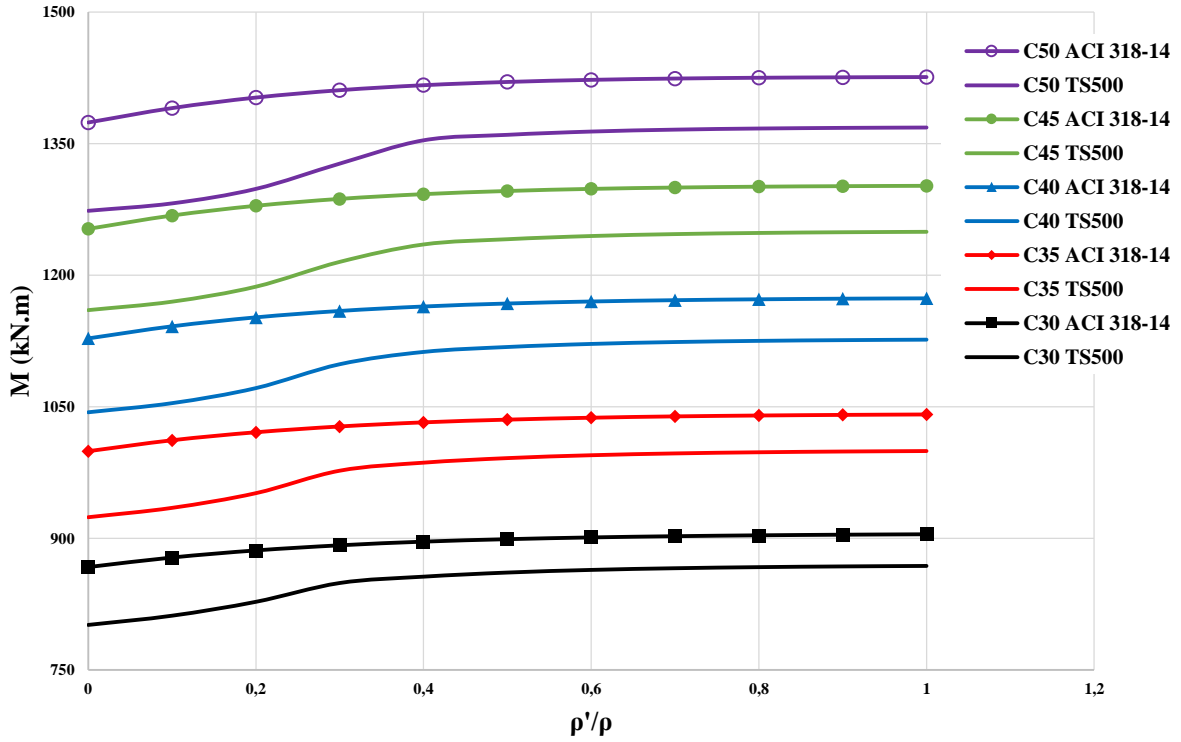
TS500-2000					ACI318-14			
$f_{ck}$ (MPa)	$f_{cd}$ (MPa)	$f_{yk}$ (MPa)	$f_{yd}$ (MPa)	$k_1$	$f_{ck} = f_{cd}$ (MPa)	$f_{yk} = f_{yd}$ (MPa)	$\beta_1$	$\phi$
25	16.7	420	365	0.85	25	420	0.85	0.9
30	20.0	420	365	0.82	30	420	0.84	0.9
35	23.3	420	365	0.79	35	420	0.80	0.9
40	26.7	420	365	0.76	40	420	0.76	0.9
45	30.0	420	365	0.73	45	420	0.73	0.9
50	33.3	420	365	0.70	50	420	0.69	0.9

Tablo 5. Beton basınç dayanımı ve kullanılan katsayıları ile AC318-14'e göre hesaplanan taşıma kapasite momentleri

Elemanın Adı	Nominal momentin değerleri (ACI 318-14)				
	C30	C35	C40	C45	C50
	$\phi M_n$ (kN.m)	$\phi M_n$ (kN.m)	$\phi M_n$ (kN.m)	$\phi M_n$ (kN.m)	$\phi M_n$ (kN.m)
B-0	867.2	999.3	1127.9	1252.8	1374.1
B-1	878.1	1011.8	1141.7	1268.0	1390.5
B-2	886.2	1020.9	1151.9	1279.1	1402.5
B-3	892.0	1027.5	1159.2	1287.0	1410.9
B-4	896.2	1032.2	1164.3	1292.4	1416.6
B-5	899.0	1035.3	1167.7	1296.0	1420.3
B-6	901.0	1037.5	1170.0	1298.4	1422.7
B-7	902.4	1039.0	1171.5	1299.9	1424.2
B-8	903.4	1040.0	1172.5	1300.9	1425.1
B-9	904.1	1040.7	1173.2	1301.5	1425.6
B-10	904.6	1041.2	1173.6	1301.9	1425.9

Tablo 6. Beton basınç dayanımı ve kullanılan katsayıları ile TS500'e göre hesaplanan taşıma kapasite momentleri

Elemanın Adı	Taşıma gücü momentin değerleri (TS500-2000)				
	C30	C35	C40	C45	C50
	$M_r$ (kN.m)	$M_r$ (kN.m)	$M_r$ (kN.m)	$M_r$ (kN.m)	$M_r$ (kN.m)
B-0	801.25	924.05	1043.70	1160.16	1273.40
B-1	811.76	934.72	1054.08	1169.80	1281.85
B-2	827.58	951.47	1071.25	1186.90	1298.38
B-3	849.04	977.09	1098.47	1215.19	1327.19
B-4	856.27	986.24	1112.50	1235.03	1353.79
B-5	860.96	991.43	1118.12	1240.99	1360.02
B-6	863.96	994.71	1121.61	1244.64	1363.75
B-7	865.88	996.78	1123.77	1246.84	1365.94
B-8	867.13	998.09	1125.11	1248.16	1367.21
B-9	867.95	998.94	1125.95	1248.96	1367.94
B-10	868.50	999.49	1126.48	1249.44	1368.35



Şekil 5. ACI 318-14 ve TS500'e göre hesaplanan taşıma gücü momentlerinin karşılaştırması

### Sonuçlar

Araştırma bulgular ve Tartışma bölümünde özetlenen sonuçların ışığında aşağıdaki sonuçlar elde edilmiştir.

- Betonarme kirişlerde sabit beton basınç dayanımı ve çekme donatısı oranı için basınç donatısı oranının artması ile ACI 318-14'e göre hesaplanan nominal momenti artmaktadır.
- Betonarme kirişlerde sabit beton basınç dayanımı ve çekme donatısı oranı için basınç donatısı oranının artması ile TS500'e göre hesaplanan taşıma gücü momenti artmaktadır.
- Sabit basınç donatısı ve çekme donatısı oranına sahip betonarme kirişlerde beton basınç dayanımının artması ile ACI 318-14'e göre hesaplanan nominal momenti artırmaktadır.
- Sabit basınç donatısı ve çekme donatısı oranına sahip betonarme kirişlerde beton basınç dayanımının artması ile TS500'e göre hesaplanan taşıma gücü momenti artmaktadır.
- Hesaplarda, beton basınç dayanımı ACI 318-14'te beton karakteristik basınç dayanımı ( $f'_c = f_{ck}$ ) ve TS500'e göre beton hesap basınç dayanımı ( $f_{cd}$ ) olarak alınmaktadır.
- Hesaplarda donatı çeliği akma dayanımı, ACI 318-14'e göre karakteristik akma dayanımı ( $f_y = f_{yk}$ ) ve TS500'e göre hesap akma dayanımı ( $f_{yd}$ ) olarak alınmıştır.
- ACI 318-14'te  $\beta_1$  eşdeğer dikdörtgen beton gerilme dağılımı katsayısı farklı beton basınç dayanımına göre 0.85, 0.84, 0.80, 0.76, 0.73 ve 0.69 hesaplanarak alınmıştır.
- TS500'de  $k_1$  eşdeğer dikdörtgen beton gerilme dağılımı katsayısı farklı beton basınç dayanımına göre 0.85, 0.82, 0.79, 0.76, 0.73 ve 0.70 olarak hesaplanarak ele alınmıştır.
- ACI 318-14'te  $\phi$  dayanım azaltma katsayısı hesaplarda kullanılmaktadır.
- TS500-2000'de  $\phi$  dayanım azaltma katsayısı olmadığı için hesaplarda beton ve donatı için malzeme katsayısı sırasıyla  $\gamma_{mc} = 1.5$ ,  $\gamma_{ms} = 1.15$  olarak alınmıştır.
- TS500-2000 yönetmeliğine göre hesaplanan taşıma gücü momentlerinin değerleri  $M_r$ , ACI 318-14'e göre hesaplanan  $\phi M_n$  azaltma katsayısı ile çapılmış nominal momentlerinden daha düşük elde edilmiştir.

T en-kesitli kirişlerde ACI 318-14'e hesaplanmış moment taşıma kapasitelerinin ( $\phi M_n$ ) TS500 2000'e göre hesaplanmış moment taşıma kapasitelerinden ( $M_r$ ) %4 ila %8 kadar daha fazla elde edilmiştir. T en kesitli kirişlerde basınç donatısı oranının azalması ile iki yönetmelik arasında elde edilen

fark artmaktadır. Basınç donatısı olmaması durumunda fark %8'e ulaşmaktadır. Beton basınç dayanımının artması ile moment kapasiteleri arasındaki fark artmaktadır.

#### Referanslar

- [1] Doğangün, Adem, 2016, Betonarme yapıların hesap ve tasarımı, ISBN: 978-975-511-310-X, Birsen Yayınevi, İstanbul.
- [2] TBDY, 2018, Türkiye Bina Deprem Yönetmeliği, T.C. Bayındırlık ve İskân Bakanlığı, Ankara.
- [3] ACI 318M-14, 2014. Building Code Requirements for Structural Concrete and Commentary, ISBN: 978-1-942727-11-8, American Concrete Institute, USA.
- [4] TS500, 2000, Betonarme Yapıların Tasarım ve Yapım Kuralları, Türk Standardları Enstitüsü, TSE, Ankara.
- [5] Canbay, E., Ersoy, U., Özcebe, G., Sucuoğlu, H., Wasti, S. T., 2010. Binalar İçin Deprem Mühendisliği Temel İlkeler, ISBN: 9799789944070, ODTÜ, Akademik Kitaplar Yayınevi, Ankara.
- [6] Çağlar, N, Akkaya, A., Demir, A., Öztürk, H., 2004. Farklı Kesit Geometrilerine Sahip Betonarme Kolonların Davranışının İncelenmesi, ISITES2014, p. 2095-2105, Karabük/Türkiye.
- [7] Doğangün, Adem, 2018, Betonarme yapıların hesap ve tasarımı, ISBN: 978-975-511-310-X, Birsen Yayınevi, İstanbul.
- [8] Ersoy, U. ve Özcebe, G., 2017, Betonarme 1, ISBN: 978-975-503-233-7, Evrim Yayınevi ve Bilgisayar San. Tic. Ltd. Şti, İstanbul.
- [9] Ersoy, U. ve Özcebe, G, Tankut. T, 2003, Reinforced concrete, Middle East Technical University, Ankara.

## TBDY-2018 ve ASCE 41-17'de Betonarme Kirişlerin Lineer Olmayan Analizleri için Modelleme Parametrelerinin Karşılaştırılması

Rohullah Jamal\*, Konya Teknik Üniversitesi, Mühendislik ve Doğa Bilimleri Fakültesi, İnşaat Mühendisliği Bölümü, Konya, Türkiye

Süleyman Bahadır Yüksel, Konya Teknik Üniversitesi, Mühendislik ve Doğa Bilimleri Fakültesi, İnşaat Mühendisliği Bölümü, Konya, Türkiye

\*İletişimden sorumlu yazar: jamal.rohullah@gmail.com

**Anahtar kelimeler:** Betonarme kirişler, kesit hasar sınırı, deprem güvenliği, moment eğrilik ilişkisi, şekil değiştirme  
**Disiplin:** İnşaat Mühendisliği

### Özet

Mevcut veya yeni yapılacak betonarme bir yapının deprem güvenliğinin belirlenmesi için öncelikle her bir taşıyıcı elemanın kesit hasar seviyesinin belirlenmesi gerekmektedir. Yapılan doğrusal olmayan analiz sonucu kesitlerde oluşan şekil değiştirme ve plastik mafsal dönme değerlerinin, yönetmeliklerdeki kesit hasar seviyesine tekabül eden şekil değiştirme ve dönme açılarının sınır değerleriyle kıyaslanması ile kesitin hasar seviyesi elde edilir. ASCE 41-17 ve Türkiye Bina Deprem Yönetmeliği (TBDY, 2018) kesit hasar sınırları açısından kıyaslanmıştır. Bunun için 33 adet dikdörtgen en-kesitli betonarme kirişler tasarlanmıştır. Dikdörtgen en-kesitli kirişlerin kesit genişliği 250mm ve kesit yüksekliği 500mm olacak şekilde boyutları sabit tutulmuştur. Dikdörtgen kesitli kirişlerde beton sınıfı olarak C30, C40 ve C50 boyuna ve enine donatı olarak B420C donatı çeliği kullanılmıştır. Dikdörtgen en-kesitli betonarme kirişlerde boyuna çekme donatısı oranı  $\rho = \rho_{max}$  olacak şekilde sabit tutulmuş ve basınç donatı oranları  $\rho' = 0 \times \rho, 0.1 \times \rho, 0.2 \times \rho, \dots 1.0 \times \rho$  olacak şekilde değiştirilerek analizler yapılmıştır. Betonarme elemanların doğrusal olmayan davranışlarını dikkate alabilmek için SAP2000 (Ver.20.2.0) programında moment-eğrilik analizleri gerçekleştirilmiştir. SAP2000 programında tanımlanan beton ve donatı çeliği için hesaplarda ve malzeme modellerinde kullanılan parametreler iki farklı yönetmeliğe göre uygun olarak ele alınmıştır. Tasarlanan dikdörtgen kesitli betonarme kirişlerin elde edilen şekil değiştirme değerlerine bağlı olarak kesit hasar seviyeleri belirlenmiştir. Elde edilen sonuçlar grafik ve tablolar halinde sunulmuş aradaki farklar değerlendirilerek yorumlanmıştır. Her iki yönetmeliğe göre belirlenen sonuçlar birbiri ile kıyaslanarak arasındaki farklar belirlenmiştir. ASCE 41-17 ve TBDY (2018) yönetmeliklerine göre dikdörtgen en-kesitli betonarme kiriş kesitleri için hesaplanan hasar sınırlarında önemli farklılıklar olduğu gözlemlenmiştir.

### Giriş

Yapı sistemlerinin doğrusal olmayan davranışlarının dikkate alındığı hesap yöntemleri, son yıllarda yaygın bir biçimde kullanılmaktadır. Amerika Birleşik Devletleri'nde ASCE tarafından hazırlanan ASCE 41-06 yönetmeliği 2006'da, sonra ASCE 41-013 yönetmeliği 2013'te ve en son günümüzde ASCE 41-17 yönetmeliği 2017'de yer almıştır. Ülkemizde Deprem Bölgelerinde Yapılacak Binalar Hakkında Yönetmelik (DBYBHY, 2007) ve bu yönetmeliğin geliştirilmesiyle Türkiye Bina Deprem Yönetmeliği (TBDY, 2018) yayınlanmıştır. Bu çalışmada dikdörtgen en-kesitli kirişlerin doğrusal olmayan performans hasar sınırları TBDY 2018 ve ASCE 41-17'ye göre hesaplanarak karşılaştırma yapılmıştır.

Performansa dayalı tasarım temelde üç parametreden oluşmaktadır. Bunlar kapasite, talep ve performanstır. Kapasite; binanın taşıyıcı sistemi, malzemesi, kesit geometrisi vb. unsurların bir bileşkesi olarak düşünülebilir. Binanın yatay yer değiştirebilme kapasitesi (süneklik) ve yatay yük taşıma kapasitesi (rijitlik) genel anlamda kapasite olarak tanımlanır. Talep; sismik hareketlerin yapıdan karşılama istediği yer değiştirme ve kesit tesirleri olarak tanımlanabilir. Performans ise yapının kapasitesinin sismik talepleri hangi oranda karşılayabileceği ile ilgilidir [1].

Performans esaslı deprem mühendisliği, yapıların depreme dayanıklı tasarımında konvansiyonel dayanım esaslı tasarıma göre çok daha şeffaf bir yöntem sunmaktadır. Performans esaslı deprem mühendisliğinde kullanılan doğrusal olmayan hesap yöntemleri gerek yapısal modelleme gerek doğrusal olmayan davranışa ait verilerin hazırlanması, gerekse sonuçların derlenmesi ve yorumu aşamalarında standart mühendislik pratiğine göre daha yüksek bir mühendislik bilgi düzeyi gerektirmektedir [2].

Yapı taşıyıcı sisteminin doğrusal sınır ötesindeki kapasitesinin de dikkate alındığı hesap yöntemleri son yıllarda yaygınlaşmıştır. Yapının dayanım ve yer değiştirme kapasitelerini ortaya çıkaran, göçme aşamasına kadar oluşacak hasarların adım adım izlenebildiği doğrusal olmayan hesap yöntemleri kullanılarak, yapı davranışı daha iyi anlaşılabilir. Yapısal ve yapısal olmayan elemanlar, yapı sisteminin dayanım ve şekil değiştirme kapasitelerine katkıda bulunmaktadır. Yapı performansı, amaçlanan deprem istemi etkisinde yapıda oluşması beklenen hasar durumu ile ilişkilidir. Sağlanan kapasite ile deprem istemine ait veriler yapının tasarım ve güçlendirmesine yönelik performans düzeyinin belirlenmesinde kullanılmaktadır [3].

Performans esaslı değerlendirme yönteminin en önemli aşamalarından birisi yapısal elemanların her birinin hasar düzeylerinin belirlenmesidir. Doğrusal olmayan değerlendirme yöntemi ile analiz edilen yapıdaki yapısal elemanların kesitlerinde oluşan şekil değiştirme değerinin, yürürlükte olan yönetmelikteki kesit hasar seviyesine tekabül eden şekil değiştirme üst sınır değerleri ile kıyaslanması ile kesitin hasar seviyesi elde edilir. Dolayısı ile yapıların deprem güvenliğini belirlemede kesit hasar sınır değerlerinin doğru bir şekilde elde edilmesi oldukça önem arz etmektedir. Eleman davranışı kesit davranışından ve kesitin moment eğrilik ilişkisinden izlenilebilir [4].

TBDY (2018)'de beton şekil değiştirme üst sınır değerleri kesitteki beton sınıfı ve sargılama durumu düşük olması durumunda düşük değerlerde çıkmakta, donatı çeliği şekil değiştirme üst sınır değerleri de sargılama durumundan bağımsız sabit değerler olduğundan düşük dayanımlı malzeme kesitin hasarını ve eğrilik değerini beton belirlemiş olmaktadır [5].

Bu çalışmada, TBDY (2018) [6] ve ASCE 41-17 [7] kesit hasar sınırları açısından kıyaslanmıştır. Bunun için 3 Tip toplam 33 adet dikdörtgen en-kesitli kiriş tasarlanmıştır. Yönetmeliklerin kıyaslamasında betonarme kirişlerde, üç farklı beton sınıfı (C30, C40 ve C50), boyuna ve enine donatı olarak B420C donatı çeliği kullanılmıştır. Dikdörtgen kesitli kirişlerde çekme donatısı oranı maksimum donatı oranına sahip olacak şekilde seçilmiş, enine donatı çapı 8mm ve aralığı 50mm olacak şekilde sabit tutulmuştur. Kirişlerde eksenel yük fazla etkili olmadığı için kirişlerde eksenel yük seviyesi sıfır alınmıştır. Betonarme dikdörtgen kesitli kirişlerde basınç donatısı oranı değiştirilerek toplam 33 adet kiriş, TBDY (2018) ve ASCE 41-17 deprem yönetmeliklerine göre kesit hasar seviyesine tekabül eden şekil değiştirme üst sınır değerleri elde edilmiştir. Elde edilen şekil değiştirme üst sınır değerlerine bağlı olarak kesit hasar seviyeleri tablolar ve grafikler halinde sunulmuştur. Her iki yönetmeliğe göre belirlenen sonuçlar birbiri ile kıyaslanmıştır.

### Materyal ve Metot

Bu çalışmada dikdörtgen en-kesitli betonarme kiriş elemanlarının deprem performansının belirlenmesi için TBDY, (2018)'de verilen kurallara göre farklı parametrelere ve sabit geometriye sahip 33 adet betonarme kiriş modeli tasarlanmıştır (Tablo 1). Şekil 1'de verilen dikdörtgen en-kesitli betonarme kirişlerin kesit genişliği ( $b = 250mm$ ), kesit yüksekliği ( $h = 500mm$ ) ve faydalı yüksekliği ( $d = 450mm$ ) sabit tutulmuştur. Betonarme kiriş elemanlarında sargı donatısı ( $\emptyset 8/50mm$ ) ve çekme donatı oranı ( $\rho = 0.85\rho_b = \rho_{max}$ ) sabit alınmıştır. Elemanlarda farklı parametre olarak; basınç donatısı oranı ( $\rho' = 0.1\rho, 0.2\rho, 0.3\rho, 0.4\rho, 0.5\rho, 0.6\rho, 0.7\rho, 0.8\rho, 0.9\rho, \rho$ ) ve beton basınç dayanımı (C30, C40 ve C50) dikkate alınmıştır. Betonarme dikdörtgen kesitli kirişlerin beton ve donatı çeliği birim şekil değiştirmeleri, plastik mafsal akma dönmeleri ve plastik dönmeleri hesaplanarak performans düzeyleri araştırılmıştır. Betonarme dikdörtgen kesitli kiriş kesit hesabı ve tasarımı yapılırken dikkat edilmesi gereken en önemli husus, elde edilen kesitteki donatı oranının, dengeli orandan küçük olmasını sağlamaktır. Bu koşul yönetmeliklerce zorunlu olduğu için bu çalışmada TS500 (2000)'de verilen sınır değerler dikkate alınmıştır. TS500 (2000)'de betonarme kirişlerde sünek davranışın sağlanabilmesi için, donatı oranı Denklem (1) ile sınırlandırılmıştır. Denklem (1)'de  $\rho$ ; çekme donatısı oranı,  $\rho'$ ; basınç donatısı oranı,  $f_{cd}$  betonun hesap basınç dayanımı,  $f_{yd}$  donatı çeliğinin hesap akma dayanımıdır.

$$\rho_b = 0.85k_1 \left( \frac{f_{cd}}{f_{yd}} \right) \left( \frac{600}{600 + f_{yd}} \right), \rho = \rho_{max} = 0.85\rho_b, \quad (1)$$

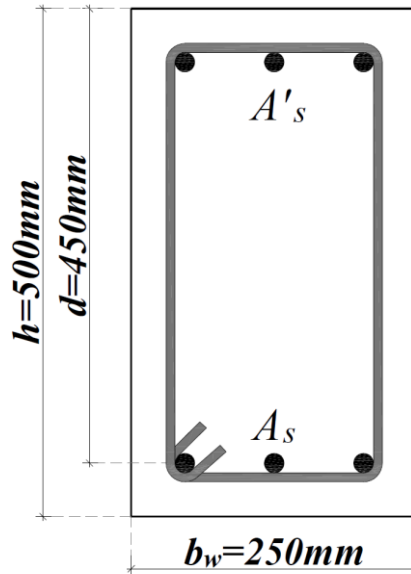
Betonarme kesitlerde süneklik, kesitin dayanımında önemli bir azalma olmadan yapabileceği doğrusal ötesi deformasyon kapasitesi olarak tanımlanır. Sayısal olarak ise süneklik, eğrilik süneklik

katsayısı ( $\mu$ ) Denklem (2) ile hesaplanmaktadır. Eğrilik süneklik katsayısı, kesitin kırılma anında yaptığı eğriliğin ( $k_u$ ), çekme donatısının aktığı anda kesitte oluşan eğriliğe ( $k_y$ ) oranıdır [8].

$$\mu = \frac{k_u}{k_y} \quad (2)$$

Tasarlanan dikdörtgen kesitli betonarme kiriş kesitlerinde gerçek malzeme davranışları esas alınarak farklı beton basınç dayanımı ve basınç donatı oranı için moment-eğrilik ilişkilerinden; akma eğriliği ( $k_y$ ), akma momenti ( $M_y$ ), göçme öncesi eğrilik (maksimum eğrilik  $k_u$ ) ve eğilme momenti kapasitesi ( $M_u$ ) değerleri SAP 2000 analizleri ile elde edilmiştir. Dikdörtgen kesitli betonarme kiriş modellerinin moment-eğrilik ilişkilerinden elde edilen sonuçlara göre kiriş kesitlerinin davranışları incelenmiştir. Tasarlanan betonarme kiriş modellerinde yapılan performans değerlendirmesinde TBDY 2018 ve ASCE 41-17'ye göre doğrusal olmayan performans hasar sınır değerleri hesaplanmıştır.

Yığılı plastik davranışına göre modellenen dikdörtgen kesitli betonarme kirişlerin moment-eğrilik ilişkilerinden elde edilen  $k_y$  ve  $k_u$  değerlerine göre plastik mafsal dönmeleri hesaplanmıştır. Malzeme modellerinde kullanılan parametreler ve farklı tip dikdörtgen en-kesitli betonarme kirişlerin çekme ve basınç donatı oranı ve alanları sırasıyla Tablo 1, 2, 3 ve 4'te özetlenmiştir. Kesitlerde kullanılan donatı oranları TS500, (2000) ve TBDY, (2018)'de verilen sınırlamalar dikkate alınarak belirlenmiştir. Beton sınıfı olarak C30, C40 ve C50 seçilmiştir. Tüm kesit modelleri için, donatı çeliği olarak B420C seçilmiştir.



Şekil 1. Tasarlanan kiriş modellerinin en-kesit detayları

Tablo 1. Malzeme modellerinde kullanılan parametreler [6]

Malzeme	Parametre	Değer
Beton Sınıfı: C30, 40 ve C50	Sargısız betonun maksimum gerilmeye ulaştığı birim şekil değiştirme değeri ( $\epsilon_{co}$ )	0.002
	Sargısız betonun nihai birim şekil değiştirmesi ( $\epsilon_{cu}$ )	0.0035
	Karakteristik beton basınç dayanımı ( $f_{ck}$ )	30, 40, 50MPa
	Donatı çeliğinin akma birim şekil değiştirmesi ( $\epsilon_{sy}$ )	0.0021
Donatı Çeliği: B420C	Donatı çeliğinin pekleşme birim şekil değiştirmesi ( $\epsilon_{sp}$ )	0.008
	Donatı çeliğinin kopma birim şekil değiştirmesi ( $\epsilon_{su}$ )	0.08
	Donatı çeliğinin karakteristik akma dayanımı ( $f_{yk}$ )	420MPa
	Donatı çeliğinin karakteristik kopma dayanımı ( $f_{su}$ )	550MPa

Tablo 2. Tip-1 olarak tasarlanan betonarme kiriş modellerine ait parametreler

Kesit Grubu	Kesit No	Sargı Donatısı	Beton sınıfı (MPa)	$A_s(mm^2)$	$A'_s(mm^2)$	$\rho_b$	$\rho$	$\rho'$	$\frac{\rho - \rho'}{\rho_b}$
Tip 1	B1-0				0			0.0000	0.85
	B1-1				227			0.0020	0.77
	B1-2				454			0.0040	0.68
	B1-3				681			0.0061	0.60
	B1-4				908			0.0081	0.51
	B1-5	Φ8/50mm	30	2269	1134	0.0237	0.0202	0.0101	0.43
	B1-6				1361			0.0121	0.34
	B1-7				1588			0.0141	0.26
	B1-8				1815			0.0161	0.17
	B1-9				2042			0.0182	0.09
	B1-10				2269			0.0202	0.00

Tablo 3. Tip-2 olarak tasarlanan betonarme kiriş modellerine ait parametreler

Kesit Grubu	Kesit No	Sargı Donatısı	Beton sınıfı (MPa)	$A_s(mm^2)$	$A'_s(mm^2)$	$\rho_b$	$\rho$	$\rho'$	$\frac{\rho - \rho'}{\rho_b}$
Tip 2	B2-0				0			0.0000	0.85
	B2-1				280			0.0025	0.77
	B2-2				561			0.0050	0.68
	B2-3				841			0.0075	0.60
	B2-4				1122			0.0100	0.51
	B2-5	Φ8/50mm	40	2804	1402	0.0293	0.0249	0.0125	0.43
	B2-6				1682			0.0150	0.34
	B2-7				1963			0.0174	0.26
	B2-8				2243			0.0199	0.17
	B2-9				2523			0.0224	0.09
	B2-10				2804			0.0249	0,00

Tablo 4. Tip-3 olarak tasarlanan betonarme kiriş modellerine ait parametreler

Kesit Grubu	Kesit No	Sargı Donatısı	Beton sınıfı (MPa)	$A_s(mm^2)$	$A'_s(mm^2)$	$\rho_b$	$\rho$	$\rho'$	$\frac{\rho - \rho'}{\rho_b}$
Tip 3	B3-0				0			0.0000	0.85
	B3-1				323			0.0029	0.77
	B3-2				646			0.0057	0.68
	B3-3				968			0.0086	0.60
	B3-4				1291			0.0115	0.51
	B3-5	Φ8/50mm	50	3228	1614	0.0338	0.0287	0.0143	0.43
	B3-6				1937			0.0172	0.34
	B3-7				2260			0.0201	0.26
	B3-8				2582			0.0230	0.17
	B3-9				2905			0.0258	0.09
	B3-10				3228			0.0287	0,00

Bu çalışmada kirişlerin doğrusal olmayan performans seviyeleri TBDY 2018 ve ASCE 41-17'e göre hesaplanarak karşılaştırılmıştır. Dikdörtgen en-kesitli kirişlerde farklı performans düzeyi için oluşan şekil değiştirme ve iç kuvvet sınır değerleri hesaplanarak tablolar ve grafikler halinde özetlenmiştir. Çalışmada iki farklı yönetmeliğe göre hesaplanan doğrusal olmayan performans seviyeleri (hasar sınırları) farklı başlıklar altında incelenmiştir.



### TBDY, 2018'e göre İzin Verilen Şekil Değiştirme Sınırları

TBDY 2018'e göre izin verilen üç farklı şekil değiştirme ve iç kuvvet sınırları belirlenmiştir. Performans değerlendirmesinde Göçmenin Önlenmesi (GÖ), Kontrollü Hasar (KH) ve Sınırlı Hasar (SH) Performans Düzeyleri tanımlanmıştır. Yüksek binalar ve yeni betonarme bina elemanlarında yayılı plastik davranış modeline göre hesaplanan beton ve donatı çeliği toplam birim şekil değiştirmeleri için izin verilen sınırlar aşağıda tanımlanmıştır. Göçmenin Önlenmesi Performans Düzeyi (GÖ), Kontrollü Hasar Performans Düzeyi (KH) ve Sınırlı Hasar Performans Düzeyi (SH) için beton birim kısalma değerleri ( $\varepsilon_c^{(GÖ)}$ ,  $\varepsilon_c^{(KH)}$  ve  $\varepsilon_c^{(SH)}$ ), donatı çeliği birim şekil değiştirme değerleri ( $\varepsilon_s^{(GÖ)}$ ,  $\varepsilon_s^{(KH)}$  ve  $\varepsilon_s^{(SH)}$ ) ve plastik dönme değerleri  $\theta_p^{(GÖ)}$ ,  $\theta_p^{(KH)}$  ve  $\theta_p^{(SH)}$ , dikdörtgen kesitli kirişler için Tablo 5'te verilen denklemler ile hesaplanmıştır.

Tablo 5. Betonarme elemanlar için izin verilen şekil değiştirme üst sınırları [6]

Betonarme Elemanları için İzin Verilen Şekil Değiştirme ve İç Kuvvet Sınırları		
Göçme Önlenmesi Performans Düzeyi (GÖ)		
$\varepsilon_c^{(GÖ)} = 0.0035 + 0.04\sqrt{\omega_{we}} \leq 0.018$		
$\varepsilon_s^{(GÖ)} = 0.40\varepsilon_{su}$		
$\theta_p^{(GÖ)} = \frac{2}{3} \left[ (k_u - k_y)L_p \left( 1 - 0.5 \frac{L_p}{L_s} \right) + 4.5k_u d_b \right]$		
Kontrollü Hasar Performans Düzeyi (KH)		
$\varepsilon_c^{(KH)} = 0.75\varepsilon_c^{(GÖ)}$	$\varepsilon_s^{(KH)} = 0.75\varepsilon_s^{(GÖ)}$	$\theta_p^{(KH)} = 0.75\theta_p^{(GÖ)}$
Sınırlı Hasar Performans Düzeyi (SH)		
$\varepsilon_c^{(SH)} = 0.0025$	$\varepsilon_s^{(SH)} = 0.0075$	$\theta_p^{(SH)} = 0$

Tablo 5'te verilen  $\varepsilon_c^{(GÖ)}$ ,  $\varepsilon_c^{(KH)}$  ve  $\varepsilon_c^{(SH)}$  sırasıyla göçmenin önlenmesi, kontrolü hasar ve sınırlı hasar performans düzeyi için izin verilen beton birim kısalmasıdır.  $\varepsilon_s^{(GÖ)}$ ,  $\varepsilon_s^{(KH)}$  ve  $\varepsilon_s^{(SH)}$  sırasıyla göçmenin önlenmesi, kontrolü hasar ve sınırlı hasar performans seviyeleri için izin verilen donatı birim şekil değiştirmesini gösterilmektedir.  $\theta_p^{(GÖ)}$ ,  $\theta_p^{(KH)}$  ve  $\theta_p^{(SH)}$  sırasıyla göçmenin önlenmesi, kontrolü hasar ve sınırlı hasar performans düzeyinde izin verilen dönme açılarıdır. Tablo 5'te verilmiş denklemlerde  $\omega_{we}$ ,  $\varepsilon_{su}$ ,  $k_u$ ,  $k_y$ ,  $L_p$ ,  $L_s$  ve  $d_b$  sırasıyla etkin sargı donatısının mekanik donatı oranını, donatının çekme dayanımına karşı gelen birim uzamayı, maksimum eğriliği, akma eğriliği, plastik mafsal uzunluğunu, kesme açıklığını ve boyuna donatı çapını göstermektedir.

Göçmenin önlenmesi performans düzeyinde izin verilen beton birim kısalması denklemindeki ilk terim (0.0035) sargısız betonun birim kısalmasına karşı gelmektedir.  $\omega_{we}$ ; etkin sargı donatısının mekanik donatı oranı Denklem (3) ile hesaplanmıştır.

$$\omega_{we} = \alpha_{se} \rho_{sh, \min} \frac{f_{ywe}}{f_{ce}} \quad (3)$$

Denklem (3)'te,  $\alpha_{se}$  sargı donatısı etkinlik katsayısını,  $\rho_{sh, \min}$  dikdörtgen kesitte iki yatay doğrultuda hacimsel enine donatı oranının küçük olanını,  $f_{ywe}$  enine donatının ortalama (beklenen) akma dayanımını göstermektedir. Sargı donatısı etkinlik katsayısı ( $\alpha_{se}$ ) ve kesitte hacimsel enine donatı oranı ( $\rho_{sh}$ ) Denklem (4) ile hesaplanmıştır.

$$\alpha_{se} = \left( 1 - \frac{\sum a_i^2}{6b_o h_o} \right) \left( 1 - \frac{s}{2b_o} \right) \left( 1 - \frac{s}{2h_o} \right), \quad \rho_{sh} = \frac{A_{sh}}{b_k s} \quad (4)$$

Denklem (4)'te  $A_{sh}$  ve  $\rho_{sh}$  gözönüne alınan doğrultuda enine donatının alanını ve hacimsel oranını,  $b_k$  dik doğrultudaki çekirdek boyutunu (en dıştaki enine donatı eksenleri arasındaki uzaklık),  $s$  enine donatı aralığını,  $b_o$  ve  $h_o$  sargı donatısı eksenlerinden ölçülen sargılı beton boyutlarını,  $a_i$  bir etriye kolu

veya çiroz tarafından mesnetlenen boyuna donatıların eksenleri arasındaki uzaklığını göstermektedir. Etkin kesit rijitlikleri kullanılarak yapılan hesapta Sınırlı Hasar Performans düzeyi için taşıyıcı sistemde plastik mafsal oluşumuna izin verilmemektedir.

Akma durumu için yer değiştirmiş plastik mafsal eksen dönmesi  $\theta_y$  Denklem (5) ile hesaplanmıştır. Kiriş ve kolonlarda  $\eta$  katsayısı,  $\eta = 1$ , perdelerde ise  $\eta = 0.5$  alınacaktır.  $f_{ce}$  ve  $f_{ye}$  ise betonun ortalama (beklenen) basınç dayanımı ile donatının ortalama akma dayanımını göstermektedir. TBDY (2018)'e göre  $f_{ce} = 1.3f_{ck}$  ve  $f_{ye} = 1.2f_{yk}$  verilmiştir.  $f_{ck}$  ve  $f_{yk}$  sırasıyla betonun karakteristik basınç dayanımı ve donatı çeliğin karakteristik akma dayanımıdır.

$$\theta_y = \frac{k_y L_s}{3} + 0.0015 \eta \left( 1 + 1.5 \frac{h}{L_s} \right) + \frac{k_y d_b f_{ye}}{8 \sqrt{f_{ce}}} \quad (5)$$

### ASCE 41-17'e göre İzin Verilen Şekil Değiştirme Sınırları

ASCE 41-17'e göre yapı ve yapı elemanlarının kontrolü amacıyla deformasyon kontrolü ve kuvvet kontrolü olmak üzere iki yöntem tanımlanmıştır. Eğilme etkisi altındaki elemanların (kirişler) deformasyon kontrolü için doğrusal ve doğrusal olmayan kriterler ASCE 41-17'de Tablo 10.7'de belirtilmiştir. Yapı elemanların bilişenleri ASCE 41-17'e göre düşük, orta ve yüksek süneklik olarak sınıflandırılmaktadır. Eksenel yük ve eğilme altında çalışan elemanların eğilme dayanımı ACI-318'e göre, beton ve çelik modellerini dikkate alan kesitlerin analizi ile hesaplanmaktadır. Eksenel yük altında olan ve olmayan elemanların deformasyon kapasitesi kayma, eğilme ve donatı deformasyonu dikkate alınarak hesaplanmaktadır. Elemanların dayanım ve deformasyon kapasiteleri hesaplanmaktadır. Eğilme deformasyon kapasiteleri mekanik temellerine göre hesaplanması durumunda kesme kapasitesinin neden olduğu deformasyon kapasitesindeki azaltmalar dikkate alınmalıdır.

Betonarme dikdörtgen kesitli kirişlerin hasar sınırları ve performans değerleri ASCE 41-17'ye göre hesaplanmıştır. Betonarme dikdörtgen kesitli kirişlerin hasar sınırları ve performans seviyeleri ASCE 41-17 Tablo 10-7'de açıklanan performans seviyelere göre hesaplanmaktadır. Betonarme dikdörtgen kesitli kirişlerin hasar sınırları ve performans seviyeleri hesaplamak için ASCE 41-17 Tablo 10-7 verilen değerler aşağıda Tablo 6'da özetlenmiştir. Betonarme kirişlerinin doğrusal olmayan modelleme prosedürü etkilenen parametreler  $(\rho - \rho')/\rho$  oranına, kesite etkiyen kesme kuvveti etkisine  $V/(b_w d \sqrt{f'_{ce}})$ , kesitin sargılanma ve kırılma durumuna bağlıdır. Betonarme dikdörtgen kesitli kirişlerin hasar sınırları ve performans seviyesinin hesaplanması için öncelikle  $(\rho - \rho')/\rho$  oranı ve  $V/b_w d \sqrt{f'_{ce}}$  değerlerinin hesaplanması gerekmektedir. ASCE 41-17'ye göre  $V$  tasarım kesme kuvvetinin lineer olmayan hesaplamalardan elde edilmesi gerekmektedir.  $V$  tasarım kesme kuvveti SAP 2000 analizinden denklem (6) ile elde edilmiştir.

$$V = \frac{2M_y}{L_n} \quad (6)$$

Denklem (6)'da  $M_y$  ve  $L_n$  sırasıyla akma momenti ve kirişin net açıklığıdır. Tablo 6'da verilen a, b, c hasar sınırları, IO, LS ve CP performans seviyesi değerleri doğrusal enterpolasyon yöntemi ile hesaplanmıştır. IO Hemen kullanım, LS Can güvenliği ve CP göçme önleme performans seviyeleri göstermektedir. Akma durumu için yerdeğiştirmiş eksen dönmesi ( $\theta_y$ ) denklem (7) ile hesaplanmıştır.

$$\theta_y = \left( \frac{M_y}{E_c I_{cr}} \right) l_p \quad (7)$$

Denklem (7)'de  $E_c I_{cr}$  değerleri ASCE 41-17'ye göre Tablo 10-5'e verilen denklemler ile hesaplanmaktadır. Dikdörtgen en-kesitli betonarme kirişlerin etkin eğilme rijitliği ASCE 41-17'ye göre denklem (8) ile hesaplanmıştır. Beton elastisite modülü ( $E_c$ ) ACI 318-14'e göre denklem (8) ile hesaplanmıştır.

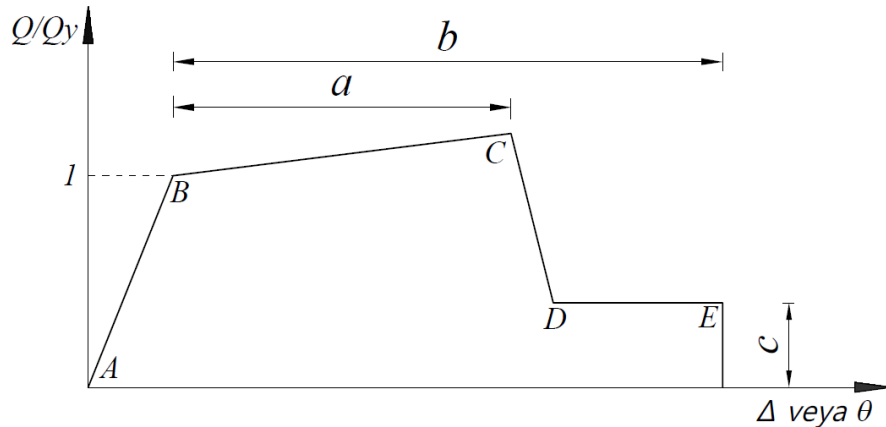
$$E_c I_{cr} = 0.3 E_c I_g, \quad E_c = 4700 \sqrt{f'_c}, \quad I = \frac{b \times h^3}{12} \quad (8)$$

Denklem (8)'de  $E_c$  ve  $I_g$  sırasıyla beton elastisite modülü ve kesit atalet momentidir. Denklem (7)'de verilen  $l_p$  plastik mafsal uzunluğudur. ASCE 41-17'de plastik mafsal uzunluğu ile ilgili herhangi bir açıklama yoktur. Bu nedenle hesaplarda plastik mafsal uzunluğu  $l_p = h/2$  olarak alınmıştır.  $h$  dikdörtgen kesitli betonarme kirişlerin kesit yüksekliğidir.

Tablo 6. ASCE 41-17'ye betonarme kirişlerinin doğrusal olmayan modelleme prosedürü için gerekli parametreler [7]

Durum	Modelleme değişkenleri			Kabul edilmiş kriterler				
	Plastik Dönme Açıları (Rad)	Artık dayanım oranı		Plastik dönme açısı (Rad)	Performans seviyesi			
Durum 1: Eğilme davranışı kontrolündeki kirişler								
$\frac{(\rho - \rho')}{\rho}$	Enine donatı	$\frac{V}{b_w d \sqrt{f'_{cE}}}$	a	b	c	IO	LS	CP
$\leq 0.0$	C	$\leq 3$ (0.25)	0.025	0.050	0.2	0.0100	0.025	0.050
$\leq 0.0$	C	$\geq 6$ (0.5)	0.020	0.040	0.2	0.0050	0.020	0.040
$\geq 0.5$	C	$\leq 3$ (0.25)	0.020	0.030	0.2	0.0050	0.020	0.030
$\geq 0.5$	C	$\geq 6$ (0.5)	0.015	0.020	0.2	0.0050	0.015	0.020
$\leq 0.0$	NC	$\leq 3$ (0.25)	0.020	0.030	0.2	0.0050	0.020	0.030
$\leq 0.0$	NC	$\geq 6$ (0.5)	0.010	0.015	0.2	0.0015	0.010	0.015
$\geq 0.5$	NC	$\leq 3$ (0.25)	0.010	0.015	0.2	0.0050	0.010	0.015
$\geq 0.5$	NC	$\geq 6$ (0.5)	0.005	0.010	0.2	0.0015	0.005	0.010
Durum 2: Kesme davranışı kontrolündeki kirişler								
Etriye Aralığı $\leq d/2$			0.003	0.020	0.2	0.0015	0.010	0.020
Etriye Aralığı $\geq d/2$			0.003	0.010	0.2	0.0015	0.005	0.010
Durum 3: Açıklık boyunca yetersiz donatı ve bindirme boyu kontrolündeki kirişler								
Etriye Aralığı $\leq d/2$			0.003	0.020	0.0	0.0015	0.010	0.020
Etriye Aralığı $\geq d/2$			0.003	0.010	0.0	0.0015	0.005	0.010
Durum 4: Kolon kiriş birleşim bölgesine yeterli derecede saplanmamış kirişler								
			0.015	0.03	0.2	0.0100	0.020	0.030

ASCE 41-17'de; Tablo 1 ve Şekil 2'de belirtilen B-C, B-E noktaları arasındaki mesafe ve E noktasında işaretlenmiş a, b ve c üç deformasyon değerleri ve performans seviyesi belirlenmiştir.



Şekil 2. Betonarme elemanlarının Genelleştirilmiş kuvvet-deformasyon ilişkisi grafiği [7]

### Analitik Çalışma

Betonarme dikkörtgen en-kesitli kiriş elemanlarının hasar sınırları TBDY 2018 ve ASCE 41-17 yönetmeliklerine göre hesaplanmıştır. Tasarlanmış dikkörtgen en-kesitli betonarme kirişlerde, beton basınç dayanımının ve basınç donatı oranının değişiminin hasar sınırlarına etkisi araştırılarak iki farklı yönetmeliğe göre elde edilen sonuçlar karşılaştırılmıştır. İki farklı yönetmeliğine göre hesaplanan hasar sınırları karşılaştırarak yorumlanmıştır. Analitik çalışmanın kapsamında toplam 33 adet farklı parametrelere sahip dikkörtgen en-kesitli betonarme kirişin analizi yapılmıştır. Elde edilen sonuçlar karşılaştırmalı olarak çizelgeler halinde özetlenmiştir. Tip 1, 2 ve 3 olarak tasarlanan ve detayları Tablo 2, 3 ve 4'te verilen dikkörtgen kesitli betonarme kiriş modelleri için sabit çekme donatısı oranı ve farklı basınç donatı oranlarına göre moment-eğrilik analizlerinden elde edilen sonuçlar kullanılarak kiriş modelleri için  $k_y$ ,  $M_y$ ,  $k_u$  ve  $M_u$  değerleri hesaplanmıştır.

TBDY 2018'de yığılı plastik davranışına göre modellenen dikkörtgen kesitli betonarme kirişlerin akma durumu için  $\theta_y$  değerleri hesaplanarak Tablo 10'da verilmiştir. Tip 1, 2 ve 3 olan betonarme kirişlerin farklı parametrelere göre hesaplanan  $\epsilon_c^{(SH)}$ ,  $\epsilon_s^{(SH)}$ ,  $\theta_p^{(SH)}$ ,  $\epsilon_c^{(KH)}$ ,  $\epsilon_s^{(KH)}$ ,  $\theta_p^{(KH)}$ ,  $\epsilon_c^{(GÖ)}$ ,  $\epsilon_s^{(GÖ)}$ ,  $\theta_p^{(GÖ)}$  değerleri sırasıyla Tablo 7, 8 ve 9'da verilmiştir.

Tablo 7. Tip-1 betonarme kirişlerin farklı performans düzeyleri için hesaplanan sonuç değerleri

Kesit Grubu	Kesit No	(SH)			(KH)			(GÖ)		
		$\epsilon_c^{SH}$	$\epsilon_s^{SH}$	$\theta_p^{SH}$	$\epsilon_c^{KH}$	$\epsilon_s^{KH}$	$\theta_p^{KH}$	$\epsilon_c^{GÖ}$	$\epsilon_s^{GÖ}$	$\theta_p^{GÖ}$
Tip 1	B1-0				0.00626		0.00974	0.00834		0.01298
	B1-1				0.00629		0.01643	0.00839		0.02190
	B1-2				0.00630		0.04083	0.00840		0.05444
	B1-3				0.00631		0.04089	0.00841		0.05451
	B1-4				0.00632		0.04092	0.00842		0.05455
	B1-5	0.0025	0.0075	0	0.00633	0.024	0.04093	0.00843	0.032	0.05457
	B1-6				0.00633		0.04095	0.00844		0.05460
	B1-7				0.00634		0.04096	0.00845		0.05461
	B1-8				0.00634		0.04097	0.00845		0.05463
	B1-9				0.00635		0.04098	0.00846		0.05465
	B1-10				0.00635		0.04100	0.00847		0.05466

Tablo 8. Tip-2 betonarme kirişlerin farklı performans düzeyleri için hesaplanan sonuç değerleri

Kesit Grubu	Kesit No	(SH)			(KH)			(GÖ)		
		$\epsilon_c^{SH}$	$\epsilon_s^{SH}$	$\theta_p^{SH}$	$\epsilon_c^{KH}$	$\epsilon_s^{KH}$	$\theta_p^{KH}$	$\epsilon_c^{GÖ}$	$\epsilon_s^{GÖ}$	$\theta_p^{GÖ}$
Tip 2	B2-0				0.00585		0.01519	0.00780		0.02026
	B2-1				0.00587		0.02563	0.00783		0.03417
	B2-2				0.00588		0.04259	0.00785		0.05679
	B2-3				0.00589		0.04263	0.00786		0.05684
	B2-4				0.00590		0.04265	0.00787		0.05687
	B2-5	0.0025	0.0075	0	0.00590	0.024	0.04267	0.00787	0.032	0.05689
	B2-6				0.00591		0.04268	0.00788		0.05691
	B2-7				0.00591		0.04269	0.00789		0.05692
	B2-8				0.00592		0.04271	0.00789		0.05694
	B2-9				0.00592		0.04272	0.00790		0.05696
	B2-10				0.00593		0.04273	0.00790		0.05697

Tablo 9. Tip 3 betonarme kirişlerin farklı performans düzeyleri için hesaplanan sonuç değerleri

Kesit Grubu	Kesit No	(SH)			(KH)			(GÖ)		
		$\varepsilon_c^{SH}$	$\varepsilon_s^{SH}$	$\theta_p^{SH}$	$\varepsilon_c^{KH}$	$\varepsilon_s^{KH}$	$\theta_p^{KH}$	$\varepsilon_c^{GÖ}$	$\varepsilon_s^{GÖ}$	$\theta_p^{GÖ}$
Tip 3	B3-0				0.00555		0.04382	0.00740		0.05842
	B3-1				0.00558		0.04386	0.00744		0.05847
	B3-2				0.00559		0.04389	0.00745		0.05852
	B3-3				0.00559		0.04391	0.00746		0.05855
	B3-4				0.00560		0.04392	0.00747		0.05857
	B3-5	0.0025	0.0075	0	0.00560	0.024	0.04394	0.00747	0.032	0.05859
	B3-6				0.00561		0.04395	0.00748		0.05860
	B3-7				0.00561		0.04396	0.00748		0.05862
	B3-8				0.00562		0.04397	0.00749		0.05863
	B3-9				0.00562		0.04398	0.00749		0.05864
	B3-10				0.00562		0.04399	0.00750		0.05866

Tablo 10. Tip 1, 2 ve 3 betonarme kirişlerin akma durumu için yer değiştirmiş eksen dönmesi

Kesit Grubu	Kesit No	$\theta_y$	Kesit Grubu	Kesit No	$\theta_y$	Kesit Grubu	Kesit No	$\theta_y$
Tip-1	B1-0	0.01353	Tip-2	B2-0	0.01308	Tip-3	B3-0	0.01216
	B1-1	0.01298		B2-1	0.01246		B3-1	0.01178
	B1-2	0.01231		B2-2	0.01194		B3-2	0.01147
	B1-3	0.01178		B2-3	0.01158		B3-3	0.01126
	B1-4	0.01149		B2-4	0.01136		B3-4	0.01114
	B1-5	0.01135		B2-5	0.01122		B3-5	0.01100
	B1-6	0.01118		B2-6	0.01108		B3-6	0.01090
	B1-7	0.01107		B2-7	0.01097		B3-7	0.01077
	B1-8	0.01093		B2-8	0.01084		B3-8	0.01067
	B1-9	0.01083		B2-9	0.01074		B3-9	0.01058
B1-10	0.01071	B2-10	0.01064	B3-10	0.01048			

Betonarme dikdörtgen kesitli kirişlerin hasar sınırları ve performans seviyelerini hesaplamak için ASCE 41-17’de Tablo 10-7’deki verileri kullanılarak betonarme dikdörtgen kesitli kirişlerin doğrusal olmayan performans seviyeleri hesaplanmıştır. Betonarme kirişlerinin doğrusal olmayan modelleme prosedürünü etkileyen parametreler  $(\rho - \rho')/\rho$  oranı, kesme kuvveti etkisi  $V/(b_w d \sqrt{f'_{CE}})$ , kesitin sargılama durumu ve kırılma durumudur. Betonarme dikdörtgen kesitli kirişlerin hasar sınırları ve performans seviyeleri Tablo 11, 12 ve 13’te performans grafikleri ise Şekil 3, 4 ve 5’te verilmiştir.

Tablo 11. Tip-1 betonarme kirişlerin hasar sınırları ve performans değerleri [7]

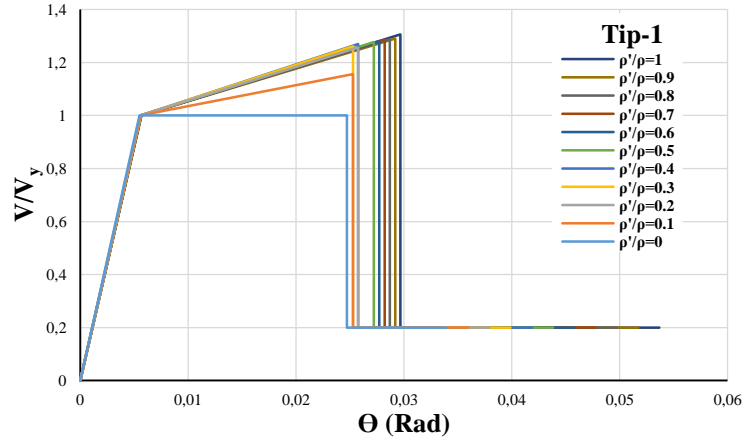
Tip-1							
$\frac{(\rho - \rho')}{\rho}$	$\frac{V}{b_w d \sqrt{f'_{CE}}}$	Modelleme Değişkenleri			Kabul edilmiş kriterler		
		Plastik Dönme Açılırları(Rad)		Artık Dayanım Oranı	Plastik dönme açılırları (Rad)		
		a	b	c	Performans seviyesi		
					IO	LS	CP
0.850	0.288	0.0192	0.0284	0.2	0.0050	0.0192	0.0284
0.765	0.292	0.0197	0.0304	0.2	0.0054	0.0197	0.0304
0.680	0.292	0.0202	0.0323	0.2	0.0058	0.0202	0.0323
0.595	0.293	0.0206	0.0343	0.2	0.0062	0.0206	0.0343
0.510	0.293	0.0211	0.0362	0.2	0.0066	0.0211	0.0362
0.425	0.293	0.0216	0.0382	0.2	0.0070	0.0216	0.0382
0.340	0.294	0.0221	0.0402	0.2	0.0074	0.0221	0.0402
0.255	0.295	0.0226	0.0421	0.2	0.0078	0.0226	0.0421
0.170	0.296	0.0230	0.0441	0.2	0.0082	0.0230	0.0441
0.085	0.296	0.0235	0.0460	0.2	0.0086	0.0235	0.0460
0.000	0.297	0.0240	0.0480	0.2	0.0090	0.0240	0.0480

Tablo 12. Tip-2 betonarme kirişlerin hasar sınırları ve performans değerleri [7]

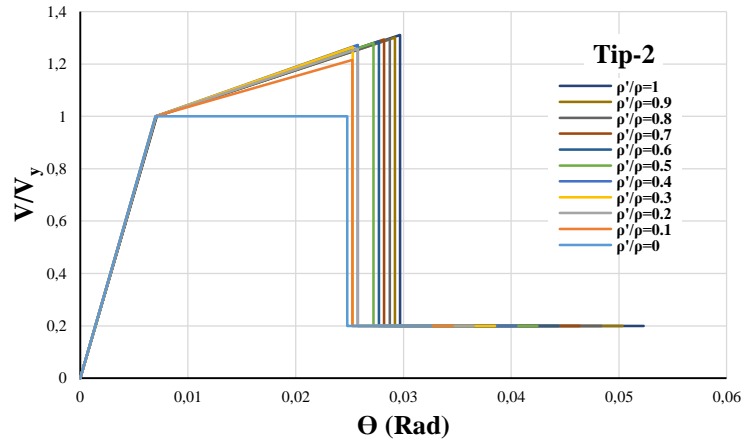
Tip-2							
$\frac{(\rho - \rho')}{\rho}$	$\frac{V}{b_w d \sqrt{f'_{CE}}}$	Modelleme Değişkenleri			Kabul edilmiş kriterler		
		Plastik Dönme Açılırları(Rad)		Artık Dayanım Oranı	Plastik Dönme Açılırları (Rad)		
		a	b	c	IO	LS	CP
0.850	0.364	0.0178	0.0256	0.2	0.0050	0.0178	0.0256
0.765	0.365	0.0183	0.0276	0.2	0.0053	0.0183	0.0276
0.680	0.366	0.0188	0.0295	0.2	0.0055	0.0188	0.0295
0.595	0.366	0.0192	0.0315	0.2	0.0058	0.0192	0.0315
0.510	0.366	0.0197	0.0334	0.2	0.0060	0.0197	0.0334
0.425	0.367	0.0202	0.0354	0.2	0.0063	0.0202	0.0354
0.340	0.367	0.0207	0.0374	0.2	0.0066	0.0207	0.0374
0.255	0.368	0.0212	0.0393	0.2	0.0068	0.0212	0.0393
0.170	0.370	0.0216	0.0413	0.2	0.0071	0.0216	0.0413
0.085	0.370	0.0221	0.0432	0.2	0.0073	0.0221	0.0432
0.000	0.370	0.0226	0.0452	0.2	0.0076	0.0226	0.0452

Tablo 13. Tip-3 betonarme kirişlerin hasar sınırları ve performans değerleri [7]

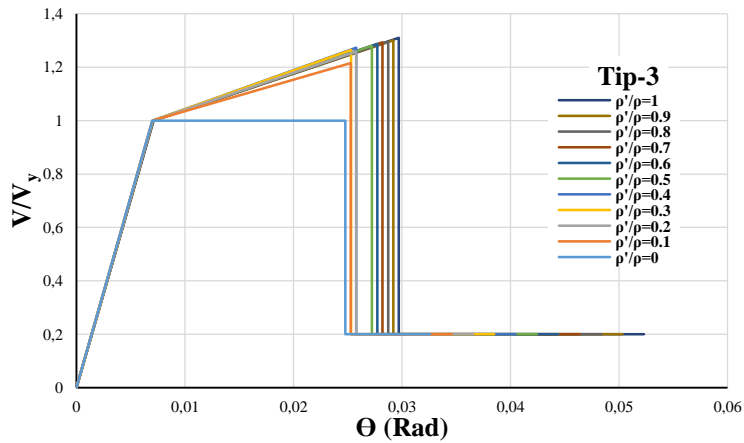
Tip-3							
$\frac{(\rho - \rho')}{\rho}$	$\frac{V}{b_w d \sqrt{f'_{CE}}}$	Modelleme Değişkenleri			Kabul edilmiş kriterler		
		Plastik Dönme Açılırları(Rad)		Artık Dayanım Oranı	Plastik Dönme Açılırları(Rad)		
		a	b	c	IO	LS	CP
0.850	0.406	0.0168	0.0236	0.2	0.0050	0.0168	0.0236
0.765	0.408	0.0173	0.0256	0.2	0.0052	0.0173	0.0256
0.680	0.408	0.0178	0.0276	0.2	0.0053	0.0178	0.0276
0.595	0.409	0.0183	0.0295	0.2	0.0055	0.0183	0.0295
0.510	0.410	0.0188	0.0315	0.2	0.0057	0.0188	0.0315
0.425	0.411	0.0193	0.0335	0.2	0.0059	0.0193	0.0335
0.340	0.411	0.0197	0.0355	0.2	0.0060	0.0197	0.0355
0.255	0.413	0.0202	0.0375	0.2	0.0062	0.0202	0.0375
0.170	0.414	0.0207	0.0394	0.2	0.0064	0.0207	0.0394
0.085	0.414	0.0212	0.0414	0.2	0.0065	0.0212	0.0414
0.000	0.415	0.0217	0.0434	0.2	0.0067	0.0217	0.0434



Şekil 3. Tip-1 betonarme kirişlerin kuvvet deformasyon ilişkileri [7]



Şekil 4. Tip-2 betonarme kirişlerin kuvvet deformasyon ilişkileri [7]

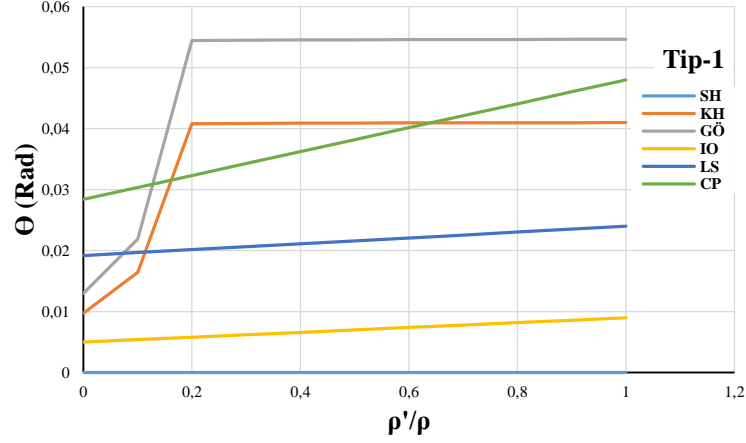


Şekil 5. Tip-3 betonarme kirişlerin kuvvet deformasyon ilişkileri [7]

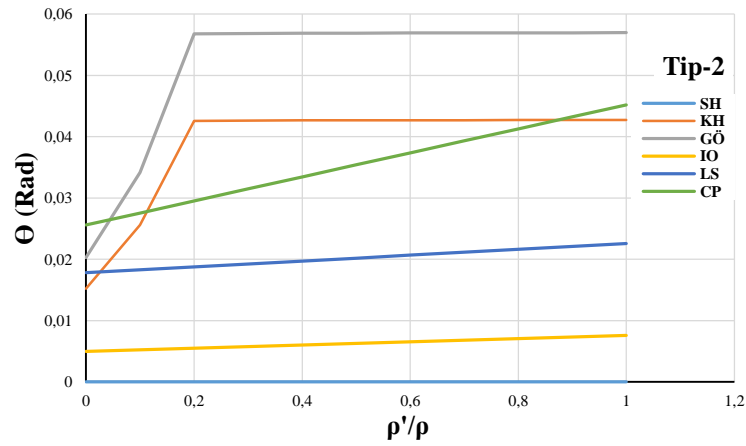
### Araştırma Bulguları ve Tartışma

Betonarme dikdörtgen kesitli kirişlerin hasar sınırları ve performans seviyeleri TBDY 2018 ve ASCE 41-17 yönetmeliklere göre elde edilmiştir. TBDY 2018'e göre hesaplanan sınırlı hasar (SH), kontrollü hasar (KH) ve göçme önlenmesi (GÖ) hasar seviyelerindeki değerler elde edilerek karşılaştırmalı olarak Tablo 7, 8 ve 9'da verilmiştir. ASCE 41-17'e göre hesaplanan performans seviyeleri de karşılaştırmalı olarak Tablo 11, 12 ve 13'te ve Şekil 3, 4 ve 5'te sunulmuştur. Dikdörtgen

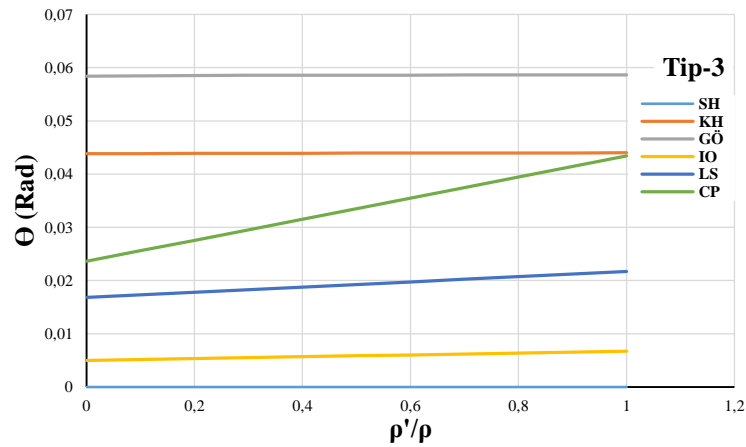
kesitli betonarme kirişlerinde TBDY (2018) ve ASCE 41-17'ye göre hesaplanan hasar sınırları ve performans seviyeleri karşılaştırmalı grafikleri Şekil 6, 7, 8 ve 9'da verilmiştir.



Şekil 6. Tip-1 betonarme kirişlerin  $\theta$  değerlerinin  $\rho'/\rho$  değerlerin göre değişimi

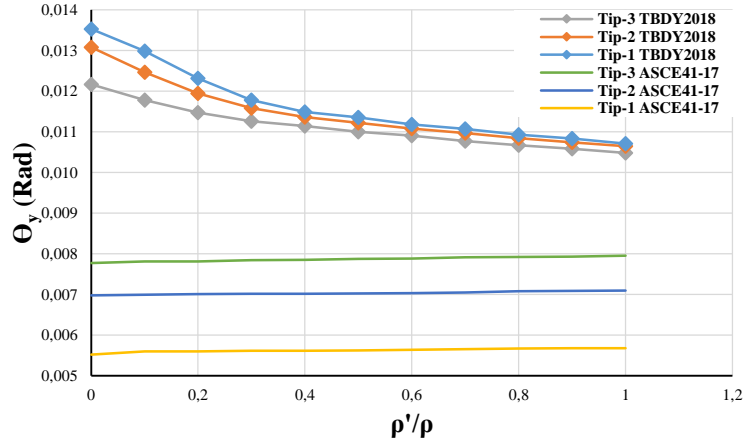


Şekil 7. Tip-2 betonarme kirişlerin  $\theta$  değerlerinin  $\rho'/\rho$  değerlerin göre değişimi



Şekil 8. Tip-3 betonarme kirişlerin  $\theta$  değerlerinin  $\rho'/\rho$  değerlerin göre değişimi





Şekil 9. Tip-1, 2 ve 3 betonarme kirişlerin  $\theta$  değerlerinin  $\rho'/\rho$  değerlerin göre değişimi

### Sonuçlar

Araştırma bulgular ve tartışma bölümünde betonarme dikdörtgen en-kesitli kirişler için özetlenen sonuçlar maddeler halinde aşağıda özetlenmiştir.

- Sabit beton basınç dayanımı ve çekme donatısı oranına sahip dikdörtgen en-kesitli betonarme kirişlerde basınç donatı oranının artması ile plastik mafsal akma dönmesinin ( $\theta_y$ ) değeri azalmaktadır (TBDY 2018).
- Betonarme dikdörtgen en-kesitli kirişlerde TBDY, 2018'e göre hesaplanan plastik mafsal akma dönmesinin ( $\theta_y$ ) değeri; sabit çekme donatısı ve basınç donatısı oranları için, artan beton basınç dayanımı ile azalmaktadır.
- Sabit beton basınç dayanımı ve çekme donatısı oranına sahip dikdörtgen en-kesitli betonarme kirişlerde basınç donatı oranının artması ile plastik mafsal akma dönmesinin ( $\theta_y$ ) değeri artmaktadır (ASCE 41-17).
- Betonarme dikdörtgen en-kesitli kirişlerde ASCE 41-17'e göre hesaplanan plastik mafsal akma dönmesinin ( $\theta_y$ ) değeri; sabit çekme donatısı ve basınç donatısı oranları için, artan beton basınç dayanımı ile artmaktadır.
- TBDY 2018'e göre hesaplanan plastik mafsal akma dönmesinin değerleri ASCE 41-17'ye göre hesaplanmış akma dönmesinden daha fazla elde edilmiştir ve yaklaşık olarak 2 katıdır.
- Sabit çekme donatısı oranı ve beton basınç dayanımı için artan basınç donatı oranı ile  $\epsilon_c^{(KH)}$  ve  $\epsilon_c^{(GÖ)}$  değerleri artmaktadır.
- Sabit çekme donatısı oranı ve beton basınç dayanımı için artan basınç donatısı oranı ile  $\theta_p^{(KH)}$  ve  $\theta_p^{(GÖ)}$  değerleri artmaktadır.
- Sabit çekme ve basınç donatısı oranı için artan beton basınç dayanımı ile  $\epsilon_c^{(KH)}$  ve  $\epsilon_c^{(GÖ)}$  değerleri azalmaktadır.
- Sabit çekme ve basınç donatısı oranı için artan beton basınç dayanımı ile  $\theta_p^{(KH)}$  ve  $\theta_p^{(GÖ)}$  değerleri artmaktadır.
- TBDY (2018)'de donatı çeliği için GÖ ve KH performans düzeylerinde verilen hasar sınırları ( $\epsilon_s^{(KH)}$ ,  $\epsilon_s^{(GÖ)}$ ), donatı çeliğinin çekme dayanımına karşı gelen birim uzama değerini sabit katsayılar ile çarparak elde edilmektedir. SH performans düzeyi için verilen hasar sınırı ise sabit bir değer olarak verilmektedir ( $\epsilon_s^{(SH)} = 0.0075$ ).
- $\epsilon_c^{(SH)}$  performans düzeyi için verilen hasar sınırı ise sabit değer olarak verilmektedir ( $\epsilon_c^{(SH)} = 0.0025$ ).
- ASCE 41-17'ye göre sabit çekme donatısı oranı ve beton basınç dayanımı için artan basınç donatısı oranı ile  $\theta_{IO}$ ,  $\theta_{LS}$  ve  $\theta_{CP}$  değerleri artmaktadır.
- ASCE 41-17'ye göre sabit çekme ve basınç donatısı oranı için artan beton basınç dayanımı ile  $\theta_{IO}$ ,  $\theta_{LS}$  ve  $\theta_{CP}$  değerleri azalmaktadır.

- Betonarme dikdörtgen en-kesitli kirişlerin performans hasar seviyeleri TBDY 2018'e göre sınırlı hasar performans durumunda dönme açısına izin verilmemektedir.
- ASCE 41-17'ye göre hesaplanan sınırlı hasara karşı gelen dönme açıları izin verilmekte ve basınç donatısı oranının artmasıyla dönme açısı artmakta ve beton basınç dayanımının artması durumunda bu değer azalmaktadır.
- ASCE 41-17'ye göre hesaplanan hasar sınırların dönme açıları TBDY 218'e göre hesaplanmış hasar sınırların dönme açıları daha az elde edilmiştir.

#### Kaynaklar

- [1] Celep, Z., ve Kumbasar N. (2004). Deprem Mühendisliğine Giriş ve Depreme Dayanıklı Yapı Tasarımı, Beta Dağıtım, İstanbul, 596s.
- [2] Sucuoğlu, H. (2015). Performans Esaslı Deprem Mühendisliği. 3. Türkiye Deprem Mühendisliği ve Sismoloji Konferansı, 14-16 Ekim 2015, DEÜ, İzmir.
- [3] Sönmez, İbrahim K, 2010. Betonarme Yapı Sistemlerinde Yapısal Performans Düzeyini Belirleyen bir Bilgisayar Programı Geliştirilmesi, Yüksek Lisans Tezi, İTÜ Fen Bilimleri Enstitüsü.
- [4] Ersoy, U. ve Özcebe G. (1998). Sarılmış Betonarme Kesitlerde Moment-Eğrilik İlişkisi Analitik Bir İnceleme. Teknik Dergi, 9(4), 1998-1827.
- [5] Ulutaş, H. (2019). DBYBHY (2007) ve TBDY (2018) Deprem Yönetmeliklerinin Kesit Hasar Sınırları Açısından Kıyaslanması. Avrupa Bilim ve Teknoloji Dergisi Sayı 17, S. 351-359, Aralık 2019.
- [6] TBDY, 2018, Türkiye Bina Deprem Yönetmeliği, T.C. Bayındırlık ve İskân Bakanlığı, Ankara.
- [7] ASCE 41-17. Seismic Evaluation and Retrofit of Existing Buildings; American Society of Civil Engineers: Reston, VA, USA, 2017.
- [8] Çağlar, N., Akkaya, A., Demir, A., Öztürk, H., 2004. Farklı Kesit Geometrilerine Sahip Betonarme Kolonların Davranışının İncelenmesi, ISITES2014, p. 2095-2105, Karabük/Türkey.
- [9] TS500, 2000, Betonarme Yapıların Tasarım ve Yapım Kuralları, Türk Standartları Enstitüsü, TSE, Ankara.
- [10] ACI 318-14, American Concrete Institute. 2014. Building Code Requirements for Structural Concrete and Commentary, Standards ACI 318–14 and ACI 318R-08. Farmington Hills: Michigan.
- [11] SAP2000. Structural software for analysis and design, Computers and Structures, Inc. Version 20.0.0. USA.

## Betonarme Kolonlar için Kesme Dayanımı ve Deformasyon Kapasite Modellerinin Araştırılması

*Saeid Foroughi\**, Konya Teknik Üniversitesi, Mühendislik ve Doğa Bilimleri Fakültesi, İnşaat Mühendisliği Bölümü, Konya, Türkiye

*Süleyman Bahadır Yüksel*, Konya Teknik Üniversitesi, Mühendislik ve Doğa Bilimleri Fakültesi, İnşaat Mühendisliği Bölümü, Konya, Türkiye

\*İletişimden sorumlu yazar: saeid.foroughi@yahoo.com

**Anahtar Kelimeler:** Betonarme taşıyıcı sistem, kesme mukavemeti, Deplasman sünekliği, Sismik değerlendirme, Eksenel yük.

**Disiplin:** İnşaat Mühendisliği

### Özet

Mevcut veya yeni tasarlanacak betonarme yapıların sismik değerlendirmesinde, betonarme kolonların yapısal davranışını tahmin etmek çok önemlidir. Betonarme kolonların kesme kırılması veya eğilme kırılmasına maruz kalması olasılığının incelenmesi en önemli parametrelerden birisidir. Sadece yüksek kesme kuvveti altında tek bir kolon davranışını araştırmak değil, aynı zamanda bu davranışın bir bütün olarak yapı üzerindeki etkilerini incelemek de önemlidir. Göçme öncesi sismik performans seviyesinde, kesmeye duyarlı betonarme kolonların yatay yük taşıma kapasitesindeki azalmayı, eksenel yük taşıma kapasitesindeki olası kaybını ve bu tür davranışların tüm yapı üzerindeki etkilerini tahmin etmeye ve modellemeye ihtiyaç vardır. Kesme dayanımı ve deformasyon kapasite modellerinin araştırılması için farklı beton sınıfı, boyuna donatı oranı, enine donatı çapı, enine donatı aralığı ve eksenel yük seviyelerine sahip betonarme kolon modelleri tasarlanmıştır. Bu çalışmada farklı parametrelerde tasarlanan betonarme kolon modellerinin kesme davranışı ile deformasyon kapasitesi; Türkiye Bina Deprem Yönetmeliği (TBDY, 2018), Amerikan Beton Enstitüsü (ACI318, 2014), Mevcut Binaların Sismik Değerlendirmesi ve Güçlendirilmesi (ASCE/SEI-41, 2017) ve farklı araştırmacılar tarafından önerilen modeller dikkate alınarak araştırılmıştır. Farklı yönetmelikler ve araştırmacılar tarafından önerilen bağıntılardan elde edilen kesme dayanımları ile betonarme kolon modellerinin deplasman süneklikleri arasındaki ilişkiler de incelenmiştir. Betonarme kolonların elastik ve plastik deplasmanları ile toplam deplasman ilişkilerinin elde edilebilmesi için kesitlerin moment-eğrilik ilişkileri oluşturularak, bu ilişkilerin karakteristik değerleri belirlenmiştir. Moment-eğrilik ilişkisindeki her bir eğrilik değerine ait deplasman değeri hesaplanarak deplasman süneklikleri elde edilmiştir. Betonarme kolonlar için kesme dayanım kapasitesi farklı yönetmelikler ve farklı araştırmacılar tarafından önerilen modeller dikkate alınarak hesaplanmıştır. Araştırma sonuçlarından elde edilen değerler farklı modeller ve parametrelere göre karşılaştırarak yorumlanmıştır.

### Giriş

Betonarme yapılarda, betonarme kolonlar deprem yükleri altında en önemli taşıyıcı sistemlerden biridir. Kolon mekanizmaları depremlerde toptan çökmeyi önlemek için çok önemlidir. Bazı kritik betonarme kolonların hasarı nedeniyle betonarme yapıların objektif performans seviyeleri sağlanamamıştır. Bu nedenle, yapıların davranışlarının belirlenmesi, depreme dayanıklı tasarım için çok önemlidir [1]. Betonarme kolonlar, çerçevesel yapıların sismik davranışını belirleyen ana taşıyıcı elemanlardır. Betonarme yapılarda depremler sonrası kolonlarda oluşan hasarlar nedeniyle yapıların objektif performans seviyeleri sağlanamamaktadır. Bu nedenle, depreme dayanıklı yapı tasarım için yapısal elemanların davranışlarının iyi bilinmesi gerekmektedir [2]. Betonarme kolonların kesme kırılması veya eğilme kırılmasına maruz kalması olasılığının incelenmesi en önemli parametrelerden birisidir. Sadece yüksek kesme kuvveti altında tek bir kolon davranışını araştırmak değil, aynı zamanda bu davranışın bir bütün olarak yapı üzerindeki etkilerini incelemek de önemlidir. Bu elemanlar temelde eksenel yükleri taşıyacak şekilde tasarlanmıştır, ancak deprem veya rüzgâr gibi yanal yüklerin bir sonucu olarak olası kesme kırılmalarını önleyecek şekilde tasarlanmalıdır [3].

Betonarme kolonların kesme dayanımı ve deformasyon kapasiteleri, kolonların tasarım ve yapımında kullanılan donatı çeliğinin ve betonun malzeme özellikleriyle ilgili çok sayıda değişkenden etkilenir. Tasarım değişkenlerini kullanarak betonarme kolonların performansını tahmin etmek, bu değişkenlerin etkileşimi nedeniyle karmaşık doğrusal olmayan bir sorundur. Bir deprem sırasında bir yapıya uygulanan döngüsel yanal yüklemenin eklenmesi, yük döngüleri devam ederken kesme

mukavemetinde ve süneklikte ciddi hasarlara neden olabilir. Kolonun kesme kırılması nispeten düşük deformasyonlarda meydana geldiğinden ve yapının yanal yüklemeye direnme kabiliyetini önemli ölçüde etkileyebildiğinden, bu durum performansı tahmin etmenin karmaşıklığını daha da artırabilir.

Betonarme kolonların kesme dayanımının tahminine yönelik mevcut modellerin çoğu, döngüsel yüklemeye tabi tutulduğunda kapasite azalmasını göz ardı etmektedir. Düşük deformasyonlarda kesme göçmesi olasılığının yüksek olması nedeniyle, düşük deplasman seviyelerinde aşırı konservatif sonuçlar elde edilir ve daha yüksek deformasyon seviyelerinde oldukça muhafazakâr sonuçlar görülür [4]. Daha yakın zamanlarda, deplasman ve döngüsel yükleme ile ilişkili kesme mukavemeti azalmasını içeren yeni modeller geliştirilmiştir. Bu modeller genellikle, deneysel sonuçlara dayalı olarak kesme dayanımına beton katkısını etkileyen bir katsayı tanımlayarak kesme dayanımının azalmasını ele alır. Bu katsayı, yapısal bir elemanın deplasman sünekliğini, genellikle akma durumu için deplasmanın, göçme durumunda nihai deplasmana oranı olarak tanımlar. Sünek kırılma, depreme dayanıklı yapı tasarım için amaçlanmıştır ve performansa dayalı deprem mühendisliğinin temel gerekliliğidir. Bir elemanı sünek eleman olarak sınıflandırmak için, eğilme ve kesme dayanımı tahmin edilmeli ve göçme tipi tanımlanmalıdır.

Betonarme kolonlarda başlıca gözlemlenen üç tür kırılma modu vardır. Bunlar kesme kırılması, eğilme kırılması ve eğilme-kesme kırılması olarak tanımlanır. Kesme kırılması, istenmeyen ve ani kırılma modunun gevrek bir türüdür. Bir kolonun kesme mukavemeti, eğilme mukavemetinin gelişebilmesi için yeterli değilse, bu kolon, neredeyse hiç deforme olmadan bir kesme kırılması yaşar. Hâkim eğimli bir çatlak açılır ve aynı anda yanal ve eksenel kapasitelerde ani kayıp meydana gelene kadar yukarı doğru genişler. Deneysel test sonuçları, kesme aralığının derinlik oranına ( $a/d$ ), ikiden küçük veya  $a/d$  oranına bakılmaksızın yetersiz enine donatı oranına sahip kolonların kesme kırılmasına duyarlı olduğunu ortaya koymuştur. Eğilme kırılma modu genellikle sünek bir kırılma türüdür. Kolon yeterli kesme dayanımına sahip olduğunda, eleman yüksek kesme talepleri altında kırılmadan önce eğilme dayanımına ulaşabilir. Kolon, bu bölgenin detaylandırılmasının uygun olması koşuluyla, yük taşıma kapasitesinde önemli bir kayıp olmaksızın en yüksek moment bölgelerinde elastik olmayan deformasyonlar yaşar. Çatlama momentinin aşıldığı bölgelerde eğilme çatlakları görülmektedir. Test veri tabanı incelendiğinde, 3.5'ten büyük  $a/d$  oranına sahip ve yeterli enine donatıya sahip kolonlarda eğilme kırılması yaşandığı görülmektedir. Kırılma modunun üçüncü tipi, eğilme-kesme kırılması olarak adlandırılır. Enine donatı miktarı, betondaki ana çekme gerilmelerinin yatay bileşenini taşımaya yeterli değildir. Eleman gövde çatlama neden olan diyagonal çekme kuvvetinin dikey bileşeni, diyagonal çatlaklar arasındaki diyagonal basınç desteğinin basınç kapasitesinden daha büyüktür. Eleman gövde çatlama neden olan çapraz çekme kuvvetinin dikey bileşeni, boyuna donatının dayanımından daha büyüktür. Bu tür bir kırılma, kesme kırılması kadar gevrek değildir. Test sonuçları, eğilme-kesme kırılmasının çoğunlukla 2 ile 3.5 arasında bir kesme aralığının derinlik oranına ( $a/d$ ), sıfır ile 0.018 arasında değişen hacimsel enine donatı oranına ve dengeli yüke yakın veya altında bir eksenel yük seviyesine sahip kolonlarda meydana geldiğini göstermektedir [5].

Deplasman sünekliği, yapıların sismik tepkisinin tasarlandıkları ilk hedeflere uygun olup olmadığının belirlenmesine yol açan önemli bir özelliktir. Deplasman sünekliği önemlidir çünkü dünya çapındaki sismik kodlardan bazıları, tepki azaltma faktörlerinin deplasman sünekliğine dayalı olarak tahmin edildiği modal-spektral analizi öngörmektedir [6]. Bir betonarme elemanın kesme dayanımı; beton dayanımı, kemer etkisi ( $a/h$ ), eksenel yük seviyesi, deplasman sünekliği, enine donatı, boyuna donatı oranı, sismik performans seviyesi ve uygulanan kuvvet-deplasman geçmişi gibi birçok parametreye bağlıdır [7]. Aşağıdaki bölüm, farklı tasarım yönetmeliklerinin ve önerilen modellerin kesme dayanımı hükümlerinin bir incelemesini sunmaktadır. Bir çok güncel yönetmelik, betonarme kolonların kesme dayanımını analiz etmek için beton ve enine donatı katkılarını içerir. Daha sonra iki bileşen, toplam kesme dayanımını tahmin etmek için toplanır.

### **Betonarme Kolonların Dayanımı için Önerilen Modeller**

Betonarme kolonların kesme dayanımı, son yıllarda araştırmalarda büyük ilgi görmektedir. Yeni binaların tasarımı ve mevcut binaların değerlendirilmesi için betonarme kolonların kesme dayanımı için çeşitli modeller önerilmiş ve kullanılmıştır. Betonarme elemanda eğilme kırılmasının olmasını sağlamak için kesme donatıları kullanılır. Kesme donatıları, çatlaklar boyunca çekme gerilmelerini karşılar, sarılma bölgesi betonunu sınırlayarak kesme kapasitesini artırır. Bu bölümde, betonarme kolonlar için çeşitli tasarım yönetmelikleri ve araştırmacılar tarafından önerilen kesme dayanımı modellerinin

incelemesi yapılmıştır. Çoğu tasarım yönetmelikleri, kesme dayanımlarını tahmin etmek için deneysel veya yarı deneysel modeller kullanır. Bu çalışmada farklı parametrelerde tasarlanan betonarme kolon modellerinin kesme davranışı ile deformasyon kapasitesi; Türkiye Bina Deprem Yönetmeliği (TBDY) [8], Amerikan Beton Enstitüsü (ACI 318) [9], Mevcut Binaların Sismik Değerlendirmesi ve Güçlendirilmesi (ASCE/SEI-41) [10] ve araştırmacılar tarafından önerilen modeller dikkate alınarak araştırılmıştır. Farklı yönetmelikler ve araştırmacılar tarafından önerilen bağıntılar ile ilgili açıklamalar aşağıda detaylı olarak özetlenmiştir.

### TBDY (2018)

Betonarme yapı elemanlarına eğilme momenti ile birlikte etkiyen kesme kuvvetlerinin oluşturduğu asal çekme gerilmeleri, beton ve uygun kesme donatısı ile karşılanacak, asal basınç gerilmelerinin de gövdede ezilme oluşturmayacak bir düzeyde tutulması sağlanacaktır [11]. Betonarme kirişler için yapılan tanımlar kolonlar için de geçerlidir. TS500'e [11] göre betonarme bir kesitin kesmede çatlama dayanımı, daha kesin hesaba gerek duyulmadığı durumlarda, Denklem (1) kullanılarak hesaplanabilir. Denklemde  $N_d$  (eksenel kuvvet) çekmede de basınçta da pozitif alınacaktır. Elverişsiz yükleme şartlarından elde edilen en büyük kesme kuvveti tasarım kesme kuvveti olarak alınır. Denklemde, eksenel basınç durumunda  $\gamma=0.07$  alınabilir.

$$V_{cr} = 0.65f_{ctd}bd \left( 1 + \gamma \frac{N_d}{A_c} \right) \quad (1)$$

Betonun kesme dayanımı; beton katkısı ve kesme donatısının yaptığı katkıdan oluşmaktadır. Betonarme kolonun kesme güvenliği için kesme dayanımı, tasarım kesme kuvvetinden küçük olmamalıdır.  $V_d$  tasarım kesme kuvveti,  $V_r$  kesitin kesme dayanımıdır, beton katkısı ( $V_c$ ) ve kesme donatısı katkısının ( $V_w$ ) toplanması ile elde edilir.

$$V_r = V_c + V_w = 0.8V_{cr} + \left( \frac{A_{sw}}{s} \right) f_{ywd}d \geq V_d \quad (2)$$

TBDY'e [8] göre kolonlarda enine donatı hesabına esas alınacak kesme kuvveti  $V_e$ , Denklem (3) ile hesaplanacaktır. Denklemde  $M_a$  ve  $M_{\bar{u}}$  kolonun serbest yüksekliğinin alt ve üst ucunda, kolon kesme kuvvetinin hesabında esas alınan moment ve  $l_n$  kolonun kirişler arasında kalan serbest yüksekliği, kirişin kolon veya perde yüzleri arasında kalan serbest açıklığıdır.

$$V_e = (M_a + M_{\bar{u}})/l_n \quad (3)$$

Denklem (3) ile hesaplanan kesme kuvveti ( $V_e$ ), yük katsayıları ile çarpılmış düşey yükler ve deprem yüklerinin ortak etkisi altında hesaplanan kesme kuvveti ( $V_d$ )'den daha küçük alınmayacak ve ayrıca Denklem (4) ile verilen koşulları sağlayacaktır. Denklem (4)'teki ikinci koşulun sağlanamaması durumunda, kesit boyutları gerektiği kadar büyütülerek deprem hesabı tekrarlanacaktır.

$$V_e \leq V_r, \quad V_e \leq 0.85A_w\sqrt{f_{ck}} \quad (4)$$

Kolon enine donatısının  $V_e$  kesme kuvvetine göre hesabında, betonun kesme dayanımına katkısı ( $V_c$ ), TS500'e [11] göre belirlenecektir. Ancak kolon sarılma bölgelerindeki enine donatının hesabında, sadece deprem yüklerinden oluşan kesme kuvvetinin depremlili durumdaki toplam kesme kuvvetinin yarısından daha büyük olması ve aynı zamanda  $N_d \leq 0.05A_c f_{ck}$  koşulunun sağlanması halinde, betonun kesme dayanımına katkısı  $V_c = 0$  alınacaktır.

### Sezen ve Moehle (2004)

Bazı araştırmacılar [13] kesme dayanımına beton katkısının artan deplasman süneklik talebi ile azaldığı kesme dayanımı modelleri önermiştir. Konwinski vd. [14], kolon kesme dayanımının deplasman süneklik talebinden bağımsız olduğunu bulmuşlardır. Daha önce yapılan çalışmalardan elde edilen gözlemlere dayanarak, artan deplasman sünekliği ile hem beton hem de donatı ve beton ile donatı

arasındaki etkileşimin mukavemet azalmasının ilerlemesine katkıda bulunduğu kaydedilmiştir. Böylece, kesme dayanımına hem beton hem de donatı katkılarında bir dayanım azalma faktörü uygulanır. Önerilen kesme dayanımı modeli Denklem (5) ile ifade edilir. Denklem (5), süneklikle ilişkili dayanım azalmasını hesaba katmak için  $k$  faktörünü içeren kesme dayanımı modelini ifade eder.

$$V_c = k \left( \frac{0.5\sqrt{f'_c}}{a/d} \sqrt{1 + \frac{P}{0.5\sqrt{f'_c}A_g}} \right) 0.8A_g, \quad V_s = k \left( \frac{A_v f_y d}{s} \right) \quad (5a)$$

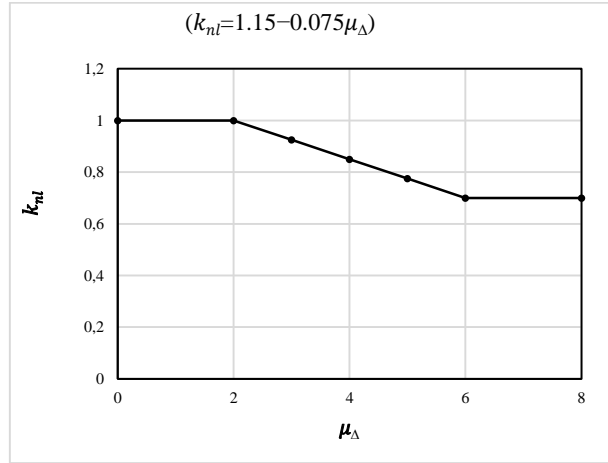
$$V_n = k(V_s + V_c) = k \left[ \left( \frac{A_v f_y d}{s} \right) + \left( \frac{0.5\sqrt{f'_c}}{a/d} \sqrt{1 + \frac{P}{0.5\sqrt{f'_c}A_g}} \right) \right] 0.8A_g \quad (MPa) \quad (5b)$$

#### ASCE Standard (ASCE/SEI 41-17)

Betonarme kolonların kesme dayanımı ve deformasyon kapasiteleri, kolonların tasarımında ve yapımında kullanılan donatı çeliği ve betonun malzeme özellikleriyle ilgili çok sayıda değişkenden etkilenir. Bir betonarme kolonun deformasyon kapasitesini belirlemek için ASCE/SEI 41 [10] kolonları, düşük süneklik talebindeki kesme dayanımının ( $V_0$ ) plastik kesme talebi ( $V_p$ ) oranına bağlı olarak üç farklı göçme modunda sınıflandırır. Plastik kesme talebi ( $V_p$ ), plastik mafsalların eğilme akmasına karşılık gelen kesme kuvvetidir.  $V_p$ , kesit analizinden elde edilen maksimum moment dayanımının kesme açıklığına ( $a = L/2$ ) bölünmesiyle hesaplanır ( $V_p = 2M_p/L$ ). ASCE/SEI 41 [10], Sezen ve Moehle [12] tarafından geliştirilen kesme dayanımı modelini benimser ve Denklem (6)'da gösterildiği gibi beton ( $V_c$ ) ve enine donatının ( $V_s$ ) katkısını toplayarak kolon kesme dayanımının ( $V_{Col}$ ) hesaplanmasını önerir.  $V_{Col0} = V_{Col}/k_{nl}$  terimi süneklik talebiyle ilgili indirgeme faktörü hariç kolon kesme dayanımıdır.

$$V_{Col} = k_{nl}V_{Col0} = k_{nl} \left[ \alpha_{Col} \left( \frac{A_v F_{ytL/E} d}{s} \right) + \lambda \left( \frac{0.5\sqrt{f'_{cL/E}}}{M_{UD}/V_{UD} d} \sqrt{1 + \frac{N_{UG}}{0.5A_g \sqrt{f'_{cL/E}}}} \right) 0.8A_g \right] \quad (MPa) \quad (6)$$

Denklemden,  $V_{Col}$  kuvvet kontrollü veya deformasyon kontrollü davranışlar için geçerli olan alt sınır veya beklenen malzeme özellikleri kullanılarak değerlendirilen betonarme kolonların kesme dayanımıdır ve  $V_{Col0}$ , 2.0'yi geçmeyen bir deplasman süneklik talebinde betonarme kolonların kesme dayanımıdır. Deplasman süneklik talebinin 2'ye eşit veya daha az olduğu bölgelerde  $k_{nl} = 1.0$ , deplasman sünekliğinin 6'ya eşit veya daha büyük olduğu bölgelerde  $k_{nl} = 0.7$  ve deplasman sünekliği için 2 ile 6 arasında doğrusal olarak değişir (Şekil 1).  $s/d \leq 0.75$  sınırı için  $\alpha_{Col} = 1$ ,  $s/d \geq 1$  için  $\alpha_{Col} = 0$  ve 0.75 ile 1.0 arasında  $s/d$  için doğrusal olarak değişir.  $A_v$  kesme donatısı alanıdır,  $f_{ytL/E}$  enine donatıların beklenen akma dayanımıdır,  $f'_{cL/E}$  beklenen beton kapsamlı dayanımıdır,  $d$  en dış basınç lifinden çekme donatısının ağırlık merkezine olan mesafe (faydalı yükseklik),  $s$  kesme donatı aralığı ve  $A_g$  betonarme kolonun brüt en-kesit alanıdır. Hafif agregalı beton için  $\lambda = 0.75$  ve normal agregalı beton için  $\lambda = 1.0$ .  $N_{UG}$  eksenel basınç kuvvetidir ve  $M_{UD}/(V_{UD} d)$ , tasarım yükleri altında kolon için momentin etkili derinlik kesme yükü oranı, ancak 4'ten büyük veya 2'den az olarak alınmamalıdır.



Şekil 1.  $k_{nI} - \mu_{\Delta}$  ilişkisi

#### ACI 318 (2014)

ACI 318 [9], tasarım kesme kuvvetinin bir kısmının beton kesme direnci mekanizması ( $V_c$ ) tarafından taşınacağını, geri kalanı ise enine donatıyı içeren kafes mekanizma ( $V_s$ ) tarafından taşınacağını kabul etmektedir. Eksenel basınç elemanları için  $V_c$  ve  $V_s$  Denklem (7)'den hesaplanacaktır.

$$V_c = 0.17 \left[ 1 + \frac{N_u}{14 A_g} \right] \lambda \sqrt{f'_c} b_w d \quad , \quad V_s = \frac{A_v f_{yt} d}{s} \quad (MPa) \quad (7)$$

ACI 318'e [9] göre nominal kesme dayanımı;  $V_n = V_c + V_s$  olarak hesaplanır. Denklemlerde;  $N_u$  eksenel basınç kuvveti ve basınç elemanlar için pozitif almır.  $A_g$  beton en-kesit alanı,  $f'_c$  betonun basınç dayanımı,  $b_w$  en-kesit genişliği veya dairesel kesitin çapı,  $d$  faydalı yüksekliği,  $A_v$  kesme donatı alanı,  $f_{yt}$  enine donatı akma dayanımı,  $s$  kesme donatılarının merkezinden merkezine olan mesafedir.

#### Betonarme Kolonlarda Doğrusal Olmayan Deplasman Kapasitesi

Yatay kuvvetlere dayanıklı elemanlar olarak, betonarme kolonların sünek deformasyon kapasitesi, yapılarda daha iyi bir sismik performans elde etmek için önemli bir faktördür. Performans/yer değiştirme tabanlı sismik tasarımın geliştirilmesiyle, yapısal deformasyon kapasitesi önemli ölçüde dikkat çekmiştir. Kolonlar tipik olarak yapıların gevrek kırılmaya karşı koruması için yeterli süneklikte tasarlanmalıdır. Yapısal sismik tasarım yalnızca dayanıma odaklanmamalı, aynı zamanda sünekliği de hesaba katmalıdır. Sünek sismik tasarımın daha iyi anlaşılması ve gerçekleştirilmesi için güçlü depremler altında yapısal deformasyon kapasitesinin tahmin edilmesi gerekir. Plastik mafsal analizinde, bir konsolun toplam tepe deplasman ( $\Delta_u$ ), akma deplasmanı ( $\Delta_y$ ) ve plastik deplasman ( $\Delta_p$ ) bileşeninin toplamı olarak elde edilir (Denklem 8). Denklemlerde  $H_w$ , kolon yüksekliğidir.  $(\phi_u - \phi_y)L_p$  terimi, plastik dönmeyi ifade eder ve plastik eğriliğin eşdeğer plastik mafsal uzunluğunun ( $L_p$ ) merkezinde toplandığı varsayımına dayanır. Plastisitenin yayıldığı gerçek fiziksel uzunluk daha büyüktür ve plastik bölge olarak adlandırılır. Plastik bölge üzerindeki kolonlarda elastik olmayan eğriliklerin doğrusal olarak değiştiği varsayılmaktadır. Çünkü plastik mafsal analizi, Şekil 2'de gösterildiği gibi  $\theta_p = \phi_p \cdot L_p$  kadar olan koşula dayanmaktadır. Her iki deplasman hesaplandıktan sonra, deplasman sünekliği ( $\mu_{\Delta}$ ) tepe deplasmanın akma deplasmanına oranı ( $\Delta_u/\Delta_y$ ) olarak belirlenir. Yığılı plastik davranış modelinde iç kuvvetlerin plastik kapasitelerine eriştiği sonlu uzunluktaki bölgeler boyunca, plastik şekil değiştirmelerin düzgün yayılı biçimde oluştuğu varsayılmaktadır. Plastik mafsal boyu olarak adlandırılan plastik şekil değiştirme bölgesinin uzunluğu ( $L_p$ ), çalışan doğrultudaki kesit boyutunun ( $h$ ) yarısına eşit alınacaktır ( $L_p = 0.5h$ ).

$$\Delta_u = \Delta_y + \Delta_p \quad ; \quad \Delta_y = \frac{\phi_y H^2}{3} \quad , \quad \Delta_p = \theta_p (H - 0.5L_p) = (\phi_u - \phi_y)L_p (H - 0.5L_p) \quad (8)$$





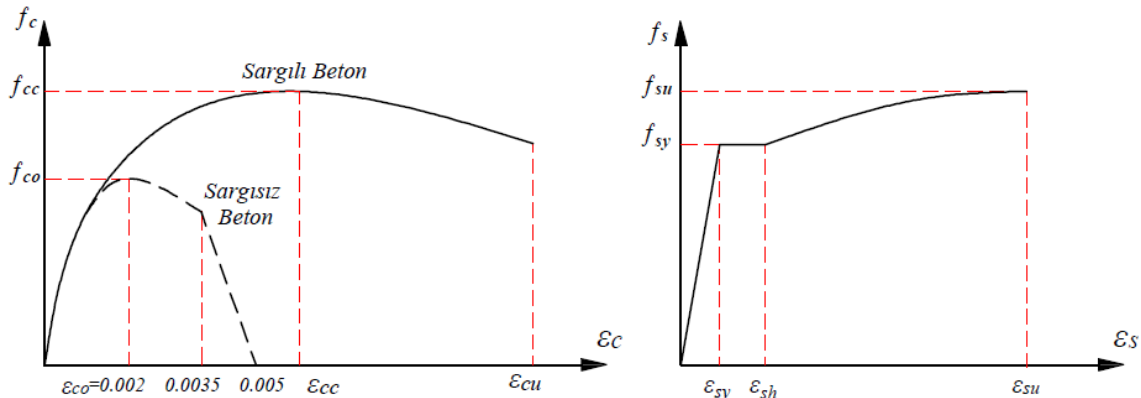
beton basınç dayanımı, enine ve boyuna donatı oranı ve eksenel yük seviyeleri dikkate alınarak SAP2000 programı ile elde edilmiştir. Düşey yükler ve deprem yüklerinin ortak etkisi altında hesaplanan eksenel basınç kuvvetlerinin en büyüğü olmak üzere,  $A_c \geq N_{dmax}/0.40f_{ck}$  koşulu sağlanmalıdır. Betonarme kolon kesitlerinde,  $N_{max} = A_c \times f_{ck}$  olmak üzere  $N/N_{max}$  oranının 0.0, 0.10, 0.20, 0.30 ve 0.40 değerleri için moment-eğrilik ilişkileri elde edilmiştir. Tasarlanan betonarme kolon modellerinde, farklı parametrelere göre moment-eğrilik ilişkilerinden akma ve kırılma koşulları için moment ( $M_y, M_u$ ) ve eğrilik ( $\phi_y, \phi_u$ ) değerleri hesaplanmıştır.

Plastik mafsal uzunluğuna göre, betonarme kolonların akma deplasman ( $\Delta_y$ ) ve plastik deplasman ( $\Delta_p$ ) değerleri hesaplanarak kolonlarının toplam tepe deplasman ( $\Delta_u$ ) değerleri elde edilmiştir. Deplasman sünekliği ( $\mu_\Delta$ ), yapısal bir sistem veya eleman konfigürasyonu ve kesit sünekliği ile ilgilidir ve yük-deplasman eğrisine dayanır. Yatay yük-tepe deplasman ilişkisinin elde edilebilmesi için öncelikle betonarme kesitin moment eğrilik ilişkisi oluşturularak, bu ilişkinin karakteristik değerleri ( $\phi_y, \phi_u$ ) belirlenmelidir. Moment eğrilik ilişkisindeki her bir eğrilik değerine ( $\phi_y, \phi_u$ ) ait deplasman değeri hesaplanmıştır. Farklı eksenel yük seviyelerine göre,  $\mu_\Delta$  değerleri betonarme kolonların  $\Delta_y, \Delta_p$  ve  $\Delta_u$  değerleri elde edilerek hesaplanmıştır.

Bazı araştırmacılar ve yönetmeliklerde kesme dayanımına beton katkısının artan deplasman süneklik talebi ile azaldığı kesme dayanımı modelleri önermişlerdir. Bazı araştırmacılar ve yönetmelikler ise betonarme kolon kesme dayanımının deplasman süneklik talebinden bağımsız olduğunu bulmuşlardır. Kolon kesitlerinden elde edilen kesme dayanımı bağıntılarına dayanarak, artan deplasman sünekliği ile hem beton hem de donatı ve beton ile donatı arasındaki etkileşimin dayanım kaybının ilerlemesine katkıda bulunduğu kaydedilmiştir. Böylece, kesme dayanımına hem beton hem de donatı katkılarına bir dayanım azaltma faktörü uygulanır. Bazı bağıntılarda ve yönetmeliklerde, süneklikle ilişkili dayanım azalması hesaba katmak için  $k$  faktörünü içeren kesme dayanımı modeli ifade edilmektedir. Önerilen bağıntılardan elde edilen kesme dayanımları ile betonarme kolon modellerinin deplasman süneklikleri arasındaki ilişkiler de incelenmiştir. TBDY'ye [8] göre kolon kesitlerinin kesme dayanımı, beton katkısı ve kesme donatısının yaptığı katkıdan oluşmaktadır.

Tablo 1. Malzeme modellerinde kullanılan parametreler

Malzeme	Parametre	Değer
Beton Sınıfı: C30-C50	Sargısız betonun maksimum gerilmeye ulaştığı birim şekil değiştirme değeri ( $\epsilon_{co}$ )	0.002
	Sargısız betonun nihai birim şekil-değiştirmesi ( $\epsilon_{cu}$ )	0.0035
	Karakteristik beton basınç dayanımı ( $f_{ck}$ )	30-50 MPa
Donatı Çeliği: B420C	Donatı çeliğinin akma birim şekil değiştirmesi ( $\epsilon_{sy}$ )	0.0021
	Donatı çeliğinin pekleşme birim şekil değiştirmesi ( $\epsilon_{sp}$ )	0.008
	Donatı çeliğinin kopma birim şekil değiştirmesi ( $\epsilon_{su}$ )	0.08
	Donatı çeliğinin karakteristik akma dayanımı ( $f_{yk}$ )	420 MPa
	Donatı çeliğinin karakteristik kopma dayanımı ( $f_{su}$ )	550 MPa



Şekil 4. Beton ve donatı çeliği için gerilme-şekil değiştirme ilişkileri

### Sayısal Çalışma

Farklı yönetmeliklere göre farklı parametrelerde tasarlanan betonarme kolonlar için elde edilen analiz sonuçları aşağıda sunulmuştur. Bazı bağıntılarda ve yönetmeliklerde, süneklikle ilişkili dayanım azalması hesaba katmak için  $k$  faktörünü içeren önerilen kesme dayanımı modeli kullanılmaktadır. Önerilen bağıntılardan elde edilen kesme dayanımları ile betonarme kolon modellerinin deplasman süneklikleri arasındaki ilişkiler araştırılmıştır. Deplasman süneklik taleplerine bağlı kesme dayanımını hesaplamak için kolon modellerinin akma eğriliği ile plastik mafsallara göre akma deplasman ve plastik deplasman değerleri hesaplanarak tepe deplasman değeri elde edilmiştir. Hesaplanan akma deplasman ile tepe deplasman değerlerine göre deplasman süneklik değerleri hesaplanmıştır. Deplasman süneklik değerlerine göre dayanım azalma faktörünün değerleri hesaplanarak kolonların kesme dayanımları hesaplanmıştır. Betonarme dairesel kolon elemanlarının  $\Delta_y$ ,  $\Delta_p$ ,  $\Delta_u$  ve  $\mu_\Delta$  değerleri plastik mafsallara göre hesaplanmıştır. Hesaplamaların sonuçları, farklı parametre seviyelerine göre sırasıyla Tablo 2, 3 ve 4'te özetlenmiştir.

Tablo 2. Farklı enine donatı çapı için betonarme dairesel kolonların deplasman değerleri

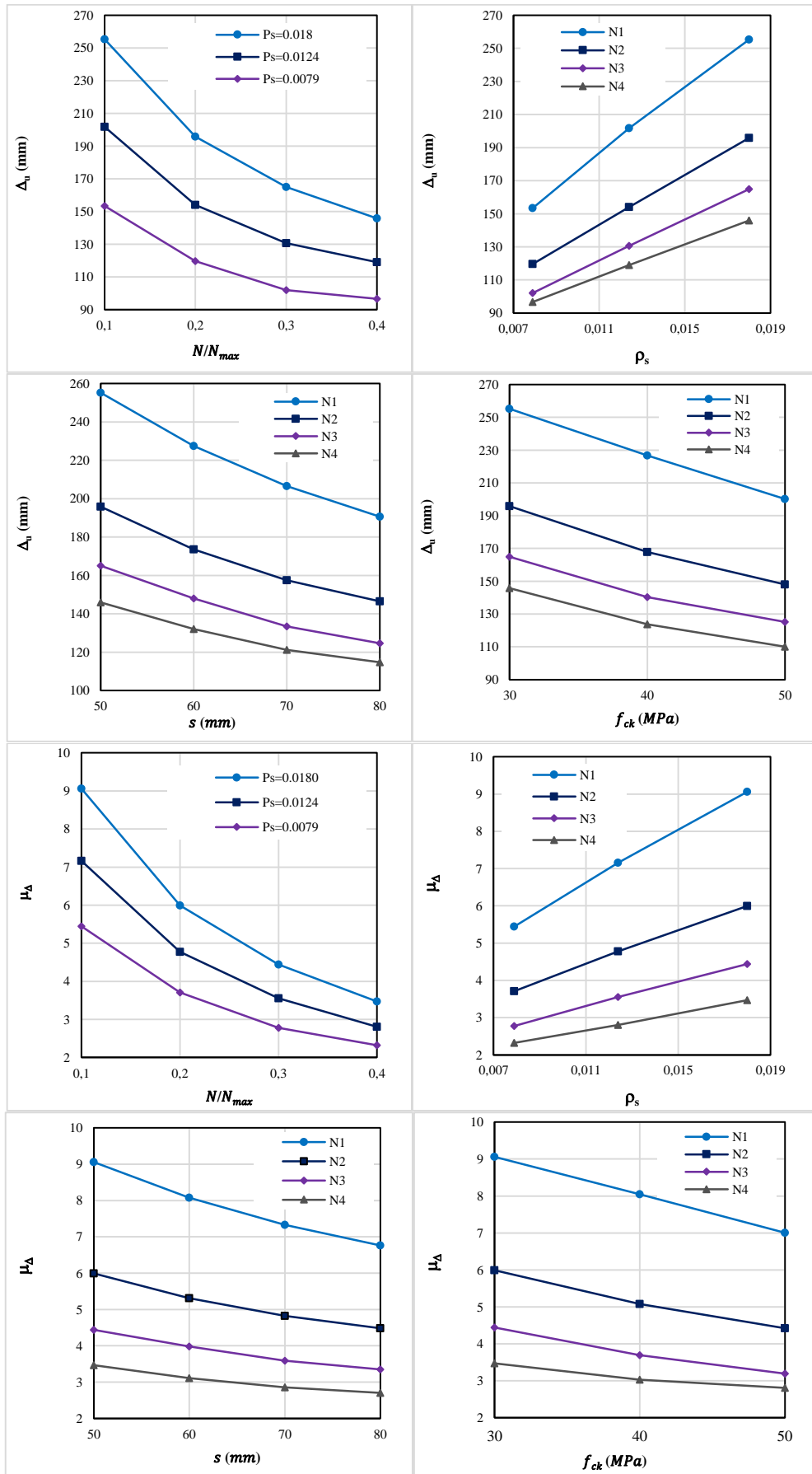
Malzeme	Spiral	$\rho_s$	$N/N_{max}$	$\Delta_y$	$\Delta_p$	$\Delta_u$	$\mu_\Delta$
C30	Φ10/50mm	0,0124	0.10	28.2	173.5	201.7	7.2
			0.20	32.3	121.8	154.1	4.8
			0.30	36.8	93.9	130.7	3.6
			0.40	42.5	76.6	119.0	2.8
	Φ12/50mm	0,0180	0.10	28.2	227.1	255.2	9.1
			0.20	32.7	163.1	195.8	6.0
			0.30	37.2	127.8	165.0	4.4
			0.40	42.1	103.8	145.9	3.5

Tablo 3. Farklı enine donatı aralığı için betonarme dairesel kolonların deplasman değerleri

Malzeme	Spiral	$\rho_s$	$N/N_{max}$	$\Delta_y$	$\Delta_p$	$\Delta_u$	$\mu_\Delta$
C30	Φ12/60mm	0,0150	0.10	28.2	199.4	227.5	8.1
			0.20	32.7	140.9	173.6	5.3
			0.30	37.2	110.8	148.0	4.0
			0.40	42.5	89.6	132.0	3.1
	Φ12/70mm	0,0128	0.10	28.2	178.4	206.6	7.3
			0.20	32.7	124.9	157.5	4.8
			0.30	37.2	96.2	133.4	3.6
			0.40	42.5	78.8	121.2	2.9
	Φ12/80mm	0,0112	0.10	28.2	162.4	190.6	6.8
			0.20	32.7	113.9	146.5	4.5
			0.30	37.2	87.4	124.5	3.4
			0.40	42.5	72.3	114.8	2.7

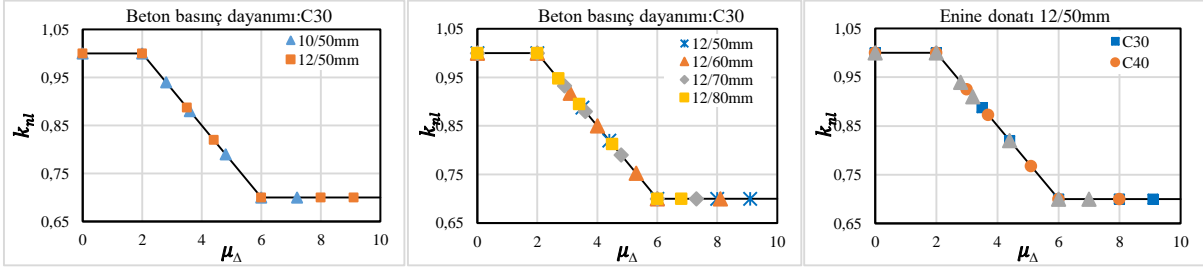
Tablo 4. Farklı eksenel yük seviyesi ile beton basınç dayanımı için betonarme dairesel kolonların deplasman değerleri

$N/N_{max}$	Spiral	$\rho_s$	Malzeme	$\Delta_y$	$\Delta_p$	$\Delta_u$	$\mu_\Delta$
0.10	Φ12/50mm	0,0180	30	28.2	227.1	255.2	9.1
			40	28.2	198.5	226.7	8.0
			50	28.6	171.6	200.2	7.0
0.20			30	32.7	163.1	195.8	6.0
			40	33.1	134.8	167.9	5.1
			50	33.5	114.6	148.1	4.4
0.30			30	37.2	127.8	165.0	4.4
			40	38.0	102.4	140.4	3.7
			50	39.2	86.0	125.2	3.2
0.40	30	42.1	103.8	145.9	3.5		
	40	40.8	82.8	123.7	3.0		
	50	39.2	70.9	110.1	2.8		

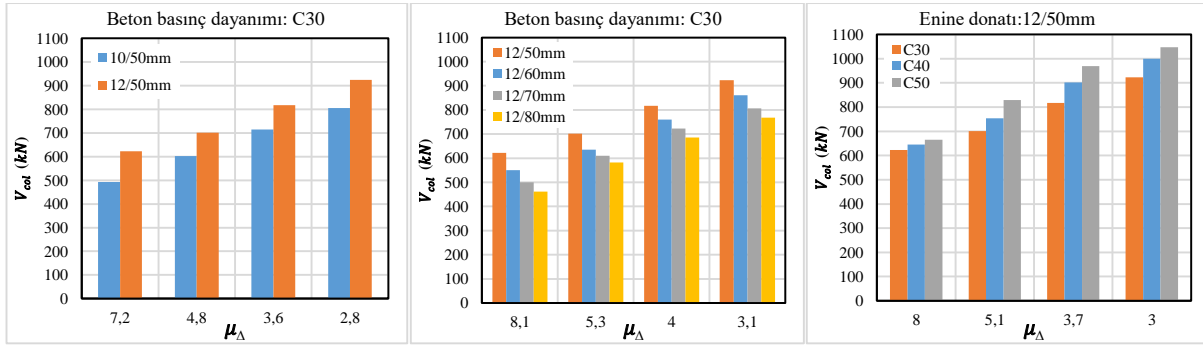


Şekil 5. Farklı parametrelerin deplasman sünekliliği üzerindeki etkisi

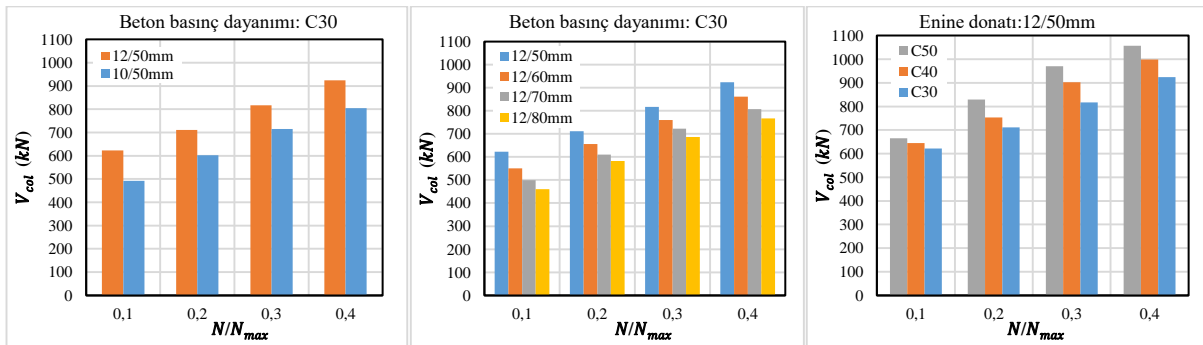
Sayısal çalışmanın bu bölümünde analiz sonuçlarından farklı parametrelerde tasarlanan dairesel enkesitli betonarme kolonların ASCE/SEI 41'e [10] göre kesme dayanımına eksenel yük seviyesi, beton basınç dayanımı, enine donatı oranı ve deplasman sünekliğinin etkisi elde edilmiştir. Elde edilen analiz sonuçları farklı parametrelere göre karşılaştırmalı olarak aşağıda sunulmuştur. TBDY [8] ve ACI318 [9] yönetmeliklerinde kesme dayanımı için önerilen ilişkilerin deplasman sünekliğinden bağımsız oluğu ve ASCE/SEI 41 [10], Sezen ve Moehle [12] tarafından geliştirilen kesme dayanımı modelini benimsediği için bu bölümde ASCE/SEI 41 [10] yönetmeliği dikkate alınmıştır.



Şekil 6. Betonarme kolonların farklı parametrelere göre elde edilen  $k_{nl} - \mu_{\Delta}$  ilişkileri



Şekil 7. Betonarme kolonların farklı parametrelere göre elde edilen  $V_{col} - \mu_{\Delta}$  ilişkileri



Şekil 8. Betonarme kolonların farklı parametrelere göre elde edilen  $V_{col} - N/N_{max}$  ilişkileri

### Sonuçlar

Betonarme kolonların kesme dayanımı ve deformasyon kapasiteleri, kolonların tasarım ve yapımında kullanılan donatı çeliğinin ve betonun malzeme özellikleriyle ilgili çok sayıda değişken tarafından etkilenir. Bu tür yapısal elemanlar için kesme dayanımı ve süneklik tahmini, tasarım yönetmeliklerde önerin bağıntılardan elde edilmiştir.

Farklı eksenel yük seviyelerine göre hesaplanan akma eğriliği, maksimum eğrilik, akma deplasmanı, plastik deplasman, toplam tepe deplasmanı ve deplasman süneklik değerlerinde farklılıklar bulunmaktadır. Eksenel yük seviyeleri arttıkça plastik deplasman, toplam tepe deplasmanı ve süneklik deplasman değerleri azalır. Betonarme dairesel en-kesitli kolonların enine donatı çapı arttıkça toplam tepe deplasmanı ve deplasman süneklik değerleri artar. Enine donatı aralığının artmasıyla toplam tepe deplasmanı ve deplasman süneklik değerleri azalmaktadır. Deplasman süneklik değeri, akma deplasman değerlerinin artması ve toplam tepe deplasman değerlerinin azalması ile azalmaktadır.

$\mu_{\Delta} \leq 2$  ve  $\mu_{\Delta} \geq 6$  değerleri için dayanım azalma faktörü ( $k_{nl}$ ) sabit bir değer ve deplasman sünekliği 2 ile 6 arasında doğrusal olarak azalmaktadır. Betonarme kolonlar için analizlerden elde edilen kesme dayanımlarının eksenel yük seviyesi, beton basınç dayanımı, enine donatı oranı ve deplasman süneklik değerlerinden etkilendiği görülmektedir. Deplasman sünekliğini artırarak, hesaplanan kesme dayanımı değerleri doğrusal olarak azalmaktadır. Artan deplasman sünekliği ile hem beton hem de donatı ve beton arasındaki etkileşimin dayanım azalmasına katkıda bulunduğu görülmektedir. Enine donatı çapının artması ile kesme dayanım değeri artmaktadır. Enine donatı aralığının artması ile hesaplanan kesme dayanım değerleri azalmaktadır. Beton basınç dayanımının artması ile hesaplanan kesme dayanım değerleri artmaktadır. Eksenel yük seviyesinin artması ile hesaplanan kesme dayanım değerleri artmaktadır. Eksenel yük seviyesinin artması ile deplasman süneklik değerleri azalmakta olduğu için  $k_{nl}$  değeri artmakta, buna göre kesme dayanım değerleri artmaktadır. Betonarme elemanların kesme dayanımını tanımlamak için sismik performans seviyesi ve empoze edilen kuvvet-deplasman geçmişi belirtilmesi gerekir.

### Referanslar

- [1] Dok G, Ozturk H, Demir A. determining moment-curvature relationship of reinforced concrete columns. The Eurasia Proceedings of Science, Technology, Engineering and Mathematics. 2017; 1:52-58.
- [2] Foroughi S, Yüksel SB. Betonarme kolonların şekil değiştirme esaslı hasar sınırlarının araştırılması. Uluslararası Mühendislik Araştırma ve Geliştirme Dergisi. 2019; 11(2):584-601.
- [3] Fiore A, Marano GC, Laucelli D, Monaco P. Evolutionary modeling to evaluate the shear behavior of circular reinforced concrete columns. Advances in Civil Engineering. 2014; 1-14.
- [4] Gordon NP. Prediction of shear strength and ductility of cyclically loaded reinforced concrete columns using artificial intelligence. Master of Science in Engineering-Civil and Environmental Engineering. University of Nevada, Las Vegas. 2015.
- [5] Wight JK, Sozen MA. Shear strength decay in reinforced concrete columns subjected to large deflection reversals. UIUL-ENG-73-2017 Report, University of Illinois, Illinois, 1973.
- [6] Ergüner K. Analytical examination of performance limits for shear critical reinforced concrete columns. Master of Science in Civil Engineering Department, Middle East Technical University. 2009.
- [7] Sasani M. Shear strength and deformation capacity models for reinforced concrete columns. 13th World Conference on Earthquake Engineering. Vancouver, B.C., Canada, August 1-6, 2004:Paper No. 1838
- [8] TBDY. Türkiye Bina Deprem Yönetmeliği, T.C. Bayındırlık ve İskân Bakanlığı, 2018, Ankara, Türkiye.
- [9] ACI 318. Building Code Requirements for Structural Concrete and Commentary, American Concrete Institute, U.S.A. 2014.
- [10] ASCE Standard, 41. Seismic Evaluation and Retrofit of Existing Buildings, (ASCE/SEI 41), Published by the American Society of Civil Engineers, Reston, Virginia, USA. 2017.
- [11] TS500. Betonarme Yapıların Tasarım ve Yapım Kuralları, Türk Standardları Enstitüsü, 2000, Ankara, Türkiye.
- [12] Sezen H, Moehle J. Shear strength model for lightly reinforced concrete columns. ASCE Journal of Structural Engineering. 2004; 130(11):1692-1703.
- [13] Aschheim AM, Moehle JP. Shear strength and deformability of RC bridge columns subjected to inelastic displacements. Technical Report: UCB/EERC 92/04. University of California, Berkeley. 1992: 93 pp.
- [14] Konwinski CM, Ramirez JA, Sozen MA. Shear strength of reinforced concrete columns subject to seismic loading. Proceedings of the National Seismic Conference on Bridges and Highways: Progress in Research and Practice, San Diego, California. December 10-13, 1995.

## Betonarme Taşıyıcı Sistem Elemanlarının Etkin Kesit Rijitliklerinin Araştırılması

*Saeid Foroughi\**, Konya Teknik Üniversitesi, Mühendislik ve Doğa Bilimleri Fakültesi, İnşaat Mühendisliği Bölümü, Konya, Türkiye

*Süleyman Bahadır Yüksel*, Konya Teknik Üniversitesi, Mühendislik ve Doğa Bilimleri Fakültesi, İnşaat Mühendisliği Bölümü, Konya, Türkiye

\*İletişimden sorumlu yazar: saeid.foroughi@yahoo.com

**Anahtar Kelimeler:** Deprem performansı, betonarme taşıyıcı sistem, etkin kesit rijitlikleri, moment-eğrilik, eksenel kuvvet

**Disiplin:** İnşaat Mühendisliği

### Özet

Ulusal ve uluslararası deprem yönetmeliklerinde betonarme yapıların deprem performanslarının belirlenmesinde tasarım aşamasında betonarme taşıyıcı elemanlarda çatlama kesite ait etkin kesit rijitliklerinin kullanılması istenmektedir. Eğilme rijitliği yapı elemanının yük alma kapasitesine etki etmektedir. Betonarme taşıyıcı sistemlerin etkin kesit rijitliklerinin hesaplanmasında, gerçekçi yollardan birisi de moment-eğrilik ilişkilerinin kullanılmasıdır. Betonarme kesitlerde çatlama kesite ait etkin kesit rijitlikleri, moment-eğrilik ilişkisi göz önüne alınarak, akma momentinin akma eğriliğine karşılık gelen oranı ile belirlenir. Çatlama kesite ait etkin kesit rijitlikleri sabit olmamakla beraber kesitin boyutu, beton dayanımı ve kesite etkiyen eksenel kuvvet gibi parametrelere bağlıdır. Bu çalışmada etkin kesit rijitliklerinin araştırılması için farklı beton sınıfı, boyuna donatı oranı, yatay donatı çapı ve yatay donatı aralığına sahip betonarme kolon ve kiriş modelleri tasarlanmıştır. Farklı parametrelerde tasarlanan betonarme taşıyıcı sistem elemanlarında çatlama kesite ait etkin kesit rijitliği ve etkin rijitlik katsayısı analitik olarak elde edilmiştir. Analitik olarak araştırılan parametreler Türkiye Bina Deprem Yönetmeliği (TBDY, 2018), Amerikan Beton Enstitüsü (ACI318, 2014), Mevcut Binaların Sismik Değerlendirmesi ve Güçlendirilmesi (ASCE/SEI-41, 2017) ve Depreme Dayanıklı Yapıların Tasarımı (Eurocode8, 2004) yönetmeliklerinden ve kesitlerin moment-eğrilik ilişkilerinden hesaplanmıştır. Moment-eğrilik ilişkileri için farklı beton sınıfı, boyuna donatı oranı, yatay donatı çapı, yatay donatı aralığı ve eksenel yük seviyeleri dikkate alınarak SAP2000 programı kullanılmıştır. Analizlerden elde edilen etkin kesit rijitlikleri, farklı yönetmeliklerde betonarme taşıyıcı sistem elemanları için verilen etkin kesit rijitliği çarpanları ile karşılaştırılmıştır. Karşılaştırma sonuçları detaylı olarak irdelenerek yorumlanmıştır. Etkin kesit rijitlikleri ile ilgili gerçekleştirilen analitik çözümler, yapılan kabuller çerçevesinde bir yaklaşık içermektedir. Bu nedenle farklı yönetmeliklere göre analitik çözümlerin sonuçlarının da birbirinden farklı olması olasıdır. Tasarlanan betonarme taşıyıcı sistem elemanlarında, eksenel yük seviyesi, beton sınıfı, yatay donatı ve boyuna donatı oranının artması ile analiz sonuçlarından elde edilen etkin kesit rijitlik değerleri ve etkin rijitlik katsayısı artmaktadır.

### Giriş

Beton çatlama, betonarme elemanların eğilme ve kesme rijitliğini azaltır. Bu nedenle, betonarme yapıların çatlama etkisini dikkate almadan analiz edilmesi gerçek davranışı temsil etmeyebilir. Beton çatlama kaynağından kaynaklanan etkili eğilme rijitliği, beton ve donatı çeliğinin sargılaması, eksenel yük seviyesi, kesit boyutları ve malzeme özellikleri gibi bazı önemli parametrelere bağlıdır [1]. Bir binanın yapısal elemanlarının varsayılan rijitlikleri, binanın yer sarsıntısına karşı hesaplanan tepkisini güçlü bir şekilde etkiler. Doğrusal analiz için, eleman rijitlikleri, yapının periyodunun tahminlerini, yapı içindeki yük dağılımını ve deformasyon taleplerini kontrol eder. Doğrusal olmayan analiz için, akma deplasmanını güvenilir bir şekilde tahmin etmek için eleman rijitliğinin doğru bir tahmini gereklidir ve bu da, tahmin edilen süneklik deplasman taleplerini etkiler [2]. Kesit rijitliği tahminindeki doğruluk seviyesi, yapısal rijitlik için gerçekçi değerlerin ve dolayısıyla uygulanan sismik kuvvetlerin belirlenmesinde çok önemli bir rol oynar. Betonarme kesitlerin teorik akmasının yanı sıra çatlamanın etkisini de yansıtan etkin rijitliği etkileyen en önemli parametreler, çeşitli betonarme kesitlerin kapsamlı moment-eğrilik analizleri ile belirlenir [3]. Betonarme yapıların sismik analizi ve tasarımı doğrusal tepkiye göre yapılır, ancak şiddetli depremler altında elastik olmayan tepki ve çatlakların kabul edildiği evrensel olarak kabul edilmektedir. Bu nedenle eleman özelliklerinin bu durumu yansıtmaması ve betonarme kiriş ve kolonların atalet momentlerinin buna göre azaltılması gerekir [4].

Betonarme taşıyıcı elemanların etkin rijitliği konusunda çeşitli araştırmalar yapılmıştır. Mirza [5], narin kolonların eğilme rijitliğini etkileyen parametreleri araştırmış ve eksantriklik oranını dikkate alarak tasarım için önerilen denklemleri incelemiştir. Paulay ve Priestley [6], betonarme elemanlarının eğilme rijitliğini etkileyen çeşitli faktörleri araştırmış ve ortalama değerleri önermiştir. Mehanny vd., [7], eksenel yük seviyesini dikkate alarak kiriş ve kolonların etkili eğilme ve kesme rijitliği katsayılarını belirlemek için basit formüller önermiştir. Panagiotakos ve Fardis [8], çatlama betonarme elemanların etkili elastik rijitliğini tahmin etmek için gerekli olan elemanların akma ve nihai deformasyon kapasiteleri için ifadeler geliştirmiştir. Khuntia ve Ghosh [9], boyuna donatı ve eksenel yükün eksantrikliğinin etkisini dikkate alarak, genel olarak çerçevelerin yanal analizinde ve kolonlarda kullanılacak basit etkili rijitlik modellerinin kullanılmasını önermiştir. Kumar ve Singh [10], bina tasarımında kullanılacak normal dayanımlı ve yüksek dayanımlı betonarme elemanlar için iki farklı etkin rijitlik modeli önermiştir. Pan vd., [11] etkin kesit rijitliği için azaltma faktörünü araştırmış ve etkin kesit rijitlik tahmininin doğruluğunu ispatlamak için farklı yöntemler önermiştir.

Bahsi geçen çalışmalar çoğu kodların ve yönetmeliklerin temelini oluşturmuştur. Yaygın olarak kullanılan yönetmeliklerde ve yönergelerde, elemanların etkili rijitliği, brüt kesit özellikleri temelinde hesaplanan, rijitliklerinin bir oranı olarak ifade edilir. Betonarme elemanların etkin rijitliklerinin dikkate alınması için; Türk Bina Deprem Yönetmeliği (TBDY, 2018) [12], Amerikan Beton Enstitüsü (ACI318, 2014) [13], Mevcut Binaların Sismik Değerlendirmesi ve Güçlendirilmesi (ASCE/SEI-41, 2017) [14], Depreme Dayanıklı Yapıların Tasarımı (Eurocode8, 2004) [15] yönetmeliklerinde çeşitli prosedürler önerilmektedir. Farklı parametrelerde tasarlanan betonarme taşıyıcı elemanlarının çatlama kesitlerinin etkin rijitliği ve etkin rijitlik katsayısı analitik olarak incelenmiştir. Analitik olarak araştırılan parametreler TBDY [12], ACI318 [13], ASCE/SEI-41 [14] ve Eurocode8 [15] yönetmeliklerinden ve kesitlerin moment-eğrilik ilişkilerinden hesaplanarak karşılaştırılmıştır. Moment-eğrilik ilişkileri için, farklı beton dayanımı, yatay ve boyuna donatı oranı ve farklı eksenel yük seviyeleri dikkate alınarak SAP2000 yazılımı [16] kullanılmıştır.

## Betonarme Taşıyıcı Sistem Elemanlarının Etkin Kesit Rijitlikleri

### Moment-eğrilik ilişkilerine göre etkili kesit rijitlik katsayısı

Çatlakların etkisini ve betonarme kesitlerinin teorik akmasını yansıtan etkin rijitliği etkileyen en önemli parametreler, betonarme kesitlerin kapsamlı moment eğrilik analizleri ile belirlenir. Etkin rijitlik sadece çatlamanın etkisini değil, aynı zamanda moment-eğrilik analizlerinden belirlenen betonarme elemanların davranışını da yansıtır. Betonarme taşıyıcı elemanların etkin rijitliği ( $EI_e$ ), moment-eğrilik ilişkilerinin başlangıç bölümünün eğimi olarak tanımlanmıştır. Bu tanım hem çatlamanın etkilerini hem de betonarme kesitlerin teorik olarak akmasını yansıtır. Betonarme elemanlardaki çatlama kesitin etkin rijitliği, moment-eğrilik ilişkisi dikkate alınarak akma momentine ( $M_y$ ) ve akma eğrisine ( $\phi_y$ ) karşılık gelen oran ( $EI_e = M_y/\phi_y$ ) ile belirlenmiştir.  $EI_e$  sabit olmayıp ve kesitin boyutu, beton dayanımı ve kesite etkileyen eksenel kuvvet gibi parametrelere bağlıdır. Betonarme kolonların brüt atalet momenti ( $I$ ) ve betonun elastisite modülü ( $E_c$ ) değerleri kullanılarak çatlama kesit rijitlikleri ( $EI$ ) hesaplanmıştır. Beton sınıfları için TS500'de [17] verilen beton karakteristik basınç dayanımlarına ( $f_{ck}$ ) göre  $E_c$  değerleri hesaplanmıştır ( $E_c = 3250 + \sqrt{f_{ck}} + 14000$ ). Betonarme taşıyıcı sistemlerin etkin kesit rijitliklerinin hesaplanmasında, gerçekçi yollardan birisi de moment-eğrilik ilişkilerinin kullanılmasıdır. Betonarme elemanların etkin rijitlik katsayısı;  $k_e = EI_e/EI$  olarak hesaplanmaktadır.

### TBDY'de önerilen etkili kesit sertlik katsayısı

Ulusal ve uluslararası deprem yönetmeliklerinde, betonarme yapıların sismik performansı belirlenirken, tasarım aşamasında betonarme yapısal elemanlarda çatlama kesitin etkin rijitliklerinin kullanılması istenmektedir. Dayanıma Göre Tasarım kapsamında betonarme taşıyıcı sistem elemanlarının kesit özelliklerinin modellenmesinde Tablo 1'de verilen etkin kesit rijitliği çarpanları kullanılacaktır. Etkin kesit rijitlikleri çarpanları, sadece deprem etkili yük birleşimleri içinde yer alan ve bu birleşimlere giren yükler altındaki hesaplarda uygulanacaktır.

Tablo 1. Betonarme taşıyıcı elemanlar için etkin kesit rijitliği çarpanları [12]

Betonarme Taşıyıcı Sistem Elemanları	Etkin Kesit Rijitlik Katsayıları	
<i>Çubuk Elemanı</i>	<i>Eğilme</i>	<i>Kesme</i>
Bağ Kirişi	0,15	1,0
Çerçeve Kirişi	0,35	1,0
Çerçeve Kolonu	0,70	1,0
Perde (Eşdeğer Çubuk)	0,50	0,50

Yığılı plastik davranışına göre modellenen kolon, kiriş, bağ kirişi ve perdelerin etkin kesit rijitlikleri  $(EI)_e$  Denklem (1)'e göre hesaplanacaktır.  $M_y$  ve  $\theta_y$  çubuk elemanın uçlarındaki plastik mafsalların etkin akma momentleri ile akma dönmelerinin ortalamalarını göstermektedir.  $L_s$ ; ise kesme açıklığıdır (M/V), betonarme kolon ve kirişlerde yaklaşık olarak açıklığın yarısı, betonarme perde duvarlarda ise her katın tabanından perde tepesine olan yüksekliğin yarısı olarak alınabilir [12].

$$(EI)_e = \frac{M_y L_s}{\theta_y 3} \quad (1)$$

Doğrusal olmayan hesap için deprem etkisi altında binaların şekil değiştirmeye göre değerlendirme ve tasarımı için etkin kesit rijitlikleri kullanılarak yapılan hesapta SH performans düzeyi için taşıyıcı sistemde plastik mafsal oluşumuna izin verilmeyecektir. Doğrusal olmayan hesap için taşıyıcı sistemlerin akma durumu için yer değiştirmiş plastik mafsal akma dönmesi ( $\theta_y$ ) Denklem (2) ile hesaplanmıştır. Yeni yapılacak binaların şekil değiştirmeye göre değerlendirilme ve tasarımında beton ve donatı çeliği için TBDY'de [12] tanımlanan beklenen dayanımları esas alınacaktır ( $f_{ce}=1.3f_{ck}$ ,  $f_{ye}=1.2f_{yk}$ ).  $f_{ce}$  ve  $f_{ck}$  sırasıyla betonun ortalama ve karakteristik basınç dayanımlarıdır. Betonarme kiriş ve kolonlarda  $\eta=1$  alınacaktır.

$$\theta_y = \frac{\phi_y L_s}{3} + 0.0015\eta \left(1 + 1.5 \frac{h}{L_s}\right) + \frac{\phi_y d_b f_{ye}}{8\sqrt{f_{ce}}} \quad (2)$$

### Eurocode 8'de önerilen etkili kesit rijitlik katsayısı

Eurocode 8'e [15] göre betonarme taşıyıcı elemanların rijitliği, donatı akmasının başlamasına karşılık gelen çatlama etkisi dikkate alınarak değerlendirilmelidir. Eurocode 8'e [15] göre, betonarme elemanlarındaki doğrusal kuvvet-deformasyon ilişkisinin elastik rijitliği, çatlak bölümlerinkine ve donatı akmasının başlamasına karşılık gelmelidir. Çatlamış elemanların daha doğru bir analizi yapılmadıkça, bu standart, betonarme elemanların elastik eğilme ve kayma direnci özelliklerinin, çatlama elemanın karşılık gelen rijitliğinin %50'si olarak alınmasını önerir.

### ACI318 standardında önerilen etkili kesit sertlik katsayısı

İkinci derece etkiler nedeniyle basınç elemanları ve çerçevelerdeki momentlerin büyütülmesi için etkili rijitlik aşağıdaki gibi belirlenir. Kirişler ve çatlamış perde duvarlar için 0.35 kolonlar ve çatlama perde duvarlar için 0.70 olarak dikkate alınmaktadır.

Tablo 2. Azaltma faktörleri [13]

Taşıyıcı eleman	Etkin rijitlik
Kiriş	$0.35I_g$
Kolon	$0.70I_g$

Tablo 2'de verilen azaltma faktörlerine ek olarak (alternatif olarak), basınç ve eğilme elemanlarının atalet momentlerinin (I), aşağıdaki şekilde hesaplanmalıdır. Basınç elemanları:

$$I = \left(0.80 + 25 \frac{A_{st}}{A_g}\right) \left(1 - \frac{M_u}{P_u h} - 0.5 \frac{P_u}{P_o}\right) I_g \leq 0.875 I_g \quad (3)$$

Eğilme elemanları:



$$I = (0.10 + 25\rho) \left(1.2 - 0.2 \frac{b_w}{d}\right) I_g \leq 0.5I_g \quad (4)$$

( $I$ ), basınç elemanları için  $0.35I_g$ 'den ve eğilme elemanları için  $0.25I_g$ 'den daha az alınmamalıdır. Denklemde,  $A_{st}$  boyuna donatı toplam alanı,  $A_g$  beton kesitin brüt alanı,  $M_u$  kesitin nihai momenti.  $P_u$  faktörlü eksenel kuvveti,  $P_o$  nominal eksenel kuvveti,  $h$  kesit yüksekliğidir.  $\rho$  düşey donatı oranı,  $b_w$  kesit genişliği ve  $d$  faydalı yüksekliktir.

#### ASCE/SEI-41 standardında önerilen etkili kesit sertlik katsayısı

Mevcut binaların sismik değerlendirmesi ve güçlendirilmesinde [14] Betonarme taşıyıcı elemanlar için rijitlik azaltma katsayı değerleri Tablo 3'te verilmiştir. .

Tablo 3. Betonarme taşıyıcı elemanlar için rijitlik azaltma katsayı değerleri [14]

Betonarme Eleman Tipi	Eğilme Rijitliği	Kayma Rijitliği	Eksenel Rijitliği
Kirişler: Ön Gerilmesiz	$0.3E_{cE}I_g$	$0.4E_{cE}A_w$	--
Kirişler: Ön Gerilmli	$E_{cE}I_g$	$0.4E_{cE}A_w$	--
Tasarım Düşey Yüklerinden dolayı kolonda oluşan eksenel kuvvet $\geq 0.5A_gf'_{cE}$	$0.7E_{cE}I_g$	$0.4E_{cE}A_w$	$E_{cE}A_g$
Tasarım Düşey Yüklerinden dolayı kolonda oluşan eksenel kuvvet $\leq 0.1A_gf'_{cE}$ veya kolonda çekme kuvveti olması.	$0.3E_{cE}I_g$	$0.4E_{cE}A_w$	$E_{cE}A_g$ (Basınç) $E_{cE}A_s$ (Çekme)

#### Materyal ve Yöntem

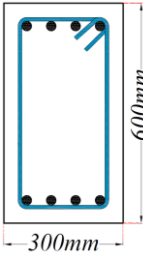
Ulusal ve uluslararası deprem yönetmeliklerinde betonarme yapıların sismik performansının belirlenmesinde, tasarım aşamasında betonarme yapı elemanlarında çatlak kesitinin etkin kesit rijitliklerinin kullanılması istenmektedir. Betonarme yapı elemanlarının etkili kesit rijitliklerini hesaplamının gerçekçi analizlerinden biri, moment-eğrilik ilişkilerinin kullanılmasıdır. Betonarme yapı elemanlarında çatlak kesitinin etkili kesit rijitlikleri, moment-eğrilik ilişkisi dikkate alınarak akma momentinin akma eğriliğine oranı ile belirlenir. Çatlaklı bölümün etkili kesit rijitlikleri, beton dayanımı ve eksenel yük seviyeleri gibi parametrelere bağlıdır. Bu çalışmada, etkili kesit rijitliğini araştırmak için farklı beton basınç dayanımı, boyuna donatı oranı, yatay donatı oranına sahip betonarme kolon ve kiriş modelleri tasarlanmıştır. Farklı parametrelerde tasarlanan betonarme yapı elemanlarının çatlaklı kesitinin etkin kesit rijitliği ve etkin rijitlik katsayısı analitik olarak araştırılmıştır. Analitik olarak incelenen parametreler TBEC [12], ACI318 [13], ASCE/SEI41 [14], Eurocode 8 [15] yönetmelikleri ve kesitlerin moment-eğrilik ilişkilerinden hesaplanmış ve karşılaştırılmıştır. Betonarme kiriş, kolon ve perde duvar modelleri, beton dayanımı, boyuna ve yatay donatı oranı ve eksenel yük seviyelerinin etkin kesit rijitliği üzerindeki etkisini incelemek için tasarlanmıştır.

Moment-eğrilik ilişkisi, kesit mukavemeti, eğilme rijitliği ve kesit sünekliğini tahmin etmek için yapıların elastik olmayan analizi için esastır. Betonarme elemanlar için, teorik moment-eğrilik analizi, hem beton hem de donatı çeliğinin gerilme-şekil değiştirme ilişkilerinin bilinmesi durumunda yapılabilir. Moment-eğrilik ilişkileri farklı beton basınç dayanımı, yatay ve boyuna donatı oranı ve eksenel yük seviyeleri dikkate alınarak SAP2000 programı [16] ile elde edilmiştir.

Betonarme kirişlerin tasarımında dikkat edilmesi gereken en önemli husus, elde edilen kesitte donatı oranının dengeli donatı oranından daha küçük olmasını sağlamaktır. Yönetmelikler bu durumu zorunlu kıldığından, bu çalışmada TS500'de [17] verilen sınır değerler dikkate alınmıştır. TS500'de [17], betonarme kirişlerde sünek davranış sağlamak için donatı oranı Denklem (5) ile sınırlandırılmıştır. Kirişlerde çekme ve basınç donatı oranları arasındaki fark, denge donatının  $0.85$ 'ini geçmemelidir. Farklı parametrelere sahip tasarlanan betonarme kiriş kesitlerinin detayları Tablo 4'te verilmiştir.

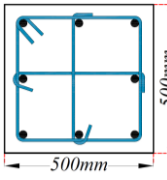
$$\rho = \frac{A_s}{b_w d} \geq \rho_{min} = 0.8 \frac{f_{ctd}}{f_{yd}}, \quad (\rho - \rho') \leq \rho_{max} = 0.85\rho_b, \quad \rho_b = 0.85k_1 \left(\frac{f_{cd}}{f_{yd}}\right) \left(\frac{600}{600 + f_{yd}}\right) \quad (5)$$

Tablo 4. Tasarlanan betonarme kiriş kesitlerinin detay ve özellikleri

En-kesit boyutları	$\rho'/\rho$	Malzeme: C30		Malzeme: C35		Malzeme: C40		Malzeme: C45		Malzeme: C50	
		$\rho_{max}$	$\rho'$	$\rho_{max}$	$\rho'$	$\rho_{max}$	$\rho'$	$\rho_{max}$	$\rho'$	$\rho_{max}$	$\rho'$
	0		0		0		0		0		0
	0.1		0.0021		0.0024		0.0026		0.0028		0.0030
	0.2		0.0043		0.0048		0.0053		0.0057		0.0061
	0.3		0.0064		0.0072		0.0079		0.0085		0.0091
	0.4		0.0085		0.0096		0.0105		0.0114		0.0121
	0.5	0.0213	0.0107	0.0240	0.0120	0.0263	0.0132	0.0285	0.0142	0.0303	0.0152
	0.6		0.0128		0.0144		0.0158		0.0171		0.0182
	0.7		0.0149		0.0168		0.0184		0.0199		0.0212
	0.8		0.0171		0.0192		0.0211		0.0228		0.0243
	0.9		0.0192		0.0216		0.0237		0.0256		0.0273
	1		0.0213		0.0240		0.0263		0.0285		0.0303

Her bir betonarme kolon modeli için altı farklı boyuna donatı çapı ve iki farklı yatay donatı çapı kullanılmaktadır. Boyuna donatı çapının etkin eğilme rijitliği üzerindeki etkisini incelemek için boyuna donatı çapları 20mm, 22mm, 24mm, 26mm, 28mm ve 30mm seçilmiştir. Betonarme kolon kesitlerinde kullanılan donatı çapları ve donatı oranları TBDY'de [12] ve TS500 [17] verilen sınırlamalar dikkate alınarak belirlenmiştir. Yatay donatı çapının aralığının etkili eğilme rijitliği üzerindeki etkisini araştırmak için farklı yatay donatı çapları (10mm ve 12mm) seçilmiştir. Her bir betonarme kolon modeli için üç farklı yatay donatı aralığı seçilmiştir (50mm, 75mm ve 100mm). Tasarlanan betonarme kolon kesitlerinin farklı parametrelere sahip detayları Tablo 5'te verilmiştir.

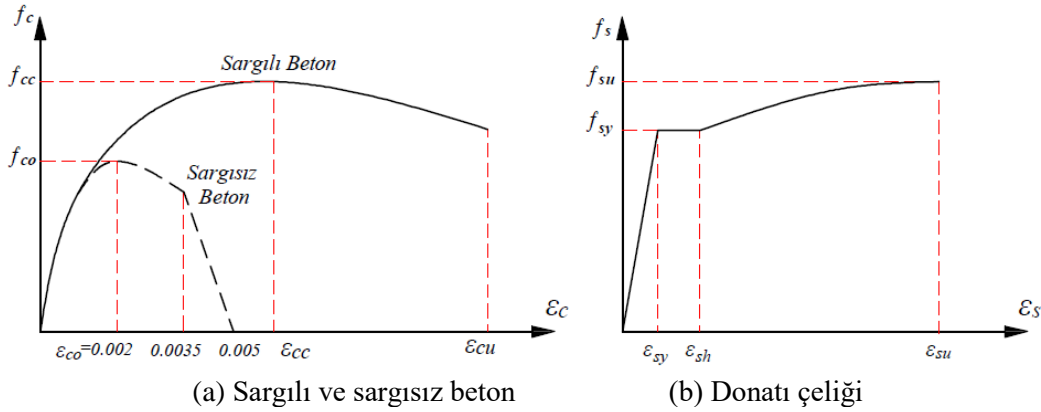
Tablo 5. Tasarlanan betonarme kolon kesitlerinin detay ve özellikleri

Malzeme	En-kesit boyutları	Boyuna donatı	Yatay donatı	Yatay donatı aralığı	Eksenel yük (N/N <sub>max</sub> )
		8Φ20mm			
C30		8Φ22mm			0.10
C35		8Φ24mm	Φ10mm	50mm	0.20
C40		8Φ26mm	Φ12mm	75mm	0.30
C45		8Φ28mm		100mm	0.40
C50		8Φ30mm			

Moment-eğrilik ilişkileri ise malzemelerin doğrusal olmayan davranışları dikkate alınarak farklı parametreler için SAP2000 programı ile elde edilmiştir. Betonarme elemanların üç farklı malzeme modelinden oluştuğu düşünülmüştür. SAP2000 programı ile yapılan moment-eğrilik analizlerinde, kabuk betonu için Mander sargısız beton modeli, çekirdek betonu için Mander sargılı beton modeli [18] ve donatı çeliği için Tablo 6'da verilen pekleşmeli model kullanılmıştır. Tüm betonarme elemanlar için beton sınıfı olarak C30, C35, C40, C45 ve C50, donatı davranış modeli için donatı olarak B420C seçilmiştir. Moment-eğrilik analizlerinde, sargısız beton ve donatı çeliği için malzeme modelleri Tablo 6 ve Şekil 1'de verilmiştir. Moment-eğrilik analizlerinde betonun çekme dayanımı ihmal edilmiştir.

Tablo 6. Malzeme modellerinde kullanılan parametreler

Malzeme	Parametre	Değer
Beton Sınıfı: C30-C50	Sargısız betonun maksimum gerilmeye ulaştığı birim şekil değ. değeri ( $\epsilon_{co}$ )	0.002
	Sargısız betonun nihai birim şekil-değiştirmesi ( $\epsilon_{cu}$ )	0.0035
	Karakteristik beton basınç dayanımı ( $f_{ck}$ )	30-50MPa
Donatı Çeliği: B420C	Donatı çeliğinin akma birim şekil değiştirmesi ( $\epsilon_{sy}$ )	0.0021
	Donatı çeliğinin pekleşme birim şekil değiştirmesi ( $\epsilon_{sp}$ )	0.008
	Donatı çeliğinin kopma birim şekil değiştirmesi ( $\epsilon_{su}$ )	0.08
	Donatı çeliğinin karakteristik akma dayanımı ( $f_{yk}$ )	420MPa
	Donatı çeliğinin karakteristik kopma dayanımı ( $f_{su}$ )	550MPa



Şekil 1. Beton ve donatı çeliği için gerilme-şekil değiştirme ilişkileri

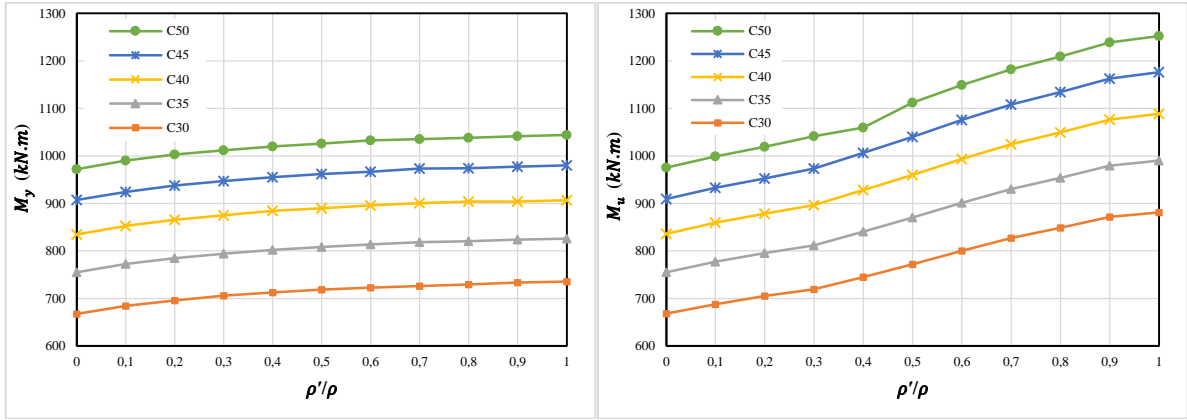
Farklı standartlar ve kodlar, betonarme elemanlarının rijitliğini değiştirmek için çeşitli yönergeler sağlar. Yapısal analiz yaparken, elemanların etkili rijitliğini belirlemek için birden fazla kod ve standardı gözden geçirmek yararlıdır. Birden çok kaynaktan elde edilen bilgiler, tasarımcının halihazırda değerlendirmekte olduğu belirli yapı için daha doğru bir analiz yöntemi ortaya çıkarabilir. Analitik olarak incelenen parametreler, farklı standart, kodlardan ve kesitlerin moment-eğrilik ilişkilerinden hesaplanmıştır. Analiz sonuçlarından elde edilen etkin rijitlik değerleri detaylı olarak Araştırma Bulguları ve Tartışma bölümünde sunulmuştur.

#### Araştırma Bulguları ve Tartışma

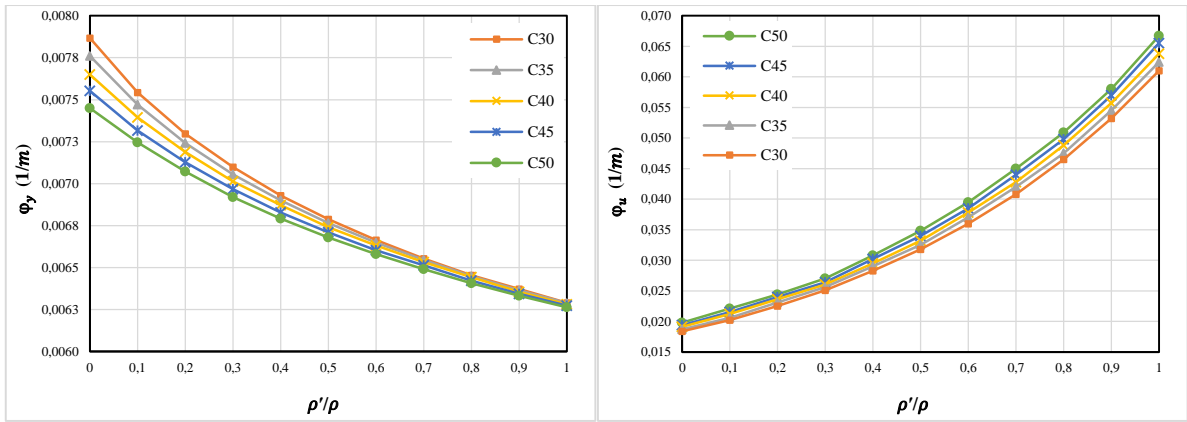
Farklı parametrelerde tasarlanan betonarme yapı elemanlarının çatlamış kesitlerinin rijitliği ve etkin rijitlik katsayısı analitik olarak elde edilmiştir. Analitik olarak incelenen parametreler, farklı deprem yönetmeliklerinden önerilen çeşitli prosedürlerden ve moment-eğrilik ilişkilerinden hesaplanmıştır. Analizlerden elde edilen etkin kesit rijitlik katsayısı, farklı yönetmeliklerde betonarme elemanlar için verilen etkin rijitlik katsayısı ile karşılaştırılmıştır. Önerilen yönetmeliklerinden ve moment-eğrilik ilişkilerinden elde edilen değerlerin karşılaştırılmasıyla yorumlanmıştır. Mevcut eğilme momentini ve eğriliği gösteren betonarme yapı elemanları için teorik moment-eğrilik analizi, hem beton hem de donatı çeliği için gerilme-şekil değiştirme ilişkilerinin bilinmesi şartıyla yapılabilir. Farklı parametrelere sahip betonarme yapı elemanlarının moment-eğrilik ilişkilerinin hesaplanması aşağıdaki paragraflarda hesaplanmıştır. Çalışmanın bu bölümünde, moment-eğrilik ilişkileri tasarım parametreleri değiştirilerek elde edilmiştir. Etkili rijitlik ( $EI_{eff}$ ), bu çalışmada moment-eğrilik diyagramının ilk segmentinin eğimi olarak tanımlanmıştır. Bu tanım hem çatlamadan etkilerini hem de betonarme kesitlerinin teorik akmasını yansıtır. İlk akmaya karşılık gelen noktanın tanımı ve moment-eğrilik ilişkisi elde etme prosedürü oldukça önemlidir. Tasarlanan betonarme yapı modellerinde, farklı parametrelere göre moment-eğrilik ilişkilerinden akma ve kırılma durumları için moment ( $M_y$ ,  $M_u$ ) ve eğrilik ( $\phi_y$ ,  $\phi_u$ ) değerleri, etkin eğilme rijitliği ( $EI_e$ ) ve etkin rijitlik katsayısı ( $k_e$ ) hesaplanmıştır.

#### Dikdörtgen en-kesitli betonarme kiriş

Farklı beton basınç dayanımı, farklı çekme ve basma donatı oranlarına sahip toplam 55 adet betonarme kiriş modeli tasarlanmıştır (Tablo 4). Betonarme kiriş modellerinin tasarımında TBDY [12] ve TS500 [17] hükümleri dikkate alınmıştır. Farklı parametrelerde tasarlanan betonarme kiriş modellerinde çekme donatısının oranı olarak;  $\rho_{max} = 0.85\rho_b$  ve basınç güçlendirme oranı olarak;  $\rho'_s = 0.0, 0.1\rho_{max}, 0.2\rho_{max}, 0.3\rho_{max}, 0.4\rho_{max}, 0.5\rho_{max}, 0.6\rho_{max}, 0.7\rho_{max}, 0.8\rho_{max}, 0.9\rho_{max}$  ve  $\rho_{max}$  değerleri dikkate alınmıştır. Betonarme kiriş modellerinde C30, C35, C40, C45 ve C50 olarak beş farklı beton sınıfı dikkate alınır. Kiriş modellerinde, her beton dayanımı için çekme donatı oranı  $\rho_{max} = 0.85\rho_b$  ile sabit tutulmuştur. Tasarlanan betonarme kiriş modellerinde, farklı parametrelere göre moment-eğrilik ilişkilerinden akma ve kırılma koşulları için moment ( $M_y$ ,  $M_u$ ) ve eğrilik ( $\phi_y$ ,  $\phi_u$ ) değerleri, etkin rijitlik katsayısı ( $k_e$ ) hesaplanmıştır. Betonarme kirişlerde maksimum eksenel yük değeri  $N = 0.10 \times A_c \times f_c$  ile sınırlı olduğundan bu analizlerde  $N = 0$  olarak dikkate alınmıştır.

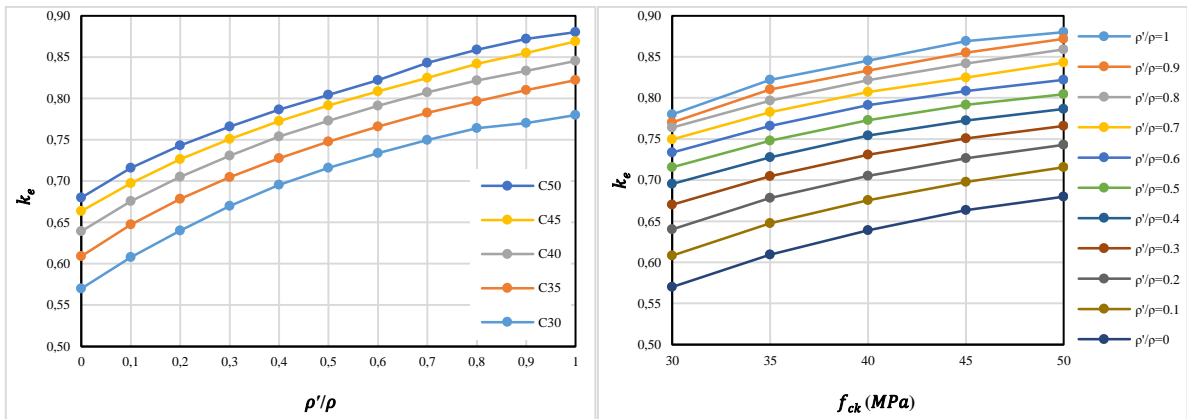


Şekil 2.  $\rho'/\rho$  ve beton basınç dayanımının akma ve maksimum moment üzerindeki etkisi

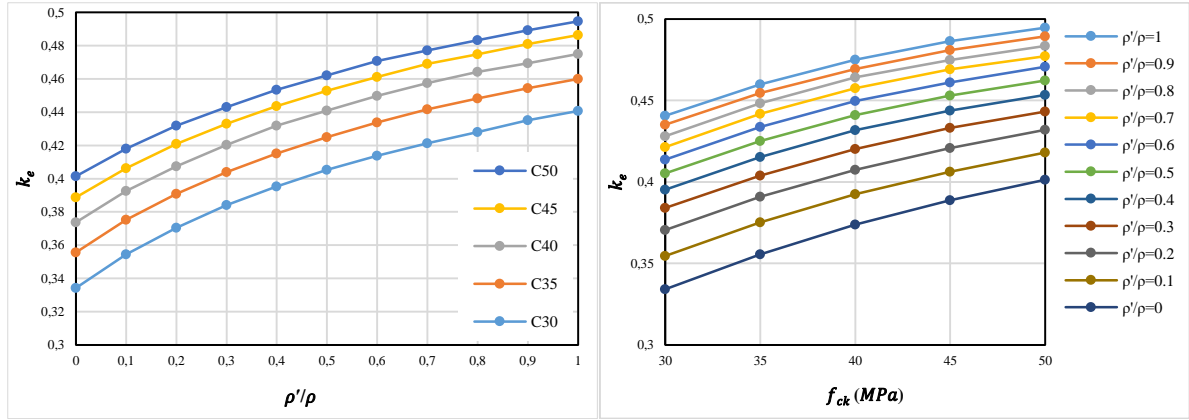


Şekil 3.  $\rho'/\rho$  ve beton basınç dayanımının akma ve maksimum eğrilik üzerindeki etkisi

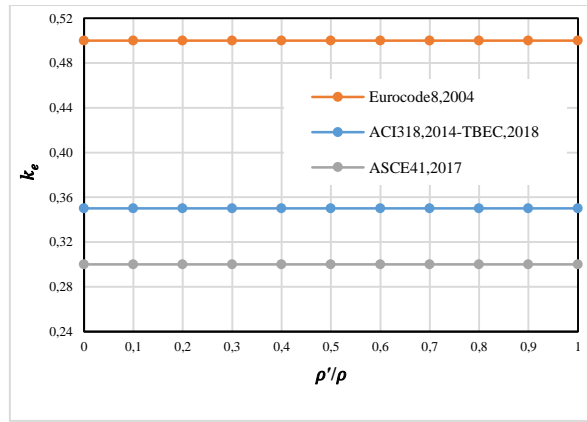
On bir farklı boyuna donatı oranına ve beş farklı beton basınç dayanımına sahip dikdörtgen kesitli kirişlerin etkin rijitlik katsayılarını belirlemek için toplam 55 farklı analiz yapılmıştır. Farklı parametrelere sahip dikdörtgen kiriş elemanlarının moment-eğrilik analizi sonuçlarından elde edilen efektif kesit rijitlik oranları ve yönetmeliklerden elde edilen analiz sonuçları Şekil 4-6'da verilmiştir. Şekil 4'teki moment-eğrilik ilişkilerine göre  $k_e - \rho'/\rho$  ilişkisi (SAP2000), Şekil 5'te TBDY'de [12] verilen yığılı plastik davranışa göre ve Şekil 6'da farklı sismik kodlara göre özetlenmiştir. Dikdörtgen kirişler için farklı prosedürlere göre analiz sonuçlarından elde edilen etkili kesit rijitlik oranlarının karşılaştırması Şekil 7'de verilmiştir.



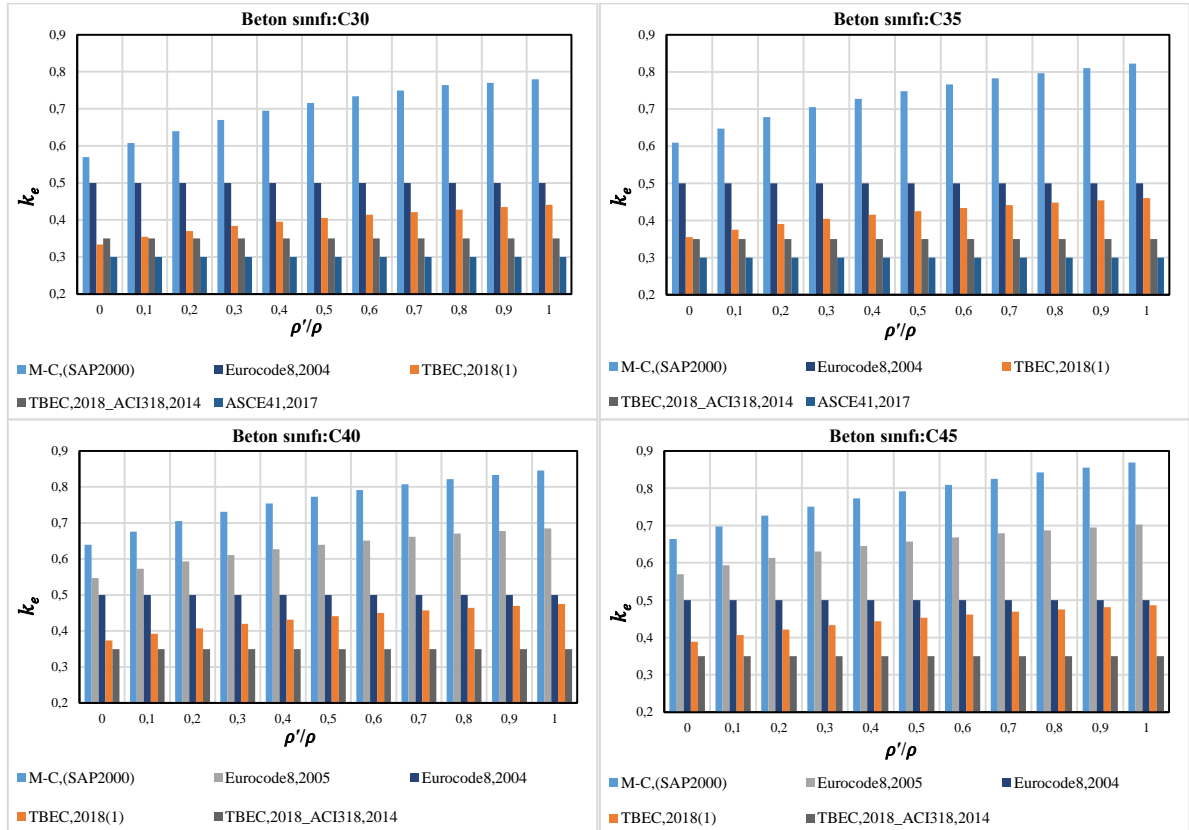
Şekil 4. Farklı parametrelere göre moment-eğrilik ilişkilerinden elde edilen  $k_e$  değerleri

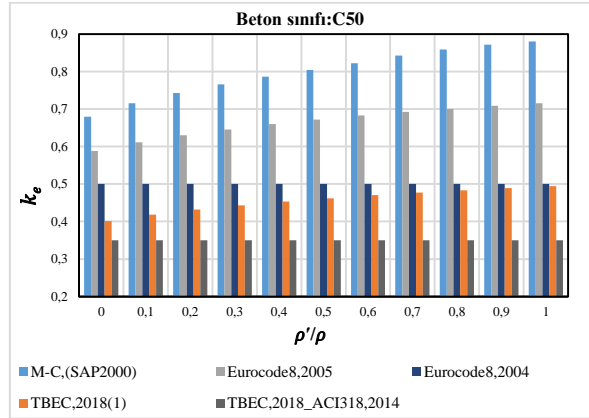


Şekil 5. TBDY (2018)'de verilen doğrusal olmayan davranışa göre elde edilen  $k_e$  değerleri



Şekil 6.  $\rho'/\rho$  ve beton basınç dayanımının etkin kesit rijitlik katsayısı üzerindeki etkisi

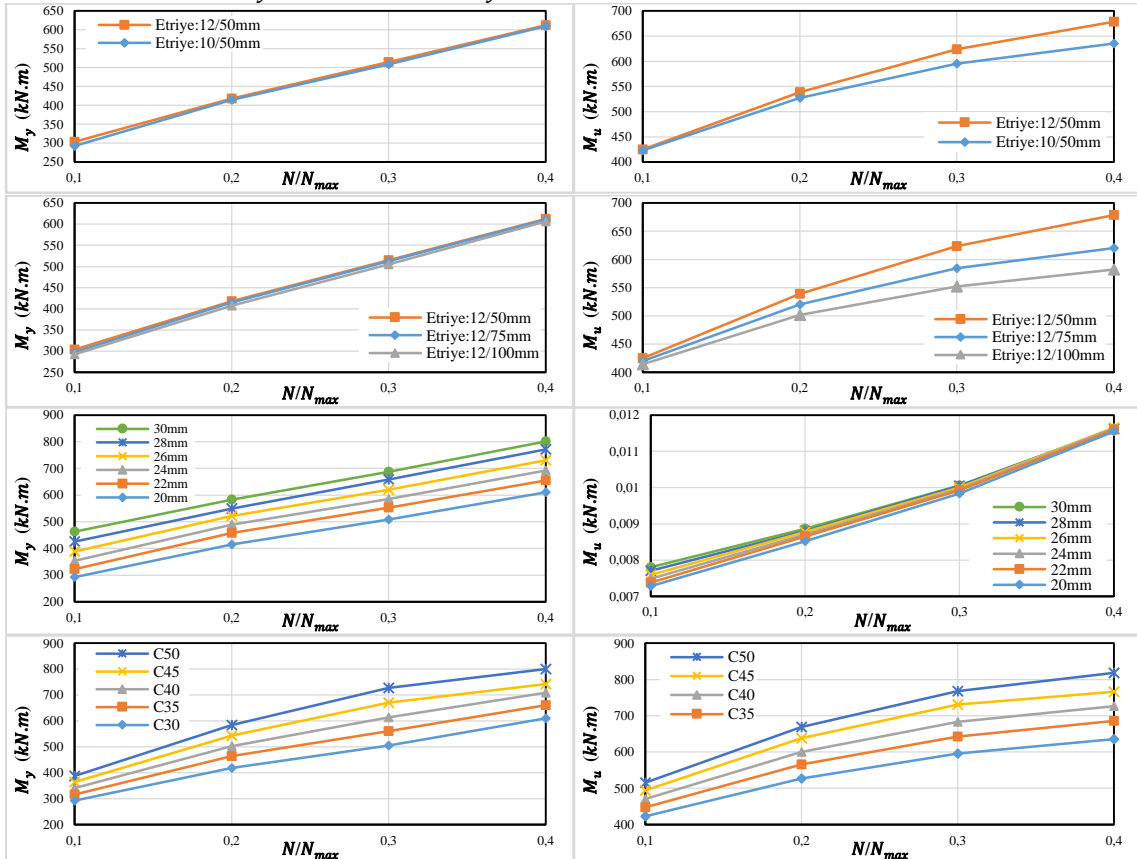




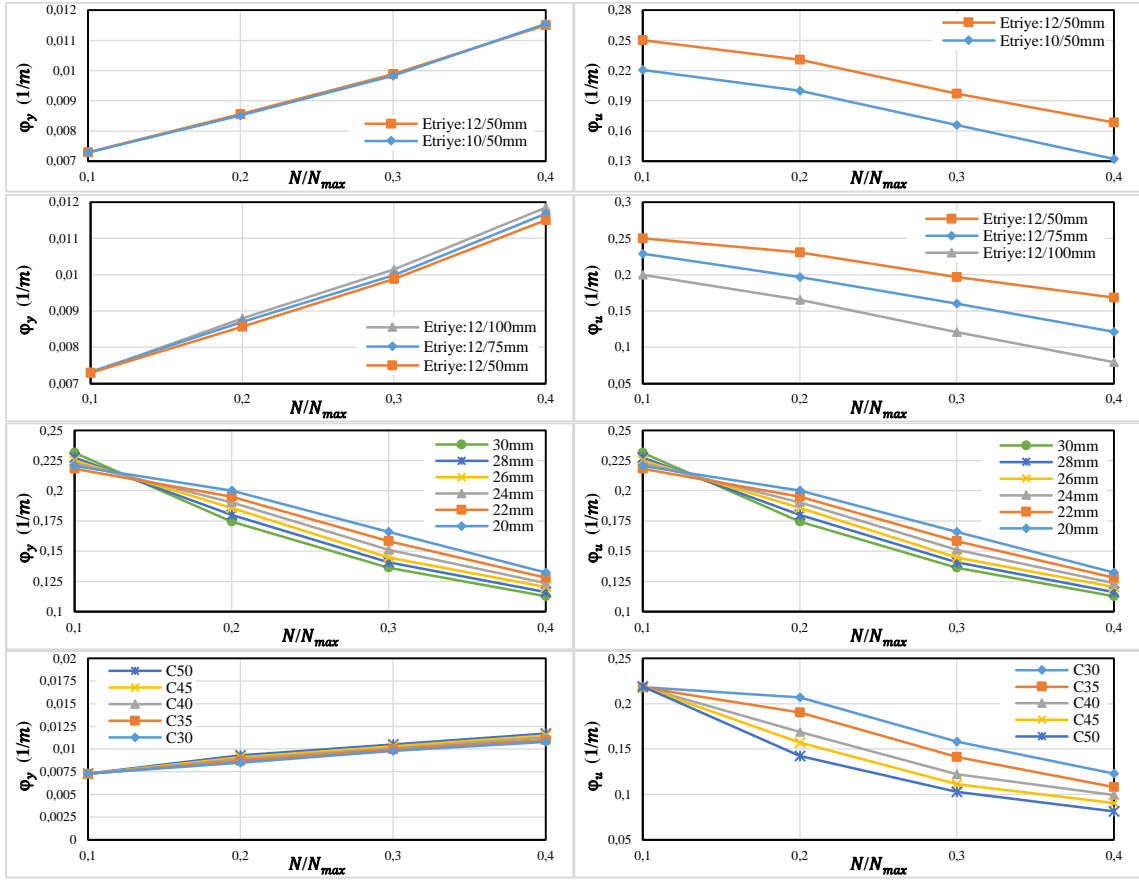
Şekil 7. Farklı parametrelere göre karşılaştırmalı  $k_e - \rho'/\rho$  ilişkileri

### Betonarme Kolonlar

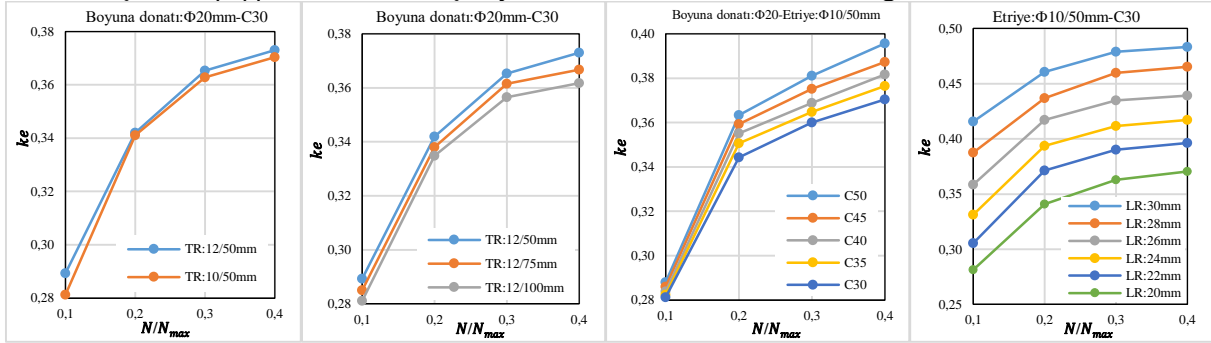
Bu çalışmada, beton basınç dayanımı, boyuna donatı oranı, yatay donatı çapı, yatay donatı aralığı ve eksenel yük seviyelerinin tasarlanan kare en-kesitli betonarme kolon modellerin etkin kesit rijitliğine etkileri incelenmiştir. Betonarme kolon modellerinin davranışı moment-eğrilik ilişkisi ile incelenmiştir. Farklı parametrelerde tasarlanan kare en-kesitli kolonların moment-eğrilik ilişkilerini ve etkin rijitlik katsayılarını belirlemek için toplam 720 farklı analiz yapılmıştır. Kombine eğilme altındaki bir kesitin moment-eğrilik ilişkileri, eksenel yük seviyelerine bağlıdır. Düşey yükler ve deprem yüklerinin ortak etkisi altında hesaplanan eksenel basınç kuvvetlerinin en büyüğü olmak üzere,  $A_c \geq N_{dmax}/0.40f_{ck}$  koşulu sağlanmalıdır. Betonarme kolon kesitlerinde,  $N_{max} = A_c \times f_{ck}$  olmak üzere  $N/N_{max}$  oranının 0.0, 0.10, 0.20, 0.30 ve 0.40 değerleri için moment-eğrilik ilişkileri elde edilmiştir. Tasarlanan betonarme kolon modellerinde, farklı parametrelere göre moment-eğrilik ilişkilerinden akma ve kırılma koşulları için moment ( $M_y$ ,  $M_u$ ) ve eğrilik ( $\phi_y$ ,  $\phi_u$ ) değerleri, etkin rijitlik katsayısı ( $k_e$ ) hesaplanmıştır.



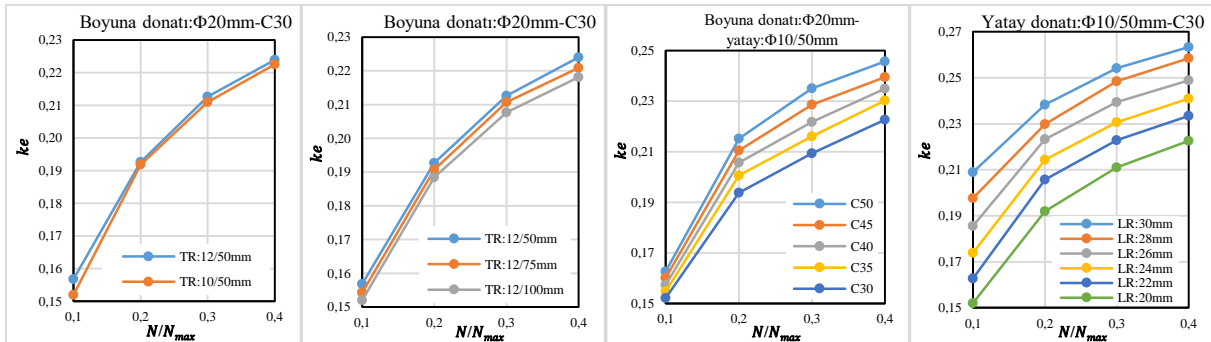
Şekil 8.  $\rho'/\rho$  ve beton basınç dayanımının akma ve maksimum moment üzerindeki etkisi



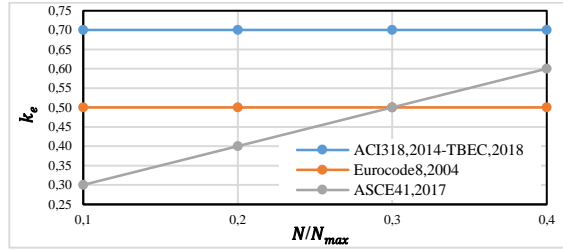
Şekil 9.  $\rho' / \rho$  ve beton basınç dayanımının akma ve maksimum eğrilik üzerindeki etkisi



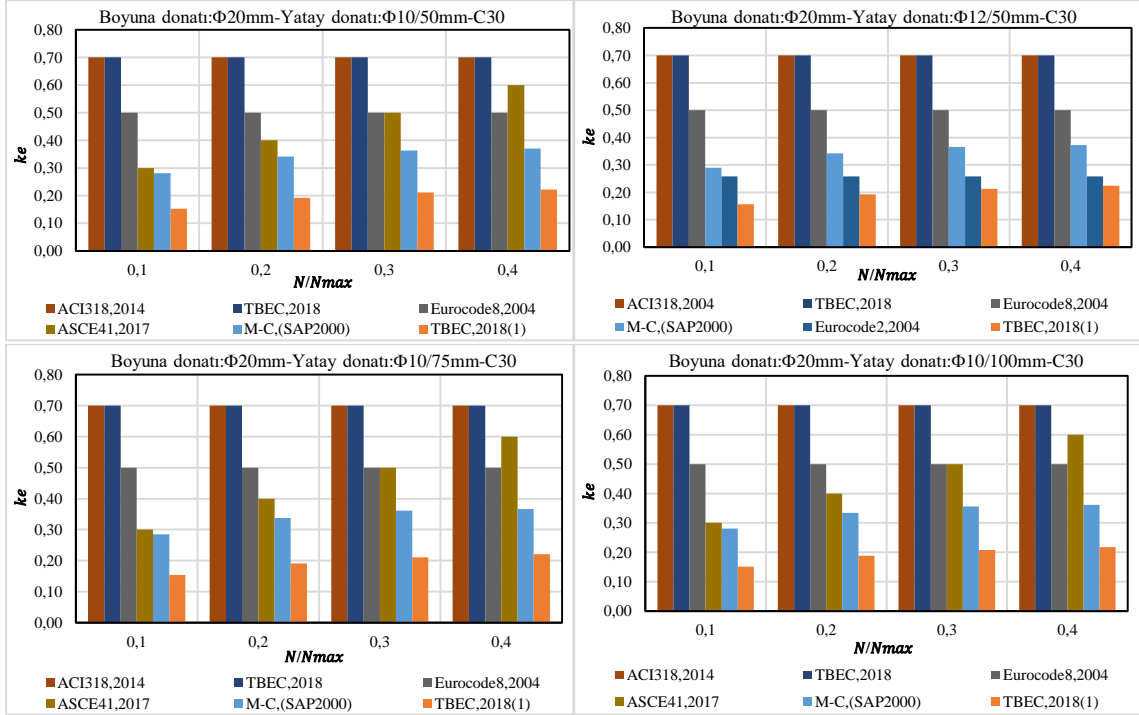
Şekil 10. Farklı parametrelere göre moment-egrilik ilişkilerinden elde edilen  $k_e$  değerleri



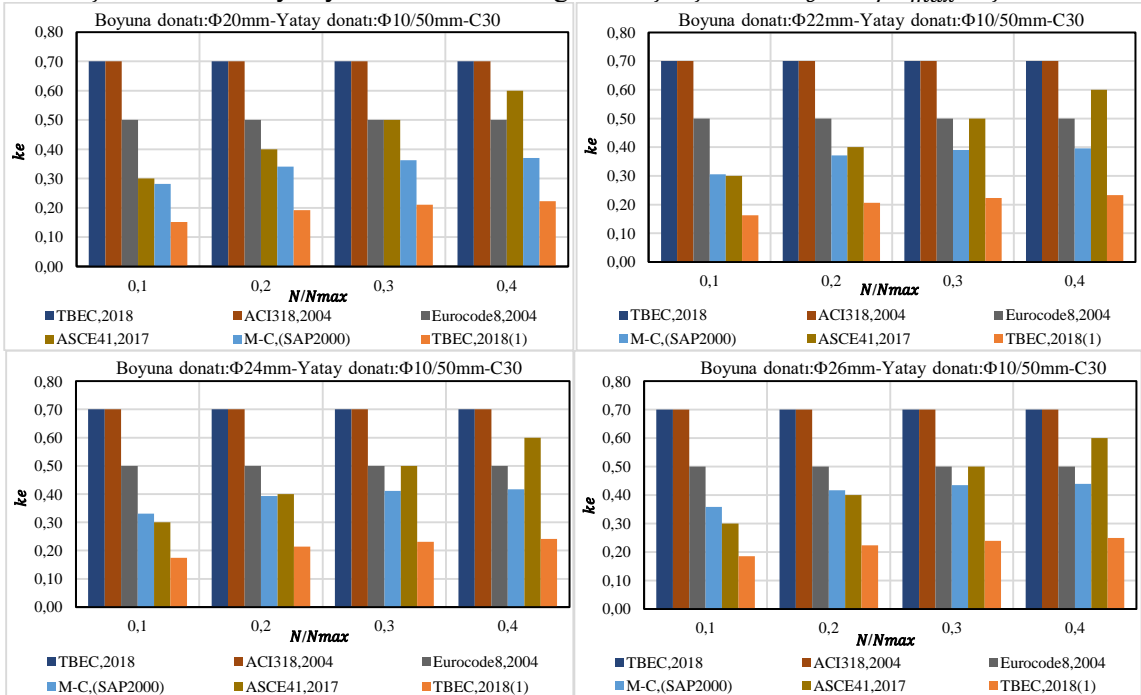
Şekil 11. TBDY (2018)'de verilen doğrusal olmayan davranışa göre elde edilen  $k_e$  değerleri



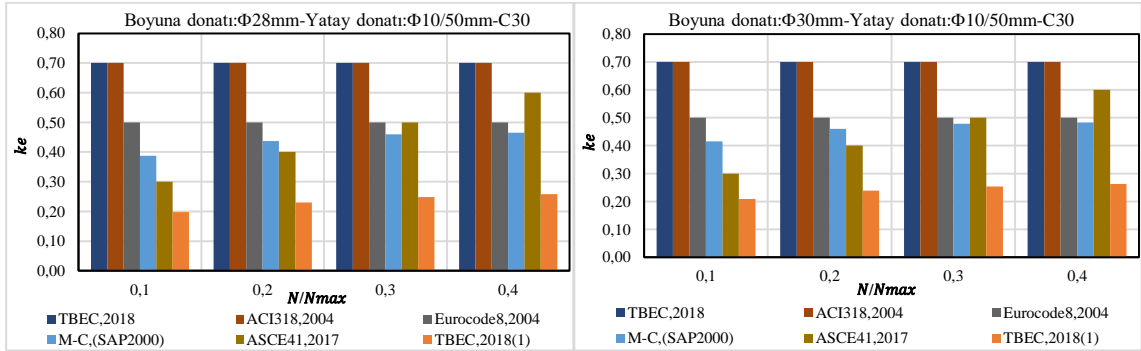
Şekil 12. Farklı yönetmeliklere göre elde edilen  $k_e$  değerleri



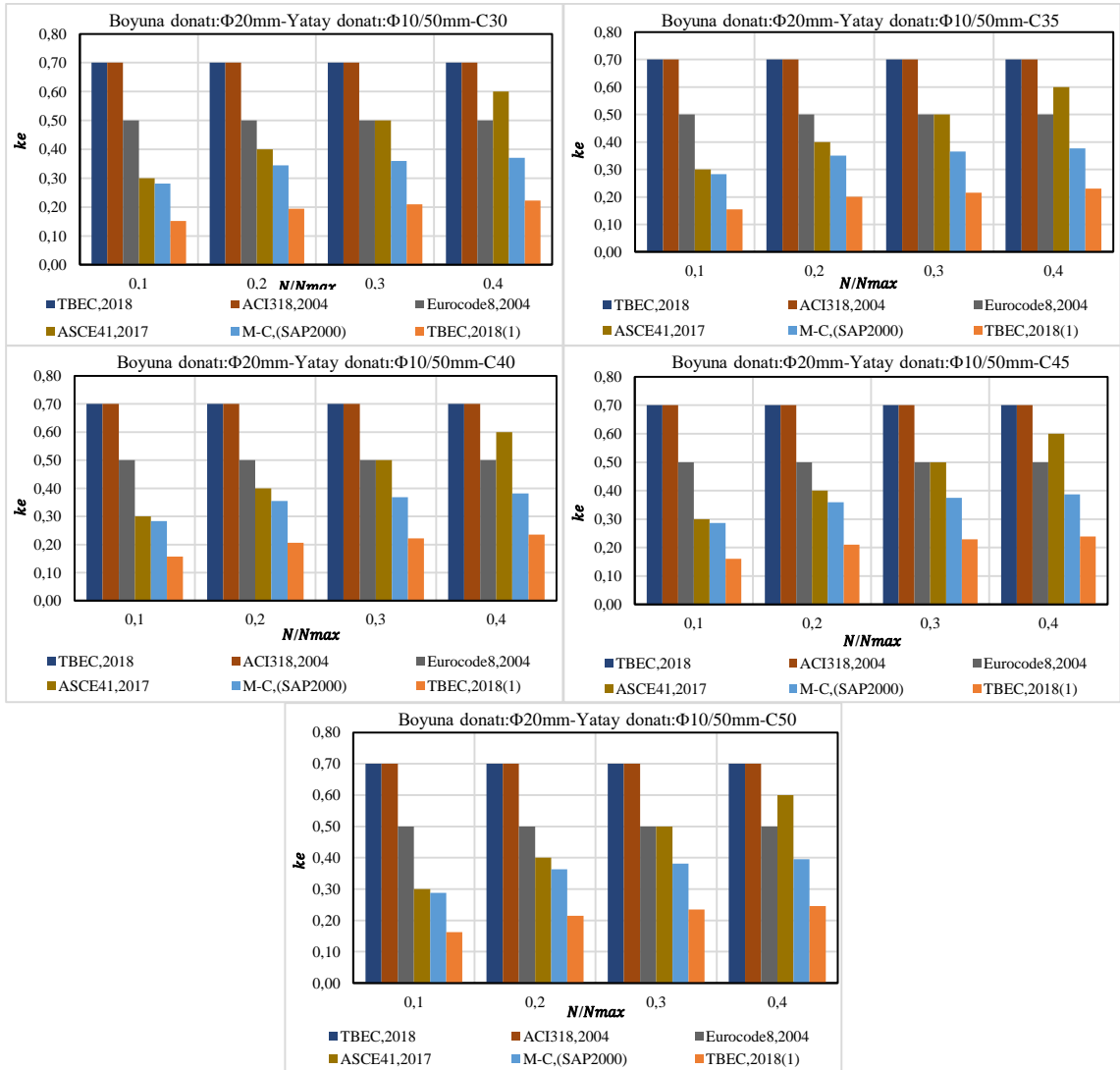
Şekil 13. Farklı yatay donatı oranlarına göre karşılaştırmalı  $k_e - N/N_{max}$  ilişkileri







Şekil 14. Farklı boyuna donatı oranlarına göre karşılaştırmalı  $k_e - N/N_{max}$  ilişkileri



Şekil 15. Farklı beton basınç dayanımlarına göre karşılaştırmalı  $k_e - N/N_{max}$  ilişkileri

### Sonuçlar

Betonarme kirişlerde farklı parametrelerinin etkin rijitlik katsayısı, farklı yönetmeliklerde önerilen ilişkilere ve doğrusal olmayan moment-eğrilik analizi kullanılarak kapsamlı parametrik çalışmalarla incelenmiştir. ACI318'de [13], bir betonarme kirişin akmaya kadar etkili rijitliği, eğilme ve kesme çatlağının etkisini hesaba katmak için bir azaltma faktörüyle birlikte kesitsel atalet momenti ile tahmin edilir. ACI318 [13], kolonlar için sabit bir  $0.70E_cI_c$  oranı ve betonarme kirişler için  $0.35E_cI_c$  oranı verilmektedir. ASCE/SEI-41'de [14],  $EI_{eff}$  öngerilmemiş kirişler için  $0.3E_cI_g$  olarak belirtilmiştir. Tasarım düşey yükü  $0.1A_gf_c$ 'den az olan kolonlar için  $EI_{eff}$ , 0.3 olarak belirtilmiştir.  $0.5A_gf_c$ 'den büyük

basınç kuvvetine sahip kolonlar için bu katsayı 0.7 olarak verilmiştir. Eurocode 8’de [15] verilen çatlak kesitin efektif kesit rijitlik değeri sabittir. Çatlamış kesitin etkin rijitliği, başlangıçtaki rijitliğin yarısı olarak kabul edilir. Eurocode 8’de [15] beton dayanımı, kesit geometrisi, boyuna ve yatay donatı oranı ve kesite etki eden eksenel kuvvet gibi özellikler dikkate alınmamaktadır. Benzer şekilde TBDY’de [12] etkin kesit rijitliğinin sabit olduğu varsayılırken, kirişler için çatlamış kesitin etkin rijitlik katsayısı değerleri 0.35 ve betonarme kolonlar için 0.70 olarak kabul edilmektedir. TBDY’de [12] yığılı plastik davranışına göre modellenen betonarme kirişlerin etkin kesit rijitliği, etkin akma momentleri, akma dönmesi ve kesme açıklığına bağlı olarak hesaplanabilir. Etkin kesit rijitliğinin sabit olmadığı düşünülerek kesit boyutu, donatı oranı ve beton dayanımı gibi parametrelere dayalı bir formülasyon önerilmektedir.

Kesit akma noktasını ve kesitin etkin rijitliğini etkileyen en önemli faktörler olarak geometri, beton dayanımı ve basınç ve çekme donatılarının miktarı belirlenmiştir. Etkili kesit rijitlik katsayısı için bazı araştırmacılar tarafından önerilen ilişkilerde yatay donatı etkisi yönetmeliklerde olduğu gibi dikkate alınmamaktadır. Dolayısıyla kesit boyutu, beton basınç dayanımı, yatay donatı etkisi ve kesite etki eden eksenel kuvvet gibi parametrelerin etkilerinin ihmal edilmesi anlamına gelmektedir. Bu durum, betonarme elemanlarının tasarımında ve değerlendirilmesinde gerçekçi olmayan sonuçlara yol açabilir. Bu nedenle betonarme elemanların tasarımında ve değerlendirilmesinde moment-eğrilik ilişkisinin belirlenmesi ve etkin kesit rijitlik değerlerinin elde edilmesi daha gerçekçi sonuçlar elde etmek için büyük önem taşımaktadır.

Analiz sonuçları incelendiğinde betonarme donatı oranı, basma donatı oranı ve beton dayanımındaki değişimin betonarme kirişlerin moment-eğrilik davranışı üzerinde önemli bir etkiye sahip olduğu görülmektedir. Betonarme kirişlerde basınç donatı oranının artmasıyla moment-eğrilik ilişkilerinden elde edilen  $M_y$ ,  $M_u$  ve  $\varphi_u$  değerleri artmakta ve  $\varphi_y$  değerleri azalmaktadır. Basınç donatı oranının artması ile kesitlerin maksimum moment taşıma kapasitesi ve sünekliği artar. Beton basınç dayanımının artmasıyla birlikte betonarme kirişlerin maksimum moment taşıma kapasitesi artar.

Betonarme kolonların moment-eğrilik davranışı üzerinde eksenel yük, boyuna donatı çapı, enine donatı oranının değişiminin önemli bir etkiye sahip olduğu görülmektedir. Yatay donatı aralığının azalması ile kesitlerin akma ve nihai moment kapasiteleri artar. Yatay donatı oranı, betonarme kolonların kesit davranışları üzerinde etkili bir parametredir. Yatay donatı çapı arttıkça kolon kesitlerinin moment kapasitesi artar. Yatay donatı çapındaki artış, nihai moment, nihai eğrilik ve eğrilik süneklik değerlerini artırır, ancak akma momenti ve akma eğriliği değerleri neredeyse sabit kalır (enine donatı aralığı ve eksenel yük seviyeleri sabittir). Akma momenti, akma eğriliği, nihai moment ve nihai eğrilik değerleri artar. Eksenel yük seviyesindeki artış eğrilik değerlerinin azalmasına neden olur. Eksenel yükün düşük olduğu durumlarda, betonarme bölümler sünek bir davranış sergiler. Boyuna donatı oranının artmasıyla elemanların akma ve nihai moment kapasiteleri artar.

Karşılaştırma sonuçlarından da görülebileceği gibi, SAP2000 programından [16] ve farklı yönetmeliklerden hesaplanan etkin kesit sertlik değerleri birbirinden farklıdır. Etkili kesit rijitliğinin gerekli değerden daha yüksek alınması, yapısal rijitliğin fazla tahmin edilmesine neden olacaktır. Sonuç olarak, yapıların hesaplanmasında ve değerlendirilmesinde sorunlar ortaya çıkacaktır.

Farklı parametrelerde tasarlanan betonarme kirişler için moment-eğriliğinden elde edilen etkin kesit rijitlik katsayısı değerlerinin karşılaştırılmasından da anlaşılacağı gibi; Betonarme kirişlerde sabit beton dayanımı ve çekme donatı oranı için basınç donatı oranı arttıkça etkin rijitlik katsayısı değerleri artar. Sabit basınç ve çekme dayanım oranına sahip betonarme kirişlerde, beton dayanımı arttıkça etkin rijitlik katsayısı değerleri artar. Basınç donatı oranının, betonarme kirişlerin maksimum moment taşıma kapasitesi, etkili eğilme rijitliği ve kesitlerin etkili rijitlik katsayısı ve sünekliği üzerinde etkili olduğu kanıtlanmıştır.

Farklı parametrelerde tasarlanan betonarme kolon için farklı yönetmelik ve moment-eğrilik ilişkilerinden elde edilen efektif rijitlik katsayı değerlerinin karşılaştırılmasından da anlaşılacağı gibi; Betonarme kolonlar için hesaplanan etkin rijitlik, artan enine donatı oranı, boyuna donatı oranı ve beton dayanımı ile artar. Eksenel kuvvetin artması nedeniyle betonun etkin rijitlik değerleri artmıştır.

### Referanslar

- [1] Çağlar N, Demir A, Ozturk H, Akkaya A. A simple formulation for effective flexural stiffness of circular RC columns, *Engineering Applications of Artificial Intelligence*. 2015; 38: 79-87.
- [2] Elwood KJ, Eberhard MO. Effective stiffness of RC columns. *ACI Structural Journal*. 2009; 106(4): 476-484.
- [3] Avşar Ö, Bayhan B, Yakut A. Effective flexural rigidities for ordinary reinforced concrete columns and beams. *The Structural Design of Tall and Special Buildings*. 2014; 23: 463-482.
- [4] Pique JR, Burgos M. Effective rigidity of reinforced concrete elements in seismic analysis and design. *The 14th World Conference on Earthquake Engineering 12-17 October, 2008, China*.
- [5] Mirza SA. Flexural stiffness of rectangular RC columns. *ACI Structural Journal*. 1990; 87(4): 425-435.
- [6] Paulay T, Priestley MJN. *Seismic design of RC and masonry buildings*. John Wiley & Sons: New York, 1992.
- [7] Mehanny SSF, Kuramoto H, Deierlein GG. Stiffness modeling of RC beam-columns for frame analysis. *ACI Structural Journal*. 2001; 98(2): 215-225.
- [8] Panagiotakos TB, Fardis MN. Deformations of RC members at yielding and ultimate. *ACI Structural Journal*. 2001; 98(2): 135-148.
- [9] Khuntia M, Ghosh SK. Flexural stiffness of RC columns and beams: analytical approach. *ACI Structural Journal*. 2004; 101(3): 351-363.
- [10] Kumar R, Singh Y. Stiffness of RC frame members for seismic analysis. *ACI Structural Journal*. 2010; 107(5): 607-615.
- [11] Pan Z, Li B, Lu Z. Effective shear stiffness of diagonally cracked RC beams. *Engineering Structure*. 2014; 59: 95-103.
- [12] TBDY. *Türkiye Bina Deprem Yönetmeliği*, T.C. Bayındırlık ve İskân Bakanlığı, 2018, Ankara, Türkiye.
- [13] ACI 318. *Building code requirements for RC and commentary*, American Concrete Institute Committee. 2014.
- [14] ASCE Standard, 41. *Seismic Evaluation and Retrofit of Existing Buildings*, (ASCE/SEI 41), Published by the American Society of Civil Engineers, Reston, Virginia, USA. 2017.
- [15] Eurocode 8. *Design of structures for earthquake resistance: Part 1: General rules, seismic actions and rules for buildings*, BS EN 1998-1:2004.
- [16] SAP2000, *Structural Software for Analysis and Design*, Computers and Structures, Inc, USA.
- [17] TS500. *Betonarme Yapıların Tasarım ve Yapım Kuralları*, Türk Standardları Enstitüsü, 2000, Ankara, Türkiye.
- [18] Mander JB, Priestley MJN, Park R. Theoretical stress-strain model for confined concrete. *Journal of Structural Engineering*. 1988; 114(8): 1804-1826.

## Earthquake Resilience of Infilled Reinforced Concrete Frames with Innovative Wall Solutions

*İbrahim Serkan Mısır\**, Dokuz Eylül University, Civil Engineering Department, İzmir, Turkey  
*Prost Iverden Balenda Bakala*, Dokuz Eylül University, Graduate School of Natural and Applied Sciences, İzmir, Turkey

\*Corresponding author: serkan.misir@gmail.com

**Keywords:** Reinforced concrete frames, infill frame, shear strength, concrete damaged plasticity, embedded constraint

**Discipline:** Civil Engineering

### Abstract

Reinforced concrete frames are usually infilled by masonry walls, but in most design, the shear strength response of these walls is ignored. Therefore, the nonlinear numerical modeling of masonry infilled frames is one of the most complex problems in structural engineering, especially when such structure is under the influence of lateral loads. It has been well understood that masonry infilled wall will affect the seismic responses of the RC frame in terms of load carrying capacity, ductility, damage pattern etc. Various methods are used for modeling of masonry walls of the structures. Three different approaches that have been well explained by Lourenço in 1996 [12]: details micro models, simplified micro models or meso-model and macro models are diverse modeling techniques. The aim of this study is to assess the reliability of numerical results provided by selected modeling approaches available in finite element codes. One of the three approaches is considered to model structural masonry by numerical analysis, namely a macro-modeling approach. In this case of modeling strategy, the masonry is treated as a homogeneous, isotropic continuum. The commercial software ABAQUS is used to simulate the in-plane seismic behavior of infilled RC frame. The nonlinear behavior of the concrete and masonry is properly represented by the Concrete Damage Plasticity (CDP) model. Steel rebars are modelled as elastic-plastic with hardening and are assumed to have a perfect adhesion with the surrounding concrete by means of the embedded constraint.

### Introduction

Infill walls are generally considered as non-structural components. Moreover, their effects are considered to be positive and hence ignored in the design phase. Research works and experimental studies on frame with masonry infill walls have shown that there is an increase in lateral stiffness, strength and energy dissipation capacity as compared to bare frames [9, 11, 19]. Paolo and Verzeletti in 1996 [17] state that, masonry panel strongly affect the behavior of the main structure. In general, the presence of non-structural masonry panels has a beneficial effect, because they significantly increase the global strength of the structure. On the other hand, they also increase the initial stiffness, so that the inertial forces may be increased to a large extent. They state that infill walls cause major changes on both the stiffness and the drift behavior of the frame, and the effect of changes can be either advantageous or disadvantageous depending on the failure mode of the wall. The advantageous means that the presence of masonry infill improves the capacity of the structure to resist lateral loads, such as earthquake. In another words, the composite system (masonry-infill RC frame) might resist an earthquake, whereas the weak frame would not. The disadvantageous of infills is related mainly to the formation of short columns or a soft story, which can lead to global or local failure of the structure. The formation of a short columns occurs when masonry infill leaves a short portion of the column clear, leading to column shear collapse. Although a soft story is typically observed when the distribution of infill walls along the height of the structure is irregular, the mechanism can also appear even in the cases of a uniform distribution when: a) the ground motion is strong compared to demand design, the global ductility of the bare frame and structural elements is low, the infill walls are relatively weak and brittle, as discussed in detail by Dolsek and Fajfar in 2001[8]. Based on earlier studies [9, 17, 18], it is well known that infill walls can change strongly the deformation properties of the frame structures due to strength and stiffness contribution of the wall.

However, experiences after some major earthquakes [1, 2, 3, 4] have illustrated the undesired damage phenomenon such as soft story, short column effect, torsion and out-of-plane collapse. Because

of these complications, and performing evaluation of seismic behavior and parametric study, numerical simulation becomes essential.

Numerical analysis is usually employed as a complement to experimental works, contributing to a better understanding of infill and frame behavior. As shown in Figure 1, the infill can be modelled via three different approaches: details micro models, simplified micro models and macro models [12]. The micro modeling of infill walls involves consideration of the individual masonry units, mortar joints and the frame wall interface and their appropriate constitutive models, units and mortar in the joints are represented by continuum elements whereas the unit-mortar interface is represented by discontinuous elements; the simplified micro-modeling, expanded units are represented by continuum elements whereas the behavior of the mortar joints and unit-mortar interface is lumped in discontinuous elements; and in macro-modeling, units, mortar and unit-mortar interface are smeared out in the continuum. Equivalent strut method is minimalistic model and is suitable for analysis of building with infill walls. In this model, infill walls are replaced by a diagonal strut (single or multiple) with appropriate geometrical and mechanical characteristics. However, these macro models have deficiency in capturing some failure mechanism of infilled frames.

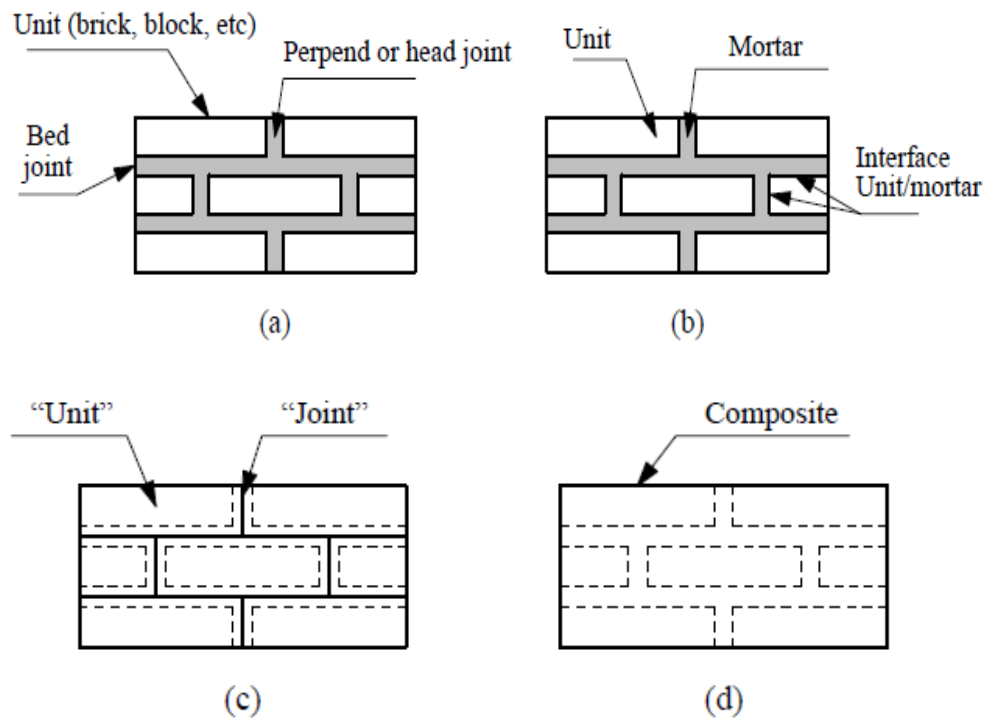


Figure 1. Modeling strategies for masonry structures: (a) masonry sample; (b) detailed micro-modeling; (c) simplified micro-modeling; (d) macro-modeling.

In this study, a 3D finite element model of infilled frame is developed in a commercially available software ABAQUS [5] and is validated against the experimental results. The model can be used to study the in-plane behavior and failure modes of the infilled RC frames under lateral loading.

### Description of Test Specimen

The parameters in the experiment performed by Misir et al in 2012 [16] are used. The specimens were cast at a precast concrete facility and were transported to the laboratory, and infill walls were constructed in the laboratory. The dimensions and the reinforcement details of test frames are shown in Fig. 2. The amount of steel bars used for the columns and beam are 8Φ8 and 4Φ8, respectively. It is noted here that confinement reinforcements were used in the beam column connections which is required by the Turkish Earthquake Design Code (2007). Concrete with a maximum diameter of 10 mm for coarse aggregate was used. The material tests both for concrete and reinforcement steel were conducted to characterize the materials used for the test. The effective compressive strength of concrete was

measured 20 MPa, and the yield and ultimate stresses of reinforcing steel were measured 472 MPa and 538 MPa, respectively. The dimensions of the foundation were 3500 mm in length, 650 mm in width, and 525 mm in height.

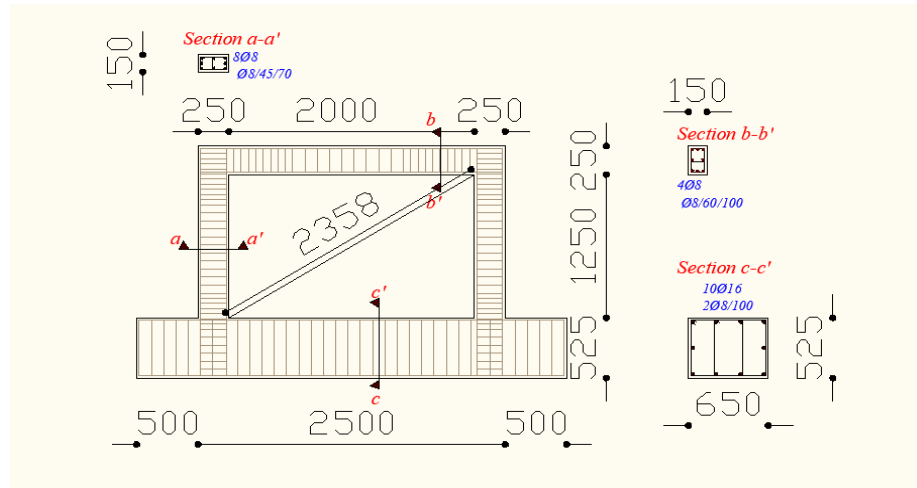


Figure 2. Dimensions and reinforcement details of test frames

### Numerical Simulation of Masonry Wall (Specimen 1)

The finite element method gives the opportunity to study wall specimens in more depth due to the large amount of results that can be analyzed. Therefore, FE method provides the opportunity to understand how and not just that, a parameter affects the results. This means that the need for experiments can be greatly reduced by using the finite element method. However, experiments are still needed to verify that FE method match actual behavior. Therefore, when experiments and nonlinear finite element method are used together, they can become very powerful tools to better understand the structural behavior of masonry walls under lateral load. In this regard, detailed finite element method of the wall specimens is carried out using the nonlinear finite element program, ABAQUS version 2019.[5]

### Description of Finite Element Model

#### Finite element analysis

The finite element analysis package ABAQUS/standard [5] is used to model the infilled RC frame with masonry infill wall. A brief description of the constitutive models (specimen 1) that are used in the model is presented below. Figure 2 illustrates the first specimen components of RC frame with infilled masonry wall.

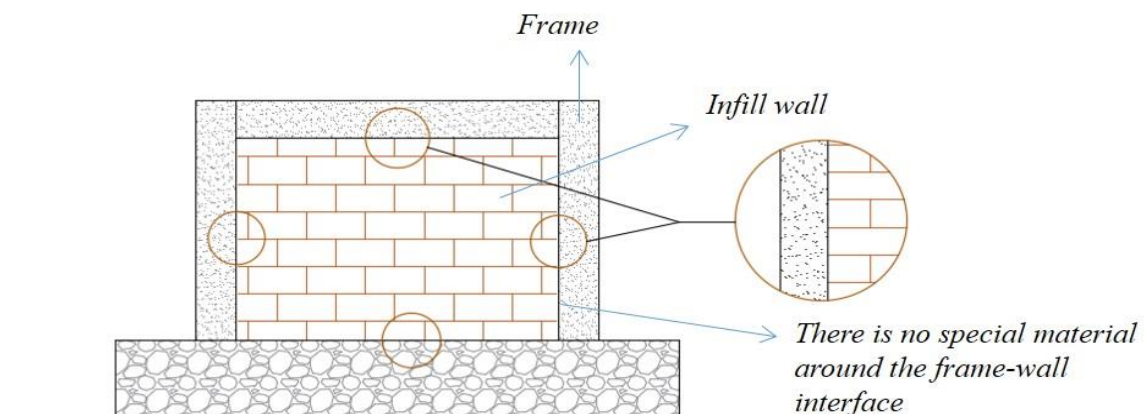


Figure 2. Details of first specimen components of RC frame with infilled masonry wall

### Model characterization

In this research, the macro-modelling approach proposed by Lourenço [12] is used for modeling masonry walls that has been adopted for this specimen. In this way, the bricks, mortar, concrete, and their contact interfaces are not modelled separately (Fig. 3a). Rather, all components are treated as homogeneous and isotropic materials. The modelling process is carried out in the commercial software package ABAQUS as was mentioned before. The model employed element C3D8R, which is a linear 8-node solid element for concrete and masonry elements, and element T3D2 a linear 2-node 3D-truss element for the steel rebars as shown in Fig. 3. The elements are connected together with appropriate constraints to represent the interaction between various components of the wall assembly. In this respect, to simulate the bond between concrete and reinforcement, the reinforcement is embedded in the concrete using the “Embedded Constraint” (Fig. 5b) option that is available in Abaqus, which enforces full compatibility and assumes full bond. This means that no slip is taken into account between these two materials.

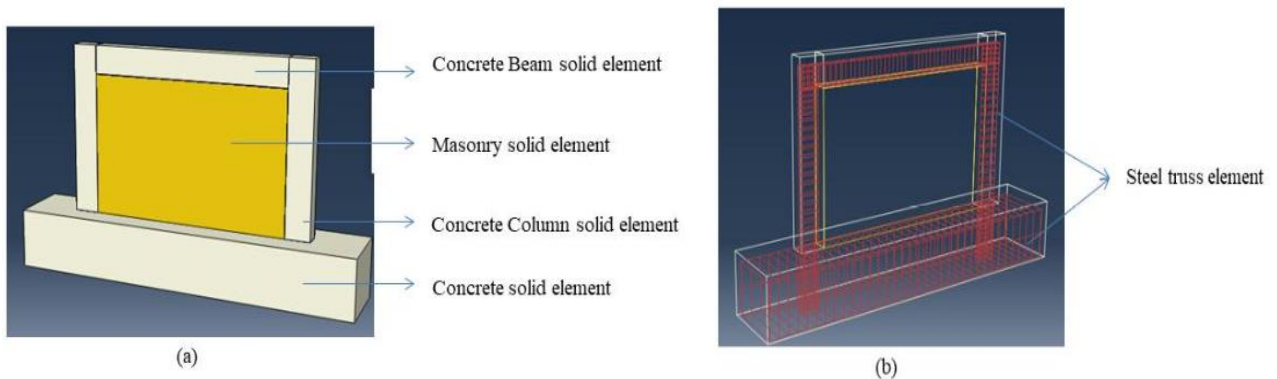


Figure 3. (a) Solid element for concrete and masonry, (b) Truss element for the steel rebars

### Concrete Damage Plasticity Model (CDPM)

Concrete Damage Plasticity (CDP) is a continuum plasticity-based damage model for concrete and other quasi-brittle materials in any type of structure. This model was theoretically described by Lubliner et al. in 1989 [14]. It is assumed that the failure of a material is governed by two main mechanisms: tensile cracking and compressive crushing. For a full definition of CDP model in Abaqus the following obligatory parameters should be input: dilation angle, flow potential eccentricity  $e$ , the ratio  $fb_0/fc_0$  of biaxial compressive yield stress to uniaxial compressive yield stress, the ratio  $K$  of the second stress invariant on the tensile meridian to that on the compressive meridian for the yield function, the viscosity.

All the parameters involved in CDP can be obtained from uniaxial, biaxial and triaxial tests, as described by Jankowiak and Lodygowski in 2005 [10]. Regarding the dilation angle,  $\psi$ , values of  $30^\circ$  and  $35^\circ$  are used for concrete and masonry, respectively, as were correctly used by Breveglieri et al. in 2018 [6]. Regarding the rest of parameters, in the absence of experimental data,  $e$ ,  $fb_0/fc_0$  and  $K$  can be taken by default values from ABAQUS as is the case for this work: 0.1, 1.16 and 0.667, respectively. Regarding the parameter of viscosity, it is taken to be 0.0001, following the recommendations of Michał S. and Andrzej [15] as it is shown in Tables 1 and 2. For the uni-axial compression stress-strain curve of the concrete, the stress–strain relationship proposed by Hognestad is used and the work conducted by Chaudhari and Chakrabarti [7] was useful. To specify the peak stress tension failure behavior of concrete, the stress strain curve for concrete under uniaxial tension is used.

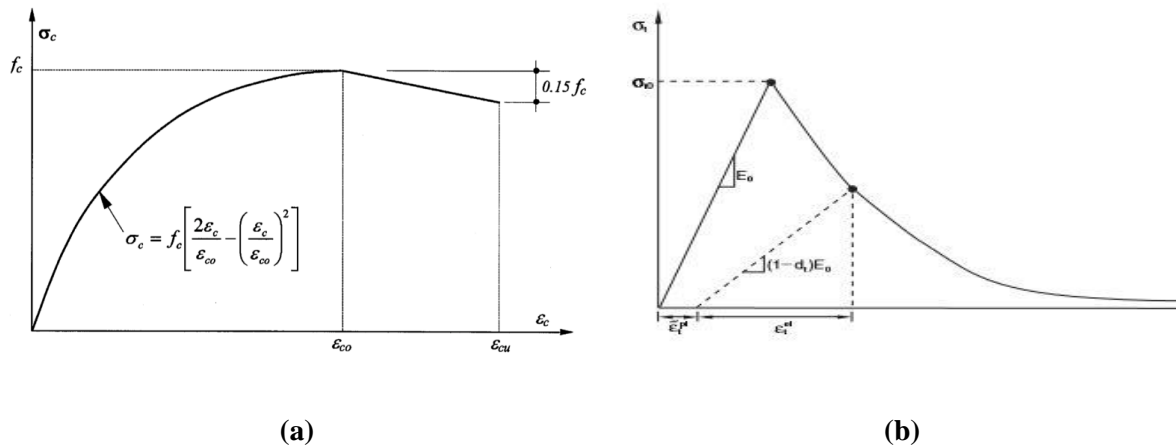


Figure 4. (a) Hognestad stress-strain model for concrete, (b) Concrete response under uniaxis loading in tension

Table 1. Parameters involved in concrete damaged plasticity for concrete

Dilation angle	Eccentricity	Fbo/fco	k	Viscosity
30	0.1	1.16	0.667	0.0001

Table 2. Parameters involved in concrete damaged plasticity for masonry wall

Dilation angle	Eccentricity	Fbo/fco	k	Viscosity
35	0.1	1.16	0.667	0.0001

### Interaction between concrete frame and Infill panel

The wall is constructed conventionally touching the frame elements and not including any special material among the frame-infill interface (as a first option proposed in the code). ABAQUS/standard [5] provides a node-to-node interaction method using Cartesian connector element. Cartesian connector element provides a connector between two nodes that allows independent behavior in the three local Cartesian directions. To define the Cartesian connectors' properties in the present model, the normal and tangential mechanical behavior must be defined. The interface between the masonry panel and the concrete frame is modeled as a “hard contact” for the normal direction. The tangential behavior is defined using the penalty friction formulation with a friction coefficient equal to 0.5 as shown in Figure 5.

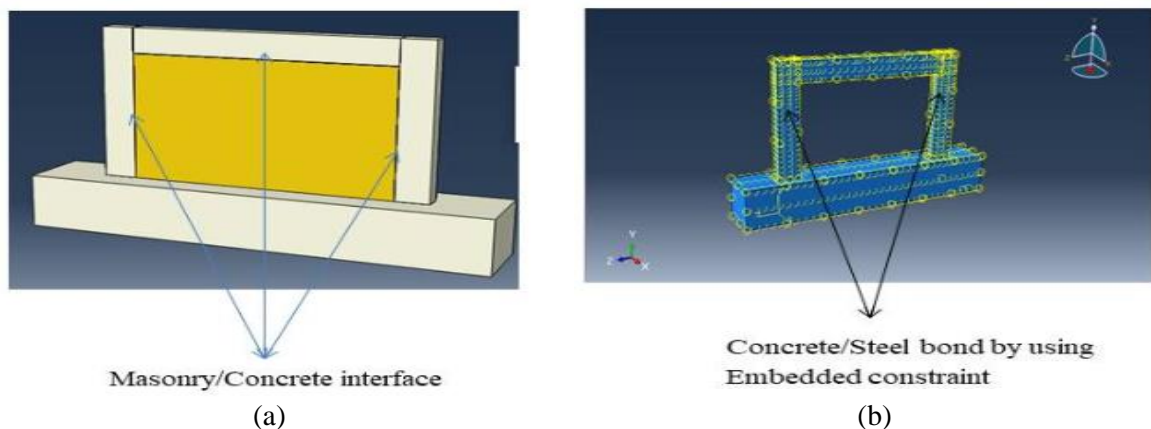


Figure 5. (a) Interface between Masonry and RC frame, (b) reinforcement is embedded in the concrete using the “Embedded Constraint”

### Load modeling

The loading of the model is similar to that conducted by Misir et al [16] in the experimental campaign (Fig. 6). According to the test setup, the load was applied in two different steps. A vertical load of 600 KN was applied on each column and the horizontal load was applied by a displacement of



60.0mm assigned at the top surface as a boundary condition of shear models. Besides, 9.81N is taken into account and represent the force of gravitational attraction. The other degrees of freedom of defined control point are assumed equal to 0 (Fig. 7). As far as boundary conditions, the base of the concrete footing possesses locked translational degrees of freedom in all directions. C20 concrete is used for frame and base. Standard brick is used for masonry infill wall. The properties of steel reinforcement are based on the test on the steel rebars presented in Misir et al [16]. The properties of materials are provided in Table 3.

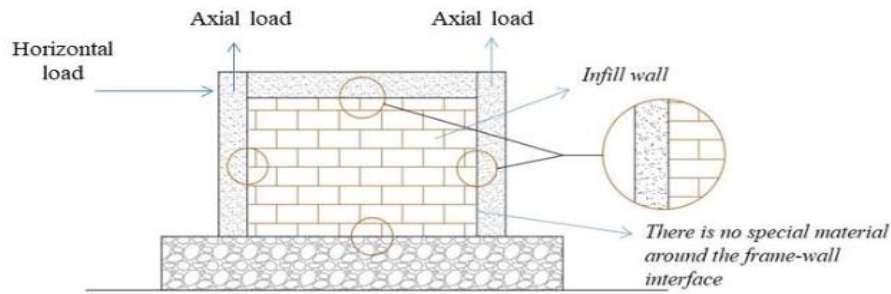


Figure 6. Load details of first specimen

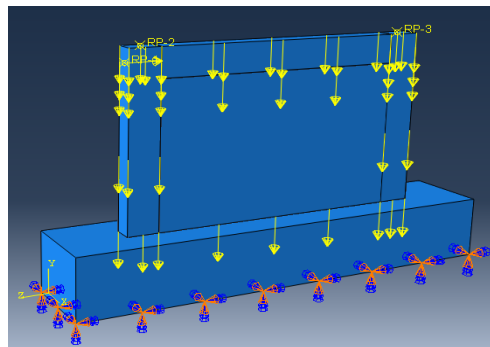


Figure 7. Boundary conditions for the three-dimensional model

Table 3. Material property of all experimental models

Material	Properties
Concrete	Poisson ratio = 0.2 Compressive strength = 20 MPa Modulus of elasticity = 22360,68 MPa Density = 2.4 e-9 ton/mm <sup>3</sup> (2400kg/m <sup>3</sup> )
Block	Poisson ratio = 0.15 Compressive strength = 11,7 MPa Modulus of elasticity = 17102,63 MPa Density = 1800kg/m <sup>3</sup> Thickness = 150mm
Reinforcing steel	Poisson ratio = 0.3 Yield stress = 472 MPa Modulus of elasticity = 214000 MPa Density = 7.8 e-9 ton/mm <sup>3</sup> (7800kg/m <sup>3</sup> )

### Results of Finite Element Analysis

The results of the finite element analysis in terms of deformed collapse shapes, stress distribution and equivalent plastic strain are presented below. The predicted collapse mechanisms, as well as the distribution of stresses (Fig. 8a) and equivalent plastic strains (Fig. 8b) of the macro-model as illustrated in the Figure 8, agree with the typical failure mode of a brittle material under a lateral load.

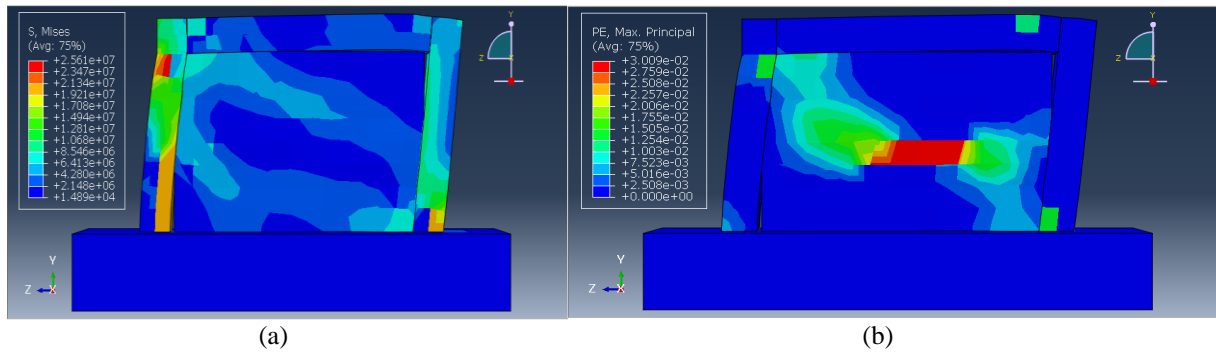


Figure 8. Predicted collapse mechanisms: (a) distribution of stress on the interface of wall, (b) Equivalent plastic strain of macro model subjected to lateral load

According to the numerical analysis performed, when the in-plane lateral load is applied to the structure, the infilled frame acts as a monolithic resisting system at low lateral load level. As the load increases, the infill panel tends to partially separate from the enclosure frame and the severe cracks are developed in the right-hand side column, ends of construction column, mid area of infill wall along the diagonal as shown in Fig. 9. Likewise, formation of diagonal strut is presented by stress distribution in the diagonal region of the wall. This behavior is schematically shown in Figure 9b. The upper left and right corner of infill detach from the RC frame at lateral load of 353,64 kN which correspond to the drift of 2,2%. (33,44mm)

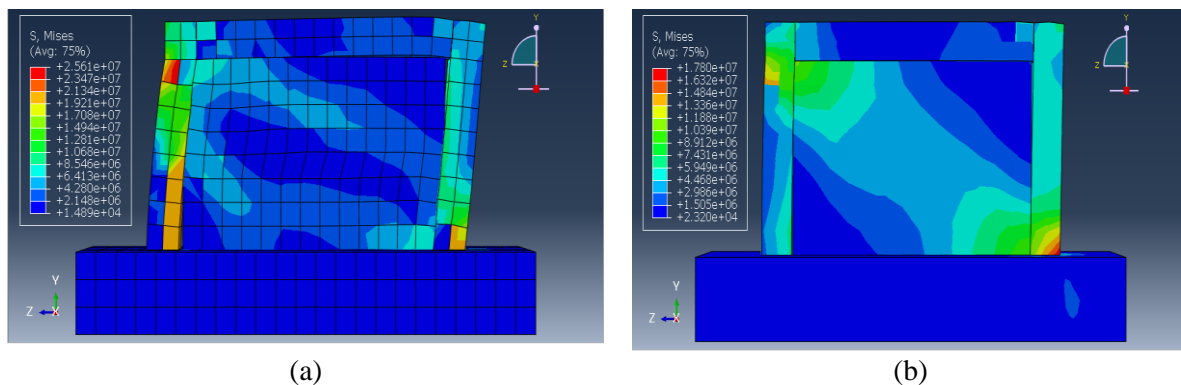


Figure 9. (a) cracks developed in the right-hand side column, ends of construction column, mid area of infill wall along the diagonal, (b) schematically formation of diagonal strut presented by stress distribution in the diagonal region of the wall.

It should be also noticed that, the failure mode of the numerical model is compatible with that recorded in the experimental results in terms of damages. As shown in the Figure 10, the deformed mesh observed in the numerical model of the infill panel at failure demonstrates the crushing of the infill at the extremities of the diagonal compression strut. This result corresponds to the failure mode of the test results shown in figure (Crushing of load corner in a test specimen).

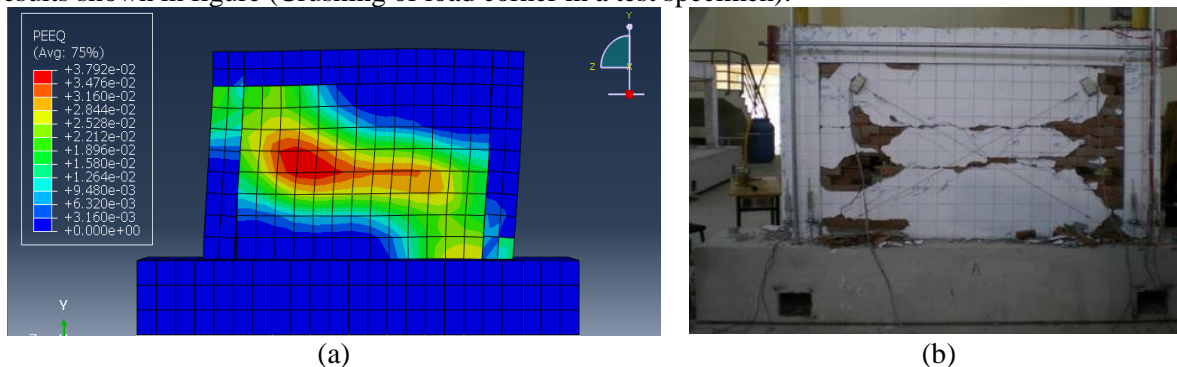


Figure 10. (a) deformed mesh of infill wall at failure, (b) Crushing of load corner in test specimen

### Comparisons with experimental test in terms of damages

Comparison of the experimental and numerical results in terms of damage distribution showed some similarity in the prediction of failure response. The behavior of the wall is well captured by the model as illustrated in Fig. 11. In these figures, the word "damage" is used for the equivalent plastic strain (PEEQ) from each mode of the composite interface model. Note that the "damage" of the compressive strut is only shown in the softening regime, not during hardening. Initially, two horizontal tension cracks develop at the bottom and top of the wall. A stepped diagonal crack immediately follows as explained above.

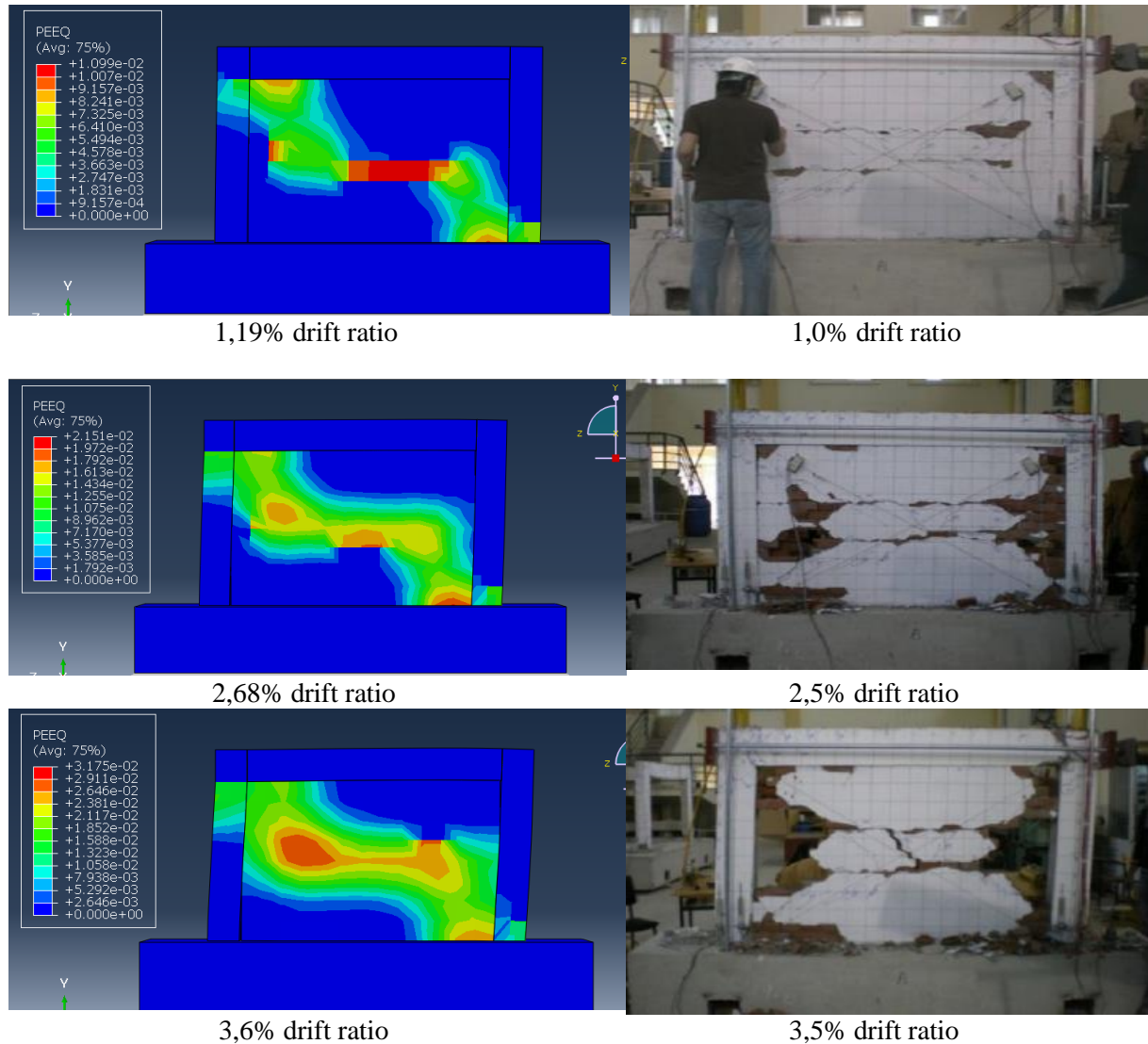


Figure 11. Damages patterns at different level drift

A comparison of the force displacement diagrams obtained during the experiment and the numerical campaign of specimen 1 (RC frame with Infill wall) cannot be underline in this part. The specimen in the experiment was subjected to "push and pull" loading. In despite of lack of some information, it was concluded to conducted the numerical analysis to monotonic loading. This is well illustrated in Figure 12 and 13. From this figure, it is well seen the numeric monotonic curve in terms of lateral load and deformation. There is also a good agreement in terms of the pre-peak regime, where the linear stiffness and the nonlinear pre-peak regime are well described.

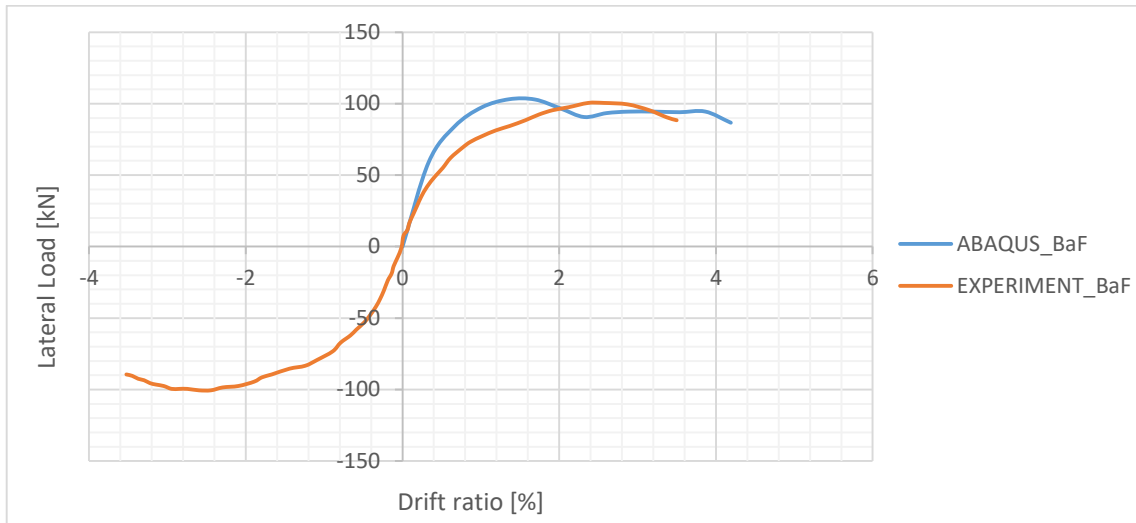


Figure 12. Comparison of monotonic curve for Numerical analysis and Pushover Experiment analysis for BaF

Note: BaF: Bare without any infill wall

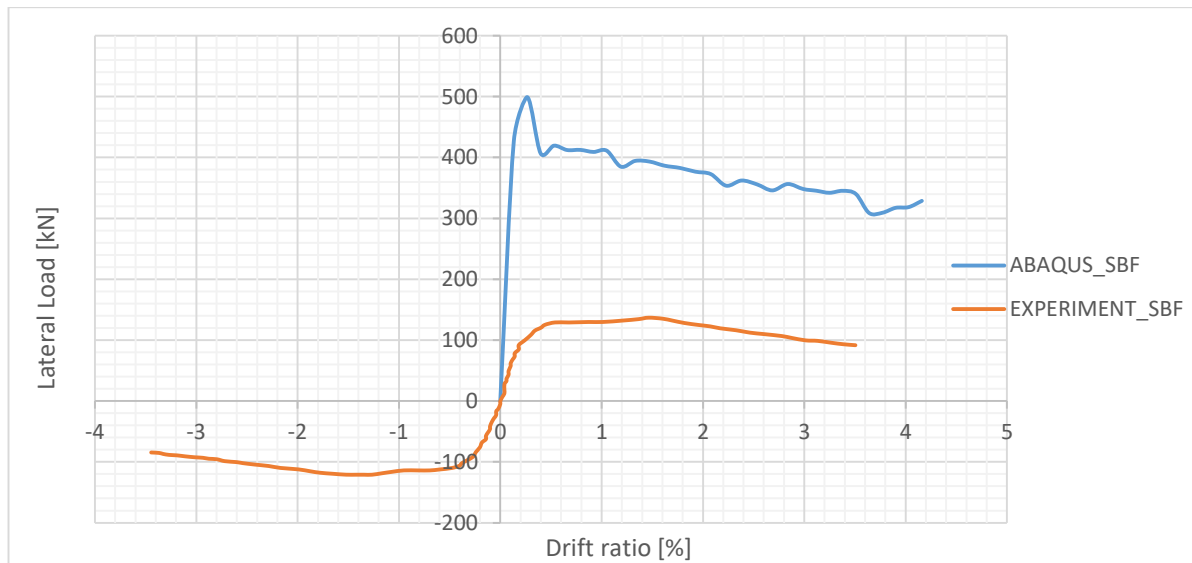


Figure 13. Comparison of monotonic curve for Numerical analysis and Pushover Experiment analysis for SBF

Note: SBF: Standard Brick with Infill frame

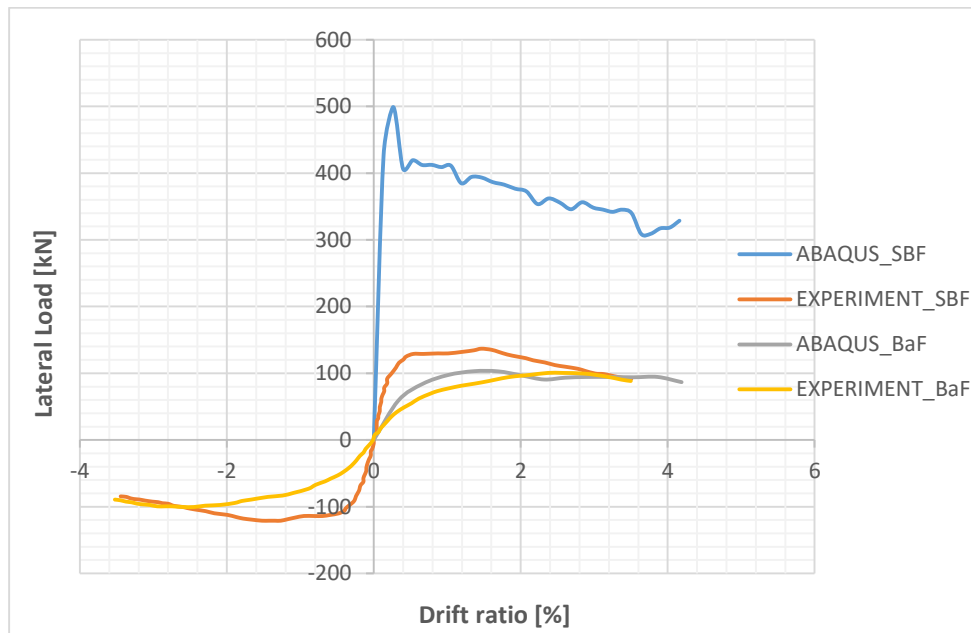


Figure 14. Comparison of monotonic curve for Numerical analysis and Pushover Experiment analysis for both BaF and SBF

Note: BaF: Bare without any infill wall  
SBF: Standard Brick with Infill frame

Diagonal cracking characterizes the shear failure mode through the panel wall depending upon the path of least resistance. Diagonal cracking marks the ultimate or peak load carrying capacity of the wall which is 499,18kN and 103,08kN for Bar without infill (BaF), as illustrated in Figure 12 above. Figure 13 shows the various stages observed in the diagonal shear cracking failure. After diagonal cracking, the load-deformation curve shows a softening response for both numerical and experiment results. From Table 4, damages and force level for specimen are illustrated.

Table 4. Damages states and corresponding loads level for the Specimen 1

Specimen	First separation of wall		First diagonal crack on SBF wall		Observed max. lateral load	
	Drift ratio [%]	Load [kN]	Drift ratio [%]	Load [kN]	Drift ratio [%]	Load [kN]
BaF	-	-	-	-	1,36	103,08
SBF	2,22	353,64	0,13	406,59	0,26	499,18

### Conclusion

The modelization of reinforced concrete infill frame with masonry wall under monotonic lateral loading through a finite element method is presented in the study. Abaqus version 2019 was performed to fulfill this work. The force-displacement curve, the cracks pattern shows that the methodologies of using finite element program are able to simulate the behavior of infilled frame. The results of the numerical analysis and comparison with selected experimental tests even in the despite of lack of some data showed that the use of macro model approach allows a good prediction of response to be achieved, both in terms of failure loads and collapse mechanisms.

The lack of experimental data for the evaluation of the Push pull behavior of the specimens introduces uncertainties in the numerical modelling of the structure's response. Even though, the material properties calibrated and used in this work represent well the experimental behavior of the tested wall in monotonic loading, there is a need extensive experimental campaigns aimed at characterizing the mechanical properties of materials. Provided additional material test data is available,

numerical analyzes such as those presented in this paper should be added to gain insight into the seismic behavior of structures subjected to cyclic loads.

The study also shows that the technique of macro-modeling with a cohesive surface is suitable for reproducing understandable results. Further research will focus on DIANA Software in order to reach the experiment campaign.

### References

- [1] Miranda E, Bertero VV. The Mexico Earthquake of September 19, 1985-Performance of Low-Rise Buildings in Mexico City. *Earthquake Spectra*. 1989; 5:121-43.
- [2] Elnashai AS. Analysis of the damage potential of the Kocaeli (Turkey) earthquake of 17 August 1999. *Engineering Structures*. 2000 ; 22 :746-54.
- [3] Jain SK, Lettis WR, Murty CVR, Bardet JP. Bhuj, India Earthquake of January 26, 2001 Reconnaissance Report. *Earthquake Spectra*. 2002 ; Supplement A to Vol 18.
- [4] Braga F, Manfredi V, Masi A, Salvatori A, Vona M. Performance of non-structural elements in RC buildings during the L'Aquila, 2009 earthquake. *Bull Earthquake Eng*. 2011 ; 9:307-24.
- [5] ABAQUS, V. (2014). 6.14 Documentation. Dassault Systemes Simulia Corporation.
- [6] Breveglieri M, Camata G, Spacone E. Strengthened infilled RC frames: Continuum and macro modeling in nonlinear finite element analysis. *Compos Part B: Eng* 2018.
- [7] Chaudhari S.V., Chakrabarti M.A. Modeling of concrete for nonlinear analysis Using Finite Element Code ABAQUS. *International Journal of Computer Applications (0975 – 8887) Volume 44– No.7, April 2012*
- [8] Dolsek M., Fajfar P. (2001) The effect of masonry infills on the seismic response of a four-storey reinforced concrete frame - a deterministic assessment. University of Ljubljana, Faculty of Civil and Geodetic Engineering, Jamova 2, SI-1000 Ljubljana, Slovenia
- [9] Hashemi A. and Mosalam K.M. (2006) Shake-table experiment on reinforced concrete structure containing masonry infill wall. Department of Civil and Environmental Engineering, University of California, Berkeley, CA 94720-1710, U.S.A.
- [10] Jankowiak T, Lodygowski T. Identification of parameters of concrete damage plasticity constitutive model. *Found Civil Environ Eng* 2005;6(1):53–69.
- [11] Jiang, H., Liu, X., and Mao, J. (2015). "Full-scale experimental study on masonry infilled RC moment-resisting frames under cyclic loads". *Engineering Structures*, 91, 70-84.
- [12] Lourenco, P. J. B. B., (1996), Computational Strategies for Masonry Structures, PhD Dissertation, Delft University of Technology, Holland
- [13] Lourenco, P. B., & Rots, J. G. (1997). Multi-surface interface model for analysis of masonry structures. *Journal of Engineering Mechanics*, 123(7), 660–668.doi :10.1061/(ASCE) 0733-9399(1997)123 :7(660)
- [14] Lubliner, J., Oliver, J., Oller, S., and Onate, E. (1989). A plastic-damage model for concrete. *International Journal of Solids and Structures*, 25(3), 299-326.
- [15] MichałS, Andrzej W. Calibration of the CDP model parameters in ABAQUS; 2015.
- [16] Misir I.S., Ozcelik O., Girgin S.G., and Kahraman S. (2012) Experimental work on seismic behavior of various types of masonry infilled RC frames. *Structural Engineering & Mechanics* · December 2012
- [17] Negro P. and Verzeletti G. (1996) Effect of infills on the global behavior of RC frames: Energy considerations from pseudodynamic tests. ELSA Laboratory, Joint Research Centre of the European Commission TP 480. I21020 Ispra (VA), Italy.
- [18] Pinto A. and Taucer F. (2006) "Assessment and retrofit of full-scale models of existing RC frames" in *Advances in Earthquake Engineering for Urban Risk Reduction*, ed. S. T. Wasti and G. Ozcebe (NATO Science Series, Istanbul, Turkey), vol. 66, pp. 353–367.
- [19] Pujol, S., & Fick, D. (2010). The test of a full-scale three-story RC structure with masonry infill walls. *Engineering Structures*, 32(10), 3112-3121

## Derivation of Equation of Motions of Rotating Beams Using Biot Stress

*Betül Üstüner, Celal Bayar University, Department of Civil Engineering, Manisa, Turkey*  
*Berra Gültekin Sınır, Celal Bayar University, Department of Civil Engineering, Manisa, Turkey*  
*\*Corresponding author: betul.celik@cbu.edu.tr*

**Keywords:** Elasticity theory, rotating beam, biot stress

**Discipline:** Civil Engineering

### Abstract

Beam theory is used to model helicopter rotor blades, aircraft wings, aviation propeller blades, prop-fan blades, wind-turbine blades, robot manipulators, large space structures, arm-type positioning mechanisms of magnetic disk drives, links of slider-crank mechanism. Beams are major construction components of aircraft. The post buckling strength of beams plays an important role in the design of aircraft structures. It is also used in experimental characterization of materials. Moreover, beams are major construction components of aircraft. Because the post buckling strength of beams plays an important role in the design of aircraft structures [1]. In this study, uniform beam with homogeneous and isotropic material was discussed. The stress equation of the system was obtained using Biot stress stresses [2]. According to Biot stresses, two stresses are applied to the beams as initial stress and incremental stress. The problems related to the initial tension of deformable. The initial stresses occur in structural elements after manufacturing and assembly. The initial stresses are present in the Earth's crust due to the action of geostatic and geodynamic forces in composite materials, in rocks, in blood vessels of living organisms and so on. Moreover, stresses in the structural elements caused by exploitation forces as well as by their own weight can be taken as initial stresses. [3].

The theory of elasticity [4] is used to solve some linear, inplane deflection problems for isotropic beams. Beam theories are one-dimensional mathematical models, one of which is much larger than the other two. Modelling of beams more difficult than modelling of plates and shells. Because the former involves the transformation of a three-dimensional problem in nature into a one-dimensional problem whereas the latter involves the transformation of a three-dimensional problem into a two-dimensional problem. However, solving beam problems are easier than solving plates and shells problems because the former deals with only one dependent spatial variable, whereas the letter deal with two independent spatial variables. In this study the mathematical model of beams was obtained from the theory of elasticity. Stress values are replaced in the biot equation. In biot stress equation, values related to the coordinate set are written. In stress equations, integrals are taken along the cross-sectional area. When the equation is arranged, the motion equation is obtained for the rotating beam.

### Introduction

Many investigators studied rotating tapered beams, which are very important for the design. Several engineering applications are such as rotating machinery, helicopter blades, robot manipulators, spinning space structures, etc. The dynamic characteristics natural frequencies and related mode shapes of rotating tapered beams are required to determine resonant responses and perform forced vibration analysis [5].

This work introduces the physics of the material in the form of linear relations between the incremental stresses and the strain. Such linear relations do not necessarily imply that the material is elastic. They are applicable to non-elastic media undergoing an incremental deformation in the vicinity of a prestressed condition. More precisely, we consider deformations which are elastic for the incremental deformations alone, irrespective of the manner by which the state of initial stress has been generated. For example, in geophysical applications the state of initial stress in the earth is the result of a slow but highly irreversible process of a viscous or plastic nature. Rapid deformations, however, may be approximately elastic [2].

Modeling beams is more difficult but solving problems are easier. The mathematical model was obtained from the theory of elasticity. Using biot stresses the equation is obtained. In biot stress equation, values related to the coordinate set are written. Acceleration equations found for rotating beam Two-dimensional beam equations are obtained. Equations were combined using normal force. Equation of motion was obtained for rotating beam.

### Equation of Motion

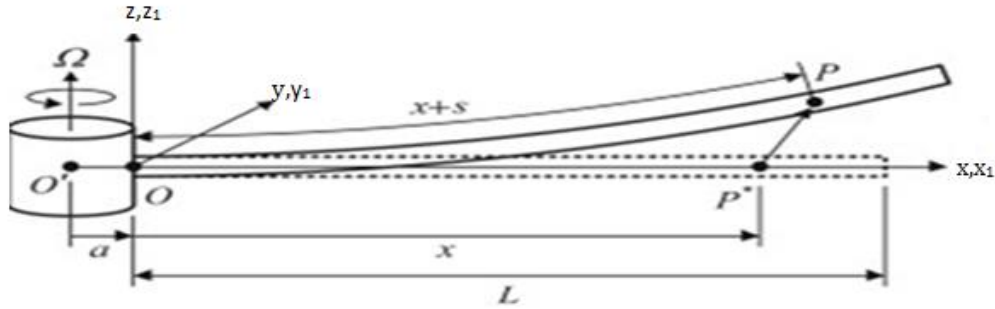


Figure 1. Uniform rotating beam

Figure 1 is a schematic representation of a rotating, cantilever, uniform, Euler Bernoulli beam. The length of the beam  $L$  is given as the center  $O$  of the beam with a fixed rigid shaft, the radius  $R$  and the constant angular velocity. The cross-section width of the beam is  $b$  and its height is  $h$ . The area of the cross section is shown as  $A$ , the moment of inertia  $I$ . Material behavior is linear elastic. Second-order effects are neglected. The material from which the beams are made is homogeneous and isotropic. The damping effect is neglected. Axial deformations are not taken into account. The Coriolis effect has been neglected.

Displacements in the Euler Bernoulli beam;

$$u_x = -z \frac{\partial w}{\partial x}, \quad u_y = 0, \quad u_z = w(x, t) \quad (1)$$

Here  $x$  is the axis along the beam,  $y$  is the neutral axis,  $z$  is the axis that indicates the positive direction of the beam's transverse displacement.  $u_x, u_y, u_z$  are displacements.  $w$  is vertical displacement.  $-\partial w / \partial x$  is rotation.

It is accepted that the deformations that occur under external effects are small. First order theory is valid.

$$\varepsilon_{xx} = \frac{\partial u_x}{\partial x} = -z \frac{\partial^2 w}{\partial x^2} + \frac{1}{2} \left( \frac{\partial w}{\partial x} \right)^2 \quad (2)$$

$$\varepsilon_{xz} = \frac{1}{2} \left( \frac{\partial u_x}{\partial z} + \frac{\partial u_z}{\partial x} \right) = \frac{1}{2} \left( -\frac{\partial w}{\partial x} + \frac{\partial w}{\partial x} \right) \quad (3)$$

$$\varepsilon_{zz} = \frac{1}{2} \left( \frac{\partial u_z}{\partial z} + \frac{\partial u_z}{\partial z} \right) = 0 \quad (4)$$

### Equilibrium Equation

Biot stress equation,

$$\frac{\partial s_{ij}}{\partial x_j} + \rho \Delta X_i - \rho \omega_{ik} X_k(x_1) - \rho e \Delta X_i(x_1) + S_{jk} \frac{\partial \omega_{ik}}{\partial x_j} + S_{ik} \frac{\partial \omega_{jk}}{\partial x_j} - e_{jk} \frac{\partial S_{ik}}{\partial x_j} = \rho a_i \quad (5)$$

$s_{ij}$  is stress value,  $X_i(x_1) = X_j(x_1) = X_k(x_1) = 0$  is body force,  $\omega_{ik}$  is rotation  $S_{ik}$  is initial stress.

Shear stress and moment values on the beam are calculated. It is necessary to substitute these terms in the equations of motion. The equation of motion of the system has been obtained by using Biot stress stresses.



Matrix elements are written in general form;

$$\begin{aligned}\omega_{ij} &= 0 & \text{eğer } i &= j \\ \omega_{ij} &= -ij & \text{eğer } i &\neq j\end{aligned}\quad (6)$$

It is arranged according to Cartesian coordinates,

$$\begin{aligned}\omega_{11} &= \omega_{22} = \omega_{33} = 0 \\ \omega_{32} &= -\omega_{23} = \omega_x \\ \omega_{13} &= -\omega_{31} = \omega_y \\ \omega_{21} &= -\omega_{12} = \omega_z\end{aligned}\quad (7)$$

Coordinates are defined

$$x = x_1 \quad y = x_2 \quad z = x_3 \quad (8)$$

Displacements are defined

$$u = u_1 \quad v = u_2 \quad w = u_3 \quad (9)$$

$i = 3, \quad j = 1,2,3, \quad k = 1,2,3$  substituting these values into Eq. (5)

$$\begin{aligned}\frac{\partial s_{31}}{\partial x_1} + \frac{\partial s_{32}}{\partial x_2} + \frac{\partial s_{33}}{\partial x_3} + S_{11} \frac{\partial \omega_{31}}{\partial x_1} + S_{12} \frac{\partial \omega_{32}}{\partial x_1} + S_{13} \frac{\partial \omega_{33}}{\partial x_1} \\ + S_{21} \frac{\partial \omega_{31}}{\partial x_2} + S_{22} \frac{\partial \omega_{32}}{\partial x_2} + S_{23} \frac{\partial \omega_{33}}{\partial x_2} \\ + S_{31} \frac{\partial \omega_{31}}{\partial x_3} + S_{32} \frac{\partial \omega_{32}}{\partial x_3} + S_{33} \frac{\partial \omega_{33}}{\partial x_3} \\ + S_{31} \frac{\partial \omega_{11}}{\partial x_1} + S_{32} \frac{\partial \omega_{12}}{\partial x_1} + S_{33} \frac{\partial \omega_{13}}{\partial x_1} \\ + S_{31} \frac{\partial \omega_{21}}{\partial x_2} + S_{32} \frac{\partial \omega_{22}}{\partial x_2} + S_{33} \frac{\partial \omega_{23}}{\partial x_2} \\ + S_{31} \frac{\partial \omega_{31}}{\partial x_3} + S_{32} \frac{\partial \omega_{32}}{\partial x_3} + S_{33} \frac{\partial \omega_{33}}{\partial x_3} \\ - e_{11} \frac{\partial S_{31}}{\partial x_1} - e_{12} \frac{\partial S_{32}}{\partial x_1} - e_{13} \frac{\partial S_{33}}{\partial x_1} \\ - e_{21} \frac{\partial S_{31}}{\partial x_2} - e_{22} \frac{\partial S_{32}}{\partial x_2} - e_{23} \frac{\partial S_{33}}{\partial x_2} \\ - e_{31} \frac{\partial S_{31}}{\partial x_3} - e_{32} \frac{\partial S_{32}}{\partial x_3} - e_{33} \frac{\partial S_{33}}{\partial x_3} = \rho a_3\end{aligned}\quad (10)$$

In this study, beam axis is located in x and z planes. Rotation occurs on the y-axis. For this reason, 2-dimensional equations are handled and expressions are made simpler

$$\begin{aligned}\frac{\partial s_{31}}{\partial x_1} + \frac{\partial s_{33}}{\partial x_3} + S_{11} \frac{\partial \omega_{31}}{\partial x_1} + S_{31} \frac{\partial \omega_{31}}{\partial x_3} + S_{33} \frac{\partial \omega_{13}}{\partial x_1} + S_{31} \frac{\partial \omega_{31}}{\partial x_3} - e_{11} \frac{\partial S_{31}}{\partial x_1} \\ - e_{13} \frac{\partial S_{33}}{\partial x_1} - e_{31} \frac{\partial S_{31}}{\partial x_3} - e_{33} \frac{\partial S_{33}}{\partial x_3} = \rho a_3\end{aligned}\quad (11)$$

If the expressions given in Equation 24-25 are replaced in the equation,

$$\frac{\partial s_{31}}{\partial x} + \frac{\partial s_{33}}{\partial z} + \frac{\partial \omega_y}{\partial x} (-s_{11} + s_{33}) + \frac{\partial \omega_y}{\partial z} (-s_{31} - s_{31}) - e_{11} \frac{\partial s_{31}}{\partial x} - e_{13} \frac{\partial s_{33}}{\partial x} - e_{31} \frac{\partial s_{31}}{\partial z} - e_{33} \frac{\partial s_{33}}{\partial z} = \rho a_3 \quad (12)$$

$$s_{33} = s_{31} = 0 \quad (13)$$

General equation of rotation in beam

$$\omega_{ij} = \frac{1}{2} \left( \frac{\partial u_i}{\partial x_j} - \frac{\partial u_j}{\partial x_i} \right) \quad (14)$$

Rotation in the beam,

$$\omega_{13} = \omega_y = \frac{1}{2} \left( -\frac{\partial w}{\partial x} - \frac{\partial w}{\partial x} \right) = -\frac{\partial w}{\partial x} \quad (15)$$

Rotation substitute in Eq (12),

$$\frac{\partial s_{31}}{\partial x} + \frac{\partial s_{33}}{\partial z} + s_{11} \frac{\partial^2 w}{\partial x^2} = \rho a_z \quad (16)$$

$i = 1, j = 1,3, k = 1,3$  substituting these values into Eq (5)

$$\begin{aligned} \frac{\partial s_{11}}{\partial x_1} + \frac{\partial s_{13}}{\partial x_3} + s_{11} \frac{\partial \omega_{11}}{\partial x_1} + s_{31} \frac{\partial \omega_{11}}{\partial x_3} \\ + s_{13} \frac{\partial \omega_{13}}{\partial x_1} + s_{33} \frac{\partial \omega_{13}}{\partial x_3} + s_{11} \frac{\partial \omega_{31}}{\partial x_1} + s_{11} \frac{\partial \omega_{31}}{\partial x_3} + s_{13} \frac{\partial \omega_{31}}{\partial x_1} \\ + s_{13} \frac{\partial \omega_{33}}{\partial x_3} - e_{11} \frac{\partial s_{11}}{\partial x_1} - e_{13} \frac{\partial s_{13}}{\partial x_1} - e_{31} \frac{\partial s_{11}}{\partial x_3} - e_{33} \frac{\partial s_{13}}{\partial x_3} = \rho a_x \end{aligned} \quad (17)$$

Following similar way, it is obtained that,

$$\frac{\partial s_{11}}{\partial x} + \frac{\partial s_{13}}{\partial z} = \rho a_x \quad (18)$$

The above equation is also used by multiplying  $z$ ,

$$z \frac{\partial s_{11}}{\partial x} + z \frac{\partial s_{13}}{\partial z} = z \rho a_x \quad (19)$$

This equation is the equation of motion derived from the Biot stress stress equations.

Here  $\rho(z)$  is the density of the beam.  $\sigma_{xx} = s_{11}$  is the normal stress,  $\tau_{xz} = s_{13}$  is the shear stress. Sections are integrated across the area.

$$\int_A \frac{\partial \sigma_{xx}}{\partial x} dA + \int_A \frac{\partial \tau_{xz}}{\partial z} dA = \int_A \rho(z) \frac{\partial^2 u_x}{\partial t^2} dA \quad (20)$$

$$\int_A z \frac{\partial \sigma_{xx}}{\partial x} dA + \int_A z \frac{\partial \tau_{xz}}{\partial z} dA = \int_A z \rho(z) \frac{\partial^2 u_x}{\partial t^2} dA \quad (21)$$

$$\int_A \frac{\partial \tau_{xz}}{\partial x} dA + \int_A \frac{\partial \sigma_{xx}}{\partial z} dA + S_{11} \frac{\partial^2 w}{\partial x^2} = \int_A \rho(z) \frac{\partial^2 u_z}{\partial t^2} dA \quad (22)$$

where  $S_{11} = N$  and

$$\frac{\partial^2 u_x}{\partial t^2} = a_x = a_1 \quad (23)$$

$$\frac{\partial^2 u_z}{\partial t^2} = a_z = a_3 \quad (24)$$

Integrals are arranged.

$$N = \int \sigma_{xx} dA, \quad Q = \int \tau_{xz} dA, \quad M = \int z \sigma_{xx} dA, \quad q = \int \frac{\partial \sigma_{zz}}{\partial z} dA \quad (25)$$

Equations are arranged by writing instead of cross-section effect values,

$$\int z \frac{\partial \tau_{xz}}{\partial z} dA = \int_{-h/2}^{h/2} bz \frac{\partial \tau_{xz}}{\partial z} dz = z \tau_{xz} \int_{-h/2}^{h/2} z dz - \int_{-h/2}^{h/2} b \frac{\partial \tau_{xz}}{\partial z} dz = -Q, \quad \frac{\partial Q}{\partial z} = 0 \quad (26)$$

Shear and moment values are putting into the Eq (16).

$$\frac{\partial Q}{\partial x} + q + N \frac{\partial^2 w}{\partial x^2} = 0 \quad \frac{\partial M}{\partial x} - Q = \int z \rho \frac{\partial^2 u_x}{\partial t^2} dA \quad (27)$$

The additional shear stress and moment value from the components of the normal force which are the bending of the beam are added to the shear stress and moment value.

Obtaining the term of acceleration

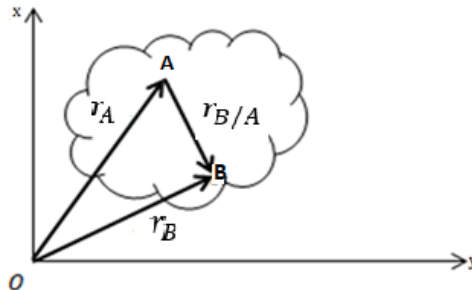


Figure 2. Rotating and translating coordinate axis

$O, x, y$  represent rotating and translating coordinate system in the Figure 2. Position vector on the rotating and shifting coordinate axis;

$$r_B = r_A + r_{B/A} \quad (28)$$

The velocity is found by taking derivate of the position.

$$V_B = \left( \frac{dr_B}{dt} \right)_{XY} \Rightarrow V_B = V_A + \left( \frac{dr_{B/A}}{dt} \right)_{XY} \quad (29)$$

According to the rotating and translating coordinate system  $A(x, y)$ , the length of the vector  $r_{B/A}$  is variable.

$$\left( \frac{dr_{B/A}}{dt} \right)_{XY} = (V_{B/A})_{xy} + \omega \times r_{B/A} \quad (30)$$

Substituting Eq (29) into Eq (30),

$$V_B = V_A + (V_{B/A})_{xy} + \omega \times r_{B/A} \quad (31)$$

Here,  $V_A$ , is the absolute velocity vector for point A.  $V_B$ , is the velocity for point B.  $(V_{B/A})_{xy}$ , It is the relative velocity vector of point B with respect to point A.  $r_{B/A}$ ,  $B$  The position vector of point B relative to the moving axis set at point A.  $\omega \times r_{B/A}$ , The relative velocity of point B with respect to the fixed axis.

The acceleration term is obtained by deriving the velocity vector with respect to time.

$$a_B = \left( \frac{dV_B}{dt} \right)_{XY} \Rightarrow a_B = a_A + \frac{d(V_{B/A})_{xy}}{dt} + \frac{d(\omega \times r_{B/A})}{dt} \quad (32)$$

Eq (32) is arranged

$$a_B = a_A + \alpha \times r_{B/A} + 2\omega \times (V_{B/A})_{xy} + \omega \times (\omega \times r_{B/A}) \quad (33)$$

$a_A$ , the acceleration at point A,  $a_B$ , the acceleration at point B,  $\alpha$  angular acceleration vector,  $\omega$ , angular velocity vector,  $r_{B/A}$ , position vector of point B according to A point,  $(V_{B/A})_{xy}$ , velocity vector of point B according to A point,  $(a_{B/A})_{xy}$ , acceleration vector of point B according to A point,  $\alpha \times r_{B/A}$  angular acceleration effect,  $\omega \times (\omega \times r_{B/A})$  angular velocity effect,  $2\omega \times (V_{B/A})_{xy}$  coriolis acceleration [6].

The resulting acceleration terms apply to the rotating beam.

$$a_x = \frac{\partial^2 u_0}{\partial t^2} - z \frac{\partial^3 w}{\partial x \partial t^2} - \omega^2 \left( u_0 - z \frac{\partial w}{\partial x} + R + u \right) \quad (34)$$

$$a_z = \frac{\partial^2 w}{\partial t^2} \quad (35)$$

$$\int \rho a_x dA = \int \rho \left[ \frac{\partial^2 u_0}{\partial t^2} - z \frac{\partial^3 w}{\partial x \partial t^2} - \omega^2 \left( u_0 - z \frac{\partial w}{\partial x} + R + u \right) \right] dA \quad (36)$$

Since the transverse displacement of the beam is smaller than the longitudinal displacement, it can be neglected.

$$\ddot{u}_0 \approx 0, \frac{\partial \ddot{w}}{\partial x} \approx 0 \quad (37)$$

Acceleration components of the beam,

$$\int \rho a_x dA = \int -\rho \omega^2 \left( u_0 - z \frac{\partial w}{\partial x} + R + u \right) dA = -\rho_0 \omega^2 (u_0 + R + u) + \rho_1 \frac{\partial w}{\partial x} \quad (38)$$

In this study, the beam has a symmetrical cross-section and homogeneous material.

$$\rho_0 = \rho A = m, \quad \rho_1 = 0, \quad \rho_2 = \rho I \quad (39)$$

$$\int \rho a_x dA = -\rho A \Omega^2 (R + x + u_0) \quad (40)$$

$$\int \rho z a_x dA = -\rho I \left( \frac{\partial \ddot{w}}{\partial x} + \Omega^2 \frac{\partial w}{\partial x} \right) \quad (41)$$

$$\int \rho a_z dA = \rho A \ddot{w} \quad (42)$$

When the equation is simplified, the expressions are edited.

$$\begin{aligned} (-EI)''w'' + (-EI)'w''' + (-EI)w^{iv} + N''w + N'w' + N'w' + Nw'' - N \frac{\partial^2 w}{\partial x^2} \\ + N \frac{\partial^2 w}{\partial x^2} - N'w' = \rho A \ddot{w} \end{aligned} \quad (43)$$

The equation is regulated,

$$(-EI)w^{iv} + 2(-EI)'w''' + [(-EI)'' + N]w'' + N'w' + N'w' = \rho A \ddot{w} \quad (44)$$

Equation of motion for rotating beam is obtained

In a cantilever beam, integrals are taken along the beam at any point.

$$\frac{\partial N}{\partial x} = -\rho A \Omega^2 (R + x + u_0) \quad (45)$$

$$\int_x^L \partial N = \int_x^L -\rho A \Omega^2 (R + x + u_0) \partial x \quad (46)$$

Point  $L$  equals to 0 at the free end of the cantilever beam.

$$N(x) = \int_x^L \rho A \Omega^2 (R + x + u_0) \partial x \quad (47)$$

### Conclusion

Rotating beams were discussed in this study. The motion equation of rotating beams is derived from biot stresses. Acceleration terms relative to axes are obtained for the moving system. Stress terms are derived from the theory of elasticity. Equation of motion for the rotating beam were obtained by writing the equations into the biot equation. This equation has been investigated for compatibility with the literature.

### References

- [1] Nayfeh A. H., Pai F. B. Linear ve nonlinear Mechanics, John Wiley and Sons, New York, 2004.
- [2] Biot M.A. Mechanics of Incremental Deformations, John Wiley and Sons, New York, 2008

- [3] Akbarov S.B. Dynamics of Pre-Strained Bi-Material Elastic Systems, Springer International Publishing Switzerland, 2015
- [4] Reddy J. N. Mechanics of Laminated Composite Plates and Shells Theory And Analysis, New York, 2004
- [5] Ozgümüş, O. Ozdemir; Kaya, M. O. Flapwise bending vibration analysis of a rotating double-tapered Timoshenko beam. Archive of Applied Mechanics, 2008, 78.5: 379-392.
- [6] Pakdemirli, M. Mühendislik Dinamiği, Ankara, 2010.

## Parametrical Resonance Analysis of a Rotating Beam

*Betül Üstüner, Celal Bayar University, Department of Civil Engineering, Manisa, Turkey*  
*Berra Gültekin Sınır, Celal Bayar University, Department of Civil Engineering, Manisa, Turkey*  
*\*Corresponding author: gultekin.sinir@cbu.edu.tr*

**Keywords:** Rotating Beam, Parametrical Resonance Analysis, Perturbation Method  
**Discipline:** Civil Engineering

### Abstract

Rotating beams are used in many engineering applications. For example, these structures such as helicopters, turbine blades, wind turbines, ventilation systems, submarines, turning area structures.

Dynamic characteristics and natural frequencies of rotating beams are very important. Therefore, many investigators have studied rotating beams. Most of these studies have used Euler Bernoulli beam theory in their model [1-3].

In this study, the parametrical resonance case of a rotating beam is analyzed. In this model, Euler Bernoulli beam theory is considered. The beam has cantilever beam support conditions. The beam is connected to a rigid shaft. This shaft with a certain diameter and rotates at a constant angular velocity. The angular velocity is time depended. The variation of the angular velocity with time is harmonic around mean value. The cross-section of the beam is not uniform. The height of beam varies along the length of the beam. The mathematical model of the beam is a partial differential equation. The mathematical model has the terms centrifugal force, bending stiffness and acceleration. The centrifugal force is written in the integral form. The centrifugal force depends on the square of the beam's rotational speed. The originality of this study is the application of Galerkin and Multiple Scale Perturbation methods to the parametrical analysis of the rotating beam. In order to perform parametric resonance analysis, firstly, the as a perturbation technique is applied directly to the mathematical model [4]. In this method, the time is divided into multi scales. After application of the perturbation technique, the mathematical models become more than one equation. These equations are linear partial differential equations. The perturbation technique is a kind of serial solution which is using a small parameter denoted with  $\varepsilon$ . According to the power of  $\varepsilon$ , the mathematical model is separated. At minimum order of  $\varepsilon$ , the equation is a linear partial differential equation. In the application of these two methods together, a numerical integration method is necessary at the application of solvability conditions. The parametric resonance case is only seen when the angular velocity of the system is close to two times of the natural frequency of the beam.

### Introduction

Many physical models such as beam [5-7], plate and shell [8,9] model are recommended for rotating objects. Beams encounter problems of axial deformation, bending and torsion under a certain external force. The cross section of the beam can be uniform or variable cross section. Beams with variable cross-section are used as rotating beam elements in engineering applications such as machinery, construction and aviation. Examples of this are many advanced engineering structures such as helicopter blades, turbine blades, wind turbines, ventilation systems, submarine propellers [10]. It is important to know the dynamic behavior of the building in the design of these structures. Rotating beams have a wide range of applications. Therefore, studies on dynamic analysis and solution methods have gained momentum. It is mathematically modeled and analyzed to find the displacement of these beams. Some theories are used in beams during this modeling. The Euler-Bernoulli beam theory is also at the top of these theories [11-13]. Beams can have different material properties such as composite beams, functional graded beams. All the same time, the movement of the beams can also change. In this study, flapwise motion is discussed. Flapwise movement is seen, which is the wing movement that rotates around the z axis. It is the flapwise vibrations that examine the vibrations of the movement of the beams perpendicular to the plane they rotate. In this vibration motion, the beam moves up and down.

### Equation of motion

The schematic representation of the Euler Bernoulli beam, rotating, cantilever, varying in height is as follows.  $h_0$

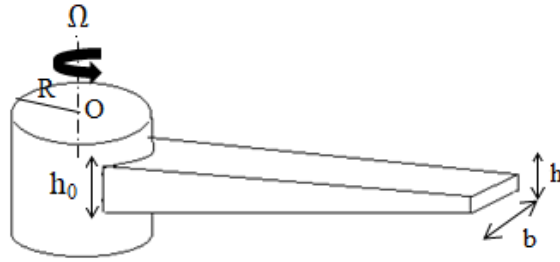


Figure 1. The non-uniform Euler Bernoulli beam

In Figure 1,  $L$  is the length of the beam, the center  $O$  of the beam held by a fixed rigid shaft,  $R$  is the radius and  $\Omega$  is angular velocity. Section width is shown as constant  $b$ , varying beam height  $h$  and height of  $h_0$  at the root.

The motion equation of the rotating beam is taken from Özdemir, Kaya (2006) [13],

$$\frac{\partial^2}{\partial x^2} \left( EI \frac{\partial^2 w}{\partial x^2} \right) - \frac{\partial}{\partial x} \left( N \frac{\partial w}{\partial x} \right) + \rho A \frac{\partial^2 w}{\partial t^2} + \mu \frac{\partial w}{\partial t} = 0 \quad (1)$$

Centrifugal force in this equation,

$$N(x) = \int_x^L \rho A(x) \Omega^2 (r + x) dx \quad (2)$$

In this equation  $N$  is the centrifugal force,  $\rho$  is the density,  $\mu$  is the damping ratio,  $EI$  is the bending stiffness. Boundary conditions of fixed-free end support in Euler Bernoulli beam,

$$x(0) = x'(0) = 0 \quad (3)$$

$$x''(L) = x'''(L) = 0 \quad (4)$$

( ) <sup>$l$</sup>  shows the derivation with respect to  $x$ .

### Nondimensionalization

For the purpose of nondimensionalization [14], the following dimensionless terms are introduced:

$$\tilde{w}(t, \tilde{x}) = \frac{w}{L}, \quad \tilde{x} = \frac{x}{L}, \quad \tilde{t} = t \sqrt{\frac{EI_0}{\rho A_0 L^4}}, \quad \delta = \frac{R}{L} \quad (5)$$

The hat ( $\tilde{\quad}$ ) mark will not be used in the rest of the work for ease of display.

Where  $L$  is the length of the beam,  $R$  is the radius of shaft,  $E$ ,  $\rho$ ,  $A$  are Young's modulus, density and the cross-sectional area of the beam, respectively.  $I$  is the cross sectional moment of inertia along the bending axis.

$$\frac{\partial^2}{\partial x^2} \left( I(x) \frac{\partial^2 w}{\partial x^2} \right) - \frac{\partial}{\partial x} \left( N \frac{\partial w}{\partial x} \right) + A(x) \frac{\partial^2 w}{\partial t^2} + \mu \frac{\partial w}{\partial t} = 0 \quad (6)$$

### Solution Methods

In this section we try to find approximate analytical solutions for Eq. (1) subject to the related boundary conditions. We apply the method of multiple time scales [44], to the partial equation and boundary conditions directly. We assume the following approximate solution for the deflection in the form



$$w(x, T_0, T_1, \varepsilon) = w_0(x, T_0, T_1) + \varepsilon w_1(x, T_0, T_1) \quad (7)$$

where,  $T_0$  and  $T_1$  represent the fast and slow time scales, respectively. Time derivatives are

$$\frac{\partial}{\partial t} = D_0 + \varepsilon D_1 + \dots \quad (8)$$

$$\frac{\partial^2}{\partial t^2} = D_0^2 + 2\varepsilon D_0 D_1 + \dots \quad (9)$$

Substituting Eqs.(8) into Eq(7) and ordering of the terms at each power of  $\varepsilon$ , one obtains;

$$O(1): (I(x)w_0'')'' - (N_0 w_0')' + D^2_0 A(x)w_0 = 0 \quad (10)$$

$$O(\varepsilon): (I(x)w_1'')'' - (N_0 w_1')' + D^2_0 w_1 A(x) \\ = -\mu D_0 w_0 + (N_1 w_0')' - 2D_0 D_1 w_0 A(x) \quad (11)$$

At  $O(1)$  the problem is linear. We assume the following form of solution,

$$w_0 = (B_n(T_1)e^{i\omega_n T_0} + \bar{B}_n(T_1)e^{-i\omega_n T_0})X_n(x) \quad (12)$$

where  $\omega_n$  is the natural frequencies  $B_n$  is the amplitude of motion and  $X_n(x)$  is the mode shapes. Substituting Eq.(12) into :Eq.(10), one has

$$(I(x)X_n'')'' - (N_0 X_n')' - \omega_n^2 X_n = 0 \quad (13)$$

Fixed-free support boundary conditions are respectively as

$$X_n(0) = X_n'(0) = 0 \quad (14)$$

$$X_n(1)'' = X_n(1)''' = 0 \quad (15)$$

It is difficult to solve problems with variable coefficients depending on the location. The solution of the linear part of the equation is done by the Galerkin method. This method is a semi-analytical method. In Galerkin method, shape functions satisfying boundary conditions are written as series sum.

$$y^{iv} - \lambda^4 y = 0 \quad (16)$$

Static solution of the simplest beam equation,

$$y = c_1 \cosh \lambda x + c_2 \sinh \lambda x + c_3 \cos \lambda x + c_4 \sin \lambda x \quad (17)$$

Boundary conditions for fixed-free support are written instead in the solution

$$y(0) = 0 \quad , \quad y'(0) = 0 \quad (18)$$

$$y''(1) = 0 \quad , \quad y'''(1) = 0 \quad (19)$$

The shape function is determined while solving the equation in the Galerkin method.

$$X_n = \sum_{i=1}^{\infty} q_i y_i \quad (20)$$

Here  $q_i$  is a constant number,  $y_i$  is the equation to be applied to the boundary conditions.

$$y_i = \cosh \lambda x - \cos \lambda x - \frac{\cosh \lambda + \cos \lambda}{\sinh \lambda + \sin \lambda} (\sin \lambda x - \sin h \lambda x) \quad (21)$$

In order to solve the equation system, the determinant of the equation is set to 0. ( $\det(A) = 0$ ).

$$\begin{aligned} \lambda_1 &= 1.875104069 \\ \lambda_2 &= 4.694091133 \\ \lambda_3 &= 7.854757438 \\ \lambda_4 &= 10.99554073 \\ \lambda_5 &= 14.13716839 \end{aligned}$$

At  $O(\varepsilon)$  the assume the following form of solution,

$$w_1 = (\psi(X_1, T_1)e^{i\omega_n T_0} + \bar{\psi}(X_1, T_1)e^{-i\omega_n T_0}) \quad (22)$$

Boundary conditions,

$$\psi(0) = 0 \quad , \quad \psi'(0) = 0 \quad (23)$$

$$(x)\psi''(1) = 0 \quad , \quad (I(x)\psi'')' = 0 \quad (24)$$

$\psi(X_1, T_1)$  is the part related to secular terms  $\bar{\psi}(X_1, T_1)$  indicates the complex conjugate part. Substituting Eq.(22) into Eq.(11), one has

$$\begin{aligned} e^{i\omega_n T_0} [(I(x)\psi'')'' - (N_0\psi')' - \omega_n^2 A(x)] \\ = [-\mu i \omega_n X_n] B_n e^{i\omega_n T_0} - 2i \omega_n X_n D_1 A(x) B_n e^{i\omega_n T_0} \\ + (N_1 X_n') \bar{B}_n e^{i\omega_n T_0} \end{aligned} \quad (25)$$

To solve this equation, it is necessary to edit the expression

$$\Omega = \Omega_0 + \varepsilon \Omega_1 \cos \theta T_0 \quad (26)$$

$$\Omega^2 \cong \Omega_0^2 + 2\varepsilon \Omega_0 \Omega_1 \cos \theta T_0 \quad (27)$$

$$\cos \theta T_0 = \frac{1}{2} (e^{i\theta T_0} + e^{-i\theta T_0}) \quad (28)$$

Here  $\Omega_0$  is the average velocity and,  $\Omega_1$  is the amplitude of the change around the average velocity.  $\theta$  is the frequency of change of angular velocity with time.  $\varepsilon \ll 1$  small value.

Perturbative solution is applied to centrifugal force.

$$N = N_0 + \varepsilon N_1 \quad (29)$$

$$N = \Omega_0^2 + 2\varepsilon \Omega_0 \Omega_1 \cos \theta T_0 \int_x^L A(x) (\delta + x) dx \quad (30)$$

$$N_0 = \Omega_0^2 \int_x^L A(x) (\delta + x) dx \quad (31)$$

$$\begin{aligned} N_1 &= 2\varepsilon \Omega_0 \Omega_1 \cos \theta T_0 \int_x^L A(x) (\delta + x) dx \\ &= \Omega_0 \Omega_1 \frac{1}{2} (e^{i\theta T_0} + e^{-i\theta T_0}) \int_x^L A(x) (\delta + x) dx \end{aligned} \quad (32)$$

To obtain secular terms it is necessary to operate on the right side of the equation.

$$\begin{aligned}
 R. H. S. = & [-\mu i \omega_n X_n] B_n e^{i \omega_n T_0} - 2i \omega_n X_n D_1 A(x) B_n e^{i \omega_n T_0} \\
 & + \left( \left( \Omega_0 \Omega_1 \int_x^L A(x) (\delta + x) dx X_n' \right) \right)' B_n (e^{(\theta + \omega_n) i T_0} \\
 & + e^{(\omega_n - \theta) i T_0}) + \overline{B}_n (e^{(\theta - \omega_n) i T_0} + e^{(-\omega_n - \theta) i T_0})
 \end{aligned} \quad (33)$$

There are  $\theta$  values that make up the secular term.

$$\theta = 2\omega_n + \varepsilon S \quad (34)$$

Here,  $\omega_n$  is natural frequency,  $S$  is detuning parameter,  $\varepsilon$  is small value.

$$\begin{aligned}
 e^{i \omega_n T_0} [(I(x)\psi'')'' - (N_0\psi')' - \omega_n^2 A(x)] \\
 = & \left[ [-\mu i \omega_n X_n - 2i \omega_n X_n D_1 A(x)] B_n \right. \\
 & \left. + \left( \left( \Omega_0 \Omega_1 \int_x^L A(x) (\delta + x) dx X_n' \right) \right)' \overline{B}_n e^{i S T_1} \right] e^{i \omega_n T_0} + N. S. T
 \end{aligned} \quad (35)$$

N.S.T. means non-secular term. To solve the equation, it is necessary to multiply both sides of the equation by the function  $u$  and integrate.

$$\begin{aligned}
 \int_0^1 \psi \left[ (I(x)u)'' - 2(I(x)u)'''' + ((I(x)'' + \varepsilon \Omega I(x))u)'' - ((\varepsilon \Omega I(x))u)' \right. \\
 + N'u \Big] dx + (I(x)u\psi'''' - [(I(x)u)' - 2I(x)u]\psi'' \\
 + [(I(x)u)'' - 2(I(x)u)' + I(x)'' + \varepsilon \Omega I(x)u]\psi' \\
 - [(I(x)u)'''' - 2(I(x)'u)'' + ((I(x)'' + \varepsilon \Omega I(x))u)' \\
 - \varepsilon \Omega I(x)u] \psi) \Big|_0^1 = \int_0^1 R. H. S. u dx
 \end{aligned} \quad (36)$$

The function  $u$  is taken as the function  $X_n$  in order to satisfy the solubility condition and carried to the equation by partial integration

$$[(I(x)X_n'')' - (N_0X_n')' - \omega_n^2 X_n' A(x)]\psi + \psi'' X_n \Big|_0^1 = \int_0^1 [R. H. S.] X_n dx \quad (37)$$

Equations are arranged.

$$D_1 B_n + (i\alpha_{im} + \alpha_{re}) B_n + b_n \overline{B}_n e^{i S T_1} = 0 \quad (38)$$

To solve this equation;

$$B_n = \frac{1}{2} \alpha(T_1) e^{i\beta(T_1)} \quad (39)$$

The stability regions equation is obtained.

$$S = 2 \left( -\alpha_{im} \pm \sqrt{b_n^2 - \alpha_{re}^2} \right) \quad (40)$$

$\Omega = 2\omega_n$  Parametric resonance occurs when the angular velocity is equal to twice the natural frequency.

Here S is detuning parameter. Indicates the stability regions of the system. When it approaches 2 times the resonance state is seen.

### Numerical Results

Parametric resonance analysis was performed. Stability zones of the system have been determined. Stability zones are shown in graphs. Stability regions graphs were created with the data obtained from these equations.

$$S_1 = 2 \left( -\alpha_{im} + \sqrt{b_n^2 - \alpha_{re}^2} \right) \quad (41)$$

$$S_2 = 2 \left( -\alpha_{im} - \sqrt{b_n^2 - \alpha_{re}^2} \right) \quad (42)$$

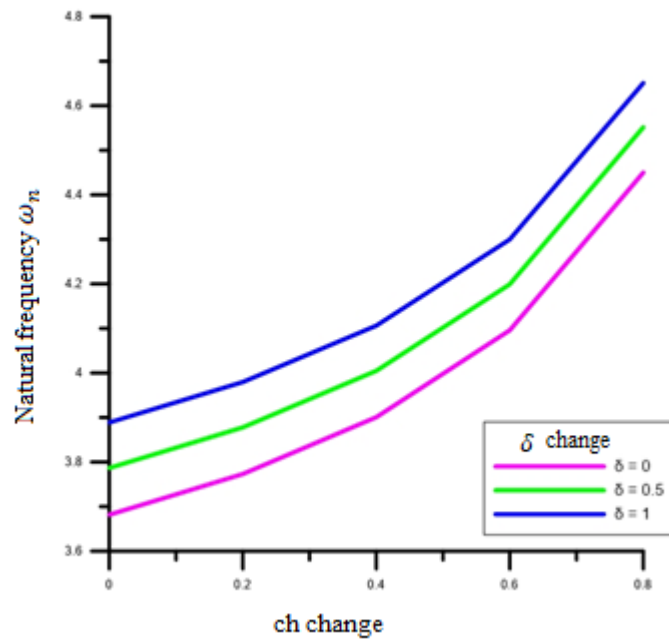


Figure 3. Natural frequency values for beam with decreasing height ( $\Omega = 1$ ,  $\delta = 0$ ,  $\delta = 0.5$ ,  $\delta = 1$ )

In Figure 3, as the  $\delta$  value increases, the natural frequency values increase.

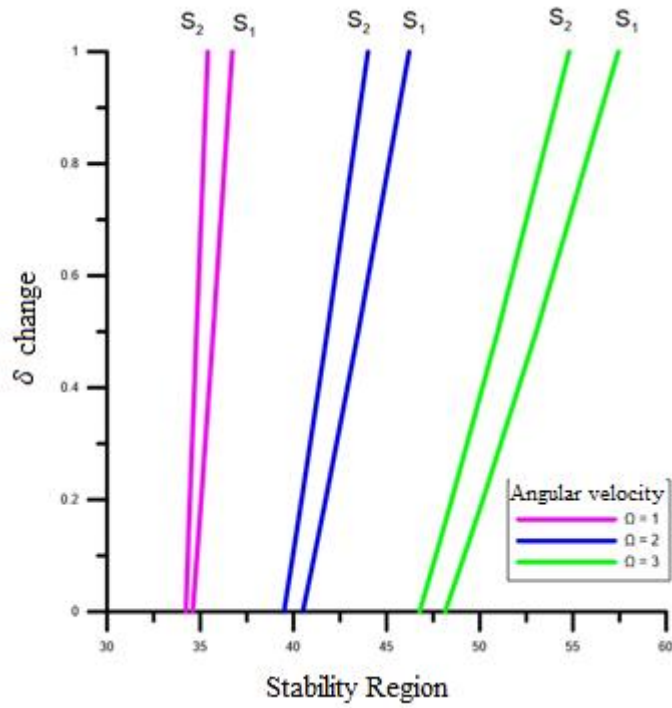


Figure. 4. The effect of angular velocity on stability regions

In Figure 4, stability regions increase as the angular velocity increases.

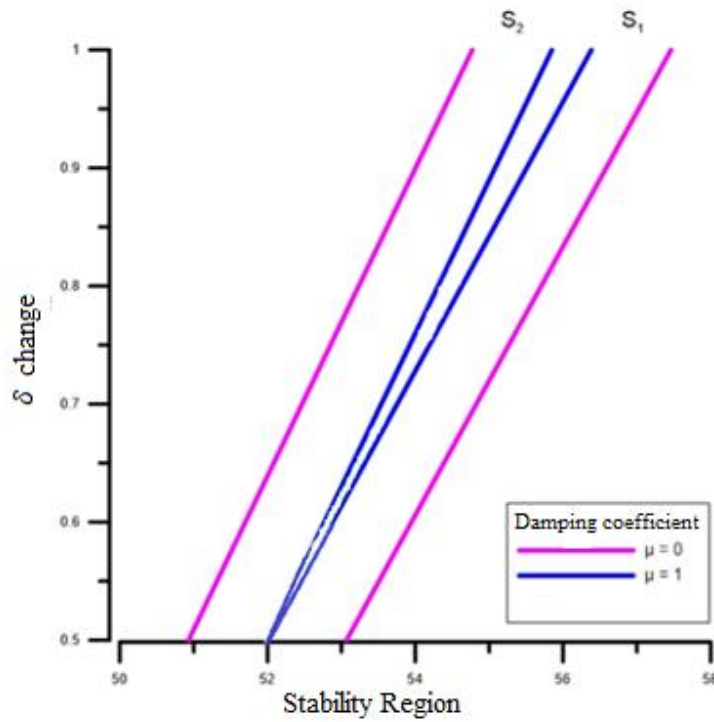


Figure 5. Effect of damping value on angular velocity

In Figure 5, as the damping value gets smaller, the unstable region increases.

Table 1.  $\delta$  and  $\Omega$  natural frequency, height decreasing beam ( $c_b = 0, c_h = 0.3, n = 1$ )

$\delta \backslash \Omega$	1	2	3
0	3.83108	4.28432	4.94270
	20.03294	20.48248	21.21086
	53.48196	53.92467	54.65406
	103.47892	103.93430	104.68897
	174.23289	174.71289	175.51014
0.1	3.85220	4.35910	5.08684
	20.05299	20.56076	21.38054
	53.50241	54.00568	54.83359
	103.50038	104.01975	104.87979
	174.25700	174.80907	175.72560
0.2	3.87320	4.432584	5.22689
	20.07301	20.63874	21.54884
	53.52285	54.08656	55.01232
	103.52184	104.10513	105.07025
	174.28111	174.90521	175.94084
0.5	3.935515	4.64589	5.62563
	20.13294	20.87086	22.04570
	53.58411	54.32837	55.54484
	103.58619	104.36086	105.63955
	174.35343	175.19338	176.58517
1	4.037184	4.98066	6.23222
	20.23243	21.25189	22.84883
	53.68605	54.72874	56.41983
	103.69334	104.78567	106.58159
	174.47389	175.672739	177.65451

In Table 1 depending on the values  $c_b = 0, c_h = 0.3, n = 1, \Omega$  and  $\delta$  change table was obtained. Data were obtained for 5 different mode values. It is seen that the natural frequency values increase for each mode. Mode 1 has the smallest natural frequency value.

### Conclusion

In this study, dynamic behaviors of the rotating beam are analyzed. Euler-Bernoulli theory is used to model the rotating beam. A hybrid method which is perturbation-Galerkin method is used to analyze. It is main novelty of this study. The stability boundaries are obtained for the parametric resonance case. The unstable region is getting smaller as increasing damping coefficient. For higher values of rotating velocity, larger unstable regions are obtained.

### References

- [1] W. J. Book 1990 Proceedings of the 29<sup>th</sup> Conference on decision and control, Honolulu, Hawaii, 500-506. Modeling, design, and control of flexible manipulator arm: a tutorial review.
- [2] SPECTOR A. FLASHNER H. ASME Journal of Dynamic Systems, Measurements and control 112, 186-193. Modeling design implications of noncolocated control in flexible systems. 1990.

- [3] NORGUL WO., IEEE Transactions on Automatics Control, Dynamic boundary control of Euler Bernoulli beam. 1992; 37, 639-642.
- [4] NAYFEH A. H. Introduction To Perturbation Techniques, John Wiley and Sons, New York, 1981.
- [5] Liu, T., Ren Y., Vibration and flutter of wind turbine blade modeled as anisotropic thin-walled closed-section beam. Science China Technological Sciences, 2011, 54(3), 715-722.
- [6] Larsen, J. W., Nielsen, S. R., Non-linear dynamics of wind turbine wings. International Journal of Non-Linear Mechanics, 2006, 41(5), 629-643.
- [7] Larsen, J. W., Nielsen, S. R. Nonlinear parametric instability of wind turbine wings. Journal of Sound and Vibration, 2007, 299(1-2), 64-82.
- [8] Young, T. H., & Liou, G. T., Dynamic response of a rotating blade with time-dependent rotating speed. Journal of sound and vibration, 1993, 164(1), 157-171.
- [9] Rao, J. S., Gupta, K. Free vibrations of rotating small aspect ratio pretwisted blades. Mechanism and Machine Theory, 1987, 22(2), 159-167.
- [10] Ozgumus, O. O., Kaya, M. O. Flapwise bending vibration analysis of a rotating double-tapered Timoshenko beam. Archive of Applied Mechanics, 2008, 78(5). 379-392.
- [11] Huang, C. L., Lin, W. Y., Hsiao, K. M. Free vibration analysis of rotating Euler beams at high angular velocity. Computers & Structures, 2010, 88(17-18), 991-1001.
- [12] Ozdemir, O., Kaya. M. O., Flapwise bending vibration analysis of a rotating tapered cantilever Bernoulli–Euler beam by differential transform method. Journal of Sound and Vibration, 2006, 289(1-2), 413-420.
- [13] Ozgumus, O. O., Kaya, M. O., Flapwise bending vibration analysis of double tapered rotating Euler–Bernoulli beam by using the differential transform method. Meccanica, 2006, 41(6), 661-670.
- [14] Sınır, S., Çevik, M., Sınır, B. G. Nonlinear free and forced vibration analyses of axially functionally graded Euler-Bernoulli beams with non-uniform cross-section. Composites Part B: Engineering, 2018, 148, 123-131.

## Punching Behavior of Fiber Reinforced Concrete Thin Panels

*Jamalullah Naseri\**, İzmir Institute of Technology, Dept. of Civil Engineering, İzmir, Türkiye  
*Selçuk Saatci*, İzmir Institute of Technology, Dept. of Civil Engineering, İzmir, Türkiye  
*\*Corresponding author: jamalnasari@iyte.edu.tr*

**Keywords:** Fiber reinforced concrete, punching, thin panels  
**Discipline:** Civil Engineering

### Abstract

In this study, the punching behavior of Steel fiber reinforced concrete (SFRC) thin panels was investigated. Two panel specimens with dimensions of 1700x1700 mm<sup>2</sup> in thicknesses of 50 and 70 mm were cast. Steel fiber of type Dramix® 60/80 with a ratio of 0.5% by volume was used. The panel tests were supplemented by flexural tests on one-way panels. It was therefore possible to assess the flexural behavior of the tested panels. The yield line theory was also used to evaluate the load carrying capacity of the panels. From the results of the tests, it was observed that the panels experienced ductile punching failure.

### Introduction

Flat plate is a reinforced concrete structural system consists of slabs supported directly by columns without beams. This system is typically used in structures that have comparatively low levels of gravity loads (George & Tian, 2012). Flat plate systems are commonly used due to their numerous advantages. Effective formworks reduce the construction duration and cost compared to other structural systems. In addition, flat plate systems have low ceiling height, reducing overall height of the structure and decreasing material cost. On the other hand, due to lack of beams, required column capitals and drop panels makes a flexible design difficult (Li et al., 2007). Punching shear failure is a significant problem in flat plate systems due to high localized stresses around column support connections. The brittle nature of punching shear results in a very risky failure. After the initiation of punching failure, the structure's resistance is substantially decreased, letting the column and slab to be separated, and then allow the entire system to collapse (Nguyen-Minh et al., 2011). (See Figure 6)



Figure 6. Top story collapse at Pipers Row Car Park, UK. (Wood, 1997)

Several methods are developed to improve punching strength of flat plates. These include increasing the thickness of the slabs or using column's capitals and different types of shear reinforcement. Recently, researchers are interested in fiber reinforced concrete to increase the punching strength (Barros et al. (2015); Saatci et al. (2018); Gouveia et al. (2018)). As long as suitable mix compositions of SFRC



are used, steel fibers could be appropriate shear reinforcement for reinforced concrete flat plates, by enhancing the load carrying strength and energy absorption capacity of the slab column connection. These advantages are obtained from the mechanisms of fiber reinforcement offered by fibers bridging the micro-cracks that avoid the spread of cracks, preferring the existence of numerous cracks of small width (Moraes Neto et al., 2013). Also, latest experimental studies demonstrate the feasibility of constructing steel fiber reinforced concrete slab without conventional reinforcement (Tan & Venkateshwaran, 2019).

This paper presents an experimental study to investigate the punching shear behavior of steel fiber reinforced concrete thin panels without traditional reinforcement. In this study, two panels with different thicknesses having same type of steel fibers and ratios were tested and two one-way panels of identical concrete mixture were tested under flexure. The yield line theory was also used to evaluate the load carrying capacity of the two-way panels.

### Experimental program

#### Material

In this study, same concrete mixture was used for both one-way and two-way panel specimens. The mixture ingredients contain, Portland cement (PC), CEM I 42.5 R, consistent with TS EN 197-1: 2012, fly ash (FA) of class F, crushed limestone coarse aggregate with maximum aggregate size ( $D_{max}$ ) of 16 mm, river sand and hooked-end steel fiber of type Dramix® 60/80. The steel fiber length and diameter were 80 mm and 0.75 mm.

#### Test specimens and setup

In this research, two panel specimens with dimensions of 1700x1700 mm<sup>2</sup> in thicknesses of 50 and 70 mm were cast. The panels were named as J50 and J70, where the numbers after letter J represent the thickness of the panel specimens. Steel fiber ratio of 0.5% by volume was used in both specimens. After casting, the specimens were kept in humid environment for about a month before testing. In order to define the mechanical properties of the concrete, three cylinders ( $\phi$ 100 x 200 mm) were cast for each specimen as well and tested at the same day as the panel specimens were tested. Average concrete compressive cylinder strength after approximately three months was 41.8 MPa for both panels.

Panels were tested in a simply supported system with a clear span of 1600 mm from support to support. The simply supported system was provided by steel bars of 30 mm diameter placed on the flanges of four steel beams which sat on footings. Footings were mounted on the strong floor of the lab (Figure 2). Panels were loaded on the midpoint by a hydraulic loading machine with a constant speed of 3 mm/min. The load was applied through a steel plate of 120 mm diameter. Midpoint displacement and applied load were measured.

Usually direct tension and flexural tests are performed to define the tensile behavior of fiber reinforced concrete (Gouveia et al., 2019). In this study, two one-way panels with dimensions of 500 x 2000 mm and thickness of 50 mm and 70 mm were cast to determine the one-way flexural behavior of the tested panels. These one-way panels were named as F50 and F70, where the numbers after the letter F represent the thickness of the panel specimen. The panels were tested under three-point loading with clear span of 1700 mm. Panels were supported by two steel cylinders, which worked as a simply supported system. A steel rod with a diameter of 30 mm was placed under the hydraulic loading machine and a linear load was obtained at the midpoint (Figure 3). The load was applied at constant speed of 3 mm/min. Midpoint displacement and load were measured.



Figure 7. Test setup



Figure 8. One-way panel test

### Experimental Results

The load displacement curve obtained from one-way flexural tests are shown in Figure 4. As it is observed from the curve, the panel F70 bears more load and displays a much more ductile behavior than F50. F50 withstood a maximum load of 1.34 kN and quickly lost its strength after the first crack. On the other hand, F70 showed a gradual decrease after the maximum load of 2.6 kN.

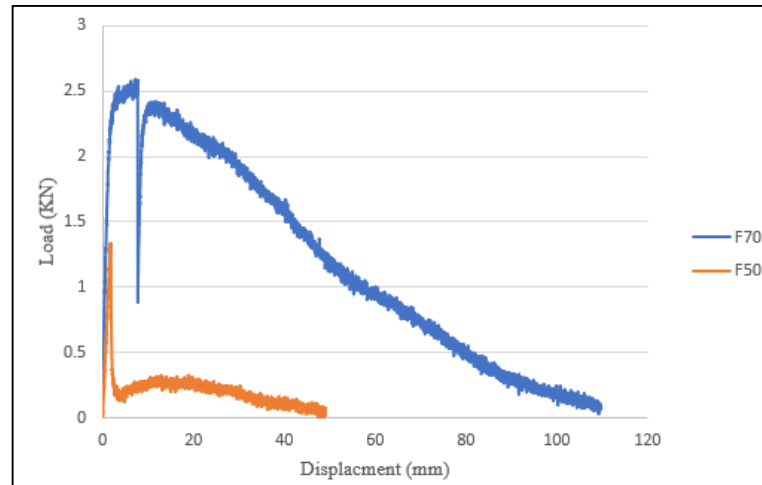


Figure 9. Load displacement curve of one-way panels

Relation between the applied load and the displacement at the center of the tested two-way panels is shown in Figure 5. As seen in the figure, change in thickness of the specimens resulted in a significant change in the strength. However, their general behavior is very similar. In both panels, applied load increased linearly up until cracking. After cracking occurred, both panels' stiffnesses reduced significantly. The first crack occurred in J50 and J70 were approximately at loads of 11 kN and 17 kN, respectively, almost at the same displacement of 3.5 mm. The maximum applied load in F50 and F70 were measured to be 17 kN and 28 kN, at displacements of 54 mm and 64 mm, respectively. The applied load capacity increased by 64.71 % in panel J70 compared to J50. The maximum load achieved in both panels occurred long after the initial cracks. If these unreinforced panels did not contain steel fiber, they were expected to collapse with the first crack, while these steel fiber reinforced concrete panels have shown a very ductile behavior. The ductility of the steel fiber reinforced concrete allowed the panels to resist to higher load levels and show a ductile punching behavior.

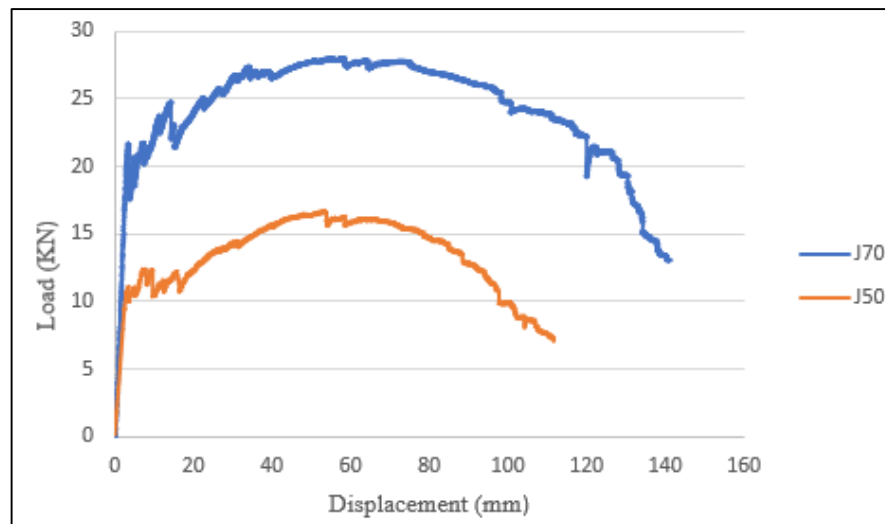


Figure 10. Load- displacement behavior of two-way panels

In both panels, first flexural crack occurred on the bottom surface. The cracks formed from the midpoint right below the loading plate and extended radially on diagonals towards the edges. Flexural cracks' widths increased with increasing load. Near the peak load, cracks started to appear on the top surface in tangential direction around the steel plate. As the tangential cracks became exceedingly wide, the load dropped gradually. Finally, the loading plate started to punch through, and a punching failure observed in both panels evidenced by the formation of a punching cone (Figure 11 and Figure 12).



Figure 11. Crack patterns of panel J50 (a) flexural crack (b) tangential crack



Figure 12. Crack patterns of panel J70 (a) flexural crack (b) tangential crack

Yield line theory can be used to determine the flexural capacities of the tested two-way panels and verify their failure modes. Yield line theory relies on predicting a collapse mechanism with compatible boundary conditions and calculating the maximum load using the virtual work principle. A failure load of  $P_u = 8M_y$ , where  $M_y$  is the one-way flexural yield strength for a unit width, is given by the basic yield line pattern which is formed by the midpoint load and extended from the center to corners on diagonals (Park & Gamble, 1999)

One-way panels result was used to define flexural capacity for two-way panels. As one-way panels were 0.5 mm in width, flexural strength obtained from one-way tests were multiplied by two in order to determine  $M_y$ . The yield line theory and experimental results are presented in Table 1. The flexural capacity calculated from the yield line theory was higher than the experimental result, which verifies that the panels failed in punching.

Table 4. Experimental and calculated results

Specimen	Flexural strength for a unit strip kN m/m	Experimental strength kN	Calculated two-way flexural strength kN
J50	2.68	17.0	21.44
J70	5.20	28.0	41.60

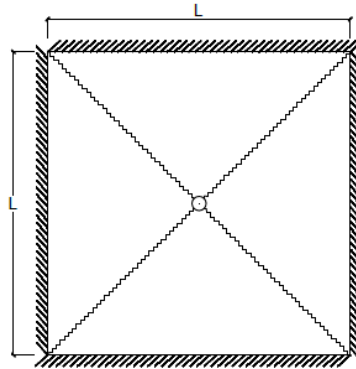


Figure 13. Yield line mechanism for a simply supported square slab (Batarlar, 2013)

### Conclusion

The following conclusions can be drawn based on the results obtained from the study:

- Steel fibers significantly enhanced the panels' punching behavior.
- Panel thickness is a major factor for panels' strength. Applied load increased by 64.71 %, as the thickness of panel increased from 50 mm to 70 mm.
- Panel thickness is also a major factor for flexural strength of one-way panels. The flexure strength enhanced by 94.0 % when the panel thickness changed from 50 mm to 70 mm. This increase is significantly higher than the increase that would be expected due to the increase in the effective depth.
- Strength calculated from the yield line theory were higher than experimental results, which confirmed that the presence of fibers increased the flexural capacity and resulted in final punching failure in these panels.

### Acknowledgement

This study was conducted with the support provided by the Scientific and Technological Research Council of Turkey (TUBITAK), project number 217M442.

### References

- [1] Barros, Joaquim A. O., Bernardo N. Moraes Neto, Guilherme S. S. A. Melo, and Cristina M. V. Frazão. "Assessment of the Effectiveness of Steel Fibre Reinforcement for the Punching Resistance of Flat Slabs by Experimental Research and Design Approach." *Composites Part B: Engineering* 78 (2015): 8-25. <https://doi.org/10.1016/j.compositesb.2015.03.050>.
- [2] Batarlar, Baturay. "Behavior of Reinforced Concrete Slabs Subjected to Impact Loads." 2013.
- [3] George, Sara J., and Ying Tian. "Structural Performance of Reinforced Concrete Flat Plate Buildings Subjected to Fire." *International Journal of Concrete Structures and Materials* 6, no. 2 (2012): 111-21. <https://doi.org/10.1007/s40069-012-0011-2>.
- [4] Gouveia, Nuno D., Duarte M. V. Faria, and António Pinho Ramos. "Assessment of Sfrc Flat Slab Punching Behaviour – Part I: Monotonic Vertical Loading." *Magazine of Concrete Research* 71, no. 11 (2019): 587-98. <https://doi.org/10.1680/jmacr.17.00343>.
- [5] Gouveia, Nuno D., Massimo Lapi, Maurizio Orlando, Duarte M. V. Faria, and António M. P. Ramos. "Experimental and Theoretical Evaluation of Punching Strength of Steel Fiber Reinforced Concrete Slabs." *Structural Concrete* 19, no. 1 (2018): 217-29. <https://doi.org/10.1002/suco.201700136>.
- [6] Li, Ran, Young Sang Cho, and Sumei Zhang. "Punching Shear Behavior of Concrete Flat Plate Slab Reinforced with Carbon Fiber Reinforced Polymer Rods." *Composites Part B: Engineering* 38, no. 5-6 (2007): 712-19. <https://doi.org/10.1016/j.compositesb.2006.07.017>.
- [7] Moraes Neto, Bernardo N., Joaquim A. O. Barros, and Guilherme S. S. A. Melo. "A Model for the Prediction of the Punching Resistance of Steel Fibre Reinforced Concrete Slabs Centrally Loaded." *Construction and Building Materials* 46 (2013): 211-23. <https://doi.org/10.1016/j.conbuildmat.2013.04.034>.

- [8] Nguyen-Minh, L., M. Rovňák, T. Tran-Quoc, and K. Nguyenkim. "Punching Shear Resistance of Steel Fiber Reinforced Concrete Flat Slabs." *Procedia Engineering* 14 (2011): 1830-37. <https://doi.org/10.1016/j.proeng.2011.07.230>.
- [9] Park, R., and W. Gamble. "Reinforced Concrete Slabs, 2nd Edition." 1999.
- [10] Saatçı, Selçuk, Süleyman Yaşayanlar, Yonca Yaşayanlar, and Baturay Batarlar. "Çelik Fiber Katkısının Farklı Boyuna Donatı Oranına Sahip Betonarme Döşemelerin Zımbalama Davranışı Üzerinde Etkileri." *Gazi Üniversitesi Mühendislik-Mimarlık Fakültesi Dergisi* 2018, no. 18-2 (2018). <https://doi.org/10.17341/gazimmfd.460507>.
- [11] Tan, Kiang Hwee, and Akshay Venkateshwaran. "Punching Shear in Steel Fiber-Reinforced Concrete Slabs with or without Traditional Reinforcement." *ACI Structural Journal* 116, no. 3 (2019). <https://doi.org/10.14359/51713291>.
- [12] Wood, J.G.M. "Pipers Row Car Park, Wolverhampton: Quantitative Study of the Causes of the Partial Collapse on 20th March 1997." *Structural Studies & Design Ltd* (1997).

## Unconfined Compression Strength of Polypropylene Fiber Reinforced Alluvial Deposits

*Hasan Fırat Pulat\**, İzmir Kâtip Çelebi University, Department of Civil Engineering, İzmir, Turkey  
*Abdulmuner Malikzada*, İzmir Kâtip Çelebi University, Department of Civil Engineering, İzmir, Turkey  
*Özge Oğur*, İzmir Kâtip Çelebi University, Department of Civil Engineering, İzmir, Turkey  
*Levent Çümen*, İzmir Kâtip Çelebi University, Department of Civil Engineering, İzmir, Turkey  
\*Corresponding author: [hfirat.pulat@ikcu.edu.tr](mailto:hfirat.pulat@ikcu.edu.tr)

**Keywords:** Alluvial soil, compaction behavior, polypropylene fiber, unconfined compressive strength  
**Discipline:** Civil Engineering

### Abstract

Alluvial deposits are generally defined as problematic soils in terms of civil engineering applications because of low bearing capacity, high organic matter content, and void ratio. Therefore, alluvial deposits should be stabilized. Using geosynthetics in geotechnical engineering for treating soil properties is advantageous because they are economic and eco-friendly. Fiber reinforcement causes considerable improvement in shear strength, tensile strength and other engineering properties of soil.

In this research, fundamental engineering properties, compaction behaviors of alluvial deposits, and the influence of discrete and randomly oriented polypropylene fiber reinforcement on unconfined compressive strength of alluvial soil are presented. Alluvial soil is taken from Çiğli, Balatçık (İzmir, Turkey). Polypropylene fiber is mixed with soil (1% by dry weight of soil). To determine compaction behavior and geotechnical index properties; wet sieve analysis, plastic limit, liquid limit, specific gravity, pH, standard compaction and organic matter content tests were conducted. In order to determine compressive strength, the soil was subjected to an unconfined compressive strength test. As a result of laboratory tests; the liquid limit values of the alluvial soil samples varied between 21.8 – 66.5%. The specific gravities ranged between 2.62 and 2.83. According to the results of wet sieve analysis and consistency limit tests, it was stated that the soil contains large amounts of silt and clay. The washed sieve analysis and consistency limit experiment results were rated according to USCS, it was determined that the soil covers large amounts of low plasticity silt and high plasticity clay (ML and CH), and the particle sizes increase with depth. The pH value ranged between 7.65 and 8.76. The conducted test results have shown that maximum dry unit weight varies between 14.8 - 19.2 (kN/m<sup>3</sup>), and optimum moisture content varies between 11.5 - 22%. Maximum and minimum compressive strength for unreinforced soil is 180 (kN/m<sup>2</sup>), 11.5 (kN/m<sup>2</sup>), respectively, maximum and minimum compressive strength for reinforced soil is 130 (kN/m<sup>2</sup>) and 10.5 (kN/m<sup>2</sup>) respectively which show the negative effect of 1% polypropylene fiber on unconfined compressive strength of alluvial soils.

### Introduction

Alluvial soils cover a very wide spectrum of soils, both in terms of condition and the type of soil. This results from the facies alteration of the river valley system at the cross-section and especially along the river course. With the enhancement distance from the river head, rivers carry and deposit increasingly fine material, sometimes include notable mixtures of the organic fraction [1].

Such soils changes in thickness, varying from layers of around a dozen to several dozen centimeters up to complexes of deposits several meters thick. Deposition under periglacial conditions and the vicinity of the ice-sheet resulted in a relatively small proportion of organic admixtures, as well as considerable contents of calcium carbonate, characteristic of Pleistocene soils genetically connected with the Vistula glaciation [2].

In projects involving the design of a building foundation, it is great importance to examine and evaluate the geotechnical properties of the foundation base in detail. Alluvial deposits are loose soils that do not fully complete geological formation. So, they have high void ratio and high organic matter content. These negative properties of alluvial deposits affect the design process negatively. Therefore, the geotechnical engineering properties of alluvial soil with low bearing capacity and liquefaction potential must be examined comprehensively [3].

According to the previous studies, Ahmet Sahin ZAIMOGLU (2012) examined the unconfined compressive strength of fine-grained soils modified with polypropylene fibers and additive materials.

This experimental study was performed to investigate the effect of randomly distributed Polypropylene fibers (PP) and some additive materials [e.g., Borogypsum (BG), Fly Ash (FA) and Cement (C)] on unconfined compressive strength of a fine-grained soil cured for 7, 14 and 28 days. The Taguchi method was applied to the experiments and a standard L9 Orthogonal Array (OA) with four factors and three levels were chosen. A series of unconfined compression tests (7, 14 and 28 days) were conducted on each specimen. 0-20% BG, 0-20% FA, 0-0.25% PP and 0-3% of C by total dry weight of mixture were used in the preparation of specimens. Experimental results showed that the most effective material for increasing the unconfined compressive strength of the samples was polypropylene fiber. The values of unconfined compressive strength for curing times of 7, 14 and 28 days in optimum conditions were 0.94 MPa, 1.25 MPa and 1.95 MPa, respectively [4].

Lei Gao et al (2015) investigated the unconfined compressive strength of basalt fiber reinforced clay soil. For this purpose, a series of unconfined compressive strength tests conducted on clay soil reinforced with basalt fiber have been performed under the condition of optimum water content and maximum dry density. Both the content and length of basalt fiber are considered. When the effect of content is studied, the 12 mm long fibers are dispersed into clay soil at different contents. When the effect of length is researched, different lengths of basalt fibers with 4 mm, 8 mm, 12 mm, and 15 mm are put into soil at the same content of 0.05%. Experimental results show that basalt fiber can effectively improve the UCS of clay soil. And the best content and length are 0.25% and 12 mm, respectively. The results also show that the basalt fiber reinforced clay soil has the “post strong” characteristic [5].

M.M Hossain et al (2018) studied the improvement of soil characteristics using lime and polypropylene fiber. polypropylene fibers and lime were used with soil to examine its effect on the bearing capacity. Different proportions of lime (0 to 15%) by weight of soil and 2% polypropylene fibers by weight of lime were mixed with different soil samples according to the soil categories like sandy and clay and silt soil. The necessary parameters of the soil were determined and the unconfined compressive strength of the soil was also measured by laboratory testing machine with different curing days. The result revealed the optimum value of the unconfined compressive strength was obtained for the concentration of 10% lime for clay and silt soil on the other hand 7.5% for the sandy soil [6].

In this research, fundamental engineering properties, compaction behaviors of alluvial deposits, and the influence of discrete and randomly oriented polypropylene fiber reinforcement on unconfined compressive strength of alluvial soil are presented. Alluvial soil is taken from Çiğli, Balatçık (İzmir, Turkey). Polypropylene fiber is mixed with soil (1% by dry weight of soil). To determine compaction behavior and geotechnical index properties; wet sieve analysis, plastic limit, liquid limit, specific gravity, pH, standard compaction and organic matter content tests were conducted. In order to determine compressive strength, the soil was subjected to an unconfined compressive strength test.

## Materials

### Alluvial Deposits

Alluvial deposits are those which are formed as a result of the deposition of sediments by rivers. They consist of clay, silt, sand, and gravel. Alluvial soils are generally most common in the down part of a river's route, forming deltas and floodplains, but they may form at any point where the river runovers its banks or where the flow of a river is checked.

Alluvial deposits have high void ratio because they have not completed their geological formation yet. For this reason, they have low bearing capacity. Due to these properties, buildings that are constructed on alluvial soils cause high damage during earthquakes. So that they are defined as a problem in geotechnical engineering. They have also liquefaction potential. Alluvial soils that are used in our experiments were taken from Çiğli – Balatçık region (İzmir, Turkey). The samples were taken from a construction site where is located at İzmir Kâtip Çelebi University. The total exploration depth was 30 m and alluvial soil samples were taken for each 1.50 m from boreholes. The samples were immediately coated with nylon to protect its natural properties and they were transferred to the soil mechanics laboratory and kept in airtight boxes.





Figure 1. General view of Çiğli-Balatçık

### Polypropylene Fiber

Polypropylene fiber is a thermoplastic polymer produced from the polymerization of the propene under 25-30 atm at 100°C in the presence of a catalyst system. Propene is a product of petroleum. This material is cost. Its linear structure is  $C_nH_{2n}$ . There are two catalyst systems to manufacture the polypropylene fiber. One is the Ziegler Natta Catalyst and the other is Metallocene. There are two principal processes to use the Ziegler Natta Catalyst. These are the bulk process and the gas phase process. The length of the fiber is 1,5 cm and mixed with soil in 1% by dry weight of the soil. Physico – mechanical properties of the polypropylene fiber are given below.

Table 1. Properties of the polypropylene fiber

Properties	Value
Size (mm)	15
Specific gravity ( $gr/cm^3$ )	0.92
Elasticity modulus (GPa)	3,15
Tensile strength (MPa)	620
Maximum elongation (%)	22
Electric permeability	Low
Melting point (°C)	160
Burn point (°C)	590
Thermal Conductivity	Low
Resistance to alkalis	High
Resistance to acids	High
Resistance to salts	High

### Methods

#### Index Properties of Alluvial Deposits

All experiments were conducted according to the process given in the American Society for Testing and Materials (ASTM) and British Standards (BS). The organic matter content (OMC) of the alluvial soil was determined by standing in the furnace with ceramic pot at 440 °C for 24 hours according to ASTM D2974 – 14 [7]. The specific gravities of alluvial soil samples were determined according to ASTM D854-14. In this experiment, a vacuum pump, air-free distilled water, pycnometer, and 25 g sample were used [8]. The pH values of samples were obtained by digital pH meter. The mixture was prepared by mixing 125 ml distilled water and 50 g sample and to stand for 24 hours (Figure 2). Then pH measurement was done [9]. To check repeatability each measurement was performed two times.

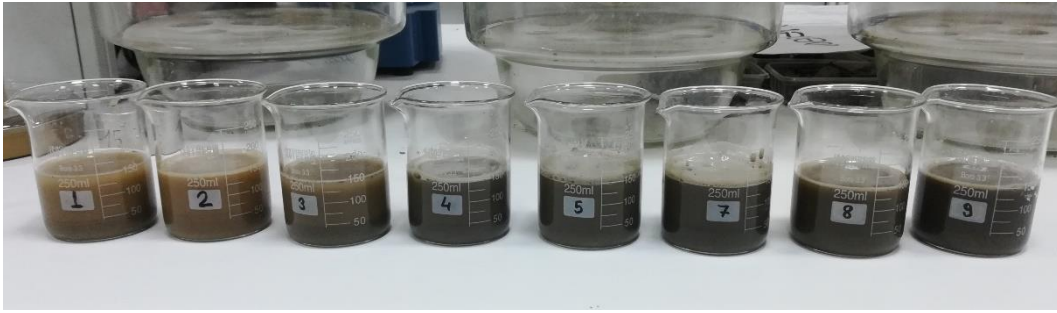


Figure 2. Alluvial samples for pH tests

The grain size distributions were determined with wet and dry sieve analysis for all specimens. After the wet sieve analysis was completed, dry sieve analysis was organized [10, 11]. Plastic limits were determined according to ASTM D4318-10 [12]. Liquid limits were defined with the fall cone test method in accordance with BS1377-1:2016 [13]. The alluvial soil specimens were classified using grain size distribution's parameters and Atterberg's limits according to the Unified Soil Classification System (USCS) [14]. The unconfined compression tests were performed according to ASTM D2166.

### Compaction Test

The compaction properties of soil were defined using standard laboratory tests. There are three methods for the standard proctor compaction test in ASTM D698. The soil is compacted in a cylindrical mold using a standard compaction energy. In the Proctor test, the volume of the mold is 943 cm<sup>3</sup> and the soil (with all particles larger than 20 mm removed) is compacted by a rammer in existence of a 2.5 kg mass falling freely through 305 mm: the soil is compacted in three layers, each layer getting 25 blows with the rammer. After compaction, the bulk density and water content of the soil are defined and the dry density is calculated. For a certain soil, the process is repeated at least five times, the water content of the sample being increased each time. The dry unit weight is plotted versus water content, and the curve of maximum dry unit weight against optimum moisture content is plotted [15].



Figure 3. Sample preparation of compaction test

### Unconfined Compression Test

This test method contains the definition of the unconfined compressive strength of cohesive soil in the remolded, intact, or recomposed condition, using strain-controlled application of the axial load. In order to carry out the Unconfined Compressive Strength Test, the sample is extruded from the mold. The cylindrical sample is trimmed. Because its ends must be smooth. The sample is placed on the bottom platen. When the bottom platen is raised, an axial load is applied to the sample. The strain rate is constant. The load increases and readings are recorded for each 15 seconds of the force applied to the sample. The loading is continued until the soil develops a potential failure surface. The data are used to determine the compressive strength and the stress-strain characteristics. In the unconfined compression test, it is pretended that there is no pore water lost from the sample during the experiment. 3 specimens were prepared for each 1,5 m. In this test, in order to calculate the required amount of the soil that must be compacted in the mold, values of maximum dry unit weight and optimum water content which are obtained from standard compaction tests are used. Figure 4 shows the procedure of the unconfined compressive strength test in the geotechnical laboratory of İzmir Kâtip Çelebi University [16].

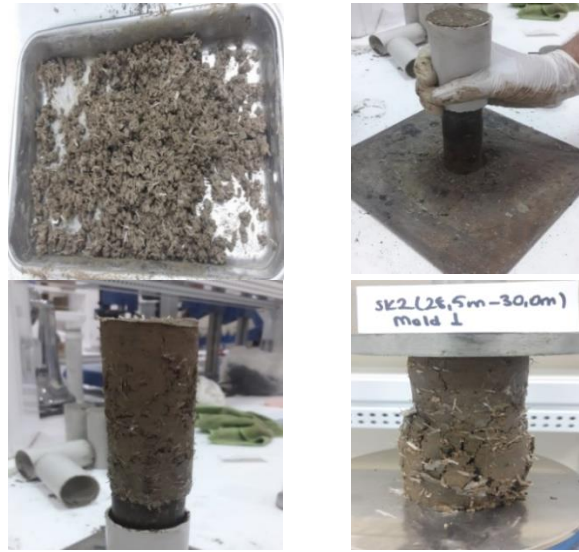


Figure 4. Unconfined compressive test procedure

## Results and Discussion

### Results of Index Properties and Idealized Soil Profile

The idealized soil profile obtained from the results of sieve analysis and Atterberg's limit tests have been shown in Figure 5.

SC	G = 0.7%, S = 60.3%, M and C = 39.1%	0.0 m
CL	G = 2.0%, S = 28.8%, M and C = 69.2%	1.5 m
SC	G = 1.6%, S = 79.2%, M and C = 19.2%	3.0 m
CL	G = 0.8%, S = 33.4%, M and C = 65.8%	9.0 m
SC	G = 0.2%, S = 72.6%, M and C = 27.2%	10.5 m
SM	G = 0.1%, S = 74.0%, M and C = 25.9%	13.5 m
SC	G = 0.0%, S = 88.5%, M and C = 11.5%	16.5 m
ML	G = 0.0%, S = 22.0%, M and C = 78.0%	18.0 m
CH	G = 13.0%, S = 22.3%, M and C = 64.7%	22.5 m
GM	G = 47.8%, S = 22.1%, M and C = 30.1%	28.5 m
		30.0 m

Figure 5. Idealized soil profile

The specific gravity ( $G_s$ ), pH, OMC, liquid limit (LL) and plastic limit (PL) values of alluvial samples have been listed in Table 1.

Table 2. Index properties of soil

Depth	LL (%)	PL (%)	G <sub>s</sub>	pH
0.0 – 1.5	45.6	NP	2.62	8.41
1.5 – 3.0	25.7	NP	2.75	8.76
3.0 – 9.0	34.7	NP	2.83	8.15
9.0 – 10.5	34.3	18.8	2.81	7.65
10.5 – 13.0	21.8	NP	2.68	8.01
13.0 – 16.5	24.1	NP	2.82	7.82
16.5 – 18.0	26.1	NP	2.64	8.45
18.0 – 22.5	29.1	19.7	2.73	8.44
22.5 – 28.5	30.3	26.2	2.67	8.41
28.5 – 30.0	66.5	NP	2.68	8.29

The typical alluvial deposit behavior has been shown by basic physicochemical parameters. Also, the results were consistent with previous literature studies [18, 19, 20, 21].

### Compaction Tests Results

Maximum dry unit weight and optimum moisture content for boreholes 2, 3, and 4 obtained from standard proctor compaction tests are shown in Table 3. The compaction curves for boreholes 2, 3, and 4 are shown in Figure 6. Maximum dry unit weight varies between 14.75 (kN/m<sup>3</sup>) to 19.21 (kN/m<sup>3</sup>) and optimum moisture content varied between 11.5% and 22%.

Table 3. Maximum dry unit weight and optimum moisture content of bore Hole 2, 3, and 4

Bore Hole 2			Bore Hole 3			Bore Hole 4		
Depth (m)	g <sub>drymax</sub>	% w <sub>c</sub>	Depth(m)	g <sub>drymax</sub>	% w <sub>c</sub>	Depth (m)	g <sub>drymax</sub>	% w <sub>c</sub>
0,0-1,5	16,05	16,5	0,0-1,5	16,41	14,95	0,0-1,5	17,13	13,47
1,5-3,0	16,35	16,5	1,5-3,0	16,8	15,5	1,5-3,0	16,9	14,35
4,5-6,0	15,18	19	4,5-6,0	15,5	21	3,0-4,5	17,58	11,5
9,0-10,5	15,32	21,7	9,0-10,5	15,63	22	4,5-6,0	16,15	12,55
10,5-12,0	15,82	16,99	10,5-12,0	16,19	19,2	7,5-9,0	14,75	17
16,5-18,0	15,4	15	15,0-16,5	15,05	15	15,0-16,5	14,95	16,8
18,0-19,5	16,14	13,5	16,5-18,0	15,7	18	16,5-18,0	17,18	13
27,0-28,5	18,02	12	21,0-22,5	15,42	17,97	18,0-19,5	14,74	22,5
28,5-30,0	19,21	11,5	27,0-28,5	17	15	28,5-30,0	18,95	12,2

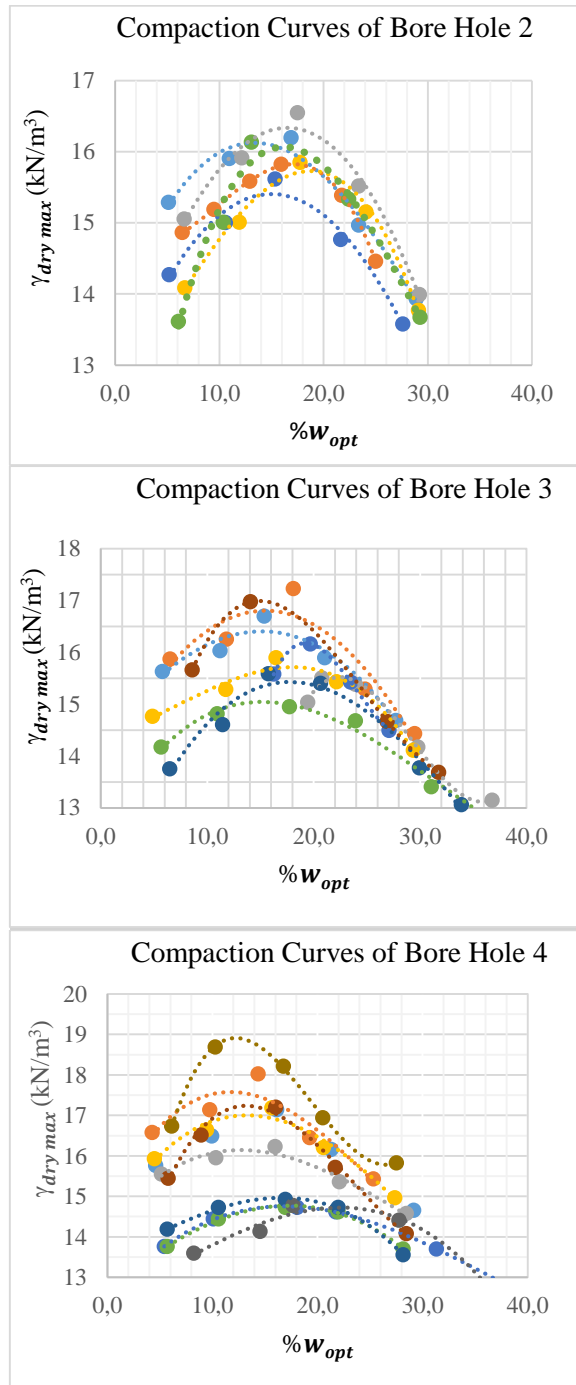


Figure 6. Compaction Curves for Bore Hole 2, 3, and 4

### Unconfined Compression Tests Result

The test is performed for both fiber-reinforced and unreinforced soils. Using polypropylene fiber more than 0.75% can affect negatively on unconfined compressive strength of soil [22]. Since 1% of polypropylene fiber has been used, in most cases an increase in unconfined compressive strength has not been seen. Strain-stress curves obtained from the unconfined compression test for some depth of borehole 2 are shown in Figures 7, 8, and 9.

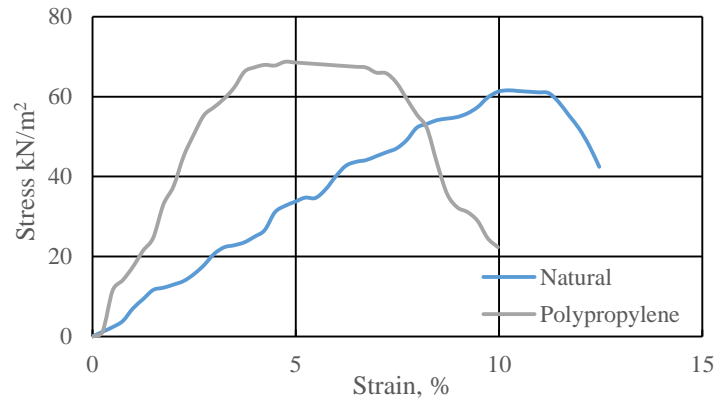


Figure 7. Stress-strain curve of borehole 2 ( 1,5-3,0 m)

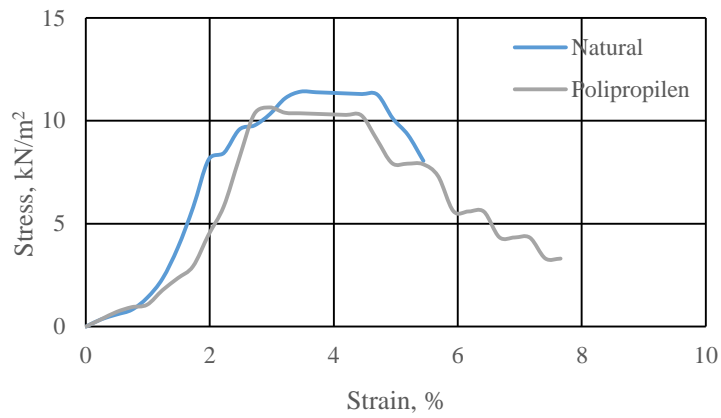


Figure 8. Stress-strain curve of borehole 2 (4,5- 6,0 m)

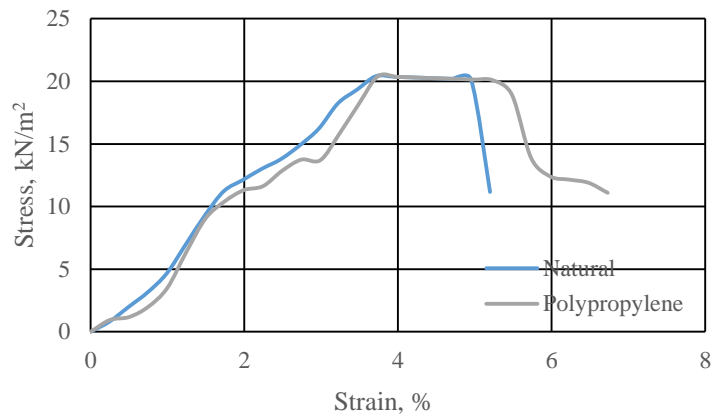


Figure 9. Stress-strain curve of borehole 2 (10,5-12,0 m)

The results for boreholes 2, 3, and 4 for both reinforced and unreinforced are shown in Table 4.

Table 4. Reinforced and unreinforced unconfined compression stress of bore holes

Depth (m)	UCS (kN/m <sup>2</sup> ), Unreinforced	UCS (kN/m <sup>2</sup> ), Reinforced	UCS (kN/m <sup>2</sup> ), Unreinforced	UCS (kN/m <sup>2</sup> ), Reinforced	UCS, (kN/m <sup>2</sup> ), Unreinforced	UCS (kN/m <sup>2</sup> ), Reinforced
0-1,5	-	-	31	24	45	47,5
1.05.2003	62	69	83	70	55	70
3-4,5	-	-	-	-	34.5	25
4.05.2006	11.5	10.5	-	-	-	-
6.07.2005	79	88	-	-	-	-
7,5-9,0	-	-	-	-	88	100
9-10,5	-	-	34	18	-	-
10.05.2012	20	20	59	31	-	-
12-13,5	-	-	48	37	-	-
13,5-15	-	-	-	-	-	-
15-16,5	-	-	14	20	14	14.5
16.05.2018	30.5	33	12	24	62	69
18-19.5	27.5	20	-	-	41	65
19.05.2021	69	70	-	-	-	-
21-22,5	-	-	80	65	-	-
22,5-24	-	-	-	-	70	82
27-28.5	150	130	180	100	-	-
28.05.1930	79	79	-	-	31	59

### Conclusion

A general problem for building projects in many countries is the building of construction and road work on alluvial, soft, and inadequate soils. This subject causes a great challenge in finding solutions to improve the problematic and inadequate soil which is utilized for building projects. Recently, soil reinforcement with polypropylene fiber as a cost-effective and environmentally friendly method is widely used. In this study, the effects of fiber reinforcement on alluvial soil were studied by using results obtained from unconfined strength tests. Based on the results presented in this paper the following conclusions are drawn:

1. Maximum and minimum compressive strength for unreinforced soil is 180 (kN/m<sup>2</sup>), 11.5 (kN/m<sup>2</sup>), respectively, maximum and minimum compressive strength for reinforced soil is 130 and 10.5 (kN/m<sup>2</sup>) respectively.
2. The maximum dry unit weight varies between 19.21-14.75 (kN/m<sup>3</sup>), and optimum moisture content varies between 22-11.5%.
3. It is observed that the failure of the fiber-reinforced specimens takes a longer time than the original soil, which indicates an increase in the ductility of the soil using polypropylene fiber.
4. Using polypropylene fiber more than 0.75% can affect negatively on unconfined compressive strength of soil. Since in this study, 1% of polypropylene fiber has been used, in most cases an enhancement in unconfined compressive strength has not been observed.
5. Using 1% or more polypropylene fiber can effect negatively on unconfined compressive strength of alluvial soils.

### References

- [1] Z. Młynarek, K. Stefaniak, J. Wierzbicki Geotechnical Parameters of Alluvial Soils from in-situ Tests, Archives of Hydro-Engineering and Environmental Mechanics Vol. 59 (2012), No. 1–2, pp. 63–81
- [2] J R, Cornell, C A Benjamin Probability, statistics, and decision for civil engineers. Published by McGraw-Hill, 1970 ISBN 10: 0070045496 / ISBN 13: 9780070045491
- [3] B. Semerci, I. Develioglu and H.F. Pulat, Geotechnical Characterization of Alluvial Soil in Çiğli - Balatçık Region, “Eurasian Journal of Civil Engineering and Architecture” (2018).

- [4] Ahmet Sahin Zaimoglu, Optimization of Unconfined Compressive Strength of Fine-grained Soils Modified with Polypropylene Fibers and Additive Materials, *KSCE Journal of Civil Engineering* (2015) 19(3):578-582
- [5] Lei Gao, Guohui Hu, Nan Xu, Junyi Fu, Chao Xiang, and Chen Yang, Experimental Study on Unconfined Compressive Strength of Basalt Fiber Reinforced Clay Soil, *Advances in Materials Science and Engineering* (2015): 561293, 8.
- [6] M. M. Hossain\*, R. C. Malo & M. H. Safi, Soil Improvement Using Lime And Polypropylene Fibers, 4th International Conference on Advances in Civil Engineering (2018).
- [7] *Standard test methods for moisture, ash, and organic matter of peat and other organic soils*, 2014. American Society of Testing and Materials, West Conshohocken, PA, USA.
- [8] *Standard test methods for specific gravity of soil solids by water pycnometer*, 2014. American Society of Testing and Materials, West Conshohocken, PA, USA.
- [9] Kocasoy, arıtma çamuru ve katı atık ve kompost örneklerinin analiz yöntemleri, Bogazici University Publisher, İstanbul, 1996.
- [10] *Standard test method for particle-size analysis of soils (Withdrawn 2016)*, 2007. American Society of Testing and Materials, West Conshohocken, PA, USA.
- [11] *Standard test method for particle-size analysis of soils (Withdrawn 2016)*, 2007. American Society of Testing and Materials, West Conshohocken, PA, USA.
- [12] *Standard test methods for liquid limit, plastic limit, and plasticity index of soils*, 2010. American Society of Testing and Materials, West Conshohocken, PA, USA.
- [13] *Methods of test for soils for civil engineering purposes*, 2016. British Standard Institution, London, UK.
- [14] ASTM D2487 - 17e1 Standard Practice for Classification of Soils for Engineering Purposes (Unified Soil Classification System)
- [15] ASTM D698 Standard Test Method for Laboratory Compaction Characteristics of Soil Using Standard Effort.
- [16] *Standard Test Method for Unconfined Compressive Strength of Cohesive Soil*. West Conshohocken, US: American Society Testing and Materials.
- [17] Masaud, Geotechnical evaluation of the alluvial soils for urban land management zonation in Gharbiya governorate, Egypt. *Journal of African Earth Sciences*, (2015), 101, 360- 374.
- [18] Yilmaz, I. And Karacan, Geotechnical Properties of Clayey Alluvial Soils in the Erbaa Basin, Turkey. *International Geology Review*, (2002), 44, 179 - 190.
- [19] Bolat, Burcu; Gürpınar, Okay; Yalçın, M. Namık;. İstanbul Ömerli'deki Alüvyal Zeminin Jeoteknik Özellikleri. *İstanbul Üniv. Müh. Fak. Yerbilimleri Dergisi*, (2005), 18(1), 95-111.
- [20] Cai, Yi; Shi, Bin; Ng, Charles W.W; Tang, Chao-sheng, Effect of polypropylene fibre and lime admixture on engineering properties of clayey soil. *Engineering Geology*, (2006), 230-240.
- [21] Çobanoğlu, İbrahim; Bozdağ, Şaziye. Adana Yerleşim Alanındaki Alüvyonların Jeoteknik Özellikleri Ve Coğrafi Bilgi Sistemi Yardımıyla Değerlendirilmesi. *S.Ü. Müh.-Mim. Fak. Derg.*, (2007), 23(3), 107-120.
- [22] Mechanical Behavior of Loose Sand Reinforced With Synthetic Fibers. *Soil Mechanics and Foundation Engineering*, (2016), 53(1), 12-18.



## Statistical Analysis of Monthly and Annual Precipitation and Monthly Mean Air Temperature in Black Sea (Turkey)

Waheedullah Mohammad khail\*, İzmir Kâtip Çelebi Univ., Dept. of Civil Engineering, İzmir, Türkiye  
Gökçen Bombar, İzmir Kâtip Çelebi Univ., Dept. of Civil Engineering, İzmir, Türkiye  
Ebru Eriş, Ege Univ., Dept. of Civil Engineering, İzmir, Türkiye  
Yalçın İşler, İzmir Kâtip Çelebi Univ., Dept. of Biomedical Engineering, İzmir, Türkiye  
\*Corresponding author: waheed.mohammadkhail@gmail.com

**Keywords:** Monthly precipitation, monthly mean air temperature and SPSS

**Discipline:** Civil Engineering

### Abstract

Turkey is one of the precision regions to climate variation particularly to precipitation changes in the World. The purpose of this study was to determine the annual, seasonal, monthly precipitation and monthly mean air temperature on the origin of the Black Sea in Turkey, moreover, SPSS software was used to analyze statistical the changes in the annual, seasonal, monthly precipitation and monthly air mean temperature overall 2 meteorological stations (HOPA and ARTVIN) covering the year from 1975 to 2006. The maximum temperature occurs in summer in ARTVIN station and another hand in HOPA station the maximum precipitation occurs in autumn but the maximum temperature occurs in summer and spring and autumn is the homogenous season in terms of temperature.

### Introduction

Water is completely necessary for all living things including human beings and rain is one of the most important incomes of water. Worldwide warming and climate change meaningfully make a different change in environmental variables in many countries around the world. This situation could have important effects on the population as well as agriculture, environment, economy and industry. Changes in precipitation patterns directly affect water resources management, agriculture, and hydrology. All the necessary water for life on earth comes from rain. For this reason, it is important to understand the spatial and temporal patterns of precipitation and their variability to gain knowledge about the balance of water dynamics for water resources management.

Air temperature and precipitation are standard elements of weather systems, so that investigation of their behavior is important for the understanding of climate variability because both are highly variable spatially and temporarily at different local, regional and global scales. For the calculation of future climate conditions, the level of variability of these two weather elements must be studied and understood. Therefore, recently, the focus on climate variability bases mostly on the discovery of trends in instrumental records of precipitation and temperature.

In the world, Turkey is between those countries which most likely to experience climatic variations for short and long time periods. Inter-annual variation of precipitation and temperature in Turkey is relatively large from the annual mean. As a result of climatic variations, natural resources of the country, such as vegetation, and the existing resources are easily damaged by changes in precipitation patterns. Many recent studies show that there is an increasing trend in climate variability [1].

In recent years, climatic change has been analyzed by many researchers and their results get more attention than ever. Global warming in precipitation regimes has been affected by many people directly or indirectly. Temperature and precipitation changes have not been uniform globally, many studies in different countries of the world have been investigated. for example, Yavuz and Erdogan (2012) analyzed precipitation trends by using MK rank correlation test for all regions of Turkey and performed by using monthly and annual precipitation data, recorded at 120 stations during the period 1975-2009 [2]. Haktanir et al. (2013) investigated on 48 years long complete and 79 years long incomplete maximum daily precipitation series recorded at Alexandria, Egypt, and on 61 years long maximum daily precipitation series recorded at Antalya [3]. Dinpashoh et al. (2014) analyzed trends of precipitation by using the MK trend detection test and determined the trends on monthly, seasonal, and annual time scales by using the precipitation data for the period of time 1955-2004 of the 16 stations selected from Iran [4].

This study aims to determine the change in the precipitation and temperature statistically in the Black Sea Region (HOPA and ARTVIN) covering the period 1975 to 2006 using SPSS software.

### Study area and data

Data on the daily precipitation and monthly mean air temperature recorded at the Black Sea were used in this study, the name of the gauging stations for both variables are HOPA and ARTVIN. Table 1 shows the basic statistics of monthly total precipitation and monthly mean air temperature for the period 1975-2006. There is no missing data in all of the temperature time series. There are some unrecorded precipitation data in some months (for example for HOPA and ARTVIN in 2006 in September, November and December) unpaid to non-existing monthly mean air temperature data. Figure 1 presents the annual precipitation for both stations. Figure 2 represents the annual mean air temperature for both stations.

Table 1. The basic statistics of monthly total precipitation and monthly mean air temperature for HOPA and ARTVIN

	Monthly total precipitation (mm)	Monthly mean air temperature (°C)
Date ranges	1975-2006	1975-2006
Number of data	384	384
Minimum value	1.30	-2.10
Maximum value	588.9	26.00

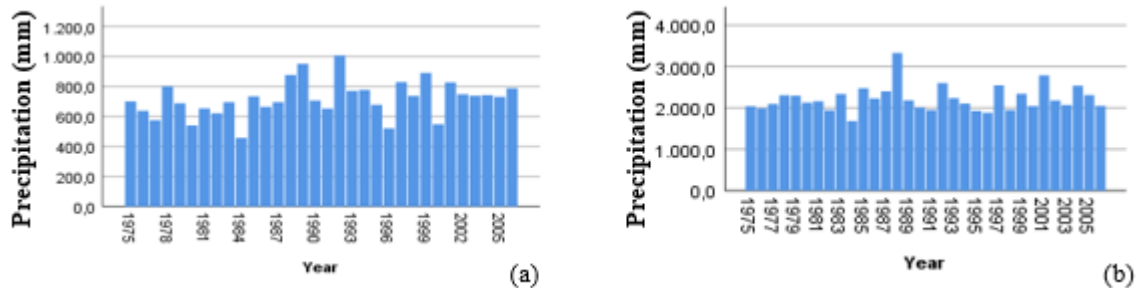


Figure 1. Annual precipitation for a) ARTVIN b) HOPA station.

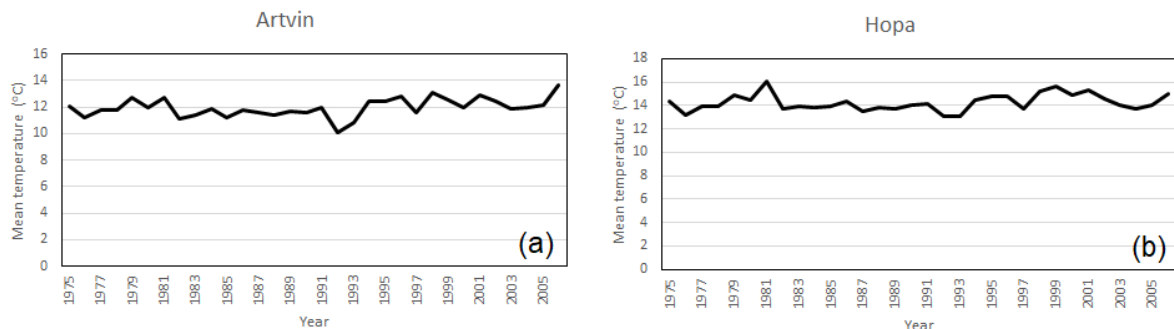


Figure 2. Annual mean air temperature (a) ARTVIN and (b) HOPA station.

### Methodology

In this study, the daily precipitation and mean air temperature data are collected in the Black Sea Region and two meteorological stations were used from 1975 to 2006. Daily precipitation and monthly mean air temperature data were first calculated as monthly and annually. For the precipitation data set, the seasonal amount was calculated by summing precipitation quantity from monthly precipitation, even though the location of this station has not been changed during the period of observation.

After the data has been arranged and double-checked, the following step is to calculate Descriptive Statistics. The three key types of descriptive statistics are frequencies, measures of central tendency (also called averages), and measures of variability. Frequency statistics simply count the number of times that each variable occurs

### Results and Discussions

Statistical properties of monthly precipitation series were presented in Table 2. The result shows that the minimum monthly precipitation occurs in September and the maximum in January. Table 3 shows the seasonal air mean temperature.

Even though the results of the two stations are different from each other, the maximum precipitation occurs in winter (see Figure 3) but the maximum temperature occurs in summer in ARTVIN station.

Table 2. Statistical summary of monthly precipitation series for ARTVIN.

		JAN	FEB	MAR	APR	MAY	JUN	JUL	AUG	SEPT	OCT	NOV	DEC
N	Valid	32	32	32	32	32	32	32	32	32	31	31	31
	Missing	0	0	0	0	0	0	0	0	0	1	1	1
MEAN		97.8	73.4	56.7	57.8	54.3	49.6	31.1	27.7	32.7	64.3	77.1	95.9
STANDARD ERROR		14.3	9.1	5.3	4.3	4.9	3.6	4.1	2.7	2.8	6.2	9.5	7.9
MEDIAN		82.2	60.0	52.6	59.2	50.2	47.5	25.0	26.3	31.1	57.0	57.6	94.3
STANDARD DEVIATION		80.8	51.6	29.8	24.1	27.8	20.1	22.9	15.3	15.8	35.1	54.0	44.9
SAMPLE VARIANCE		6535.6	2664.6	885.9	579.2	771.9	405.6	526.2	235.5	248.8	1234.5	2916.5	2019.6
KURTOSIS		3.2	0.3	0.2	1.4	2.0	0.2	0.5	-1.1	0.3	2.9	0.2	-0.4
SKEWNESS		1.7	1.0	0.8	0.5	1.3	0.4	1.1	0.3	0.5	1.5	0.9	0.3
RANGE		336.7	200.6	122.9	116.7	124.1	89.3	87.6	49.4	72.7	167.0	210.0	175.4
MINIMUM		5.5	6.2	15.7	12.1	9.6	13.2	3.3	4.8	1.3	12.6	7.5	14.8
MAXIMUM		342.2	206.8	138.6	128.8	133.7	102.5	90.9	54.2	74.0	179.6	217.5	190.2

Table 3. Statistical summary of seasonally mean air temperature for ARTVIN.

	winter	summer	spring	autumn
Valid	32	32	32	32
Missing	0	0	0	0
mean	3.21	19.80	11.31	13.35
median	3.20	19.80	11.60	13.40
mode	2.40	17.90	7.50	17.50
minimum	-2.10	16.70	2.50	5.30
maximum	8.50	24.70	18.20	21.70

Statistical properties of the monthly precipitation series of HOPA station was given in Table 4. The results showed that the data have a slight positive skewness. According to the results, the maximum precipitation occurs in August. May represented the minimum precipitation. January and February months have same precipitation which means that these months are the homogenous months in terms of precipitation variations. The maximum temperature occurs in summer. Table 5 shows the seasonal air mean temperature for HOPA station. In HOPA station the maximum precipitation occurs in autumn Figure 4.

Table 4. Statistical summary of monthly precipitation series for HOPA.

	Jan	Feb	Mar	Apr	May	Jun	Jul	Aug	Sept	Oct	Nov	Dec
N	Valid	32	32	32	32	32	32	32	32	31	31	31
	Missing	0	0	0	0	0	0	0	0	1	1	1
Mean	202.0	166.2	137.2	87.8	93.1	153.1	142.7	179.2	254.0	319.5	256.6	233.0
Standard Error	16.9	14.8	8.2	8.3	8.8	9.3	11.9	19.7	14.8	17.5	21.8	12.4
Median	191.2	158.9	127.9	82.2	89.5	154.2	141.9	171.6	259.7	297.7	246.5	230.5
Standard Deviation	95.5	83.8	46.4	47.1	49.9	52.4	67.1	111.4	83.4	98.9	123.3	70.1
Sample Variance	9123.1	7021.7	2154.1	2215.2	2492.8	2744.1	4495.9	12415.9	6963.3	9781.5	15203.7	4909.7
Kurtosis	0.1	4.0	0.9	5.7	0.9	-0.6	1.1	5.0	0.2	-0.2	-0.2	0.7
Skewness	0.5	1.4	0.9	1.8	0.9	0.3	1.0	1.7	-0.4	0.6	0.5	-0.2
Range	408.2	413.8	198.6	246.3	225.5	182.8	289.4	551.4	344.7	399.2	477.2	326.4
Minimum	51.3	51.8	73.3	20.5	9.3	69.8	41.1	37.5	62.6	161.6	54.0	47.3
Maximum	459.5	465.6	271.9	266.8	234.8	252.6	330.5	588.9	407.3	560.8	531.2	373.7

Table 5. Statistical summary of seasonally mean air temperature for HOPA.

	winter	summer	spring	autumn
Valid	32	32	32	32
Missing	0	0	0	0
mean	7.58	21.64	12.07	15.54
median	7.80	21.80	12.00	15.10
mode	7.90	22.00	15.10	19.30
minimum	0.00	17.70	5.00	8.30
maximum	14.80	26.00	18.50	22.40

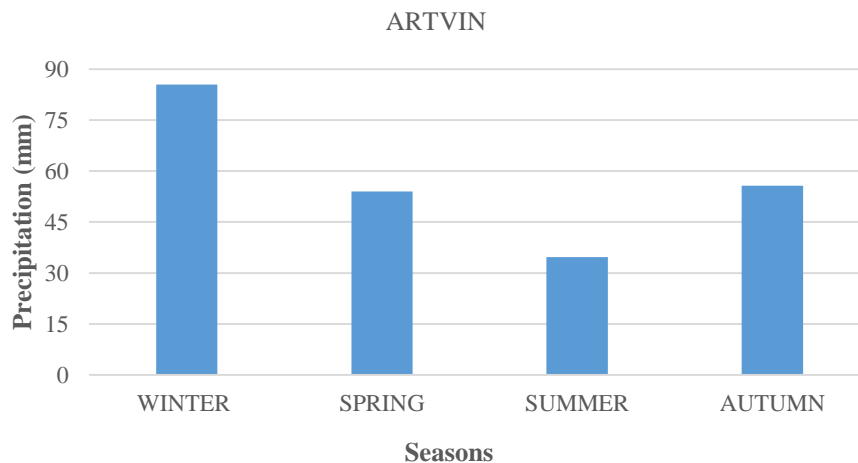


Figure 3. Seasonally precipitation for ARTVIN station from year 1975 to 2006.

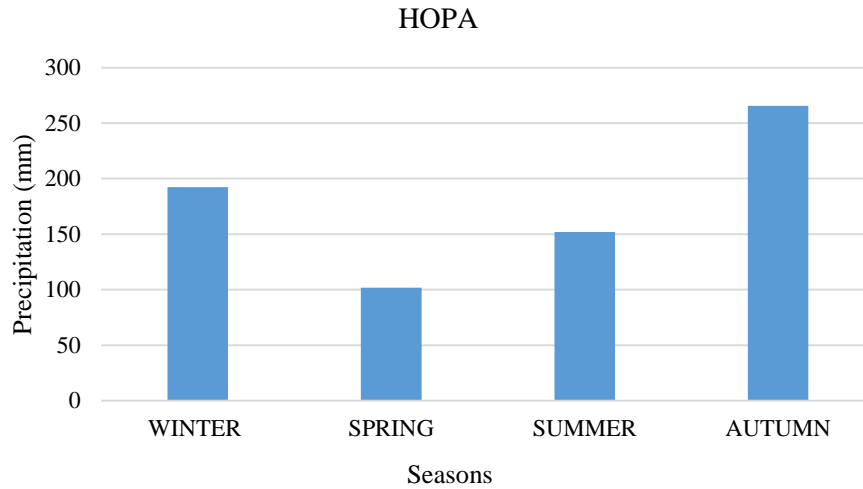


Figure 4. Seasonally precipitation for HOPA station from year 1975 to 2006.

### Conclusion

In this study precipitation and temperature data from 1975 to 2006 were used to identify statistically seasonality, annually and monthly precipitation and temperature in the Black Sea Region (Turkey). From the analysis of annual, seasonal and monthly precipitation data series, Black Sea Region has a significant precipitation amount such that it is experienced disaster of flood and landslide. On the other hand, the climate in the Black Sea region is wet, warm and humid, with summer temperatures about 24°C. The climate is effective mainly on the slopes of the North Anatolian Mountains facing the Black Sea. Maximum precipitations are seen in autumn and winter whereas minimums are seen in spring and summer. The average annual temperature is 11-15 °C

### References

- [1] Kadioğlu, M. Trends Surface Air Temperature Data Over Turkey. *International Journal of Climatology*. 1997, 17:511-520.
- [2] Yavuz H, Erdogan, S. Spatial Analysis of Monthly and Annual Precipitation Trends in Turkey. *Water Resource Management*. 2012. 26: 609-612.
- [3] Haktanir T, Bajabaa S, Masoud M, 2013. Stochastic Analyses of Maximum Daily Precipitation Series Recorded at Two Stations Across the Mediterranean Sea. *Arabian Journal of Geoscience*, 2013. 6(10):3943-3958
- [4] Dinpashoh Y, Mirabbasi R, Jhajharia D, Abianeh H Z, Mostafaeipour A. Effect of Short Term and Long-term Persistence on Identification of Temporal Trends. *Journal of Hydrologic Engineering*, 2014. 19(3), doi:10.1061/(ASCE)HE.1943-5584.0000819
- [5] BeyeneA N. Precipitation and Temperature Trend Analysis in Mekelle city, Northern Ethiopia, the Case of Illala Meteorological Station. *Journal Earth Science & Climate Change*, . 2016. 7(1):1-6.
- [6] Mohsin T, Gough W A. Trend Analysis of Long-term Temperature Time Series in the Greater Toronto Area. *Theoretical and Applied Climatology*. 2010. 101:311-327.
- [7] Jones R J, Schwartz, S J, Ellis N K, Hathaway, MJ, Jawdy M C. Temporal Variability of Precipitation in the Upper Tennessee Valley. *Journal of Hydrology*. 2015. 3:125-138.
- [8] Turkes, M. Spatial and Temporal Analysis of Annual Precipitation Variations in Turkey. *International Journal of* 12. Buffoni, L., Maugeri, M., Nanni, T., 1999. Precipitation in Italy from 1833 to 1996. *Theoretical and Applied Climatology*. 1996. 63:33-40.

## Computer Science and Engineering / Bilgisayar Bilimi ve Mühendisliği

## Survey on Implementation of Lattice-based Identification Schemes

Azhar Murzaeva\*, Meryem Soysaldi, Sedat Akleylek  
Ondokuz Mayıs Univ., Dept. of Computer Engineering, Samsun, Türkiye  
\*Corresponding author: azhar.murzaeva@bil.omu.edu.tr

**Keywords:** Post-quantum cryptography, lattice-based cryptography, identification schemes, implementation of identification schemes

**Discipline:** Computer Science and Engineering, Information Technologies

### Abstract

In providing a secure data flow during the communication between parties identification plays an important role. With a threat of quantum computers to the traditional cryptosystems and due to a big interest of researchers towards post-quantum cryptosystems, different identification schemes are developed. These schemes are based on different computational problems in areas such as lattices, multivariate quadratic polynomials or codes. During this study, identification schemes based on lattice problems are overviewed.

We analyze schemes based on hard problems in lattices (SVP, LWE, SIS, NTRU) and compare them by categories such as soundness, communication cost, commitment length, base problem. Since proving the secureness of an identification theoretically and practically is important, we summarize functions and operations required for the implementation of each scheme. Implementation of identification schemes that provide a 80-bit security level is performed on Java and Javascript languages. The results show that for the same security level Xagawa's identification scheme demonstrates the best performance.

### Introduction

Identification is the "first step" of defense. Identification is the process of recognizing entities by assigning them unique labels. Due to the verification of the conformity (authenticity) of the entity, that entity is allowed to access the system of an organization with some privileges. There are many methods on performing the identification and verification of the party (entity) such as using a password, using a protocol with hash function, using a protocol based on public key encryption (Schnorr identification protocol [3], Feige Fiat Shamir Identification scheme [2]), using a protocol that uses biometric data (voice, fingerprints, DNA sample, etc.), using identification cards and electronic keys (such as contactless smartcards and USB-keys). Therefore, it plays an important role in providing a secure communication between parties (client and server, human and machine, machine and machine) in the emerging IoT technologies, where RFID chips and cards are the main components. In addition, many EU countries use 'electronic identity cards' (eIDs) that are capable to identify and authenticate the user online [1]. Estonia launched the national eID cards integration in 2002, which is used in all digital services available in the country.

In this study, we consider identification protocols based on public key cryptography, where identifying an individual party is performed by following the steps of an identification scheme. Identification scheme is a cryptosystem that consists of several steps in order to identify the user. In the basis of this cryptosystem, computationally hard problems that can be solved in polynomial time by a quantum computer, which is proved using Shor's algorithm [5]. In this case, current cryptosystems seem to be insecure towards quantum computers. Therefore, there are many researches on construction of quantum resistant cryptosystems. Examples include encryption/decryption systems [10], key exchange and encapsulation mechanisms [18], [37] digital signatures [38]. These cryptosystems are based on one of the post-quantum cryptographic areas and we are concerned by identification schemes that are based on lattice-based cryptography. Lattice-based cryptography contains several quantum resistant hard problems that became a base for different quantum secure cryptosystems. Key encapsulation mechanisms (KEM) [17], [18], [19], signature schemes [20], [21], [28], [38] construction of collision-resistant hash function [29], secure encryption, key exchange and authenticated key exchange [37] are examples to such cryptosystems. Together with them, quantum resistant identification schemes are being developed [13], [22], [11], [21], [14], [12].

Proving that identification scheme is secure theoretically and practically is important. Thus, we overview properties of several lattice-based identification schemes to show their secureness theoretically

and for practical experiments, implementation of those schemes has been performed. For implementations the cross-platform languages Java and JavaScript are chosen. Java is widely used in mobile applications while JavaScript is used in web browsers, web pages and in IoT developments. Due to the property of being cross-platform languages, it is easy to modify and implement them in any other Java/JavaScript environment.

### Motivation and Contribution

Identification is the process of determining the individual. The scope of identification protocols' usage is very large: industry, transportation, medicine, sports, e-commerce, etc. It has an essential role for the upcoming Internet of Things technology. There are also attempts to build a quantum computer [33], [34]. With these recent developments, Shor proposed his algorithm that solves concurrent hard problems in polynomial time on quantum computers [5]. Thus, National Institute of Standards and Technology (NIST) has started a project for standardization quantum secure algorithms [35]. For the third round of the NIST's call for standardization project, 7 main (where 5 of them are lattice-based) and 8 (2 of them are lattice-based) alternative cryptographic algorithms became the finalists. Most of those candidates for NIST's standardization are based on lattice-based cryptography. Therefore, lattice-based cryptography is the main candidate for post-quantum cryptography and there are many researches directed on this area. Thus, we reviewed lattice-based identification schemes with their properties and analyzed each of them. This work is the first in literature that overviews all lattice-based identification schemes and evaluates their performance by implementing them on Java and JavaScript languages in one paper. As the main contribution, we develop cryptographic libraries in these languages. Later, we implement the schemes using these libraries and perform their comparison.

### Organization

The rest content of this paper is organized as follows. Section II involves some definitions of problems and main properties of an identification scheme. Section III introduces selected identification schemes with their properties. Section IV contains comparison tables of presented identification schemes. Finally, Section V concludes this survey by presenting and comparing results obtained during the implementation.

### Preliminaries

In this section, we review some basics that help to understand and analyze an identification scheme. We give definitions of some hard problems and present some identification specific properties.

**Definition 1. Short Integer Solution (SIS)** SIS problem was proposed by Ajtai in 1996 [7], [16]. Given a uniform  $\in Z_q^{m \times n}$ , find  $x \in Z^m \setminus \{0\}$  such that  $\|x\| \leq \beta$  and  $x^T \cdot A = 0 \pmod{q}$ . There is no polynomial algorithm known to solve this problem [7].

**Definition 2. Learning With Errors (LWE)** LWE problem was proposed by Regev in 2005 [8]. Let  $\in Z_q^n$  be a secret vector, where  $q$  is prime;  $a_i \in Z_q^n$  be uniformly generated random values from  $Z_q^n$  and errors' vector  $e$  is sampled from a discrete normal probability distribution (e.g. continuous Gaussian). ( $a_i b_i = a_i s + e$ ). It's needed to find a secret vector  $s$ . The hardness of this problem is due to that LWE runs in exponential time and depends on the hardness of the standard lattice problem SIVP (Shortest Independent Vectors Problem) [8] and other reasons [9].

**Definition 3. NTRU Key Recovery Problem (NTRU)** Let  $N, p, q$  be integers and  $L_f, L_g, L_m, L_r, L_q$  are sets of polynomials of degree  $N - 1$  with integer coefficients. NTRU is defined in the ring  $R = Z[X]/(X^N - 1)$ . An element  $F \in R$  will be written as a polynomial or a vector:

$$F = \sum_{i=0}^{N-1} F_i x^i = [F_0, F_1, \dots, F_{N-1}]$$

\* denotes a multiplication in  $R$ . This *star multiplication* is a cyclic convolution product:



$$F * G = H, \text{ where } H_k = \sum_{i=0}^k F_i G_{k-i} + \sum_{i=k+1}^{N-1} F_i G_{N+k-i} = \sum_{i+j=k(\text{mod})N} F_i G_j$$

Secureness of the NTRU problem is related to the SVP (Shortest Vector Problem) hard problem in lattices. For details of the NTRU problem see the original paper [10].

**Definition 4. Shortest Vector Problem (SVP)** SVP is a problem on finding the shortest non-zero vector in lattice:  $\|v\| = \lambda_1(L)$ . It is not too hard to find short vectors in low dimensions, but with the increase of dimensions it becomes very hard. SVP is a NP-hard problem for  $\gamma = \sqrt{d(2(\log)^{\frac{1}{2}-\epsilon(d)})}$  [6]

### A. Identification Scheme

An identification protocol is a set of rules that is composed of key generation, computation of commitments and verification stages. The general structure for a three-pass identification scheme is illustrated in Figure 1. Properties needed for a secure construction of an identification scheme are presented in the following subsections.

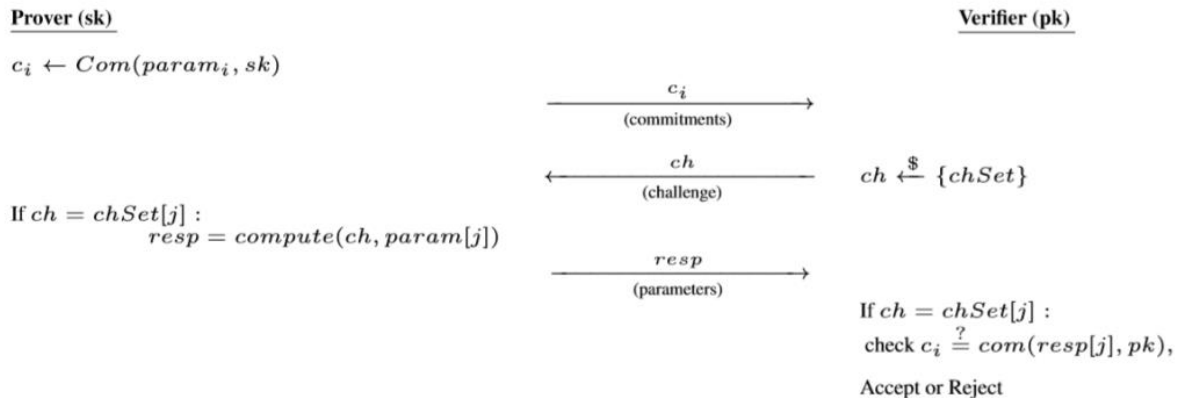


Figure 14. General construction of an identification scheme

1. *Zero-knowledge Proof of Knowledge.* The typical interactive proof involves two parties Prover and Verifier, where Verifier tries to identify the Prover. Interaction between parties consists of these main moves:

- the Prover computes and sends "commitment" to the Verifier
- the Verifier sends "challenge" to the Prover
- the Prover sends parameters as a "response"
- the Verifier verifies the Prover and either accepts or rejects it.

This identification process without revealing any important information to a third party (adversary) is known as zero-knowledge proof. The essence of the zero-knowledge can be very popularly explained using the example of "Aladdin's cave" by Jean Jacques Quisquater and Louis Guillou [27] which is shown in Figure 2.

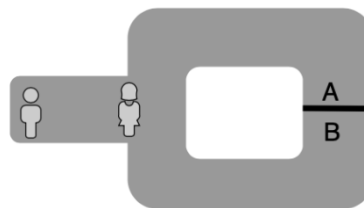


Figure 15. "Alladin's cave" example

In the cave there is a secret door A-B, which can only be opened by someone who knows the magic words. Alice wants to prove to Bob that she knows the magic words, but does not want to reveal them to him. Thus, Alice can convince Bob as follows: Alice goes to point A or B. Then, Bob invites Alice

to appear from the left side or from the right side. Alice fulfills the request using, if necessary, magic words. Alice and Bob repeat these steps  $n$  times.

2. *Completeness.* It asserts that interaction between parties during the protocol is successful with a high probability [26]. In short, an honest Verifier is always able to verify an honest Prover. For the formal definition, see [2], [26] and the formal proof of this property is presented in [26].

3. *Soundness.* During the interaction protocol between parties, where a secret knowledge is protected from being revealed, an adversary can (accidentally) obtain a possible secret value. On practice, an adversary who does not possess the secret key, can not be verified as a regular user [26]. In short, a cheating Prover can not convince an honest Verifier that he is an honest one (except of a small probability). For the formal definition, see [2], [26] and the formal proof of this property is presented in [26].

**Notations:**

$Com(\dots)$	→ commitment function (hash function is used)
$\pi$	→ permutation function
$x \xleftarrow{\$} \mathbb{F}_2^m$	→ generate $m$ –dimensional vector with random values in $\text{mod } 2$
$A \xleftarrow{\$} \mathbb{Z}_q^{n \times m}$	→ generate matrix with dimension $n \times m$ with random values in $\text{mod } q$
$hw(x) = m/2$	→ Hamming weight
$Ax, Ar$	→ matrix-vector product
$(x + r), (r_t + x_t)$	→ vector addition
$a_h \otimes x_h, a_t \otimes x_t$	→ polynomial product (vectors product is used)
$P^{-1}$	→ matrix inversion
$AB$	→ matrix product
$\ z\ $	→ norm

Figure 16. List of functions and operations needed for the implementation of an identification scheme

4. *Witness Indistinguishability.* In a protocol with two (Prover and Verifier) parties, Prover possesses several witnesses and uses them for the computation of the result. This concept with witnesses is known as *witness indistinguishability* [23], and it is ensured if the Verifier can not determine which witness is used, even if the Verifier knows all the witnesses [2].

5. *Security Analysis.* Data transmitted during the communication must be protected from the eavesdropping and must be prevented from being caught by adversaries in accordance to security requirements (confidentiality, integrity, availability, non-repudiation, authenticity) [36]. Thus, cryptographic schemes are widely used as techniques of secure communication between clients and servers, between tags and readers. They have been constructed to deal with security issues for the protection of information [15]. Cryptographic schemes are expected to be secure against different attacks.

7. *String Commitment schemes.* Commitment schemes take a crucial part in the design of cryptographic protocols such as zero-knowledge. It is considered as an honest trusted party that sets up system parameters for the sender and receiver. For the construction of the commitment schemes collision-resistant hash functions were used by Damgard et. al [24], by Halevi and Micali [25] and by Stern [26]. These collision-resistant hash functions, also known as message-digest functions, are widely used in digital signatures, authentication schemes etc. As security properties, commitment schemes provide hiding and binding properties. For the formal definition of these properties, see [24].

Together with the overview on the theoretical side of identification schemes, we implement them on practice. For that, we drew up the list of demanded operations. Functions and operations required for the implementation of an identification scheme are given in Figure 2. It is a general list of operations needed for the execution of a general structure of an identification scheme, where *vectors product*, *matrix inversion*, *matrix product*, *norm* operations are specific to a particular identification scheme.

### Identification Schemes

This section presents zero-knowledge Kawachi's [11], Cayrel's [13], Soysaldi's [22], Silva's [14], Xagawa's [12] and non zero-knowledge Lyubashevsky's [21] constructions. The rough structures of these schemes depending on used protocol (zero-knowledge or witness indistinguishability) and underlying problems are demonstrated in Figure 4. Details are described in subsections.

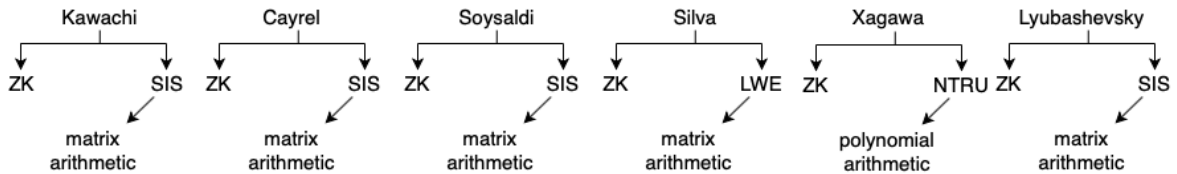


Figure 17. Comparison among basic structures of identification schemes

#### A. SIS-based identification schemes

**KeyGen:**

$$x \leftarrow_{\$} \mathbb{F}_2^m, hw(x) = m/2$$

$$y = Ax, A \leftarrow_{\$} \mathbb{Z}_q^{n \times m},$$

$\pi$  is a random permutation over  $\{1, \dots, m\}$ .

**Prover:**  $(sk, pk)$

$$r \leftarrow_{\$} \mathbb{Z}_q^m,$$

$$c_1 \leftarrow Com(\pi, Ar)$$

$$c_2 \leftarrow Com(\pi(r))$$

$$c_3 \leftarrow Com(\pi(x+r))$$

If  $c=1$ :  $resp = (\pi(x), \pi(r))$

If  $c=2$ :  $resp = (\pi, (x+r))$

If  $c=3$ :  $resp = (\pi, r)$

**Verifier:**  $(pk)$

$$\begin{array}{c} \xrightarrow{c_1, c_2, c_3} \\ \xleftarrow{c} \end{array} \quad c \leftarrow_{\$} \{1, 2, 3\}$$

$$\xrightarrow{resp}$$

If  $c=1$ :  
check  $c_2 \stackrel{?}{=} com(\pi(r)), c_3 \stackrel{?}{=} com(\pi(r) + \pi(x))$ ,  
If  $c=2$ :  
check  $c_1 \stackrel{?}{=} com(\pi, A(r+x) - y)$ ,  
 $c_3 \stackrel{?}{=} com(\pi(r+x))$   
If  $c=3$ :  
check  $c_1 \stackrel{?}{=} com(\pi, Ar), c_2 \stackrel{?}{=} com(\pi(r))$

Figure 18. Kawachi's identification scheme

##### a) Kawachi's identification scheme

Kawachi et. al. [11] proposed a scheme based on hardness of SIS (Shortest Integer Solution) problem in lattices. It is a three-pass scheme. Stages of Kawachi's interactive proof are given in Figure 5. In the Key Generation stage, private and public keys are generated. In proposed scheme,  $x$  is a secret key, while matrix  $A$  and values of  $y$  are public keys. Vector  $x$  is a vector with random values in  $F_2^m$  ( $x \leftarrow F_2^m$ ) with a Hamming weight  $m/2$ ; a public matrix  $A$  is randomly generated from  $Z_q^{n \times m}$  ( $A \leftarrow Z_q^{n \times m}$ ) and values of  $y$  are computed by using SIS problem:  $y = Ax$ . Then, these keys are used by Prover and Verifier to compute commitments and responses. Kawachi's scheme concerns the concurrent attack. It is a zero-knowledge protocol, it provides completeness and its soundness error equals  $2/3$ .

##### b) Cayrel's identification scheme

Cayrel et. al. [13] proposed an interactive proof that is based on SIS (Shortest Integer Solution) problem in lattices. This scheme possesses five passes. Structure of Cayrel's interactive proof is illustrated in Figure 6. In the Key Generation stage private and public keys are generated. In proposed scheme,  $x$  is a secret key, while matrix  $A$  and values of  $y$  are public keys. Vector  $x$  is a vector with random values in  $F_2^m$  ( $x \leftarrow F_2^m$ ) with a Hamming weight  $m/2$ ; a public matrix  $A$  is randomly generated from  $Z_q^{n \times m}$  ( $A \leftarrow Z_q^{n \times m}$ ) and values of  $y$  are computed by using SIS problem:  $y = Ax \bmod p$ . Then, these keys are used by Prover and Verifier to compute commitments and responses. Cayrel's scheme concerns

concurrent attacks. It is a zero-knowledge protocol, it has a completeness and its soundness error equals  $1/2$ .

**c) Soysaldi's identification scheme**

Soysaldi et. al. [22] proposed a new identification scheme based on SIS (Shortest Integer Solution) problem in lattices. The structure of the scheme and computational operations are similar to the structure and operations of the Cayrel's [13] identification scheme. For its implementation it needs functions such as matrix-vector product, addition of vectors, scalar vector multiplication. It differs from Cayrel's scheme in the number of phases. There are three phases in Soysaldi's scheme while the number of phases in Cayrel's is five. Structure of Soysaldi's interactive proof is illustrated in Figure 7. In the Key Generation stage private and public keys are generated. In proposed scheme,  $x$  is a secret key, while matrix  $A$  and values of  $y$  are public keys. Vector  $x$  is a vector with random values in  $F_2^m$  ( $x \leftarrow F_2^m$ ) with a Hamming weight  $m/2$ ; a public matrix  $A$  is randomly generated from  $Z_q^{n \times m}$  ( $A \leftarrow Z_q^{n \times m}$ ) and values of  $y$  are computed by using SIS problem:  $y = Ax$ . Then, these keys are used by Prover and Verifier to compute commitments and responses. Soysaldi's scheme is a zero-knowledge protocol, it provides completeness and its soundness error equals  $1/2$ .

**KeyGen:**

$$x \leftarrow_{\$} F_2^m, hw(x) = m/2$$

$$A \leftarrow_{\$} Z_q^{n \times m},$$

$$y \leftarrow Ax$$

**Prover:**

$$u \leftarrow_{\$} Z_q^m, z \leftarrow_{\$} P_\sigma x,$$

$$\sigma \leftarrow_{\$} S_m,$$

$$P_\sigma^{m \times m} \leftarrow \text{is a binary matrix}$$

$$r_0 \leftarrow_{\$} F_2^n, r_1 \leftarrow_{\$} F_2^n.$$

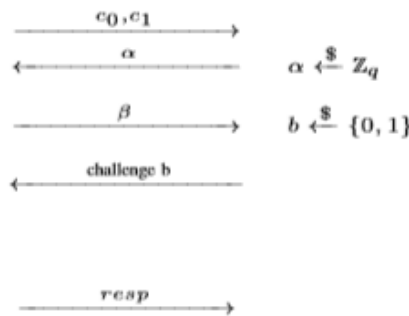
$$c_0 \leftarrow Com(\sigma || Au; r_0);$$

$$c_1 \leftarrow Com(z || P_\sigma u; r_1);$$

$$\beta \leftarrow P_\sigma (u + \alpha x)$$

If  $b=0$ :  
 else:  
 $resp = (\sigma, r_0)$   
 $resp = (z, r_1)$

**Verifier:**



If  $b=0$ :  
 check  $c_0 \stackrel{?}{=} Com(\sigma || AP_\sigma^{-1}\beta - \alpha y; r_0)$   
 $\sigma \stackrel{?}{\in} S_m$   
 else:  
 check  $c_1 \stackrel{?}{=} Com(z || \beta - \alpha z; r_1)$   
 $z \stackrel{?}{\in} \{0, 1\}^m$   
 $hw(z) \stackrel{?}{=} m/2$

Figure 19. Cayrel's identification scheme

**KeyGen:**

$$x \leftarrow_{\$} \mathbb{F}_2^m, hw(x) = m/2$$

$$y = Ax, A \leftarrow_{\$} \mathbb{Z}_q^{n \times m},$$

$\pi$  is a random permutation over  $\{1, \dots, m\}$ .

**Prover:**

$$r \leftarrow_{\$} \mathbb{Z}_q^m, seed_1 \leftarrow_{\$} \mathbb{F}_2^n, seed_2 \leftarrow_{\$} \mathbb{F}_2^n,$$

$$c_0 \leftarrow Com(\pi(r); seed_1)$$

$$c_1 \leftarrow Com(\pi, Ar; seed_2)$$

If  $b = 0$ :

$$\beta_0 = \pi(r + \alpha x)$$

$$s = \pi(x)$$

$$resp = (s, \beta_0, seed_1)$$

If  $b = 1$ :

$$\beta_1 = A(r + \alpha x)$$

$$\phi = \pi(x)$$

$$resp = (\phi, \beta_1, seed_2)$$

**Verifier:**

$$\begin{array}{c} \xrightarrow{c_0, c_1} \\ \xleftarrow{\alpha, b} \end{array} \quad \alpha \leftarrow_{\$} \mathbb{Z}_q, b \leftarrow_{\$} \{0, 1\}$$

$$\begin{array}{c} \xrightarrow{resp} \\ \text{If } b = 0: \\ \text{check } c_0 \stackrel{?}{=} Com(\beta_0 - \alpha s; seed_1) \\ \text{If } b = 1: \\ \text{check } c_1 \stackrel{?}{=} Com(\pi, (\beta_1 - \alpha y); seed_2) \end{array}$$

Figure 20. Soysaldi's identification scheme

**B. LWE-based identification schemes**

**a) Silva's identification scheme**

Silva et. al. [14] proposed a scheme based on LWE (Learning With Errors) problem in lattices. It is a three-pass scheme. Structure of Silva's interactive proof is illustrated in Figure 8. In the Key Generation stage, private and public keys are generated. In proposed scheme,  $s$  is a secret key, while matrix  $A$  and values of  $b$  are public keys. Vector  $s$  is a vector with random values in  $F_q^m$  ( $x \leftarrow F_q^m$ ); a public matrix  $A$  is randomly generated from  $Z_q^{n \times m}$  ( $A \leftarrow Z_q^{n \times m}$ ) and values of  $b$  are computed by using LWE problem:  $b = As + e$ , where errors in  $e$  are generated from  $F_q^n$  ( $x \leftarrow F_q^n$ ). Silva's scheme concerns the active attack. It is a zero-knowledge protocol, it provides completeness and its soundness error equals  $2/3$ .

**C. NTRU-based identification schemes**

**a) Xagawa's identification scheme**

Xagawa et. al. [12] proposed a scheme based on hardness of NTRU problem in lattices. It is a three-pass scheme. Structure of Xagawa's interactive proof is illustrated in Figure 9. In the Key Generation stage, private and public keys are generated. Private keys are  $x_h, x_t$  and public key is a tuple of  $(a_h, a_t, y)$ . Structure of NTRU problem can be noticed in computation of the public key  $y = a_h \otimes x_h + a_t \otimes x_t$ , where  $\otimes$  denotes the vectors product operation. Xagawa's scheme is a zero-knowledge protocol, it provides a perfect completeness and has a soundness error of  $2/3$ . This scheme is resistant against active and passive attacks.

**KeyGen:**

$$A \leftarrow \mathbb{F}_q^{m \times m}, s \leftarrow \mathbb{F}_q^m, e \leftarrow \mathbb{F}_q^m,$$

$$b = As + e$$

$$p = hw(e)$$

**Prover:**

$$u \leftarrow \mathbb{F}_q^m, r_1 \leftarrow \mathbb{F}_q^n, r_2 \leftarrow \mathbb{F}_q^n, r_3 \leftarrow \mathbb{F}_q^n,$$

$$\gamma \leftarrow \mathbb{F}_q^m, \gamma \neq 0, \forall i \in 1, \dots, m, \Sigma \leftarrow \mathbb{S}_n,$$

$$c_1 \leftarrow Com(\Pi_{\gamma, \Sigma}; r_1)$$

$$c_2 \leftarrow Com(\Pi_{\gamma, \Sigma}(A(u + s)); r_2)$$

$$c_3 \leftarrow Com(\Pi_{\gamma, \Sigma}(Au + b); r_3)$$

If c=1:  $resp = (r_1, r_2, (u + s), \Pi_{\gamma, \Sigma})$

If c=2:  $resp = (r_2, r_3, \Pi_{\gamma, \Sigma}(A(u + s)), \Pi_{\gamma, \Sigma}(e))$

If c=3:  $resp = (r_1, r_3, \Pi_{\gamma, \Sigma}, u)$

**Verifier:**

$$\xrightarrow{c_1, c_2, c_3}$$

$$\xleftarrow{c} c \leftarrow \mathbb{S} \{1, 2, 3\}$$

$$\xrightarrow{resp}$$

If c=1:  
check  $c_1 \stackrel{?}{=} Com(\Pi_{\gamma, \Sigma}, r_1)$  and  
 $c_2 \stackrel{?}{=} Com(\Pi_{\gamma, \Sigma}(A(u + s)), r_2)$

If c=2:  
check  $c_2 \stackrel{?}{=} Com(\Pi_{\gamma, \Sigma}(A(u + s)), r_2)$  and  
 $c_3 \stackrel{?}{=} Com(\Pi_{\gamma, \Sigma}(A(u + s)) + \Pi_{\gamma, \Sigma}(e)),$   
 $hw(\Pi_{\gamma, \Sigma}(e)) \stackrel{?}{=} p$

If c=3:  
check  $c_1 \stackrel{?}{=} Com(\Pi_{\gamma, \Sigma}, r_1)$  and  
 $c_3 \stackrel{?}{=} Com(\Pi_{\gamma, \Sigma}(Au + b); r_3)$

Figure 21. Silva's identification scheme

**KeyGen:**

$x_h, x_t$  – enumeration sets

$$y = a_h \otimes x_h + a_t \otimes x_t$$

$$(a_h, a_t, y) \in \mathbb{R}_q^3$$

**Prover:** (sk, pk)

$$a_h \leftarrow \mathbb{Z}^n, a_t \leftarrow \mathbb{Z}^n, x_h \leftarrow \mathbb{Z}_2^n, x_t \leftarrow \mathbb{Z}_2^n,$$

$\pi$  is a random permutation over  $\{1, \dots, m\}$ .

$$r \leftarrow \mathbb{Z}_q^m,$$

$$c_1 \leftarrow Com(\pi_h, \pi_t, y)$$

$$c_2 \leftarrow Com(\pi_h(r_h), \pi_t(r_t))$$

$$c_3 \leftarrow Com(\pi_h(r_h + x_h), \pi_t(r_t + x_t))$$

If c=1:  $resp = (\pi_h(x_h), \pi_t(x_t), \pi_h(r_h), \pi_t(r_t))$

If c=2:  $resp = (\pi_h, \pi_t, r_h + x_h, r_t + x_t)$

If c=3:  $resp = (\pi_h, \pi_t, r_h, r_t)$

**Verifier:** (pk)

$$\xrightarrow{c_1, c_2, c_3}$$

$$\xleftarrow{c} c \leftarrow \mathbb{S} \{1, 2, 3\}$$

$$\xrightarrow{resp}$$

If c=1:  
check  $c_2 \stackrel{?}{=} Com(\pi_h(r_h), \pi_t(r_t))$ , and  
 $c_3 \stackrel{?}{=} Com(\pi_h(r_h) + \pi_h(x_h), \pi_t(r_t) + \pi_t(x_t))$ ,  
 $\pi(x_h) \in \text{enumeration set}, \pi(x_t) \in \text{enumeration set}$

If c=2:  
check  $c_1 \stackrel{?}{=} Com(\pi_h, \pi_t, y)$  and  $c_3 \stackrel{?}{=} Com(\pi_h(r_h + x_h), \pi_t(r_t + x_t))$

If c=3:  
check  $c_1 \stackrel{?}{=} Com(\pi_h, \pi_t, y)$  and  $c_2 \stackrel{?}{=} Com(\pi_h(r_h), \pi_t(r_t))$

Figure 22. Xagawa and Tanaka's identification scheme

## D. SVP-based identification schemes

### a) Lyubashevsky's identification scheme

Lyubashevsky et. al. [21] proposed an identification scheme that is based on SVP (Shortest Vector Problem) problem in lattices. This scheme possesses three passes. Structure of Lyubashevsky's interactive proof is illustrated in Figure 10. In the condition  $\tilde{y} + \tilde{w} \notin \{1 \dots 5m - 1\}^m$  SVP problem can be noticed. Lyubashevsky's scheme concerns active attacks. It is not a zero-knowledge protocol and it

is based on concept of witness indistinguishability. It has a completeness and its soundness error is less than  $2^{-80}$ .

**KeyGen:**

$$\begin{aligned} \tilde{w} &\leftarrow_{\$} \mathbb{F}_2^m, \\ A &\leftarrow_{\$} \mathbb{Z}_q^{n \times m}, \\ \tilde{w} &\leftarrow A\tilde{w}, \end{aligned}$$

**Prover:**

$$\begin{aligned} \tilde{y} &\leftarrow_{\$} \{0, 1, \dots, 5m-1\}^m, \\ y &\leftarrow A\tilde{y}, \end{aligned}$$

If  $c=1$  and  $\tilde{y} + \tilde{w} \notin \{1, \dots, 5m-1\}^m$

$$\begin{aligned} \text{else:} \quad z &\leftarrow \perp \\ z &\leftarrow \tilde{y}|cw \end{aligned}$$

**Verifier:**

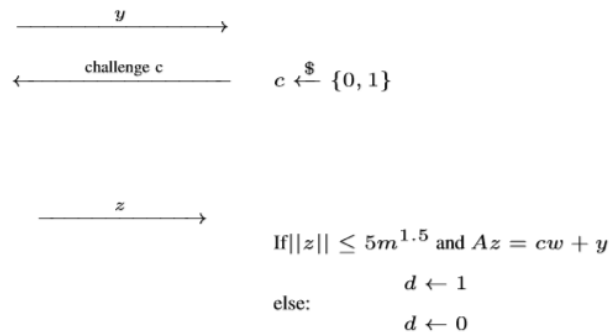


Figure 23. Lyubashevsky's identification scheme

**Comparison of Presented Identification Schemes**

In this section, we present SIS-based, LWE-based, NTRU-based and SVP-based identification schemes in terms of comparison. Main properties of identification schemes, computational cost of identification schemes and their implementation results are summarized in Table 1, Table 2 and Table 3, respectively.

Main properties of identification schemes and their resistance against attacks are shown and described in Table 1. Categorized properties of an identification scheme show the possession of the zero-knowledge concept, possession of the number of passes in a scheme, the base problem, the possession of the completeness and the threshold of the soundness error. Within these properties, resistance of identification schemes against active attack, passive attack and concurrent attack is considered. SIS-based Kawachi's, SIS-based Cayrel's, NTRU-based Xagawa's and LWE-based Silva's schemes take place in the zero-knowledge protocols, while SVP-based Lyubashevsky's scheme is the non zero-knowledge protocol. All considered schemes provide the completeness property. Cayrel's scheme possesses 5 passes and all other remaining schemes possess 3 passes. Majority of the schemes is resistant against at least on one type of the attacks.

Table 1. Main properties of identification schemes

Identification Scheme	ZK	NP	Problem	Completeness	Soundness	Resistance Against		
						AA	PA	CA
Kawachi et. al [11]	✓	3	SIS	✓	2/3	✗	✗	✓
Cayrel et. al [13]	✓	5	SIS	✓	1/2	✓	✗	✓
Soysaldi et. al [22]	✓	3	SIS	✓	1/2	✓	✗	✓
Silva et. al [14]	✓	3	LWE	✓	2/3	✓	✗	✓
Xagawa et. al [12]	✓	3	NTRU	✓	2/3	✓	✓	✗
Lyubashevsky et. al [21]	✗	3	SVP	✓	$<2^{-80}$	✗	✗	✓

**ZK** Zero Knowledge  
**NP** Number of Passes  
**AA** Active Attack  
**PA** Passive Attack  
**CA** Concurrent Attack

### A. Operations list for the implementation

For the implementation of each scheme, required operations are figured out. Number of operations for each scheme is computed and given in Table 2. Number and the length of commitments are also added to the table as a computational cost.

Table 2. Computational cost of identification schemes

Identification Scheme	Number of Operations			NC	CL
	Key Generation	Computation of Commitments	Verification		
Kawachi et. al [11]	1mv	1mv + 4p + 2v	$(4p + 2mv + 4v)/3$	3	3h
Cayrel et. al [13]	1mv	4mv + 1sv + 1v	$(1mm + 1inv + 1mv + 2sv + 2v + 1hw)/2$	2	2h
Soysaldi et. al [22]	1mv	$1mv + 1p + (3p + 2sv + 2v + 1mv)/2$	$(2sv + 2v)/2$	2	2h
Silva et. al [14]	1mv + 1v	$2mv + 2v + 2p + (2p + 1v)/3$	$(4mv + 5v + 5p)/3$	3	3h
Xagawa et. al [12]	2vp + 1v	6p + 2v	$(10p + 4v)/3$	3	3h
Lyubashevsky et. al [21]	1mv	1mv + 1v + 1sv(0.5)	1n + 1mv + 1v	-	-

NC Number of commitments

CL Commitments' length

representation of operations:

mv → matrix-vector product

mm → matrix-matrix product

md → mod

inv → matrix inversion

v → vectors addition/subtraction

h → hash length

sv → scalar vector multiplication

vp → vectors product

hw → Hamming weight

p → permutation function

n → norm

### B. Parameter set values

Parameter values selected for the implementation provide the 80-bit security level and are presented in Table 3. Parameter set values for the Cayrel's scheme are proposed in [13]. Kawachi et. al [11] and Soysaldi et. al [22] did not provide parameter values, so the values listed in Table 3 are extracted from [13]. Parameter set values for the Xagawa's scheme [12] are recommended in [31]. For the Silva's [14] identification schemes, parameter values were not given in their original works, therefore, parameters suggested for the LWE in [32] are used. For the Lyubashevsky's [21] scheme, parameter values are recommended in [30]. Additionally, in Table 3, commitment length is considered for all schemes.

Table 3. System parameters

Identification Scheme	n	m	q	CL (bits)
Kawachi et. al [11]	512	2048	257	768
Cayrel et. al [13]	512	2048	257	512
Soysaldi et. al [22]	512	2048	257	512
Silva et. al [14]	608	960	1024	768
Xagawa et. al [12]	677	-	2048	768
Lyubashevsky et. al [21]	608	960	1024	-

CL Commitments' length

### C. Practical implementation results

Implementation results of identification schemes in Java and Javascript are given in Table 4. Results of practical implementation of schemes are demonstrated. Key generation, computation of commitments and verification stages are measured separately.

Depending on total time required for the implementation of a scheme, Xagawa's scheme demonstrated the best results (63.331 ms in JavaScript and 30.157 ms in Java), while Cayrel's scheme demonstrated the worst results in the implementation in both JavaScript(71387 ms) and Java(80,319.459 ms) languages. These results are obtained due to the operations needed in the problems that these identification schemes are based on. In Xagawa's scheme, vectors product and vector addition operations



are needed while in Cayrel's scheme computationally hard operations such as the matrix-matrix product, matrix inversion and matrix-vector product are required.

Table 4. Implementation results of identification schemes

Identification Scheme	JavaScript (ms)			Java (ms)		
	Key Generation	Computation of Commitments	Verification	Key Generation	Computation of Commitments	Verification
Kawachi et. al [11]	133.797	89.644	83.484	47.013	49.09	4.158
Cayrel et. al [13]	115	329	70.943	76.185	437.677	80,319.459
Soysaldi et. al [22]	128.569	79.155	30.338	55.659	63.221	2.625
Silva et. al [14]	82.147	78.099	18.294	33.114	38.303	5.023
Xagawa et. al [12]	4.312	42.812	16.207	3.508	25.279	1.37
Lyubashevsky et. al [21]	77.328	13.216	65.257	36.319	5.881	11.525

#### Use of identification in RFID, IoT, Cloud Systems and Industry 4.0

In the emerging Internet of Things technologies identification is performed using the RFID (Radio-frequency Identification) technology. Scope of RFID are industry (an RFID tag with a set of final requirement for the product can be placed on its (part of) body (e.g., car can be automatically painted in a certain way/color); an operator with an RFID card can control equipment in a specific location); transportation (in sea container shippings, each container is equipped with an RFID tag containing information about the cargo and the owner of the cargo get the opportunity to track the location of it; since 2004, the Smart Key/Smart Start function has become available in the Toyota Prius. The key contains an active RFID chip that allows the machine to identify it from a distance of 1 meter. The driver can open the door and start the car without removing the key from his pocket); transport payments (in Hong Kong, transportation is paid mainly using RFID technology called the Octopus Card. It also can be used in vending machines and supermarkets; the Super Urban Intelligent Card Suica is used to pay rail travel in Japan); access control systems (identification and restriction to a given territory; accounting for working hours; automatic unlocking of emergency exits and closing fire doors in event of a fire alarm); medicine (RFID bracelets are used to identify the baby with the mother; search for a patient suffering from Alzheimer's disease who has left his ward); libraries (accounting for the movements of books and documents and protection against theft or accidental removal; control of the correct placement of books; one of the largest applications of RFID is the Vatican Library, which has more than two billion books in its collection); human implants (nightclubs in Barcelona nad Rtterdam use an implantable label to identify their VIP visitors, who, in turn, use them to pay for a drink); passport control (the first RFID passports were introduced in Malaysia in 1998; RFID have been included in the new biometric passports of Russian citizens since 2006); sport (RFID wristbands worn by athletes are used in orienteering, triathlon and some other sports) [4]. Through these given examples we see that production and service is becoming more intelligent; various automated devices are generating more and more information. IDC (International Data Corporation) predicts that the summation of all data (including from the IoT devices) will grow from 33 Zettabytes in 2018 to 175 Zettabytes by 2025 [39]. Such a growth in data increases the deployment of cloud. Most of companies use cloud technology to store and process data and the results of their activities. Service systems such as Healthcare, Smart environments, financial services and Entertainment upload their collected data to the cloud. For example, in the Gagarin Project [40] for the Russian telecommunications company "MegaFon", it is planned to transfer the procurement to an electronic format, where all actions will be carried out online in a single system. Due to this, paper will disappear altogether and the approval of contracts will be performed by the electronic digital signature. Note that in the basis of the electronic digital signature identification scheme underlies. Those concurrent and developing technologies such as IoT, cloud computing, cybersecurity take a place in the list of main components of the Industry 4.0. All these examples show the importance of the identification process on daily basis and global level.

#### Conclusion

In this paper, we have introduced identification schemes that are based on lattices in the post-quantum cryptography. We have shown and analysed constructions of Kawachi's [11], Cayrel's [13], Soysaldi's [22], Silva's [14], Xagawa's [12] and Lyubashevsky's [21] identification schemes. Each identification scheme is described in details. Main properties such as number of passes in a scheme, base

problem, existence of the zero-knowledge concept, existence of the completeness and the threshold of the soundness error are outlined. Some of the presented schemes are zero knowledge interactive proofs, while some of them are witness indistinguishable schemes. Those schemes were summarized in tables that demonstrate properties of schemes in different categories. Practical implementations of identification schemes are performed. As a consequence, obtained results of their executions are demonstrated and compared in a common table. The results show that Cayrel's scheme which contains computationally hard operations such as the matrix-matrix product, matrix inversion took the longest time as expected. Xagawa's scheme which contains computational operations such as the vectors product, vectors addition/subtraction and permutation took the shortest time for the execution. Future work includes the study and development of those schemes in C language with optimizations in required operations.

### References

- [1] ENISA Position Paper, “Privacy Features of European eID Card Specifications”, February 2009, <https://www.enisa.europa.eu/publications/eid-cards-en>
- [2] U. Feige, A. Fiat, A. Shamir, “Zero-knowledge proofs of identity,” *J. Cryptology* 1988; pp. 77–94.
- [3] M. Just, “Schnorr Identification Protocol,” *Encyclopedia of Cryptography and security*, Springer, Boston, 2011.
- [4] V. Anisimov, “Cryptographic methods of information security: Identification Protocols,” (Lecture Notes), available: [sites.google.com/site/anisimovkhv/learning/kripto/lecture/tema11/](https://sites.google.com/site/anisimovkhv/learning/kripto/lecture/tema11/)
- [5] P.W. Shor, “Polynomial-time algorithms for prime factorization and discrete logarithms on a quantum computer,” *SIAM J Comput* 1997; 26: 1484-1509.
- [6] T.Laarhoven, J. Pol and B. Weger, “Solving Hard Lattice Problems and the Security of Lattice-Based Cryptosystems,” in *J. IACR Cryptology ePrint Archive*, vol:2012, 2012.
- [7] M. Ajtai, “Generating hard instances of lattice problems,” in *Quaderni di Matematica*, 2004. Preliminary version in *STOC* 1996.
- [8] O. Regev, “On lattices, learning with errors, random linear codes, and cryptography,” in *Proceedings of the 37th Annual ACM Symposium on Theory of Computing* 2005; pp.84-93.
- [9] O. Regev, “The Learning with Errors Problem,” 2010 IEEE 25th Annual Conference on Computational Complexity, Cambridge, 2010, pp. 191-204. doi: 10.1109/CCC.2010.26
- [10] J. Hoffstein, J. Pipher and J.H. Silverman, “NTRU: A ring-based public key cryptosystem,” in *Buhler, Algorithmic Number Theory, 1998; Lecture Notes in Computer Science*, Springer, Berlin, Heidelberg, vol: 1423.
- [11] A. Kawachi, K. Tanaka, and K. Xagawa “Concurrently Secure Identification Schemes Based on the Worst-Case Hardness of Lattice Problems,” *J. Advances in Cryptology - ASIACRYPT* 2008; pp. 372-389.
- [12] K. Xagawa and K. Tanaka, “Zero-Knowledge Protocols for NTRU: Application to Identification and Proof of Plaintext Knowledge,” *Lecture Notes in Computer Science*, 2009; pp. 198–213.
- [13] P.-L. Cayrel, R. Lindner, M. Ruckert, and R. Silva, “Improved Zero Knowledge Identification with Lattices,” *J. TatraMountains Mathematical Publications*, vol: 53, 2010; pp. 1-17.
- [14] R. Silva, A. Campello and R. Dahab, “LWE-based identification schemes”, *CoRR*, abs/1109.0631, 2011.
- [15] J. Menezes, P. C. Oorschot, S. A. Vanstone, *Handbook of Applied Cryptography*, 1996, <http://www.cacr.math.uwaterloo.ca/hac/>
- [16] M. Ajtai, “Generating Hard Instances of Lattice Problems”, *J. Electronic Colloquium on Computational Complexity (ECCC)*, vol:3, 1996.
- [17] J. H. Cheon, D. Kim, J. Lee, and Y. Song, “Lizard: Cut off the Tail! Practical Post-Quantum Public-Key Encryption from LWE and LWR,” *arXiv:1126*, 2016.
- [18] J. Bos, C. Costello, L. Ducas, I. Mironov, M. Naehrig, V. Nikolaenko, A. Raghunathan, D. Stebila, “Frodo: Take off the ring! Practical, quantumsecure key exchange from LWE,” In *ACM Conference on Computer and Communications Security (CCS)* 2016. doi:10.1145/2976749.2978425, eprint: <http://eprint.iacr.org/2016/659>.
- [19] E. Alkim, L. Ducas, T. Poppelmann and P. Schwabe, “Post-quantum key exchange - a new hope,” *arXiv:1092*, 2015.

- [20] R. E. Bansarkhani and J. A. Buchmann, “Improvement and Efficient Implementation of a Lattice-Based Signature Scheme,” *Selected Areas in Cryptography 2014*; pp. 48-67. doi: 10.1007/978-3-662-43414-7
- [21] V. Lyubashevsky, F. Shamir, “Applications to lattice and factoring-based signatures,” *Advances in Cryptology – ASIACRYPT 2009, Lecture Notes in Computer Science*; Springer Berlin Heidelberg, 2009; pp. 598–616
- [22] M. Soysaldi, S. Akleylek, “A new 3-pass Zero-knowledge Lattice-based Identification Scheme,” 4th International Conference on Computer Science and Engineering (UBMK) 2019.
- [23] U. Feige, A. Shamir, “Witness indistinguishable and witness hiding protocols,” *Proceedings of the Twenty-Second Annual ACM Symposium on Theory of Computing - STOC '90*, 1990. doi: 10.1145/100216.100272
- [24] I. B. Damgard, T. P. Pederson and B. Pfitzmann, “On the Existence of Statistically Hiding Bit Commitment Schemes and Fail-Stop Signatures,” in: *Journal of Cryptology* 10, 1997; pp. 163–194.
- [25] S. Halevi and S. Micali, “Practical and provably-secure commitment scheme from collision - free hashing,” in *CRYPTO '96*, 1996; pp. 201–215.
- [26] J. Stern, “A new paradigm for public key identification,” *IEEE Transactions on Information Theory* 42, 1996; pp. 749–765
- [27] J. J. Quisquater and Louis Guillou, “How to Explain Zero-Knowledge Protocols to Your Children,” in: *Advances in Cryptology — CRYPTO' 89 Proceedings, CRYPTO 1989, Lecture Notes in Computer Science*, vol 435, 1990, Springer, New York
- [28] T. Guneysu, V. Lyubashevsky and T. Poppelmann, “Practical lattice-based cryptography: A signature scheme for embedded systems,” *Cryptographic Hardware and Embedded Systems – CHES 2012, Lecture Notes in Computer Science*; Springer Berlin Heidelberg, 2012; pp. 530–547.
- [29] O. Goldreich, S. Goldwasser and S. Halevi, “Collision-Free Hashing from Lattice Problems,” *Electronic Colloquium on Computational Complexity*, vol. 3, no. 42, 1996; pp. 1–10.
- [30] V. Lyubashevsky, “Fiat-shamir with aborts: Applications to lattice and factoring-based signatures,” in Springer, *ASIACRYPT, Lecture Notes in Computer Science*, vol: 5912, 2009; pp. 598–616.
- [31] P. Hirschhorn, J. Hoffstein, N. Howgrave-Graham and W. Whyte, “Choosing NTRUEncrypt parameters in light of combined lattice reduction and MITM approaches,” in *Applied cryptography and network security*, Springer, 2009; pp. 437–455
- [32] J. H. Cheon, D. Kim, J. Lee and Y. Song, “Lizard: Cut off the Tail! Practical Post-Quantum Public-Key Encryption from LWE and LWR,” *Cryptology ePrint Archive Report* 2016/1126.
- [33] R. de Wolf, “Quantum computing: Lecture notes,” 2019, arxiv:1907.09415v1
- [34] G. Lichfield, “Inside the race to build the best quantum computer on Earth,” *MIT Technology Review*, 2020: [technologyreview.com/2020/02/26/916744/quantum-computer-race-ibm-google/](https://technologyreview.com/2020/02/26/916744/quantum-computer-race-ibm-google/)
- [35] L. Chen, S. Jordan, Y. K. Liu et al., “Report on post-quantum cryptography,” *National Institute of Standards and Technology*
- [36] J. Menezes, P. C. Oorschot, S. A. Vanstone, (1996), *Handbook of Applied Cryptography*, <http://www.cacr.math.uwaterloo.ca/hac/>
- [37] J. Bos, L. Ducas, E. Kiltz, T. Lepoint, V. Lyubashevsky, J. M. Schanck, P. Schwabe, G. Seiler, D. Stehlé, “CRYSTALS – Kyber: a CCA-secure module-lattice-based KEM,” In *IEEE European Symposium on Security and Privacy*, 2018, doi:10.1109/EuroSP.2018.00032
- [38] T. Prest, P. A. Fouque, J. Hoffstein, P. Kirchner, V. Lyubashevsky, T. Pornin, T. Ricosset, G. Seiler, W. Whyte and Z. Zhang, “Falcon,” *Technical report*, National Institute of Standards and Technology, 2017, <https://csrc.nist.gov/Projects/Post-Quantum-Cryptography/r-2-submissions>
- [39] D. Reinsel, J. Gantz, J. Rydning, “The Digitization of the World from Edge to Core,” in: *An IDC White Paper*, November 2018, <https://www.seagate.com/files/www-content/our-story/trends/files/idc-seagate-data-age-whitepaper.pdf>
- [40] Tadviser news, “Information Technologies in MegaFon”, 2020, available : <https://www.tadviser.ru/index.php/>

## Support Vector Machines: From Classical Version to Quantum

Gildas Decadjevi\*, Department of Computer Engineering, Ondokuz Mayıs University, 55139 Samsun, Turkey

Sedat Akleylek, Department of Computer Engineering, Ondokuz Mayıs University, 55139 Samsun, Turkey

Gazmor Abdiu, Department of Computer Engineering, Ondokuz Mayıs University, 55139 Samsun, Turkey

Omar Halabi, Department of Computer Engineering, Ondokuz Mayıs University, 55139 Samsun, Turkey

\*Corresponding author: gildasdeca@gmail.com

**Keywords:** Support vector machine, machine learning, quantum computing, qubit

**Discipline:** Computer Science and Engineering

### Abstract

Machine learning algorithms are used to analyze and process large amounts of data in order to get useful insights from them. Its combination with quantum computing gives rise to the field of quantum machine learning based on the implementation of machine learning algorithms on quantum computers in order to compare their performances and evaluate the possibilities to improve them. One of these algorithms is the support vector machine (SVM). This one is based on the determination of the optimum hyper plane that will separate the data in different classes. It has a time complexity of  $\mathcal{O}(M^2(M + N))$  on classical computers. However, its quantum version, the quantum SVM are theoretically proved to have logarithmic complexity. Through this work we carry out the SVM algorithm's study, its implementation on classical and quantum computers as well as a comparative analysis of the results. It shows that while the quantum SVM are faster than the classical SVM in matter of time, its accuracy still needs to be improved. For that purpose, we propose that the development and application of noise reduction methodologies will help getting better performances.

### Introduction

Machine learning algorithms are used to build models for data analysis in various domains such as financial services, health care, sales, retail, transport, and much more. They are used in financial services for fraud detection, credit scoring, and stock trading [1]. In health care, machine learning has enhanced the processes of drug design, disease detection, and treatment effectiveness evaluation [2]. It's also improving the sales and retail sector through sales forecasting, data-driven decision making, recommendation systems, and customer relationship management [3], [4]. All these areas have in common the concept of data. With the continual growth of the amount of data available, making sense of it, analyzing it, drawing useful insights that will help in decision making becomes a global necessity [5]. Thus, we have different machine learning algorithms that are developed and continuously improved for this purpose and implemented on our classical computers [6]. Although there are many algorithms for a good analysis of the data, classical machine learning is facing different challenges such as the performance of its algorithms and their complexity: the processing performance, the curse of modularity, the curse of dimensionality, the class imbalance, feature engineering, and non-linearity [5]. The larger the amount of data to analyze is, the higher the required computing power is [7]. Classical devices do not always execute such tasks easily due to their limited capacities of computation and memory. It's then important to look for possible ways to increase the computation capabilities of those devices as well as trying to improve the existing machine learning algorithms in order to have lesser complexity.

Quantum computing's main promise to machine learning is to provide not only a higher capacity of computation on quantum computers but also a new way to apply those algorithms so as to get more efficient results [8]. Quantum physics makes it possible to encode and process information in ways that completely exceed what classical computers would actually be capable to do [9]. Quantum entanglement and teleportation are some non-classical phenomena that give quantum computing an edge over classical computing [10]. With these features, quantum computers are expected to run quantum versions of many existing algorithms with an exponential speedup [11]. The study of machine learning algorithms with a quantum-based approach enabled the emerging of the new field of quantum machine learning (QML). QML is focused on the research and implementation of software that will enable the use of the advantages made available by quantum computing to enhance machine learning and its quest for efficiency and speed in a world of voluminous data [12]. In data analysis, one of the most known algorithms is the support vector machines (SVM). It is mainly used in classification or regression

problems with multiple applications [13]. The quantum version of the SVM namely the quantum support vector machine (QSVM) is theoretically proved to have an exponential speed-up comparatively to the classical SVM [14]. It will be then a great revolution to get such a result practically by implementing successfully this widely used algorithm.

### Motivation and Contribution

The field of quantum machine learning presents a lot of sub-areas to explore. Due to the fact that it is a new domain, the researches, as well as the implementations, are still at an early stage, making it possible to engage in one of its sub-areas for new discoveries or to work on ways to translate the theoretical knowledge available into practical applications that will enable its use in the industry. Different quantum machine learning algorithms have been developed but not implemented on the real quantum devices for reasons such as their unavailability or their inaccessibility. But now, with the different simulators and even some real devices made available online by some high-tech companies, the implementations of those algorithms have started. In the same direction, in this work, we apply classical SVM to classify a breast cancer data set and applied quantum SVM on the same data set but on IBM quantum devices namely `Ibmq_melbourne`, `Ibmq_rome` and `Ibm_qasm` simulator. After the analysis and implementation of the SVM and QSVM algorithm, we performed a comparison of their speed and accuracy which shows that the theoretical supremacy of the QSVM is not yet practically obtainable with the available devices due to the noise factor.

### Organization

The rest of this paper is structured as follows. In Section II, we present the main background and explanation of the studied algorithm which is the SVM. In Section III, we explain the quantum SVM. In Section IV, the algorithm implementation, the data set, and the results have been presented followed by an analysis and suggestions for future results improvement. The conclusion of the work is provided in Section V.

### Preliminaries

In this section, the SVM algorithm is clearly explained. Machine learning includes a large variety of algorithms that can be classed as supervised learning, unsupervised learning, and reinforcement learning algorithms [15]. In supervised learning, the data is labeled. Thus, the model basing on the expected output of the received input infers a function which' accuracy is measured during the testing phase. Contrarily to that, in unsupervised learning, the data is unlabeled and should be classified in groups based on some common characteristics or properties to be detected by the model. In reinforcement learning, the model receives the inputs and is directed or taught while producing an output for the different inputs basing on a rewarding system. SVM are among supervised learning algorithms. SVM's main use is to classify the data into the right groups while striving to find and establish the optimum hyper plane that will enable the categorization. The sought hyper plane's equation is given in Equation (1) [16].

$$w^T x \pm b = 0 \quad (1)$$

Accordingly, to the number of data groups, there are binary SVM and multi category SVM. Binary SVM are used when the data can be classified into two groups. In binary classification, the training set is of the type  $\{(X_1, Y_1), (X_2, Y_2), \dots, (X_n, Y_n)\}$  with  $Y \in \{-1, 1\}$  having  $X_i$  as input and  $Y_i$  as output. The data is said to be linearly separable when the two groups can be divided by a straight line and it is qualified as non-linear in the opposite case. In Figure 1, a representation of linearly separable data is given.

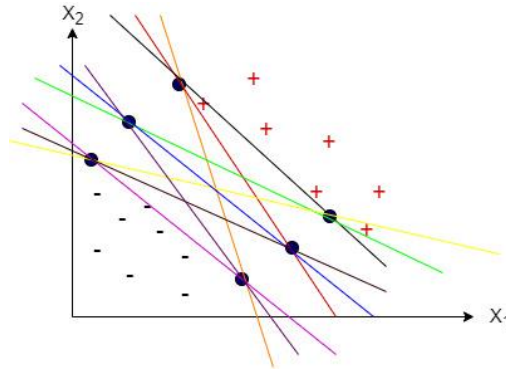


Figure 24. Linearly separable data

In this figure the goal is to classify the positive data points (+1) from the negatives (-1). There are many possible lines that can divide them but the SVM looks for the hyper plane that will yield the maximum gap between the data points of the two classes. That distance is the margin and the model is named hard margin SVM. The data points present on the boundaries are the support vectors. The equations of the plans of the positive and the negative support vectors are respectively given in (2) and (3) [16].

$$w^T x - b = +1 \quad (2)$$

$$w^T x - b = -1 \quad (3)$$

$w$  is the normal vector to the hyper plane, and  $b$  is the bias parameter helping to determine the offset of the hyper plane from the origin. When the plans are parallel, they have the same normal vector but their bias value is not the same. Thus, we can determine the gap between the positive and negative boundary plans as given in Equation (4).

$$\frac{|b_1 - b_2|}{\|w\|} = \frac{|1 - (-1)|}{\|w\|} = \frac{2}{\|w\|} \quad (4)$$

As the goal of the SVM model is to maximize the margin, then  $\frac{2}{\|w\|}$  is to be maximized, which means that we will minimize  $\frac{1}{2} \|w\|^2$ . For the optimum classification of the positive and negative data points, it is expected that none of them will fall into the space delimited by the margin. This condition is expressed by the Equations (5), (6) and generalized in (7) [16].

$$w^T x - b \geq +1 \text{ with } y = +1 \quad (5)$$

$$w^T x - b \leq -1 \text{ with } y = -1 \quad (6)$$

$$y(w^T x - b) \geq 1, \text{ for } x = 1, \dots, N \quad (7)$$

These conditions lead to the primal formulation of hard margin SVM given in a reduced way in Equation (8) so that for positive data points  $f(x) = +1$  and for negative ones  $f(x) = -1$  [17].

$$f(x) = \text{sign}(wx - b) \quad (8)$$

For optimization purposes in linear SVM, we apply the method of Lagrange multipliers to the primal expression so as to obtain the dual formulation of hard margin SVM given in the Equations (9), (10), (11) and (12) [18].

$$\max_{\vec{\alpha}} L(\vec{\alpha}) \sum_{j=1}^M -\frac{1}{2} \sum_{j,k=1}^M \alpha_j x_j \alpha_k x_k, \sum_{j=1}^M \alpha_j y_j = 0 \quad (9)$$

$$\vec{w} = \sum_{i=1}^N \alpha_i y_i \vec{x}_i \quad (10)$$

$$f(\vec{x}) = \text{sign}\left(\sum_{i=1}^N \alpha_i y_i \vec{x}_i \cdot \vec{x} + b\right) \quad (11)$$

$$b = \frac{1}{|\{i: \alpha_i \neq 0\}|} \sum_{i: \alpha_i \neq 0} (w^T x_i - y_i) \quad (12)$$

Due to factors such as noise in the data set, some data points may fall on the wrong side of the hyper plane creating confusion in the classification. In that case, we define a trade-off variable  $C$  slack variable representing the distance between the outliers and the hyper plane with the goal to minimize these distances. This forms the soft margin SVM model expressed through the Equations (13) and (14). In the same way, the primal formulation of soft margin linear SVM as well as the dual formulation are given in the Equations (15), (16) and (17), respectively [16].

$$w^T x_i + b \geq 1 - \xi_i \text{ for } y_i = +1 \quad (13)$$

$$w^T x_i + b \leq -1 + \xi_i \text{ for } y_i = -1 \quad (14)$$

$$\min \frac{1}{2} \sum_{i=1}^n w_i^2 + C \sum_{i=1}^N \xi_i \quad (15)$$

$$y_i(\vec{w} \cdot \vec{x}_i + b) \geq 1 - \xi_i, i = 1, \dots, N \quad (16)$$

$$\max \sum_{i=1}^n \alpha_i - \frac{1}{2} \sum_{i,j=1}^N \alpha_i \alpha_j y_i y_j \vec{x}_i \cdot \vec{x}_j \quad (17)$$

$$0 \leq \alpha_i \leq C \text{ and } \sum_{i=1}^N \alpha_i y_i = 0, i = 1, \dots, N$$

When the trade-off value  $C$  is very high, the soft margin SVM tends to be equivalent to the hard margin SVM. However, when  $C$  is very low, the probability of erroneous classification increases [16]. When the binary classification is to be done on a data set of which the points are not linearly separable, the SVM translates the data from its original space to a higher dimensional space named the feature space so as to determine the classification hyper plane in that space.

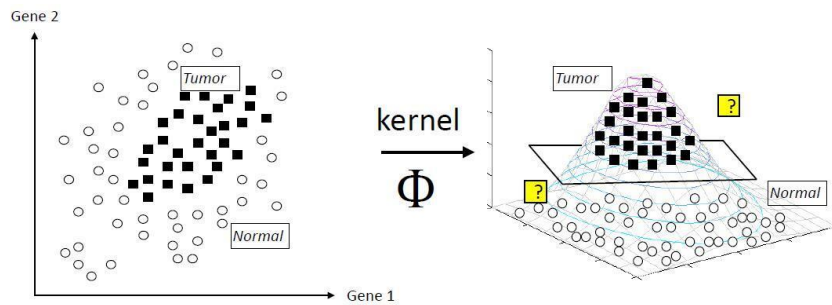


Figure 25. Classification with non-linear SVM

In Figure 2, an example is given showing the space translation and data classification by non-linear SVM [16]. The primal formulation of hard margin non-linear SVM is given in Equations (18), (19), and (20) as follows [16].

$$w \cdot \phi(x) + b = 0 \quad (18)$$

$$\text{argmin}_{w,b} \frac{1}{2} \|w\|^2 \quad (19)$$

$$y_i(w \cdot \phi(x_i) + b) \geq 1, \quad (20)$$

$\phi(x)$  is the mapping function from the input space to the feature space. Equations (21) and (22) presents the state in input space while (23) and (24) present it in the feature space [16].

$$f(x) = \text{sign}(\bar{w} \cdot \vec{x} + b) \quad (21)$$

$$\bar{w} = \sum_{i=1}^N \alpha_i y_i \vec{x}_i \quad (22)$$

$$f(x) = \text{sign}(\bar{w} \cdot \phi(\vec{x}) + b) \quad (23)$$

$$\bar{w} = \sum_{i=1}^N \alpha_i y_i \phi(\vec{x}_i) \quad (24)$$

When we replace  $w$  in  $f(x)$  we get the equations (25) and (26).

$$f(x) = \text{sign}\left(\sum_{i=1}^N \alpha_i y_i \phi(\vec{x}_i) \cdot \phi(\vec{x}) + b\right) \quad (25)$$

$$f(x) = \text{sign}\left(\sum_{i=1}^N \alpha_i y_i K(\vec{x}_i, \vec{x}) + b\right) \quad (26)$$

$$\phi : R^N \rightarrow H \text{ for } K : R^N \times R^N \rightarrow R$$

In data classification and regression analysis, another version of SVM are Least-squares support vector machines (LSSVM). They are summarized into the optimization problem expressed in Equation (28) under the constraints presented in Equation (29) [18].

$$\text{argmin} \frac{1}{2} w^T w + \frac{\gamma}{2} \sum_{i=1}^M e_i^2 \quad (28)$$

$$y_i (w^T \phi(x_i) + b) = 1 - e_i, \quad (29)$$

The parameter  $\gamma$  determines the cost or the trade-off value. By applying the method of Lagrange, we obtain the Equation (30) with  $K$  as kernel matrix [18].

$$\begin{pmatrix} 0 & 1^T \\ 1 & K + \gamma^{-1} I \end{pmatrix} \begin{pmatrix} b \\ \alpha \end{pmatrix} = \begin{pmatrix} 0 \\ y \end{pmatrix} \quad (30)$$

Apart from binary SVM, there are multi category SVM used when the data should be categorized into more than two classes. One of the main methods used is the one-versus-rest multi category SVM method. In this method, we determine the hyper plane corresponding to the classification of the element of only one class against all the other classes. In this case it is considered as if it were a binary classification where the  $i^{th}$  class is the first and all the  $(n - 1)$  rest of class constitute second different class and the corresponding hyper plane is defined. After applying this to each of the  $n$  classes, we finally get  $n$  hyper planes which are analyzed with the decision functions so as to define the complete hyper plane of the multi category classification. The disadvantage of this method is related to all the computations that it requires.



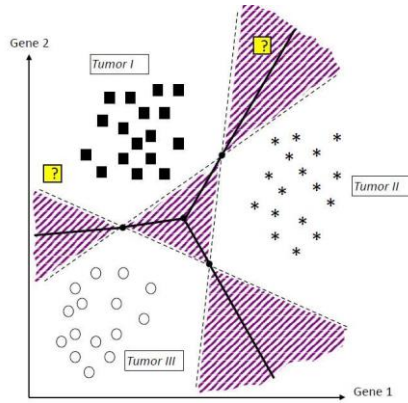


Figure 26. Example of one-versus-rest multi category SVM method.

In Figure 3, an example of multi category classification based on one-versus-rest is presented [16]. When this method is applied, the different equations explaining the functioning of the SVM model are presented in Equation (31), (32) and (33) [18].

$$\min_{w^i, b^i, \xi^i} \frac{1}{2} (w^i)^T w^i + C \sum_{j=1}^N \xi_j^i \quad (31)$$

$$(w^i)^T \phi(x_j) + b^i \geq 1 - \xi_j^i, \quad y_i = i \quad (32)$$

$$(w^i)^T \phi(x_j) + b^i \leq -1 + \xi_j^i, \quad y_i \neq i \quad (33)$$

### Quantum Support Vector Machines

In this section, the quantum SVM are explained. As for classical SVM, quantum SVM are used in classification and regression processes. The main goal is also the determination of the optimum hyper plane. The difference between classical SVM and quantum SVM is how the algorithm is implemented leading then to differences of performance. Quantum SVM was developed primarily to solve the Least Square problem. The training set is expressed as a quantum state via the quantum random access memory (QRAM). Mathematically, the state's representation is given in Equation (34) [19]:

$$|\vec{x}_j\rangle = \frac{1}{|\vec{x}_j|} \sum_{k=1}^N (\vec{x}_j)_k |k\rangle \quad (34)$$

Quantum SVM can be realized using the Grover search algorithm when the data used is a classical one. The Grover search algorithm finds an element in an unordered set in  $\mathcal{O}(\sqrt{n})$  steps whereas classically at least  $\mathcal{O}(n)$  steps are required. This added to the adiabatic quantum optimization leads to a quadratic speed up of the QSVM comparatively to classical SVM. If the data is already in quantum state or has been converted to quantum state, then the LS-SVM's quantum version can be executed on quantum devices. Thus the kernel matrix is calculated using quantum algorithm for inner product on QRAM, [20] and the other operations are performed using the quantum algorithm for solving linear equations. Finally, the trained qubits are used for the data classification with a logarithmic complexity  $\mathcal{O}(\log(MN))$ . To get these results, the matrix problem that has been solved is expressed in Equation (35) with ways to find its inverse given in Equation (36) and (37) [18].

$$F \begin{pmatrix} b \\ \vec{\alpha} \end{pmatrix} = \begin{pmatrix} 0 & \vec{1}^T \\ \vec{1}^T & K + \gamma^{-1}I \end{pmatrix} \begin{pmatrix} b \\ \vec{\alpha} \end{pmatrix} = \begin{pmatrix} 0 \\ \vec{y} \end{pmatrix} \quad (35)$$

$$F = \begin{pmatrix} 0 & \vec{1}^T \\ \vec{1}^T & K + \gamma^{-1}I \end{pmatrix} \quad (36)$$

$$F = J + K\gamma \text{ such that}$$

$$J = \begin{pmatrix} 0 & \vec{1}^T \\ \vec{1} & 0 \end{pmatrix} \text{ and } K\gamma = \begin{pmatrix} 0 & 0 \\ 0 & K + \gamma^{-1}I \end{pmatrix} \quad (37)$$

When the different quantum matrix algorithms and *Lie* algebra are applied, the normalization process of  $K$  and  $F$  matrices are performed and the inverse of  $F$  matrix is found. If it were the classic SVM, the complexity would be  $\mathcal{O}(M^2(M + N))$ , however, with this method of QSVM an exponential speedup is noticed [18]. In algorithm 1, the pseudocode of QSVM algorithm is presented [21].

**Algorithm 1** Quantum SVM

**Input:**

- Training data set  $(\vec{x}_j, y_j)$ ,  $j = 1, 2, 3, \dots, M$
- A query data  $\vec{x}$

**Output:**

- Classification of  $\vec{x}$  : +1 or -1

**Procedure:**

- Calculate kernel matrix  $K_{ij} = \vec{x}_i \cdot \vec{x}_j$  using quantum inner product algorithm.
- Solve the linear equations and find  $|b\vec{\alpha}\rangle$  using a quantum algorithm for solving linear equations (training step)
- Perform the classification of the query data  $\vec{x}$  against the training results  $|b\vec{\alpha}\rangle$  using a quantum algorithm.

In Table 5, a general comparison of classical SVM and quantum SVM is given [18] [17].

Table 5. General comparison of classical and quantum SVM

Comparison	Classical SVM	Quantum SVM
Learning type	Supervised learning	Supervised learning
Intended use	Classification and regression	Classification and regression
Hyper plane equation	$\vec{w}\vec{x} + b = 0$	$\vec{w}\vec{x} + b = 0$
Complexity	$\mathcal{O}(M^2(M + N))$ , with $M$ the number of training instances and $N$ the number of dimensions in the feature space.	$\mathcal{O}(M^2N)$ , with Grover search algorithm $\mathcal{O}(\log(MN))$ with quantum matrix Optimization algorithms.
Algorithms that are used in the background	Standard matrix multiplication, linear equation solving and matrix inversion method.	Grover search algorithm, quantum linear equation solving algorithm, quantum sparse matrix method, PCA.

**Experimental Results**

In this section, the classical and the quantum version of SVM algorithm have been implemented, compared and analyzed. The two versions of the algorithm have been executed on the breast cancer Wisconsin diagnostic data set. It is available in the Scikit-learn library and has 569 instances with 30 numeric predictive attributes and the class. A cell can be classified either as benign or malignant. The data set has been initially preprocessed and normalized so as to ease the classification process. In each case, 70% of the data set constituted the training set and 30% the test set. On the classical device, the average result is given in the Figure 4.

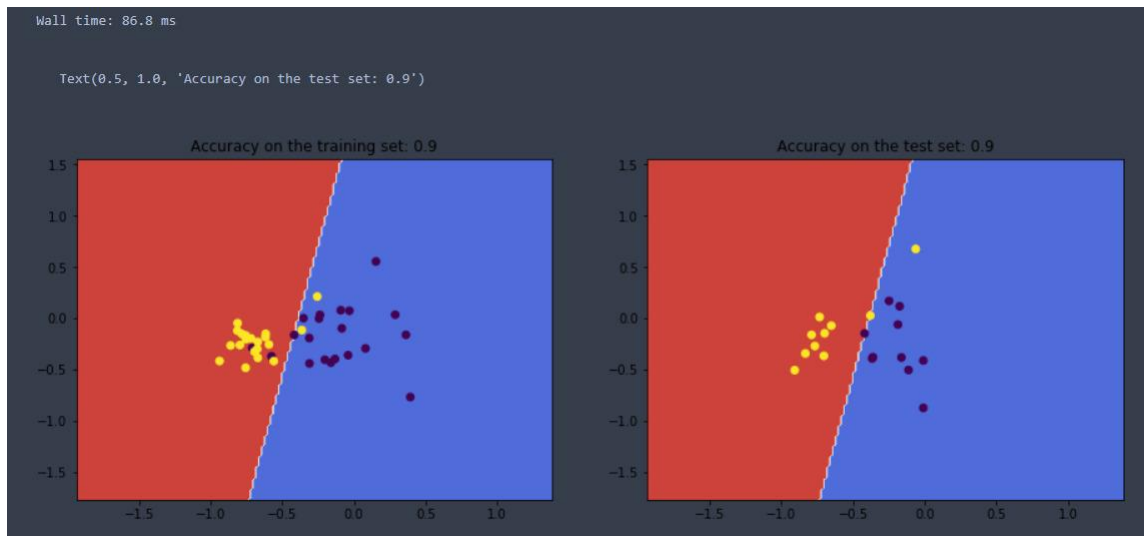


Figure 27. Data classification with classical SVM

For the quantum SVM, the dimensionality of the data has been reduced using the principal component analysis (PCA) before its classification.

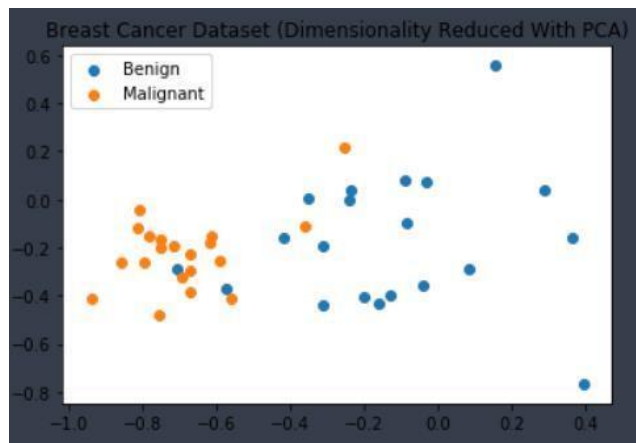


Figure 28. Data set with dimensionality reduced with PCA

In Figure 5, the representation of the data after dimensionality reduction with PCA is given. The quantum SVM has been run on the IBM Qiskit simulator as well as two of the real quantum devices made available by IBM and reachable online for experimental purposes. In Table 2, the comparison of the performance results of the classical SVM and quantum SVM is provided. In Figure 6, the circuit of the representation of QSVM on a 5-qubits real device is presented [22].

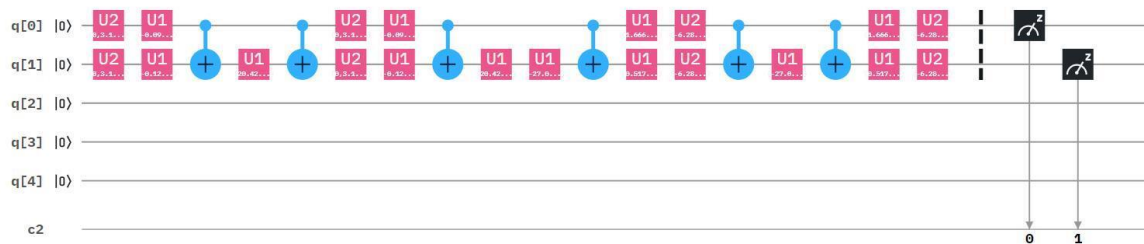


Figure 29. Representation of QSVM circuit

Table 6. The performance differences based on the type of the SVM algorithm and the implementation device

Comparison	Average Time	Average Accuracy
Classical SVM on classical computer	75.8ms	90%
QSVM on local qasm_simulator	Seconds	95%
Quantum SVM on ibmq_16_melbourne (16 qubits)	50ms	70%
Quantum SVM on ibmq_rome (5 qubits)	50ms	70%

For instance, quantum SVM's execution on the two real quantum devices with different numbers of qubit results in average into the same performance in matter of time and accuracy. This means that the number of qubits unused does not influence considerably the result yielded by those in use. The fact that the classification time on the real quantum devices is lower than the classical one shows that the quantum computers are really faster than classical devices at computing tasks and that quantum SVM too are faster than classical SVM. The fact that the local simulator "qasm" has an average time that is higher than all the others proves how hard and costly it is to implement and test quantum properties on classical devices. The qasm-simulator is available offline to run directly on classical devices while approximating an ideal quantum environment (void of noise).

As shown in the table, the qasm simulator presents the highest accuracy among all the implementations. Given that the qasm simulator represents the ideal quantum computer environment, then it means that the real quantum devices used have not been able to work up to their full potential. It's also to be noticed that although those real quantum computers are faster than classical computers, they are not yet as accurate as classical computers are. In fact, if the quantum computers were working in ideal mode, they would produce at least the result of the local simulator or even better due to the limitations of the simulator on classical devices. Thus, one of the main reasons that could be hindering us from getting the best out of the quantum SVM expected to produce practically the exponential speedup, is the noise factor. In fact, quantum computers are designed to be held at a temperature that is completely close to the absolute zero which is not easy to achieve. For this reason, every modification or derangement of the environment may be an eventual source of noise, causing some errors to happen in the quantum information processing and leading consequently to less accuracy. Toward this situation, the suggestion of our work would be the exploration of possible ways of noise mitigation. Actually, one of the libraries being developed for quantum devices is the "Ignis" library that is an IBM framework for characterizing and mitigating noise in quantum devices. The study and application of this library to quantum SVM would then surely help to enhance the performances obtained actually on quantum devices for QSVM execution.

### Conclusion and Future Works

In this paper, we carry out a large study of the quantum SVM, a QML algorithm starting from its main concepts as classical SVM until its implementation and the performance analysis. We find out that the theoretically proved exponential speedup of the quantum SVM comparatively to the classical SVM still requires some improvements before being achievable in practice. One of those requirements is the noise mitigation due to the fact that quantum devices are exposed to this factor that may corrupt their execution process and their results. For this reason, as future work, it is possible and preferable look for ways to minimize it by taking advantage of existing noise mitigation libraries or by building more efficient ones so as to be able to get the best out of these computers that have the capacity to revolutionize completely the way we process data.

### References

- [1] P. Domingos, "A few useful things to know about machine learning," *Commun. ACM*, vol. 55, p. 78–87, Oct. 2012.
- [2] M. Haddadi and M. Dehghanian, "Strictly proximal in normed spaces," *World Applied Sciences Journal*, vol. 16, no. 2, pp. 250–252, 2012.

- [3] M. Bohanec, M. K. Borštnar, and M. Robnik-Šikonja, “Explaining machine learning models in sales predictions,” *Expert Systems with Applications*, vol. 71, pp. 416–428, 2017.
- [4] I.-F. Chen and C.-J. Lu, “Sales forecasting by combining clustering and machine-learning techniques for computer retailing,” *Neural Computing and Applications*, 02 2016.
- [5] A. L’heureux, K. Grolinger, H. F. Elyamany, and M. A. Capretz, “Machine learning with big data: Challenges and approaches,” *IEEE Access*, vol. 5, pp. 7776–7797, 2017
- [6] Y. Liu, J.-W. Bi, and Z.-P. Fan, “Multi-class sentiment classification: The experimental comparisons of feature selection and machine learning algorithms,” *Expert Systems with Applications*, vol. 80, pp. 323 - 339, 2017.
- [7] A. Katal, M. Wazid, and R. H. Goudar, “Big data: issues, challenges, tools and good practices,” in *2013 Sixth international conference on contemporary computing (IC3)*, pp. 404–409, IEEE, 2013.
- [8] T. A. Shaikh and R. Ali, “Quantum computing in big data analytics: A survey,” in *2016 IEEE International Conference on Computer and Information Technology (CIT)*, pp. 112–115, IEEE, 2016.
- [9] A. Galindo and M. A. Martin-Delgado, “Information and computation: Classical and quantum aspects,” *Reviews of Modern Physics*, vol. 74, no. 2, p. 347, 2002.
- [10] R. Jozsa, “Entanglement and quantum computation,” arXiv preprint [quantph/9707034](https://arxiv.org/abs/quantph/9707034), 1997.
- [11] J. Biamonte, P. Wittek, N. Pancotti, P. Rebentrost, N. Wiebe, and S. Lloyd, “Quantum machine learning,” *Nature*, vol. 549, no. 7671, pp. 195–202, 2017.
- [12] W. S. Noble, “What is a support vector machine?” *Nature biotechnology*, vol. 24, no. 12, pp. 1565–1567, 2006.
- [13] P. Rebentrost, M. Mohseni, and S. Lloyd, “Quantum support vector machine for big data classification,” *Physical review letters*, vol. 113, no. 13, p. 130503, 2014.
- [14] S. Shalev-Shwartz and S. Ben-David, *Understanding Machine Learning: From Theory to Algorithms*. USA: Cambridge University Press, 2014.
- [15] R. Jozsa and N. Linden, “On the role of entanglement in quantum computational speed-up,” *Proceedings of the Royal Society of London. Series A: Mathematical, Physical and Engineering Sciences*, vol. 459, no. 2036, pp. 2011–2032, 2003.
- [16] A. Statnikov, *A gentle introduction to support vector machines in biomedicine: Theory and methods*, vol. 1. world scientific, 2011.
- [17] E. R. Johnson, N. Harrigan, and M. Gimeno-Segovia, *Programming Quantum Computers: Essential Algorithms and Code Samples*. O’Reilly Media, Incorporated, 2019.
- [18] P. Wittek, *Quantum Machine Learning: What Quantum Computing Means to Data Mining*. 08 2014.
- [19] Y. Huang, H. Lei, and X. Li, “A survey on quantum machine learning,” *Chin. J. Comput*, vol. 41, no. 1, pp. 145–163, 2018.
- [20] S. Lloyd, M. Mohseni, and P. Rebentrost, “Quantum algorithms for supervised and unsupervised machine learning,” arXiv preprint [arXiv:1307.0411](https://arxiv.org/abs/1307.0411), 2013.
- [21] P. Coles and S. Eidenbenz et al., “Quantum algorithm implementations for beginners,” 04 2018.
- [22] V. Silva, “Enter the ibm q experience: A one-of-a-kind platform for quantum computing in the cloud,” in *Practical Quantum Computing for Developers*, pp. 77–141, Springer, 2018.

## **Control and Automation Engineering / Kontrol ve Otomasyon Mühendisliği**

## An Application of Offset-Free Linear Quadratic Optimal Control

Hazin Inci\*, Ege University, Department of Electrical and Electronics Engineering, İzmir, Turkey  
Musa Alci, Ege University, Department of Electrical and Electronics Engineering, İzmir, Turkey  
Aydoğan Savran, Ege University, Department of Electrical and Electronics Engineering, İzmir, Turkey  
\* Corresponding author: hazininici@gmail.com

**Keywords:** Feedback control, linear quadratic optimal control, ball-beam system, rotary inverted pendulum  
**Discipline:** Control and Automation Engineering

### Abstract

In this work, the control of ball-beam and rotary inverted pendulum systems with linear quadratic optimal control method is considered. Firstly, the reference-tracking performance of the control system is investigated by assuming that the plant is represented by a linear model with an integrator. The expected steady state error performance was achieved by tracking the reference without any off-set in the simulation. However, it is observed that the expected steady state error performance could not be obtained in the application for the real plant. An integrator is added to cope with model uncertainties of the systems and to achieve zero off-set. Then, a linear quadratic optimal controller is designed and applied to the augmented system. The reference tracking performance is investigated.

In simulation, the controller performances are tested for the nonlinear model by taking into consideration noise and disturbance. The results of the simulation and real system application are compared. The designed linear quadratic optimal controller with integrator is applied to the real system and the good reference tracking performance is obtained without off-set.

It is aimed to take the attention of the students and control researchers about systems that have integrator in their linear model may not track the reference without off-set in the real application because of the model mismatch and to mention how to solve this issue.

### Introduction

Linear Quadratic Regulator (LQR) is one of the controllers that is used in many control applications extensively. Besides regulating the systems, it can be used for controlling systems to track a nonzero reference. Controller design is usually related to a cost function in optimal control theory. In LQR, the term linear refers to the model of the controlled plant being linear and the term quadratic refers to the cost function that includes the quadratic of an error and control signal. Since LQR is designed such that to minimize a cost function, it is called an optimal control method.

Applications of LQR control method are presented in many different types of systems and in many different structures in the literature. In [1], performances of PID and LQR controllers are compared in simulation and in real system for controlling orientation angles of a micro Vertical Take-Off and Landing (VTOL) system. This work showed that LQR control caused a steady state error if it is used without adding an integrative action. An LQR control with integrative action application performed for trajectory tracking of a quadrotor and good results in trajectory tracking are provided in [2]. In [3], besides adding integrative action to LQR control method, derivative of control signal  $u$  is also introduced in cost function for second LQR control method. Therefore, comparison of two methods is presented for two continuous stirred-tank reactor (CSTR)'s in series. LQR with integrative action named as LQI in [4] and used to control the twin rotor multi input-multi output (MIMO) system with a Luenberger observer to provide the full state feedback. Proposed controller is compared to two different methods which are Linear Quadratic Gaussian (LQG) and sliding mode controller with a nonlinear state observer. It is presented that the LQI controller provided superior performance to the other controllers. In [5], a robust fuzzy controller based on LQR method is presented and applied to a nonlinear 4 degree of freedom (DOF) quadrotor. The fuzzy controller is designed as a supervisory controller to regulate the LQR gains for each DOF due to the uncertainties and nonlinearities of the system.

In this paper, the laboratory setups which are ball-beam and rotary inverted pendulum systems produced by Quanser are used to show the performance of the controllers. A linearized model of these systems are used to design LQR control method with and without integral action. The applications of the control structure on nonlinear models of the systems in simulation and in real systems are investigated in a manner that the reference is being tracked without any offset or not. Mainly, the reference trajectory is applied to control the ball position for the ball-beam system and the rotary arm

angle for the rotary inverted pendulum system. The reference signal for other states are set to zero for both systems.

The main contributions of this paper are emphasizing the fact that mathematical models are approximately representing the actual plants even for the laboratory setups and therefore revisions of the controllers might be required before applying to the actual plants. It is also shown that in spite of having integrator in linear model of the system that does not mean reference trajectory would be tracked without steady state error. The application of model-based LQR control with integrative action is performed in simulation and real systems for two aforementioned systems.

This paper is organized as follows: brief information and linear models of the experimental setups are given in section 2; control methodology is presented in section 3; in section 4 experimental results are presented and analyzed; in last section this work is concluded.

### Experimental Setups

#### Ball-Beam System

The ball-beam system which is used in this work is manufactured by Quanser and shown in Figure 1. The informations about system's specification and modelling is utilized from manuals provided by Quanser [6]. So, the details of modelling from first principles will not be given in this paper for simplicity.

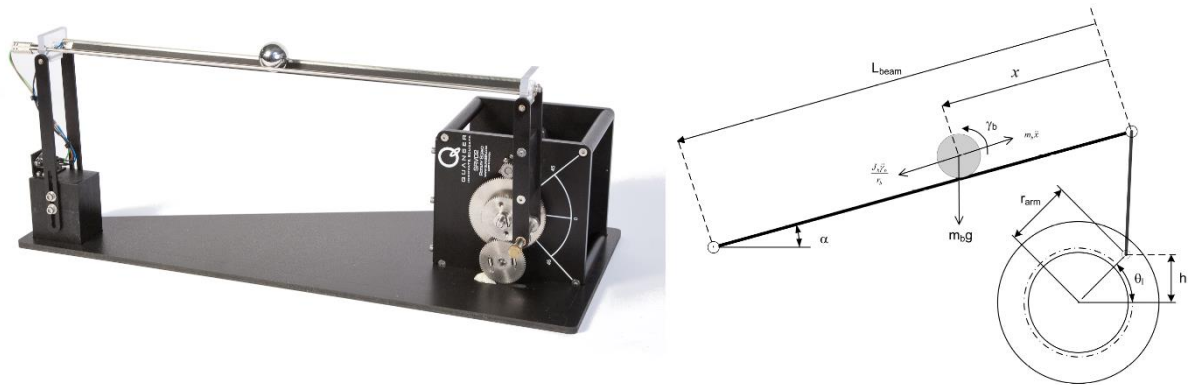


Figure 30. Ball-Beam system and its free-body diagram [6]

Ball-Beam system is formed of two plants as shown in Figure 2. They are the Rotary Servo and the Ball-Beam.

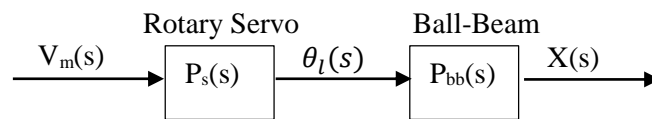


Figure 2. Ball-Beam open-loop block diagram

The linear transfer function model of Rotary Servo is given as,

$$P_s(s) = \frac{\theta_l(s)}{V_m(s)} = \frac{K}{s(\tau s + 1)}$$

The linear transfer function model of Ball-Beam is given as,

$$P_{bb}(s) = \frac{X(s)}{\theta_l(s)} = \frac{K_{bb}}{s^2}$$

Servo voltage to ball displacement transfer function can be written as,



$$P(s) = \frac{X(s)}{V_m(s)} = \frac{KK_{bb}}{s^3(\tau s + 1)}$$

As the control method of LQR will be applied to control the position of the ball, state-space model of the system is needed. The states of system selected as,

$$x = [\theta_l; \dot{\theta}_l; x; \dot{x}]$$

where  $\theta_l$  is the load angle of the servo,  $x$  is the linear displacement of the ball and the other two states are velocities of these states. State space matrices can be derived from transfer function models as,

$$A = \begin{bmatrix} 0 & 1 & 0 & 0 \\ 0 & -1/\tau & 0 & 0 \\ 0 & 0 & 0 & 1 \\ K_{bb} & 0 & 0 & 0 \end{bmatrix}, B = \begin{bmatrix} 0 \\ K/\tau \\ 0 \\ 0 \end{bmatrix}, C = [0 \ 0 \ 1 \ 0], D = 0$$

Controllability matrix for this system can be calculated as follows

$$M = [B \ : \ AB \ : \ A^2B \ : \ A^3B]$$

Since the rank of matrix M is full, the system is therefore completely state controllable around operating points. That means it is possible to move the eigenvalues of the control system to a region that will make the system stable.

Table 7. Parameters of Ball-Beam

Parameters	Value
$K_{bb}$	30
K	0.73
$\tau$	0.02

The DC motor that is mounted on our Ball-Beam system is replaced by another. So, the parameters' values given in Table 1 are updated values.

### Rotary Inverted Pendulum

This system which is used in this work as well is manufactured by Quanser and shown in Figure 3. The details about system can be found from manuals provided by the company [7]. Nevertheless, some information about the system will be given briefly like ball-beam system.

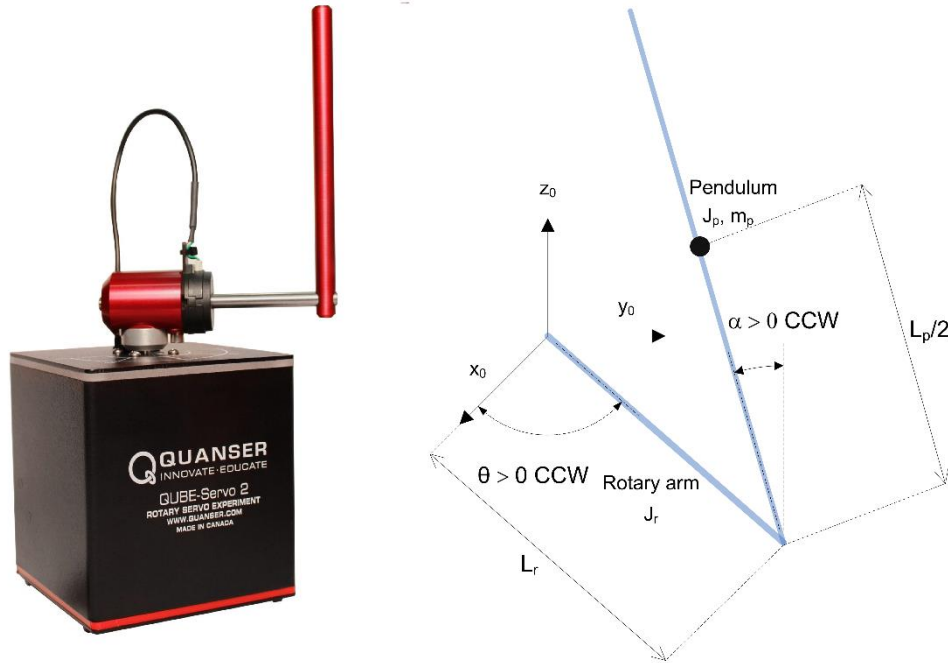


Figure 31. Rotary Inverted Pendulum and its diagram [7]

The rotary arm angle is denoted by  $\theta$  and the pendulum angle is denoted by  $\alpha$ . These variables are being measured with incremental encoders. There are some conventions for this system:

- $\alpha = 0$  means the pendulum is perfectly upright. It is expressed mathematically using
- 

$$\alpha = \alpha_{full} \bmod 2\pi - \pi$$

where  $\alpha_{full}$  is the pendulum angle measured by the encoder.

- $\theta$  and  $\alpha$  are defined as positive when rotated in the counter-clockwise (CCW) direction.
- When a positive voltage is applied to the motor, the rotary arm moves in the positive CCW direction.

The states of system selected as,

$$x = [\theta; \alpha; \dot{\theta}; \dot{\alpha}]$$

Linearized state-space model matrixes of rotary inverted pendulum system around operating points are,

$$A = \begin{bmatrix} 0 & 0 & 1 & 0 \\ 0 & 0 & 0 & 1 \\ 0 & 149.2751 & -0.0104 & 0 \\ 0 & 261.6091 & -0.0103 & 0 \end{bmatrix}, B = \begin{bmatrix} 0 \\ 0 \\ 49.7275 \\ 49.1493 \end{bmatrix}, C = [1 \ 0 \ 0 \ 0], D = 0$$

It can be seen from linear transfer function model of rotary inverted pendulum system has integrator. Motor voltage to rotary arm angle transfer function can be written as

$$G(s) = \frac{49.73s^2 - 5672}{s(s^3 + 0.01044s^2 - 261.6s - 1.191)}$$

Controllability matrix for this system as well checked and its rank is full. Therefore, the system is completely state controllable around operating points.

### Problem Formulation and Methodology

The Linear Quadratic Regulator (LQR) is an optimal control technique and it uses full state-feedback. It was mentioned that ball-beam and rotary inverted pendulum systems are completely state controllable and all states can be measured. Therefore, these systems can be controlled with LQR to track a reference.

A system to be controlled can be defined in state space representation as

$$\begin{aligned}\dot{x} &= Ax + Bu \\ y &= Cx + Du\end{aligned}$$

where  $x \in \mathbb{R}^{n \times 1}$  is the vector of state variables,  $u \in \mathbb{R}^{r \times 1}$  is the control input vector,  $y \in \mathbb{R}^{m \times 1}$  is the output vector,  $A \in \mathbb{R}^{n \times n}$  is the system matrix,  $B \in \mathbb{R}^{n \times r}$  is the input matrix,  $C \in \mathbb{R}^{m \times n}$  is the output matrix, and  $D \in \mathbb{R}^{m \times r}$  is the feedforward matrix.

LQR control technique calculates a control input  $u$  to minimize a cost function chosen as

$$J = \int_0^{\infty} (x^T Q x + u^T R u) dt$$

$Q$  and  $R$  are the penalties on the state variables and the control actions, respectively. Performance of the controller depends on the selection of  $Q$  and  $R$  matrices and some techniques for their selection are discussed in [8]. Let  $u$  be control law as

$$u = -Kx$$

where  $K \in \mathbb{R}^{m \times n}$  is the feedback gain. The computation of the optimal gains is performed through

$$K = R^{-1} B^T P$$

where the positive-definite matrix  $P$  can be found from the steady-state Riccati equation:

$$A^T P + PA - PBR^{-1}B^T P + Q = 0$$

If a nonzero reference is desired to be tracked, then control law would be as

$$u = -Kx + k_1 r$$

$k_1$  is used because the output signal assumed to be equal to first state.  $r$  is the reference signal. Calculation of  $K$  is not changed. But the control diagram is changed. For reference tracking with LQR controller, control block diagram will be as in Figure 4.

To deal with steady state error, an integrator can be added to the control structure as shown in Figure 5. This addition ensures eliminating steady state error due to constant disturbances and model mismatches.

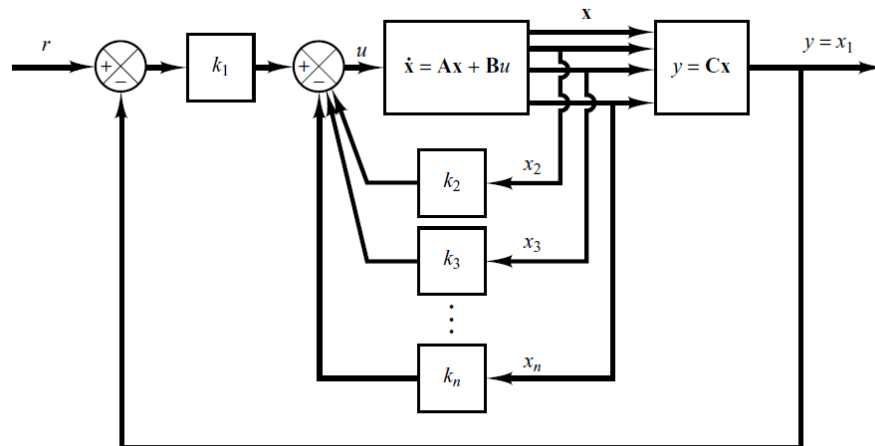


Figure 4. Control System with LQR [9]

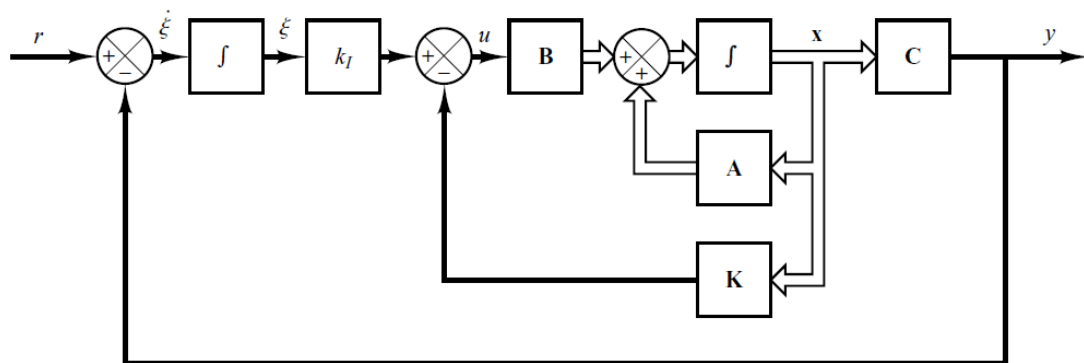


Figure 5. Control System with LQR where plant is augmented with an integrator [9]

The system state-space model should be updated by this addition and will be called as augmented system. Difference between reference signal and output of the system can be denoted as  $\xi$  which enters integrator. Augmented system will be as

$$\begin{aligned}\dot{\bar{x}} &= \bar{A}\bar{x} + \bar{B}\bar{u} \\ \bar{y} &= \bar{C}\bar{x} + \bar{D}\bar{u}\end{aligned}$$

where

$$\bar{x} = \begin{bmatrix} x \\ \xi \end{bmatrix}, \bar{A} = \begin{bmatrix} A & 0 \\ -C & 0 \end{bmatrix}, \bar{B} = \begin{bmatrix} B \\ 0 \end{bmatrix}, \bar{C} = [C \quad 0], \bar{D} = D$$

Calculation of optimal gains with augmented system is in same way as presented formerly and will be get as

$$\bar{K} = [K \quad -k_I]$$

where  $k_I$  is the gain for the integrative action.

### Experimental Studies

In simulation works only, noise and disturbance applied to both systems. Disturbance is applied at 15 seconds. For ball-beam system, position of the ball is controlled and for rotary inverted pendulum system, angle of rotary arm is controlled by the controller. The other states for each system are set to

zero. For rotary inverted pendulum, setting reference to zero for angle of pendulum means that pendulum is desired to be inverted.

Q and R matrices are defined as identity matrix for all simulation and real system works presented below. For better or any different desired results, penalizing matrixes Q and R could be changed. For example; the weight of relevant state which is desired to track a reference could be increased for faster tracking. On the other hand, the weight of matrix R could be increased for lesser control effort.

To emphasize the elimination of steady state error, only figures of error signals and tracking performances are presented.

In real system application of rotary inverted pendulum control, y-axis of figure that shows pendulum angle  $\alpha$  is limited. Because, at the beginning of the application pendulum is downward which means that  $\alpha$  will begin with a value that is 180 degree away from where it should be. Manually pendulum is inverted to near operating region and released when the controller takes action.

## Results for Ball-Beam System

### a. Simulation and Real System Results of LQR Control without Integrative Action

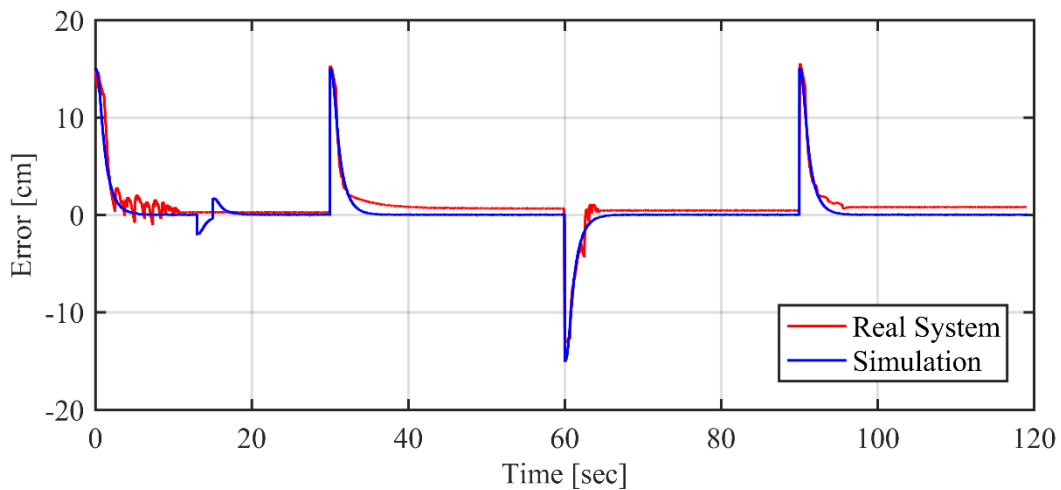


Figure 6. Error signal

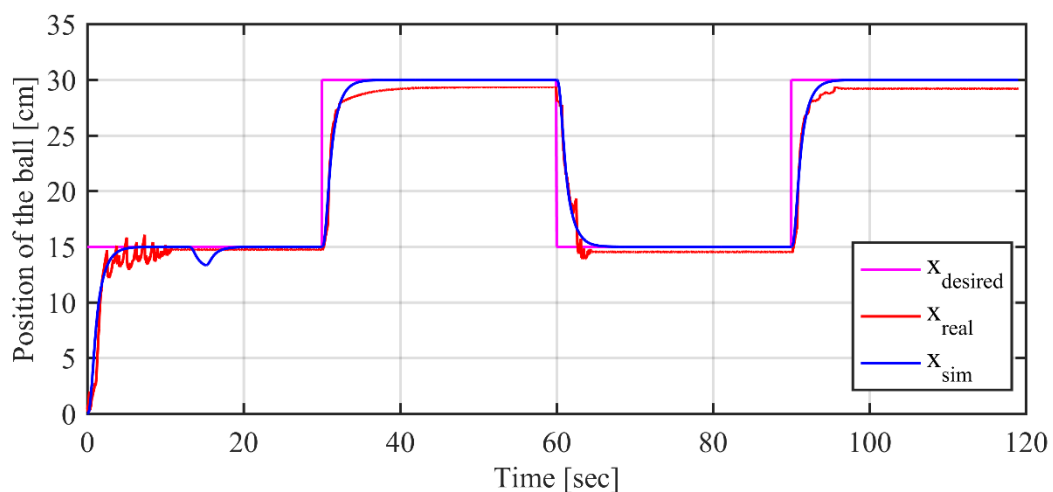


Figure 7. Reference tracking result for ball position

In simulation work, it can be seen from Figures 6 and 7 that there is no steady state error due to having integrator in plant's linear model and disturbance rejection at 15 seconds is achieved. But in real system application, there is an offset between reference signal and output signal.

**b. Simulation and Real System Results of LQR Control with Integrative Action**

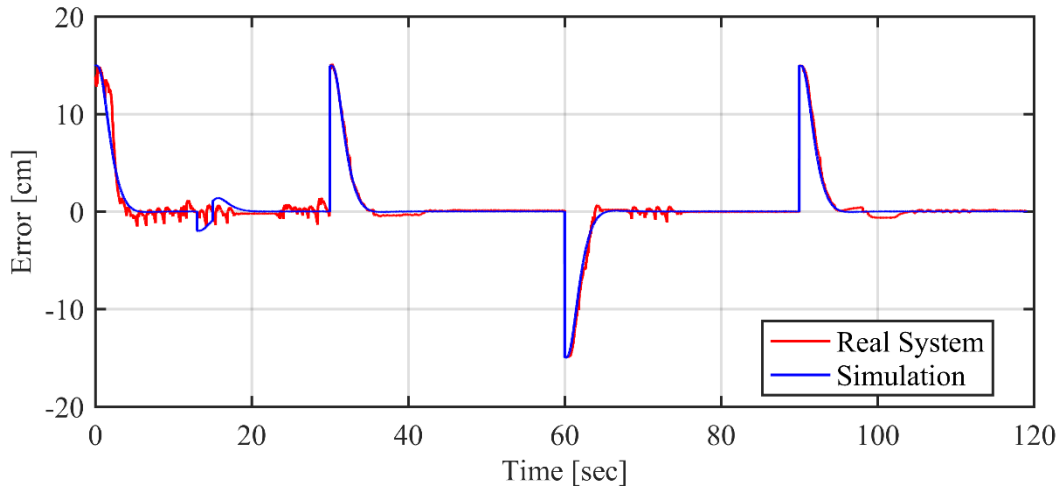


Figure 8. Error signal

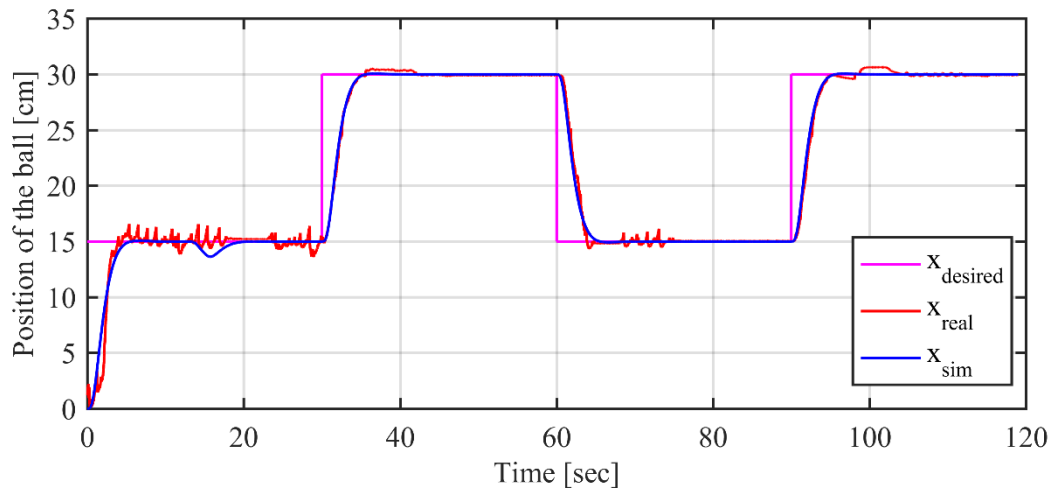


Figure 9. Reference tracking result for ball position

After augmenting system with an integrator, it can be seen from Figures 8 and 9 that steady state error is eliminated in real system application and there is no offset between reference and output signals.

**Results for Rotary Inverted Pendulum System**

**c. Simulation and Real System Results of LQR Control without Integrative Action**

In simulation work, it can be seen from Figures 10, 11 and 12 that there is no steady state error due to having integrator in plant's linear model and disturbance rejection at 15 seconds is achieved as well. But in real system application, tracking performance is poor while pendulum is inverted successfully.

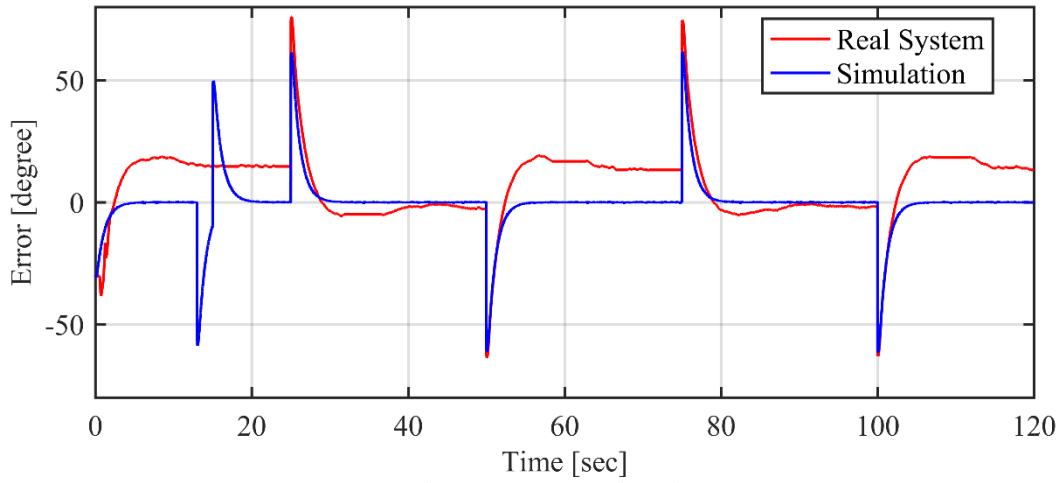


Figure 10. Error signal

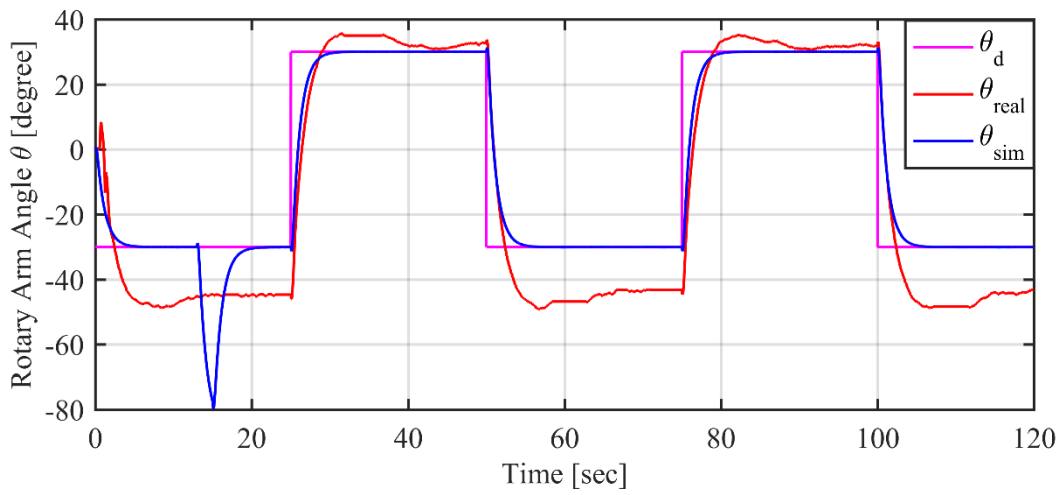


Figure 11. Reference tracking result for rotary arm angle

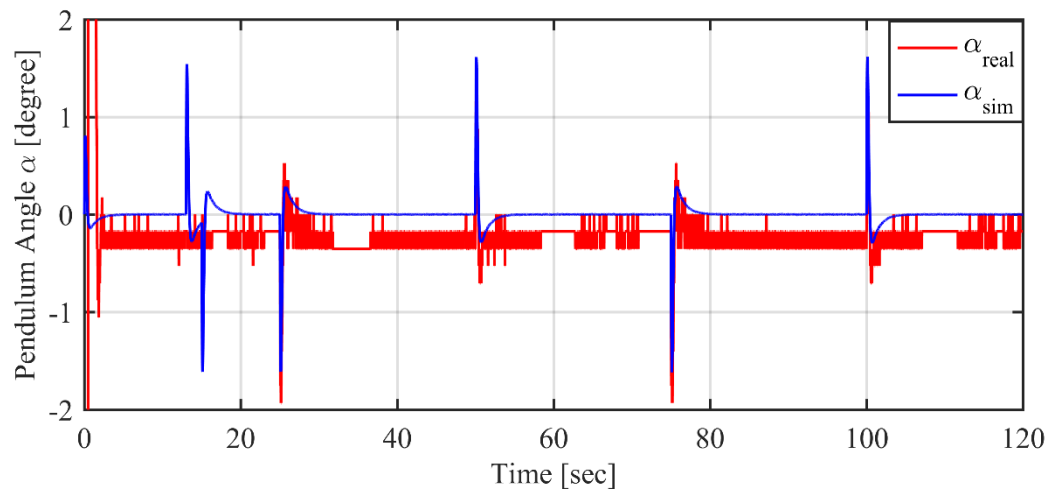


Figure 12. Pendulum angle

**d. Simulation and Real System Results of LQR Control with Integrative Action**

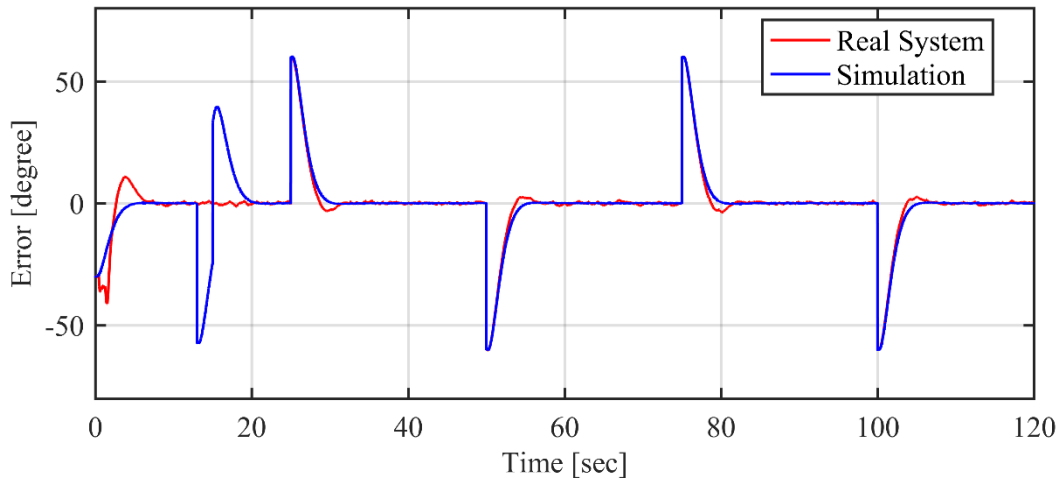


Figure 13. Error signal

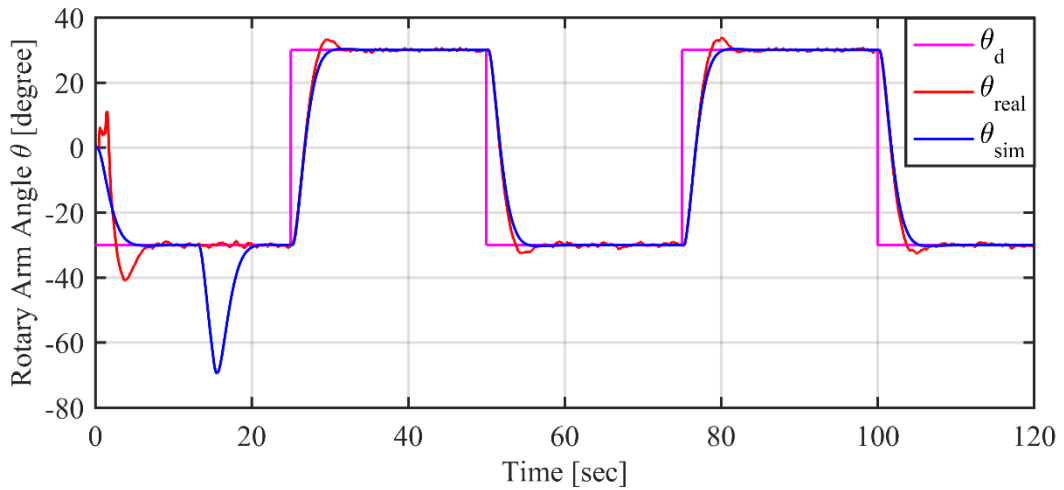


Figure 14. Reference tracking result for rotary arm angle

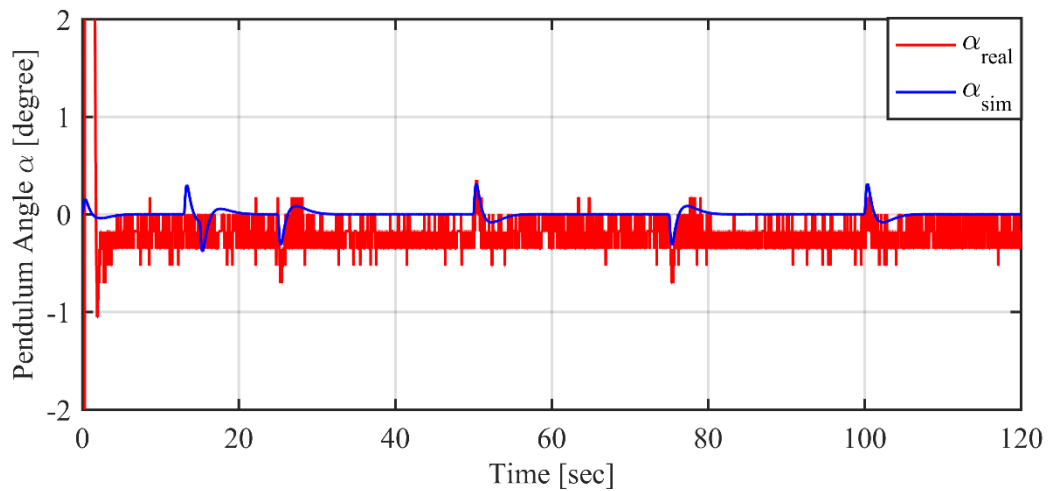


Figure 15. Pendulum angle



It can be seen from Figures 13, 14 and 15 that steady state error is eliminated in real system application after augmenting system with an integrator. Reference tracking performance is as good as simulation work and pendulum is also stayed inverted successfully.

### Conclusion

Since the controlled systems have integrators in their transfer function models, we obtained zero steady state error for the step response in the case of simulation. However, in real system application, there is offset between output and reference signals. To deal with this issue, control structure is changed and an integrator is added. As it is shown from real system results, steady state error is eliminated with this augmented structure.

From the given results, it is concluded that mathematical models are approximately representing the real systems and therefore revisions of the controllers might be required to have desired performance before applying to the real systems. On the other hand, it is also shown that having integrator in linear model of the system does not mean desired trajectory would be tracked without any steady state error in reality.

### References

- [1] Bouabdallah S, Noth A, Siegwart R. PID vs LQ control techniques applied to an indoor micro quadrotor. In: 2004 IEEE/RSJ International Conference on Intelligent Robots and Systems (IROS) (IEEE Cat No04CH37566). IEEE; 2005.
- [2] Martins L, Cardeira C, Oliveira P. Linear quadratic regulator for trajectory tracking of a quadrotor. IFAC-PapersOnLine. 2019; 52(12):176–81.
- [3] Malkapure HG, Chidambaram M. Comparison of two methods of incorporating an integral action in linear quadratic regulator. IFAC proc vol. 2014;47(1):55–61.
- [4] Phillips A, Sahin F. Optimal control of a twin rotor MIMO system using LQR with integral action. In: 2014 World Automation Congress (WAC). IEEE; 2014.
- [5] Mahmoodabadi MJ, Rezaee Babak N. Robust fuzzy linear quadratic regulator control optimized by multi-objective high exploration particle swarm optimization for a 4 degree-of-freedom quadrotor. *Aerosp Sci Technol*. 2020;97(105598):105598.
- [6] Quanser, Ball and Beam User Manuals, 2011.
- [7] Quanser, QUBE-Servo User Manuals, 2014.
- [8] Anderson BDO, Moore JB. Optimal control: Linear quadratic methods. Old Tappan, NJ: Prentice Hall; 1989.
- [9] Ogata K. Modern Control Engineering: International Edition. 5th ed. Upper Saddle River, NJ: Pearson; 2010.

## **Electrical and Electronics Engineering / Elektrik ve Elektronik Mühendisliği**

## Photovoltaic Potential Assessment in the Democratic Republic of Congo

Joseph Tshitumbu Kazadi\*, Ege University., Dept. of Electrical Engineering, İzmir, Türkiye

\*Corresponding author: kazadijoseph02@gmail.com

**Keywords:** Democratic Republic of Congo (DRC), electrification rates, National Energy Commission, photovoltaics

**Discipline:** Electrical Engineering

### Abstract

The Democratic Republic of the Congo has enormous potential in renewable energy. Of which the most widely used and most widely used are hydroelectricity and biomass. However, the electrification threshold for the whole city remains low, less than 20%. Thus, the use of renewable energies, particularly solar energy, is one of the conditions necessary to raise the electrification rate of the country. The measurements of the sun obtained by the National Energy Commission are average values over the year between 3.34 and 6.73 kWh / m<sup>2</sup>, from this information, we see that the integration of solar electricity production will contribute to significantly increase the electrification rate in the DRC.

The objective of this document is to give an overview of the power supply situation in the DRC. With the firm conviction that the integration of photovoltaic systems will actively contribute to the positive development of the country.

### Introduction

World energy demand is still mostly satisfied by traditional fossil energy sources. In fact, in 2007, more than three quarters of the primary energy used globally was of fossil origin [10].

The various fossil fuels are not renewable energies and produce a lot of carbon dioxide and other harmful gases such as methane. Renewable energies seem to be a relevant response to the current energy challenge. These resources are essentially inexhaustible on the scale of human times, their recovery and their conversion into electrical energy represents a lower impact on the environment than fossil and fissile sources. In addition, the multiplicity of means of recovery coupled with the excellent geographical distribution of the resource makes it possible to consider these production methods over the entire globe and in the Democratic Republic of Congo in our case. Thus, systems for producing electrical energy from renewable energy have experienced extremely high growth rates in recent years. Among these renewable resources, solar energy offers the greatest potential.

Indeed, solar energy received each year at the surface of the globe is equivalent to several thousand times the annual world consumption of primary energy [10].

### Geographical description



Figure 1. The geographic map of the DRC

The Democratic Republic of Congo, DRC also called Congo-Kinshasa to differentiate it from Congo-Brazzaville (or Republic of Congo), is a country with an area of 2,345,410 km<sup>2</sup>, or about 33 times larger than the Benelux (Belgium, the Netherlands and Luxembourg), 4 times more than France or 2 times more than Quebec (Canada). In Africa where it is located, only Algeria is more extensive. It is limited to the west by Congo Brazzaville, to the north by the Central African Republic and Sudan, to the east by Uganda, Rwanda, Burundi, and Tanzania and to the south by Zambia and Angola. Sharing nine borders with its neighbors, Congo-Kinshasa is a completely landlocked country, except for a few kilometers of coastline bordering the Atlantic Ocean. Due to its large area, its enormous wealth and its large population, the DRC remains one of the giants of Africa, along with Egypt, Nigeria, and South Africa. It is made up of the city of Kinshasa (its capital) and 25 following provinces: Bas Uele, Equateur, Haut Lomami, Haut Katanga, Haut Uele, Ituri, Kasai, Kasai Oriental, Kongo central, Kwango, Kwilu, Lomami, Lualaba, Lulua, Maindombe, Maniema, Mongala, Nord-Kivu, Nord Ubangi, Sankuru, Sud-Kivu, Sud Ubangi, Tanganyika, Tshopo and Tshuapa [7].

Populated by nearly 90 million inhabitants, Congo-Kinshasa is considered to be the “first French-speaking country in the world”, after France. Its official language is French, its currency is the Congolese franc, its hymn is the Congolese, its national languages are Lingala, Tshiluba, Swahili and Kikongo, with 250 tribes and more than 400 dialects.

### National Energy resources and potentials

The Democratic Republic of the Congo is a country-continent which alone contains 52% of Africa's total freshwater reserves and lush vegetation typical of three major natural regions namely:

- The dense humid forest in the central basin and to the west,
- Dry forests and savannas in the southern part and on the northern fringe,
- Mountain ecosystems along the eastern border.

With its 155 million hectares of forests, the DRC is one of the largest forest countries in the world. The importance of its tropical forest (covering 60% of the forest mass of the Congo Basin, the second largest tropical massif in the world by area), its freshwater resources and its rich biodiversity, make it bear a real responsibility in the building a better future, not only for the Congolese population, but also for all of humanity [7].

In terms of the global environment, the volume and strategic nature of its natural resources give it a special role at the international level for the reduction of greenhouse gases and the preservation of biodiversity. The country is also full of abundant and varied energy potential and resources, the conservation and sustainable management of which are major issues for the Congolese and for the rest of the world, we can cite: biomass, hydraulic power, solid, liquid and hydrocarbons. gaseous (including methane gas from Lake Kivu), mineral coal, oil shales, solar wind potential, uranium ore, etc.

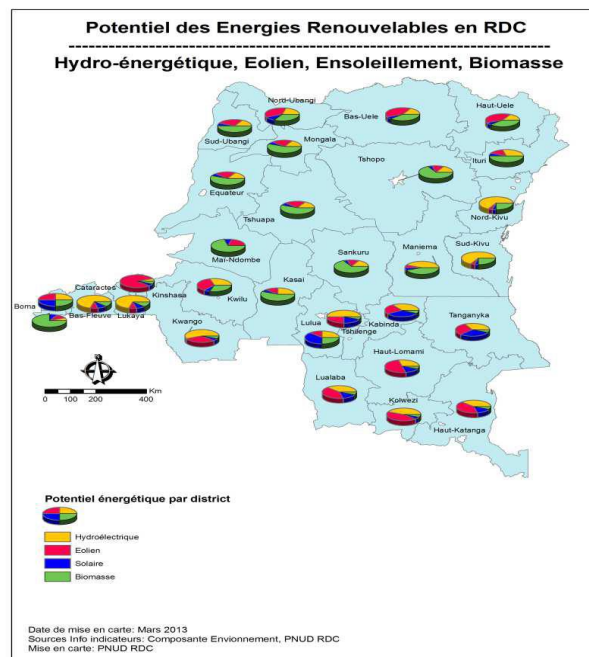


Figure 2. Potential of Renewable Energies in the DRC

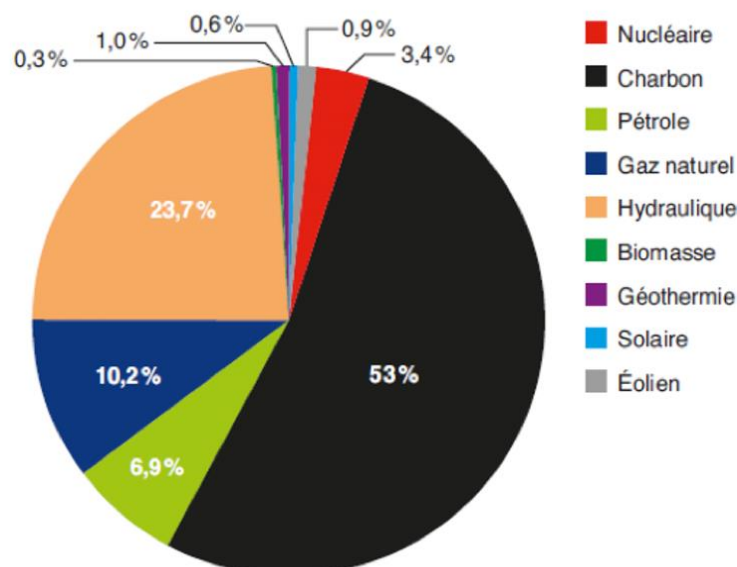


Figure 3. Percentage Distribution of the energy potential of the DRC

### Methodology

There are several approaches to estimating the photovoltaic energy potential in a country. In this work it will be question of the evaluation of the latter based on the approach known as: Resource potential. This approach only indicates the amount of radiation on the surface of the country. This methodology aims to assess the potential of extractable photovoltaic energy for the future (horizon 2030) energy in the Democratic Republic of Congo. The approach considers solar radiation, hours of sunshine and suitable lands available for photovoltaic implementation as the basic input for our study.

### Influence of temperature and illumination

The characteristic of a photovoltaic cell (or a photovoltaic generator) is directly dependent on illumination and temperature [9].

We notice that, at a given temperature, here 25 ° C:

- The short-circuit current  $I_{cc}$  varies proportionally to the illumination  $E$ ,
- No-load voltage  $V_{co}$  varies little with illumination. It can be considered as a constant for a given installation.

The influences of these parameters therefore result in variations of the useful characteristic of the photovoltaic generator with the lighting conditions.

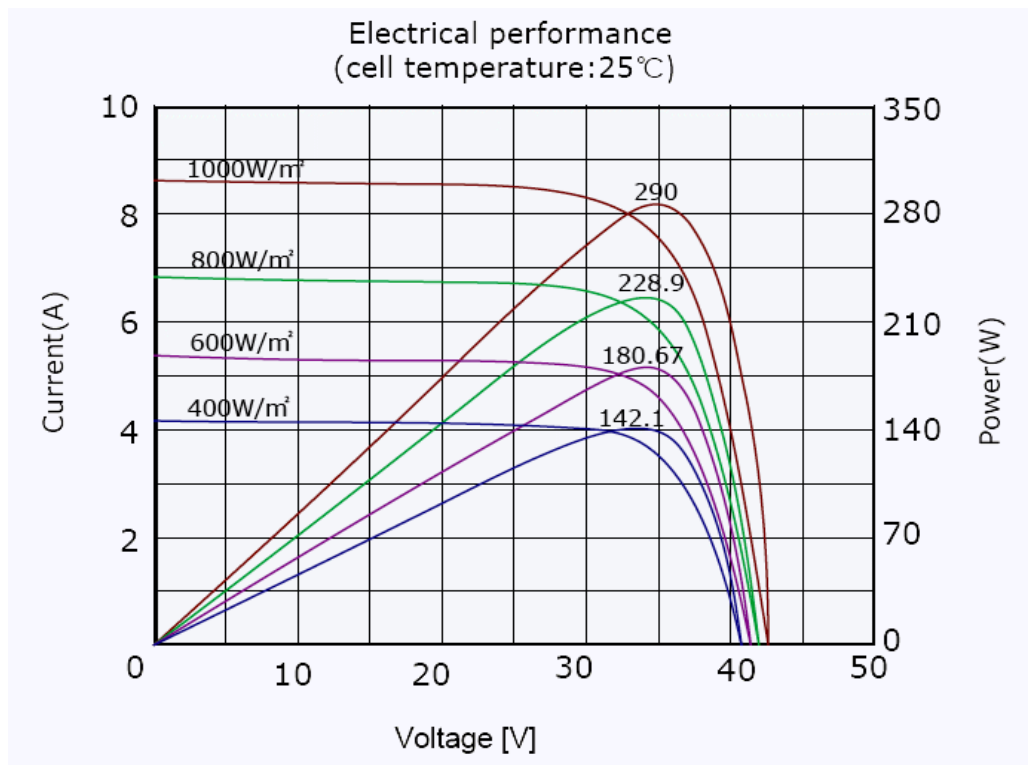


Figure 4. General appearance of the electrical characteristics of a photovoltaic generator for different illuminances

Temperature also has an influence on the characteristic of a photovoltaic generator.

We notice that at given illumination:

- The open circuit voltage  $V_{co}$  decreases with temperature. The higher the temperature, the lower the  $V_{co}$ ,
- The short-circuit current  $I_{sc}$  increases with temperature. This rise is much less important than the drop in voltage. The influence of temperature on  $I_{sc}$  can be neglected in most cases.

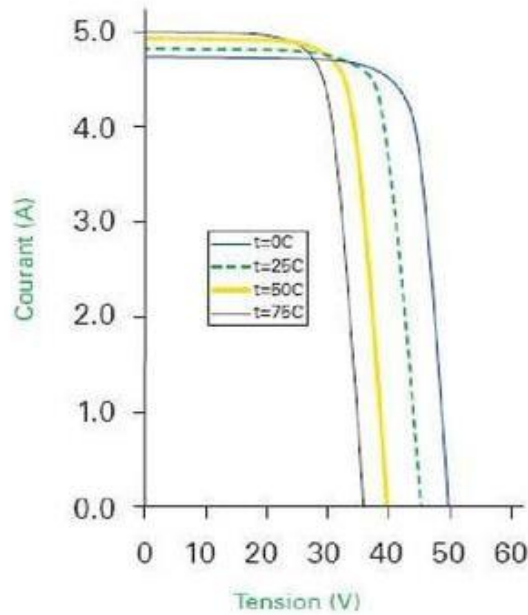


Figure 5. The variation in the characteristics of a 160W photovoltaic generator as a function of the temperature at a given illumination. The illumination here is set at  $1000\text{W} / \text{m}^2$

Temperature and lighting are therefore the two main parameters that will modify the characteristics of a photovoltaic generator. These two parameters should therefore be carefully considered when setting up a photovoltaic installation.

### Types of resource potentials

- Theoretical potential model

The theoretical potential of solar energy involves the evaluation of the latter received on the surface of the study area. This potential consists of identifying the limit and size of the study area including the annual average magnitude of solar radiation. Thus, this potential will be calculated using equation (1) below:

$$E_{TH} = A_S * H_r * T_{tot} \quad (1)$$

With:  $E_{TH}$  which is the theoretical solar energy potential (MWh / year),  $A_S$  which is the area of the active surface ( $\text{km}^2$ ),  $H_r$  which is the solar irradiance ( $\text{MW} / \text{km}^2$ ) and  $T_{tot}$  which is the number total annual sunshine hours (hours / year) [5].

- Geographic potential model

The geographic potential of solar energy consists of the evaluation of the latter received over an appropriate area. Thus, the process of assessing this potential first involves the exclusion of restricted land areas for the deployment of solar energy technologies. These are agricultural areas, roads, water bodies, protected national parks, game reserves and forest reserves. Second are the transmission and distribution line areas and the area unsuitable for the deployment of solar energy technologies and developments such as land with bad slopes (more than 3% slopes). Therefore, the remaining land will be considered the most suitable area for the deployment of solar energy technologies (which is estimated at 54% for the DRC). Thus, this potential will be estimated by equation (2) below:

$$E_G = A_S * H_r \quad (2)$$

With:  $E_G$  which is the geographic solar energy potential (kWh / year),  $A_S$  which is the appropriate available surface ( $\text{m}^2$ ) and  $H_r$  which is the average annual solar radiation ( $\text{kWh} / \text{m}^2\text{-year}$ ).

- Technical potential model

Industrial scale photovoltaic is defined as a large-scale photovoltaic power plant that can be deployed in an open space on the borders of the country [14]. The process of assessing the extractable energy potential of the sun for any country first involves excluding areas that are not suitable for large-scale PV systems within defined limits [14, 15].

Thus, taking into account the technical characteristics of photovoltaic systems to convert solar energy into electric energy, the technical potential of solar energy will be estimated using equation (3) below:

$$E_{TH} = A_S * p_{PD} * C_f * T_{tot} \quad (3)$$

With:  $E_{TH}$  which is the theoretical solar energy potential (MWh / year),  $A_S$  which is the area of the active surface (km<sup>2</sup>),  $p_{PD}$  which is the power density of the study area (MW / km<sup>2</sup>),  $C_f$  which is the capacity factor of the study area (%) and  $T_{tot}$  which is the total number of annual hours of sunshine 8760 (hours / year).

## Results and discussion

### Photovoltaic potential

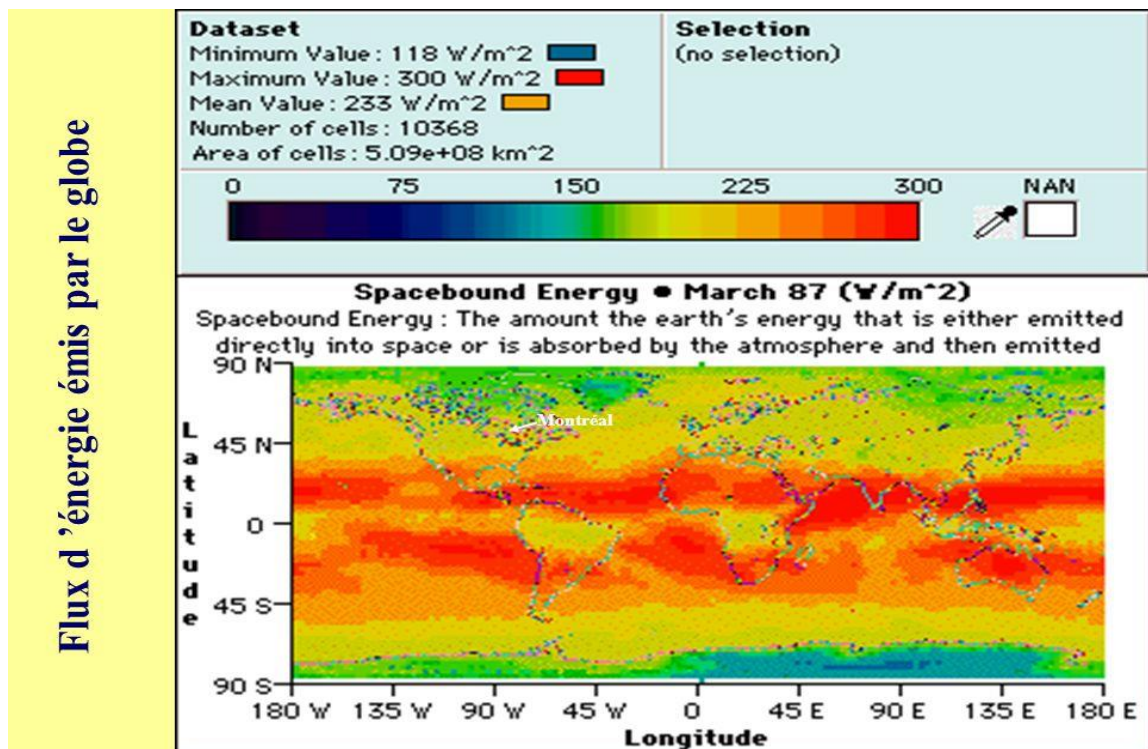


Figure 6. Solar belt of the terrestrial globe

We are based on solar measurements carried out by the National Energy Commission. Indeed, the country sits on the Equator, just below the solar belt, but it was no less important to confirm these facts with scientific and quantifiable measurements.

The sunshine measurements obtained by the National Energy Commission are average values over the year between 3.34 and 6.73 KWh / m<sup>2</sup>. We can conclude that solar energy offers huge untapped potential because the minimum value for electrification by photovoltaic system is 1 KWh / m<sup>2</sup> [8].



Table 2. Daily global radiation and sunshine (annual average) in the Democratic Republic of Congo.

N°	STATION	RADIATION (Kcal / m <sup>2</sup> )	SUNSHINE (KWh /m <sup>2</sup> )
1	Kongolo	5.80	6.73
2	Manono	4.70	5.45
3	Kolwezi	4.70	5.45
4	Bukavu	4.60	5.34
5	Bunia	4.20	4.87
6	Kalemie	4.10	4.76
7	Bandundu	4.00	4.64
8	Inongo	4.00	4.64
9	Kisangani	4.00	4.64
10	Goma	4.00	4.64
11	Mbandaka	3.90	4.52
12	Tshikapa	3.80	4.41
13	Mbuji - mayi	3.80	4.41
14	Lubumbashi	3.80	4.41
15	Kindu	3.80	4.41
16	Kananga	3.70	4.29
17	Lodja	3.70	4.29
18	Kikwit	3.80	4.25
19	Kinshasa	3.30	3.34
20	Moanda	3.30	3.83
21	Boma	3.25	5.45
22	Matadi	2.80	5.45

#### Assessment of photovoltaic potential in the DRC

We used the Geometric Potential Model to determine the photovoltaic potential of the DRC. The lands considered to be the most suitable area for the deployment of solar energy technologies are spread over 15 provinces with a total area of 1,275,690 km<sup>2</sup> ( $A_s = 1,275,690,000,000$  km<sup>2</sup>) and  $H_r = 104.22$  kWh/m<sup>2</sup>-year

Therefore, the geographic solar energy potential  $E_G$  is 132,952,411.8 GWh / year.

#### Kinshasa Solar City

The President of the Republic, Félix-Antoine Tshisekedi Tshilombo, this Wednesday, August 19, laid the foundation stone for the construction of the 600 MW photovoltaic solar power plant, called "Kinshasa Solar City", located in Menkao in the town from Maluku. This solar energy production project provides for a total of 1,000 MW, spread over several sites across the city of Kinshasa.

Knowing that the total number of hours of sunshine per year is 8,760 hours, the "Kinshasa Solar City" photovoltaic solar power plant will produce a total solar energy of 8,760 GWh / year, or 0.007% of the country's geographic solar energy potential.



Figure 7. Felix Tshisekedi lays the foundation stone for the construction of Kinshasa Solar City

### Conclusion

The Democratic Republic of Congo is an underdeveloped country, its economic and social development necessarily implies an increase in its energy consumption. This is how our work was based on the evaluation of the photovoltaic potential of the latter.

To do this, greater recourse to renewable energies is one of the necessary conditions for achieving sustainable development for our country because they offer advantages for solving energy, environmental and economic and social development problems.

Finally, the Democratic Republic of Congo has enormous potential in renewable energies, this is no longer any doubts and they are very present and tangible all over the country. However, the country is sorely lacking in scientific data that can help better analyze and quantify these potentials. The National Energy Commission is still doing measurement work and collecting remarkable data on hydro and solar energy, which is what allowed us to develop this document.

### References

- [1] Politique énergétique intégrée en République Démocratique du Congo. Leçon publique donnée le 6 octobre 2001 à l'occasion de l'inauguration solennelle de l'Académie, par Michel Maldague, Président-fondateur de l'Académie Nationale des sciences du développement Professeur émérite de l'Université Laval à la Faculté de Foresterie.
- [2] <http://www.uqac.ca/jmt-sociologue/>
- [3] [http://www.uqac.ca/Classiques\\_des\\_sciences\\_sociales/](http://www.uqac.ca/Classiques_des_sciences_sociales/)
- [4] <http://bibliotheque.uqac.ca/>
- [5] Assessment of Solar Energy Source Distribution and Potential in Zambia: ISEM2016, 3rd International Symposium on Environment and Morality, 4-6 November 2016, Alanya\_Turkey
- [6] Bulletin africain, n<sup>o</sup>11, Juillet 1999, p.13
- [7] Rapport national « énergie durable pour tous a l'horizon 2030 », aout 2013
- [8] Les Energies Renouvelables en République Démocratique du Congo Novembre 2011
- [9] Thèse de doctorat: Systèmes photovoltaïques raccordés au réseau : Choix et dimensionnement des étages de conversion, Septembre 2010.
- [10] Thèse de doctorat : Optimisation des profils de consommation pour minimiser les coûts économique et énergétique sur cycle de vie des systèmes photovoltaïques autonomes et hybrides - Evaluation de la technologie Li-ion, Juillet 2010.
- [11] [https://www.memoireonline.com/02/07/362/m\\_exercice-droits-libertes-individuelles-collectif-gouvernance-afrique-noire-rdc4.html](https://www.memoireonline.com/02/07/362/m_exercice-droits-libertes-individuelles-collectif-gouvernance-afrique-noire-rdc4.html)
- [12] Recensement du potentiel d'énergie solaire Thermique et photovoltaïque dans le Département des Ardennes, Mars 2010.
- [13] Système d'énergie solaire photovoltaïque pour les installations et les services communautaires, Avril 2012.
- [14] Anthony Lopez, Billy Roberts, Donna heimiller, Nate Blair, Gian Porro, 2012, "U. S Renewable Energy Technical Potentials: A GIS-Based Analysis" Technical Report NREL/TP-6A20-5146, July 2012.
- [15] Yan-wei Sun, Angela Hof, Run Wang, Jian Liu, Yan-jie Lin, De-wei Yang, 2013 "GIS-based approach for potential analysis of solar PV generation at the regional scale: A case study of Fujian Province" Energy Policy 58 (2013) 248-259, ScienceDirect.
- [16] Richesses Renouvelables : comment le solaire et l'éolien peuvent électrifier la RDC et l'Afrique du Sud, Septembre 2017.
- [17] Etat des lieux des énergies solaires et éoliennes en République Démocratique du Congo par Monsieur François DIKETE LUMU, Chef de Département Adjoint Chargé du CEDENR à la Commission National de l'Énergie, mars 2011.

## Environmental Engineering / Çevre Mühendisliği

## Remediation of Nickel Ions from Contaminated Solutions Using Mandarin Peels as Non-Valuable Biosorbent Media

Mohammed Nsaif Abbas<sup>1</sup>, Suha Anwer Ibrahim<sup>\*1</sup>, Hala Husham Nussrat<sup>1</sup>, Mustafa Mohammed Hathal<sup>2</sup>

<sup>1</sup>Environmental Engineering Department, College of Engineering, Mustansiriyah University, Iraq

<sup>2</sup>Department of Chemical Engineering and Petroleum Industries, Al-Mustaqbal University College, Iraq

\*Corresponding Author: suhaanwer@uomustansiriya.edu.iq

**Keywords:** Adsorption, aqueous solutions, nickel, mandarin peels and ZRL

**Discipline:** Chemical Engineering, Ecology, Waste Management

### Abstract

The removing process of nickel (as one of heavy metals types) from aqueous solutions using a simple and effective method which is adsorption technique was investigated in this paper. The adsorption media used were mandarin peels (*Citrus reticulata*) as a non-valuable biosorbent material. The adsorption process was conducted in a unit of batch mode at various operating conditions of the acidic function (pH) of the contaminated solutions, initial concentrations of Ni<sup>2+</sup> ions, agitation speed, contact time, amount of mandarin peel and temperature. The obtained results showed that the mandarin peels were of adequate efficacy to remove nickel ions from synthetic aqueous solutions and the maximum efficiency was 86.031%. The efficiency of removal was inversely proportional with the initial concentration and directly with the other operating variables. By this way, a sustainable method was reached to treat the polluted aqueous solutions and get rid of more than one type of waste at the same time, using cheap, non-valuable and available materials, a simple unit, a low treatment cost, an economical, beneficial, and environmentally friendly manure accessing to the zero-residual level (ZRL) concept.

### Introduction

Heavy metals are considered as one of the most harmful types of pollutants, due to the diversity of their use and their toxicity [1]. The wastewater of its various kinds, medical, industrial, agricultural, domestic, etc. contains many heavy metals such as lead (Pb), nickel (Ni), cadmium (Cd), mercury (Hg), copper (Cu), zinc (Zn), cobalt (Co), iron (Fe), etc [2]. The presence of these elements in aquatic environments poses much jeopardy; among them it is not biologically degradable and can accumulate in the tissues of living organisms and even soil [3]. This would lead to contaminate the surface and underground water and poses a real threat to public health, livestock and fisheries [4]. One of the most important of these elements is nickel which is used as a raw material or auxiliary material in many industries and applications such as batteries, stainless steel, electroplating, alloys, gas turbines, jet engine parts, electric wires, coins, and highly specialized military equipment, in addition to its use in most of the catalysts used in petroleum refineries, vegetable oils, and some kinds of soaps [5]. As a result of its wide and diversified use, wastewater which is discharged as liquid waste from these industries must contain a nickel metal of no more than 0.2 ppm in the industrial water discharged to the river and in drinking water less than 0.02 ppm according to the Iraqi specification [6]. The risks associated with the presence of nickel in contaminated water include the possibility of allergic diseases such as skin irritation, congenital malformations, poor liver function, while the high levels of this metal leading to bone, lungs and nose cancers in addition to damage of the nervous system and other injuries [7]. Therefore, removing the highest possible concentration of this metal from the water contaminated with it is considered as a crucial issue to reduce its toxic effects on humans and aquatic ecosystems in particular [8]. There are many conventional methods that deal with removing nickel from waste water, including adsorption [9], biological treatment [10], cationic exchange resins [11], chemical reduction [12], chemical precipitation [13], electrochemical treatments [14], evaporative recovery [15], coagulation-flocculation [16], electrocoagulation [17], filtration, flotation, membrane technologies, ion exchange, reverse osmosis, sedimentation, solvent extraction, ultrafiltration [18] etc. Adsorption technology is considered a one of the most important methods that attracted the attention of researchers over the near last decades. It is a simple technology that does not require high costs or complicated equipment or pre-treatments [19]. At the same time, it has proven its efficiency in treating heavy metals, especially with the use of activated carbon, which is considered one of the most famous and most efficient adsorption materials due to its high surface area. However, the high cost of activated carbon

synthesis and losing of 10-15% from its weight after each regeneration process prompted researchers in the field of water treatment to search for alternative medias that are used either as adsorbents directly instead of activated carbon or as a raw material in its preparation [20]. Among the most important and well-known alternatives that have aroused interest are agricultural waste because of its availability in large quantities, non-valuable or cheap price materials, negligible toxicity, and appropriate efficiency compared to activated carbon [21]. The removal process of heavy metals from wastewater was studied using rice husks [22], potato peels [23], pomegranate peels [24], banana peels [25], lemon peels [26], orange peels [27], and others, and it proved their ability to treat polluted different aqueous solutions with high efficiency. But another problem arose from the accumulation of toxic residues after the end of adsorption processes, which required solutions to get rid of it, i.e. additional costs added to the previously treatment costs [19]. Several solutions were proposed to this problem through a new concept, which considered these wastes as materials that could be used up reaching to the zero residues level (ZRL) [21]. The present paper aims to study the use of mandarin peels as biosorbent which is one of available and non-valuable agricultural wastes to remediate the contaminated solutions by nickel ions. The adsorption process performs in a unit of batch mode at different operating conditions and infers optimal conditions that achieve the highest efficiency in removing nickel ions from contaminated aqueous solutions. By this way, more than one type of waste can be disposed at the same time in a beneficial, economical and eco-friendly manner, accessing to the zero residues level (ZRL).

### Experimental Work

#### Preparation of Mandarin Peels (*Citrus reticulata*)

The peels used in the conduct of this study were from the mandarin fruit crop, which was produced from Muqdadiyah District farms - Diyala Governorate in eastern Iraq, about 80 km northeast of Baghdad. The peels were collected from the domestic use for the period from 1/1/2019 to 1/7/2019 with an average consumption of 2-4 kg per week, and were kept in sealed and closed dark bottles to avoid exposure to putrefy. The collection process was continued until the required quantity was available. After obtaining a sufficient amount, the collected mandarin peels were washed, first with an excess of tap water and then with distilled water and before boiled in water for 60 minutes to remove any impurities that might be stuck with them during the storage period and to restore their freshness. After that the washed peels were dried by two steps, the first one was naturally using sunlight and continued for three days in the summer season while the next step drying by oven for 24 hours at 50 °C to avoid the disintegration of the composition structure at high temperature. To obtain a biosorbent material, the dried peels was cut into small pieces ranged between 1-3 mm and used by their final shape without any further treatment.



Figure 1. The mandarin peels used in this study

#### Preparation of Nickel (Ni<sup>2+</sup>) ions Stock Solutions

The treatment process has been studied using pre-synthesis laboratory solutions that mimic the real contaminated solutions. These solutions were used in order to obtain accurate results about the susceptibility of mandarin peel to adsorb nickel ions. Moreover to avert any kind of inconsistency that may occur between ions, molecules or other compounds present in the real wastewater. The required

stock solution of 1000 ppm concentration nickel ions was prepared in a laboratory at  $28 \pm 2^\circ\text{C}$  by dissolving 4.05 g of nickel hexahydrate ( $\text{NiCl}_2 \cdot 6\text{H}_2\text{O}$ ) in a one liter of deionized water. The salt of nickel hexahydrate supplied by (Sigma-Aldrich Corporation) (CAS No. 7791-20-0) was light green with 99.9% purity (99.9% trace metals basis). Whereas, deionized water was obtained from the Al-Mansour Company-Iraq. All solutions used were obtained from diluting the prepared stock solution to the required concentration with deionized water. Nickel hexahydrate and stock solution prepared in this study are shown in Figure 2.



Figure 2. Nickel hexahydrate and stock solution prepared in this study

### Calibration Curve

The famous method applied for determining the concentrations of heavy metal, including nickel, in aqueous solutions is by using the Atomic Absorption Spectroscopy AAS and with the help of the calibration curve for each metal. To detect the concentration of nickel metal in aqueous solutions after the completion of the treatment process, the AAS calibration curve of nickel ions was prepared through preparing multi standard solutions of different nickel ion concentrations and tested by Atomic Absorption Spectroscopy of type (AA-7000 Shimadzu) at a wavelength of ( $\lambda = 341.5 \text{ nm}$ ). The value of absorbance obtained for each concentration was recorded. So, the relationship between concentration of nickel ions and the absorbance can be plotted to obtain the correction curve. When the relationship between two variables (concentration and absorbance) is linear and of high correlation coefficient the concentration of nickel in the solution can be determined with greater accuracy. The concentrations of the prepared solutions for preparing the calibration curve ranged from the lowest concentration to the highest concentration that can make relationship between concentration and absorbance is linear (i.e. between 1-16 ppm). Figure 3 shows the calibration curve for nickel ions using the Atomic Absorption Spectroscopy.

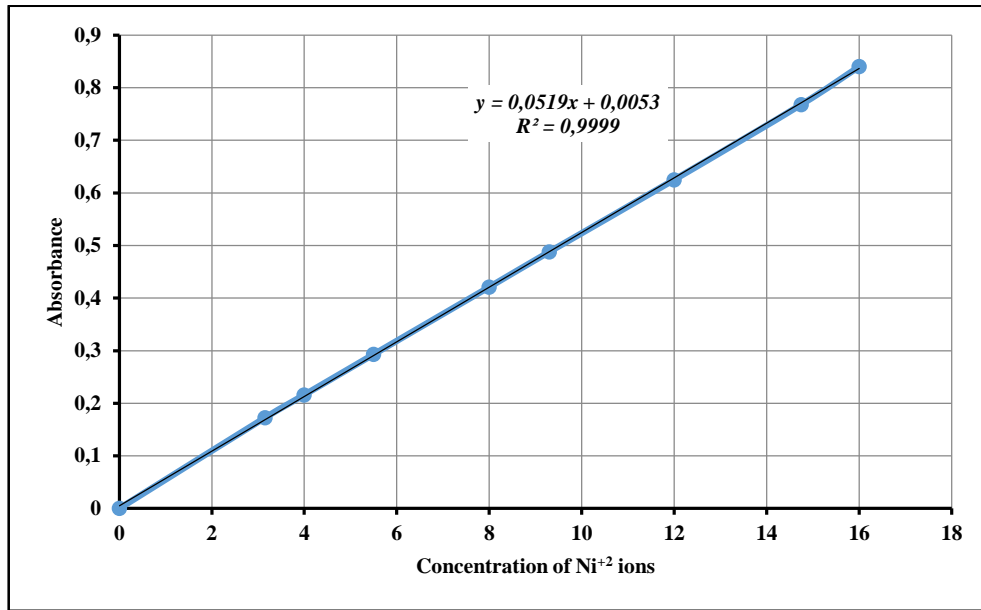


Figure 3. The calibration curve of nickel ions using the AAS @  $\lambda = 341.5$  nm

#### Adsorption Experiments in Batch Mode Unit

All treatment experiments were performed using a batch mode adsorption unit (Thermo Scientific MaxQ SHKE7000 Benchtop Water Bath Shaker, Model 4303) at different operating conditions. The operating conditions studied included the initial concentration of nickel ions, acidic function (pH), agitation speed, contact time, amount of adsorbent and temperature. The acidic function was changed within a range (1-9) using 0.1 M concentration of sodium hydroxide (NaOH) and hydrochloric acid (HCl) supplied by Sigma-Aldrich Corporation as basic and acidic solutions respectively to arrive the required pH studied while the effect of temperature ranging between (25-55) °C was studied in the unit. The remaining studied operating parameters were varied between (1-100 mg/L), (50-500 rpm), (0.05-3.0 g), (10-180 min) for the initial concentration of nickel, agitation speed, the amount of the adsorbent media and the contact time respectively. Laboratory experiments were performed by 50 ml of the contaminated solution in an appropriate flask using the adsorption unit and each experiment was performed repeated triplicate in order to reduce the percentage of experimental error. Samples are drawn from the treatment flasks at specific time intervals, then filtered with filter paper and centrifuged, then tested by AAS device and using calibration curve to detect the concentration of nickel ions after treatment process ending. The tests of sample were also triplicated. Figure 4 shows the water bath shaker used in the current study, which represents the batch adsorption unit. The percentage removal of nickel ions from contaminated aqueous solutions after the end of the treatment process was calculated from the mathematical relationship described in equation (1), while equation (2) represents the capacity of mandarin peels to adsorb of nickel ions.

$$R = \frac{C_i - C_o}{C_i} \times 100 \quad (1)$$

$$q = \frac{V}{m} \times (C_i - C_o) \Rightarrow q = \frac{RC_i}{100} \left( \frac{V}{m} \right) \quad (2)$$

Where:  $R$ : is the percent removal of Ni<sup>2+</sup> ions (-),  $q$ : is the capacity of adsorption by mandarin peels (mg/g),  $C_i$  and  $C_o$ : initial and final concentrations of Ni<sup>2+</sup> ions respectively (mg/L),  $m$ : mass of mandarin peels used for adsorption (g) and  $V$ : volume of solution (L).



Figure 4. The water bath shaker used in the current study

### Results and Discussion

The process of treating aqueous solutions contaminated with nickel ions prepared in the laboratory was accomplished by a low-cost substance, which are Iraqi mandarin peels as a biosorbent material using a batch mode adsorption unit. The percentage removal of pollutant material was measured at various designing variables and with different ranges of acidic function (pH), initial nickel concentration, agitation speed, amount of adsorbent material, contact time and temperature to determine the optimum conditions that achieve maximum removal efficiency.

#### Acidic function (pH)

The acidic function value of the contaminated aqueous solutions is considered of great importance and one of the most operational factors affecting the adsorption process, especially by using non-valuable materials such as agricultural waste. Therefore, the effect of this important operational factor was studied by changing the value of the acidic function of nickel contaminated solutions within a range between (1-9) and by fixing the rest operational variables constant at optimal values. Figure 5 shows the effect of changing the acidic function on the removing efficiency of the nickel ions from the contaminated aqueous solutions. It is noticed from the figure that the relationship between the pH and the removal percentage has increased since the removal is increased from 14.522% at pH = 1 to 86.031% at pH = 6. The reason for this results is because the hydrogen ions (protons) increase at low values of the acidic function, which will make them in strong competition with nickel ions which is positive also on the active sites located on the surface of the adsorbent material and the chance of protons will be greater in adsorption because they have a +1 equivalence while nickel ions would be equivalent to +2. Thus, the number of nickel ions dispersed in the solution will increase, and as the volume is constant, the final concentration will increase and the removal percentage will decrease. At pH values greater than 6, nickel ions in the solution will be precipitated in the form of nickel hydroxide ( $\text{Ni}(\text{OH})_2$ ), which is slightly soluble in water, and the percentage removal will increase. Therefore, the value of pH = 6 is the optimal acidic function for nickel adsorption using mandarin peels.



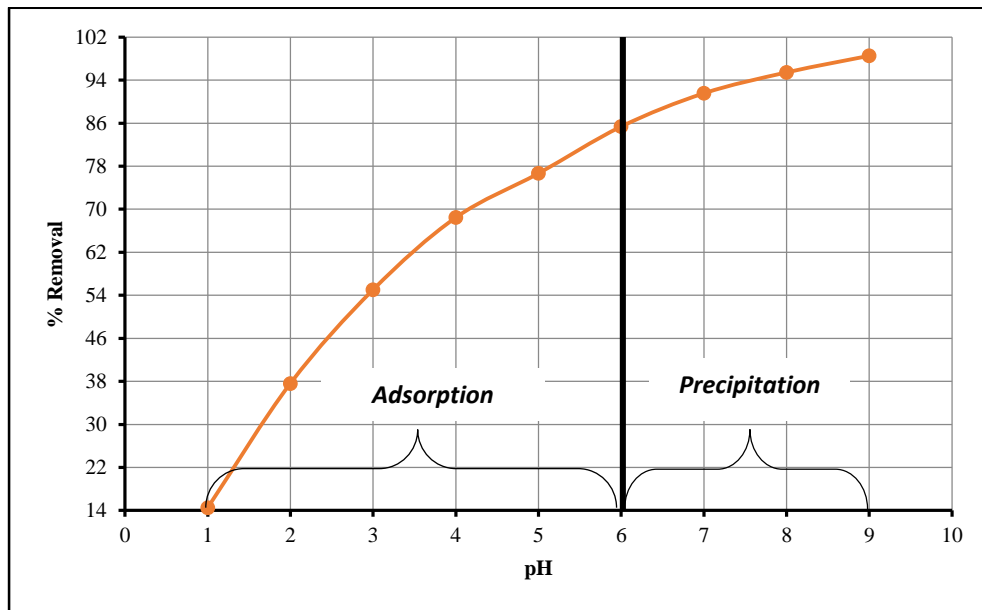


Figure 5. The effect of changing the acidic function on the removing efficiency of the nickel ions

### Agitation speed

Figure 6 represents the effect of changing the agitation speed within a range between (100-500) rpm on the percentage removal of nickel ions from contaminated aqueous solutions when all other variables are constants at optimal values. From the figure, it can be seen that the relationship is directly proportional between 100 rpm and up to 400 rpm, then become steady and there is no change in the removal efficiency despite increasing the value of agitation speed. The agitation speed is always related with the diffusion of ions in the solution, as the increase in velocity leads to increased diffusion. Therefore, the removal value increased from 44.391% to the maximum value 86.031% due to the increase in speed from 100 rpm to 400 rpm, respectively. This is due to the increase in the speed of the diffusion of nickel ions in the solution, which will increase the chance of these ions to reach the functional groups present in the active sites on the surface of the adsorbent material. On a related level, the high agitation velocity prevents the material from accumulating at the bottom of the beaker, thus making the contact period with the mandarin peels longer and thus increasing the chance of adsorption. On the other hand, increasing the agitation speed leads to the destruction of any boundary layers surrounding the surface of the adsorbent material, which prevents nickel ions from reaching the effective sites, which leads to an increase in the number of nickel ions adsorbed and thus the number of nickel ions in the solution will decrease and the percentage removal will increase. It is also noted that increasing the agitation speed beyond 400 rpm does not affect in any way the percentage removal, which means that the adsorbent particles have reached saturation state and cannot adsorb any other amount of nickel ions. Therefore, the removal efficiency will remain constant at the maximum value and cannot be changed at those specific operating conditions.

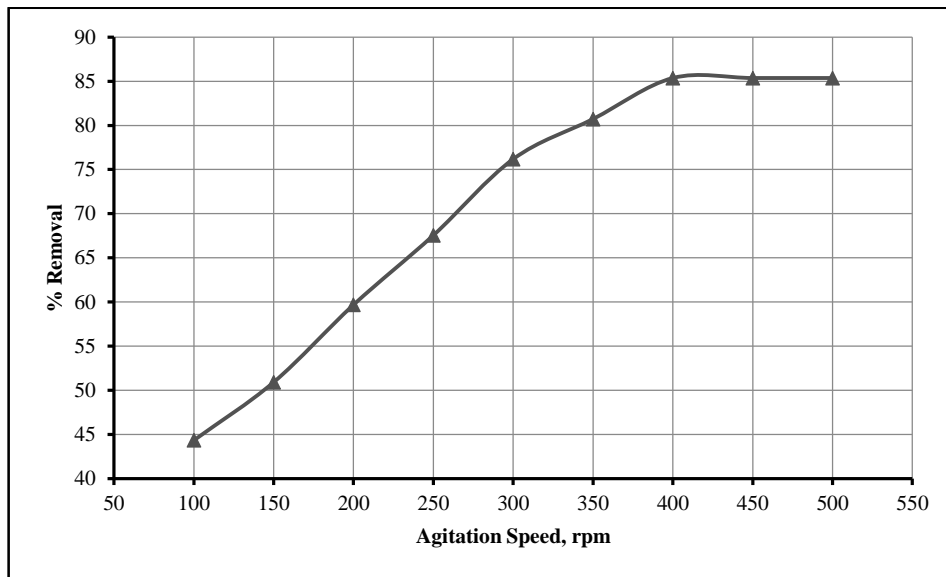


Figure 6. The effect of agitation speed on the removing efficiency of the nickel ions

### Initial concentration

Experiments related with changing the initial concentration of nickel ions in aqueous solutions were carried out within a range between (1-100 mg/L) and the validation of the remaining design factors under ideal conditions. The practical results obtained from conducting the experiments are represented in Figure 7 which shows that the relationship is completely inversely proportional between the removal efficiency and the initial concentration. The increase in the initial concentration leads to a decrease in the removal efficiency, as the removal rate decreased from 86.031% at  $C_0 = 1$  mg/L to 14.522% at  $C_0 = 100$  mg/L. The reason for this result is attributed to the fact that the higher concentration of nickel, meaning more ions in the solution (at constant volume), this would lead to an increase in the number of competing ions on the same number of active sites in the unit weight of the adsorbent material, and in turn will lead to a decrease in the number of ions adsorbed in the solution to a constant surface area, which will reduce the removal efficiency.

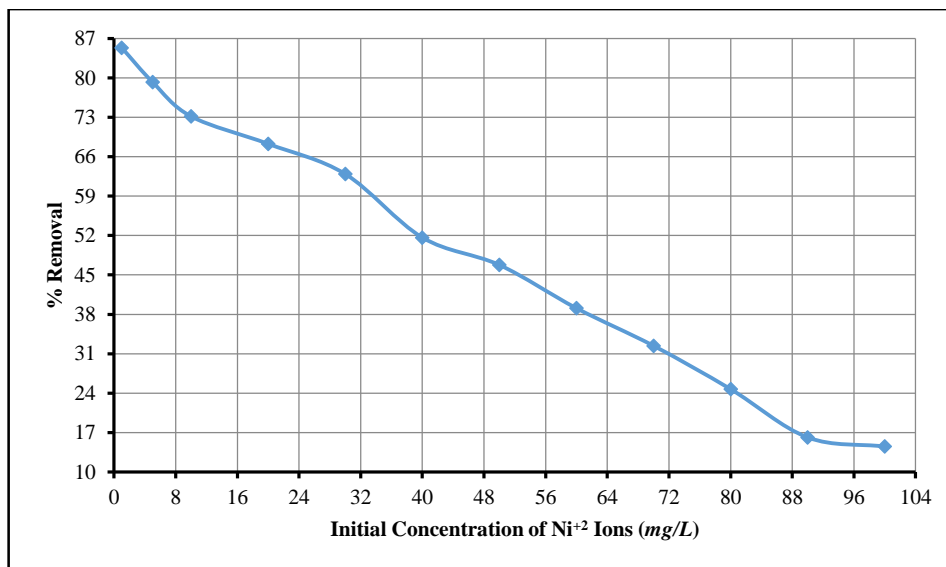


Figure 7. The effect of initial concentration on the removing efficiency of the nickel ions

### Contact Time

The treating time is a vital design factor in adsorption experiments as it represents the time required for the adsorbent material to remain in contact with the pollutant ions dispersed in the aqueous solution and complete the adsorption process. The results obtained from a set of contact time experiments were

conducted with time intervals ranging from 10 minutes to 180 minutes, keeping other operational variables constant at optimal values. Figure 8 indicates that increasing the contact time from 10 minutes to 120 minutes increases the percentage removal from 14.5% to the maximum value 86.031%, respectively. The concept of contact time is related with agitation speed. If the agitation velocity is constant, then nickel ions will spend more time in contact with the active substance and thus the possibility of metal adsorption by the functional groups found on the surface of the mandarin peels will increase and thus the efficiency of removal will increase. It is also noticed from Figure 8 that the efficiency of nickel removal remains constant after the time exceeds 120 minutes and the reason for this may be due to of active sites on the surface of the adsorbent material arrived to the saturation state and thus unable to adsorb additional numbers of ions. This leads to the fixed of the removal efficiency at the maximum value.

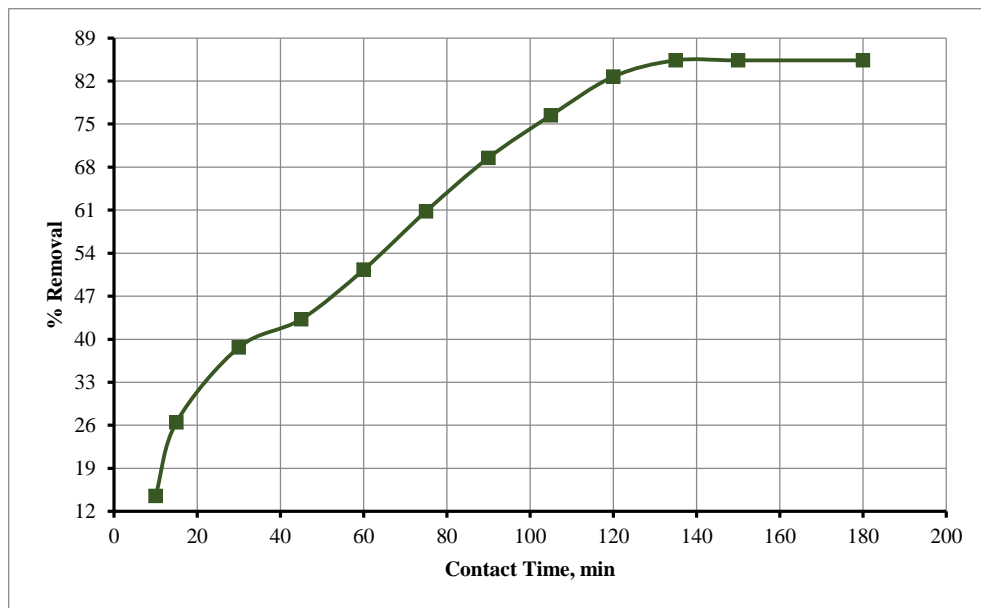


Figure 8. The effect of contact time on the removing efficiency of the nickel ions

#### Adsorbent media dose

Figure 9 represents the results of the removal efficiency obtained as a result of changing the dose of adsorbent media while other design variables remaining constant at optimum values. It is clear that the relationship between the percentage removal of nickel and the dose of adsorbent media is directly proportional. Increasing the amount of adsorbent material means increasing the surface area, which in turn means increasing the number of active sites on the surface of the adsorbent media that will be in contact with the pollutant ions, which will increase the chance of adsorption of nickel ions, and thus the percentage removal will increase. It is also noted that increasing the amount of mandarin peels from 1.0 g to 4.0 g raises the removal efficiency from 14.522% to 86.031%, respectively. But at a dose of 4 grams or more of the adsorbent substance, the percentage removal remains constant at the maximum value. This may be attributed to the fact that other operating conditions and the adsorbent behavior will lead to the distribution of adsorbed nickel ions over all the amount of the adsorbent material without exploiting the additional surface area in adsorption. Or, the increase in the amount of mandarin peels will lead to generate an additional barriers and film layers surrounding the adsorbent material that prevent additional numbers of polluted ions from reaching the active sites in the pores of the adsorbent material, which leads to an increase in the number of nickel ions in the solution and thus the stability of the removal rate when it reaches the maximum value. What supports these two explanations is the constant removing of nickel efficiency of, despite the increase in the dose of adsorbent material.

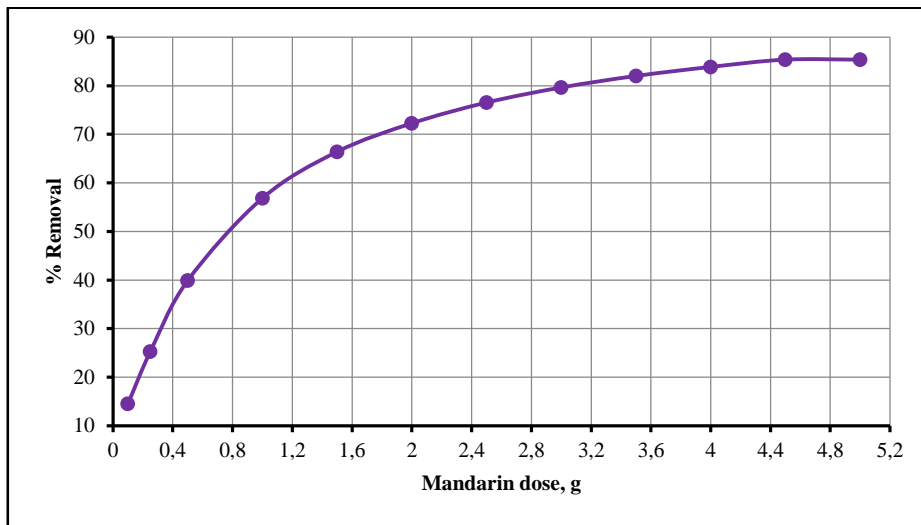


Figure 9. The effect of mandarin dose on the removing efficiency of the nickel ions

### Temperature

The effect of temperature is directly related to chemical and physical processes, where this operational factor plays an important role in determining the efficiency of surface transport processes (i.e. adsorption). A set of laboratory experiments were conducted to study the effect of temperature on the susceptibility of mandarin peels for adsorption of nickel ions from contaminated aqueous solutions within different temperatures ranged between (25-55) °C while other operational factors were fixed at optimum values. The obtained results indicated that increasing the temperature will improve the processing efficiency of nickel-contaminated solutions from 14.522% to 86.031% at 25 to 55 °C, respectively, as shown in Figure 10. The direct relationship between temperature and percentage removal can be attributed to a number of interpretations, the first one is the increasing the temperature leads to increase the kinetic energy of nickel ions, which will lead to an increase in the ion diffusion speed in the solution, which will increase the chance of ions reaching functional groups in the effective locations. The second is that increasing the temperature will expand the pores in the mandarin peels and thus allow a greater number of ions to reach the active sites distributed over the surface of the mandarin peels, which increases the number of nickel adsorbed ions. The third explanation is that increasing the temperature is likely to increase the effectiveness of the active sites by breaking down the layers of barriers that block the ions' path to reach the active sites, which in turn will allow more ions to adsorb. The end result of all the previous explanations is that the removing of nickel ions is increased by about 17%.

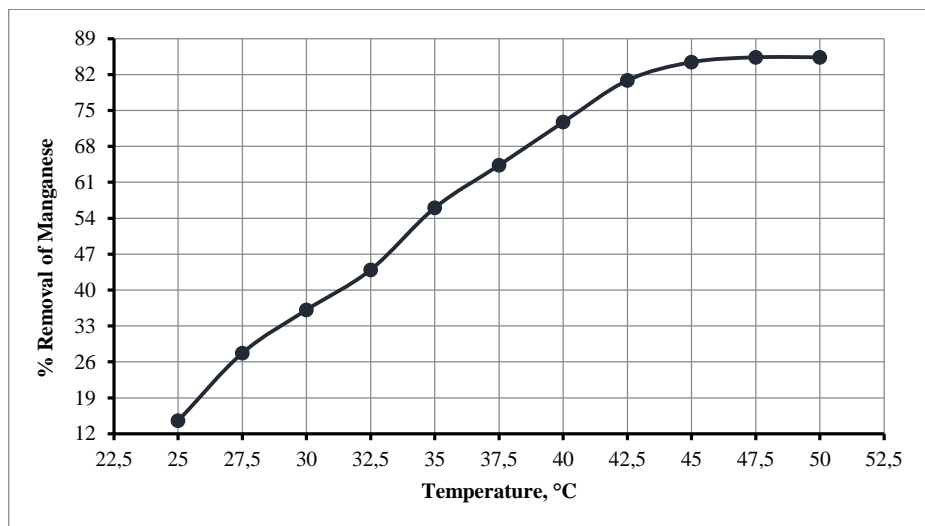


Figure 10. The effect of temperature on the removing efficiency of the nickel ions

## Conclusions

This study draws attention to agricultural waste as a sustainable source for many activities at the agricultural, industrial and environmental levels. In addition to its traditional use in preparing compost and using it as a source of animal and livestock feed, it has become of great importance at the industrial level in preparing many materials, including biofuels, and at the environmental level as treating materials that attracted the attention of researchers to it for its availability, cheapness and efficiency. One of the most important conclusions of the current study is that raw mandarin peels are considered a material with a high ability to adsorb nickel ions as one of the heavy, dangerous and widely used metals of contaminated aqueous solutions. The highest removal efficiency was 86.031% at an initial concentration of 1 mg/L, an acidic value of 6, a contact time of 120 minutes, a temperature of 55 °C, and a agitation speed of 400 rpm on a 4.0 g surface of mandarin peels. This study also indicated that the efficiency of removal is inversely proportional to the initial concentrations and directly with the rest of the variables within certain limits and then is fixed at the maximum value and is not affected by any increase in operational factors.

## References

- [1] Engwa G. A., Ferdinand P. U., Nwalo F. N. and Unachukwu M. N., (2019), “Mechanism and Health Effects of Heavy Metal Toxicity in Humans”, Chapter 5 in “Poisoning in the Modern World - New Tricks for an Old Dog?” Authord by Karcioğlu O. and Arslan B., IntechOpen, doi: 10.5772/intechopen.82511. ISBN: 978-1-83880-786-3. Available from: <https://www.intechopen.com/books/poisoning-in-the-modern-world-new-tricks-for-an-old-dog-/mechanism-and-health-effects-of-heavy-metal-toxicity-in-humans>
- [2] Singh, R., Gautam, N., Mishra, A. and Gupta, R., (2011), “Heavy metals and living systems: An overview”, Indian journal of pharmacology, volume 43, Issue 3, pp: 246–253. <https://doi.org/10.4103/0253-7613.81505>
- [3] Ali H., Khan E. and Ilahi., (2019), “Environmental Chemistry and Ecotoxicology of Hazardous Heavy Metals: Environmental Persistence, Toxicity, and Bioaccumulation” Journal of Chemistry, Volume 2019, Article ID 6730305, 14 pages, <https://doi.org/10.1155/2019/6730305>
- [4] Sasakova N., Gregova G., Takacova D., Mojzisoava J., Papajova I., Venglovsky J., Szaboova T. and Kovacova S., (2018), “Pollution of Surface and Ground Water by Sources Related to Agricultural Activities”, Frontiers in Sustainable Food Systems, Volume 2, Article 42, 27 July, 11 pages, <https://doi.org/10.3389/fsufs.2018.00042>
- [5] (IQS/417/2001) Iraqi Standard Specification for drinking water, 1<sup>st</sup> Revised, 2001.
- [6] Khadim H. J. Ammar S. H. Ebrahim S. E., (2019), “Biom mineralization based remediation of cadmium and nickel contaminated wastewater by ureolytic bacteria isolated from barn horses soil”, Environmental Technology & Innovation, Volume 14, May, 100315. <https://doi.org/10.1016/j.eti.2019.100315>
- [7] Gillespie P. A., Kang G. S., Elder A., Gelein R., Chen L., Moreira A. L., Koberstein J., Tchou-Wong K. M., Gordon T., Chen L. C., (2010), “Pulmonary response after exposure to inhaled nickel hydroxide nanoparticles: short and long-term studies in mice”, Nanotoxicology, March 1, Volume 4, Issue 1, pp:106-119. <https://doi.org/10.3109/17435390903470101>
- [8] Abbas M. N. and Abbas F. S., (2013), “Utilization of Iraqi Rice Husk in the Removal of Heavy Metals from Wastewater”, *Research Journal of Environmental and Earth Sciences*, Volume 5, Number 7, pp: 370-380, ISSN: 2041-0484.
- [9] Gupta S. and Kumar A., (2019), “Removal of nickel (II) from aqueous solution by biosorption on *A. barbadensis* Miller waste leaves powder”, Applied Water Science, Volume 9, Issue 4, June, Article No. 96, 11 pages. <https://doi.org/10.1007/s13201-019-0973-1>
- [10] Kamika I. and Momba M. N., (2015), “Effect of nickel on nutrient removal by selected indigenous protozoan species in wastewater systems”, Saudi Journal of Biological Sciences, Volume 22, Issue 2, pp: 147–156, <https://doi.org/10.1016/j.sjbs.2014.09.010>
- [11] Kamika I. and Momba M. N., (2015), “Effect of nickel on nutrient removal by selected indigenous protozoan species in wastewater systems”, Saudi Journal of Biological Sciences, Volume 22, Issue 2, pp: 147–156, <https://doi.org/10.1016/j.sjbs.2014.09.010>

- [12] Kamika I. and Momba M. N., (2015), “Effect of nickel on nutrient removal by selected indigenous protozoan species in wastewater systems”, *Saudi Journal of Biological Sciences*, Volume 22, Issue 2, pp: 147–156, <https://doi.org/10.1016/j.sjbs.2014.09.010>
- [13] Phetla T. P., Ntuli F. and Muzenda E., (2011), “Removal and recovery of Ni, Cu and Fe from heavy metal effluent by reduction crystallization”, *Water Resources Management VI*, Volume 145, pp: 681 – 690. doi: 10.2495/WRM110611.
- [14] Phetla T. P., Ntuli F. and Muzenda E., (2011), “Removal and recovery of Ni, Cu and Fe from heavy metal effluent by reduction crystallization”, *Water Resources Management VI*, Volume 145, pp: 681 – 690. doi: 10.2495/WRM110611.
- [15] Aryal, M. and Liakopoulou-Kyriakides, M., (2015), “Bioremoval of heavy metals by bacterial biomass”, *Environmental Monitoring and Assessment*, Volume 187, Issue1, 26 pages, Article: 4173. <https://doi.org/10.1007/s10661-014-4173-z>
- [16] Amuda, O.S, Amoo, I. A. and Ipinmoroti, K. O., Ajayi, O. O., (2006), “Coagulation / flocculation process in the removal of trace metals present in industrial wastewater”, *Journal of Applied Sciences and Environmental Management*, Volume 10, Issue 3, pp:159- 162 September.
- [17] Mansour S. E. and Hasieb I. H., (2012), “Removal of Nickel from Drinking Water by Electrocoagulation Technique Using Alternating Current”, *Current Research in Chemistry*, Volume: 4, Issue: 2, pp: 41-50. <https://doi.org/10.3923/crc.2012.41.50> .
- [18] Kumar P. S., Ramakrishnan K., Gayathri R., (2010), “Removal of Nickel (II) from Aqueous Solutions By CERALITE IR 120 Cationic Exchange Resins”, *Journal of Engineering Science and Technology*, Volume 5, Number 2, pp: 232 – 243.
- [19] Abbas M. N. and Abbas F. S., (2014), “Rice Husk as a Biosorbent Packed bed, Management, Utilization and Improvement compressive strength of concrete”, *LAMBERT Academic Publishing*, ISBN-10: 3659504483; ISBN-13: 978-3659504488
- [20] Saleem, J., Shahid, U., Hijab, M. McKay G., (2019), “Production and applications of activated carbons as adsorbents from olive stones”, *Biomass Conversion and Biorefinery*, Volume 9, Issue 4, pp 775–802, December. <https://doi.org/10.1007/s13399-019-00473-7>
- [21] Abbas M. N., (2014), “Application of Used Tea Leaves for Multi Functions”, *European Academic Research*, Volume II, Issue 7/ October, ISSN 2286-4822.
- [22] Alalwan H. A., Abbas M. N., Abudi Z. N. and Alminshid A. H., (2018), “Adsorption of thallium ion (Tl<sup>3+</sup>) from aqueous solutions by rice husk in a fixed-bed column: Experiment and prediction of breakthrough curves”, *Environmental Technology and Innovation*, Volume 12, November, pp: 1-13. <https://doi.org/10.1016/j.eti.2018.07.001>
- [23] Prasad D. A. G. and Abdullah A. M., (2009), “Biosorption potential of potato peel waste for the removal of nickel from aqueous solutions: Equilibrium and kinetic studies”. *International Journal of Chemical Engineering Research*, Volume 1, Number 2, pp: 77-87.
- [24] Khawaja M., Mubarak S., Zia-Ur-Rehman M., Kazi A. A. and Hamid A., (2015), “Adsorption Studies of Pomegranate Peel Activated Charcoal for Nickel (II) Ion”, *Journal of the Chilean Chemical Society*, Volume 60, Number 4, pp: 2642-2645. <https://doi.org/10.4067/S0717-97072015000400003>
- [25] Abbasi Z., Alikarami M., Nezhad E. R., Moradi F. and Moradi V., (2013), “Adsorptive Removal of Co<sup>2+</sup> and Ni<sup>2+</sup> by Peels of Banana from Aqueous Solution”, *Universal Journal of Chemistry*, Volume 1, Issue 3, pp: 90-95. <https://doi.org/10.13189/ujc.2013.010303>
- [26] Sudha R., Srinivasan and Premkumar K. P., (2015), “Removal of nickel(II) from aqueous solution using *Citrus Limettioides* peel and seed carbon”, *Ecotoxicology and Environmental Safety*, Volume 117, pp: 115-123, July. <https://doi.org/10.1016/j.ecoenv.2015.03.025>
- [27] Gönen F. and Serin D. S., (2012), “Adsorption study on orange peel: Removal of Ni(II) ions from aqueous solution”, *African Journal of Biotechnology*, Volume 11, Number 5, pp: 1250-1258. <http://dx.doi.org/10.5897/AJB11.1753>

## **Fisheries / Balıkçılık**

## Utilization of Blood Meal as an Alternative Protein Source on Growth and Feed Efficiency in Fingerlings Nile Tilapia (*Oreochromis Niloticus*)

*Obey Alnaiem\**, Kocaeli University, Dept. of Aquaculture, Kocaeli, Türkiye  
*Ahmed El nouman Babiker Moh, Al-Neelain University, Dept. of Fish Sciences, Khartoum, Sudan*  
*\*Corresponding author: gadain76@gmail.com*

**Keywords:** Fish, Tilapia, protein, blood meal, feeding

**Discipline:** Fisheries

### Abstract

The study aims to investigate the feasibility of utilizing blood meal in diets for feeding Nile tilapia fingerlings and determine the optimum level for the blood meal. Four pelleted diets were prepared. One diet was used as a control without blood meal, the other three contained 5%, 10% and 15% blood meal in terms of weight. All diets contained the same protein level of 35%. The experiment continued for six weeks and was conducted in four circular fiberglass tanks each of 300 liters capacity. Thirty fingerlings averaging 6.9-7.0g were placed in each tank. The fish were weighed together in the beginning of the experiment. They were also weighed once weekly to follow growth rates and re-estimate daily food allowance for the subsequent week. At the end of the experiment the fish were weighed individually. Fish in all tanks were fed the same daily allowance of food which ranged between 4% to 6% of their body weight per day. The daily ration was given in two equal doses. Blood meal improved growth rates in fish that were fed the diets containing 10% and 15% blood meal as compared to the all-plant control diet that contained no blood meal. Average percentage weight gain was 165% and 157% in fish which were fed the diets containing 10% and 15% blood meal, respectively, as compared to 140% for the control diet. Blood meal also improved food conversion ratios (FCR) which were 2.06 and 2.16 for the 10% and 15% blood meal treatments, respectively, as compared to 2.33 for the control diet. Moreover, addition of blood meal to the basic diet reduced the cost of the diet substantially. The study showed that the 10% blood meal treatment gave slightly better performance than the 15% blood meal treatment. This probably relates to the known effect of blood meal on palatability of diets particularly at high inclusion levels. Hence, it is recommended – based on the results obtained in this study – not to exceed a level of 10% of blood meal in fish diets.

### Introduction

Fish farming is the process of raising fish in a specific aquatic environment under human control regarding water quality and food. This is done by controlling the variables influencing the lives of fish to help maximize fish production at the shortest time and at the lowest cost [1]. The ten most generally cultivated fish are six distinctive carp species (family Cyprinidae), Nile tilapia (*Oreochromis niloticus*), Atlantic salmon (*Salmo salar*) rainbow trout (*Oncorhynchus mykiss*) and milkfish (chanos) [2]. Aquaculture production needs to increase to meet the growing demand for fish as food, especially since fish is an important source of essential amino acids, fatty acids, vitamins, and minerals for the human population. In addition, fish production in low-income regions and countries is important to increase economic gains and food supplies that may be lacking [3]. The success of fish culture has been driven by a number of factors, including: (i) depletion of the fish stocks as a result of overfishing; (ii) higher fishing costs; and (iii) reduced freshwater stocks due to pollution [1]. Furthermore, aquaculture constitutes the cheapest source of animal protein for poorer households, and plays a great role in poverty alleviation through capital accumulation [4]. Fish, like other animals, need good protein sources to ensure rapid growth. Protein quality is increasingly important in intensive culture systems, where there is total reliance on artificial food for fish and little or no natural food contribution. Animal protein sources are particularly important for early age nutrition and, particularly fish in intensive breeding systems. This has resulted in two great challenges, (i) First, there is increasing pressure on already overfished stock due increasing demand for fish meal (FM) [5] [6]. And high prices of FM, derived from the growing demand, is affecting the recommended inclusion levels of FM in fish diet [7] [8]. Consequently, the aquafeed business had to search for affordable alternative protein sources to reduce their reliance on FM [9] [1]. Clearly the developing aquaculture industry cannot keep on depending on finite stocks of fish meal from wild-caught fish, a figure, which was formerly classified as completely



abused overexploitation [10]. Therefore, a sustainable aquaculture requires cost-effective and high-quality alternative protein source as a substitute for fish meal. Other animal protein sources such as blood meal (BM) presents an excellent alternative [11]. Attaining a cost-effective and high-quality protein alternative implies improving aquaculture revenue and reducing high fishing pressure. In production research, attention has been directed towards the assessment and utilization of unconventional protein sources, particularly from animal products that are neglected and unexploited, such as; fish waste, poultry waste, slaughterhouse wastes, dried blood powder, and other byproducts [12] [13] [14] [15] [16] [17] [18] [19] [20] [21]. Due to insufficient information available from local studies, the present study analyzes the utilization of bloodmeal as a fish meal substitute in the diet of Nile tilapia fry (*Oreochromis niloticus*).

## Material and methods

### Experimental system and Fish feeding

The experiment was conducted at the fish farm of the Faculty of Agricultural Technology and Fish Sciences at Neelain University, located south of the Jabal Awliya Reservoir. The experiment period was 6 weeks, conducted in four cylindrical fiberglass tanks (volume 0.3 m<sup>3</sup>). The source water was the groundwater well for the college farm. The fiberglass tanks were thoroughly washed with soap and water, disinfected with formalin (10%) and exposed to sunlight to dry completely. Fingerlings of *Oreochromis niloticus* were obtained from the Jawars fish hatchery. Prior to stocking experimental units, fingerlings were conditioned in a fiberglass tank for a week. Fingerlings were fed 4% body weight during conditioning. The present experiment consisted of three (3) treatments and a control. The treatments are defined as; 5% Blood meal, 10 Blood meal, and 15% Blood meal. Both treatments and the control had one (1) replicate, making a total of eight (8) experimental units. Each experimental unit was stocked with 15 fingerlings of weight 6.9±0.1 g. All tanks were aerated using aquarium aerators with air stones for diffusion.

Feeding was done manually, and three times (3) per day, at 09:00, 13:00 and 17:00 hours. Uneaten food was collected from the bottom of the tank using pipe before every morning before the first feeding throughout the experimental period. Fingerlings were feed 6% BW in the first three (3) weeks and 5% BW in the last three weeks.

### Preparation for the blood meal

The blood of the cows was obtained from the Sahafa slaughterhouse in Khartoum, where blood was collected from one cow immediately after its slaughter and was weighed, as the weight reached 5.3 kg. The blood was stored in a deep freezer for the next day, where it was treated (sterilized and dried) thermally by heating it to a boil for 15 minutes [22]. It was then dried under the sun for eight hours, when its weight then reached 1.05 kg, and accordingly, the percentage of moisture removed from fresh blood by heating and solar drying reached 80.2%. The dried blood was fine grinded for use in diets.

### Diet formulation and manufacture

Four diets were installed using fava beans, wheat rose, cornmeal, in addition to the blood powder being studied. The first feed contains a diet (reference control) that does not contain dried blood powder, the second diet contains blood powder dried by 5%, the third diet contains 10% of dried blood powder, while the fourth diet contains 15% blood powder. The diets were synthesized so that each contained 35% protein (Table 1). The diets were constructed on feed components of nutrients (Nutrients) as indicated in the [23]. (Table 2).

### Evaluation of growth parameters

The fish were weighed every week to calculate their mean body weight of Scale (QEA 00) accuracy of 1 g, the biomass present in each tank, and to re-estimate the amount of daily food needed for feeding during the following week. At the end of the experiment, all fish were weighed individually in each tank. Growth and feed efficiency of the fish were monitored in terms of weight gain (WG), feed intake (FI), feed conversion ratio (FCR), specific growth rate (SGR) and survival (S). The biological indicators were calculated as follows:

Average final weight (g)= Total fish weight(g)/ Number of fish

Weight gain (WG) = final mean weight (g) – initial weight (g)

Feed intake (FI) =  $\Sigma$  In [(total feed consumption (g)) / (No: of fish)] / number of days

Feed conversion ratio (FCR) = feed intake (g) /weight gain (g)

Specific growth rate (SGR)= [In (final weight–initial weight) /number of days] X 100

Survival (S) = (Number of fish / Number of fish) X100

### Statistical analysis

All data were subjected to a one-way analysis of variance ANOVA and the significance of the differences between means was tested using Duncan's multiple range test (P<0.05). The software used was Statistica ®, Version 5.1 (Statsoft Inc., Tulsa, USA). Values are expressed as means±standard deviation.

Table 1. The composition of the diets used in the experiment (%) \*

Ingredients	Diet (protein35%)			
	Control	BM %5	BM %10	BM %15
Soybean meal	69.8	59.5	49.5	39.1
Wheat rose	22.7	26.6	30.4	34.4
Corn flour	7.5	8.9	10.1	11.5
Blood meal	-	5	10	15
Total	100	100	100	100

\*BM=Blood meal

Table 2. Feed ingredients used to form feed (%) \*

Ingredients	moisture	Crude protein	Diet (protein35%)		
			Crude lipid	Ash	Carbohydrates
Soybean meal	10.0	44.0	7.3	5.3	33.1
Wheat rose	11.0	15.1	3.9	6.2	63.4
Corn flour	10.0	11.3	2.8	1.7	73.9
Dried blood meal	8.0	75.3	1.6	5.4	9.5

\* The results are taken from the NRC Feed Analysis Tables (1977).

### Results

The current study, which spanned six weeks during the period from 12/5/ to 23/6, showed that the average weight of fish in treatment control No (1) – in which fish were fed with a diet that did not contain dried blood powder – increased from 7.0 g at the beginning of the experiment to 16.8 g at the end of the experiment, with an average weight of 9.8 g. The average weight of fish in treatment (2) – in which fish were fed with a diet containing BM 5% – increased from 6.9 g at the beginning of the experiment to 15.8 g at the end of the experiment period, with an average acquired weight of 8.9 g. The average weight of fish in treatment No. (3) – in which fish were fed with a diet containing BM10% – increased from 6.9 g at the beginning of the experiment to 18.3 g at the end of the experiment, with an average weight of 11.4 g. The average weight of fish in treatment (4) – whose diet contained BM 15% – increased from 6.9 g at the beginning of the experiment to 17.7 g at the end of the experiment period, with an average weight of 10.8 g. (Table 3, Figures 1 and 2).

Based on the visual observation during feeding time and on the behavior of fish, palatability or acceptability of feed was a constraint in this study. In the beginning, particularly in weeks 1 and 2 of the experiment, fish fed with diets 5%, 10%, and 15% were slightly reluctant to consume the offered feed. Accordingly, the percentage of gained weight reached 140% in the treatment control (1), whose diet did not contain dried blood powder, and 129% in the treatment (2), whose diet contained BM 5%, and 165% in the treatment (3) Their diet contained 10% of the BM, and 157% of the treatment (4) whose diet contained 15% of the BM (Table 3, Figure 3).

The daily growth rate was 0.23 g / day for the control (1), 0.21 g / day for the treatment (2), 0.27 g / day for the treatment (3), and 0.26 g / day for the treatment (4), as in (Table 3). The food conversion rate in the control was 2.33, while it reached 2.80, 2.06 and 2.16 for the treatments in which the diet of fish contained dried blood powder at rates of 5%, 10% and 15%, respectively. Survival% in the control treatment was 100%, while the ratio was 43.3%, 96.7% and 90% in the treatments in which the fish were fed with diets containing dried blood powder at 5%, 10% and 15%. % respectively (Table 3).

The temperatures recorded daily in all tanks were almost equal, as they were almost constant throughout the experiment period, where the weekly average in different treatments ranged between 30.1 ° C and 30.7 ° C. The lowest temperature was recorded at 29 ° C and the highest temperature of 31.5 ° C during the trial period (Table 4, Figure 3).

Statistical analysis of (One Way ANOVA) using the computer program in its third edition to compare between final weight averages showed that the differences between the four treatments were not significant at 95% (0.05), except for the difference between the two treatments 5% and 10%, which was a significant difference when non-confidence is (0.05).

Table 3. Fish performance in experiments

Ingredients	Diet (protein35%)			
	Control	BM %5	BM %10	BM %15
Average Initial weight (g)	7.0	6.9	6.9	6.9
Average Final weight (g)	16.8	15.8	18.3	17.7
Weight gain (g)	9.8	8.9	11.4	10.8
Weight gain (%)	140	129	165	157
Specific growth rate SGR	0.23	0.21	0.27	0.26
Feed conversion ratio FCR	2.33	2.80	2.06	2.16
Survival	100	43.3	96.7	90.0

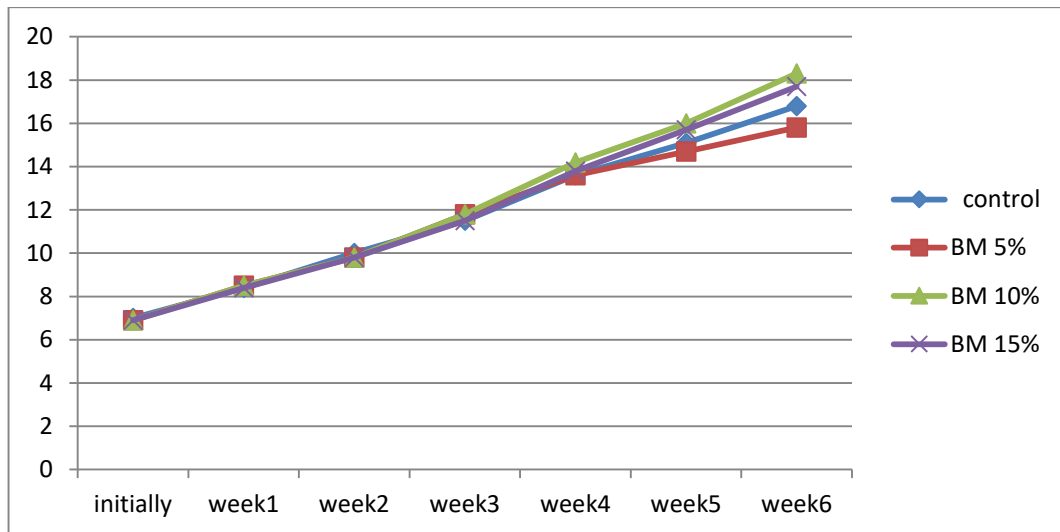


Figure 1. Fish growth rate in the four treatments average weight (g)

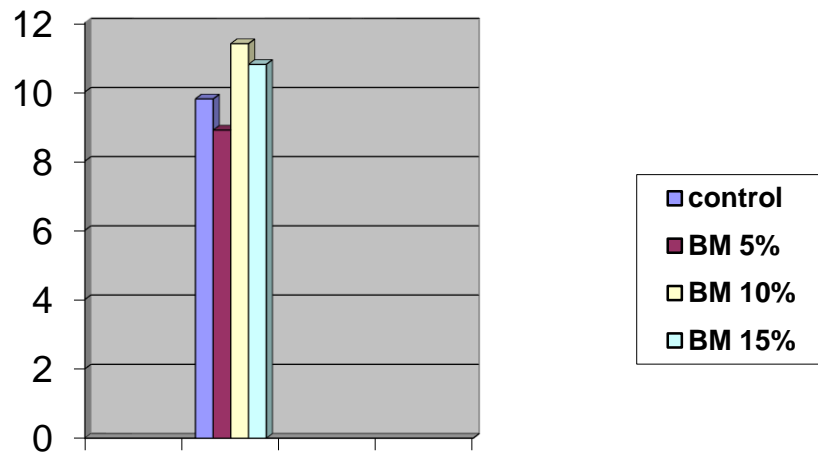


Figure 2. Weight gained in the four parameters (g)

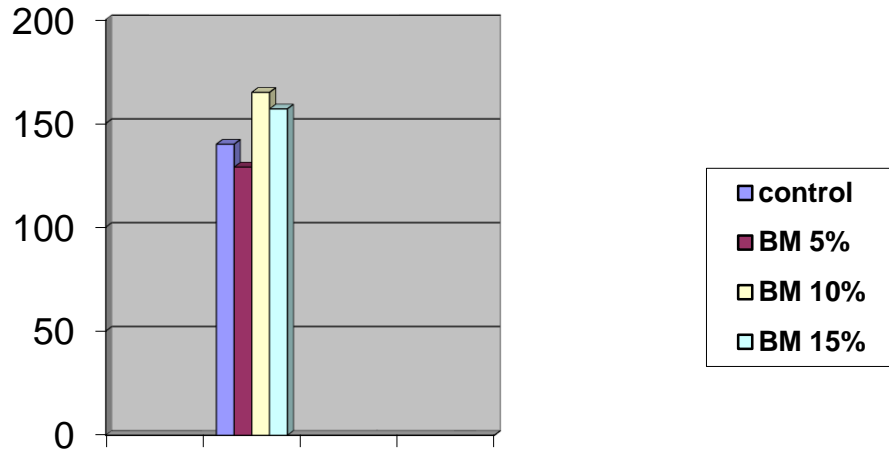


Figure 3. Weight gained in the four factors (%)

Table 4. Average weekly temperatures (° C)

Diet	Week 1	Week 2	Week 3	Week 4	Week 5	Week 6	Average
Control	30.7	30.1	30.3	30.5	30.6	30.4	30.4
BM 5%	30.2	30.1	30.1	30.3	30.6	30.1	30.2
BM 10%	30.7	30.1	30.4	30.3	30.6	30.4	30.4
BM 15%	30.6	30.3	30.4	30.4	30.6	30.4	30.5
Average	30.6	30.2	30.3	30.4	30.6	30.3	30.4

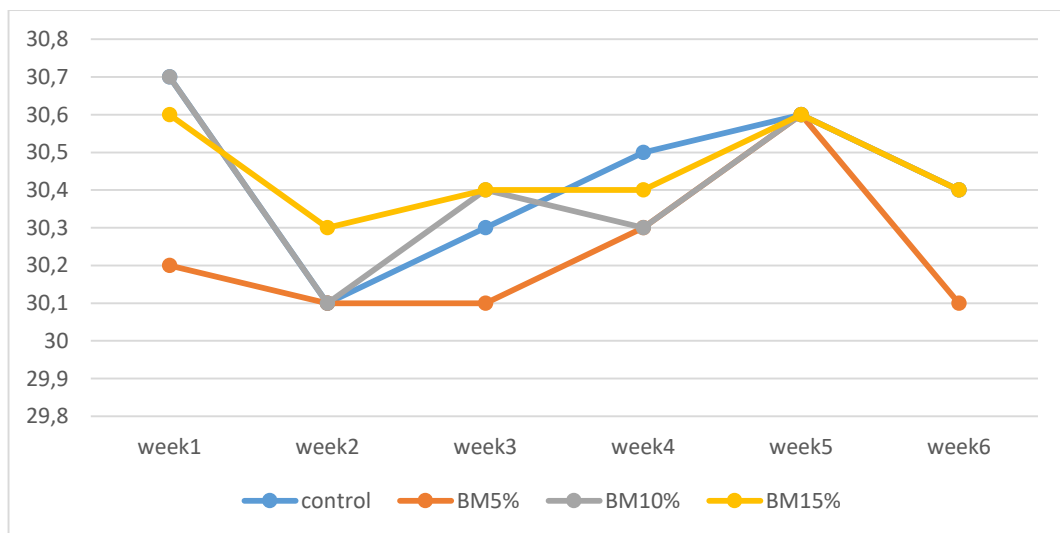


Figure 4. Average weekly temperatures for each treatment separately during the experiment (° C)

### Discussion

The current study showed an increase in the weight of fish in the four treatments during the six-week trial period, and with no other food source in the fiberglass tank, except for the provided feeds, this indicates that the fish have accepted the four feed provided to them and fed them, although they have differed in the extent of their utilization, which was reflected in some difference in the rates of fish growth in the four treatments. The results showed that there was no significant difference in fish performance between the different treatments according to the performance criteria that were used in the study. Treatment (3) in which the diet contained 10% of the dried cows blood powder showed little superiority to the rest of the treatments as the weight ratio Gain was 165% compared to transactions (1), (2), (4) in which the weight gain ratios were 140%, 129%, and 157%, respectively. It is noted that the

differences in the rate of growth between the different feeds did not appear at the beginning of the experiment, but began to appear more and more as the days of the experiment progressed and perhaps the differences would be greater, clearer and more significant if the experiment extended for a longer period. with the exception of treatment (2) (5% dried blood powder) whose result seemed abnormal due to the large unexplained mortality rate that occurred in it compared to the rest of the treatments, we find that the addition of dried blood powder (by 10% and 15% of the diet) led to an increase in Fish growth rate compared to the reference diet that contained plant protein sources only, It also improved the food transformation rates which reached 2.06 and 2.16 for the diets 10% and 15%, respectively, compared to the control diet, which recorded the food transformation rate of 2.33. This is in line with the findings of [24]. And other animal protein is better than vegetable protein in feeding tilapia. The results of the current study indicate that the blood powder led to an improvement in the quality of the protein, which was reflected in the better growth of the fish fed on the feed containing it, compared to the dietary diet control, noting that all experiment diets contain the same protein content of 35%. It was found that dried blood powder can replace 50-75% of dried fish meal in tilapia diets [25], which indicates the relative quality of its protein, as dried fish powder is one of the best sources of animal protein in diets. Fish is the most used but it is defective in its high cost.

The high mortality rate (56.7%) in treatment (2) in which fish were fed with a diet containing dried blood powder at 5% was not - as it is noted - related to feeding fish on blood powder since the other two treatments that contained blood powder at a higher rate reached 10% and 15% had a significantly lower death rate than treatment (2), where the mortality rate was 3.3% and 10%, respectively. There was no clear reason for the high mortality rate in the treatment to be explained (2), as it received the same rate of ventilation and the same rate of water regeneration in the aquarium as the rest of the treatments, and the fish did not have any apparent pathological symptoms.

The results of the current study showed that the diet containing 10% of the dried blood powder led to a growth rate and a rate of food transformation slightly better than the diet containing the blood powder by 15%, as the weight gained was 165% compared to 157%. Perhaps this is due to the effect of blood powder on the palatability of the diet if the percentage in the diet increases, and this corresponds to what Martinez- the effect of non-palatability of blood powder and the necessity of not exceeding 10% in the diet due to the negative effect on fish growth and sensory imbalances.

In summary, the results showed that commercial BM appeared to be a good feed ingredient for tilapia in terms of growth performance and nutrient composition as long as dietary levels remain 10% or less These results may serve to aid in the formulation of cost-effective diets for tilapia and as a basis to explore ways to improve the palatability of diets containing BM.

### Acknowledgments

The authors like to thank the Neelain University department of Fish Science for allowing the hatchery to be used for the purposes of this research. Thanks to the anonymous reviewer for their review and very useful comments and recommendations on the manuscript.

### References

- [1] Abdul Bari Muhammad Mahmoud. 2004 m. Essential fish farming and farm management. Knowledge facility. Alexandria, second edition, (272 pages).
- [2] Piracha, Awais. 2015. CUPUM 2015 - 14th International Conference on Computers in Urban Planning and Urban Management *EDevelopment-Assessment as "Smart Eplanning" for New South Wales (NSW) Australia.*
- [3] Avault, J.W. , Jr.(editor). 1970-1985.Proceedings (Journal) of the World Mariculture Society. Louisiana: Louisiana State University Division of Philippines. Aquaculture Magazine 13(6):51-52.
- [4] Kassam, L. (2014). Aquaculture and food security, poverty alleviation and nutrition in Ghana: Case study prepared for the Aquaculture for Food Security, Poverty Alleviation and Nutrition project. WorldFish, Penang, Malaysia. Project Report: 2014-48.
- [5] Naylor, R.L., Hardy, R.W., Bureau, D.P., Chiu, A., Elliot, M., Farrell, A.P., Forster, I., Gatlin, D.M., Goldberg, R.J., Hua, K., Nichols, P.D., 2009. Feeding aquaculture in an era of finite resources. Proceedings of the National Academy of Sciences of the United States of America 106, 15103–15110.
- [6] Hannesson, R., 2003. Aquaculture and fisheries. Marine Policy 27, 169–178.

- [7] (FAO), Food and Agricultural Organization of the United Nations 2009. The State of World Fisheries and Aquaculture 2008 (SOFIA). FAO Fisheries and Aquaculture Department, Rome.
- [8] Tacon, A.G.J., Metian, M., 2008. Global overview on the use of fish meal and fish oil in industrially compounded aquafeeds: trends and future prospects. *Aquaculture* 285, 145–158.
- [9] Hardy, R.W., 2010. Utilization of plant proteins in fish diets: effects of global demand and supplies of fishmeal. *Aquaculture Research* 41, 770–776.
- [10] NRC (National Research Council), 1999. *Sustaining Marine Fisheries*. National Academy Press, Washington, DC.
- [11] Naylor, R.L., Goldburg, R.J., Primavera, J.H., Kautsky, N., Beveridge, M.C.M., Clay, J., Folke, C., Lubchenco, J., Mooney, H., Troell, M., 2000. Effect of aquaculture on world fish supplies. *Nature* 405, 1017–1024.
- [12] Olvera-Novoa, M.A., Martinez-palacios, C.A., Galvan, C.R., Chavez, S.C., 1988. The use of seed of the leguminous plant *Sesbania grandiflora* as a partial replacement for fish meal in diets for tilapia (*Oreochromis mossambicus*). *Aquaculture* 71, 51–60.
- [13] El-Sayed, A.F.M., 1999. Alternative dietary protein sources for farmed tilapia, *Oreochromis* spp. *Aquaculture* 179, 149–168.
- [14] Makkar, H.P.S., Becker, K., 1999. Plant toxins and detoxification methods to improve feed quality of tropical seeds – review. *Asian- Australas. J. Anim. Sci.* 12 (3), 467–480.
- [15] Siddhuraju, P., Becker, K., Makkar, H.P.S., 2000. Studies on the nutritional composition and antinutritional factors of three different germplasm seed materials of an under-utilised tropical legume, *Mucuna pruriens* var. *utilis*. *J. Agric. Food Chem.* 48, 6048–6060.
- [16] Hossain, M.A., Focken, U., Becker, K., 2001a. Evaluation of an unconventional legume seed, *Sesbania aculeata*, as a dietary protein source for common carp, *Cyprinus carpio* L. *Aquaculture* 198, 129–140.
- [17] Siddhuraju, P., Becker, K., 2001. Preliminary nutritional evaluation of *Mucuna* seed meal (*Mucuna pruriens* var. *utilis*) in common carp (*Cyprinus carpio* L.): an assessment by growth performance and feed utilisation. *Aquaculture* 196, 105–123.
- [18] Siddhuraju, P., Becker, K., 2002. Effect of phenolic non-protein amino acid, L-Dopa (L-3, 4-dihydroxyphenylalanine), on growth performance, metabolic rates and nutrient utilisation in common carp (*Cyprinus carpio* L.). *Aquac. Nutr.* 8, 69–77.
- [19] Siddhuraju, P., Becker, K., 2003. Comparative nutritional evaluation of differentially processed mucuna seeds [*Mucuna pruriens* (L.) DC. Var. *utilis* (Wall ex Wight) Barker ex Burk] on growth performance, feed utilisation and body composition in Nile tilapia (*Oreochromis niloticus* L.). *Aquaculture* 34, 487–500.
- [20] Afuang, W., Siddhuraju, P., Becker, K., 2003. Comparative nutritional evaluation of raw, methanol extracted residues and methanol extracts of moringa (*Moringa oleifera* Lam.) leaves on growth performance and feed utilisation in Nile tilapia (*Oreochromis niloticus* L.). *Aquacult. Res.* 34, 1147–1159.
- [21] Richter, N., Siddhuraju, P., Becker, K., 2003. Evaluation of the quality of (*Moringa oleifera* Lam.) leaves as an alternative protein source for Nile tilapia (*Oreochromis niloticus* L.). *Aquaculture* 217, 599–611.
- [22] Göhl, B., 1982. *Les aliments du bétail sous les tropiques*. FAO, Division de Production et Santé Animale, Roma, Italy.
- [23] NRC series. 1977. *Nutrient Requirements of Domestic Animals: Nutrient Requirements of Warmwater Fishes*. National Academy of Science, Washington D.C., USA. 76 pp.
- [24] Wu, J. and L. Jan. 1997. Comparison of Nutritive Value of Dietary Protein in *Tilapia aurea*. *J. Fish. S. Taiwan.* 5(2): 55-60.
- [25] Dongmeza, Euloge, Perumal Siddhuraju, George Francis, and Klaus Becker. 2006. “Effects of Dehydrated Methanol Extracts of Moringa (*Moringa Oleifera* Lam.) Leaves and Three of Its Fractions on Growth Performance and Feed Nutrient Assimilation in Nile Tilapia (*Oreochromis Niloticus* (L.))” *Aquaculture* 261(1): 407–22.

## **Food Engineering / Gıda Mühendisliği**

## Gıda Mühendisliğinde Dijitalleşme ve Önemi

*Mesut Emre Çetin, Özlem Çağındı*  
*Manisa Celal Bayar Üniv., Gıda Mühendisliği Bölümü, Manisa, Türkiye*  
*\*İletişimden sorumlu yazar: ozlem.cagindi@cbu.edu.tr*

**Anahtar Kelimeler:** Dijitalleşme, Gıda mühendisliği, endüstri 4.0, plm, sürdürülebilirlik  
**Disiplin:** Gıda Mühendisliği

### Giriş

İmalat şirketleri, son zamanlarda müşterilerden ve tedarikçilerden kaynaklanan çeşitli zorluklarla karşı karşıya kalmaktadırlar. Bu durum değer zincirini doğrudan etkilemektedir (Burger ve ark. 2017). Bu zorlukların üstesinden gelmek için Alman yüksek teknoloji stratejisi “Industrie 4.0” (endüstri 4.0) veya İtalyan kümesi “Fabbrica Intelligente” gibi üretim sistemlerinde yeni teknolojik yol haritaları ve önerilen müdahaleler uygulanmaktadır. Bu çözümler, endüstride hızla ilerleyen bilgi ve iletişim teknolojilerinin devam eden etkisinden kaynaklanan yüksek inovasyon ve ekonomik potansiyeli kullanmayı amaçlamaktadır. Endüstri 4.0, geleceğe yönelik ve oldukça esnek bir sistemdir ve pek çok fırsat sunar. Bu fırsatlara örnek olarak kalite, verimlilik ve rekabet gücünü arttırmak için yeni teknolojilerin tanıtılması ve entegrasyonu verilebilir.

Diğer sektörler nazaran, gıda sektörü insanların hayatında daha önemli bir yere sahiptir. Zira temel besin ihtiyaçlarından farklı tekstür ve tatlara hitap eden tüm gıda ürünlerini üreten bu sektör küresel olarak insanların gıda teminini ve hayatta kalmasını sağlamak amacıyla sahiptir. Bu sektördeki talep değişikliği, müşterilerin tüketim eğiliminin ve hammaddenin temininin değişken olması, üretim hacminin ayarlanması konuları fazlasıyla önem taşımaktadır. Dolayısıyla gıda sektörüne yeni teknolojilerin getirdiği çözümlerin uygulanması elzem bir konu haline gelmiştir. Özellikle, yakın zamanda sektörler tarafından sunulan arzın müşterilerin ne yiyip ne içmek istediklerini belirtmeleri üzerine olmaya başlamasıyla az önce bahsi geçen değişkenliklerin büyüklüğü daha iyi anlaşılmaktadır (Almada-Lobo, 2016).

Bu sorunların altından kalkılabilmesi için atılacak adımlardan bir tanesi üretim aşamasında oluşan problemleri en aza indirmektir. Bunun için üretim esnasında üretimi yapan makineler, depolama sistemleri, yardımcı programlar birbirleri ile bilgi paylaşımında bulunarak otonom şekilde üretim yapabilmeli ve birbirlerini kontrol edebilmelidirler (Anderl ve Reiner, 2015).

### Dijitalleşme

Dijitalleşme veya sayısallaşma, fiziki olarak erişilebilecek olan verileri dijital ortama aktarıp yedeklemek olarak tanımlanmaktadır. Bu verilerin daha sonradan da fiziksel olarak elde edilebilmesi, güvenli şekilde saklanabilmesi, fiziksel hasarlara maruz kalma riskinin olmaması nedeni ile pek çok yönden tercih edilme sebebi olarak kabul edilebilir.

Genel olarak şirketlerin dijitalleşmeye geçiş amacı ise 3 sebeple özetlenebilir:

- Kalite, güvenlik ve düzenleyici kısıtlamalar:** Gıda Güvenliği, kalite mükemmelliği ve düzenleyici kısıtlamalara uyum sağlayabilmek, şirket için en önemli önceliktir. Artan küresel rekabet ve müşteri taleplerinin artması ve zorlaşması ile birlikte teknolojinin hızlı gelişmesi, ürün ve süreçlerin kalitesini arttırmak için şirket üzerindeki baskıları şiddetli hale getirmektedir. Ayrıca, gıda endüstrisi, şirketlerin farklı ülkelerde rekabet edebilmesi için yapılan düzenlemelerin kritik ve önemli bir hale geldiği karmaşık bir sistemdir (Boland ve Mike, 2008).
- Çevresel rekabet gücü:** Piyasa rekabet gücü, küreselleşme ve yerelleştirme ve çevresel sürdürülebilirlik gibi konuları içermektedir. Şirketler, insan ve çevre sağlığına zarar vermemeyi taahhüt ederek faaliyetlerini sürdürmektedirler. Ayrıca, hammadde, enerji ve su fiyatları ciddi şekilde artmakta ve şirketlerin mali giderlerini arttırmaktadır. Şirketler, bu dalgalanmalardan daha az etkilenmek için sürdürülebilirlik uygulamalarını optimize etmek istemektedirler (Taticchi ve Tonelli, 2013).
- Sosyal sürdürülebilirlik:** Sosyal sürdürülebilirlik, şirketler için birincil hedeftir. Şirketlerin faaliyetlerini sürdürdüğü ve kaynaklarını temin ettiği toplumlara yönelik sosyal ve etik sorumlulukların farkındalığı önemli bir konudur. Yapılan anket çalışmalarında şirketler tarafından verilen cevaplardan, şirketlerin “çevresel rekabet konusuna hususi önem verdikleri



açık bir şekilde belli olmaktadır. Bu gerçek şirketlerin bazıları tarafından da doğrulanmıştır (Pinna ve ark., 2016).

Şirketler, dijitalleşmede yol almak için şu konulara daha çok önem vermektedirler;

- Çevresel Sürdürülebilirlik
- Küreselleşme ve yerelleştirme
- Pazar rekabet gücü.

Görüşülen şirketlerin diğer bir ortak amaçları ise şirket değerini artırmak ve piyasada daha rekabetçi olabilmek için tasarım ve üretim süreçlerini dijitalleştirmek olarak belirlendi. Bu hedeflere ulaşabilmek amacıyla izledikleri yol “Gezegende az iz bırakma ve atık azaltma” politikası olarak belirtilmiştir (Tonelli ve ark, 2013).

#### Endüstri 4.0

Tarih boyunca 4 büyük endüstriyel devrim gerçekleşmiştir. Bu devrimlerin getirilerini şu şekilde özetlemek mümkündür ;

1. Endüstriyel devrim ; Su ve buhar gücünü kullanan mekanik sistemlerin kullanılmaya başlanması.
2. Endüstriyel devrim: Elektriğin ve Henry Ford’un tasarladığı üretim bandı tasarımının seri üretimde kullanılmaya başlanması ile üretim hattının geliştirilmesi.
3. Endüstriyel devrim: Günümüzün de içinde bulunduğu, 1970’ler itibari ile başlayan, üretimde dijital teknolojilerin kullanılmaya başlanıp mekanik teknolojilerin devre dışı bırakılması.
4. Endüstriyel devrim: Almanya’da 2011 yılında Hannover fuarında tanıtılan, üretim sürecinde sadece siber fiziksel sistemlerin kullanıldığı, insan faktörünün neredeyse tamamen üretim sürecinin dışına çıkarıldığı, akıllı fabrikalar ile üretime geçiş yapılan atılım (Schwab ve Klaus, 2015).

Günümüzde otomotiv sektörü gibi pek çok sektör, üretim veriminin artırıldığı endüstri 4.0 üretim modeline geçmiş bulunmaktadır. Ancak bazı firmalar henüz yaygın olmayan bu sistem için gerekli olan yatırım maliyetini yüksek bulduğundan geçiş işlemine başlamamıştır. Gıda sektörü de henüz geçiş sürecinde olan sektörler aşamasında bulunmaktadır (Sisca ve ark., 2016).

#### PLM (Ürün Yaşam Döngüsü)

PLM kısaltması, pek çok farklı görüşlere sahip topluluklar tarafından benimsenmiş ve kullanılmıştır. PLM hakkındaki tüm tanımları inceleyen ve özetleyen Terzi şu tanımları ortaya koymuştur ; ‘ *PLM, ürün ve ilgili hizmetler için istenen performansları ve sürdürülebilirliği elde etmek için ürün yaşam döngüsünün farklı aşamalarında aktörler, süreçler ve kuruluşlar arasında ürün verilerinin paylaşıldığı ve bilgi teknolojileri tarafından desteklenen yaşam döngüsü odaklı bir iş modelidir.* ’

Teknolojik bir çözüm olarak PLM, ürün yaşam döngüsünün çeşitli aşamalarında bilgi akışını kolaylaştıran ve doğru zamanda doğru bilgileri sağlamaya çalışan araç ve teknolojilerin birleşimidir (Terzi ve ark., 2010).

PLM çeşitli bilgi ve iletişim teknolojileri ve araçları, platformları ve sistemlerinden oluşur. PLM’nin özellikle ürün yaşam başlangıç fazında özel bir etkisi vardır. PLM çözümleri şu yöntemleri barındıran bilgi sistemlerini içermektedir;

- a) Bilgisayar destekli teknolojiler entegrasyonu,
- b) Ürün veri yönetimi,
- c) Bilgisayarla tümleşik üretim
- d) Konfigürasyon yönetim sistemleri (Flavio ve Demartini, 2016).

Ürün geliştirmeye ait tüm bilgiler, ürün geliştirilmesi sırasında oluşturulan ve kullanılan sistemlerin tanımlanmasını ve standardize edilmesini sağlayabilmek için tek bir veri tabanında toplanmaktadır. PLM sistemleri, firmalar için ürün bilgilerini düzenleyerek yeni ürün geliştirme sürecinde ürünle ilgili bilgilerin oluşturulmasını, çeşitlenmesini, değişimini ve firmaların bu değişimleri yönetmelerine yardımcı olmaktadır (Godoi ve ark., 2016).

PLM sistemlerinin uygulanması, firmaların üretim süreçlerini daha verimli bir şekilde kontrol edebilmelerini ve yönetmelerini sağlayacaktır (Demartini ve ark., 2017). PLM çözümlerini benimseyen firmalar yeni ürün geliştirme süreçlerini düzenli hale getirebilmektedirler. Böylece süreç verimliliği artmakta ve yeni ürün geliştirme süresini ve maliyetini azaltmaktadır. PLM sistemleri, sanal ürün tasarımına dayanan ve firmaların fizibilite analizini hızlandırmasını ve konsept doğrulama ve ürün testi maliyetlerini azaltmasını sağlayan bir platform sunmaktadır (Nee ve ark., 2013). PLM çözümlerini benimseyen firmalar yeni ürün geliştirme sürecinde optimizasyon yeteneğini sürekli olarak geliştirmektedirler. PLM işlevleri, şirketlerin veritabanlarında ürün tasarımlarının yeniden kullanımı veya değiştirilmesi için ürün bilgilerinin korunmasına sağlamakta ve kaynakların daha verimli değerlendirilmesine yardımcı olmaktadır.

PLM çözümünün uygulanmasının başka bir olumlu etkisi süreç yönetimi kabiliyeti üzerinedir. Bu sayede yeni ürün geliştirilmesinde kaynaklardan daha çok tasarruf yapılmakta, AR-GE çalışmaları daha verimli hale gelmektedir

PLM çözümleri, yeni ürün geliştirme departmanının çalışanları arasında iletişimi ve veri paylaşımını kolaylaştıran ve ürünün güncel bilgilerinin paylaşılmasını, yeni ürün geliştirme sürecini ve faaliyetlerinin daha rahat yürütülebilmesini sağlayan bir koordinasyon çözümleri işlevi de görmektedir.

PLM sistemleri, büyük miktarlarda veri ve bilgiyi yönetmek, ürün geliştirme departmanı çalışanları arasında iletişimi ve bilgi alışverişini yönetmek, böylece ürün geliştirme süreçlerinde işbirliğiyle yapılacak çalışmaları desteklemek için tasarlanmıştır. (D. shepherd ve ark., 2011). PLM, yeni ürün geliştirme ve yaşam döngüsü boyunca bilgi odaklı çalışmaları ve ürün bilgi paylaşımını basitleştirmeli, doğru ve hızlı karar alma ve değişiklikler için gerekli tüm veri ve bilgileri sağlamalıdır.

### Gıda Üretiminde Otomasyon ve Sürdürülebilirlik

"Gıda endüstrisi" terimi, gıda ile ilgili tüm üretimleri, hammaddelerin temininden gıda ürününün insanlara arz edilmesine kadar olan tüm olar zincirini kapsayan bir terimdir. Tüm bu süreçlerde sosyal ve çevresel sürdürülebilirlik sorumluluğu olmakla birlikte, sosyal ve çevresel sürdürülebilirlik konusunda bu süreçler içindeki en önemli süreç gıda üretim sürecidir.

Gıda üretim sürecinde, enerji tüketimi, su kullanımı, atık ve emisyon üretiminin yanı sıra gıda üretiminde kullanılan hammadde ve arz edilen ürün fiyatlarının da dengede tutulması ve ürünlerin topluma uygun bir maliyetle arz edilebilmesi gerekmektedir (Akkerman ve ark., 2008).

Bir firmanın üretim sistemlerini optimize etmesi, gıda üretimi açısından verimli süreçlerin geliştirilmesi ve işletilmesi anlamına gelir. Bu süreçlerin verimliliği aşağıdaki yöntemlerle sağlanır (Akkerman ve ark., 2009):

1. Kaynakların dikkatli kullanımının ve yönetiminin sağlanması,
2. Atıkların önemli ölçüde azaltılmasını ve geri dönüştürülmesini sağlanması,
3. Yüksek kaliteli ve uygun fiyatlı ürünlerin üretimini devam ettirilebilmesi.

Gıda üretiminde sürdürülebilirliğin, yüksek verimli üretimin ve kalkınma hedeflerine ulaşmanın yolu otomasyon sistemlerdir. Çünkü otomasyon sistemler, gıda üretim süreçlerinde daha önceden belirlenmiş olan hedeflere yönelik müdahaleleri sağlayan uygun teknolojiyi ve yöntemleri içermektedir. Yüksek doğruluk, güvenilir tekrar, yüksek güvenlik ve hijyen önlemleri gerektiren işlerde, insan işçilerin yerine otomatik araçlar ve prosedürler kullanılır. Özetlendiği gibi çok sayıda önemli faydayı sağlar:

1. Çalışmalar mümkün olan en yüksek verimde gerçekleştirilir.
2. Tüm maliyetler yüksek doğrulukla takip edilebildiği için işletme ekonomisi sıkı bir şekilde düzenlenir.
3. Hata ihtimali pratik olarak ortadan kaldırıldığı için ürün kalitesi önemli ölçüde artar.
4. Güvenli olmayan veya hijyenik olmayan görevleri yerine getirmek için sadece mekanik ekipman kullanıldığı için insanlar tehlikeli işlerden korunmuş olur.
5. Gerekli işgücü, sert fiziksel veya monoton işleri gerçekleştiren iş gücünden, ilgili otomasyon ekipmanını yönetmek için gereken özel becerilerle donatılmış iş gücüne dönüştürülür.

Bu faydalar, çoğunlukla otomasyon teknolojilerinin uygulanması için ana hedef olarak kabul edilen üretim süreçleri ile ilgilidir. Son zamanlarda bilgi işlem ve bilgi teknolojilerinin yaygınlaşmasıyla birlikte, otomatik teknolojilerin süreç tasarımı ve geliştirme alanına genişletilmesinin de önemli faydalar

sağlayabileceği anlaşılmıştır. Bunun asıl sebebi ise, sürdürülebilirlik, esneklik ve küreselleşme gibi modern gereksinimlerin, endüstriyel işlemlerin tasarlanmasında, insanın hesaplama yapma yeteneklerinin üstüne çıkan karmaşık kısıtlamalar eklemesidir (Balsa -Canto ve ark., 2002)

Ürünlerin ve süreçlerin tasarımı, sistematik bilgisayar destekli yöntem ve araçların kullanılmasını gerektiren önemli zorluklar getirir. Bu tür gereksinimlerin tipik bir örneği, bir sürecin enerji gereksinimlerinden kaynaklanan çevresel ve ekonomik etkilerin tanımlanması ve en aza indirilmesi için oldukça karmaşık bir görevdir. Sürecin ekonomik, çevresel ve işletme performansı arasında optimum değiş tokuşları belirlemek için seçenekler, kısıtlamalar ve hedefler şeklinde çok sayıda karar içerir.

Endüstri 4.0 ve PLM çözümlerini uygulayarak dijitalleşmeye geçiş yapmış olan uluslararası boyutta üretim yapan bir İtalyan makarna üreticisine SIEMENS in uyguladığı bir anket çalışması ile dijitalleşmenin bu firma üzerinde yaptığı etkileri ve getiriler göz önüne konulmaya çalışıldı (Tonelli ve ark., 2013).

Bahsi geçen firma, Avrupa kıtasında lider makarna üreticisidir. Aynı zamanda soslar, unlu mamuller, İskandinav ülkelerinde gevrek ekmekleri üreten bir kaliteli ürünler ailesidir. Şirketin ürünleri 100'den fazla ülkede satılmaktadır. Şirketin İtalya'da 14, diğer ülkelerde 28 olmak üzere toplam 42 adet üretim yapan fabrikası bulunmaktadır. Şirketin yıllık toplam ürettiği gıda ürünü miktarı ise 1.800.000 tondur. Şirket farklı ürünlerde farklı üretim tesislerine sahiptir (Mourtzis ve ark., 2016).

SIEMENS tarafından yapılan çalışmada bu şirketin İtalya'da bulunan bir üretim tesisi ele alındı. Araştırmanın bu şirkette yapılma sebepleri ise;

- Şirketin İtalyan pazarında lider konumda olması
- Büyük bir küresel pazar payına sahip olması
- Şirket içinde sürekli iyileştirmelerin gerekmesi
- Şirketin, ürettiği ürünler ve kaliteleri konusunda mükemmel bir durumda olması

Şirketin Ar-Ge departmanına ve şirketin üretim bölgesinden sorumlu yöneticilerine bir anket hazırlanıp sunuldu (Tonelli., 2016). Anketin geliştirilmesinde Siemens endüstri yöneticileri gıda sektörü uzmanları yer aldı. Anketin yapısı, üretim modelinin anketin yapısı, şu 3 bölümden oluşmaktadır:

1. Dış etki faktörleri: eğilimler;
2. İç etki faktörü: etkileri ve fırsatları
3. Çözümler: yetenekler ve teknolojiler.

Bu bölümlere dair sonuçlar, yapılan araştırmanın tasarım ve üretim bölümleri ile sınırlı olduğu göz önünde bulundurularak açıklanmıştır. Bunun sonucunda, her iki evre için de farklı model adımlarının her bir sonucu incelenip analiz edilmiş ve her bir model basamağına ait faktörlerin etkilerinin tespit edilmesi sayesinde çalışma sonucunda endüstri 4.0 ve PLM sistemlerinin bu firmaya yaptığı katkılar tespit edilmiştir.

### **Dış Etki Faktörleri : Eğilimler**

Dış etkiler, üretim ortamını etkileyen üretim zorluklarının rapor edildiği Tablo 1'de gösterildiği gibi şirket dışından gelen zorlukları temsil eder. Bu bölüm gıda sektörünün üretim hattı dışından kaynaklı karşılaştığı zorluklar hakkında bir fikir verir.

Bu zorluklarla genel olarak şu konularda karşılaşılmaktadır: endüstrinin yönelimi ve endüstride meydana gelen önemli değişimler.

Tablo 1. Dış etki faktörleri

Dış Etki Faktörleri: Eğilimler	Açıklama
Çevresel sürdürülebilirlik	Çevresel sürdürülebilirlik, doğal kaynakların doğal rejenerasyonun altında bir oranda tüketilmesi sınırlı emisyon üretilmesi ve ekosistemi bozabilecek faaliyetlerde bulunmamak anlamına gelmektedir (Longori ve Cagliano, 2014).
Sağlık ve zindeliğe odaklanmak	Eğitim, sağlıklı yaşamı hızlandırır. “Bir gezegenin sınırları içinde iyi yaşamayı destekleyen yaşam tarzları gereklidir (Dipiazza ve ark. 2010).
Gıda güvenliği ve kalitede mükemmellik	Gıda sektörü çeşitli değişikliklere yol açmakta ve gıda güvenliğini politika gündeminin ana önceliklerinden biri haline getirmektedir (Lehmann, Reiche ve Schiefer, 2012). Güvenlik, yaralanma veya kayıplardan korunma koşulu olarak tanımlanmaktadır (Mish ve ark 1990). Gıda güvenliğinin güvencesi, gıdanın zararlı olmayacağını garantisidir. Öte yandan kalite mutlak değildir ve üzerinde anlaşılan şartnamelerin yerine getirilmesi olarak tanımlanır (Holleran ve ark, 1999).
Küreselleştirme ve yerelleştirme	Küreselleşme eğilimi, müşterilere ürün sağlama yollarını ve dolayısıyla analiz edilen nesnelere, şirketlerin üretim ağını veya tedarik zincirini değiştirdi (Rudberg ve Olhager, 2003).
Pazar rekabet edilebilirliği	Küresel endüstri, şirketleri yeni üretim stratejileri ve üretim yöntemlerini benimsemeye ve geliştirmeye zorlayan rekabet gücünde artan bir artışla karşı karşıya (Azevedo ve Almeida, 2011).
Hammaddelerin fiyat baskısı	Geçtiğimiz yıl boyunca endüstriyel hammadde fiyatları küresel pazarlarda tüm zamanların en yüksek seviyesine yükselmiştir. Bu hammaddeler üretim sürecine önemli girdiler getirmektedir (Lehmann ve ark, 2012).
Ürün portföyü çeşitlendirme	Kitlesele kişiselleştirme yeni bir eğilimdir. Ürünler kitlesele kişiselleştirme çerçevesinde üretilmekte ve tüketicilerin isimlerinin ürünler üzerinde etiketlenmesi gibi ayrı bir özellik içermektedir (Chen ve ark, 2015).
Düzenleyici kısıtlamalar	Düzenleyici yada tüketici bakış açısına göre kalite; gıdaların güvenli, kontamine olmadığından, hileli olmadığından veya sahtekarlıkla tanıtılmadığından emin olmak için mevcut yasalar uyarınca temel amaç gerekliliklerini ifade eder. Gıda kalitesi ve güvenlik gereklilikleri isteğe veya pazarlığa bağlı değildir (Lehmann ve ark, 2012).
Sosyal sürdürülebilirlik	Sosyal sürdürülebilirlik, gelecek nesillerin yeteneklerinin yanı sıra becerilerin korunmasını ve oluşturulmasını aktif olarak desteklemeyi, sağlığı teşvik etmeyi ve şirket bağlamının içinde ve dışında iyi bir yaşam kalitesine izin veren eşit ve demokratik tedavileri desteklemeyi ifade eder (Longori ve Cagliano, 2014).

### İç Etki Faktörleri ve Etkileri

İç etki faktörleri, üretimi yapan şirketin hedeflerini ve stratejilerini belirtir. Farklı iç etki faktörleri; etkiler ve fırsatlar olarak tanımlanabilir. Etkiler, bölgesel eğilimler tarafından yönlendirilen şirketin, işletme üzerindeki etkisini tanımlar ve bu eğilimlerin şirket stratejisini nasıl etkilediğine dikkat çeker.

Tablo 2 gıda yaşam döngüsü üzerine odaklanmış analizleri ve gıda üretiminde dijitalleşme için atılması gereken adımların hangi aşamalarda olduğunu içermektedir.

Tablo 2. İç etki faktörleri ve Etkileri (Tonelli ve ark., 2017)

İç Etki Faktörleri ve Etkileri	Aşama
Küresel ve standart bir çözümün ve homojen KPI'ların benimsenmesi	Dizayn /Üretim
Düzenleyici kısıtlamalarla uyum	Dizayn / Üretim
İş güvenliğini ve çalışanların zindeliğini sağlamak	Üretim
Kağıtsız fabrika	Dizayn / Üretim
Gezegen izi ve atık azaltma	Dizayn ve üretim
İşlem izlenilebilirliği	Dizayn ve üretim
Maliyeti düşürmek ve üretim performansını arttırmak	Dizayn ve üretim
Kağıtsız fabrika	Dizayn ve üretim

### İç etki faktörleri: Fırsatlar

Bir şirketin iç sürecini tanımlamak ve tanımlanmasını sağlamak için:

1. Şirketin uygulamadan kaynaklanan bir fırsat veya riske değinmesi
2. Bir fırsatı yakalamak veya riski azaltmak için atılan adımlar.

Tablo 3, gıda sektörü için fırsatları göstermektedir. Ayrıca, bu durumda, içerik tasarımı ve üretime odaklanarak ürün yaşam döngüsü aşamaları analiz edilmiştir.

Tablo 3. Gıda Sektörü için Fırsatlar (Tonelli ve ark., 2017)

İç etki faktörleri: Fırsatlar	Aşama
Otomatik veri toplama ve evrak azaltma	Dizayn / Üretim
Ar - Ge, laboratuvar ve üretim arasında sorunsuz işbirliği sağlamak	Dizayn/ Üretim
Tüm süreç boyunca verimli operatör rehberliği sağlamak	Dizayn / Üretim
Küresel şartname yönetimi	Dizayn
Kurumsal düzeyde veri görünürlüğü uygulamak	Dizayn / Üretim
Üretim performansını arttırmak ve en iyi pratikleri paylaşmak	Dizayn / Üretim
İş güvenliği ve çalışanların refahını izlemek	Üretim
Çöp üretimini en aza indirmek	Dizayn / Üretim
Mevcut kaynakların daha iyi kullanımı sayesinde kapasiteyi optimize etmek	Dizayn / Üretim
Cihazların güvenliği ve prosedür takibi	Üretim
Ürünler hakkında tarifler ve kaliteli operatif bilgi gönderimi	Dizayn / Üretim

### Çözümler: Yetenekler ve Teknolojiler

Çözümler, fırsatları gerçekleştirmeyi destekleyen en iyi uygulama, yetenek ve teknolojilerin belirlenmesine olanak tanır. Tablo 4, her çözüm için süreç iyileştirme ve ilgili teknolojiler açısından ilgili açıklamayı göstermektedir.

Tablo 4. Süreç İyileştirmeleri (Tonelli ve ark., 2017)

Fırsatlar	Çözümler	Süreç İyileştirmeleri
Veri toplamayı otomatikleştirme ve evrak azaltma	Büyük veri Analizleri	IIoT
Ar-Ge, laboratuvar ve üretim arasında sorunsuz işbirliği sağlanması	CPPS	Bulut Sistemli İmalat
Süreç boyunca etkin operatör rehberliği sağlama	Hologram (AR,VR)	Tesis personeli sezgisel olarak yönlendirilir ve basitleştirilmiş bir işlem sırası yürütülmesi sağlanır.
Küresel tanımlama yönetimi	CPPS	Bulut Sistemli İmalat
Kurumsal görünürlükte veri görünürlüğü uygulama	Bulut Sistemli İmalat	Büyük Veri Analizleri
		Formül yönetimi
		Kurumsal veri analitiği
		İnsan hatası indirgeme
		Mevzuata uygunluk maliyetini azaltır
		Tesis önceliklerini, kısıtlarını ve çatışmalarını yönetme

### Anahtar ve Temsilci Teknolojiler

Gıda sektörü dijitalleşmesi için seçilen anahtar ve temsilci teknolojiler şunlardır:

- Siber-fiziksel Üretim Sistemleri (CPP'LER)
- Endüstriyel nesnelerin interneti (IIoT)
- Bulut üretimi (CM)
- Büyük veri analitiği
- Hologram

### Siber-fiziksel Üretim Sistemleri (CPPS)

Akıllı üretim gerçekleştirmek için önemli bir teknolojidir ve aşağıda açıklanan teknolojiler ile yakın bir ilişki içinde incelenmektedir:

- Tak ve üret: Bu kavram, ürün merkezli bir yaklaşımı takip eder. Ürünün örnekleri kendi üretimini yönlendirir ve bu yüzden merkezi koordinasyona gerek yoktur. Üretim sistemleri, kendilerini yapılandırabilen ve bu seviyede sadece en az mühendislik çabası gerektiren akıllı üretim birimlerinden oluşur.
- Akıllı ürünler: Endüstri 4.0'ın arkasındaki temel fikirlerden biri, veri toplama -iletişim kurma ve birbirleriyle ağ kurma yeteneğine sahip gömülü sistemlerle ürün ve bileşenleri düzenlemektir. Bu amaçla, gömülü sistemlerin haricinde çipler ve mikro işlemciler geliştirmek gereklidir. Bu bileşenler, Makine ve üretim ekipmanının çalışmasını hızlandırılarak verilerin tek bir yerde depolanmasına izin verir. Böylece manuel yapılandırma adımlarına gerek kalmaz.
- Çalışma sürecinden elde edilen veriler bileşen üzerinde saklanır. Böylece bu veriler ile ürünü geliştirir veya verilerin bakım için kullanılması sağlanır.

### Endüstriyel Nesnelerin İnterneti (IIoT)

Endüstriyel nesnelerin interneti, üretim yapan makinelerin kendi aralarında kurduğu iletişim ağını belirtir. Bu aynı zamanda, otomasyonun sistematik olarak genişletilmesi ve makinelerin üretim alanında

birbirleri ile kurduğu iletişimden yola çıkarak bunun iyileştirilmesini sağlayacak veriyi de elde edilmesini sağlar. Bu veriler aynı zamanda kullanıcılara olayları ve üretim faaliyetlerini anlık ve geriye dönük izlemek için yardımcı olur. Ayrıca kullanıcılara cihazlarını uzaktan izleme ve kontrol etme fırsatı verir (Almada-Lobo 2016).

### **Bulut Sistemli Üretim**

Üretim alanına uygulanan bulut bilgi işlem teknolojisi. Üretim verimliliğini artıran, ürün yaşam döngüsü maliyetlerini azaltan ve buna bağlı olarak en uygun kaynakların yüklenmesine izin veren geçici veya yeniden yapılandırılabilir üretim hatları oluşturmak için, çeşitlendirilmiş ve dağıtılmış üretim kaynaklarının tek bir yerde depolanabildiği ve tüm üretim sistemlerinden erişiminin sağlanabilmesine olanak veren bir üretim sistemidir.

### **Büyük Veri Analitiği**

Büyük veri genellikle geniş bir yelpazesi, karmaşık yapısı ve büyüklüğü nedeniyle geleneksel veri işlem yöntemleri tarafından kullanılması uygun olmayan bir veri kümesi anlamına gelir. Bu nedenle, analiz, yakalama, veri küratörlüğü arama, paylaşım, depolama, aktarma, görselleştirme ve bilgi gizliliği gibi teknik ve özel sistemler ve metodolojiler, tahmine dayalı analitik yapmak, verilerden değer elde etmek ve nadiren belirli bir değere ulaşmak için gereklidir. Akıllı Üretim'in gerçekleştirilmesi, ürün geliştirme ve üretim sistem mühendisliği süreçlerinden kaynaklanan çeşitli verilerin tahmin ve modelleme için kullanılacak imalat sahalarına etkin bir şekilde görselleştirilmesini, analiz edilmesini ve paylaşılmasını gerektirir (Niesen ve ark. 2016).

### **Hologram**

Hologram, VR (Sanal Gerçeklik) ve AR (Artırılmış Gerçeklik) ile birlikte görselleştirme yöntemlerinden biridir. Arttırılmış gerçeklik temelli sistemler sayesinde parça bir depoda kullanılacak parça seçimi, hareketli cihazlara onarım talimatı gönderebilmek gibi çeşitli işlemler yapılabilir. Veya insan faktörünün devreye girmesi gereken durumlar için sanal bir uygulama denemesi yapılabilir. Teşhis, öğrenme, montaj gibi çeşitli adımların da gerçek cihazlar kullanılması ve karşılaşılabilecek sorular sonucu kayıplar oluşması riskine gerek kalmadan atılabileceği rapor edilmiştir. VR ve AR'nin ana uygulamaları ise robotik, fabrika yerleşimi ve bakımdır (Mourtzis ve ark., 2016).

### **Sonuç**

Endüstri 4.0 ve dijitalleşme, gıda sektörü için henüz yeni bir sistemdir. Ve daha çok araştırma ve çalışma yapılması gerektiği açıktır. Ancak Siemens'in pilot bölgeye uygulayarak bize ispat ettiği gibi Endüstri 4.0 ve dijitalleşmenin gıda sektörüne pek çok katkısı olacaktır. Küresel çaptaki tüm gıda firmalarının mücadele etmesi gereken düzenli hammadde temini sorunu, müşteri odaklı sorunlar, çevreye ve ürün arzı yapılan toplumlara olan etik sorumluluk gibi konular ile daha kolay başa çıkılması için gerekli olan bu sistemin uygulanabilirliği açıktır.

### **Kaynakça**

- [1] Akkerman R, and Van Donk DP. Development and application of a decision support tool for reduction of product losses in the food processing industry. *Journal of Cleaner Production*. 2008 ; 16, 335 –342.
- [2] Akkerman R, Wang Y, and Grunow M. MILP approaches to sustainable production and distribution of meal elements', *International Conference on Computers and Industrial Engineering, CIE .2009; art. No: 5223667, 973 –978.*
- [3] Almada-Lobo F. The Industry 4.0 Revolution and the Future of Manufacturing Execution Systems (MES). *Journal of Innovation Management*. 2016; 3(4):17.
- [4] Anderl R. Industrie 4.0 -Technological Approaches, Use Cases, and Implementation. *Automatisierungstechnik*. 2015; 63(10):753–65.
- [5] Azevedo A and Almeida. Factory Templates for Digital Factories Framework. *Robotics and Computer-Integrated Manufacturing*. 2011; 27(4):755– 71.

- [6] Balsa-Canto E, Banga JR and Alonso AA. A novel, efficient and reliable method for thermal process design and optimization. Part II : applications ', *Journal of Food Engineering*, 2002 ; 52, 235 –247.
- [7] Boland M. Innovation in the Food Industry: Personalised Nutrition and Mass Customisation. *Innovation: Management, Policy and Practice*. 2008; 10(1):53–60.
- [8] Burger N, Demartini M, Tonelli F, Bodendorf F, and Testa C. Investigating Flexibility as a Performance Dimension of a Manufacturing Value Modeling Methodology (MVMM): A Framework for Identifying Flexibility Types in Manufacturing Systems. *Procedia CIRP*; 2017.
- [9] Claudia P, Ramundo L, et al. Additive Manufacturing Applications within Food Industry: An Actual Overview and Future Opportunities. *Scopus* 6; 2016.
- [10] Danfang C et al. Direct Digital Manufacturing: Definition, Evolution, and Sustainability Implications. *Journal of Cleaner Production*. 2015; 107:615–25.
- [11] Demartini M, Tonelli F, Damiani L, and Revetria R. Digitalization of Manufacturing Execution Systems: The Core Technology for Realizing Future Smart Factories. In XXII edition of the Summer School Francesco Turco; 2017.
- [12] Godoi Fernanda C, Prakash S, and Bhandari BR. 3d Printing Technologies Applied for Food Design: Status and Prospects. *Journal of Food Engineering*. 2016; 179:44–54.
- [13] He Y, Keung Lai K, Sun H, Chen H, The impact of supplier integration on customer integration and new product performance: the mediating role of manufacturing flexibility under trust theory. *Int. J. Prod. Econ*. 2014; 147:260–270.
- [14] Holleran E, Bredahl ME, and Zaibet L. Private Incentives for Adopting Food Safety and Quality Assurance. *Food Policy*. 1999; 24(6):669–83.
- [15] Lehmann R J, Reiche R, and Schiefer G. Future Internet and the Agri-Food Sector: State-of-the-Art in Literature and Research. *Computers and Electronics in Agriculture*. 2012; 89:158–74. Retrieved (<http://dx.doi.org/10.1016/j.compag.2012.09.005>).
- [16] Longori A and Cagliano R. Environmental and Social Sustainability Priorities. *International Journal of Operations & Production Management*. 2014; 12(4):564–78.
- [17] Mish F, Gilman EW, Lowe JG, McHenry RD, and Pease RW. Webster's Ninth New Collegiate Dictionary; 1990.
- [18] Mourtzis D, Vlachou E, Giannoulis C, Siganakis E, and Zogopoulos V. Applications for Frugal Product Customization and Design of Manufacturing Networks. *Procedia CIRP*. 2016; 52:228–33. Retrieved (<http://dx.doi.org/10.1016/j.procir.2016.07.055>).
- [19] Nee AYC, and Ong SK, Virtual and Augmented Reality Applications in Manufacturing. *IFAC*. Retrieved (<http://dx.doi.org/10.3182/20130619-3-RU3018.00637>); 2013.
- [20] Niesen T, Houy C, Fettke P, and Loos P. Towards an Integrative Big Data Analysis Framework for Data- Driven Risk Management in Industry 4.0. 49th Hawaii International Conference on System Sciences (HICSS) 5065–74; 2016.
- [21] Rudberg M, and Olhager J. Manufacturing Networks and Supply Chains: An Operations Strategy Perspective. *Omega*. 2003; 31(1):29–39.
- [22] Schuh G, Anderl R, Hompel GJ, Wahister MW(Hrsg): *Industrie 4.0 Maturity Index. Die digitale Transformation von Unternehmen gestolten (acatech STUDIE)*, München: Herbert Utz Veriag; 2017.
- [23] Schwab K, *The Fourth Industrial Revolution: what it means, how to respond*. World Economic Forum. Retrieved; 2017.
- [24] Shepherd D, Patzelt H, Wolfe M. Moving forward from project failure: negative emotions, affective commitment, and learning from the experience, *Acad. Manag. J*. 2011; 54, 1229–1259, <http://dx.doi.org/10.5465/amj.2010.0102>.
- [25] Sisca FG, Angioletti CM, Taisch M, and Colwill JA. Additive Manufacturing as a Strategic Tool for Industrial Competition; 2016.
- [26] Taticchi P, Tonelli F, and Pasqualino R. Performance Measurement of Sustainable Supply Chains: A Literature Review and a Research Agenda. *International Journal of Productivity and Performance Management*. 2013; 62(8):782–804 (Retrieved <http://0->



[www.emeraldinsight.com.pugwash.lib](http://www.emeraldinsight.com.pugwash.lib).

[warwick.ac.uk/journals.htm?issn=17410401&volume=62&issue=8&articleid=17098324&show=html%5Cnhttp://www.emeraldinsight.com/10.1108/IJPPM-03-2013-0037](http://warwick.ac.uk/journals.htm?issn=17410401&volume=62&issue=8&articleid=17098324&show=html%5Cnhttp://www.emeraldinsight.com/10.1108/IJPPM-03-2013-0037)).

- [27] Tonelli F, Demartini M, Loelo A, and Testa C. A Novel Methodology for Manufacturing Firms Value Modeling and Mapping to Improve Operational Performance in the Industry 4.0 Era; 2016.
- [28] Tonelli F. Industrial Sustainability: Challenges, Perspectives, Actions. *International Journal of Business Innovation and Research*.2013; 7(2):143–63.

## Badem Sütü Üretimi ve Gıdalarda Kullanım Olanakları

Feyza Nur Yıldırım\*, Sağlık Bilimleri Üniv., Beslenme ve Diyetetik Bölümü, İstanbul, Türkiye  
Sibel Bölek, Sağlık Bilimleri Üniv., Gıda Teknolojisi Ana Bilim Dalı, İstanbul, Türkiye  
\*İletişimden sorumlu yazar: feyza.yildirim@outlook.com

**Anahtar Kelimeler:** Fonksiyonel gıda, badem sütü, Çölyak, Laktoz intoleransı  
**Disiplin:** Gıda Mühendisliği

### Özet

Bireylerin yaşam boyu tükettiği süt, besin öğelerini yeterli miktarda ihtiva eden önemli bir besin kaynağıdır. Dünya’da birçok süt çeşidi olup bunlardan biri içerdiği diyet lifi, yağ asitleri, B grubu vitaminler, A ve E vitaminleri ile bitkisel bazlı fonksiyonel gıda olan badem sütüdür. Badem sütü, bademlerin suyla birlikte ince öğütülerek üretilebilen, kremli dokusu ve çatlak tadı olan bir bitki sütüdür. Tartışmasız derecede besleyicidir, inek sütünden farklı olarak doymuş yağ ve laktoz içermez. Ortaçağ’da Avrupa tariflerinde sıkça kullanılmış aynı zamanda Orta Doğu’da da daima popüler bir içecek olmuştur. Geçmişteki popülerliğini kuru bademlerin kolay depolanmasına borçludur. Modern blender ile bileşimi daha da kolaylaşmıştır, harmanlanmış bademden diğerlerine göre daha ince kıvamlı bir süt elde edilir.

### Badem Sütü

Badem sütü gluten, laktoz, doymuş yağ ve kolesterol içermez (Vanga vd., 2018). Bununla beraber inek sütüyle aynı yoğunluğa sahip olduğu için aynı amaçlar için kullanılabilir. Aynı zamanda düşük kalorili olan bu içecek (50 kalori/1 su bardağı) E vitamini içeriğiyle; bir bireyin günlük ihtiyacından fazlasını karşılar ve bu da kansere, yaşlanmaya ve cilt hastalıklarına karşı savaşacak bir antioksidan desteğidir. Buna ek olarak E vitamininin yanı sıra A ve D vitaminleri, proteinler, omega-6, çinko, kalsiyum, demir, magnezyum ve potasyum içerir. Laktoz intoleransı ve çölyak hastalığı bulunan bireyler için iyi bir alternatif olan badem sütü diğer taraftan bitkisel bir gıda olması sebebiyle vegan/vejetaryen bireyler için de değerli bir kaynaktır. Probiyotik özelliği bulunan badem sütü, yapılan bir çalışmada standart yoğurtlara alternatif fermente ürün elde edilmesinde başarıyla kullanılmıştır (Bernat vd., 2015). Yeni fonksiyonel gıda üretimini amaçlayan bir çalışmada probiyotik yoğurtlar badem sütü ile zenginleştirilmiş ve yapılan analizlerin sonucunda, badem sütü ilavesinin probiyotik yoğurdun fiziko-kimyasal özellikleri üzerine olumsuz bir etkisi olmadığı saptanmıştır (Ersan vd., 2019).

### İnek Sütü & Badem Sütü & Soya Sütü Kıyaslaması (Bernat vd., 2015)

- Badem sütünün enerji içeriği/ kalorisi, inek (az yağlı süt) ve soya sütünden daha azdır.
- Badem sütünün kalsiyum içeriği, inek sütünden daha düşüktür ancak soya sütünden daha yüksektir.
- Badem sütü inek sütünün aksine kolesterol ve doymuş yağ içermez.
- Laktoz içermez, intolerantları tarafından kullanılabilir.

Badem sütü günlük kalsiyum ihtiyacının %30’u, E vitamininin %125’ini ve D vitamininin %25’ini karşılayarak osteoporoz ve artrit riskini düşürür. Bitkisel bir ürün olması sebebiyle kolesterol ve doymuş yağ içermez ve elzem yağ asitlerince zengindir. Böylece kan basıncını dengeler ve kalp rahatsızlığı riskini düşürür. Yüksek miktarda çözülebilir lif içeren badem sütü bağırsak duvarlarını ve kolonu korur, şeker emilimini dengeler ve kolesterol seviyelerini dengede tutar. İçindeki B2 vitamini saçları ve tırnakları güçlendirir. Cildi nemlendirir. Kasları güçlendirir (Torluoğlu, 2017). Şekersiz badem sütü düşük karbonhidratlı bir içecektir (%0,6 yani 1.5 g/fincan) kan şekeri seviyesini yükseltmez. Ayrıca karbonhidrat içeriğine göre yağ ve protein açısından da zengin olduğundan diyabet hastaları için iyi bir seçenektir. İyi kolesterol seviyesini geliştirirken, kötüyü düşürür.

Badem guatrojenik bir yiyecektir. Barındırdığı kimyasallar sebebiyle tiroide olumsuz etki edebilir. İnek sütü yerine soya veya badem sütü içmek bebekler için faydalı değildir. Badem sütü bir bebeğin ihtiyacı olan besinleri vermez. Bunun yanı sıra Amerikan Diyetetik Birliği’nin (ADA) bulgularına göre badem sütü içen bebeklerde otoimmün tiroid hastalığı görülmüştür. İçeriğindeki kimyasallar bebek vücudunda yetişkinlere oranla daha fazla guatr birikimine yol açabilir.

Yapılan bir çalışmada çok fazla badem sütü içeren besin tükettikleri düşünülen 3 çocukta disüri (idrar zorluğu), hematüri (kanlı idrar) veya böbrek taşı ile hiperoksalürisi bulunuyor. Bu araştırma yaygın kullanılan süt alternatifi bitkisel ürünlerin oksalat miktarına yönelik. Piyasadaki çoğu badem sütlü ürünün yüksek miktarda diyet oksalat bulundurduğu görülüyor. Badem sütü ve bundan elde edilen ürünlerin kesilmesinin ardından söz konusu rahatsızlıklar çözülüyor. Bundan dolayı, çocuk sağlığı uzmanları badem sütü ve adı geçenlerin arasındaki olası bağın farkında olmalılar. Araştırmada gözlemlenen hastalar az sayıda olsa da bu çocukların önceden çok sağlıklı olduğu ve badem sütünün kesilmesinden sonra bahsedilen sorunların tekrar meydana çıkmadığına dikkat çekiliyor (Ellis vd., 2015).

Badem sütü ve bundan elde edilen yan ürünler marketlerde yaygın bir şekilde bulunur. Türk hastaların yorumlarına bakıldığında doktorlarının sıklıkla badem sütü önerdikleri görülüyor. Saklama koşullarına dayanıklılığı özellikle pazarı canlı tutan etmenlerden.

Badem sütü üretimiyle alakalı yapılmış bir diğer çalışmada ham badem sütü 350 MPa basınç ve 85 °C ultra yüksek basınçlı homojenizasyon tekniği kullanılarak üretilmiştir ve bu tekniğin gıdadaki mikroorganizmaları ortadan kaldırdığı bilinir ve uzun süreli tüketim gıdaları hazırlanırken kullanılır (Briviba vd., 2016).

Bu uygulamadan sonra;

- Badem sütünde B1 ve B2 vitamin değerleri değişmeden kalıyor.
- Protein izlerini takip etmede kullanılan antijen özelliği neredeyse tamamen kayboluyor.
- Açığa çıkmış serbest sülfhidrillerde düşüş oluyor.
- Ultra yüksek basınçlı homojenizasyon tekniği (350 Mpa, 85°C) vitamin değerlerini değiştirmiyor.
- Sitotoksik ve genotoksik etki gerçekleşmiyor.
- Bağırsak hücrelerini demire karşı koruyan antigenotoksik kabiliyetler yapay ortamda hamıyla aynı miktarda DNA hasarına yol açıyor.

Piyasadaki sağlık vaat eden ürün talebini karşılamak için badem ve yararlı bakterilerin (probiyotikler) özelliklerini birleştiren bir badem sütü elde edilmesi amaçlanmış olan yapılmış bir başka çalışmada ise *Lactobacillus reuteri* ve *Streptococcus thermophilus* bakterileri kullanılmış, merkezi karma tasarım ve yanıt yüzey yönteminden yararlanılmıştır.

Çalışma süresince glukoz, fruktoz, inülin ve başlangıç yemleri bakterilerin çıktı ürününde yüksek hayatta kalma oranı tutturabilmeleri için en iyi duruma getiriliyor. En iyi formüleleştirme fizyokimyasal olarak 28 günlük soğuk depolama boyunca karakterize ediliyor. Yapay ortamdaki sindirim ve protein parçalanması gözleniyor. Elde edilen ürün 28 günün sonunda yüksek miktarda yararlı bakteri bulunduruyor (>107 koloni oluşturabilen birim/mL).

- Glukozun ana besin olarak kullanıldığı ve manitolün *L. Reuteri* tarafından üretildiği tespit edildi.
- Mayalama sürecinde viskozite arttı, cıvık jel kıvamında ve fiziksel özellikleri kolayca değiştirilemeyen bir ürün elde edildi.
- Yapay ortamdaki sindirim sırasında yararlı bakteriler %51 oranında hayatta kaldı, kesin olarak inülin varlığına bağlıyoruz bu da geliştirilen ürünün tüketiminin sağlığa olumlu etkisini artıracaktır.

Badem sütü evde de çok kolay elde edilen bir besin olmakla beraber gerekli malzemeleri sadece çiğ badem, biraz su, tuz ve şeker. Bademler en az 8 saat suda bekletilir ve ardından süzülüp sudan geçirilir. 3 bardak su ve suda bekletilmiş bademler robottan geçirilir. 10 dakika karıştırıp robotun hızı ara sıra değiştirilir (3 dakika düşük hızda, 3 dakika yüksek hızda gibi). Karışım beyaz bir sıvı halini alınca içine biraz bal veya şeker eklenir, bir tutam da tuz. Sonra tüm karışım bir bez yardımıyla süzülür ve böylece badem sütü eldesi gerçekleşir (Kundu vd., 2018).

### Sonuç

Yapılan araştırmaların büyük çoğunluğu badem sütünün günlük tüketim gıdası olarak fonksiyonel görebileceğini gösteriyor. Ancak bu bitkisel sütün ev koşullarında elde edilme işlemi de oldukça kolay olduğu ve raf ömrü uzatılırken bazı özellikleri kaybedildiği için piyasadaki ürünler tercih edilmeyebilir.

Bununla beraber tüketilirken guatrojenik etkisi dolayısıyla dikkatli olunmalı ve küçük yaş grubu bireylerde tüketimine özel olarak dikkat edilmelidir.

#### Kaynakça

- [1] Abi. “Almond Milk Nutrition - What You Need to Know.” Almond Milk, 2013, [almondmilk.net/almond-milk-nutrition/](http://almondmilk.net/almond-milk-nutrition/)
- [2] Almond Milk: Benefits, Side Effects, Recipes, Nutrition Facts, [www.seedguides.info/almond-milk/](http://www.seedguides.info/almond-milk/).
- [3] Arnarson, PhD Atli. “Seven benefits of almond milk.” Medical News Today, MediLexicon International, 1 Aug. 2017, [www.medicalnewstoday.com/articles/318612.php](http://www.medicalnewstoday.com/articles/318612.php).
- [4] Bernat, Neus, et al., 2014. Development of a non-dairy probiotic fermented product based on almond milk and inulin. <https://doi.org/10.1177/1082013214543705>
- [5] Brady, Krissy. “11 Benefits of Almond Milk You Didn't Know About.” Lifehack, Lifehack, 5 May 2017. [www.lifehack.org/articles/lifestyle/benefits-almond-milk.html](http://www.lifehack.org/articles/lifestyle/benefits-almond-milk.html).
- [6] Briviba, Karlis, et al., 2016. Ultra high-pressure homogenization of almond milk: physicochemical and physiological effects. <https://doi.org/10.1016/j.foodchem.2015.06.063>
- [7] Ellis, Demetrius and Jessica Lieb., 2015. Hyperoxaluria and Genitourinary Disorders in Children Ingesting Almond Milk Products. <https://doi.org/10.1016/j.jpeds.2015.08.029>
- [8] Ersan, L. Y., & Topçuoğlu, E., 2019. Badem Sütü ile Zenginleştirilmiş Probiyotik Yoğurtların Mikrobiyolojik ve Bazı Fiziko-Kimyasal Özellikleri <https://dergipark.org.tr/tr/download/article-file/866422>
- [9] Kundu, P., Dhankhar, J., & Sharma, A., 2018. Development of non-dairy milk alternative using soymilk and almond milk. doi: <http://dx.doi.org/10.12944/CRNFSJ.6.1.23>
- [10] Torluoğlu, Melis. “Almond Milk.” The Journal of Global Health, Sept. 2017, p. 122.
- [11] Vanga, S. K., & Raghavan, V., 2018. How well do plant-based alternatives fare nutritionally compared to cow’s milk? <https://doi.org/10.1007/s113197-017-2915-y>

## **Information Technologies / Bilgi Teknolojileri**

## Implementation and Evaluation of Distributed Algorithms in Peer-to-Peer and Multi-hop Smartphone Networks

*Malath T. Nejres\**, Ege Univ., International Computer Institute, Information Technologies, İzmir, Turkey

*Vahid Akram*, Ege Univ., International Computer Institute, İzmir, Turkey

\*Corresponding author: [malath.nejres@gmail.com](mailto:malath.nejres@gmail.com)

**Keywords:** Distributed systems, distributed algorithms, peer-to-peer networks (P2P), leader election, Minimum Spanning Tree (MST)

**Discipline:** Computer Science and Engineering, Information Technologies

### Abstract

Nowadays, the increasing prevalence and lower costs of smartphones, coupled with support for rapidly evolving operating systems that can communicate directly between devices at close range, have reduced costs and made it easier to set up peer-to-peer networks. Smartphones have many communication hardware such as Bluetooth, Wi-Fi, and 3G, there exist many standard applications that use these communications hardware. Local peer-to-peer connections between smartphones can be used as a distributed system infrastructure for the implementation and evaluation of distributed algorithms.

In this study, a communication and messaging infrastructure will be developed for the implementation and evaluation of distributed algorithms in peer-to-peer and multi-hop smartphone networks. The aim of this study is to develop a software library based on Java that uses existing peer-to-peer smartphone communication services to efficiently support tasks such as communication, synchronization and event sequencing. With this developed library, it can be faster and easier to implement and evaluate various distributed algorithms, such as leader election, spanning tree creation, synchronization, routing and clustering in peer-to-peer networks of smartphones.

### Introduction

Distributed systems consist of a set of processors located in different locations and cooperating with each other to achieve a common goal. In distributed systems, each processor has its own memory. The communication and interaction between these processors can happen through messages passing.

Due to the high cost, spatial constraints and resource limits of central systems, they are not used in many applications. In recent years, the increase in network technology speed has significantly reduced the data transmission process between processors. Therefore, the application and usage of distributed systems is increasing day by day. Programs implemented in distributed systems are used in many fields such as economics, science and automation.

On the other hand, the developments of mobile phone technologies in recent years have significantly increased the memory and processing power of these devices. Today, smart mobile phones support various communication tools such as Bluetooth, Wi-Fi and 3G. The powerful processor and various communication tools of these devices have turned them into an infrastructure candidate suitable for distributed systems.

In this study, a communication and messaging infrastructure will be developed for the implementation and evaluation of distributed algorithms in peer-to-peer and multi-hop smartphone networks. The aim of this study is to develop a software library based on Java that uses existing peer-to-peer smartphone communication services to efficiently support tasks such as communication, synchronization and event sequencing. With this developed library, it can be faster and easier to implement and evaluate various distributed algorithms, such as leader election, spanning tree creation, synchronization, routing and clustering in peer-to-peer networks of smartphones.

### Related Works

Most smartphone communication leverages one-hop radio links to cell towers or Wi-Fi access points. In recent years, the major smartphone operating systems have included increasingly stable and useful support for local peer-to-peer communication that allows a device to talk directly to a nearby device (using local radio broadcast) while avoiding cellular and Wi-Fi infrastructure. The ability to create these local links, combined with the ubiquity of smartphones, enables scenarios in which large groups of nearby smartphone users run applications that create peer-to-peer meshes supporting

infrastructure-free networking. Developing useful applications for this smartphone peer-to-peer setting requires distributed algorithms that can provide global reliability and efficiency guarantees on top of an unpredictable collection of local links. The models that describe this emerging setting are different from existing models that new algorithms and analysis techniques are required. Newport [1] addressed this need by describing and analyzing new algorithms for the gossip problem in the mobile telephone model. This problem assumes a subset of nodes starts with messages (also called tokens). The goal is to spread these messages to the entire network.

The mobile telephone model abstracts the basic scan and-connect dynamics of the Multi peer framework as follows. Time proceeds in synchronous rounds. In each round, a connected graph describes the underlying network topology for that round. At the beginning of each round, each device (also called a node) learns its neighbors in the topology graph (e.g., as the result of a scan). Each device can then attempt to initiate a connection with a neighbor. Each node can support at most one connection—so if multiple nodes attempt to connect with the same target, only one connection will succeed. If two nodes connect, they can perform a bounded amount of reliable communication before the round ends. In recent study of Newport [2] he parameterized the mobile telephone model with a tag length  $b \geq 0$ . At the beginning of each round, each node can choose a tag consisting of  $b$  bits to advertise. When performing a scan, each node learns both the ids and chosen tags of its neighbors (where  $b = 0$  means there are no tags). These tags can change from round to round. They also parameterized the model with a stability factor  $\tau \geq 1$ . The underlying network topology must stay stable for at least  $\tau$  rounds between changes. For  $\tau=1$ , for example, the network topology can change completely in every round, while for  $\tau = \infty$ , the topology never changes. Newport focused in his study on describing and analyzing new provably correct and efficient leader election algorithms that can be implemented and executed on top of existing smartphone peer-to-peer services. These algorithms provide a key primitive that supports the development of more sophisticated distributed systems by simplifying tasks such as event ordering, agreement, and synchronization. He studied leader election algorithms that require no advance knowledge of a stability factor  $\tau$ , and can gracefully adapt to whatever level of stability they encounter in an execution. The leader election problem in the mobile telephone model assumes that each device starts with a unique id (UID), and requires the devices to stabilize to the same UID as the leader. Newport studied how many rounds are required to reach this stabilization point with high probability in the network size.

Zamora et al. [3] presented a heuristic-based pairwise gossip algorithm, which will calibrate smartphone-based pressure sensors with respect to fixed weather stations as referential ground truth. Similar to how weather instruments are calibrated and maintained, smartphone-based data should undergo similar data correction processes to yield reliable synoptic weather data. Therefore, they investigated how to correct or adjust smartphone-based environmental data even when the device is normally used as a smartphone. Using commercial weather instruments and built-in smartphone sensors, the device-based measurement is adjusted with a heuristic-based pairwise gossip algorithm. The contribution of their study is the formulation of a heuristic-based pairwise gossip algorithm that will adjust pressure values as measured by the embedded sensors in the smartphone-based on normal usage. A limitation of this method is that the smartphone requires being located nearby a weather station at present.

By using P2P network as a domain, Alexandre De Masi [4] proposed LoadIoT, a peer-to-peer load balancing scheme that can distribute tasks onto cluster of smartphones in the IoT world he called this mobile far-edge computing for the IoT world, and then he developed an android-based load-balancing application to implement and evaluate this concept. The proposed LoadIoT scheme employs a publish-subscribe message exchange pattern over a peer-to-peer (P2P) network. The exchange of information between the different entities is one the higher concern in this study.

Nowadays, many smartphones use android as a main operating system because Google has made it easy for developers to create Android applications. Android Studio is also provided by Google as an Android Development Tools (ADT). The ADT gives developers access to the AVD, an emulator configuration that models an actual device (smartphone) by defining hardware and software options to be emulated by the Android Emulator. The problem is that the Android emulator does not support P2P communication between instances of the Android Virtual Device (AVD). Since many new Android smartphones support Near Field Communication (NFC) and the Android SDK provides an NFC API that can be used to develop NFC applications that conduct peer-to-peer (P2P) data exchange, Doug

Serfass and Kenji Yoshigoe [5] created JNFC by using the JavaMail API to emulate the functionality of the Android NFC P2P API. The purpose is to prove that JNFC and the Android AVD are a platform for NFC and WSN research.

### Communication systems

Three types of communication systems can be used for implementing distributed algorithms. Wi-Fi, Bluetooth and P2P. The best communication technologies to use is Wi-Fi, 3G communication is discarded because the energy consumption of 3G communication on Android based smart devices is higher than Wi-Fi for the same amount of data Kalic et al. [6].

#### WiFi-Based Infrastructure

To implement the distributed algorithm based on Wi-Fi, we have developed an Android program that solves one of the problems of distributed systems which is the leader election problem. The program was written in Java for the Android studio platform. We have made a java class called "**WiFiLeaderElection**" that includes some functions for broadcasting messages, receiving messages and function for starting the leader election process. We can use this class as a java library to be invoked whenever needed.

For end-to-end data transmission, we have used IP with UDP socket (User Datagram Protocol). Despite of UDP lacks many advantages that founded in TCP like reliability, in-order segment delivery, connection-oriented and retransmission of messages, but UDP is the best choice because it offers a small header size compare to TCP and can blast away as fast as desired and also it is simple (no connection state at sender and receiver) [7]. Furthermore, because the UDP is a connectionless protocol, a broadcast message is possible.

The method in "**WiFiLeaderElection**" class that was used for electing a leader amongst a number of nodes (devices) depends on the node's id. The method can be abstracted by the following steps:

1. When a node starts the leader election process, it broadcasts an election message contains its id to the other nodes on the network.
2. When a receiver node receives a broadcast message, it will examine the id in the received message with its own id. Then, if the received id is smaller than its own id, it will send Ok message to the sender node and restart the election process with its own id. Else, if the received id is greater than its own id, the receiver node will remain idle and wait for a message from the leader node.
3. When the node that started the leader election process receives an Ok message, it will remain idle and wait for a message from the leader node.
4. When a node starts the leader election process and sends its own id, it will wait for a specific amount of time. If no response message is received (this means, it is the node with the greatest id), then it will send back the leader message with its own id to the other nodes on the network.

By using the "**WiFiLeaderElection**" class, we can build a program that implements distributed systems and solves the leader election problem. After running the program in all devices and start the leader election process, one node will be chosen as leader and the leader id will be sent to all nodes on the network.

### Implementation of distributed algorithms

The use of distributed systems offers many benefits such as horizontal scalability, fault tolerance, and low latency. Horizontal scalability means adding more computers rather than upgrading the hardware of a single one. Fault tolerance means that the system generally doesn't experience any disruptions if a single machine fails. The implementation of distributed systems overcomes many issues by allowing different machines (nodes) to communicate and work together through distributed algorithms to accomplish common goals. Regarding this aspect, we have developed an android-based mobile phone application that implements the distributed algorithm in peer-to-peer networks. The application was written in java for the Android studio platform and solve one of the distributed algorithms problems, which is the leader election problem. Two types of communication systems were used in this application to implement the distributed algorithms, which are Wi-Fi and Bluetooth. In this study, we will present the implementation of the Wi-Fi based Infrastructure. When the user open the application, he/she will select which communication system is to be used in order to implement the distributed algorithms like in Figure 1.



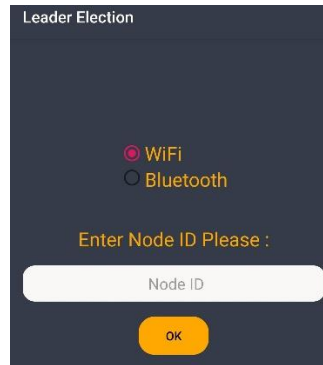


Figure 32. Selection of the preferred communication system.

Once the Wi-Fi is selected by the user in the interface shown in Figure 1, the Wi-Fi device can be used to implement the distributed algorithms. By using the previously mentioned "**WiFiLeaderElection**" class, we can send and receive messages between the network's nodes. Furthermore, we can use this class to solve the problem of the leader election. The leader election process chooses one network's node as a task leader or an organizer of some task distributed among some network's nodes.

The use case diagram in Figure 2 shows how the system integrates and works together from the beginning of entering the unique id for each node by the user until starting the leader election process and choose the leader node. The scenario is as follows:

1. The user enters a unique id for each node.
2. Any node can act as a server or as a client at the same time.
3. When the id is entered, the client node sends a request for id checking to the server node.
4. The server will check this id to see if another node takes this id or not.
5. The user can send a broadcast message or start the election process.
6. The server receives a broadcast message coming from the user by listening to a specified port number.
7. After receiving the election message, the server restarts the election process if necessary.

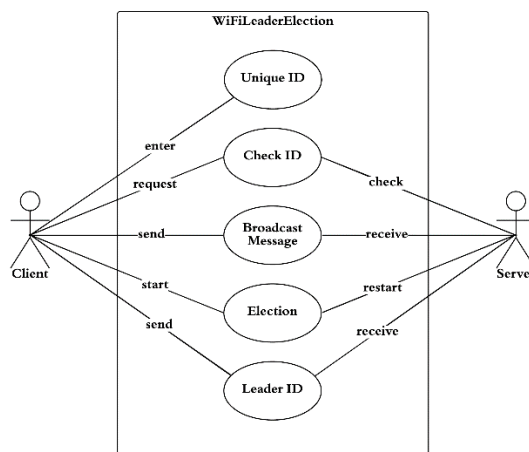


Figure 33. Use Case Diagram

After entering node id and pressing the ok button, the id entered by the user is checked to ensure that each node has a unique id. After checking the id entered by the user and find out another node uses it, a toast message will inform the user to enter another id. If no other node uses it, the **WiFiActivity** class will be opened. This class contains a **ListView** to show all messages exchanging between nodes. Furthermore, we can use this class to send a broadcast message and/or start the leader election process by clicking the menu item at the top right of the screen, see Figure 3.

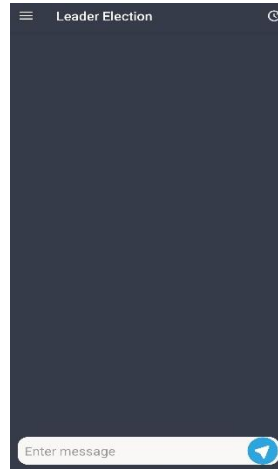


Figure 34. Wi-Fi Activity

When a user clicks the start election button at the top right of the screen, the leader election process will be started. The leader node will be elected from among a number of nodes in the network and a popup message will inform the user that the node with a specific id (9 in our example) is the leader node, see Figure 4.

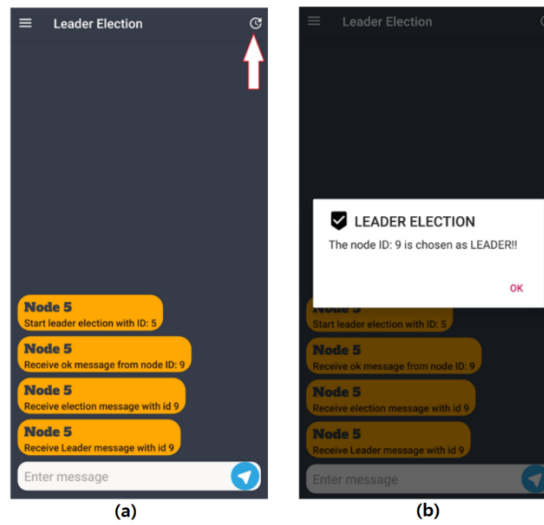


Figure 35. (a) when starting the leader election, (b) when receiving the leader id

In the same way, all other nodes will be informed that the leader node was elected. Figure 5 shows what happened with the leader node (node id 9):

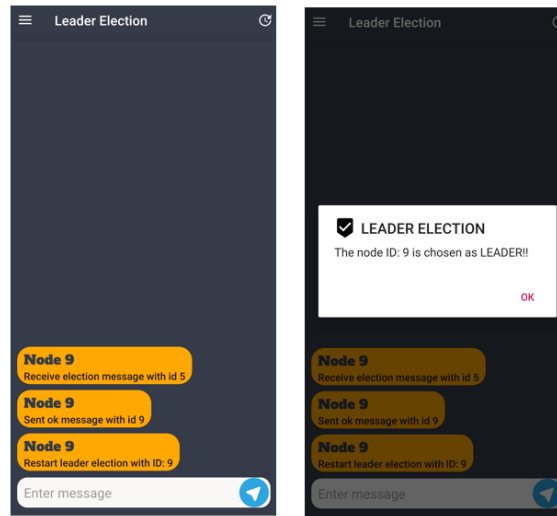


Figure 36. Leader Node

### Conclusion

In distributed systems, nodes can communicate with each other by sending messages over a communications network. Distributed systems have several advantages over centralized systems (systems with a single processor and a single memory). One of the advantages of distributed systems is resource sharing. Many problems can occur when trying to access to central systems like the bottleneck in that central site. Distributing resources such as databases and peripherals over a network overcomes these problems. The fault-tolerant design allows the system to continue to operate instead of completely failing when some part of the system fails. This type of fault tolerance is an important reason for using distributed systems.

With the widespread use of smartphones in recent years, the memory capacity, processing power and connectivity of these devices have increased. Therefore, these devices can be an application platform for the distributed systems. Most smartphone communication leverages one-hop radio links to cell towers or Wi-Fi access points. In recent years, smart phone operating systems have allowed to communicate directly with a nearby device, while avoiding cellular and Wi-Fi infrastructure. Thus, local peer-to-peer communication can be made by using local radio broadcasts. The ability to create these local links, combined with the ubiquity of smartphones, enables scenarios in which large groups of nearby smartphone users run applications that create peer-to-peer meshes supporting infrastructure-free networking. Developing useful applications for this smartphone peer-to-peer setting requires distributed algorithms that can provide global reliability and efficiency guarantees on top of an unpredictable collection of local links.

In this study, a distributed infrastructure consisting of smartphones has been created. The developed system supports both Wi-Fi and Bluetooth connections. When using the Wi-Fi connection, all nodes (devices) connect to the same Wi-Fi network. When connected to the same Wi-Fi network, each node can send a broadcast message to all other nodes and/or start the leader election process. When a node starts the leader election process, it sends an election message containing its identification number to all other nodes on the network at the same time. After  $n$  rounds, a leader node will be elected and the leader ID will be sent to all other nodes on the network.

### References

- [1] Newport C. Gossip in a smartphone peer-to-peer network. In Proceedings of the ACM Symposium on Principles of Distributed Computing 2017 Jul 25 (pp. 43-52).
- [2] Newport C. Leader election in a smartphone peer-to-peer network. In 2017 IEEE International Parallel and Distributed Processing Symposium (IPDPS) 2017 May 29 (pp. 172-181). IEEE.
- [3] Zamora JL, Kashihara S, Yamaguchi S. Calibration of smartphone-based weather measurements using pairwise gossip. The Scientific World Journal. 2015 Sep 2;2015.
- [4] De Masi A. Load balancing in P2P smartphone based distributed IoT systems.

- [5] Serfass D, Yoshigoe K. Wireless sensor networks using android virtual devices and near field communication peer-to-peer emulation. In 2012 Proceedings of IEEE Southeastcon 2012 Mar 15 (pp. 1-6). IEEE.
- [6] Kalic G, Bojic I, Kusek M. Energy consumption in android phones when using wireless communication technologies. In 2012 Proceedings of the 35th International Convention MIPRO 2012 May 21 (pp. 754-759). IEEE.
- [7] Kurose JF. Computer networking: A top-down approach featuring the internet, 3/E. Pearson Education India; 2005.

## **Materials Science and Engineering / Malzeme Bilimi ve Mühendisliği**

## Stochastic Optimization of Graphene Sheets Subjected to Drilling Operation Using Neuro-Regression Approach for Maximum Mechanical Strength

*K. Bartu Aydın, İzmir Kâtip Çelebi Univ., Dept. of Materials Science and Engineering, İzmir, Turkey  
Levent Aydın\*, İzmir Kâtip Çelebi Univ., Dept. of Mechanical Engineering, İzmir, Turkey  
Melih Savran, İzmir Kâtip Çelebi Univ., Dept. of Mechanical Engineering, İzmir, Turkey  
Harun Sayı, İzmir Institute of Technology, Dept. of Mechanical Engineering, İzmir, Turkey  
Ozan Ayakdaş, İzmir Institute of Technology, Dept. of Mechanical Engineering, İzmir, Turkey  
H. Seçil Artem, İzmir Institute of Technology, Dept. of Mechanical Engineering, İzmir, Turkey  
\*Corresponding author: levent.aydin@ikcu.edu.tr*

**Keywords:** Drilling operation, graphene sheets, stochastic optimization, neuro-regression approach  
**Discipline:** Materials Science and Engineering

### Abstract

Drilling operation is one of the primary machining processes in manufacturing of functional components. In this study, optimization of drilling process has been achieved using neuro-regression analysis. In the analysis, the effect of design parameters, namely, temperature, drill bit velocity and the feed rate of the drill bit on the mechanical strength of graphene sheets subjected to the drilling operation at the nanoscale level have been investigated. In the optimization, Nelder-Mead, Simulated Annealing, Differential Evolution and Random Search algorithms are used to obtain the optimum design parameters for maximum mechanical strength. The results have indicated that all of these optimization methods give the same value for the mechanical strength and design variables.

### Introduction

Graphene is carbon dependent, two-dimensional nano-material that has drawn considerable interest in nano-technology recently because of its outstanding mechanical and physical properties. For this reason, graphene has found wide application areas owing to its two-dimensional superior properties. Recently, there are many studies in literature which demonstrate the advantageous of the graphene with nanopores. It is shown that a single nanopore in graphene is the sophisticated candidate with the great potential for nanopore-based DNA sequencing with current-blocking method [1-5]. The other potential applications related to graphene with multi nanopores have been investigated in significant areas, such as biosensors, seawater desalination, ionic sieves of high selectivity and transparency, etc [6-9]. All of these applications require machining process at nanoscale for graphene for production of graphene-based nanocomponents of complex geometry and functionality. With the increase of manufacturing requirements for applications in aerospace, defence, and electronics, the drilling process of graphene has come forward as an important issue handled in literature. Many investigations have been done to estimate the drilling process performance of the graphene. Molecular dynamics (MD) simulation and ab initio calculations are popular modes of research among the theoretical studies for the drilling process. MD simulations have been employed to investigate the mechanical properties of graphene sheet at high temperatures [10]. It is found that graphene sheet demonstrates great performance despite of its high temperature. Due to experiments for monitoring machining process at the nanoscale are time-consuming and very expensive, theoretical models come forward as viable alternative compare to them. Recently, the evolutionary approach of multi-gene genetic programming (MGGP) and artificial neural networks (ANN) have been rising methods among soft computing techniques [11-16]. There are also many investigations in literature related to optimization of the machining operations' unit production cost by novel soft computing approaches such as hybridizing differential evolution algorithm with receptor editing property of immune system [17-19], artificial bee colony algorithm with Taguchi's method [20,21], the differential algorithm with Taguchi's method [22], cuckoo search algorithm (CS) [23] and immune algorithm with hill climbing local search algorithm [24,25]. All of these methods need to input training data which is determined by the analytical tools based on a specific geometry and temperature. Meaningful solutions can be achieved for complicated nanoscale problems utilizing soft computing methods in case of consistent input data [26-27]. In addition to these studies, evolutionary approach provides an advantageously fast and cost-effective explicit mathematical model including multiple

variables with no existing analytical models [28-29]. In another study, multi-gene genetic programming (MGGP) compared with ANN model for prediction of mechanical strength of the graphene subjected to drilling process [30]. MGGP model demonstrates better performance than that of the ANN model. Thus, it is required a complete understanding and investigation for modelling of the drilling process of graphene in the future applications.

In this present study, it is aimed to maximize the mechanical strength of graphene sheets subjected to drilling process at nanoscale for a certain temperature, feed and rotational velocity. Nelder-Mead (NM), Simulated Annealing (SA), Differential Evolution (DE) and Random Search (RS) have been used as stochastic optimization methods to obtain maximum mechanical strength of graphene sheets.

### Methods

In the present study, a regression analysis was first performed to establish a mathematical model to determine the mechanical strength of the graphene sheets affected by design variables which are feed rate, temperature and rotational velocity. The total number of data used to carry out regression analysis were 63; 70% of it were training data and the remaining amount are testing ones. The accuracy of the mathematical model was performed by R-Squared ( $R^2$ ) and R-Squared adjusted ( $R^2_{adjusted}$ ) values obtained by the following equation:

$$R^2 = 1 - \frac{SS_{res}}{SS_{tot}} \quad (1)$$

$$R^2_{adjusted} = 1 - \left[ \left( \frac{n-1}{n-k-1} \right) \times (1 - R^2) \right] \quad (2)$$

where

$$SS_{tot} = \sum_i (y_i - \bar{y})^2 \quad (3)$$

and

$$SS_{res} = \sum_i (y_i - f_i)^2 \quad (4)$$

Here,  $\bar{y}$  is the mean of the output values and  $f_i$  is the prediction by the proposed model for corresponding inputs. The parameters  $n$  and  $k$  are the number of observations and number of independent variables, respectively. In this case, the  $R^2$  and  $R^2_{adjusted}$  values being above 0.85 were qualified for training and testing data for appropriate model.

After examining the appropriateness of the model by considering the relevant coefficients, the boundedness of the model is to be the next step to be checked. In this process, the bounds of the objective function were obtained in the manner of maximum and minimum values. The reason behind this process is to determine whether fitted model is in the logical terms of engineering. If proposed model gives realistic results for engineering, it can be interpretable as bounded.

In the present study, all mathematical relations and calculations were performed using Wolfram Mathematica 11.3. Here, the functions of NMaximize and NMinimize were used to find constrained global optimum values. Maximization of the mechanical strength value of graphene sheets using stochastic search algorithms, Nelder-Mead, Differential Evolution, Simulated Annealing and Random Search, is the main objective in this study.

### Nelder-Mead

Also, known as simplex, Nelder-Mead algorithm is one of the direct search methods. The algorithm sets  $n+1$  points generating the vertices of a polytope in  $n$ -dimensional space for a function variable. There is also simplex method known for linear programming which should not be confused with [31].

In each iteration,  $n+1$  points;  $x_1, x_2, \dots, x_{n+1}$  generate a polytope. The points are arrayed according to inequality of  $f(x_1) \leq f(x_2) \leq \dots \leq f(x_{n+1})$ . Then, a new point is produced to change the worst point of  $x_{n+1}$ .

The centroid of the polytope ( $c$ ) including the best performing  $n$  points has following relation,  $c = \frac{1}{n} \sum_{i=1}^n x_i$ . A trial point  $x_t$  is produced by reflecting the worst point through the centroid,  $x_t = c + \alpha(c -$

$x_{n+1}$ ), where  $\alpha > 0$  is a parameter. If the new point  $x_t$  is neither a new worst point nor a new best point,  $f(x_1) \leq f(x_t) \leq f(x_n)$ ,  $x_t$  changes with  $x_{n+1}$ .

When the new point  $x_t$  is better than last best point,  $f(x_t) < f(x_1)$ , the reflection is assumed as achieved and it can be continued further to  $x_e = c + \beta(x_t - r)$  where  $\beta > 1$  is a parameter to enlarge the polytope. If the expansion is achieved,  $f(x_e) < f(x_t)$ ,  $x_e$  changes with  $x_{n+1}$ ; otherwise  $x_t$  replaces  $x_{n+1}$ .

On the other hand, if the new point  $x_t$  is worse than the second worst point,  $f(x_t) \geq f(x_n)$ , the polytope is supposed to be too large and needs to be contracted. A new trial point is expressed as

$$x_c = \begin{cases} c + \gamma(x_{n+1} - c), & \text{if } f(x_t) \geq f(x_{n+1}) \\ c + \gamma(x_t - c), & \text{if } f(x_t) < f(x_{n+1}) \end{cases} \quad (5)$$

where  $0 < \gamma < 1$  is a parameter. If  $f(x_c) < \text{Min}(f(x_{n+1}), f(x_t))$ , the contraction is achieved, and  $x_c$  changes with  $x_{n+1}$ . Contrary, a further contraction is fulfilled.

As a result, if the difference between best values in the new and old polytope and the distance between new best and old points are not in conflict with the tolerances supplied by the Accuracy Goal and Precision Goal features, the algorithm process agrees to be converged.

In addition, because of Nelder-Mead is not a true global optimization algorithm, it performs significantly well for problems having fewer local minima.

### Simulated Annealing

Simulated annealing is one of the simple stochastic optimization methods in finding minimum. The idea of the method relies on the physical process of annealing where a metal object is heated first to elevated temperature, then it is allowed to cool slowly. By this way, the atomic structure of the annealed metal settles to a lower energy state making it a tougher metal. In optimization terminology, the aim of the method is to reach better minimum value. However, it is not guaranteed that the new value is global minimum [32].

In iteration process, a new point,  $x_{new}$ , is produced in the neighbourhood of the current point,  $x$ . The radius of the value neighbourhood reduces by each iteration. The best point,  $x_{best}$  is tracked in each process.

If  $f(x_{new}) \leq f(x_{best})$ ,  $x_{new}$  replaces  $x_{best}$  and  $x$ . Otherwise,  $x_{new}$  replaces  $x$  with a probability of  $e^{b(i, \Delta f, f_0)}$  where  $b$ ,  $i$ ,  $\Delta f$ ,  $f_0$  denote the function defined by Boltzmann Exponent, the current iteration, the change in the objective function value and the value of the objective function from the previous iteration, respectively. The default function of Boltzmann Exponent,  $b$  is  $\frac{-\Delta f \log(i+1)}{10}$  in Mathematica.

Simulated Annealing holds multiple starting points and finds an optimum initial point from each of them. The initial points given by the option SearchPoint is  $\text{min}(2d, 50)$ , where  $d$  is the number of variables. Until the maximum number of iterations is attained, this process is repeated for each initial point. After the new best point is found, the method converges to that point. Otherwise, the method stays at the last best point for the following number of iterations.

### Differential Evolution

Similar to Simulated Annealing, Differential Evolution is also a kind of maximization or minimization algorithm. In this method, a population of  $m$  points,  $\{x_1, x_2, \dots, x_j, \dots, x_m\}$ , is maintained where  $m$  is significantly larger than  $n$ , with  $n$  being the number of variables.

A new population of  $m$  points is produced in each iteration. The  $j^{\text{th}}$  new point is generated by picking three random points,  $x_u$ ,  $x_v$  and  $x_w$ , from the old population. Then it forms,  $x_s = x_w + s(x_u - x_v)$ , where  $s$  is a real scaling factor. Then a new point  $x_{new}$  is determined from  $x_j$  and  $x_s$  by taking  $i^{\text{th}}$  coordinate from  $x_s$  with probability  $\rho$  and otherwise taking the coordinate from  $x_j$ . If  $f(x_{new}) < f(x_j)$ , then  $x_{new}$  changes with  $x_j$  in the population. The probability  $\rho$  is controlled by the "CrossProbability" feature of the algorithm settings in Mathematica platform.

If the tolerances determined by AccuracyGoal and PrecisionGoal are more than the new and old populations as well as the distance between the new best point and the previous best point, the process is assumed convergent [33].



Though this search method is computationally expensive, it proves to be relatively robust algorithm when especially dealing with problems having more local minima.

### Random Search

As its name indicating, Random Search method carries out with a population generated by random starting points (similar with Simulated Annealing) to converge to a local minimum. The solution is realized when the best local minimum is determined. “Automatic” and “InteriorPoint” are the possible local search methods in Mathematica program [32].

First method is default option which uses “FindMinimum” solver with unrestricted methods applied to a system with error terms added for the constraints. On the other hand, there is an alternative method called nonlinear interior-point method. “SearchPoint” gives the default number of initial points which are min (10d, 100), where d is the number of variables.

Convergence of the local method for each initial point determines the convergence for RandomSearch algorithm. While this algorithm gives quick result in optimization, it doesn’t scale well with the dimension of the search space. In addition, it lacks many limitations also seen in FindMinimum. Moreover, RandomSearch is not well suited in discrete problems where derivatives don’t give much useful information.

### Problem Definition

In the present study, the effect of design parameters i) temperature, ii) rotational velocity of the drill bit and iii) the feed rate of the drill bit on the mechanical strength of graphene sheets subjected to the drilling operation at the nanoscale level are investigated. Single objective optimization approach is used to maximize mechanical strength by means of different direct search methods including stochastic optimization approach (DE, SA, NM, RS). Detailed explanation about the problem is given as follow:

### Single Objective Problem

#### Find

$$\{x_1 \in [300, 600] \wedge x_2 \in [10, 30] \wedge x_3 \in [50, 90]: \{x_1, x_2, x_3\} \}$$

#### Maximizing

$$MS(x_1, x_2, x_3)$$

#### Constraints

$$\text{Scenario 1 } 300 \leq x_1 \leq 600, 10 \leq x_2 \leq 30, 50 \leq x_3 \leq 90$$

$$\text{Scenario 2 } 300 \leq x_1 \leq 600, 10 \leq x_2 \leq 30, 50 \leq x_3 \leq 90 \quad \{x_1, x_2, x_3\} \in \text{Integers}$$

#### Design variables

$$x_1, x_2, x_3$$

where  $x_1, x_2,$  and  $x_3$  represent temperature, feed and rotational velocity, respectively. Mechanical strength is an objective function named as MS.

### Results and Discussion

In this section, results of mechanical strength for optimized graphene sheets subjected to the drilling operation are given. Neuro-regression approach and stochastic optimization methods are employed to solve the optimization problems. For modelling stage, the data are divided into two parts as 30% and 70% of it. The multiple nonlinear regression model is constituted using 70% of the data, and the 30% ones are used for testing. The training and testing data with the corresponding mechanical strength values are given in Tables 1 and 2, respectively [30].

Table 1. Training data [30]

Data	Temperature (K)	Feed (m/s)	Rotational velocity (rad/s)	Mechanical Strength (GPa)
1	300	30	70	92.7
2	300	20	90	84.9
3	300	10	70	84.9
4	300	30	90	92.4
5	300	20	50	103.8
6	300	20	70	102.5
7	350	20	90	67.98
8	350	30	90	66.22
9	350	10	90	71.12
10	350	20	70	76.19
11	350	30	50	87.38
12	350	10	70	85.35
13	350	20	50	87.03
14	375	30	70	69.61
15	375	20	70	71.39
16	375	20	90	61.28
17	375	30	90	59.2
18	400	20	90	55.7
19	400	20	50	74.6
20	400	10	50	88.3
21	400	10	70	71.9
22	400	30	50	74.6
23	400	30	90	55.7
24	425	20	70	60.78
25	425	30	70	58.32
26	425	10	70	65.24
27	425	20	90	50.94
28	425	10	50	81.36
29	425	20	50	59.82
30	425	30	90	49.65
31	425	30	50	70.87
32	425	10	90	53.51
33	500	20	90	40.4
34	500	10	70	55.4
35	500	20	70	47.1
36	500	10	50	64.7
37	500	30	90	20.8
38	500	30	70	29.5
39	500	20	50	51.6
40	600	30	50	29.81
41	600	20	70	34.81
42	600	20	90	20.13
43	600	30	50	39.18
44	600	30	90	18.02
45	600	10	90	24.88

Table 2. Testing data [30]

Data	Temperature (K)	Feed (m/s)	Rotational velocity (rad/s)	Mechanical Strength (GPa)
1	300	10	50	115.6
2	300	10	90	93.3
3	300	30	50	103.2
4	350	10	50	103.14
5	350	30	70	77.56
6	375	10	50	92.83
7	375	10	70	77.17
8	375	10	90	65.03
9	375	20	50	79.58
10	375	30	50	82.02
11	400	10	90	59.1
12	400	20	70	64.9
13	400	30	70	64.9
14	500	10	90	43.8
15	500	30	50	37.9
16	600	10	50	52.15
17	600	10	70	40.17
18	600	20	50	42.16

Multiple nonlinear regression model for mechanical strength using all the parameters given in Tables 1 and 2 have been obtained as follows:

### Mechanical Strength (MS)

$$MS = 319.483 - 0.569542 t - 0.000313985 t^2 + 7.13911 \times 10^{-7} t^3 - 2.29166 f + 0.0000220282 t f + 6.36863 \times 10^{-6} t^2 f - 0.075102 f^2 - 0.000150723 t f^2 + 0.0055828 f^3 - 1.35902 r + 0.00861395 t r - 4.28365 \times 10^{-6} t^2 r + 0.0571693 f r - 0.0000165963 t f r - 0.0023607 f^2 r - 0.0234939 r^2 - 0.0000309551 t r^2 + 0.000380661 f r^2 + 0.000138964 r^3$$

where the parameters  $t$ ,  $f$ , and  $r$  are temperature, feed and rotational velocity, respectively.

In Table 3, the statistical accuracy of the model is shown. The results of  $R^2$  for training and testing data are founded as 0.9838 and 0.9636, and  $R^2_{\text{adjusted}}$  values are 0.9826 and 0.9559, respectively.

Table 3. Results of neuro regression model for fitting parameters and boundedness

	Number of Data	$R^2$	$R^2_{\text{adjusted}}$	Maximum Mechanical Strength (GPa)	Minimum Mechanical Strength (GPa)
Training	45	0.9838	0.9826	115.6	18.02
Testing	18	0.9636	0.9559		

In order to determine whether the fitted regression model is bounded, the boundedness control stage has performed by checking the maximum and minimum values taken by the model in the search space of design variables specified in this study. As it is seen from the Tables 1 and 2, the maximum and minimum values of mechanical strength are obtained as 115.6 GPa and 18.02 GPa, respectively. Thus, the proposed model gives realistic results for engineering and hence, it can be interpretable as bounded.

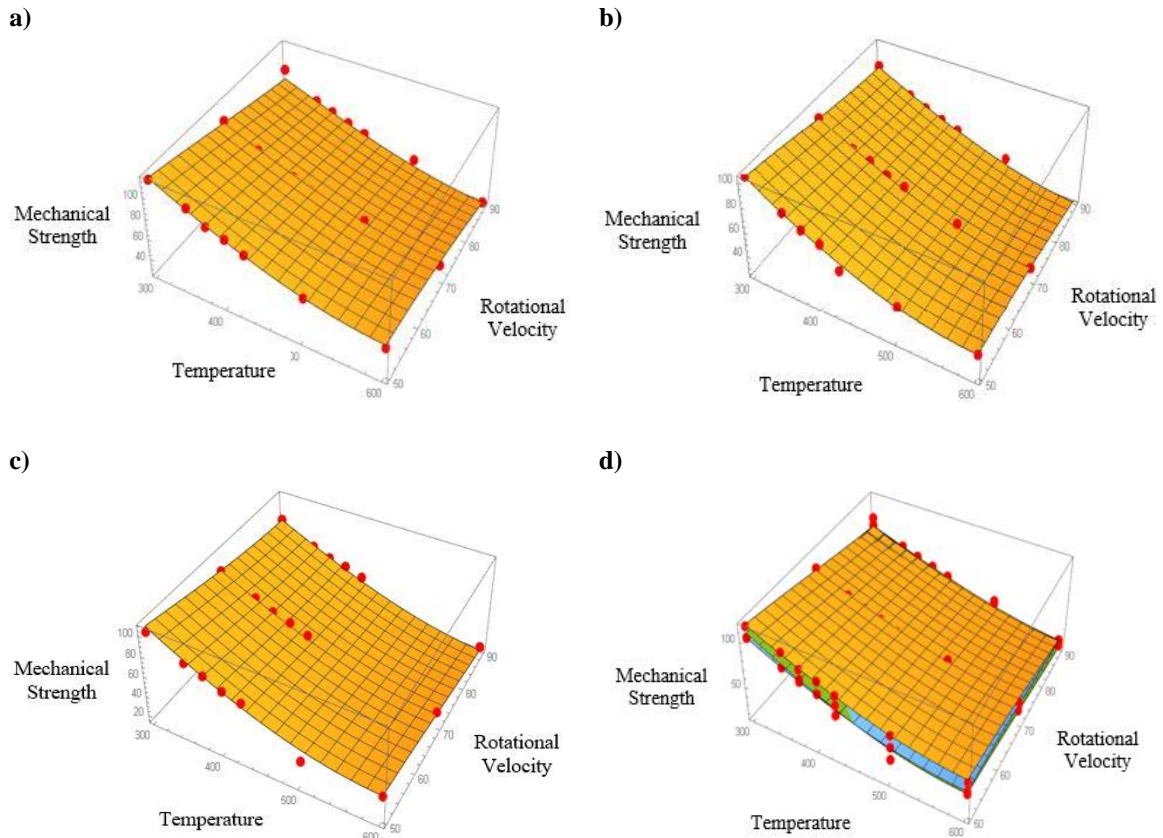


Figure 1. 3D plot representations of comparison between experimental and recommended model results on mechanical strength in terms of rotational velocity and temperature.

3D-graphs about mechanical strength results of the graphene sheet are given in Fig.1 so as to see a graphical comparison of the experimental data and proposed regression model function. In Figs.1a), b) and c), the feed parameters are taken as 10 m/s, 20 m/s and 30 m/s, respectively. Figure d) includes a combined representation of Figures a), b) and c). As it is seen from the figures that the proposed model fit well with experimental results.

Table 4 shows the optimum mechanical strength of graphene sheets utilizing stochastic optimization methods NM, SA, DE and RS, considering continuous and integer search spaces. It is seen that all the optimization methods give the same mechanical strength value as 115.6 GPa. This value is exactly the same as the maximum mechanical strength value obtained by the experimental study in the reference article [30].

Table 4. Results of optimization problem considered for continuous and integer search spaces

Optimization Methods	Design Variables			Mechanical Strength (GPa)
	Temperature (K)	Feed (m/s)	Rotational velocity (rad/sec)	
NM	300	10	50	115.6
SA	300	10	50	115.6
DE	300	10	50	115.6
RS	300	10	50	115.6

Moreover, the obtained results in this present study are identical for both continuous and integer search spaces. The design parameters: temperature, feed and rotational velocity have been obtained as 300 (K), 10 (m/s) and 50 (rad/s), respectively in case of maximum strength. It has been understood from

here that the interval values of design variables do not provide higher mechanical strength for drilling operation problem handled in this study.

### Conclusion

In this study, optimization of mechanical strength of graphene sheets affected by drilling operation parameters such as temperature, feed rate, rotational velocity, is investigated. The neuro-regression approach is used to define the objective function for mechanical strength to be used in optimization process. Optimization is achieved using Nelder-Mead (NM), Simulated Annealing (SA), Differential Evolution (DE) and Random Search (RS) algorithms. It is seen that all methods gave the same result in terms of maximum mechanical strength value (115.6 GPa) and corresponding optimum design parameters are temperature (300 K), feed (10 m/s) and rotational velocity (50 rad/s). In addition, the performance of the optimization result is compared to that of experimental result in the literature [30]. Also, this paper demonstrated that the stochastic optimization algorithms give a reasonable estimation of output variables based on different values of input variables by using the neuro-regression approach.

### References

- [1] Schneider GF, Kowalczyk SW, Calado VE, Pandraud G, Zandbergen HW, Vandersypen LMK, Dekker C. DNA Translocation through Graphene Nanopores. *Nano Lett.* 2010; 10: 3163 – 7.
- [2] Merchant CA, Healy K, Wanunu M, Ray V, Peterman N, Bartel J, Fischbein MD, Venta K, Luo Z, Johnson ATC, Drndic M. DNA Translocation through Graphene Nanopores. *Nano Lett.* 2010; 10: 2915 – 21.
- [3] Postma HWC. Rapid sequencing of individual DNA molecules in graphene nanogaps. *Nano Lett.* 2010; 10: 420 –5.
- [4] Bayley H. Holes with an edge. *Nature* 2010; 467: 164 –5.
- [5] He H, Scheicher RH, Grigoriev A, Ahuja R, Long S, Huo ZL, Liu M. Enhanced DNA sequencing performance through edge-hydrogenation of graphene electrodes. *Adv. Funct. Mater.* 2011; 21: 2674 –9.
- [6] Humplik T, Lee J, O’Hern SC, Fellman BA, Baig MA, Hassan SF, Atieh MA, Rahman F Laoui T, Karnik R, Wang EN. Nanostructured materials for water desalination. *Nanotechnology* 2011; 22(29): 19
- [7] Siwy ZS, Davenport M. Graphene opens up to DNA. *Nat. Nanotechnol.* 2010; 5: 697 –8.
- [8] Sint K, Wang B, Kral P. Selective ion passage through functionalized graphene nanopores. *Am. Chem. Soc.* 2008; 130: 16448 –9.
- [9] Garaj S, Hubbard W, Reina A, Kong J, Branton D, Golovchenko JA. Graphene as a subnanometre trans-electrode membrane. *Nature* 2010; 467: 190 –3.
- [10] Zhao H, Min K, Aluru NR. Size and chirality dependent elastic properties of graphene nanoribbons under uniaxial tension. *Nano Lett.* 2009; 9(8): 3012–5
- [11] Gopalakrishnan K, Kim S, Ceylan H, Khaitan SK. Natural selection of asphalt mix stiffness predictive models with genetic programming. St. Louis, Missouri: ANNIE 2010, Artificial Neural Networks in Engineering; 2010.
- [12] Desai CK, Shaikh A. Prediction of depth of cut for single-pass laser micro-milling process using semi-analytical, ANN and GP approaches. *Int. J. Adv. Manuf. Technol.* 2012; 60: 865–2.
- [13] Gandomi AH, Alavi AH. A new multi-gene genetic programming approach to nonlinear system modeling. Part I: materials and structural engineering problems, *Neural Comput. Appl.* 2012; 21: 171–87.
- [14] Gandomi AH, Alavi AH. A new multi-gene genetic programming approach to nonlinear system modeling. Part II: geotechnical and earthquake engineering problems, *Neural Comput. Appl.* 2012; 21: 189–201.
- [15] Rezaei M, Eftekhari M, Mahin S, Ranjbar M. A CO<sub>2</sub>-oil minimum miscibility pressure model based on multi-gene genetic programming. *Energy Expl. Exploit.* 2013; 31: 607–22.
- [16] Muduli PK, Das SK. CPT-based seismic liquefaction potential evaluation using multi-gene genetic programming approach. *Ind. Geotech. J.* 2014; 44(1): 86-93.
- [17] Yıldız AR. A comparative study of population-based optimization algorithms for turning operations. *Inf. Sci.* 2012; 210: 81–8.

- [18] Yıldız AR. Comparison of evolutionary based optimization algorithms for structural design optimization. *Eng. Appl. Artif. Intell.* 2013; 26(1), 327–33.
- [19] Yıldız AR. A new hybrid differential evolution algorithm for the selection of optimal machining parameters in milling operations. *Appl. Soft Comput.* 2013; 13(3): 1561–6.
- [20] Yıldız AR. A new hybrid artificial bee colony algorithm for robust optimal design and manufacturing. *Appl. Soft Comput.* 2013; 13(5): 2906–12.
- [21] Yıldız AR. Optimization of cutting parameters in multi-pass turning using artificial bee colony-based approach. *Inf. Sci.* 2013; 220: 399–407.
- [22] Yıldız AR. Hybrid Taguchi-differential evolution algorithm for optimization of multi-pass turning operations. *Appl. Soft Comput.* 2013; 13(3): 1433–9.
- [23] Yıldız AR. Cuckoo search algorithm for the selection of optimal machining parameters in milling operations. *Int. J. Adv. Manuf. Technol.* 2013; 64(1-4): 55–61.
- [24] Yıldız AR. A novel hybrid immune algorithm for global optimization in design and manufacturing. *Robot. Comput. – Integr. Manuf.* 2009; 25(2): 261–70.
- [25] Yıldız AR. An effective hybrid immune-hill climbing optimization approach for solving design and manufacturing optimization problems in industry. *J. Mater. Process. Technol.* 2009; 209(6): 2773–80.
- [26] Gandomi AH, Alavi AH. Multi-stage genetic programming: a new strategy to nonlinear system modeling. *Inf. Sci.* 2011; 181(23): 5227–39.
- [27] Gandomi AH, Alavi AH, Arjmandi P, Aghaeifar A, Seyednoor M. Genetic programming and orthogonal least squares: a hybrid approach to modeling the compressive strength of CFRP-confined concrete cylinders. *J. Mech. Mater. Struct.* 2010; 5(5): 735–53.
- [28] Çevik A, Göğüs MT, Güzelbey IH, Filiz H. Soft computing-based formulation for strength enhancement of CFRP confined concrete cylinders. *Adv. Eng. Softw.* 2010; 41(4): 527–36.
- [29] Garg A, Sriram S, Tai K. Empirical analysis of model selection criteria for genetic programming in modeling of time series system. Singapore: Proceedings of 2013 IEEE Conference on Computational Intelligence for Financial Engineering and Economics (CIFER); 2013; 84–8.
- [30] Vijayaraghavan V, Garg A, Wong CH, Tai K, Mahapatra SS. Measurement of properties of graphene sheets subjected to drilling operation using computer simulation. *Measurement* 2014; 50: 50–62.
- [31] Savran M, Sayi H, Aydin L, Chapter 3: Mathematica and Optimization. In: L. Aydin, H.S. Artem, S. Oterkus, editors. *Designing Engineering Structures Using Stochastic Optimization Methods*. CRC Press Taylor & Francis Group; 2020.
- [32] Polatoğlu İ, Aydin L, Nevruz BÇ, Özer S. A Novel Approach for the Optimal Design of a Biosensor. *Anal Lett* 2020; 53(9): 1428–45.
- [33] Akçair M, Savran M, Aydin L, Ayakdaş O, Öztürk S, Küçükdoğan N. Optimum design of anti-buckling behavior of graphite/epoxy laminated composites by differential evolution and simulated annealing method. *Res Eng Struct Mat* 2019; 5(2): 175–88.

## Stochastic Optimization of Friction Stir Welded AA7039 Aluminum Alloy Joints Using Neuro-Regression Approach for Maximum Tensile Strength

Gülperi Feyza Yavuz, *İzmir Kâtip Çelebi Univ., Dept. of Materials Science and Engineering, İzmir, Turkey*  
Levent Aydın\*, *İzmir Kâtip Çelebi Univ., Dept. of Mechanical Engineering, İzmir, Turkey*  
Melih Savran, *İzmir Kâtip Çelebi Univ., Dept. of Mechanical Engineering, İzmir, Turkey*  
Harun Sayı, *İzmir Institute of Technology, Dept. of Mechanical Engineering, İzmir, Turkey*  
H. Seçil Artem, *İzmir Institute of Technology, Dept. of Mechanical Engineering, İzmir, Turkey*  
\*Corresponding author: levent.aydin@ikcu.edu.tr

**Keywords:** Stochastic optimization, neuro-regression approach, friction stir welding

**Discipline:** Materials Science and Engineering

### Abstract

Friction stir welding (FSW) is an important solid-state joining technique and has been employed in automotive, aerospace and marine industries to join aluminum, zinc, magnesium and copper alloys. In this regard, the main goal of the present study is to maximize the tensile strength of friction stir welded AA7039 aluminum alloy joints by considering the FSW process parameters such as tool rotational speed, welding speed and axial force. The neuro-regression approach has been used to model friction FSW process mathematically. The optimum FSW process parameters required to obtain the maximum tensile strength is determined using direct search algorithms, namely, Random Search, Simulated Annealing, Differential Evolution and Nelder-Mead. The results of this study exhibit that these four optimization algorithms give the same results and a reasonable estimation by considering the same design variables.

### Introduction

The technique known as FSW is a type of solid-state joining process. Thus, the welded material using the technique does not recast and melt [1]. FSW has significant advantages over fusion welding such as solution for solidification cracks and porosity when the case in the absence of the parent metal melting. There are some unwieldable materials like 2xxx and 7xxx series high strength aluminium alloys by conventional fusion welding processes. The use of FSW technique overcomes this problem [2]. Its usage has significant importance especially in aerospace, shipbuilding, marine, automotive and railway industry [3,4].

Material flow and temperature distribution around the area of the weld form the main characteristic of the FSW. The attributes are directly affected by pin/shoulder geometry and welding parameters such as rotational speed, welding speed and axial force [4,5]. Other certain properties of the tool such as homogeneous microstructure, uniform joint properties and governing of process forces are related to the pin/shoulder geometry of the tool. In welding process, heat generation and lower displacement volumes of the softened materials increases, hence to relief these, welding forces must be reduced. Therefore, Whorl™ and MX Triflute™ tool geometries are used [6].

Stirring, mixing and the amount of heat generated over unit time of the material around the pin are determined by rotary speed of the tool [7]. The speed of welding process or the traverse speed of the tool have direct effect on the highest temperature produced during welding and the total time passed when the material is subjected to the welding [8]. The welding speed is inversely correlated with the cost of friction welded joints. Therefore, high welding speed is generally preferred especially in mass productions. On the other hand, high welding speed with constant rotational speed causes the formation of void under the top surface of the welded area or the advancing side at the edge of weld nugget. In addition, the defects in size of wormhole compounds due to the increment in welding speed [9]. This is caused due to leading inadequate material flow through the bottom of the well by reduced heat input.

In literature, there are number of studies dealing with the various aspects of the friction stir welded aluminium alloys such as material flow [10-12], mechanical properties and the development of the microstructure [13]. However, the number of research studies about friction stir welding of precipitation hardenable AA7039 aluminium alloy seems to be marginal. Balasubramanian [14] reveal yield strength, hardness and ductility of the alloy carry a major importance for weld quality of friction welded joints. In another study, the effect of welding speed and post weld heat treatment (T6) on mechanical properties

and microstructure was investigated by Singh et al. [15]. The research team revealed that the strength of the welded area is directly proportional with welding speed.

Friction stir welding (FSW) is highly preferred solid-state joining technique in vast majority of large industries such as aerospace, marine, rail and automotive in welding of aluminium, zinc, magnesium and copper alloys. In this respect, the main objective of the present study was to determine the maximum tensile strength of the FSW welded AA7039 aluminium alloy joints by taking into consideration of the FSW process parameters welding speed (S), rotational speed of the tool (N) and axial force (F). The neuro-regression approach was utilized as the base of optimization in this study. Random Search (RS), Simulated Annealing (SA), Differential Evolution (DE) and Nelder-Mead (NM) algorithms were adopted to optimize the tensile strength of the FSW AA7039 aluminium alloy joints.

## Materials and Methods

### Regression Analysis

Regression analysis is a statistical method to develop a mathematical model that gives the relationship between independent variables and the dependent variable. In the literature, there are many types of regression models such as linear, nonlinear, rational, logistic and stepwise with the object of identifying physical processes. While the linear regression model could be used to describe phenomena in problems containing linear relationship between input and output parameters, nonlinear regression model which includes more general class of functions, such as logarithmic, trigonometric, power and rational forms, might be necessary to define many engineering processes [16].

Herein, before constructing the nonlinear regression model some basic definitions are highlighted:

SSE (error sum of squares) is the sum of the squared differences between each observation and experimental value can be used as a measure of variation within a cluster. If all cases within a cluster are identical, the SSE would then be equal to 0. The formula for SSE is

$$SSE = \sum_{i=1}^n (x_i - x_{fit})^2$$

where n is the number of rows.

SST (the total sum of squares) is a quantity that appears as part of a standard way of presenting results of such analyses. It is defined as being the sum, over all observations, of the squared differences of each observation from the overall mean. The formula for SST is

$$SST = \sum_{i=1}^n (x_i - x_{mean})^2$$

Coefficient of determination ( $R^2$ ) is used to represent a relation between two quantitative variables. It comprises estimating the best function to summarize the relationship. The value of  $R^2$  is often mentioned to as a percentage and it ranges from 0 to 1, and the higher its value, the regression model is the more accurate. The expression for  $R^2$  is

$$R^2 = 1 - \frac{SSE}{SST}$$

### Optimization Algorithms

Optimization is defined as a mathematical process to acquire the best or the most convenient design by maximizing or minimizing the objective function under specified constraints. There are several optimization algorithms to achieve the optimum result in a design problem. These algorithms can be classified as traditional and non-traditional methods. Traditional methods such as constrained variation and Lagrange multipliers are analytical and include only continuous and differentiable functions to find the optimum result [17]. It should be considered here that optimization problems can be involved highly nonlinear terms and these kinds of optimization problems can be estimated with the rare error by using



non-traditional methods. For this reason, stochastic optimization methods from non-traditional methods, such as RS, SA, and DE, methods, become more popular and convenient among other algorithms. A detailed review about optimization methods can be found in the study by Rao, S.S [17]. RS, SA, DE, and NM algorithms were briefly explained as follows:

*Random Search* is a stochastic method based on generating a population of random starting points. It converges to a local minimum by using a local optimization method from each starting point and the best local minimum is chosen as a solution. The main advantage of this algorithm is that it enables to acquire the global optimum for non-convex, non-differentiable objective functions containing continuous, discrete domains, or a mix of them for large-scale problems [18].

*Simulated Annealing* is one of the most popular methods which is motivated from the physical process of annealing. Annealing is a type of heat treatment process wherein a metal is heated to a high temperature and allowed to cool slowly. Since this process allows the atomic structure of the material to settle to a lower energy state, metallic material becomes tougher. In SA algorithm, annealing process enables the structure to recover of a local minimum, and to settle on a better global optimum point. SA algorithm has also more advantageous to solve several optimization problems such as continuous, discrete, or mixed-integer [18].

*Differential Evolution* is a type of stochastic optimization method that maximizes or minimizes the design problem iteratively. Although it permits alternative and convergent global optimum solutions, it is not assured to find the global optimum. It includes initialization, mutation, crossover, and selection steps [18].

*Nelder-Mead* is an optimization method and enables to achieve minimum or maximum response of objective function for the unconstrained optimization problem. Even though this method is not a global optimization algorithm, it can give reasonable results for problems that do not have many local minima in practical use [18].

### Problem Definition

In the present study, the effect of design parameters; rotational speed, welding speed and axial force on the tensile strength of friction stir welded AA7039 aluminum alloy joints are investigated. Single objective optimization approach is employed to maximize tensile strength by means of different direct search methods including stochastic optimization approaches (DE, SA, NM, RS). Detail explanation about the problem description is given as follow:

#### Single Objective Problem

##### Find

$$\{x_1 \in [1200, 1600] \wedge x_2 \in [22, 75] \wedge x_3 \in [4, 8]: \{x_1, x_2, x_3\}$$

##### Maximize

$$TS (x_1, x_2, x_3)$$

##### Constraints

$$\text{Scenario 1: } 1200 \leq x_1 \leq 1600, 22 \leq x_2 \leq 75, 4 \leq x_3 \leq 8$$

$$\text{Scenario 2: } 1200 \leq x_1 \leq 1600, 22 \leq x_2 \leq 75, 4 \leq x_3 \leq 8 \quad \{x_1, x_2, x_3\} \in \text{Integers}$$

##### Design variables

$$x_1, x_2, x_3$$

where  $x_1$ ,  $x_2$  and  $x_3$  represent the parameters rotational speed, welding speed and axial force respectively. Tensile strength is an objective function and named as TS.

### Results and Discussion

In this section, mechanical strength of friction stir welded AA7039 aluminum alloy joints are presented by considering the process parameters which are tool rotational speed, welding speed and axial force. The neuro-regression approach has been used to mathematically model the friction FSW process. The optimum FSW process parameters required to gain maximum tensile strength are

determined using direct search methods Nelder-Mead, Random Search, Simulated Annealing and Differential Evolution.

The data used in the present study is divided into two parts as 75% for training and 25% for testing. The multiple nonlinear regression model is composed employing 75% part of the data, and the remaining 25% ones are utilized to test the regression model. The training and testing data and their corresponding mechanical strength values taken from the paper in literature [19] are given in Table 1.

Table 1. Training, testing data and corresponding observed response [19]

	Experimental Run Numbers	Rotational Speed "N" (r/min)	Welding Speed "S" (mm/min)	Axial Force "F" (kN)	Tensile Strength "TS" (MPa)
Training	1	1200	22	4	180
	2	1200	22	8	200
	3	1200	45	6	255
	4	1200	75	8	209
	5	1400	22	6	258
	6	1400	45	4	296
	7	1400	45	8	298
	8	1600	22	8	224
	9	1600	45	6	292
	10	1600	75	4	211
	11	1600	75	8	214
Testing	12	1400	75	6	243
	13	1200	75	4	170
	14	1600	22	4	238
	15	1400	45	6	317

Then, using data in Table 1, multiple nonlinear regression model for mechanical strength has been obtained as follow:

### Tensile Strength

$$TS = -2028.66 + 2.68085 N - 0.000848771 N^2 + 8.18779 S - 0.00101347 NS - 0.0804298 S^2 + 65.746 F - 0.0274144 NF + 0.128317 SF - 2.61271 F^2$$

Here, N, S and F represent rotational speed, welding speed and axial force, respectively.

Table 2 shows boundedness check result and values of SSE, SST and R<sup>2</sup> for training and testing process. A well-described model provides two conditions: (i) the obtained R<sup>2</sup> training and testing values should converge to 1 and (ii) as a result of the check of the boundedness of the candidate models for prescribed values, the obtained results should be realistic. For this study, R<sup>2</sup> training and testing values are found as 0.9989 and 0.9747, respectively. To evaluate whether the proposed model bounded or not, the maximum and minimum values of the models in the given interval for each design variables are calculated. The maximum and minimum tensile strength values in this problem are found as 319.91 MPa and 169.781 MPa, respectively. These results are realistic and appropriate for the defined problem in this study. In this regard, it can be said that the proposed second order multiple non-linear model is valid for friction stir problem.

Table 2. Results of neuro regression model for fitting parameters and boundedness

	Number of Data	Error Sum of Squares SSE	Total Sum of Squares SST	Coefficient of Determination R <sup>2</sup>	Maximum Tensile Strength (MPa)	Minimum Tensile Strength (MPa)
Training	11	20.1306	17686.2	0.9989	319.91	169.781
Testing	4	274.361	10826	0.9747		

Comparison of tensile strength values of the friction stir welded AA7039 aluminium alloy joints for the proposed model and experimental is presented in Figure 1. Here, axial force is taken as 4 kN, 6 kN and 8 kN, in Figure 1a, 1b and 1c, respectively. Results in Figures 1a, 1b and 1c are presented in Figure 1d together. It is seen that the second order regression model fit well with experimental results given in [19]. It is seen that the proposed model fit well with the experimental results.

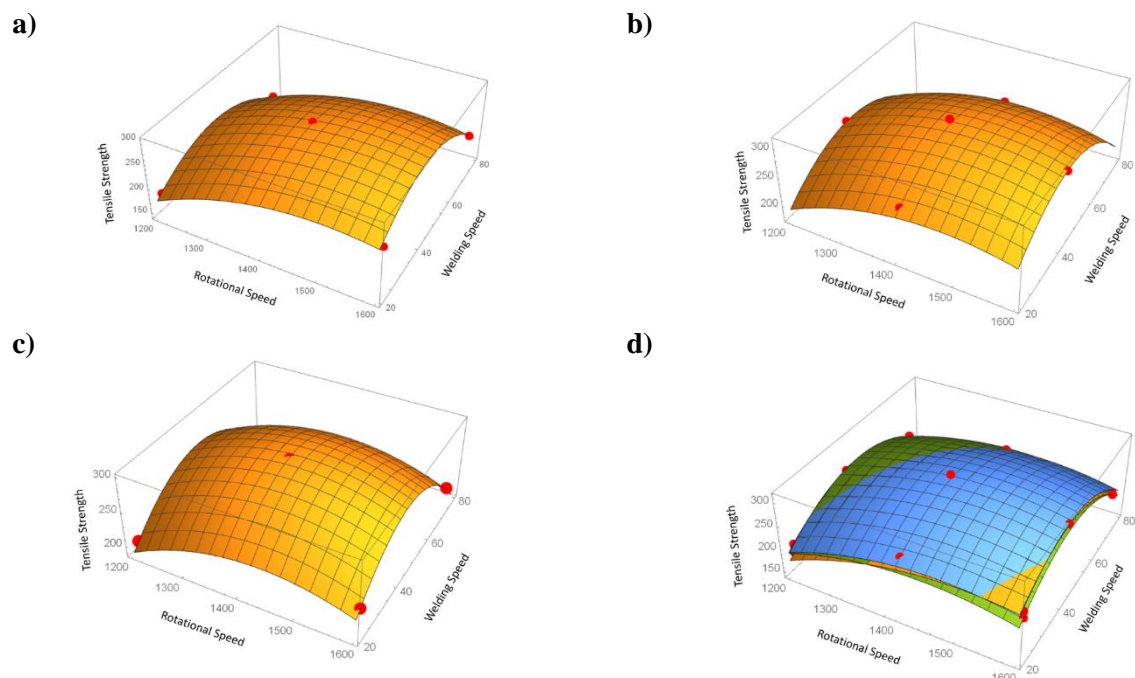


Figure 1. Comparison between experimental and recommended model results on tensile strength in terms of rotational speed and welding speed

Table 3 shows the optimum tensile strength of friction stir welded AA7039 aluminium alloy joints employing different direct search methods, including stochastic approaches: NM, SA, DE and RS. Here, all of the design variables are assumed to be real numbers and the search space is continuous. It is seen that all optimization methods give same mechanical strength value as 319.91 MPa. As a result of experimental study which is carried out in [19] obtained maximum tensile strength value is 317 MPa. The values of design parameters rotational speed, welding speed, axial force have been gained as 1452.84 (r/min), 46.62 (mm/min) and 6.10 (kN), respectively.

Table 3. Results of optimization problem considered for continuous search space

Optimization Methods	Design Variables			Tensile Strength (MPa)
	Rotational Speed (r/min)	Welding Speed (mm/min)	Axial Force (kN)	
NM	1452.84	46.62	6.10	319.91
SA	1452.84	46.62	6.10	319.91
DE	1452.84	46.62	6.10	319.91
RS	1452.84	46.62	6.10	319.91

Table 4 denotes optimum design of friction stir welded AA7039 aluminium alloy joints for maximum tensile strength by four different algorithms when the search space is selected as integer. Unlike continuous space, all algorithms have not given the same tensile strength values in the optimization performed considering the integer space assumption. While DE and NM find maximum tensile strength as 319.87 MPa, SA and RS find it as 319.84 MPa and 316.82 MPa, respectively.

Table 4. Results of optimization problem considered for integer search space

Optimization Methods	Design Variables			Tensile Strength (MPa)
	Rotational Speed (r/min)	Welding Speed (mm/min)	Axial Force (kN)	
NM	1454	47	6	319.87
SA	1449	47	6	319.84
DE	1454	47	6	319.87
RS	1474	47	5	316.82

When an overall assessment is made of the effect of search space on design of friction stir welded AA7039 aluminium alloy joints, it can be said that the higher tensile strength has been obtained under continuous search space compared to integer search space; however, this value is not a significant difference providing improvement in design.

### Conclusion

This paper has focused on a solid-state joining technique which is the FSW. The effect of design parameters; rotational speed, welding speed and axial force on the tensile strength of friction stir welded AA7039 aluminium alloy joints are investigated. Automotive, aerospace and marine industries consider this process to join aluminium, zinc, magnesium and copper alloys. The neuro-regression approach has been used to model the friction FSW process. The optimum process parameters required to obtain maximum tensile strength are determined using Nelder-Mead, Random Search, Simulated Annealing and Differential Evolution. The results of the study show that the proposed optimization algorithms give the same result (319.91 MPa) and provide good predictions by considering the same design variables. The followings can be advised as optimum process parameters for FSW: Rotational speed =1452.84 r/min; Welding speed=46.62 mm/min; Axial force=6.10 kN.

### References

- [1] Liu H J, Fujii H, Maedaa M, Nogi K. Tensile properties and fracture locations of friction-stir-welded joints of 2017-T351 aluminum alloy. *J Mater Process Technol.* 2003;142(3):692-6.
- [2] Lakshminarayanan AK, Balasubramanian V & Elangovan K. Effect of welding processes on tensile properties of AA6061 aluminium alloy joints. *Int J Adv Manuf Technol.* 2009;40:286-96.
- [3] Threadgill PL, Leonard AJ, Shercliff HR, Withers PJ. Friction stir welding of aluminium alloys. *Int Mater Rev* 2009;54(2): 49-93.
- [4] Mishra RS, Ma ZY. Friction stir welding and processing. *Mater Sci Eng, R.* 2005; 50:1-78.
- [5] Nandan R, Deb Roy T, Bhadeshia HKDH. Recent advances in friction stir welding – Process, weldment structure and properties. *Progress Mater Sci* 2008; 53:980-1023.
- [6] Sharma C, Dwivedi DK, Kumar P. Effect of welding parameters on microstructure and mechanical properties of friction stir welded joints of AA7039 aluminum alloy. *Mater Des,* 2012;36:379-90.
- [7] Peel M, Steuwer A, Preuss M, Withers PJ. Microstructure, mechanical properties and residual stresses as a function of welding speed in AA5083 friction stir welds. *Acta Materilia* 2003;51(16):4791-801.
- [8] Liu HJ, Fujii H, Maeda M, Nogi K. Mechanical properties of friction welded joints of 1050-H24 aluminum alloy. *Sci Technol Weld Joining* 2003;8(6):450-4.
- [9] Crawford R, Cook GE, Strauss AM, Hartman DA, Stremmer MA. Experimental defect analysis and force prediction simulation of high weld pitch friction stir welding. *Sci Technol Weld Joining* 2006;11(6):657-65.
- [10] Reynolds AP. Visualisation of material flow in autogenous friction stir welds, *Sci Technol Weld Joining* 2000;5(2):120-4.

- [11] Colligan K. Material flow behavior during friction stir welding of aluminum. *Weld J* 1999; 78:229–37.
- [12] Krishnan KN. On the formation of onion rings in friction stir welds. *Mater Sci Eng* 2002;327:246–51.
- [13] Sakthivel T, Senger GS, Mukhopadhyay J. Effect of welding speed on microstructure and mechanical properties of friction stir welded aluminum. *Int J Adv Manuf Technol* 2009; 43:468–73.
- [14] Balasubramanian V. Relationship between base metal properties and friction stir welding process parameters. *Mater Sci Eng* 2008;480:397–403.
- [15] Singh RKR, Chaitanya Sharma, Dwivedi DK, Mehta NK, Kumar P. The microstructure and mechanical properties of friction stir welded Al–Zn–Mg alloy in as welded and heat treated conditions. *Mater Design* 2011; 32:682–7.
- [16] Ozturk S, Aydin L, Kucukdogan N, & Celik E. Optimization of lapping processes of silicon wafer for photovoltaic applications. *Solar Energy*, 2018;164, 1-11.
- [17] Rao S S. *Engineering optimization: theory and practice*: John Wiley & Sons. 2019
- [18] Savran M, Aydin L. Stochastic optimization of graphite-flax/epoxy hybrid laminated composite for maximum fundamental frequency and minimum cost. *Eng Struct* 2018;174:675–87.
- [19] Lakshminarayanan AK, Balasubramanian V. Comparison of RSM with ANN in predicting tensile strength of friction stirwelded AA7039 aluminium alloy joints. *Trans NonferrousMet Soc China* 2009;19(1):9–18.

## Investigation in Graphene/Silicon-based Schottky Junction Solar Cell

*Ala K. Jehad\**, Dokuz Eylül Univ., Dept. of Physics, İzmir, Turkey  
*Metin Yurddaşkal*, Dokuz Eylül Univ., Dept. of Metallurgical and Materials Engineering, İzmir, Turkey  
*Kemal Kocabaş*, Dokuz Eylül Univ., Dept. of Physics, İzmir, Turkey  
*\*Corresponding author: ala.jehad13@gmail.com*

**Keywords:** Graphene, photovoltaics, Schottky junction, efficiency, silicon solar cell, I-V characteristics  
**Discipline:** Physics, Materials Science, Renewable energy

### Abstract

Graphene has recently attracted much attention in solar applications due to its astonishing physical and chemical properties. Graphene has excellent electrical conductivity, high transparency, good mechanical flexibility, high carrier mobility, and large surface area. Graphene has been utilized for different purposes in photovoltaic technologies. It has been used as a transparent conducting film, active light-harvesting material, transparent electrode, and hole-transporting material. Graphene/silicon Schottky junction solar cell has been considered as a high-efficiency and low cost-effective solar cell. Recently, the power conversion efficiency (PCE) has reached up to 15.8% and 22.55% for p-G/n-Si and n-G/p-Si Schottky junction solar cell respectively. However, these efficiencies are still limited to fundamental principles of Schottky junction. Assorted methods have been used to improve the cell-efficiency, such as texturing silicon surface, anti-reflection coating, doping graphene, and using multi-layer graphene. In this study, graphene sheet has been synthesized by chemical vapor deposition (CVD) was transfer onto the top of silicon substrate of 1cm<sup>2</sup> area to fabricate Schottky junction solar cell. The cell was examined by IV characterization, Raman spectroscopy and Scanning electron microscopy (SEM).

### Introduction

The finding of graphene (G) urged the scientific community to study more theoretically and experimentally about this wonder material [1]. The sp<sup>2</sup> structure of graphene has shown numerous remarkable properties such as highly optical transparence, near-zero bandgap, highly electrical conduction, highly mobility of carriers, good mechanical flexibility and high optical transparency [2]–[4]. Graphene has been investigated widely in the applications of solar cells. Many studies have been reported about using graphene in the photovoltaic filed, where graphene has been used as a transparent electrodes anode, cathode and catalytic counter [5]–[7]. Graphene has been also used as an active layer material to harvest sun light [8] by making a Schottky junction with semiconductor [9]. As an electron/hole transport layer [10] and as interfacial layer in the configuration of tandem solar cell [11].

Numerous studies have been focused on using graphene as a metal to construct the Schottky junction with a different semiconductor (Sc) materials [12], [13]. The G/Sc Schottky junction is considered to be the simplest device that illustrate the physical phenomena at the interface between graphene 2D and bulk semiconductor 3D [14].

In Schottky junction, the semiconductor which is silicon in this study is fit in between two metals where one metal forms a Schottky contact (graphene in our study case) and other forms an Ohmic contact (silver) with the silicon (Si). The G/Si junction creates a voltage barrier which prevents electrons to move from graphene to the silicon called Schottky barrier [15]. This barrier acts as a rectifier with a current-voltage (I-V) characteristic similar to that of a metal/semiconductor Schottky diode [14].

Graphene/silicon Schottky junction can be fabricated by wet transferring of a CVD graphene layer on the top of Si substrate. The fabrication cost of this cell is much cost-effective in comparison to the p-n junction solar cells.

The first G/n-Si solar cell was achieved in 2010 with a power conversion efficiency (PCE) of 1.5 % [16], and this value has reached to 15.6% in five years [17].

In this study, Graphene/silicon Schottky junction solar cell with the top-window structure has been fabricated. High quality graphene layer has been synthesized by chemical vapor deposition (CVD) method. Two different types of silicon were used to examine the behavior of the cell. The morphology and microstructure of the cells were examined using scanning electron microscopy (SEM). The quality

of graphene layer was checked by Raman spectroscopy and cell performance (I-V characteristics) was calculated under illumination of 100 mW/cm<sup>2</sup> at AM1.5G.

### Materials and Methods

In this study, two types of silicon wafer have been used as a semiconductor substrate as shown in Table 1. The structure of the study case G/Si Schottky junction solar cell is illustrated in Figure 1. Graphene layer with high quality was synthesized using chemical vapor deposition (CVD) method. Gold (Au) and silver (Ag) were used as a front and back contact of the cell.

Table 1. The properties of used silicon wafers in this study

Si wafers	Doping Conc.	R <sub>s</sub> (Ωcm)	Thickness (μm)
n-type Si <111>	Phosphor doped	< 0.04	250-300
p-type Si <100>	Boron doped (N <sub>A</sub> = 10 <sup>17</sup> cm <sup>-3</sup> )	10-20	100-300

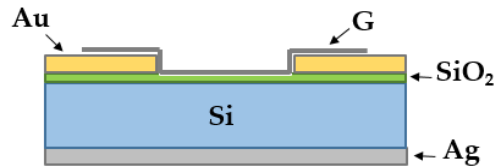


Figure 1. The schematic view of the study case

The solar cell has been fabricated through by following steps. First step was preparation of the cell substrate which include cutting the Si substrate to samples of 1×1cm<sup>2</sup> and then cleaning them with standard set of wafer cleaning steps (general clean, particle removal, metal contamination removal and oxide removal) [18] after each cleaning step, silicon substrates were washing with rinse of DI water and then dried with N gas. The second step was deposition of metal contacts where thermal deposition system was used in vacuum to deposit 150 nm of silver on the back surface of the silicon (unpolished side) and a frame of gold 50 nm with width of 2mm and open window of 4×4cm<sup>2</sup> as the front contact on the polished side of the silicon. Later, the front surface of the cell was totally covered with scotch tape then open window of 3.5×3.5cm<sup>2</sup> was made to etch the SiO<sub>2</sub> layer by soaking them in 1% of HF for 90s before transferring graphene layer.

The third step was synthesizing the graphene layer using CVD technique with the assistance of copper foils [19]. Cu foils with 1cm<sup>2</sup> area were gradually heated at 1074 °C in a flow of H<sub>2</sub> (60 sccm) and Ar (1000 sccm) for 30 min, then CH<sub>4</sub> (10 sccm) was introduced for 2 min and then samples were cooled down to the room temperature. Later, G/Cu was protected by spin-coating the top graphene with 2% of poly (methyl methacrylate) (PMMA) at 2000 rpm for 60 s. Cu foil was etched away by soaking PMMA/G/Cu in Ferric chloride (FeCl<sub>3</sub>) solution for 40 min then washed 3 times in DI water.

Last step was fabrication the schottky junction between graphene and silicon, where PMMA/graphene layer/s was transfer directly on the top of silicon substrate while it was floating in the DI water and placed into the furnace for 40 min at 60°C to dry. To remove PMMA layer, PMMA/G/Si were hold in acetone at 50°C for 8 min then placed onto hot plate for more 20 min. The device is ready for characterizations.

### Results and Discussion

In this study, two different silicon substrates have been using to fabricate schottky junction with CVD graphene. G/n-Si and G/p-Si Schottky junction solar cell. Raman Spectroscopy characteristics have been performed on a RENISHAW in via Raman microscope, with laser monochromatic light at 532nm, with lenses 20x, and 50x. The morphology of the two solar cell were examined using SEM, COXEM EM-30 Plus with magnification rate ×500–×10k at 20 kV. The I-V measurements were performed by OptoSense cell simulator characterization system under AM1.5 G illuminations. The IV measurements were taken at room temperature.

## Raman Spectroscopy

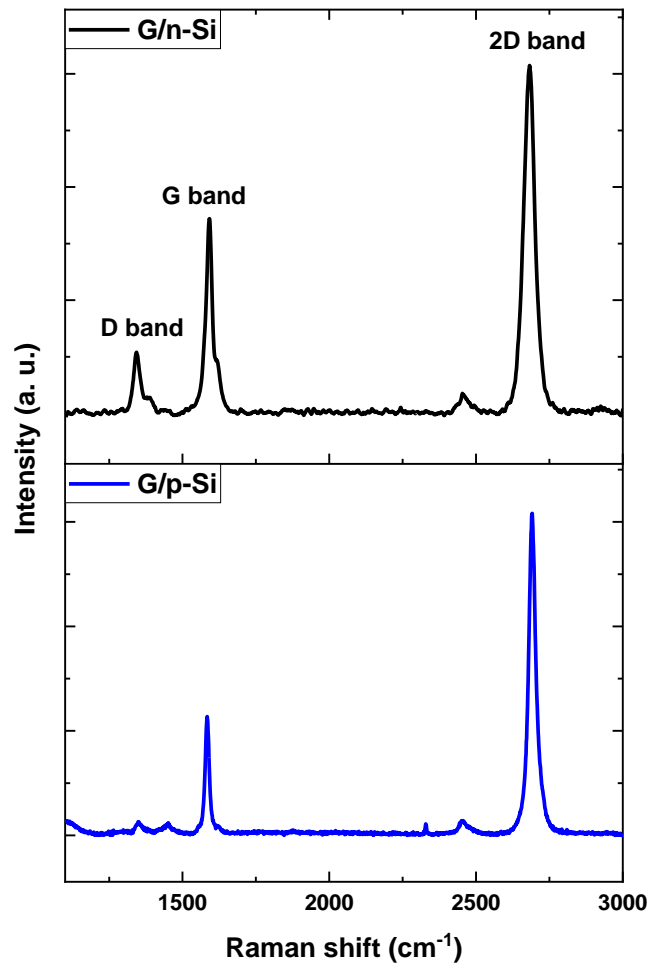


Figure 2. Raman spectra of mono-graphene layer transferred on n-Si and p-Si respectively

Figure 2 shows Raman spectra of mono graphene layer transferred onto Si substrate. Raman results exhibit the significant characteristic peaks G-band at  $1584\text{ cm}^{-1}$  and 2D-band  $\sim 2680\text{ cm}^{-1}$  in both devices. Table 2 illustrates the related data of these Raman spectra where defect density and thickness layer ratio are shown. It has been proof that high quality mono-layer graphene was successfully synthesized with a very sharp 2D band which is confirmed by thickness layer ratio ( $I_{2D}/I_G = 2.71$ ) [20] with low defect density ratio ( $I_D/I_G = 0.12$ ) for the first sample on n-Si.

While in the second p-Si, Raman spectrum exhibits the thickness layer ratio ( $I_{2D}/I_G = 1.79$ ) with defect density ratio ( $I_D/I_G = 0.31$ ).

Table 2. Raman data of synthesized CVD graphene

Sample	$I_D/I_G$	$I_{2D}/I_G$
mono-G/n-Si	0.12	2.71
mono-G/p-Si	0.31	1.79

## Scanning Electron Microscopy (SEM)

Figure 3 shows the morphology image of the graphene layer after transferred onto the silicon substrate. In the first image (a) three different colors can be distinguished Au, SiO<sub>2</sub>, and Si from left to right all covered with one layer of graphene. While in the second image (b) the wrinkles of graphene



layer is shown especially at the corners of the active area. The morphology of the graphene in the active area is shown in Figure 3 (c) where PMMA residue was seen.

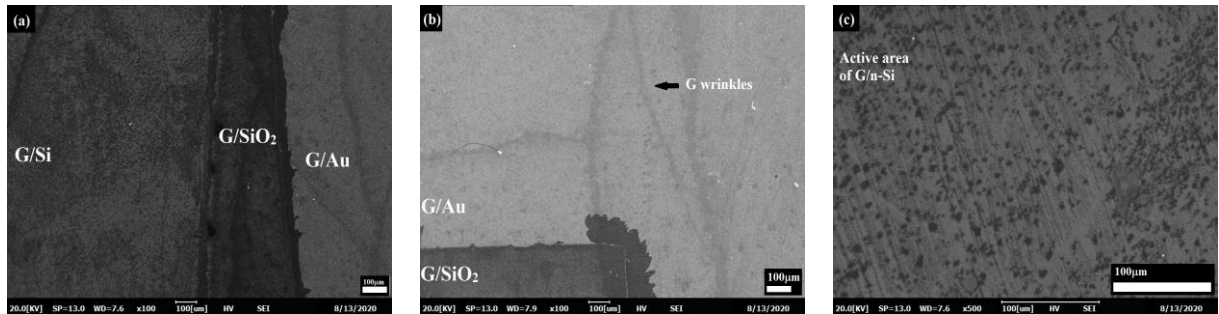


Figure 3. SEM images of mono layer graphene on Si substrate

### Measurements of IV characteristics

Figure 4 shows the I-V characteristics of the fabricated G/n- and p- Si Schottky junction solar cell under illumination of light. Table 3 illustrates the main parameters of the solar cell performance; open circuit voltage ( $V_{oc}$ ), short circuit current ( $J_{sc}$ ), Fill factor (FF) and the power conversion efficiency. The recorded IV data of our cells showed different photovoltaic respond.

The  $J_{sc}$  was found to be higher in the case of n-Si than p-Si, while  $V_{oc}$  was decreased to 150 mV in the case of n-Si. The power conversion efficiency was 0.23 in G/n-Si cell while it was 0.017 in the case of G/p-Si solar cell. The main reason is that the majority carriers in p-Si are holes so it would be more difficult to the electrons in the p-type to cross the Schottky barrier and reach the graphene. The low efficiencies in our cell it might be due to the thickness of  $SiO_2$  layer, and the techniques of depositing the front contact. More research and investigations will be continued to overcome these obstacles in fabricating this device.

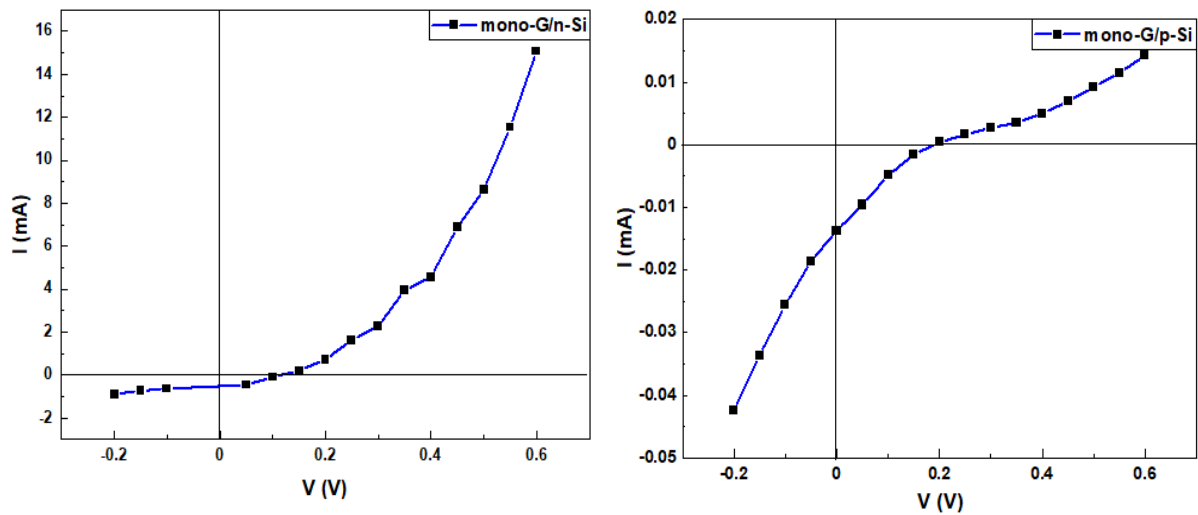


Figure 4. IV characteristic curve of the two fabricated cells

Table 3. IV main parameters of G/Si Schottky junction solar cell

Sample	$I_{sc}$ (mA/cm <sup>2</sup> )	$V_{oc}$ (mV)	FF	$\eta$ (%)
Mono-G/n-Si	0.50	150	0.31	0.23
Mono-G/p-Si	0.33	220	0.22	0.017

### Conclusions

In this study, graphene/silicon Schottky junction solar cells with a top-window structure have been fabricated. High quality mono-layer graphene sheets were successfully synthesized on copper foil using chemical vapor deposition (CVD) method. Raman spectra shows high quality mono-layer graphene sheet with thickness layer ratio 2.7 with low defect density 0.12. SEM images illustrate the morphology

of the top surface of the fabricated cell. I-V characteristics shows 0.23% power conversion efficiency in the case of mono-G/n-Si Schottky junction solar cell.

### References

- [1] A. K. Geim and K. S. Novoselov, "The rise of graphene," in *Nanoscience and technology: a collection of reviews from nature journals*, World Scientific, 2010, pp. 11–19.
- [2] A. H. C. Neto, F. Guinea, N. M. R. Peres, K. S. Novoselov, and A. K. Geim, "The electronic properties of graphene," *Rev. Mod. Phys.*, vol. 81, no. 1, p. 109, 2009.
- [3] K. S. Novoselov, V. I. Fal, L. Colombo, P. R. Gellert, M. G. Schwab, and K. Kim, "A roadmap for graphene," *Nature*, vol. 490, no. 7419, pp. 192–200, 2012.
- [4] C. Lee, W. Xiaoding, and W. Jeffrey, "K.; James, H," *Meas. Elastic Prop. Intrinsic Strength Monolayer Graphene. Sci.*, vol. 321, pp. 385–388, 2008.
- [5] S. Bae *et al.*, "Roll-to-roll production of 30-inch graphene films for transparent electrodes," *Nat. Nanotechnol.*, vol. 5, no. 8, p. 574, 2010.
- [6] H. Bi *et al.*, "Large-scale preparation of highly conductive three dimensional graphene and its applications in CdTe solar cells," *J. Mater. Chem.*, vol. 21, no. 43, pp. 17366–17370, 2011.
- [7] L. Yan *et al.*, "Chemistry and physics of a single atomic layer: strategies and challenges for functionalization of graphene and graphene-based materials," *Chem. Soc. Rev.*, vol. 41, no. 1, pp. 97–114, 2012.
- [8] Z. Liu *et al.*, "Organic photovoltaic devices based on a novel acceptor material: graphene," *Adv. Mater.*, vol. 20, no. 20, pp. 3924–3930, 2008.
- [9] C. Ciminelli, F. Dell'Olio, G. Brunetti, D. Conteduca, and M. N. Armenise, "Graphene/Silicon Schottky Junction Solar Cells," in *2018 20th International Conference on Transparent Optical Networks (ICTON)*, 2018, pp. 1–4.
- [10] S. Kim *et al.*, "Robust Magnetized Graphene Oxide Platform for In Situ Peptide Synthesis and FRET-Based Protease Detection," *Sensors*, vol. 20, no. 18, p. 5275, 2020.
- [11] E. Lamanna *et al.*, "Mechanically Stacked, Two-Terminal Graphene-Based Perovskite/Silicon Tandem Solar Cell with Efficiency over 26%," *Joule*, 2020.
- [12] S. Tongay *et al.*, "Graphene/GaN Schottky diodes: Stability at elevated temperatures," *Appl. Phys. Lett.*, vol. 99, no. 10, p. 102102, 2011.
- [13] Y. Lin *et al.*, "Graphene/semiconductor heterojunction solar cells with modulated antireflection and graphene work function," *Energy Environ. Sci.*, vol. 6, no. 1, pp. 108–115, 2013.
- [14] A. Di Bartolomeo, "Graphene Schottky diodes: An experimental review of the rectifying graphene/semiconductor heterojunction," *Phys. Rep.*, vol. 606, pp. 1–58, 2016.
- [15] S.-J. Liang, W. Hu, A. Di Bartolomeo, S. Adam, and L. K. Ang, "A modified Schottky model for graphene-semiconductor (3D/2D) contact: A combined theoretical and experimental study," in *2016 IEEE International Electron Devices Meeting (IEDM)*, 2016, p. 14.
- [16] X. Li *et al.*, "Graphene-on-silicon Schottky junction solar cells," *Adv. Mater.*, vol. 22, no. 25, pp. 2743–2748, 2010.
- [17] Y. Song *et al.*, "Role of interfacial oxide in high-efficiency graphene–silicon Schottky barrier solar cells," *Nano Lett.*, vol. 15, no. 3, pp. 2104–2110, 2015.
- [18] K. Igarashi and T. Abe, "Method for cleaning silicon wafer." Google Patents, May 28, 2020.
- [19] X. Li, L. Colombo, and R. S. Ruoff, "Synthesis of graphene films on copper foils by chemical vapor deposition," *Adv. Mater.*, vol. 28, no. 29, pp. 6247–6252, 2016.
- [20] A. C. Ferrari, "Raman spectroscopy of graphene and graphite: disorder, electron–phonon coupling, doping and nonadiabatic effects," *Solid State Commun.*, vol. 143, no. 1–2, pp. 47–57, 2007.

## Investigating the effect of Vacancy Defect on Graphene/Hexagonal Boron Nitride In-plane Heterostructure

*Habibu Aminu Hussain\**, İzmir Kâtip Çelebi Univ., Graduate School of Natural and Applied Sciences,  
Nanotechnology, Çiğli Main Campus, İzmir, Türkiye

*Cem Özdoğan*, Department of Engineering Science, İzmir Kâtip Çelebi Univ. Çiğli Main Campus, İzmir, Türkiye  
*Nurten Akman*, Department of Physics, Mersin University, 33343 Içel, Turkey

\*Corresponding author: habaminu@gmail.com

**Keywords:** Graphene, h-BN, defect

**Discipline:** Physics

### Abstract

In this study we have successfully investigated the effect of mono vacancy on structural, electronic and magnetic properties of an in-plane (GBN) nanosheet structure. We create the in-plane GBN structure by implanting graphene island on hexagonal boron nitride substrate. We create vacancy defect at different location on the hybrids, by removing one atom of either C, B or N. The effect of these vacancies and their positions on electronic, magnetic, and physical properties of the hybrids were fully investigated.

### Introduction

The extraction of single-atom-thick graphene from bulk graphite in 2004 has led to the massive interest in other single layer materials, with or without honeycomb structure by the scientific community [1]. One of the stable one similar to graphene is the boron nitride in hexagonal form (h-BN) [2]. The ideal lattice match between graphene and h-BN make it practicable to create graphene/h-BN in-plane hybrids (GBN) structure. The honeycomb lattice of carbon atoms makes it an attractive structure in fundamental physics and electronic devices, such as capacitors and field effect transistors (FETs) [3]. Moreover, tuning it's band gap might further increase its application in optoelectronics and nanoelectronics devices. Several techniques have been suggested to open an energy gap between the valence and conduction band. One basic approach involves chemical modification such as chemical doping of graphene with foreign atoms [4]. Using liquid precursor based chemical vapor deposition (CVD) techniques, nitrogen-doped graphene was grown directly on Cu current collector and studied for its reversible Li-ion intercalation properties by Reddy [5]. The properties of purest graphene are outstanding. Being the strongest material ever tested, conduct heat and electricity efficiently and nearly transparent. Graphene is one of the favorable materials for researchers in nanotechnology.

Structural defect in graphene is inevitable during the growth or processing. The defect which often perceived as limiters somehow found their application in thermoelectric devices [6]. Graphene lattice can be reconstructed by forming non-hexagonal rings, which does not involve added or removed atoms. For example, hexagons are transformed into two pentagons and heptagons by rotating one of the C-C bonds by 90° forming what is known as Stone-Wales defect [7]. Foreign atoms can intentionally be introduced into graphene as impurities forming extrinsic defect that alter the type and amount of charge defect in the system. Nitrogen or boron are desirable dopants in carbon nanostructures since they have one electron more or less respectively. Single vacancy defect in graphene has been experimentally observed by transmission electron microscope [8] and Scanning tunneling microscope. The presence of single vacancy has fascinating and unanticipated implication. It leads to the emergence of a stable unit charge localized at the vacancy site and interacting with other charges of the conductor by means of an unscreened coulomb potential. It also breaks the symmetry between the two graphene sublattice hence inducing zero energy state at the Dirac point. Perfect graphene is nonmagnetic, but the existence of vacancy can cause magnetism, by breaking the symmetry of  $\pi$ -electron system [9].

An h-BN is the isoelectric equivalent of graphite. The boron and nitrogen atoms are alternatively arranged to form planar conjugated layers, which bundle such that the two atom types in the neighboring layers eclipse on top of one another because of polarity mismatch. Within each layer of h-BN, boron and nitrogen atoms are bound by strong covalent bonds, whereas the layers are held together by weak van der Waals forces, as in graphite. Many experimental [10] and theoretical [11] studies were carried out to investigate the effect of defect on h-BN. For instance, a pristine h-BN samples containing

micrometer sized hexagonal crystalline particles were mechanically treated using a ball-milled to intentionally introduce defect on the h-BN. Common defects observed in h-BN monolayer are the missing boron or nitrogen atoms. Another type of defect found in h-BN is the substitution of either boron or nitrogen atom with carbon atom. This type of defect has its own implication. It was found that substituting single boron atom with carbon atom in an N-rich growth or a nitrogen atom in a B-rich medium, lowers the formation energy as compares to creating a vacancy defect of either boron or nitrogen. It is also observed that two deep defect level, largely localized on the carbon atom appears slightly below the conduction band.

### Computational Method

We performed electronic structure calculations within the DFT framework.[12] The exchange correlation potential was handled through the generalized gradient approximation (GGA) together with the Perdew-Wang parametrization (PW91) [13]. For geometry optimizations, electronic and density of states (DOS) computations we used the Vienna Ab Initio Simulation Package (VASP, version 5.3) [14;15] employing the projected augmented wave (PAW) method [16,17].

### Result

In this section we will discuss the electronic and magnetic properties of pristine h-BN and in-plane GBN hybrids systems, energetics of island implantation and defect formation energy. The total energy difference between NSP and SP is called as the magnetization energy  $\Delta E_M$

$$\Delta E_M = E_{NSP} - E_{SP} \quad (1)$$

Positive  $\Delta E_M$  means that the system has a SP ground state, otherwise it refers to as NSP ground state. Each nanosheet is made of 9 x 9 unit cell with 162 atoms. Although h-BN thin film was described as an indirect band gap semi-conductor, a recent study has reported that it has a direct band gap of 5.9 eV [18]. The band gap of monolayer h-BN sheet is calculated through the LDA and G0W0 method, respectively, as 4.61 and 6.57eV. While the LDA underestimate the band gap value GGA overestimate the value, but GW method usually estimates it more accurately. We calculated the BN bond length as 1.45Å, which is consistent with the literature. [19] Calculated  $\Delta E_M$  value for h-BN is 0.4meV.

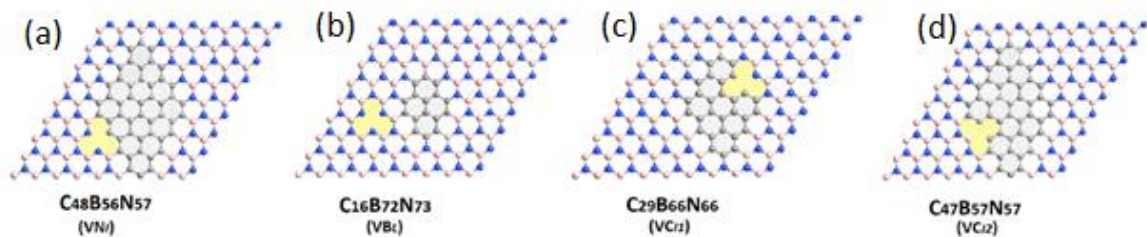


Figure 1. Optimized geometry of in-plane hybrid of graphene and h-BN GBN heterostructure. The dark blue, grey and the light orange colors show N, C and B atoms respectively. It shows a graphene layout hosting a diamond shaped h-BN island at the middle. (a) B vacancy at the interface between Cand N (b) B vacancy at the middle of N atoms (c) C vacancy at the interface between C and N (d) C vacancy at the interface between C and B

Table 8. Island formation energies for pristine GBN hybrids. The G island is in the shape of diamond (D), each having 4, 9 or 16 hexagons. Energy per atom and minimum and maximum island formation energies,  $E_{if\ min}$  and  $E_{if\ max}$  are given in eV. Minimum and maximum island formation energies per total number of atoms involved by the G island are given in eV/atom in the next two columns. The total magnetic moment  $\mu$  and band gap  $E_g$  are given in units of  $\mu_B$  and eV, respectively. Here, NM means that the hybrid is in a non-magnetic state or has no magnetic moment each.

Hybrid	Name	Energy (eV/atom)	$\mathcal{E}_{if\ min}$ (eV)	$\mathcal{E}_{if\ max}$ (eV)	$\mathcal{E}_{if\ min}$ (eV/atom)	$\mathcal{E}_{if\ max}$ (eV/atom)	$\mu$ $\mu_B$	$E_g$ (eV)
$B_{81}N_{81}$	h-BN	-8.837						4.59
$C_{16}B_{73}N_{73}$	4G(D)@h-BN	-8.843	-102.229	120.518	-6.389	7.532	NM	2.13
$C_{30}B_{66}N_{66}$	9G(D)@h-BN	-8.861	-193.582	224.068	-6.453	7.469	NM	1.12
$C_{48}B_{57}N_{57}$	16G(D)@h-BN	-8.887	-311.652	356.588	-6.493	7.429	NM	0.65

As is seen in Table 1, each hybrid system has a wide range of formation energies. The energetics prove that the reactions can both be endothermic (positive  $\mathcal{E}_{if\ max}$  values) or exothermic (negative  $\mathcal{E}_{if\ min}$  values) ion implantation processes. Energetics of hexagonal and triangular shaped island implantation for the pristine hybrids have been discussed through the solid-state reactions in our previous work.

### References

- [1] Allen, Matthew J., Vincent C. Tung, and Richard B. Kaner. "Honeycomb carbon: a review of graphene." Chemical reviews 110.1 (2009): 132-145.
- [2] Gao, Gao, Yabo, et al. "Toward single-layer uniform hexagonal boron nitride graphene patchworks with zigzag linking edges." Nano letters 13.7 (2013): 3439-3443.
- [3] Westervelt, R. M. "Graphene nanoelectronics." Science 320.5874 (2008): 324-325.
- [4] Long, Donghui, et al. "Preparation of nitrogen-doped graphene sheets by a combined chemical and hydrothermal reduction of graphene oxide." Langmuir 26.20 (2010): 16096-16102.
- [5] Reddy, Arava Leela Mohana, et al. "Synthesis of nitrogen-doped graphene lms for lithium battery application." ACS nano 4.11 (2010): 6337-6342.
- [6] Quandt, Alexander, et al. "Functionalizing graphene by embedded boron clusters." Nanotechnology 19.33 (2008): 335707.
- [7] Meyer JC, Kisielowski C, Erni R, Rossell MD, Crommie MF, Zettl A. Direct imaging of lattice atoms and topological defects in graphene membranes. Nano letters. 2008 Jun 19;8(11):3582-6.
- [8] Zhou, Wu, et al. "Direct determination of the chemical bonding of individual impurities in graphene." Physical review letters 109.20 (2012): 206803.
- [9] Gonzalez-Herrero, H., et al. "Atomic-scale control of graphene magnetism by using hydrogen atoms." Science 352.6284 (2016): 437-441.
- [10] Museur, Luc, Eduard Feldbach, and Andrei Kanaev. "Defect-related photoluminescence of hexagonal boron nitride." Physical Review B 78.15 (2008): 155204.
- [11] Hussain, Habibu Aminu, Nurten Akman, and Cem Özdoğan. "Investigation of the mono vacancy effects on the structural, electronic and magnetic properties of graphene hexagonal-boron nitride in-plane hybrid embracing diamond shaped graphene island." Solid State Sciences (2020): 106395.
- [12] Kohn, Walter, and Lu Jeu Sham. "Self-consistent equations including exchange and correlation effects." Physical review 140.4A (1965): A1133.
- [13] Perdew, John P., and Yue Wang. "Accurate and simple analytic representation of the electron-gas correlation energy." Physical Review B 45.23 (1992): 13244.
- [14] Perdew, John P., et al. "Atoms, molecules, solids, and surfaces: Applications of the generalized gradient approximation for exchange and correlation." Physical review B 46.11 (1992): 6671.
- [15] Kresse, Georg, and Jrgen Furthmüller. "Efficient iterative schemes for ab initio total energy calculations using a plane-wave basis set." Physical review B 54.16 (1996): 11169.
- [16] Blöchl, Peter E., Ove Jepsen, and Ole Krogh Andersen. "Improved tetrahedron method for Brillouin-zone integrations." Physical Review B 49.23 (1994): 16223.

- [17] Kresse, Georg, and Daniel Joubert. "From ultrasoft pseudopotentials to the projector augmented-wave method." *Physical review b* 59.3 (1999): 1758.
- [18] Watanabe, Kenji, Takashi Taniguchi, and Hisao Kanda. "Direct-bandgap properties and evidence for ultraviolet lasing of hexagonal boron nitride single crystal." *Nature materials* 3.6 (2004): 404.
- [19] Zhi, Chunyi, et al. "Large scale fabrication of boron nitride nanosheets and their utilization in polymeric composites with improved thermal and mechanical properties." *Advanced Materials* 21.28 (2009): 2889-2893.

## Mathematics / Matematik

## Numerical Solution of IVPs using Adaptive Nelder-Mead Optimization

Muhammad Jalil Ahmad\*, Aydın Adnan Menderes University, Graduate School of Natural and Applied Sciences, Dept. of Mathematics, Aydın, Türkiye  
Korhan Günel, Aydın Adnan Menderes University, Faculty of Arts & Sciences, Dept. of Mathematics, Aydın, Türkiye  
\*Corresponding author: jalilahmad82@hotmail.com

**Keywords:** Ordinary differential equation, initial value problems, derivative-free optimization, Direct Search Algorithm, Neural Network, Nelder Mead, Adaptive Nelder Mead, particle swarm optimization  
**Discipline:** Mathematics

### Abstract

In this study, we propose a numerical approach for solving first order differential equations with an initial value condition using a feed-forward neural network. Adaptive Nelder Mead Simplex (ANMS) algorithm is preferred to train the network, because ANMS is one of the derivative-free optimization algorithms, which reduce the time-consuming workloads in the training stage.

The proposed approach is compared with the state-of-art Particle Swarm Optimization (PSO) and classical Nelder-Mead Simplex (NMS) algorithms, which are well known in derivative-free algorithms. The performance analysis of these algorithms is examined using Dolan-More benchmarking optimization software tool.

### Introduction

Differential equations are substantial tools for making a mathematical model of real-world problems. Most of these problems have nonlinear characteristics, and are difficult to obtain analytical solution, in spite of knowing the existence of a single solution. In such cases, an approximate solution is tried to be obtained by numerical methods. The main bottleneck of the numerical methods is that the approximate solutions are obtained at only the quadrature nodes, which are generated via discretization or meshing procedure on the problem domain. The numerical solution at other points are only derived using interpolation methods, and this approach causes the cumulative error to increase. Alternatively, Lee and Kang (1990) show that the neural networks are capable of solving differential equations numerically [1]. Since, the researchers try to develop neural networks having different topology for solving various types of differential equations with initial and boundary conditions. The detailed literature review can be found in [2].

In this study, we propose to use Adaptive Nelder-Mead Simplex (ANMS) algorithm to train the neural networks getting numerical solutions of first order initial value problems for ordinary differential equations. The procedure is as follows.

First, we will transform the initial value problem to an optimization problem so that we can use ANMS [3]. ANMS is a derivative-free optimization algorithm [4]. Then, the results will be compared to Nelder-Mead Simplex (NMS) algorithm [4] and Particle Swarm Optimization (PSO) [5]. Finally, a performance analysis will be conducted using Dolan-More optimization software performance analysis [6].

We transform the initial value problem given in Eq. (1) to an optimization problem using Eq. (2).

$$\begin{cases} y'(t) = f(t, y(t)), a \leq t \leq b \\ y(a) = A \end{cases} \quad (1)$$

where  $y_t$  is the trial solution as defined in Eq. (2). The trial solution satisfies the initial condition, and it depends on the neural network solution in Eq. (3).

$$y_t(t, \vec{p}) = A + (t - a)Net(t, \vec{p}) \quad (2)$$

where  $x$  represents the network input, and  $\vec{p} \in \mathbb{R}^{3m+1}$  is the vector of arbitrary parameters of the neural network such that  $m$  is the total number of the neurons of the network.



$$Net(t, \vec{p}) = \sum_{j=1}^m \alpha_j \sigma(\omega_j t + \beta_{1,j}) + \beta_2 \quad (3)$$

where  $\omega_j$  values represent the weights of the connection between the input layer and the hidden layer, and  $\alpha_j$  values represent the weights of the connection between the hidden layer and the output layer for  $j = 1, 2, \dots, m$ . Similarly,  $\beta_{1,j}$  values are the bias values of the neurons in the hidden layer for  $j = 1, 2, \dots, m$ , and  $\beta_2$  is the bias for the output of the network. In Eq. (3),  $\sigma$  is sigmoid function acting as an activation function.  $\vec{p} = \vec{p}(\vec{\alpha}, \vec{\beta}, \vec{\omega})$  are unknown parameters of the neural network. To train the network, we prefer to use Adaptive Nelder-Mead Simplex algorithm as a derivative free optimization method. The network inputs, in training stage, are obtained via the discretization of the interval  $[a, b]$  using  $t_i = a + i \cdot h$  where  $h > 0$  is the step size for  $i = 1, 2, \dots, n$ . After training stage, the network gives the numerical solutions of the initial value problem given in Eq. (1) on whole of the interval  $[a, b]$ .

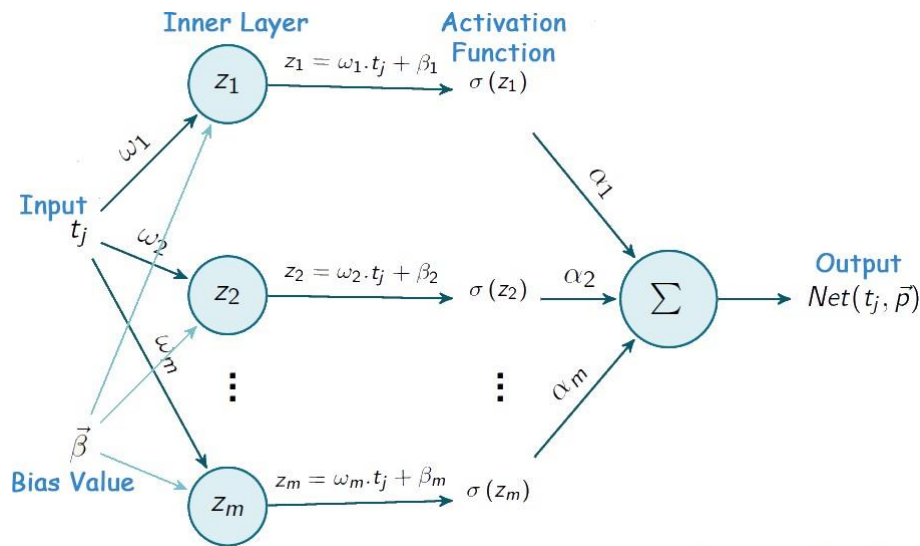


Figure 1. Topological Structure of Neural Network.

This is the major difference from the classical numerical methods for solving differential equations. In the classical methods, the numerical solutions are only obtained at the discretization points.

In the beginning, the output of the neural network is calculated for arbitrary parameters  $\vec{p} = \vec{p}(\vec{\alpha}, \vec{\beta}, \vec{\omega})$ . Of course this will result into a different output value than the expected one. Generally backpropagation algorithm is used to minimize this error.

$$E = \frac{1}{n} \sum_{i=1}^n \left( \frac{\partial y_t(x_i)}{\partial x_i} - f(x_i, y_t(x_i)) \right)^2 \quad (4)$$

### Method

The Nelder-Mead simplex algorithm is a direct search method for solving the unconstrained optimization problems.

$$\min f$$

where  $f: \mathbb{R}^n \rightarrow \mathbb{R}$  is called the objective function and  $n$  is the dimension. A simplex is a geometric figure in  $n$  dimensions that is the convex hull of  $n + 1$  vertices. The simplex is a triangle for two variables. The value of the objective function is evaluated on the vertices of the triangle. At each iteration, the vertices of the simplex are ordered according to the objective function values. The vertex at which the objective function has biggest value is changed with some other vertex and a new triangle is formed and the search continues.

### Nelder - Mean Simplex Algorithm

1. **Sort** Evaluate  $f$  at the vertices of the simplex and sort the vertices so that

$$f(x_1) \leq f(x_2) \leq \dots \leq f(x_{n+1})$$

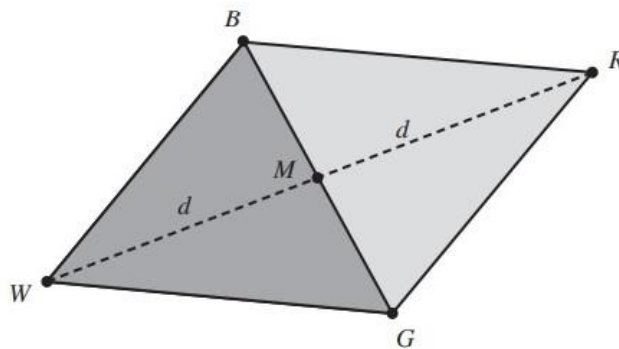
holds where  $x_i \in \mathbb{R}^n$  for  $i = 1, 2, \dots, n + 1$ .

2. **Reflection** Compute the reflection point  $x_r$  from

$$x_r = \bar{x} + \alpha(\bar{x} - x_{n+1})$$

where  $\alpha$  is real valued reflection coefficient.

Evaluate  $f_r = f(x_r)$ . If  $f_1 \leq f_r < f_n$ , replace  $x_{n+1}$  with  $x_r$



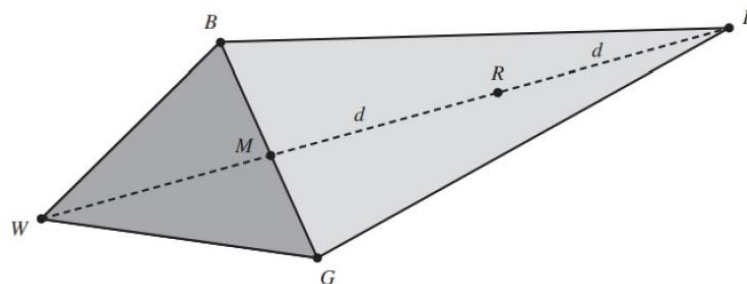
The simplex is a triangle for two variables. The vertex with worst value is denoted with  $W$ , good with  $G$  and best with  $B$ .  $M$  is the mid-point of the side  $[BG]$  and  $R$  is the reflection of the vertex  $W$ . Also  $|WM| = |MR| = d$ .

3. **Expansion** If  $f_r < f_1$  then compute the expansion point  $x_e$  from

$$x_e = \bar{x} + \beta(x_r - \bar{x})$$

where  $\beta$  is real valued expansion coefficient.

Evaluate  $f_e = f(x_e)$ . If  $f_e < f_r$ , replace  $x_{n+1}$  with  $x_e$ ; otherwise replace  $x_{n+1}$  with  $x_r$ .



Here  $E$  denotes the vertex after expansion.

4. **Inside Contraction** If  $f_r \geq f_{n+1}$ , compute the inside contraction point  $C_1$  from

$$C_1 = \bar{x} - \gamma(x_r - \bar{x})$$

where  $\gamma$  is real valued inside contraction coefficient.

Evaluate  $f_{ic} = f(C_1)$ . If  $f_{ic} < f_{n+1}$ , replace  $x_{n+1}$  with  $C_1$ ; otherwise, go to step 5.

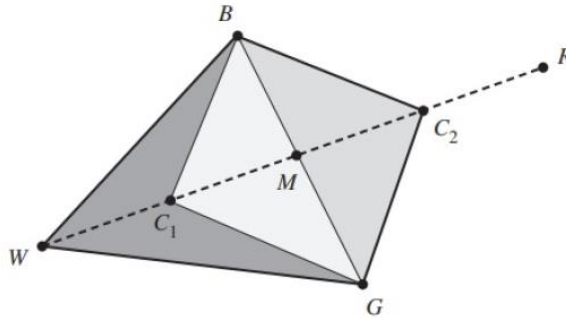
5. **Outside Contraction** If  $f_n \leq f_r < f_{n+1}$ , compute the outside contraction point

$$C_2 = \bar{x} + \gamma(x_r - \bar{x})$$

Evaluate  $f_{oc} = f(C_2)$ . If  $f_{oc} \leq f_r$ , replace  $x_{n+1}$  with  $C_2$ ; otherwise go to step 6.

6. **Shrink** For  $2 \leq i \leq n + 1$ , define

$$x_i = x_1 + \delta(x_i - x_1)$$



Here denotes  $C_1$  inside contraction and  $C_2$  denotes outside contraction.

#### Adaptive Nelder – Mead Algorithm

Let  $\Delta$  be a simplex in  $\mathbb{R}^n$  with vertices  $\{x_1, x_2, \dots, x_{n+1}\}$ . Using these vertices let's define the functional

$$F(\Delta) = f(x_1) + f(x_2) + \dots + f(x_{n+1}).$$

Now the reduction in the functional  $F(\Delta)$  caused by an expansion or contraction step depends on the factor  $\frac{n-1}{2n^2}$ . It decreases for  $n \geq 2$  and converges to 0 as  $n \rightarrow \infty$ . This indicates that the efficiency of the expansion and contraction steps diminishes as the dimension  $n$  increases. Reducing the chances of using reflection steps and avoiding the rapid reduction in the simplex diameter should help improve the performance of the Nelder-Mead simplex method for large dimensional problems. New parameters are:

$$\alpha = 1, \beta = 1 + \frac{2}{n}, \gamma = 0.75 - \frac{1}{2n}, \delta = 1 - \frac{1}{n}$$

#### Experiments

##### Example

Consider the following IVP:

$$\begin{cases} y'(t) = e^{-t} - y \\ y(0) = 1 \end{cases} \quad (5)$$

The analytical solution of this problem is

$$y(t) = \frac{t+1}{e^t}$$

The trial solution for this problem can be written as

$$y_t(t, \vec{p}) = 1 + t \text{Net}(t, \vec{p})$$

### Results

Table 1 shows comparison of results obtained from NMS and ANMS. The table also gives the number of times of evaluation of reflection, expansion, contraction and shrink points. It is clear that best cost obtained from ANMS is better than as compared to NMS.

Table 1. NMS and ANMS Comparison

	NMS	ANMS
Best cost	$1.946 \times 10^{-6}$	$4.654 \times 10^{-8}$
Worst cost	$2.302 \times 10^{-2}$	$9.401 \times 10^{-2}$
Mean of costs	$0.0026 \pm 0.0063$	$0.0096 \pm 0.0218$
Number of cost function evaluation	1449	1696
No. of reflection point evaluation	1000	92
No. of expansion point evaluation	144	92
No. of inside contraction point evaluation	249	469
No. of outside contraction point evaluation	23	22
No. of shrink point evaluation	16	96
Mean of elapsed time	$5.712 \times 10^{-2} \pm 2.142 \times 10^{-2}$	$5.976 \times 10^{-2} \pm 7.183 \times 10^{-3}$

Table 2 shows the error for the test set. In addition to NMS and ANMS here the results are also compared with Particle Swarm Optimization Algorithm which clearly shows that PSO (Particle Swarm Optimization Algorithm) gives better results as compared to NMS and ANMS. Hence the error is much less for PSO as compared to NMS and ANMS.

Table 2. Error comparison for Test Set

<i>i</i>	<i>t<sub>i</sub></i>	Errors For		
		NMS	ANMS	PSO
1	0.000	0.000	0.000	0.000
2	0.020	$2.925 \times 10^{-06}$	$6.803 \times 10^{-07}$	$7.580 \times 10^{-06}$
3	0.040	$1.209 \times 10^{-05}$	$5.836 \times 10^{-07}$	$3.551 \times 10^{-05}$
4	0.060	$2.270 \times 10^{-05}$	$3.336 \times 10^{-08}$	$7.359 \times 10^{-05}$
5	0.080	$3.156 \times 10^{-05}$	$9.675 \times 10^{-07}$	$1.142 \times 10^{-04}$
6	0.120	$3.744 \times 10^{-05}$	$3.201 \times 10^{-06}$	$1.830 \times 10^{-04}$
7	0.140	$3.337 \times 10^{-05}$	$4.299 \times 10^{-06}$	$2.052 \times 10^{-04}$
8	0.160	$2.494 \times 10^{-05}$	$5.300 \times 10^{-06}$	$2.172 \times 10^{-04}$
9	0.180	$1.287 \times 10^{-05}$	$6.171 \times 10^{-06}$	$2.187 \times 10^{-04}$
10	0.220	$1.832 \times 10^{-05}$	$7.468 \times 10^{-06}$	$1.922 \times 10^{-04}$
11	0.240	$3.538 \times 10^{-05}$	$7.902 \times 10^{-06}$	$1.661 \times 10^{-04}$
12	0.260	$5.209 \times 10^{-05}$	$8.210 \times 10^{-06}$	$1.333 \times 10^{-04}$
13	0.280	$6.760 \times 10^{-05}$	$8.412 \times 10^{-06}$	$9.540 \times 10^{-05}$
14	0.300	$8.119 \times 10^{-05}$	$8.532 \times 10^{-06}$	$5.393 \times 10^{-05}$
15	0.320	$9.233 \times 10^{-05}$	$8.592 \times 10^{-06}$	$1.055 \times 10^{-05}$
16	0.340	$1.006 \times 10^{-04}$	$8.614 \times 10^{-06}$	$3.317 \times 10^{-05}$
17	0.360	$1.059 \times 10^{-04}$	$8.617 \times 10^{-06}$	$7.573 \times 10^{-05}$
18	0.380	$1.081 \times 10^{-04}$	$8.617 \times 10^{-06}$	$1.158 \times 10^{-04}$
19	0.420	$1.036 \times 10^{-04}$	$8.652 \times 10^{-06}$	$1.835 \times 10^{-04}$
20	0.440	$9.740 \times 10^{-05}$	$8.696 \times 10^{-06}$	$2.093 \times 10^{-04}$
21	0.460	$8.909 \times 10^{-05}$	$8.756 \times 10^{-06}$	$2.285 \times 10^{-04}$
22	0.480	$7.905 \times 10^{-05}$	$8.825 \times 10^{-06}$	$2.408 \times 10^{-04}$
23	0.520	$5.563 \times 10^{-05}$	$8.935 \times 10^{-06}$	$2.430 \times 10^{-04}$
24	0.540	$4.315 \times 10^{-05}$	$8.942 \times 10^{-06}$	$2.327 \times 10^{-04}$
25	0.560	$3.073 \times 10^{-05}$	$8.887 \times 10^{-06}$	$2.149 \times 10^{-04}$

26	0.580	$1.878 \times 10^{-05}$	$8.747 \times 10^{-06}$	$1.899 \times 10^{-04}$
27	0.620	$2.371 \times 10^{-06}$	$8.109 \times 10^{-06}$	$1.202 \times 10^{-04}$
28	0.640	$1.104 \times 10^{-05}$	$7.562 \times 10^{-06}$	$7.680 \times 10^{-05}$
29	0.660	$1.816 \times 10^{-05}$	$6.834 \times 10^{-06}$	$2.882 \times 10^{-05}$
30	0.680	$2.363 \times 10^{-05}$	$5.905 \times 10^{-06}$	$2.281 \times 10^{-05}$
31	0.720	$2.940 \times 10^{-05}$	$3.399 \times 10^{-06}$	$1.327 \times 10^{-04}$
32	0.740	$2.975 \times 10^{-05}$	$1.815 \times 10^{-06}$	$1.885 \times 10^{-04}$
33	0.760	$2.855 \times 10^{-05}$	$1.902 \times 10^{-08}$	$2.432 \times 10^{-04}$
34	0.780	$2.595 \times 10^{-05}$	$1.969 \times 10^{-06}$	$2.953 \times 10^{-04}$
35	0.820	$1.747 \times 10^{-05}$	$6.380 \times 10^{-06}$	$3.860 \times 10^{-04}$
36	0.840	$1.215 \times 10^{-05}$	$8.700 \times 10^{-06}$	$4.214 \times 10^{-04}$
37	0.860	$6.555 \times 10^{-06}$	$1.100 \times 10^{-05}$	$4.481 \times 10^{-04}$
38	0.880	$1.062 \times 10^{-06}$	$1.318 \times 10^{-05}$	$4.645 \times 10^{-04}$
39	0.920	$7.914 \times 10^{-06}$	$1.674 \times 10^{-05}$	$4.593 \times 10^{-04}$
40	0.940	$1.046 \times 10^{-05}$	$1.781 \times 10^{-05}$	$4.344 \times 10^{-04}$
41	0.960	$1.104 \times 10^{-05}$	$1.819 \times 10^{-05}$	$3.923 \times 10^{-04}$
42	0.980	$9.113 \times 10^{-06}$	$1.766 \times 10^{-05}$	$3.313 \times 10^{-04}$
43	1.000	$4.099 \times 10^{-06}$	$1.599 \times 10^{-05}$	$2.496 \times 10^{-04}$

Table 3 shows the comparison of Mean Square Root Error for the test set. From the table, it is clear that ANMS gives better results as compared to NMS and PSO.

Table 3. MSE (Mean Square Root) Error Comparison

Method	MSE for test set
NMS	$7.635 \times 10^{-06}$
ANMS	$1.370 \times 10^{-06}$
PSO	$3.586 \times 10^{-05}$

Figure 1 shows the analytical solution and the numerical solution for the test set obtained from NMS, ANMS and PSO, of the IVP given in Eq. 5. Clearly, NMS and ANMS are efficient in solving the IVP give in Eq. 5.

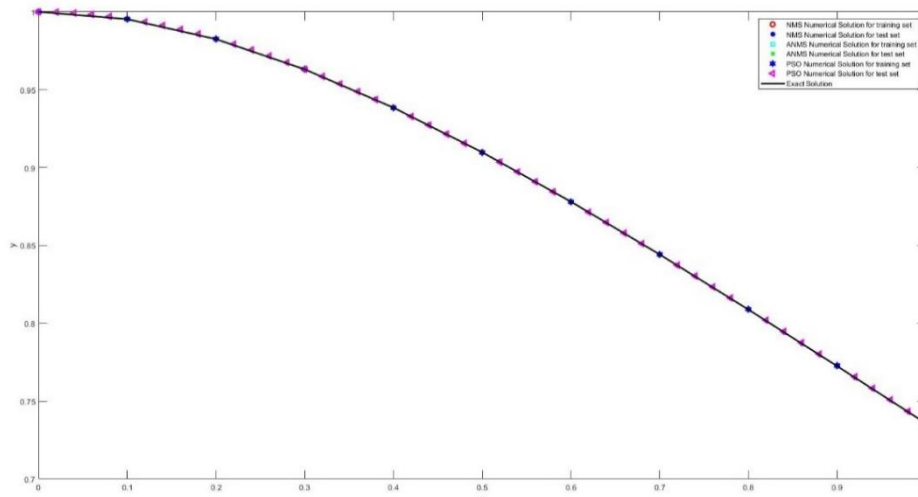


Figure 1. Analytical and Numerical Solution

Figure 2 show the Dolan More Performance Analysis for NMS, ANMS and PSO. Despite the fact that PSO shows very low error in Table 2, NMS and ANMS have an edge in terms of performance as they give solution much quickly.

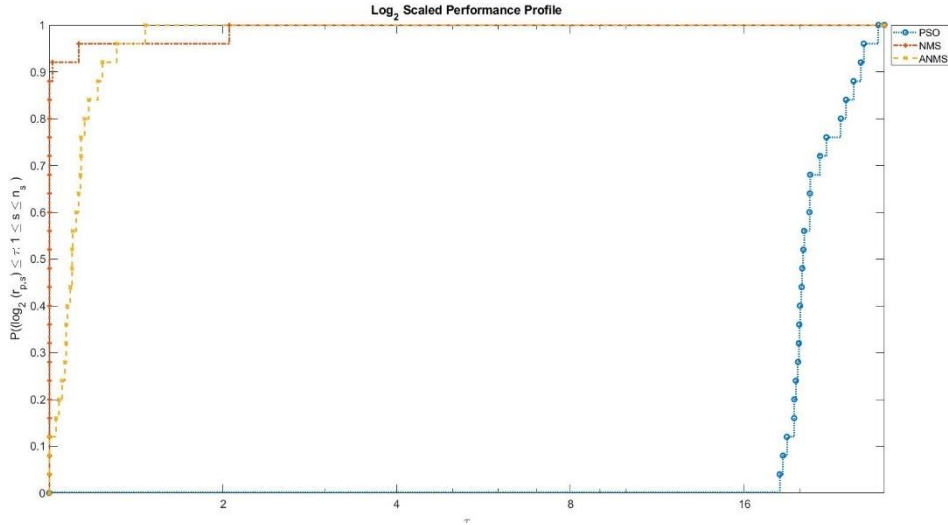


Figure 2. Dolan More Performance Analysis

### Conclusions

In this study an IVP is solved using Feed-Forward Neural Network, which is trained by Adaptive Nelder-Mead Simplex optimization method upgrading from classical Nelder-Mead Simplex algorithm. The results show that ANMS is preferred to train the neural network for solving IVP numerically. In our future work, Adaptive Nelder-Mead Simplex method will be upgraded using different approaches such as introducing a new weighting schema for enhancing adaptability of the parameters of optimization method. So that more robust parameter tuning approach for NMS will be presented.

### References

- [1] Lee H, Kang IS. 1990. Neural algorithms for solving differential equations. Journal of Computational Physics, 91(1): 110-131.
- [2] Gör I. Diferansiyel denklemlerin yapay sinir ağları ile nümerik çözümleri (en: Numerical solutions of differential equations by artificial neural networks), Phd. Thesis, Aydın Adnan Menderes University, Graduated School of Natural and Applied Sciences, Dept. of Mathematics, 2020, 91 pages.
- [3] Gao F, Han, L. Implementing the Nelder-Mead simplex algorithm with adaptive parameters. Comput Optim Appl. 2012; 51(1):259-277.
- [4] Audet C, Hare W. Derivative-Free and Blackbox Optimization. Switzerland: Springer; 2017.
- [5] Kennedy J, Eberhart R. Particle swarm optimization, Proceedings of IEEE International Conference on Neural Networks, Vol. 4, pp. 1942–1948, 1995.
- [6] Dolan ED, Moré JJ. Benchmarking optimization software with performance profiles. Math Program. 2002; 91: 201–213.

## A Numerical Algorithm to Solve a Class of Neutral Type Functional Integro-Differential Equations by Using Shifted Gegenbauer Polynomials

Tuğçe Özalp\*, Manisa Celal Bayar Üniv., Dept. of Mathematics Manisa, Türkiye  
Mehmet Sezer, Manisa Celal Bayar Üniv., Dept. of Mathematics, Manisa, Türkiye  
\* Corresponding author: tugce.mollaoglu@hotmail.com

**Keywords:** Neutral type functional integro-differential equations, shifted Gegenbauer polynomials  
**Discipline:** Mathematics

### Abstract

In this study, an operational matrix method based on collocation points and Shifted Gegenbauer polynomials is developed for solving the approximate solutions of high-order neutral integro differential equations involving variable coefficients and mixed delays. These kinds of equations characterized by the presence of functional delays play an important role in explaining many different phenomena and, particularly, arise in industrial applications and in studies based on biology, economy, electrodynamics, physics and chemistry. The proposed algorithm reduces the solution of the mentioned neutral integro-differential equation subject to the initial conditions to the solution of a matrix equation with the unknown Gegenbauer coefficients. Moreover, the approximate solution is obtained in terms of Shifted Gegenbauer polynomials. Besides, some examples along with residual error techniques are performed to illustrate the efficiency of the method; the obtained results are scrutinized and interpreted.

### Introduction

In this study, the finite shifted Gegenbauer matrix-collocation method is established to solve second-order linear neutral type functional integro-differential equations with variable delays in the form

$$\sum_{k=0}^2 P_k(t)y^{(k)}(t) + \sum_{j=0}^2 Q_j(t)y^{(j)}(a_j t - \beta_j) = G(t) + \int_0^{h(t)} \sum_{r=0}^2 K_r(t,s)y^{(r)}(\mu_r s + \gamma_r) ds \quad (1)$$

under the condition

$$y^{(k)}(0) = \lambda_k, k = 0, 1, \dots, m - 1 \quad (2)$$

where  $P_k(t), Q_j(t), G(t)$  and  $K_r(t, s)$  are defined on  $0 \leq t, s \leq 1$ ;  $a_j, \beta_j$ , and  $\lambda_l$  are appropriate constants. Linear functional integro-differential equation involved in Eq.(1) is a combination of neutral differential with variable delay and Volterra integral equations. These type equations explore many physical phenomena arising in applied sciences, such as mathematics, engineering, electrodynamics, mechanics, physics and biology etc. [10-11]. In recent year, the mentioned equations have been enquired by many authors for their analytic and numerical solutions; so numerical methods are required [4-9]. Our purpose in this study is to establish the matrix-collocation method based on shifted Gegenbauer polynomials and to find the approximate solution of the problem (1)-(2) in the truncated shifted Gegenbauer series form

$$y(t) \cong y_N(t) = \sum_{n=0}^N a_n S_n(t, \lambda), 0 \leq t \leq 1 \quad (3)$$

where  $a_n, n = 0, 1, \dots, N$  are unknown coefficients and  $S_n(t, \lambda)$  is shifted Gegenbauer polynomials, which are defined as

$$S_n(t, \lambda) = G_n(2t - 1, \lambda), 0 \leq t \leq 1$$

$$G_n(t, \lambda) = \sum_{k=0}^{\lfloor \frac{n}{2} \rfloor} (-1)^k \frac{(\lambda)_{n-k}}{k! (n-2k)!} (2t)^{n-2k}, -1 \leq t \leq 1 \quad (4)$$

Note that  $G_n(t, \lambda)$ , classical polynomials orthogonal on the interval  $[-1, 1]$  with respect to the weight function,  $w \rightarrow (1 - t^2)^{\lambda-1/2}$  ( $\lambda > -1/2$ ), denote the Gegenbauer polynomials defined by (4).

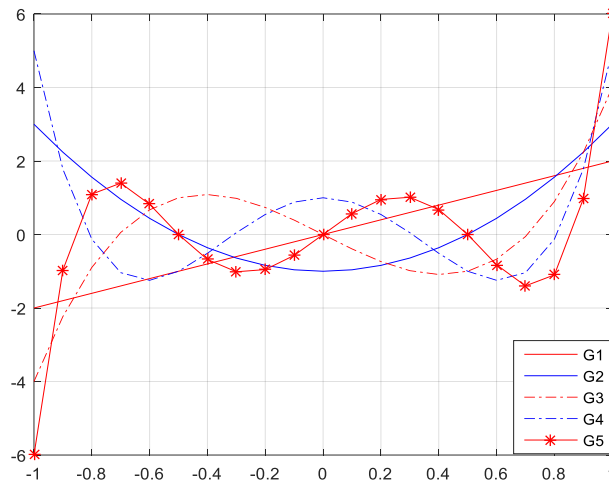


Figure 1. The first five Gegenbauer polynomials for  $\lambda = 1$ .

### Fundamental Matrix Relations

In this section, the matrix forms related to the problem (1)-(2) are generated. For this purpose, the approximate solution (3) can be written as the truncated shifted Gegenbauer series

$$y_n(t) = \mathbf{S}(t, \lambda) \mathbf{A} \quad (5)$$

where  $\mathbf{S}(t, \lambda) = [S_0(t, \lambda) \ S_1(t, \lambda) \ \dots \ S_N(t, \lambda)]$  and  $\mathbf{A} = [a_0 \ a_1 \ \dots \ a_N]^T$ . Here, the matrix form  $\mathbf{S}(t, \lambda)$  can be obtained as follows: using the matrix form of (4) defined by [12]

$$\mathbf{G}(t, \lambda) = \mathbf{X}(t) \mathbf{T}(\lambda); \quad \mathbf{X}(t) = [1 \ t \ t^2 \ \dots \ t^N]$$

We have the matrix form  $\mathbf{S}(t, \lambda)$  as

$$\mathbf{S}(t, \lambda) = \mathbf{G}(2t - 1, \lambda) = \mathbf{X}(2t - 1, \lambda) \mathbf{T}(\lambda) = \mathbf{X}(t) \mathbf{B}(2, -1) \mathbf{T}(\lambda) \quad (6)$$

where

$$\mathbf{B}(2, -1) = \begin{bmatrix} \binom{0}{0} 2^0 (-1)^0 & \binom{1}{0} 2^0 (-1)^1 & \binom{2}{0} 2^0 (-1)^2 & \dots & \binom{N}{0} 2^0 (-1)^N \\ 0 & \binom{1}{1} 2^1 (-1)^0 & \binom{2}{1} 2^1 (-1)^1 & \dots & \binom{N}{1} 2^1 (-1)^{N-1} \\ 0 & 0 & \binom{2}{2} 2^2 (-1)^0 & \dots & \binom{N}{2} 2^2 (-1)^{N-2} \\ \vdots & \vdots & \vdots & \ddots & \vdots \\ 0 & 0 & 0 & \dots & \binom{N}{N} 2^N (-1)^0 \end{bmatrix}$$

If N is odd,



$$\mathbf{T} = \begin{bmatrix} 1 & 0 & (-1)^1 \frac{2^0(\lambda)_1}{1!0!} & 0 & \dots & 0 \\ 0 & (-1)^0 \frac{2^1(\lambda)_2}{0!1!} & 0 & (-1)^1 \frac{2^1(\lambda)_2}{1!1!} & \dots & (-1)^{\binom{N-1}{2}} \frac{2^1(\lambda)_{\binom{N+1}{2}}}{\left(\frac{N-1}{2}\right)!1!} \\ 0 & 0 & (-1)^0 \frac{2^2(\lambda)_2}{0!2!} & 0 & \dots & 0 \\ 0 & 0 & 0 & (-1)^0 \frac{2^3(\lambda)_3}{0!3!} & \dots & (-1)^{\binom{N-3}{2}} \frac{2^3(\lambda)_{\binom{N+3}{2}}}{\left(\frac{N-3}{2}\right)!3!} \\ \vdots & \vdots & \vdots & \vdots & \ddots & \vdots \\ 0 & 0 & 0 & 0 & \dots & (-1)^0 \frac{2^N(\lambda)_N}{0!N!} \end{bmatrix}$$

If N is even,

$$\mathbf{T} = \begin{bmatrix} 1 & 0 & (-1)^1 \frac{2^0(\lambda)_1}{1!0!} & 0 & \dots & (-1)^{\binom{N}{2}} \frac{2^0(\lambda)_{\binom{N}{2}}}{\left(\frac{N}{2}\right)!1!} \\ 0 & (-1)^0 \frac{2^1(\lambda)_2}{0!1!} & 0 & (-1)^1 \frac{2^1(\lambda)_2}{1!1!} & \dots & 0 \\ 0 & 0 & (-1)^0 \frac{2^2(\lambda)_2}{0!2!} & 0 & \dots & (-1)^{\binom{N-2}{2}} \frac{2^2(\lambda)_{\binom{N+2}{2}}}{\left(\frac{N-2}{2}\right)!2!} \\ 0 & 0 & 0 & (-1)^0 \frac{2^3(\lambda)_3}{0!3!} & \dots & 0 \\ \vdots & \vdots & \vdots & \vdots & \ddots & \vdots \\ 0 & 0 & 0 & 0 & \dots & (-1)^0 \frac{2^N(\lambda)_N}{0!N!} \end{bmatrix}$$

Besides, by substituting the relation (6) into (5), we get the matrix form of the solution  $y_N(t)$  as follows:

$$y_N(t) = \mathbf{S}(t, \lambda) \mathbf{A} = \mathbf{X}(t) \underbrace{\mathbf{B}(2, -1) \mathbf{T}(\lambda)}_{\mathbf{M}(\lambda)} \mathbf{A} \quad (7)$$

and its derivative for  $k = 0, 1$ ,

$$y_N^{(k)}(t) = \mathbf{X}(t) \mathbf{B}^k \mathbf{B}(2, -1) \mathbf{T}(\lambda) \mathbf{A} \quad (8)$$

Where

$$\mathbf{B} = \begin{bmatrix} 0 & 1 & 0 & \dots & 0 \\ 0 & 0 & 2 & \dots & 0 \\ \vdots & \vdots & \vdots & \ddots & \vdots \\ 0 & 0 & 0 & \dots & N \\ 0 & 0 & 0 & \dots & 0 \end{bmatrix}, \mathbf{B}^0 = \begin{bmatrix} 1 & 0 & 0 & \dots & 0 \\ 0 & 1 & 0 & \dots & 0 \\ 0 & 0 & 1 & \dots & 0 \\ \vdots & \vdots & \vdots & \ddots & \vdots \\ 0 & 0 & 0 & \dots & 1 \end{bmatrix}$$

In similar manner; the matrix form of the delay term, form (8):

$$y^{(k)}(a_j t - \beta_j) = \mathbf{X}(a_j t - \beta_j) \mathbf{B}^k \mathbf{B}(2, -1) \mathbf{T}(\lambda) \mathbf{A} = \mathbf{X}(t) \mathbf{B}(a_j, -\beta_j) \mathbf{B}^k \mathbf{M}(\lambda) \mathbf{A} \quad (9)$$

Such that

$$\mathbf{B}(a_j, -\beta_j) = \begin{bmatrix} \binom{0}{0} a_j^0 (-\beta_j)^0 & \binom{1}{0} a_j^0 (-\beta_j)^1 & \binom{2}{0} a_j^0 (-\beta_j)^2 & \cdots & \binom{N}{0} a_j^0 (-\beta_j)^N \\ 0 & \binom{1}{1} a_j^1 (-\beta_j)^0 & \binom{2}{1} a_j^1 (-\beta_j)^1 & \cdots & \binom{N}{1} a_j^1 (-\beta_j)^{N-1} \\ 0 & 0 & \binom{2}{2} a_j^2 (-\beta_j)^0 & \cdots & \binom{N}{2} a_j^2 (-\beta_j)^{N-2} \\ \vdots & \vdots & \vdots & \ddots & \vdots \\ 0 & 0 & 0 & \cdots & \binom{N}{N} a_j^N (-\beta_j)^0 \end{bmatrix}$$

The matrix form of Volterra integral part, from (7) ;

$$\begin{aligned} \mathbf{V}(t) &= \int_0^{h(t)} \sum_{r=0}^{m_1} K_r(t, s) y^r(\mu_r s + \gamma_r) ds = \int_0^{h(t)} \mathbf{X}(t) \mathbf{K} \mathbf{X}^T(s) \mathbf{X}(s) \mathbf{B}(\mu_r, \gamma_r) \mathbf{B}^r \mathbf{M}(\lambda) \mathbf{A} ds \\ &= \mathbf{X}(t) \mathbf{K} \mathbf{I}(t) \mathbf{B}(\mu_r, \gamma_r) \mathbf{B}^r \mathbf{M}(\lambda) \mathbf{A} \quad (10) \end{aligned}$$

Where

$$\begin{aligned} \mathbf{I}(t) &= \int_0^{h(t)} \mathbf{X}^T(s) \mathbf{X}(s) ds = [r_{pq}], \quad r_{pq} = \frac{v(t)^{m+n+1} - u(t)^{m+n+1}}{m+n+1} \\ \mathbf{K} &= [k_{mn}], k_{pq} = \frac{1}{m! n!} \frac{\partial^{m+n} K(0,0)}{\partial t^m \partial s^n}, m, n = 0, 1, 2, \dots, N \end{aligned}$$

On the other hand, firstly we write the neutral term with delay of Eq.(1) in the form and then, by substituting the expressions (7)-(10) into Eq.(1), we obtain the matrix equation

$$\begin{aligned} \sum_{j=0}^m \mathbf{Q}_j(t) \mathbf{X}(t) \mathbf{B}(1, -\beta(t)) \mathbf{B}^k \mathbf{M}(\lambda) \mathbf{A} + \sum_{k=0}^m \mathbf{P}_k(t) \mathbf{X}(t) \mathbf{B}^k \mathbf{M}(\lambda) \mathbf{A} - \mathbf{X}(t) \mathbf{K} \mathbf{I}(t) \mathbf{B}(\mu_r, \gamma_r) \mathbf{B}^r \mathbf{M}(\lambda) \mathbf{A} \\ = \mathbf{G}(t) \end{aligned} \quad (11)$$

### Matrix – Collocation Method

By using the collocation points defined by  $t_i = \frac{1}{N} i, i = 0, 1, \dots, N$  into Eq.(11), and by simplifying the system of the obtained matrix equations, the fundamental matrix equation is obtained as

$$\left\{ \sum_{j=0}^m \mathbf{Q}_j \bar{\mathbf{X}} \bar{\mathbf{B}}(1, -\beta(t)) \mathbf{B}^k \mathbf{M}(\lambda) + \sum_{k=0}^m \mathbf{P}_k \bar{\mathbf{X}} \mathbf{B}^k \mathbf{M}(\lambda) - \bar{\mathbf{X}} \bar{\mathbf{K}} \bar{\mathbf{I}} \mathbf{B}(\mu_r, \gamma_r) \mathbf{B}^r \mathbf{M}(\lambda) \right\} \mathbf{A} = \mathbf{G} \quad (12)$$

$$\text{or } \mathbf{W} \mathbf{A} = \mathbf{G} \rightarrow [\mathbf{W}; \mathbf{G}]$$

where

$$\mathbf{X} = \begin{bmatrix} \mathbf{X}(t_0) \\ \mathbf{X}(t_1) \\ \vdots \\ \mathbf{X}(t_N) \end{bmatrix}, \mathbf{G} = \begin{bmatrix} g(t_0) \\ g(t_1) \\ \vdots \\ g(t_N) \end{bmatrix}, \bar{\mathbf{I}} = \begin{bmatrix} \mathbf{I}(t_0) \\ \mathbf{I}(t_1) \\ \vdots \\ \mathbf{I}(t_N) \end{bmatrix}, \bar{\mathbf{B}}(1, -\beta(t)) = \begin{bmatrix} \mathbf{B}(1, -\beta(t_0)) \\ \mathbf{B}(1, -\beta(t_1)) \\ \vdots \\ \mathbf{B}(1, -\beta(t_N)) \end{bmatrix},$$

$$\mathbf{P}_k = \text{diag}[\mathbf{P}(t_0) \quad \mathbf{P}(t_1) \quad \cdots \quad \mathbf{P}(t_N)], \bar{\mathbf{K}} = \text{diag}[\mathbf{K} \quad \mathbf{K} \quad \cdots \quad \mathbf{K}]$$

$$\bar{\mathbf{X}} = \text{diag}[\mathbf{X}(t_0) \quad \mathbf{X}(t_1) \quad \cdots \quad \mathbf{X}(t_N)], \mathbf{Q}_j = \text{diag}[\mathbf{Q}(t_0) \quad \mathbf{Q}(t_1) \quad \cdots \quad \mathbf{Q}(t_N)]$$

Also, we can write the matrix form for the condition (2), by using the relation (7),

$$\sum_{k=0}^1 (a_{kl}\mathbf{X}(a) + b_{kl}\mathbf{X}(b)) \mathbf{B}^k \mathbf{M}(\lambda) \mathbf{A} = \lambda_l, l = 0, 1,$$

or  $\mathbf{U}\mathbf{A} = [\lambda] \rightarrow [\mathbf{U}; \lambda]$  (13)

where

$$\mathbf{U} = \sum_{k=0}^1 (a_{kl}\mathbf{X}(a) + b_{kl}\mathbf{X}(b)) \mathbf{B}^k \mathbf{M}(\lambda) = [\mathbf{U}_{00} \quad \mathbf{U}_{01} \quad \cdots \quad \mathbf{U}_{0N}],$$

Finally, we replace any one row of (12) by the row matrix (13) and thus we have the required augmented matrix as

$$[\tilde{\mathbf{W}}; \tilde{\mathbf{G}}] \text{ or } \tilde{\mathbf{W}}\mathbf{A} = \tilde{\mathbf{G}} \quad (14)$$

If  $\text{rank}\tilde{\mathbf{W}} = \text{rank}[\tilde{\mathbf{W}}; \tilde{\mathbf{F}}] = N + 1$ , then we can write  $\mathbf{A} = (\tilde{\mathbf{W}})^{-1}\tilde{\mathbf{G}}$ . Thus, the matrix  $\mathbf{A}$  (thereby the coefficients  $a_0, a_1, \dots, a_N$ ) is uniquely determined. Eq. (1) under the conditions (2) has a unique solution. Hence, the problem (1) – (2) has a unique solution in terms of Gegenbauer polynomials in the form (3).

### Accuracy of Solutions and Residual Error Estimation

We can easily check the accuracy of the obtained solutions as follows. Since the truncated Gegenbauer series (3) is approximate solution of (1), when the function  $y_N(t)$  and its derivatives are substituted in Eq.(1), the resulting equation must be satisfied approximately; that is, for  $t = t_q \in [a, b], q = 0, 1, \dots$

$$R_N(t_q) = \sum_{j=0}^m Q_j(t_q)y_N^{(j)}(a_j t_q - \beta_j) + \sum_{k=0}^m P_k(t_q)y_N^{(k)}(t_q) - V(t_q) - G(t_q) \cong 0$$

or

$$R_N(t_q) \leq 10^{-k_q}, (k_q \text{ is any positive integer}).$$

If  $\max 10^{-k_q} = 10^{-k}$  ( $k$  is an positive integer) is prescribed, then the truncation limit  $N$  is increased until the difference  $R_N(t_q)$  at each of the points becomes smaller than the prescribed  $10^{-k}$ . Therefore, if  $R_N(t_q) \rightarrow 0$ , when  $N$  is sufficiently large enough, then the error decreases. On the other hand, by means of the residual function defined by  $R_N(t)$  and the mean value of the function  $|R_N(t)|$  on the interval  $[a, b]$ , the accuracy of the solution can be controlled and the error can be estimated [6 – 9]. Also, we can estimate the upper bound of the mean error  $\bar{R}_N$  as follows:

$$\left| \int_a^b R_N(t) dx \right| = (b-a)|R_N(c)| \leq \int_a^b |R_N(t)| dt, a \leq c \leq b$$

$$(b-a)|R_N(c)| \leq \int_a^b |R_N(t)| dt \Rightarrow |R_N(c)| \leq \frac{\int_a^b |R_N(t)| dt}{b-a} = \overline{R_N}$$

### Numerical Example

Let us consider neutral type differential equation

$$y''(t) - \frac{3}{4}y(t) - y\left(\frac{t}{2}\right) - y'\left(\frac{t}{2}\right) - \frac{1}{2}y''\left(\frac{t}{2}\right) = g(t)$$

with the initial condition  $y(0) = 0, y'(0) = 0$ . The exact solution of problem is  $y(t) = t^2, \lambda = 1$  and  $g(t) = 1 - t - t^2$ . Firstly, let us compute the approximate solution defined by

$$y_2(t) = \sum_{n=0}^2 a_n S_n(t, \lambda)$$

The set of the collocation points for  $N = 2$  is calculated as  $\{t_0 = 0, t_1 = 1/2, t_2 = 1\}$  and from Eq.(12), the fundamental matrix equation of the problem is written as

$$\left\{ \sum_{j=0}^2 \mathbf{Q}_j \overline{\mathbf{X}} \mathbf{B} (1, -\beta(t)) \mathbf{B}^k \mathbf{M}(\lambda) + \sum_{k=0}^2 \mathbf{P}_k \mathbf{X} \mathbf{B}^k \mathbf{M}(\lambda) - \overline{\mathbf{X}} \mathbf{K} \mathbf{I} \mathbf{B} (\mu_r, \gamma_r) \mathbf{B}^r \mathbf{M}(\lambda) \right\} \mathbf{A} = \mathbf{G}$$

From Eq. (13), we obtain the matrix form for the initial condition:

$$\begin{aligned} [\mathbf{U}_0; \boldsymbol{\lambda}_0] &= [1 \quad -2 \quad 3 \quad ; \quad 0] \\ [\mathbf{U}_1; \boldsymbol{\lambda}_1] &= [0 \quad 4 \quad -16 \quad ; \quad 0] \end{aligned}$$

Therefore, from Eq. (14), the new augmented matrix is calculated as

$$[\tilde{\mathbf{W}}; \tilde{\mathbf{G}}] = \begin{bmatrix} 1 & -2 & 3 & ; & 0 \\ 0 & 4 & -16 & ; & 0 \\ 0 & 0 & -16 & ; & -1 \end{bmatrix}$$

Solving this system, the unknown coefficients matrix is obtained as  $\mathbf{A} = [5/16 \quad 1/4 \quad 1/16]^T$ . Therefore, we obtain the approximate solution  $y_2(t) = t^2$ .

### Conclusion

In this study, a numerical method for solving the finite shifted Gegenbauer series is proposed to find approximate solutions of second-order linear neutral type functional integro-differential equations involving variable bounds and variable delays under the mixed conditions has been developed. Also, the approximate solutions in terms of the finite series have been obtained by using Gegenbauer polynomials. An error analysis technique has introduced for the method by using the residual function. Also, when the exact solution of the problem is not known, the solution can be approximately computed by means of residual error estimation. In addition, it is observed from the numerical values of the approximate solutions and the error estimations that the developed method is quite effective and applicative.

### References

- [1] Kim D. S., Kim T., Rim S-H (2012) Some identities involving Gegenbauer polynomials, *Advance in Difference Equations*, 2012: 219.
- [2] Rashed M.T. (2004) Numerical solution of functional differential, integral and integro-differential equations, *Appl. Numer. Math.* 156:485–492.
- [3] Khan S., Al-Gonah A. A., Yasmin G. (2012) Generalized and mixed type Gegenbauer polynomials, *J. Math. Anal. Appl.* 390:197-207.
- [4] Gümgüm S., Savaşaneril N. B., Kürkçü Ö. K., Sezer M. (2018) A numerical technique based on Lucas polynomials together with standard and Chebyshev-Lobatto collocation points for solving functional integro-differential equations involving variable delays, *Sakarya University Journal of Science*, 22 (6),1659-1668.
- [5] Baykuş N., Sezer M. (2017) Hybrid Taylor-Lucas Collocation Method for Numerical Solution of High-Order Pantograph Type Delay Differential Equations with Variables Delays, *Appl. Math. Inf. Sci.* 11, No. 6, 1795-1801.
- [6] B. Gürbüz, M. Sezer, C. Güler, (2014) Laguerre collocation method for solving Fredholm integro-differential equations with functional arguments, *J.Appl. Math.*2014, Article ID 682398,12 pages.
- [7] Ş. Yüzbaşı, E. Gök, M. Sezer, (2014) Laguerre matrix method with the residual error estimation for solutions of a class of delay differential equations, *Math. Meth. Appl. Sci.*, 453-463.
- [8] Özalp, T., Sezer, M. (2019) Gegenbauer - Taylor Matrix Technique for Neutral Type Second Order Functional Integro - Differential Equations with Variable Bounds, 3rd International Students Science Congress, Full Text Book, 314-320.
- [9] Özalp, T., Sezer, M. (2018) Polynomial Solutions of Linear Integro Differential Equations with Variables Delays by Using Gegenbauer Collocation Method, II. International Symposium on Multidisciplinary Academics Studies, Full Text Book, 461-472.
- [10] Mollaoğlu T., Sezer M. (2017) A numerical approach with residual error estimation for solution of high-order linear differential-difference equations by using Gegenbauer polynomials, *CBU J. of Sci.*, Volume 13, Issue 1, p 39-49.
- [11] Özalp, T., Sezer, M. (2019) Gegenbauer Polynomial Approach for A Kind of First Order Nonlinear Neutral Integro-Differential Equations with Delays, Mas 10th International European Conference on Mathematics, Engineering, Natural & Medical Sciences, Full Text Book, 185-193.
- [12] Özalp, T., Sezer, M., (2019) Shifted Gegenbauer-Taylor Matrix-Collocation Method for Second Order Linear Neutral Type Integro-Differential Equations with Variable Delays, Mas 10th International European Conference on Mathematics, Engineering, Natural & Medical Sciences, Full Text Book, 195-201.

## An Approximate Solution of 3D Partial Differential Equation by the Pell Matrix Collocation Method

Seda Çayan\*, Manisa Celal Bayar University, Department of Mathematics, Manisa, Turkey  
Mehmet Sezer, Manisa Celal Bayar University, Department of Mathematics, Manisa, Turkey  
\*Corresponding author: seda\_cayan@hotmail.com

**Keywords:** Pell polynomials and series, matrix and collocation methods, partial differential equation, initial value problem.

**Discipline:** Mathematics

### Abstract

In this study, a Pell matrix collocation method is presented to solve three-dimensional linear partial differential equation with variable coefficients under the initial conditions. Presented method based on the truncated Pell polynomials, the matrix operations and standard collocation points. The accuracy of the proposed method is demonstrated with some examples.

### Introduction

In this study, we develop a numerical technique based on Pell polynomials to solve three-dimensional linear partial differential equation with variable coefficients [1-5]

$$\sum_{i,j,k,i+j+k \leq n} f_{i,j,k}(x,y,z) \frac{\partial^{i+j+k} u(x,y,z)}{\partial x^i \partial y^j \partial z^k} = g(x,y,z), \quad (x,y,z) = [a,b] \times [c,d] \times [e,f] \quad (1)$$

under the initial conditions

$$u(x,y,0) = \rho_1(x,y), \quad u_z(x,y,0) = \rho_2(x,y) \quad (2)$$

where  $f_{i,j,k}(x,y,z)$  ( $i,j,k=0,1,\dots,n$ ),  $\rho_1(x,y)$  and  $\rho_2(x,y)$  are the known continuous functions.

For our purpose, we first assume the approximate solution of the problem (1) - (2) in the truncated Pell series form

$$u(x,y,z) \cong u_N(x,y,z) = \sum_{m=0}^N \sum_{n=0}^N \sum_{r=0}^N a_{m,n,r} P_{m+1,n+1,r+1}(x,y,z); \quad (3)$$

$$P_{m+1,n+1,r+1}(x,y,z) = P_{m+1}(x) P_{n+1}(y) P_{r+1}(z)$$

where  $u_N(x,t)$  is the approximate solution of Eq. (1);  $a_{m,n}$ , ( $m,n=0,1,\dots,N$ ) are the unknown Pell polynomial coefficients;  $N$  is chosen as any positive integer such that  $N \geq n$ .

Pell polynomials  $P_n(x)$  are defined by the recurrence relations [6,7]:

$$P_n(x) = 2xP_{n-1}(x) + P_{n-2}(x); \quad (4)$$

$$P_0(x) = 0, \quad P_1(x) = 1, \quad n \geq 2.$$

$$\underbrace{\begin{bmatrix} P_1(x) \\ P_2(x) \\ P_3(x) \\ P_4(x) \\ P_5(x) \\ \vdots \\ P_N(x); \\ (N \text{ odd}) \\ P_N(x); \\ (N \text{ even}) \end{bmatrix}}_{\mathbf{P}(x)^T} = \underbrace{\begin{bmatrix} 1 & 0 & 0 & 0 & 0 & \cdots & 0 \\ 0 & 2^1 \binom{1}{0} & 0 & 0 & 0 & \cdots & 0 \\ 2^0 \binom{1}{1} & 0 & 2^2 \binom{2}{0} & 0 & 0 & \cdots & 0 \\ 0 & 2^1 \binom{2}{1} & 0 & 2^3 \binom{3}{0} & 0 & \cdots & 0 \\ 2^0 \binom{2}{2} & 0 & 2^2 \binom{3}{1} & 0 & 2^4 \binom{4}{0} & \cdots & 0 \\ \vdots & \vdots & \vdots & \vdots & \vdots & \ddots & \vdots \\ 2^0 \binom{N-1}{\frac{N-1}{2}} & 0 & 2^2 \binom{N+1}{\frac{N-3}{2}} & 0 & 2^4 \binom{N+3}{\frac{N-5}{2}} & \cdots & 2^{N-1} \binom{N-1}{0} \\ 0 & 2^1 \binom{N}{\frac{N-2}{2}} & 0 & 2^3 \binom{N+2}{\frac{N-4}{2}} & 0 & \cdots & 2^{N-1} \binom{N-1}{0} \end{bmatrix}}_{\mathbf{S}^T} \underbrace{\begin{bmatrix} x^0 \\ x^1 \\ x^2 \\ x^3 \\ x^4 \\ \vdots \\ x^{N-1} \\ x^{N-1} \end{bmatrix}}_{\mathbf{X}(x)^T}$$

### Matrix Relations

By using relation (4), we can write the matrix form of Pell polynomials as follows:

$$\mathbf{P}(x)^T = \mathbf{S}^T \mathbf{X}(x)^T \Rightarrow \mathbf{P}(x) = \mathbf{X}(x) \mathbf{S}. \quad (5)$$

Then, by substituting the matrix relation (5) into the truncated Pell polynomial form (3), the matrix forms of the approximate solution of the problem (1)-(2) is obtained as

$$\begin{aligned}
 u_N(x, y, z) &= \mathbf{P}(x) \bar{\mathbf{P}}(y) \bar{\bar{\mathbf{P}}}(z) \bar{\mathbf{A}}; & (6) \\
 \mathbf{P}(x) &= [P_1(x) \ P_2(x) \ \cdots \ P_{N+1}(x)], \\
 \bar{\mathbf{P}}(y) &= \begin{bmatrix} \mathbf{P}(y) & 0 & \cdots & 0 \\ 0 & \mathbf{P}(y) & \cdots & 0 \\ \vdots & \vdots & \ddots & \vdots \\ 0 & 0 & \cdots & \mathbf{P}(y) \end{bmatrix}, & \bar{\bar{\mathbf{P}}}(z) &= \begin{bmatrix} \bar{\mathbf{P}}(z) & 0 & \cdots & 0 \\ 0 & \bar{\mathbf{P}}(z) & \cdots & 0 \\ \vdots & \vdots & \ddots & \vdots \\ 0 & 0 & \cdots & \bar{\mathbf{P}}(z) \end{bmatrix}, \\
 \bar{\mathbf{A}} &= [a_{0,0,0} \ a_{0,0,1} \ \cdots \ a_{0,0,N} \ a_{0,1,0} \ a_{0,1,1} \ \cdots \ a_{0,1,N} \ \cdots \ a_{N,N,0} \ a_{N,N,1} \ \cdots \ a_{N,N,N}]^T.
 \end{aligned}$$

Eq. (6) can be rewritten as follows:

$$u_N(x, y, z) = \mathbf{X}(x) \mathbf{S} \bar{\mathbf{X}}(y) \bar{\bar{\mathbf{X}}}(z) \bar{\bar{\mathbf{S}}} \bar{\mathbf{A}} \quad (7)$$

where

$$\mathbf{X}(x) = [1 \ x \ x^2 \ \cdots \ x^N],$$

$$\bar{\mathbf{X}}(y) = \begin{bmatrix} \mathbf{X}(y) & 0 & \cdots & 0 \\ 0 & \mathbf{X}(y) & \cdots & 0 \\ \vdots & \vdots & \ddots & \vdots \\ 0 & 0 & \cdots & \mathbf{X}(y) \end{bmatrix}, \quad \bar{\bar{\mathbf{X}}}(z) = \begin{bmatrix} \bar{\mathbf{X}}(z) & 0 & \cdots & 0 \\ 0 & \bar{\mathbf{X}}(z) & \cdots & 0 \\ \vdots & \vdots & \ddots & \vdots \\ 0 & 0 & \cdots & \bar{\mathbf{X}}(z) \end{bmatrix},$$

$$\mathbf{S}^0 = \mathbf{I} = \begin{bmatrix} 1 & 0 & \cdots & 0 \\ 0 & 1 & \cdots & 0 \\ \vdots & \vdots & \ddots & \vdots \\ 0 & 0 & \cdots & 1 \end{bmatrix}, \quad \bar{\mathbf{S}} = \begin{bmatrix} \mathbf{S} & 0 & \cdots & 0 \\ 0 & \mathbf{S} & \cdots & 0 \\ \vdots & \vdots & \ddots & \vdots \\ 0 & 0 & \cdots & \mathbf{S} \end{bmatrix}, \quad \bar{\bar{\mathbf{S}}} = \begin{bmatrix} \bar{\mathbf{S}} & 0 & \cdots & 0 \\ 0 & \bar{\mathbf{S}} & \cdots & 0 \\ \vdots & \vdots & \ddots & \vdots \\ 0 & 0 & \cdots & \bar{\mathbf{S}} \end{bmatrix},$$

The relation between the matrix  $\mathbf{X}(x)$  and its  $i$  th order derivative  $\mathbf{X}^{(i)}(x)$  is given by

$$\mathbf{X}'(x) = \mathbf{X}(x)\mathbf{B}, \quad \mathbf{X}''(x) = \mathbf{X}(x)\mathbf{B} = \mathbf{X}(x)\mathbf{B}^2, \quad \dots, \quad \mathbf{X}^{(i)}(x) = \mathbf{X}(x)\mathbf{B}^i. \quad (8)$$

In a similar way, the relation between the matrix  $\bar{\mathbf{X}}(y)$  and its  $j$  th order derivative  $\bar{\mathbf{X}}^{(j)}(y)$  is

$$\bar{\mathbf{X}}'(y) = \bar{\mathbf{X}}(y)\bar{\mathbf{B}}, \quad \bar{\mathbf{X}}''(y) = \bar{\mathbf{X}}'(y)\bar{\mathbf{B}} = \bar{\mathbf{X}}(y)\bar{\mathbf{B}}^2, \quad \dots, \quad \bar{\mathbf{X}}^{(j)}(y) = \bar{\mathbf{X}}(y)\bar{\mathbf{B}}^j \quad (9)$$

and the relation between the matrix  $\bar{\bar{\mathbf{X}}}(z)$  and its  $k$  th order derivative  $\bar{\bar{\mathbf{X}}}^{(k)}(z)$  is

$$\bar{\bar{\mathbf{X}}}'(z) = \bar{\bar{\mathbf{X}}}(z)\bar{\bar{\mathbf{B}}}, \quad \bar{\bar{\mathbf{X}}}''(z) = \bar{\bar{\mathbf{X}}}'(z)\bar{\bar{\mathbf{B}}} = \bar{\bar{\mathbf{X}}}(z)\bar{\bar{\mathbf{B}}}^2, \quad \dots, \quad \bar{\bar{\mathbf{X}}}^{(k)}(z) = \bar{\bar{\mathbf{X}}}(z)\bar{\bar{\mathbf{B}}}^k. \quad (10)$$

Here

$$\mathbf{B} = \begin{bmatrix} 0 & 1 & 0 & \cdots & 0 \\ 0 & 0 & 2 & \cdots & 0 \\ \vdots & \vdots & \vdots & \ddots & \vdots \\ 0 & 0 & 0 & \cdots & N \\ 0 & 0 & 0 & \cdots & 0 \end{bmatrix}, \quad \mathbf{B}^0 = \mathbf{I} = \begin{bmatrix} 1 & 0 & \cdots & 0 \\ 0 & 1 & \cdots & 0 \\ \vdots & \vdots & \ddots & \vdots \\ 0 & 0 & \cdots & 1 \end{bmatrix}, \quad \bar{\mathbf{B}} = \begin{bmatrix} \mathbf{B} & 0 & \cdots & 0 \\ 0 & \mathbf{B} & \cdots & 0 \\ \vdots & \vdots & \ddots & \vdots \\ 0 & 0 & \cdots & \mathbf{B} \end{bmatrix}, \quad \bar{\bar{\mathbf{B}}} = \begin{bmatrix} \bar{\mathbf{B}} & 0 & \cdots & 0 \\ 0 & \bar{\mathbf{B}} & \cdots & 0 \\ \vdots & \vdots & \ddots & \vdots \\ 0 & 0 & \cdots & \bar{\mathbf{B}} \end{bmatrix}.$$

### Pell Matrix Collocation Method for 3D Partial Differential Equation

From relations (5), (7), (8), (9) and (10), the matrix form of the Eq.(1) can be obtained as

$$\frac{\partial^{i+j+k} u(x, y, z)}{\partial x^i \partial y^j \partial z^k} \cong \frac{\partial^{i+j+k} u_N(x, y, z)}{\partial x^i \partial y^j \partial z^k} = \mathbf{X}^{(i)}(x) \mathbf{S} \bar{\mathbf{X}}^{(j)}(y) \bar{\bar{\mathbf{S}}} \bar{\bar{\mathbf{X}}}^{(k)}(z) \bar{\bar{\mathbf{S}}} \bar{\mathbf{A}}. \quad (11)$$

Substituting the relations (11) into Eq.(1), the fundamental matrix equation is gained as follows:

$$\sum_{i,j,k} f_{i,j,k}(x, y, z) \mathbf{X}(x) \mathbf{B}^i \mathbf{S} \bar{\mathbf{X}}(y) \bar{\mathbf{B}}^j \bar{\bar{\mathbf{S}}} \bar{\bar{\mathbf{X}}}(z) \bar{\bar{\mathbf{B}}}^k \bar{\bar{\mathbf{S}}} \bar{\mathbf{A}} = g(x, y, z)$$

or shortly



$$\mathbf{W}(x, y, z) \bar{\mathbf{A}} = g(x, y, z) \quad (12)$$

where

$$\mathbf{W}(x, y, z) = \sum_{i,j,k} f_{i,j,k}(x, y, z) \mathbf{X}(x) \mathbf{B}^i \mathbf{S} \bar{\mathbf{X}}(y) \bar{\mathbf{B}}^j \bar{\mathbf{S}} \bar{\mathbf{X}}(z) \bar{\mathbf{B}}^k \bar{\mathbf{S}}.$$

Thereafter, by putting the collocation points  $x_\gamma$ ,  $y_\mu$  and  $z_\psi$ , for  $x \in [a, b]$ ,  $y \in [c, d]$  and  $z \in [e, f]$ ,

$$x_\gamma = a + \frac{b-a}{N} \gamma, \quad y_\mu = c + \frac{d-c}{N} \mu, \quad z_\psi = e + \frac{f-e}{N} \psi, \quad \gamma, \mu, \psi = 0, 1, 2, \dots, N \quad (13)$$

into Eq.(12), the system of matrix equations is obtained as

$$\mathbf{W}(x_\gamma, y_\mu, z_\psi) \bar{\mathbf{A}} = g(x_\gamma, y_\mu, z_\psi), \quad \gamma, \mu, \psi = 0, 1, 2, \dots, N$$

or

$$\mathbf{W}_{\gamma,\mu} \bar{\mathbf{A}} = \mathbf{G}_{\gamma,\mu} \quad \gamma, \mu = 0, 1, 2, \dots, N. \quad (14)$$

Briefly, Eq.(14) can be written as

$$\mathbf{W} \bar{\mathbf{A}} = \mathbf{G} \quad \text{or} \quad [\mathbf{W}; \mathbf{G}] \quad (15)$$

where

$$\mathbf{W} = \begin{bmatrix} \mathbf{W}_{0,0} \\ \mathbf{W}_{0,1} \\ \vdots \\ \mathbf{W}_{0,N} \\ \vdots \\ \mathbf{W}_{N,0} \\ \mathbf{W}_{N,1} \\ \vdots \\ \mathbf{W}_{N,N} \end{bmatrix}; \quad \mathbf{W}_{\gamma,\mu} = \begin{bmatrix} \mathbf{W}(x_\gamma, y_\mu, z_0) \\ \mathbf{W}(x_\gamma, y_\mu, z_1) \\ \vdots \\ \mathbf{W}(x_\gamma, y_\mu, z_N) \end{bmatrix} \quad \text{and} \quad \mathbf{G} = \begin{bmatrix} \mathbf{G}_{0,0} \\ \mathbf{G}_{0,1} \\ \vdots \\ \mathbf{G}_{0,N} \\ \vdots \\ \mathbf{G}_{N,0} \\ \mathbf{G}_{N,1} \\ \vdots \\ \mathbf{G}_{N,N} \end{bmatrix}; \quad \mathbf{G}_{\gamma,\mu} = \begin{bmatrix} \mathbf{G}(x_\gamma, y_\mu, z_0) \\ \mathbf{G}(x_\gamma, y_\mu, z_1) \\ \vdots \\ \mathbf{G}(x_\gamma, y_\mu, z_N) \end{bmatrix}.$$

Lastly, by following the same way for the initial conditions (2), the matrix equations are obtained as follows:

$$\begin{aligned} \xi_1 u(x, y, 0) &= \xi_1 \mathbf{X}(x) \mathbf{S} \bar{\mathbf{X}}(y) \bar{\mathbf{S}} \bar{\mathbf{X}}(0) \bar{\mathbf{S}} \bar{\mathbf{A}} = \rho_1(x, y), \\ \xi_2 u_z(x, y, 0) &= \xi_2 \mathbf{X}(x) \mathbf{S} \bar{\mathbf{X}}(y) \bar{\mathbf{S}} \bar{\mathbf{X}}(0) \bar{\mathbf{B}} \bar{\mathbf{S}} \bar{\mathbf{A}} = \rho_2(x, y), \end{aligned}$$

or

$$\mathbf{U}_1(x, y, 0) \bar{\mathbf{A}} = \rho_1(x, y), \quad \mathbf{U}_2(x, y, 0) \bar{\mathbf{A}} = \rho_2(x, y) \quad (16)$$

where

$$\mathbf{U}_1(x, y, 0) = \xi_1 \mathbf{X}(x) \mathbf{S} \bar{\mathbf{X}}(y) \bar{\mathbf{S}} \bar{\mathbf{X}}(0) \bar{\mathbf{S}}, \quad \mathbf{U}_2(x, y, 0) = \xi_2 \mathbf{X}(x) \mathbf{S} \bar{\mathbf{X}}(y) \bar{\mathbf{S}} \bar{\mathbf{X}}(0) \bar{\mathbf{B}} \bar{\mathbf{S}}.$$

By using the collocation points, for  $\gamma, \mu = 0, 1, \dots, N$ , into (16), the matrix equations of the conditions (2) are obtained as

$$\mathbf{U}_1(x_\gamma, y_\mu, 0) \bar{\mathbf{A}} = \rho_1(x_\gamma, y_\mu), \quad \mathbf{U}_2(x_\gamma, y_\mu, 0) \bar{\mathbf{A}} = \rho_2(x_\gamma, y_\mu)$$

or

$$\mathbf{U}_i \bar{\mathbf{A}} = \Phi_i \quad \text{or} \quad [\mathbf{U}_i; \Phi_i], \quad (i=1,2). \quad (17)$$

Here

$$\mathbf{U}_1 = \begin{bmatrix} \mathbf{U}_1(x_0, y_0, 0) \\ \mathbf{U}_1(x_0, y_1, 0) \\ \vdots \\ \mathbf{U}_1(x_0, y_N, 0) \\ \vdots \\ \mathbf{U}_1(x_N, y_0, 0) \\ \mathbf{U}_1(x_N, y_1, 0) \\ \vdots \\ \mathbf{U}_1(x_N, y_N, 0) \end{bmatrix}, \quad \mathbf{U}_2 = \begin{bmatrix} \mathbf{U}_2(x_0, y_0, 0) \\ \mathbf{U}_2(x_0, y_1, 0) \\ \vdots \\ \mathbf{U}_2(x_0, y_N, 0) \\ \vdots \\ \mathbf{U}_2(x_N, y_0, 0) \\ \mathbf{U}_2(x_N, y_1, 0) \\ \vdots \\ \mathbf{U}_2(x_N, y_N, 0) \end{bmatrix}, \quad \Phi_1 = \begin{bmatrix} \rho_1(x_0, y_0) \\ \rho_1(x_0, y_1) \\ \vdots \\ \rho_1(x_0, y_N) \\ \vdots \\ \rho_1(x_N, y_0) \\ \rho_1(x_N, y_1) \\ \vdots \\ \rho_1(x_N, y_N) \end{bmatrix}, \quad \Phi_2 = \begin{bmatrix} \rho_2(x_0, y_0) \\ \rho_2(x_0, y_1) \\ \vdots \\ \rho_2(x_0, y_N) \\ \vdots \\ \rho_2(x_N, y_0) \\ \rho_2(x_N, y_1) \\ \vdots \\ \rho_2(x_N, y_N) \end{bmatrix}.$$

Replacing the rows of the matrices (17) by any rows of the matrix (15), the following new augmented matrix is constructed

$$\tilde{\mathbf{W}} \bar{\mathbf{A}} = \tilde{\mathbf{G}} \quad \text{or} \quad [\tilde{\mathbf{W}}; \tilde{\mathbf{G}}].$$

If  $\text{rank}(\tilde{\mathbf{W}}) = \text{rank}(\tilde{\mathbf{W}}; \tilde{\mathbf{G}}) = (N+1)^3$ , then the unknown Pell coefficients matrix  $\bar{\mathbf{A}}$  is computed as  $\bar{\mathbf{A}} = (\tilde{\mathbf{W}})^{-1} \tilde{\mathbf{G}}$  and  $\bar{\mathbf{A}}$  is uniquely determined. Hence, Eq. (1) under the initial conditions (2) has unique solution in the truncated Pell polynomial form (3).

### Numerical Examples

Example 1. Let us consider three-dimensional linear partial differential equation with variable coefficients

$$(x + y - z)u_{xx}(x, y, z) + u_{yy}(x, y, z) + u_{zz}(x, y, z) = -2y^2 - 2z^2 + 2(x + y - z) \quad (18)$$

under the initial conditions

$$u(x, y, 0) = x^2, \quad u_z(x, y, 0) = 0, \quad 0 \leq x, y, z \leq 1.$$

The analytical solution to Eq. (18) is



which is the exact solution.

Example 2. [5,8] Consider three-dimensional linear partial differential equation with variable coefficients

$$u_{zz}(x, y, z) = \frac{x^2}{12}u_{xx}(x, y, z) + \frac{y^2}{12}u_{yy}(x, y, z) \quad (19)$$

under the initial conditions

$$u(x, y, 0) = x^4, \quad u_z(x, y, 0) = y^4, \quad 0 \leq x, y, z \leq 0.25.$$

The analytical solution to Eq. (19) is given as

$$u(x, y, z) = x^4 \cosh(z) + y^4 \sinh(z).$$

The approximate solutions are found by using the Pell matrix collocation method. Numerical results can be seen in Table 1 and Figures 1-3.

Table 1. Comparison of the absolute errors in Example 2

$x$	$y$	$z$	$e_7(x, y, z)$	$e_8(x, y, z)$	$e_9(x, y, z)$	$e_{10}(x, y, z)$
0.025	0.025	0.025	6.44E-08	4.61E-10	6.24E-15	1.36E-16
0.050	0.050	0.050	1.21E-07	1.09E-09	1.41E-14	1.39E-16
0.075	0.075	0.075	4.98E-08	1.38E-09	2.40E-14	4.15E-16
0.100	0.100	0.100	1.23E-07	1.22E-09	4.95E-14	5.15E-16
0.125	0.125	0.125	3.05E-07	2.20E-11	1.32E-13	9.16E-16
0.150	0.150	0.150	3.10E-07	4.63E-09	4.85E-13	6.61E-15
0.175	0.175	0.175	1.64E-07	2.33E-08	2.63E-12	1.40E-13
0.200	0.200	0.200	1.70E-06	1.16E-07	3.09E-11	6.38E-12
0.225	0.225	0.225	1.09E-05	9.92E-07	1.48E-09	8.06E-10
0.250	0.250	0.250	1.38E-04	2.62E-05	1.66E-08	1.07E-08

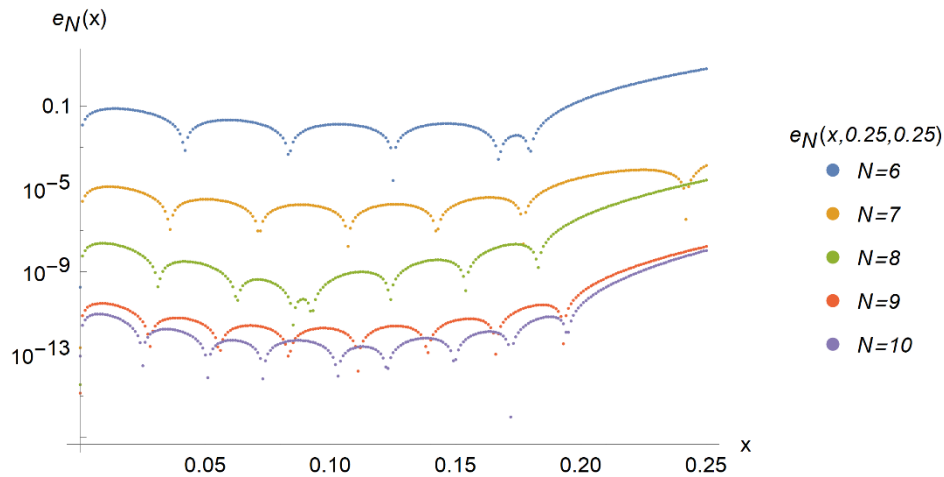


Figure 1. Comparison of the absolute errors for  $y = 0.25$  and  $z = 0.25$  in Example 2.

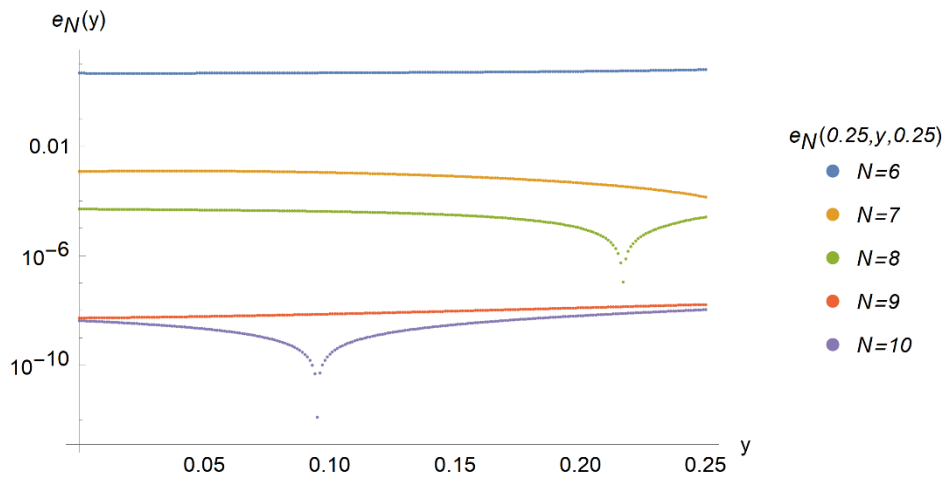


Figure 2. Comparison of the absolute errors for  $x = 0.25$  and  $z = 0.25$  in Example 2.

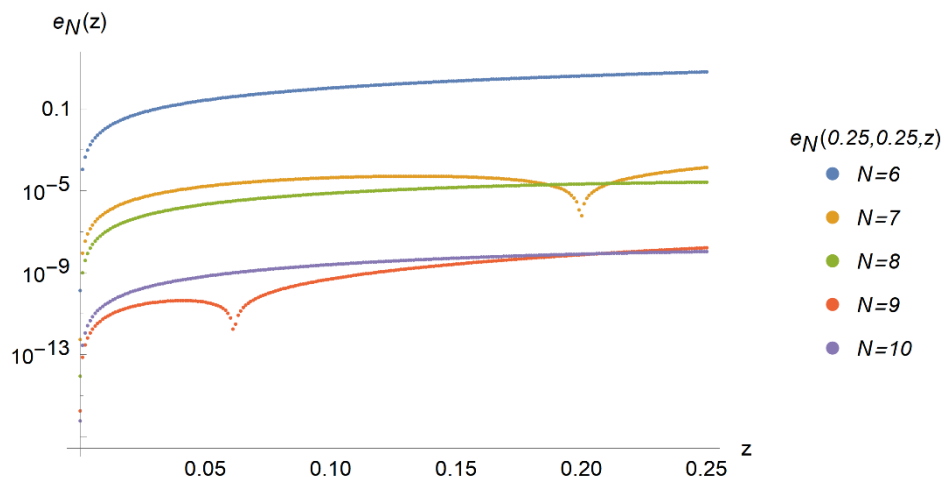


Figure 3. Comparison of the absolute errors for  $x = 0.25$  and  $y = 0.25$  in Example 2.

### Conclusion

In the present study, we consider three-dimensional linear partial differential equation with variable coefficients under the initial conditions. The approximate solutions of this equation are obtained by using Pell matrix collocation method.

We applied to two numerical examples to show usefulness of the Pell matrix collocation method and we obtained numerical results of this examples. It is seen from Table 1 and Figures 1-3 that the

approximate solutions are close to the analytical solution when the values of  $N$  are selected big enough. In other words, the numerical results show that the accuracy improves when the values of  $N$  are increased.

### References

- [1] Bülbül, B, Sezer, M. A Taylor matrix method for the solution of a two-dimensional linear hyperbolic equation. *Applied Mathematics Letters*. 2011; 24:1716-1720.
- [2] Yüzbaşı, Ş. A collocation approach for solving two-dimensional second order linear hyperbolic equations. *Applied Mathematics and Computation*. 2018; 338:101-114.
- [3] Singh, I, Kumar, S. Wavelet methods for solving three-dimensional partial differential equations. *Mathematical Sciences*. 2017; 11(2):145-154.
- [4] Enadi, MO, Tawfiq, LNM. New approach for solving three-dimensional space partial differential equation. *Baghdad Science Journal*. 2019; 16(3):786-792.
- [5] Taha, BA. The use of reduced differential transform method for solving partial differential equations with variable coefficients. *Journal of Basrah Researches ((Sciences))*. 2011; 37(4):226-233.
- [6] Djordjevic, GB, Milovanovic, GV. Special cases of polynomials. Leskovac: University of Nis, Faculty of Technology; 2014.
- [7] Koshy, T. Pell and Pell-Lucas numbers with applications. New York: Springer; 2014.
- [8] Jin, L. Homotopy perturbation method for solving partial differential equations with variable coefficients. *Int. J. Contemp. Math. Sciences*. 2008; 3(28):1395 – 1407.

## Shifted Legendre Matrix Method for Solving Second Order Linear Neutral Integro Differential Equations Involving Delays

Ülker Başar\*, Manisa Celal Bayar Univ., Dept. of Mathematics, Manisa, Turkey

Mehmet Sezer, Manisa Celal Bayar Univ., Dept. of Mathematics, Manisa, Turkey

\*Corresponding author: ulkerbasar@hotmail.com

**Keywords:** Shifted Legendre polynomials and series, Taylor polynomials, Neutral integro-differential equation with delays, matrix and collocation methods, residual error technique, variable bounds

**Discipline:** Mathematics

### Abstract

In this study, a novel matrix-collocation method based on the finite shifted Legendre series and the collocation points is presented to find approximate solutions of second-order linear neutral type functional integro-differential equations involving variable bounds and variable delays under the initial conditions. The method is based on the matrix forms of the shifted Legendre polynomials and their derivatives by means of the collocation points. Then the solution of the problem is converted into the solution of a matrix equation created by the unknown Legendre coefficients and the solutions are obtained in terms of the orthogonal shifted Legendre polynomials defined on the interval  $[a, b]$  or Taylor polynomials. Also, by using an efficient residual error technique of the operator equation, an error differential equation is constructed and thus the approximate solution obtained by shifted Legendre collocation method is corrected. Furthermore, we give an upper bound of the absolute errors for the corrected shifted Legendre solution. Finally, the numerical examples together with tables and figures are performed to illustrate the validity and the applicability of the method and the obtained results are discussed. All of the numerical computations have been performed on the computer using a program written in Mathematica.

### Introduction

In this study, the finite shifted Legendre matrix-collocation method is established to solve second-order linear neutral type functional integro-differential equations with variable delays in the form

$$\sum_{j=0}^2 Q_j(t) y^{(j)}(t) + \sum_{k=0}^2 R_k(t) y^{(k)}(t - \tau(t)) = G(t) + \int_{u(t)}^{v(t)} K(t, s) y(s) ds \quad (1)$$

under the initial conditions

$$\sum_{k=0}^1 a_{kl} y^{(k)}(0) = \lambda_l, \quad l = 0, 1 \quad (2)$$

where  $Q_j(t), R_k(t), \tau(t), G(t), K(t, s), u(t)$  and  $v(t)$  are defined on  $a \leq t, s \leq b$ ;  $a_{kl}$  and  $\lambda_l$  are appropriate constants. The linear functional integro-differential equation involved in Eq. (1) is a combination of the neutral differential equation with variable delay and Volterra integral equations with functional bounds. These type equations explore many physical phenomena arising in applied sciences, such as mathematics, engineering, electrodynamics, mechanics, physics and biology etc. [2-15]. In recent years, the mentioned equations have been enquired by many authors for their analytic and numerical solutions; so numerical methods are required [5-10].

Our purpose in this study is to establish the matrix-collocation method based on shifted Legendre polynomials and to find the approximate solution of the problem (1) – (2) in the truncated shifted Legendre series form

$$y(t) \cong y_N(t) = \sum_{n=0}^N a_n S_n(t), \quad a \leq t \leq b \quad (3)$$

where  $a_n, n=0,1,\dots,N$  are unknown coefficients and  $S_n(t)$  is shifted Legendre polynomials, which are defined as

$$S_n(t) = P_n(\alpha t + \beta), \quad \alpha = \frac{2t}{b-a}, \quad \beta = \frac{a+b}{b-a}, \quad a \leq t \leq b \quad (4)$$

Note that  $P_n(x), n=0,1,\dots,N$  are classical Legendre polynomials which are orthogonal on the interval  $[-1,1]$  with respect to the weight function,  $w(x) = 1$ , denote the Legendre polynomials defined by (5) and are given by the forms [19]

$$P_n(x) = \frac{1}{2^n} \sum_{k=0}^{\lfloor \frac{n}{2} \rfloor} (-1)^k \binom{n}{k} \binom{2n-2k}{n} x^{n-2k}, \quad n=0,1,\dots,N, \quad -1 \leq x \leq 1 \quad (5)$$

$$\lfloor \frac{n}{2} \rfloor = \begin{cases} \frac{n}{2}, & n \text{ even} \\ \frac{n-1}{2}, & n \text{ odd} \end{cases}.$$

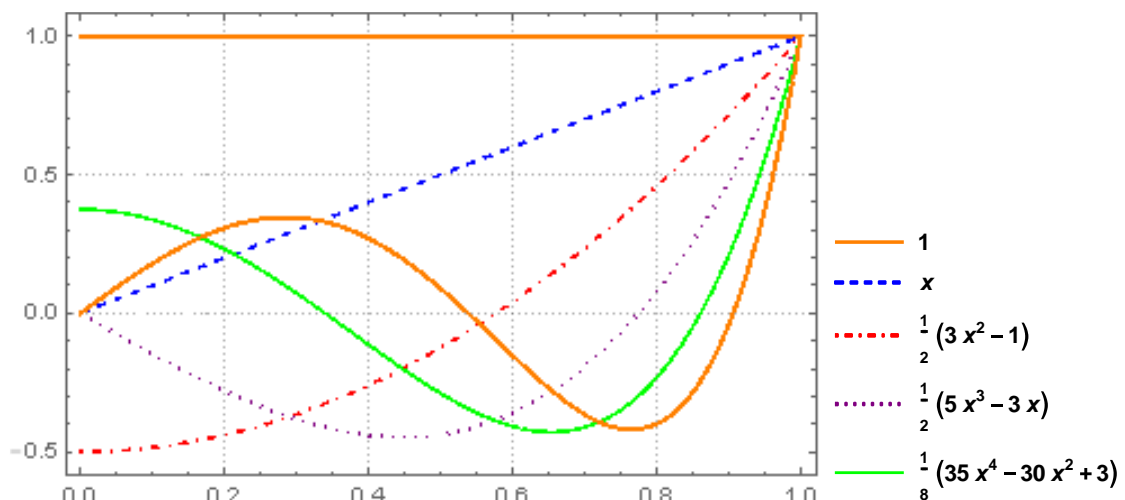


Figure 1. The first five Legendre polynomials

Legendre polynomials are examples of eigenfunctions of singular Sturm-Liouville problems [3] and have been used extensively in the solution of the boundary value problems and in computational fluid dynamics [17]. On the other hand, the methods based on the shifted Legendre polynomials may be more efficient for solving linear and nonlinear neutral integro-differential equations [19].

Since the beginning of the 1994s, Taylor matrix and Taylor collocation methods to solve linear differential, integral, integro-differential, difference, integro-difference and systems of integro-differential equations have been used by Sezer et al. [13-14].

In this paper, by means of the matrix relation between the Taylor and shifted Legendre polynomials, the mentioned methods above are modified and developed for solving the second order linear neutral integro-differential equation with delays and functional argument.



### Fundamental Matrix Relations

In this section, the matrix forms related to the problem (1) – (2) are generated. For this purpose, the approximate solution (3) can be written as the truncated shifted Legendre series

$$y(t) \cong y_N(t) = \mathbf{S}(t)\mathbf{A} \quad (6)$$

where  $\mathbf{S}(t) = [S_0(t) \ S_1(t) \ \dots \ S_N(t)]$  and  $\mathbf{A} = [a_0 \ a_1 \ \dots \ a_N]^T$ . Here the matrix form  $\mathbf{S}(t)$  can be obtained as follows; using the matrix form of Legendre polynomials (5) defined by (see [19])

$$\mathbf{P}(x) = \mathbf{X}(x)\mathbf{D}; \quad \mathbf{X}(x) = [1 \ x \ \dots \ x^N],$$

We have the matrix form  $\mathbf{S}(t)$  as

$$\mathbf{S}(t) = \mathbf{P}(\alpha t + \beta) = \mathbf{X}(\alpha t + \beta)\mathbf{D} = \mathbf{X}(t)\mathbf{B}(\alpha, \beta)\mathbf{D} \quad (7)$$

where

$$x = \alpha t + \beta, \quad \alpha = \frac{2}{b-a}, \quad \beta = -\frac{a+b}{b-a};$$

$$\mathbf{X}(\alpha t + \beta) = \mathbf{X}(t)\mathbf{B}(\alpha, \beta), \text{ [19],}$$

$$\mathbf{B}(\alpha, \beta) = \begin{bmatrix} \binom{0}{0} \alpha^0 \beta^0 & \binom{1}{0} \alpha^0 \beta^1 & \binom{2}{0} \alpha^0 \beta^2 & \dots & \binom{N}{0} \alpha^0 \beta^N \\ 0 & \binom{1}{1} \alpha^1 \beta^0 & \binom{2}{1} \alpha^1 \beta^1 & \dots & \binom{N}{1} \alpha^1 \beta^{N-1} \\ 0 & 0 & \binom{2}{2} \alpha^2 \beta^0 & \dots & \binom{N}{2} \alpha^2 \beta^{N-2} \\ \vdots & \vdots & \vdots & \vdots & \vdots \\ 0 & 0 & 0 & \dots & \binom{N}{N} \alpha^N \beta^0 \end{bmatrix},$$

where, for odd values of  $N$ ;

$$\mathbf{D}^T = \begin{bmatrix} \frac{(-1)^0}{2^0} \binom{0}{0} \binom{0}{0} & 0 & 0 & \dots & 0 \\ 0 & \frac{(-1)^0}{2^1} \binom{1}{0} \binom{2}{1} & 0 & \dots & 0 \\ \frac{(-1)^1}{2^2} \binom{2}{1} \binom{2}{2} & 0 & \frac{(-1)^0}{2^2} \binom{2}{0} \binom{4}{2} & \dots & 0 \\ \vdots & \vdots & \vdots & \dots & \vdots \\ 0 & \frac{(-1)^{\frac{N-1}{2}}}{2^N} \binom{N}{\frac{N-1}{2}} \binom{N+1}{N} & 0 & \dots & \frac{(-1)^0}{2^N} \binom{N}{0} \binom{2N}{N} \end{bmatrix},$$

for even values of  $N$  ;

$$D^T = \begin{bmatrix} \frac{(-1)^0}{2^0} \binom{0}{0} \binom{0}{0} & 0 & 0 & \dots & 0 \\ 0 & \frac{(-1)^0}{2^1} \binom{1}{0} \binom{2}{1} & 0 & \dots & 0 \\ \frac{(-1)^1}{2^2} \binom{2}{1} \binom{2}{2} & 0 & \frac{(-1)^0}{2^2} \binom{2}{0} \binom{4}{2} & \dots & 0 \\ \vdots & \vdots & \vdots & \dots & \vdots \\ \frac{(-1)^{\frac{N}{2}}}{2^N} \binom{N}{\frac{N}{2}} \binom{N}{N} & 0 & \frac{(-1)^{\frac{N-2}{2}}}{2^N} \binom{N}{\frac{N-2}{2}} \binom{N+2}{N} & \dots & \frac{(-1)^0}{2^N} \binom{N}{0} \binom{2N}{N} \end{bmatrix}$$

Besides, by substituting the relation (7) into (6), we get the matrix form of the solution  $y_N(t)$  as follows:

$$y_N(t) = S(t)A = X(t)B(\alpha, \beta)DA \quad (8)$$

and its derivative  $y_N^{(k)}$ , for  $k = 0, 1, [13-14]$

$$y_N^{(k)}(t) = X(t)B^k B(\alpha, \beta)DA \quad (9)$$

where

$$B = \begin{bmatrix} 0 & 1 & 0 & \dots & 0 \\ 0 & 0 & 2 & \dots & 0 \\ \vdots & \vdots & \vdots & \dots & \vdots \\ 0 & 0 & 0 & \dots & N \\ 0 & 0 & 0 & \dots & 0 \end{bmatrix}, B^0 = \begin{bmatrix} 1 & 0 & 0 & \dots & 0 \\ 0 & 1 & 0 & \dots & 0 \\ 0 & 0 & 1 & \dots & 0 \\ \vdots & \vdots & \vdots & \dots & \vdots \\ 0 & 0 & 0 & \dots & 1 \end{bmatrix}$$

On the other hand, the matrix form of the delay term, by means of (9):

$$\begin{aligned} y_N^{(k)}(t - \tau(t)) &= X(t - \tau(t))B^k B(\alpha, \beta)DA \\ &= X(t)B(1, -\tau(t))B^k B(\alpha, \beta)DA \end{aligned} \quad (10)$$

Such that

$$\mathbf{B}(1, -\tau(t)) = \begin{bmatrix} \binom{0}{0}(-\tau(t))^0 & \binom{1}{0}(-\tau(t))^1 & \binom{2}{0}(-\tau(t))^2 & \dots & \binom{N}{0}(-\tau(t))^N \\ 0 & \binom{1}{1}(-\tau(t))^0 & \binom{2}{1}(-\tau(t))^1 & \dots & \binom{N}{1}(-\tau(t))^{N-1} \\ 0 & 0 & \binom{2}{2}(-\tau(t))^0 & \dots & \binom{N}{2}(-\tau(t))^{N-2} \\ \vdots & \vdots & \vdots & \dots & \vdots \\ 0 & 0 & 0 & \dots & \binom{N}{N}(-\tau(t))^0 \end{bmatrix}$$

The matrix form of Volterra integral part, from (8);

$$\begin{aligned} V(t) &= \int_{u(t)}^{v(t)} K(t,s)y(s)ds = \int_{u(t)}^{v(t)} \mathbf{X}(t)\mathbf{K}\mathbf{X}^T(s)\mathbf{X}(s)\mathbf{B}(\alpha, \beta)\mathbf{D}\mathbf{A}ds \\ &= \mathbf{X}(t)\mathbf{K}\mathbf{I}(t)\mathbf{B}(\alpha, \beta)\mathbf{D}\mathbf{A} \end{aligned} \quad (11)$$

where

$$\mathbf{I}(t) = \int_{u(t)}^{v(t)} \mathbf{X}^T(s)\mathbf{X}(s)ds = [\mathbf{r}_{pq}(t)]; \mathbf{r}_{pq}(t) = \frac{(v(t))^{p+q+1} - (u(t))^{p+q+1}}{p+q+1}$$

and

$$\mathbf{K} = [\mathbf{k}_{mn}]; \mathbf{k}_{mn} = \frac{1}{m!n!} \cdot \frac{\partial^{m+n} K(0,0)}{\partial t^m \partial s^n}, \quad m, n, p, q = 0, 1, \dots, N$$

On the other hand, firstly we write the neutral term with delay of Eq. (1) in the form and then, by substituting the expressions (9), (10) and (11) into Eq. (1), we obtain the matrix equation

$$\left\{ \sum_{j=0}^2 \mathbf{Q}_j(t)\mathbf{X}(t)\mathbf{B}^j + \sum_{k=0}^2 \mathbf{R}_k(t)\mathbf{X}(t)\mathbf{B}(1, -\tau(t))\mathbf{B}^k - \mathbf{X}(t)\mathbf{K}\mathbf{I}(t) \right\} \mathbf{B}(\alpha, \beta)\mathbf{D}\mathbf{A} = \mathbf{G}(t). \quad (12)$$

#### Shifted Legendre Matrix Method

By using the collocation points defined by  $t_i = \frac{1}{N}i$ ,  $i = 0, 1, \dots, N$  into Eq. (12), and by simplifying the system of the obtained matrix equations, the fundamental matrix equation is obtained as

$$\left\{ \sum_{j=0}^2 \mathbf{Q}_j \mathbf{X} \mathbf{B}^j + \sum_{k=0}^2 \mathbf{R}_k \bar{\mathbf{X}} \bar{\mathbf{B}}(\tau) - \bar{\mathbf{X}} \bar{\mathbf{K}} \bar{\mathbf{I}} \right\} \mathbf{B}(\alpha, \beta)\mathbf{D}\mathbf{A} = \mathbf{G} \quad (13)$$

$$\text{or } \mathbf{W}\mathbf{A} = \mathbf{G} \Leftrightarrow [\mathbf{W}; \mathbf{G}]$$

where

$$X = \begin{bmatrix} X(t_0) \\ X(t_1) \\ \vdots \\ X(t_N) \end{bmatrix}, G = \begin{bmatrix} G(t_0) \\ G(t_1) \\ \vdots \\ G(t_N) \end{bmatrix}, \bar{I} = \begin{bmatrix} I(t_0) \\ I(t_1) \\ \vdots \\ I(t_N) \end{bmatrix}, \bar{B}(\tau) = \begin{bmatrix} B(1, -\tau(t_0)) \\ B(1, -\tau(t_1)) \\ \vdots \\ B(1, -\tau(t_N)) \end{bmatrix},$$

$$Q_j = \text{diag}[Q_j(t_0) \quad Q_j(t_1) \quad \dots \quad Q_j(t_N)], R_k = \text{diag}[R_k(t_0) \quad R_k(t_1) \quad \dots \quad R_k(t_N)],$$

$$\bar{X} = \text{diag}[X(t_0) \quad X(t_1) \quad \dots \quad X(t_N)], \bar{K} = \text{diag}[K \quad K \quad \dots \quad K],$$

In addition, we can write the matrix form for the conditions (2), by using the relation (9),

$$\sum_{k=0}^1 a_{kl} X(0) B^k B(\alpha, \beta) D A = \lambda_l, \quad l = 0, 1$$

or  $UA = \lambda \Rightarrow [U; \lambda]$  (14)

where

$$U = \sum_{k=0}^1 a_{kl} X(0) B^k B(\alpha, \beta) D, \quad U = \begin{bmatrix} U_0 \\ U_1 \end{bmatrix}, \quad \lambda = \begin{bmatrix} \lambda_0 \\ \lambda_1 \end{bmatrix},$$

Finally, we replace any one row of (13) by the row matrix (14) and thus we have the required augmented matrix as

$$[\tilde{W}; \tilde{G}] \text{ or } \tilde{W}A = \tilde{G}. \quad (15)$$

If  $\text{rank } \tilde{W} = \text{rank} [\tilde{W}; \tilde{G}] = N + 1$ , then we can write  $A = (\tilde{W})^{-1} \tilde{G}$ . Thus the matrix  $A$  (thereby the coefficients  $a_0, a_1, \dots, a_N$ ) is uniquely determined and the problem (1) – (2) has the unique solution in terms of shifted Legendre polynomials in the form (5).

### Accuracy of Solutions and Residual Error Estimation

We can easily check the accuracy of the obtained solutions as follows. Since the truncated shifted Legendre series (3) is approximate solution of Eq. (1), when the function  $y_N(t)$  and its derivatives are substituted in Eq. (1), the resulting equation must be satisfied approximately; that is, for

$$t = t_q \in [a, b], \quad q = 0, 1, \dots$$

$$R_N(t_q) = \sum_{j=0}^2 Q_j(t) y_N^{(j)}(t_q) + \sum_{k=0}^2 R_k(t_q) y_N^{(k)}(t - \tau(t_q)) - V(t_q) - G(t_q) \cong 0$$

or

$$R_N(t_q) \leq 10^{-k_q}, \quad (k_q \text{ is any positive integer}).$$

If  $\max 10^{-k_q} = 10^{-k}$  ( $k$  is an positive integer) is prescribed, then the truncation limit  $N$  is increased until the difference  $R_N(t_q)$  at each of the points becomes smaller than the prescribed  $10^{-k}$ . Therefore, if  $R_N(t_q) \rightarrow 0$ , when  $N$  is sufficiently large enough, then the error decreases.

On the other hand, by means of the residual function defined by  $R_N(t)$  and the mean value of the function  $|R_N(t)|$  on the interval  $[a, b]$ , the accuracy of the solution can be controlled and the error can be estimated [19-20]. Also, we can estimate the upper bound of the mean error  $\bar{R}_N$  as follows:

$$\left| \int_a^b R_N(t) dt \right| = (b-a) |R_N(c)| \leq \int_a^b |R_N(t)| dt, \quad a \leq c \leq b$$

$$(b-a) |R_N(c)| \leq \int_a^b |R_N(t)| dt \Rightarrow |R_N(c)| \leq \frac{\int_a^b |R_N(t)| dt}{b-a} = \bar{R}_N.$$

### Numerical Examples

**Example 1.** Let us consider linear neutral type integro-differential equation

$$y''(t) - y(t-t^2) + \frac{1}{2}ty'(t-t^2) + \frac{1}{2}t^4y''(t-t^2) = g(t) + \int_{t-1}^t 3y(s)ds$$

with the initial condition  $y(0) = 0, y'(0) = 0$ . The exact solution of problem is  $y(t) = t^2$  and  $g(t) = t^3 - 3t^2 + 3t + 1$ . Firstly, let us compute the approximate solution defined by

$$y_2(t) = \sum_{n=0}^2 a_n S_n(t)$$

The set of the collocation points for  $N=2$  is calculated as  $\left\{ t_0 = 0, t_1 = \frac{1}{2}, t_2 = 1 \right\}$  and from Eq.

(13), the fundamental matrix equation of the problem is written as

$$\left\{ \sum_{j=0}^2 Q_j \bar{X} B^j + \sum_{k=0}^2 R_k \bar{X} \bar{B}(\tau) - \bar{X} \bar{K} I \right\} B(\alpha, \beta) D A = G$$

From Eq. (14), we obtain the matrix form for the initial condition:

$$[U_0; \lambda_0] = [1 \quad -2 \quad 3; \quad 0]$$

$$[U_1; \lambda_1] = [0 \quad 4 \quad -16; \quad 0]$$

Therefore, from Eq. (15), the new augmented matrix is calculated as

$$[\tilde{W}; \tilde{G}] = \begin{bmatrix} -4 & 14 & -20; & 1 \\ 1 & -2 & 3; & 0 \\ 0 & 4 & -16; & 0 \end{bmatrix}$$

Solving this system, the unknown coefficients matrix is obtained as

$$A = \left[ \frac{5}{16} \quad \frac{1}{4} \quad \frac{1}{16} \right]^T. \text{ Therefore, we obtain the approximate solution } y_2(t) = t^2.$$

**Example 2.** Let us consider the linear neutral Volterra integro-differential equation

$$y''(t) - ty(t) + y'(t - t^2) = g(t) + \int_{t-1}^t y(s) ds; \quad 0 \leq t \leq 1$$

with the initial conditions  $y(0) = -1$ ,  $y'(0) = 1$ . Here  $g(t) = -t^2 + 2t + \frac{1}{2}$ . The exact solution of problem is  $y(t) = t - 1$ . Firstly, let us compute the exact solution  $y_3(t)$  by the truncated shifted Legendre series for  $N = 3$  is given by

$$y(t) = \sum_{n=0}^3 a_n S_n(t).$$

The set of the collocation points (2) for  $N = 3$  is calculated as

$$\left\{ x_0 = 0, x_1 = \frac{1}{3}, x_2 = \frac{2}{3}, x_3 = 1 \right\},$$

and from Eq. (13), the fundamental matrix equation of the problem is written as,

$$\left\{ \sum_{j=0}^2 Q_j X B^j + \sum_{k=0}^2 R_k \bar{X} \bar{B}(\tau) - \bar{X} \bar{K} \bar{I} \right\} B(\alpha, \beta) D A = G$$

So, by applying the procedure given in this article, we get the shifted Legendre polynomial solution  $y(t) = t - 1$  which is the exact solution of the problem.

**Example 3.** Our last example is the first-order linear differential equation

$$y(t+1) - y(t) + 2y(t-1) = 3t^2 + 6t + 5,$$

with the condition  $y(0) = 1$ ,  $y(1) = 4$ .

For  $N = 3$ , the matrix form of the problem is defined by

$$\left\{ \sum_{j=0}^2 Q_j \mathbf{X} \mathbf{B}^j + \sum_{k=0}^2 \mathbf{R}_k \overline{\mathbf{X}} \overline{\mathbf{B}}(\tau) - \overline{\mathbf{X}} \overline{\mathbf{K}} \mathbf{I} \right\} \mathbf{B}(\alpha, \beta) \mathbf{D} \mathbf{A} = \mathbf{G} .$$

After the augmented matrices of the system and conditions are computed, we obtain the solution  $y(t) = t^2 + 2t + 1$ , which is exact solution.

### Conclusion

In this study, a numerical method for solving the finite shifted Legendre series is proposed to find approximate solutions of second-order linear neutral type functional integro-differential equations involving variable bounds and variable delays under the mixed conditions has been developed. Also, the approximate solutions in terms of the finite series have been obtained by using Legendre polynomials. An error analysis technique has introduced for the method by using the residual function. Also, when the exact solution of the problem is not known, the solution can be approximately computed by means of residual error estimation. In addition, it is observed from the numerical values of the approximate solutions and the error estimations that the developed method is quite effective and applicative.

### References

- [1] Baykuş N, Sezer M. Hybrid Taylor-Lucas collocation method for numerical solution of high-order pantograph type delay differential equations with variables delays, *Appl. Math. Inf. Sci.* 2017; 11(6): 1795-1801.
- [2] Candan T. Existence of positive solutions of higher-order nonlinear neutral equations, *Journal of Inequalities and Applications* 2013; 573.
- [3] Everitt WN, Littlejohn LL, Wellman R. Legendre polynomials Legendre-Stirling numbers and the left-definite spectral analysis of the Legendre differential expressions, *J. Comput. Appl. Math.* 2002; 148: 213-238.
- [4] El-Mikkawy MEA, Cheon GS. Combinatorial and hypergeometric identities via the Legendre polynomials a computational approach, *Appl. Math. Comput.* 2005; 166: 181-195.
- [5] Gümgüm S, Savaşaneril NB, Kürkçü ÖK, Sezer M. A numerical technique based on Lucas polynomials together with standard and Chebyshev-Lobatto collocation points for solving functional integro-differential equations involving variable delays, *Sakarya University Journal of Science* 2018; 22(6):1659-1668.
- [6] Gürbüz B, Sezer M, Güler C. Laguerre collocation method for solving Fredholm integro-differential equations with functional arguments, *J. Appl. Math.* 2014; Article ID 682398, 12 pages.
- [7] Gülsu M, Sezer M. The approximate solution of high-order linear difference equation with variable coefficients in terms of Taylor polynomials, *Appl. Math. Comput.* 2005; 168: 76-88.
- [8] Gülsu M, Sezer M. Polynomial solution of the most general linear Fredholm integro-differential-difference equation by means of Taylor matrix method, *Int. J. Complex Variables* 2005; 50(5): 367-382.
- [9] Gülsu M, Sezer M. A method for the approximate solution of the high-order linear difference equations in terms of Taylor polynomials, *Int. J. Comput. Math.* 2005; 82(5): 629-642.
- [10] Işık OR, Güney Z, Sezer M. Bernstein series solutions of pantograph equations using polynomial interpolation, *J. Differ. Equ. Appl.* 2012; 18(3): 357-374.
- [11] Marzban HR, Razzaghi M. Optimal control of linear delay systems via hybrid of block-pulse and Legendre polynomials, *J. Franklin Inst.* 2004; 341: 279-293.
- [12] Özalp T, Sezer M. Gegenbauer-Taylor matrix technique for neutral type second order functional integro-differential equations with variable bounds, *3rd International Students Science Congress Proceeding Book.* 2019; 314-321.
- [13] Sezer M, Yüzbaşı Ş, Şahin N. A Bessel collocation method for numerical solution of generalized pantograph equations, *Numer. Methods Partial Differ. Equ.* 2012; 28(4): 1105-1123.

- [14] Sezer M, Akyüz-Daşçiođlu A. A Taylor method for numerical solution of generalized pantograph equations with linear functional argument, J. Comput. Appl. Math. 2007; 200: 217-225.
- [15] Soualhia I, Ardjouni A, Djoudi A. Fixed points and stability in nonlinear neutral integro-differential equations with variable delay, Filomat 2014; 28(4): 781-795.
- [16] Şahin N, Yüzbaşı Ş, Sezer M. A Bessel polynomial approach for solving general linear Fredholm integro-differential-difference equations, Int. J. Comput. Math. 2011; 88(14): 3093-3111.
- [17] Yousefi S, Razzaghi M. Legendre wavelets method for the nonlinear Volterra-Fredholm integral equations, Math. Comput. Simulat. 2005; 70(1): 1-8.
- [18] Yüzbaşı Ş, Gök E, Sezer M. Laguerre matrix method with the residual error estimation for solutions of a class of delay differential equations, Math. Meth. Appl. Sci. 2014; 453-463.
- [19] Yüzbaşı Ş, Sezer M. Shifted Legendre approximation with the residual correction to solve pantograph-delay type differential equations, Applied Mathematical Modelling 2015; 39: 6529-6542.
- [20] Yüzbaşı Ş, Sezer M. An exponential approximation for solutions of generalized pantograph-delay differential equations, Appl. Math. Model. 2013; 37: 9160-9173.



## Approximation Properties of Some Bernstein Type Operators

Faruk Özger

İzmir Kâtip Çelebi Univ., Dept. of Engineering Sciences, Çiğli Main Campus, İzmir, Türkiye  
Corresponding author: farukozger@gmail.com

**Keywords:** Convergence of operators, approximation results

**Discipline:** Mathematics

### Abstract

Bernstein's famous polynomials have been used in many theories including proof of Weierstrass's fundamental theorem. Approximation properties of certain Bernstein type operators have been investigated by many researchers for the last two decades. In this work, we investigate convergence of Bernstein operators via computer graphics and consider some recent Bernstein type operators.

### Bernstein type operators and graphs

Bernstein used famous polynomials nowadays called Bernstein polynomials, in 1912, to obtain an alternative proof of Weierstrass's fundamental theorem [2]. Approximation properties of Bernstein operators and their applications in Computer Aided Geometric Design and Computer Graphics have been extensively studied in many articles.

Bernstein basis of degree  $n$  on  $x \in [0,1]$  is defined by

$$b_{n,i}(x) = \binom{n}{i} x^i (1-x)^{n-i} \quad i = 0, \dots, n.$$

In Figure 1, we show Bernstein polynomials for certain values of  $n$ .

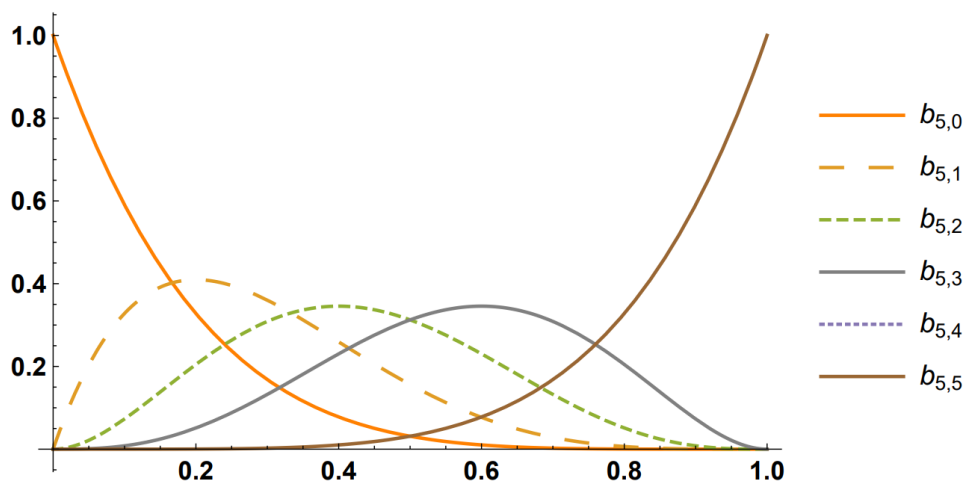


Figure 1. Bernstein polynomials  $b_{n,i}$

Bernstein operators are defined as

$$B_n(f; x) = \sum_{i=0}^n f\left(\frac{i}{n}\right) b_{n,i}(x).$$

Now consider the function  $f(x) = \frac{e^{x^3}}{x^2+1}$  on the interval  $[0,1]$ . In the following figure we give the approximation of  $B_n(f; x)$  operators for certain  $n$  values.

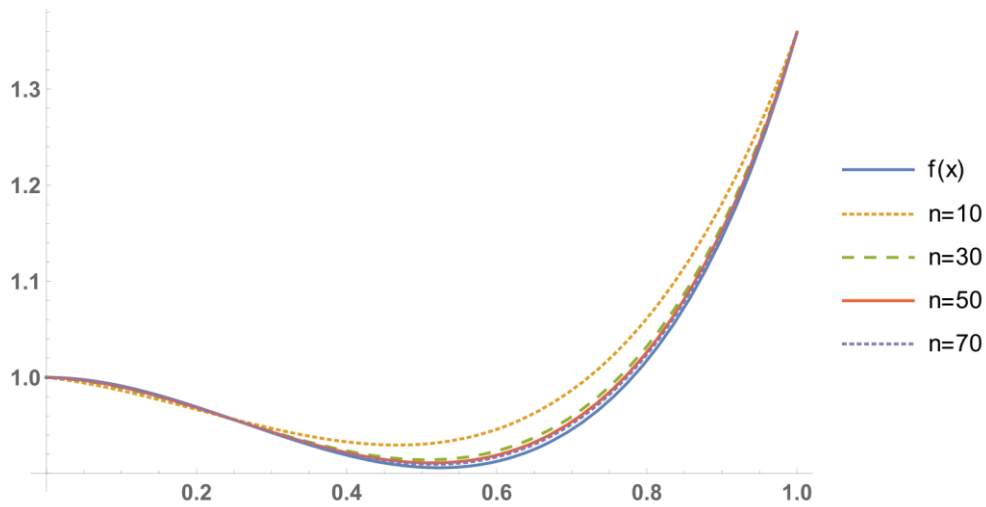


Figure 2. Approximation of  $B_n(f; x)$  operators

We also consider the function  $f(x) = \cos(\pi x^3)$  on the interval  $[0,1]$ . In Figure 3, we give the approximation of  $B_n(f; x)$  operators for certain  $n$  values.

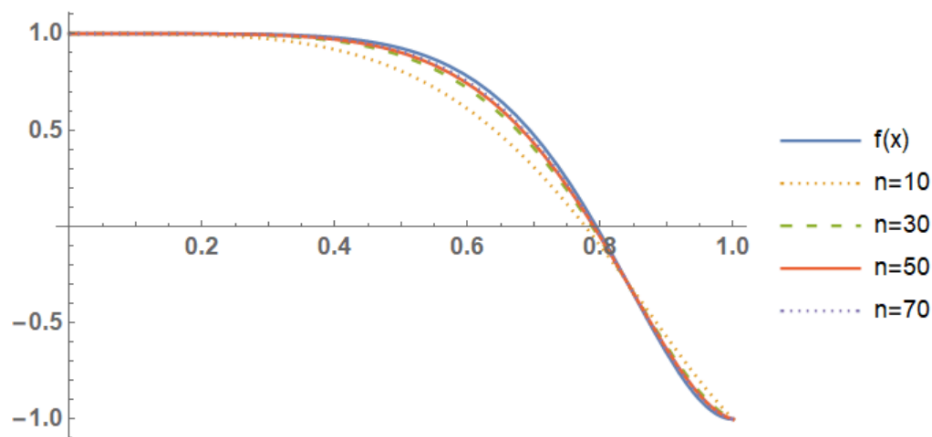


Figure 3. Approximation of  $B_n(f; x)$  operators

In 2018, Cai et al. have introduced a new type  $\lambda$  –Bernstein operators [1]

$$B_{n,\lambda}(f; x) = \sum_{i=0}^n f\left(\frac{i}{n}\right) \tilde{b}_{n,i}(\lambda; x)$$

with Bézier bases  $\tilde{b}_{n,i}(\lambda; x)$  [3]:

$$\begin{aligned} \tilde{b}_{n,0}(\lambda; x) &= b_{n,0}(x) - \frac{\lambda}{n+1} b_{n+1,1}(x), \\ \tilde{b}_{n,i}(\lambda; x) &= b_{n,i}(x) + \lambda \left( \frac{n-2i+1}{n^2-1} b_{n+1,i}(x) - \frac{n-2i-1}{n^2-1} b_{n+1,i+1}(x) \right), \\ \tilde{b}_{n,n}(\lambda; x) &= b_{n,n}(x) - \frac{\lambda}{n+1} b_{n+1,n}(x), \end{aligned}$$

where shape parameters  $\lambda \in [-1,1]$ .

Results in the following lemma were obtained for  $\lambda$  –Bernstein operators in [1, Lemma 2.1].

**Lemma 1.** We have following equalities for  $\lambda$  –Bernstein operators:

$$\begin{aligned}
 B_{n,\lambda}(1; x) &= 1; \\
 B_{n,\lambda}(t; x) &= x + \frac{1-2x+x^{n+1}-(1-x)^{n+1}}{n(n-1)} \lambda; \\
 B_{n,\lambda}(t^2; x) &= x^2 + \frac{x(1-x)}{n} + \left[ \frac{2x-4x^2+2x^{n+1}}{n(n-1)} + \frac{x^{n+1}+(1-x)^{n+1}-1}{n^2(n-1)} \right] \lambda; \\
 B_{n,\lambda}(t^3; x) &= x^3 + \frac{3x^2(1-x)}{n} + \frac{2x^3-3x^2+x}{n^2} + \left[ \frac{6x^{n+1}-6x^3}{n^2} + \frac{3x^2-3x^{n+1}}{n(n-1)} \right. \\
 &\quad \left. + \frac{9x^{n+1}-9x^2}{n^2(n-1)} + \frac{4x^{n+1}-4x}{n^3(n-1)} + \frac{1-x^{n+1}+(1-x)^{n+1}}{n^3(n^2-1)} \right] \lambda; \\
 B_{n,\lambda}(t^4; x) &= x^4 + \frac{6x^3(1-x)}{n} + \frac{7x^2-18x^3+11x^4}{n^2} + \frac{x-7x^2+12x^3-6x^4}{n^3} \\
 &\quad + \left[ \frac{6x^2-2x^3-8x^4+4x^{n+1}}{n^2} + \frac{17x^{n+1}+16x^4-32x^3-x^2}{n^3} + \frac{x-x^{n+1}}{n^4} \right. \\
 &\quad \left. + \frac{7x^2-7x^{n+1}}{n^2(n-1)} + \frac{x-23x^2+22x^{n+1}}{n^3(n-1)} + \frac{(1-x)^{n+1}+x-1}{n^4(n-1)} \right] \lambda.
 \end{aligned}$$

In [4], a comprehensive literature review about  $\lambda$ -Bernstein-type operators, Bernstein operators, Schurer operators, and Schurer and Bernstein polynomials were provided. Some Voronovskaja-type theorems, including a Grüss-Voronovskaja and a quantitative Voronovskaja-type theorem for  $\lambda$  -Schurer-Kantorovich operators were given. A family of GBS operators of bivariate tensor product of  $\lambda$ -Kantorovich type was constructed in [5]. An estimate for the rate of convergence of such operators was given for B-continuous and B-differentiable functions.

Also, a Voronovskaja-type asymptotic formula was established for the bivariate case. Many researchers established some Kantorovich-type operators by modifying Bernstein-type operators to have better error estimation [6-8]. More recently, statistical approximation properties of univariate and bivariate  $\lambda$ -Kantorovich operators were considered by Özger in [9]. The rate of weighted A-statistical convergence was estimated. A Voronovskaja-type approximation theorem by a family of linear operators was proved using the notion of weighted A-statistical convergence. Some estimates for differences of  $\lambda$ -Bernstein and  $\lambda$ -Durrmeyer, and  $\lambda$ -Bernstein and  $\lambda$ -Kantorovich operators were given. Finally, a Voronovskaja-type approximation theorem by weighted A-statistical convergence was established for the bivariate case of operators.

### References

- [1] Q-B. Cai, B-Y. Lian, G. Zhou, Approximation properties of  $\lambda$ -Bernstein operators, J. Ineq. and App., (2018), 2018:61.
- [2] S. N. Bernstein, Demonstration du theoreme de Weierstrass fondee sur le calcul des probabilites, Communications of the Kharkov Mathematical Society (1912), 13(2), 1-2.
- [3] Z. Ye, X. Long, X-M. Zeng, Adjustment algorithms for Bezier curve and surface, International Conference on Computer Science and Education, (2010), 1712-1716.
- [4] Özger, Faruk, and Kamil Demirci. Approximation by Kantorovich Variant of  $\lambda$ —Schurer Operators and Related Numerical Results. Topics in Contemporary Mathematical Analysis and Applications. CRC Press, 2020. 77-94.
- [5] Cai QB, Zhou G. Blending type approximation by GBS operators of bivariate tensor product of  $\lambda$ -Bernstein-Kantorovich type. J Inequal Appl. 2018; 2018:268.
- [6] Mohiuddine SA, F. Özger. Approximation of functions by Stancu variant of Bernstein-Kantorovich operators based on shape parameter  $\alpha$ , Rev. R. Acad. Cienc. Exactas Fis. Nat. Ser. A Math. RACSAM 2020; 114:70.
- [7] Rahman S, Mursaleen M, Acu AM. Approximation properties of  $\lambda$ - Bernstein Kantorovich operators with shifted knots. Math Meth Appl Sci. 2019; 42(11):042–4053.
- [8] Özger F. On new Bezier bases with Schurer polynomials and corresponding results in approximation theory. Commun Fac Sci Univ Ank Ser A1 Math Stat. 2019; 69(1):376–393.
- [9] Özger F. Weighted statistical approximation properties of univariate and bivariate  $\lambda$ -Kantorovich operators. Filomat 2019; 33(11):3473–3486.

## A Numerical Approach Based on Bell Polynomials to Solve Volterra Integro Differential Equations with Variable Coefficients

Gökçe Yıldız\*, Manisa Celal Bayar Univ., Dept. of Mathematics, Manisa, Türkiye  
Mehmet Sezer, Manisa Celal Bayar Univ., Dept. of Mathematics, Manisa, Türkiye  
\*Corresponding author: gokceyldz3@gmail.com

**Keywords:** Bell polynomials and series, collocation points and matrix method, Volterra integro- differential equations

**Discipline:** Mathematics

### Abstract

The main purpose of this study is to apply Bell polynomials to the solution of high order linear Volterra integro-differential equations with variable coefficients under initial and boundary conditions. The used technique in this study is essentially based on the truncated Bell series, their derivatives and its matrix representations along with collocation points; also it reduces the solution of the mentioned equation under the initial -boundary conditions to the solution of a matrix equation with the unknown Bell coefficients. Therefore, when the problem is solved, the approximate solution is written in terms of Bell polynomials. Also, by using the Mean-Value Theorem and residual function, an efficient error estimation technique is proposed, and some illustrative examples are presented to demonstrate the validity and applicability of the method. The numerical results obtained by using this method are compared in tables and figures. The method is easy to implement and produces accurate results. All numerical computations have been performed on the computer algebraic system MATLAB.

### Introduction

Volterra integro-differential equations (VIDEs), which are a combination of differential equation and Volterra integral equations, have been of great interest to researchers for many years and their solutions play a major role in the fields of science and engineering. There are many application areas to illustrate engineering, mechanics, physics, chemistry, astronomy, biology, economics potential theory, electrostatics etc. Since the fore mentioned VIDEs usually difficult to solve analytically, a numerical method is needed. In recent years, for solving these equation, numerical methods have been developed. For example, Adomian decomposition method [1,6], Legendre spectral-collocation method [6], hybrid function method [7], variational iteration method [18], the Haar function method [9], Chebyshev collocation method [13], Taylor collocation method [11], Bernoulli matrix collocation Method [5] and etc.

In this study, we consider the approximate solutions of high order linear Volterra integro differential equations with variable coefficients

$$\sum_{k=0}^m P_k(x)y^{(k)}(x) = g(x) + \lambda \int_a^x K(x,t)y^{(k)}(t)dt \quad a \leq x, t \leq b \quad (1)$$

with initial-boundary conditions

$$\sum_{k=0}^{m-1} (a_{jk}y^{(k)}(a) + b_{jk}y^{(k)}(b)) = \lambda_j, j = 0, 1, \dots, m-1 \quad (2)$$

where  $P_k(x)$ ,  $g(x)$  and the kernel function  $K(x, t)$  are known functions defined on the interval  $a \leq x, t \leq b$ ;  $a_{jk}$ ,  $b_{jk}$  and  $\lambda_j$  are suitable constants.

Our aim is to obtain an approximate solution of (1) in the following truncated Bell series form

$$y(x) \cong y_N(x) = \sum_{n=0}^N a_n B_n(x) \quad (3)$$

where  $a_n, n = 0, 1, \dots, N$  are unknown Bell coefficients and  $B_n(x), n = 0, 1, \dots, N$  are Bell polynomial defined by

$$B_n(x) = \sum_{k=0}^n S(n, k) x^k \quad (4)$$

where

$$S(n, k) = \sum_{j=0}^k \frac{(-1)^{k-j}}{k!} \binom{k}{j} \cdot j^n$$

is Stirling numbers of the second kind [2,4,10].

### Fundamental matrix relations

First of all, we can write the Bell polynomials  $B_n(x)$  in the matrix form as follows:

$$\mathbf{B}(x) = \mathbf{X}(x)\mathbf{S} \quad (5)$$

where

$$\mathbf{B}(x) = [B_0(x) \ B_1(x) \ \dots \ B_N(x)] \ , \ \mathbf{X}(x) = [1 \ x \ x^2 \ \dots \ x^N]$$

and

$$\mathbf{S} = \begin{bmatrix} S(0,0) & S(1,0) & S(2,0) & \dots & S(N,0) \\ 0 & S(1,1) & S(2,1) & \dots & S(N,1) \\ 0 & 0 & S(2,2) & \dots & S(N,2) \\ \vdots & \vdots & \vdots & \ddots & \vdots \\ 0 & 0 & 0 & \dots & S(N,N) \end{bmatrix}$$

Let us show Eq. (1) in the form:

$$D(x) = g(x) + V(x) \quad (6)$$

where the functional differential part is

$$D(x) = \sum_{k=0}^m P_k(x) y^{(k)}(x)$$

and Volterra integral part is

$$\mathbf{V}(x) = \int_a^x \mathbf{K}(x, t) \mathbf{y}^{(k)}(t) dt \quad a \leq x, t \leq b$$

Now we transform the parts  $D(x), V(x)$  and the conditions (2) to matrix forms.

### Matrix relation for the differential part $\mathbf{D}(x)$

Let us consider the solution  $y(x)$  of (1) and its  $k$ -th derivative  $y^{(k)}(x)$  of defined by the truncated Bell series (3). Then, we can put the finite series (3) in the matrix form  
Then, we can put the finite series (3) in the matrix form

$$y(x) = \mathbf{B}(x)\mathbf{A}; \mathbf{A} = [a_0 \ a_1 \ \dots \ a_N]^T \quad (7)$$

and its  $k$ -th derivative becomes

$$y^{(k)}(x) = \mathbf{B}^{(k)}(x)\mathbf{A} \quad (8)$$

By substituting (5) into (7) we obtain that

$$y(x) = \mathbf{X}(x)\mathbf{S}\mathbf{A} \quad (9)$$

On the other hand it is clearly seen that [14] the relation between the matrix  $\mathbf{X}(x)$  and its  $k$ th derivative  $\mathbf{X}^{(k)}(x)$  is

$$\mathbf{X}^{(k)}(x) = \mathbf{X}(x)\mathbf{M}^k \quad (10)$$

where

$$\mathbf{M} = \begin{bmatrix} 0 & 1 & 0 & \cdots & 0 \\ 0 & 0 & 2 & \cdots & 0 \\ \vdots & \vdots & \vdots & \cdots & \vdots \\ 0 & 0 & 0 & \cdots & N \\ 0 & 0 & 0 & \cdots & 0 \end{bmatrix}, \mathbf{M}^0 = \begin{bmatrix} 1 & 0 & 0 & \cdots & 0 \\ 0 & 1 & 0 & \cdots & 0 \\ 0 & 0 & 1 & \cdots & 0 \\ \vdots & \vdots & \vdots & \ddots & \vdots \\ 0 & 0 & 0 & \cdots & 1 \end{bmatrix}$$

From the matrix relations (8), (9) and (10) we can write the following matrix form

$$y^{(k)}(x) = \mathbf{B}^{(k)}(x)\mathbf{A} = \mathbf{X}^{(k)}(x)\mathbf{S}\mathbf{A} = \mathbf{X}(x)\mathbf{M}^k\mathbf{S}\mathbf{A} \quad (11)$$

By substituting the expression (10) into Eq. (6), we get the matrix relation [12]

$$D(x) = \sum_{k=0}^m P_k(x)\mathbf{X}(x)\mathbf{M}^k\mathbf{S}\mathbf{A}$$

### Matrix Representation for Volterra Integral Part

Let us find the matrix form for the Volterra integral part  $V(x)$ . The kernel function can be  $K_l(x, t)$  approximated by the truncated Maclaurin series [16]

$$K(x, t) = \sum_{p=0}^N \sum_{q=0}^N k_{pq} x^p t^q \quad (12)$$

where

$$k_{pq} = \frac{1}{p!q!} \frac{\partial^{p+q} K(0,0)}{\partial x^p \partial t^q}, \quad p, q = 0, 1, \dots, N$$

The expression (12) converts to the matrix form

$$K(x, t) = \mathbf{X}(x)\mathbf{K}\mathbf{X}^T(t) \quad \text{where } \mathbf{K} = [k_{pq}]. \quad (13)$$

Substituting relations (10) and (13) in the Volterra integral part, we obtain

$$\begin{aligned} V(x) &= \int_0^x \sum_{l=0}^{m_1} \mathbf{X}(x)\mathbf{K}\mathbf{X}^T(t)\mathbf{X}(t)\mathbf{M}^l\mathbf{S}\mathbf{A} \, dt \\ &= \sum_{l=0}^{m_1} \mathbf{X}(x)\mathbf{\Theta}(x)\mathbf{M}^l\mathbf{S}\mathbf{A} \end{aligned} \quad (14)$$

where

$$\Theta(x) = [\varphi_{ij}(x)] = \int_a^x \mathbf{X}^T(t)\mathbf{X}(t)dt \text{ and } \varphi_{ij}(x) = \frac{x^{i+j+1} - a^{i+j+1}}{i+j+1} ; i, j = 0, 1, 2, \dots, N.$$

### Matrix relation for the conditions

Let us define the matrix form of the conditions given by (2) using expression (11) that can be written as

$$\left\{ \sum_{k=0}^{m-1} (a_{jk}\mathbf{X}(a)\mathbf{M}^k\mathbf{S} + b_{jk}\mathbf{X}(b)\mathbf{M}^k\mathbf{S}) \right\} \mathbf{A} = \lambda_j, j = 0, 1, \dots, m-1 \quad (15)$$

### Method of Solution

In an attempt to construct a fundamental matrix equation, substituting the matrix relations (12) and (16) into (1) we obtain that

$$\sum_{k=0}^m \mathbf{P}_k(x)\mathbf{X}(x)\mathbf{M}^k\mathbf{S} = g(x) + \lambda\mathbf{X}(x)\mathbf{KQ}(x)\mathbf{M}^k\mathbf{SA} \quad (16)$$

The collocation points  $x_i$  are defined by

$$x_i = a + \frac{b-a}{N}i, \quad i = 0, 1, \dots, N \quad (17)$$

And by using this points (19) the systems of the matrix equations are obtained as

$$\sum_{k=0}^m \mathbf{P}_k(x_i)\mathbf{X}(x_i)\mathbf{M}^k\mathbf{S} = g(x_i) + \lambda\mathbf{X}(x_i)\mathbf{KQ}(x_i)\mathbf{M}^k\mathbf{SA} \quad (18)$$

or shortly

$$\underbrace{\left\{ \sum_{k=0}^m \mathbf{P}_k\mathbf{X}\mathbf{M}^k\mathbf{S} - \lambda\bar{\mathbf{X}}\bar{\mathbf{K}}\bar{\mathbf{Q}}\mathbf{S} \right\}}_{\mathbf{W}} \mathbf{A} = \mathbf{G}$$

where

$$\mathbf{X} = \begin{bmatrix} 1 & x_0 & \dots & x_0^N \\ 1 & x_1 & \dots & x_1^N \\ \vdots & \vdots & \ddots & \vdots \\ 1 & x_N & \dots & x_N^N \end{bmatrix}, \bar{\mathbf{X}} = \begin{bmatrix} \mathbf{X}(x_0) & 0 & \dots & 0 \\ 0 & \mathbf{X}(x_1) & \dots & 0 \\ \vdots & \vdots & \ddots & \vdots \\ 0 & 0 & \dots & \mathbf{X}(x_N) \end{bmatrix}$$

$$\mathbf{K} = \begin{bmatrix} k_{00} & k_{01} & \dots & k_{0N} \\ k_{10} & k_{11} & \dots & k_{1N} \\ \vdots & \vdots & \ddots & \vdots \\ k_{N0} & k_{N1} & \dots & k_{NN} \end{bmatrix}, \bar{\mathbf{K}} = \begin{bmatrix} \mathbf{K} & 0 & \dots & 0 \\ 0 & \mathbf{K} & \dots & 0 \\ \vdots & \vdots & \ddots & \vdots \\ 0 & 0 & \dots & \mathbf{K} \end{bmatrix}, \bar{\mathbf{Q}} = \begin{bmatrix} \mathbf{Q}(x_0) \\ \mathbf{Q}(x_1) \\ \vdots \\ \mathbf{Q}(x_N) \end{bmatrix}$$

$$\mathbf{P}_k = \begin{bmatrix} P_k(x_0) & 0 & \dots & 0 \\ 0 & P_k(x_1) & \dots & 0 \\ \vdots & \vdots & \ddots & \vdots \\ 0 & 0 & \dots & P_k(x_N) \end{bmatrix}, \mathbf{M} = \begin{bmatrix} 0 & 1 & 0 & \dots & 0 \\ 0 & 0 & 2 & \dots & 0 \\ \vdots & \vdots & \vdots & \dots & \vdots \\ 0 & 0 & 0 & \dots & N \\ 0 & 0 & 0 & \dots & 0 \end{bmatrix}, \mathbf{G} = \begin{bmatrix} g(x_0) \\ g(x_1) \\ \vdots \\ g(x_N) \end{bmatrix}$$

The fundamental matrix equation (18) for (1) corresponds to a system of  $(N + 1)$  algebraic equation for the  $(N + 1)$  unknown coefficients  $a_0, a_1, a_2, \dots, a_N$ . Concisely we can write as

$$\mathbf{WA} = \mathbf{G} \quad \text{or} \quad [\mathbf{W}; \mathbf{G}] \quad (19)$$

On the other hand, the matrix form (15) for the conditions can be written as

$$\mathbf{U}_j \mathbf{A} = \lambda_j \quad \text{ya da} \quad [\mathbf{U}; \lambda_j], \quad j = 0, 1, \dots, m - 1 \quad (20)$$

where

$$\mathbf{U}_j = [u_{j0} \quad u_{j1} \quad \dots \quad u_{jN}] = \sum_{k=0}^{m-1} a_{jk} \mathbf{X}(a) \mathbf{M}^k \mathbf{S} + b_{jk} \mathbf{X}(b) \mathbf{M}^k \mathbf{S}, \quad j = 0, 1, \dots, m - 1$$

To obtain the solution of (1) under conditions (2), by replacing the  $m$  rows in matrix equation (20) into the matrix equation (19), we have the required new augmented matrix system [15,17]

$$\widetilde{\mathbf{W}} \mathbf{A} = \widetilde{\mathbf{G}} \quad \text{or} \quad [\widetilde{\mathbf{W}}; \widetilde{\mathbf{G}}] \quad (21)$$

If  $\text{rank}(\widetilde{\mathbf{W}}) = \text{rank}[\widetilde{\mathbf{W}}; \widetilde{\mathbf{G}}] = N + 1$ , then we can write

$$\mathbf{A} = (\widetilde{\mathbf{W}})^{-1} \widetilde{\mathbf{G}}.$$

Thus, the matrix  $\mathbf{A}$  (there by the coefficients  $a_0, a_1, a_2, \dots, a_N$ ) is uniquely determined and the Eq. (1) under the coefficient equation (2) has unique solution. This solution is given by truncated Bell series

$$y(x) \cong y_N(x) = \sum_{n=0}^N a_n B_n(x).$$

### Residual Correction and Error Estimation

We can easily check the accuracy of the obtained solutions as follows. Since the truncated Bell series (3) is approximate solution of (1), when the function  $y_N(x)$  and its derivatives are substituted in (1), the resulting equation must be satisfied approximately, that is, for  $x = x_q \in [a, b]$ ,  $q = 0, 1, \dots$

$$R_N(x_q) = \sum_{k=0}^m P_k(x_q) y_N^{(k)}(x_q) - \lambda \int_a^{x_q} K(x_q, t_q) y^{(k)}(t_q) dt - g(x_q) \cong 0$$

or

$$R_N(x_q) \leq 10^{-k_q}, \quad (k_q \text{ is any positive integer}).$$

If  $\max 10^{-k_q} = 10^{-k}$  ( $k$  is an positive integer) is prescribed, then the truncation limit  $N$  is increased until the difference  $R_N(x_q)$  at each of the points becomes smaller than the prescribed  $10^{-k}$ . Therefore, if  $R_N(x_q) \rightarrow 0$  when  $N$  is sufficiently large enough, then the error decreases [8].



On the other hand, by means of the residual function defined by  $R_N(x)$  and the mean value of the function  $|R_N(x)|$  on the interval  $[a, b]$ , the accuracy of the solution can be controlled and the error can be estimated [7]. Thus, we can estimate the upper bound of the mean error  $\overline{R_N}$  as follows:

$$\left| \int_a^b R_N(x) dx \right| \leq \int_a^b |R_N(x)| dx$$

and

$$\begin{aligned} \int_a^b |R_N(x)| dx &= (b-a)|R_N(c)|, a \leq c \leq b \\ \Rightarrow \left| \int_a^b R_N(x) dx \right| &= (b-a)|R_N(c)| \Rightarrow (b-a)|R_N(c)| \leq \int_a^b |R_N(x)| dx \\ &\Downarrow \\ |R_N(c)| &\leq \frac{\int_a^b |R_N(x)| dx}{b-a} = \overline{R_N} \end{aligned}$$

### Numerical Examples

Using exact solution  $y(x)$  and the approximate solution  $y_N(x)$ , the error function  $e_N$  is calculated by the following form

$$e_N = y(x) - y_N(x).$$

**Example 1.** Let us first consider the first order linear Volterra type integro-differential equation

$$y'(x) + xy(x) = 1 + x^2 - x^4/3 + \int_0^x xty(t)dt$$

with initial conditions  $y(0) = 0$  and the approximate solution  $y_2(x)$  by the truncated Bell series

$$y_2(x) = \sum_{n=0}^2 a_n B_n(x)$$

where  $m=1, N=2, P_0(x) = x, P_1(x) = 1, K(x, t) = xt, g(x) = 1 + x^2 - x^4/3$  and  $\lambda = 1$ .

Hence the collocation points for  $N = 2$  becomes

$$\{x_0 = 0, x_1 = 1/2, x_2 = 1\}$$

and from the eq. (18), the Fundamental matrix equation of the given VIDE becomes

$$\{P_0 X M^0 S + P_1 X M S - \lambda \bar{X} \bar{K} \bar{Q} S\} A = G$$

$$P_0 = \begin{bmatrix} 0 & 0 & 0 \\ 0 & 1/2 & 0 \\ 0 & 0 & 1 \end{bmatrix}, P_1 = \begin{bmatrix} 1 & 0 & 0 \\ 0 & 1 & 0 \\ 0 & 0 & 1 \end{bmatrix}, S = \begin{bmatrix} 1 & 0 & 0 \\ 0 & 1 & 1 \\ 0 & 0 & 1 \end{bmatrix},$$

$$\bar{\mathbf{K}} = \begin{bmatrix} 1 & 0 & 0 & 0 & 0 & 0 & 0 & 0 & 0 \\ 0 & 0 & 0 & 0 & 0 & 0 & 0 & 0 & 0 \\ 0 & 0 & 0 & 0 & 0 & 0 & 0 & 0 & 0 \\ 0 & 0 & 0 & 1 & 0 & 0 & 0 & 0 & 0 \\ 0 & 0 & 0 & 0 & 0 & 0 & 0 & 0 & 0 \\ 0 & 0 & 0 & 0 & 0 & 0 & 0 & 0 & 0 \\ 0 & 0 & 0 & 0 & 0 & 0 & 1 & 0 & 0 \\ 0 & 0 & 0 & 0 & 0 & 0 & 0 & 0 & 0 \\ 0 & 0 & 0 & 0 & 0 & 0 & 0 & 0 & 0 \end{bmatrix}, \bar{\mathbf{Q}} = \begin{bmatrix} 0 & 0 & 0 \\ 0 & 0 & 0 \\ 0 & 0 & 0 \\ 1/2 & 1/8 & 1/24 \\ 1/8 & 1/24 & 1/64 \\ 1/24 & 1/64 & 1/160 \\ 1 & 1/2 & 1/3 \\ 1/2 & 1/3 & 1/4 \\ 1/3 & 1/4 & 1/5 \end{bmatrix}$$

$$\bar{\mathbf{X}} = \begin{bmatrix} 1 & 0 & 0 & 0 & 0 & 0 & 0 & 0 & 0 \\ 0 & 0 & 0 & 1 & \frac{1}{2} & \frac{1}{4} & 0 & 0 & 0 \\ 0 & 0 & 0 & 0 & 0 & 0 & 1 & 1 & 1 \end{bmatrix}, \mathbf{M} = \begin{bmatrix} 0 & 1 & 0 \\ 0 & 0 & 2 \\ 0 & 0 & 0 \end{bmatrix}, \mathbf{G} = \begin{bmatrix} 1 \\ 59/48 \\ 5/3 \end{bmatrix}$$

The augmented matrix for this fundamental matrix equation is calculated as

$$[\mathbf{W}; \mathbf{G}] = \begin{bmatrix} 0 & 1 & 1 & ; & -1 \\ 7/16 & 59/48 & 901/384 & ; & 59/48 \\ 1/2 & 5/3 & 53/12 & ; & 5/3 \end{bmatrix}$$

From Eq. (20), the matrix forms for the initial condition is

$$[\mathbf{U}_0; \lambda_0] = [1 \quad 0 \quad 0 \quad ; \quad 0]$$

From system (21), the new augmented matrix based on conditions can be obtained as follows:

$$[\tilde{\mathbf{W}}; \tilde{\mathbf{G}}] = \begin{bmatrix} 0 & 1 & 1 & ; & -1 \\ 1 & 0 & 0 & ; & 0 \\ 1/2 & 5/3 & 53/12 & ; & 5/3 \end{bmatrix}$$

Solving this system, the unknown Bell coefficient matrix is obtained as

$$\mathbf{A} = [0 \quad 1 \quad 0]^T$$

By substituting the above Bell coefficient matrix into equation (7), we obtain the approximate solution  $y(x) = x$  which is the exact solution.

Example 5.2. Let us consider the Bell series solution second order linear Volterra type integro-differential equation given by

$$y''(x) + y'(x) + xy(x) = -2\cos x - 2x\sin x + x + \int_0^x xy(t)dt$$

with initial condition  $y(0) = 1$  and  $y'(0) = -1$ . The exact solution of problem is  $\cos x - \sin x$  and we seek the approximate solution  $y_N(x)$  as a truncated Bell series

$$y(x) \cong y_N(x) = \sum_{n=0}^N a_n B_n(x)$$

where  $P_0(x) = x, P_1(x) = 1, P_2(x) = 1, K(x, t) = x, g(x) = -2\cos x - 2x\sin x + x$  ve  $\lambda = 1$ . For  $N = 4, 7$  and  $8$  the obtained approximate solutions are

$$y_4(x) = 1 - x - 0.5000x^2 + 0.1705x^3 + 0.0302x^2$$

$$y_7(x) = 1 - x - 0.5000x^2 + 0.1667x^3 + 0.0417x^4 - 0.0083x^5 - 0.0014x^6 + 2.5398e^{-04}x^7$$

$$y_8(x) = 1 - x - 0.5000x^2 + 0.1667x^3 + 0.0417x^4 - 0.0083x^5 - 0.0014x^6 + 2.1402e^{-04}x^7 + 1.3981e^{-05}x^8$$

Table 1. Comparison of the absolute errors of Example 2 for N= 4, 7 and 6

$x_i$	$y(x) = \cos(x^i) - \sin \cos(x^i)$	$ e_4(x_i) $	$ e_7(x_i) $	$ e_8(x_i) $
0	1	0	0	0
0.2	0.7814	$1.4745e^{-05}$	$1.3539e^{-09}$	$1.0844e^{-10}$
0.4	0.5316	$3.9381e^{-05}$	$2.5795e^{-09}$	$2.0933e^{-10}$
0.6	0.2607	$3.6800e^{-05}$	$3.5357e^{-09}$	$2.8962e^{-10}$
0.8	0.0206	$2.8321e^{-04}$	$4.2170e^{-09}$	$3.1687e^{-10}$
1	0.3012	0.0018	$1.2702e^{-09}$	$1.6465e^{-80}$

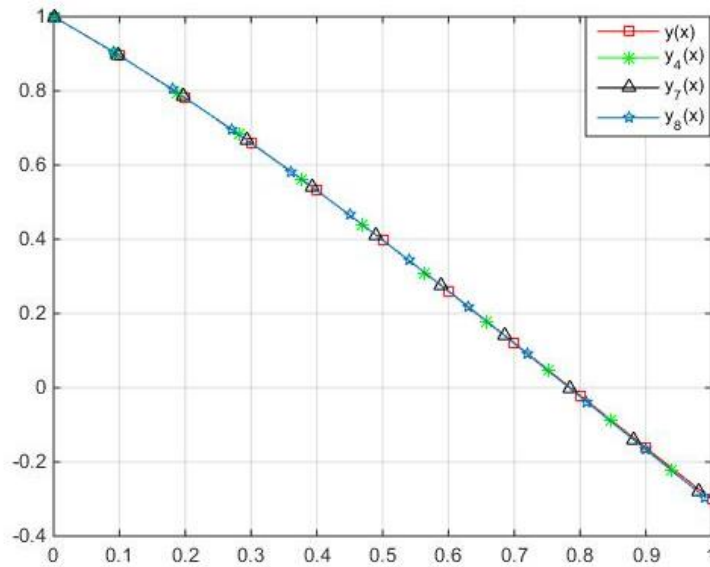


Figure 1. Numerical and exact solutions of Example 2 for N = 4, 7 and 8

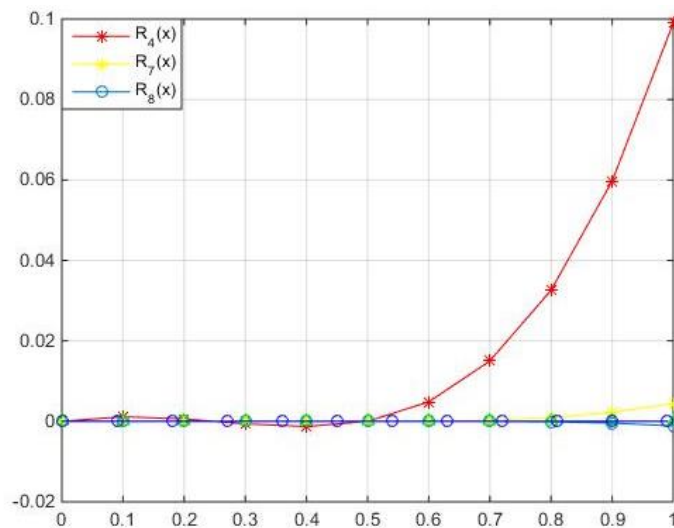


Figure 2. Residual Error Functions of Example 2 for N = 4, 7 and 8.

### Conclusion

In this study, a new method was developed by using Bell polynomials for the solution of high order linear Volterra integro differential equations. To illustrate the validity and applicability of this method, explanatory examples were solved, and an error analysis based on the residual function was performed to show the accuracy of the results. These comparisons and error estimates show that the proposed method is highly effective. We have calculated the solutions with the help of Matlab.

### References

- [1] Biazar J, Babolian E and Islam R. Solution of a system of Volterra integral equations of the first kind by Adomian method, *Appl Math Comput* 2003;139 ,249–258.
- [2] Bell E.T, Exponential polynomials, *Ann. Math.*1934; 35(2):258-277.
- [3] Chen Y, Gu Z. Legendre spectral-collocation method for Volterra integral differential equations with nonvanishing delay, *Communications in Applied Mathematics and Computational Science* 8 (2013), 67–98.
- [4] Çam Ş. Stirling Sayıları. *Matematik Dünyası* 2005, 30-34.
- [5] Erdem K, Sezer M. Bernoulli matrix collocation Method for solving general functional integro differential equations with hybrid delays. *Journal of Inequalities and Special Functions* 2017; 8(3), 85-99.
- [6] Goghary HS, Javadi S and Babolian E. Restarted Adomian method for system of nonlinear Volterra integral equations, *Appl Math Comput* 2005;161,745–751.
- [7] Hsiao CH, Hybrid function method for solving Fredholm and Volterra integral equations of the second kind, *J. Comput. Appl. Math.* 2009;230,59–68.
- [8] Mollaoğlu T, M Sezer, A numerical approach with residual error estimation for solution of high-order linear differential-difference equations by using Gegenbauer polynomials, *CBU J. of Sci.* 2017;13(1):39-49.
- [9] Reihani MH, Abadi Z. Rationalized Haar functions Method for solving Fredholm and Volterra integral equations, *J. Comput. Appl. Math.* 2007; 200, 12–20.
- [10] Van Gorder R A, Recursive Relations for Bell Polynomials of Arbitrary Positive Non-Integer Order, *International Mathematical Forum* 2010; 5(37):1819-1821.
- [11] Yalçınbaş S, Sezer M. The approximate solution of high-order linear Volterra–Fredholm integro-differential equations in terms of Taylor polynomials, *Appl. Math. Comput.* 2000; 112,291–308.
- [12] Yıldız G, Tınaztepe G and Sezer M. Bell polynomial approach for the solutions of Fredholm Integro differential equations with variable coefficients. *Computer Modeling in Engineering & Sciences*, 2020; 123(3), 973-993(21).
- [13] Yüksel G, Gülsu M and Sezer M. A Chebyshev Polynomial Approach for High-Order Linear Fredholm-Volterra Integro-Differential Equations. *Gazi University Journal of Science* 2012; 25(2):393-401.
- [14] Yüzbaşı Ş, Şahin N and Sezer M. Bessel polynomial solution of high-order linear Volterra integro-differential equations, *Computers & Mathematics with Applications*, 2011; 62(4), 1940-1956.
- [15] Yuzbası S. Laguerre approach for solving pantograph-type Volterra integro-differential equations, *Appl. Math. and Comput.* 2014; 232, 1183–1199.
- [16] Yuzbası S., An exponential method to solve linear Fredholm–Volterra integro-differential equations and residual improvement. *Turk J Math* 2018;42: 2546 – 2562.
- [17] Yusufoglu E, An efficient algorithm for solving integro-differential equations system, *Appl Math Comput* 2007; 192, 51–55.
- [18] Wang SQ, He JH. Variational iteration method for solving integro-differential equations, *Phys Lett A* 2007; 367, 188–191.

## **Mechanical Engineering / Makina Mühendisliği**

## Compression-after Impact Behavior of Laminated Composites Plates

*Samet Kıyık\**, Dokuz Eylül University, Graduate School of Natural and Applied Sciences, İzmir, Turkey

*Ramazan Karakuzu*, Dokuz Eylül University, Department of Mechanical Engineering, İzmir, Turkey

*Halis Kandaş*, Dokuz Eylül University, Graduate School of Natural and Applied Sciences, İzmir, Turkey

\*Corresponding author: sam\_46\_sam@hotmail.com

**Keywords:** S2 glass, epoxy, laminated composite compression-after impact, low velocity impact

**Discipline:** Mechanical Engineering

### Abstract

In this study, S2 glass/epoxy laminated composite at different thicknesses were produced by using the vacuum assisted resin infusion method (VARIM). 15-layer and 18-layer S2 glass composites were used to investigate the effect of thickness of the composite on compression-after impact (CAI) strength. Impact tests were conducted by using Ceast 9350 Fractovis Plus impact test machine at 30J, 40J and 50J impact energies. In order to determine the effect of the impact damage on the residual compressive strength of the specimen, Compression-after impact (CAI) tests were carried out by using Universal Shimadzu testing machine with Boeing CAI fixture (ASTM D 7137) for impacted and unimpacted specimens. CAI strength of composites decreases with increase of impact energy.

### Introduction

E-glass and S-glass fibers are generally preferred glass fibers for fiber-reinforced composites [1]. S-glass fiber has the highest tensile strength among all types of glass fibers [2]. The epoxy matrix material used in manufacturing has good resistance to water, acid, oil and chemicals. Therefore, it has a wide field of use. Some of these fields are aerospace industry, automotive and marine industries. The most commonly used reinforcement material in composites is glass fibers, due to their compressive strength is very high than other fiber types. As they are extremely resistant to temperature, they can easily use in aerospace industry.

CAI is a method used to determine the degradation in the compressive strength of the composite plate after impact loading to the material. Therefore, the CAI problem has been a very important area of research. There were many studies on the CAI problem. Aktas et al. [3] used to glass/epoxy composite plates (two different laminate orientation) was applied different impact energies at room temperature (20 °C) and high temperatures. After then two different laminate orientations tested to investigate the effects of laminate orientation on CAI strength and CAI damage mechanism. They showed that impact test temperature has remarkable effect on the CAI strength of the laminates. Ruixiang et al. [4] performed low-velocity impact test on composite foam-core sandwich (FCS) panels and the CAI tests. CAI experiments showed that as the impact energy applied to FCS panels increases, compressive strength decreases. Tay and Shen et al. [5] investigated the effects of thermal residual stresses for buckling and post buckling on woven and non-woven composite materials. Their results showed that the local strain energy had a negligible effect on the distribution of the release rate in the post-buckling regime, but the thermal residual stresses had a significant effect at the beginning of the buckling. Hongliang et al. [6] investigated the failure and damage mechanism of unidirectional carbon/epoxy prepreg under various impact energies and CAI loading situation by numerical and experimental methods. Their results showed that CAI strength decreases with increase of impact energy and multiple impacts.

In this study, S2 glass/epoxy composites were manufactured by vacuum assisted resin infusion method (VARIM). Firstly, impact tests were applied to the composite specimens then CAI tests carried out. The effects of the composite thickness and impact energy on CAI strength investigated experimentally.

### Methodology

Firstly, the manufacturing plate covered with mold release agent to prevent the epoxy from sticking to the plate and all edges covered with adhesive sealant. Subsequently, S2 glass fibers laid on the mold release agent. Peel ply placed on S2 glasses. The reason for this is that S2 glasses can be adhered to the resin dispenser and vacuum bag by this process. A resin dispenser placed on the peel ply to distribute the resin well. Finally, as shown in the Figure 1.b on both sides, after the spiral pipes were placed, they

are covered with a vacuum bag. After opening the vacuum and drawing the air inside, leak check done. If there is no leakage after the control, the mixture of epoxy and hardener is prepared so that the hardener/epoxy ratio is 1/3. In production process, pre-curing established at 50 °C for 30 minutes and then curing process applied at 80 °C for 8 hours. The specimens were cut at dimensions of 100x150mm. Firstly, impact tests were carried out by Ceast 9350 Fractovis Plus impact test machine at 30J, 40J and 50J impact energies for different thicknesses. After that, the CAI tests were applied to composite specimens.



Figure 1. (a) Preparing of S2 Glass Fibers, (b) Composite manufacturing system

### Results

In order to better comparison of the test results, results of 15 and 18-layer S2 glass/epoxy composites are shown separately. 15-layer S2 glass/epoxy composites thickness are 2.72mm and 18-layer S2 glass/epoxy composites thickness are 3,02mm. First CAI test results for 15- layer S2 / epoxy are given in Figure 2.

When the 15-layer S2 glass/epoxy composites are examined, it is first seen that the specimen with the highest resistance is 15-layer-0J without impact. Additionally, it is clearly seen that the lowest force is 15-layer-50J specimen. Maximum forces and CAI strength are given in Table 1.

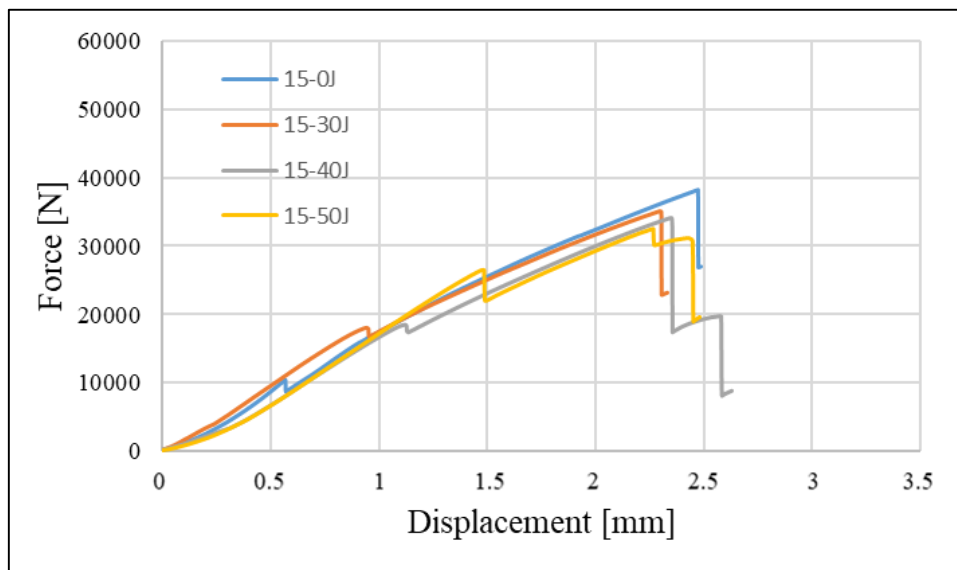


Figure 2. CAI test results of 15-Layer S2 glass / epoxy

Table 1. Maximum forces and CAI strengths of CAI tests for 15-layer S2 glass / epoxy composites

Specimen	Maximum force [N]	CAI strength [MPa]
15-0J	38225	139
15-30J	35024	127
15-40J	34177	124
15-50J	32604	118

Figures 3-6 show CAI damage 15-layer S2 glass / epoxy for impacted and unimpacted specimens.

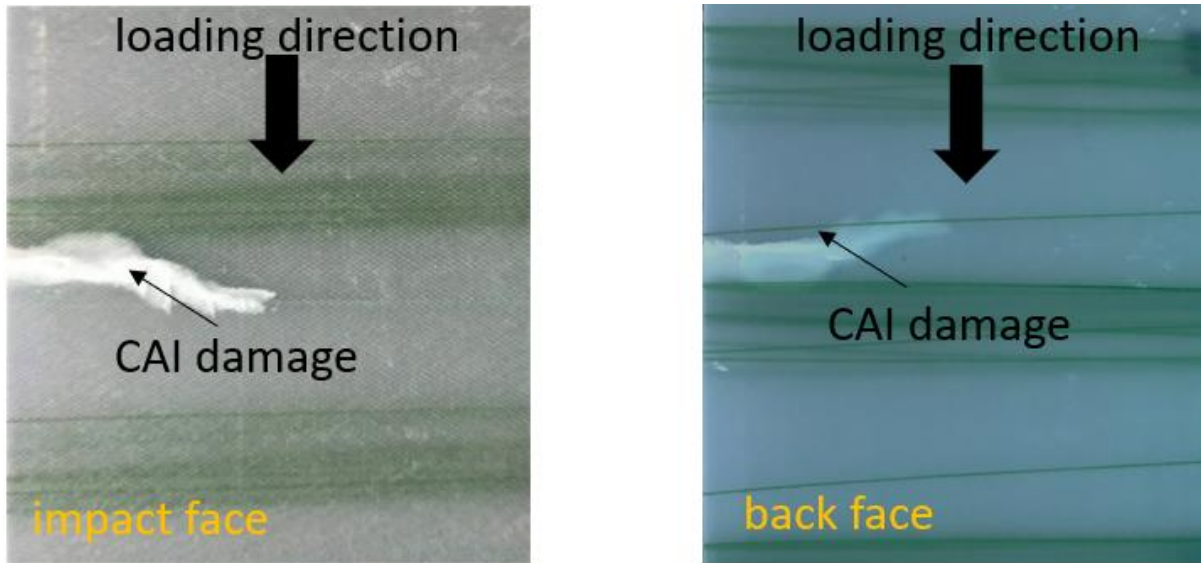


Figure 3. CAI damage of S2 glass / epoxy specimen for 15-0J (unimpacted)

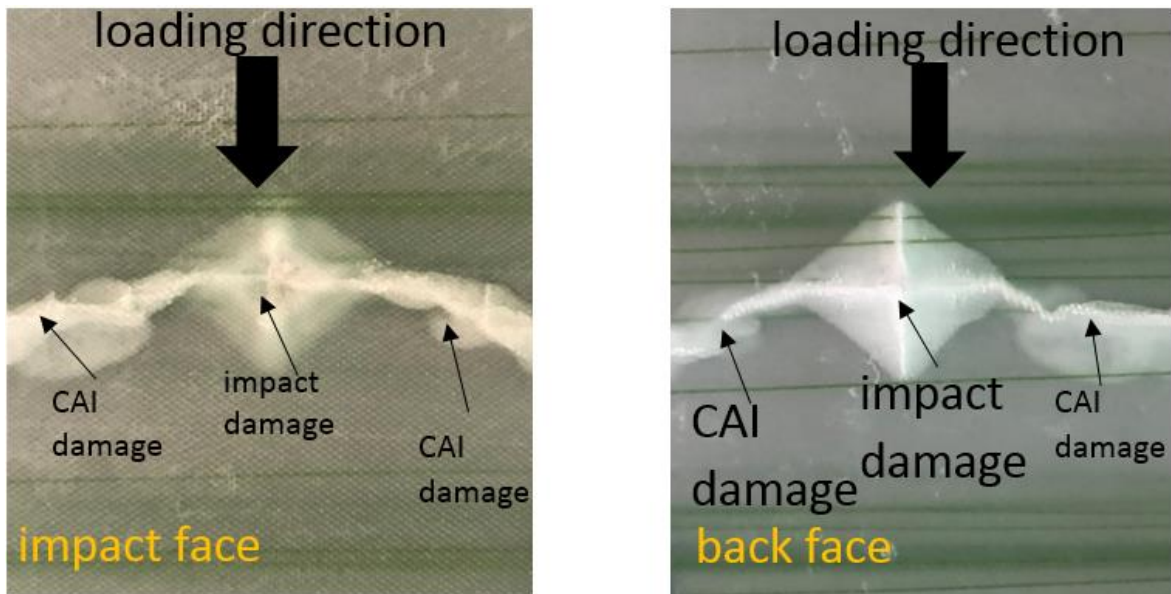


Figure 4. CAI damage of S2 glass / epoxy specimen for 15-30J



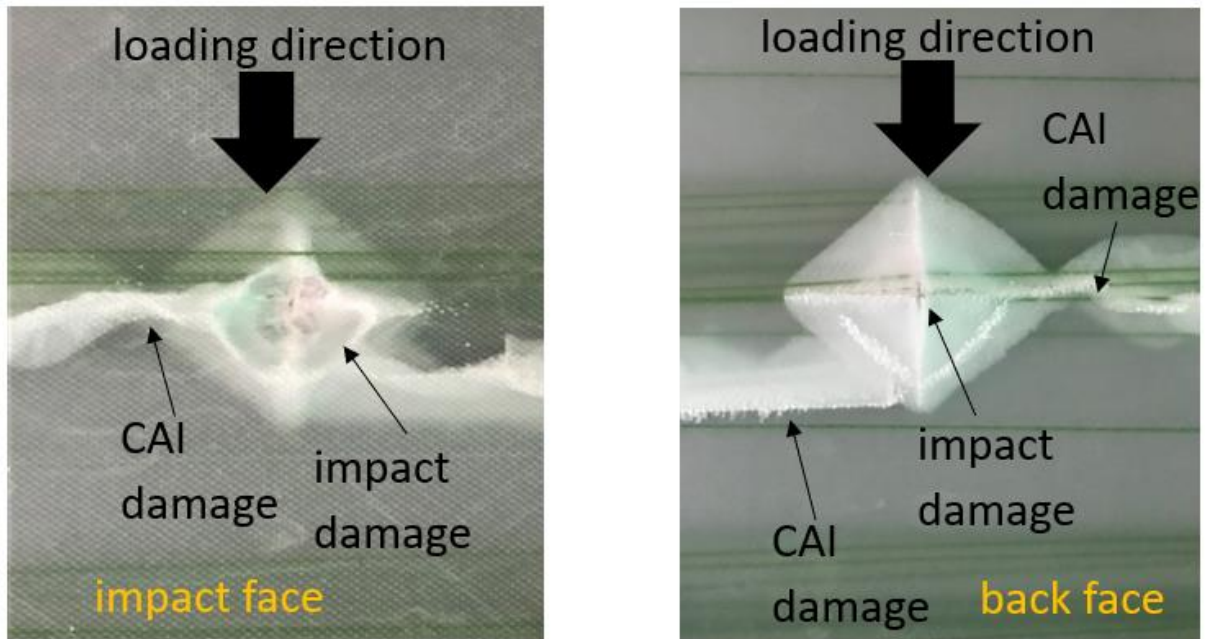


Figure 5. CAI damage of S2 glass / epoxy specimen for 15-40J

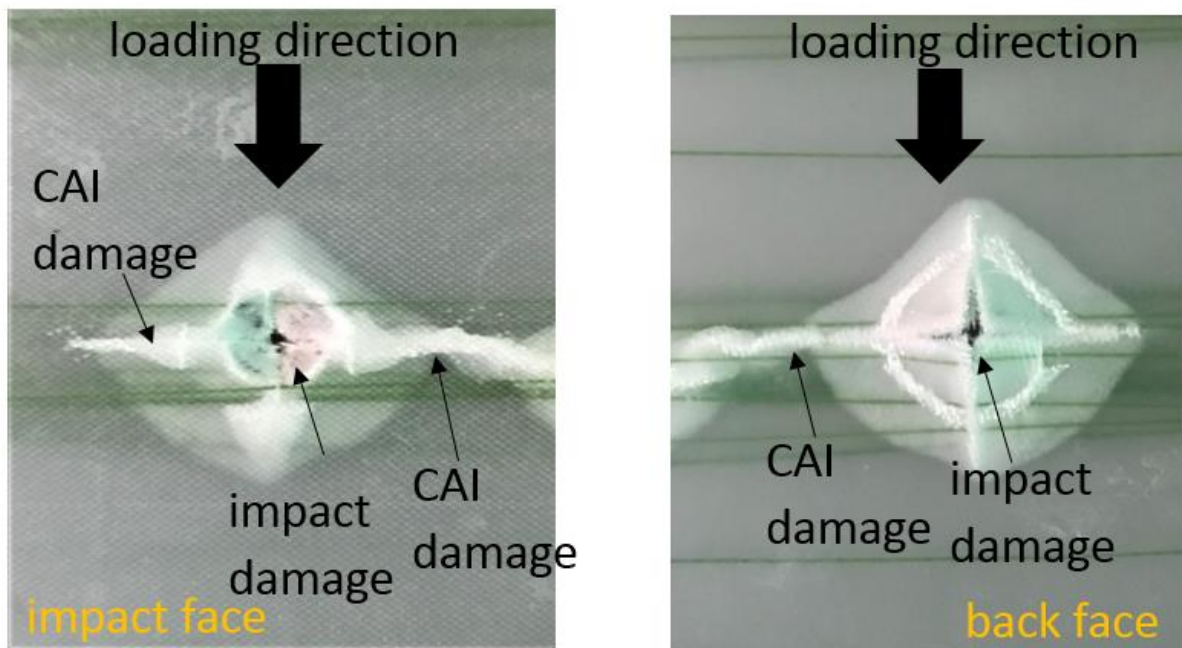


Figure 6. CAI damage of S2 glass / epoxy specimen for 15-50J

As can be seen from Figures 3-6, CAI damage occurred in the region where the impact damage occurred. From these figures, it can be said that stiffness of composite around the damaged area increases and therefore CAI damage starts from this region. As seen in the figures, even though there was no perforation in 15-layer S2 glass / epoxy for 30J and 40J impact energies, perforation occurs in 50J impact energy. Figure 7 shows the CAI test results for 18-layer S2 / glass epoxy composites.

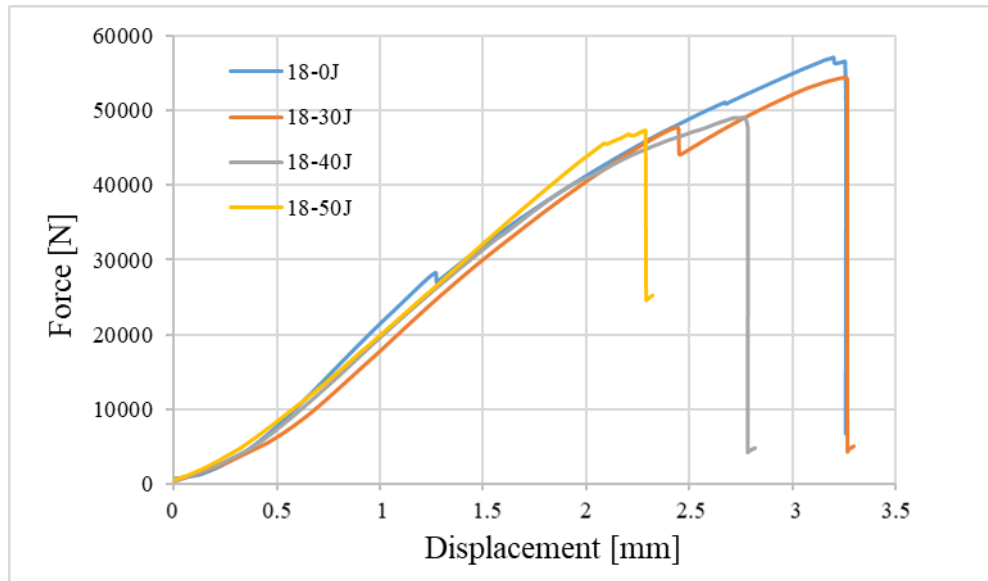


Figure 7. CAI test results of 18-layer S2 glass / epoxy

As can be seen from Figure 7, as the impact energy increases the maximum force of 18-layer S2 glass/epoxy decreases, just like 15-layer S2 glass/epoxy. The specimen with the highest strength resistance is the specimen that has not been exposed to 18-0J impact damage. The specimen with the lowest strength resistance is the specimen that has been exposed to 18-50J impact damage. The values of maximum forces and CAI strengths are seen in Table 2.

Table 2. Maximum forces and CAI strengths of CAI tests for 18-layer S2 glass / epoxy composites

Specimen	Maximum force [N]	CAI strength [MPa]
18-0J	57159	189
18-30J	54486	180
18-40J	49043	162
18-50J	47350	156

Figures 8-11 show CAI damage 18-layer S2 glass / epoxy for impacted and unimpacted specimens

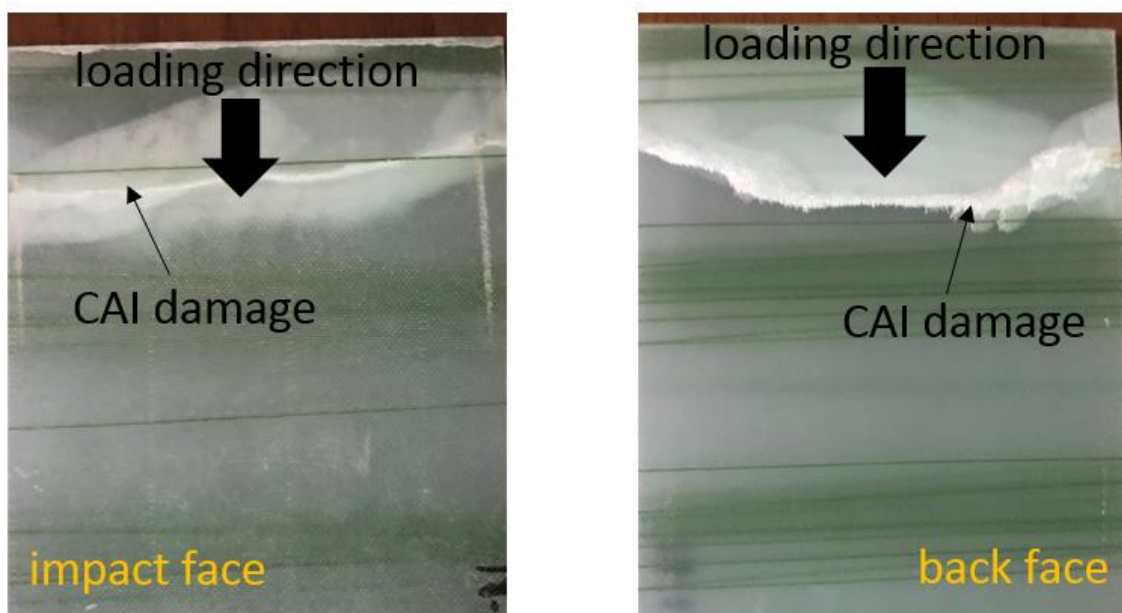


Figure 8. CAI damage of S2 glass / epoxy specimen for 18-0J (unimpacted)

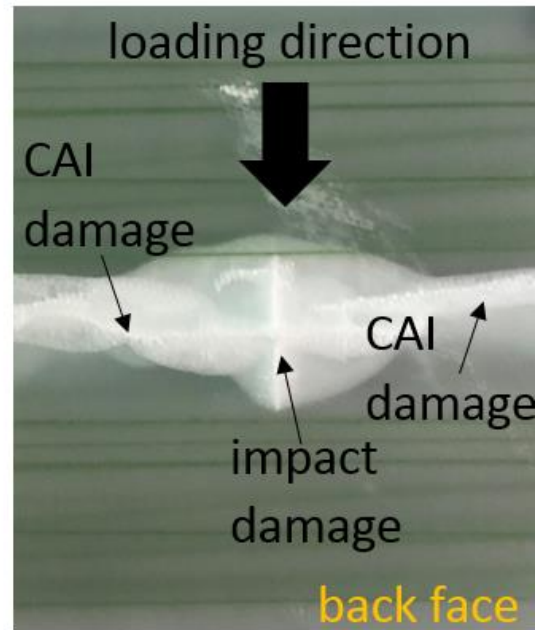
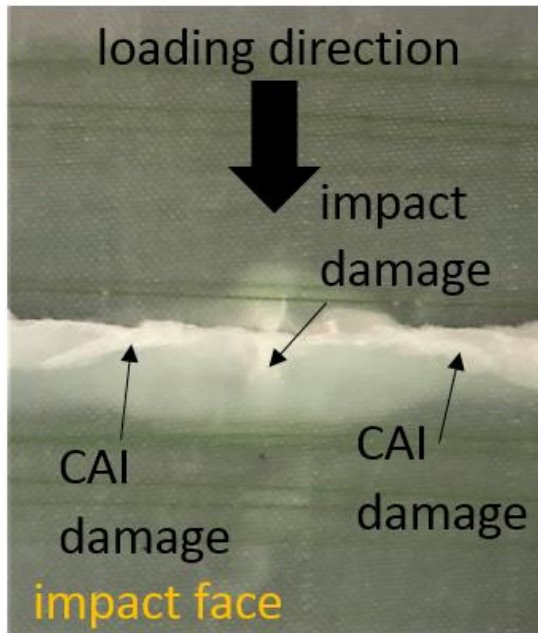


Figure 9. CAI damage of S2 glass / epoxy specimen for 18-30J

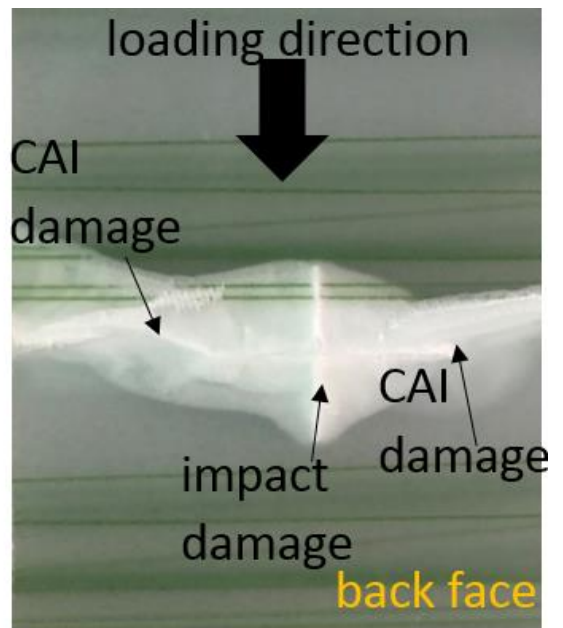
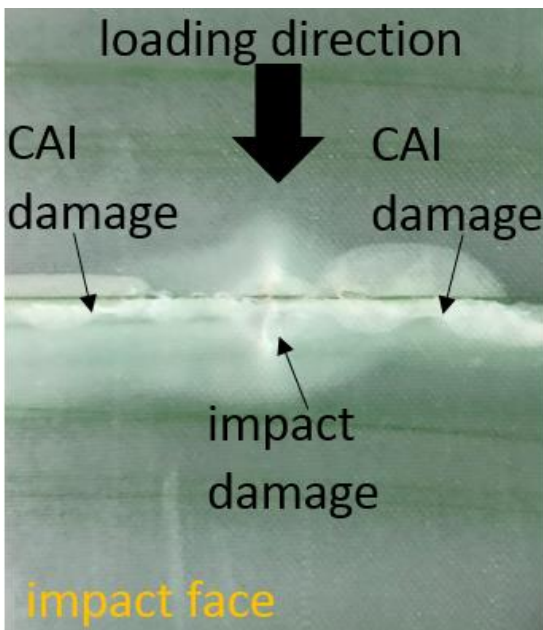


Figure 10. CAI damage of S2 glass / epoxy specimen for 18-40J

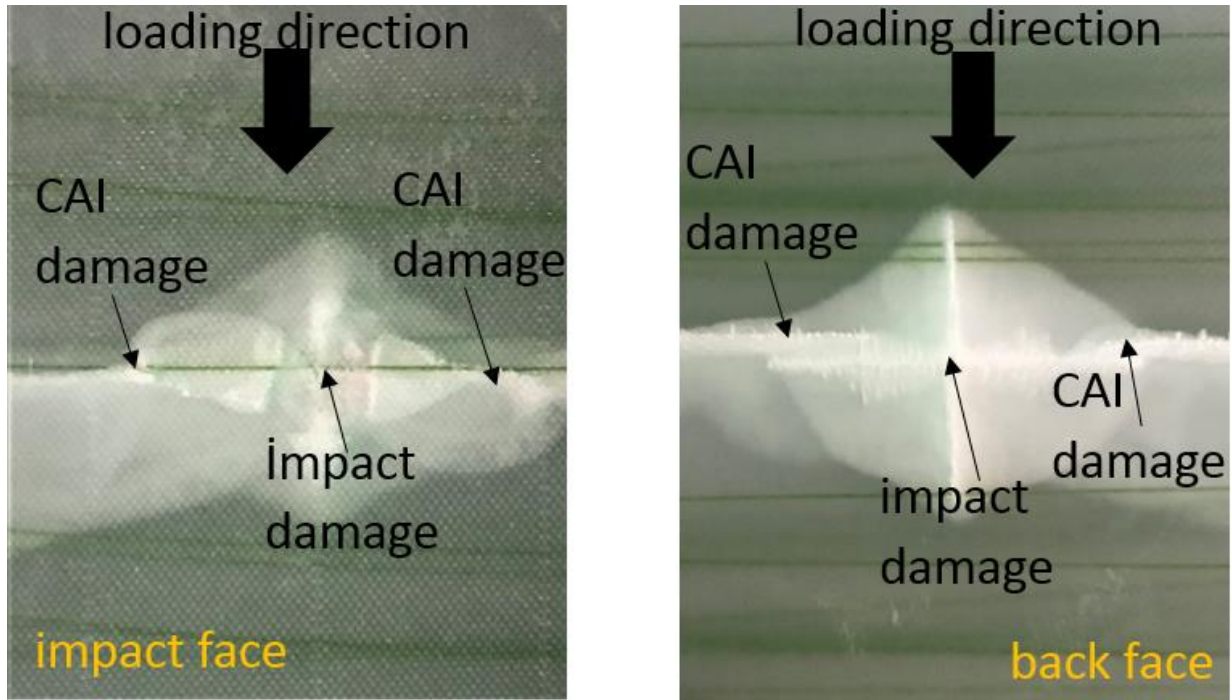


Figure 11. CAI damage of S2 glass / epoxy specimen for 18-50J

When visual inspection was conducted after CAI tests, wherever CAI damage occurred in 15-layer, CAI damage in 18-layer S2 glass / epoxy occurs in the region where impact damage occurred. From these figures, it can be seen that stiffness of composite around the damaged area increases and therefore CAI damage starts from this region. As seen in the figures, there was no perforation in 18-layer S2 glass / epoxy for 30J, 40J and 50J impact energies.

### Conclusion

In this study, the effects of impact energy and the thickness of composite on CAI strength were studied for S2 glass / epoxy composite. Firstly, 15-layer and 18-layer S2 glass / epoxy composites were subjected to 30J, 40J and 50J impact energies. Then, CAI test was applied on impacted and unimpacted specimens. From obtained results, the following conclusions were drawn:

1. 18-layer S2 glass / epoxy composite has more CAI strength than 15 layers.
2. The lowest CAI strength was revealed in the specimen with 50J impact energy applied for both 18-layer and 15-layer specimens.
3. The highest CAI strength was the 15 and 18-layer S2 glass / epoxy in unimpacted specimens. This was followed by specimens with 30J and 40J impact energies, respectively.
4. CAI damage occurred at the place where impact damage was applied. The reason for this can be said that stiffness of composite around the damaged area decreases and therefore CAI damage starts from this region.

### References

- [1] Zhang M, Matinlinna J. E-glass fiber reinforced composites in dental applications. *Silicon* 2012; 4: 73–8.
- [2] Qiting H, Sufyan G, Zhengmei L, Jingwei H, Wei Q, Fang L, Pekka KV, Lippo VJL. Properties of discontinuous S2-glass fiber-particulate-reinforced resin composites with two different fiber length distributions. *Journal of Prosthodontic Research* 2017; 61: 471-479.
- [3] Mehmet Aktas, Cesim Atas, Bulent Murat Icten, Ramazan Karakuzu. An experimental investigation of the impact response of composite laminates. *Composite Structures* 2019; 87: 307-313.
- [4] Ruixiang Bai, Jingjing Guoa, Zhenkun Leia Da Liua, Yu Maa, Cheng Yan. Compression after impact behavior of composite foam-core sandwich panels. *Composite Structures* 2019; 225: 111181

- [5] Tay, T. E., Shen, F. Analysis of delamination growth in laminated composites with consideration for residual thermal stress effects. *Journal of composite materials* 2002, 36.11: 1299-1320.
- [6] Hongliang Tuo, Zhixian Lu, Xiaoping Ma, Chao Zhang, Shuwen Chen. An experimental and numerical investigation on low-velocity impact damage and compression-after-impact behavior of composite laminates. *Composites Part B: Engineering* 2019; 167: 329-341.

## Cooling Analysis of a Horizontally Oriented Piezofan in Longitudinal Channel

Salim Ibrahim Hasan\*, Mosul University, Dept. of Mechanical Engineering, Mosul, Iraq  
Serhan Küçükka, Dokuz Eylül University, Dept. of Mechanical Engineering, İzmir, Turkey

\*Corresponding author: mediansalim@gmail.com

**Keywords:** Electronic cooling, heated surface, piezoelectric fan, cantilever motion, COMSOL analysis

**Discipline:** Mechanical Engineering

### Abstract

Most surveys and conclusions in the past have clearly shown that more than 55% of electronic devices failures are related to the inability to fully control high heat generated. Although many thermal management techniques have been applied, they are no longer able to work adequately with high performance, compact size and increased heat generated advanced electronic devices. Conventional cooling methods are increasingly inadequate in meeting the cooling requirements of these high-power electronic packages. The main aims of this investigation are to analyze the flow and heat transfer of a single piezofan oscillating transversally to longitudinal horizontal channel airflow, to show its applicable to achieve a successful thermal management in compact electronics components. The analysis was performed on a 2D-laminar flow model, by combining the cantilever motion analysis with fluid flow and heat transfer using COMSOL Multiphysics software. The model based on the finite element method (FEM) is determined using an Arbitrarily Lagrange-Euler scheme (ALE) in Fluid-Structure-Interaction (FSI) analysis. The cooling performance of piezofan is computed by evaluating the average forced convective heat transfer coefficient at the heated section of the channel surface with inlet flow velocity ( $u_{in}=0.1\text{m/s}$ , i.e.  $Re_m=1040$ ). The results of the simulation have shown the high performance of these fans compare without piezofan flow condition, and the best performance was obtained at which the moving tip of the fan at the middle of the heated surface ( $\Delta x_p=-20\text{mm}$ ). Compared with the laminar flow conditions without piezofan, the convection heat transfer coefficient is increased by (231%).

### List of symbols

#### Nomenclature

$A_c$  Cross section Area of piezofan ( $\text{m}^2$ ).  
 $C_p$  specific heat at constant pressure ( $\text{kJ/kg.K}$ ).  
 $D_h$  Hydraulic diameter of channel,  $D_h = \frac{4A}{P} = 2H = 16\text{ mm}$ .  
 $E$  Young's modulus (Pa).  
 $f_r$  First resonant frequency (Hz).  
 $G$  Relative vertical distance of piezofan to the heated surface (mm).  
 $H$  Channel height (cm).  
 $h$  Convective heat transfer coefficient ( $\text{W/m}^2.\text{K}$ ).  
 $I$  Second moment of area ( $\text{m}^4$ ), ( $I=w*th^3/12$ ).  
 $k_a$  Thermal conductivity of air ( $\text{W/m.K}$ ).  
 $L_c$  Length of channel (cm).  
 $L_f$  Distance between the channel entrance and the heated surface (cm).  
 $L_s$  Length of heated surface (cm).  
 $L_{pz}$  Length of piezofan (mm).  
 $\dot{m}$  Mass flow rate of air through channel (kg/s).  
 $m_{pz}$  Mass of piezofan (g).  
 $Nu$  Nusselt number.  
 $P$  pressure (Pa).  
 $q$  Heat transfer rate (W).  
 $q''$  Heat flux ( $\text{W/m}^2$ ).  
 $Re_m$  Reynolds number of mainstream channel flow,  
 $Re_m = \frac{\rho u_{in} D_h}{\mu}$ .  
 $T$  Temperature (K).

$u$  Velocity of air in x-direction (m/s).  
 $u_{pz}$  Velocity of piezofan (m/s).  
 $v$  Velocity of air in y-direction (m/s).  
 $w$  Piezofan width (mm).  
 $x,y$  Cartesian coordinates.  
 $x$  Position on the horizontally oriented piezofan.  
 $x_p$  Horizontal distance between piezofan tip and the heated surface leading edge (mm).  
 $Y_{pz}$  Piezofan displacement (mm).  
 $y_{pz}$  Piezofan amplitude (mm).

#### Subscripts

$a$  air.  
 $c$  channel.  
 $e$  enthalpy.  
 $f$  fluid.  
 $h$  hydraulic.  
 $in$  channel inlet .  
 $m$  mainstream flow.  
 $out$  channel outlet.  
 $pz$  piezofan.  
 $s$  heated surface.

#### Greek Symbols

$\Delta$  drop, change or difference .  
 $\beta$  frequency coefficient.  
 $\sigma$  Poisson's ratio.  
 $\mu$  viscosity ( $\text{kg/m.s}$ ).  
 $\rho$  density ( $\text{kg/m}^3$ ).

$t$  Time (s).  
 $th$  Piezofan thickness (mm).

$\psi$  dimensionless drive coefficient.

### Introduction

With the development of electronic units and packaging technologies, the conventional cooling processes and heat dissipation technologies can't meet the allowable temperature requirement. Therefore, in recent decades, the rapid development of modern electronic technology has attracted the attention of scientists and engineers to research, introduce and innovate new cooling techniques to meet the requirements and challenges of high heat generation in these continued miniaturization electronic parts. Air cooling is one of the simplest methods of thermal management that used most widely in a variety range of portable and large electronic systems, due to its availability and ease of use. In air cooling the heat is dissipated from hotspots via thermal management components by passive or active novels.

One of the smart materials that correspond to electronic intelligence world is the phenomenon of piezoelectricity. Piezoelectricity, derived from the Greek roots, means pressure and electricity, substances that produce an electric charge from dimensional changes, and vice versa, as shown in Figure 1 [1].

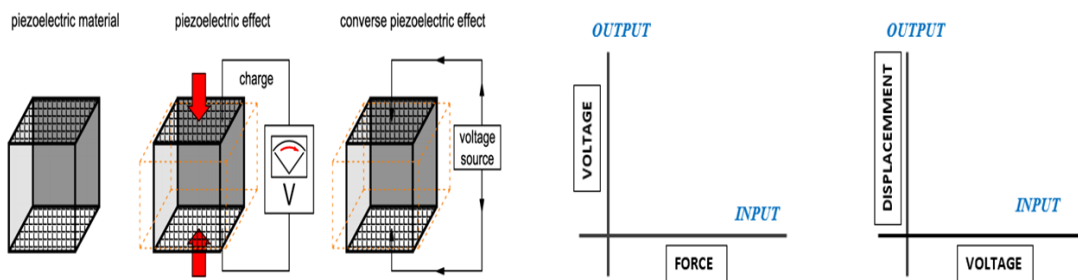


Figure 37 . Piezoelectric effect

Piezoelectric materials are either ceramic or polymeric electromechanical transducers, its' reversibility effect make it act as both sensors and actuators. Piezofans (also known as piezoelectric fans or piezoceramic fans) developed in the 1970's, and received some attention over the past few decades in cooling applications. Since the beginning of Toda's work ([2] and), it has been developed over 25 years in analytical and experimental work, and has issued many patents for its applications. Figure 2 shows the simple structure of piezoelectric fan with its' cantilever motion to generate airflow.

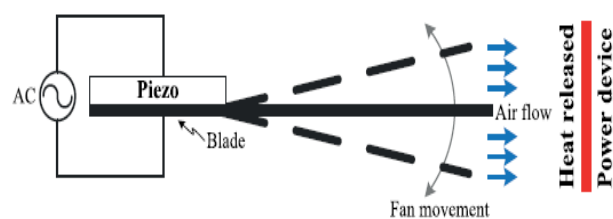


Figure 38. Piezoelectric fan [3]

Tseng et.al [4] explained the operation principle and characteristics of piezofans by inverse piezoelectric effect and their available applications in electronic cooling. Different techniques have been studied theoretically and experimentally to investigate the effects of piezofans on the thermal characteristics and performance of electronic components. Some studies have carried out experimental observations and numerical simulations on the air flow characteristics generated by a single piezofan. Others discussed the effects of the airflow generated by these fans on the heat transfer. Another group of researches focused on how to move air with low noise, lower power consumption without using large size conventional fans. Recent works consider the effects of multi and/or embedded piezofans on thermal characteristics and new designs of heat sinks performance. Most of these studies investigate the influences of the geometry, orientation and oscillation parameters on thermo-fluid properties and

cooling performance. They have reached distinctive conclusions that have already entered in many electronics applications as a major or complementary component of the cooling process.

The works that deal with flow in a channel have been conducted to analyze the characteristics of fluid flow and/or to investigate the methods of the convective heat transfer from heated surfaces. In general, the heat transfer from the internal surfaces of the longitudinal channels increases with increasing the flow rate. However, a turbulence increase occurred at a certain region increases also heat transfer [5]. But what if the turbulence increase occurred at a certain point in the flow field? This introduces a largely unexplored subject area that uses piezofans to induce a turbulence at specific point [5]. The importance of these type of analyses and its summaries will be useful to achieve a successful and advanced thermal management for meeting a variety of cooling needs in compact portable and small-scale electronic devices, as well as in larger scale thermal systems and power electronics components. Florio and Harnoy (2007) [6], introduced a 2D model to investigate the transverse oscillation of piezofan in a vertical channel. They obtained up to 52% increase in the local heat transfer coefficient relative to standard natural convection. Jeng and Liu (2015) [7] conducted experiments to discuss the influence of transverse and axial piezofan oscillation to channel airflow to enhance the heat transfer of different constructions heat sinks. They concluded that the square pin–fin heat sink achieved the best heat transfer enhancement, and the transverse oscillation promoted slightly more enhancement than the axial oscillation. Li et al. (2017) [8] proved that in the presence of cross-flow with piezofan oscillation, the convective heat transfer coefficient increased by 56% compared with pure piezofan oscillation condition. This enhancement is reduced to 46.4% with increasing the cross-flow velocity from 0.94 to 1.56 m/s. They also confirmed an improvement in heat transfer when the oscillating piezofan tip to the heated surface gap is small (i.e.3mm).

As there are very few researches that has reported piezofan oscillations transverse to channel airflow, there is an important developmental aspect that is still quite incomplete in this topic and the possibility of developing their distinctive applications. Accordingly, the main objective of our current study is to propose an effective Multiphysics method by COMSOL software to analyze the cooling effects (convective heat transfer) of the air flow generated by oscillations of a single piezofan transverse to channel airflow, to show its capability to improve the heat dissipation from a flat heated surface compare with the flow inside the channels without this fan.

### Definition of the Problem

For addressing issue of this study, a horizontal 2D channel model has been set up, which is heated by constant heat flux from below at a specific part, and a cantilever fan placed above it. Then combining the cantilever motion analysis with fluid flow and heat transfer in fluid-structure analysis and non-isothermal flow Multiphysics. This simulation was done using a moving mesh scheme by defining the function of motion using variable displacement in a time-dependent study. In the results, the horizontal position of piezofan to the heated surface leading edge ( $\Delta x_p$ ) have been investigated. The average means convective heat transfer coefficient ( $\bar{h}$ ) and Nusselt number ( $\overline{Nu}$ ) on the heated surface are analyzed with details, and a prominent enhancement of heat transfer was shown.

In this problem, a heater with a length of  $L_s$  is placed at the bottom wall of a channel and is exposed to the forced convection. Figure 3 shows the model with its coordinates and the boundary conditions. The distance between the channel entrance and the leading edge of the heater is  $L_f$ . A constant heat flux of  $q''=1000 \text{ W/m}^2$  is applied to the heater. A piezofan is horizontally placed above the heated surface to enhance the heat transfer between the heater and the flowing fluid. The spacing between the piezofan and the heater  $G = 10 \text{ mm}$ .

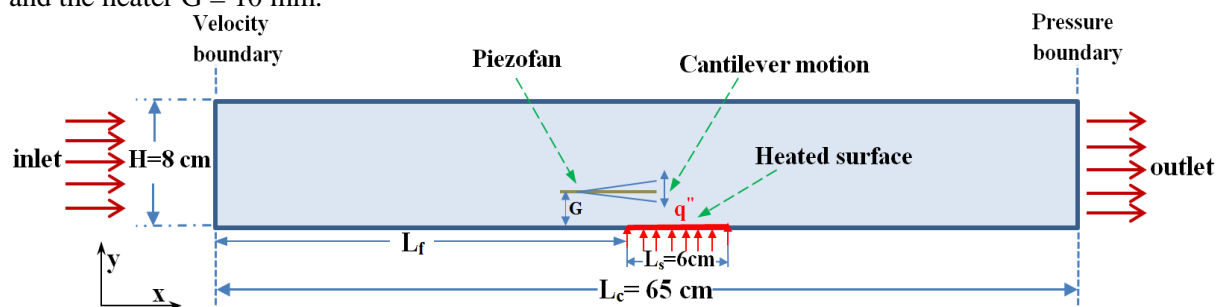


Figure 3. The 2D channel model with horizontally oriented piezofan.



The piezofan has a structure of a uniform cantilever beam, which is fixed on one end, and the other end is allowed to move freely. It is oriented horizontally above the surface to be cooled, as illustrated in Figure 4. The tip of the piezofan is placed with a distance of  $\Delta x_p$  from the heated surface.

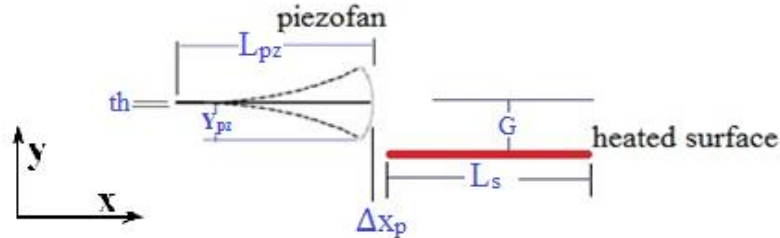


Figure 4. Piezofan dimensions and the alignment with the heated surface.

The piezofan specifications summarized in Table 1, have been selected according to the literature review data [5] and experimental data in ref. [9].

Table 1. Piezofan specifications [5,9]

SPECIFICATION	VALUE
Material	Stainless Steel
Size (mm)	60( $L_{pz}$ ) x 0.12(th) x 12.5(w)
Density $\rho_{pz}$ (kg/m <sup>3</sup> )	7850
Young's modulus $E_{pz}$ (Pa)	$2 \cdot 10^{11}$
Mass of piezofan $m_{pz}$ (g)	0.706
Poisson's ratio ( $\sigma$ )	0.28

The solution of stable and uniform free beam oscillations can be found in many textbooks of mechanics and some piezofan reviews [5,10,11,12]. The piezofan oscillation frequency and amplitude are governed by its geometrical and material properties in Table 1. It has been investigated in several previous studies [13,14]. As a widely followed method, the oscillation frequency is defined as the first mode of the resonant frequency of the blade. Accordingly, the resonant frequency is  $f_r = 20$  Hz. Eq. (1) represents the equation of motion as a function of position ( $x$ ) along the piezofan length ( $L_{pz}$ ).

$$Y_{pz}(x) = \psi \cdot A_c \cdot [(\sin(\beta \cdot L_{pz}) - \sinh(\beta \cdot L_{pz})) \cdot (\sin(\beta \cdot x) - \sinh(\beta \cdot x)) + (\cos(\beta \cdot L_{pz}) - \cosh(\beta \cdot L_{pz})) \cdot (\cos(\beta \cdot x) - \cosh(\beta \cdot x))] \quad (1)$$

where  $A_c$  is the cross-section area of piezofan beam, and  $\beta$  is the frequency coefficient and defined as

$$\beta = \sqrt[4]{\frac{2\pi \cdot f_r \cdot m_{pz}}{L_{pz} \cdot I \cdot E_{pz}}} \quad (2)$$

Although the general equation that describing the cantilever motion of piezofan (Eq. 1 and 3) depends on different operational and geometric factors, the displacement ( $Y_{pz}$ ) and frequency ( $f_r$ ) represent the main factors affecting the motion. Many previous experiments and theoretical works have demonstrated the relationship between the drive input power (applied voltage) and piezofan tip amplitude; for example, Tseng et al. [4] proved the direct relationship between them. Therefore, it is possible to adjust the amplitude without affecting the other characteristics, which is theoretically defined by dimensionless drive coefficient  $\psi$  [5].

$$y_{pz}(x, t) = \psi \cdot Y_{pz}(x) \cdot \sin(2\pi \cdot f_r \cdot t) \quad (3)$$

## Mathematical model and meshing

### Setting of initial and boundary conditions

Through our follow-up of different numerical and simulation models in the literature, we have found several flow and related numerical assumptions that must consider setting up the piezofan models. Using the assumptions of the boundary and initial conditions as inputs, which specified as follows; inlet conditions defined as inlet velocity to satisfy incompressible laminar flow conditions ( $Re_m < 2300$ ), while the outlet defined as pressure boundary. Both top and bottom boundaries are considered as insulated walls no-slip condition except the heated surface location. The ambient air temperature is set to (293.15K), and uniform heat flux of ( $q''=1000 \text{ W/m}^2$ ) has been applied on the heated surface. To satisfy other general solution, -buoyancy and radiative effects are neglected. All these assumptions are conducted in the time-dependent study to combine airflow and heat transfer with solid mechanics using a moving boundary option to calculate the deformation in the fluid domain due to the induced forces from the cantilever motion of piezofan simultaneously. Moving boundary conditions have been created as an automatic remeshing option by using the ALE (*Arbitrary Lagrangian-Eulerian*) method to reduce the computational time required for large-displacement in fluid-structure interactions analysis (FSI).

So the summary of the initial and boundary conditions defined as:

$$x=0 : u=u_{in}, v=0, T=T_{in} \text{ (Normal uniform inflow condition).}$$

$$x=L_c : \frac{\partial u}{\partial x} = 0, v=0 \text{ (Normal flow without suppressing backflow condition).}$$

$$y=0 \text{ and at } y=H : u = v = 0 \text{ ( Non-slip conditions on the channel walls).}$$

### Governing Equations

The specified fluid flow physic in COMSOL includes the general Navier-Stokes governing Eqs. 4 to 7;

$$\text{Continuity: } \frac{\partial \rho}{\partial t} + \rho \frac{\partial}{\partial x}(u) + \rho \frac{\partial}{\partial y}(v) = 0 \quad (4)$$

$$\text{Momentum: } \rho \frac{\partial}{\partial t}(u) + \rho u \frac{\partial}{\partial x}(u) + \rho v \frac{\partial}{\partial y}(u) = -\frac{\partial P}{\partial x} + \mu \left( \frac{\partial^2 u}{\partial x^2} + \frac{\partial^2 u}{\partial y^2} \right) \quad (5)$$

$$\rho \frac{\partial}{\partial t}(v) + \rho u \frac{\partial}{\partial x}(v) + \rho v \frac{\partial}{\partial y}(v) = -\frac{\partial P}{\partial y} + \mu \left( \frac{\partial^2 v}{\partial x^2} + \frac{\partial^2 v}{\partial y^2} \right) \quad (6)$$

$$\text{Energy: } \rho c_p \frac{\partial T}{\partial t} + \rho c_p u \frac{\partial T}{\partial x} + \rho c_p v \frac{\partial T}{\partial y} = k \left( \frac{\partial^2 T}{\partial x^2} \right) + k \left( \frac{\partial^2 T}{\partial y^2} \right) \quad (7)$$

where  $\rho$  is the fluid density,  $P$  is the pressure in the fluid,  $C_p$  specific heat of air at constant pressure and  $k$  is thermal conductivity. The average convective heat transfer coefficient ( $\bar{h}$ ) and average Nusselt number ( $\overline{Nu}$ ), defined as follows:

$$\bar{h} = \frac{q''}{(\bar{T}_s - T_a)} \quad (8)$$

$$\overline{Nu} = \frac{\bar{h} \cdot L_s}{k_a} \quad (9)$$

$k_a$  (thermal conductivity of air) is calculated at film air temperature ( $T_f$ );

$$T_f = \frac{\bar{T}_s + T_a}{2} \quad (10)$$

### Multiphysics and meshing set up

As it is mentioned in the previous sub-section, to solve the oscillation of the beam, it is needed to combine solid mechanics, fluid mechanics, and heat transfer equations. The combined fluid flow physics with solid mechanics physic using FSI (Fluid-Structure Interaction) configuration, and combining the laminar flow physic with heat transfer physic using Non-isothermal flow configuration and combining all above physics in the time-dependent study with (9829 elements mesh as shown in Figure 5) using automatic re-meshing solver, and the time step per piezofan oscillation cycle was 100 time steps (i.e.  $\Delta t = 1 / (20 * 100) = 0.0005s$ ) step-size iteration to avoid failures or errors during computation, Which regenerate all mesh with each time step to reach a suitable mesh with changing the piezofan motion

within domain geometry changes . Finally, the model took about 32 hours to get the first results in Intel (R) core i7-6700HQ CPU @ 2.60GHz (8 CPUs), ~2.6GHz 16GB RAM PC laptop.

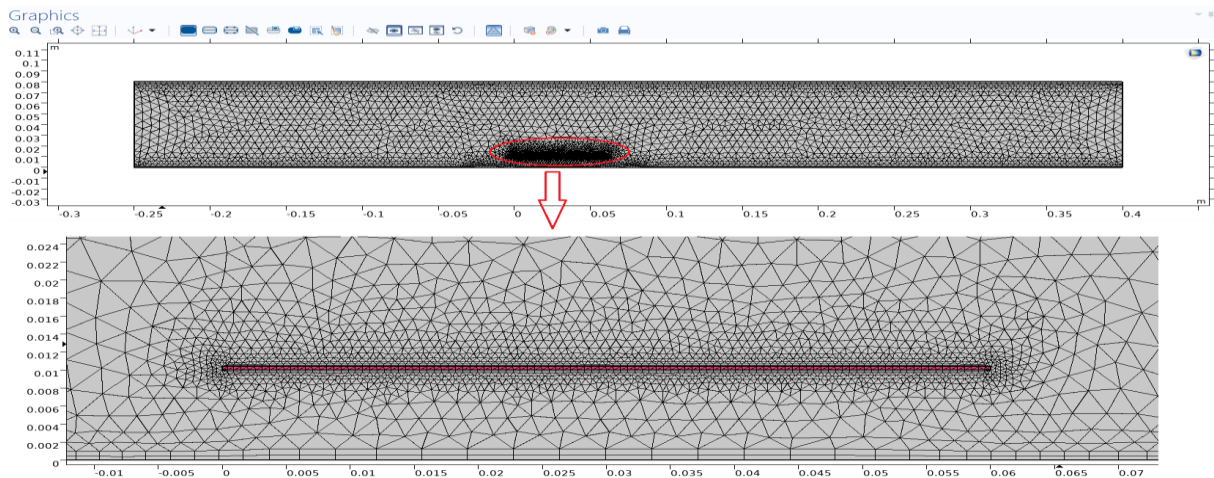


Figure 5. The used mesh grid in simulation model.

### Results and Discussion

In order to verify the results obtained from this simulation, we applied the same characteristics, boundary and initial conditions that were used by Acikalin & Garimella (2009) [15,16] study. As shown in Figure 6 for temperature and convective heat transfer coefficient at a specific point on the heated surface, the comparison error bars show a good agreement with maximum deviation not exceed 1.6 %.

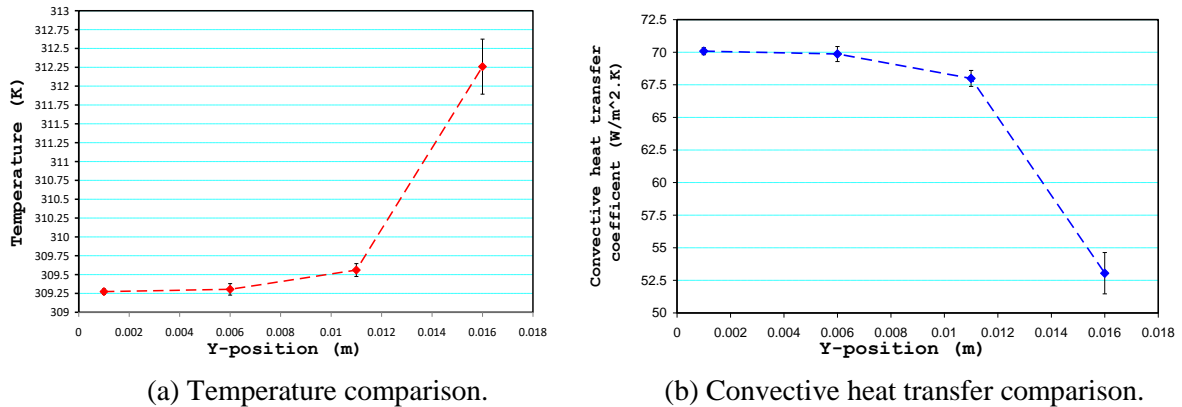


Figure 6. Comparison of temperature and heat transfer coefficient predicted on the heated surface with Acikalin & Garimella (2009) [11].

The variation of temperature with time during the operation of piezofan is showed in Figure 7 the temperature reached to steady state at (1.5s), so the period of simulation is selected according to this as minimum computation time.

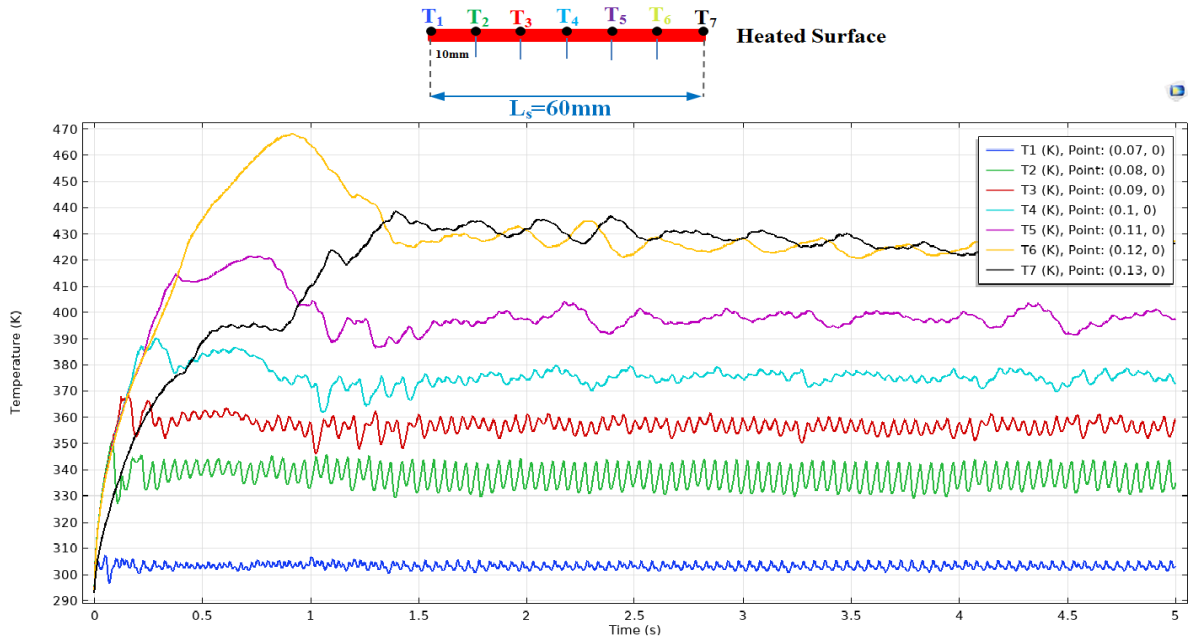


Figure 7. Variation of Temperature over time for different point on the heated surface.

Then the average convective heat transfer coefficient ( $\bar{h}$ ) on heated surface for these different position cases is plotted in (Figure 9), which show the maximum value (i.e. the optimal heated surface position ( $\Delta x_p = -20$  mm)).

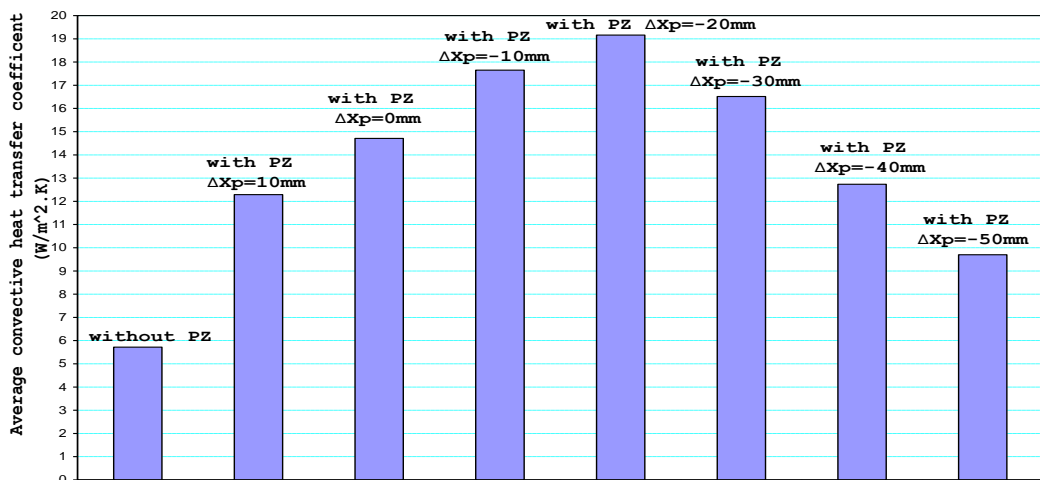


Figure 9. The average convective heat transfer coefficient for different positions of heated surface to the piezofan tip at (5 s) of operation.

### Conclusions

In this study, using of piezofans to increase heat dissipation from hot spot flat surfaces inside longitudinal channels was investigated, to prove the ability of these smart piezoelectric materials to cool small compact electronic devices and replace high-noise, high-power consumption and large-size conventional fans. The thermal analysis results show that, these fans have a good performance compared to the natural flow under the same conditions. There are various factors that can improve the performance of these fans, but the horizontal positions to the heated surface are the most influential factors. The piezofan positions ( $x_p = -20$  mm) were selected as optimal positions, which showed high average convective heat transfer coefficient ( $\bar{h}$ ) and average Nusselt number ( $\overline{Nu}$ ). The research will continue to analyze another structure inside the channel, for example: adding baffles beside the heated

surface and changing the piezofan orientations to get the best turbulence, or embedding the piezofan between a finned heated surface.

### References

- [1] Piezoelectric Fans and Their Application In Electronics Cooling, Qpedia Thermal Magazine 411\_V3\_lorez. Aprile 211 Vol.3.
- [2] M. Toda, "Voltage-induced Large Amplitude Bending Device PVF2 Bimorph – Its Properties and Applications," *Ferroelectrics*, vol. 32, pp. 127-133, 1981.
- [3] Tseng, K. H., Mochizuki, M., Mashiko, K., Kosakabe, T., Takenaka, E., Yamamoto, K., & Kikutake, R. (2010). Piezo fan for thermal management of electronics. In Proc. 2nd Int. Forum Heat Transfer (pp. 1-4).
- [4] Tseng, K. H., Mochizuki, M., Mashiko, K., Kosakabe, T., Takenaka, E., Yamamoto, K., & Kikutake, R. (2010). Piezo fan for thermal management of electronics. In Proc. 2nd Int. Forum Heat Transfer (pp. 1-4).
- [5] Hales, A., & Jiang, X. (2018). A review of piezoelectric fans for low energy cooling of power electronics. *Applied Energy*, 215, 321-337.
- [6] Florio, L. A., & Harnoy, A. (2007). Use of a vibrating plate to enhance natural convection cooling of a discrete heat source in a vertical channel. *Applied thermal engineering*, 27(13), 2276-2293.
- [7] Jeng, T. M., & Liu, C. H. (2015). Moving-orientation and position effects of the piezoelectric fan on thermal characteristics of the heat sink partially filled in a channel with axial flow. *International Journal of Heat and Mass Transfer*, 85, 950-964.
- [8] Li, X. J., Zhang, J. Z., & Tan, X. M. (2017). Convective heat transfer on a flat surface induced by a vertically-oriented piezoelectric fan in the presence of cross flow. *Heat and Mass Transfer*, 53(9), 2745-2768.
- [9] Acikalin, T., Wait, S. M., Garimella, S. V., & Raman, A. (2004). Experimental investigation of the thermal performance of piezoelectric fans. *Heat Transfer Engineering*, 25(1), 4-14.
- [10] Maaspuro, M. (2016). Piezoelectric oscillating cantilever fan for thermal management of electronics and LEDs—A review. *Microelectronics Reliability*, 63, 342-353.
- [11] Gere, J. M. (1984). Timoshenko SP. Mechanics of Materials. *Brooks Cole, Monterey, CA.*
- [12] Meirovitch, L. (1967). Analytical methods in vibrations.
- [13] Kimber, M., & Garimella, S. V. (2009). Measurement and prediction of the cooling characteristics of a generalized vibrating piezoelectric fan. *International Journal of Heat and Mass Transfer*, 52(19-20), 4470-4478.
- [14] Lin, C. N., Jang, J. Y., & Leu, J. S. (2016). A study of an effective heat-dissipating piezoelectric fan for high heat density devices. *Energies*, 9(8), 610.
- [15] Acikalin, T. (2007). *Thermal and fluidic characterization of piezoelectric fans* (Doctoral dissertation, Purdue University).
- [16] Acikalin, T., & Garimella, S. V. (2009). Analysis and prediction of the thermal performance of piezoelectrically actuated fans. *Heat transfer engineering*, 30(6), 487-498.

## Effects of Crosshead Speed and Penetrator Shape on the Punch Shear Behaviors of Sandwich Composites

Rifat Sarioğlu \*, Dokuz Eylül University, Graduate School of Natural and Applied Sciences, İzmir, Turkey

Ramazan Karakuzu, Dokuz Eylül University, Department of Mechanical Engineering, İzmir, Turkey

Halis Kandaş, Dokuz Eylül University, Graduate School of Natural and Applied Sciences, İzmir, Turkey

\*Corresponding author: sarioglugurifat@gmail.com

**Keywords:** Sandwich composite, S2 glass fabric, PVC core, punch shear test

**Discipline:** Mechanical Engineering

### Abstract

Sandwich composites are widely used in aerospace industry due to their high strength. Face sheets should be designed to be resistant against compression and tensile stresses and the core should be resistant to shear and compression stresses. In this study, sandwich composite was produced by vacuum assisted resin infusion method (VARIM). In the manufacturing, PVC core material with thickness of 10 mm and S2 glass fabric with areal density of 190 g/m<sup>2</sup> were used. For each face sheet material, S2 glass fabrics of four layers were used. Samples were cut in the dimensions of 100 mmx100 mm. Then quasi-static punch shear test was applied to sandwich composite by using the Universal Shimadzu Test machine with both penetrators of flat and hemispherical noses and punch shear test fixture. Tests are conducted at five various crosshead speeds and three repeats for each tests. Flat nose and hemispherical nose penetrators with a cylindrical punch diameter of 12.70 mm were mounted to the test machines. After the experiments, force-deflection diagrams were drawn and results were compared with each other.

### Introduction

Sandwich structures are increasing in the aviation, defense and aerospace industries as technology is developing day by day. The purpose of use of these materials is that they are light in weight compared to other materials found in nature and have high resistance against external loads. However, composite sandwich structures are susceptible to damage and failure due to transverse contact and to impact by foreign object [1]. Composite materials are subjected to various dynamic and static loads over their lifetime. The composite plays the crucial role of absorbing energy due to various interlaminar and intralaminar damage mechanisms such as delamination, fiber breakage and matrix cracking [2]. This is why the development and strength of face sheets have recently gained importance.

Many researchers carry out various tests on the energy absorption and strength of composite structures. These tests are the low speed impact test, the high-speed impact test, and the quasi static test, respectively. In particular, the quasi static test is one of the appropriate tests used to determine the material's crushing strength and punch shear strength. When subjected to low- or high velocity impact, the composites behavior becomes very complicated due to phenomena such as fibers breakage, delamination, dishing deformation, plugging failure [3]. Study of materials behavior and failure analysis of quasi-static penetration indicates that failures and damages depend on several parameters such as the fibers and matrix mechanical properties, bonding strength, shape and dimensions of indenter, span ratio, and loading velocity. The indenter shape determines the type and amount of its contact with the target. In addition, the composite reaction against the indenter is dependent on the strain rate or loading velocity [4]. Indenter nose shape has great influence on the indentation and impact resistance of sandwich panels. [5] In this study, the amount of energy absorption of the material was investigated by the quasi-static punch shear test at five various crosshead speeds and with two different penetrators.

### Experimental Procedure

The experiments were performed on the sandwich composites. Sandwich composite was produced by vacuum assisted resin infusion method (VARIM) (Figure 1). In the manufacturing, PVC core material with thickness of 10 mm and S2 glass fabric with areal density of 190 g/m<sup>2</sup> were used. For each face sheet material, S2 glass fabrics of four layers were used. Samples were cut in the dimensions of 100 mm x100 mm (Figure 2). Then quasi-static punch shear test was applied to sandwich composite by using the Universal Shimadzu Test machine with both penetrators of flat and hemispherical noses and punch

shear test fixture (Figure 3). Tests are conducted at five various crosshead speeds and three repeats for each test. Various speeds 1mm/min, 5mm/min, 15mm/min, 25mm/min and 50mm/min of crosshead were chosen for quasi-static tests. Flat nose and hemispherical nose penetrators with a cylindrical punch diameter of 12.70 mm were mounted to the test machines. After the experiments, force-deflection diagrams were drawn and results were compared with each other.



Figure 1. Production of sandwich composite by vacuum assisted resin infusion method



Figure 2. Sandwich composite specimen

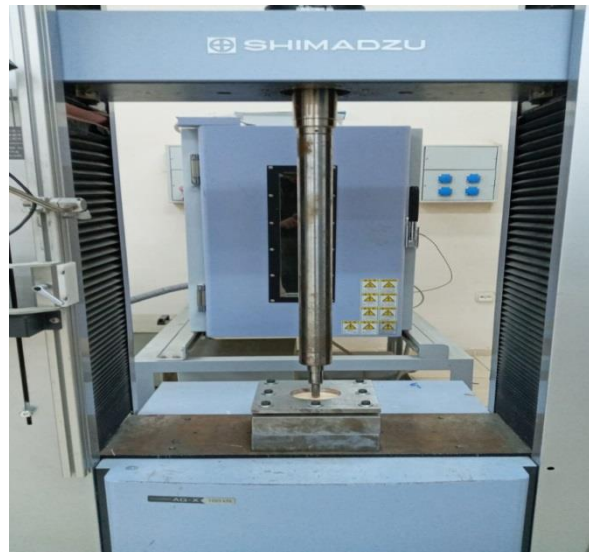


Figure 3. Test machine with punch-shear test apparatus

### Results

In Figure 4, Force- Displacement diagrams of S2 glass /PVC sandwich composite in quasi-static test at various speeds for hemispherical nose shown. It was observed at diagrams that the hemispherical nose perforated the sandwich composite specimens. In Table 1, peak force values of S2 glass /PVC sandwich composite in quasi-static test for various speeds given. The maximum contact force for the hemispherical nose was found 2082 N.

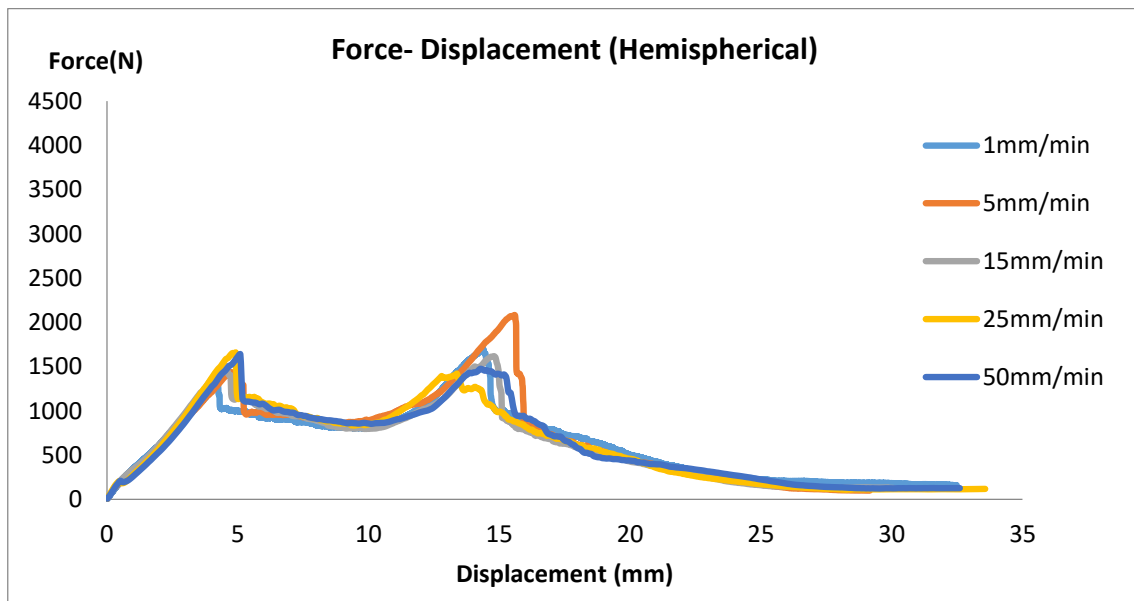


Figure 4. Force- Displacement diagram of S2 glass /PVC sandwich composite in quasi-static tests for hemispherical nose

Table 1. Peak force values of S2 glass/PVC sandwich composite in quasi-static tests for hemispherical nose

	1 mm/min	5 mm/min	15 mm/min	25 mm/min	50 mm/min
1 <sup>st</sup> Peak (N)	1305	1438	1508	1658	1638
2 <sup>nd</sup> Peak (N)	1697	2082	1417	1419	1473



When the sandwich composite is loaded with the hemispherical nose, the shear stress is softer in the first sandwich. The foam crushing with the contact force acting on the sandwich after the first sandwich was crushed smoothly as seen in the graph. When the hemispherical nose passed through the foam and reached the second sandwich layer, it reached the maximum shear force and properly punched the material.

The damage geometry of the perforated with the hemispherical nose was determined more uniformly (Figure 5).

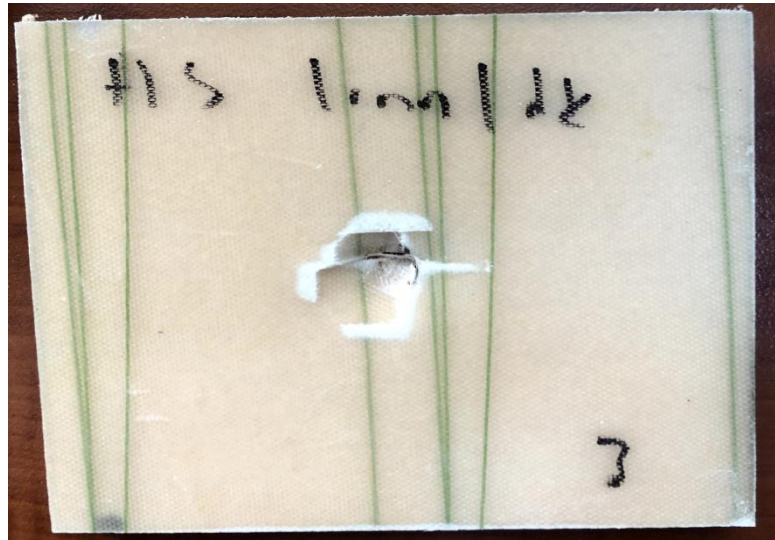


Figure 5. Specimen of hemispherical nose after loading

In Figure 6, Force- Displacement diagrams of S2 glass /PVC sandwich composite in quasi-static test at various speeds for flat nose given. In Table 2, peak force values of S2 glass /PVC sandwich composite in quasi-static test for various speeds given. The maximum contact force for the hemispherical nose has found 3848 N. In flat nose experiments, a sharper rise in shear stress was observe in the first sandwich. After the first sandwich has damaged, fluctuations appear in the contact force of the flat nose to the foam. This is due to the improper contact of the foam nose .Then the contact force in the second sandwich was quite high and the sudden rise and fall here was observed to be higher than the contact force applied to the first sandwich.

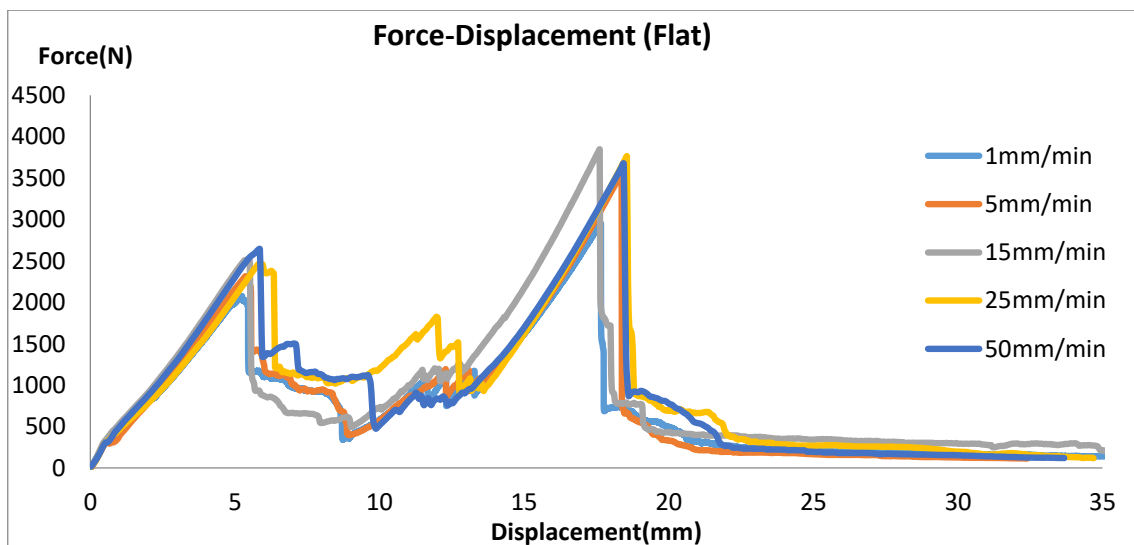


Figure 6. Force- Displacement diagram of S2 glass /PVC sandwich composite in quasi-static test for flat nose

Table 2. Peak force values of S2 glass/PVC sandwich composite in quasi-static tests for flat nose

	1 mm/min	5 mm/min	15 mm/min	25 mm/min	50 mm/min
1 <sup>st</sup> Peak (N)	2075	2314	2520	2464	2641
2 <sup>nd</sup> Peak (N)	2954	3553	3848	3762	3674

The appearance of damage in samples pierced with a flat nose appears to be sharp-edged and, in some corners, exposed to bending (Figure 7).

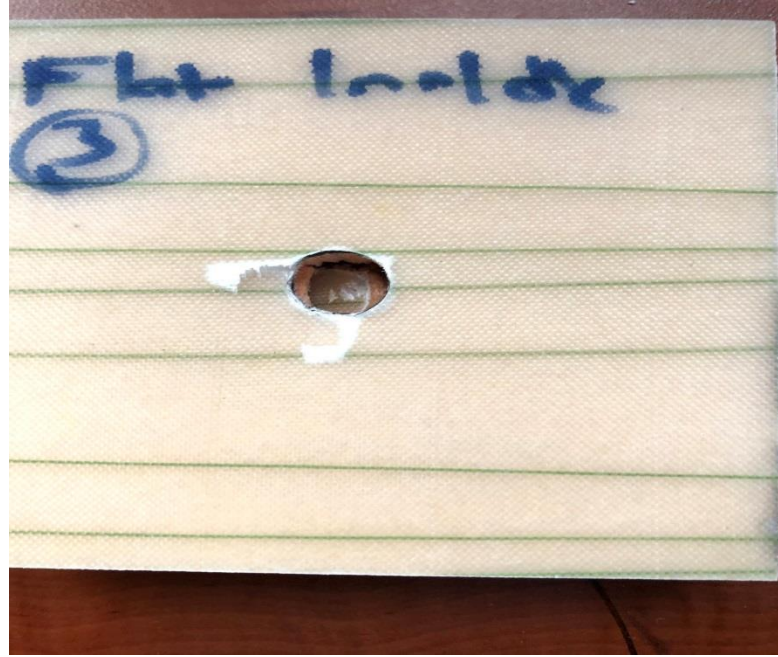


Figure 7. Specimen of flat nose after loading

### Conclusion

As results of the tests, it was determined that the contact force at the hemispherical nose was lower than the contact force at the flat nose. The reason for this is the difference of geometric shapes at the noses.

In tests with the hemispherical nose, the first peak contact forces have increased by rise the speed of the nose. In the second contact forces, the maximum value was seen at the time of 5 mm / min, and a decrease in the forces was observed with the increase in speed.

When the sandwich composite is loaded with the hemispherical nose, the shear stress is softer in the first sandwich.

In tests with flat nose, first peak contact forces increased up to 15mm / min and decreased after 15mm / min. In the same way, the second peak contact forces increased by 15mm / min and decreased after 15mm / min.

The reason why the graphics come out with sharp corners in the tests made with the flat nose is because the flat nose forces the material to shear.

### References

- [1] Zhu Shengqing, Chai Gin Boay (2013) Damage and failure mode maps of composite sandwich panel subjected to quasi-static indentation and low velocity impact. *Composite Structures*; 13(101):204-14.
- [2] Xiao JR, Gama BA, Gillespie Jr. JW (2007) Progressive damage and delamination in plain weave S-2 glass/SC-15 composites under quasi-static punch-shear loading. *Composites Structures* 78(2): 182-196.

- [3] Sadeghi M, Pol MH (2017) Investigation of behaviors of glass/epoxy laminate composites reinforced with carbon nanotubes under quasi-static punch shear loading. *Journal of Sandwich Structures and Materials*. 21(4):1535-1556.
- [4] Sadeghi M and Pol MH. Experimental investigation of the effect of the addition of carbon nanotubes on the quasi-static punch shear penetration of the laminated glass/epoxy composite. *Modares Mech Eng* 2015; 15: 416–424
- [5] Wen HM, Reddy TY, Reid SR, Soden PD. Indentation, penetration and perforation of composite laminate and sandwich panels under quasi-static and projectile loading. *Key Eng Mat* 1998; 141–143:501–52.

## Optimization Study of Ballistic Impact Tests on Carbon-Carbon Composites

Latif Tibet Aktas\*, İzmir University of Economics, Dept. of Mechanical Engineering, Balçova, İzmir, Turkey  
Levent Aydın, İzmir Kâtip Çelebi Univ., Dept. of Mechanical Engineering, Çiğli Main Campus, İzmir, Turkey  
\*Corresponding author: tibet.aktas@ieu.edu.tr

**Keywords:** Carbon-carbon composites, ballistic impact, multiple nonlinear regression  
**Discipline:** Mechanical Engineering

### Abstract

In this study it is intended to optimize a high velocity impact case of a composite plate. The case is selected from the literature based on its dataset properties (e.g. amount of inputs and outputs, number of tests, physical relations with real life situations and relations between the properties studied on). The base study focused on failure response of advanced carbon-carbon composites under high velocity impacts. In the present study, two unique models are introduced within the scope of the present study as dimensionless damage areas of front and back sides of the composite plate. Multiple nonlinear regression method is used for objective functions of the optimization problem. The prediction models found in the present study are in first order trigonometric multiple nonlinear regression form; thus, these models can be considered as the basic prediction functions of high velocity impact response of carbon-carbon composites under high temperatures, in processing power terms. Since the determination coefficient values have been found quite similar with the ones in the base study, the presented models in this study can be considered successful to predict the results.

### Introduction

Carbon-carbon composites are known about their unique behaviors. These relatively new developed engineering materials show ceramic behavior in nature but behave in a range from brittle to pseudoplastic. These materials have a wide range of real-life applications depending on their thermo-structural properties. These application areas include rocket nozzles, re-entry nose tips, aircraft brake discs etc. Working on these types of materials will enhance the performance of aerospace vehicles against basic natural drawbacks of the application area.

One of the experimental ballistic studies from literature is chosen as the base study and it is intended to develop a model to predict results of different experimental parameters by using optimization methods.

Xue et al. [1] worked on effects of hypervelocity impact on SiC coated carbon-carbon composites. In their study, ablation response of SiC coated carbon-carbon composites is investigated, and they concluded that impact velocity affects ablation rates. Also, they concluded that coating carbon-carbon composites with SiC improves ablation response of the plates.

Grujicic et al. [2] conducted a transient non-linear-dynamics-based analysis to investigate damage and failure response of carbon-carbon/carbon-foam composites under hypervelocity impact. These types of panels are used in common aero vehicles and they concluded that the damage is depending on normal component of the momentum of the projectile just before the impact. Additionally, it was observed that carbon-foam increases the hypervelocity impact resistance of common aero vehicles.

The study of Park and Fahrenthold [3] is shaped on the concern of orbital debris impact hazard on spacecrafts. They simulated the impact experiments of hypervelocity impacts on space shuttle wing leading edge made of carbon-carbon composite. They concluded that momentum scaling method can predict perforations accurately and validated simulations can bring results of beyond experiment conditions.

Curry et al. [4] discussed the arcjet test results of reinforced carbon-carbon composites impacted by hypervelocity debris. These tests are conducted at the NASA Johnson Space Center and test specimens were exemplar of the ones used in Space Shuttle Orbiter. They presented the correlation functions for front and back face mass loss and oxidation characteristics of reinforced carbon-carbon composites discussed in consideration of the results.

Xie et al. [5] investigated the structural integrity of advanced carbon-carbon composites under high temperature environments. In their study, heated carbon-carbon composites are exposed to high velocity projectile impacts to observe their mechanical responses and obtain the effects of different impact

parameters. They conducted tensile tests on the carbon-carbon samples to measure residual stresses after the high velocity impact tests. This study is selected as the base study and the dataset of their experiments are taken as the examples to the present study. Their impact test results are shown in Table 1.

Table 1. Impact test results [5] (“1” represents perforation while “0” represents no perforation)

T (°C)	$v_0$ (km/s)	Test result	$t_w/d_p$	$A_{front}/d_p^2$	$A_{back}/d_p^2$	Impact energy (J)
1205	1.690	1	1.667	3.537	4.207	69.449
1206	1.680	1	1.667	1.781	2.498	68.629
1225	1.710	1	2.5	1.268	2.198	21.067
1230	1.700	0	5	2.95	0	2.603
25	1.690	1	1.667	3.501	5.519	69.449
1212	1.980	1	1	3.100	3.225	441.334
1218	1.676	0	3	3.42	0	2.530
1270	2.000	0	5	3.82	0	3.602
1230	1.704	1	1	3.376	3.999	326.871
1193	1.760	1	1.667	2.928	3.799	131.374
1205	1.700	1	1	2.640	3.303	70.273
900	1.700	1	3.333	2.090	3.591	70.273
819	1.886	1	1.667	8.998	10.956	86.492
1429	1.608	1	1.667	4.143	10.754	62.873
1220	4.600	1	1.667	21.32	25.169	514.525
1205	3.090	1	1.667	11.133	11.364	232.171
1234	3.900	1	5	12.554	14.52	13.698

The base study presented an experimental and analytical investigation on the effects of high velocity impact ( $1608 \text{ m.s}^{-1} - 4600 \text{ m.s}^{-1}$ ) and related damage on carbon-carbon composites at high temperatures (between  $25 \text{ °C}$  and  $1429 \text{ °C}$ ) using a fast-electric heating system and two-stage light gas gun.

Two equations were presented as prediction of the effect of high velocity impact on the structural integrity of advanced carbon-carbon composites for high temperature applications in the base study. They concluded that the residual strength of the carbon-carbon composite samples improved by 47% by heating the samples.

### Method

To obtain accurate models of objective functions, regression analysis method is used. Regression analysis method can accurately determine which variables have how much impact on the interested phenomena. Operating this method gives crucial information about the process of phenomena. First order trigonometric multiple nonlinear regression analysis method is used for the optimization process of this study. Standard form of first order trigonometric multiple nonlinear regression is:

$$Y = a_0 + a_1 \sin x_1 + a_2 \sin x_2 + a_3 \sin x_3 + a_4 \cos x_1 + a_5 \cos x_2 + a_6 \cos x_3 \quad (1)$$

Multiple form of nonlinear regression defines that there are more than one independent variables (for the present case, input types) in the objective function. The design variables are temperature of the composite sample during the impact test ( $\text{°C}$ ), impact velocity of the projectile (km/s), and the fraction between the laminate thickness and diameter of the projectile ( $t_w/d_p$ ). The system outputs are dimensionless frontal damage area ( $A_{front}/d_p^2$ ) and dimensionless back damage area ( $A_{back}/d_p^2$ ) for the present case. Optimization process has been done by using Wolfram Mathematica 11.0 software.

## Results

In the base study, the models are presented with the additional variables of  $T_0$  as room temperature and  $c_t$  as speed of sound in carbon-carbon composites, beside design variables. The presented models for dimensionless front and back damage areas in the base study are [5]:

$$\frac{A_{front}}{d_p^2} = 11.090 \left(\frac{T}{T_0}\right)^{-0.027} \left(\frac{v_0}{c_t}\right)^{1.175} \left(\frac{t_w}{d_p}\right)^{-0.150} - 4.925 \quad (2)$$

$$\frac{A_{back}}{d_p^2} = 11.219 \left(\frac{T}{T_0}\right)^{-0.117} \left(\frac{v_0}{c_t}\right)^{1.655} \left(\frac{t_w}{d_p}\right)^{-0.223} - 2.068 \quad (3)$$

The new first order trigonometric multiple nonlinear regression models presented in this study are:

$$\begin{aligned} \frac{A_{front}}{d_p^2} = & 10.487 - 0.677 \cos x_1 + 0.259 \cos x_2 + 0.314 \cos x_3 + 0.881 \sin x_1 \\ & - 7.406 \sin x_2 + 1.370 \sin x_3 \end{aligned} \quad (4)$$

$$\begin{aligned} \frac{A_{back}}{d_p^2} = & 12.102 - 2.510 \cos x_1 + 2.345 \cos x_2 + 0.503 \cos x_3 + 2.059 \sin x_1 \\ & - 8.389 \sin x_2 + 3.653 \sin x_3 \end{aligned} \quad (5)$$

where  $x_1$ ,  $x_2$  and  $x_3$  represent temperature of the composite plate ( $^{\circ}\text{C}$ ), impact velocity of the projectile (km/s), and the ratio between the laminate thickness and diameter of the projectile ( $t_w/d_p$ ), respectively.

After obtaining the models of the system, the determination coefficients ( $R^2$ ) values are calculated for each of the output functions. Global minimum values of the system are determined for each of the two objective functions of damage areas. To consider the models as successful, determination coefficients should be over 0.9 ( $\leq 1$ ), and this is the defined criteria of the success of the present study.

Comparison of the determination coefficient results found in the present study with the results given in the base study are shown in Table 2.

Table 2. Comparison of the determination coefficients

	Present study	Base study [5]
$A_{front}/d_p^2$	0.910	0.998
$A_{back}/d_p^2$	0.978	0.944

The new models presented in this study shows different determination coefficient agreements with the ones in the base study and it shows that, for one of the objective functions, optimization process of the present study has higher success rate than the one in the base study. Finally, global minimum optima outputs are found with applied constraints.

To obtain the effect of the ratio between the plate thickness and the diameter of the projectile, other input types are kept equal and the results are shown in Table 3. Similarly, same study is done for the effect of impact velocity and the results are shown in Table 4.

Table 3. Optimized input results and the effect of  $t_w/d_p$  value

Outputs	Minimized values	$x_1$ ( $^{\circ}\text{C}$ )	$x_2$ (km/s)	$x_3$ ( $t_w/d_p$ )
$A_{front}/d_p^2$	0.883	25	1.608	4.487
$A_{back}/d_p^2$	$7.1 \times 10^{-9}$	25	1.608	3.294

Table 4. Optimized input results and the effect of impact velocity

Outputs	Minimized values	$x_1$ (°C)	$x_2$ (km/s)	$x_3$ ( $t_w/d_p$ )
$A_{front}/d_p^2$	0.883	25	1.608	4.487
$A_{back}/d_p^2$	$6.3 \times 10^{-8}$	25	2.275	4.489

### Conclusion

To determine the dimensionless damage areas, two novel equations are presented. The new models presented in this study show good determination coefficient agreements with the ones in the base study. The new presented model of dimensionless front damage area is better than the base model to predict the phenomena. According to the global optima results, it is seen that the effect of the impact velocity on the impact resistance of carbon-carbon composites appears to be more important than the dimensions of the projectile diameter, the testing temperature and the thickness of the samples. Dimensionless damage area can be minimized by decreasing the ratio between the laminate thickness and diameter of the projectile.

### References

- [1] Xue LZ, Li KZ, Jia Y, Zhang SY, Ren JJ, You ZY. Effects of hypervelocity impact on ablation behavior of SiC coated C/C composites. *Materials and Design* 2016; 108:151-156.
- [2] Grujicic M, Pandurangan B, Zhao C, Biggers S, Morgan D. Hypervelocity impact resistance of reinforced carbon-carbon/carbon-foam thermal protection systems. *Appl Surf Sci* 2006; 252(14):5035e50.
- [3] Park Y-K, Fahrenthold EP. Simulation of hypervelocity impact effects on reinforced carbon-carbon. *J Spacecr Rockets* 2006; 43(1):200e6.
- [4] Curry DM, Pham VT, Norman I, Chao DC. Oxidation of hypervelocity impacted reinforced carbon-carbon. *J Spacecr Rockets* 2000; 37(3):310e7.
- [5] Xie WH, Meng SH, Ding L, Jin H, Han GK, Wang LB, et al. High velocity impact tests on high temperature carbon-carbon composites. *Compos B Eng.* 2016; 98:30-38.

## Impact and Compression-after Impact Behaviors of Laminated Composite Plates

*Aidel Kadum Jassim Al-shamary\**, University of Diyala, Dept. of Mechanical Engineering, Diyala, Iraq  
*Halis Kandas*, Dokuz Eylul University, Department of Mechanical Engineering, İzmir, Turkey  
*Okan Ozdemir*, Dokuz Eylul University, Department of Mechanical Engineering, İzmir, Turkey  
*Ramazan Karakuzu*, Dokuz Eylul University, Department of Mechanical Engineering, İzmir, Turkey  
*\*Corresponding author: adel\_kadum500@yahoo.com*

**Keywords:** Kevlar/Carbon, compression test, composite material, low velocity impact  
**Discipline:** Mechanical Engineering

### Abstract

Owing to their specific advantages like high stiffness, light weight, acoustic damping, and high bending stiffness, the composite materials have been used in the several main sectors, such as aerospace, automobile, wind turbines, and sport part etc. This study presents the experimental study of the impact loading on the composite laminates. In this context, the composite laminates were subjected to the impact loading by using flat impactor nose. Kevlar/Carbon fibers were chosen as reinforcing materials. Epoxy resin and hardener were used as matrix material to manufacture laminated composite. The obtained results show that the maximum contact force by using the flat impactor nose increases by increasing the impact energy levels.

### Introduction

Kevlar and carbon fibers are significant structure in various applications of engineering fields such as aeronautics, construction, and marine industries etc. The effectiveness of stitching in containing size damage was studied by Hosur et al. [1]. Composites materials were manufactured with carbon fabric by using Vacuum Assisted Resin Infusion Molding (VARIM) process. In another study, sandwich composites with carbon and kevlar/hybrid face sheets were subjected to low velocity impact energies at different temperatures [2]. They obtained that low velocity impact performance of sandwich composites was highly affected with temperature changes. Al-Shamary [3] tested three type configurations of sandwich composite experimentally and found that core number and core thickness of sandwich composite have a significant impact on the low velocity impact performances. Li et al. [4] produced composite specimens by using woven Kevlar fabrics in the stacking sequence of 0/90°. They observed that instantaneous deflections of specimens are larger than the permanent deflections.

Along with the experimental studies, finite element method was carried out in the numerical study conducted by Abdel-Nasser et al. [5]. They used two different models utilizing E-glass, kevlar and carbon fibers. Selection of boundary condition in the impact analysis of composite laminate is very important to determine the failure modes. Ansari & Chakrabarti [6] have carried out the experimental and numerical studies on the kevlar/epoxy sandwich composite plates. They found that penetration resistances of kevlar/epoxy sandwich composite laminate are better than the single kevlar/epoxy composite plates. Dogan & Arman [7] performed a study in order to investigate effects of impactor nose diameter and temperature. They showed that maximum contact force was obtained at the impactor nose with a diameter of 20 mm. Al-Shamary et al. [8] studied effects of low velocity impact on the compression test. Their results showed that the damage occurred at the impact point of the specimen during the compression test.

### Experimental Methodology

In this study, the composite laminates were fabricated by vacuum-assisted resin infusion molding method (VARIM). Figure 1 shows the fabrication stage of composite laminates. The composite laminates were cured at 80°C for 8 h and then temperature decreased progressively to room temperature. After that, specimens were cut from the composite panel.

Prepared specimens were then subjected to different impact energy levels (5J, 7.5J, 10J, 12.5J and 15J). Circular support with an inner diameter of 76.2 mm was used in order to clamp the specimens (Figure 2). Low velocity impact (LVI) tests were carried out by using the impact testing machine as shown in Figure 3. Flat nose impactor with a diameter 12.7 mm was used during the tests. All the



impacted specimens were then subjected to compression test by using the Shimadzu AG testing machine.

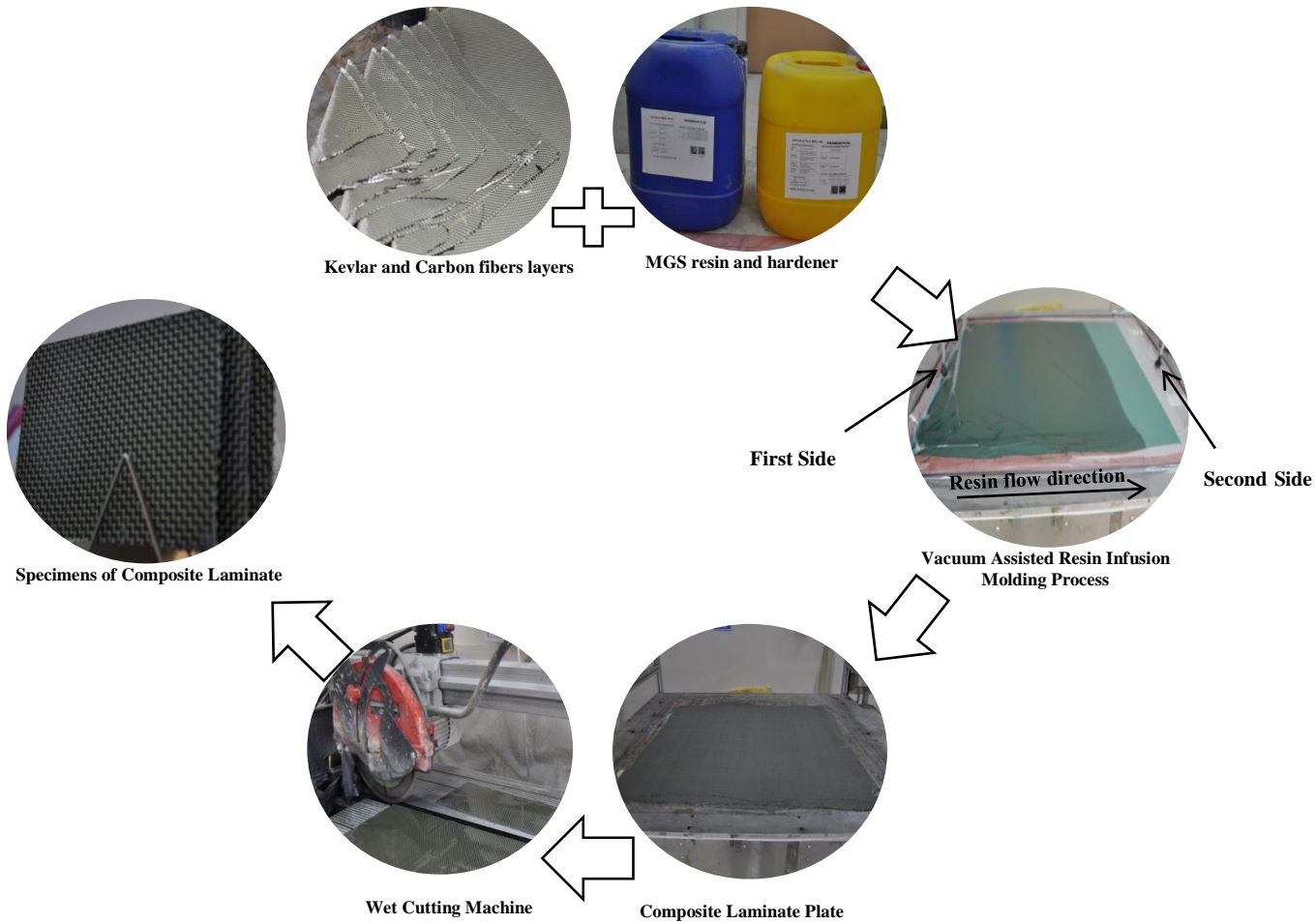


Figure 1. Fabrication stages of composite laminate

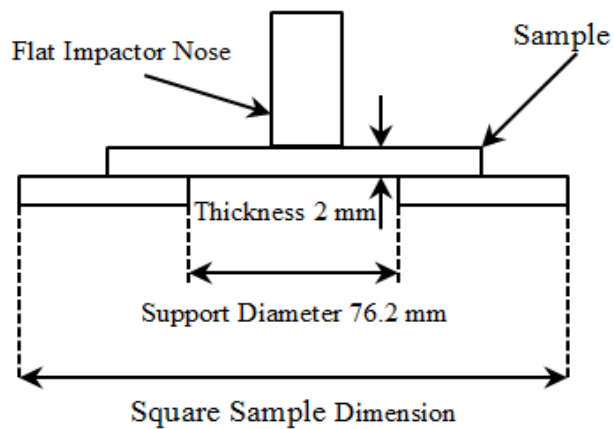
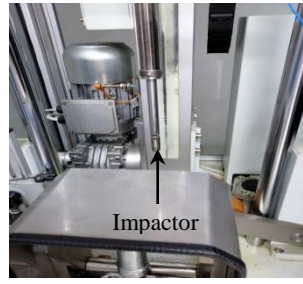


Figure 2. Dimension of test specimen



Ceast 9350 Fractovis Plus  
Impact Testing Machine



Impactor



Flat Impactor



The Shimadzu Test Machine



Apparatus of Compression Test

Figure 3. Tests procedure of composite laminates

### Results and Discussions

The Figure 4 explains the impact energy versus maximum contact force curves of the composite laminates. The maximum contact force of specimens increases with increasing the impact energy levels. The maximum contact force values are given in Table 1 for the flat impactor nose at different impact energy levels.

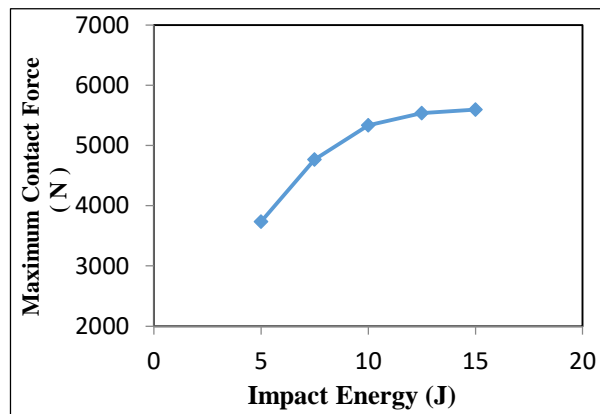


Figure 4. Maximum contact force – impact energy

Table 1. Variation of maximum contact force according to the impact energy level

Impact Energy (J)	Maximum contact force (N)
5	3736
7.5	4767
10	5337
12.5	5538
15	5598

The stress-deflection curves of specimens in the compression test are given in Figure 5. All the specimens were subjected to uniaxially loaded compression until the failure occurs. The results showed that the maximum stress occurs in specimens impacted at 0 J in the compression test. The stress value of specimens decreases by increasing the impact energy levels. The maximum stress values of CAI are given in Table 2 for the flat impactor nose at different impact energy levels.

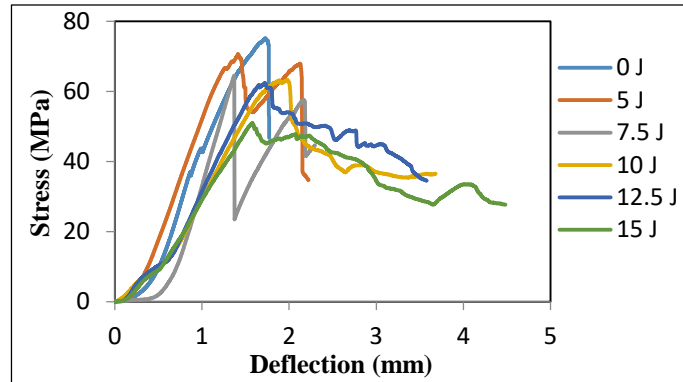


Figure 5. Stress-Deflection curves of compression test after impacted at 5J, 7.5J, 10J, 12.5J and 15J

Table 2. Variation of maximum stress of CAI according to the impact energy level

Impact Energy (J)	Maximum stress of CAI (MPa)
0	75.2
5	70.7
7.5	64.6
10	63.2
12.5	62.4
15	51.1

Figure 6 shows the time versus velocity curves of specimen during the impact loading tests. The results show that velocity increases by increasing the impact energy until the 5 ms. The positive velocity values implies the lowdown motion of impactor. On the other hand, the negative values represent the rebounding case. The impactor cannot penetrate the samples when impact energy of 5 J to 12.5 J was applied. Applying 15 J to specimens, the impactor penetrated the specimens in the flat impactor nose during low velocity impact tests. It is also concluded that time remains constant during impact test with flat impactor nose after the 5 ms.

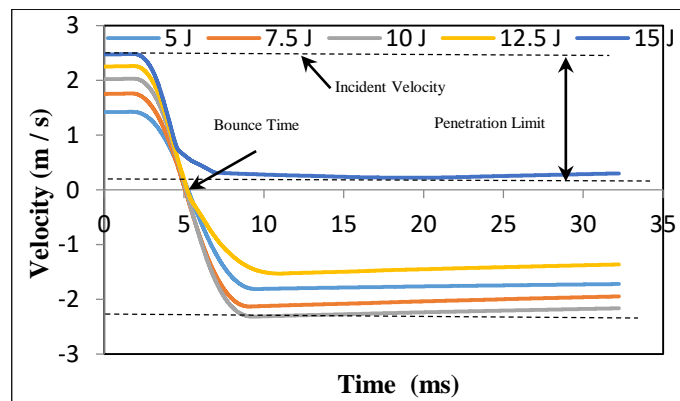


Figure 6. Velocity-time responses curves of the specimens under various impact energies

The most important factor in composite laminates is absorbed energy. Absorbed energy is calculated from the energy profile diagram as shown in Figure 7. The perforation case was occurred after the impact energy level of 15 J was applied to specimens. The absorbed energy is rising for all applied energy levels in the flat nose impactor. The absorbed energy values of the specimens are also given in Table 3.

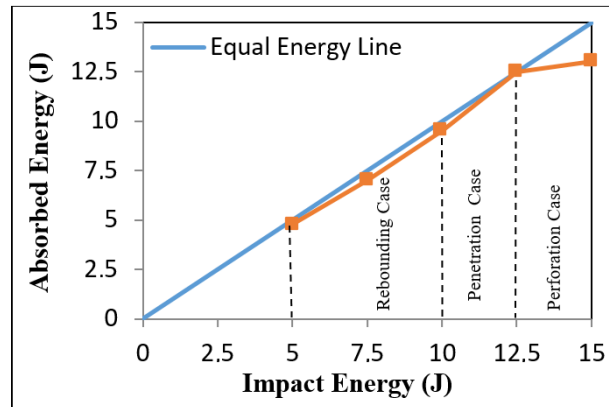


Figure 7. Energy profile diagram of composite laminates

Table 3. Variation of absorbed energy according to the impact energy level

Impact Energy (J)	Absorbed energy (J)
5	4.8
7.5	7.0
10	9.5
12.5	12.5
15	13.0

### Conclusions

In the current study, the effects of impactor nose on the hybrid composite materials under the low velocity impact were studied experimentally at room temperature. The CAI tests of the impacted specimens were also carried out. The brief summary of the paper is given below;

- The final velocity value stays in positive side after the penetration case (15J).
- The maximum contact force increases by increasing the impact energy level by using impactor with flat nose.
- The absorbed energy value increases by increasing the impact energy level.
- Maximum stress of CAI of hybrid composites decreases with increasing the impact energy levels.

### References

- [1] Hosur MV, Adya M, Alexander J, Jeelanı S. (2003) Studies on Impact Damage Resistance of Affordable Stitched Woven Carbon/Epoxy Composite Laminates. *Journal of Reinforced Plastics and Composites*. (22): 927-952.
- [2] Salehi-Khojin A, Mahinfalah M, Bashirzadeh R, Freeman B. (2007) Temperature effects on Kevlar/hybrid and carbon fiber composite sandwiches under impact loading. *Composite Structures*. 78: 197-206.
- [3] Al-Shamary A. K. J. (2014) Investigation of energy absorption capacity of sandwich composites subjected to the impact loadings. \_İzmir: MSc Thesis, Dokuz Eylül University.

- [4] Li X, Nia A B, Ma X, Yahya M Y, Wang Z. (2016) Dynamic response of Kevlar®29/epoxy laminates under projectile impact-experimental investigation. *Mechanics of Advanced Materials and Structures*. 24:2, 114-121.
- [5] Abdel-Nasser Y, Elhewy A M H, Al-Mallah I. (2017) Impact analysis of composite laminate using finite element method. *Ships and Offshore Structures*. 12(2): 219-226.
- [6] Muslim Ansari Md, Chakrabarti A. (2016) Impact behaviour of GFRP and Kevlar/epoxy sandwich composite plate Experimental and FE analyses. *Journal of Mechanical Science and Technology*. 31(2): 771-776.
- [7] Dogan A, Arman Y. (2018) Effects of temperature and impactor nose diameter on the impact behavior of PA6 and PP thermoplastic composites. *Journal of Elastomers & Plastics*. 51(1): 64-74.
- [8] Al-shamary A K J, Dogan A, Ozdemir O, Karakuzu R. (2018) Impact and Post Impact Behavior of Hybrid Composites. *Diyala Journal of Engineering Sciences*. 11(4): 46-52.

## Linear Vibration Analysis of Axially Forced Euler-Bernoulli Beam Graded Trigonometric Material with Variable Cross-Section

Sümeyye Sınır\*, Manisa Celal Bayar Univ., Dept. of Mechanical Engineering, Şehit Prof. Dr. İlhan Varank Campus, Manisa, Türkiye

Mehmet Çevik, İzmir Kâtip Çelebi Univ., Dept. of Mechanical Engineering, Çiğli Main Campus, İzmir, Türkiye  
B. Gültekin Sınır, Manisa Celal Bayar Univ., Dept. of Civil Engineering, Şehit Prof. Dr. İlhan Varank Campus, Manisa, Türkiye

\*Corresponding author: sumeyyesinir@gmail.com

**Keywords:** Functionally graded beam (FGM), differential quadrature method, vibration

**Discipline:** Mechanical Engineering

### Abstract

Axially functionally graded material beam has been performed in terms of Euler – Bernoulli beam theory. The properties of the material being used in the beam vary along the beam in terms of trigonometric functions. Linear variations on both width and height have been taken into account for the cross section of the beam. The beam is forced with axially parametric force. The equation of motion is given with dimensional variables and parameters. Then, the dimensionless form of the equation is obtained. Differential Quadrature Method is utilized to solve the equation of motion, natural frequencies and critical forces are obtained. The graphics of natural frequency – critical force variation are drawn.

### Introduction

Functionally Graded Materials (FGMs) are one kind of new inhomogeneous composite materials containing two or more constituents whose material composition continuously and smoothly varies along certain direction(s).

The FGM concept originated in Japan in 1984 during the space-plane project, in the form of a proposed thermal barrier material capable of withstanding a surface temperature of 2000 K and a temperature gradient of 1000 K across a cross-section.

Why FGMs are preferred? This question can be answered by illustrating about disadvantages of the classical composites and advantages of the FGMs. The main disadvantages of the classical composites are cracking, delamination phenomenon, fiber separation, large residual stress accumulation, large local plastic deformation. The main advantages of the FGMs are prevention or reduction large residual stress accumulation, prevention or reduction large local plastic deformation, stretching, high strength, light weight, isolation, damping vibrations, resistance to friction [1-8].

Moreover, there are organic FGMs which are bones, teeth, human skins bamboo etc. in nature. And then, produced FGMs structure elements are rods, beams, plates and shells. Some examples of application areas can be given as space structures, automotive industry, nuclear industry, energy, defense industry, electrical-electronics/communications, optoelectronic, biomedical, marine structures, sports equipments etc. [1-8].

Tribune blades, helicopter rotor blades, robot arms, space adjustable booms (lifting arms) etc. are given as examples of FGMs beams. Material property variations of the beam are seen in Fig. (1).

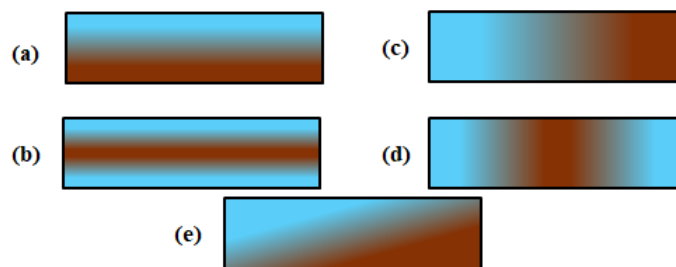


Figure 1. Material properties variations of the beam

Especially, axially varying material properties are shown in cases (c) and (d) of Figure 1.

In the literature, the well-known material gradient is Power Law Material Gradient [9]. Axial direction Power Law Material Gradient is as [1-4]

$$P_x(x) = (P_L - P_R) \left(1 - \frac{x}{L}\right)^{k_1} + P_R \quad (1)$$

Here,  $P_x$  is axially material properties variation function,  $P_L$  is material property of left side beam,  $P_R$  is material property of right-side beam,  $L$  is length of the beam and  $k_1$  is material gradient coefficient.

Other commonly used material gradients are exponential material gradient, trigonometric material gradient, polynomial material gradient etc. [6-9].

In this study, axially trigonometric functionally graded material Euler-Bernoulli beam is considered and the equation of motion is solved with Differential Quadrature Method. Natural frequencies and critical loads are calculated. Then, the effects of coefficient of material gradient on natural frequencies and critical loads are shown in tables and figures.

### Equation of Motion

The equation of motion of axially functionally graded Euler-Bernoulli beam is as [2-5],

$$(\hat{E}(\hat{x})\hat{I}(\hat{x})\hat{w}''')'' + \hat{P}\hat{w}'' + \hat{\rho}(\hat{x})\hat{A}(\hat{x})\hat{w} = 0 \quad (2)$$

Here  $\hat{w} = \hat{w}(\hat{x}, \hat{t})$  denotes transverse deflection of a point on the  $\hat{x}$ -axis,  $\hat{x}$ -axis coincides with the centroidal axis of the undeformed beam,  $\hat{t}$  is time,  $E(\hat{x})$  is the Young's modulus,  $\rho(\hat{x})$  is the density of the material  $\hat{I}(\hat{x})$  is the area moment of inertia,  $\hat{A}(\hat{x})$  is the cross-sectional area,  $\hat{P}$  is axially force.  $(\dot{\quad})$  is the derivative of time ( $t$ ) and  $(\prime)$  is the derivative of ( $x$ ).

The properties of the material being used in the beam vary along the beam in terms of trigonometric functions. The functions of elasticity modulus and density are defined according to trigonometric material gradient [6]

$$\hat{E}(\hat{x}) = E_0 \left[1 + k_2 \cos\left(\pi \frac{\hat{x}}{L}\right)\right] \quad (3)$$

$$\hat{\rho}(\hat{x}) = \rho_0 \left[1 + k_2 \cos\left(\pi \frac{\hat{x}}{L}\right)\right] \quad (4)$$

Here,  $E_0$  is the elasticity modulus at the starting configuration of the beam,  $\rho_0$  is the density at the starting configuration of the beam and  $k_2$  is material gradient coefficient.

In Fig. 2, variations of the elasticity modulus for different material gradient coefficient ( $k_2$ ) values are shown.

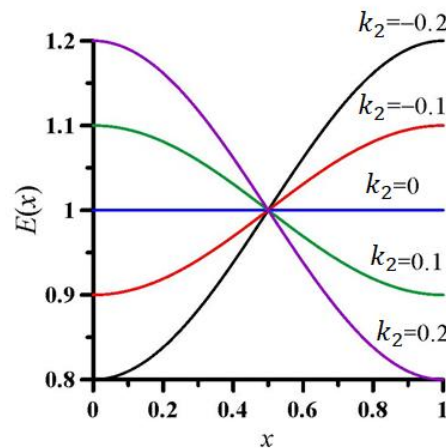


Figure 2. Variations of the elasticity modulus for different  $k_2$  values

For the non-uniform beam, cross section area and inertia moment are defined as respectively [1],

$$\hat{A}(\hat{x}) = A_0 \left(1 + \alpha_b \frac{\hat{x}}{L}\right) \left(1 + \alpha_h \frac{\hat{x}}{L}\right) \quad (5)$$

$$\hat{I}(\hat{x}) = I_0 \left(1 + \alpha_b \frac{\hat{x}}{L}\right) \left(1 + \alpha_h \frac{\hat{x}}{L}\right)^3 \quad (6)$$

Here,  $A_0$  is cross section area at the starting configuration of the beam,  $I_0$  is inertia moment at the starting configuration of the beam,  $\alpha_b$  is width variation coefficient and  $\alpha_h$  is height variation coefficient.

For material and geometry independent solutions, the equation of motion is dimensioned. The defined non dimensional terms are follows [1],

$$x = \frac{\hat{x}}{L}, \quad t = \frac{\hat{t}}{L^2} \sqrt{\frac{E_0 I_0}{\rho_0 A_0}}, \quad w = \frac{\hat{w} L}{r^2} \quad (7)$$

According to non-dimensional terms which are given with Eq. (7), the non-dimensional equation of motion is obtained

$$Gw^{iv} + 2G'w'''' + G''w'' + m\dot{w} + Pw'' = 0 \quad (8)$$

Here, the obtained non dimensional terms as,

$$G = E(x)I(x) = \frac{E(\hat{x})\hat{I}(\hat{x})}{E_0 I_0}, \quad (9)$$

$$m = \rho(x)A(x) = \frac{\hat{\rho}(\hat{x})\hat{A}(\hat{x})}{\rho_0 A_0}, \quad (10)$$

$$P = \frac{\hat{p}L^2}{E_0 I_0} \quad (11)$$

and the boundary conditions for pinned-pinned supports are given as follows [1],

$$w''(1, t) = w(0, t) = 0 \text{ and } w(1, t) = w(0, t) = 0 \quad (12)$$

### Solution with Differential Quadrature Method

For the solution, Differential Quadrature Method is used. In this method, the derivative of a function may be represented as the weighted linear sum of the function values at all discrete points [1].

$$\frac{dX_n(x_i)}{dx} = \sum_{j=1}^S c_{ij}^{(1)} X_n(x_j) \quad (13)$$

The higher order derivative of a function can be given as follows,

$$\frac{d^\xi X_n(x_i)}{dx^\xi} = \sum_{j=1}^S c_{ij}^{(\xi)} X_n(x_j), \quad (14)$$

$$i = 1, 2, \dots, S$$

The grid points are defined as

$$x_i = \frac{i-1}{S-1}, \quad i = 1, 2, \dots, S \quad (15)$$

The following relations for calculating the weighting coefficients are given



$$M(x) = \prod_{i=1}^H (x - x_i) \quad (16)$$

$$M^{(1)}(x_i) = \prod_{j=1, j \neq i}^S (x_i - x_j), \quad i = 1, 2, \dots, S \quad (17)$$

$$c_{ij}^{(1)} = \frac{M^{(1)}(x_i)}{(x_i - x_j)M^{(1)}(x_j)}, \quad i \neq j; i, j = 1, 2, \dots, S \quad (18)$$

$$c_{ii}^{(1)} = -\sum_{j=1, j \neq i}^S x_{ij}^{(1)}, \quad i = 1, 2, \dots, S \quad (19)$$

$$c_{ii}^{(\xi)} = -\sum_{j=1, j \neq i}^S x_{ij}^{(\xi)}, \quad i = 1, 2, \dots, S \quad (20)$$

The solution of the linear equation is as

$$w = X_n(x)e^{i\omega_n t} \quad (21)$$

Here,  $X_n(x)$  are the shape functions and  $\omega_n$  are the natural frequencies. Substituting the solution given in Eq. (21) into Eqs. (8) and (12), one can obtain

$$GX_n^{iv} + 2G'X_n''' + (G'' + P)X_n'' - \rho\omega_n^2 X_n = 0 \quad (22)$$

and the boundary conditions are,

$$X_n''(1) = X_n''(0) = 0 \text{ and } X_n(1) = X_n(0) = 0 \quad (23)$$

The discretized equation of motion is obtained as

$$\begin{aligned} G(x_i) \sum_{j=1}^S c_{ij}^{(4)} X_n(x_j) \\ + 2G'(x_j) \sum_{j=1}^S c_{ij}^{(3)} X_n(x_j) + (G''(x_j) \\ + P) \sum_{j=1}^S c_{ij}^{(2)} X_n(x_j) - \omega_n^2 \rho(x_j) X_n(x_j) = 0, \quad (24) \\ i = 1, 2, 3, \dots, S \end{aligned}$$

The discretized boundary conditions for pinned-pinned supports are

$$X_n(x_1) = 0, \quad \sum_{j=2}^{S-1} c_{1j}^{(2)} X_n(x_j) = 0 \quad (25a)$$

$$X_n(x_S) = 0, \quad \sum_{j=2}^{S-1} c_{Sj}^{(2)} X_n(x_j) = 0 \quad (25b)$$

From the discretized boundary conditions, one can obtain,

$$X_n(x_2) = -\frac{1}{K} \sum_{j=3}^{S-2} K_1 X_n(x_j) \quad (26a)$$

$$(26b)$$

$$X_n(x_{S-1}) = -\frac{1}{K} \sum_{j=3}^{S-2} K_2 X_n(x_j)$$

Here,

$$K_1 = c_{Sj}^{(2)} c_{1,S-1}^{(2)} - c_{1j}^{(2)} c_{S,S-1}^{(2)} \quad (27a)$$

$$K_2 = c_{S2}^{(2)} c_{1,j}^{(2)} - c_{12}^{(2)} c_{Sj}^{(2)} \quad (27b)$$

Substituting the discretized boundary conditions into the discretized equation of motion, we obtain

$$\begin{aligned} G(x_i) \sum_{j=3}^{S-2} \left( c_{ij}^{(4)} - \frac{c_{i2}^{(4)} K_1 + c_{iS}^{(4)} K_2}{K} \right) X_n(x_j) \\ + 2G'(x_i) \sum_{j=3}^{S-2} \left( c_{ij}^{(3)} - \frac{c_{i2}^{(3)} K_1 + c_{iS}^{(3)} K_2}{K} \right) X_n(x_j) \\ + (G''(x_i) \\ + P) \sum_{j=3}^{S-2} \left( c_{ij}^{(2)} - \frac{c_{i2}^{(2)} K_1 + c_{iS}^{(2)} K_2}{K} \right) X_n(x_j) \\ - \omega_n^2 \rho(x_i) X_n(x_i) = 0, \quad i = 3, \dots, S-2 \end{aligned} \quad (28)$$

The natural frequencies and critical loads are obtained from algebraic equations system (28).

### Numerical Results

Linear natural frequencies of axially trigonometric functional graded material beam with uniform cross section area are given in Table 1. Linear natural frequencies of the beam with non-uniform cross section area are given in Table 2 and critical loads are given in Table 3. In Fig. 3 and Fig. 4, the variations of natural frequencies depending on the critical loads at different  $k_2$  values are given.

In cases of  $k_2$  and  $-k_2$ , linear natural frequencies of axially trigonometric functional graded material beam with uniform cross section area are same as seen in Table 1.

Table 1. Linear natural frequencies of axially trigonometric functional graded material beam with uniform cross section area ( $\alpha_b = 0, \alpha_n = 0$ ).

<b>n</b>	$k_2 = -0.2$	$k_2 = -0.1$	$k_2 = 0.1$	$k_2 = 0.2$
<b>1</b>	9.7953	9.8514	9.8514	9.7953
<b>2</b>	39.4116	39.4622	39.4622	39.4116
<b>3</b>	88.7617	88.8106	88.8106	88.7617

In Table 2,  $k_2$  increases, linear natural frequencies of the beam with non uniform cross section area increase.

Table 2. Linear natural frequencies of axially trigonometric functional graded material beam with non-uniform cross section area ( $\alpha_b = 0.1, \alpha_n = 0.2$ ).

<b>n</b>	$k_2 = -0.2$	$k_2 = -0.1$	$k_2 = 0.1$	$k_2 = 0.2$
<b>1</b>	10.3056	10.5262	10.8270	10.9152
<b>2</b>	42.9196	43.0827	43.2912	43.3422
<b>3</b>	97.1069	97.2611	97.4570	97.5029

In cases of  $k_2$  and  $-k_2$ , critical loads of the uniform cross section beam are same and  $k_2$  increases, critical loads of the non uniform cross section beam increase in Table 3.

Table 3. Critical loads ( $P$ ) of axially trigonometric functionally graded material beam (For mode 1)

$k_2$	$\alpha_b = 0, \alpha_h = 0$	$\alpha_b = 0.1, \alpha_h = 0.2$
-0.2	9.5704	11.8775
-0.1	9.7954	12.6647
0.1	9.7954	13.6728
0.2	9.5704	13.8795

The effects of coefficient of material gradient  $k_2$  on natural frequencies and critical loads are shown in tables and figures.

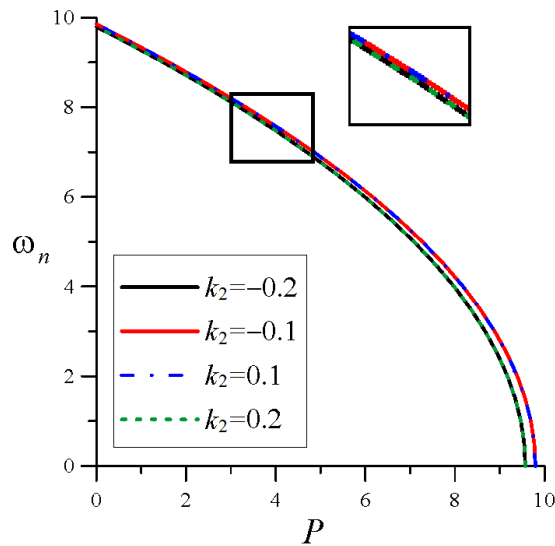


Figure 3.  $\omega_n - P_0$  graph of axially trigonometric functional graded material beam with uniform cross section area ( $\alpha_b = 0, \alpha_h = 0$ ).

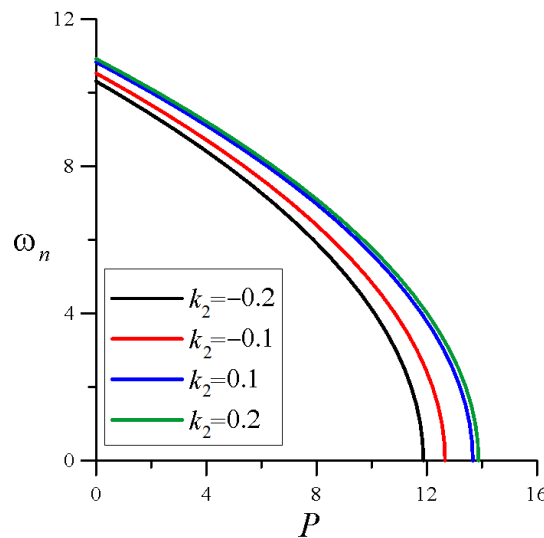


Figure 4.  $\omega_n - P_0$  graph of axially trigonometric functional graded material beam with non-uniform cross section area ( $\alpha_b = 0.1, \alpha_h = 0.2$ ).

### Conclusion

The equation of motion is defined. The natural frequencies and the critical loads are obtained by solving the linear equation of motion solved. The effect of coefficient of material gradient  $k_2$  on natural frequencies and critical loads are illustrated.

### References

- [1] Sınır S, Çevik M, Sınır BG (2018) Nonlinear free and forced vibration analyses of axially functionally graded Euler-Bernoulli beams with non-uniform cross-section, *Composites Part B* 148: 123-131.
- [2] Huang Y, Li XF (2010) A new approach for free vibration of axially functionally graded beams with non-uniform cross-section. *Journal of Sound and Vibration* 329 : 2291–303.
- [3] Lee JW, Lee JY (2017) Free vibration analysis of functionally graded Bernoulli-Euler beams using an exact transfer matrix expression, *International Journal of Mechanical Sciences* 122: 1–17.
- [4] Kumar S, Mitra A, Roy H (2015) Geometrically nonlinear free vibration analysis of axially functionally graded taper beams, *Engineering Science and Technology, An International Journal* 18:579-593
- [5] Huang Y, Yang LE, Luo QZ (2013) Free vibration of axially functionally graded Timoshenko beams with non-uniform cross-section, *Composites: Part B* 45: 1493-1498.
- [6] Şimşek M (2010) Non-linear vibration analysis of a functionally graded Timoshenko beam under action of a moving harmonic load, *Composite Structures* 92: 2532–2546.
- [7] Jin C., Wang X. (2015) Accurate free vibration analysis of Euler functionally graded beams by the weak form quadrature element method, *Composite Structures* 125: 41-50.
- [8] Pradhan KK., Chakraverty S. (2013) Free vibration of Euler and Timoshenko functionally graded beams by Rayleigh-Ritz method, *Composites: Part B* 51: 175–184.
- [9] Sınır S, Çevik M, Sınır BG (2019) Free vibration analysis of axially exponentially functionally graded beams by Differential Quadrature Method. *Proceedings of 3<sup>rd</sup> International Students Science Congress*, 491-496.

## Design of ABS Plastic Scrap Recycling Process for 3D Printer Filaments

*Alif Ngimbi Diambu\**, İzmir Kâtip Çelebi Univ., Graduate School of Natural and Applied Sciences, Çiğli Main Campus, İzmir, Turkey

*Ziya Haktan Karadeniz*, İzmir Kâtip Çelebi Univ., Dept. of Mechanical Engineering, Çiğli Main Campus, İzmir, Turkey

\*Corresponding author: [anasrouline1@gmail.com](mailto:anasrouline1@gmail.com)

**Keywords:** Plastic recycling, 3D printer, ABS, extruder

**Discipline:** Mechanical Engineering

### Abstract

Resources are running out as the amount of waste increases. Recycling thus becomes a compulsory practice. Since most plastic materials are not biodegradable, plastic recycling is of paramount importance. Developed countries are increasingly focusing on promoting sustainable waste management. Most plastic waste ends up in the trash. A recycling idea of this plastics scrap would enable a good management of those plastics for further use as filaments for 3D printers. This study focused on designing an extrusion process for ABS (Acrylonitrile Butadiene Styrene) plastic scrap material into filaments. An extrusion process involving melting, homogenization and pressurization of the polymer melt in a plastic extruder is used by exploiting thermodynamic and heat transfer approaches to assess the amount of heat required to melt the plastic and the work required to pressurize the material in the extruder. The choice of ABS is motivated by its thermal properties as other thermoplastics to be meltable and reusable. Although the purity of the material tends to degrade with each reuse cycle, it is shown that recycling of ABS does not cause deterioration in its properties up to three repeated extrusion with the exception of impact properties. This study can be used as a reference for recycling 3D printer ABS plastic scrap into reusable filaments. It has shown that to recycle 1 kg of ABS scrap with a flow rate of 0.25 g/s, a screw of 520 mm long, 20 mm of diameter shall be used where a heater power of 90.4 W and a motor power of 100 W are enough for thermal and mechanical needs of the process, respectively.

### Introduction

3D printing, otherwise known as additive manufacturing, has a very promising future in many areas of current life. 3D printers are becoming more and more accessible with more local service providers offering outsourcing services for different manufacturing tasks.

Most 3D printed parts need some cleaning up to remove support materials from the build. These support materials can be large, depending on the size of the printed component or its complexity. Removed support materials end up as waste. Moreover, many users prefer to restart over printing rather than resuming it in case an interruption occurred during printing. In this case too, interrupted parts end up as waste. Sometimes, to obtain the right needed prototype, several tests may be necessary. All failed prototypes or designs that do not meet the expected result are thrown into the trash and end up as waste as well. Any waste that is not recycled and disposed of in nature is a step away from the goals of sustainable waste management. Recycling those scrap into 3D printer filaments for further usage is a cost-effective solution.

Some of the previous studies related to this context are presented below. Gyárfás A. & Gergely A. (2019) designed a small-scale plastic extruder machine and presented the polymer processing technologies by student-built machines and emphasized the importance of plastic recycling. Dongoh L. et al. (2018) developed a distributed recycling system for making filaments reused in 3D printers and presented the design procedures of a system for making recycled filaments for 3D printers from waste polymer. Maria de T.G. et al. (2016) investigated an attempt to overcome some of the barriers that hinder the progress of Acrylonitrile Butadiene Styrene (ABS) plastic recycling process using injection molding machine. Vinod Kumar B. et al. (2018) designed a single screw extruding machine for bio-composites focusing on compacting the size of the extruding machine without harming its ability to extrude. Nana Levi N. (2012) analyzed the energy consumption during the extrusion of plastics and they focused on quantifying and qualifying the flow of energy that is transferred in the cooling medium (air or water), by suggesting different methods so that this energy can be valuable to the industry. Bishwash N. et al. (2019) designed and manufactured a plastic extrusion machine for plastic recycling.

In this current study, a thermodynamic-heat transfer-based approach to recycle ABS 3D printer scrap into 3D printer filament is presented. The choice of ABS is motivated by its thermal properties as other thermoplastics to be melted and reused. ABS is widely used in industrial and domestic appliances due to its excellent mechanical properties, dimensional stability and chemical resistance performance. At the end, design parameters to recycle 1 kg of ABS material are determined.

### Design of ABS Recycling Process

A mechanical and heat transfer study allows to determine the dimensions and technical characteristics of components, the amount of energy required, etc. At first, the amount of plastic to recycle is proposed on a daily base and approximate duration to recycle it. All other design parameters are evaluated accordingly. A single screw extruder is chosen for its easy assembly. Key components in a single screw extruder are shown in Figure 1. A single screw extruder has five major equipment components [17]:

- Drive system
- Feed system
- Screw, barrel, and heaters system
- Head and die assembly
- Control system

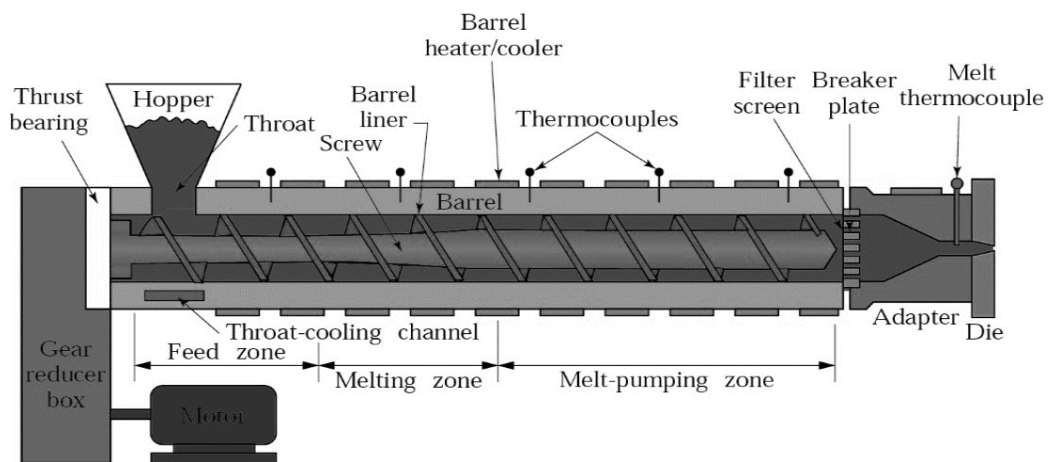


Figure 1. Basic extrusion process [26]

The drive system basically consists of the gear reducer box and thrust bearing group. In the feed system, there are the hopper, the throat, throat cooling and the screw feed zone. The screw, barrel, heaters and thermocouple systems are where the mixing, melting and pumping of plastic occurs. Plastic scrap from the hopper moves down by gravity and is conveyed forward by the screw to the die. The control system controls all the process with feedback loops that automatically influence the process settings, it allows for instance to increase or decrease the heaters temperature, the puller and screw speed in order to reach the desired filament diameter [17]. To prevent polymer degradation, some polymers require drying prior to extrusion. Moisture results in poorer property performance. Therefore, proper drying is critical to acquire the optimum property performance in the end product.

### ABS properties

ABS important properties for this design are summarized in Table 1 below.

Table 1. ABS properties

1. Density	1.05 g/cm <sup>3</sup> [7]
2. Melting temperature	220~240°C [2]
3. Glass transition temperature	106.9°C [2]
4. Glass transition heat	207 kJ/kg [7]

5. Heat transfer coefficient	600–1600 W/m <sup>2</sup> K [4] (For ABS/Steel barrel)
6. Extrusion temperature	165~175°C [2] (Reaches 185°C in practice)
7. Dynamic viscosity	See graphic presented later from [23]
8. Specific heat Cp	See DSC from [21], Figure 7 later.
9. Average thermal conductivity	0.17 [7]

ABS is an amorphous, meaning that it doesn't have a melt point.

To realize this design, some parameters are required. Those parameters are the length and diameter of the screw together with its detailed characteristics such as the pitch, the channel depth and width, different zone length, screw flight or land width, for a given filament flow rate (Mass or Volume). To determine the pressure, drop inside the barrel, the shear rate at the top of the screw nozzle, the dynamic viscosity, the flow rate in the barrel, the length to be covered by the heating system, the heater power (After evaluating the heat transfer), the rotation speed of the screw, the screw driving motor power, etc. (Figure 2).

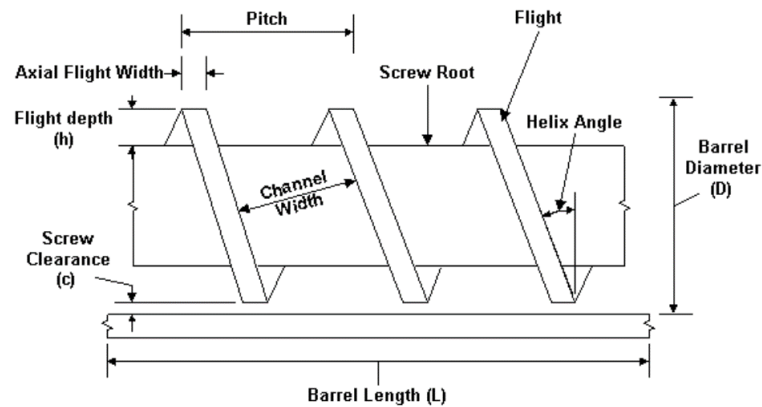


Figure 2. Extruder screw terminology [11]

### Screw diameter and length

The length of the screw is determined based on the ratio  $L/D$ . This ratio is recommended to be higher than 24 [20, 16] for better results. For that purpose, we choose first the screw diameter from standard screw diameter available on the market [24]. For the GT-20 screw, the diameter is 20 mm. Considering a  $L/D$  ratio of 26, the screw active length (The length of the 3 zones of the screw, see Figures 3 and 4) is 520 mm.

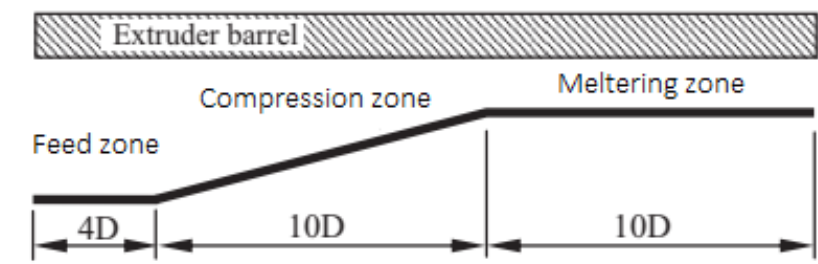


Figure 3. Zone of the extruder screw [12]

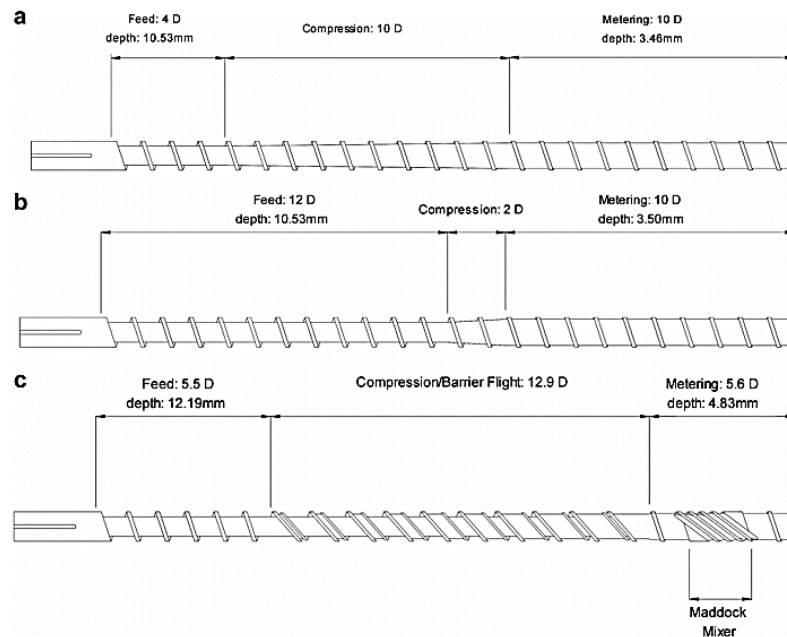


Figure 4. Types of screws: a) Single flighted, tapered compression. b) Single flighted, stepped compression, c) Barrier flighted with spiral mixer [10].

### Shear rate calculation

The shear rate allows to find the average viscosity and therefore to find the pressure drop inside the barrel.

The shear rate  $\dot{\gamma}$  is given by:

$$\dot{\gamma} = \frac{4q}{\pi r^3} \quad [19] \quad (1)$$

where  $q=\dot{v}$  is the volume flow rate of ABS and  $r$  the radius of the screw (10 mm). To recycle 1 kg of ABS, with a speed of 0.1 m/s (100 mm/s), a volume flow rate of 240.53 mm<sup>3</sup>/s is found using the density of ABS and mass flow evaluated considering a target diameter of 1.75 mm (Standard 3D printer filament diameter) for the die, allowing to find the cross section). Therefore, the shear rate of 0.30625 /s is found by exploiting formula (1). From this shear rate, the average dynamic viscosity is found.

### Average dynamic viscosity

The average dynamic viscosity is given in Figure 5, using the target temperature and previously found shear rate.

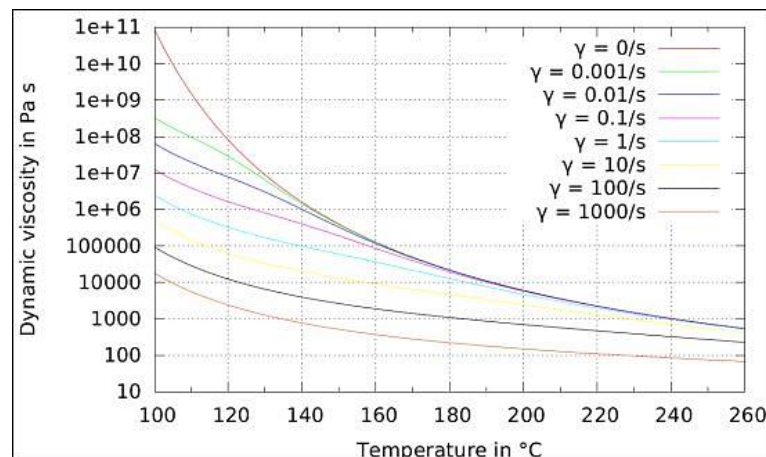


Figure 5. Dynamic viscosity as function of temperature of different flow rates [23]



0.30625 /s as shear rate is very close to the 0.1 /s shear rate and curves almost intersect at the target temperature (185°C). At that temperature, the dynamic viscosity ( $\eta$ ) is roughly equal to 18000 Pa.s ( $1000 \cdot 10^{(0.255)}$ ).

### Pressure drop inside the barrel

The pressure drop inside the barrel is given by the following expression:

$$\Delta P = \frac{8q\eta L}{\pi r^4} \quad [19] \quad (2)$$

L is the active length of the screw.

Hence,  $\Delta P = 573300$  Pa.

### Length of the heater

The length of the heating system is determined based on the first law of thermodynamics and fundamentals of heat transfer by convection, that is;

$$\Delta H + \Delta PE + \Delta KE = \Delta Q + \Delta W \quad (3)$$

where,

$\Delta H = H_2 - H_1$ : Enthalpy increase per unit of polymer mass. (J/kg)

$\Delta PE$ : Potential energy increase per unit of polymer mass. (J/kg)

$\Delta KE$ : Kinetic energy increase per unit of polymer mass. (J/kg)

$\Delta Q$ : Net thermal input per unit of polymer mass. (J/kg)

$\Delta W$ : Net mechanical input per unit of polymer mass. (J/kg) (From the motor)

$\Delta PE$  and  $\Delta KE$  contributions are negligible in comparison to  $\Delta H$  in extrusion [11], Expression (3) reduces to:

$$\Delta H = \Delta Q + \Delta W \Rightarrow \Delta Q = \Delta H - \Delta W \quad (4)$$

The heat transfer from the heater is calculated by,

$$\Delta Q = h A (T_{surface} - T_{ave. Scrap}) \quad (5)$$

$T_{surface}$  is the temperature of the heater contact surface with the barrel. Since the target temperature of the ABS scrap is 185°C,  $T_{surface}$  should be a bit higher than that, let's roughly take  $T_{surface} = 200^\circ\text{C}$ . And the average temperature of the ABS scrap throughout the extrusion process is changing from the feed zone to the melt zone. A rough approach is to consider an average value between 20°C and 185°C ( $T_{ave.scrap} = 102,5^\circ\text{C}$ ). A is the heat transfer area of the heater and h is the heat transfer coefficient.

$$A = \pi D_{BO} l \quad (6)$$

where,  $l$  is the length of the heater and  $D_{BO}$  is the heater diameter which can be deduced from the standard heater catalog diameter size. A standard heater diameter of 25 mm is considered in this study [14]. With a clearance of 0.1 mm between the heater and the barrel, the barrel outer diameter is equal to 24.8 mm.

With  $D_B = D + \delta$ , the barrel inner diameter, and extruder screw diameter (D), for  $\delta = 0.002D - 0.005D$  (Clearance screw-barrel) [1, 18]. Taking the upper limit, therefore  $\delta = 0.005 \cdot 20 \text{ mm} \Rightarrow \delta = 0.1 \text{ mm}$ . The inner diameter of the barrel will be then,  $D_B = 20.1 \text{ mm}$ . Hence, the thickness of the barrel shall be 2.35 mm (Assumed enough to withstand the pressure created inside the barrel).

By substituting Expression 6 in Expression 5, we get;

$$\Delta Q = h \pi D_{BO} l (T_{surface} - T_{ave.scrap}) \quad (7)$$

From Expression 4,  $\Delta Q = \Delta H - \Delta W$ ,  $\Delta H$  can be evaluated considering 3 different stages of the process (See Figure 6).

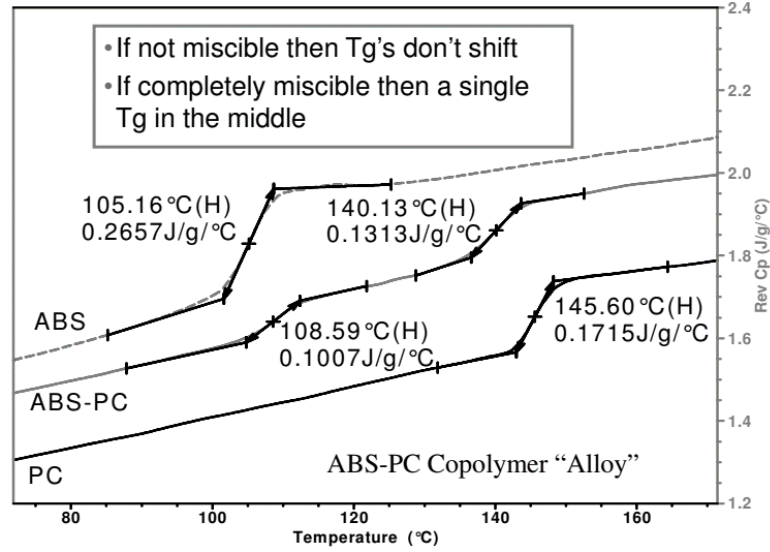


Figure 6. DSC (Differential Scanning Calorimetry) for ABS, PC and ABS-PC [21].

$$\Delta Q = \Delta H - \Delta W = \dot{m} * \bar{c}_{p_{gi}}(T_{gl} - T_i) + \dot{m} * H_g + \dot{m} * \bar{c}_{p_{fg}}(T_f - T_{gr}) \quad (8)$$

The first stage starts from  $T_i$  to a temperature close to  $T_g$  (Glass transition temperature) designated  $T_{gl}$  (l as left), the second stage takes into account the glass transition heat  $H_g$  and the last stage starts a little bit after the glass transition temperature at  $T_{gr}$  (r as right), to the target temperature  $T_f$ . From Figure 6,  $T_{gl} \approx 102^\circ\text{C}$  and  $T_{gr} \approx 108^\circ\text{C}$ .

$\dot{m}$  is the mass flow rate,  $\dot{m} = 0.000252555 \text{ kg/s}$  (By using the volume flow rate and the density)?  $\bar{c}_{p_{gi}}$  is the average specific heat for the first stage,  $\bar{c}_{p_{gi}} \approx 1.6 \text{ J/g}^\circ\text{C}$  (kJ/kg°C).  $\bar{c}_{p_{fg}} \approx 2.05 \text{ J/g}^\circ\text{C}$ .  $H_g = 207 \text{ kJ/kg}$ .

Therefore,

$$\Delta H = 125.28 \text{ W}$$

$$\Delta W = \dot{m} * \frac{\Delta p}{\rho} \quad [12] \quad (9)$$

Therefore,

$$\Delta W = 0.137895 \text{ W}$$

Thus,

$$\Delta Q = \Delta H - \Delta W = 125.14 \text{ W}.$$

Previous studies mentioned that over 40% of the energy supplied to the small-scale extruder is lost without being effectively used (in other words, heating efficiency ( $\eta$ ) is 60%) through drive/transmission losses, radiation, convection, conduction to the surroundings etc. [22]. We should therefore consider these losses in the overall energy calculation. The heat transferred from the heater must be considered as

$$\Delta Q_{\text{real}} = \frac{\Delta Q}{\eta} = 208.6 \text{ W}$$

A similar assumption is valid for the power consumption of the electric motor, therefore,

$$\Delta W_{\text{real}} = \frac{\Delta W}{\eta} = 0.23 \text{ W}$$

From Expression 5, by using  $\Delta Q_{\text{real}}$  found lately,  $l$  the length to be covered by the heater will be:

$$l = \frac{\Delta Q_{\text{real}}}{h \cdot \pi \cdot D_{BO} \cdot (T_{\text{surface}} - T_{\text{ave.scrap}})} \quad (10)$$

By considering an average value of heat transfer coefficient  $h=1100 \text{ W/m}^2\text{K}$  [4] (See Table 1).

$l = 24,7 \text{ mm}$ . (Length of the heater unit).

From the catalog sheet of standard heater having an inner diameter ( $D_{BO}$ ) of 25 mm with a power at least of 208.6 W, Mica heater coded M2530C25A3 providing 250 W with 30 mm of length is more suitable [14].



Figure 7. Mica heater M2525C20A3

In addition, we calculate the power of the driving motor.

#### Power of the screw driving motor

Theoretically speaking, we may be tempted to consider the mechanical power calculated above as the power of the screw driving motor  $\Delta W=0.23 \text{ W}$ . However, the reality is different, providing that the size of a 0.2 W DC motor is too small (Figure 8). A decision should be made from the total power required to melt the plastic, by splitting that power in order to find a standard convenient DC motor to use and a convenient standard heater.

The total power required is  $P = \Delta H = (208.6+0.23) = 208.83 \text{ W}$ . From this total power, the decision to be made will consist of using for example a 100 W DC motor (Figure 9) to drive the screw and 108.83 W for the heater. Attention should be paid for the choice of the driving motor by considering the torque.



Figure 8. 6mm 3.0V DC motor 0.2Watt (Model ZWPD006006-136)



Figure 9. 100 W DC motor (Model SZGH-04010D)

Common motor drives have about 85% of efficiency. Therefore, we should expect 85 W of power transmitted instead of a 100 W DC motor. Thus, the heater to use should have at least 123.83 W of power. For this end, Mica L2535C12A5 (125 W with 35 mm of length) heater would be a right choice.

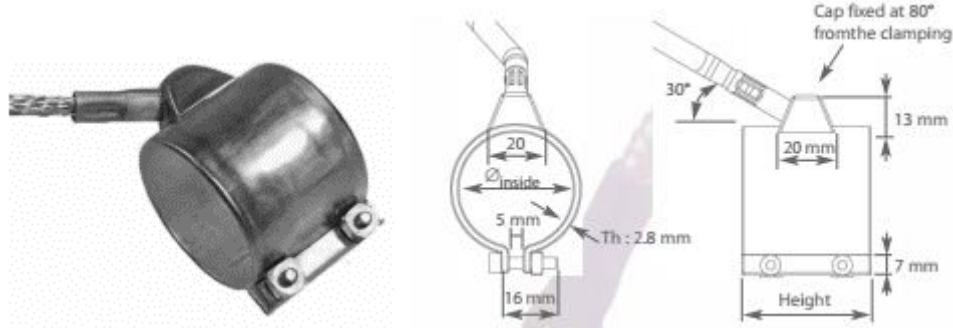


Figure 10. Mica heater L2530C10A5

### Screw additional characteristics

The pitch of the screw

$$p = \pi D \tan \phi \quad [15] \quad (11)$$

$\phi$ : screw channel inclination or helix angle. It is chosen to optimize the feeding characteristics. It's about 17.5° [18].

$$p = \pi D \tan \phi = 19.81 \text{ mm} [15]$$

$$H_f = 0.2D = 4 \text{ mm (Feed section depth)} [15].$$

$$H_m = \frac{H_f}{C.R.} \text{ (Metering section depth)} [15].$$

C.R: Compression ratio. A compression ratio of 2.5:1 to 4:1 is usually used [11]. Considering 2.5:1,  $H_m = 1.6 \text{ mm}$ .

The flight  $e = 0.1 * D = 2 \text{ mm} [15]$ .

The channel width  $W = (p - e) \cos \phi = (\tan \phi - e) \cos \phi = 17 \text{ mm} [15]$ .

To evaluate the screw speed in rpm we use the mass flow rate relation in the screw given by:

$$\text{Rate} = 2.3 D^2 H_m \rho N \quad [11] \quad (12)$$

$\dot{m} = 0.000252555 \text{ kg/s} = 15.15327582 \text{ g/min}$ , equalizing with Rate expression, we get  $N = 9.8 \text{ rpm}$ , a value of 10 rpm can be considered for the screw speed. Therefore, a speed reducer might be necessary providing that most motor are designed with a higher speed range. These characteristics are essential to define the screw.

### Conclusion

This study presented a design of a process for recycling 3D printer ABS plastic scrap to produce ABS filaments to use for printing new components. 1 hour 6 minutes is necessary to recycle 1 kg of ABS scrap with a mass flow rate of 0.252555 g/s. For this end, a screw of 520 mm long, 20 mm of diameter should be used. The heater power of 123.83 W model Mica L2535C12A5 (125 W with 35 mm of length) with a DC motor of 100 W shall be used. The barrel is in Stainless steel with threaded top for the nozzle (die) to be fixed.

The steps presented in this study is a general guide for any other recyclable plastic material. However, we should mention that a more accurate approach would consider the heat transfer coefficient changing value throughout the extrusion process (600-1600 W/m<sup>2</sup> K). For instance, using 1600 W/m<sup>2</sup> K at the beginning of feed zone, decreasing this value stepwise until 600 W/m<sup>2</sup> K in the melt zone. In the same way, instead of considering an average value for the ABS scrap temperature in the barrel, different temperatures, stepwise, starting from 20°C to 185°C would give more accurate results.

This design should be completed with a cooling route. Water cooling is the best solution for this small-scale extruder. The implementation of this study results shall allow to reach a sustainable waste management and make some savings.

### References

- [1] Gyárfás A. & Gergely A. (2019) The Design of a Small-Scale Plastic Extruder Machine, *Műszaki Tudományos Közlemények*, vol. 11, 73–76 <https://doi.org/10.33894/mtk-2019.11.14>.
- [2] Dongoh L. et al. (2018) Development and Evaluation of a Distributed Recycling System 2 For Making Filaments Reused in 3-D Printers, *Journal of Manufacturing Science & Engineering*.
- [3] Lakemeyer C. & Schöppner V. (2014) Temperature calculation for extruder screws with internal heat pipes, *AIP Conference Proceedings*, 1593, 544–548 <https://doi.org/10.1063/1.4873840>
- [4] Maksims B. et al. (2018) Evaluation of Heat Transfer at The Cavity-polymer Interface in Microinjection Moulding Based on Experimental and Simulation Study, *Applied Thermal Engineering*, 130, 865–876. <https://doi.org/10.1016/j.applthermaleng.2017.11.022>.
- [5] Orisaleye JI. (2018) Parametric analysis and design of a screw extruder for slightly non-Newtonian (pseudoplastic) materials, *Engineering Science & Technology, an Int. Journal*, 21, 229-237.
- [6] Van den Berg J.B. et al. (2000) *Thermal Modeling in Polymer Extrusion*, SWI.
- [7] Miftahur R. et al. (2016) Glass Transition of ABS in 3D Printing, *COMSOL Conference*, Boston.
- [8] Amir Sohel Md. (2017) Thermal analysis of ABS/PA6 polymer blend using differential scanning calorimetry, doi 10.1007/s10973-017-6312-6
- [9] Maria de gracia T.G. et al. (2016) Recycling of Acrylonitrile Butadienne Styrene Using Injection Moulding Machine, *Procedia Technology*, 22, 399-406.
- [10] Vera-Sorroche J. et al. (2013) Thermal Optimisation of Polymer Extrusion Using in-process Monitoring Techniques, *Applied Thermal Engineering*, 53, 405-413.
- [11] Nana Levi N. (2012) Energy Analysis of the Extrusion of Plastics (Thesis Plastics Engineering Technology), Arcada University of Applied Sciences, Finland.
- [12] Chamil A. et al. (2014) Process Efficiency in Polymer Extrusion: Correlation Between the Energy Demand and Melt Thermal Stability, *Applied Energy*, 135, 560–571
- [13] David OK. *Plastics Manufacturing Systems Engineering A Systems Approach*, Hanser Publishers, 46-83, Munich.
- [14] Acim J. Mica band heaters catalog, France.
- [15] Vinod Kumar B. et al. (2018) Design and Development of Single Screw Extruding Machine for Bio-Composites, *IJERMCE*, vol. 3. 191-193.
- [16] Carlos B. *Introduction to Polymers (Lecture notes)*, SUNY Buffalo, USA.
- [17] Harold F, John R. (2005) *Extrusion: The Definitive Processing Guide and Handbook*, W Andrew.
- [18] Syed Ali A. (2014) *Thermoforming of Single and Multilayer Laminates*, Elsevier Amsterdam.
- [19] Bishwash N. et al. (2019) *Design and Fabrication of Plastic Extrusion Machine (Final Report)*, Kathmandu University.
- [20] Dynisco, *The Screw and Barrel System (Catalog)*, Franklin, USA.
- [21] Charles P. et al. *Materials Characterization by Thermal Analysis (DSC & TGA), Rheology, and Dynamic Mechanical Analysis*, TA Instruments, Newcastle, USA.
- [22] Chamil A. et al. (2014) Investigation of the process energy demand in polymer extrusion: A brief review and an experimental study, *Applied Energy* 136, 726–737,
- [23] Thomas H. et al. (2015) Simulation of a Downsized FDM Nozzle, <https://www.researchgate.net/publication/292962364>.
- [24] Plabor, *Single Screw Extruder*, Research Laboratory of Plastics Technology Co. Retrieved January 12<sup>th</sup>,2020 from [www.plabor.co.jp/en/products/single/index.html](http://www.plabor.co.jp/en/products/single/index.html)
- [25] Mohammed M. et al (2019) Investigation of closed loop manufacturing with Acrylonitrile Butadiene Styrene (ABS) over multiple generations using Additive Manufacturing, *ACS Sustainable Chemistry & Engineering*, doi: 10.1021/acssuschemeng.9b02368
- [26] *Mechanical Engineering, Extrusion Process Principles*, Retrieved December 14<sup>th</sup>,2020 from <http://mechanicalinventions.blogspot.com/2016/04/plastic-extrusion-process-principles.html>

## Neuro-Regression Approach in Optimization of Predicted Enthalpy of a Refrigeration System with Two-Stage Compression and Intercooling

Alif Ngimbi Diambu\*, İzmir Kâtip Çelebi Univ., Graduate School of Natural and Applied Sciences, Çiğli Main Campus, İzmir, Turkey

Levent Aydın, İzmir Kâtip Çelebi Univ., Department of Mechanical Engineering, İzmir, Turkey

\*Corresponding author: anasroudine1@gmail.com

**Keywords:** Optimization, neuro-regression, refrigeration system, boundedness

**Discipline:** Mechanical Engineering

### Abstract

Two-stage compression and intercooling are one of the enhancements made to refrigeration systems to increase efficiency and reduce the size of installations. When engineers design cooling machines, the goal is not just sizing but also to insure their optimum operation. Therefore, this leads to system optimization. Some design-optimization studies based on regression analysis are found to be misleading in a realistic point of view even if  $R^2$  values of the regression models are quite high. In order to overcome this drawback, the present study performed a hybrid approach based on multiple nonlinear regression-artificial neural networks to measure the accuracy of predictions of objective functions for the enthalpy taking into consideration their realistic characters. For this end,  $R^2_{\text{training}}$  and  $R^2_{\text{testing}}$  check are performed for different models based on the data (Enthalpy values for vapor phase) retrieved from a previous publication on a Refrigeration System with Two-Stage and Intercooler. A subsequent boundedness check allowed to choose the appropriate models for the optimization process using Wolfram Mathematica. First, all the models were analyzed ( $R^2$  training and testing check). After that, the models having high  $R^2_{\text{training}}$  and  $R^2_{\text{testing}}$  values, were also checked whether the functions are bounded or not. It's seen that only one model satisfies the three criteria mentioned above. Hence, this study showed how useful boundedness check is in design modelling and optimization of engineering systems.

### Introduction

Refrigeration cycle systems are used to remove heat from a low-temperature environment and reject it to a high-temperature reservoir (typically ambient air). They are generally designed to operate optimally at a particular maximum cooling load condition, which is termed the 'design point' of the system. However, in practice, these systems are often operated far away from their design point [1]. The pressure difference between evaporation and condensation is low for the simple vapor compression systems. For high temperature or pressure difference, the multi-stage systems should be suggested. In particular, two-stage systems use one refrigerant to optimize the inter-stage conditions [2].

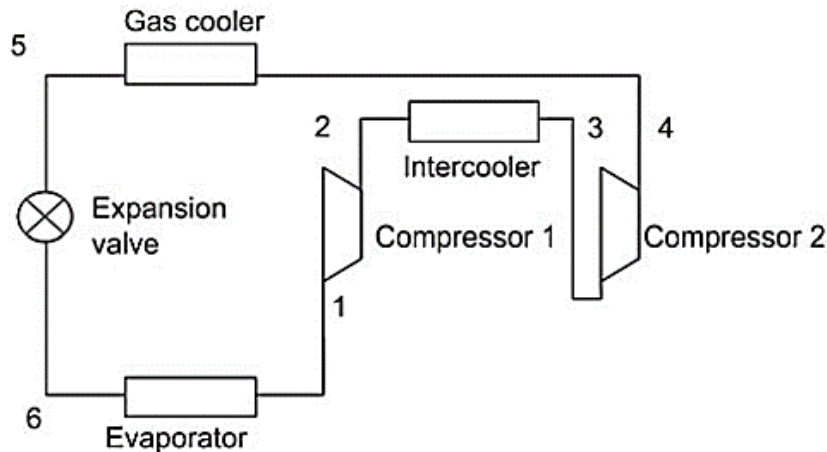


Figure 1. Schematic diagram for a two-stage cycle with inter-cooling [3]

Traditional thermodynamic optimization of refrigeration systems deals with maximizing the coefficient of performance (COP) or minimizing the irreversibility of cycles. Unfortunately, these do not yield a realistic optimum because as you approach the optimum the sizes of the heat exchangers go to infinity [4]. Novel approach of optimization as used in this study deals with constructing mathematical models fitting the best experimental data and optimizing them. Some regression-based design-optimization are found to be misleading in a realistic point of view of results even if  $R^2_{\text{training}}$  and  $R^2_{\text{testing}}$  values are high. The boundedness check of models is a very important further test to perform in order to check if the models are realistic or not. This study presents a hybrid approach combining Artificial Neural Network and regression analysis in Optimization of Predicted Enthalpy a Refrigeration System with Two-Stage Compression and Intercooling.

In the literature, Neera & Andrew, (2011) investigated multiple degree of freedom (MDOF) optimization of steady-state vapor-compression cycle (VCC) operation where five degrees of freedom (DOFs) of the vapor-compression cycle are optimized using an objective function which minimizes the rate of exergy destruction in the cycle. Razavi-Far et al. (2013) investigated on Optimizing the Performance of a Refrigeration System Using an Invasive Weed Optimization Algorithm. They have shown that by using adequate knowledge on plant operation, the plant wide performance can be optimized with respect to a small set of variables. David (2014) on Optimization of Vapor Compression Cycles showed that the only viable objective function for the optimization of cooling systems is the total life cycle costs. In a study by Nejatolahi & Sayyaadi (2011) on Multi-objective optimization of a cooling tower assisted vapor compression refrigeration system, two objective functions including the total exergy destruction of the system (as a thermodynamic criterion) and the total product cost of the system (as an economic criterion), have been considered simultaneously. Ridha et al. (2017) study on Optimization of Absorption Refrigeration Systems by Design of Experiments Method apply the method of experimental design to optimize configurations proposed by the absorption pairs used and the operating conditions by focusing on both acceptable COP and low operating generator temperature. Kılıç, (2017) investigated on Optimization of Refrigeration System with Two-Stage and Intercooler Using Fuzzy Logic and Genetic Algorithm. Pekka et al. (2009) investigated on Optimizing the refrigeration cycle with a two-stage centrifugal compressor and a flash intercooler. The performance of the centrifugal compressor is evaluated based on semi-empirical specific-speed curves and the effect of the Reynolds number, surface roughness and tip clearance have also been taken into account. Aydin et al. (2020) investigated on A Novel Approach for the Optimal Design of a Biosensor. A detailed study on multiple nonlinear neuro-regression analysis has been performed methodically in order to overcome the insufficient approaches on modeling-design-optimization of a biosensor.

In our present study, the boundedness of two candidate models is checked after the calculation of  $R^2_{\text{training}}$  and  $R^2_{\text{testing}}$  values to reveal whether the models are realistic or not. For this end, a study including linear and quadratic neuro-regression analysis to generate objective functions is performed for the enthalpy as output. Finally, the different direct search methods including stochastic optimization algorithms (Modified versions of Differential Evaluation, Nelder-Mead, Random Search and Simulated Annealing algorithms) have been performed methodically.

### Methodology

Neuro-regression approach and different direct search optimization algorithms is used for this study. The process is subdivided into two substeps including modeling and optimization. Any design optimization process starts with defining optimization (Design of variables, Objective function and constraints). Then follows the design of experiments if necessary. For our current study, the design experiments have not been performed providing that inputs and outputs are already set. In the process represented in Figure 2, each subsequent step refers to the previous ones. For any ambiguity the procedure requires to fall back on one of previous steps to fix the issue. The three first steps represent the modeling process and the last three steps the optimization.

The image below is a diagram of the process.

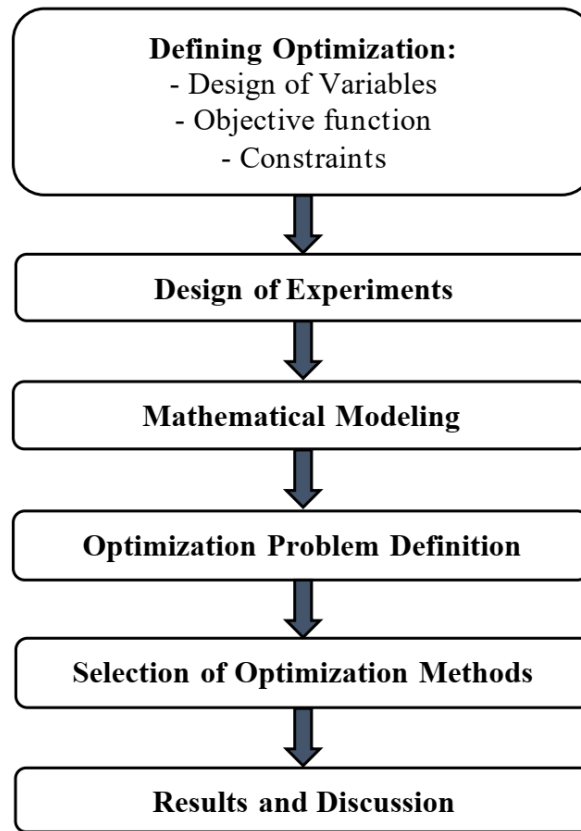


Figure 2. Process diagram of Neuro-regression optimization

### Modelling

A hybrid method is used in the modeling phase in order to test the accuracy of the predictions. This method combines the advantages of regression analysis and Artificial Neural Network (ANN). In this approach, data are split into two sets representing each 80% and 20% of the data set respectively. The first set of the data is used for the training routine while the second set is used for the testing routine.

The general structure of these routines is explained in the following steps:

- Step 1: 80% of data is selected randomly.
- Step 2: Use regression analysis to those data to create a model. Check if  $R^2_{\text{training}}$  is high enough ( $>0.85$  or close to 1). If yes, go to Step 3. If not, use a modified training regression model type or use a higher order function.
- Step 3: Check if  $R^2_{\text{testing}}$  is high enough ( $>0.85$  or close to 1). If yes, go to Step 4. If not, use a modified training regression model type or use a higher order function.
- Step 4: Check the boundedness of the training model. If it's bounded (In an acceptable range depending on expected results), go to optimization. If not, use a modified training regression model type or use a higher order function.



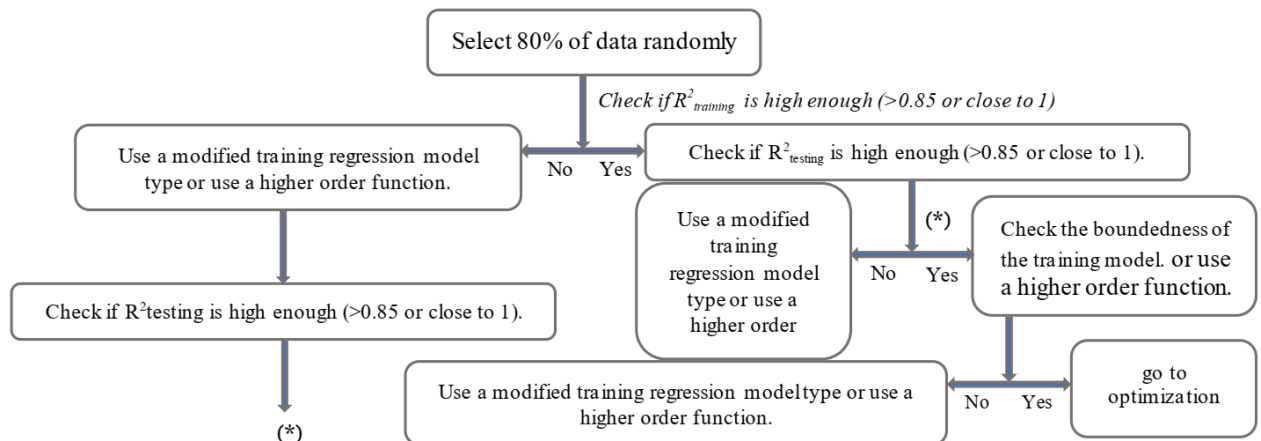


Figure 3. Neuro-regression optimization representative diagram

In the training process, the aim is to minimize the error between the experimental and predicted values by adjusting the regression models and their coefficients. Table 1 summarizes different regression model types including linear, quadratic, trigonometric, logarithmic, and their rational forms.

Boundedness check is performed to see if the model is realistic or not. In this regard, after obtaining the appropriate models in terms of  $R^2_{\text{training}}$  and  $R^2_{\text{testing}}$ , the maximum and minimum values of the models in the given interval for each design variables are calculated to see if it's close to the reality.

Table 1. Multiple regression model types including linear, quadratic, trigonometric, logarithmic, and their rational forms [5]

Model Name	Formula
Multiple linear (L)	$Y = \alpha_0 + \alpha_1 x_1 + \alpha_2 x_2$
Multiple linear rational (LR)	$Y = (\alpha_0 + \alpha_1 x_1 + \alpha_2 x_2) / (\beta_0 + \beta_1 x_1 + \beta_2 x_2)$
Second order multiple nonlinear (SON)	$Y = \alpha_0 + \alpha_1 x_1 + \alpha_2 x_2 + \alpha_3 x_1^2 + \alpha_4 x_2^2 + \alpha_{12} x_1 x_2$
Second order multiple nonlinear rational (SONR)	$Y = (\alpha_0 + \alpha_1 x_1 + \alpha_2 x_2 + \alpha_3 x_1^2 + \alpha_4 x_2^2 + \alpha_{12} x_1 x_2) / (\beta_0 + \beta_1 x_1 + \beta_2 x_2 + \beta_3 x_1^2 + \beta_4 x_2^2 + \beta_{12} x_1 x_2)$
First order trigonometric multiple nonlinear (FOTN)	$Y = \alpha_0 + \alpha_1 \sin x_1 + \alpha_2 \sin x_2 + \alpha_3 \cos x_1 + \alpha_4 \cos x_2$
First order trigonometric multiple nonlinear rational (FOTNR)	$Y = (\alpha_0 + \alpha_1 \sin x_1 + \alpha_2 \sin x_2 + \alpha_3 \cos x_1 + \alpha_4 \cos x_2) / (\beta_0 + \beta_1 \sin x_1 + \beta_2 \sin x_2 + \beta_3 \cos x_1 + \beta_4 \cos x_2)$
Second order trigonometric multiple nonlinear (SOTN)	$Y = \alpha_0 + \alpha_1 \sin x_1 + \alpha_2 \sin x_2 + \alpha_3 \cos x_1 + \alpha_4 \cos x_2 + \alpha_5 \sin^2 x_1 + \alpha_6 \sin^2 x_2 + \alpha_7 \cos^2 x_1 + \alpha_8 \cos^2 x_2$
Second order trigonometric multiple nonlinear rational (SOTNR)	$Y = (\alpha_0 + \alpha_1 \sin x_1 + \alpha_2 \sin x_2 + \alpha_3 \cos x_1 + \alpha_4 \cos x_2 + \alpha_5 \sin^2 x_1 + \alpha_6 \sin^2 x_2 + \alpha_7 \cos^2 x_1 + \alpha_8 \cos^2 x_2) / (\beta_0 + \beta_1 \sin x_1 + \beta_2 \sin x_2 + \beta_3 \cos x_1 + \beta_4 \cos x_2 + \beta_5 \sin^2 x_1 + \beta_6 \sin^2 x_2 + \beta_7 \cos^2 x_1 + \beta_8 \cos^2 x_2)$
First order logarithmic multiple nonlinear (FOLN)	$Y = \alpha_0 + \alpha_1 \ln x_1 + \alpha_2 \ln x_2$
First order logarithmic multiple nonlinear rational (FOLNR)	$Y = (\alpha_0 + \alpha_1 \ln x_1 + \alpha_2 \ln x_2) / (\beta_0 + \beta_1 \ln x_1 + \beta_2 \ln x_2)$
Second order logarithmic multiple nonlinear (SOLN)	$Y = \alpha_0 + \alpha_1 \ln x_1 + \alpha_2 \ln x_2 + \alpha_3 \ln^2 x_1 + \alpha_4 \ln^2 x_2 + \alpha_5 \ln x_1 x_2$
Second order logarithmic multiple nonlinear rational (SOLNR)	$Y = (\alpha_0 + \alpha_1 \ln x_1 + \alpha_2 \ln x_2 + \alpha_3 \ln^2 x_1 + \alpha_4 \ln^2 x_2 + \alpha_5 \ln x_1 x_2) / (\beta_0 + \beta_1 \ln x_1 + \beta_2 \ln x_2 + \beta_3 \ln^2 x_1 + \beta_4 \ln^2 x_2 + \beta_5 \ln x_1 x_2)$

Some useful command in Mathematica presented below was used in the modelling process.

Input = {Enter input or output values separated with commas}: allows to assign input or outvalue to a case named here Input.

Table [expr, {i, Subscript[i, max]}] : generates a list of values of expr when i runs from 1 to Subscript[i, max].

NonlinearModelFit[data, b<sub>0</sub> + b<sub>1</sub> x<sub>1</sub> + b<sub>2</sub> x<sub>2</sub>, {b<sub>0</sub>, b<sub>1</sub>, b<sub>2</sub>}, {x<sub>1</sub>, x<sub>2</sub>}: Generates a nonlinear (or linear) model by replacing suitable coefficients b that represent the best the data set.

Nlm ["SinglePredictionConfidenceIntervalTable"]: For a nonlinear model named "Nlm", this command generates a table of observed data, predicted data, error and confidence interval.

Nlm [{"RSquared", "AdjustedRSquared", "AIC", "BIC"}]: generates Rsquared and adjusted Rsquared value for a nonlinear model.

RSquared testing using SSE and SST.

$$SSE = \sum_{i=1}^5 (\text{RealOutput}[[i]] - \text{testingprediction}[[i]])^2 \quad (1)$$

$$SST = \sum_{i=1}^5 (\text{RealOutput}[[i]] - \text{MeanRealOutP})^2 \quad (2)$$

Both are used for evaluating R<sup>2</sup> testing. SSE (Squared Estimated Error) gives the square of the difference between real testing values and the predicted testing value obtained from the training model. SST (Total Sum of Squares) is the square of the difference between real testing values and their mean.

$$R^2_{\text{Testing}} = 1 - SSE/SST \quad (3)$$

NMaximize and NMinimize: allow to check the boundedness of models. An extension of this command provides the optimization using the syntax:

NMaximize[{Objective function, Constraints }, {Input1,...}, Method→ "DifferentialEvolution, NelderMead, SimulatedAnnealing or RandomSearch"]

### Optimization

An optimization problem is to find a maximizer or minimizer of a given function subject to a given set of constraints that must be satisfied by any solution [6]. Optimization techniques can be classified as traditional and non-traditional. Traditional optimization techniques, such as constrained variation and Lagrange multipliers, are analytical and find the optimum solution of only continuous and differentiable functions [7]. In engineering design problems, traditional optimization techniques cannot be used because of specificity. In these cases, the stochastic optimization (Non-traditional) methods such as genetic algorithms (GA), particle swarm (PS), and simulated annealing (SA) are favorable. Because of the nature of stochastic methods, the exact solution cannot be obtained and using more than one method with a different phenomenological basis for the same optimization problem increases the reliability of the solution [5]. In this study, four different optimization algorithms (MDE, MNM, MSA, MRS) have been selected to solve optimization problems.

The most difficult mathematical optimization problems have the following issues [5]:

1. Multiple nonlinear objective functions
2. Objective functions having many local extremum points
3. Mixed-integer (discrete) - continuous nature of the design variables
4. Nonlinear Constraints.

#### Modified Nelder-Mead Algorithm (MNM)

Nelder-Mead (NM) is one of the simplest direct search methods optimization algorithms since it does not require any derivative information and starts with simplex for minimization of the function. The iteration steps of the Nelder-Mead algorithm are Ordering, Centroid, and Transformation. [5].

#### Modified Differential Evolution Algorithm (MDE)

DE is one of the suitable ways of the stochastic optimization method. It can be used in complex structured composite design problems to find the optimum result. The productive parameters of the DE algorithm are population size, crossover, and scaling factor. It handles a population of solutions instead of iterating over solutions. DE algorithm is proposed as robust and efficient in the literature even it does not satisfy the global optimum points for all optimization problems [5].

### Modified Simulated Annealing Algorithm (MSA)

MSA is based on the physical annealing process of metal is Simulated Annealing. The material moves to a lower energy state throughout the melting process and becomes tougher. Because of the intrinsic structure of the algorithm, it is better at finding the global optimum. It can solve continuous, mixed-integer, or discrete optimization problems [5].

### Modified Random Search Algorithm (MRS)

In the traditional random search algorithm, the first step is to produce a population of random starting points. It uses a local optimization method from each starting point to get closer to a local extremum point at this stage. As a solution, the best local minimum is selected [5].

### Problem Definition

In this section, different steps for Optimization of Predicted Enthalpy a Refrigeration System with Two-Stage Compression and Intercooling are presented. The starting point is the data selection from the paper by Kılıç, B. (2017) on Optimization of Refrigeration System with Two-Stage and Intercooler Using Fuzzy Logic and Genetic Algorithm. Data are presented in Table 2 below. Temperatures and pressures are inputs and enthalpy for vapor phase are outputs. The second step is to check the boundedness related to  $R^2_{\text{training}}$  and  $R^2_{\text{testing}}$  in order to choose the best model (Objective function).

Table 2. Measured data from Solkane software [7]

T (°C)	P (bar)	Vapor Phase Enthalpy measured (kJ/kg)
-24	1.11	384.04
-23	1.16	384.66
-22	1.22	385.28
-21	1.27	385.89
-20	1.33	386.51
-19	1.39	387.12
-18	1.45	387.73
-17	1.51	388.34
-16	1.57	388.95
-15	1.64	389.56
-14	1.71	390.17
-13	1.78	390.77
-12	1.85	391.38
-11	1.93	391.98
-10	2.01	392.58
-9	2.09	393.18
-8	2.17	393.78
-7	2.25	394.37
-6	2.34	394.97
-5	2.43	395.56
-4	2.53	396.15
-3	2.62	396.74
-2	2.72	397.32
-1	2.82	397.91
0	2.93	398.49

Two cases are considered for the optimization:

- The first case is to consider all the data set of inputs (Temperature and pressure) as  $-24^{\circ}\text{C} < T < 0^{\circ}\text{C}$  and  $1.11 \text{ bar} < P < 2.93 \text{ bar}$ .
- The second case is to consider some values of temperatures and pressures from the data set as  $-20^{\circ}\text{C} < T < -3^{\circ}\text{C}$  and  $1.33 \text{ bar} < P < 2.62 \text{ bar}$ .

Outputs are Enthalpies H for vapor phases.

### Results and Discussion

Different regression models for optimizing the outputs of the considered refrigeration system are used. Two cases were discussed. One taking into consideration all the data set  $-24^{\circ}\text{C} < T < 0^{\circ}\text{C}$  and  $1.11 \text{ bar} < P < 2.93 \text{ bar}$ , and the other one isolating a set inside the big set  $-20^{\circ}\text{C} < T < -3^{\circ}\text{C}$  and  $1.33 \text{ bar} < P < 2.62 \text{ bar}$ .

Results have shown that both linear and second order nonlinear model exhibit good  $R^2$  values. However, second order model is more stable providing that it gives more accurate results. This can be seen from the boundedness check of the models from Table 3 and in Table 4, results provided by the linear model is contradictory. The slope of the enthalpy is positive (Values increase for increasing temperature and pressure), surprisingly, the linear model exhibits an opposite behavior. While the temperature and enthalpy increase, optimized values of the pressure decrease. Second order model fit the best the expected results.

Table 3. Results of selected models

	Model	Vapor phase			
		$R^2_{\text{training}}$	$R^2_{\text{testing}}$	$H_{\text{vap.max}}$	$H_{\text{vap.min}}$
1.	$400.407 + 0.651637 x_1 - 0.653087 x_2$	0.999	0.999	399.682	382.854
2.	$397.958 + 0.590939 x_1 - 0.000341096 x_1^2 + 0.217937 x_2 - 0.00886466 x_1 x_2 - 0.0121391 x_2^2$	0.999	0.999	398.492	384.042

Table 4. Optimization results using different proposed cases and optimization algorithms

Objective function	Case	Constraints	Optim.Alg.	Enthalpy Vapor	Suggested design
L	1	$-24^{\circ}\text{C} < T < 0^{\circ}\text{C}$ and $1.11 \text{ bar} < P < 2.93 \text{ bar}$ .	MNM	399.682	$x_1 \rightarrow 0., x_2 \rightarrow 1.11$
			MDE	399.682	$x_1 \rightarrow 0., x_2 \rightarrow 1.11$
			MSA	399.682	$x_1 \rightarrow 0., x_2 \rightarrow 1.11$
			MRS	399.682	$x_1 \rightarrow 0., x_2 \rightarrow 1.11$
	2	$-20^{\circ}\text{C} < T < -3^{\circ}\text{C}$ and $1.33 \text{ bar} < P < 2.62 \text{ bar}$ .	MNM	397.583	$x_1 \rightarrow -3., x_2 \rightarrow 1.33$
			MDE	397.583	$x_1 \rightarrow -3., x_2 \rightarrow 1.33$
			MSA	397.583	$x_1 \rightarrow -3., x_2 \rightarrow 1.33$
			MRS	397.583	$x_1 \rightarrow -3., x_2 \rightarrow 1.33$
SON	1	$-24^{\circ}\text{C} < T < 0^{\circ}\text{C}$ and $1.11 \text{ bar} < P < 2.93 \text{ bar}$ .	MNM	398.492	$x_1 \rightarrow 0., x_2 \rightarrow 2.93$
			MDE	398.492	$x_1 \rightarrow 0., x_2 \rightarrow 2.93$
			MSA	398.492	$x_1 \rightarrow 0., x_2 \rightarrow 2.93$
			MRS	398.492	$x_1 \rightarrow 0., x_2 \rightarrow 2.93$
	2	$-20^{\circ}\text{C} < T < -3^{\circ}\text{C}$ and $1.33 \text{ bar} < P < 2.62 \text{ bar}$ .	MNM	396.739	$x_1 \rightarrow -3., x_2 \rightarrow 2.62$
			MDE	396.739	$x_1 \rightarrow -3., x_2 \rightarrow 2.62$
			MSA	396.739	$x_1 \rightarrow -3., x_2 \rightarrow 2.62$
			MRS	396.739	$x_1 \rightarrow -3., x_2 \rightarrow 2.62$

### Conclusion

In this study, Optimization of Predicted Enthalpy of a Refrigeration System with Two-Stage Compression and Intercooling using Neuro-regression approach was investigated. The study has shown that boundedness check is a very important step in optimization. The best model to fit the experiments

data has a more realistic boundedness (Very close to the experiments values). At  $-24^{\circ}\text{C}$  for instance, the enthalpy of vapor phase at 1.11 bar is 384.04 kJ/kg. When predicted data of the enthalpy for the second order model gives 384.042 kJ/kg at the same temperature, the linear model gives 382.854 kJ/kg, which is a major difference for this case study. Even if  $R^2$  values are high, it doesn't allow to make the last decision on whether the model is appropriate or not. Four different optimization algorithms were used for the optimization. The results provided by these algorithms were the same for each specific case studied. It's found that a second order function is more appropriate for optimization.

### References

- [1] Neera J, Andrew G. (2011) Thermodynamics-Based Optimization and Control of Vapor-Compression Cycle Operation: Optimization Criteria, 2011 American Control Conference, San Francisco, CA, USA.
- [2] Mancuhan E. (2019) Comparative evaluation of a two-stage refrigeration system with flash intercooling using different refrigerants, Thermal Science, doi: 10.2298/TSCI180921011M.
- [3] Shilliday, J. et al. (2009) Comparative Energy and Exergy Analysis of R744, R404a and R290 Refrigeration Cycles, International Journal of Low-carbon Technologies, doi: 10.1093/ijlct/ctp014
- [4] David, C. (2014) Optimization of Vapor Compression Cycles, 121st ASEE Annual Conference & Exposition, Indianapolis.
- [5] Aydin, L. et al. (2020) A Novel Approach for the Optimal Design of a Biosensor, Analytical Letters, doi: 10.1080/00032719.2019.1709075
- [6] Fukuda K. (2011) Introduction to Optimization, Institute for Operations Research, and Institute of Theoretical Computer Science, ETH Zurich, Switzerland.
- [7] Aydin, L. et al. (2016) Design of dimensionally stable composites using efficient global optimization method, Journal of Materials: Design and Applications, 1–13, doi: 10.1177/1464420716664921.
- [8] Nejatolahi, M. & Sayyaadi, H. (2010) Various Criteria in Optimization of a Vapor Compression Refrigeration System, ASME 2010 10th Biennial Conference on Engineering Systems Design and Analysis, doi:10.1115/ESDA2010-24510.
- [9] Razavi-Far, R. et al. (2013) Optimizing the Performance of a Refrigeration System Using an Invasive Weed Optimization Algorithm, Smart Innovation, Systems and Technologies, doi: 10.1007/978-3-642-36651-2\_5.
- [10] Kılıç, B. (2017) Optimization of Refrigeration System with Two-Stage and Intercooler Using Fuzzy Logic and Genetic Algorithm. International Journal of Engineering & Applied Sciences (IJEAS), 9, 42-54, <http://dx.doi.org/10.24107/ijeas.290336>.
- [11] Nejatolahi, M. & Sayyaadi, H. (2011) Multi-Objective Optimization of a Cooling Tower Assisted Vapor Compression Refrigeration System, International Journal of Refrigeration, 34, 243-256, doi:10.1016/j.ijrefrig.2010.07.026.
- [12] Ridha, B. et al. (2017) Optimization of Absorption Refrigeration Systems by Design of Experiments Method, International Conference on Materials and Energy, 139, 280-287, 10.1016/j.egypro.2017.11.209.
- [13] Pekka, R. et al. (2009) Optimising the refrigeration cycle with a two-stage centrifugal compressor and a flash intercooler, International Journal of Refrigeration, 32, 1366-1375, doi:10.1016/j.ijrefrig.2009.01.006.

## Cross Akışkanın Sınır Tabakası Denklemleri ve Benzerlik Çözümleri

Yiğit Aksoy\*, Manisa Celal Bayar Üniv., Makine Mühendisliği Bölümü, Manisa, Türkiye  
Hikmet Sümer, Manisa Celal Bayar Üniv., Makine Mühendisliği Bölümü, Manisa, Türkiye  
\*İletişimden sorumlu yazar: ygtaksoy@gmail.com

**Anahtar Kelimeler:** Newtonyen olmayan akışkan, non-Newtonyen, sınır tabakası akışı, benzerlik çözümleri  
**Disiplin:** Makine Mühendisliği

### Özet

Bu çalışmada sonsuzdan gelen uniform bir Newtonyen olmayan akışkanın akışa paralel hareketsiz plaka üzerindeki viskoz davranışı analitik yollar ile incelenecektir. Newtonyen olmayan akış düzlemsel plakaya temas ettikten sonra uniform hız profili bozulacak ve sürtünmeli akış gereği mekana göre değişen hız profiline sahip olacaktır. Bu davranışın değişimini inceleyebilmek için laminer ve kararlı iki boyutlu momentum sınır tabakası denklemleri Newtonyen olmayan Cross akışkan modeli üzerinden kartezyen koordinatlarda türetilmiştir. Özünde kısmi diferansiyel olan bu denklemlerin simetrisi hesaplanarak elde edilen benzerlik değişkenleri ile adi diferansiyel formda benzerlik sınır tabakası denklemleri elde edilmiştir. Denklemlerin çözümü için Matlab altında bir sonlu farklar algoritması kullanan bvp4c komutu kullanılmıştır. Çözümlerin sayısal verileri ile çizilen grafikler ile sistemi tanımlayan boyutsuz parametrelerin sınır tabakası kalınlığı üzerindeki etkileri tartışılmıştır.

### Giriş

Newtonyen akışkan tanımının akışkanlar mekaniğinin gelişmesi ile eksik veya kısıtlayıcı olduğu araştırmacılar tarafından fark edilmiş ve “akma davranışı” gösteren klasik tanıma uymayan katı veya akışkan cisimler için reoloji [1] yani “akışın bilimi” geliştirilmiştir. Bundan dolayı çoğunlukla katılar ve akışkanlar arasındaki çizgi kesin olmamakla beraber, katı bir cisim olduğu halde akışkan davranışı gösteren veya akışkan olup da bazı özel durumlarda katı cisim haline dönüşen cisimler gözlemlenebilir. Bu durum sıcaklık değişiminden dolayı gerçekleşen faz dönüşümlerinden farklıdır. Örneğin bir dış macunu, tüp içerisinde ya da dış fırçasının üzerinde katı cisim halindeyken, tüp sıkıldığında ya da fırçalarken akışkan hale gelir. Bu yüzden doğada gözlemlenen çoğu akışkan doğrusal kayma gerilmesi-deformasyon hızı ilişkisine sahip Newtonyen davranışa uymamaktadır. Bu davranışa uymayan akışkanlara Newtonyen olmayan (non-Newtonyen) akışkan denir. Newtonyen akışkanlar, doğrusal kayma gerilmesi deformasyon hızı ilişkisi sonucu ortaya çıkan sabit viskoziteye sahipken, Newtonyen olmayan akışkanların tümü için böyle bir doğrusal ilişkiden veya sabit viskoziteden bahsedilmez. Bu çalışma kapsamında incelenecek olan akışkan tipi non-Newtonyen özelliğini doğrusal olmayan kayma gerilmesi deformasyon hızı ilişkisine borçlu olduğu için viskozitenin sabit değil, deformasyon hızına bağlı olduğu ‘genelleştirilmiş Newtonyen akışkan’ (GNA) modelleri [2] üzerinde durulacaktır. Söz konusu akışkan modeli aşağıdaki Cross [3] formülü olup oldukça geniş deformasyon hızı aralıklarında görünür (değişken) viskozite tahmininde başarılı sonuçlar vermektedir.

$$\mu(|\dot{\gamma}|) = \mu_{\infty} + \frac{\mu_0 - \mu_{\infty}}{1 + \eta|\dot{\gamma}|^n} \quad (1)$$

Burada  $\mu$  görünür viskozite,  $|\dot{\gamma}|$  deformasyon hızlarını içeren tensörün şiddeti,  $\mu_0$  ve  $\mu_{\infty}$  çok düşük ve yüksek deformasyon hızlarındaki viskozite değerleri olmakla birlikte,  $\eta$  ise zaman sabiti olup limit viskozite değerleri arasındaki geçiş bölgesinin karakterini belirler. Benzer şekilde  $n$  power-law sabitidir.

### Problemın Fiziksel Tanımı

Sonsuzdan  $x^*$  koordinatı doğrultusunda gelen sürtünmesiz  $U_{\infty}$  üniform hız profiline sahip sıkıştırılamaz akış, kendisine paralel yerleştirilmiş hareketsiz  $L$  uzunluğundaki plakaya temas ettikten sonra kaymama şartı gereği hızı sıfırlanmakta ve plakaya dik koordinatı temsil eden  $y^*$  koordinatı boyunca hızını artırarak tekrar  $U_{\infty}$  hızını yakalamaktadır. Hızın sıfır olduğu plaka üzerindeki bir nokta ile bu noktaya dik doğrultuda akışkanın  $U_{\infty}$  hızını yakaladığı mesafe,  $y^*$  koordinatında oldukça dar bir mesafe işgal etmekte ve  $x^*$  doğrultusunda artmakla birlikte plaka üzerinde belirli bir mesafeden sonra değişim durmaktadır. Değişken hız profilinin gözlemlendiği bu dar bölgeye sınır tabakası denir ve

dışarıda kalan bölgeler sürtünmesiz kabul edilip, momentum denklemleri sadece bu bölge için tanıma uygun fiziksel kabuller ile sadeleştirilir. Benzer şekilde basitleştirilmiş momentum denklemlerine sınır tabakası denklemleri denir.

### Yönetici Denklemler

Akışkan modelinden ya da diğer bir deyişle kayma gerilmesi fonksiyonundan bağımsız olarak kartezyen koordinat bileşenleri  $x^*$  ve  $y^*$  momentum denklemleri iki boyutta şu şekilde verilir.

$$\rho \left[ u^* \frac{\partial}{\partial x^*} + v^* \frac{\partial}{\partial y^*} \right] u^* = -\frac{\partial P}{\partial x^*} + \frac{\partial}{\partial x^*} \tau_{xx} + \frac{\partial}{\partial y^*} \tau_{xy} \quad (2)$$

$$\rho \left[ u^* \frac{\partial}{\partial x^*} + v^* \frac{\partial}{\partial y^*} \right] v^* = -\frac{\partial P}{\partial y^*} + \frac{\partial}{\partial x^*} \tau_{xy} + \frac{\partial}{\partial y^*} \tau_{yy} \quad (3)$$

Burada  $\rho$  akışkanın yoğunluğu,  $P$  basınç,  $\tau_{xx}$ ,  $\tau_{yy}$ ,  $\tau_{xy}$  ise  $\tau$  kayma gerilmesi tensörünün ilgili doğrultulardaki bileşenleridir. Deformasyon hızlarını içeren  $\dot{\gamma}$  tensörünün şiddeti aşağıdaki şekilde hesaplanır.

$$|\dot{\gamma}| = \left( 2 \left( \frac{\partial u^*}{\partial x^*} \right)^2 + 2 \left( \frac{\partial v^*}{\partial y^*} \right)^2 + \left( \frac{\partial v^*}{\partial x^*} + \frac{\partial u^*}{\partial y^*} \right)^2 \right)^{\frac{1}{2}} \quad (4)$$

Yukarıdaki ifade Denklem (1)' e yerleştirilirse görünür viskozite Cross akışkan için

$$\mu |\dot{\gamma}| = \mu_{\infty} + (\mu_0 - \mu_{\infty}) \left( 1 + \eta \left( 2 \left( \frac{\partial u^*}{\partial x^*} \right)^2 + 2 \left( \frac{\partial v^*}{\partial y^*} \right)^2 + \left( \frac{\partial v^*}{\partial x^*} + \frac{\partial u^*}{\partial y^*} \right)^2 \right)^{\frac{n}{2}-1} \quad (5)$$

olarak elde edilir.  $\tau = \mu(|\dot{\gamma}|) \dot{\gamma}$  olduğunu hatırlatarak Denklem (2) ve (3) için aşağıdaki kayma gerilmeleri hesaplanır.

$$\tau_{xx} = 2 \left( \mu_{\infty} + (\mu_0 - \mu_{\infty}) \left( 1 + \eta \left( 2 \left( \frac{\partial u^*}{\partial x^*} \right)^2 + 2 \left( \frac{\partial v^*}{\partial y^*} \right)^2 + \left( \frac{\partial v^*}{\partial x^*} + \frac{\partial u^*}{\partial y^*} \right)^2 \right)^{\frac{n}{2}-1} \right) \frac{\partial u^*}{\partial x^*} \quad (6)$$

$$\tau_{xy} = \left( \mu_{\infty} + (\mu_0 - \mu_{\infty}) \left( 1 + \eta \left( 2 \left( \frac{\partial u^*}{\partial x^*} \right)^2 + 2 \left( \frac{\partial v^*}{\partial y^*} \right)^2 + \left( \frac{\partial v^*}{\partial x^*} + \frac{\partial u^*}{\partial y^*} \right)^2 \right)^{\frac{n}{2}-1} \right) \left( \frac{\partial v^*}{\partial x^*} + \frac{\partial u^*}{\partial y^*} \right) \quad (7)$$

$$\tau_{yy} = 2 \left( \mu_{\infty} + (\mu_0 - \mu_{\infty}) \left( 1 + \eta \left( 2 \left( \frac{\partial u^*}{\partial x^*} \right)^2 + 2 \left( \frac{\partial v^*}{\partial y^*} \right)^2 + \left( \frac{\partial v^*}{\partial x^*} + \frac{\partial u^*}{\partial y^*} \right)^2 \right)^{\frac{n}{2}-1} \right) \frac{\partial v^*}{\partial y^*} \quad (8)$$

Burada  $\tau$  tensörü simetrik olması dolayısıyla  $\tau_{xy} = \tau_{yx}$  olduğu belirtilmelidir. Genellikle yukarıda verilen kayma gerilmeleri Denklem (2) ve (3)' e yerleştirilerek sıkıştırılmaz ve daimî Cross akışkanı için iki boyutlu kartezyen koordinatlarda en genel momentum denklemleri hesaplanıp, sınır tabakası basitleştirmeleri bu denklemler üzerinde yürütülebilir. Ancak sınır tabakasının basitleştirici kabullerinin doğrudan yukarıdaki eşitliklere de uygulanabileceği bir sonraki kısımda gösterilecektir. Son olarak momentum korunumuna ek olarak kütle korunumu gereği süreklilik denklemi kartezyen koordinatlar iki boyutlu sıkıştırılmaz daimî bir akış için şu şekilde verilir.

$$\frac{\partial u^*}{\partial x^*} + \frac{\partial v^*}{\partial y^*} = 0 \quad (9)$$

### Sınır Tabakası Denklemleri

Sınır tabakası daha önce değindiğimiz gibi değişimin gerçekleştiği dar bir bölgeyi temsil etmektedir. Bu değişimin gerçekleştiği dar bölgeye ilişkin kabuller GNA modelleri için devasa büyüklükteki

momentum denklemlerini ciddi şekilde basitleştirir. Kısaca bu kabuller ve ilişkili matematiksel hallerine değinelim. Sınır tabakası kalınlığı  $\delta^*$  oldukça küçük bir büyüklüktür,  $\delta^* \ll 1$ . Dolayısıyla  $y^*$  koordinatı da çok küçük olmalıdır ya da diğer bir değişle  $y^*$ ,  $\delta^*$  mertebesinde,  $y^* \sim O(\delta^*)$ .  $x^*$  koordinatı ise küçük olmamakla birlikte 1 mertebesinde,  $x^* \sim O(1)$ . Kütle korunumunda mertebeli ihlali olmaması için  $u^* \sim O(1)$  ve  $v^* \sim O(\delta^*)$  olması gerektiği hemen görülür. Bu kabuller ışığında kayma gerilmelerinin içinde bulunan aşağıdaki kısmi türevlerin mertebeleri hakkında sonuçlar çıkarılabilir.

$$\frac{\partial u^*}{\partial x^*} \sim O(1), \frac{\partial u^*}{\partial y^*} \sim O\left(\frac{1}{\delta^*}\right), \frac{\partial v^*}{\partial x^*} \sim O(\delta^*) \quad (10)$$

Bu kabuller yapılırken  $\delta^* \ll 1$  olduğundan  $\frac{1}{\delta^*} \gg 1 \gg \delta^*$  şeklinde bir mertebeli hiyerarşinin olduğu unutulmamalıdır. Benzer hiyerarşiler Denklem (10) ile ele alınıp Denklem (5)' de verilen görünür viskozite fonksiyonuna uygulanır ve en büyük mertebeye sahip terimler tutulup diğer terimler elde edilirse

$$\mu(\dot{\gamma}) = \mu_\infty + (\mu_0 - \mu_\infty) \left(1 + \eta \left|\frac{\partial u^*}{\partial y^*}\right|^n\right)^{-1} \quad (11)$$

şeklinde sınır tabakasının içi için geçerli basitleştirilmiş görünür viskozite fonksiyonu elde edilir. Aynı kabuller ile Denklem (6-8) verilen kayma gerilmesi bileşenleri şu hallerde basitleştirilir.

$$\tau_{xx} = 2 \left( \mu_\infty + (\mu_0 - \mu_\infty) \left(1 + \eta \left|\frac{\partial u^*}{\partial y^*}\right|^n\right)^{-1} \right) \frac{\partial u^*}{\partial x^*} \quad (12)$$

$$\tau_{xy} = \left( \mu_\infty + (\mu_0 - \mu_\infty) \left(1 + \eta \left|\frac{\partial u^*}{\partial y^*}\right|^n\right)^{-1} \right) \frac{\partial u^*}{\partial y^*} \quad (13)$$

$$\tau_{yy} = 2 \left( \mu_\infty + (\mu_0 - \mu_\infty) \left(1 + \eta \left|\frac{\partial u^*}{\partial y^*}\right|^n\right)^{-1} \right) \frac{\partial v^*}{\partial y^*} \quad (14)$$

Denklem (2)'de her terimin mertebesi incelendiğinde ilk kayma gerilmesi teriminin ikinciye göre ihmal edilebilir olduğu fark edilir ve  $x^*$  momentum eşitliği

$$\rho \left[ u^* \frac{\partial}{\partial x^*} + v^* \frac{\partial}{\partial y^*} \right] u^* = - \frac{\partial p}{\partial x^*} + \frac{\partial}{\partial y^*} \tau_{xy} \quad (15)$$

haline indirgenir. Bu eşitliğe Denklem (13)' de verilen  $\tau_{xy}$  yerleştirilirse

$$\rho \left( u^* \frac{\partial u^*}{\partial x^*} + v^* \frac{\partial u^*}{\partial y^*} \right) = - \frac{\partial p}{\partial x^*} + \frac{\partial^2 u^*}{\partial y^{*2}} \left( \eta_\infty + (\eta_0 - \eta_\infty) \frac{1 - \eta n \left|\frac{\partial u^*}{\partial y^*}\right|^n \left(1 + \eta \left|\frac{\partial u^*}{\partial y^*}\right|^n\right)^{-1}}{1 + \eta \left|\frac{\partial u^*}{\partial y^*}\right|^n} \right) \quad (16)$$

elde edilir. Yukarıdaki denklemi boyutsuz hale getirebilmek için aşağıdaki boyutsuz parametreleri tanımlayalım.

$$\delta = \frac{\delta^*}{L}, u = \frac{u^*}{U_\infty}, v = \frac{v^*}{\delta U_\infty}, x = \frac{x^*}{L}, y = \frac{y^*}{\delta L} \text{ ve } p = \frac{P}{\rho U_\infty^2} \quad (17)$$

Bu değişkenler cinsinden Denklem (16) aşağıdaki hale gelir.

$$u \frac{\partial u}{\partial x} + v \frac{\partial u}{\partial y} = - \frac{\partial p}{\partial x} + \frac{\partial^2 u}{\partial y^2} \left( \frac{\eta_\infty}{\delta^2 U_\infty L \rho} + \frac{(\eta_0 - \eta_\infty)}{\delta^2 U_\infty L \rho} \frac{1 - \frac{\eta n U_\infty^n}{\delta^n L^n} \left|\frac{\partial u}{\partial y}\right|^n \left(1 + \frac{\eta U_\infty^n}{\delta^n L^n} \left|\frac{\partial u}{\partial y}\right|^n\right)^{-1}}{1 + \frac{\eta U_\infty^n}{\delta^n L^n} \left|\frac{\partial u}{\partial y}\right|^n} \right) \quad (18)$$

Bu denklemdeki katsayılar boyutsuz olmakla birlikte aşağıdaki şekilde tanımlayalım.



$$\epsilon_1 = \frac{\eta_0}{U_\infty L \rho}, \quad \epsilon_2 = \frac{\eta_\infty}{U_\infty L \rho} \quad \text{ve} \quad \epsilon_3 = \frac{\eta U_\infty^n}{L^n} \quad (19)$$

Yukarıdaki boyutsuz katsayılar cinsinden Denklem (18)

$$u \frac{\partial u}{\partial x} + v \frac{\partial u}{\partial y} = -\frac{\partial p}{\partial x} + \frac{\partial^2 u}{\partial y^2} \left( \frac{\epsilon_2}{\delta^2} + \frac{(\epsilon_1 - \epsilon_2) 1 - \frac{n \epsilon_3}{\delta^n} \left| \frac{\partial u}{\partial y} \right|^n \left( 1 + \frac{\epsilon_3}{\delta^n} \left| \frac{\partial u}{\partial y} \right|^{n-1} \right)}{\delta^2 \left( 1 + \frac{\epsilon_3}{\delta^n} \left| \frac{\partial u}{\partial y} \right|^n \right)} \right) \quad (20)$$

şeklinde düzenlenir. Yukarıdaki denklemde sol taraftaki terimler ivme terimleri olup  $O(1)$  mertebesindedirler. Ancak sağ taraftaki  $1/\delta^2$  diğer terimlere göre çok küçük olup önceki kısımlardaki gibi ihmal edilmesi gerekir. Bu sınır tabakası içinde gerçekleşen bir akış için çok doğru bir önerme olmaz. Dolayısıyla bu ivme terimlerinin kaybolmaması için sağdaki terimlerin de 1 mertebesi olması gerekir, yani  $\epsilon_1 \sim O(\delta^2)$ ,  $\epsilon_2 \sim O(\delta^2)$  ve  $\epsilon_3 \sim O(\delta^n)$ . Bu nedenle  $\epsilon_1 = \delta^2 k_1$ ,  $\epsilon_2 = \delta^2 k_2$  ve  $\epsilon_3 = \delta^n k_3$  dönüşümlerini yaparsak  $x^*$  momentum denkleminin son hali

$$u \frac{\partial u}{\partial x} + v \frac{\partial u}{\partial y} = -\frac{\partial p}{\partial x} + \frac{\partial^2 u}{\partial y^2} \left( k_2 + (k_1 - k_2) \frac{1 - n k_3 \left| \frac{\partial u}{\partial y} \right|^n \left( 1 + k_3 \left| \frac{\partial u}{\partial y} \right|^{n-1} \right)}{1 + k_3 \left| \frac{\partial u}{\partial y} \right|^n} \right) \quad (21)$$

şeklini alır.  $x^*$  momentum denkleminin üzerinde uygulanan sınır tabakası kabullerinden gelen  $\eta_0 \sim O(\delta^{*2})$ ,  $\eta_\infty \sim O(\delta^{*2})$  ve  $\eta \sim O(\delta^{*n})$  sonuçları gereği  $y^*$  yönündeki momentum denkleminin boyutsuz son hali aşağıdaki şekilde elde edilir.

$$\frac{\partial p}{\partial y} = 0 \quad (22)$$

Bu sonuç bize basıncın sadece plaka doğrultusunda değiştiğini söyler, kısaca  $p = p(x)$ ' dir. Potansiyel yani sürtünmesiz teori gereği sonsuzdaki akış için Bernoulli denkleminde aşağıdaki şekilde basınç hesaplanır.

$$p = -\frac{1}{2} U_\infty^2 + \text{sabit} \quad (23)$$

Bu ifadenin  $x'$  e göre türevi alınırsa,

$$\frac{dp}{dx} = -U_\infty \frac{dU_\infty}{dx} \quad (24)$$

hesaplanır. Bu ifade Denklem (21)' e yerleştirilirse sınır tabakası içerisindeki  $x$  doğrultusundaki aşağıdaki boyutsuz momentum denklemi elde edilir.

$$u \frac{\partial u}{\partial x} + v \frac{\partial u}{\partial y} = U_\infty \frac{dU_\infty}{dx} + \frac{\partial^2 u}{\partial y^2} \left( k_2 + (k_1 - k_2) \frac{1 - n k_3 \left| \frac{\partial u}{\partial y} \right|^n \left( 1 + k_3 \left| \frac{\partial u}{\partial y} \right|^{n-1} \right)}{1 + k_3 \left| \frac{\partial u}{\partial y} \right|^n} \right) \quad (25)$$

Süreklilik denklemi aşağıdaki şekilde boyutsuz olarak yazılır.

$$\frac{\partial u}{\partial x} + \frac{\partial v}{\partial y} = 0 \quad (26)$$

Problemin sınır şartları: plaka üzerinde akışkanın hız bileşenleri kaymama koşulu gereği sıfırdır;  $u^*(x^*, 0) = v^*(x^*, 0) = 0$ . Yeteri kadar plakadan yukarıda akışkan hızının  $x^*$  bileşeni sonsuzdan gelen akışın hızına eşittir;  $u^*(x^*, \infty) = U_\infty$ . Bu şartın gerçekleşmesi ile alakalı olarak akışkan hızının  $x^*$

bileşeni yönündeki artışın durması ise  $\partial u^*/\partial y^*(x^*, \infty) = 0$  olarak ifade edilir. Tüm bu şartların boyutsuz karşılıkları aşağıdaki şekilde hesaplanır.

$$u(x, 0) = v(x, 0) = 0, u(x, \infty) = 1 \text{ ve } \frac{\partial u}{\partial y}(x, \infty) = 0 \quad (27)$$

Bundan sonraki kısımda kısmi diferansiyel formda olan bu denklemler benzerlik dönüşümleri ile adi diferansiyel forma indirgenecektir.

### Denklemlerin Simetrileri ve Benzerlik Dönüşümleri

Sınır tabakası denklemleri aşağıdaki Lie grup dönüşümlerinin [4] özel bir hali olan ölçekleme dönüşümleri altında invaryant (değişmez) kaldıklarını kabul edelim.

$$\bar{x} = e^a x, \bar{y} = e^b y, \bar{u} = e^c u, \bar{v} = e^d v, \bar{U}_\infty = e^\epsilon U_\infty \quad (28)$$

Burada  $a, b, c, d, \epsilon$  ölçekleme dönüşümüne ait parametrelerdir. Yukarıdaki yeni değişkenlerin bir önceki kısımda verilen sınır tabakası ve süreklilik denklemlerine yerleştirilir ve ölçekleme parametrelerinin hangi değerlerinde orijinal denklemlerin aynısı elde edileceği araştırılırsa ;

$$e = c, b = c, a = 3c, d = -c \quad (29)$$

olması gerektiği bulunur. Simetriler ve orijinal değişkenler arasında aşağıdaki diferansiyel formların eşitliği ilkesi aşağıdaki şekilde yazılabilir.

$$\frac{d\bar{x}}{a\bar{x}} = \frac{d\bar{y}}{b\bar{y}} = \frac{d\bar{u}}{c\bar{u}} = \frac{d\bar{v}}{d\bar{v}} = \frac{d\bar{U}_\infty}{\epsilon\bar{U}_\infty} \text{ veya } \frac{d\bar{x}}{3\bar{x}} = \frac{d\bar{y}}{\bar{y}} = \frac{d\bar{u}}{\bar{u}} = \frac{d\bar{v}}{-\bar{v}} = \frac{d\bar{U}_\infty}{\bar{U}_\infty} \quad (30)$$

Yukarıdaki son ifadeden kısmi diferansiyel denklemleri adi denkleme indirmek için gerekli benzerlik değişkeni ve benzerlik fonksiyonları aşağıdaki şekilde elde edilir, detaylar için [5].

$$\xi = x^{-\frac{1}{3}}y, f(\xi) = x^{-\frac{1}{3}}\bar{u}, g(\xi) = x^{\frac{1}{3}}\bar{v} \text{ ve } h(\xi) = x^{-\frac{1}{3}}\bar{U}_\infty \quad (31)$$

Genellikle kayıp olmaksızın  $U_\infty$  ile ilişkili benzerlik fonksiyonu  $h(\xi) = 1$  alınabilir. Yeni değişkenler cinsinden sınır tabakası denklemi

$$f^2(\xi) - \xi f(\xi)f'(\xi) + 3g(\xi)f'(\xi) = 1 + 3 \left( k_2 + (k_1 - k_2) \frac{1-n k_3 |f'(\xi)|^n (1+k_3 |f'(\xi)|^n)^{-1}}{(1+k_3 |f'(\xi)|^n)} \right) f''(\xi) \quad (32)$$

ve süreklilik denklemi

$$f(\xi) - \xi f(\xi)f'(\xi) + 3g'(\xi) = 0 \quad (33)$$

olarak adi diferansiyel denklem haline indirgenir. Dönüştürülmüş sınır şartlarımız ise aşağıdaki şekildedir.

$$f(0) = 0, g(0) = 0, f(\infty) = 1, f'(\infty) = 0, f''(\infty) = 0 \quad (34)$$

Plaka üzerindeki kayma gerilmesinin benzerlik dönüşümü ile Denklem (13) ele alınarak şöyle bulunur.

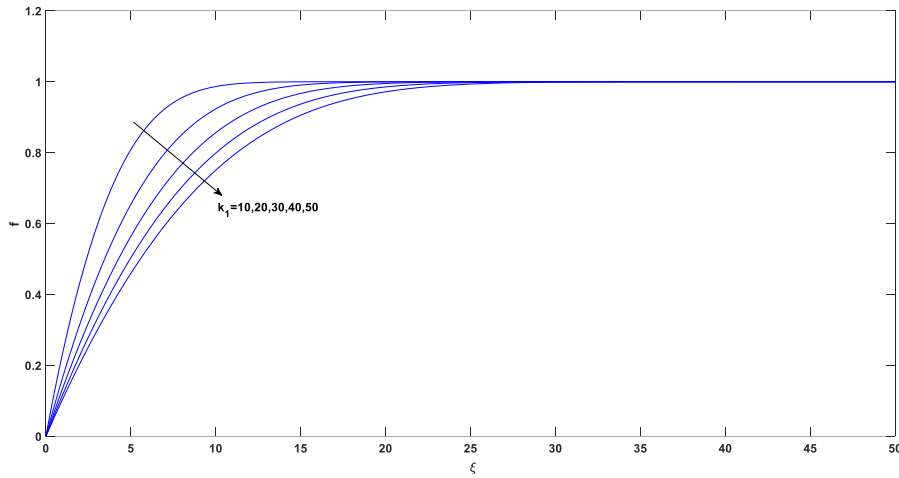
$$\tau^* = k_2 f'(0) + (k_1 - k_2)(1 + k_3 |f'(0)|^n)^{-1} f'(0) \quad (35)$$

Denklem (32) ve (33), Denklem (34) şartları altında Matlab programının bir sonlu farklar çözücüsü olan bvp4c kullanılarak çözülmüştür. Matlab yazılımının bvp4c komutu standart halde ele aldığımız

problemin her değerinde hata toleransını sağlamış ve başarılı sonuçlar verdiği için herhangi bir sonlu farklar algoritmasının bilgisayar programı uyarlamasına gerek duyulmamıştır.

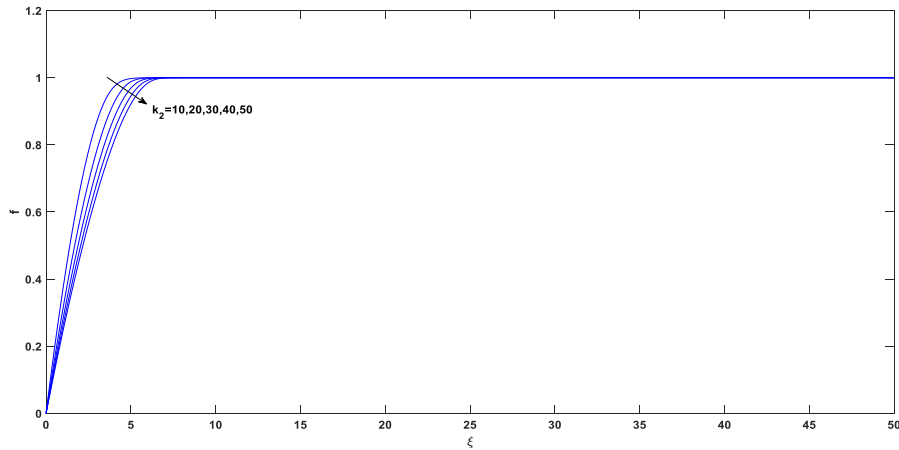
### Sayısal Sonuçlar ve Tartışma

Şekil 1’ de farklı  $k_1$  değerlerinde akışkan hızının plaka doğrultusunda bileşeniyle alakalı benzerlik fonksiyonu  $f'$  in benzerlik değişkeni  $\xi$  'ye göre değişimi verilmiştir. Benzerlik fonksiyonunun yapısı gereği  $f$  deki artış  $u$  hızındaki artış ile ilişkilendirilebilir.  $k_1$  Cross akışkan özelliğinin artan değerlerinde akışkan hızının,  $f$  değerindeki azalış dolayısıyla azaldığı söylenebilir. Azalan akışkan hızı momentumun korunumu gereği daha kalın sınır tabakasına işaret etmektedir. Başka türlü, sınır tabakası içerisindeki bir noktada  $k_1$  değeri arttığında akışkan hızı azalacaktır. Bu demek oluyor ki, hızı az olan noktadan uniform ya da en yüksek hıza ulaşmak için daha çok akışkan tabakası geçmemiz gerekmektedir. Dolayısıyla o noktadaki sınır tabakası kalınlığı daha büyük olmalıdır.



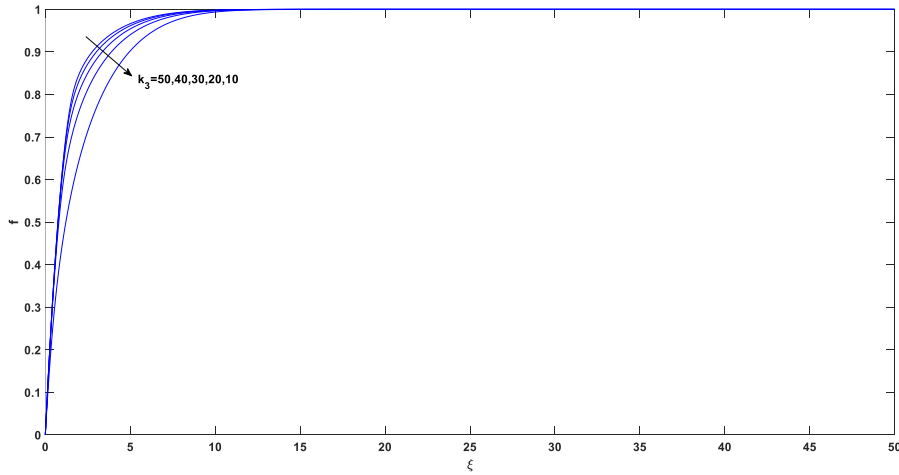
Şekil 1. Benzerlik fonksiyonu  $f'$  nin farklı  $k_1$  değerleri için benzerlik değişkeni  $\xi$ 'ye göre değişimi.  
( $k_2 = 1$ ,  $k_3 = 1$ ,  $n = 1,5$ )

Şekil 2’ de benzerlik fonksiyonu  $f'$  in farklı  $k_2$  değerleri için benzerlik değişkeni  $\xi$  'ye göre değişimi verilmiştir.  $k_2$  parametresi aslında limit viskozite değeri ile ilişkili olduğundan, önceki grafiklerdeki gibi arttıkça akışkan hızında azalmaya yol açacaktır. Bu da aynı şekilde daha kalın sınır tabakasına yol açar. Yalnız dikkat edilirse aynı değerlerde  $k_1$  ile karşılaştırıldığında  $k_2$ ' nin akışkan hızı üzerindeki etkisi daha az gözükmektedir. Bunun nedeni viskozite-deformasyon hızı grafiklerindeki power-law bölgesine daha ileride girilmesi ile açıklanabilir.



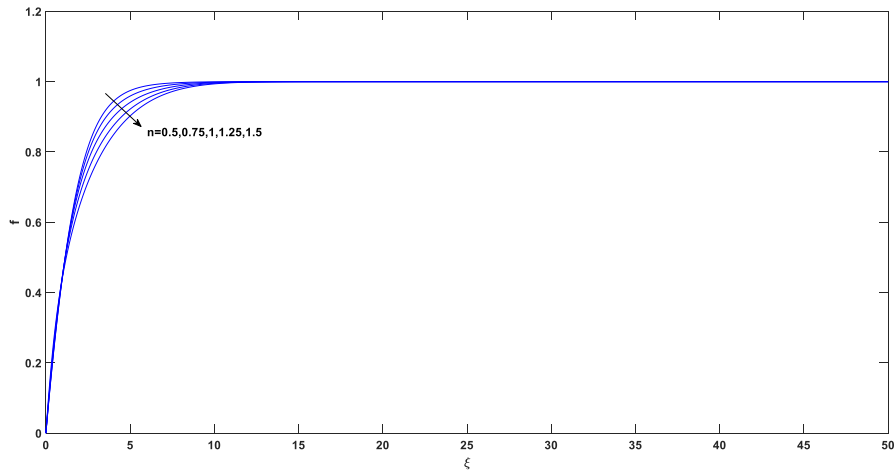
Şekil 2. Benzerlik fonksiyonu  $f'$  nin farklı  $k_2$  değerleri için benzerlik değişkeni  $\xi$  'ye göre değişimi.  
( $k_1 = 1$ ,  $k_3 = 1$ ,  $n = 1,5$ )

Şekil 3'te akışkan hızının yatay bileşeni ile alakalı benzerlik fonksiyonu  $f'$ ' nin farklı  $k_3$  değerleri için benzerlik değişkeni  $\xi$ ' ye göre değişimi verilmiştir.  $k_1$  ve  $k_2$  parametrelerinin viskozite ilişkilerinin aksine  $k_3$  parametresi power-law bölgesinin davranışını belirleyen zaman sabiti ile ilişkilidir. Dikkat edilirse nihai denklemlerden, akışkan modelinin power-law kısmını çarpan etkisi ile kontrol edenin  $k_3$  parametresi olduğu görülür. Bu matematiksel gözlemlerin uyumlu olarak da  $k_1$  ve  $k_2$  parametrelerinin aksine  $k_3$  değerlerinde artışla birlikte akışkan hızı artmakta ve sınır tabakası daha ince hale gelmektedir.  $k_3$  parametresinin artışı limit değerlerin ya da  $k_1$  ve  $k_2$ ' nin akışkan davranışı üzerindeki etkisini azaltmaktadır.

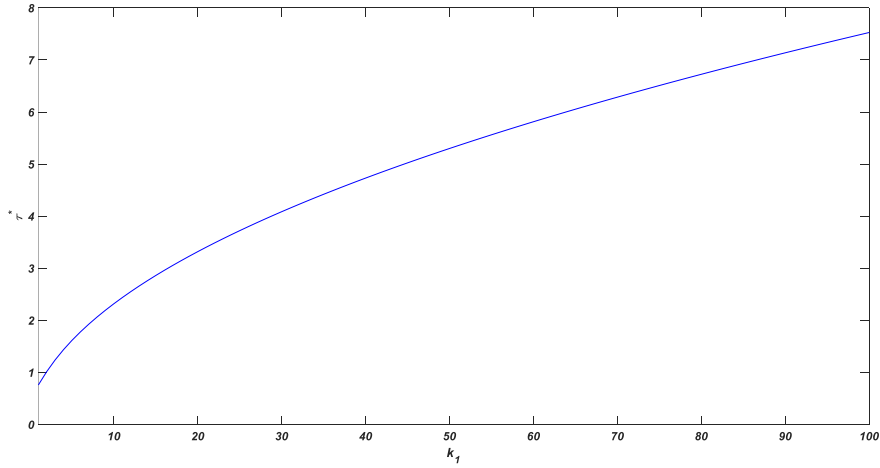


Şekil 3. Benzerlik fonksiyonu  $f'$  nin farklı  $k_3$  değerleri için benzerlik değişkeni  $\xi$ 'ye göre değişimi.  
( $k_1 = 11$ ,  $k_2 = 1$ ,  $n = 1,5$ )

Şekil 4'te akışkan hızı ile alakalı benzerlik fonksiyonumuz  $f'$  nin benzerlik değişkeni  $\xi$ ' ye göre değişimi, farklı power-law indeksi  $n$  değerlerinde gösterilmiştir. Dikkat edilirse  $n$  değeri arttıkça akışkan hızı sadece çok dar bir bölgede değişmektedir. Bu değişim akışkan hızındaki azalış ve daha kalın sınır tabakasına işaret eder. Plakanın başlangıcı ve yakın bölgelerde akışkan davranışı  $n$  değerine göre neredeyse hiç değişmediği, ancak düşük  $n$  değerlerinde akış hızının, sonsuzdan gelen akışkan hızını daha çabuk yakaladığı söylenir. Buradaki  $n$  değerinin artması ile akışkanın hareketinin zorlaşması Ostwald-de Waele modeli ile benzerdir.

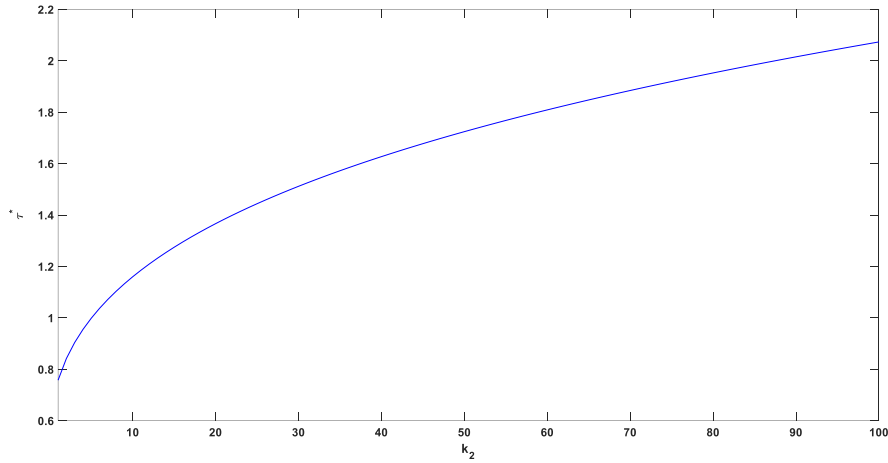


Şekil 4. Benzerlik fonksiyonu  $f'$  nin benzerlik değişkeni  $\xi$ 'ye göre değişiminin, farklı power-law indeksi  $n$  değerlerinde gösterimi. ( $k_1 = 11$ ,  $k_2 = 1$ ,  $k_3 = 10$ )



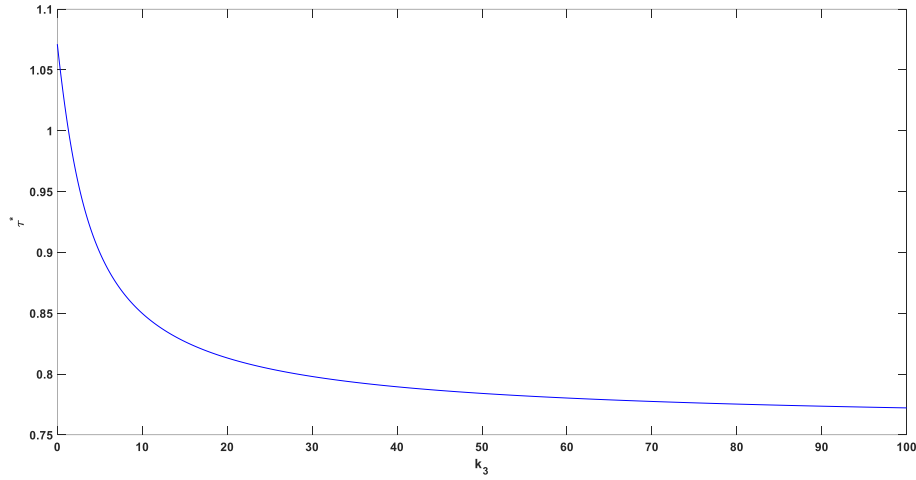
Şekil 5. Kayma gerilmesinin  $k_1$  değerleri ile değişimi.  
( $k_2 = 1$ ,  $k_3 = 1$ ,  $n = 1,5$ )

Şekil 5 ve 6'da limit viskoziteler ile ilişkili  $k_1$  ve  $k_2$  parametreleri Newtonyen akışkanlarda olduğu gibi daha viskoz bir akışa yol açarak plaka üzerindeki kayma gerilmesini önce exponansiyel ve daha sonra doğrusala yakın bir şekilde arttırmaktadır.



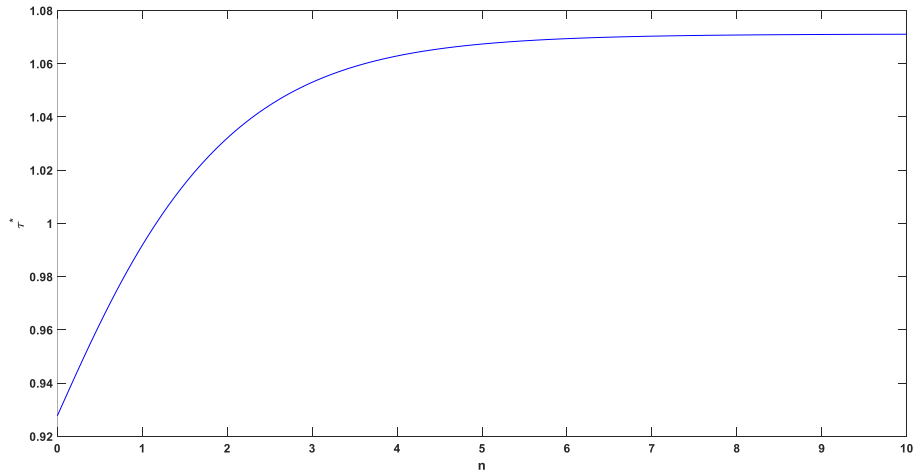
Şekil 6. Kayma gerilmesinin  $k_2$  değerleri ile değişimi.  
( $k_1 = 1$ ,  $k_3 = 1$ ,  $n = 1,5$ )

Zaman sabiti ile ilgili boyutsuz parametremiz  $k_3$ 'ün kayma gerilmesi üzerindeki etkisi Şekil 7'de verilmiştir. Kayma gerilmesi  $k_3$ 'e göre exponansiyel bir şekilde azalmaktadır. Benzer şekilde artan  $k_3$  değerleri akışkan hızını arttırdığından daha ince bir sınır tabakasına yol açmaktaydı. İnce sınır tabakası akışkanın plakaya daha az bir kuvvet uyguladığına işaret etmektedir.



Şekil 7. Kayma gerilmesinin  $k_3$  değerleri ile değişimi.  
( $k_1 = 2$ ,  $k_2 = 1$ ,  $n = 1,5$ )

Şekil 8’de power-law indeksinin kayma gerilmesi üzerindeki etkisi gösterilmiştir. Artan power-law indeksi ile akışkanın aynı miktarda deforme edebilmek için daha yüksek deformasyona maruz bırakmamız gerekir. Dolayısıyla akışkanın kabaran davranışı ortaya çıkmakta ve hızı azalmaktadır. Böylece artan  $n$  değerleri için plaka üzerinde kayma gerilmesi artmaktadır. Bu nihai artış, bir limit viskozite ile sonlandırılması gerektiğinden söz konusu artış bir değere yakınsayacak şekilde eksponansiyel olacaktır.



Şekil 8. Kayma gerilmesinin power-law indeksi  $n$  değerleri ile değişimi.  
( $k_1 = 2$ ,  $k_2 = 1$ ,  $k_3 = 1$ )

Dikkat edilirse sınır tabakası kalınlığı sadece plaka doğrultusundaki hız baskın olduğu için ilk benzerlik fonksiyonu  $f$  üzerinden grafikler vasıtası ile tartışılmış. Düşey doğrultuda hız ile alakalı ikincil benzerlik değişkeni  $g$  fonksiyonu ele alınmamıştır.

### Sonuçlar

Cross akışkanına ait viskozite terimlerinin artması ile akışkan hızı azalmakta ve sınır tabakası kalınlığı azalmaktadır. Akışkanın power-law ya da incelen davranışı ile alakalı zaman sabiti, akışkanın viskozitelerinin yol açtığı akış hızını azaltan davranışını engellemektedir. Dolayısı ile artan zaman sabiti değerlerinde akışkanın hızı artmakta ve sınır tabakası incelmektedir. İncelen davranışı temsil etmek için en önemli parametre olan üstel ya da power-law indeksi azaldıkça daha akışkan daha akıcı hale gelmekte hızı artmaktadır. Bu davranış klasik power-law akışkanı ile uyumludur. Dolayısıyla power-law indeksi

azaldıkça akışkanın hızı artmakta ve sınır tabakası incelmektedir. Tam tersi durumda ise yani indeksin artan değerlerinde akışkan hızı yavaşlamakta ve sınır tabakası kalınlaşmaktadır. Son olarak plaka üzerindeki kayma gerilmesi başlangıç ve limit viskozite değerleri ile ilişkili boyutsuz parametrelerin artışı ile artmakta, zaman sabiti ile ilişkili boyutsuz parametrenin artışı ile de azalmaktadır. Viskozite ile ilgili boyutsuz parametrelere benzer şekilde artan power-law indeksi değerlerinde kayma gerilmesi artmakta, ancak bu artış viskozite parametrelerindeki doğrusal artıştan farklı olarak sonsuz bir değer yerine sonlu bir değere eksponansiyel yakınsayarak sonlanmaktadır.

#### Referanslar

- [1] Morrison, FA. Understanding Rheology, Oxford University Press, Newyork ABD, 2001.
- [2] Bird RB. Usefull Non-newtonian models. Annual Review of Fluid Mechanics.197, 8, 13-34.
- [3] Cross MM. Rheology of non-Newtonian Fluids: A new flow equation For pseudoplastic Systems. Journal of Colloid Science. 1965, 20(5), 417-437
- [4] Aksoy Y, Pakdemirli M, Khaliq CM. Boundary layer equations and stretching sheet solutions for the modified second grade fluid. International Journal of Engineering Science. 2007, 45(10), 829-841.
- [5] Sümer H. Newtonyen olmayan cross akışkanının sınır tabakası içerisindeki davranışının incelenmesi. Manisa Celal Bayar Üniversitesi Fen Bilimleri Enstitüsü, 2019.

## Bir Gıda Üretim Tesisinde Konfor Soğutmada Amonyak ve Freon R-134a Akışkanlı Sistemlerin Verimliliklerinin Karşılaştırılması

*Kaan Vatansever\**, Dr. Oetker Gıda San. ve Tic. A.Ş., İzmir, Türkiye  
*Mustafa Demirbağ*, Dr. Oetker Gıda San. ve Tic. A.Ş., İzmir, Türkiye  
*Mehmet Çevik*, İzmir Kâtip Çelebi Üniversitesi, Makine Mühendisliği Bölümü, İzmir, Türkiye  
*\*İletişimden sorumlu yazar: k\_vs94@hotmail.com*

**Anahtar Kelimeler:** Soğutma, amonyak, freon, konfor, performans katsayısı  
**Disiplin:** Makina Mühendisliği

### Özet

Endüstriyel tesislerde çeşitli soğutma sistemleri bulunmaktadır. Otomotiv, tekstil, gıda, mobilya gibi sektörler soğutma sistemlerini farklı amaçlar için kullanmaktadır. Örneğin otomotiv sektöründe, yalnızca fabrikanın çalışma alanlarının konfor soğutması için kullanılmaktadır.

Bu çalışmada, dondurulmuş pizza üreten bir gıda fabrikası incelenmiştir. Bu fabrikada soğutma iki amaç için kullanılmaktadır. Bunlardan ilki, sırasıyla, soğuk hava depoları ve pizzanın üretimi esnasında donmasını sağlayan spiral dondurucu için  $-24^{\circ}\text{C}$  ve  $-40^{\circ}\text{C}$  ortam sıcaklığı ihtiyacını karşılamak üzere kullanılacak olan amonyaklı soğutma sistemidir. İkincisi, konfor iklimlendirmesi için kullanılan freonlu soğutma sistemidir. Çalışmamızda, iki sistemin konfor iklimlendirmesi açısından verimliliklerin karşılaştırılarak, mevcut uygulamada var olan amonyaklı soğutma sisteminin konfor iklimlendirmesinde kullanılmasının verimli olup olmayacağı tartışılmıştır. Bu amaçla, önce iki sistemdeki tüm ekipmanlar tanıtılacak, ardından performans katsayısı, entalpi ve soğutma yüklerini içeren termodinamik hesaplamalar ve sonlu elemanlar analizleri yapılmıştır. Son olarak, yapılan analizlerin konfor iklimlendirmesinde pratik uygulaması yapılacak, enerji izleme sisteminden kompresörlerin harcadığı enerjiler ve soğutma yükleri karşılaştırılarak, elde edilen sonuçlar değerlendirilmiştir.

### Giriş

İklimlendirme sistemleri, fabrikalarda çalışanların sağlık ve konforunu temin etmek suretiyle iş veriminin artırılmasına katkıda bulunur. Ayrıca birçok endüstri kolunda daha kaliteli mal ve ürün elde edilmesinde yine iklimlendirme sistemleri etkilidir. Buna örnek olarak tütün ve gıda endüstrisi gösterilebilir.

Gıda endüstrisinde iklimlendirmenin önemi büyüktür. Gıda maddelerinin üretim mekânlarına yeterli miktarda temiz hava verilmelidir. Oluşturulacak iç iklim şartları, gıda maddelerinin bozulmasına, buharlaşma yolu ile fazla nem kaybederek kötü görünümüne ve tatlarının bozulmasına engel olacaktır. Gıda endüstrisinde iklimlendirme ilk olarak ekmek üretiminde kullanılmıştır. Mayanın fermantasyonunu kontrol etmek, kullanılan maya özelliklerini sabit tutmak ve üretilen her ekmeğin aynı özelliklerde olmasını sürdürmek ancak iklimlendirme ünitelerinin kullanımıyla mümkündür.

Bir soğutma çevriminde ısının bir ortamdaki alınıp başka bir ortama nakledilmesinde ara madde olarak yararlanılan soğutucu akışkanlar ısı alışverişini genellikle, sıvı halden buhar haline (soğutucu- evaporatör devresinde) ve buhar halden sıvı haline (yoğuşturucu-kondenser devresi) dönüştürerek sağlarlar. [1]

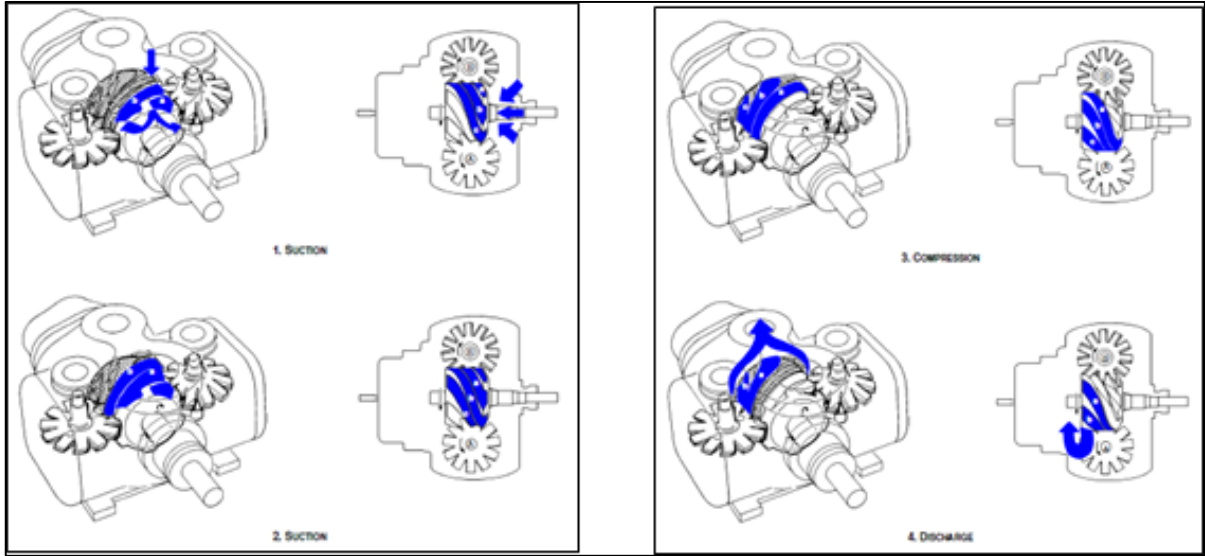
Kimyasal simgesi  $\text{CF}_2\text{CH}_2\text{F}$  olan R134A, termodinamik ve fiziksel özellikleri Freon 12'ye en yakın olan bir gaz olup, ozon tüketme katsayısı sıfırdır; diğer özellikleri açısından da en uygun soğutucu maddedir. Araç soğutucuları ve ev tipi soğutucular için de uygun bir alternatiftir. [2]

Bugün, fluo-karbon ailesinin dışında geniş ölçüde kullanılmaya devam edilen tek soğutucu akışkan amonyaktır. Zehirleyici ve bir ölçüde yanıcı-patlayıcı olmasına rağmen mükemmel ısı özelliklerine sahip olması sebebiyle, iyi eğitilmiş işletme personeli ile ve zehirleyici etkisinin fazla önem taşımadığı hallerde, büyük soğuk depoculukta, buz üretiminde, buz pateni sahalarında ve donmuş paketleme uygulamalarında başarıyla kullanılmaktadır. Buharlaşma ısısının yüksek oluşu ve buhar özgül hacminin oldukça düşük olması sistemde dolaştırılması gereken akışkan miktarının düşük seviyede olmasını sağlar. [3]

Amonyak ( $\text{NH}_3$ ) çok eskiden beri en yaygın şekilde kullanılan bir soğutucu maddedir. Normal atmosfer basıncında  $-33^{\circ}\text{C}$ 'da buharlaşır. Endüstride benimsenen bir soğutucu olması, düşük hacimsel deplasman gerektirmesi, ucuz, hafif ve yüksek verimli olması, amonyağın önemli yararları arasındadır.







Şekil 2. Tek vidalı çift yıldız kitli kompresör çalışma bölgeleri

### Evaporatif Kondenser

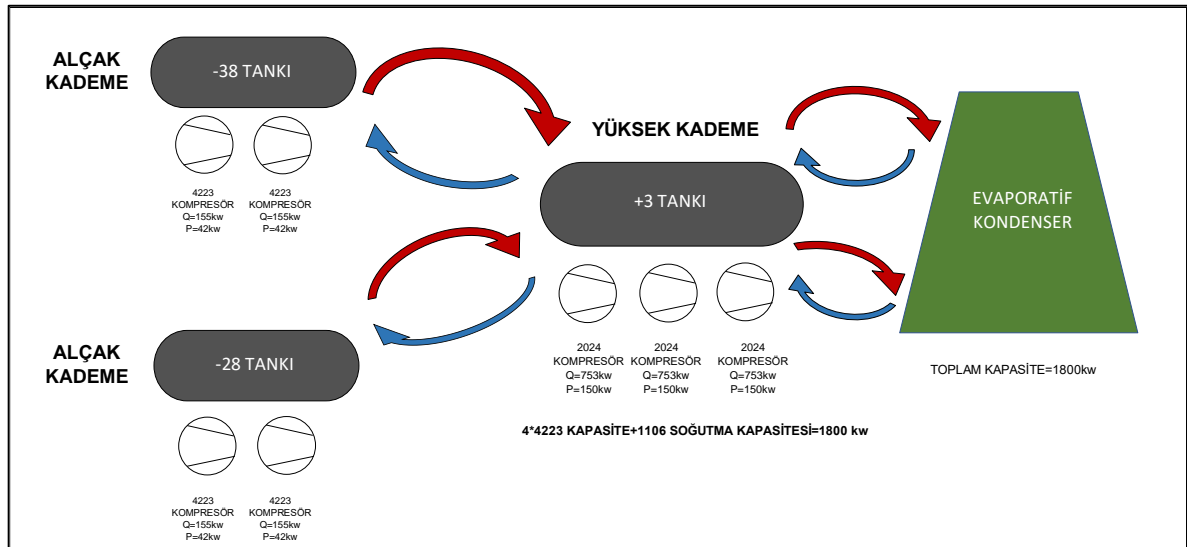
1800 kW gücünde tek sprey pompalı, çift fanlı

### Alçak Kademe Tankları

- 38°C sıcaklığında 11 m<sup>3</sup> kapasiteli
- 28°C sıcaklığında 11 m<sup>3</sup> kapasiteli

### Yüksek Kademe Tankı

+3°C sıcaklığında 20 m<sup>3</sup> kapasiteli



Şekil 3. Sistemin en genel ifadesi

Şekil 3'te sistemin ana ekipmanlarıyla son durumu görülmektedir. Kırmızı renkli oklar basma hattını, mavi renkli oklar dönüş hatlarını temsil etmektedir. Alçak kademe bölgesinde -38°C ve -28°C tanklarını besleyen 2 adet 55 kW gücünde kompresör bulunmaktadır. Yüksek kademede ise +3°C tankını besleyen 160 kW gücünde 3 adet kompresör bulunmaktadır. Bunlardan 1 tanesi mahal soğutma için kullanılacaktır. Mahal soğutma kapasitesi yüksek kademe kompresörlerinden 1 tanesinden karşılanacaktır.

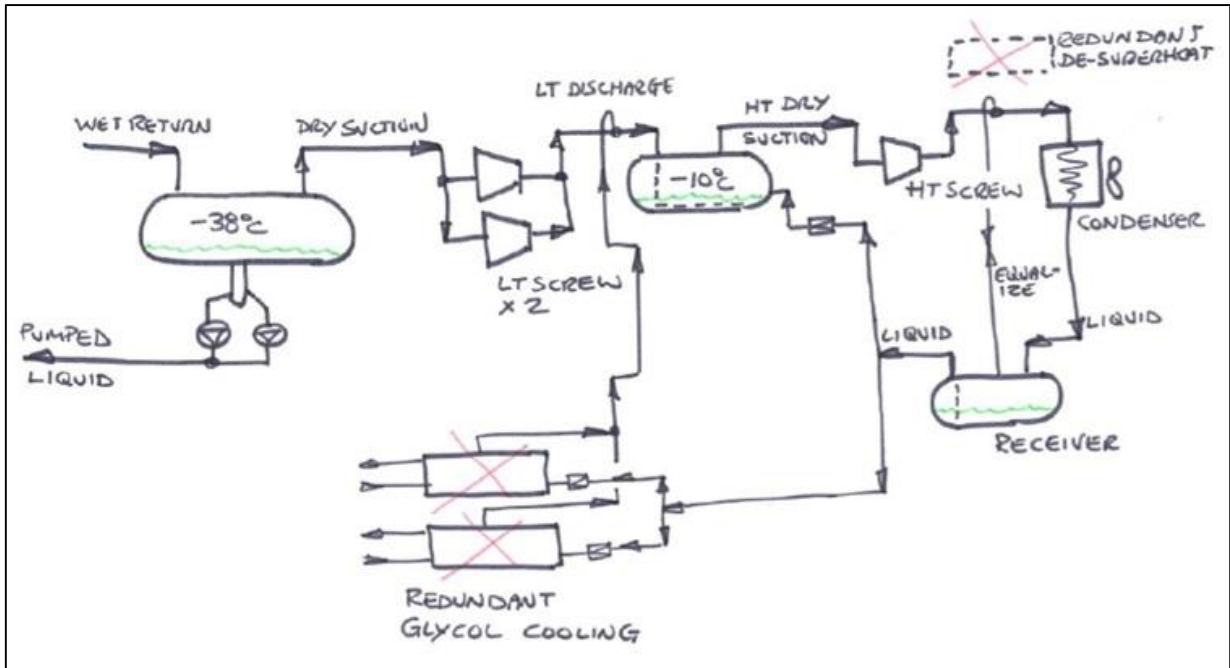
### Bulgular ve Tartışma

İki soğutma sisteminin verdikleri kapasite, ulaştıkları sıcaklık ve Performans Katsayısı (CoP) değerleri Tablo 1’de gösterilmiştir. Mahal soğutmanın freonlu soğutmadan amonyaklı soğutma sistemine geçmesiyle 4,1 olan CoP değeri yaklaşık %60 artarak 6,7 olmuştur. Ayrıca evaporatör maksimum sıcaklığı da 7°C’den 0°C’ye düşürülmüştür.

Tablo 1. Sistem karşılaştırma tablosu

Sistem	Mahale verilen Kapasite	Ulaşılan Sıcaklık	CoP
Amonyaklı Soğutma Sistemi	668 kWh	0°C	6,7
Freon R134A Soğutma Sistemi	668 kWh	7°C	4,1

Şekil 4 ve Şekil 5’te sistemin, sırasıyla, eski ve yeni durumu görülmektedir. Alçak kademe bölgesinde mevcutta olan tek bir -40°C tankı yerine 1 adet -38°C ve 1 adet -28°C tankı oluşturulmuştur. Ayrıca yüksek kademede sıcaklık farkları göz önünde bulundurularak -10°C tankı yerine +3°C tankı devreye alınmıştır. Mahalden gelen ek soğutma kapasitesi bu kademeye eklenmiş olup, enerji tasarrufu açısından da -10°C yerine +3°C’ye ayarlanıp ek enerji maliyetleri giderilmiştir.



Şekil 4. Sistemin eski durumu



## Accurately Capturing Heat Transfer in a Turbulent U-Bend Flow

Deniz Hakyemez\*, İzmir Kâtip Çelebi University, Mechanical Engineering Department, İzmir, Turkey  
Sercan Acarer, İzmir Kâtip Çelebi University, Mechanical Engineering Department, İzmir, Turkey

\*Corresponding author: denizhkymz@gmail.com

**Keywords:** Heat transfer, CFD, turbulence modeling, U-bend flow

**Discipline:** Mechanical Engineering

### Abstract

One of the challenging problems in Computational Fluid Dynamics (CFD) is turbulence. Achieving an accurate turbulent model is important for time-averaged CFD analyses. Fluid flow and heat transfer problems in u-bend geometries are complex problems in this regard because streamline curvature and the associated secondary flows forms complex fluid patterns. Two-equation eddy-viscosity models may play an important role for such a problem. However, these simple and computationally efficient models can be insufficient to express such flow fields. Reynolds Stress Models (RSM) are much more elaborate, however they are computationally more expensive and convergence behaviors are weak. By using ANSYS Fluent software, this work compares two-equation k-epsilon realizable model with the recent Menter-Lechner near-wall model and Reynolds Stress-Omega model against a published u-bend experimental data of Verstrate et al. [1] at a Reynolds number of 40,000.

### Introduction

Turbulence is fluid eddy motion characterized by chaotic changes and most flow occurring in nature is turbulent. All turbulent flows are unsteady and irregular in space and time. Even if the mean flow is only 2-Dimensional, turbulence is 3-Dimensional because of vorticity fluctuations. Another property of turbulence is diffusivity. It is the reason for increasing the rate of momentum, heat, and mass transfer [2]. All of these properties cause complex mathematical description of turbulence. Therefore, predicting turbulence is problematic in engineering applications.

Computational fluid dynamics (CFD), is a science that simulates fluid-flow phenomena by using governing equations (conservation of mass, momentum, and energy) with the help of computers. It has an important role in several engineering applications such as the aerodynamics of aircraft and vehicles (lift and drag), hydrodynamics of ships, power plants (combustion in internal combustion engines and gas turbines), meteorology (weather prediction), and biomedical engineering (blood flows through arteries and veins) [3]. In this science, turbulence models, which predict the effects of turbulence with using mathematical models, are used to estimate the evolution of turbulence. These models contain a set of relations and equations which determine unknown turbulent correlations (Reynolds stresses, transport terms etc.). It is unnecessary to resolve the details of these turbulent fluctuations. Thus, using The Reynolds-averaged Navier–Stokes (RANS) equations is the most common technique for turbulence modeling which is time-averaged equations of fluid flow motion [3].

A useful turbulence model in CFD must be widely applicable, accurate, and economical to run. In this regard, the most common RANS turbulence models for CFD are mixing length model (zero transport equation), Spalart–Allmaras model (one transport equation), k-ε model and k-ω model (two transport equation), Reynolds stress model (seven transport equation). These models are significant for standard turbulence calculation in currently available commercial CFD codes [3].

In this study, a reference experimental study and CFD simulations are compared by using the turbulence models mentioned above. Especially, in pipe flow, turbulence occurs when the flow path has a sudden expansion, sudden contraction, or bendings as the effects of the streamline curvature and the associated secondary flows are typically challenging to reproduce in numerical simulations. On the other hand, heat transfer is a considerable parameter for turbulence modeling as mentioned in the properties. Hence, the reference experimental study was chosen by taking these cases into consideration.

### Experimental Study

Verstraete et al [1] studied the design of a U-bend for serpentine internal cooling channels optimized for minimal pressure loss. In Fig. 1, the u-bend geometry and dimensions are shown which are used for the experiment. Also, the same geometry and dimensions are studied in this study. The experimental

setup shown in Fig 2. A 2.2-kW centrifugal blower discharging into a settling chamber arranges the air flow. Then, fluid flow passes through the test section, which is made of Plexiglas channel. These channels consist of a square cross-section of hydraulic diameter  $D_h=75$  mm and the length is 2 m. The walls are 15mm thick and hermetically sealed. Inlet and outlet location planes are shown in Fig. 2. The operating conditions are measured in the inlet section by a traversing Pitot probe (diameter 1.5 mm), and a thermocouple located  $16 D_h$  downstream of the settling chamber. At this location, the fluid properties, the bulk velocity, and the hydraulic diameter define the Reynolds number, which is kept at 40,000 for all measurements (the bulk velocity is about 8.8 m/s).

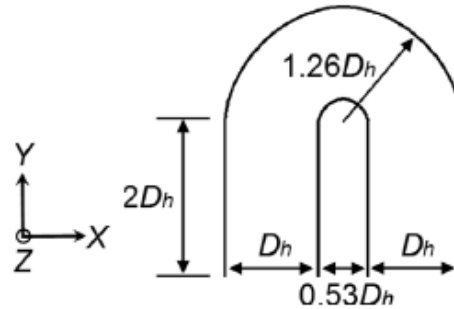


Figure 39. U-bend geometry

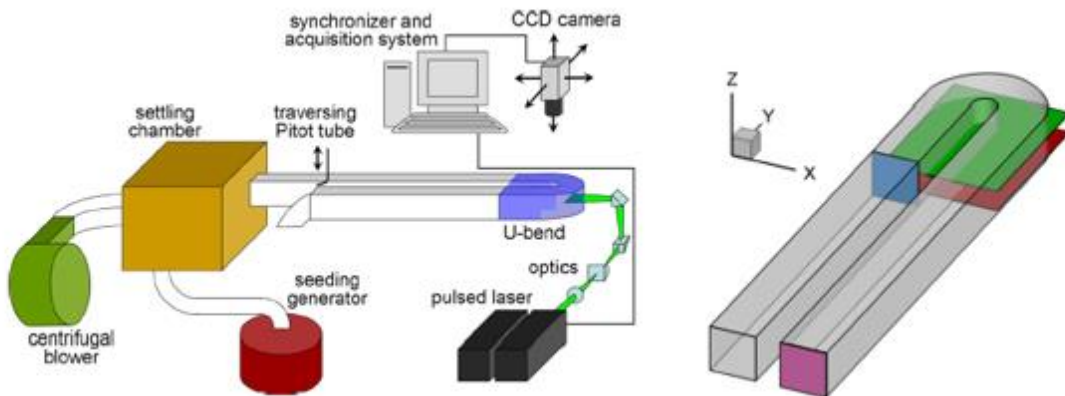


Figure 40. Schematic representation of the experimental set up (left) and location of the measurement planes (right)

In the experimental study, Nusselt number was used to quantify the heat transfer rate which is,

$$Nu = \frac{hD_h}{k_{air}} \quad (1)$$

where  $k_{air}$  is the air thermal conductivity and the heat transfer coefficient  $h$  is calculated as

$$h = \frac{q - q_{loss}}{(T_w - T_b)} \quad (2)$$

$q_{loss}$  includes both the conduction losses and the radiation losses. The Nusselt number is normalized by the Dittus–Boelter correlation for a fully developed turbulent flow in a smooth circular tube,

$$Nu_0 = 0.023Re^{0.8} Pr^{0.4} \quad (3)$$

Normalized Nusselt number distribution of the experiment is shown in Fig 3 and according to this distribution, simulation results have been compared.

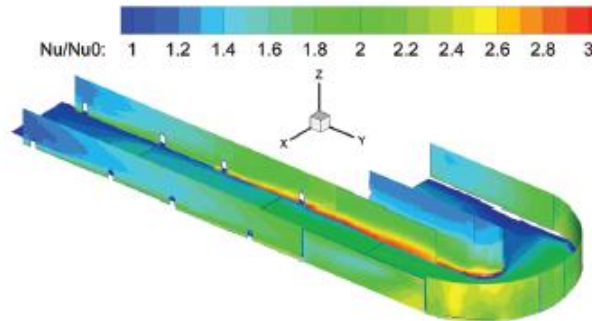


Figure 41. 3D view of the normalized Nusselt number distribution.

### CFD Simulation

In this study, only the measurement part of the u-bend geometry analyzed, which is between inlet and outlet planes. These inlet and outlet locations have been taken from the reference study as shown in Fig 4 and the geometry has been designed according to given dimensions. Also, the mesh configuration of simulation is shown in Fig 4. In the simulation setup, several turbulence models are used such as k-omega, k-epsilon realizable, Reynolds stress omega model with different wall functions.

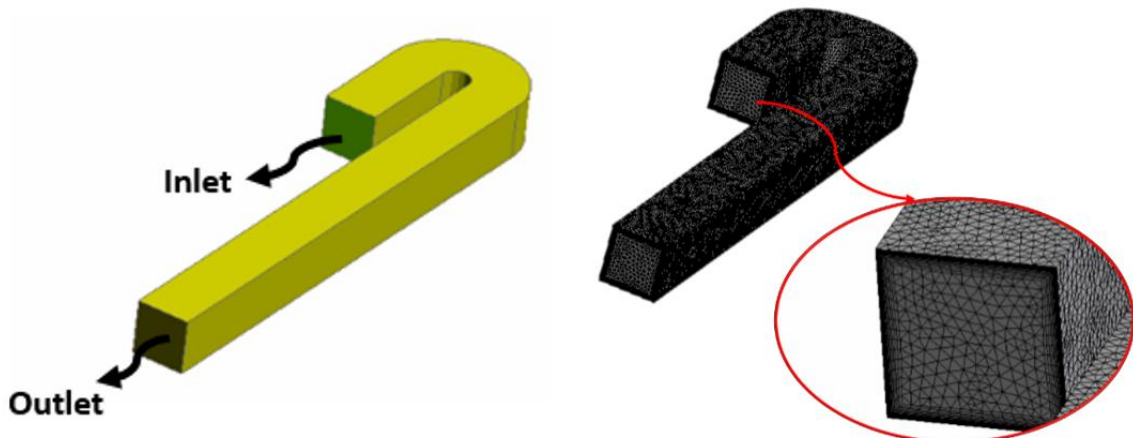


Figure 42. The simulation geometry and mesh configuration

### Results

The simulation results are compared with the Nusselt number distribution of the experimental study. Fig 5 (a) shows Nusselt number distribution of the experimental study. Fig 5 (b) presents k-omega with standard wall function (c) presents k-epsilon realizable with scable wall function (d) presents k-epsilon realizable with enhanced wall treatment, (e) presents Reynolds stress omega model with low Reynolds number option and (f) presents Reynolds stress omega model without low Reynolds number option. These results were not close enough to experimental Nusselt number distribution. Therefore, k-epsilon realizable model analyzed with Menter Lechner near-wall treatment. The results of k-epsilon realizable / Menter Lechner have been obtained similar with experiment as shown in Fig 6. Figure 6 (b) and (c) present k-epsilon model with Menter Lechner near-wall treatment for coarse and fine meshes, respectively. Hence simulations were continued with coarse mesh to avoid wasting of the time. Finally, Menter Lechner has been compared with all used models as turbulent kinetic energy (Fig 7), turbulent intensity (Fig 8), turbulent dissipation rate (Fig 9), and wall shear stress (Fig 10), respectively.

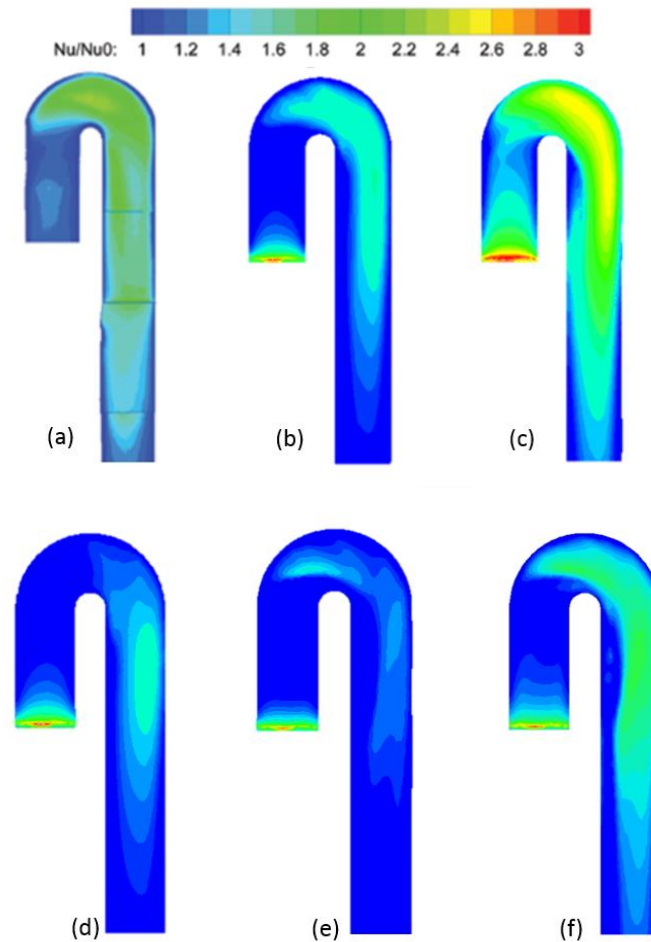


Figure 43. Normalized Nusselt number distributions of (a) experimental data [1], (b) k-omega / standard wall function (c) k-epsilon realizable / scable wall function (d) k-epsilon realizable / enhanced wall treatment (e) Reynolds stress omega model with low Re number option (f) Reynolds stress omega model without low Re number option

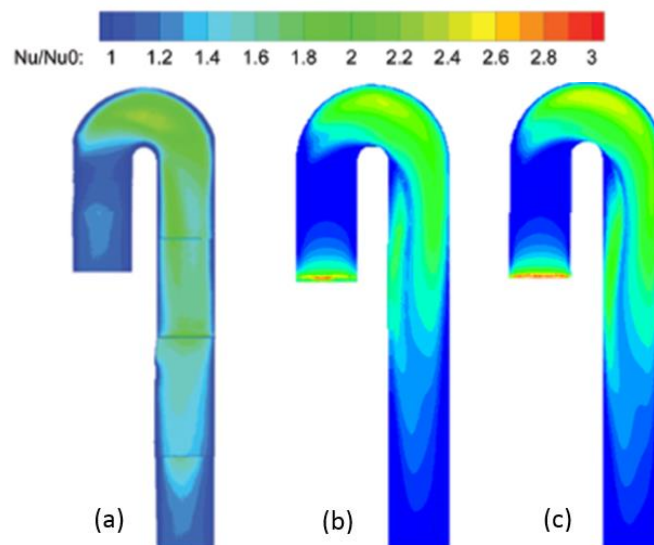


Figure 6. Normalized Nusselt number distributions of (a) experimental data [1], (b) k-epsilon realizable Menter Lechner with coarse mesh (c) the same model with fine mesh



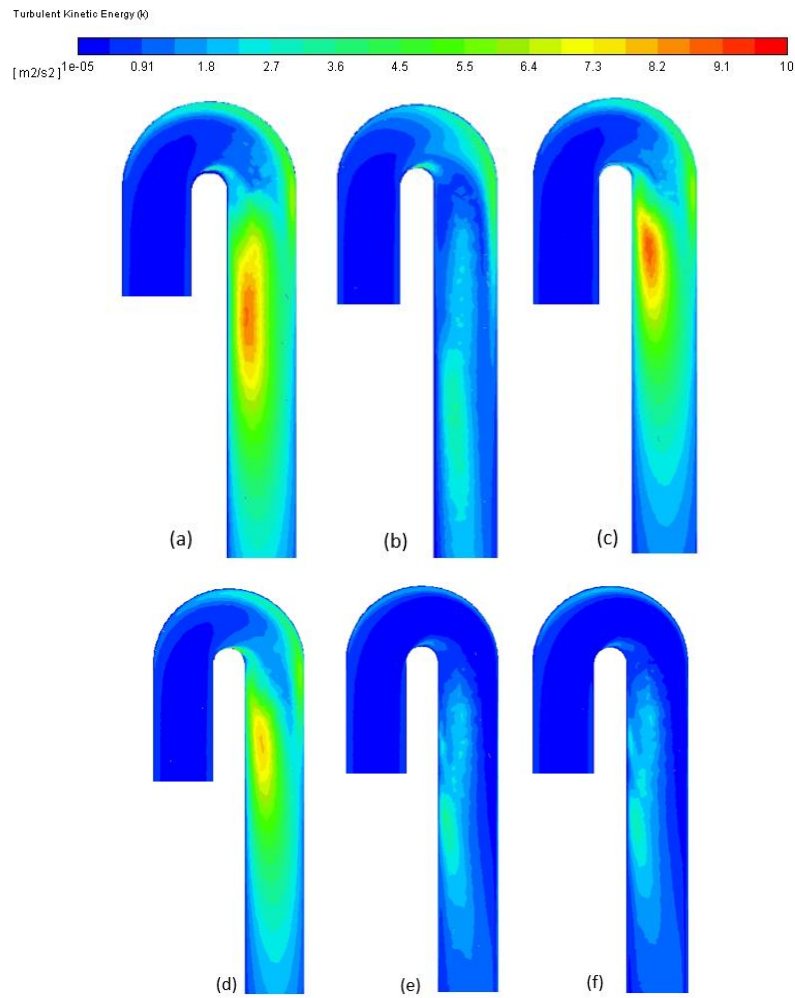
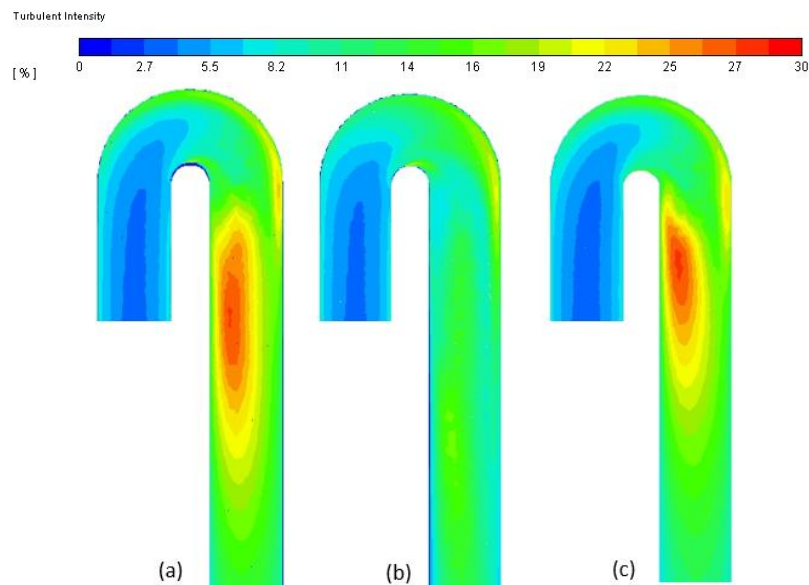


Figure 7. Turbulent kinetic energy (k) distributions of (a) k-epsilon realizable Menter Lechner (b) k-omega / standard wall function (c) k-epsilon realizable / scable wall function (d) k-epsilon realizable / enhanced wall treatment (e) Reynolds stress omega model with low Re number option (f) Reynolds stress omega model without low Re number option



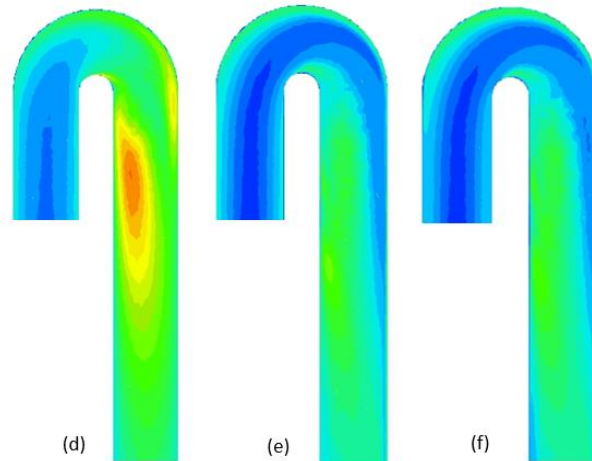


Figure 8. Turbulent intensity distributions of (a) k-epsilon realizable Menter Lechner (b) k-omega / standard wall function (c) k-epsilon realizable / scable wall function (d) k-epsilon realizable / enhanced wall treatment (e) Reynolds stress omega model with low Re number option (f) Reynolds stress omega model without low Re number option

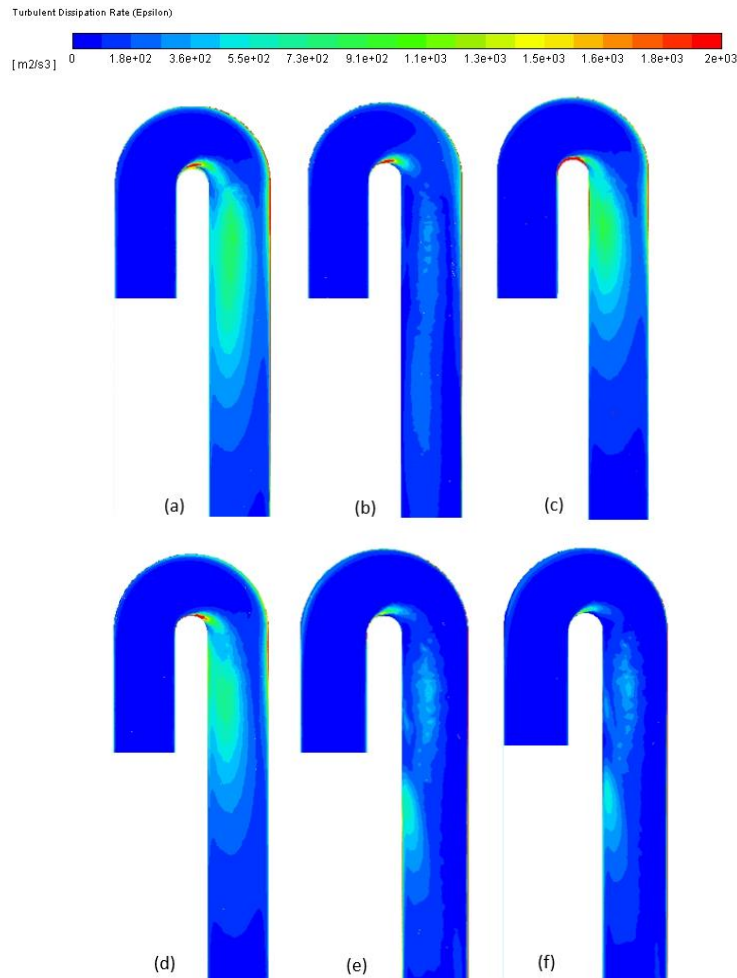


Figure 9. Turbulent dissipation rate (Epsilon) distributions of (a) k-epsilon realizable Menter Lechner (b) k-omega / standard wall function (c) k-epsilon realizable / scable wall function (d) k-epsilon realizable / enhanced wall treatment (e) Reynolds stress omega model with low Re number option (f) Reynolds stress omega model without low Re number option

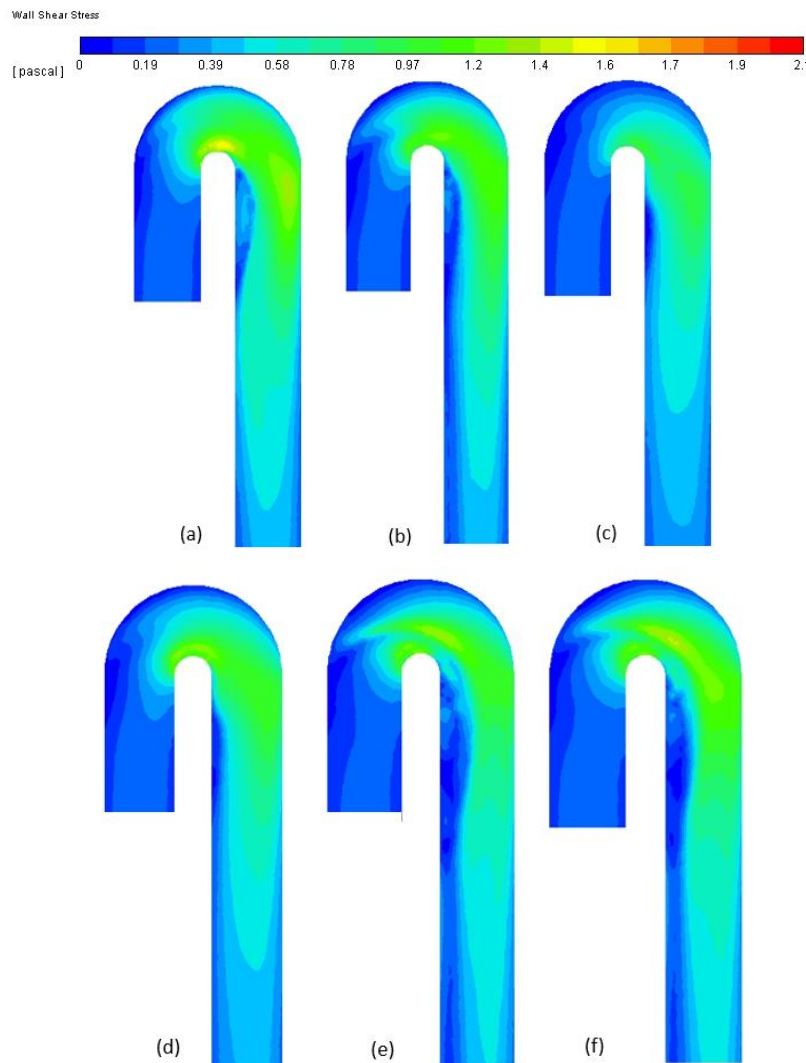


Figure 10. Wall shear stress distributions of (a) k-epsilon realizable Menter Lechner (b) k-omega / standard wall function (c) k-epsilon realizable / scable wall function (d) k-epsilon realizable / enhanced wall treatment (e) Reynolds stress omega model with low Re number option (f) Reynolds stress omega model without low Re number option

### Concluision

U-bent pipe experimental data, which includes both turbulence and heat transfer criteria, has been analyzed in CFD and compared with the experimental results according to Nusselt number distribution. Surprisingly, the more complex RSM model fails to reproduce the normalized Nusselt number distribution. On the other hand, the simpler k-epsilon realizable model with the recent Menter-Lechner near-wall treatment yields to the most accurate results in reference to the experimental data. Moreover, the coarse mesh is not much different from the finer mesh. Therefore, coarse mesh and a two-equation turbulence model is appropriate to model such complex fluid flow and heat transfer problem.

### References

- [1] Verstraete, T., Coletti, F., Bulle, J., Van der Wielen, T., and Arts, T., "Optimization of a U-Bend for Minimal Pressure Loss in Internal Cooling Channels: Part II— Experimental Validation," *Journal of Turbomachinery*, 135(5), 2013.
- [2] H. Tennekes & J. L. Lumley, *A first course in turbulence*, 6<sup>th</sup> Edition, MIT Press, 1972.
- [3] H K Versteeg and W Malalasekera, *An Introduction to Computational Fluid Dynamics*, 2<sup>nd</sup> Edition 2007.

## Hasara Uğramış Bir Manuel Vites Mekanizmasının Ömür ve Güvenirlik Analizi

Çağlar Hocalar\*, Manisa Büyükşehir Belediyesi, Manisa, Türkiye  
Muharrem Er, Milli Savunma Üniversitesi, Kara Aştsubay Meslek Yüksek Okulu, Balıkesir, Türkiye  
Can Çivi, Manisa Celal Bayar Üniversitesi, Mühendislik Fakültesi, Makine Mühendisliği Bölümü, Manisa, Türkiye

\*Sorumlu yazar: hocalarcaglar@gmail.com

**Anahtar kelimeler:** Dişli çark ömür analizi, güvenirlik, hasar analizi

**Disiplin:** Makine Mühendisliği

### Özet

Bu çalışmada; önden çekişli bir otomobilin beş ileri, bir geri manuel vites kutusunun üçüncü vites dişlisinde oluşan hasar durumu incelenmiştir. Dişlilerde oluşabilecek hasar mekanizmaları değerlendirilerek, diş dibi zorlaması açısından minimum ömür hesabı ve yüzey yorulması (pitting) hesabı yapılarak dişlinin güvenirliliği hesaplanmıştır. Hasarın nedeninin tespiti için metalografik incelemelerde bulunulmuş, sertlik testi ve spektral analiz sonuçları ile stereo mikroskop görüntüleri incelenmiştir. Deneysel analizler hasara uğrayan ve uğramayan bir dişli için ayrı ayrı yapılarak sonuçlar karşılaştırılmıştır. Çalışma sonucunda deneysel analizlerin sonuçları ve teorik ömür hesapları karşılaştırılarak hasar mekanizması tespit edilmiş ve yorumlanmıştır.

### Giriş

Dişli çarklar, eski çağlardan beri yaygın olarak kullanılan makine elemanlarıdır. Çeşitli boyut, malzeme ve uygulamalarla dişli çarklar; her makinede giriş ve çıkış milleri arasında kuvvet ve hareket ileten, aynı zamanda en uzun ömürlü olması istenilen elemanlardır [1]. Büyük yüklerin taşınmasının yanında dinamik yük ve gürültü seviyesinin en az seviyede tutulması gereken makine elemanlarında helisel dişli çarklar tercih edilmektedir. [2]. Yüksek basınç ve zorlamalara maruz kalan bu makine elemanları, genel olarak hatalı yağlama sebebiyle, dayanımından daha yüksek ve sürekli zorlamalara bağlı olarak hasara uğramaktadır. Aşınma, yüzey yorulmaları (pitting), kırılma ve plastik akma gibi tipik hasarlar bu elemanlarda sıklıkla görülmektedir. Yağ sıcaklığı ve ısınma, dişlinin mikroyapısını önemli ölçüde etkilemekte; aşırı ısınma hasar oluşumuna sebep olmaktadır [3,4]. Aşınma ve yüzey yorulması gibi hasarlar hatalı yağlama ve hatalı kavrama açıları ile ilgiliyken, diş dibinde oluşan kırılma; kademeli hasar olarak meydana gelir ve dişliyi tamamen kullanılmaz hale getirir [5]. Dişli mekanizmaları bu tarz hasarları önleyebilmek için ısıl işlemler ile yüzey sertleştirilmesi işlemine tabi tutulmaktadır [6]. Bu yüzey sertleştirme işlemi sonucunda yüzeyin aşınma ve yorulma dayanımı büyük ölçüde artırılmaktadır [7].

Dişli tasarımlarında çoğu zaman minimum boyut istenirken yüksek yüklere dayanması beklenmektedir. Bu nedenle optimal bir üretim sağlamak için oluşabilecek hasar mekanizmalarına hakim olmak gerekmektedir [8]. Dişlilerin diş dibinde oluşabilecek küçük çatlakların veya dişli temas yüzeylerinde oluşan yorulma çatlaklarının (pitting) önceden saptanamaması nedeniyle birçok makine kullanılmaz hale gelene kadar çalıştırılmaktadır [9]. Kritik yerlerde çalışan dişliler için maliyet kaybının ve daha büyük hasarların oluşmasının önlenmesi için: minimum ömür hesabı ve yüzey basıncı güvenirlik hesabı önem kazanmıştır [9-10]. Hasar tiplerinden biri olan yorulma hasarının önceden saptanabilmesi; makinelerde daha büyük hasarların oluşmasının ve tamamen kullanılmaz hale gelmelerinin önlenmesinde önemli bir etkidir [11]. Değişken yüklemelere maruz kalan makine parçalarında ömür değerleri gerilme-ömür (Wöhler) eğrilerinden saptanabilmektedir. Bu grafiklere göre 103 süreli ömür; 106 çevrim ve sonrası sürekli ömür olarak adlandırılmaktadır [12].

Bu çalışmada önden çekişli bir otomobilin 5 ileri 1 geri manuel vites kutusunun; 3'üncü vites helisel dişlisinde oluşan hasar durumu incelenmiştir. Çalışma sonucunda deneysel analizlerin sonuçları ve teorik ömür hesapları karşılaştırılarak hasar mekanizması tespit edilmiş ve yorumlanmıştır.

### Materyal ve Metot

Bu çalışmada vites kutusunda hasara uğrayan dişli için metalürjik incelemeler ve matematiksel mukavemet ve ömür hesapları bir arada gerçekleştirilerek hasar mekanizması araştırılmıştır. İncelenen vites kutusunda 3'üncü vites dişlisinde (vites çıkış mili dişlisi) aşınma hasarı ve plastik akma oluştuğu gözlemlenmiştir. Hasara uğrayan dişli mekanizması Şekil 1'deki gibidir. Hasara uğrayan dişli şekilde açıkça görülmektedir.



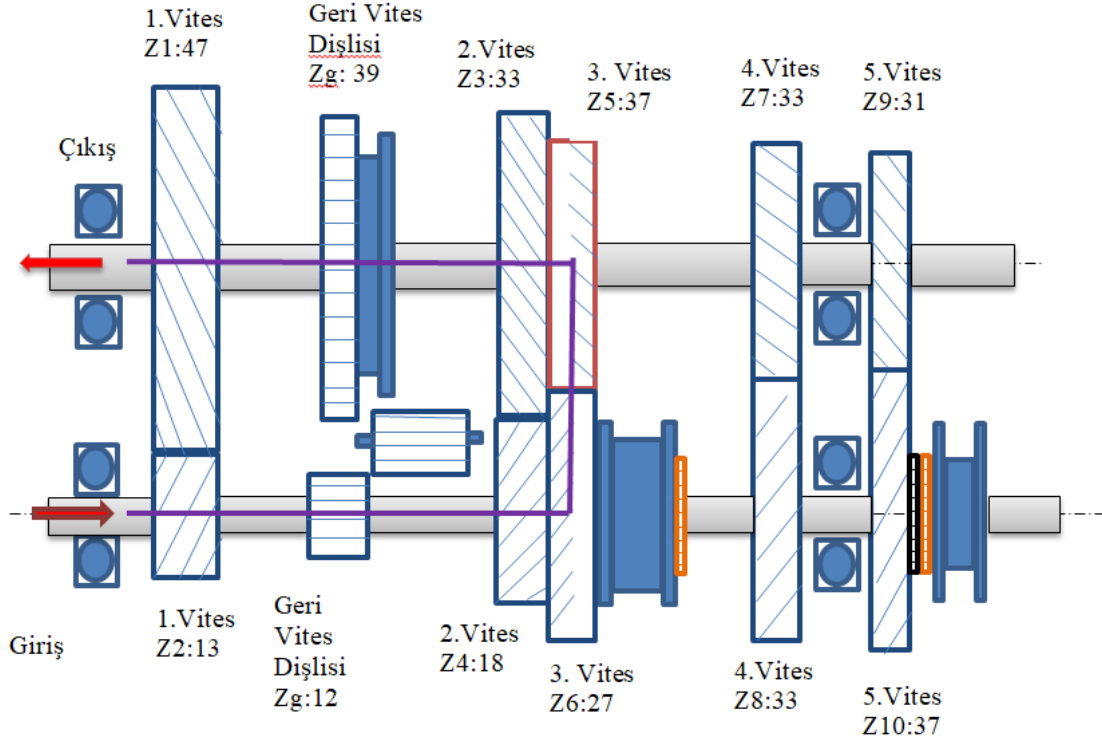
Şekil 1. Hasara uğrayan dişli mekanizması

Kullanılan malzemenin tayini ve hasara uğrayan dişli işe uğramayan dişli arasında kompozisyon farklılıkları olup olmadığını tespit etmek için spektral analiz yapılmıştır. Metalografik incelemeler ile malzemenin ısıl işlemi tahmin edilmiştir. İki numune arasındaki farklılıklar mikro sertlik ölçümleri ile desteklenmiştir. Deneysel sonuçlar incelenmiş iki numune arasındaki farklılıklar ile malzemenin yüzeyi ve çekirdeği arasındaki farklılıklar yorumlanmıştır.

Makine elemanlarında daha büyük hasarların ve kayıpların önlenmesi için büyük önem arz eden güvenilirlik ve teorik ömür hesapları yapılmıştır. Deneysel sonuçlar ve bu hesaplar karşılaştırılarak hasar mekanizması konusunda yorumlarda bulunulmuştur.

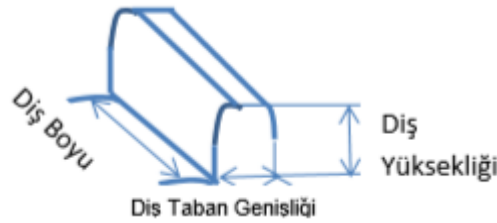
### Diş Dibi Zorlaması Açısından Minimum Ömür Hesabı ve Yüzey Basıncı (Pitting) Hesabı Veriler

Şekil 2'de vites dişli mekanizması şematik olarak verilmiş; 3'cü vites hareket iletme durumu oklar ile gösterilmiştir. Hasar kırmızı olarak gösterilen; çıkış mili üzerindeki dişlide gerçekleşmektedir.



Şekil 2. Üçüncü vites hareket iletme durumu

Dişlinin boyutlarının şematik gösterimi Şekil 3'te verilmiştir.



Şekil 3. Dişli boyutlarının şematik gösterimi

Tablo 1'de dişli üzerinden kumpas yardımıyla alınan ölçüler verilmiştir. Hesaplar bu ölçüler referans alınarak yapılmıştır.

Tablo 1. Dişlinin üzerinden alınan ölçüler

	Dişli Çapları (mm)	Diş Boyu (Dişli genişliği) (mm)	Diş Yüksekliği (mm)	Diş Taban Genişliği (mm)
1.Vites	D1: 112	16,2	5,0	5,4
	D2: 37,2	17,4	5,0	5,4
2.Vites	D3: 97,6	14,6	4,9	5,7
	D4: 51,9	17,0	4,9	5,7
3.Vites	D5: 81,6	14,6	4,9	5,7
	D6: 62,0	14,1	4,9	5,7
4.Vites	D7: 75,2	13,6	4,9	5
	D8: 75,2	13,6	4,9	5
Geri Vites	Dg1: 35	18	5	5
	Dg2: 112,9	11,7	5	5
	Avare Dişli: 78,8	11,30	5,0	5,4

### Giriş Milindeki Moment ( $M_d$ ) Hesabı

Motor gücü, çalışma devri vb. özellikleri aracın özellikleri kapsamında bilinmektedir. Bu doğrultuda mil üzerindeki döndürme momenti 258,37 Nm olarak hesaplanmıştır. Motor gücü: 110 HP=80,85 kW 3'üncü Vites Durumundaki Giriş Mili Devri: 3000 dev/dak, Giriş Mili Döndürme Momenti:  $M_d=257,37$  Nm olarak belirlenmiştir.

### V<sub>3</sub> Dişli için Hesaplar

Tablo 2'de 3'üncü vites dişlisine ait veriler gösterilmiştir. Tablodaki veriler doğrultusunda 3'üncü vites dişlisine ait dönme hızı (6,17 m/s), etkiyen dönme momenti ( $M_{b3}$ ) ve teğetsel kuvvet ( $F_{t3}$ ) hesaplanmıştır:

Tablo 2. Dişli verileri

$d_0$	$z_2$	$z_1$	$b$	$m_n$	$n$	$M_t$
76,7mm	37	27	14,6mm	1,8mm	3000dev/dk	2mm

$$d_0 = m_t \cdot z \quad (1)$$

$$m_t = d_0 / z \quad (2)$$

$$m_t = 2,07 \text{mm} \approx 2 \text{mm} \quad (3)$$

$$m_n = m_t / \cos \beta, m_n = 1,8 \quad (4)$$

$$V_1 = \pi \cdot m_1 \cdot z_1 \cdot n = 508680 \text{mm/dak} \quad (5)$$

$$V_3 = (z_1 / z_2) \cdot V_1 = 371198,92 \text{mm/dak} = 6,17 \text{ m/s} \quad (6)$$

$$M_{b3} = M_d \cdot i = 352,69 \text{ Nm} \quad (7)$$

$$F_{t3} = (2 \cdot M_{b3}) / m \cdot z = 9532,16 \text{ N} \quad (8)$$

Bu değerler dikkate alınarak mukavemet hesapları gerçekleştirilmiştir.

### Diş Dibindeki Zorlama

Diş dibindeki zorlama aşağıda hesaplandığı gibidir. Malzemeye ait veriler literatürden alınan genel geçer bilgilerdir. Diş dibindeki zorlama hesabı için bazı faktörler Tablo 3'te verilmiştir.

$$\sigma_z = \frac{F_t}{m \cdot b} * K_f * K_o * K_v * K_m * K_\beta * K_\epsilon \quad (9)$$

Dişli özelliklerine bağlı değerler ve kabuller;

Malzeme 20CrMo5,  $\sigma_{GD} = 1000 \text{ N/mm}^2$ ,  $P_{HD} = 1250 \text{ N/mm}^2$ ,  $\sigma_{DT} = 0,44 * \sigma_K * 1,7 \sigma_{DT} = 748 \text{ N/mm}^2$

Tablo 3. Dişli hesap faktörleri

$K_f$	$K_o$	$K_v$	$K_m$	$\alpha$	$\beta$	$b$
Form Faktörü	Çalışma Faktörü	Hız Faktörü	Yük Faktörü	Profil Kavrama Açısı	Helis Açısı	Dişli Genişliği
2,55	1,25	1,1	1	20°	30°	14,6

$\epsilon_\alpha = 1,6$  kabul edilmiştir.

$$\epsilon_\beta = \frac{b \cdot \sin \beta}{\pi \cdot m_n} = 1,3 \text{ (Helis faktörü)} \quad (10)$$

$$K_\epsilon = 0,25 + \frac{0,75}{\epsilon_\alpha} \cdot \cos^2 \beta = K_\epsilon = 0,6 \text{ (Kavrama faktörü)} \quad (11)$$

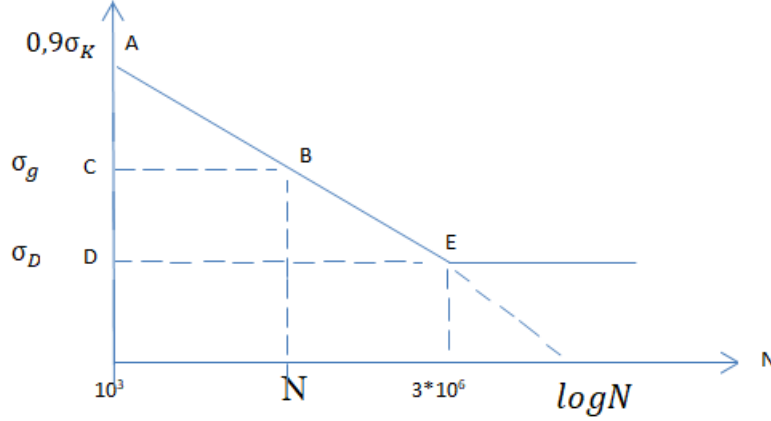
Kalan faktörler de hesaplandıktan sonra değerler formülde aşağıdaki gibi yazılmıştır ve 3'üncü vites diş dibindeki zorlama ( $\sigma_z$ ) 515,07N/mm<sup>2</sup> olarak hesaplanmıştır.

$$\sigma_z = \frac{F_t}{m \cdot b} * K_f * K_o * K_v * K_m * K_\beta * K_\epsilon \quad (13)$$

Bu değerler emniyetli sınırlar içerisinde bulunmuştur.

#### Wöhler Diyagramı ile Dişli Ömür Hesabı

Dişli çarklarda sürekli mukavemet bölgesi sınır değeri DIN 3990 normunda  $3 \times 10^6$  olarak belirtilmektedir [13]. Böylece gerilme-ömür diyagramı Şekil 4'deki gibi çizilebilir.



Şekil 4. Wöhler Diyagramı

$$\log N = 3 + \frac{3,4771 * (0,9\sigma_K - \sigma_g)}{0,9\sigma_K - \sigma_D} \quad (14)$$

Yukarıda Wöhler diyagramından çıkarılan denklemde veriler yerine yazılırsa;

$$\log N = 3 + \frac{3,4771 * (0,9\sigma_K - \sigma_g)}{0,9\sigma_K - \sigma_D} = 17,6968 \quad (15)$$

olarak hesaplanır. Buradan dişli için teorik ömür  $10^{17,6968}$  çevrim olarak bulunmaktadır. Bu da oldukça yüksek bir değer olup, dişlinin ömrünün teorikte bitmediğini göstermektedir.

#### Yüzey Basınç Kontrolü

Dişli çarklarda en sık görülen hasar mekanizmalarından biri olan yüzey basıncı yorulması için gerekli hesaplar aşağıdaki gibidir. Bu hesaplar sonrasında yüzey basıncı açısından güvenli olduğu belirlenmiştir.

$$K_E = \text{Elastiklik Faktörü} = 192, \quad K_\alpha = \text{Kavrama açısı faktörü} = 2,25$$

$$K_i = \sqrt{\frac{i_{12} + 1}{i_{12}}} = 1,32 \quad (16)$$

$$P_{Hmax} = K_E * K_\alpha * K_\beta * K_\epsilon * K_i * \sqrt{\frac{F_t * K_o * K_v * K_m}{b * d_o}} = 879,9 \text{ N/mm}^2 \leq P_{Hlimit} \quad (17)$$

$879,9 \text{ N/mm}^2 \leq 1250 \text{ N/mm}^2$  olarak güvenli sınırlar içerisinde tespit edilmiştir. Tüm hesaplar dikkate alındığında, teorik olarak dişlinin doğru malzemeye ve geometrik boyutlara sahip olduğu tespit edilmiştir. Hasarın kaynağının malzeme ya da boyutlandırma olmadığı, hasarın başka unsurlar nedeniyle oluştuğu düşüncesi oluşmuştur. Bunun üzerine hasarı oluşturması muhtemel unsurlardan olan yağlama ve mekanik hata durumları incelenmiştir. Sonuçlar ve tartışma kısmında bu incelemenin sonuçları yer almaktadır.



### Deneysel Sonuçlar

Spektral analiz sonucunda hasara uğrayan ve uğramayan dişli arasında; kimyasal kompozisyon farkı bulunmadığı tespit edilmiştir. Malzemenin kimyasal kompozisyonu incelendiğinde 20CrMo5 ıslah çeliği olduğu tespit edilmiştir. Spektral analiz sonucunda tespit edilen malzeme kompozisyonları Tablo 4 ve Tablo 5'te verilmiştir. Bu da hasarın malzeme kaynaklı olmadığını göstermiştir.

Tablo 4. Büyük dişli için spektral analiz sonucu malzemenin kimyasal kompozisyonu

Cr	C	Mn	Al	Cu	Mo	Ni	Si	V	S	Co,Nb,Ti,P,W
1.333	0.184	0.943	0.018	0.074	0.091	0.062	0.0242	0.010	0.021	<0.01

Tablo 5. Küçük dişli için spektral analiz sonucu malzemenin kimyasal kompozisyonu

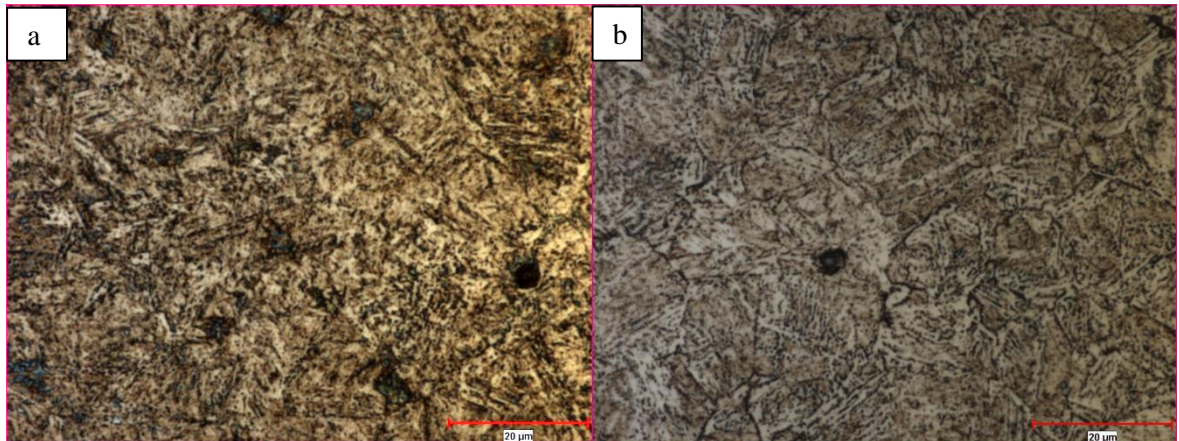
Cr	C	Mn	Al	Cu	Mo	Ni	Si	V	S	Co,Nb,Ti,P,W
1.340	0.188	0.955	0.021	0.089	0.099	0.056	0.0261	0.010	0.015	<0.01

Stereo mikroskop ile çekilen görüntülerde (Şekil 5) görüldüğü gibi hasara uğrayan dişli aşınmış, plastik akmaya uğramış ve sıvanmıştır. Hasara uğrayan dişlinin pinyon dişlisinde hasar meydana gelmemiştir.



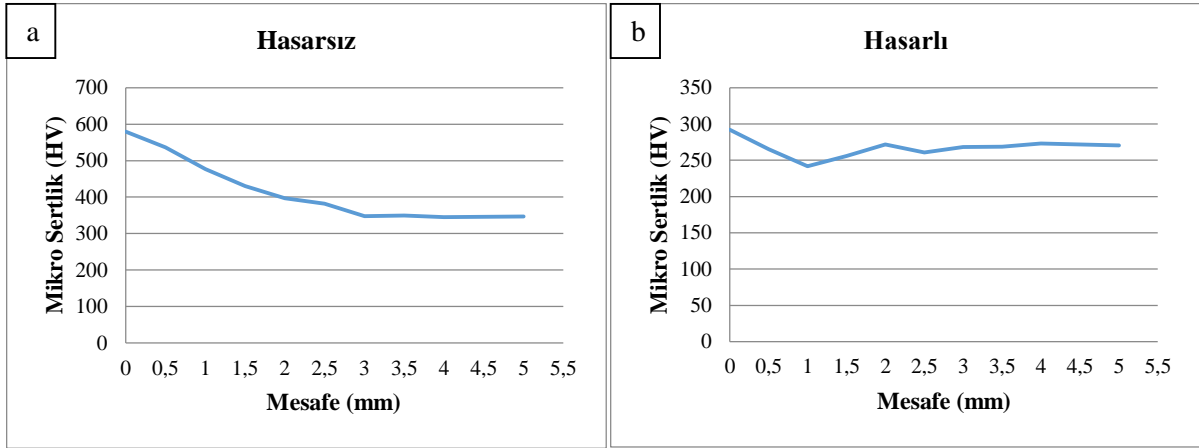
Şekil 5. Hasarsız (a) ve hasarlı (b) numune kesitlerinin stereo mikroskop görüntüleri

Dişlilerin kesit mikroyapıları optik mikroskop yardımıyla incelenmiştir. Şekil 6'da hasarlı numunede temperlenmiş martenzit yapılar göze çarparken; hasarsız olan numunede sert martenzitik yapıların ön planda olduğu gözlemlenmiştir. Buradan hasara uğrayan dişlide daha yumuşak fazların oluştuğu söylenebilir.



Şekil 6. Hasarsız (a) ve hasarlı (b) dişli için mikro yapı incelemesi

Hasarsız ve hasarlı dişlilerin mikro sertlik ölçümleri Şekil 7’de verilmiştir. Ölçümler stereo mikroskopta verilen parça kesitleri üzerinden; diş başından başlanarak ortasına doğru on adet ölçüm yapılmıştır. Hasarsız dişli kesiti üzerinden yapılan ölçümlerde; diş başından ortasına doğru sertliğin azaldığı gözlemlenmiştir. Diş başında yaklaşık 580HV olan sertlik ortalarına doğru 345HV’ye kadar düşmüştür. Bu da dişlilerde yüzey sertleştirme ısı işlemleri uygulandığını göstermektedir. Bunun aksine hasarlı numunede yapılan ölçümlerde sonuçlar düzenli bir azalış veya artış göstermemiş; 242HV ile 292HV arasında değişiklik göstermiştir.



Şekil 7. Hasarsız (a) ve hasarlı (b) dişli için mikro sertlik grafikleri

### Sonuçlar ve Tartışma

Genel olarak vites kutusu dişlileri; yüksek moment iletimi esnasında yüzey basıncı (pitting) ve diş dibi zorlamalarından dolayı hasara uğramaktadır. İncelemiş olduğumuz vites kutusunda ise 3’üncü vites dişlisinde (vites çıkış mili dişlisi) aşınma ve plastik akma olduğu gözlemlenmiştir.

- Yapılan hesaplar sonucunda dişlinin teorik ömür ve yüzey basıncı açısından emniyetli olduğu görülmüştür.
- Senkromeç mekanizmasında veya vites kutusu kilit mekanizmasında oluşan bir arıza sonucunda araç vitesi, 3’üncü vites durumunda takılı kalmış, yetersiz yağlama ve uzun süre 3’üncü vites durumunda çalışma sebebiyle hasar meydana gelmiştir.
- Pinyon (hasarsız dişli) altta bulunduğu düşünüldüğünde yağ seviyesi düşük olduğu için üstteki dişli yeterince yağlanamamıştır ve aşınma başlamıştır.
- Yüzey sertleştirme işlemine tabi tutulan bu tür dişlilerde işlem sırasında hatalar olabilmektedir. Hasara uğrayan dişli için bu durum da söz konusu olabilir.
- Aşınma nedeniyle ısınan dişli yeniden tavllanmış ve mikroyapısının sert martenzitik yapıdan temperlenmiş martenzit yapıya kaydığı gözlemlenmiştir.
- Yapılan mikro sertlik testleri sonucunda hasara uğramayan dişlinin yüzeyinin sertliğinin yüksek olduğu ve içeriye doğru gidildikçe sertliğin düştüğü görülmüştür. Hasara uğrayan dişlinin mikro sertlik ölçümleri hasara uğramayan dişliye göre çok düşük çıkmış ve diş başı ile ortası arasında doğrusal bir farklılık olmadığı gözlemlenmiştir. Bu da hasara uğrayan dişlinin aşırı ısınmadan dolayı yeniden tavlansın mikro yapısının değiştiğinin ispatıdır.

### Referanslar

- [1] Karpat, F., Çavdar, K., & Babalık, F. C. (2002). Bilgisayar yardımıyla düz, helisel, konik ve sonsuz vida dişli mekanizmalarının boyutlandırılması ve analizi. Mühendis ve Makine Dergisi, (510).
- [2] Asi, O. (2006). Fatigue failure of a helical gear in a gearbox. Engineering failure analysis, 13(7), 1116-1125.
- [3] Höhn, B. R., & Michaelis, K. (2004). Influence of oil temperature on gear failures. Tribology International, 37(2), 103-109 Fernandes, P. J. L., & McDuling, C. (1997). Surface contact fatigue failures in gears. Engineering Failure Analysis, 4(2), 99-107.

- [4] Wang, W., Liu, H., Zhu, C., Wei, P., & Wu, W. (2019). Micromechanical analysis of gear fatigue-ratcheting damage considering the phase state and inclusion. *Tribology International*, 136, 182-195.
- [5] Fernandes, P. J. L. (1996). Tooth bending fatigue failures in gears. *Engineering Failure Analysis*, 3(3), 219-225. P. J. L., & McDuling, C. (1997). Surface contact fatigue failures in gears. *Engineering Failure Analysis*, 4(2), 99-107 .
- [6] BOZCA, M. Sertleştirilmiş Silindirik Düz Dişli Çarkın Statik Eğilme Dayanımının Güvenirlik Analizi. *Marmara Fen Bilimleri Dergisi*, 30(4), 388-397.
- [7] Juvinall, R. C., & Marshek, K. M. (2000). *Fundamentals of Machine Component Design*, Jon Wiley & Sons. Inc., Englewood Cliffs, NJ.
- [8] Glodež, S., Ren, Z., & Flašker, J. (1999). Surface fatigue of gear teeth flanks. *Computers & structures*, 73(1-5), 475-483.
- [9] Ulus, Ş., Erkaya, S., & Kayseri, K. (2015). Dişli Çark Mekanizmalarındaki Hataların Akustik Yöntemler ve Titreşim Metodu ile Karşılaştırmalı Analizi. *Uluslararası Katılımlı*, 17, 14-17.
- [10] Nagamura, K., Terauchi, Y., & Martowibowo, S. Y. (1994). Study on gear bending fatigue strength design based on reliability engineering: Prediction of crack propagation and fatigue life of MAC14 supercarburized steel gear. *JSME international journal. Ser. C, Dynamics, control, robotics, design and manufacturing*, 37(4), 795-803.
- [11] Saatçı, G. E., & Tahralı, N. (2003). Birikimli hasar teorileri ve yorulma çatlağına göre ömür değerlendirmeleri. *Journal of Aeronautics and Space Technologies*, 1(2), 33-39.
- [12] Tahralı N., Dikmen F., 1995, "Konstrüksiyon Elemanlarında Güvenirlik ve Ömür Hesapları", Y.T.Ü. Makine Fakültesi, sayı : 303, İstanbul.
- [13] Din 3990 Tragfähigkeitsberechnung Von Stirnrädern; 1987 (Teil 3.)

## **Mining Engineering / Maden Mühendisliği**

## Characterization of Triple Superphosphate for Removal of Heavy Metals

*Mahamane Chapiou Souley Garba\**, Dokuz Eylül University, Graduate School of Natural and Applied Sciences

*Erol Kaya, Fatih Turan, Abdullah Seyrankaya, Dokuz Eylül University, Mining Engineering Department, İzmir, Turkey.*

*Mertol Göknelma and Gabriella Tranell, Norwegian University of Science and Technology, Department of Materials Science and Engineering, Trondheim, Norway*

*\*Corresponding author: mahamane.souley@ogr.deu.edu.tr*

**Keywords:** Triple superphosphate, heavy metals, precipitation

**Discipline:** Mining Engineering

### Abstract

Triple superphosphate or monocalcium phosphate monohydrate has several advantages in soil fertilization. This inorganic fertilizer is water-soluble and has been extensively investigated for the immobilization of heavy metals. The aims of this paper were to characterize triple superphosphate (TSP), its solubility in water, moisture contents, and the impurities released from the TSP. Furthermore, TSP was evaluated for the removal of pure metal ions of Pb and Fe separately from the aqueous environment. The results showed that TSP removed 74.88 % of Pb and 63.96 % of Fe.

### Introduction

Triple superphosphate (TSP) is an inorganic fertilizer and its chemical name is monocalcium phosphate monohydrate [Ca(H<sub>2</sub>PO<sub>4</sub>). H<sub>2</sub>O]. TSP is obtained by adding concentrated phosphoric acid to phosphate rock. The amount of P in triple superphosphate is about 20%, and 80-90% of P is water-soluble [1]. Commercial TSP fertilizer is the most commonly used in the agriculture area for soil fertilization. It is also heavily investigated for the removal of heavy metals, and the remediation of polluted soil.

The use of TSP can be considered as an alternative way for the removal of heavy metals from wastewater or a sludge matrix because of its low cost when compared to other methods [2]. The heavy metals Pb and Fe can be removed from contaminated soil using TSP through a precipitation reaction. A research confirmed that when soluble P (TSP) is added to a waste material, reactions appeared in the solution range from surface sorption of metals to particulate surfaces in waste materials, through the formation of new surface metal precipitates, and the formation of discrete heterogeneous or homogeneous metal precipitates [3]. Valipour et al [4] reported that triple superphosphate adding to contaminated soil reduces the mobility of heavy metals like Cd and Pb by transforming the metals non-leachable. It has been also identified that the immobilization of heavy metals by P amendments including triple superphosphate is carried out through the formation of metal phosphates with reduced solubility and enhanced geochemical stability in a wide range of environmental conditions [5]. Although triple superphosphate fertilizers are effective in the immobilization of heavy metal from waste, they may also contain different quantities of potentially toxic heavy metals or compounds, derived mainly from parent rock materials [6].

The present work focuses on the characterization of TSP by determining its solubility and heavy metal contents. Triple superphosphate was also tested for the removal of pure metals of Pb and Fe.

### Materials and Methods

#### Triple superphosphate solubility and moisture tests

The fertilizer triple superphosphate (TSP) used in this study was received from the fertilizer industry (GÜBRETAŞ-Turkey) in a granular form with no crushing and no grinding. For the solubility tests of TSP, the different masses of granular triple superphosphate were weighed (5g, 10g, 20g, 40g, and 80 g) and dissolved in distilled water. The procedure was as follows: mixing of each weighed mass with 500 ml in beaker glass containing magnetic mixer, then the solution was put on a hot plate adjusted to 3000 revolutions per minute of speed at room temperature. The dissolution time ranged from 1 to 60 minutes and the pH of TSP solution measured by pH meter at the starting and ending time of tests was about 3.3. After solubility time, the solution of TSP was filtered through a funnel glass containing filter paper until

no water dripped anymore. Then, the sludge obtained was put in an oven maintained at 105° C for 1-hour drying, then the masses of dry solids were put desiccator for cooling and the last step was weighing of remained solid by precision balance.

The moisture of TSP was measured by weighing 5g of TSP granular sample on a crucible. Then the crucible containing TSP were put inside a drying oven at a temperature of 105°C. After one hour, the crucibles with the TSP sample were cooled in a desiccator and weighed. The same process was repeated with 2 and 3 hours to measure the maximum of triple superphosphate moisture.

### Chemical analysis of TSP sample

The sample preparation procedures employed in different studies for chemical analysis of fertilizers were the Association of Official Agricultural Chemists (AOAC) methods [7]. The modified method was used by dissolving 5 g of TSP in a 500 ml beaker through the addition of 10 ml of HCl as a reagent. The beaker was covered with a watch glass, and the contents were boiled on a hot plate. The boiled contents were then evaporated to near dryness, and 20 ml of 2 M of HCl were added after cooling. A second boiling was conducted, then the contents were filtered through a funnel glass with filter paper after cooling by using 0.1 M HCl, and the filtrate was collected in a 250 ml volumetric flask. The residue as slurry was washed with 0.1 M HCl, and the volume adjusted with the same solution. For chemical analysis by Inductively Coupled Plasma (ICP), the device was started half an hour before and calibrate with standard solutions of metals Al, Ca, Cd, Co, Cr, Cu, Fe, K, Mg, Mn, Ni, Pb, Sr, and Zn. Thus, the elements released in the filtrate were detected and quantified by employing emission spectrometry with Inductively Coupled Plasma.

### Precipitation test

The standard stock solutions of pure metals Pb<sup>2+</sup> and Fe<sup>2+</sup> used for precipitation tests were received from Merck KGaA company-Germany. Firstly, 5 g of granular TSP (equivalent to 0.04M) were mixed with 500 ml of distilled water in a beaker. At the same time, the beaker covered with a watch glass was put in a hot plate at room temperature, then the dissolution of TSP was accelerated by a magnetic mixer. After 30 minutes, 10 ppm of metal ions of Pb<sup>2+</sup> and Fe<sup>2+</sup> were added separately, into the beaker containing solubilized TSP, and pH measured by pH meter device at the starting and end of the experiment. 5ml of solution were sampled at different reaction times of 0, 5, 10, 30, 60 minutes. Before the sample being analyzed with atomic absorption (AA), calibration curves for each of the selected metals of Pb and Fe were prepared using standard solutions of 0,5 ppm, 3 ppm, 5ppm, 10 ppm, and 20 ppm. Finally, the concentration of the metal ions present in the sample was determined by reading their absorbance using the atomic absorption spectrometry device.

## Results and Discussions

### Solubility and moisture content in TSP

The results presented in Table 1 show that about 82% of TSP is solubilized in the water after mixing 5 g of TSP with 500 ml of distilled water. The pH of the solution was measured as 3.3. No pH adjustment was made. Literature data have shown 80-90% of triple superphosphate is water-soluble [8]. Research has also demonstrated that phosphate-based materials containing 30% of total P in water-soluble, has the solubility rate ranged from 82 to 96 % [9]. As seen from Table 1, the results indicated that the solubility increased with increasing time and it decreased with increasing mass of triple superphosphate.

For the moisture of TSP, the results obtained from TSP drying in the oven at 1, 2, 3 hours were 4.926g, 4.909g, 4.900g respectively. Thus, the moistures of TSP calculated through the difference in the weight of the initial weight and the dry sample were 1.42%; 1.76%; 1.94%; respectively. We can conclude from the result that the moisture of TSP is approximatively 2% which is slightly greater than obtained by De la Vega [10] which is 1.04 ± 0.01 % during the gravimetric determination of moisture and phosphorus in Fertilizer Samples.

### Chemical analysis of TSP

The experimental analyses of the TSP fertilizer sample indicated that TSP contains trace and non-trace elements. As reported in the literature, commercial fertilizers produced in many countries such as India, Italy, Australia, New Zealand, England, and United State contain important concentration values

of Cd, Cu, Cr Ni, Pb, and Zn [11,12]. This presence of heavy metals is due to the origins, i.e. originated from the phosphate rock, and characteristics of TSP fertilizers. Except for the concentrations of Co, Cu, Ni, and Pb, all the concentration of trace elements in this study were in the interval of trace elements concentration values in 24 TSP samples analyzed by Charter et al.; 1993 [13] (see Table 2). Also, the high concentration of Ca ([Ca]=229.8g/kg) explained the solubility of TSP in water. The observation made is that Triple superphosphate fertilizers from different countries have a difference in terms of metal content or heavy metals released. For example, the analytical results of triple superphosphate samples collected according to the different locations in Sri Lanka have demonstrated that the presence of uranium radioactive elements [14]. The concentration value of Pb in TSP sample is lesser than the maximum permissible concentration (MPC) in the soil for Turkey and Europe, while the other trace element concentrations exceed the permissible limit values [15, 16].

### Lead and iron removal

The results of the precipitation test with pure lead indicate that 5g of TSP (0.04 M) precipitates Pb metal efficiently (Table 3). The removal of Pb by TSP occurs in two steps: the dissolution of TSP and the formation of insoluble lead-phosphate. A research confirmed that the principal mechanism of Pb removal by phosphate base-material such as carbonate-hydroxyapatite was the conjunction of dissolution-precipitation with surface sorption [17]. The pH of the solution during lead precipitation with triple superphosphate was measured as acidic 3.3. Similarly, a previous study has also reported that the formation of an insoluble lead-phosphate compound (PbHPO<sub>4</sub>) appeared at pH 3. Figure 1 shows more than 74 % of [Pb] are removed within 60 minutes of reaction times. Comparing to the research on immobilization of Pb by phosphate rock with 65 % as a yield of Pb of removal [18], we can conclude that TSP is more effective than phosphate rock (PR). Even though Brown et al.; [19] reported that excess dosage of TSP (20 g P/Kg) is used to immobilize Pb, the results obtained from analysis confirmed that a maximum yield of Pb removal can be achieved with less dosage of TSP (5g). In addition, many studies have been demonstrated that triple superphosphate immobilizes Pb<sup>2+</sup> efficiently with different methods [20, 21, 22].

Regarding to Fe removal test, a presence of Iron concentration ([Fe] =3.29ppm) in a solution of the TSP sample before was detected by the atomic absorption analysis. Even though the TSP sample contained Fe, the results in Table 3 show an optimum removal rate of [Fe]. In Figure 1, the rate of removal increases slightly from 34.43 to 40.11% between 5 and 10 minutes of sampling time. The maximum iron removal was observed at 60 minutes (63.96%), and the mechanism of Fe removal is attributed to the formation of Iron-phosphate in acidic conditions (pH ≥3). Similar finding reported that the interaction of iron with phosphate species promoted the formation of colloidal Fe-phosphate solid [23]. In addition, the study demonstrated that the reaction of Fe<sup>2+</sup> with phosphate provides the formation of insoluble species (FeH<sub>2</sub>PO<sub>4</sub>) at pH below 5.05 in the thermodynamic equilibrium of iron with triple superphosphate [24].

Table 1. Solubility test results of TSP with different masses in water

Sample Weight, (g)	Time (minutes)	Solubility rate (%)
5g	30	82.25
10g	30	73.78
20g	1	60.99
20g	5	65.45
20g	10	72.73
20g	20	74.35
20g	30	74.92
20g	40	75.48
20g	50	75.59
20g	60	76.11
40g	30	69.34
80g	30	63.83

Table 2. Chemical analysis showing impurities of triple superphosphate sample

Elements in TSP Sample	Concentration of trace elements (mg/kg)								
	Cd	Co	Cr	Cu	Mn	Ni	Pb	Sr	Zn
Sample	38.5	37	343.9	43.6	79.6	120.6	49.6	1301.8	500.2
*Literature, range	6.8-47	9-15	63-548	2.1-13	14-352	14-40	9-16	363-1016	77-696
(MPC) Turkey**	3	20	100	14	NA	75	300	NA	300
(MPC) Europe ***	2	NA	200	50	NA	100	500	NA	300
Elements in TSP Sample	Concentration of Non-trace elements (g/kg)								
	Al	Ca	Fe	K	Mg	Na			
Sample	3.7	229.8	1.96	2.8	7.3	2.9			
*Literature, range	2.3-6.9	99-168	3-10	1.2-4.7	3.1-6.7	2-8.9			
(MPC) Turkey**	NA	NA	NA	NA	NA	NA			
(MPC) Europe ***	NA	NA	NA	NA	NA	NA			

References: [13] \*, [15] \*\*, [16] \*\*\*.

MPC: Maximum permissible concentration of heavy metals in soil.

NA: not available.

Table 3. Pb and Fe removal treated with 5 grams TSP separately in 500ml of distilled water (5ml samples are taken)

Metals	Initial concentration at starting (ppm)	pH	% of metal removal at different times				
			0min	5min.	10min.	30min.	60min.
Pb	10	3.3	40.5	51.25	60.12	68.15	74.88
Fe	10	3.2	25.6	34.43	40.11	53.42	63.96



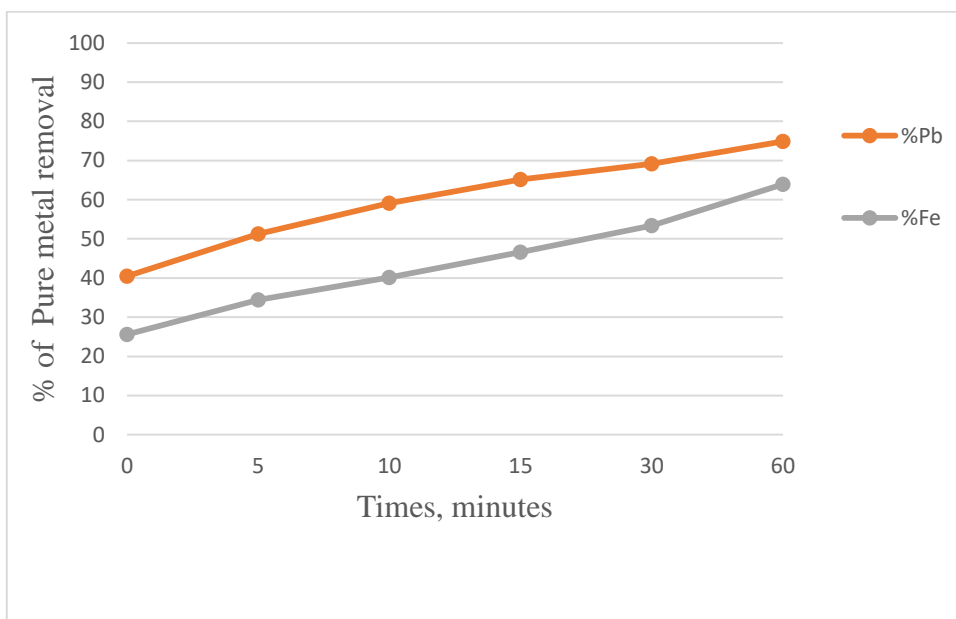


Figure 1. Heavy metals removal using 0,04M (5g) of TSP separately; [Pb]=10ppm; [Fe]=10ppm.

### Conclusion

Based on the results obtained, the following conclusions are drawn:

- The solubility of triple superphosphate (TSP) is about 82 % in water at measured solution pH of 3.3 and its granular form as received has about 2% moisture.
- The chemical analysis of TSP sample indicated that triple superphosphate releases heavy metals of Cd, Cr, Cu, Fe, Mn, Ni, Pb, Sr, and Zn into water.
- The precipitation test result of the TSP with pure metals demonstrated that TSP is effective for the removal of Pb and Fe (74.88%, 63.96 % respectively) from the water.

### Acknowledgments

The authors would like to thank Dokuz Eylul University, İzmir-Turkey, Scientific Research Projects Coordination council (BAP), and Norwegian University of Science and Technology (NTNU), Faculty of Natural Materials and Engineering for partially funding this research.

### References

- [1] B. H. Byrnes, B. L. Bumb, B. H. Byrnes, and B. L. Bumb, "Population Growth, Food Production and Nutrient Requirements Population Growth, Food Production and Nutrient Requirements," October 2014, pp. 37–41, 2008.
- [2] E. P. Agency and R. W. Regan, "Pennstate (814)863-0291," no. 814, 1995.
- [3] McBride NW. Environmental chemistry of soils. New York: Oxford University Press, 1990.
- [4] M. Valipour, K. Shahbazi, and A. Khanmirzaei, "Chemical Immobilization of Lead, Cadmium, Copper, and Nickel in Contaminated Soils by Phosphate Amendments," *Clean - Soil, Air, Water*, 44(5): 572–578, 2016.
- [5] Cao, Rocky X., Lena Q. Ma, Ming Chen, Satya P. Singh, and Willie G. Harris. "Phosphate-induced metal immobilization in a contaminated site." *Environmental Pollution* 122(1): 19-28, 2003.
- [6] D. K. Gupta, S. Chatterjee, S. Datta, V. Veer, and C. Walther, "Role of phosphate fertilizers in heavy metal uptake and detoxification of toxic metals," *Chemosphere*, vol. 108, pp. 134–144, 2014.
- [7] Williams, Sidney. Official methods of analysis. No. 630.24 A8 1984. Association of Official Analytical Chemists, 1984.
- [8] S. H. Chien, "Solubility assessment for fertilizer containing phosphate rock," *Fertile. Res.*, 35(1–2): 93–99, 1993.

- [9] Chien, S.H., Sale, P.W.G. and Hammond, L.L. Comparison of the effectiveness of phosphorus fertilizer products. Phosphorus requirements for sustainable agriculture in Asia and Oceania. Int. Rice Res. Inst., Manila, Philippines, 143-156, 1990.
- [10] De la Vega, G. Z. Gravimetric Determination of Moisture and Phosphorus in Fertilizer Samples, 2014.
- [11] Lee, K.W. and Keeney, D.R. Cadmium and zinc additions to Wisconsin soils by commercial fertilizers and wastewater sludge application. *Water, Air, and Soil Pollution*, 5(1), 109-112, 1975.
- [12] Arora CL, Nayyar VK, Randhawa NS. Note on secondary and microelement contents of fertilizers and manures. *Indian journal of agricultural sciences*. 1975.
- [13] R. A. Charter, M. A. Tabatabai, and J. W. Schafer, "Metal contents of fertilizers marketed in Iowa," *Commun. Soil Sci. Plant Anal.*, 24(9-10): 961-972, 1993.
- [14] C. B. Dissanayake and R. Chandrajith, "Phosphate Mineral Fertilizers, trace metals and human health," *J. Natl. Sci. Found. Sri Lanka*, 37(3): 153-165, 2009.
- [15] Anonim, Toprak Kirliliğinin Kontrolü Yönetmeliği, 25831 Sayılı Resmi Gazetede, Ankara. <https://www.resmigazete.gov.tr/eskiler/2001/12/20011210.htm#3>, 2001.
- [16] Kabata -Pendias, A. Trace elements in soils and plants, *CRC Press*, Inc. Boca Raton, Florida, USA.: 3-18, 1995.
- [17] Xu, H., Yang, L., Wang, P., Liu, Y. and Peng, M. Kinetic research on the sorption of aqueous lead by synthetic carbonate hydroxyapatite. *Journal of Environmental Management*, 86(1): 319-328, 2008.
- [18] X. Cao, L. Q. Ma, D. R. Rhue, and C. S. Appel, "Mechanisms of lead, copper, and zinc retention by phosphate rock," *Environ. Pollut.*, 131(3): 435-444, 2004.
- [19] S. Brown et al., "An inter-laboratory study to test the ability of amendments to reduce the availability of Cd, Pb, and Zn in situ," *Environ. Pollut.*, 138(1): 34-45, 2005.
- [20] Brown, S., Chaney, R., Hallfrisch, J., Ryan, J.A. and Berti, W.R. In situ soil treatments to reduce the phyto-and bioavailability of lead, zinc, and cadmium. *Journal of Environmental Quality*, 33(2): 522-531, 2004.
- [21] R. Melamed, X. Cao, M. Chen, and L. Q. Ma, "Field assessment of lead immobilization in a contaminated soil after phosphate application," 305: 117-127, 2003.
- [22] G. M. Hettiarachchi, G. M. Pierzynski, and M. D. Ransom, "In situ stabilization of soil lead using phosphorus and manganese oxide," *Environ. Sci. Technol.*, 34(21): 4614-4619, 2000.
- [23] Gschwend, P.M. and Reynolds, M.D., 1987. Monodisperse ferrous phosphate colloids in an anoxic groundwater plume. *Journal of Contaminant Hydrology*, 1(3): 309-327.
- [24] Kaya, E., Regan Sr, R.W. and Osseo-Asare, K. Thermodynamic equilibrium of lead and iron with triple superphosphate. *Transactions of the American Foundrymen's Society*, 104: 651-658, 1996.

## **Nanotechnology / Nanoteknoloji**

## Preparation and Characterization of Chitosan-Based Hydrogels Reinforced by Mesoporous Silica Nanoparticles

Ahmet Aykaç\*, İzmir Kâtip Çelebi University, Faculty of Engineering and Architecture, Department of Engineering Sciences, İzmir, Turkey

İzel Ok, İzmir Kâtip Çelebi University, Institute of Natural & Applied Sciences, Department of Nanoscience & Nanotechnology, İzmir, Turkey

\*Corresponding Author e-mail: ahmet.aykac@ikcu.edu.tr

**Keywords:** Hydrogel, chitosan-based hydrogel, mesoporous silica nanoparticle, mesoporous silica nanoparticles/chitosan-based hydrogel

**Discipline:** Nanotechnology and Materials Science

### Abstract

Hydrogels are three-dimensional, cross-linked organizations that can absorb a large of water without dissolving structures. Hydrogels have many applications in many scientific fields. Mainly they are used in bioengineering as a component of tissue engineering and 3D structures that act as a support for cells and help the formation of an ideal tissue; in pharmaceutical science as a drug delivery carrier, and in material science engineering as a smart material. Mesoporous silica nanoparticles can be defined as a mesoporous form of silica that has applications in catalysis, drug delivery systems, and imaging. Due to the increasing demand for new materials with improved thermal, mechanical, physical, and chemical properties, the application of silica nanoparticles as fillers in the preparation of nanocomposites especially in hydrogels has attracted great attention. So that, we have envisaged to the reinforcement of chitosan-based hydrogels by mesoporous silica nanoparticles might be helpful to overcome mechanical problems of chitosan-based hydrogels.

In this study, we have synthesized and characterized chitosan-based hydrogel (CS), mesoporous silica nanoparticles (MSNPs), and finally, chitosan-based hydrogels reinforced by the mesoporous silica nanoparticles (CS/MSNPs). Characterizations of the prepared MSNPs and the hydrogel were carried out by Fourier transform infrared spectroscopy (FTIR), nano zeta sizer, and scanning electron microscopy (SEM).

### Introduction

Hydrogels were first reported by Wichterle and Lím in 1960 [1] and they are three-dimensional (3D), cross-linked soft materials that are composed of a large amount of water without dissolving or losing their structure. Hydrogels may have hydrophilic or hydrophobic functional groups due to the polymers which compose the hydrogels. Hydrophilic functional groups, such as hydroxyl (–OH), amine (NH<sub>2</sub>), and amide (–CONH–CONH<sub>2</sub>) facilitate the water absorption ability of hydrogels. Hydrophilic chains have higher water swelling capacity than hydrophobic chains such as polylactic acid [2]–[4]. Owing to this high-water content (typically 70–99%) property, hydrogels exhibit excellent biocompatibility, the capability to easily encapsulate hydrophilic drugs, and decrease the risk of drug denaturation and aggregation upon exposure to organic solvents as well as they can act like tissues [5]. Therefore, they are one of the most in-demand materials used in many different kinds of applications like drug delivery, tissue engineering, contact lens, wound dressing in terms of biomedical applications [6], [7]. Depending on methods of preparation, hydrogels can be classified into physically crosslinked hydrogels that have secondary forces interaction networks such as ionic, hydrogen bonding, or hydrophobic bonds and chemically crosslinked hydrogels that have covalently bonded cross-linked networks and they are stronger than physically crosslinked hydrogels [3], [6]. The cross-linked polymer network was high sensitivity to stimuli such as solvent composition, solutes, pH, temperature, electric field, and light [8]. Moreover, their porous structure can be tuned by controlling the crosslinking density in the gel matrix and correspondingly the swelling ratio in the aqueous environment [9].

Generally, hydrogels can be prepared from synthetic or natural polymers. Among these hydrogels, chitosan-based hydrogels are the most widely studied [6]. Chitosan is a naturally occurring polymer obtained by deacetylation of chitin and it is one of the most studied polymers in wound dressing applications especially as hydrogel material due to its biodegradable, biocompatible, non-toxic, antibacterial properties. Also, amino and hydroxyl groups found on the structure of chitosan enable a desirable and controllable chemical structure [10], [11]. Many studies reported the production of

chitosan-based hydrogels and their applications on tissue repairing, wound dressing, and drug delivery applications. For example, Tamahkar et al. synthesized chitosan (CS)-based poly- $\epsilon$ -caprolactone (PCL) hydrogels by using polyvinyl alcohol (PVA), polyethylene glycol (PEG), and polyvinyl pyrrolidone (PVP). PVA-CS-PCL hydrogels to observe the drug delivery potential of this composite for wound dressing applications [12]. Besides, Abdel-Mohsen et al. produced a physically cross-linked polyvinyl alcohol (PVA)/chitosan hydrogel for the release of sparfloxacin antibiotic by using the eco synthesis method [13]. On the other hand, chitosan-based hydrogels have some disadvantages such as low mechanical strength because of the high-water content, a comparatively loose three-dimensional (3D) network, and unsatisfied releasing time of some small drug molecules from the chitosan hydrogel [11]. In order to overcome these problems, chitosan has been blended with various materials to obtain mechanical and chemically reinforced chitosan-based composites [6].

Mesoporous silica nanoparticles have provided new solutions recently in nanomedicine and biomedical applications by incorporated with hydrogels due to their large surface area, controllable mesopore size, modifiable surface, good chemical and thermal stabilities, and biocompatibility properties. MSNs have the ability to boost both the mechanical strength of the chitosan hydrogel and control the drug-releasing time [11], [14], [15]. In the literature, there are many studies about the uses of MSNPs in biomedical applications. Among them, for instance, the study of Zhu et al. developed an MSNPs/chitosan hydrogel and investigated its mechanical properties and drug delivery behaviours by loading of gentamicin (GS) and bovine serum albumin (BSA) as small drug models [11].

In this study, we aimed to develop a chitosan hydrogel reinforced by mesoporous silica nanoparticles (CS/MSNPs) to investigate the effect of the MSNPs on the chitosan-based hydrogels as a reinforcement factor. The main purpose of this investigation is to evaluate the properties of this hydrogel in terms of the possibility of being a potential drug delivery system candidate for our future studies. Regarding our study, the preparation steps are shown in Figure 1.

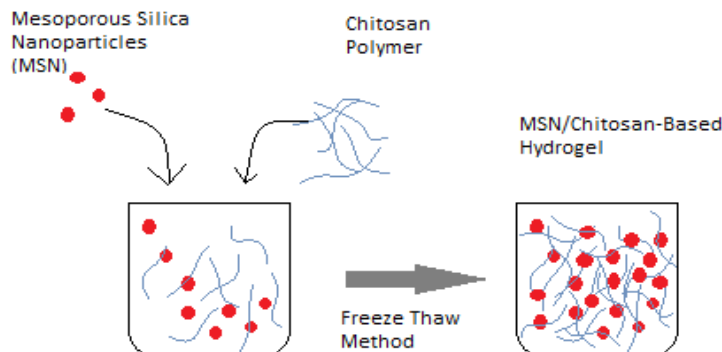


Figure 1. The preparation steps of MSNPs/CS based hydrogel. Firstly, MSNPs were synthesized by doing slight modifications in sol-gel method at our laboratory. Secondly, chitosan and MSNPs were blended to obtain MSNPs/CS based hydrogel.

## Methodology

### Preparation of Mesoporous Silica Nanoparticles (MSNPs)

During the preparation process, cetyltrimethylammonium bromide (CTAB) was used as a structure-directing agent and tetraethoxysilane (TEOS) was used as a silicon source. MSNPs were obtained by doing slight modifications in the sol-gel method. In this process, 0,32 gr cetyltrimethylammonium bromide (CTAB, 99%), was dissolved in 110 mL water, and then 2 ml of tetraethoxysilane (TEOS, 98%), 52 mL of anhydrous ethanol, and 2 mL of ammonium hydroxide (NH<sub>4</sub>OH) were added into the mixture of water. The mixture was stirred for 3 h to produce a white precipitate. After the reaction, white precipitations were obtained, washed with a large amount of water, and kept dried [15-17].

The size distributions of nanoparticles were measured by using a Malvern Nano ZS90 Zetasizer. Besides, the morphology of the MSNPs was investigated by using a Carl Zeiss 300VP Scanning Electron Microscope (SEM). FTIR spectra were recorded using a Thermo Scientific Nicolet iS50 FT-IR Spectrometer in the spectral range 4000-500 cm<sup>-1</sup>.

### Preparation of Mesoporous Silica Nanoparticles/Chitosan (MSNPs/CS) Based Hydrogel

200 mg of CS powder was dissolved into 1.0 % aqueous acetic acid (9 mL) at room temperature. 100 mg of MSNPs were then added to the acidic suspension by under magnetic stirring at 45 °C. The viscous solution was transferred into petri dishes and dried overnight. Hydrogels were pre-frozen at -20 °C for 12 h and then they were lyophilized in a freeze drier [11]. The morphology of the MSN/CS-based hydrogels was investigated using a Carl Zeiss 300VP Scanning Electron Microscope (SEM). Also, FTIR spectra were recorded using a Thermo Scientific Nicolet iS50 FT-IR Spectrometer in the spectral range 4000-500 cm<sup>-1</sup>.

### Results

#### Result of FTIR Analysis of the Mesoporous Silica Nanoparticles (MSNPs), Pure Chitosan-Based Hydrogel and MSNPs/CS-Based Hydrogels

The FTIR spectrum of mesoporous silica nanoparticles (MSNPs) presented in Figure 2 shows a broad band at 3443 cm<sup>-1</sup>, attributed to O-H stretching, the band at 2922 cm<sup>-1</sup> represents -CH<sub>2</sub> aliphatic groups. The band at 1029 cm<sup>-1</sup> shows the silica groups.

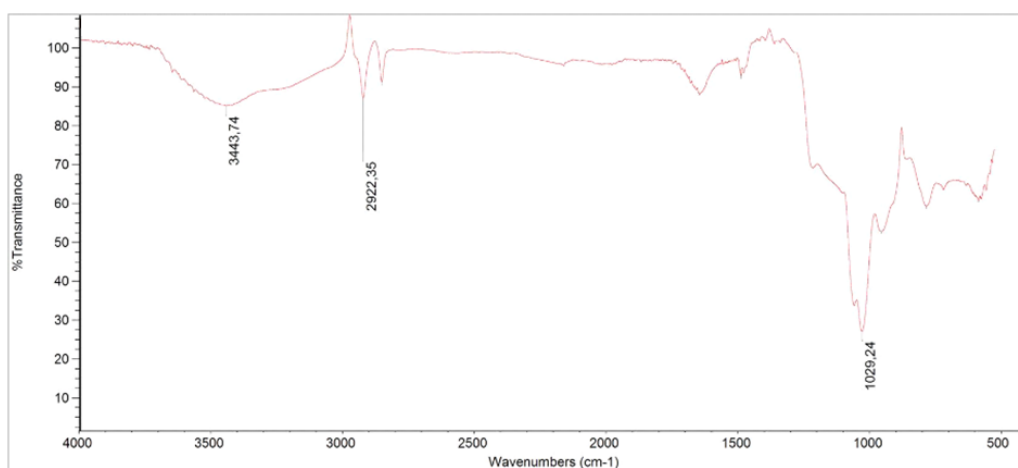


Figure 2. FTIR spectra of mesoporous silica nanoparticles (MSN)

The FTIR spectrum of pure chitosan-based hydrogel presented in Figure 3 shows a broad band at 3253 cm<sup>-1</sup>, attributed to O-H stretching, the band at 2922 cm<sup>-1</sup> represents -CH<sub>2</sub> aliphatic groups. The band at 1635 cm<sup>-1</sup> is the N-H bending vibration. Also, the band at 1538 cm<sup>-1</sup> refers to N-O stretching.

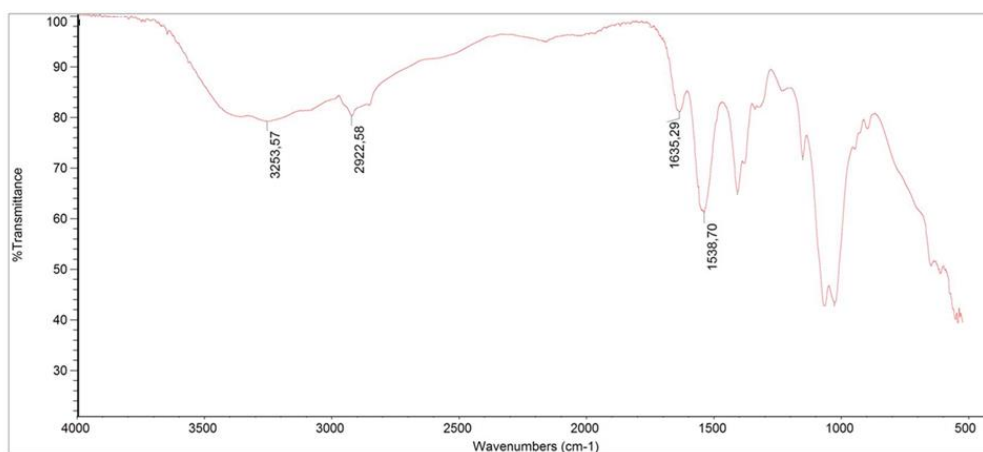


Figure 3. FTIR spectra of chitosan hydrogel

Moreover, the FTIR spectrum of MSNPs/CS based hydrogel is presented in Figure 4. This graphic shows a broad band at  $3261\text{ cm}^{-1}$ , attributed to O-H stretching, the band at  $1548\text{ cm}^{-1}$  is the regarding as N-H bending vibration. Also, the band at  $1072\text{ cm}^{-1}$  represents silica groups.

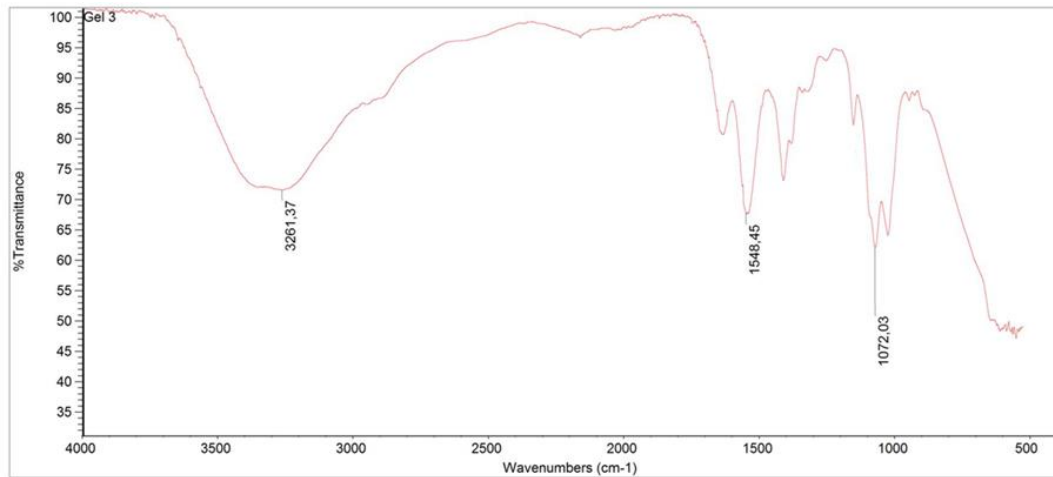


Figure 4. FTIR spectra of MSN/CS based hydrogel

#### Results of size distribution analysis of MSNPs

The size distributions of MSNs were exhibited in Figure 5. The average hydrodynamic diameter of MSNs dispersed in water is between 300-400 nm, which is in agreement with the SEM analysis.

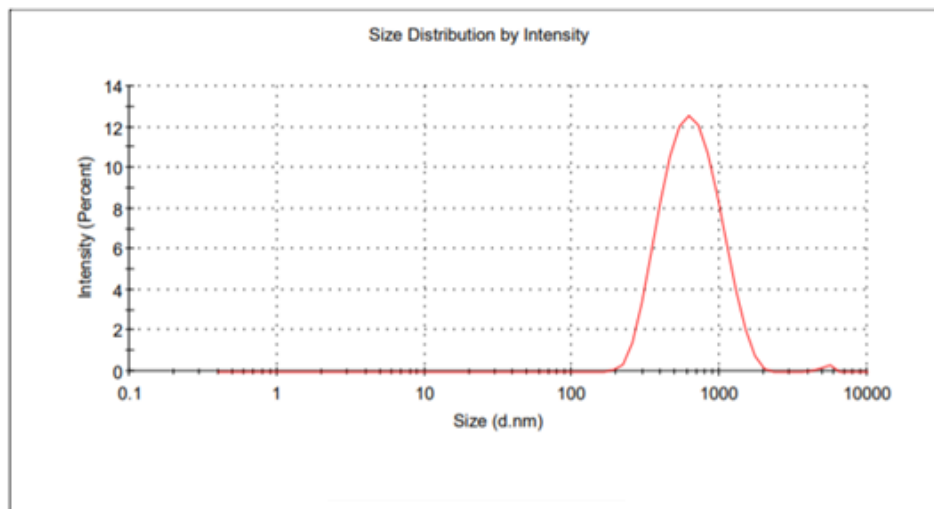


Figure 5. The size distribution of MSN

#### Results of Scanning Electron Microscope Analysis of MSNPs and MSNPs/CS-Based Hydrogel

Morphology analysis is important evidence of whether the study was successful. Therefore, both MSNPs and MSNPs/CS-based hydrogels structures were characterized by using SEM. SEM images of the samples are given in Figure 6. As can be seen in Figure 6 (a) diameter of MSNPs is approximately 340-360 nm and the nanoparticles have been dispersed. Besides, Figure 6 (b) shows the 3D structure of MSNPs/CS-based hydrogels which MSNPs were dispersed homogeneously on the hydrogel surface.

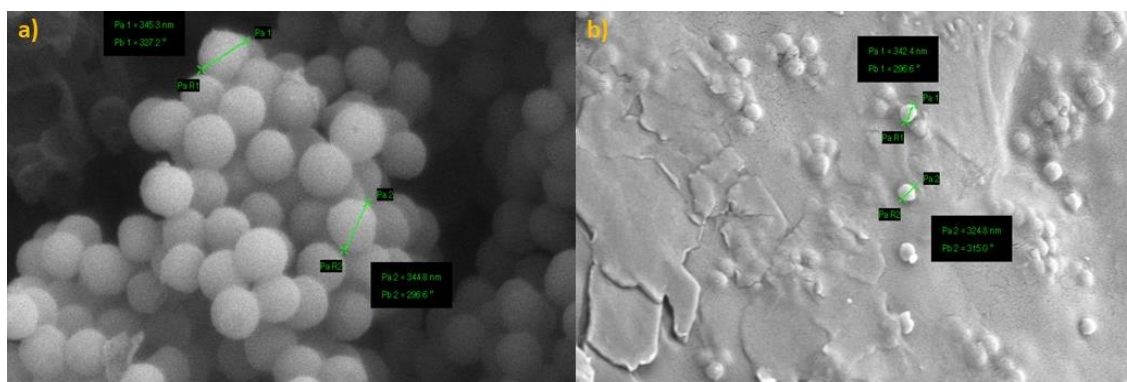


Figure 6. a) The SEM image of MSNPs, b) The SEM image of MSNPs/CS based hydrogel

### Conclusion and Future Perspective

In a conclusion, we have synthesized and characterized the mesoporous silica nanoparticles successfully and we have produced the chitosan-based hydrogels that reinforced by mesoporous silica nanoparticles. We anticipate that these current advancements will yield next-generation delivery systems as we gain a further understanding of the dynamics of mixed chitosan chain networks. Once we fully optimized the parameters for the production of chitosan-based hydrogel that contains a certain amount of the MSNPs we believe that, a cheap, non-toxic, efficient, and novel MSNPs-chitosan-based hydrogel network will be available for drugs as a carrier system not only on lab-scale but also in clinical trials. We believe that the result of this study will lead to further investigations and it will be able to adapt delivery systems for different drug formulations, release conditions, and treatment intervals.

### References

- [1] Wichterle O, Lim D. Hydrophilic Gels for Biological Use. *Nature* [Internet]. 1960;185(4706):117–8. Available from: <https://doi.org/10.1038/185117a0>
- [2] Bahram M, Mohseni N, Moghtader M. An Introduction to Hydrogels and Some Recent Applications. In 2016.
- [3] Hamedi H, Moradi S, Hudson SM, Tonelli AE. Chitosan based hydrogels and their applications for drug delivery in wound dressings: A review. *Carbohydr Polym* [Internet]. 2018;199:445–60. Available from: <http://www.sciencedirect.com/science/article/pii/S0144861718307690>
- [4] Damiri F, Bachra Y, Bounacir C, Laaraibi A, Berrada M. Synthesis and Characterization of Lyophilized Chitosan-Based Hydrogels Cross-Linked with Benzaldehyde for Controlled Drug Release. Bai L, editor. *J Chem* [Internet]. 2020;2020:8747639. Available from: <https://doi.org/10.1155/2020/8747639>
- [5] Li J, Mooney DJ. Designing hydrogels for controlled drug delivery. *Nat Rev Mater* [Internet]. 2016;1(12):16071. Available from: <https://doi.org/10.1038/natrevmats.2016.71>
- [6] Wu T, Li Y, Lee DS. Chitosan-based composite hydrogels for biomedical applications. *Macromol Res* [Internet]. 2017;25(6):480–8. Available from: <https://doi.org/10.1007/s13233-017-5066-0>
- [7] Shin MS, Kang H seok, Park TG, Yang J-W. Synthesis and characterization of pH/temperature-sensitive hydrogels based on chitosan derivative. *Polym Bull* [Internet]. 2002;47(5):451–6. Available from: <https://doi.org/10.1007/s002890200008>
- [8] Thoniyot P, Tan MJ, Karim AA, Young DJ, Loh XJ. Nanoparticle–Hydrogel Composites: Concept, Design, and Applications of These Promising, Multi-Functional Materials. *Adv Sci* [Internet]. 2015 Feb 1;2(1–2):1400010. Available from: <https://doi.org/10.1002/advs.201400010>
- [9] Alemdar N. Synthesis of chitosan-based hydrogel by using photopolymerization technique. *Anadolu Univ J Sci Technol Appl Sci Eng*. 2016 Jul 14;17.
- [10] Sámano-Valencia C, Martínez-Castañón GA, Martínez-Gutiérrez F, Ruiz F, Toro-Vázquez JF, Morales-Rueda JA, et al. Characterization and Biocompatibility of Chitosan Gels with Silver and Gold Nanoparticles. Wang R, editor. *J Nanomater* [Internet]. 2014;2014:543419. Available from: <https://doi.org/10.1155/2014/543419>
- [11] Zhu M, Zhu Y, Zhang L, Shi J. Preparation of chitosan/mesoporous silica nanoparticle composite



- hydrogels for sustained co-delivery of biomacromolecules and small chemical drugs. *Sci Technol Adv Mater* [Internet]. 2013 Jul 23;14(4):45005. Available from: <https://pubmed.ncbi.nlm.nih.gov/27877598>
- [12] Tamahkar E, Özkahraman B. Synthesis of Chitosan-Based Hydrogels as a Novel Drug Release Device for Wound Healing. *Hittite J Sci Eng*. 2017 Jan 1;4:137–44.
- [13] Abdel-Mohsen AM, Aly AS, Hrdina R, Montaser AS, Hebeish A. Eco-Synthesis of PVA/Chitosan Hydrogels for Biomedical Application. *J Polym Environ* [Internet]. 2011;19(4):1005–12. Available from: <https://doi.org/10.1007/s10924-011-0334-0>
- [14] Liu W. Facile and simple preparation of pH-sensitive chitosan-mesoporous silica nanoparticles for future breast cancer treatment. *Express Polym Lett*. 2015 Oct 1;9:1068–75.
- [15] Şen Karaman D, Sarwar S, Desai D, Björk EM, Odén M, Chakrabarti P, et al. Shape engineering boosts antibacterial activity of chitosan coated mesoporous silica nanoparticle doped with silver: a mechanistic investigation. *J Mater Chem B* [Internet]. 2016;4(19):3292–304. Available from: <http://dx.doi.org/10.1039/C5TB02526E>
- [16] Li Z, Zhang Y, Feng N. Mesoporous silica nanoparticles: synthesis, classification, drug loading, pharmacokinetics, biocompatibility, and application in drug delivery. *Expert Opin Drug Deliv*. 2019 Mar;16(3):219–37.
- [17] Zhao P, Liu H, Deng H, Xiao L, Qin C, Du Y, et al. A study of chitosan hydrogel with embedded mesoporous silica nanoparticles loaded by ibuprofen as a dual stimuli-responsive drug release system for surface coating of titanium implants. *Colloids Surfaces B Biointerfaces* [Internet]. 2014;123:657–63. Available from: <http://www.sciencedirect.com/science/article/pii/S092777651400544X>

## **Petroleum and Natural Gas Engineering / Petrol ve Doğalgaz Mühendisliği**

## Miscible Displacement Simulator Using Novel Adjustable Flux Limiter

Osman Ünal\*, İzmir Kâtip Çelebi Univ., Dept. of Petroleum Engineering, İzmir, Türkiye

\*Corresponding author: osman.unal1992@gmail.com

**Keywords:** Flux limiter, high resolution scheme, reservoir simulation

**Discipline:** Petroleum and Natural Gas Engineering

### Abstract

Numerical reservoir simulations are used to predict performance of the oil and gas reservoirs. Due to the inherent of the numerical calculations, reservoir simulation engineers encounter some significant problems such as numerical dispersion and unphysical oscillation.

The use of first order methods leads to huge numerical dispersion. Numerical dispersions cause incorrectly prediction of reservoir performance. Therefore, reservoir simulation engineers need to use higher order techniques to diminish effects of the numerical dispersion. Leonard, Zhang and Jiang improved higher order spatial discretization schemes using Quick (without flux limiter function), TCDF (third order continuously differentiable function) flux limiter and Adaptive flux limiter methods respectively. First objective of this study is to propose application of second order Crank-Nicolson time accuracy method to previously developed spatial discretization techniques. Because using second order semi-implicit Crank-Nicolson time accuracy method significantly reduces effects of numerical dispersion especially at large time steps.

Although use of higher order techniques gives to us sharper flood front compared with the first order methods, they lead to unacceptable and unphysical oscillations in some cases for instance at large courant number. Second objective of this study is to present novel adjustable flux limiter function which works at large courant number without any unphysical oscillation compared with the previously developed flux limiter such as TCDF and Adaptive flux limiter functions.

### Introduction

Decreasing the numerical dispersion and suppressing non-physical oscillation have been a major problem of CFD researchers for many years. Higher-order techniques are recommended to reduce numerical dispersion [1]. However, in some cases, especially for large Courant numbers, higher order techniques cause non-physical oscillations. In the Quick method proposed by Leonard [2] in 1979, both the numerical dispersion was reduced and non-physical oscillations were suppressed by using the third order differentiation method. However, the Quick method causes large non-physical oscillations in the convection dominated flows. In 2015, Zhang [3] proposed the TCDF method in order to both suppress the oscillations occurring in the Quick method and to optimize the number of Newton iterations. In 2017, Jiang [4] reduced the upper limit of the limiter function from 2 to 1.5 constant value, further reducing the number of Newton iterations. In 2020, Unal [5] proposed the flexible flux limiter function by defining the upper limit of the limiter function as a function of the Courant number instead of 1.5 fixed number value. Flexible flux limiter captures higher order scheme by bringing the upper limit of the limiter function closer to 2 at low Courant values, while suppressing non-physical oscillations by approaching the upper limit of the limiter function to 1.15 at high courant values. Although the Courant number is a good parameter to determine the upper limit of the limiter function, in order to obtain more stable and more accurate results, it is necessary to determine the upper limit of the limiting function by considering the total variation (TV) and Newton iteration numbers. This study proposes the Adjustable Flux Limiter function, which determines the highest limit of the limiter function, using the parameters of Courant number, TV and Newton iteration with the help of fuzzy logic.

### Application of Crank-Nicolson Method to TCDF and Adaptive 1.5 Limiters

Unsteady convection-diffusion equation [6] consists of diffusion term, convection term and accumulation term. Eq. (1) shows general form of unsteady convection-diffusion equation.

$$D\nabla^2 C - u \cdot \nabla C = \frac{\partial C}{\partial t} \quad (1)$$

In Eq. (1), first left-hand side term is diffusion term and D refers to the physical dispersion coefficient. Second left-hand side term is convection term and u refers to the velocity. Right-hand side term is accumulation term. Eq. (2) indicates one-dimensional form of the Eq. (1).

$$D \frac{\partial^2 C}{\partial x^2} - u \frac{\partial C}{\partial x} = \frac{\partial C}{\partial t} \quad (2)$$

Space discretization of one-dimensional convection-diffusion equation can be expressed as Eq. (3).

$$D \frac{C_{i+1} - 2C_i + C_{i-1}}{\Delta x^2} - u \frac{C_{i+1/2} - C_{i-1/2}}{\Delta x} = \frac{\partial C}{\partial t} \quad (3)$$

According to Eq. (3), there is not any problem of space discretization of diffusion term. Because only block center values are required to know for diffusion term. On the other hand, block face values have to be predicted for space discretization of convection term. But there is no any knowledge about block face values. Only block center values are known in numerical methods. Therefore, block face values are predicted according to some techniques.

$$C_{i+1/2} \approx C_i \quad (4)$$

Eq. (4) shows single point upwinding technique. According to upwinding or upstream technique [7], the previous central block value is assumed to be the right face value.

$$C_{i+1/2} \approx \frac{C_{i+1} + C_i}{2} - \frac{C_{i+1} - 2C_i + C_{i-1}}{8} \quad (5)$$

Eq. (5) implies third order Quick method. It is very good method to suppress unphysical oscillation. But it cause large unphysical oscillation when physical dispersion coefficient approaches to zero [8]. Thus, limiter functions should be used to calculate grid block face values. Eq. (6) shows general form of the limiter functions.

$$C_{i+1/2} \approx C_i + \frac{1}{2} \varphi(r) [C_i - C_{i-1}] \quad (6)$$

Generally, limiter functions consist of upwinding term and anti-diffusive term. In Eq. (6), first right-hand side term is upwinding or upstream term and second right-hand side term is anti-diffusive term. In Eq. (6),  $\varphi$  is limiter which is a function of concentration gradient ratio (r). Eq. (7) shows concentration gradient ratio.

$$r = \frac{C_{i+1} - C_i}{C_i - C_{i-1}} \quad (7)$$

Total variation diminishing (TVD) technique [9, 10] is used to suppress unphysical oscillation. In order to get second order accurate and TVD scheme, limiter have to pass through grey shaded area in

Figure 1. There are a number of limiter function to satisfy TVD criteria but two of them stand out: TCDF and Adaptive 1.5. Eqs. (8) and (9) are mathematical expression of TCDF and Adaptive 1.5 methods respectively.

$$\varphi(r) = \begin{cases} r^3 - 2r^2 + 2r & \text{if, } 0 \leq r < 0.5 \\ 0.75r + 0.25 & \text{if, } 0.5 \leq r < 2 \\ \frac{2r^2 - 2r - 9/4}{r^2 - r - 1} & \text{if, } 2 \leq r < +\infty \end{cases} \quad (8)$$

$$\varphi(r) = \begin{cases} r^3 - 2r^2 + 2r & \text{if, } 0 \leq r < 0.5 \\ -\frac{1.5}{15} \log \left( e^{\left(\frac{-1.5}{15}\right)(0.75r+0.25)} + e^{-15} \right) & \text{if, } 0.5 \leq r \end{cases} \quad (9)$$

Main difference between TCDF and Adaptive 1.5 methods is the upper limit of these methods. While upper limit of the TCDF method is fixed to 2 constant values, upper limit of the Adaptive 1.5 is fixed to 1.5 constant value. Due to the lower limit of the Adaptive 1.5, Adaptive 1.5 is better method than TCDF method to suppress unphysical oscillations. But it is required to increase upper limit of the limiter functions to get more accurate results. Figure 1 shows TCDF and Adaptive 1.5 methods in TVD region.

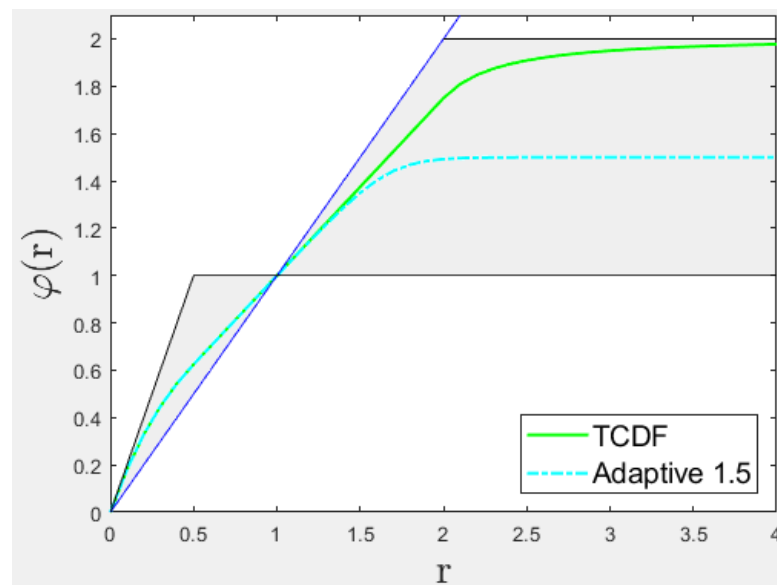


Figure 1. TVD region

In this study, two time discretization techniques will be discussed as fully implicit method (Eq. (10)) and semi-implicit method [11] (Eq. (11)). Both techniques are unconditionally stable but fully implicit method has first order time accuracy. On the other hand, semi-implicit or Crank-Nicolson method has second order time accuracy. Therefore, it reduces numerical dispersion significantly.

$$-u \frac{C_{i+1/2}^{n+1} - C_{i-1/2}^{n+1}}{\Delta x} = \frac{C_i^{n+1} - C_i^n}{\Delta t} \quad (10)$$

$$-u \frac{0.5(C_{i+1/2}^n - C_{i-1/2}^n) + 0.5(C_{i+1/2}^{n+1} - C_{i-1/2}^{n+1})}{\Delta x} = \frac{C_i^{n+1} - C_i^n}{\Delta t} \quad (11)$$

It is assumed that velocity is 1, Courant number ( $N_c$ ) is 1 and flow is convection dominated flow for each case.

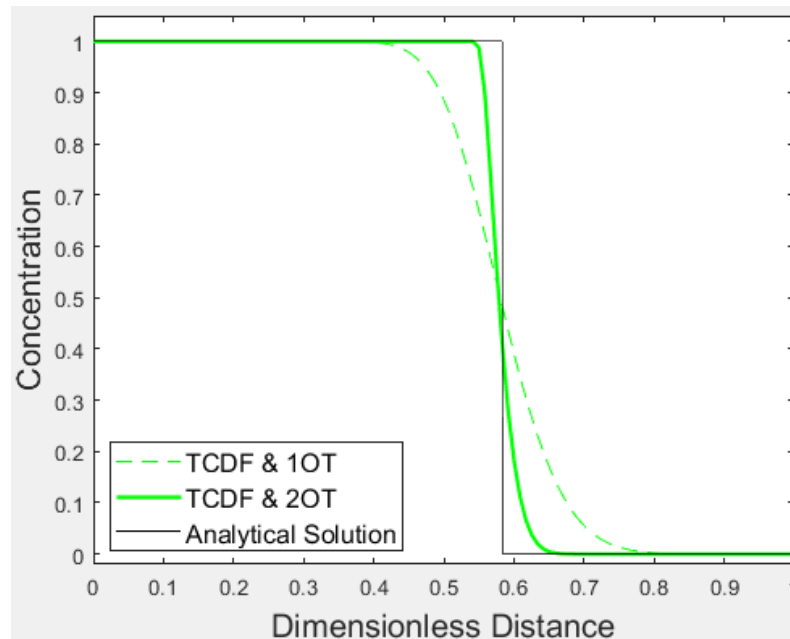


Figure 2. Application of Crank-Nicolson method to TCDF limiter ( $N_c=1$ ).

First objective of this study is to present application of Crank-Nicolson (CN) technique to TCDF and Adaptive 1.5 methods. Figures 2 and 3 show both implicit and CN time discretization methods. Crank-Nicolson method reduces nearly more than half of numerical dispersion for both schemes.

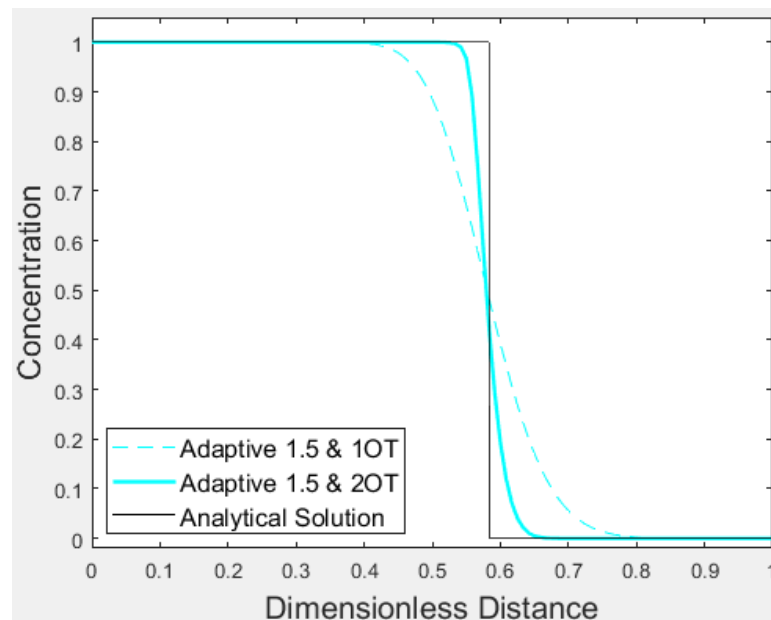


Figure 3. Application of Crank-Nicolson method to Adaptive 1.5 limiter ( $N_c=1$ ).

### Novel Adjustable Flux Limiter Using Fuzzy Logic

Courant number is very good indicator of the oscillations. When Courant number is close to 1, oscillation can be observed. In that case, upper limit of the limiter function should be decreased. Flexible flux limiter uses only Courant number to determine upper limit of the limiter function. But Courant number is not a single parameter of the oscillations and stable results. Therefore, total variation (TV)

and Newton iteration should be taken into account to get more stable and more accurate results. TV can be defined as summation of differences of each grid block concentration with their neighbors. Newton iteration is number of steps to obtain reasonable convergence of results. To sum up, there are three input data to determine upper limit of the novel adjustable limiter function which are Nc, TV and Newton iterations. Table 1 and table 2 show input and output data to design fuzzy logic function.

Table 1. Fuzzy logic input data.

INPUT					
Nc		TV		Iterations	
Level	Range	Level	Range	Level	Range
L (trimf)	[0 0 1]	L (trimf)	[1 1 1.001]	L (trimf)	[1 1 5]
M (trimf)	[0.9 1.2 1.35]	M (trimf)	[1.001 1.3 1.5]	H (trimf)	[4 9 9]
H (trimf)	[1.3 1.9 1.9]	H (trimf)	[1.4 1.75 1.75]	-	-

In input data, the range of the Courant number (Nc) varies from 0 to 1.9. For the low range of the Nc, generally there is no any danger to observe oscillation and for that case high range of output (LF) data can be used. If there are not any oscillations, total variation (TV) will be 1 or very close to 1. Similarly, for that case, high range of output (LF) data can be used. Three Newton iterations are optimal to obtain reasonable numerical solutions. If Newton iterations are higher than five, probably convergence problem will be observed because of the large oscillations. Therefore, upper limit of the limiter function (LF) must be decreased. In brief:

1. If (TV is L) and (it is L) and (Nc is L) then (LF is H)
2. If (TV is L) and (it is L) and (Nc is M) then (LF is H)
3. If (TV is L) and (it is L) and (Nc is H) then (LF is M)
4. If (TV is M) and (it is L) and (Nc is M) then (LF is L)
5. If (TV is M) and (it is L) and (Nc is H) then (LF is LL)
6. If (TV is H) or (it is H) or (Nc is H) then (LF is LL)

Table 2. Fuzzy logic output data.

OUTPUT (LF)	
Level	Range
LL (trimf)	[1.1 1.1 15]
L (trimf)	[1.14 1.24 1.4]
M (trimf)	[1.3 1.55 1.8]
H (trimf)	[1.7 2 2]

## Results

In order to compare all spatial discretization techniques, it is assumed that Nc equals to 1.4, velocity is 1 and physical dispersion is zero. In addition, that supposition, second order semi-implicit Crank-Nicolson time discretization technique is applied to all numerical methods. Figure 4 shows numerical results with analytical solution. According to Figure 4, TCDF method gives huge unphysical oscillation and it is very far away from the analytical solution. Adaptive 1.5 and Flexible flux limiter schemes have moderate unphysical oscillation. No oscillation has been observed on novel Adjustable flux limiter function and it is closest method to analytical solution.

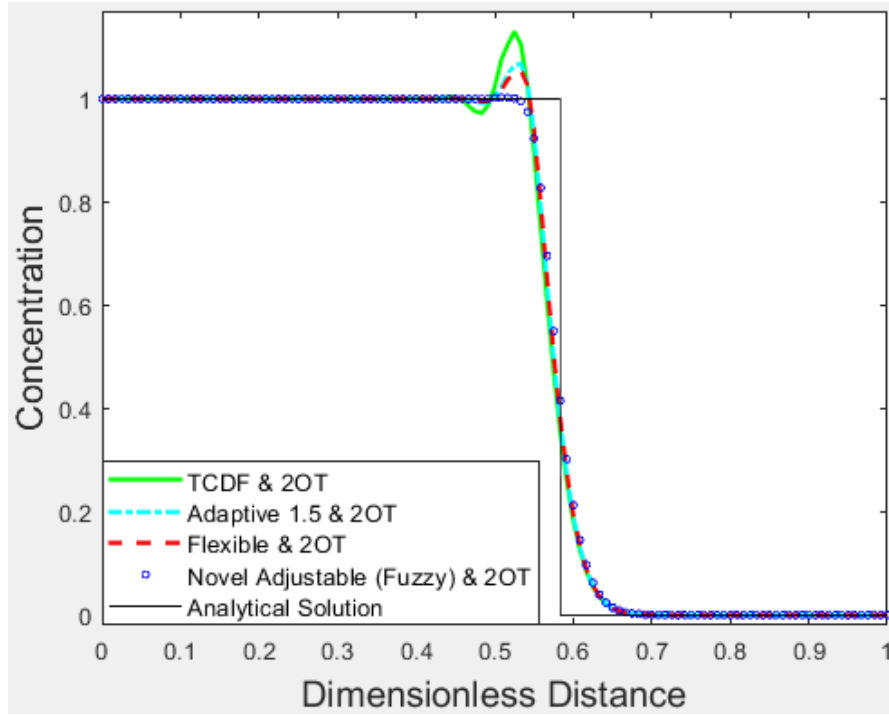


Figure 4. Comparison of Novel Adjustable Limiter with previous studies ( $N_c=1.4$ ).

### Conclusions

Basically, CFD researchers encounter two main problems which are numerical dispersion and unphysical oscillation. In order to decrease numerical dispersion, higher order discretization techniques should be used. But higher order schemes cause unphysical oscillations especially at large Courant numbers. Therefore, flux limiter should be used to suppress oscillations. In order to get adaptation of the flux limiter to every numerical problem, using Courant number to design upper limiter of the flux limiter is very good technique. On the other hand, Courant number is not a single parameter to obtain stable solutions. Thus, total variation (TV) and Newton iterations must be taken into account. Novel Adjustable flux limiter has been designed by  $N_c$ , TV and Newton iterations number using fuzzy logic algorithm. No oscillation has been observed on novel Adjustable flux limiter even Courant number equals to 1.4.

### Nomenclature

$C$  = concentration

$D$  = physical dispersion

$N_c$  = courant number

$r$  = concentration gradient ratio or flux ratio

$\Delta t$  = timestep

$u$  = velocity

$\phi$  = limiter function

### Subscripts

$i$  = index for blocks in the x direction

$i - \frac{1}{2}$  = index for left face values

$i + \frac{1}{2}$  = index for right face values



### Superscripts

$n$  = old timestep

$n+1$  = current timestep

### References

- [1] Wolcott, D., H. Kazemi, and R. Dean. A practical method for minimizing the grid orientation effect in reservoir simulation. in SPE Annual Technical Conference and Exhibition. 1996. Society of Petroleum Engineers.
- [2] Leonard B.P. A stable and accurate convective modelling procedure based on quadratic upstream interpolation. *Computer Methods in Applied Mechanics and Engineering* 197;. 19(1): 59-98.
- [3] Zhang, D., et al., A review on TVD schemes and a refined flux-limiter for steady-state calculations. *J Comput Physics*. 2015; 302: 114-154.
- [4] Jiang, J. and R.M. Younis. An Efficient Fully-Implicit MFD-MUSCL Method Based on a Novel Multislope Limiting Procedure. in SPE Reservoir Simulation Conference. 2017. Society of Petroleum Engineers.
- [5] Ünal, O., Simulation of Immiscible Displacement of Petroleum via Second and Third Order Finite Differencing Techniques. 2020.
- [6] Peaceman, D.W., Fundamentals of numerical reservoir simulation. 2000: Elsevier.
- [7] Ertekin, T., J.H. Abou-Kassem, and G.R. King, Basic applied reservoir simulation. 2001.
- [8] Liu, J., High-resolution methods for enhanced oil recovery simulation. 1993, University of Texas at Austin.
- [9] Harten A. On a class of high resolution total-variation-stable finite-difference schemes. *SIAM J. Numer. Anal.* 1984. 21(1): 1-23.
- [10] Sweby PK. High resolution schemes using flux limiters for hyperbolic conservation laws. *SIAM J. Numer. Anal.* 1984. 21(5): 995-1011.
- [11] Crank, J. and P. Nicolson. A practical method for numerical evaluation of solutions of partial differential equations of the heat-conduction type. in *Mathematical Proceedings of the Cambridge Philosophical Society*. 1947. Cambridge University Press.

## Physics / Fizik

## Determination of Inelastic Longitudinal Electron Scattering Form Factors in <sup>58</sup>Ni

Doaa Murshedi\*, Adie D. Salman  
Department of Physics, Karbala University, IRAQ  
\*Corresponding author: doaa.r244@gmail.com

**Keywords:** Inelastic scattering, core polarization, form factor  
**Discipline:** Physics

### Abstract

There are two kinds of electron scattering: elastic and inelastic scattering. In the first type, the nucleus is left in the ground state, so one can measure the static properties, such as the static distribution of charge and magnetization. While in the second type, the nucleus is left in an excitation state from which nuclear dynamical properties, such as the transition densities and current densities can be obtained. In this study, the calculations of inelastic longitudinal electron scattering form factors for C2 transition have been examined in <sup>58</sup>Ni. The F5PVH effective interaction for the fp-shell is used with the nucleon-nucleon realistic interaction Michigan three-range Yukawa (M3Y) and Modified surface delta interaction (MSDI) as a two-body interaction. The core polarization effects are considered as the first-order perturbation theory with the effective charge of both proton and neutron. The harmonic oscillator potential has been applied to calculate the wave functions of radial single-particle matrix elements. The results were calculated from two shell model codes, CP and the OXBASH code using the F5PVH interaction. Based on the obtained results for the MSDI, the core polarization found to be essential to get the exact shape of the form factor, the underestimation of the curve can be solved by introducing an effective charge to the proton and neutron. It has seen that the calculations including effective charge are in good agreement with the experimental data in the first and third peaks, but the second peak is underestimated. The theoretical calculations did not show a good agreement to describe the form factors using M3Y interaction.

### Introduction

Shell model calculations of the ground state and low-lying excited states are of interest for our understanding of nuclear dynamics and the nuclear forces. They are also of great interest for the prediction and analysis of various processes such as electromagnetic transition probabilities [1].

The Conventional multi-particle shell model with configuration mixing deals explicitly with only the distribution and coupling of the valence nucleons (assuming an inert core) within a few “Model-Space” orbits. In any shell- model calculation, one has to start by defining a “model space”, namely by specifying a set of active single-particle (SP) orbits. However, it was found that a truncated model “model space” was not able to reproduce the measured static moments or transition strengths without scaling factors, so the so-called “Core polarization effects” need to be included, which takes the higher configurations into account [2].

In the present work we seek to investigate inelastic longitudinal electron scattering in fp- shell nuclei. The calculations of the longitudinal form factors have been performed in the fp- shell model. The multi-nucleon shell model with mixed configuration is adopted here. According to this model, the nucleus contains an inert core and other additional active orbits. The valence nucleons distribute among these active orbits according to Pauli’s principle. <sup>56</sup>Ni was chosen to be the inert core for the <sup>58</sup>Ni nucleus.

The core- polarization effects have been included with the effective charges. Core polarization matrix elements are calculated with MSDI and M3Y effective interaction. The strength of the MSDI denoted by A<sub>T</sub>, B and C are set equal to A<sub>0</sub>=A<sub>1</sub>=B=0.4 MeV and C=0. The choice of the strength parameters brings the calculated B (C2<sub>↑</sub>) value very close to the measured values.

### Theory

Inelastic longitudinal electron scattering form factors involving angular momentum J and momentum transfer q, which can be written as [3]

$$|F_J(q, \theta)|^2 = \frac{4\pi}{Z^2(2J_i+1)} |\langle J_f || \hat{T}_\lambda^\eta(q) || J_i \rangle|^2 |F_{cm}(q)|^2 |F_{fs}(q)|^2 \quad (1)$$

where  $F_{cm}$  is the center of mass correction, which removes the spurious states that arise due to the fact that the interaction potential represents an average potential with respect to a fixed origin, and this correction can be written as [4]

$$F_{cm}(q) = e^{\frac{q^2 b^2}{4A}} \quad (2)$$

where  $b$  is the harmonic-oscillator size parameter,  $A$  is the nuclear mass number and  $q$  is the momentum transfer.

Another correction to the form factor formula is the nucleon finite size correction, which takes into account the finite size of the nucleon and is given as [4]

$$F_{fs}(q) = [1 + (q/4.33 fm^{-1})^2]^{-2} \quad (3)$$

The reduced matrix elements in spin and isospin space of the longitudinal operator between the final and initial for many particles states of the system including the configuration mixing are given in terms of the One Body Density Matrix (OBDM) elements times the single-particle matrix elements of the longitudinal operator [5], i.e.

$$\langle \Gamma_f || \hat{T}_\Lambda^\eta || \Gamma_i \rangle = \langle \Gamma_f || \hat{T}_\Lambda^\eta || \Gamma_i \rangle_{ms} + \langle \Gamma_f || \delta \hat{T}_\Lambda^\eta || \Gamma_i \rangle_{cp} \quad (4)$$

where  $\eta$  represents the longitudinal ( $L$ ), or transverse form factors (electric ( $E$ ) and magnetic ( $M$ )). The model space matrix elements can be written as

$$\langle \Gamma_f || \hat{T}_\Lambda^\eta || \Gamma_i \rangle_{ms} = \sum_{\alpha, \beta} OBDM(\Gamma_i, \Gamma_f, \alpha, \beta) \langle \alpha || \hat{T}_\Lambda^\eta || \beta \rangle_{fp} \quad (5)$$

The OBDM is obtained from OXBASH code [6], the core polarization matrix elements are given as

$$\langle \Gamma_f || \delta \hat{T}_\Lambda^\eta || \Gamma_i \rangle_{cp} = \sum_{\alpha, \beta} OBDM(\Gamma_i, \Gamma_f, \alpha, \beta) \langle \alpha || \delta \hat{T}_\Lambda^\eta || \beta \rangle_{cp} \quad (6)$$

According to the first-order perturbation theory, the single-particle core-polarization term is given by [7]

$$\langle \alpha || \delta \hat{T}_\Lambda^\eta || \beta \rangle = \langle \alpha | \hat{T}_\Lambda^\eta \frac{Q}{E-H(0)} V_{res} | \beta \rangle + \langle \alpha | V_{res} \frac{Q}{E-H(0)} \hat{T}_\Lambda^\eta | \beta \rangle \quad (7)$$

where the operator  $Q$  is the projection operator onto the space outside the model space. The single-particle core-polarization terms given in equation (7) are written as:

$$\begin{aligned} \langle \alpha | \hat{T}_\Lambda^\eta \frac{Q}{E-H(0)} V_{res} | \beta \rangle &= \sum_{\alpha_1 \alpha_2 \Gamma} \frac{(-1)^{\beta + \alpha_2 + \Gamma}}{e_{\beta^-} - e_{\alpha^-} - e_{\alpha_1} + e_{\alpha_2}} (2\Gamma + 1) \begin{Bmatrix} \alpha & \beta & \Lambda \\ \alpha_2 & \alpha_1 & \Gamma \end{Bmatrix} \langle \alpha \alpha_1 | V_{res} | \beta \alpha_2 \rangle \\ &\times \langle \alpha_2 | \hat{T}_\Lambda^\eta | \alpha_1 \rangle \sqrt{(1 + \delta_{\alpha_1 \alpha}) (1 + \delta_{\alpha_2 \beta})} + \end{aligned}$$

term with  $\alpha_1$  and  $\alpha_2$  exchange with an over minus sign. (8)

where the index  $\alpha_1$  runs over particle states and  $\alpha_2$  over hole states and  $e$  is the single-particle energy, and is calculated according to [7]:

$$e_{nlj} = (2n + l - \frac{1}{2}) \hbar \omega + \begin{cases} -\frac{1}{2}(l+1) \langle f(r) \rangle_{nl} & \text{for } j = l - \frac{1}{2} \\ \frac{1}{2} l \langle f(r) \rangle_{nl} & \text{for } j = l + \frac{1}{2} \end{cases} \quad (9)$$

with  $\langle f(r) \rangle_{nl} \approx -20A^{-2/3}$  and  $\hbar \omega = 45A^{-1/3} - 25A^{-2/3}$  (10)

For the residual two- body interaction  $V_{res}$ , MSDI and M3Y interaction of Bertsch et al. [8] are adopted.

### Results and Discussion

The  $^{58}\text{Ni}$  nucleus is excited from the ground state  $j_i^\pi T_i = 0^+ 1$  to the state  $j_i^\pi T_i = 2^+ 1$  with the excitation energy of 1.454 MeV.

The experimental reduced transition probability  $B(C2\uparrow)$  is equal to  $695 \pm 20 e^2 \text{fm}^4$  [9], while the theoretically calculated reduced transition probability is equal to  $23.199 e^2 \text{fm}^4$ , which is low in comparison with the measured value. When the core polarization effects are included, the  $B(C2)$  becomes  $538.2 e^2 \text{fm}^4$ , which is lower than the experimental values with about 29%, this is because the effect of adjustable parameters of MSDI which are adjusted for all nuclei under consideration

The calculation is performed within a model space consisting of  $1f_{5/2}$ ,  $2p_{3/2}$  and  $2p_{1/2}$  orbital's for  $^{58}\text{Ni}$  nuclei, which have 2 neutrons outside the closed major shell leaving  $^{56}\text{Ni}$  as an inert core. In this work for the residual two-body interaction, two different potentials are used, which are MSDI and M3Y.

The radial wave function was calculated with a harmonic oscillator (HO) potential for the single-particle matrix elements, the oscillator length parameter  $b=1.96\text{fm}$  was chosen to produce the measured root mean square charge radius [10], the core-polarization effects are taking into account through giving the model space nucleon effective charge. These effects calculated using OXBASH code, the effective proton and neutron charges chosen were equal to 1.8e and 0.64e respectively. The radial part of the single-particle wave function was those of a harmonic oscillator (HO) potential, rather than the Woods-Saxon (WS) [11] potential is used.

Figure 1 displays C2 transition using MSDI interaction. The core polarization found to be essential to get the exact shape of the form factor (the dashed dot curve), the underestimation of the curve can be solved by introducing an effective charge (the solid curve) to the proton and neutron. It's seen that the calculations including effective charge are in good agreement with the experimental data in the first and third peaks, but the second peak is underestimated.

The theoretical calculations fail to describe the form factors using M3Y interaction as it shown in Figure 2 only two peaks had formed.

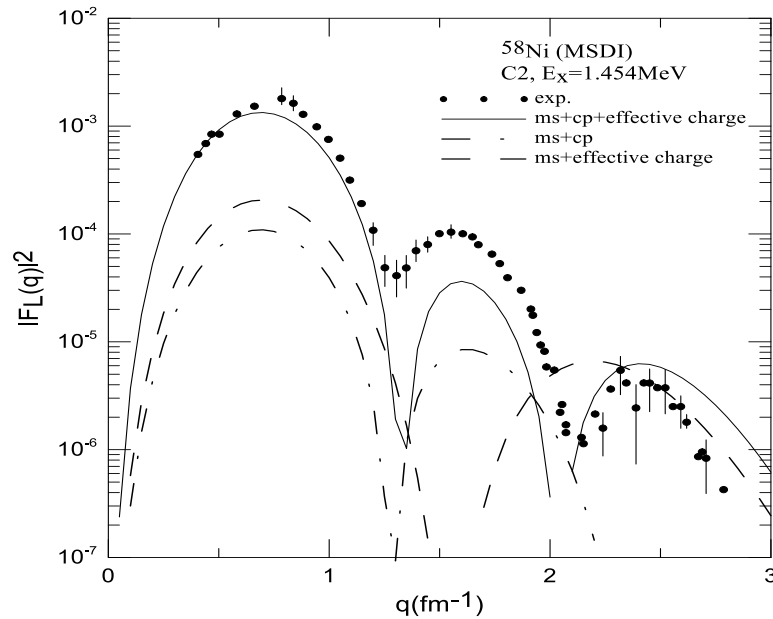


Figure 1. Inelastic longitudinal form factors for the transition to the  $2_1^+$  state in the  $^{58}\text{Ni}$  nucleus using MSDI interaction, the exp. data are taken from Ref. [12]

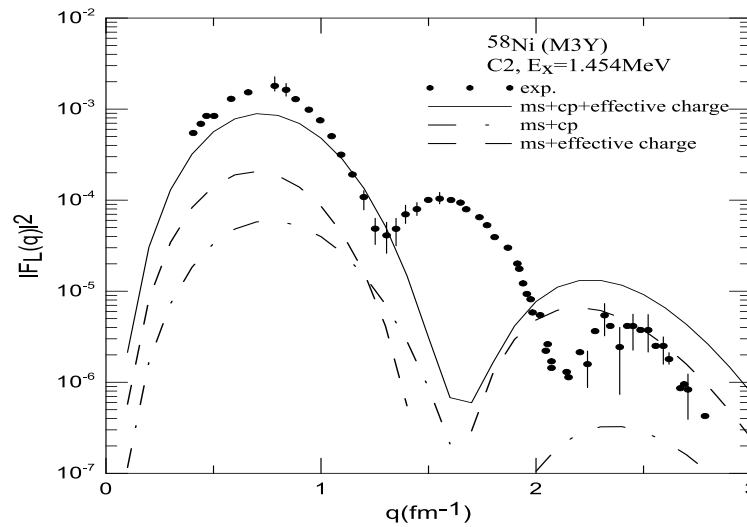


Figure 2. Inelastic longitudinal form factors for the transition to the  $2_1^+$  state in the  $^{58}\text{Ni}$  nucleus using M3Y interaction, the exp. data are taken from Ref. [12]

### Conclusion

In the present work, the shell model calculation was carried out in (1f5/2, 2p3/2, 2p1/2) orbitals. The nucleon–nucleon realistic interaction Michigan three-range Yukawa and Modified surface delta interaction as two-body interactions have been unable to describe the experimental data without addition the core polarization effects. The core polarization effects were included with the effective charges, which enhanced the results, however, it is still need more theoretical efforts to get the best results.

### References

- [1] Radhi RA, Salman EA. Collective E2 transitions in 18O. Nuclear Physics A. 2008 Jun 15;806(1-4):179-90.
- [2] Radhi RA. Perturbative role in the inelastic electron scattering from 29 Si. The European Physical Journal A. 2007 Oct 1;34(1):107-11.
- [3] Salman AD, Kadhim DR. Longitudinal electron scattering form factors for 54, 56 Fe. International Journal of Modern Physics E. 2014 Oct 4;23(10):1450054.
- [4] Tassie LJ, Barker FC. Application to electron scattering of center-of-mass effects in the nuclear shell model. Physical Review. 1958 Aug 1;111(3):940.
- [5] Glickman JP, Bertozzi W, Buti TN, Dixit S, Hersman FW, Hyde-Wright CE, Hynes MV, Lourie RW, Norum BE, Kelly JJ, Berman BL. Electron scattering from Be 9. Physical Review C. 1991 Apr 1;43(4):1740.
- [6] Brown BA, Etchegoyen A, Godwin NS, Rae WD, Richter WA, Ormand WE, Warburton EK, Winfield JS, Zhao L, Zimmerman CH. Oxbash for windows PC. MSU-NSCL Report. 2004;1289.
- [7] Brussaard PJ, Glaudemans PW, Klein A. Shell-Model Applications in Nuclear Spectroscopy. PhT. 1978;31(11):68.
- [8] Bertsch G, Borysowicz J, McManus H, Love WG. Interactions for inelastic scattering derived from realistic potentials. Nuclear Physics A. 1977 Jul 11;284(3):399-419.
- [9] Raman S, Nestor Jr CW, Tikkanen P. Transition probability from the ground to the first-excited 2+ state of even–even nuclides. Atomic Data and Nuclear Data Tables. 2001 May 1;78(1):1-28.
- [10] Salman AD, Al-Ramahi SA, Oleiwi MH. Inelastic electron-nucleus scattering form factors for 64, 66, 68Zn isotopes. In AIP Conference Proceedings 2019 Aug 22 (Vol. 2144, No. 1, p. 030029). AIP Publishing LLC.
- [11] Woods RD, Saxon DS. Diffuse surface optical model for nucleon-nuclei scattering. Physical Review. 1954 Jul 15;95(2):577.
- [12] Raina PK, Sharma SK. Form factors and transition charge densities for the quadrupole and hexadecupole electroexcitation of some 2p-1f shell nuclei. Physical Review C. 1988 Apr 1;37(4):1427.

## Urban Design / Kentsel Tasarım

## Re-Examine Conventional Concepts in Urban Design: the Conflict Between Urban Space Utilization and The Elements of Power and Control - Case of Hawkers within Amman, Jordan

Dania Abdel-Aziz\*, *Izmir Institute of Technology, Dept. of Architecture, İzmir, Turkey*  
\*Corresponding author: [archdania.aziz@gmail.com](mailto:archdania.aziz@gmail.com)

**Keywords:** Street Vendors, Central business district, convivial urban space, National Policy, Hawking Space  
**Discipline:** Urban Design

### Abstract

Architecture and urbanism are disciplines based on knowledge of space. From this point of view, this research aims to study the challenges of dealing with hawkers (Street Vendors) in the urban centers of Jordan generally by shedding light on downtown Amman. Although they succeed in acquiring and controlling space informally in Amman, hawkers have been ignored by local planners and even been harassed by local authorities by not being given space to operate their businesses. Rigid transformations should be carried in urban planning strategies in downtown Amman and local policies need to be enforced to end this conflict and provide suitable conditions and capacities to read and respond to the needs of the hawkers as they represent an integral part of the urban fabric of the region. This study is based on reviewing related literature, field survey and observations that were carried out for two months in the study area, in addition to several informal discussions that were held with the hawkers, pedestrians, the merchants and the local authorities as well and to clarify certain issues questionnaires were used. To resolve this conflict the study suggests a few recommendations that can help in the fulfillment of effective utilization of urban centers as well as harmonize the operation of both the formal activities and the hawkers. The study found that street hawkers are only considered as trouble makers and have never been involved in decision making processes when urban planning takes place. These will be an ongoing issue not unless they are integrated into the planning processes. The study suggests different scenarios for proper allocation of hawking space can be done regarding accommodating them according to their space requirements worked out the basis of the products sold, as has been done in the present study. In short, this will help in providing suitable trading environments for the hawkers, creating a pedestrian-friendly neighborhood, decreasing the unemployment rate among other advantages.

### Introduction

With the constantly increasing population due to the crises in its neighboring countries (Nilsson & Borges, 2019) and pressure on jobs, Jordan is witnessing a noticeable increase in the problem of unemployment, especially among youth. The government is now unable to provide suitable job opportunities for their citizen; that's why many Jordanians were forced to work in the informal sector to escape worsening unemployment in the country, especially as many of them support their families. Despite the limited income and the high cost of living, they face daily pursuit by the local authorities who seize their goods; they are forced to pay fines or give up what was confiscated from them, and this makes their situation worse.

Jordan's unemployment rate has been alarming and has increased from 11% in 2010 to 19% by 2019 (DoS, 2020). The participation rate of Jordan's workforce has remained one of the lowest in the world at about 40% (Husseini, 2016). The youth unemployment rate in 2018 was very high about 37.2% and among the highest globally (The World Bank, 2019).

The unemployment rates have traditionally been higher in rural areas than in urban areas and that is due to the concentration of jobs in urban governorates and the lack of transportation or reluctance to use it (Husseini, 2016). This reason made many people move from rural areas running from poverty to urban areas (rural-urban migration). But those migrants do not possess the skills or the education to enable them to find a good paid and secure employment in the formal sector. This made them settle for work in the informal sector. Sharma (2016) discussed another reason why people are pushed to work in the informal sector. According to her, many business, factories and workshops were closed and the previous workers could not find a proper job hence they had to work in the informal sector to survive.

The meaning of the informal sector has been discussed by many researchers (Schneider, 1986), (Smith, 1994), (Saunders & Loots, 2015), (Dhakal, 2015) and others. The informal sector as Smith



(1994) defines it is a market-based production of goods and services, whether legal or illegal, that escapes detection in the official estimates of GDP. According to the definition by the International Labor Office (ILO) states that the informal sector is: “The informal economy is broadly characterized as consisting of units engaged in the production of goods and services with the primary objective of generating employment and income to the persons concerned.” (ILO, 1993).

The activities in the informal sector can be categorized into two sections; (1) the self-employed and (2) the non-permanent labour (Sharma, 2016). Self-employment is one of the modern development concepts that switched perspectives in the world of business and employment, which means the individual's quest to find a job for themselves through the reliance on their ideas, experiences, and their educational and training level. A major section of the self-employed workers are hawkers or street vendors. The rise in the number of street hawkers is due to the lack of employment in other sectors and directly linked to the expansion of the informal sector.

The term “Hawkers” is an interchangeable phrase which refers to people who tends to sell goods or offer services to the public informally in any street or public place. These activities are not being protected or supervised by the government that’s why they do not have a fixed place or a permanent built-up structure. Hawkers tend to spread or display goods in open spaces or temporary static structure with intention of attracting buyers and make sales. It also refers to the person who moves from one place to another or goes to people's homes to sell goods or merchandise that he offers for sale or deals in his craft or industry by roaming (GAM, 2009). The hawker may use a trolley, kiosk, canopy or simply using the pavement.

Modernist planning is focusing on the requirements of cars rather than the needs and expectations of pedestrians, which made cities, lose many qualities (Israt, 2019). Good accessibility is directly related to the pedestrians’ thoughts and experience. It acts as a direction for the pedestrians that in result affect their perception. We can not neglect the fact that there are many problems associated with mobility and accessibility resulted from hawking in the streets of Amman downtown. At the same point if planners when planning to pedestrians, took hawkers into account, many problems could be avoided.

An external view of hawking in Jordan, gives the impression of the randomness of this sector in terms of distribution and spread, while in reality it is a sector with a remarkable degree of control, and over time it had its traditions and inner life. There are families working in hawking for three generations, and there is a great deal of specialization in the sector.

The Greater Amman Municipality's (GAM) Campaigns against the phenomenon of street vending began in 1997. Some of these campaigns were very sever and targeted local markets as well (Khalil, 2019). Hawkers at that time tended to move between many locations while some chose to work during the night or early morning. While GAM did not provide alternative markets.

GAM as a regulatory body is working to violate this sector because of the quality of goods that are handled, since they are usually poor and not suitable for consumption. Moreover, since these workers do have a specific place or are evading paying taxes and fees, it leads to a breach of security and order, the use of sidewalks, and obstructing the movement of citizens. Another justification for GAM’s campaigns can be in the urban landscape. But this contradicts reality, as these hawkers, especially in Amman downtown, constitute a cultural and heritage character and reflect a true image of the people. That's why these campaigns to date do not have the capabilities to withstand and continue.

The GAM should see the other sides of the informal sector and be aware of the important role that the urban informal sector plays in the urban economy worldwide. An organized street vending in Amman or other urban space in Jordan could be part of city precedence for the benefit of the city community.

### **Problem Statement**

With high unemployment rates, increasing poverty and the high cost of living in Jordan, the flow of hawkers into urban centers has become a distinguishing feature of most of the cities but they are often regarded as an 'element out of place' (Widjajanti, 2016). Basically, their problem is due to the absence of reference in determining the location of their activity in the city plan. Their random distribution causes many problems.

For a sustainable community for its inhabitants; it must be livable. To achieve a suitable and orderly urban intervention in urban centers, policy guidelines concerned with the effective use of urban centers must be formulated, customized and developed to address the users of urban space. At downtown

Amman for example, most urban spaces are conquered by hawkers. Hawkers' rugs are spread over a wide range of different forms, on the sidewalk inside the bazaars and local markets, in front of the Grand Husseini Mosque.

GAM has always fought against the hawkers. But at the same time, it did not try to understand their needs, did not provide them with job opportunities that would spare them all these conflicts. The government must provide solutions to overcome this crisis and help the people. Hence the importance of recognizing them, laying down laws that regulate their work and their whereabouts in a way that achieves balance and the public interest. Sustainable planning should address issues of spatial integration and resolve conflicts and the movement of hawkers within the urban fabric.

The purpose of this study is to examine the spatial processes and requirements in the areas where street hawkers are present. Urging the authority to propose suitable sites for hawkers, relocate them within urban spaces, plan their activities, and direct their growth and development in an organized pattern. The study assumes that the population of hawkers will continue to increase in Amman downtown. This means extra urban space is required to conduct their activities. The GAM has to restore economic growth, generate employment opportunities to absorb the large numbers of the unemployed, particularly the youth, and reduce poverty levels.

### Study Objectives

Public spaces are open for all to use and from this point raise the difficulties in balancing the right of pedestrians to move freely in the city and the hawkers to work legally and earn money to live a better life. The research will try to solve this conflict and filling the gap and help in building sustainable city community by suggesting scenarios where hawkers can be relocated in desirable urban spaces within the urban structure where they can conduct their business taking into consideration accessibility, comfort, and characteristics referring their activity. From this point the research aims to provide quantitative norms theories and concepts for accommodating street hawkers legally in Amman downtown. See Figure (1).

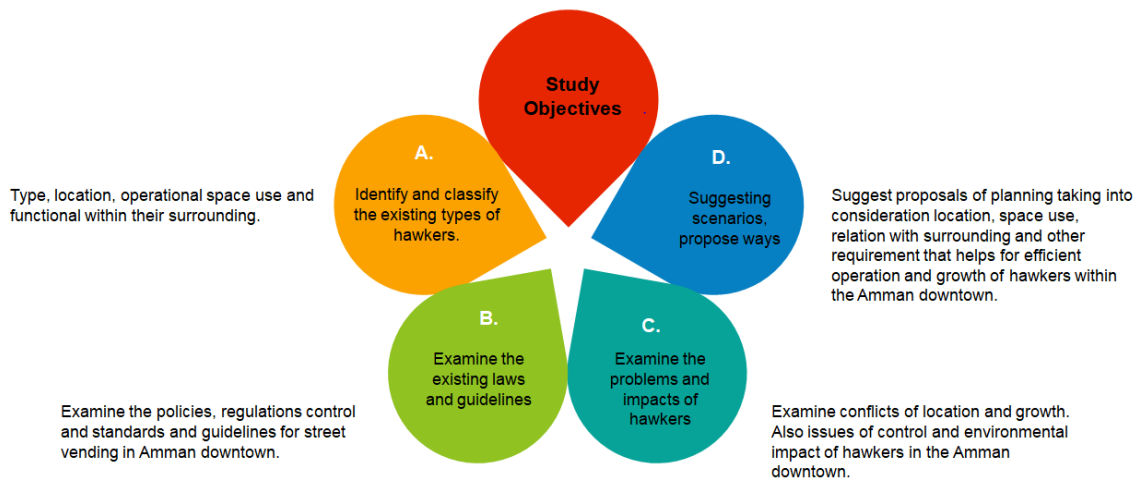


Figure 1. Study objectives

### Study Methodology

This study is based on quantitative descriptive method; (1) reviewing related literature; searching the concept of the informal sector, conflicts between hawkers, merchants, pedestrians and government, (2) field survey and of hawking establishments in the Amman downtown, the type of the goods, the size of the unit, etc., walking within the study area and observing pedestrian movement, the road network, how the hawkers related to the urban space and taking photographs of the activities (3) informal discussions with hawkers to collect information about the related problems and difficulties they face, the nature of their work, their needs, nature of their business, characteristics of their specific activity, their dependence on the site context, (4) questionnaires were carried out for formal business operators,

pedestrians and study area visitors (5) Analysis of primary and secondary information and (6) conclusion and recommendations.

The field survey was carried out after preliminary studies were made from related literatures. The analysis of all collected data was presented using analytical tables. While the questionnaires were analyzed using Statistical Package for Social Science (SPSS). Figure 2 summarizes the data collection sources.

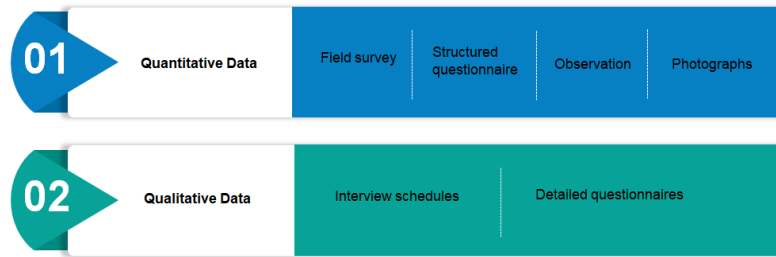


Figure 2. Data collection methods

### Study Area

Amman is the capital of Jordan and it covers 1680 km<sup>2</sup> of land area. 38% of Jordan's population live there hence it is considered the most densely populated region (Potter et al., 2009). Lack of adequate housing, unemployment, poor air quality, transportation, water shortages, rapid population growth, hawking or street vending in urban centers are among the most common problems of urbanization in Amman. These challenges are putting Amman in a huge problem in terms of its sustainability.

The detailed study area in Amman downtown was defined by the area enclosed by King Faisal Square, Als-Saadeh Street, Ar-Reda Street, and the illustrated parts of King Talal Street and Shaaban Street; as shown in Figure 3 below. In the selected study area, the subjects of observation were (1) spaces the hawkers were occupying and (2) the specific business venture the hawkers were engaged in. For the purpose of this study, the famous Friday market was excluded.

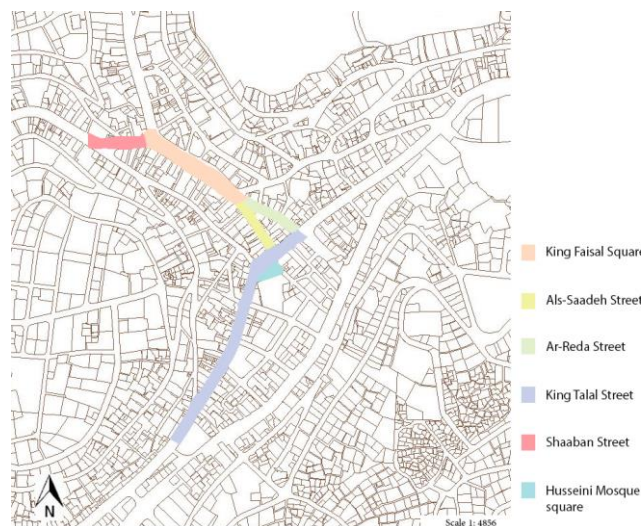


Figure 3. Study area

The target population for this research was; (1) all the hawkers who trade in the alleys of the study area, (2) pedestrians, (3) the merchants or the formal businesses owners in the surrounding area which hawkers located near their businesses and (4) the local authorities and Greater Amman Municipality departments.

The activities of hawkers were very wide, this study classified them into three main “relatively” homogeneous categories; (a) food activities (such as; seasonal fruits and vegetables, local sweets, boiled corn and light snacks), (b) clothing activities (such as; clothes (second hand and new ones), sunglasses, accessories, shoes, belts, watches and bags) and (c) entertainment activities (such as; accessories,

stationary, books, toys, lottery, perfumes, mobile accessories and magic tricks shows and home accessories). The reason for classifying them into categories was to assess the different needs and specifications for each group to take them into consideration when relocating is being suggested.

### Study Sample

The fieldwork was carried out between May 2019 and June 2019 in the selected area in Amman downtown. The observed hawkers units were 168 units, check Table 1. The observation was carried out in order to examine the everyday use, re-use, occupation and allocation of the urban space and the conditions and challenges facing the hawkers. It was noted that 152 hawking units were working at the same space uniformly. That's why for the purpose of this study the total sample size is 152 units. The floor space occupied by hawkers is 88.5 m<sup>2</sup>. For selecting respondents, this study adopted simple random sampling to select hawkers in each category. This technique gave an equal chance to each hawker of being included in the sample.

Table 1. The total number and the occupied space by hawkers in the study area.

Parameter	Unit
Total number of hawking units	168 unit
Total sample size	152 unit
Floor space area occupied by hawkers	88.5 m <sup>2</sup>

In the case of merchants, as a representative of the formal sector a sample size of 12 business owners was selected to listen to their opinions regarding relocating the hawkers next to their shops/business. While two interviews were held with the GAM staff and data were collected from 170 respondents to the questionnaire which was spread through this internet and targeted people who often visit Amman downtown only (respondents must be frequent visitors to the study).

A questionnaire survey was done with hawkers in the study area, most of whom cooperated by answering the questions whilst others refused to answer due to fear. That's why observation was also performed to validate the results and strengthen the findings. This survey included structured questions to collect information about the relationship between hawking and public space to build a holistic perception of the current situation in Amman downtown. The questionnaire survey collected data on activities, hawking duration, access, the chosen location, sociability, the informal sector, safety, comfort, uses, faced problems and the user's desires. The data was analyzed using SPSS.

## Analysis and Discussion

### Site potentials

Amman Downtown which has served as a central commercial area has many other different land-use activities which have led to a high frequency passing for local people as well as tourists every day. Hawkers assessed this situation as an opportunity to be a selling location and utilizing the space for trading activities, Table 2 below summarizes the spatial dimensions of the streets and hawkers' percentage in the study area.

The accessibility to this area was easy since it is served with public transportations from different locations. Although it is considered to be a crowded area, the affordable prices of goods and services offered around this area gets an influx of consumers. These conditions make this place an attractive area for hawkers to construct their businesses. Moreover, the easy access to public transportation relieves the load for hawkers.

Table 2. Spatial dimensions of the streets and hawkers' percentage in the study area

Street name	Street length*	Percentage of hawkers
King Faisal Square	205.90 m	50.66%
Ar-Reda Street	102.50 m	8.55%
As-Saadeh Street	103.30 m	9.21%
King Talal Street	380.50 m	30.26%
Shaaban Street	77 m	1.32%

\* The street's length represents the covered part that the study managed to collect data about.

### Strategic Location

As can be concluded from field survey; hawking activities operate in the open, on the pavement, and along the lanes and alleys. The desirable location for hawkers, are located within busy pedestrian routes with different activities (shops, hotels, restaurants...etc.), around public transport terminals and within bazaars. In other words, the land use activities influenced them to select the space they operate from. Each day hawkers take their respective positions with their wares ready to sell to potential buyers. They take in mind the particular space is in an attractive position for consumers and is located between various activities which have a high rate of visitors and a high frequency of mobility.

Every specific space has an owner; as indicated from interviewed hawkers, that no other trader would occupy the space without the approval of the original space owner and this is a rule that should not be broke. Many hawkers have worked at the same space for more than 40 years going generation to generation. Youth hawkers indicated that their fathers were working at the same space before and now it's their turn to keep working in order to live. This means that even this informal sector has its own rules. These locations, as hawkers noted, should be safe. In other words, space should be easy to run away from, and easy to be mobile in a bid to avoid arrest.

As concluded from the interviews, hawkers transport their goods by two means; 1) on foot. This is done by buying goods from a walking distance market in downtown, carrying them on their backs and walking to their trading space, 2) by use of public transportation to move their goods. From this point, another influence can be seen on selecting their desirable location, which is; the availability of public transportation. Public transportation facilitates the movement of goods as well as access to the site from their homes.

### Right in urban space

The general problem the hawkers faced in their daily operations can be summarized as not being provided with ideal urban space to perform their activities which protects them from climatic conditions (sun, rain), insecurity and harassment by the GAM.

From the interviews, hawkers pointed out a few key needs to achieve a convenient place to trade; availability of ample space, ease of modification of goods' means, ease of preparation and presentation of goods, and freedom of movement to serve buyers. They are not governed by the time schedules such as the formal sector, which gives this sector an advantage of being flexible.

As indicated from the survey, the hawkers use trolleys, wooden stands, tables and mats which they put on the ground to display their goods and services. They tend to use light materials and structures to help them easily run away from the GAM. The hawkers who traded in shoes and clothes displayed their goods on light mats to make it easy for customers to pick. The size of hawking unit varies depending on the goods they sell, as indicated in Table 3. The most used common unit size for food activities category was 1.0\*1.0 m<sup>2</sup> while 2.0\*2.0 m<sup>2</sup> and 2.5\* 2.0 m<sup>2</sup> for clothing and entertainment activities categories.

Table 3. Space occupied by hawkers within the study area.

Product type	Occupied Space (m <sup>2</sup> )											
	1.0*1.0	1.0*1.5	1.5*1.5	1.5*2.0	2.0*2.0	2.5*2.0	2.5*3.0	2.0*3.0	3.0*3.0	2.5*3.5	3.0*4.0	2.5*4.0
Food activities	28.5%		12.4%	16.5%		13.6%		16.5%		18.5%		
Clothing activities	15.8%	16.5%	5.5%	11.5%	17.3%	8.5%	6.5%	4.5%	6.9%	3.8%		3.2%
Entertainment activities	15.4%		20.3%	10.3%	17.4%	21.5%	3.4%		7.5%		2.2%	2.0%

### GAM Act with Regards to Hawking

The Greater Amman Municipality (GAM) carries out the responsibility of regulating hawking activities in Amman. The primary law is "System for monitoring and organizing hawkers, rugs, umbrellas and kiosks within the boundaries of the municipal areas No. 81 for the year 2009" (GAM, 2009). The provision of this law applies to all municipalities in Jordan with the exception of Greater Amman Municipality.

It should be mentioned that in the study area few hawkers were legally working. And examining these cases, we can see the special situation behind every one of them -family inheritance- One trader has been working for 40 years having inherited it from his past generation. The trader specializes in the selling of Islamic rosaries and other religious products due to its location in the Grand Hussein Mosque plaza. It should be noted that it has been allowed by the King Hussein bin Talal.

Another licensed unit is located in King Faisal Street, which is owned by a person with special needs. This particular trader possesses a license and identification papers that exempt him from paying any fees to the GAM due to his health condition. He noted that it was his only source of income. The third one is in King Faisal Street located at a corner in front of the Gold Market and is dedicated to selling fresh peanuts and has been trading for more than 60 years. This selling unit was distinguished by the fact that tourists were attracted to that particular sight of the owner doing his business. And taking a picture of him and with him is no less important to them than taking a picture in Roman amphitheater in the same area.

From here it should be noted that the hawkers in Amman downtown are part of the cultural heritage of the place, and they are what attracts tourists to the place. The GAM should help in the economic recovery by supporting hawkers; provide them with permanent trading spaces to overcome the crisis of poverty and the high unemployment rates. This will help in achieving improved services, by making the urban spaces an attractive place for everyone to live and a place to do business legally without the fear of harassment.

### Product/activity type

The field study showed that there were many different types of goods hawkers tend to deal with such as; fruits and vegetables, clothes and bags (second hand and new ones), sunglasses, toys, stationary, lottery, mobile accessories, light snacks. The distribution and percentage of their activities are summarized in table (4). The field survey indicates that within the different hawking activities distributed along the study area; clothes and toys (28.29%, 21% respectively) were the most percentage of the sample size. As mentioned above this study classified those various types of activities into three categories (check table (5)). Results showed that the maximum concentration of the different categories was located in King Faisal Square.

Table 4. Distribution of hawking units as per their product type.

Product type	King Faisal Square	As-Saadeh Street	Ar-Reda Street	King Talal Street	Shaaban Street	In Total
Toys	15.07%	2.63%	1.98%		1.32%	21.00%
Stationary & Books	1.98%	0.66%	1.32%	1.32%		5.28%
Watches	0.66%			0.66%		1.32%
Accessories	6.58%		0.66%	1.32%		8.56%
Perfumes			0.66%	2.63%		3.29%
Clothes	8.55%	2.63%	1.32%	15.79%		28.29%
Mobile acc.	5.26%		0.66%			5.92%
Sunglasses	1.2%			1.97%		3.17%
Shoes	2.63%	1.32%	0.66%	0.66%		5.27%
Bags	2.63%	0.66%		0.66%		3.95%
Home stuff	3.29%	1.32%		3.23%		7.84%
Food	3.23%		1.68%	1.20%		6.11%

Table 5. Distribution of hawking units as per their main category

Main category	King Faisal Square	As-Saadeh Street	Ar-Reda Street	King Talal Street	Shaaban Street
Food activities	3.23%		1.68%	1.20%	
Clothing activities	21.71%	4.61%	2.64%	21.06%	
Entertainment activities	26.14%	4.61%	4.62%	7.18%	1.32%

### The formal businesses

The study showed that most of the problem faced by formal business sector was that there existed an unfair competition between them and the hawkers, especially if they happen to be selling the same product. However, they have no problem with the presence of hawkers in the area, as long as it does not affect their work.

The study also noted that the formal business sector is the suppliers of goods and customers to the hawkers trading in the study area. Some shop owners at the study area used to supply hawkers with products that were sold at competitive prices, or that they accumulated and wanted to dispose them off and sell them at bargaining prices because there was not enough space in their warehouses.

Not only, but also one of the interviewed hawkers noted that many of them tended to pay a fixed price for the adjacent shop owners as a guarantee of a specific place for them on the street. While another one said that he has been working for 8 years at the same space because the adjacent shop belongs to one of his relatives and this means that he will not pay this amount of money. This is evidence of the presence of many points of agreement, as well as points of disagreement between the two parties.

### The size of hawking unit

The size of the hawking unit is important to be taken into consideration because planners need to ensure that the units are not infringing on the pavements and are not an obstacle to the pedestrian movements. The size of a hawking unit varies depending on the specific type of product offered. Standardizing could be difficult in general but it would be much more efficient in the same category.

The GAM would get revenue in regards to the space occupied. The study recommends that the rates charged by the GAM should reflect the space a hawking unit occupies. This will mean that hawkers pay the GAM for the size of space they need taking into consideration that every potential location has maximum and minimum occupancy area controlling the number of hawkers that can be accommodated in an urban space.

Taking into consideration that the desired unit size depends on the spatial needs of each activity this study suggested space requirements for hawking unit as follows:

- Hawking zones should be at the entry/exit points of transport nodes and parking areas. Those zones should be at certain static structures located on pavements and footpaths so it assures buses and cars smooth movement.
- The GAM allowed 7 markets in Amman that work during the weekdays. The Friday Market at Ras Alain area was one of them. It is open every Friday and located at an empty parking area. From here rises the point of spreading this successful case by allowing specific parking areas during the non-working days to accommodate the hawkers.
- To avoid clashes with the official shop owners, care must be taken into consideration; (1) maintain a clear distance between the shops and the hawking units, (2) ensure that the hawking units and the shops are not offering the same type of goods and services, (3) maintain sufficient distance for pedestrians to move between the official store and the hawking unit.
- The width of the pathways should also be taken into consideration. The pathways' minimum width in which it's considered suitable for hawking should not be less than 4 meters, while units should be separated by a distance of 5 meters minimum to assure the free movement of pedestrians and for hawkers to work sufficiently.

### Conclusion

Planning should take into account the importance of making hawking zones in different streets/cities in Jordan a legal space to work in. Because it is believed that an organized street hawking in the urban spaces could be part of city precedence for the benefit of the city community. Planners should know the need of street hawkers to locate them in certain places maybe even at certain times too. Those strategic locations should be selected due to accessibility, main activity, demand and space comfort. For sure much care should be placed on the street design and assure smooth flow for pedestrian movements and the interests of the local merchants.

Through participatory planning - while organizing the activity of hawkers - planners should make sure to achieve the integration of all stakeholders to ensure equality, sustainability and durability of this activity. Hawkers - the urban poor - should be involved in formulating and implementing a street roaming activity as part of the stakeholders. Participation will contribute to raising awareness about the problem situation; make them more understanding of proposed improvements as well as feel more responsible and committed to change. By this success has a better chance. In short, instead of treating hawkers as outlaw that only create chaos on the streets, they should be allowed to contribute, Street hawkers can be assets to the development of the urban system.

Pedestrian pathways, transport nodes and parking areas have the potential to accommodate hawkers. If properly located in spite of the small space they occupy, they will succeed in finding a stable job, a better income and equal dignity as other citizens. By this, hawkers will become a part of the city's socio-economic fabric and not as a problem in this fabric.

### Recommendations

The Greater Amman Municipality through the development process for Amman's new master plan should provide detailed enforcement procedures for customizing its standards for hawking by specifying the implementing authority, the mechanism and criteria for allocating hawking space and assuring that hawking space allocation is being taken into consideration while planning and designing.

The size of the space hawkers need has been discussed in this research but it cannot be generalized to including all the streets or cities in Jordan. Every street and city has its own different case scenario. For sure there are some fixed specifications but it is advised that the space norms for hawking should be included in each zonal development plan for each city alone in Jordan.

### References

- [1] Bank, T. W. (2019). *World Development Indicators / The World Bank*. <http://wdi.worldbank.org/tables>
- [2] Dhakal, R. C. (2015). *Classification of Informal sector activities in Chitwan District*. September.



- [3] DoS. (2020). *Unemployment rate during the first quarter of 2020*. [http://dos.gov.jo/dos\\_home\\_a/main/archive/unemp/2020/Emp\\_Q1\\_2020.pdf](http://dos.gov.jo/dos_home_a/main/archive/unemp/2020/Emp_Q1_2020.pdf)
- [4] Hussein, J. Al. (2016). Challenges Facing Jordan's Labour Market. In *Atlas of Jordan* (pp. 354–368). Presses de l'Ifpo. <https://doi.org/10.4000/books.ifpo.5039>
- [5] International Labour Organization. (1993). *Resolution concerning statistics of employment in the informal sector*. January, 300.
- [6] Khalil, A. A. (2019). *Fighting rugs is definitely a losing battle*. <http://www.zamancom.com/?p=2960>
- [7] Kjell & Borges. (2019). *Amman, one of the fastest grown cities in the world, is moving towards sustainable city planning | Nordregio*. <http://nordregio.org/amman-one-of-the-fastest-grown-cities-in-the-world-is-moving-towards-sustainable-city-planning/>
- [8] Municipality, G. A. (2009). *System for monitoring and organizing street vendors, rugs, umbrellas and kiosks within the boundaries of the municipal areas No. 81 for the year 2009*.
- [9] Saunders, S., & Loots, E. (2015). Measuring the informal economy in South Africa. *South African Journal of Economic and Management Sciences*, 8(1), 92–101. <https://doi.org/10.4102/sajems.v8i1.1286>
- [10] Schneider, F. (1986). Estimating the Size of the Danish Shadow Economy using the Currency Demand Approach: An Attempt. *The Scandinavian Journal of Economics*, 88(4), 643. <https://doi.org/10.2307/3440435>
- [11] Sharma, S. (2016). Hawking Space and National Policy on Urban Street Hawkers: A Study of NDMC, Delhi. *Procedia Technology*, 24, 1734-1741. <https://doi.org/10.1016/j.protcy.2016.05.207>
- [12] Smith, P. (1994). Assessing the Size of the Underground Economy: The Statistics Canada Perspective - ARCHIVED. *Canadian Economic Observer*, 3(11–010), 16–33. <https://www150.statcan.gc.ca/n1/en/catalogue/13-604-M1994028>
- [13] Potter, R. B., Darmame, K., Barham, N., and Nortcliff, S. (2009), “Ever-growing Amman”, Jordan: Urban expansion, social polarisation and contemporary urban planning issues. *Habitat International*, 33(1), 81- 92
- [14] Widjajanti, R. (2016). The space utilization by street vendors based on the location characteristics in the education area of Tembalang, Semarang. *Procedia-Social and Behavioral Sciences*, 227, 186-193.

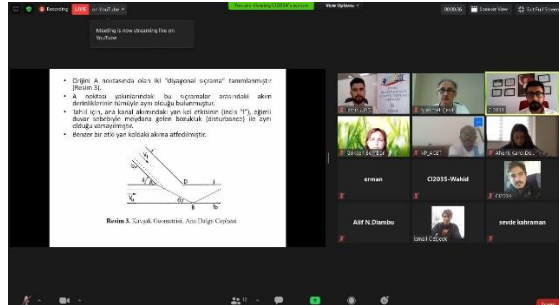
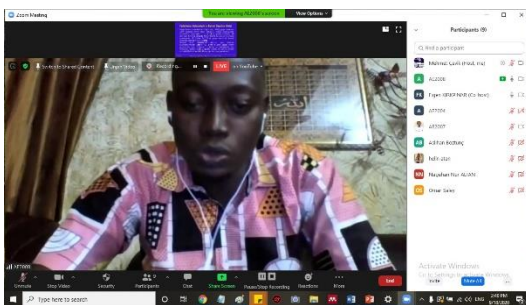
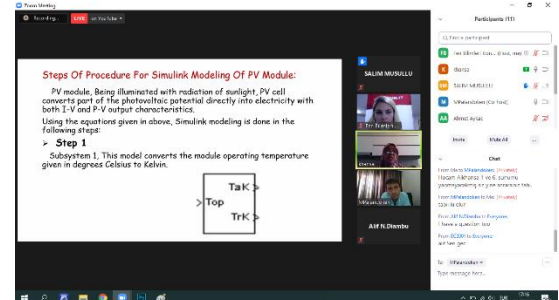
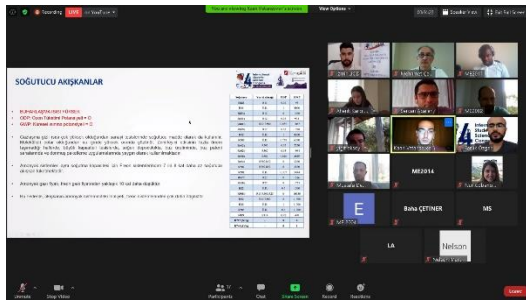
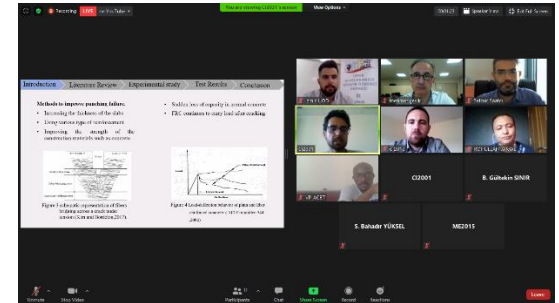
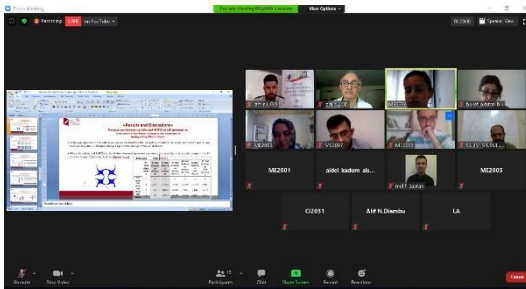
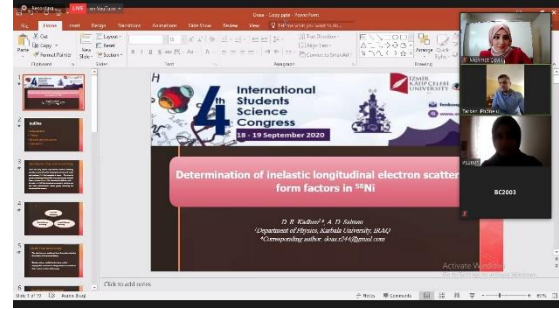
## Congress Photograph Gallery / Kongre Fotoğraf Galerisi

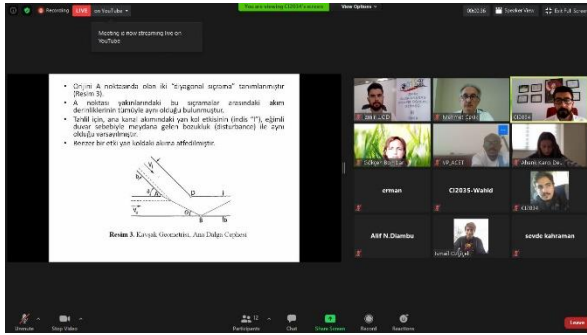
## Organizing Committee / Düzenleme Kurulu



On Air / Yayındayız



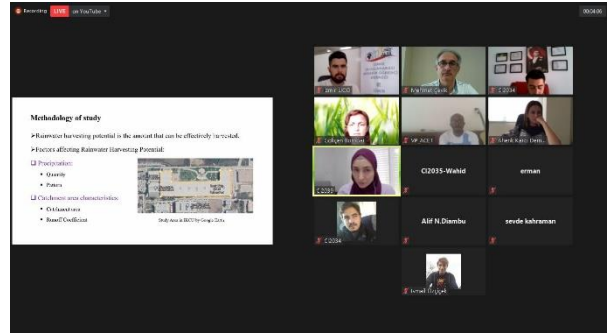




Meeting is now displaying live on YouTube

• Çizim A noktasında birinci iki "yapısal açıyı" tanımlanıyor (Şekil 3)  
• A noktası yapraklarındaki bir segmentin ortasında diğer açıları belirlemek amacıyla yapıldığı kabulünüç.  
• İkinci açı, ana köşe atomdaki yan köşe atomuna (indeksi "1"), eşitli açıları belirlemek amacıyla diğer köşeye (indeksi "2") bir çizim yapıldığı varsayılıyor.  
• Köşeler birer birer çizimle aynı şekilde tanımlanıyor.

Şekil 3. Karışık Geometrik Alan Dikiz Çizimi

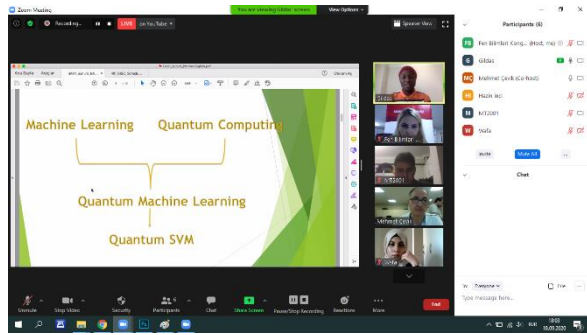


Methodology of study

► Researcher having potential in the amount that can be effectively in trouble.

► Factors affecting Rotavirus Inactivation Process:

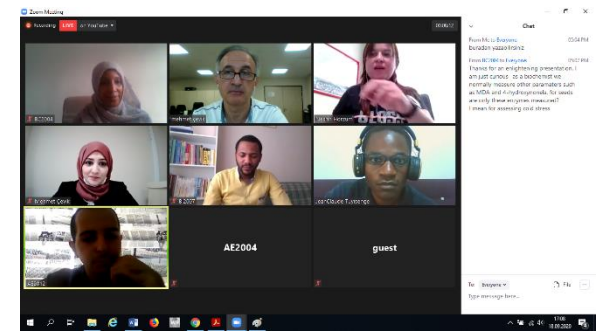
- pH
- Temperature
- UV Radiation
- Chlorination
- Boiling/Disinfection



Machine Learning Quantum Computing

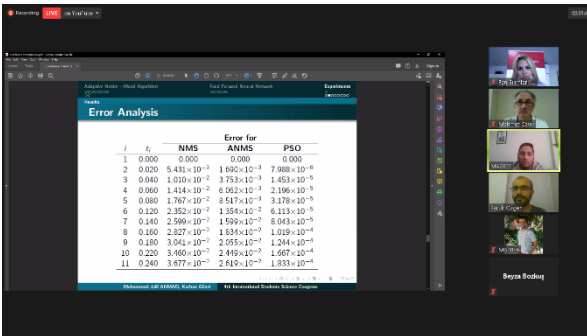
Quantum Machine Learning

Quantum SVM



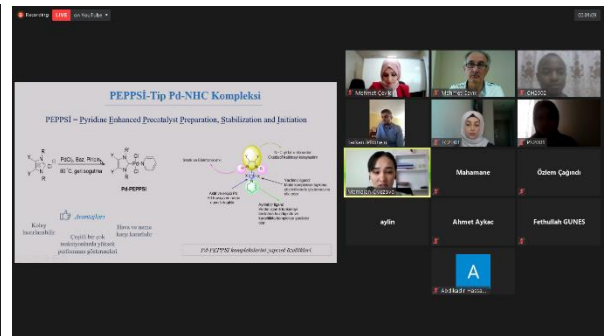
Chat

Beşim: Hello to everyone!  
Eğretir: Hello to all engineering preparation!  
anil: Hello to all participants!  
I have a question about the presentation!  
I mean for assessing soil stress



Error Analysis

	$\delta$	NMS	ANMS	PSO
1	0.000	0.000	0.000	0.000
2	0.020	$5.431 \cdot 10^{-3}$	$1.690 \cdot 10^{-3}$	$7.988 \cdot 10^{-6}$
3	0.040	$1.010 \cdot 10^{-2}$	$3.753 \cdot 10^{-3}$	$1.453 \cdot 10^{-5}$
4	0.060	$1.414 \cdot 10^{-2}$	$6.262 \cdot 10^{-3}$	$2.106 \cdot 10^{-5}$
5	0.080	$1.767 \cdot 10^{-2}$	$8.517 \cdot 10^{-3}$	$3.178 \cdot 10^{-5}$
6	0.120	$2.250 \cdot 10^{-2}$	$1.354 \cdot 10^{-2}$	$6.113 \cdot 10^{-5}$
7	0.140	$2.599 \cdot 10^{-2}$	$1.529 \cdot 10^{-2}$	$8.943 \cdot 10^{-5}$
8	0.160	$2.827 \cdot 10^{-2}$	$1.634 \cdot 10^{-2}$	$1.019 \cdot 10^{-4}$
9	0.180	$3.041 \cdot 10^{-2}$	$1.685 \cdot 10^{-2}$	$1.244 \cdot 10^{-4}$
10	0.220	$3.469 \cdot 10^{-2}$	$2.419 \cdot 10^{-2}$	$1.667 \cdot 10^{-4}$
11	0.240	$3.877 \cdot 10^{-2}$	$2.615 \cdot 10^{-2}$	$1.833 \cdot 10^{-4}$

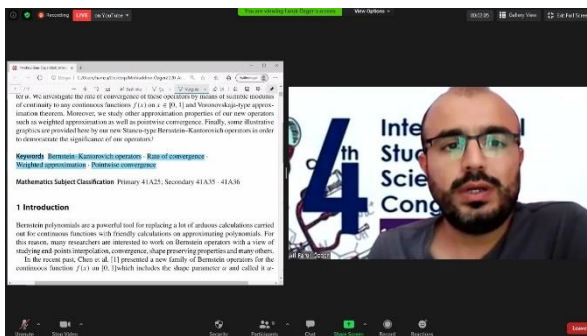


PEPPSI-Tip Pd-NHC Kompleksi

PEPPSI = Pyridine Enhanced Precatalyst Preparation, Stabilization and Initiation

Activity Initiatorlar: Çiftli bir Pd, heteroaromatik ligand, profenone/olefin/alken

Pd(PEPPSI) = Pd(PEPPSI) kompleksiyle ilgili özellikler



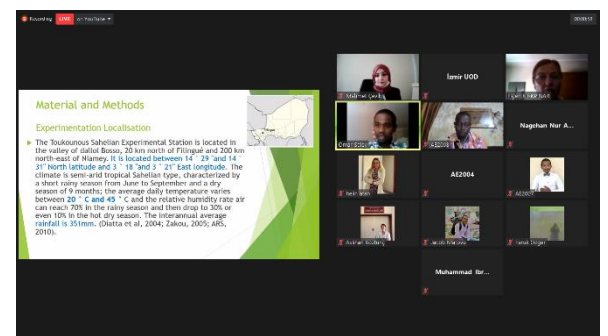
4<sup>th</sup> International Students Science Congress

Keywords: Berezin, Berezin operators, Berezin convergence, Berezin approximation, Berezin convergence

Mathematics Subject Classification: Primary 41A25, Secondary 41A55, 41A58

1 Introduction

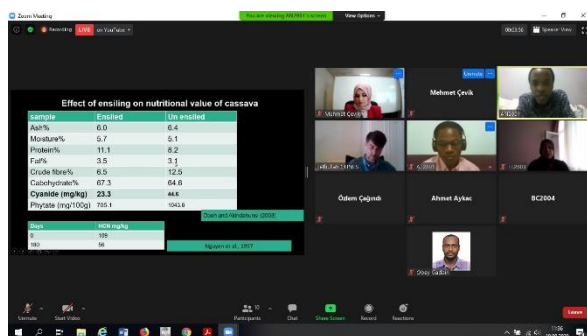
Berezin polynomials are a powerful tool for replacing a lot of arduous calculations carried out for continuous functions with friendly calculations on approximating polynomials. For this reason, many researchers are interested to work on Berezin operators with a type of stability and point approximation, convergence, shape preserving properties and many others. In the recent past, Chen et al. [1] presented a new family of Berezin operators for the continuous function  $f(x)$  on  $[0, 1]$  which includes the shape parameter and called it as...



Material and Methods

Experimentation Localisation

► The Bekoukou Sahelian Experimental Station is located in the valley of dioulou Bassa, 20 km north of Fatick and 200 km north-east of Niakhar. It is located between 14° 23' and 14° 31' North latitude and 5° 18' and 5° 21' East longitude. The climate is semi-arid tropical Sahelian type, characterized by a short rainy season from June to September and a dry season of 9 months; the average daily temperature varies between 20° C and 40° C and the relative humidity rate air can reach 70% in the rainy season and then drop to 30% or even 10% in the hot dry season. The interannual average rainfall is 351mm. (Diatta et al, 2004; Zakou, 2005; ARS, 2010).



Effect of ensiling on nutritional value of cassava

Parameter	Ensilaged	Un ensilaged
Moisture%	6.0	6.4
Moisture%	6.7	6.1
Protein%	11.1	8.2
Fats%	3.5	3.3
Crude fibre%	6.5	12.9
Carbohydrate%	67.3	64.0
Cyanide (ppm/kg)	23.3	NAK
Proximate (mg/100g)	725.1	684.1

Source: [1] Njiru et al., 2017



4<sup>th</sup> International Students Science Congress

ST2002: Unit Root Tests Comparison in the Presence of Structural Breaks

Authors:  
Dilek Altın, Doktor Eğitimci, Dept. of Statistics, Izmir University  
Prof. Dr. Emin Fıratlıoğlu, Doktor Öğretim Üyesi, Dept. of Statistics, Izmir University

16.09.2020

